

collected-reprints-1972-73

WAVE PROPAGATION LABORATORY



NATIONAL OCEANIC AND
ATMOSPHERIC ADMINISTRATION

Environmental
Research Laboratories



U.S. DEPARTMENT OF COMMERCE

Frederick B. Dent, Secretary

NATIONAL OCEANIC AND ATMOSPHERIC ADMINISTRATION

Robert M. White, Administrator

ENVIRONMENTAL RESEARCH LABORATORIES

Wilmot N. Hess, Director


Collected Reprints: 1972 - 73

Wave Propagation Laboratory

BOULDER, COLO.

August 1974

For sale by the Superintendent of Documents, U. S. Government Printing Office, Washington, D. C. 20402



Digitized by the Internet Archive
in 2012 with funding from
LYRASIS Members and Sloan Foundation

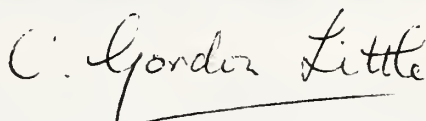
<http://archive.org/details/collectedreprin197273wave>

FOREWORD

The Wave Propagation Laboratory acts as the focal point within NOAA for the development and initial application of new methods for remote sensing of man's geophysical environment. Since its creation in May 1967, the Laboratory has pioneered in the development of new methods for remote measurement of atmospheric parameters. The new techniques have many significant advantages over standard, in situ methods: in particular, automatic 24 hr per day observations can generally be obtained over wide areas. With more frequent and more closely-spaced data, totally new insights on atmospheric structure and processes are becoming possible.

This third volume of Collected Reprints comprises work published from 1 January 1972 through 31 December 1973. The papers included in this volume have been selected to minimize duplication or extraneous material. Only abstracts rather than the full text of WPL NOAA Technical Reports are included. Following the Author Index is a section listing references for further reading as well as the complete table of contents for the volume Remote Sensing of the Troposphere, published in August, 1972.

It is hoped that this and subsequent volumes will provide a summary of the results of this laboratory that will be useful and stimulating to both researchers and interested laymen. The insights already provided by these new techniques of remote sensing clearly demonstrate the potential of this field.



C. Gordon Little, Director
Wave Propagation Laboratory

ORDERING INFORMATION

Wave Propagation Laboratory NOAA Technical Reports and Memoranda Reports are obtainable through the National Technical Information Service, Operations Division, Springfield, Virginia 22151.

Wave Propagation Laboratory Collected Reprints (1970-1971) as well as additional copies of the present volume are obtainable from the N.T.I.S. at the above address.

Copies of Collected Reprints of the Wave Propagation Laboratory, May 1967 through Dec. 1969 are for sale by the Superintendent of Documents, U.S. Government Printing Office, Washington, D.C. 20402, Stock Number 0323-0003, price \$4.50.

Remote Sensing of the Troposphere, V.E. Derr, editor, can also be obtained from the U.S. Government Printing Office, Stock Number 0323-0011, Catalog No. C55.602: T75, price \$9.00. (A microfiche, #Com-72-51061 is available for \$.95)

COVER:

A microwave radiometer (lower right) of the type used to infer the integrated liquid water content of clouds.

CONTENTS

SECTION I

BASIC WAVE PROPAGATION STUDIES

Theoretical and experimental studies of the
propagation of waves through geophysical media

Page

A. Acoustic and Acoustic Gravity Wave Propagation

1. Brown, E. H., and S. F. Clifford, Amplitude Spectra of Acoustic Pulses in the Ocean, *The Journal of Acoustical Society of America* 54, No. 2, 461-464, 1973. 1
2. Brown, E. H., and S. F. Clifford, Spectral Broadening of an Acoustic Pulse Propagating Through Turbulence, *The Journal of the Acoustical Society of America* 54, No. 1, 36-38, 1972. 5
3. Cook, J. C., T. Goforth, and R. K. Cook, Seismic and Underwater Responses to Sonic Boom, *The Journal of the Acoustical Society of America* 51, No. 2 (Part 3, 729-741, 1972. 9
4. Georges, T. M., Acoustic Ray Paths Through a Model Vortex with a Viscous Core, *The Journal of the Acoustical Society of America* 51, No. 1 (Part 2), 1972. 20
5. Georges, T. M., 3D Ray Tracing for Acoustic-Gravity Waves *AGARD Conference Proceedings No. 115*, NATO, Wiesbaden, Germany, April 1972, 2.1-2.8, 1972. 24
6. Georges, T. M., and S. F. Clifford, Acoustic Sounding in a Refracting Atmosphere, *The Journal of Acoustical Society of America* 52, No. 5 (Part 2), 1397-1405, 1972. 32

See also paper 16

B. Wave Propagation at Optical Frequencies

7. Calfee, R. F., and R. L. Schwiesow, Nu-Averaged Infrared Absorption Coefficients of Water Vapor, *NOAA Technical Report ERL 274-WPL 24*, 21 pages, August 1973. (Abstract only). 41

8. Schwiesow, R. L., and N. L. Abshire, Relative Raman Cross Section of O_3 for Four Ar^+ Laser Frequencies, *Journal of Applied Physics* 44, No. 8, 3808-3809, August 1973. 42

See also papers 31, 36, 43, and 44

SECTION II

REMOTE SENSING CONCEPTS

Theoretical and experimental studies of remote sensing concepts.

A. Remote Sensing, Using Acoustic and Acoustic Gravity Waves

9. Beran, D. W., and S. F. Clifford, Acoustic Doppler Measurements of the Total Wind Vector, *AMS Second Symposium on Meteorological Observations and Instrumentation*, San Diego, California, March 27-30, 1972. 44
10. Beran, D. W., W. H. Hooke, and S. F. Clifford, Acoustic Echo-Sounding Techniques and Their Application to Gravity-Wave, Turbulence, and Stability Studies, *Boundary Layer Meteorology* 4, 133-153, 1973. 54
11. Beran, D. W., F. F. Hall, Jr., J. W. Wescott, and W. D. Neff, Application of an Acoustic Sounder to Air Pollution Monitoring, *Proceedings of Symposium in Air Pollution, Turbulence and Diffusion*, December 7-10, 1971, 66-72, March 1972. 75
12. Emmanuel, C. B., and P. A. Mandics, A Feasibility Study for the Remote Measurement of Underwater Currents Using Acoustic Doppler Techniques, *NOAA Technical Report ERL 278-WPL* 25 August 1973. (Abstract only). 82
13. Georges, T. M., Infrasound from Convective Storms: Examining the Evidence, *Reviews of Geophysics and Space Physics* 11, No. 3, 571-594, August 1973. 83
14. Georges, T. M., Infrasound from Severe Storms, *Proceedings of Eighth Conference on Severe Local Storms*, October 15-17, 1973. 107
15. Gossard, E. E., J. H. Richter, and D. Atlas, Reply, *Journal of Geophysical Research* 77, No. 3, 510-522, January 1972. 110

16. Little, C. G., On the Detectability of Fog, Cloud, Rain and Snow by Acoustic Echo-Sounding Methods, *Journal of Atmospheric Sciences* 29, No. 4, 748-755, May 1972. 112

See also papers 1-6

B. Remote Sensing with Radio Waves

17. Barrick, D. E., First-Order Theory and Analysis of MF/HF/VHF Scatter from the sea, *IEEE Transactions on Antennas and Propagation* AP-20, No. 1, 2-10, January 1972. 120
18. Barrick, D. E., The Use of Skywave Radar for Remote Sensing of Sea States, *Marine Technology Society Journal* 7, No. 1, 29-33, January-February 1973. 129
19. Barrick, D. E., and E. R. Westwater, Interpretation and Application of Second-Order HF Sea-Echo Doppler Spectrum, *Proceedings of IEEE, OCEAN '73*, 191-197, September 1973. 134
20. Chadwick, R. B., and G. R. Cooper, Measurement of Distributed Targets with the Random Signal Radar, *IEEE Transactions on Aerospace and Electronic Systems* AES-8, No. 6, 743-750, November 1972. 141
21. Decker, M. T., F. O. Guiraud, and E. R. Westwater, Correction of Electrical Path Length by Passive Microwave Radiometry, *Proceedings of Conference on Propagation of Radio Waves at Frequencies above 10 GHz*, London, April 10-13, 1973. 149
22. Headrick, J. M., D. E. Barrick, and J. B. Snider, Some Features of Sea Echo at HF (U), OHD Technical Review Meeting, *Proceedings of Conference at U.S. Air Force Academy*, Colorado Springs, May 2-3, 1973. 154
23. Miller, L. J., Dual-Doppler Radar Observations of Circulation in Snow Conditions, *15th Radar Meteorology Conference*, October 10-12, 1972, 309-314, 1972. 167
24. Snider, J. B., Ground-Based Sensing of Temperature Profiles from Angular and Multi-Spectral Microwave Emission Measurements, *Journal of Applied Meteorology* 11, No. 6, 958-967, September 1972. 173
25. Snider, J. B., Recent Results in Ground-Based Sensing of Atmospheric Temperature Profiles, *Proceedings of Symposium on Air Pollution, Turbulence and Diffusion*, March 1972. 183

26. Taylor, W. L., An Electromagnetic Technique for Tornado Detection, *Weatherwise* 26, No. 2, 70-71, April 1973. 193
27. Taylor, W. L., Electromagnetic Radiation from Severe Storms in Oklahoma during April 29-30, 1970, *Journal of Geophysical Research* 78, No. 36, 8761-8777, December 1973. 195
28. Taylor, W. L., Evaluation of an Electromagnetic Tornado-Detection Technique, *Eighth Conference on Severe Local Storms*, October 15-17, 1973. 212
29. Westwater, E. R., Ground-Based Determination of Low Altitude Temperature Profiles by Microwaves, *Monthly Weather Review* 100, No. 1, 15-28, January 1972. 216
30. Westwater, E. R., Microwave Emission from Clouds, *NOAA Technical Report ERL 219-WPL 18*, 55 pages, January 1972. (Abstract only.) 230

See also papers 47, 49, 52-53

C. Remote Sensing by Optical Techniques

31. Cohen, A., The Size Spectrum Determination of Spherical Aerosols by Light Scattering. Part I: Method, *Proceedings of Air Pollution, Turbidity and Diffusion Symposium Committee*, 93-99, March 1972. 231
32. Cohen, A., V. E. Derr, G. T. McNice, and R. E. Cupp, Measurement of Mie Scattering Intensities from Monodispersed Spherical Particles as a Function of Wavelength, *Applied Optics* 12, No. 4, 779-782, April 1973. 238
33. Derr, V. E., Research Problems in the Use of Lidar in Anti-Pollution Studies, *Proceedings of Workshops on Research Problems in Air and Water Pollution*, University of Colorado on August 3-15, 1970, 309-321, February 1972. 242
34. Earnshaw, K. B., and E. N. Hernandez, Two-Laser Optical Distance-Measuring Instrument that Corrects for the Atmospheric Index of Refraction, *Applied Optics* 11, No. 4, 749-754, April 1972. 254
35. Hall, F. F., Jr., New Heights for Atmospheric Optics, *Optical Spectra*, Part I, 21-22, January 1972. 260

36. Hernandez, E. N., and E. B. Earnshaw, Field Tests of a Two-Laser (4416 A and 6328 A) Optical Distance-Measuring Instrument Correcting for the Atmospheric Index of Refraction, *Journal of Geophysical Research* 77, No. 35, 6994-6998, December 1972. 262
37. Lawrence, R. S., G. R. Ochs, and S. F. Clifford, Use of Scintillations to Measure Average Wind Across a Light Beam, *Applied Optics* 11, No. 2, 239-243, February 1972. 267
38. McNice, G. T., Raman Spectroscopy with a Tunable Dye Laser and a Narrow-Band Filter, *Applied Optics* 11, No. 3, 699-700, March 1972. 272
39. Ochs, G. R., and R. S. Lawrence, Temperature and C_n^2 Profiles Measured Over Land and Ocean to 3 km Above the Surface, *NOAA Technical Report ERL 251-WPL 22*, 39 pages, October 1972. (Abstract only.) 274
40. Ochs, G. R., and G. F. Miller, The NOAA Optical System for Measuring Average Wind, *NOAA Technical Memorandum ERL WPL-9*, 27 pages, July 1973. (Abstract only.) 275
41. Ochs, G. R., S. F. Clifford, and Ting-i Wang, A Feasibility Study of an Optical Crosswind Monitor, *NOAA Technical Memorandum ERL WPL-10*, 45 pages, September 1973. (Abstract only.) 276
42. Schwiesow, R. L., Optical Measurement of Capillary Wave Structure, *NOAA Technical Report ERL 263-WPL 23*, 26 pages, February 1973. 277
43. Schwiesow, R. L., Raman Scattering from Pollutant Gases and Air-Water Interfaces, *AIAA Journal* 11, No. 1, 87-90, January 1973. 278
44. Strauch, R. G., V. E. Derr, and R. E. Cupp, Atmospheric Water Vapor Measurement by Raman Lidar, *Remote Sensing of Environment* 2, No. 2, 101-108, February 1972. 282
45. Westwater, E. R., and A. Cohen, Application of Backus-Gilbert Inversion Technique to Determination of Aerosol Size Distributions from Optical Scattering Measurements, *Applied Optics* 12, No. 6, 1340-1348, June 1973. 290

D. Combination Methods and Comparisons

46. Bean, B. R., A. S. Frisch, L. G. McAllister, and J. R. Pollard, Planetary Boundary-Layer Turbulence Studies from Acoustic Echo Sounder and In-Situ Measurements, *Boundary Layer Meteorology* 4, 449-474, 1973. 299
47. Chadwick, R. B., and C. G. Little, The Comparison of Sensitivities of Atmospheric Echo-Sounders, *Remote Sensing of Environment* 2, 223-234, 1973. 325
48. Hooke, W. H., J. M. Young, and D. W. Beran, Atmospheric Waves Observed in the Planetary Boundary Layer Using an Acoustic Sounder and a Microbarograph Array, *Boundary Layer Meteorology* 2, 371-380, March 1972. 336
49. Little, C. G., Remote Sensing of the Atmosphere, *Atmospheric Technology-NCAR*, No. 2, 51-56, June 1973. 346
50. Little, C. G., Status of Remote Sensing of the Troposphere, *Bulletin of the American Meteorological Society* 53, No. 10, 936-949, October 1972. 352
51. Ottersten, H., K. R. Hardy, and C. G. Little, Radar and Sodar Probing of Waves and Turbulence in Statically Stable Clear-Air Layers, *Boundary Layer Meteorology* 4, 47-89, April 1973. 366

SECTION III

GEOPHYSICAL STUDIES

Theoretical and experimental studies
of the environment.

52. Gossard, E. E., and J. H. Richter, FM/CW Radar Studies of Production of Turbulent Instability Within Thermally Stable Layers by Internal Waves, *AGARD Conference Proceedings No. 115*, 20.0-20.14, 1972. 409
53. Gossard E. E., J. H. Richter, and D. R. Jensen, Effect of Wind Shear on Atmospheric Wave Instabilities Revealed by FM/CW Radar Observations, *Boundary Layer Meteorology*, 4, 113-131, 1973. 423
54. Hooke, W. H., F. F. Hall, Jr., and E. E. Gossard, Observed Generation of an Atmospheric Gravity Wave by Shear Instability in the Mean Flow of the Planetary Boundary Layer, *Boundary Layer Meteorology* 5, 29-41, 1973. 442

55. Mandics, P. A., Generation and Dissipation of Microwave Refractive-Index Fluctuations in the Boundary Layer, *Boundary Layer Meteorology* 4, 311-322, 1973. 455

SECTION IV

DEVELOPMENT OF INSTRUMENTS AND TECHNIQUES

Acoustic, radio, and optical instrumentation for the study of wave propagation in geophysical media.

56. Barrick, D. E., Demonstration of Distortion in Envelope Detection of SSB Signals, *IEEE Transactions on Education E-16*, No. 1, 53-54, February 1973. 467
57. Barrick, D. E., FM/CW Radar Signals and Digital Processing, *NOAA Technical Report ERL 283-WPL 26*, 22 pages, July 1973. (Abstract only.) 469
58. Bedard, A. J., Jr., The Design of a Temperature-Independent DC Flow Resistor, *Fluidics Quarterly* 5, No. 2, 31-50, April 1973. 470
59. Hernandez, E. N., Analysis of Four Optical Distance Measuring Instrument Configurations Using Electrooptical polarization Modulators, *Applied Optics* 11, No. 3, 609-612, March 1972. 490
60. Klemperer, W. K., Non-Redundant Phased-Array Radar, *Proceedings IEE Conference Publication No. 105*, RADAR, Present and Future, London, October 23-25, pp 74-80, 1973. 494
61. Ochs, G. R., and G. F. Miller, Pattern Velocity Computers: Two Types Developed for Wind Velocity Measurement by Optical Means, *The Review of Scientific Instruments* 43, No. 6, 879-882, June 1972. 501
62. Schwiesow, R. L., Analytical Representation for Standards of Spectral Irradiance over the 300-1200 nm Range, *Applied Optics* 12, No. 5, 929-930, May 1973. 505
63. Schwiesow, R. L., Departures from the Electrostatic Crystal-Field Model for Gd^{3+} in Six Hexagonal Crystals, *Journal of Optical Society of America* 62, No. 5, 649-653, May 1972. 507
- Author Index 513
- References for Further Reading 521

Reprinted with permission from the Journal of Acoustical Society of America Vol. 54, No. 2, 461-464, 1973.

Amplitude spectra of acoustic pulses in the ocean

Edmund H. Brown and Steven F. Clifford

NOAA/ERL, Boulder, Colorado 80302

(Received 23 March 1972; revised 6 December 1972)

An acoustic pulse propagating in the ocean encounters weak thermal patches that scatter energy. If these patches are moving with a mean current perpendicular to the direction of propagation, a temporal fluctuation in the pulse-averaged amplitude occurs. This study calculates the temporal frequency spectrum of the pulse-to-pulse amplitude fluctuations and finds the result in terms of a frequency convolution of Tatarski's CW spectrum found for the electromagnetic case, and the spectral distribution of the initial pulse. The result easily generalizes to amplitude, phase, and phase-difference spectra, for plane, spherical, and beam-wave pulses.

Subject Classification: 13.2; 11.2, 11.7.

INTRODUCTION

Knowledge of the effects of forward scatter by random refractive index fields on the transmission of an acoustic pulse has important applications both to underwater detection and communication and to basic research on the dynamic structure of the oceans. Motion of a random field due either to mean ocean currents or to actual motions of source or target produces spectral broadening and Doppler shifting of the initial pulse spectrum. This paper uses the general solution found by Brown¹ and several reasonable approximations to determine the shape of the temporal forward-scatter spectrum of the amplitude fluctuations in an underwater acoustic pulse propagating through turbulence carried by a mean transverse current. Earlier, Tatarski,² using Taylor's hypothesis and the two-dimensional spatial spectrum of the amplitude fluctuations, obtained a similar spectrum for CW electromagnetic propagation through atmospheric turbulence transported by a transverse mean wind. The analysis of Clifford and Brown³ provided the equivalent spatial spectra for line-of-sight CW acoustic propagation and showed the equivalence of the acoustic and electromagnetic problems. The present result assumes an especially simple and elegant form when expressed as a convolution with respect to frequency of Tatarski's CW result and the pulse spectral shape of the initial (unscattered) power. This form illustrates and supports the conjecture of Su and Plonus⁴ that the statistical properties of the wave field averaged over the pulse length are a linear transformation of the statistical properties of a CW wave field.

I. BACKGROUND

Whitmarsh, Skudrzyk, and Urlick⁵ simultaneously measured the random temperature fluctuations in the ocean (finding them representable by a Kolmogorov structure function) and the fluctuations of a forward-scattered underwater sound pulse. A somewhat crude

scattering theory gave reasonable agreement between experiment and theory with the assumption that the refractive index field depended on temperature fluctuations alone and, tacitly, that the speed of sound was a linear function of temperature. Shvachko^{6,7} reported on similar studies which measured fluctuations in the index of refraction directly with an acoustic refractometer and compared the scattering data by means of the more sophisticated diffraction theory developed by Tatarski² for the atmosphere.

Recently, Kaufman⁸ suggested that the fluctuations in sea temperature usually remain small enough for a linear relation between speed of sound and temperature (with the temperature fluctuation coefficient $\alpha c_0/T_0$, where α becomes equal to $\frac{1}{2}$ for the atmosphere) to give a good approximation to the scattering. This permits many results in the literature, such as the spatial amplitude and phase spectra of Clifford and Brown³ or the temporal power spectrum of Brown and Clifford,⁹ to apply also to the ocean by replacing the temperature-structure constant C_T by $2\alpha C_T$. In addition, Kaufman's analysis of previous data confirms that temperature fluctuations, rather than velocity fluctuations, provide the principal random scattering mechanism of sound in the ocean. Similarly, the theoretical analysis in Chap. 12 of Ref. 2 for CW propagation applies to the ocean on substituting the temperature spectrum $4\alpha^2\Phi_T$ for the refractive index spectrum Φ_n .

II. ANALYSIS

For a transverse mean current, the forward-scatter wave found by Brown¹ reduces to

$$P'(L, k, x_a) = \int_{(i)} d\phi(\kappa_i) \exp(i\kappa_a x_a) k_1 D_0(\Delta k_1 L) \times \exp(i\kappa_3 L) \frac{\exp(ik_1 L) - \exp[-i(\kappa_3 - q)L]}{k_1 + \kappa_3 - q}. \quad (1)$$

Here, P' is the scattered acoustic pressure; L is the path length; $k = \omega/c_0$, with ω the angular frequency and c_0 the equilibrium sound velocity; $d\phi(\kappa_i)$ is the Fourier-Stieltjes measure of the refractivity field over the wave-number space κ_i ($i=1, 2, 3$; $\alpha=1, 2$); x_α are the coordinates in the plane perpendicular to the direction of propagation and z is the coordinate along the path; $k_1 = k - \kappa_\alpha m_\alpha$, where $m_\alpha = v_\alpha/c_0$, the ratio of the velocity components of the mean transverse current to the sound velocity; and $\Delta k_1 = k_1 - k_0$, with k_0 the carrier frequency. The function D_0 is the spectrum of the initial pulse shape, l is the half half-length of the pulse, and q is defined by $q^2 = k_1^2 - k_0^2$, where $k_0^2 = \kappa_\alpha \kappa_\alpha$.

Since the desired final form will relate the amplitude spectrum of the pulse to the CW result of Tatarski,² changing the representation of the fluctuations from three-dimensional measure $d\phi$ to Tatarski's two-dimensional measure $d\nu$ simplifies the analysis. The measure $d\nu$ is related to $d\phi$ by

$$d\nu(\kappa_\alpha, z) = - \int_{(3)} d\phi(\kappa_i) \exp(ik_3 z), \quad (2)$$

where $\kappa_\alpha = \kappa_1, \kappa_2$. Under the κ_3 integration in Eq. 1, the Fourier transformation Eq. 2 inverts as if $d\nu$ and $d\phi$ were functions,

$$\int_{(3)} d\phi(\kappa_i) F(\kappa_3) = - \int_{(3)} \frac{1}{2\pi} dz \exp(-ik_3 z) \times d\kappa_3 d\nu(\kappa_\alpha, z) F(\kappa_3). \quad (3)$$

The combination of restricting $d\nu(\kappa_\alpha, z)$ to zero for negative z , assuming the pressure fluctuations are the limit for zero damping (thus, that the k_3 -integration is equivalent to a contour integration), and using Eq. 3, transform Eq. 1 to the form

$$P'(L, k, x_\alpha) = -i \int_{(a)} \int_0^L dz d\nu(\kappa_\alpha, z) \times \exp[i\kappa_\alpha x_\alpha + iqL + i(k_1 - q)z] k_1 D_0(\Delta k_1 l). \quad (4)$$

Some of the approximations used to obtain the normalized amplitude spectrum of CW waves in k -space breakdown when applied to pulses. This awkward snag in the analysis occurs when there are frequencies for which the initial pulse spectrum vanishes but the scattered wave spectrum is not zero. First defining the amplitude in terms of the time t , or rather the equivalent distance $\eta = c_0 t$, avoids this difficulty. After the transformation $\eta \rightarrow \eta + L$ (for a system where the time origin is at the center of the received initial pulse) the initial wave becomes

$$p_0(L, \eta) = d_0(\eta) \exp(-ik_0 \eta), \quad (5)$$

where d_0 is the inverse Fourier transform

$$d_0 = \mathcal{F}^{-1} D_0 = \int dk \exp(-ik\eta) D_0(kl)$$

of the initial spectrum. Here d_0 is a unit pulse of characteristic length $2l$, where the area under the pulse is $2l$ and the peak is 1. Then, the total pressure at the receiver, letting the x_α in $P'(L, k) = P'(L, k, x_\alpha)$ be understood, is

$$p(L, \eta) = d_0(\eta) \exp(-ik_0 \eta) + \int dk \exp[-ik(\eta + L)] P'(L, k). \quad (6)$$

Defining $p(\eta) = a(\eta) \exp i\psi(\eta)$, with the real functions $a(\eta) = d_0(\eta) + a_1(\eta)$ and $\psi(\eta) = -k_0 \eta + \psi_1(\eta)$, the amplitude is given by

$$a^2(\eta) = \left\{ d_0(\eta) + \operatorname{Re} \exp(ik_0 \eta) \times \int dk \exp[-ik(\eta + L)] P'(L, k) \right\}^2 + \left\{ \operatorname{Im} \exp(ik_0 \eta) \int dk \exp[-ik(\eta + L)] P'(L, k) \right\}^2. \quad (7)$$

Retaining only first-order terms in the scattered field P' in the interval $-l < \eta < l$ (and neglecting the tail for $\eta > l$ added by off-axis contributions traveling a greater distance), the total amplitude becomes

$$a(\eta) \approx 1 + \operatorname{Re} \int dk \exp(-i\Delta k \eta) [\exp(-ikL) P'(L, k)], \quad (8)$$

or, with the abbreviation $\bar{P}(L, k) = \exp(-ikL) P'(L, k)$, and $\Delta k = k - k_0$, the scattered pulse amplitude is

$$a_1(\eta) = \operatorname{Re} \int dk \exp(i\Delta k \eta) \bar{P}(L, k). \quad (9)$$

Now, transformation back to k -space gives

$$A_1(k) = \mathcal{F} a_1(\eta) = \frac{1}{2\pi} \int d\eta \exp(ik\eta) \times \operatorname{Re} \int dk' \exp[-i(k' - k_0)\eta] \bar{P}(L, k'), \quad (10)$$

or,

$$A_1(k) = \frac{1}{2} \bar{P}(L, k + k_0) + \frac{1}{2} \bar{P}^*(L, -k + k_0). \quad (11)$$

From Eq. 4 and the definitions of \bar{P} ,

$$\bar{P}(L, k) = -i \int_{(a)} \int_0^L dz d\nu(\kappa_a, z) \exp[i\kappa_a(x_a - m_a L)] \\ \times k_1 D_0(\Delta k_1 l) \exp[-i(k_1 - q)(L - z)]. \quad (12)$$

Substituting Eq. 12 in Eq. 11 and using the property that the refractivity is real, or $d\nu^*(-\kappa_a, z) = d\nu(\kappa_a, z)$, leads to the following expression for the amplitude

$$A_1(k) = \frac{1}{2i} \int_{(a)} \int_0^L dz d\nu(\kappa_a, z) \\ \times \exp[i\kappa_a(x_a - m_a L) - ik_1(L - z)] D_0(k_1 l) \\ \times \{ (k_1 + k_0) \exp[-i(k_0 - q^+)(L - z)] \\ + (k_1 - k_0) \exp[i(k_0 - q^-)(L - z)] \}, \quad (13)$$

where $q^\pm = [(k_1 \pm k_0)^2 - \kappa^2]^{1/2}$. Since D_0 is negligibly small for $k_1 l$ outside the range $(-\pi, \pi)$, the condition $k_0 l \gg 1$ (equivalent to many waves in each pulse) implies that only values of the coefficients for which $k_1/k_0 \ll 1$ contribute to the amplitude or, $k_1 \pm k_0 \approx \pm k_0$. A similar approximation in the phase requires the conditions $L_0 \leq 2l$ and $\lambda \leq L_0$, where L_0 is the outer scale of turbulence. The analysis of Tatarski² relies on the condition $\lambda \ll l_0$, with l_0 the inner scale of turbulence, to obtain the equivalent of the expansions of the square roots q^\pm . Clifford and Brown,³ however, have shown that these expansions still give good results when $\lambda \leq L_0$. With the above approximations, and with the transformation $z \rightarrow L - z$, Eq. 13 now becomes

$$A_1(k) = -k_0 \int_{(a)} \int_0^L dz d\nu(\kappa_a, L - z) \\ \times \exp[i\kappa_a(x_a - m_a L)] D_0(k_1 l) \sin \frac{\kappa^2 z}{2k_0}. \quad (14)$$

If the covariance of $a_1(\eta)$ is averaged over the pulse length $2l$, (see Brown and Clifford⁹ for a more extensive discussion of averaging procedures for a sequence of pulses) and the averaging integration expressed as a Fourier transform (which introduces a factor 2π), the spectrum $W(k)$ of the amplitude covariance becomes

$$W(k) = (\pi/l) \langle A_1(k) A_1^*(k) \rangle, \quad (15)$$

where $\langle \rangle$ indicate ensemble averaging over a series of pulses. Substituting Eq. 14 in Eq. 15 and using the relation

$$\langle d\nu(\kappa_a, z) d\nu^*(\kappa_a', z') \rangle$$

$= F_n(\kappa_a, z - z') \delta(\kappa_a - \kappa_a') d^2\kappa_a d^2\kappa_a'$, where F_n is the two-dimensional spectrum of the refractivity defined by

Tatarski,² gives

$$W(k) = (\pi/2l) k_0^2 \\ \times \int d^2\kappa_a \int_0^L dz \int_0^L dz' F_n(\kappa_a, z - z') D_0^2(k_1 l) \\ \times \left[\cos \frac{\kappa^2}{2k_0} (z - z') - \cos \frac{\kappa^2}{2k_0} (z + z') \right]. \quad (16)$$

Making the familiar transformation $\xi = z - z'$, $\zeta = z'$, integrating, and using the relation obtained from Eq. 1.53 of Tatarski² and the fact that F_n is even in ξ ,

$$\Phi_n[(\kappa^2 + \alpha^2)^{1/2}] = \frac{1}{\pi} \int_0^\infty d\xi \cos \alpha \xi F_n(\kappa, \xi), \quad (17)$$

reduces $W(k)$ to

$$W(k) = (\pi/2l) \int d^2\kappa_a D_0^2(k_1 l) \pi k_0^2 L \Phi_n \left(\left[\kappa^2 + \left(\frac{\kappa^2}{2k_0} \right)^2 \right]^{1/2} \right) \\ \times \left[1 - \frac{k_0}{\kappa^2 L} \sin \frac{\kappa^2 L}{k_0} \right], \quad (18)$$

or, in terms of the two-dimensional amplitude spectrum F_A found in Eq. 7.48 by Tatarski,² and using the facts that $\Phi_n(\kappa)$ is slowly varying and, from Clifford and Brown,³ that the approximations remain valid for $\kappa/k_0 \leq 1$,

$$W(k) = (\pi/2l) \int d^2\kappa_a D_0^2(k_1 l) F_A(\kappa, 0). \quad (19)$$

Express $D_0^2(k_1 l)$ as a transform

$$D_0^2(k_1 l) = \frac{1}{2\pi} \int d\eta \exp(ik_1 \eta) f_\Delta(\eta/2l), \quad (20)$$

and write $d^2\kappa_a = \kappa d\kappa d\theta$ and $m_a \kappa_a = m\kappa \cos\theta$. Then, the θ -integration gives

$$\int_0^{2\pi} d\theta \exp(ik_1 \eta) = 2\pi \exp(ik\eta) J_0(m\kappa\eta). \quad (21)$$

Substituting Eq. 21 in Eq. 20 yields

$$\int d\theta D_0^2(k_1 l) = 2D_0^2(k l) \frac{Y(m\kappa - k)}{(m^2\kappa^2 - k^2)^{1/2}}, \quad (22)$$

where $Y(k)$ is the Heaviside step-function, equal to one for positive k , and zero for negative k , and the convolution $\frac{*}{k}$ is defined by

$$f(k) \frac{*}{k} g(k) = \int dk' f(k - k') g(k').$$

Finally, introducing Eq. 22 in the result Eq. 19 gives

$$W'(k) = (\pi/l) D_0^2(kl) \star \int_{k/m}^{\infty} d\kappa \frac{\kappa F_A(\kappa, 0)}{(m^2 \kappa^2 - k^2)^{1/2}} \quad (23)$$

The right-hand side of the convolution in Eq. 23 is exactly the CW spectrum of Tatarski.² In the CW case, $\pi/l D_0^2(kl) \rightarrow \delta(k)$ and, thus, Eq. 23 transforms to Tatarski's result. Note that, for convenience, we have used the spectrum as a function of temporal wave number $k = \omega/c_0$ rather than angular frequency ω , and that $W'(k) = c_0 W'(\omega)$.

III. CONCLUSIONS

The temporal frequency spectrum of the amplitude fluctuations of a plane-wave acoustic pulse propagating over a path-length L through the ocean, modeled as a random isotropic refractive index field moving with a constant mean transverse current, has been found. The result is expressed in the form of a convolution with frequency of the spectral shape of the initial power per unit pulse length with the spectrum found by Tatarski

for the propagation of CW waves. With increasing pulse length the result approaches that of Tatarski. The result Eq. 23 quickly generalizes to phase and phase difference temporal frequency with the insertion of the appropriate spatial spectra $F_S(\kappa, 0)$ and $F_{\Delta S}(\kappa, 0)$ from Tatarski.¹⁰ It also gives the results for amplitude, phase and phase difference for spherical pulses using the spectra found by Clifford¹¹ and ultimately to any physical pulse using the recent results of Ishimaru.¹²

¹E. H. Brown, J. Acoust. Soc. Amer. (to be published).

²V. I. Tatarski, *Wave Propagation in a Turbulent Medium* (McGraw-Hill, New York, 1961).

³S. F. Clifford and E. H. Brown, J. Acoust. Soc. Am. **48**, 1123 (1970).

⁴H. H. Su and M. A. Plonus, J. Opt. Soc. Am. **60**, 256 (1971).

⁵D. C. Whitmarsh, E. Skudrzyk, and R. J. Urlick, J. Acoust. Soc. Am. **29**, 1124 (1957).

⁶R. F. Shvachko, Sov. Phys.-Acoust. **9**, 280 (1964).

⁷R. F. Shvachko, Sov. Phys.-Acoust. **13**, 93 (1967).

⁸C. Kaufman, J. Acoust. Soc. Am. **49**, 930 (1971).

⁹E. H. Brown and S. F. Clifford, J. Acoust. Soc. Am. **54**, 36 (1973).

¹⁰V. I. Tatarski, *Propagation of Waves in a Turbulent Atmosphere* (Nauka, Moscow, 1967) (in Russian).

¹¹S. F. Clifford, J. Opt. Soc. Am. **61**, 1285 (1971).

¹²A. Ishimaru, IEEE Trans. Antennas Propag. **20**, 10 (1972).

Spectral broadening of an acoustic pulse propagating through turbulence

E. H. Brown and S. F. Clifford

National Oceanic and Atmospheric Administration, Environmental Research Laboratories, Boulder, Colorado 80302

(Received 14 December 1971; revised 27 April 1972)

The following analysis develops the equation for the scattered acoustic power and spectral broadening of a plane acoustic pulse propagating through atmospheric turbulence that is moving with a uniform wind transverse to the beam. Assuming weak single scattering, the resulting propagation broadening is proportional to the wind velocity divided by the outer scale of turbulence and is independent of the strength of turbulence and total propagation range. Further, the broadening for a medium with variable outer scale and wind shear (e.g., a vertical propagation path) is determined primarily by the highest ratio of transverse wind to outer scale encountered by the pulse.

Subject Classification: 11.3, 11.7, 11.9.

INTRODUCTION

The application of acoustic Doppler radar techniques^{1,2} to atmospheric sounding requires that the signal spectra returned from the scattering volume are not too severely distorted by propagation through intervening turbulent layers for useful analysis. That is, spectral broadening due to the presence of wind-driven turbulence along the path from source to scatterer and back must not mask the Doppler shift and spread due to motions within the scattering volume. We consider here propagation broadening due to the mean cross-wind advecting turbulent refractivity fluctuations, a function of both the wind and temperature variations, through the propagating wave.

I. ANALYSIS

Consistent with the above assumptions, the following analysis assumes a zero component of the mean wind parallel to the propagation direction. Brown³ has generalized the equation for the scattered acoustic field $P'(k)$, found by Tatarski,⁴ to the case of turbulence moving with a mean wind with the vector components \bar{w}_i , $i=1, 2, 3$; here P' is the Fourier time transform of the acoustic pressure in the scattered wave and k is the ratio $k=\omega/c_0$, of angular frequency ω to the mean sound speed c_0 . Using the symbol $m_i=\bar{w}_i/c_0$, the generalized equation is

$$\nabla^2 P' + (k + im_i \partial_i)^2 P' = 2\partial_i (N'^* \partial_i \bar{P}), \quad (1)$$

where $\partial_i = \partial/\partial x_i$, N' is the Fourier time transform of the refractivity fluctuation field n' , \bar{P} is the initial, unscattered field, and the convolution operator \star_k is defined by

$$f(x) \star_k g(x) = \int_{-\infty}^{\infty} dx' f(x-x') g(x'). \quad (2)$$

Equation 1 is solved by Brown by obtaining a Green's function and substituting the three-dimensional Fourier-Stieltjes transform⁴ of the refractive index field

n' determined from assuming Taylor's hypothesis

$$n'(x_i, t) = \int d\phi(\kappa_i) \exp[i\kappa_j(x_j - \bar{w}_j t)]; \quad (3)$$

the symbol $d\phi(\kappa_i)$ represents the Fourier-Stieltjes measure of the refractive index field over the three-dimensional wavenumber space κ_i . The initial field \bar{P} is assumed a plane wave pulse in the z direction. Let $k_0 = \omega_0/c_0$, where ω_0 is the carrier frequency, $\Delta k = k - k_0$ and $\hat{k} = k(1 - m)$, where m is the component of $m_i = \bar{w}_i/c_0$ in the direction of the initial wave; thus, \hat{k} is the wavenumber corrected for the refractive effects of the mean wind. Then the initial wave is

$$\bar{P}(z, k) = D_0(\Delta k l) e^{ikz}, \quad (4)$$

where $D_0(\Delta k l)$ is the frequency spectrum of the initial pulse shape with a pulse characteristic length $2l$. As a particular example the rectangular unit pulse $d_0(z - c_0 t)$ produced by turning the transmitter on and off for the time interval $2l/c_0$ has the frequency spectrum $D_0(\Delta k l) = l \sin \Delta k l / \pi \Delta k l$.

The resulting solution for P' (see Brown³ for details) in the forward hemisphere at a distance L from the source is

$$P'(k) = \int d\phi(\kappa_i) \exp(i\kappa_a x_a) k D_0(\Delta k l) \times \frac{\exp[i(k_1 + \kappa_3)L] - \exp(iqL)}{k_1 + \kappa_3 - q}, \quad (5)$$

where x_a are the coordinates in the plane perpendicular to the direction of propagation, $k_1 = k - m_a \kappa_a$, with $m_a = \bar{w}_a/c_0$ the components of the ratio of the mean cross-wind to the sound velocity, and q is defined by $q^2 = k_1^2 - \kappa^2$ with $\kappa^2 = \kappa_a \kappa_a$. Equation 5 is the first-order scattered field found in the single scattering approximation. The scattering is weak in the sense that the refractivity fluctuation n' that scatters the incident wave satisfies the condition $n' \ll \langle n \rangle$, where $\langle n \rangle$ is the mean refractive

index. Both phase and amplitude scintillations occur with a total phase deviation of many radians.

True measurements of acoustic intensity (energy flux) are rare since they require simultaneous use of pressure and velocity microphones (see, e.g., p. 265 of Beranek⁵). Ordinarily, observations are made of the pressure and, thus, the relevant quantity required of the theory for application to Doppler spectrum measurements is the spectral density of the scattered pressure field. This can easily be seen in the design of Doppler experiments.⁶ An echo sounder emits a series of pressure-wave pulses, each scattered pulse is Fourier transformed individually, and the resulting spectrum is averaged over successive pulses. Mathematically, we can follow the same procedure by constructing the time autocorrelation function for each pulse:

$$B_p(\tau, \Omega) = \lim_{T \rightarrow \infty} \frac{1}{2T} \int_{-T}^T dt p'(t, \Omega) p'(t + \tau, \Omega), \quad (6)$$

where p' is the pressure and Ω labels each pulse. Then, averaging $B_p(\tau, \Omega)$, which is still a random variable, over the ensemble of many successive pulses gives

$$B_p(\tau) = \langle B_p(\tau, \Omega) \rangle_{\Omega}. \quad (7)$$

The Doppler spectrum observed by the experimentalist now becomes

$$I(k) = c_0 I(\omega) = c_0 \int_{-\infty}^{\infty} d\tau e^{-i\omega\tau} B_p(\tau). \quad (8)$$

On following the above steps and introducing

$$p'(t) = \int_{-\infty}^{\infty} dk e^{ik\omega t} p'(k) \quad (9)$$

we finally obtain

$$I(k) = (\pi/l) \langle P'(k) P'^*(k) \rangle_{\Omega}. \quad (10)$$

Inserting $P'(k)$ from Eq. 5 into 10 and using the relation from Tatarski⁴

$$\langle d\phi(\kappa_i) d\phi^*(\kappa_i') \rangle = \Phi_n(\kappa) \delta(\kappa_i - \kappa_i') d^3\kappa_i d^3\kappa_i', \quad (11)$$

valid for a statistically homogeneous and isotropic random field n' having the three-dimensional wave-number spectrum $\Phi_n(\kappa)$, the pressure spectrum 10 becomes

$$I(k) = (\pi/l) \langle P P^* \rangle = (\pi/l) \int d^3\kappa_1 \Phi_n(\kappa) k_1^2 D_0^2(\Delta k_1 l) \times \left[2 \frac{\sin(k_1 + \kappa_3 - q)(\frac{1}{2}L)}{k_1 + \kappa_3 - q} \right]^2. \quad (12)$$

Since $k_1 = k - m\alpha\kappa_\alpha$ does not involve κ_3 , it is useful to consider the κ_3 -integration first. Note that $\Phi_n(\kappa) = \Phi_n[(\kappa^2 + \kappa_3^2)^{1/2}]$, assumed a monotonic decreasing function, varies slowly as a function of κ_3 when $\kappa_3 \leq \kappa$. The expression in brackets in Eq. 12 is sharply peaked at $\kappa_3 = k_1 - q$. From the definition $q = (k_1^2 - \kappa^2)^{1/2}$, we must

have $k_1 - q \leq \kappa$. Therefore, in the important region of integration, we have $\kappa_3 \leq \kappa$ and, thus $\Phi_n[(\kappa^2 + \kappa_3^2)^{1/2}] \approx \Phi_n(\kappa)$. This result depends on the "sharpness" of the peak in the term in brackets in Eq. 12. Since this term has a width $\Delta\kappa_3 \approx 1/L$, if $\kappa L \gg 1$, the sharpness will be sufficient to permit factoring Φ_n out of the κ_3 -integration. The worst case for which the condition $\kappa L \gg 1$ must remain valid is when $\kappa = 1/L_0$ where L_0 is the outer scale of turbulence. For this case the condition becomes $L \gg L_0$, that is, the requirement that there be a statistically significant number of largest eddies in the total propagation path. After making this approximation and performing the κ_3 -integration, Eq. 12 becomes.

$$I(k) = (2\pi^2 L/l) \int d^2\kappa_\alpha k_1^2 D_0^2(\Delta k_1 l) \Phi_n(\kappa). \quad (13)$$

Represent $D_0^2(\Delta k_1 l)$ by a Fourier transform,

$$D_0^2(\Delta k_1 l) = \frac{1}{2\pi} \int_{-\infty}^{\infty} dz e^{-i\Delta k_1 z} f_\Delta(z, l), \quad (14)$$

where the notation reflects the fact that, if $d_0(z/l) = F^{-1} D_0(\Delta k_1 l)$ is a rectangular unit pulse of length $2l$, then $f_\Delta(z/l)$ is a triangular pulse of length $4l$ given by $f_\Delta(z/l) = (l/\pi)(1 - |z/2l|)d_0(z/2l)$. Then, in polar coordinates, $d^2\kappa_\alpha = \kappa d\kappa d\theta$ and $k_1 = k - m\alpha \cos\theta$, where $m^2 = m_\alpha m_\alpha$, Eq. 13 becomes

$$I(k) = (2\pi^2 L/l) \int_0^\infty d\kappa \cdot \kappa \Phi_n(\kappa) \int_{-\infty}^\infty dz \times \exp(ik_0 z) f_\Delta(z/l) (-1) \partial_z^2 \times \left[\exp(-ikz) \frac{1}{2\pi} \int_0^{2\pi} d\theta \exp(im\alpha z \cos\theta) \right] \quad (15)$$

$$= (2\pi^2 L/l) \int_0^\infty d\kappa \cdot \kappa \Phi_n(\kappa) \int_{-\infty}^\infty dz \times \exp(ik_0 z) f_\Delta(z/l) (-1) \partial_z^2 [\exp(-ikz) J_0(m\alpha z)], \quad (16)$$

where $\partial_z = \partial/\partial z$.

On interchanging the order of integrations and performing the κ -integrations first, Eq. 16 reduces to

$$I(k) = (\pi k^2 L/l) \int_{-\infty}^\infty dz \exp(-i\Delta\kappa z) f_\Delta(z/l) B_n(mz), \quad (17)$$

where $B_n(mz)$ is the two-dimensional covariance of the refractive-index fluctuations⁴ defined by

$$B_n(mz) = 2\pi \int_0^\infty d\kappa \cdot \kappa J_0(mz\kappa) \Phi_n(\kappa). \quad (18)$$

The second partial ∂_z^2 in Eq. 16 has been replaced by $-k^2$ since $m \ll 1$, and therefore $k \gg m l_0^{-1}$, where l_0 is the turbulence "inner scale." This inequality implies that the carrier frequency is large compared to the maximum rate of modulation $m c_0/l_0$ imposed by the turbulence.

The κ -integration in Eq. 17 is possible in the case of a von Kármán spectrum (see Strohbehn⁷):

$$\Phi_n(\kappa) = \frac{\Gamma(11/6)}{1.9\pi^{1/2}\Gamma(3/2)} C_n^2 L_0^{11/3} (1 + L_0^2 \kappa^2)^{-11/6}, \quad (19)$$

where C_n is the "structure constant" of the turbulent refractive index fluctuations and L_0 is the "outer scale." For a line-of-sight path C_n depends on both the temperature-structure constant C_T and the wind-structure constant, C_v . For a folded radar path of length $L = 2R$, where R is the radar range, use $C_n = C_T$, since, to first order, the refractive effects of wind eddies cancel in a round trip through the same volume. That is, if the pulse transit time, $2R/c_0$, is much smaller than time associated with eddy motions, the wave will interact with the same wind eddies twice on a round trip and any phase advance on outward passage will be cancelled by an equal phase retardation on return. This anisotropic refractivity contribution is of course true only for wind eddies; temperature eddies cause cumulative effects. Using formula 11.4.44 of the NBS Handbook⁸ gives

$$I(k) = \frac{\sqrt{\pi}}{2^{6/6}\Gamma(3/2)} C_n^2 L_0^{5/2} (L/l) k^2 \int dz \exp(-i\Delta k z) f_\Delta(z/l) \times \left| \frac{mz}{L_0} \right|^{6/6} K_{5/6} \left(\left| \frac{mz}{L_0} \right| \right), \quad (20)$$

where $K_\nu(x)$ is the modified Bessel function of the second kind. For $k_0 l \gg 1$, the factor k^2 in front of the integral can be replaced by k_0^2 .

Using the Fourier transform from Vol. 2 of Erdelyi *et al.*⁹

$$F[\mu \zeta^{5/6} K_{5/6}(|\mu \zeta|)] = \frac{\Gamma(3/2)}{3 \cdot 2^{1/6} \sqrt{\pi} \mu} \left[1 + \left(\frac{\Delta k l}{\mu} \right)^2 \right]^{-1}, \quad (21)$$

where $\mu = ml/L_0$, allows Eq. 20 to be rewritten in the final form

$$I(k) = \frac{\pi}{3} C_n^2 L_0^{5/2} (L/l) k_0^2 D_0^2(\Delta k l) \times_{\Delta k l}^* \left\{ \frac{1}{\mu} \left[1 + \left(\frac{\Delta k l}{\mu} \right)^2 \right]^{-1} \right\}, \quad (22)$$

or, writing out the convolution as an integral over k'

$$I(k) = \frac{\pi}{3} C_n^2 L_0^{5/2} (L/ml) k_0^2 \int_{-\infty}^{\infty} dk' \times D_0^2[(\Delta k - k')l] \left[1 + \left(\frac{k' L_0}{m} \right)^2 \right]^{-1}. \quad (23)$$

Since $D_0^2(\Delta k l)$ is the "power spectrum" of the initial pulse, and since the convolution of two functions

always has a width greater than either of them, Eq. 22 represents a spectrum whose peak is decreased by the factor $\frac{1}{3} C_n^2 L_0^{5/2} (L/l) k_0^2$ and by the convolution process (for $\mu > 0$), and whose width is increased for any $\mu > 0$.

For $\mu = 0$, Eq. 21 reduces to

$$\lim_{\mu \rightarrow 0} F[\mu \zeta^{5/6} K_{5/6}(|\mu \zeta|)] = \frac{\Gamma(3/2)}{2^{1/6}} \delta(\Delta k l), \quad (24)$$

and Eq. 22 becomes

$$\lim_{\mu \rightarrow 0} I(k) = \frac{\pi \sqrt{\pi} \Gamma(3/2)}{\Gamma(3/2)} C_n^2 L_0^{5/2} (L/l) k_0^2 D_0^2(\Delta k l), \quad (25)$$

that is, a spectrum with the same shape as the initial pulse. A second limiting form occurs when the pulse halflength l becomes arbitrarily large, for then, since $\lim_{l \rightarrow \infty} (\pi/l) D_0^2(kl) = \delta(k)$, Eq. 23 reduces to the CW broadened spectrum

$$\lim_{l \rightarrow \infty} I(k) = \frac{1}{3} C_n^2 L_0^{5/2} L k_0^2 \frac{L_0 m}{[1 + (\Delta k L_0/m)^2]^3}. \quad (26)$$

As $m \rightarrow 0$, this last expression, Eq. 26, approaches zero; that is, there is no broadening of a CW wave in the absence of wind.

II. DISCUSSION

The solution for the forwardscatter spectrum Eq. 22 has a number of interesting properties. The "weight" of the spectrum—equivalently, the area under the curve—is a constant independent of the mean wind,

$$a = \int dk I(k) = \frac{\pi \sqrt{\pi} \Gamma(3/2)}{\Gamma(3/2)} C_n^2 L_0^{5/2} (L/l) k_0^2 \times \int dk D_0^2(\Delta k l). \quad (27)$$

Thus, the effect of increasing mean wind is merely to distribute "power" from the peak of the spectrum into the wings.

For some initial pulse shapes (e.g., rectangular), the "width" defined by the 2nd moment does not exist. The most useful measure, then, is the "equivalent width" defined by $b = a/I_{\text{peak}}$, since I_{peak} is always finite, nonzero. Using a Gaussian initial pulse shape with pulselength $2l$, then, the equivalent spatial-frequency bandwidth of the spectrum of the initial wave is $b_0 = \pi/l$ and a rough estimate of the equivalent bandwidth b_s of the forward-scattered wave is

$$b_s \lesssim \frac{\pi}{l} \left(1 + \frac{ml}{L_0} \right), \quad L \gg L_0, \quad (28)$$

or equivalently, in terms of the temporal-frequency

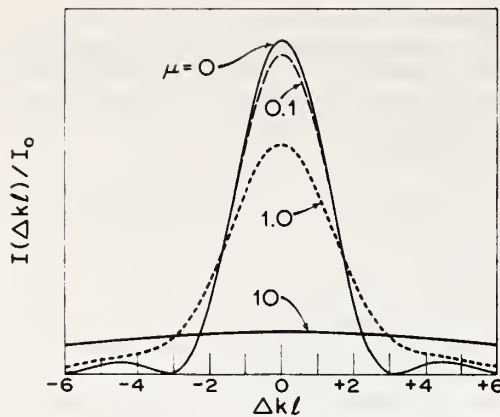


Fig. 1. Normalized power spectrum I/I_0 versus normalized wavenumber difference, $\Delta kl = (k - k_0)l$, plotted for different values of the parameter $\mu = ml/L_0$.

bandwidth

$$b_s \lesssim \frac{\pi}{\tau} \left(1 + \frac{ml}{L_0} \right),$$

where τ is half the pulse duration, m is the ratio of the magnitude of the mean cross wind to the equilibrium sound velocity, and L_0 is the outer scale of turbulence. It is of particular interest that neither the structure constant C_n nor the range enters Eq. 28, except in the weak restriction $L \gg L_0$.

Computer-calculated normalized values of $I(k)$ as given by Eq. 13 for the particular case of a rectangular pulse of half-width l are shown in Fig. 1 as a function of Δkl for several values of the parameter $\mu = ml/L_0$. With increasing μ , the peak decreases and the equivalent width increases linearly. For high values of μ , $I(k)$ approaches a low-intensity white-noise spectrum. Typical acoustic echo soundings^{1,2} in the atmosphere to heights of 1 km involve, $0.01 \lesssim \mu \lesssim 0.2$. [$I(k)$ is the spatial frequency spectrum and has units of variance per unit wavenumber. To convert to the more common variance per unit frequency divide by c_0 , i.e., $I(\omega) = c_0^{-1} I(k)$.]

III. CONCLUSIONS

For isotropic turbulence moving with a given mean cross wind, the analysis has obtained the power spectrum, Eq. 22, of the forward-scattered solution associated with an initial acoustic pulse of arbitrary shape. In addition, Eq. 28 gives an estimate of the broadening produced by the cross wind. The equivalent width found in Eq. 28 is independent of range, path length, or strength of turbulence, a result of con-

siderable importance for the feasibility of acoustic Doppler radar.

It is informative to rewrite the fractional change in bandwidth in Eq. 28 in the form, $ml/L_0 = f_m \tau$, where $f_m = \bar{w}/L_0$ is the turbulence-induced modulation frequency. Clearly, the turbulence, as it drifts through the beam with mean velocity \bar{w} , induces a phase modulation on the passing pulse. This produces an effective frequency modulation that spreads the pulse spectrum. (Note that the analysis used to develop Eq. 28 implicitly assumes³ that the weak atmospheric refractivity fluctuations produce less than one radian phase modulation *per eddy*. The analysis therefore is comparable to the narrow-band FM case. This assumption is valid except for horizontal propagation in the first few meters near the ground.) The most effective eddy size is the outer scale since it produces the maximum phase deviation, an effect more important for determining the change in bandwidth than the higher frequency but smaller amplitude-phase modulation produced by smaller eddies drifting with the same velocity. The influence of smaller eddies is severely attenuated by the $\kappa^{-11/3}$ decay of the refractivity spectrum shown in Eq. 19 for $\kappa > L_0^{-1}$. Therefore, the resulting spectral broadening depends only on L_0 , the largest size eddy in the medium. A further most interesting result of Eq. 28 is that as the wave progresses through a medium that contains variations of the wind velocity and L_0 (assuming that these changes occur smoothly over distance on the order of L_0), the total broadening of the spectrum will depend primarily on the highest modulation frequency, $f_m = \bar{w}/L_0$, that the wave encounters along its path.

ACKNOWLEDGMENT

The authors gratefully acknowledge the helpful discussions with Dr. C. Gordon Little of the Wave Propagation Laboratory, during the preparation of this paper.

¹D. W. Beran, C. G. Little, and B. C. Willmarth, *Nature* (Lond.) **230**, 160 (1971).

²D. W. Beran and B. C. Willmarth, *Proc. Seventh Int. Symp. on Remote Sensing of Environment*, Univ. of Michigan (1971).

³E. H. Brown, *J. Acoust. Soc. Am.* **52**, 1391 (1972).

⁴V. I. Tatarski, *The Effects of the Turbulent Atmosphere on Wave Propagation* (National Technical Information Service, Dept. of Commerce, Springfield, Va., 1971) (TT 68-50464).

⁵L. L. Beranek, *Acoustic Measurements* (Wiley, New York, 1949).

⁶D. W. Beran and S. F. Clifford, *Proc. AMS Acoust. Symposium on Meteorological Observations and Instrumentation*, San Diego, Calif. (1972).

⁷J. W. Strohbehn, *Proc. IEEE* **56**, 1301 (1968).

⁸M. Abramowitz and I. A. Stegun, Eds., *NBS Handbook of Mathematical Functions* (U. S. GPO, Washington, D.C., 1964).

⁹A. Erdelyi et al., *Tables of Integral Transforms* (McGraw-Hill, New York, 1954), Vol. 2.

Reprinted with permission from The Journal of Acoustical Society of America, Vol. 51, No. 2 (part 3) 729-741, 1972.

Seismic and Underwater Responses to Sonic Boom

J. C. COOK AND T. GOFORTH

Teledyne Geotech, Dallas, Texas 75228

R. K. COOK

National Bureau of Standards, Washington, D. C. 20234

Sonic booms produced by aircraft moving at supersonic speeds apply moving loads to the earth's surface. In deep water, a moving underwater pressure field is observed to accompany the hyperbolic boom trace sweeping over the surface. The pressure waveform underwater near the surface is almost identical to that of the N wave in air, but it is rapidly smoothed and attenuated with depth, typically becoming one-tenth as large at a depth less than 0.6 of the N wavelength. Overpressures may exceed background noise pressures by factors of up to 100 at moderate depths for frequencies between 2 Hz and 100 Hz, but are less than 0.16% of pressures known to harm marine life in single exposures. Adequate quantitative theories for the underwater effect have been developed, and have been verified by scale-model experiments. On land, which is generally stratified, there are two major effects: the "static" deformation field traveling with the surface load, and air-coupled Rayleigh wavetrains following each N -wave transient. The latter have frequencies and amplitudes determined by the geology and the aircraft speed. The former has always been the largest effect in over 1000 seismograms recorded in field tests. Its amplitude is proportional to the sonic-boom overpressure. The maximum ground motion recorded was about 100 times the largest natural, steady seismic noise background, but was still less than 1% of the accepted seismic damage threshold for residential structures. Movement is greater in soft ground than on hard rock, and decreases rapidly with depth. Present quantitative theories for the major seismic effects agree reasonably well with the experiments. Seismic forerunner waves, which begin at least 7 sec before arrival of the sonic boom, might be exploited for automatic warnings to lessen the startle effect. Sonic booms probably cannot trigger earthquakes, but might possibly precipitate incipient avalanches or landslides in exceptional areas which are already stressed to within a few percent of instability.

INTRODUCTION

The purpose of this paper is to review and summarize several studies made since 1965 on the seismic and underwater effects of sonic booms. We have not attempted to include all research done on these topics, but we consider the work reported here to be sufficiently representative of present knowledge to support a tutorial paper.

There is both theoretical and experimental work to report. Some agreement between theory and experiment is apparent, but there are also poorly explored areas, phenomena predicted but not yet observed, and imperfectly explained observations. Ecological and cultural implications can be surmised at this time, but additional research is clearly desirable. This paper will emphasize the phenomena, the physical reasoning followed, the research results obtained, and their interpretation.

In the interests of brevity, most mathematical and experimental details are omitted; these are given in full in the original papers referenced. The several topics are treated in order of increasing complexity: first, the underwater effects, since deep water may be considered, to a first approximation, to be a homogeneous half-space bounded by a flat surface; second, the seismic effects, wherein a layered, flat earth must often be taken into account; and finally, the little-explored topic of sonic-boom effects upon incipient avalanches, landslides, and earthquakes is briefly considered.

I. UNDERWATER RESPONSES

For an aircraft in flight over a plane surface, such as a smooth body of water, the intersection of the Mach cone with the interface is one branch of a hyperbola, whose vertex advances over the surface with the supersonic velocity of the aircraft. At the sides of the hyper-

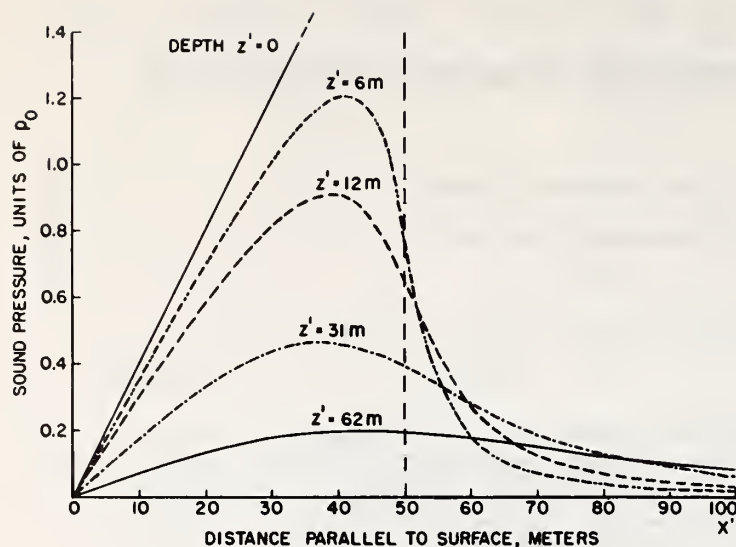


FIG. 1. Underwater sound pressure at various depths $z' = h/\mu$ below the surface, for an N wave (centered at the abscissa origin) of length = 100 m, $\mu = 0.80$ (from Cook²).

bola, the wave propagates obliquely and its speed tends towards the speed of sound in air. The overpressure waveform of the sonic boom at ground level is nominally N shaped. The length of the N wave is typically much less than the least radius of the hyperbolic trace, for example 100 m compared with 8000 m for a Mach 2.7 flight at 20-km elevation. Therefore the assumption of a plane N wave of pressure traveling over the surface is locally valid for purposes of analysis.

The air speeds of present and planned supersonic aircraft in level flight are less than 1000 m/sec and therefore are substantially less than the speed of sound in water (about 1500 m/sec). At speeds less than 1000 m/sec, the N wave from an aircraft in level flight has an angle of incidence on the water surface greater than 19° . This minimum angle of incidence is greater than the critical angle for the passage of a sound wave from air into water, which is about 14° . Each sinusoidal component of the N wave is therefore totally reflected from the surface and is accompanied by a nonradiating pressure field in the water having a subsonic phase velocity equal to the aircraft speed, whose amplitude decreases exponentially with depth below the surface. Such plane waves are referred to as "inhomogeneous" by Brekhovskikh.¹

A diving supersonic aircraft can, of course, create an N wave which arrives at an angle less than the critical, so that acoustic radiation can propagate into the water to the bottom. Nevertheless, because of the large impedance mismatch between air and water, more than 99.8% of the impinging acoustic energy will still be reflected back into the air.

A. Theory

The theory describing the underwater pressure field from a sonic boom has been worked out by R. K. Cook² for the idealized case of level, constant-speed supersonic flight over a flat air-water interface. The general procedure is use of the Fourier-integral method to solve the Cauchy problem posed by the sonic-boom penetration into water. The first step is to find the reflected and refracted waves for an incident sinusoidal wave. The second step is to find the Fourier transform of the incident N wave, and so finally to determine the total reflected and refracted waves (caused by the N wave) by linear superposition of the effects of the incident sinusoidal components.

The following boundary conditions apply:

- (1) the sound pressure is continuous across the air-water boundary surface;
- (2) the perpendicular component of particle velocity is continuous at the boundary; and
- (3) the sound pressure approaches zero at infinite depth underwater.

The complete exact solution consists of two parts, a principal function and a "spike" function. The latter has (logarithmically) infinitely high positive pressure spikes just at the surface, associated with the jump discontinuities of the leading and trailing edges of the N wave. But the spike-function energy is less than 10^{-6} of the energy of the principal function.

The main part $I_1(x', h)$ of the underwater sound pressure, in a coordinate system moving at the same velocity as the incident N wave on the surface, has a wavefield which is stationary in time in the moving coordinates. This occurs because the incident, reflected,

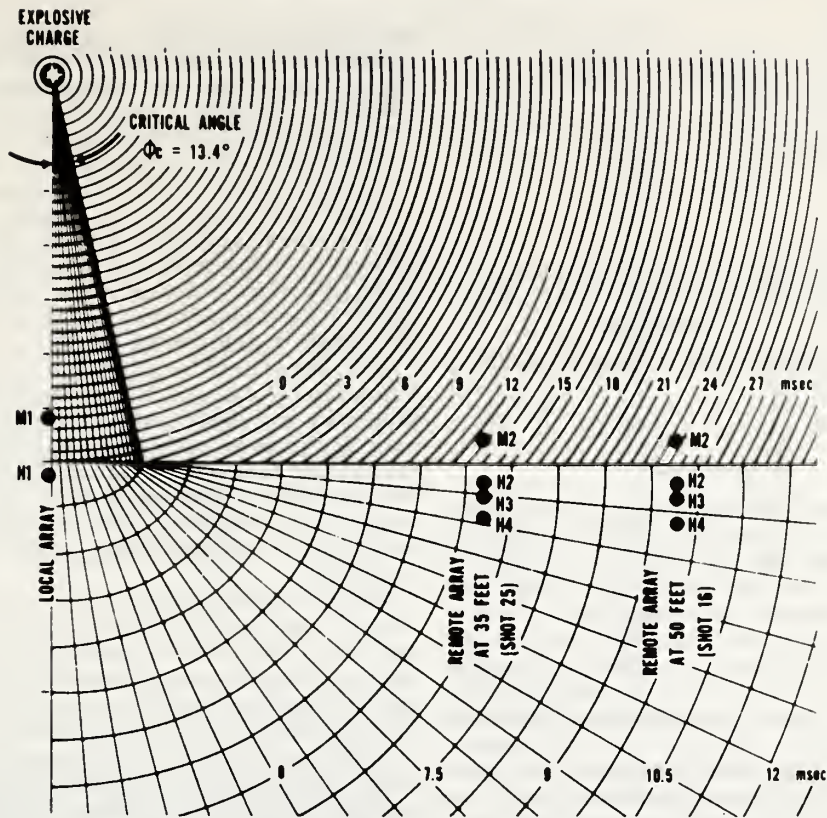


FIG. 2. Locations of sensors for measurements of penetration of sound wave energy into water (from Waters and Glass³).

and underwater wavefields all move in the same direction at the same speed (i.e., the aircraft's speed). The exact expression for the principal wave function is

$$\pi I_1(x', h) = -\frac{h}{2} \log \left[\frac{h^2 + (x' + 1)^2}{h^2 + (x' - 1)^2} \right] + x' \tan^{-1} \left[\frac{2h}{h^2 - 1 + (x')^2} \right],$$

where x' is the horizontal distance from the center of the N wave, $h = \mu z'$ is the normalized depth below the surface, $\mu = (1 - M^2/W^2)^{1/2}$, and z' is the actual depth below the surface. M is the speed of the N wave over the surface, and W is the speed of sound in water. The function I_1 has an N waveform just at the surface ($z' = 0$) but no infinite spikes.

The total sound pressure is $p_w = 2I_1 p_0$ (very nearly, except for the spikes) where p_0 is the peak pressure of the incident N wave. Plots of the total underwater sound pressure as a function of x' , at various depths $z' (=h/\mu)$ below the surface, are shown in Fig. 1. The

total pressure is not quite an odd function of x' . But, practically speaking, the curves of Fig. 1 can be used both for the forward half of the wavefield ($x' > 0, p_w > 0$) and for the trailing half ($x' < 0, p_w < 0$).

At the surface, the function $I_1(x', 0)$ has the N waveform, which we referred to earlier, and therefore $I_1(x', h)$ is the solution for the sound pressure due to a traveling pressure N waveform applied to the surface. Sawyers³ has also worked out the solution for this; his Eq. 13 agrees with $I_1(x', h)$. But the spike function is also a part of the complete underwater sound field when the incident sonic boom, reflected waves, and all the boundary conditions are fully considered. Similar spikes may be generated by sonic booms at atmospheric inhomogeneities.⁴

The function $I_1(x', h)$ spreads out underwater so as to have infinitely long precursor and tail waves. This comes about because the sound field was initiated at $t = -\infty$ (so to speak), and so the underwater sound runs ahead of the atmospheric sonic boom to form a precursor.

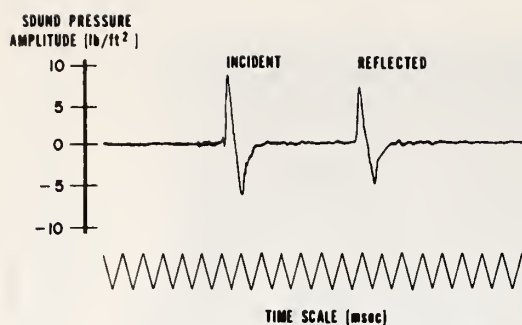


FIG. 3. Airborne pressure *N* wave due to 6-grain dynamite cap (from Waters and Glass⁶).

B. Experiments

In contrast to the well-developed theory of the underwater effects of sonic booms, there are few experimental results to report. Only one full-scale experiment is known to have been performed.⁵ The waveforms reported with microphones at average heights of 1 and 12 ft above the perturbed ocean surface were similar, but "quite different" from the waveform observed with a hydrophone 20 ft deep. The hydrophone signal was also only $\frac{1}{10}$ as large in amplitude, and those from deeper hydrophones were weaker yet. Unfortunately, the flight track of the Mach 1.1 aircraft relative to the instrument position was not determined.

A number of careful scale-model experiments were performed in a flooded rock quarry by Waters and Glass.⁶ The sensors were suspended from a steel cable spanning the quarry, and the sound pulse from the explosion of a 6-grain electric blasting cap was used to simulate the traveling sonic boom, in the manner illustrated in Fig. 2. The angle of incidence of the wave

upon the smooth water surface varied with horizontal position; two of the many positions of the sensor array used, corresponding to sonic booms generated at from Mach 1.2 to Mach 1.5, are shown in Fig. 2.

The special condenser microphones used had good response from 0.1 Hz to 10 kHz and were linear up to pressure amplitudes of 10 lb/ft². The hydrophones used responded down to 10 Hz. Signals were recorded on magnetic tape with a passband of 0 to 10 kHz, and were subsequently reproduced at reduced tape speed for good oscillograph response. Several methods of calibration were employed, and absolute pressure measurements were considered correct within ± 2 dB.

The explosion provided a reasonably good approximation to an *N* wave, as shown in Fig. 3, except that its duration was only 1% of that of a sonic-boom *N* wave. This reduction in the time scale was appropriate and necessary because of the limited size of the model. The underwater signals agreed fairly well, in both amplitude and waveform, with the predictions of Sawyers's or R. K. Cook's theory, as shown in Fig. 4 and Table I.

There were interferences peculiar to the model which would not apply to a full-scale experiment at sea. These were later echoes from the bottom and sides of the quarry, and weak but earlier arrivals refracted into the water at less than the critical angle, as would be expected from Fig. 2. It was also observed that an inner-tube float above the hydrophones radiated a second, later signal into the water. From this it is surmised that sonic-boom recordings made with hydrophones suspended below a ship will be similarly distorted.

C. Implications

The model experiments indicate that the present theories are useful for describing the traveling pressure

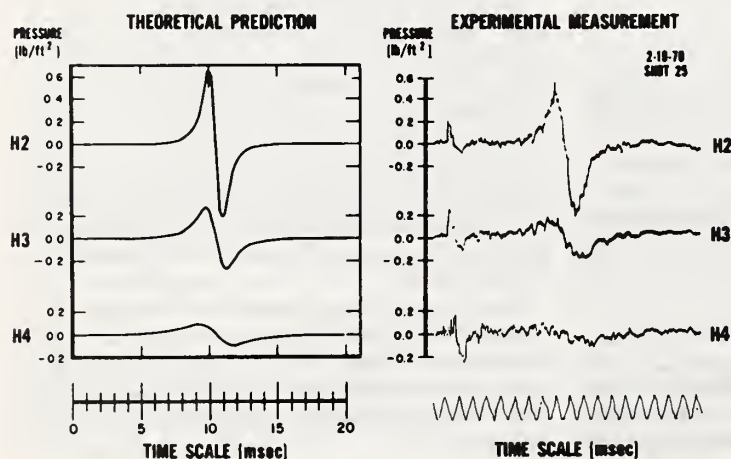


FIG. 4. Comparison between theoretical prediction and experimental measurement of penetration of sound wave energy into water, shot 25 (from Waters and Glass⁶).

SEISMIC AND UNDERWATER RESPONSES TO BOOMS

TABLE I. Summary of peak amplitudes (from Waters and Glass⁶).

| Shot number | Distance (ft) | Mach number | Measured p_1 (lb/ft ²) | Measured T (msec) | Depth (ft) | Peak pressure amplitude (lb/ft ²) | |
|-------------|---------------|-------------|--------------------------------------|---------------------|------------|-----------------------------------------------|-----------|
| | | | | | | Measured | Predicted |
| 12 | 25 | 1.66 | 6.2 | 1.22 | 1.2 | 0.78 | 1.63 |
| | | | | | 2.2 | 0.22 | 0.63 |
| | | | | | 4.2 | 0.10 | 0.19 |
| 13 | 30 | 1.41 | 5.6 | 1.42 | 1.3 | 0.56 | 0.78 |
| | | | | | 2.3 | 0.16 | 0.29 |
| | | | | | 4.3 | 0.06 | 0.09 |
| 14 | 35 | 1.32 | 5.9 | 1.54 | 1.5 | 0.29 | 0.28 |
| | | | | | 2.5 | 0.11 | 0.11 |
| | | | | | 4.5 | 0.07 | 0.03 |
| 15 | 40 | 1.25 | 5.3 | 1.54 | 1.6 | 0.28 | 0.46 |
| | | | | | 2.6 | 0.07 | 0.19 |
| | | | | | 4.6 | 0.04 | 0.06 |
| 6 | 45 | 1.20 | 5.4 | 1.42 | 1.7 | 0.18 | 0.37 |
| | | | | | 2.7 | 0.08 | 0.16 |
| | | | | | 4.7 | 0.04 | 0.05 |
| 16 | 50 | 1.17 | 4.2 | 1.50 | 1.9 | 0.16 | 0.21 |
| | | | | | 2.9 | 0.04 | 0.09 |
| | | | | | 4.9 | 0.02 | 0.03 |
| 17 | 55 | 1.14 | 3.1 | 1.46 | 2.0 | 0.12 | 0.13 |
| | | | | | 3.0 | 0.03 | 0.06 |
| | | | | | 5.0 | 0.02 | 0.02 |
| 18 | 60 | 1.12 | 3.9 | 1.43 | 2.1 | 0.19 | 0.39 |
| | | | | | 3.1 | 0.05 | 0.19 |
| | | | | | 5.1 | 0.02 | 0.07 |

field generated underwater by a sonic boom. The general conclusion is that the N wave is rapidly smoothed and attenuated with depth, typically being reduced to one-tenth of its amplitude at the surface at a depth of a few tens of feet.

A beginning has been made toward interpreting underwater sonic-boom effects in ecological terms, by comparing the underwater pressure spectra of typical sonic booms with those of normal ambient noises, in sea state 3 (moderate waves) and heavy ship traffic. Figure 5 is typical of the results,⁶ which show that sonic boom pressures can be expected to exceed the ambient-noise pressures (momentarily) by up to 50 dB, from the surface down to depths of a few hundred feet, between frequencies of 0.5 to a few hundred Hz. The particle displacements are less than 0.05 mm. It is clear, that, according to the treatment of Waters and Glass,⁶ all sea life in the continental shelf regions, all plankton and other organisms in the near-surface illuminated zone, as well as the organisms of the worldwide "deep scattering layer" when they rise to the surface at night, will be subjected to a detectable amount of momentary overpressure from the passage of a sonic boom.

However, experiments in clear seawater with electric "sparker" underwater seismic pulse sources have shown that the most sensitive small fish (anchovies, menhaden) are not stunned outside a radius of 1 m from the spark,⁷ at which distance the peak sound pressure in a passband of 20 to 100 Hz is 1 bar, or 2100 lb/ft². This value is at

least 600 times the peak overpressure of typical sonic booms. Experiments with explosive charges have shown that oysters, blue crabs, and shrimp are less vulnerable than fish.⁸ The clear inference is that typical sonic booms will not harm these organisms.

II. SEISMIC RESPONSES

The effects of sonic booms upon solid ground are similar in only one respect to those upon liquid water:

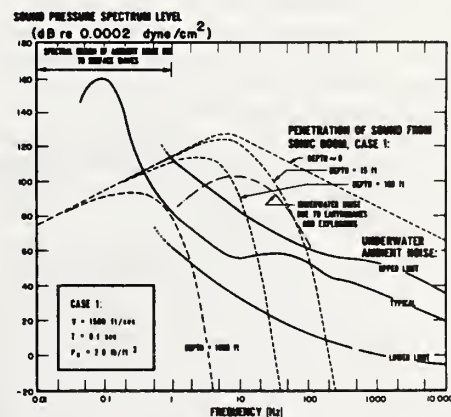


FIG. 5. Comparison of underwater sound-pressure spectrum levels for sonic boom and ambient noise, case (1) (from Waters and Glass⁶).

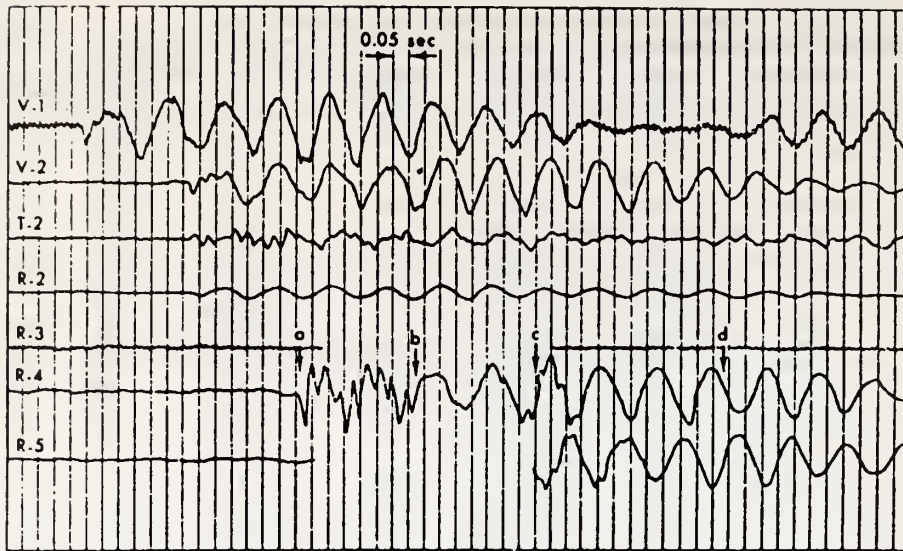


FIG. 8. Seismic coupled waves from a sonic boom (from Espinosa *et al.*¹⁰).

and complicated. Briefly, they include trapped or leaky mode expressions, expressions related to the singularities, and line integrals which give the static solution as the load speed goes to zero. The speed of the aircraft relative to the seismic shear (S) and compressional (P) velocities in the underlying half-space (the basement rock) determines which modes are possible and the extent to which each contributes to the total deformation. There are three cases:

- (1) When the aircraft speed is less than the S velocity of the half-space, the solution includes the trapped modes, a solution similar to the load distribution and the line integral contribution.
- (2) When the aircraft speed is between the S and P velocities of the half-space, the solution is similar except that leaking modes replace the trapped modes and energy is radiated into the basement rock.
- (3) In the case of the aircraft speed being greater than the P velocity of the half-space, the line integral disappears and only the leaky modes and a delayed version of the load pulse remain.

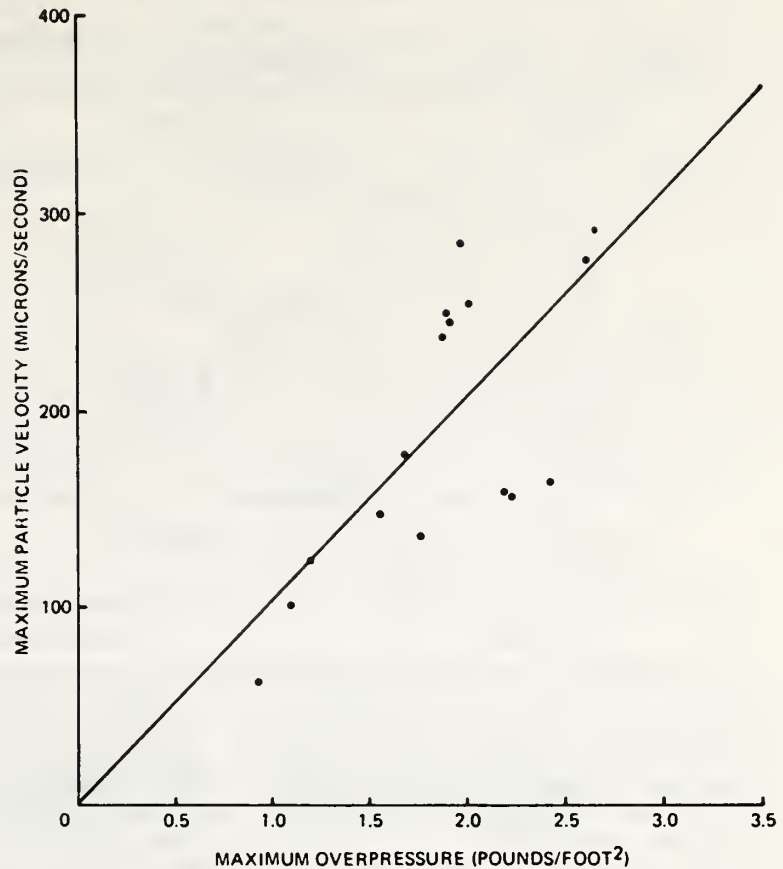
Dunkin and Corbin¹¹ have calculated curves of frequency and amplitudes as functions of the aircraft speed and the depth for a particular, simple case of a single low-velocity layer overlying a homogeneous half-space. They also present calculated velocity waveforms for various depths and aircraft speeds, for both vertical and horizontal in-line ground motions. Unfortunately, none of these results can be compared with available experimental data, because the aircraft speeds chosen

were too high, and correspond to cases 2 and 3 described above. All the experiments to be described correspond to case 1, or else involve more than one layer. Also, the Dunkin and Corbin waveforms assume a single line load, whereas sonic-boom N waves apply two in succession.

B. Experiments

Some of the first substantial measurements of ground motion from sonic booms were those of Espinosa, Sierra, and Mickey.¹² An array of ten seismographs, some 275 m in length, including a three-component set, was used near the Cape Kennedy missile launching area. At least two sonic booms were observed to produce strong air-coupled seismic wavetrains. An example is shown in Fig. 8. The predominant frequencies, interpreted as trapped Rayleigh waves, when combined with seismic velocity data for the area, provided two predicted values of surface-layer thickness which correspond reasonably well to values measured by a seismic survey. The high-frequency signals were identified as higher normal seismic modes. Unfortunately, in these experiments, narrow-band seismographs responding only from about 0.2 to 20 Hz were used, so that the major effects in the audible frequency range were not recorded. [In a later short study, the band was extended to 80 Hz; see A. F. Espinosa and W. V. Mickey, *Acustica* 20, 88-91 (1968).] There is also a lack of data on the speeds, climbing attitudes, and flight tracks of the aircraft, and also of high-resolution acoustic recordings, all of which are needed for a complete interpretation of seismic data.

FIG. 9. Relation of maximum overpressure for XB-70 overflights to peak earth particle vertical velocity observed on a clay lake bed (from Cook and Goforth¹⁴).



For this reason, only a limited interpretation was attempted.

Espinosa, Sierra, and Mickey point out two important facts: First, a diving aircraft can produce an acoustic wave traveling along the ground at up to infinite speed; for example, a wave speed of 100 000 m/sec will result from a 50° dive at only Mach 1.3. Second, alluvium and other soft or loose earth materials may move much more than hard rock in response to a sonic boom.

The most extensive experimental data now available are those of McDonald and Goforth.^{13,14} Altogether, 178 level overflights on prescribed flight tracks were monitored, chiefly at Edwards Air Force Base (EAFB), California. Four kinds of aircraft were used, the B-58, F-104, SR-71, and XB-70. Speeds were between Mach 1.3 and 2.5, and altitudes were 5 to 18 km. The 17 flights by the XB-70 are of greatest interest, since the size of this plane (57.1 m long, 136+ tons) most nearly approaches that of an SST.

Five identical velocity-sensing seismographs were used, with a frequency response flat to ± 1 dB from

1 to 100 Hz. The seismometers used have been shown to be free of spurious resonances below 100 Hz, and to be unaffected by air pressure transients, especially when buried. The system was calibrated daily. Both Visicorder and magnetic tape recordings were made. Three of the seismographs were used as a three-component set directly under the usual flight track, buried 1 m deep in the clay of a small playa (dry lake bed). Vertical seismometers were buried also at other positions on the playa, and on a nearby outcrop of the quartz monzonite basement rock. NASA microphones were provided at each seismometer location to record the air overpressure signals. Radar tracking of the aircraft and meteorology were also provided. Eight B-58 missions were flown over Tonto Forest Seismological Observatory (TFSO), a government seismic observatory in Arizona, where a seismometer array 9 km wide is available to study energy distribution outside and inside the sonic-boom hyperbola and possible focusing effects at the axis. Three B-58 missions were also flown over Uinta Basin Seismological Observatory (UBSO), a seismic observa-

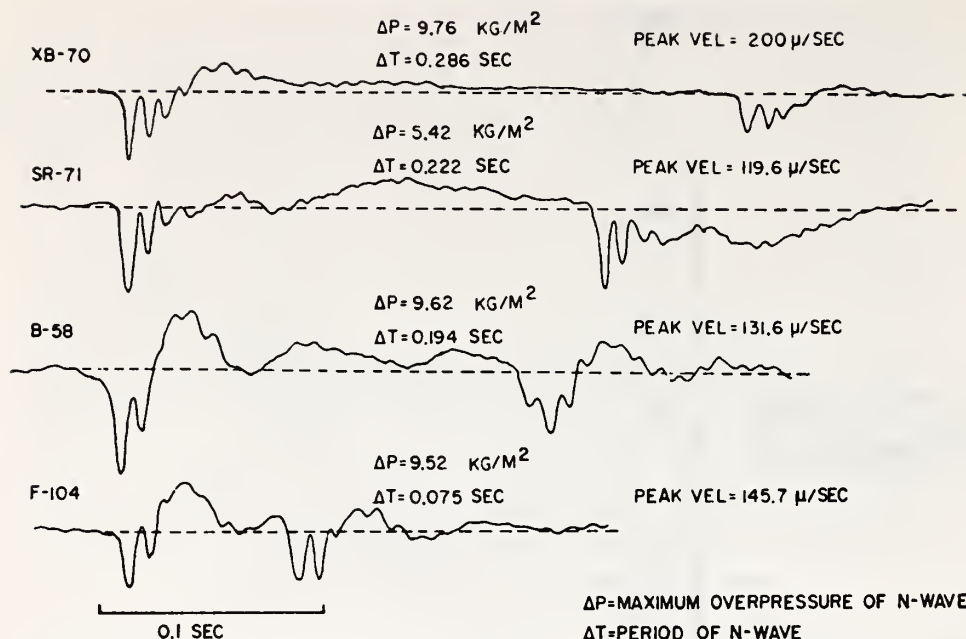


FIG. 10. Variation of seismograms recorded on rock with different types of aircraft (from McDonald and Goforth¹³).

tory in Utah where seismometers were available at various depths in a sealed deep well, to study attenuation with depth. These locations also afforded geology different from that at EAFB.

The seismograms shown in Fig. 6 are typical of most of more than 1000 which were made. In all cases, the greatest particle velocities occurred in the two sharp downward peaks which coincided with the front and rear of the air N wave. The vertical velocity was always greatest, the radial (in-line) component averaged two-thirds as great, and the transverse one-third as great. Regardless of aircraft type, the maximum particle velocity was roughly proportional to air overpressure, as is shown in Fig. 9 for the XB-70 flights. For the same sonic boom (and same overpressure), the peak particle velocity observed on the rock outcrop averaged only two-thirds that observed on the lake bed clay, as expected.¹² The seismograms recorded on the rock were also simpler, being nearly free of the prolonged air-coupled wavetrains present on the clay, as can be seen by comparing Figs. 10 and 11. This result is in accordance with theory. It was found that the recorded waveforms varied considerably, and in a complicated manner, in different geological environments (Fig. 12). At a given location, the frequencies of the air-coupled Rayleigh waves varied with aircraft speed. This too would be expected from theory.

Forerunner waves were always seen at high gain settings. These waves had frequencies of the order of

2 Hz,¹⁴ amplitudes around 5 to 10 μ /sec, and began as much as 7 sec before the arrival of the sonic boom. They are tentatively attributed to seismic body waves propagated through the ground in advance of the hyperbolic trace, at speeds as great as Mach 20, the speed of P waves in hard rocks.

No evidence was seen of large ground motions caused by "focusing," that is, meeting of reinforcing wavetrains from the two arms of the hyperbola at its axis. This is probably a consequence of attenuation over the hundreds of meters separating each arm from the axis, since according to Fig. 11 the coupled wavetrains die out in about 0.2 sec, corresponding to about 80 m of travel. Outside the hyperbola, at a lateral distance of 32 km from the flight trace, TFSO equipment recorded a maximum particle velocity only 17% of that on the flight axis. Also, there was evidently rapid vertical attenuation at UBSO. At a depth of 13.4 m, the maximum particle velocity was only 1.3% of that at the surface.

C. Implications

The largest sonic-boom effect measured for present supersonic aircraft in level flight at normal altitudes was a vertical ground velocity of 340 μ /sec at a frequency around 90 Hz, caused by a sonic-boom overpressure of 2.5 lb/ft². This value is equivalent to the ground vibration caused by automobiles passing at

SEISMIC AND UNDERWATER RESPONSES TO BOOMS

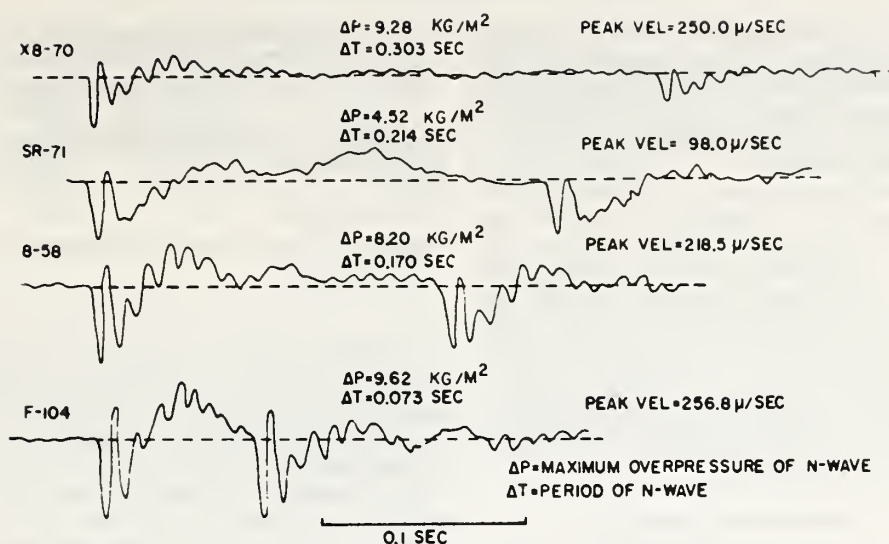


FIG. 11. Variation of seismograms recorded on clay layer with different types of aircraft (from McDonald and Goforth¹³).

30 mph, 30 ft away on a paved road.¹⁴ It amounts to less than 1% of the seismic damage threshold for residences established by the U. S. Bureau of Mines,¹⁵ which is 2.0 in./sec or 50 800 μ/sec. Seismic damage to structures as a result of even very strong sonic booms would probably be negligible compared to air-blast effects, since by a rather large extrapolation, over-

pressures of 5200 lb/ft² would be required to reach the seismic damage threshold. Underground effects of sonic booms at present aircraft speeds are essentially confined to the top few meters of the ground, and decrease rapidly with depth, as expected from theory.^{9,11,16} For aircraft speeds above perhaps 2 km/sec (Mach 6.5), this conclusion may no longer hold.

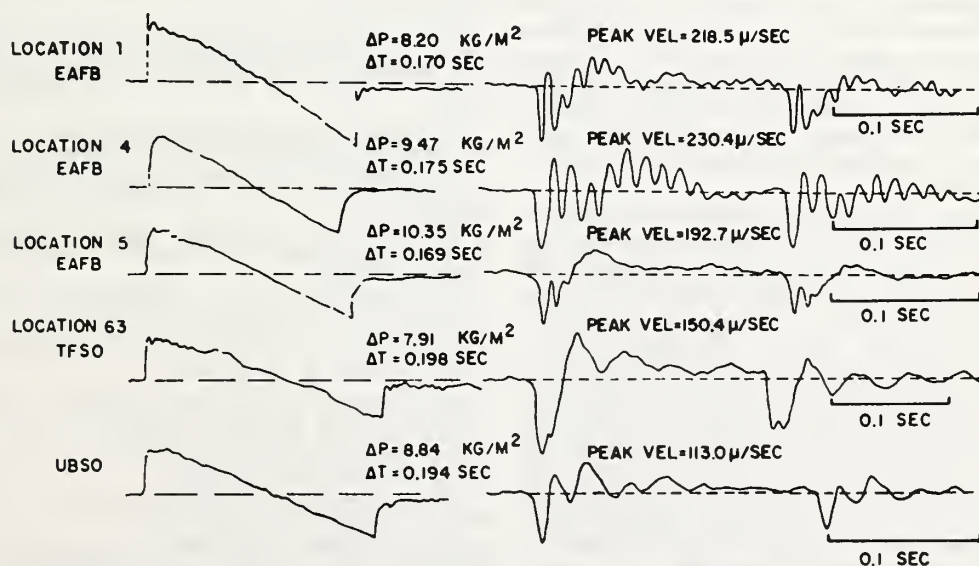


FIG. 12. Variation of seismograms with variation of geological properties (from McDonald and Goforth¹³).

Theoretically, there should be no transverse motion (along the hyperbolic trace), but transverse velocities about one-third as large as the vertical component are, in fact, observed. These velocities are attributed to departures of the natural earth from the simple layered half-space model assumed.

The seismic forerunner signal can be as much as 20 dB stronger than ambient seismic noise in quiet rural locations. There may be a possibility that it could be reliably and automatically identified, perhaps by the presence of a single autocorrelation peak at a lag time equal to the length of the N wave, or by array correlation methods. If so, automatic local warning of an approaching sonic boom by several seconds, to lessen the startle effect on people and livestock, would be feasible. There is evidence that people and animals soon learn to ignore harmless explosions when a gentle warning is consistently given.

III. SECONDARY EFFECTS

From time to time, questions have been raised as to the possibility that avalanches, landslides, earthquakes, and other catastrophic releases of stored natural energy could be triggered by sonic booms. Some light may be shed on this question by comparing the earth vibrations induced by sonic booms with those from other sources to which the stored-energy system may be subjected, and the stress required to overcome restraining effects in appropriate stored-energy systems.

Triggering of earthquakes by sonic booms is considered quite unlikely, because earthquake foci are located at depths of at least 1 km, far below the effective penetration depth of sonic booms.

The literature¹⁷ indicates that natural seismic noise levels in the 20–100-Hz frequency band most prominent in sonic-boom seismograms are practically never larger than 1% of the 340 μ /sec level measured for sonic booms. From this standpoint, sonic-boom vibrations may rank beside those of nearby railroads¹⁸ and earthquakes, as a possible triggering agency for avalanches and landslides.

Defining or measuring the approach to disequilibrium of possible slide or avalanche areas is a complex matter.^{18,19} However, for the beginning of separation of the sliding mass to occur, differential movement between adjacent masses must occur, sufficient to overcome restraining friction or adhesion. The total ground movement occurring in typical sonic booms is less than $\frac{1}{2}$ μ . This movement may occur over a rise time of perhaps 1 msec (see microphone waveforms in Fig. 12), so that the horizontal gradient of vertical strain is less than 1 μ /m for earth or rock materials. In lower density materials such as snow, the shear strain could reach perhaps 10 μ /m. The corresponding shear stresses and approximate shear strengths of some representative slide materials are shown in Table II²⁰; (here the shear stress = strain \times shear elastic modulus).

TABLE II. Sonic-boom stress effects.

| Material | Assumed strain | Shear stress, psi | Shear strength, psi | Ratio |
|-----------------------------------|------------------|-------------------|---------------------|-------|
| Wind-hardened snow ²⁰ | 10 ⁻⁶ | 5.6 | 100 | 5.6% |
| Stiff clay | 10 ⁻⁶ | 1.(?) | 50(?) | 2% |
| Brecciated limestone ^a | 10 ⁻⁶ | 3 | 1,130 | 0.26% |

^a See p. 19 of Ref. 18.

Although the values of all numbers given in Table II may be correct only to within an order of magnitude, the conclusion may be drawn that sonic booms will seldom contribute more than a few percent of the stress required to start a landslide or avalanche. The remainder must already have developed from other causes.

It is obvious that field research on the effects of sonic booms in areas prone to avalanches and landslides should be done. (One unsuccessful study has already been reported.²¹) We hope that our preliminary surmises will stimulate careful quantitative studies of these effects.

¹ L. M. Brekhovskikh, *Waves in Layered Media* (Academic, New York, 1960), p. 4.

² R. K. Cook, "Penetration of a Sonic Boom Into Water," *J. Acoust. Soc. Amer.* **47**, 1430–1436 (1970).

³ K. N. Sawyers, "Underwater Sound Pressure from Sonic Booms," *J. Acoust. Soc. Amer.* **44**, 523–524 (1968).

⁴ A. D. Pierce, "Spikes on Sonic Boom Pressure Waveforms," *J. Acoust. Soc. Amer.* **44**, 1052–1061 (1968).

⁵ R. W. Young, "Penetration of Sonic Booms into the Ocean," Abstract in *J. Acoust. Soc. Amer.* **44**, 392 (1968). Preprint available from author.

⁶ J. F. Waters and R. E. Glass, "Penetration of Sonic Boom Energy Into the Ocean: An Experimental Simulation," Hydro-space Research Corp. Tech. Rep. No. 288, Rockville, Md. Final Report on Contract No. FA60WAI-185 (N0014-70-C-0374) (1970).

⁷ C. O. Berglund and W. H. Parker, Teledyne Exploration Co., Houston, Tex., personal communication (unpublished).

⁸ R. J. Kemp, Jr., "Do Seismographic Explosives Affect Marine Life?", *Texas Game and Fish* (Austin, Texas) **14**, No. 9, 11–13 (Sep. 1956).

⁹ T. T. Goforth and J. A. McDonald, "A Physical Interpretation of Seismic Waves Induced by Sonic Booms," *J. Geophys. Res.* **57**, 5087–5092 (1970).

¹⁰ F. Press and M. Ewing, "Ground Coupling to Atmospheric Compressional Waves," *Geophysics* **16**, 416–430 (1951).

¹¹ J. W. Dunkin and D. G. Corbin, "Deformation of a Layered, Elastic Half-Space by Uniformly Moving Line Loads," *Bull. Seismol. Soc. Amer.* **60**, 167–191 (1970).

¹² A. F. Espinosa, J. P. Sierra, and M. V. Mickey, "Seismic Waves Generated by Sonic Booms: A Geoaoustical Problem," *J. Acoust. Soc. Amer.* **44**, 1074–1082 (1968).

¹³ J. A. McDonald and T. T. Goforth, "Seismic Effects of Sonic Booms," NASA CR-1137 (Sep. 1968).

¹⁴ J. C. Cook and T. T. Goforth, "Ground Motion from Sonic Booms," *J. Aircraft* **7**, 126–129 (1970).

¹⁵ W. I. Duvall and D. C. Fogelson, "Review of Criteria for Estimating Damage to Residences from Blasting Vibrations," TN 23.07, No. 5963, U. S. Dept. of the Interior, Bureau of Mines (1962).

SEISMIC AND UNDERWATER RESPONSES TO BOOMS

¹⁶ J. W. Posey, "Seismic Waves Generated by Sonic Booms," *J. Acoust. Soc. Amer.* 48, 80(A) (1970).

¹⁷ G. I. Frantti, "The Nature of High Frequency Earth Noise Spectra," *Geophysics* 28, 547-562 (1963).

¹⁸ K. Terzaghi, "Mechanism of Landslides," in *Application of Geology to Engineering Practice* (Geol. Soc. Amer., New York, 1950), Chap. 4.

¹⁹ C. Fraser, *The Avalanche Enigma* (Rand McNally, Chicago, 1966).

²⁰ M. Mellor, Properties of Snow, Rep. III-A1, U. S. Army Materiel Command, Cold Regions Res. Develop. Labs (Dec. 1964).

²¹ D. C. Lillard, T. L. Parrott, and D. C. Gallagher, "Effect of Sonic Booms of Varying Pressures on Snow Avalanches," FAA Rep. AD 468 794 (1965).

Acoustic Ray Paths through a Model Vortex with a Viscous Core

T. M. GEORGES

Environmental Research Laboratories, National Oceanic and Atmospheric Administration, Boulder, Colorado 80302

Angular deflection and the formation of a line caustic are examined for acoustic rays passing through a cylindrical vortex with a viscous core. Ray paths are displayed in normalized form and appear to be applicable to the aircraft-wake problem as well as to long-distance sound propagation through synoptic weather features.

Interest in acoustic propagation through cyclonic wind fields arises from at least two problems: the detection and diagnosis of aircraft-wake vortices, and the effects of cyclonic weather features on the propagation of sound (and infrasound) over long distances in the earth's atmosphere. The details of acoustic wave propagation through all but a few simple wind and temperature fields defy analysis in closed form; however, useful propagation information can usually be derived from ray-path calculations using geometrical acoustics, provided the medium is "slowly varying" with respect to the sound wavelength. This note briefly reviews what is already known about acoustic ray propagation through vortices and displays some ray paths through some more realistic models calculated with a three-dimensional acoustic ray-tracing program.

Lindsay¹ apparently first calculated acoustic ray paths through a vortex, using a simple line vortex as a model, in which peripheral velocity decreases as $1/r$ from the center (and where the vorticity $\nabla \times \mathbf{v}$ is zero everywhere except along the vortex axis). He obtained a differential ray equation but integrated it analytically only for the case of flow velocities that are small compared to the sound speed. His results took the form of formulas for the influence of the vortex on the relative times of arrival of a plane wavefront at pairs of points in the velocity field, but he did not illustrate the ray paths. Salant² derived a ray equation applicable to two-dimensional rotating flows with arbitrary radial variations of peripheral velocity and refractive index. He solved it for ray paths in a rigid-body flow and for a line vortex, both with constant sound speed, and demonstrated that certain rays become "trapped" in the vortex center. Some ray paths were shown for each case.

The existence of a pure line vortex (or "potential vortex") is physically impossible because its tangential velocity and velocity gradient approach infinity along its axis. In real fluids, molecular and eddy viscosity act to prevent discontinuities in the flow, and require the tangential speed at the vortex center to approach zero. Furthermore, viscosity acts to dissipate the vortex in time.

Eskinazi³ gives the velocity field of a "viscous line vortex,"

$$v_\theta = (\Gamma_0/2\pi r)[1 - \exp(-r^2/4\nu t)], \quad (1)$$

where ν is a coefficient of viscosity, r is the radius from the vortex axis, Γ_0 is the value of the vortex circulation

$$\Gamma(r, t) \equiv \int_0^{2\pi} v_\theta(r, t) d\theta$$

initially concentrated at the vortex center, and t is the time from the instant of vortex generation. Close to the center ($r \rightarrow 0$), Eq. 1 describes a nearly rigid-body rotation, while at large r (and small t) the velocity field approaches that of a line vortex. The velocity distribution is illustrated in Fig. 1, in normalized form.

Recognizing that the radius of maximum velocity (r_0) is given by

$$r_0^2/4\nu t = 1.26,$$

and that the velocity there is

$$v_{\theta m} = 0.716\Gamma_0/2\pi r_0,$$

we can rewrite the formula for v_θ in normalized form that no longer explicitly contains ν , Γ_0 , or t :

$$\frac{v_\theta}{v_{\theta m}} = 1.4 \frac{r_0}{r} \left[1 - \exp\left(\frac{-1.26r^2}{r_0^2}\right) \right]. \quad (2)$$

RAY PATHS THROUGH A VISCOUS VORTEX

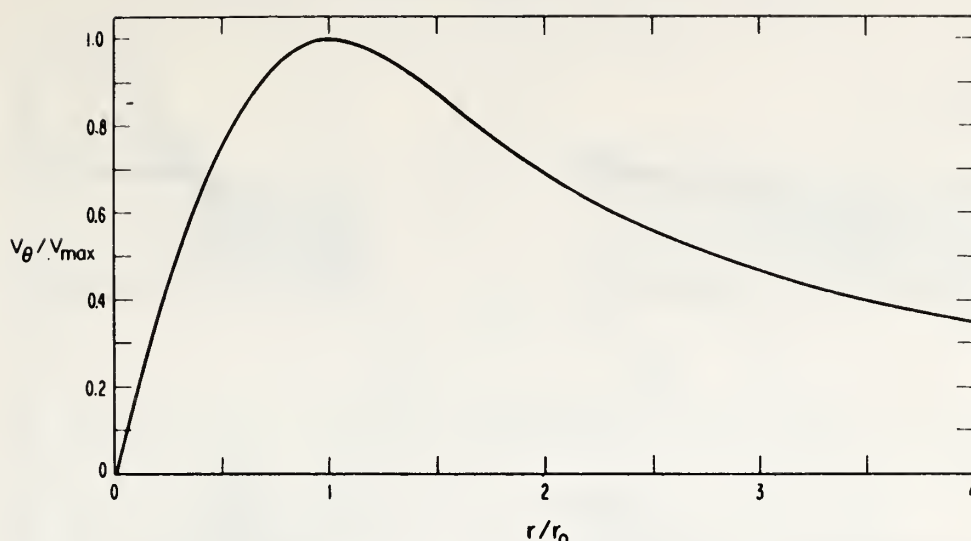


FIG. 1. Velocity field of a viscous vortex.

(The numerical constants arise from the solution of a transcendental equation.) The core diameter depends on the viscosity and the time after formation: For a time of 100 sec and a value of ν appropriate to the kinematic molecular viscosity of air at the earth's surface, r_0 is about 17 cm, independent of Γ_0 . There are observational indications that, for aircraft wakes, the core diameter is considerably larger, perhaps a few meters, only seconds after aircraft passage, indicating that eddy viscosity probably determines core size. (In this case, however, turbulent fluctuations may affect the ray paths to the same degree as the mean flow.)

Examination of atmospheric cyclonic features of synoptic scale suggests that a similar model may qualitatively describe their wind fields; there, however, the "core" dimensions, usually measured in hundreds or thousands of kilometers, are determined not by viscosity, but by scales of planetary waves (see, for example, the Tropopause Wind Analysis charts published daily by the National Weather Service).

We will show that the inclusion of such a rigid-body core drastically modifies the acoustic ray-path geometry.

Within the framework of ray theory, the geometrical ray configuration for a given refractive index field is invariant with respect to a change of spatial scale. (Reference to Snell's law makes this intuitively reasonable.) Therefore, if we calculate a ray path through a vortex described by Eq. 1, the result will apply as well to all vortices of this kind that have the same value of $v_{\theta m}/c$. In other words, we only need to vary $v_{\theta m}/c$ in order to obtain a set of ray geometries applicable to all possible vortices described by Eq. 1. The values chosen here as representative are $1/20$, $1/10$, $1/5$, and $1/3$.

The ray paths illustrated in Fig. 2 were calculated using a digital computer program for acoustic ray tracing through wind and temperature fields with arbitrary three-dimensional variability. The program,⁹ an adaptation of the ionospheric radio ray-tracing program of Jones,⁴ numerically integrates the so-called Haselgrove⁵ equations which describe ray trajectories in inhomogeneous anisotropic media in Hamiltonian form. The Haselgrove equations require the specification of the medium in terms of a refractive index field, which, in our case, is

$$\mu(\mathbf{r}) \equiv c_0 k / \omega = c_0 [c + \mathbf{v}(\mathbf{r}) \cdot \mathbf{n}]^{-1}, \quad (3)$$

where c_0 is some reference speed, c is the local sound speed in a frame moving with the fluid, \mathbf{n} is a unit vector along the wave normal, ω is the angular wave frequency, and \mathbf{v} is the vector wind field. (We assume that the temporal changes described by Eq. 1 occur very slowly compared to the time for wave transit.)

Figure 2, then, shows a set of ray paths for the four values of $v_{\theta m}/c$. Only the parallel ray geometry representing an incident plane wave is calculated; however, because of cylindrical symmetry of the wind field, the configuration due to a point source at any distance can be readily obtained by rotating ray paths about the vortex center, until they all converge at the desired "source" point. A similar procedure could be used to obtain the ray paths through a vortex pair, if the cores do not interact.

It should be mentioned that, because the ray paths are not reciprocal in the presence of winds, one cannot retrace a ray back along the same path to the source. The correct return path can be estimated, again, by a

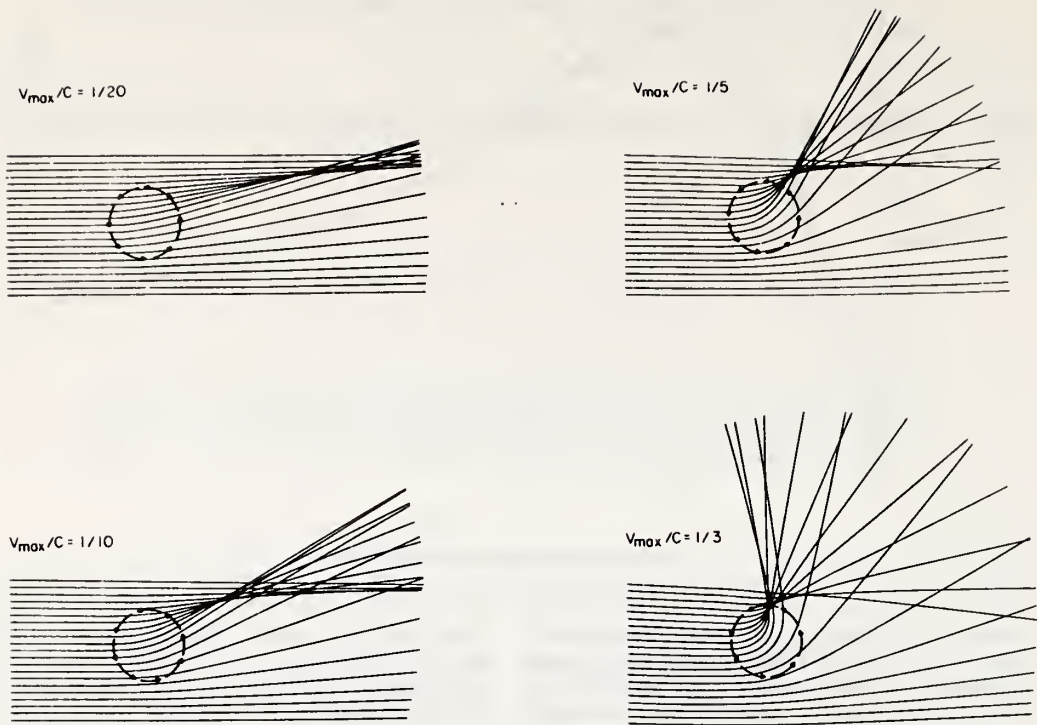


FIG. 2. Acoustic ray paths through a viscous vortex (spatial scale is arbitrary). The circle of arrows indicates r_0 .

ray-rotation process. Note also that ray theory tells us only about the geometrical paths that satisfy Fermat's principle and nothing about incoherent scattering and diffraction phenomena, which would, however, surely affect waves of finite wavelength. We would expect the ray interpretation to break down and incoherent scattering to be significant when the acoustic wavelength begins to approach r_0 in size.

Because the velocity field described by Eq. 1 is axially invariant, the axial component of the wavenumber remains constant, and these plots also represent projections, on a plane normal to the axis, of rays launched at any angle with the axis.

A qualitative explanation of the ray behavior is possible in terms of the acoustic ray equation derived by Landau and Lifshitz⁶ for a homogeneous fluid in steady motion

$$c(ds/dl) = -\mathbf{s} \times (\nabla \times \mathbf{v}), \quad (4)$$

valid to first order in v/c . Here \mathbf{s} is a unit vector tangent to the ray path, and l is length measured along the ray. Evidently, no ray deviation occurs, to first order, in the curl-free region outside the vortex core; the small deviations illustrated (which do not depend on the approximation $|v| \ll c$) are apparently due to higher-order effects and to the small vorticity present outside the

core where it blends with the line-vortex field. Inside the core, vorticity is nearly constant and the amount of ray bending depends mainly on the length of the ray path inside the core. The sign of the deviation predicted by Eq. 4 agrees with the ray plots.

One obvious effect of the vortex on the rays is angular deflection; this effect is plotted in Fig. 3, as a function of the distance of the ray from a "head-on" course and the value of $v_{\theta m}/c$. The largest ray deviation is suffered by the head-on ray, which also passes through the vortex axis, and which, incidentally, always maintains a radial wave vector. Rays do not become "trapped" in a viscous vortex unless $v_{\theta m}/c > 1$, which is physically unlikely. As $y \rightarrow \infty$, the angular deflection asymptotically approaches zero.

Another notable effect is that the rays that pass through the upper half of the vortex form a line caustic, whose location varies with $v_{\theta m}/c$. In the vicinity of such a caustic, the acoustic intensity is greatly enhanced (though the degree of enhancement can be calculated only through full-wave analysis); a corresponding region of depleted acoustic intensity is evident just below the caustic.

It is important to note that, in the presence of winds, the speed and direction of acoustic energy (ray) propagation do not generally coincide with the speed and

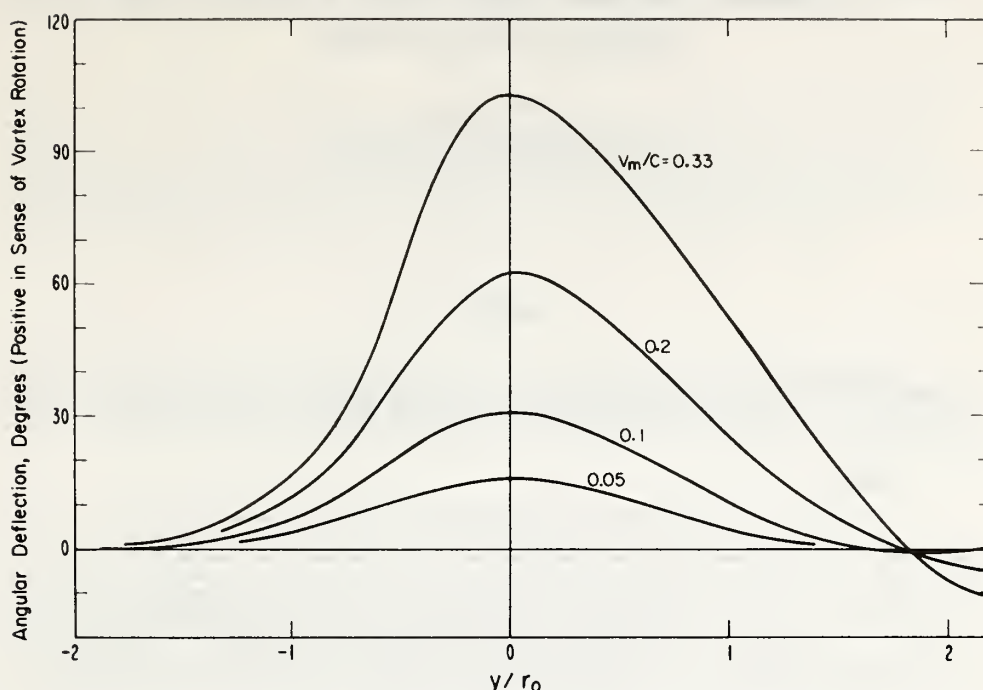


Fig. 3. Angular deflection of acoustic rays by a viscous vortex. y is the lateral distance of an incident ray from the head-on ray.

direction of wavefront travel. The general relationship between the two is given, at any point, by⁶

$$\dot{\mathbf{r}} = (c\mathbf{k}/k) + \mathbf{v}, \quad (5)$$

where $\dot{\mathbf{r}}$ is the time derivative of a point on (and is tangent to) the ray path, \mathbf{k} is the wave vector (k is its magnitude), and \mathbf{v} is the ambient wind vector. Note that $\dot{\mathbf{r}}$ represents a *group* velocity and is *not* the velocity that would be measured by, for example, an array of acoustic sensors. The *phase* velocity at any point is

$$v_p = c + [(\mathbf{k} \cdot \mathbf{v})/k]; \quad (6)$$

i.e., only the component of \mathbf{v} in the \mathbf{k} direction contributes to v_p , and then affects only its magnitude. Consequently, the velocity of a given wave measured, for example, by a closely spaced array of acoustic sensors differs in general from the velocity that would be deduced by measuring travel time from its source. These points are more relevant to geoacoustic measurements than to the aircraft-wake problem.

Refinements of the model of the aircraft trailing vortex would include radial and axial velocities, such as considered by Newman⁷ and Dosanjh *et al.*,⁸ as well as elevated temperatures within the vortex. However, further complications introduced by turbulence and

eddy diffusion may cancel any benefits of constructing more realistic models for purposes of studying sound propagation. In application to global sound propagation, one needs to include vertical temperature and wind variability of the ambient atmosphere as well as the earth's curvature.

¹ R. B. Lindsay, "Compressional Wave Front Propagation through a Simple Vortex," *J. Acoust. Soc. Amer.* **20**, 89-94 (1948).

² R. F. Salant, "Acoustic Rays in Two-Dimensional Rotating Flows," *J. Acoust. Soc. Amer.* **46**, 1153-1157 (1969).

³ S. Eskinazi, *Vector Mechanics of Fluids and Magnetofluids* (Academic, New York, 1967).

⁴ R. M. Jones, "A Three-Dimensional Ray Tracing Computer Program," ESSA Tech. Rep. IER 17-ITSA 17 (U. S. GPO, Washington, D. C., 1966).

⁵ J. Haselgrove, "Ray Theory and a New Method for Ray Tracing," in *The Physics of the Ionosphere* (Physical Society, London, 1954), pp. 355-364.

⁶ L. D. Landau and E. M. Lifshitz, *Fluid Mechanics* (Pergamon, Oxford, 1959).

⁷ B. G. Newman, "Flow in a Viscous Vortex," *Aeron. Quart.* **X**, 149 (1959).

⁸ D. S. Dosanjh, E. P. Gasparek, and S. Eskinazi, "Decay of a Viscous Trailing Vortex," *Aeron. Quart.* **XIII**, 167-188 (1962).

⁹ T. M. Georges, "A Program for Calculating Three-Dimensional Acoustic-Gravity Ray Paths in the Atmosphere," U. S. Gov. Printing Off., Washington, D. C., N.O.A.A. Tech. Rep. ERL 212-WPL16 (1971).

Reprinted from AGARD Conference Proceedings No. 115, NATO,
Wiesbaden, Germany, April 1972, 2.1-2.8, 1972.

3D RAY TRACING FOR ACOUSTIC-GRAVITY WAVES

T. M. Georges
Wave Propagation Laboratory
NOAA Environmental Research Laboratories
Boulder, Colorado, U.S.A. 80302

ABSTRACT

A new general-purpose ray tracing program for acoustic-gravity waves has been developed. It allows atmospheric wind and temperature to vary in all three spatial dimensions and with time and accounts for earth curvature. Ray plots show the characteristic acoustic ray patterns of a standard atmosphere but also some interesting and unexpected ray geometries in cases of more complex wind fields and for internal gravity waves.

1. RATIONALE

Ray tracing has been successfully employed to calculate the paths of wave-energy flow in inhomogeneous anisotropic media, most notably for radio waves in the ionospheric plasma, seismic waves in the earth, and for acoustic waves in the ocean and atmosphere. A few attempts have been made to extend acoustic-ray-tracing capabilities to low-frequency acoustic-gravity waves in the atmosphere (cf. PIERCE, 1966; JONES, 1969; CHANG, 1969; COWLING et al., 1971), but each scheme so far developed employs simplifying assumptions or idealized models that limit their applicability to the real atmosphere. In particular, the effects of winds are sometimes ignored or are at most constrained to be horizontal and to have only vertical gradients. Other approaches ignore either the effects of gravity or compressibility, and most neglect earth curvature and horizontal temperature gradients. Finally, no acoustic-gravity ray-tracing program of which we are aware is well documented and available in a "user-oriented" form, i.e., easy to use and readily adaptable to digital computers in common use.

The program described here is designed to overcome these limitations in the following ways:

- (a) Ray equations are derived from Hamilton's equations (rather than variations of Snell's Law) and allow three-dimensional gradients of atmospheric wind and temperature fields;
- (b) A Hamiltonian appropriate to acoustic-gravity waves in a windy atmosphere allows a single program to apply to the whole wave spectrum from pure acoustic to internal gravity waves;
- (c) Earth curvature is accounted for by writing Hamilton's equations in earth-centered spherical coordinates; and
- (d) Programming is modeled after the Jones-ITS ionospheric radio ray-tracing program, which has evolved, over several years of widespread use, into a thoroughly tested and highly user-oriented tool (JONES, 1966).

This paper briefly describes the workings and capabilities of the program. Further details and instructions for its use appear in a NOAA Technical Report (GEORGES, 1971) that can be supplied upon request.

2. THE RAY-TRACING EQUATIONS

Hamilton's equations, when applied to wave propagation, can be thought of as a differential expression of Fermat's Principle of Stationary Time. Their applications to geometrical optics and to geometrical acoustics are discussed, respectively, in the texts by KLINE and KAY (1965) and LANDAU and LIFSHITZ (1959). In their simplest vector form, they can be written

$$\dot{\mathbf{r}} = \frac{\partial H}{\partial \mathbf{K}}, \quad (1a)$$

and

$$\dot{\mathbf{K}} = - \frac{\partial H}{\partial \mathbf{r}}, \quad (1b)$$

where a dot indicates total time differentiation, \mathbf{K} is the wave vector, and \mathbf{r} is a point on the ray path. The Hamilton (H) is a quantity whose constancy defines the ray path, given appropriate initial conditions and a model atmosphere. For acoustic-gravity waves, H is given by the wave dispersion relation, such as that developed by HINES (1960), TOLSTOY (1963), and others for isothermal atmospheres without winds. The generalization to include winds is straightforward and is discussed by PITTEWAY and HINES (1965). The isothermal dispersion relation gives the appropriate Hamiltonian for ray tracing in nonisothermal

atmospheres because the geometrical-acoustics approximation is equivalent to assuming that the medium is locally homogeneous and is valid only when that assumption is valid. The Hamiltonian is then

$$H = \Omega^2 - \Omega^2 C^2 K^2 - \Omega^2 \omega_a^2 + C^2 k_h^2 \omega_b^2 = 0 \quad , \quad (2)$$

where Ω is the intrinsic wave frequency with respect to the air moving at a local wind velocity, \mathbf{v} , whose components are v_r , v_θ and v_ϕ in spherical coordinates, r , θ , ϕ . The wave frequency measured in a fixed frame is $\omega = \Omega + \mathbf{K} \cdot \mathbf{v}$, where \mathbf{K} is the wave vector (k_r , k_θ , k_ϕ). The horizontal component of \mathbf{K} is k_h . The local speed of sound is C , ω_a is the acoustic-cutoff frequency, $\gamma g/2C$, and ω_b^2 is the square of the Brunt frequency, $(\gamma-1)g^2/C^2 + g(\partial C^2/\partial z)/C^2$. In accordance with the analysis of EINAUDI and HINES (1970), a modified definition of ω_b is adopted, which accounts for the effects of vertical sound-speed (temperature) gradients on atmospheric stability. Substituting (2) into (1) and expressing in spherical coordinates (BRANDSTATTER, 1959), we get the six coupled differential ray-tracing equations:

$$\frac{dr}{dt} = C^2 k_r \Omega F + v_r \quad , \quad (3)$$

$$\frac{d\theta}{dt} = \frac{1}{r} \left\{ C^2 k_\theta (\Omega^2 - \omega_b^2) F / \Omega + v_\theta \right\} \quad , \quad (4)$$

$$\frac{d\phi}{dt} = \frac{1}{r \sin \theta} \left\{ C^2 k_\phi (\Omega^2 - \omega_b^2) F / \Omega + v_\phi \right\} \quad , \quad (5)$$

$$\frac{dk_r}{dt} = \frac{\Omega}{C} \frac{\partial C}{\partial r} (\omega_a^2 - C^2 k^2) F + (k_\theta^2 + k_\phi^2) \frac{\partial F}{\partial \Omega} \frac{\partial^2 C^2}{\partial r^2} - \mathbf{K} \cdot \frac{\partial \mathbf{v}}{\partial r} + k_\theta \frac{dv_\theta}{dt} + k_\phi \sin \theta \frac{dv_\phi}{dt} \quad , \quad (6)$$

$$\frac{dk_\theta}{dt} = \frac{1}{r} \left\{ \frac{\Omega}{C} \frac{\partial C}{\partial \theta} (\omega_a^2 - C^2 k^2) F + (k_\theta^2 + k_\phi^2) \frac{\partial F}{\partial \Omega} \frac{\partial}{\partial \theta} \left(\frac{\partial C^2}{\partial r} \right) - \mathbf{K} \cdot \frac{\partial \mathbf{v}}{\partial \theta} - k_\theta \frac{dv_\theta}{dt} + r k_\phi \cos \theta \frac{dv_\phi}{dt} \right\} \quad , \quad (7)$$

•

$$\frac{dk_\phi}{dt} = \frac{1}{r \sin \theta} \left\{ \frac{\Omega}{C} \frac{\partial C}{\partial \phi} (\omega_a^2 - C^2 k^2) F + (k_\theta^2 + k_\phi^2) \frac{\partial F}{\partial \Omega} \frac{\partial}{\partial \phi} \left(\frac{\partial C^2}{\partial r} \right) - \mathbf{K} \cdot \frac{\partial \mathbf{v}}{\partial \phi} - k_\phi \sin \theta \frac{dv_\theta}{dt} - r k_\theta \cos \theta \frac{dv_\phi}{dt} \right\} \quad , \quad (8)$$

where

$$F \equiv (2 \Omega^2 - \omega_a^2 - C^2 k^2)^{-1} \quad .$$

These equations, though apparently complicated, are readily integrated by standard numerical methods to yield $\mathbf{r}(t)$ and $\mathbf{K}(t)$. The addition of a seventh equation,

$$\frac{d\omega}{dt} = \mathbf{K} \cdot \left(\frac{\partial \mathbf{v}}{\partial t} \right) - \frac{\Omega}{C} \frac{\partial C}{\partial t} (\omega_a^2 - C^2 k^2) F \quad , \quad (9)$$

permits integration of Doppler shift, provided the medium does not vary appreciably during ray transit.

The program described here uses a standard Adams-Moulton integration scheme with variable step length and error checking. The user specifies the maximum tolerable fractional integration error per step and thus has the option of trading computer running time for accuracy.

3. USING THE PROGRAM

The program is designed to be used, for the most part, like a "black box," that is, without much knowledge of its inner workings. Parameters that the user may wish to vary (for example, initial conditions, wave variables, and model atmosphere parameters) are input via a data deck with one such parameter per card. Sequential ray calculations, such as stepping ray launch direction, are automatically

provided for. In addition to a comprehensive printed output, automatic ray plots may be obtained on computers with cathode-ray-tube/microfilm output capabilities.

Several simple model atmospheric wind and temperature fields with variable parameters are included in the program's repertoire, and the user may readily substitute his own models. In its present form, the program accepts only continuous analytic descriptions of wind and temperature fields, but virtually any desired field may be fitted with analytic functions.

4. ILLUSTRATIONS OF APPLICATIONS - ACOUSTIC WAVES

Figure 1 displays the kind of ray plot often produced by simpler programs: that of ordinary acoustic waves in a standard-atmosphere temperature profile. Here, however, a wind blows toward the right and increases logarithmically with height. Note particularly the influence of the wind on where rays return to the ground. The wave source in this example is near the tropopause, so that pronounced ray ducting is also evident.

Figure 2 shows acoustic ray paths through an isothermal cylindrical vortex with a solid-rotating core. The ray geometry is independent of spatial scale and so is relevant to smaller vortices, such as those generated in aircraft wakes, as well as to cyclonic weather features of synoptic scale. The only variable parameter of the problem is the ratio of the maximum wind speed in the vortex to the sound speed and is indicated on the 4 panels of the figure. This maximum is attained at the dashed circles in the figure; inside the circle, wind speed varies approximately as the radius, while outside, it falls off nearly as the inverse radius. This problem is further discussed in another paper (GEORGES, 1972).

Figure 3 shows schematically how anisotropy and nonreciprocity introduced by winds affect ray propagation in acoustic sounding of the troposphere. In general, refraction alters the location of the scattering volume, the scattering angle, and the magnitude of the Doppler shift. GEORGES and CLIFFORD (1972) further analyze refractive effects in acoustic sounding.

5. ILLUSTRATIONS OF APPLICATIONS - INTERNAL GRAVITY WAVES

Because ray paths of internal gravity waves are much more difficult to develop intuitive feelings for than are acoustic waves, one tends to use a ray-tracing program much like a new experimental tool: Internal gravity ray paths, even in simple wind and temperature fields, often exhibit unexpected behavior. An example is provided by the simple case of gravity-wave propagation in a region of linear temperature gradient. Figure 4 shows two gravity-wave rays launched upward and downward in such a temperature profile. An explanation of the cusplike reflection behavior can be found by considering the direction of the normals to the constant- ω/ω_0 surfaces in the k plane (figure 4 inset), which indicate ray direction. Waves launched in a horizontally stratified medium must maintain k_x constant as they propagate; therefore, as temperature (and thus ω_0) changes, one estimates changes in ray direction by sliding up or down a vertical line through the diagram and noting the resulting changes in direction of the surface normals. For example, a ray whose phase fronts are launched downward and that propagates upward into increasing temperature (increasing ω/ω_0) experiences a gradual ray steepening until $k_z \rightarrow 0$ when ray direction abruptly reverses, executing the cusplike reflection (not a true mathematical cusp) depicted in figure 4. The level of reflection of a gravity wave depends only on the value of k_x and can be found by setting $k_z = 0$ in the dispersion relation, giving the minimum value of ω_0/ω for a given k_x :

$$\frac{\omega_0^2}{\omega^2} = \frac{n_x^2 - 1}{n_x^2 - 1.225}$$

where

$$n_x = Ck_x/\omega \quad (10)$$

Figure 5 illustrates how internal gravity waves may be ducted in a temperature minimum. Evidently the vertical propagation of internal gravity waves tends to be restrained in the presence of temperature gradients, regardless of whether temperature increases or decreases. ECKART (1960) shows ray paths that display this behavior.

Because internal-gravity-wave phase speeds are considerably slower than those of acoustic waves, gravity waves interact much more strongly with atmospheric wind fields than do acoustic waves. Gravity-wave ray paths in a linear wind profile of gradient 0.1 m/s/km serve to illustrate that nature of the interaction. Figure 6 shows five gravity-wave rays launched downwind. Each wave eventually reaches its own "critical level," i.e., where the wind speed equals the horizontal trace speed of the wave. Each wave approaches an asymptotic condition in which the wave vector tends toward vertical and phase velocity toward zero.

Gravity waves launched upwind exhibit a quite different behavior, as illustrated in figure 7. The ray is refracted upward and is eventually turned around by the wind shear. In this example, the azimuth of k is at a 45° angle with y , and lateral ray deviation also occurs, as illustrated in the plan view in figure 7.

6. CONCLUSIONS

These few examples illustrate the capabilities of the 3D ray-tracing program in simple model atmospheres and show some ray path properties that, as yet, have not apparently been appreciated.

It is expected that the program's capabilities will be refined with use and in response to user needs and suggestions. Such suggestions are, of course, welcome.

7. REFERENCES

- BRANDSTATTER, J.J., 1959, "The Theory of Propagation of Rays in an Inhomogeneous and Anisotropic Medium," Stanford Research Institute Report, Project 2241.
- CHANG, N.J.F., 1969, "Acoustic-Gravity Waves in the Ionosphere and Their Effects on High-Frequency Radio Propagation," Ph.D. Dissertation, Electrical Engineering Dept., University of Colorado, Boulder, Colorado, U.S.A.
- COWLING, D.H., H.D. WEBB, and K.C. YEH, 1971, "Group Rays of Internal Gravity Waves in a Wind-Stratified Atmosphere," J. Geophys. Res. 76, 213-220.
- ECKART, C., 1960, "Hydrodynamics of Oceans and Atmospheres," Pergamon, New York.
- EINAUDI, F., and C.O. HINES, 1970, "WKB Approximation in Application to Acoustic-Gravity Waves," Can. J. Phys. 48, 1458-1471.
- GEORGES, T.M., 1971, "A Program for Calculating Three-Dimensional Acoustic-Gravity Ray Paths in The Atmosphere," NOAA Tech. Report ERL 212-WPL 16, U.S. Govt. Printing Office, Washington, D. C.
- GEORGES, T.M., 1972, "Acoustic Ray Paths through a Model Vortex with a Viscous Core," J. Acoust. Society of America, 51, No. 1 (Part 2), 206-209.
- GEORGES, T.M., and S.F. CLIFFORD, 1972, "Acoustic Sounding in a Refracting Atmosphere," to be submitted to J. Acoust. Society of America.
- HINES, C.O., 1960, "Internal Atmospheric Gravity Waves at Ionospheric Heights," Can. J. Phys. 38, 1441-1481.
- JONES, R.M., 1966, "A Three-Dimensional Ray-Tracing Computer Program," ESSA Tech. Report IER 17-ITSA 17, U. S. Govt. Printing Office, Washington, D. C.
- JONES, W.L., 1969, "Ray Tracing for Internal Gravity Waves," J. Geophys. Res. 74, 2028-2033.
- KLINE, M., and I.W. KAY, 1965, "Electromagnetic Theory and Geometrical Optics," Wiley, New York.
- LANDAU, L.D., and E.M. LIFSHITZ, 1959, "Fluid Mechanics," Pergamon Press, Oxford, 256 ff.
- PIERCE, A.D., 1966, "Geometrical Acoustics Theory of Waves from a Point Source in a Temperature-and Wind-Stratified Atmosphere," AVCO Scientific Report, AVSSD-0135-66-CR.
- PITTEWAY, M.L.V., and C.O. HINES, 1965, "The Reflection and Ducting of Atmospheric Acoustic-Gravity Waves," Can. J. Phys. 43, 2222-2243.
- TOLSTOY, I., 1963, "The Theory of Waves in Stratified Fluids Including the Effects of Gravity and Rotation," Rev. Mod. Phys. 35, 207-230.

ACOUSTIC WAVES IN 1962 U.S. STANDARD ATMOSPHERE

$f = 300 \text{ Hz}$; Logarithmic Wind Profile: $u = 10 \text{ m/s}$ at 1 km
Elevation Angle Varies from -20° to 200° in 10° Steps

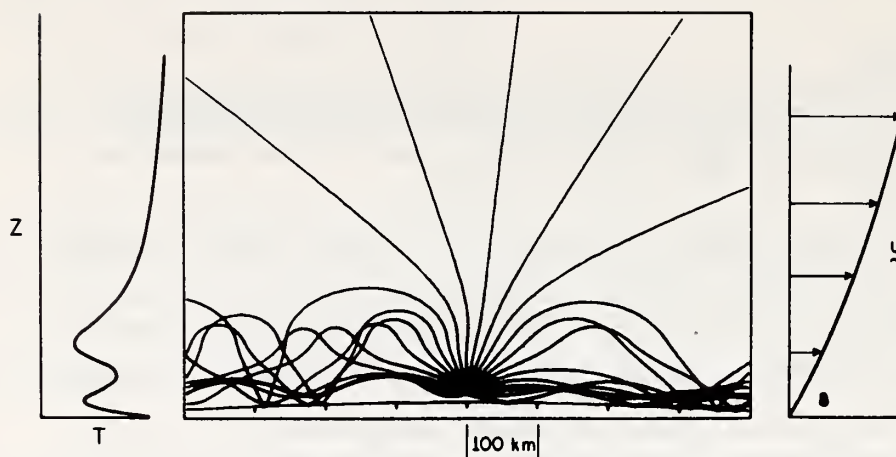


Fig.1 Acoustic waves in 1962 U.S. Standard Atmosphere temperature profile and a wind blowing to the right and increasing logarithmically with height.

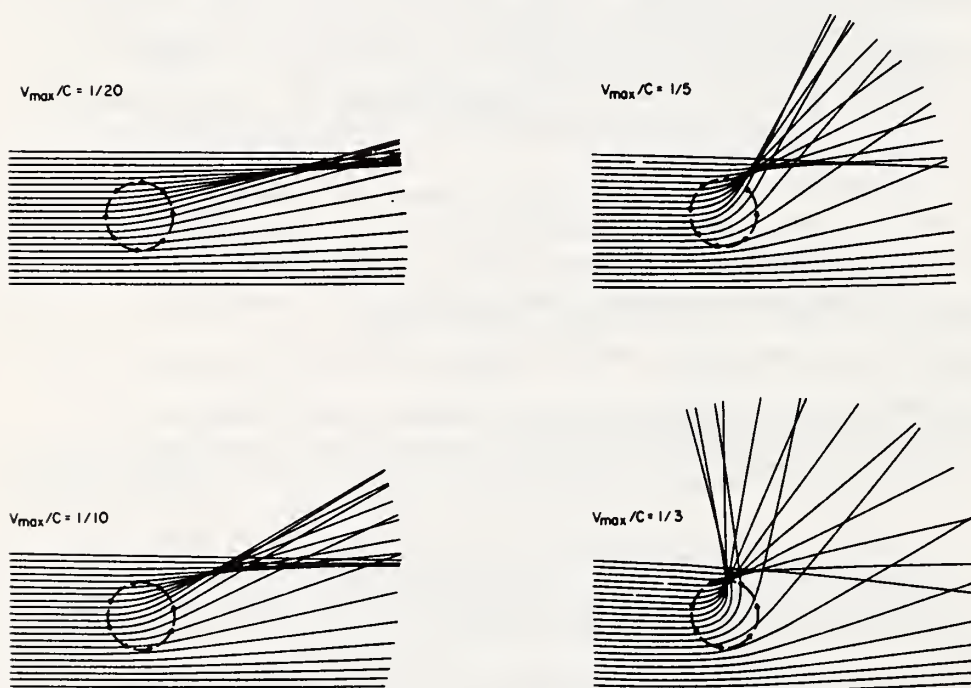


Fig.2 Acoustic ray paths through a model vortex with a viscous core. Tangential velocity maximizes along the dashed circles and has the speed indicated on each panel. (Spatial scale is arbitrary).

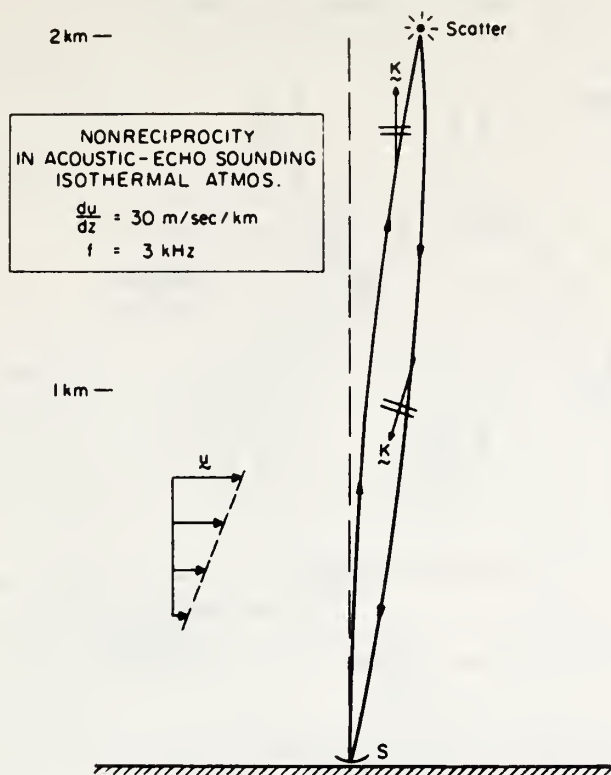


Fig.3 Acoustic ray path in an acoustic-sounding geometry illustrating nonreciprocity in the presence of wind shear.

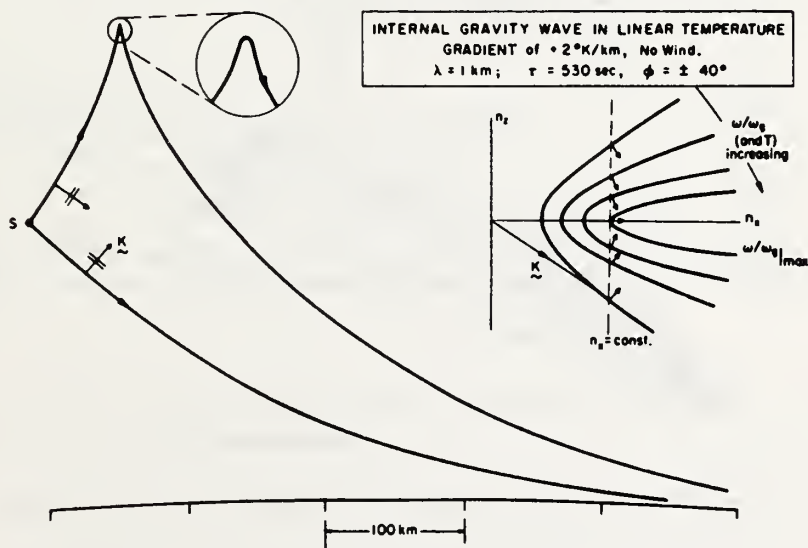


Fig.4 Internal-gravity ray paths in a positive linear temperature gradient, illustrating cusplike reflection of the upgoing ray and the asymptotic approach to horizontal of the downcoming rays.

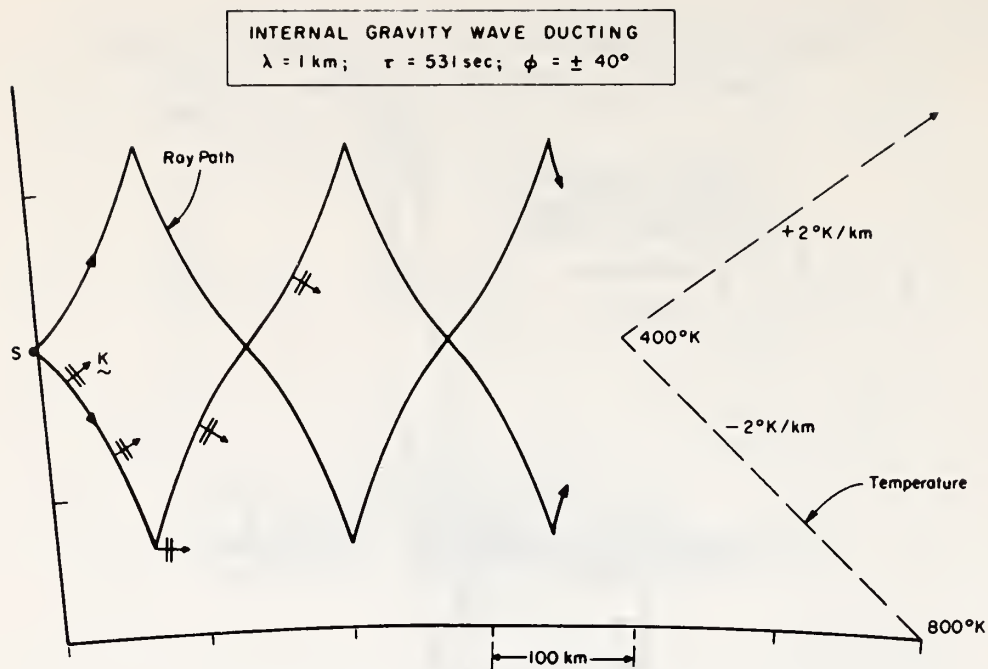


Fig.5 Internal gravity wave ducting in a piecewise linear temperature profile.

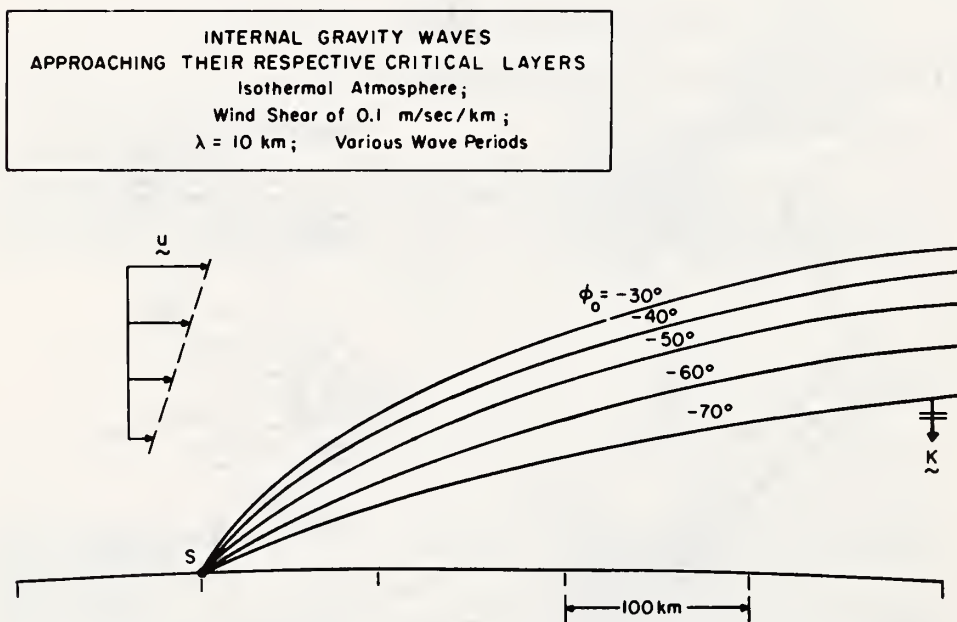


Fig.6 Internal gravity waves approaching their respective critical layers in a linearly increasing wind profile.

INTERNAL GRAVITY WAVE
 IN WIND SHEAR OF 0.1 m/sec/km
 and
 TEMPERATURE GRADIENT 0.1°K/km
 $\lambda = 10 \text{ km}$; $\tau = 475 \text{ sec}$; $\phi = -50^\circ$

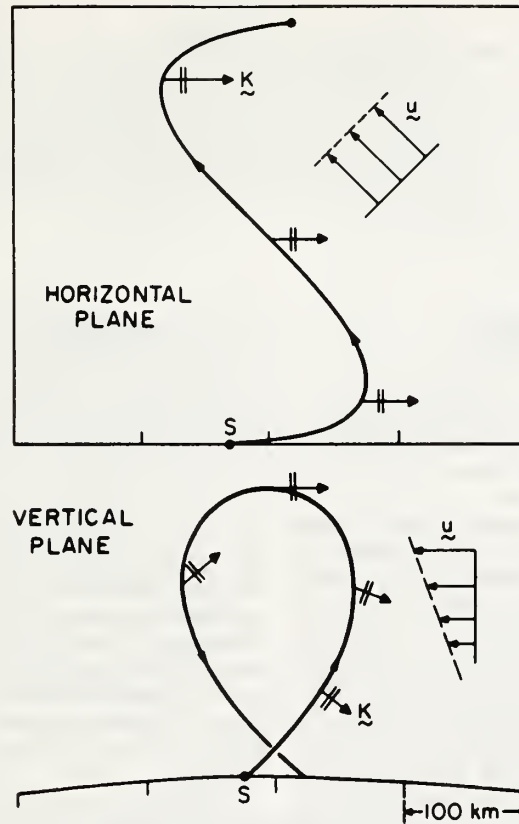


Fig.7 Three-dimensional ray path of an internal gravity wave propagating upstream in a linear wind profile.

Acoustic Sounding in a Refracting Atmosphere

T. M. GEORGES AND S. F. CLIFFORD

Wave Propagation Laboratory, NOAA Environmental Research Laboratories, Boulder, Colorado 80302

(Received 12 April 1972)

Acoustic refraction by atmospheric wind and temperature inhomogeneities affects the measurements of acoustic sounders in four ways: (a) It displaces the location of the scattering volume relative to its apparent location based on straight-line ray paths. (b) It alters the magnitude of the Doppler shift by changing the magnitude and direction of the wave vector at the scatterer. (c) It changes the scattering angle from that based on a straight-line geometry. (d) It introduces Doppler-shift contributions due to time variations of the atmospheric refractive index all along the sounding path. An idealized model of all these effects on bistatic soundings shows that most refractive corrections are small for present sounding geometries up to heights of about 1 km, but may need to be accounted for as sounding heights increase.

SUBJECT CLASSIFICATION: 11.2, 11.7, 11.9.

I. THE PROBLEM

The utility of acoustic echo sounding as a tool for displaying the dynamics of the atmospheric boundary layer has been theoretically and experimentally demonstrated by Little,¹ McAllister *et al.*,² and in the references they cite. In more recent developments, Beran *et al.*³ and Beran and Clifford⁴ have shown how wind profiles can be measured using a Doppler technique. They have produced some preliminary wind measurements that compare favorably with independent simultaneous measurements. So far, however, no attempt has been made to correct such measurements for the effects of refraction by atmospheric wind and temperature inhomogeneities. Unlike electromagnetic probes, acoustic probes interact strongly with the atmosphere, so that refractive effects can sometimes be appreciable.

If atmospheric refraction of the acoustic waves could be ignored, one would interpret bistatic Doppler observations by assuming that the waves travel at uniform speed along the line-of-sight triangular path joining source, scatterer, and receiver. In that case, Doppler shift would indicate the component of scatterer motion along the bisector of the triangle's apex angle, as is commonly assumed in electromagnetic Doppler measurements.⁵ The spatial and temporal inhomogeneity of the real atmosphere and the presence of winds give rise to several questions about the accuracy of such an interpretation, namely: (i) how much do refractive effects alter the scattering angle, (ii) how do refractive changes in wave-vector magnitude and direction affect Doppler shift, (iii) how large are displacements of the scattering volume from its apparent position, and (iv) what is the relative impor-

tance of contributions to Doppler shift due to temporal variations of refractive index all along the path?

We seek answers to these questions by analyzing an idealized problem:

Let an acoustic source be located on a flat earth (at *a* in Fig. 1), an observer at *c*, and consider the acoustic ray path *P* connecting the source and receiver via a scatterer at *b*. The source and observer employ narrow-beam antennas to look toward a small common scattering volume at *b*, which remains stationary in space unless the medium varies in time. Even though the population of scatterers in the scattering volume may continuously change (due, for example, to wind advection), the Doppler shift still represents the mean motion of individual scatterers within the volume, and not the discontinuous shifts in phase-path length as different scatterers come into view. Croft^{6,7} elaborates on this point.

In general, the ray path *P* satisfies Fermat's Principle of Stationary Time, but may itself be time-dependent if the propagation medium, or the location of the path's end points, vary with time. Furthermore, the sound propagation vector **K** does not generally lie along the ray path when winds are present, so that the propagation medium is generally anisotropic, inhomogeneous, and nonreciprocal.

We want to calculate, for this general bistatic case, the acoustic Doppler shift, the change in direction of the axis which determines the component of the wind being measured, and the relocation of the scattering volume itself, in forms which explicitly show the magnitude of refractive corrections.

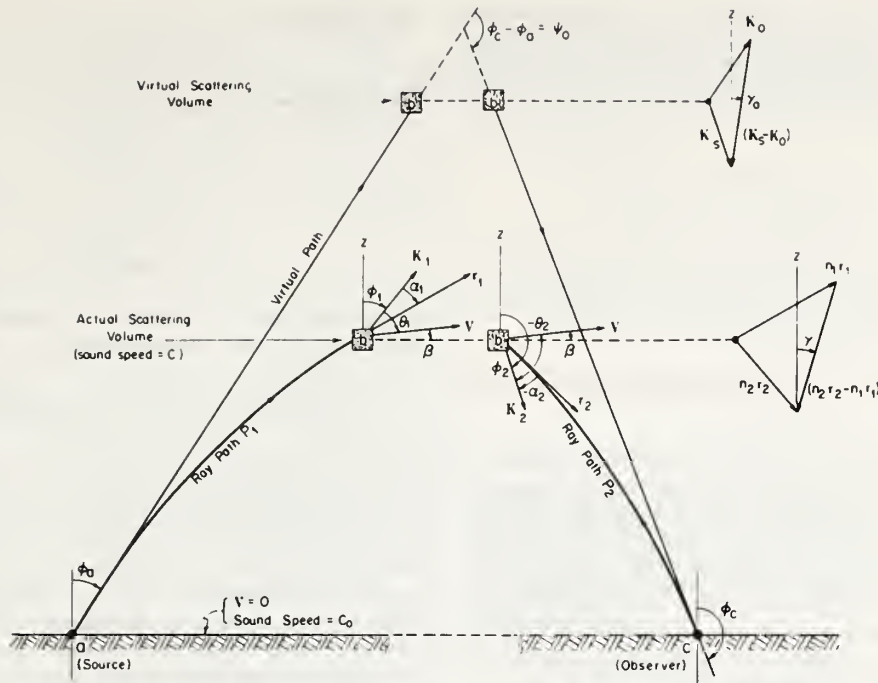


FIG. 1. Geometrical notation for the bistatic scattering of acoustic waves including refraction. The scatterer is shown split in half to illustrate quantities related to the incident wave (left) and to the scattered wave (right). Vectors shown do not in general lie in the plane of the page, but when V does, all do.

II. DOPPLER SHIFT

Fundamentally, Doppler shift (Δf) is the time rate of change of the number of wavelengths along a propagation path (P) between a source and an observer. If \mathbf{K} is the vector wavenumber (its magnitude $k = 2\pi/\text{wavelength}$), and s denotes a vector from an arbitrary origin to the ray point (ds is tangent to the ray path), then

$$-\Delta f = \frac{1}{2\pi} \frac{d}{dt} \left(\int_{P(t)} \mathbf{K} \cdot d\mathbf{s} \right). \quad (1)$$

If the path $P(abc)$ is divided into two parts (which we will denote by subscripts 1 and 2) by the scatterer at point b , and if the points a and c remain fixed, then

$$-2\pi\Delta f = \frac{d}{dt} \int_a^{b(t)} \mathbf{K}_1 \cdot d\mathbf{s}_1 + \frac{d}{dt} \int_{b(t)}^c \mathbf{K}_2 \cdot d\mathbf{s}_2. \quad (2)$$

Taking the differentiation inside the integrals

$$-2\pi\Delta f = \int_a^{b(t)} \frac{d}{dt} (k_1 \cos \alpha_1) ds_1 + \int_{b(t)}^c \frac{d}{dt} (k_2 \cos \alpha_2) ds_2 + \mathbf{K}_1(b) \cdot \hat{\mathbf{r}}_1(b) \frac{db_1}{dt} - \mathbf{K}_2(b) \cdot \hat{\mathbf{r}}_2(b) \frac{db_2}{dt}, \quad (3)$$

where α is the angle between \mathbf{K} and ds , and db_1/dt indicates the component of the motion of the scatterers at point b in the $ds_1(b)$ direction, and $\hat{\mathbf{r}}$ is a unit vector in the ds (ray) direction.

If the medium along the path is time-invariant, the integrals on the right-hand side of Eq. 3 vanish, and Doppler shift depends only on the scatterer motion at point b and the refractive properties of the medium there. Let us temporarily make this assumption and return in Sec. V to examine possible effects of ignoring these integral terms.

To evaluate the remaining terms in Eq. 3, let the scatterers move with the wind at point b , i.e., they have a velocity $V(b)$. Then

$$\frac{db_1}{dt} = V \cdot \hat{\mathbf{r}}_1 \quad (4a)$$

and

$$\frac{db_2}{dt} = V \cdot \hat{\mathbf{r}}_2, \quad (4b)$$

where $\hat{\mathbf{r}}_1$ and $\hat{\mathbf{r}}_2$ are, respectively, unit vectors in the direction of the incident ray at b and along the scattered ray at b that reaches the observer at c .

If we also define a vector refractive index \mathbf{n} whose direction is that of \mathbf{K} and whose magnitude is $C_0 k / 2\pi f_0$, where C_0 is some reference speed, here taken to be the speed of sound at the ground, and f_0 is the transmitted wave frequency, then Eq. 3 becomes

$$\frac{\Delta f}{f_0} = \frac{1}{C_0} [(\mathbf{n}_2 \cdot \hat{\mathbf{r}}_2)(\mathbf{V} \cdot \hat{\mathbf{r}}_2) - (\mathbf{n}_1 \cdot \hat{\mathbf{r}}_1)(\mathbf{V} \cdot \hat{\mathbf{r}}_1)], \quad (5)$$

where \mathbf{n}_1 and \mathbf{n}_2 refer to the refractive indices of the incident and scattered waves at b , respectively. By factoring out the wind vector \mathbf{V} , we can write the Doppler formula in an intuitively useful form:

$$\frac{\Delta f}{f_0} = \frac{\mathbf{V}}{C_0} \cdot [(\mathbf{n}_2 \cdot \hat{\mathbf{r}}_2)\mathbf{r}_2 - (\mathbf{n}_1 \cdot \hat{\mathbf{r}}_1)\mathbf{r}_1]. \quad (6)$$

This shows that the Doppler shift is proportional to the projection of the wind at b onto the bracketed vector, which will be called \mathbf{l} . In the absence of refraction along the ray paths P_1 and P_2 , this vector reduces to the bisector of the angle made by \mathbf{n}_1 and \mathbf{n}_2 , in accordance with simplified analyses that ignore refraction.

We can express Eq. 5 in terms of the wind and sound speed at b and the angles that \mathbf{n}_1 and \mathbf{n}_2 make with the wind at b : To find $(\mathbf{n} \cdot \hat{\mathbf{r}})$ and $(\mathbf{V} \cdot \hat{\mathbf{r}})$, we note that, in general, for a homogeneous flow of \mathbf{V} , \mathbf{n} and \mathbf{r} are related by

$$\mathbf{r} = C\hat{\mathbf{n}} + \mathbf{V}, \quad (7)$$

where the magnitude of \mathbf{r} is the group velocity along the ray⁸ and $\hat{\mathbf{n}}$ is a unit vector along \mathbf{n} . Also, if θ is the angle between \mathbf{n} and \mathbf{V} at b , the angle α between \mathbf{n} and \mathbf{r} is given, to first order in V/C , by

$$\tan \alpha \approx (V/C) \sin \theta, \quad (8)$$

where V is the magnitude of \mathbf{V} , and to the same order,

$$\cos \alpha \approx 1.$$

Therefore, $(\mathbf{n}_1 \cdot \hat{\mathbf{r}}_1) \approx n_1$ and $(\mathbf{n}_2 \cdot \hat{\mathbf{r}}_2) \approx n_2$. Also, if $\hat{\mathbf{V}}$ is a unit vector in the \mathbf{V} direction,

$$(\hat{\mathbf{r}} \cdot \hat{\mathbf{V}}) = \cos(\theta - \alpha) \approx \cos \theta + (V/C) \sin^2 \theta \quad (9)$$

to first order in V/C . So, combining terms, Eq. 5 becomes

$$\frac{\Delta f}{f_0} = \frac{V}{C_0} \left(n_2 \cos \theta_2 - n_1 \cos \theta_1 + \frac{V}{C} (n_2 \sin^2 \theta_2 - n_1 \sin^2 \theta_1) \right), \quad (10)$$

where θ_2 and θ_1 refer to the angles between \mathbf{n}_2 and \mathbf{V} and between \mathbf{n}_1 and \mathbf{V} , respectively.

The value of the refractive index, in terms of local sound speed C and fluid velocity \mathbf{V} , is given by Landau

and Lifshitz⁸ as

$$n = C_0 / (C + \mathbf{V} \cdot \hat{\mathbf{K}}). \quad (11)$$

If $V \ll C$, then n_1 and n_2 can be written as

$$n_1 = \frac{C_0}{C} \left(1 - \frac{V}{C} \cos \theta_1 \right), \quad (11a)$$

$$n_2 = \frac{C_0}{C} \left(1 - \frac{V}{C} \cos \theta_2 \right) \quad (11b)$$

to first order in V/C . Substituting into Eq. 10 and retaining only terms up to second order, we obtain

$$\frac{\Delta f}{f_0} = \frac{V}{C} (\cos \theta_2 - \cos \theta_1) - \frac{2V^2}{C^2} (\cos^2 \theta_2 - \cos^2 \theta_1). \quad (12)$$

Equation 12 shows that (a) Doppler shift is determined only by the wind and sound speed at the scatterer and by the angles of \mathbf{n}_1 and \mathbf{n}_2 (i.e., \mathbf{K}_1 and \mathbf{K}_2) with $\mathbf{V}(b)$; (b) a second-order correction term alters the axis of resolution (i.e., the axis which determines the component of \mathbf{V} that Doppler shift resolves) from the bisector of the angle between \mathbf{n}_1 and \mathbf{n}_2 ; and (c) when $\theta_2 = \theta_1$ no Doppler shift occurs, even to second order. Note that nothing yet has been assumed about the wind or temperature fields along P , except that they are time-invariant, and that the wind speed at b is much smaller than the sound speed.

III. HORIZONTAL STRATIFICATION

The relevant observational problem is to determine the wind \mathbf{V} (or at least its projection onto some axis) having measured Doppler shift over a path whose elevation angles at both ends are known. Therefore, we want an expression for Δf in terms of ϕ_a and ϕ_e rather than θ_1 and θ_2 . In Sec. IV, we will discuss the inversion of the resulting Doppler formula, i.e., how to get \mathbf{V} explicitly in terms of Δf .

Expressing θ_1 and θ_2 in terms of ϕ_a and ϕ_e for arbitrary wind and temperature fields along P is not generally possible analytically, and one usually resorts to numerical techniques (e.g., ray tracing), if the atmosphere cannot be represented by certain simple models. One can, however, model the atmosphere without too great a loss in generality by assuming horizontal stratification, that is, that \mathbf{V} and C are functions only of a vertical coordinate z . In such a model, the angles at the scatterer are related to the angles at the ground by Snell's Law: i.e., $n_1 \sin \phi_1 = \sin \phi_a$; $n_2 \sin \phi_2 = \sin \phi_e$. (It is still necessary, however, to use some kind of ray tracing to calculate the actual ray location, for example, the location of the scattering volume. This will be demonstrated in Sec. VI.) Note that the assumption of horizontal stratification still allows both vertical and horizontal winds as well as wind vectors lying

outside the vertical plane containing points a and c , and even winds whose direction varies with height.

Certain conceptual difficulties arise in the application of Snell's law to horizontally stratified media in which the vertical component of the wind is height-dependent, because air convergence cannot be avoided; however, Snell's law nevertheless appears to be applicable and will be applied to such media, but with the realization that significant vertical gradients of the vertical wind component necessarily violate the assumption of horizontal stratification.

A convenient way to treat the effects of a wind *not* lying in the vertical plane containing the source and observer is to resolve \mathbf{V} into a component \mathbf{u} lying in the plane and a component \mathbf{v} perpendicular to the plane and to treat the contributions of the two components separately. The validity of this type of superposition argument depends on the interaction between the two components in the Doppler formula being negligible. Inspection of Eq. 12 shows that the interaction is entirely by way of changes in the angle θ at the scatterer: If we assume that \mathbf{K} initially lies in the vertical source-observer plane, then it must remain perpendicular to \mathbf{v} up to the scatterer, because of horizontal stratification. Therefore $\mathbf{n}_1 \cdot \mathbf{v} = 0$, and \mathbf{v} cannot contribute to Doppler shift on the up-leg of the path. It does contribute on the down-leg, however. Let θ_2 momentarily represent the angle between \mathbf{n}_2 and \mathbf{u} . The change in θ_2 due to \mathbf{v} is of order v/C , causing second-order changes in $\cos\theta_2$ and third-order changes in Δf . Similar arguments apply to the \mathbf{u} -induced changes in the Doppler shift due to \mathbf{v} . Therefore, we may treat separately the contributions to Δf of \mathbf{v} and \mathbf{u} .

The Doppler shift due entirely to \mathbf{v} can be estimated by assuming that the ray's lateral deviation is small. Then

$$\theta_2 \approx \cos^{-1}(v/C). \quad (13)$$

The Doppler shift due to the perpendicular wind component is therefore v^2/C^2 , by Eq. 12, i.e., entirely second-order. It is important to note, however, that if the total wind blows mainly in the perpendicular direction, its second-order contribution may be comparable to, or even exceed, the first-order contributions of the wind component *in* the plane.

Our problem now is to express Eq. 12 in terms of the source and observer elevation angles for the two-dimensional problem where the wind field \mathbf{V} is horizontally stratified, and remains in the vertical source-observer plane, but possibly has a vertical (upward) component w in addition to a horizontal component u .

The angle of slope of the wind \mathbf{V} will be called β , so that

$$\tan\beta = w/u. \quad (14)$$

The angle \mathbf{K} makes with the vertical will be called ϕ , and subscripts 1 and 2 will refer to the incident and

scattered rays at b , and subscripts a and c denote quantities at the source and observer.

If we assume that, at the scatterer, $V \ll C_0$, $\phi_1 = \phi_a + \Delta\phi_1$, $\Delta\phi_1 \ll \phi_a$, and $C = C_0 + \Delta C$, $\Delta C \ll C_0$, then the following relations may be established, to first order in V/C_0 and $\Delta C/C_0$:

$$n_1 = \frac{C_0}{C} \left(1 - \frac{V}{C_0} \sin(\beta + \phi_a) \right), \quad (15)$$

$$\Delta\phi_1 = \phi_1 - \phi_a = \tan\phi_a \left(\frac{\Delta C}{C_0} + \frac{V}{C_0} \sin(\beta + \phi_a) \right), \quad (16)$$

$$\cos\phi_1 = \cos\phi_a - \sin\phi_a \tan\phi_a \left(\frac{\Delta C}{C_0} + \frac{V}{C_0} \sin(\beta + \phi_a) \right), \quad (17)$$

$$\alpha_1 = (V/C_0) \cos(\beta + \phi_a). \quad (18)$$

Identical relations hold for the scattered ray, i.e., if subscript 2 is substituted for 1 and c for a . Using these relations, the geometry of Fig. 1, and Eq. 6, we can calculate the x and z components of the axis of wind resolution \mathbf{l} from which other quantities of interest can be readily derived:

$$\begin{aligned} l_z &= n_2 \sin(\phi_2 + \alpha_2) - n_1 \sin(\phi_1 + \alpha_1) \\ &= (\sin\phi_c - \sin\phi_a) + (V/C_0) F_z(\beta, \phi_c, \phi_a), \end{aligned} \quad (19)$$

where

$$F_z \equiv \cos(\beta + \phi_c) \cos\phi_c - \cos(\beta + \phi_a) \cos\phi_a, \quad (20)$$

and

$$\begin{aligned} l_x &= n_2 \cos(\phi_2 + \alpha_2) - n_1 \cos(\phi_1 + \alpha_1) \\ &= (\cos\phi_c - \cos\phi_a) - (\Delta C/C_0) (\sec\phi_c - \sec\phi_a) \\ &\quad - (V/C_0) F_x(\beta, \phi_c, \phi_a), \end{aligned} \quad (21)$$

where

$$\begin{aligned} F_x &\equiv \cos(\beta + \phi_c) \sin\phi_c - \cos(\beta + \phi_a) \sin\phi_a \\ &\quad + \cos\beta (\tan\phi_c - \tan\phi_a). \end{aligned} \quad (22)$$

The Doppler shift is then obtained by substituting l_z and l_x into

$$C_0(\Delta f/f_0) = ul_z + wl_x, \quad (23)$$

yielding

$$\begin{aligned} \Delta f &= \frac{1}{2\pi} (\mathbf{K}_s - \mathbf{K}_0) \cdot \mathbf{V} + f_0 \left(\frac{V^2}{C_0^2} (F_z \cos\beta - F_x \sin\beta) \right. \\ &\quad \left. - \frac{V}{C_0} \frac{\Delta C}{C_0} \sin\beta (\sec\phi_c - \sec\phi_a) \right), \end{aligned} \quad (24)$$

where

$$\mathbf{K}_s \equiv (2\pi f_0/C_0) (\sin\phi_c \hat{\mathbf{x}} + \cos\phi_c \hat{\mathbf{z}}), \quad (25a)$$

and

$$\mathbf{K}_0 \equiv (2\pi f_0 / C_0)(\sin\phi_0 \hat{x} + \cos\phi_0 \hat{z}). \quad (25b)$$

The first term on the right-hand side of Eq. 24 is the usual nonrefractive Doppler shift.⁵ To be completely general, Eq. 24 should also contain a term $f_0 v^2 / C_0^2$ to reflect the contribution of a wind component v perpendicular to the vertical source-observer plane (see Eqs. 12 and 13). Equation 24 simplifies considerably if the vertical and perpendicular wind components are negligible:

$$\Delta f = \frac{1}{2\pi} (\mathbf{K}_s - \mathbf{K}_0) \cdot \mathbf{V} + f_0 \frac{u^2}{C_0^2} (\cos^2\phi_c - \cos^2\phi_a) \quad (26)$$

or, expressed another way,

$$\frac{\Delta f}{f_0} = \frac{u}{C_0} (\sin\phi_c - \sin\phi_a) - \frac{u^2}{C_0^2} (\sin^2\phi_c - \sin^2\phi_a). \quad (27)$$

Note that Δf no longer depends on ΔC when $\beta = 0$. If, in addition, $\phi_a = 0$, the Doppler formula reduces to the particularly simple form obtained by Beran and Clifford⁴:

$$\frac{\Delta f}{f_0} = \frac{u}{C_0} \sin\phi_c - \left(\frac{u}{C_0} \sin\phi_c \right)^2. \quad (28)$$

The orientation of the axis l upon which \mathbf{V} is projected by Doppler measurements is given in general by

$$\tan\gamma = l_z / l_s, \quad (29)$$

and its value in the absence of refraction is, from the geometry of Fig. 1,

$$\gamma_0 = (\phi_c + \phi_a - \pi) / 2. \quad (30)$$

The departure of γ from γ_0 is

$$\Delta\gamma = \gamma - \gamma_0 \ll \gamma_0, \quad (31)$$

and, to first order in $\Delta\gamma / \gamma_0$

$$\begin{aligned} \Delta\gamma &= \cos^2\gamma_0 (\tan\gamma - \tan\gamma_0) \\ &= \cos^2\gamma_0 (l_z / l_s - \tan\gamma_0), \end{aligned} \quad (32)$$

which, after substitution of Eqs. 19, 21, and 30 and considerable manipulation, becomes

$$\begin{aligned} \Delta\gamma &= \frac{\Delta C}{2C_0} (\tan\phi_c + \tan\phi_a) + \frac{V}{2C_0} \\ &\times [\cos(\beta + \phi_a) + \cos(\beta + \phi_c) + \cos\beta (\sec\phi_c + \sec\phi_a)]. \end{aligned} \quad (33)$$

In the special case where $\beta = 0$ and $\phi_a = 0$, Eq. 33 reduces to the form given by Beran and Clifford⁴:

$$\Delta\gamma = \frac{\Delta C}{2C_0} \tan\phi_c + \frac{u}{2C_0} (\cos\phi_c + \sec\phi_c + 2). \quad (34)$$

Equations 24 and 33 are the desired general formulas for Doppler shift and change in the axis of wind resolution.

In the absence of refraction, the scattering angle $\Psi_0 = \phi_c - \phi_a$, while under the influence of refraction, it changes to $\Psi = \phi_2 - \phi_1$. The change in scattering angle is thus $\Delta\Psi = \Psi - \Psi_0 = \Delta\phi_2 - \Delta\phi_1$, where $\Delta\phi$ is of the form given by Eq. 16. Note that $\Delta\Psi$ does not in general equal $2\Delta\gamma$, so that the axis of wind resolution does not bisect the angle formed by \mathbf{K}_1 and \mathbf{K}_2 at b . Furthermore, because monostatic sounding in a windy atmosphere does not in general yield $\Psi = \pi$ (backscatter), it is not generally possible to make the usual assumption¹ that wind eddies do not contribute to the monostatic scattering cross section. Clifford and Brown⁹ treat this problem in detail.

IV. INVERSION OF THE DOPPLER FORMULA AND THE NEED FOR MULTIPLE SOUNDINGS

If we write the Doppler Equation 24 in the form

$$A_i(\phi_a^i, \phi_c^i, \beta) \left(\frac{V}{C_0} \right)^2 + B_i(\phi_a^i, \phi_c^i, \beta, \Delta C) \left(\frac{V}{C_0} \right) + \left(\frac{\Delta f}{f_0} \right)_i = 0, \quad (35)$$

where the subscript or superscript i indicates a particular sounding geometry, then we can invert the system Eq. 35 to give

$$\frac{1}{B_i} \left(\frac{\Delta f}{f_0} \right)_i + \frac{A_i}{B_i^2} \left(\frac{\Delta f}{f_0} \right)_i^2 + \frac{V}{C_0} = 0, \quad (36)$$

to second order in $\Delta f / f_0$. This system involves four unknowns, V , and ΔC , and so requires four independent sounding geometries. If we assume that the four geometries all sound the same volume, then we should be able to solve the system Eq. 36 for V and ΔC . It must be recognized, however, that the ability to measure $\Delta C / C_0$ using Doppler shift depends on the presence of a vertical wind component.

It turns out that the coefficients A_i and B_i are quite unwieldy even for simple geometries, so that an analytical solution of the system Eq. 36 for ΔC and V does not appear feasible. Numerical methods should yield satisfactory results, however.

A convenient sounding geometry would use three sounders located at the vertices of a right triangle on the ground; the sounding paths would form a tetrahedron with a vertical side rising from the right angle.⁴ The apex of the tetrahedron represents the scattering volume, which could slide up and down the vertical side as the elevation angles of the other two sounders vary. Each sounder could monitor both monostatic and bistatic scattering, providing as many as nine independent sounding paths.

V. THE ROLE OF TIME-VARYING MEDIA

We now return to consider the integral terms in Eq. 3 that represent contributions to Doppler shift from temporal variations of the refractive index all along the sounding path. We want to find out if realistic temperature or wind changes along the path can ever cause significant Doppler shifts, compared to those caused by motions of the scatterers in the sounding volume.

Retaining only the integral terms, Eq. 3 can be rewritten, to first order in V/C , as

$$-C_0 \frac{\Delta f}{f_0} = \int_P \frac{d}{dt} \left(\frac{C_0}{C} \right) ds - \int_P \frac{d}{dt} \left(\frac{V}{C_0} \cos \theta \right) ds. \quad (37)$$

If we denote by angular brackets and the subscript av the average of a quantity over the sounding path, e.g.,

$$\left\langle \frac{d}{dt} \left(\frac{1}{C} \right) \right\rangle_{av} = \left\langle -\frac{1}{C^2} \frac{dC}{dt} \right\rangle_{av} = -\frac{1}{P} \int_P \frac{1}{C^2} \frac{dC}{dt} ds, \quad (38)$$

and

$$\left\langle \frac{d}{dt} (V \cos \theta_1) \right\rangle_{av} = \frac{1}{P_1} \int_{P_1} \frac{d}{dt} (V \cos \theta_1) ds_1, \quad (39)$$

then Eq. 37 becomes

$$\frac{\Delta f}{f_0} = \left\langle \frac{1}{C^2} \frac{dC}{dt} \right\rangle_{av} P + \frac{P_1}{C_0^2} \left\langle \frac{d}{dt} (V \cos \theta_1) \right\rangle_{av} + \frac{P_2}{C_0^2} \left\langle \frac{d}{dt} (V \cos \theta_2) \right\rangle_{av}. \quad (40)$$

Now compare the first term on the right-hand side of Eq. 40 with the first-order Doppler shift in Eq. 28, representing the case $\beta=0$, $\phi_c=0$, and ask what value of $\langle dC/dt \rangle_{av}$ would produce a Doppler shift equal to that of a horizontal wind u at the scatterer. We thus find that

$$\left\langle \frac{1}{C^2} \frac{dC}{dt} \right\rangle_{av} = \frac{u}{CP} \sin \phi_c. \quad (41)$$

If we let $u=10$ m/sec, $P=2$ km, $\phi_c=3\pi/4$, and C be relatively constant over the path, then

$$\left\langle \frac{1}{C} \frac{dC}{dt} \right\rangle_{av} \simeq 0.0035, \quad (42)$$

which is equivalent to an average relative temperature change of

$$\left\langle \frac{1}{T} \frac{dT}{dt} \right\rangle_{av} \simeq 0.007. \quad (43)$$

Under standard conditions, this represents an average rate of temperature change along the path of about 2°K/sec .

A similar comparison of the velocity terms in Eq. 40 yields

$$P_1 \left\langle \frac{d}{dt} (V \cos \theta_1) \right\rangle_{av} + P_2 \left\langle \frac{d}{dt} (V \cos \theta_2) \right\rangle_{av} = u C_0 \sin \phi_c. \quad (44)$$

Using the same geometry as before and making the approximations

$$\theta_1 \simeq \pi/2, \quad \theta_2 = \pi/2 = \phi_c = -\pi/4, \quad \text{and} \quad P_2 \simeq 1.17 \text{ km},$$

and letting $C_0=340$ m/sec,

$$\langle dV/dt \rangle_{av} \simeq 3 \text{ m/sec}^2. \quad (45)$$

For a purely monostatic sounding geometry

$$-P_1 \langle \cos \theta_1 \rangle_{av} \simeq P_2 \langle \cos \theta_2 \rangle_{av} \quad (46)$$

and the effects of dV/dt on Doppler shift are negligible.

Such high values of average wind or temperature changes would be expected only rarely, so that motions within the scattering volume would almost always dominate in determining the Doppler shift measured with present instruments within the atmospheric boundary layer. However, as sounding height increases with sounder development, Doppler shift becomes more sensitive to integrated refractive index changes. Furthermore, integrated changes may not be negligible in the analysis of soundings taken during the passage of the frontal discontinuities or large atmospheric waves upon which attention is often focused.

VI. DISPLACEMENT OF THE SCATTERING VOLUME

It is important to know the refractive displacement of the scattering volume from its virtual location (Fig. 1), because it is to the displaced location that the Doppler wind and temperature measurements refer. In this section, we want to see if we can provide a basis for estimating the magnitude of the vertical and horizontal displacements of the scattering volume to be expected in real wind and temperature fields.

The location of the scattering volume is determined by the intersection of two ray paths: one which leaves the source at a prescribed elevation angle, and another, which leaves a point along the upgoing ray and arrives at the observer at a prescribed angle. The size of the scattering volume is determined by the source and observer antenna beam widths. If propagation is reciprocal (i.e., no winds are present), the second ray path is identical to the one leaving the observer at its

"look angle," greatly facilitating the location of the scattering volume.

In the presence of winds, then, analysis can proceed in two directions: either to seek analytical solutions for the ray path intersections for certain simple wind fields, or to use very general numerical ray tracing techniques in iterative searching schemes. We now pursue the first alternative; ways of implementing the second will be indicated at the end of this section.

Ugincius¹⁰ (his Eq. 24) gives a formula for ray curvature κ , accurate to first order in u/C , in the presence of wind and sound-speed gradients in the z direction only. In our notation, it is

$$-\kappa = \left(\sin\phi - 2\frac{u}{C} \right) \left(\frac{1}{C} \frac{dC}{dz} \right) + \left(1 - 2\frac{u}{C} \sin\phi \right) \left(\frac{1}{C} \frac{du}{dz} \right). \quad (47)$$

Wind and sound-speed gradients thus act together in a complicated way to refract acoustic rays. However, we can derive relations that allow us to estimate scattering-volume displacement if we consider separately two further specialized cases: (a) no winds, linear sound-speed gradient, and (b) constant sound speed, linear wind-speed gradient.

In case (a), Eq. 47 reduces to

$$-\kappa = \sin\phi \left(\frac{1}{C} \frac{dC}{dz} \right), \quad (48)$$

which becomes, with the aid of Snell's law,

$$-\kappa = \sin\phi_a \left(\frac{1}{C_0} \frac{dC}{dz} \right) \equiv G \sin\phi_a, \quad (49)$$

which defines G . This is an expression of the well-known result that acoustic ray paths in a horizontally stratified medium with a linear sound-speed gradient are *circular arcs* whose centers of curvature lie at a height where the sound speed would (if extrapolated) equal zero.¹¹ It is thus a simple matter to calculate analytically (or construct graphically) acoustic ray paths in plane-stratified atmospheres whose sound-speed profiles can be approximated by linear segments.

The location of the ray-path intersection that defines the scattering volume can be calculated analytically by finding the intersection of two circular arcs. Such an analysis reveals that the x displacement, relative to the coordinate x_0 of the virtual intersection is

$$\Delta x = -GSd^2/2D(D+Gd), \quad (50)$$

with positive values indicating displacement toward the observer. Here $S \equiv \cot\phi_e + \cot\phi_a$, $D \equiv \cot\phi_e - \cot\phi_a$, and d is the horizontal separation of the points where

the rays P_1 and P_2 enter and leave the layer (e.g., the source-observer separation).

The vertical displacement of the intersection (positive upward) is

$$\Delta z \approx \Delta x \cot\phi_a - Gx^2/2 \quad (51)$$

provided $z \ll 1/G$. In the case of a symmetrical path ($\phi_a = \pi - \phi_e$), $\Delta x = 0$, and

$$\Delta z \approx -Gd^2/8. \quad (52)$$

When $\phi_e = \pi$ (or $\phi_a = 0$, by symmetry)

$$\Delta z \approx -Gd^2/2. \quad (53)$$

For case (b), i.e., an isothermal atmosphere with a constant wind shear, Eq. 47 becomes

$$-\kappa = \left(1 - 2\frac{u}{C} \sin\phi \right) \frac{1}{C} \frac{du}{dz} \approx \frac{1}{C} \frac{du}{dz} \equiv H, \quad u \ll C, \quad (54)$$

which defines H . Thus, acoustic ray paths in a constant wind shear have a nearly constant curvature as long as $u \ll C$.¹² For example, rays emanating from a point source have a spiral or "pinwheel" appearance, with all rays curving in the same sense one expects intuitively by considering the "twisting" effect of $\nabla \times \mathbf{V}$. It is important to note that, according to Eq. 54, the ray curvature in a given wind shear is always in the same sense, regardless of ray orientation, while in a sound-speed gradient, the sense of curvature depends on the sign of ϕ , according to Eq. 48, i.e., rays always curve away from the direction of increasing sound speed.

If we ignore, for cases in which $u \ll C$, the small deviation α between \mathbf{K} and the ray tangent (see Eqs. 7 and 8), ray intersection can be estimated by again computing the intersection of appropriate circular arcs. A simple approximate graphical construction is possible for acoustic ray paths in a constant wind shear: the radius of the circular ray path equals the height over which the wind speed (if extrapolated) would increase from zero to the sound speed; the circle's origin lies along a straight line through the source and perpendicular to the ray-launch direction. The two possible centers (and senses of curvature) correspond to the two opposite propagation directions through the source, and the choice is made with the knowledge of the proper sense of ray curvature for the given wind-shear profile. An identical construction serves for the ray through the observer, permitting a simple determination of the ray intersection.

The intersection of the two circular arcs can be calculated analytically using the same construction; the details of this interesting problem in analytic geometry are left to the reader. The x and z displace-

ments are given by

$$\Delta x = [H/2 \sin(\phi_e - \phi_a)] \{ (x_0^2 + z_0^2) \sin \phi_e - [(x_0 - d)^2 + z_0^2] \sin \phi_a \}, \quad (55)$$

$$\Delta z = [H/2 \sin(\phi_e - \phi_a)] \{ (x_0^2 + z_0^2) \cos \phi_e - [(x_0 - d)^2 + z_0^2] \cos \phi_a \}, \quad (56)$$

to first order in $H\Delta x$ and $H\Delta z$. In the case $\phi_a = 0$ (one sounding path vertical) the displacements reduce to

$$\Delta x = Hd^2/2 \tan^2 \phi_e, \quad (57)$$

$$\Delta z = Hd^2/2 \tan^3 \phi_e. \quad (58)$$

The coordinates of the intersection of the straight-line ray paths (corresponding to the limit $H \rightarrow 0$ or to $G \rightarrow 0$ in the sound-speed gradient case) are

$$x_0 = \frac{d \tan \phi_a}{\tan \phi_a - \tan \phi_e}, \quad (59)$$

$$z_0 = \frac{d}{\tan \phi_a - \tan \phi_e}. \quad (60)$$

Within the same order of approximation, rays under the influence of *both* linear wind and sound-speed profiles are still circular, with a net ray curvature of

$$-\kappa = G \sin \phi_a + H. \quad (61)$$

Clearly, the refractive effects of wind shear and sound-speed gradients can either reinforce or cancel each other. For example, in the case $\phi_e = \pi - \phi_a$ (a symmetrical path) the ray path in a linear wind gradient of H is identical to the ray path in a linear sound-speed gradient of $G = H/\sin \phi_a$.

Ray geometries in more complicated model atmospheres (e.g., those with three-dimensional wind and temperature variability) are readily calculated numerically with digital-computer ray-tracing programs.¹³ If refractive effects are believed small, the downcoming ray path and the location of the scattering volume can be approximately obtained with a ray-tracing program as follows: Using the intersection of the upgoing ray and the *virtual* scattering height as a source, calculate downgoing ray paths in a narrow fan of elevation angles likely to reach the ground at the required elevation angle. Select the ray that actually arrives at (or near) the required elevation angle and shift that ray parallel to the ground until it intersects the observer location. The intersection of that (shifted) ray (extended slightly, if necessary) with the upgoing ray gives the approximate location of the common volume. Further refinements, if required, can be obtained by iterating this procedure, using each new crossing point as an initial scattered-ray source. A simple alternative procedure for, in effect, tracing rays backward in time would be to define a "complementary refractive index," in which the sense of the wind vector is reversed.

Definition of a common volume is occasionally blurred by the proximity of upgoing and downcoming rays, in view of the finite dimensions of real sounding beams. One such case is that of a monostatic sounding: another arises in bistatic soundings made upwind, where a wind shear can cause upgoing and downcoming rays to intersect in more than one location. In such cases gating the echo in delay time appears to be necessary to provide adequate height resolution. Refractive corrections are then needed to convert travel time to distance along the ray path.

VII. ANGLE OF ARRIVAL IN MONOSTATIC SOUNDINGS

Mahoney *et al.* have recently suggested that one can determine wind profiles by measuring the angle of arrival of the scattered energy as a function of delay time in a vertical monostatic sounding. The dependence of angle of arrival on the wind field is difficult to calculate in general because it requires knowledge of the ray path. Furthermore, the angle depends on the temperature field as well. However, if we consider an isothermal atmosphere with $V = u(z)$, a useful estimate of the relationship can be made as follows: Equate the ground range X of a ray launched vertically in the wind field $u(z)$ with that of a ray launched at an angle ϕ_e with the vertical, in a wind field $-u(z)$, and solve for ϕ_e (reversing the wind direction allows us to "retrace" the scattered ray). Mathematically, to first order in u/C ,

$$X = \int_0^Z \phi dz = \int_0^Z \left(\int_0^z -\kappa dz' + \phi_e \right) dz = \int_0^Z \int_0^z \kappa dz' dz, \quad (62)$$

where Z is the scattering height and κ is the ray curvature of Eq. 54. We can solve for ϕ_e by defining

$$\bar{u}(Z) \equiv \frac{1}{Z} \int_0^Z u(z) dz, \quad (63)$$

which is the average value of the wind up to height Z . The arrival angle is then

$$\phi_e(Z) = 2\bar{u}(Z)/C. \quad (64)$$

Thus, if temperature gradients can be neglected, one could determine $\bar{u}(Z)$ if $\phi_e(Z)$ can be measured by delay-time gating. Then $u(Z)$ could be determined from $\bar{u}(Z)$ by a suitable inversion process.

If the wind azimuth is essentially constant up to Z , the azimuth of arrival indicates the wind azimuth. If wind azimuth varies with height, the azimuth of arrival gives approximately the average wind direction up to Z , but an exact analysis is not straightforward.

VIII. SUMMARY

The refractive correction to the magnitude of the Doppler shift is given in general by Eq. 24 and in certain special cases by simpler forms, Eqs. 26 and 28. The correction appears to be small (i.e., second-order) and is probably negligible under conditions in which acoustic sounders presently operate.

Refraction causes first-order changes in the scattering angle (Eq. 16) and in the direction upon which the wind vector is projected by Doppler measurements (Eq. 33). The axis no longer bisects the scattering angle when winds introduce anisotropy into the refractive index. Refractive corrections to the scattering angle may be required in measurements that depend critically on the attainment of a particular scattering angle.

Doppler measurements also respond to changes in refractive index caused by net wind or temperature changes along the sounding path as indicated by Eq. 3. For present sounding geometries, Doppler shift produced by motions at the scatterer appear to dominate over realistic integrated wind or temperature changes. This may not be true as sounding heights increase, however.

Refraction also displaces the atmospheric volume interrogated by acoustic sounders. Present soundings in the atmospheric boundary layer may suffer displacements of a few percent at most, but soundings to greater altitudes could encounter appreciable displacements. In extreme cases, refraction can make certain parts of the atmosphere inaccessible to acoustic sounding. Refractive displacements can be estimated in model atmospheres with linear sound-speed or wind gradients because the ray paths are circular.

Angle of arrival in monostatic vertical soundings can indicate average wind up to the scattering height.

Acoustic Doppler sounding to much greater atmospheric heights, using lower acoustic frequencies, does not appear to pose any fundamental problems.

¹ C. G. Little, "Acoustic Methods for the Remote Probing of the Lower Atmosphere," *Proc. IEEE* **57**, 571-578 (1969).

² L. G. McAllister, J. R. Pollard, A. R. Mahoney, and P. J. R. Shaw, "Acoustic Sounding—A New Approach to the Study of Atmospheric Structure," *Proc. IEEE* **57**, 579-587 (1969).

³ D. W. Beran, C. G. Little, and B. C. Willmarth, "Acoustic Doppler Measurements of Vertical Velocities in the Atmosphere," *Nature* **230**, 160-162 (1971).

⁴ D. W. Beran and S. F. Clifford, "Acoustic Doppler Measurements of the Total Wind Vector," *Proc. AMS Acoust. Symposium on Meteorological Observations and Instrumentation*, San Diego, Calif., 1972.

⁵ J. C. Owens, "Optical Doppler Measurement of Microscale Wind Velocity," *Proc. IEEE* **57**, 530-536 (1969).

⁶ T. A. Croft, "Discussion of paper by V. Agy, 'Doppler Shifts on High-Frequency Ground Backscatter,'" *J. Geophys. Res.* **74**, 3058-3063 (1969).

⁷ T. A. Croft, "Skywave Backscatter: A Means for Observing Our Environment at Great Distances," *Rev. Geophys. Space Phys.* **10**, 73-155 (1972).

⁸ L. D. Landau and E. M. Lifshitz, *Fluid Mechanics* (Pergamon, Oxford, 1959), pp. 256 ff.

⁹ S. F. Clifford and E. H. Brown, "Turbulent Scattering Cross-Sections in a Moving Fluid" (unpublished).

¹⁰ P. Ugincius, "Acoustic Ray Equations for a Moving, Inhomogeneous Medium," *J. Acoust. Soc. Amer.* **37**, 476-479 (1965).

¹¹ C. B. Officer, *Introduction to the Theory of Sound Transmission with Application to the Ocean* (McGraw-Hill, New York, 1958).

¹² U. Ingard, "A Review of the Influence of Meteorological Conditions on Sound Propagation," *J. Acoust. Soc. Amer.* **25**, 405-411 (1953).

¹³ T. M. Georges, "A Program for Calculating Three-dimensional Acoustic-Gravity Ray Paths in the Atmosphere," NOAA Technical Rep. ERL 212-WPL 16 (US GPO, Washington, D. C., 1971).

¹⁴ A. R. Mahoney, L. G. McAllister, and J. R. Pollard, "The Remote Sensing of Wind Velocity in the Lower Troposphere Using an Acoustic Sounder," *Proc. 1972 IUCRM Colloquium on Waves and Turbulence in Stratified Layers*, San Diego, Calif. (1972).

NU-AVERAGED INFRARED ABSORPTION
COEFFICIENTS OF WATER VAPOR

R. F. Calfee and R. L. Schwiesow

We report the quantitative absorption coefficients of water vapor in a format suitable for calculation of water vapor absorption spectra characterized by instrumental band-passes of 1 cm^{-1} or greater in the 670 to 1450 cm^{-1} region. These coefficients are derived from individual line parameters of H_2O and represent a useful way of reducing line parameter data to a practical volume of information for 1 cm^{-1} resolution spectra of the troposphere. Transmission spectra for three water vapor concentrations show typical applications of the absorption coefficient tables. The application of the data is restricted to conditions within 10% of 1 atmosphere pressure and a temperature of 296 K if a transmission accuracy of 2% is to be maintained.

Relative Raman cross section of O_3 for four Ar^+ laser frequencies*

R. L. Schwiesow and N. L. Abshire

Wave Propagation Laboratory, ERL/NOAA, Boulder, Colorado 80302
(Received 8 March 1973)

We have measured the relative Raman scattering cross sections of O_3 (referred to N_2) and the depolarization ratios at four argon-ion laser pump frequencies to be, respectively, 2.3 and 0.05 at 20 981 cm^{-1} , 2.5 and 0.03 at 20 487 cm^{-1} , 2.8 and 0.04 at 20 135 cm^{-1} , and 2.2 and 0.10 at 19 430 cm^{-1} . The estimated uncertainty in cross section is $\pm 12\%$ and in depolarization, ± 0.01 , although the cross sections at different frequencies are thought to intercompare to $\pm 5\%$ or less. An improved sample preparation technique was used. We found no dependence of cross section on pressure and only weak evidence for any resonance dependence on pump frequency.

A recent letter by Fouche and Chang¹ reported the Raman scattering cross section of O_3 , relative to that of N_2 , for an incident laser frequency of 19 430 cm^{-1} (5145 Å) without analysis of polarization effects. We have studied O_3 scattering for four different laser pump frequencies, with complete polarization analysis and with a sample measuring technique based on scattering and pressure measurement rather than ultraviolet absorption.

The obvious application of laser Raman scattering to air pollution and other remote real-time gas-composition analyses for atmospheric studies is well known. Additional impetus for the work is based on the possibility for resonance cross-section effects because of the Chappuis absorption bands²⁻⁴ in the visible. Reliable values for the Raman scattering cross section of O_3 are important for gas analysis, resonance enhancement, and many other studies. Our results differ significantly from the previous results for relative cross section.

The Raman spectrum of O_3 given by Selig and Claassen⁵ indicates ν_1 and ν_2 fundamentals at Raman shifts of 1103.3 and 702.1 cm^{-1} , respectively. These frequencies are consistent with our measurements. Since the ν_1 band is significantly stronger than ν_2 , we have measured the cross section of the 1103.3- cm^{-1} band only. The relative Raman cross-section values reported here are referenced to the scattering cross section, per molecule, of N_2 for the same laser pump without a ν^4 correction. To convert these O_3 values to absolute scattering cross sections, the N_2 data of Penney, Goldman, and Lapp⁶ should be used. The reported depolarization ratios are in the same notation as that of Murphy *et al.*,⁷ who give $\rho = 0.055$ for N_2 from an analysis of earlier data.⁸

Details of the data collection and analysis techniques used in our laboratory for Raman cross-section measurements of fluids will be presented in a subsequent report. Ozone sample preparation and measurement methods are important to the present discussion, however. The O_3 used for these measurements was prepared in the sample cell by a modification of the silent electric discharge technique⁹ in a cell similar to that of Zaslowsky *et al.*¹⁰ A cylindrical sample cell shown schematically in Fig. 1 is 5 cm in diameter by 7 cm long. It is fitted with a 5-cm quartz window for collecting the scattered light along the cell axis and with two 1.5-cm quartz windows for passing the incident laser beam perpendicular to the cell axis. Scattering is measured at right angles to the incident laser beam. The vacuum envelope of a Dewar, which is perpendicular to

and above the cell axis, communicates with the cell volume, as does a freeze tip below and also perpendicular to the cell axis. Foil electrodes on the inner and outer walls of the Dewar are connected to a 12-kV transformer. The cell generator is connected to a high-vacuum gas-filling station through a halocarbon-greased stop cock. The critical parameter in the system is the ratio of N_2 pressure, with the freeze tip immersed to a fixed level in liquid nitrogen, to the pressure when the entire system is at ambient temperature. This ratio was determined to a reproducibility uncertainty of 2% for the cell used in these measurements.

To prepare a sample, the cell generator is filled to a known pressure of pure O_2 and sealed off. After filling the top Dewar and cooling the freeze tip, essentially all O_2 is converted to O_3 by the silent discharge. The Dewar is warmed to the ambient temperature while the freeze tip, immersed to the predetermined level in liquid nitrogen, collects all O_3 . The system is then filled with N_2 and sealed off. Although some conversion of O_3 to O_2 occurs, both the partial pressure of N_2 and the total

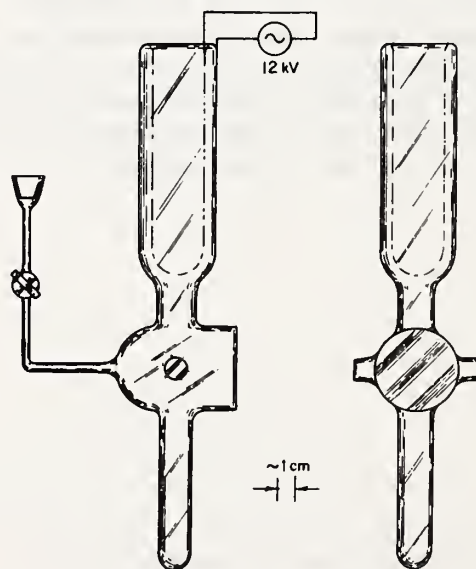


FIG. 1. Cell used for generation of O_3 and measurement of Raman scattering cross section of O_3 relative to that of N_2 .

TABLE I. Relative Raman scattering cross section of O₃.

| Incident laser (cm ⁻¹) | Relative cross section (± 12%) | Depolarization (± 0.01) |
|---------------------------------------|--------------------------------------|----------------------------|
| 20 891 | 2.3 | 0.05 |
| 20 487 | 2.5 | 0.03 |
| 20 135 | 2.8 | 0.04 |
| 19 430 | 2.2 | 0.10 |

number of O atoms in the sample are accurately known. In practice, partial pressures of O₃, approximately 400 Torr, and N₂, approximately 350 Torr, were used. Compared to the previous quantitative work,¹ the cell-generator technique has the advantage of (i) larger O₃ pressures for increased spectroradiometric accuracy, (ii) simultaneous presence of O₃ and the N₂ cross-section reference gas in the cell, and (iii) O₃ concentration deduced from pressure and Raman measurements only, without involving additional apparatus or measured (absorption) parameters.

A sampling sequence for each laser pump frequency and polarization includes measurements of the integrated Q-branch Raman scattering intensity for N₂, O₂, O₃, O₂, and N₂. Assuming an O₂ relative cross section⁶ of 1.20 and averaging the two N₂ and O₂ values, one can determine (i) the partial pressure of O₂ and therefore O₃ and (ii) the relative scattering intensity and hence the cross section of O₃. Of course, the instrument quantum efficiency as a function of frequency and polarization must be accurately known. The ratio of O₃ to N₂ cross section is based on actual pressure ratios and signal strength ratios. Results of these measurements are given in Table I. The uncertainty estimates include uncertainty in N₂ pressure (2%), O₃ pressure (4%), relative quantum efficiency determinations (2%), and relative intensity measurements (2%). The uncertainty in depolarization and an additional 2% in cross section arise principally from the necessary solid-angle corrections to the raw data.

The total sample pressure was intentionally kept near 1 atm to reproduce any pressure quenching effects on possible O₃ fluorescence. We observed no cross-section dependence on ozone or buffer gas pressure within experimental uncertainty for pressures as low as 250 Torr, and therefore, no fluorescence contribution, either broad band or sharp, exists for the O₃ scattering in this region. While no striking resonance effects were observed, the data show significant frequency dependence. The cross sections in Table I intercompare to 5% uncertainty since the same sample was used in the determinations. The Chappuis bands exhibit an increasing absorption coefficient from approximately 23 000 to

17 000 cm⁻¹, but with local slope reversals and structure. The data show a generally increasing trend with lower pump frequencies consistent with the resonance notion that larger Raman cross sections are associated with larger absorption coefficients. A smaller scattering cross section for the lowest-frequency 19 430-cm⁻¹ pump indicates that (i) obviously the relationship between cross section and absorption coefficient is not simple, and (ii) the O₃ absorption must be known in high resolution near the laser emission lines if a detailed test of resonance and preresonance Raman scattering relationships is to be made from these Raman cross-section results.

Our results are not within experimental uncertainty of the previously reported value of 4.0 (without an uncertainty estimate) for the relative Raman cross section of O₃. The difference of approximately 80% between these two values may be the result of differences in sample measurement techniques, which were previously discussed, or in achieved signal-to-noise ratios. In this experiment, the laser power of 1 W was larger by a factor of 3 and the sample concentration was larger by approximately a factor of 10 than in the previous study, which implies a 5 or 6 times better signal-to-noise ratio. If one assigns a 50% uncertainty, which may be reasonable in view of a laser signal-to-noise ratio and ultraviolet absorption coefficient uncertainty, to the early work, the results of the two studies are indeed consistent.

We have measured the relative O₃:N₂ Raman scattering cross section and the depolarization for O₃ scattering at four of the strongest argon-ion laser frequencies. These data should be useful for calibrating remote gas-composition sensors and for studying resonance scattering effects. No pressure effects were noted. No obvious resonance effects were observed. A useful extension of this work would be to use krypton-ion laser pump frequencies closer to the peak of the Chappuis absorption bands.

*Work supported in part by NASA-MSC, Houston, Tex.

¹D. G. Fouche and R. K. Chang, Appl. Phys. Lett. 20, 256 (1972).

²E. C. Y. Inn and Y. Tanaka, J. Opt. Soc. Am. 43, 870 (1953).

³A. G. Hearn, Proc. Phys. Soc. Lond. 78, 932 (1961).

⁴M. Griggs, J. Chem. Phys. 49, 857 (1968).

⁵H. Selig and H. H. Claassen, Isr. J. Chem. 6, 499 (1968).

⁶C. M. Penney, L. M. Goldman, and M. Lapp, Nat. Phys. Sci. 235, 110 (1972).

⁷W. F. Murphy, W. Holzer, and H. J. Bernstein, Appl. Spectrosc. 23, 211 (1969).

⁸T. Yoshino and H. J. Bernstein, J. Mol. Spectrosc. 2, 213 (1958).

⁹M. Griggs and S. Kaye, Rev. Sci. Instrum. 39, 1658 (1968).

¹⁰J. A. Zaslow, H. B. Urbach, F. Leighton, R. J. Wnuk, and J. A. Wojtowicz, J. Am. Chem. Soc. 82, 2682 (1960).

Reprinted from AMS Second Symposium on Meteorological Observations and Instrumentation, San Diego, California, March 27-30, 1972.

ACOUSTIC DOPPLER MEASUREMENTS OF THE TOTAL WIND VECTOR

D. W. Beran and S. F. Clifford

Wave Propagation Laboratory
National Oceanic and Atmospheric Administration
Boulder, Colorado

The ability to measure remotely a detailed profile of the winds up to heights of one kilometer would be of significance in several operational and research problems. A sensor that could make such measurements might be used for monitoring wind shear at airports, to sense the magnitude and direction of winds in an air pollution situation and to study boundary layer dynamics.

The use of an acoustic echo sounder for this purpose was suggested by Little (1969) and a similar technique, at ground level, was demonstrated by Kelton and Bricout (1964). Beran, Little, and Willmarth (1971), and Beran and Willmarth (1971) have more recently attempted to use the Doppler method, and to extend the measurements to much higher elevations.

The basic principle involves interrogating the medium with a sound pulse of a known fixed frequency. Natural turbulent scattering of this sound wave will result in the re-radiation of a portion of the acoustic energy back to a receiver. If the medium which re-radiated the sound is moving, the frequency of the returned wave will be Doppler shifted by an amount proportional to the component of the velocity of the medium along the direction of the bisector of the vertex angle formed by the incident and scattered ray paths.

The theory of acoustic wave propagation and scattering have been sufficiently covered elsewhere (see for example: Tatarski, 1961; Kallistratova, 1961; Monin, 1962; Clifford and Brown, 1971), and therefore will not be repeated here. It should be noted, however, that the scattering of an acoustic wave results primarily from naturally occurring temperature and wind inhomogeneities. The amount of energy scattered is a function of the angle between the incident ray as it leaves the scattering volume and the scattered ray. When this angle is 180° (backscatter) only temperature fluctuations contribute and when it is 90° (normal to the incident ray) no scattering will result. Knowledge of this variation in scattering strength with angle is important for determining the optimum configuration of antennas for a Doppler system. In what follows we will refer to a colocated transmitter and receiver

as a monostatic system, and to a transmitter and receiver which are separated by some distance, but aimed at a common volume as a bistatic system.

The derivation of wind speed from a Doppler shift can best be explained by referring to Figure 1. Sound transmitted from an antenna at T and having a frequency f_0 impinges upon some scattering volume at O. If this scattering volume is moving with the velocity, \vec{V} the frequency of the sound wave received at R will be some new value, f_s , and we can derive a difference frequency, $\Delta f = f_s - f_0$, proportional to \vec{V} . With the transmitted frequency expressed as a wave vector \vec{K}_0 and the scattered wave as \vec{K}_s , the difference frequency, or Doppler shift, can be written in vector notation as

$$\Delta f = \frac{1}{2\pi} (\vec{K}_s - \vec{K}_0) \cdot \vec{V} \quad (1)$$

where \vec{V} is the wind component in the plane formed by the transmitted and received beams. Writing Equation (1) in terms of the wavelength λ_0 of

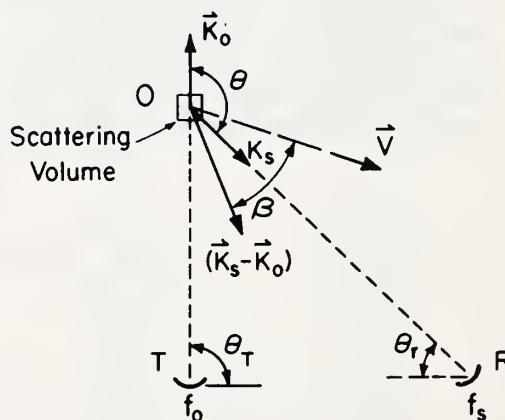


Fig. 1. Wave vector diagram showing the component of the wind measured by a Doppler shift.

the carrier wave, the angle β between the total wind vector \vec{V} in the plane and the component being measured, and the scattering angle θ we have

$$\Delta f \approx \frac{2V}{\lambda_0} \sin\left(\frac{\theta}{2}\right) \cos \beta \quad (2)$$

where $V \cos \beta$ is now the magnitude of the wind resolved along the vector $\vec{K}_s - \vec{K}_o$. Note that the direction of this component is the bisector of the angle formed by the intersection of the transmitter and receiver beams and will only be truly radial for a monostatic system.

If λ_0 is replaced by C/f_0 where C is the speed of sound, and the magnitude of the wind component being measured is solved for, we have

$$V \cos \beta = v' = \frac{C}{2 \sin \frac{\theta}{2}} \left[\frac{\Delta f}{f_0} \right] \quad (3)$$

This development assumes that refraction or bending of the beams is negligible. The effects of refraction and a more detailed development of the Doppler equation will be found in Appendix A.

Using Equation (3) and the knowledge that the direction of this wind component will be along the bisector of the antenna axes several equipment configurations can be envisioned for measuring the wind vector. For example, using a single vertically pointing, monostatic system which is pulsed, a profile of the vertical wind vector can be measured by selecting gates at successive distances along the antenna beam. The vertical wind can also be measured at a single height by using a bistatic system with the elevation angles (θ_t and θ_r in Figure 1) set equal. The first method was demonstrated by Beran, Little, and Willmarth (1971).

Clearly, in order to sense a component of the horizontal wind the axis of Doppler resolution must be off vertical. For the monostatic system, this simply requires that the beam be tilted and for the bistatic case the two antennas must be arranged with asymmetric elevation angles. A second experiment by Beran and Willmarth, (1971) tested both tilted monostatic and bistatic systems. It was concluded from this work that while the monostatic system gave better accuracy for a given elevation angle (because the component being measured was closer to the horizontal), the bistatic configuration was superior for applications requiring continual operation (because of the much stronger returned signal typical of forward scatter).

The bistatic work used only two horns, hence, measured only the component of the wind in the plane formed by the intersection of their beams.

The experiment described in this paper, extended this concept to use three antennas, one pointing vertically and the other two positioned along orthogonal axes centered on the first and tilted so as to intersect a common volume along the beam of the vertically pointing antenna. By pulsing only the vertical system and receiving the return from the common volume at all three antennas, three components of the wind can be measured and converted into the total wind vector at that height.

A sketch of the field set up for making these measurements is shown in Figure 2. The equipment van containing the sounder electronics was located near the center of the triangle formed by the three antennas. A 15 meter tower with wind sensors at 2 and 15 meters was located near this point.

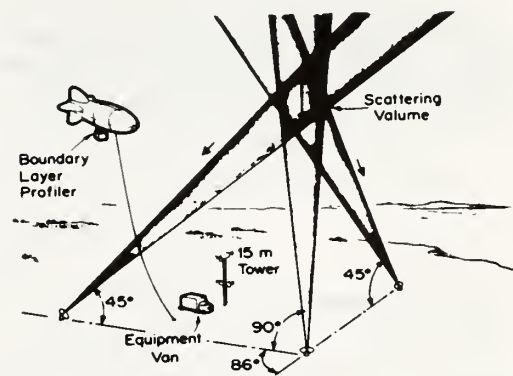


Fig. 2. Schematic of the field setup for testing the 3 axis acoustic Doppler wind technique. The spacing of the antennas was varied from 150 m to 200 m.

A major difficulty in this work was devising a method for making an independent measurement of the wind at or near the volume being interrogated by the sounder in order to obtain some estimate of the system accuracy. During a recent experiment conducted in Australia by McAllister (1971) the wind was measured by both acoustic Doppler and by an angle-of-arrival technique (McAllister et al. 1969). While McAllister's results were most encouraging the method of comparison suffered from the fact that the two winds being compared were not the same. The Doppler measurements gave a wind at some height above the ground while the angle-of-arrival method sensed the average wind between the ground and that volume.

The independent wind measurement used here and in the bistatic work described above (Beran and Willmarth, 1971), employed a tethered kiteoon operated by the National Center for Atmospheric Research. This device, called a

Boundary Layer Profiler (BLP), measures the magnitude of the wind vector, pressure, temperature and humidity and can be tethered to float at the altitude at which the Doppler measurements are being made. It was not placed in exactly the same volume, as the acoustic echo from a helium filled balloon would obliterate the return from natural scattering. The BLP has the disadvantage that it does not sense the wind direction, a factor which was difficult to resolve during the earlier work when only one component of the horizontal wind was being measured, but was of less importance for the present three-axis tests where the total wind vector was derived. The nearest wind direction available for comparison was that sensed by the wind vane on the 15 meter tower. This, combined with reports on the orientation of the kytoon, gave a crude estimate of the wind direction at the volume being interrogated.

The equipment used was similar to that described by Wescott, Simmons and Little (1969) with the exception that two receiver channels and gimbal mounted antennas were added. Basic equipment parameters are listed in Table 1.

Table 1
Acoustic Echo Sounder Parameters

| | |
|----------------------------|----------------------|
| Peak Power | 7.5 watts (acoustic) |
| Pulse Width | 50 ms |
| Pulse Repetition Frequency | .5 sec ⁻¹ |
| Maximum Range | 340 meters |
| Beam Intersection Height | 150 and 200 meters |
| Carrier Frequency | 1750 Hz |
| Antenna Diameters | 122 cm and 152 cm |
| Antenna Beamwidth | ± 4° and ± 5° |
| Elevation Angle | 90°, 45°, 45° |
| Receiver Bandwidth | 100 Hz |

For this set of trials the elevation angles θ_r , at the two passive receivers were set at 45° and the spacing between the vertical antenna and the two passive receivers was varied from 150 to 200 meters in order to gain a clearer picture of the range capability of the system. Earlier results indicated that elevation angles > 60° caused an unacceptable degradation of the derived horizontal winds, especially for bistatic operation.

Data reduction followed procedures similar to those described earlier (Beran, Little, and Willmarth 1971, and Beran and Willmarth, 1971) with the exception that a digital computer was used to determine the frequency spectra at the proper gated interval. Again, the spectra from several succeeding pulses were averaged in order to obtain greater spectral stability and wind resolution. The BLP provided an integrated

wind reading every twenty seconds. The Doppler winds were derived from the average of ten sounder pulses (20 seconds) making the two samples comparable.

Despite the advantages of using the BLP for measuring an independent value of the wind speed, there are certain drawbacks which must be accounted for when comparisons are made with the Doppler wind records. The physical separation of the BLP and the scattering volume averaged about 100 meters and was a function of the wind direction at the time of the measurement. Winds blowing from right to left (as referenced to Figure 2) would cause the separation to be greater because of the natural tendency for the kytoon to drift with the wind until the restraining force balanced the lift and wind force. In addition, small changes in the wind speed during a series of measurements caused the distance between the BLP and Doppler volume to vary as a function of time. These aspects of kytoon flight somewhat complicated the analysis procedures and no doubt were a factor in some of the observed difference between the BLP and Doppler measured winds.

The data samples from the BLP and Doppler were cross-correlated at varying lag times until maximum correlation was achieved, thus compensating for the distance between the two points being measured. As a check, this value was then compared with the lag calculated from the mean wind speed and direction during a given run and the constant separation distance between the two volumes being sensed. For

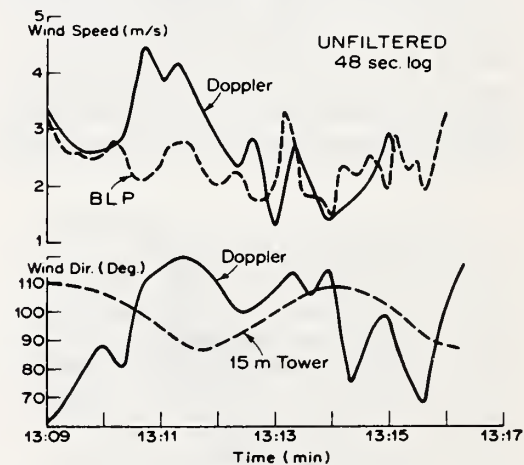


Fig. 3. Example of the horizontal wind speed measured by Doppler (solid curve) and BLP (dashed curve) and the wind direction measured by Doppler and a wind vane at 15 meters. Doppler and BLP values are at a height of 150 m and are unfiltered 20 sec average winds. The Doppler records are lagged 48 sec to compensate for the distance between the two sensors.

example, the maximum correlation for the two sets of wind data shown at the top of Figure 3 occurred with a 48 second lag. The average wind speed during this time was about 2.5 mps from the east, a direction which would tend to move the kytoon to a point about 25 m further than the 100 meter constant distance between the two volumes. Thus, the total distance separation was about 125 meters, or a lag of 50 seconds, very close to the values found by cross-correlating the two records. The Doppler wind speed trace shown in Figure 3 has been shifted 48 sec and good general agreement can be seen. Evidence of the varying lag produced by oscillations of the kytoon during the run is still present; as can be noted by the opposing shifts between the peaks in the curves at 13:13 and 13:15. A re-check of the original data for such factors as noise in the Doppler spectrum did not reveal the cause of the large deviation of the Doppler wind from the BLP wind near 13:11. One physical explanation for the presence of this apparently anomalous event might be that the measurements were made during rather strong thermal plume activity and the two data samples may have been in slightly different regions of an individual plume.

Wind direction comparisons, an example of which are shown in the lower portion of Figure 3, were quite good considering the uncertainty introduced by the large vertical separation between the two points being measured. Runs were made during both unstable and stable conditions. Not unexpectedly, the best agreement for the wind direction was found during the unstable cases when less turning of the wind with height was present. The direction measurements were considered of secondary importance for this series of tests and it was assumed that if the magnitude of the total wind vector could be correctly measured that the direction would not be far off.

A total of about two hours data were collected on the separate runs which ranged from ten minutes to 1 hour in length. An individual run consisted of first taking a vertical profile of the temperature, wind speed and pressure with the BLP, then tethering the kytoon at the altitude the Doppler measurements were being made; the run ended with a second BLP vertical profile. The level at which the BLP was tethered was determined by monitoring the pressure during its first ascent and then stopping at a pre-determined value. No adjustments in height were made during the run. This procedure proved inadequate, especially on longer runs where it was found later that the kytoon height varied up to 40 meters from its expected level. This was especially unfortunate during the run made under inversion conditions where a marked peak in the wind profile was found about 50 meters below the Doppler measurements. The BLP drifted into this stronger wind region with the result that the mean difference in the winds measured by the two

methods was about 2 m/s. This portion of the data was, of course, eliminated from the final comparison which was based on a total of 30 minutes of wind records taken under both stable and unstable conditions.

While the lag correlation technique discussed above compensated for the spacing between the BLP and the Doppler volume, there is no justification for comparing spectral wavelengths shorter than this distance. In order to derive a meaningful statistical comparison of the two data samples, these shorter wavelengths were removed from the data with a low pass filter. The time constant for the filter must be a function of the spacing between the two points measured and the mean wind speed along the path, hence the optimum filter was different for each case. For example, the observed wind speeds ranged from calm to 6 m/s and the spacing ranged from 75 to 150 meters. For higher wind speeds the time constant could have been as low as 10 or 15 seconds, but for very low wind speeds the optimum time constant was of the order of two minutes or more. An example of the effect of this filtering is shown in Figure 4, where the data have been low pass filtered with a time constant of one minute.

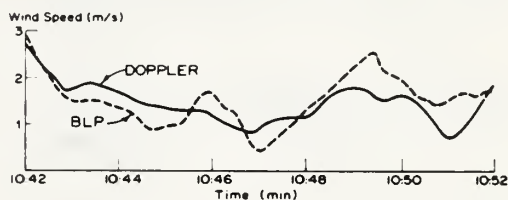


Fig. 4. Example of Doppler and BLP wind records after low pass filtering. Filter time constant was one minute.

The spacing and wind speed for this period suggest that the time constant should have been even longer, a possible explanation for the deviation shown in the figure.

The final comparison of the two data samples is shown in Figure 5, and in Table 2. Here a filter time constant of two minutes was applied to the 30 minute data sample, thus, eliminating the shorter wavelengths at even the lowest wind speeds.

The average value for the two samples are remarkably close, however, the regression line slope of .95 and Y intercept of 0.21 m/s suggests that the Doppler method may have a slight tendency to underestimate at lower speeds. This discrepancy is in part due to the start speed (0.5 m/s) of the cup anemometer used on the BLP. The anemometer output was designed so that a constant reading of 0.5 m/s was given for all speeds less than that value. While no speeds

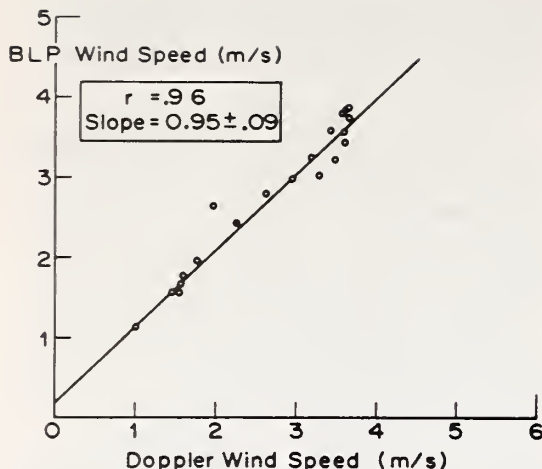


Fig. 5. Scatter diagram of Doppler vs. BLP winds. Records were lagged to compensate for spacing between the Doppler and BLP (see text)

Table 2
Comparison of BLP and Doppler Measured Winds

| | |
|------------------------------------------------|------------|
| Average Doppler | 2.33 m/s |
| Average BLP | 2.42 m/s |
| Standard Deviation, Doppler | 0.95 m/s |
| Standard Deviation, BLP | 0.94 m/s |
| Regression Line Slope and 95%Conf. Interval | 0.95 ± .09 |
| Y Intercept | 0.21 m/s |
| 95% Confidence Factor | 0.09 m/s |

this low are shown on the scatter diagram in Figure 5, these false high values would have been averaged in with the correct values above 0.5 m/s, introducing a BLP wind at low speeds which was slightly too high, and causing the regression line slope to appear low. This explanation seems more plausible than the possibility of refraction bending the beams and creating a false scatter angle, a factor which was postulated in an earlier paper (Beran and Willmarth, 1971), but in light of the calculation in Appendix A appears to be of only minor importance at the altitudes and wind speeds encountered during this experiment.

This experiment has demonstrated that acoustic Doppler techniques can be used to provide wind speeds and directions at altitudes up to at least 200 meters with a resolution as good as standard operational meteorological wind

sensors. Physical constraints imposed by the experimental setup (the distance between the Doppler scattering volume and the BLP and the rather high inertia cup anemometer on the BLP) made it impossible to assess the higher resolution capability of the Doppler technique. The limits on this resolution can be estimated, however, by noting the constraints imposed by the equipment and the analysis techniques.

Looking first at the expected spatial resolution of the system, we can assume that the winds being measured were the spatial average of all wind components within the scattering volume. For the mode of operation used the boundary of this volume is formed by the intersection of the three beams and the gate length for the vertical system. Using a beam width of 8° and a gate length of 100 ms we find a scattering volume with a maximum horizontal dimension of ≈ 30 m and a maximum vertical depth of ≈ 34 m.

The velocity resolution can be estimated by using Equation 3 and assuming that at least $1/4$ cycle of Doppler shift is the minimum detectable value. At a carrier frequency of 1750 Hz and a pulse width, τ , of 50 ms, there would be about 87 cycles of carrier in each pulse. Using this value for $f\tau$ in Equation 3 we find a resolution of ± 0.5 m/s. By averaging the spectra from pulse to pulse we improve this resolution by a factor of $(n)^{-1/2}$ where n is the number of pulses averaged. For the 10 pulse averages used above the velocity resolution would be about ± 0.15 m/s. This improved resolution is gained partially at the expense of spatial resolution, due to the mean motion of the wind stretching the effective volume being interrogated for each extra pulse that is averaged.

Other methods for improving the resolution can be used. For example, both the pulse width and the carrier frequency can be increased in order to introduce more cycles in each pulse. In the final analysis the specification of resolution must depend on each application, and then such things as the loss of range due to increased absorption at higher frequencies must be balanced against the desired increase in resolution. If the ultimate resolution of the acoustic Doppler shift, derived from the first moment of the spectrum, does not meet the requirements for certain classes of micro scale measurements it is, of course, possible to consider the information contained in the second moment of the returned frequency spectra. While improved resolution will be a high priority goal for research applications it will also be important to develop techniques for measuring complete vertical profiles of the total wind vector. This will be especially important for such operational applications as monitoring the wind shear above airports (Beran 1971), and

observing the drainage winds associated with air pollution.

Three methods for making such vertical profile measurements are at least conceptually feasible. One would use phased steerable antennas in place of the fixed beam receivers, to sweep the vertical beam. A second method might employ a fan beam segmented into smaller sectors, each connected to a separate receiver. The third method would use the same fixed beam configuration shown in Figure 2, but with all three sounders operated in an active monostatic mode at slightly different frequencies. Here, the signals at the three receivers could be gated at intervals along their respective beams, and Doppler shifted frequencies extracted for equal heights above the surface. Clearly, the three wind vectors thus measured will be in the same volume only at the height where the three beams intersect. In order to use the radial wind components at other heights, above and below the beam intersect point, it is necessary to assume horizontal homogeneity for a distance equivalent to the spacing between the volumes. For 45° elevation angles and 200 meter spacing this distance is on the order of 200 meters at the extreme top and bottom of a 500 meter profile. Employing Taylor's hypothesis of time and space stationarity and a one minute time average the assumption of horizontal homogeneity does not appear too restrictive.

The potential of the second method is clearly shown in Figure 6, a time section of the isotachs for the total horizontal wind (m/s) under an oscillating inversion. The winds used to produce these isotachs were derived solely from the Doppler shifts recorded by three separate monostatic acoustic sounders. Ten height intervals ranging from the lowest at 84 meters to the highest at 480 meters were used to make the analysis. The loss of accuracy at the extremities of the profile due to a lack of horizontal homogeneity cannot be assessed as BLP profiles were not available for the test. The remarkable continuity of the pattern, however, speaks for itself.

Acknowledgments: The authors wish to express their sincere gratitude to Margot Ackley and William Neff for their effort in preparing the computer programs, and to F. F. Hall, J. W. Wescott, B. C. Willmarth, and E. J. Owens for their help during the field measurements. Special thanks are also due to H. Baynton and R. McBeth of NCAR for providing the BLP system and to T. M. Georges for his valuable consultation during the analysis of refraction effects.

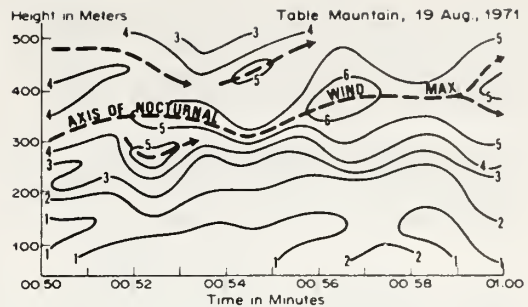


Fig. 6. Time section of isotachs for horizontal wind (m/s) winds were derived solely from acoustic Doppler measurements using three separate monostatic systems.

References

- Beran, D. W. (1971), Acoustics; A new approach for monitoring the environment near airports. To be published in Nov.-Dec., 1971 issue of AIAA, Jour. of Aircraft.
- Beran, D. W., C. G. Little, and B. C. Willmarth (1971), Acoustic Doppler measurement of vertical velocities in the atmosphere, Nature, 230, pp. 160-162.
- Beran, D. W., and B. C. Willmarth (1971), Doppler winds from a bistatic acoustic sounder, Proc. Seventh Int. Symp. on Remote Sensing of Environment, Univ. of Mich., Vol III, pp. 1699-1714.
- Brown, E. H., Acoustic Doppler Radar; Scattering equation and general solution, To be publ. IASA.
- Clifford, S. F., and E. H. Brown (1971), Propagation of sound in a turbulent atmosphere, Jour. Acoust. Soc. of Am., pp. 1123-1127.
- Kallistratova, M. A. (1961), Experimental investigation of sound wave scattering in the atmosphere, Trudy Inst. Fiz. Atmos., Atmos. Turbulentnost, 4, pp. 203-256.
- Kelton, G. and P. Bricout (1964), Wind velocity measurements using sonic techniques, Bull. Am. Met. Soc., 45, pp. 571-580.
- Little, C. G. (1969), Acoustic methods for the remote probing of the lower atmosphere. Proc. of the IEEE, 57, pp. 571-578.
- McAllister, L. G., J. R. Pollard, A. R. Mahoney, and P. J. R. Shaw (1969), Acoustic sounding - a new approach to the study of atmospheric structure. Proc. IEEE, 57, pp. 579-587.

McAllister, L. G. (1971), Wind velocity measurements in the lower atmosphere using acoustic sounding techniques, WRE Tech Note - A204(AP), Dept. of Supply, Australian Defense Sci. Serv., Weapons Res. Est. Salisbury, So. Australia, 10p.

Monin, A. S. (1962), Characteristics of the scattering of sound in a turbulent atmosphere, Akust. Zh., 7, pp. 457-461, (Sov. Phys - Acoust. 7, pp. 370-373).

Tatarski, V. I. (1961), Wave propagation in a turbulent medium, (R. A. Silverman, transl.) New York: McGraw-Hill, 285 p.

Wescott, J. W., W. R. Simmons, C. G. Little (1970), Acoustic echo-sounding measurements of temperature and wind fluctuations, ESSA Tech. Memo. ERLTM-WPL5, Boulder, Colo., 24 p.

APPENDIX A

THE DOPPLER FORMULA AND CORRECTIONS FOR REFRACTION EFFECTS

Figure 1A illustrates the changes in the scattering geometry produced by atmospheric refraction. Three basic effects are considered: first, the relocation of the scattering volume - an integrated function of wind shear and temperature gradient - second, a shift in the axis of resolution of the Doppler wind component from θ_d to θ'_d and third, a change in the magnitude of the measured wind. These changes are with respect to the scattering geometry introduced by the transmitter and receiver configuration.

Our approach for estimating the first effect was to use an acoustic ray tracing program (Georges, 1971) and insert a linear horizontal wind shear of 50 m/sec/km and a linear temperature gradient of -8°K per kilometer. For the particular case of the transmitter-receiver geometry of Figure 1A, we observed a vertical drop, $\Delta h \sim 12$ m, and a horizontal displacement, $\Delta x \sim 4$ m. These rather severe gradients have introduced a fractional uncertainty in height of $(\Delta h/h) \sim 0.06$ and in horizontal displacement of $(\Delta x/x) \sim 0.02$.

The second and third effects are solely a function of the wind velocity and temperature at the end points of the path and may be treated analytically. For simplicity we assumed a horizontally stratified temperature and horizontal wind field. Further, the displacement calculated above must not move the scattering volume to a different wind and temperature stratum than would be observed without refraction. This appears reasonable since the displacement calculation above indicates that we remain within the ideal scattering volume of the sounder even under such severe conditions.

The new scattering angle θ' is easily calculated from Snell's law, i.e., the invariance of the horizontal component of the wave vector at the scattering volume and at the receiver. From Figure 1A

$$K'_s \cos(\theta' - \frac{\pi}{2}) = K'_r \cos \theta_r \quad (1A)$$

where $K'_s = n_s K_o$ and $K'_r = n_r K_o$ are the descending wave vector magnitudes at the scattering volume and receiver respectively. (Note that the incident wave vector K_o remains vertical despite ray bending). From the definition of the acoustic refractive index,

$$n = \frac{C_o}{C + \frac{\vec{K} \cdot \vec{v}}{K}}$$

we obtain from Eq. (1A), writing $\cos(\theta' - \frac{\pi}{2}) = \sin \theta'$, the equation

$$\frac{C_o \sin \theta'}{C + v \sin \theta'} = \cos \theta_r \quad (3A)$$

where C_o is the mean speed of sound in air

($C_o \sim 340$ m/sec), and C is the speed of sound at the scatterer, which varies with temperature alone. If we now assume a small deviation in angle, i.e., $\theta' = \theta - \Delta\theta$, where $\Delta\theta \ll 1$ rad., and note from the original geometry that $\cos \theta_r = \sin \theta$, Equation (3A) gives

$$\Delta\theta = \tan \left\{ 1 - \left[\frac{C_o}{C} - \frac{v}{C} \sin \theta \right]^{-1} \right\} \quad (4A)$$

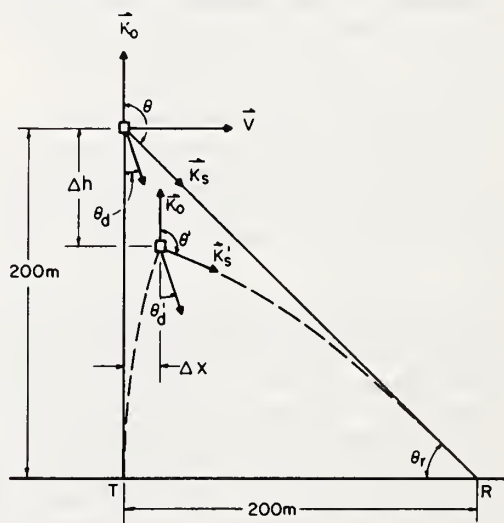


Fig. 1A. Schematic of the geometry used to analyze the effect of refraction and ray bending.

If we assume that $C = C_0 \pm \Delta C$, we obtain to first order in $\Delta C/C_0$ and v/C_0 the expression,

$$\Delta\theta = -\tan\theta \left[\frac{v}{C_0} \sin\theta \pm \frac{\Delta C}{C_0} \right]. \quad (5A)$$

Note that $\Delta\theta$ is not the change in Doppler resolution angle $\theta'_d - \theta_d$. It is only the change in angle of the wave vector \vec{K}_s from its original angle.

The third effect is the addition of first order perturbations in v/C to the Doppler equation. This effect is not included in Equation (1) of the text. To consider this problem, we must return to the basic definition of a Doppler frequency shift as the number of wavelengths per second change in phase path. This is mathematically described by

$$\Delta f = -\frac{1}{2\pi} \frac{d}{dt} \int_{a(t)}^{b(t)} K_0 n(s) \cos\alpha(s) ds. \quad (6A)$$

Equation (6A) contains the path integral of the projection of the wave vector $\vec{K}_0 n(s)$, onto the true ray path. The integral is taken between end points that vary with time. The angle $\alpha(s)$ is the angle between the tangent to the ray path and the wave vector at each point along the ray trajectory. We are counting up the number of wavelengths per second that the total path length changes.

For our discontinuous path, and ignoring time changes in the background refractivity, i.e., heating of the entire path, Equation (6A) reduces to

$$\Delta f = -\frac{k_0}{2\pi} \left[n_1(b) \cos\left[\alpha_1(b)\right] \left(\frac{db}{dt}\right)_1 - n_2(b) \cos\left[\alpha_2(b)\right] \left(\frac{db}{dt}\right)_2 \right], \quad (7A)$$

the subscripts 1 and 2 refer to the ascending and descending rays respectively. To first order in v/C , $\cos\alpha_1(b) = \cos\alpha_2(b) = 1$. This is most

easily seen in analyzing the ascending ray. The angle α_1 between the vertical \vec{K}_0 and the ray path is clearly $\alpha_1 = \tan^{-1}(v/C)$. (This is simply the direction the wave would travel when moving vertically with a velocity C and translated horizontally with a velocity v). Therefore, $\cos\alpha_1 \sim \cos(v/C)$ or, to first order, $\cos\alpha_1 \sim 1$. A similar analysis of the oblique triangle consisting of the wave vector, the tangent to the ray path and the wind velocity on the descending ray, yields,

$$\alpha_2 = -\tan^{-1} \left[\frac{\cos\theta'}{\sin\theta' + \frac{C}{v}} \right],$$

and to first order in v/C , $\alpha_2 \sim -\frac{v}{C} \cos\theta'$.

This result, as for the upward leg, results in $\cos\alpha_2 \sim 1$. Returning to Figure 1A, we have

$$n_1(b) = C_0/C \text{ and } n_2(b) = \frac{C_0}{C + v \cos(\theta' - \frac{\pi}{2})},$$

where C is the speed of sound at the scattering volume. The quantity, $\left(\frac{db}{dt}\right)_1$, is the projection of v onto the ascending ray path and is given by

$$\left(\frac{db}{dt}\right)_1 = v \cos\left(\frac{\pi}{2} - \alpha_1\right). \quad (8A)$$

Simplifying again for $v/C \ll 1$, we obtain

$$\left(\frac{db}{dt}\right)_1 \sim v \left(\frac{v}{C}\right). \quad (9A)$$

A similar calculation for $\left(\frac{db}{dt}\right)_2$ gives

$$\left(\frac{db}{dt}\right)_2 \sim v \cos(\theta' - \alpha_2 - \frac{\pi}{2}) = v \sin\theta' + v \left(\frac{v}{C}\right) \cos^2\theta'. \quad (10A)$$

Rewriting Equation (7A) after inserting Equations (9A) and (10A) and the respective indices of refraction, we obtain

$$\Delta f = -\frac{k_0 C_0}{2\pi} \left\{ \left(\frac{v}{C}\right) \frac{v}{C} - \frac{(\sin\theta' + \frac{v}{C} \cos^2\theta')}{(1 + \frac{v}{C} \sin\theta')} \right\} \quad (11A)$$

Noting that $k_0 C_0 / 2\pi = f_0$ and retaining only first order terms inside the brackets, we may write the fractional Doppler shift as:

$$\frac{\Delta f}{f_0} = \frac{v}{C} \sin\theta' - \frac{2v^2}{C^2} \sin^2\theta'. \quad (12A)$$

The angle θ' , itself a function of v/C , may be set equal to θ in the second term, valid to second order in v/C . Then, with the assumption of a small angle correction $\theta' = \theta - \Delta\theta$ in the first term, we obtain

$$\frac{\Delta f}{f_0} = \left(\frac{v}{C}\right) \sin\theta - 2 \left(\frac{v^2}{C^2}\right) \sin^2\theta - \left(\frac{v}{C}\right) \Delta\theta \cos\theta, \quad (13A)$$

where $\Delta\theta$ is given in Equation (4A). Again, assume $C = C_0 \pm \Delta C$ and disregard terms of higher than second order in $\Delta C/C_0$ or v/C_0 . Equation (13A) then becomes

$$\frac{\Delta f}{f_0} = \frac{v}{C_0} \sin\theta - \left(\frac{v}{C_0} \sin\theta\right)^2 \quad (14A)$$

The first term in Equation (14A) is exactly the term we obtain from the approximate Doppler equation (Equation (1) in text). The last term is the correction for refractive effects produced by the wind at the scattering volume. Note that in

proceeding from Equation (13A) to (14A), the temperature effects, i.e., the change in the speed of sound, C from its mean value, C_0 , are canceled by the last term involving the change in angle, $\Delta\theta$.

To find the new wind velocity, solve the quadratic Equation (14A) and select the negative square root. This gives the new wind, fractional bandwidth relation in the final form.

$$v = \frac{C_0}{2 \sin \theta} \left[1 - \left(1 - 4 \Delta f / f_0 \right)^{1/2} \right]. \quad (15A)$$

If we further assume that $\Delta f / f_0 \ll 0.25$, and expand Equation (15A) in a binomial series valid to second order in $\Delta f / f_0$, we obtain

$$v = \frac{C_0}{\sin \theta} \left(\frac{\Delta f}{f_0} \right) \left[1 + \frac{\Delta f}{f_0} \right]. \quad (16A)$$

Thus, the fractional error in velocity, ϵ_v , incurred by using Equation (1) is

$$\epsilon_v = \frac{\Delta f}{f_0}.$$

To estimate the angular displacement of the axis of wind resolution due to refraction, we return to Equation (7A) and again make the assumption $\cos \alpha_1 = \cos \alpha_2 \sim 1$, valid to first order in v/C .

Recalling that $\frac{db}{dt}$ is the projection of the wind along the tangent of the ray trajectory, we may write

$$\left(\frac{db}{dt} \right)_1 = \vec{v} \cdot \hat{t}_1 \quad \text{and} \quad \left(\frac{db}{dt} \right)_2 = \vec{v} \cdot \hat{t}_2$$

where \hat{t}_1 and \hat{t}_2 are unit vectors tangent to the ascending and descending rays respectively. Inserting the respective indices of refraction, n_1 and n_2 , and factoring out common terms, Equation (7A) becomes

$$\frac{\Delta f}{f_0} = \left(\frac{1}{C + v \sin \theta} \right) \vec{v} \cdot \left[\hat{t}_2 - \left(1 + \frac{v}{C} \sin \theta' \right) \hat{t}_1 \right]. \quad (17A)$$

Equation (17A) involves the projection of the wind vector \vec{v} onto an axis defined by the vector quantity in the brackets. We need to determine the orientation of that vector. Using the angular information in Equations (8A) and (9A), we may resolve this vector into vertical and horizontal components and compute its angle, θ_d' , shown in Figure 1A. From the geometry of Figure 1A, \hat{t}_1 is clearly

$$\hat{t}_1 = \sin \alpha_1 \hat{x} + \cos \alpha_1 \hat{z} \quad (18A)$$

where \hat{x} and \hat{z} are unit vectors in the horizontal and vertical directions respectively. Similarly,

$$\hat{t}_2 = \sin (\theta' - \alpha_2) \hat{x} + \cos (\theta' - \alpha_2) \hat{z}, \quad (19A)$$

where $\theta' = \theta - \Delta\theta$. Inserting Equations (18A) and (19A) into Equation (17A), we find the relation

$$\tan \theta_d' = \frac{\sin (\theta' - \alpha_2) - \left(1 + \frac{v}{C} \sin \theta' \right) \sin \alpha_1}{\left[-\cos (\theta' - \alpha_2) + \left(1 + \frac{v}{C} \sin \theta' \right) \cos \alpha_1 \right]} \quad (20A)$$

If we simplify (20A) to first order in $\frac{v}{C}$, it becomes

$$\tan \theta_d' = \frac{\sin \theta - (\Delta\theta + \alpha_2) \cos \theta - \alpha_1}{1 - \cos \theta - (\Delta\theta + \alpha_2) \frac{v}{C} \sin \theta} \quad (21A)$$

If we express θ_d' as $\theta_d' = \theta_d + \Delta\theta_d$ and retain terms on the left side of Equation (21A) to first order in $\Delta\theta_d$, we obtain

$$\tan \theta_d' \approx \tan \theta_d + \Delta\theta_d \sec^2 \theta_d, \quad (22A)$$

where $\theta_d = \frac{\pi - \theta}{2}$. Inserting Equation (22A) into Equation (21A) and simplifying to first order in v/C , we obtain

$$2 \Delta\theta_d = \Delta\theta + \alpha_2 - \alpha_1 - \frac{v}{C} (1 + \cos \theta). \quad (23A)$$

The estimates of α_1 and α_2 given above, inserted into Equation (23A) reduce it to the form

$$\Delta\theta_d = \frac{\Delta\theta}{2} - \frac{v}{C} (1 + \cos \theta). \quad (24A)$$

If we insert Equation (5A) into Equation (24A) after letting $C = C_0 \pm \Delta C$ and again retain terms to first order in $\Delta C/C_0$ and v/C_0 , we finally obtain

$$\Delta\theta_d = - \left[\frac{v}{C_0} \frac{(1 + \cos \theta)^2}{\cos \theta} \pm \frac{\Delta C}{2C_0} \tan \theta \right]. \quad (25A)$$

Equation (25A) defines the first order angular fluctuation of the axis of Doppler wind resolution due to refractive effects. A numerical estimate may be found by using

$$\frac{v}{C_0} = \frac{\Delta C}{C_0} = 0.05 \quad \text{and} \quad \theta = 135^\circ,$$

yielding

$$\Delta\theta_d \sim 0.025 \left[0.121 \pm 1 \right]$$

For the worst case the plus sign applies, leaving $\Delta\theta_d = 0.028$ rad. To calculate the percent error in wind, ϵ_v , caused by this angular fluctuation, we note from Figure 1A,

$$\epsilon_v = \Delta\theta_d \sin \theta_d = - \left(\Delta\theta_d \right) \cos \frac{\theta}{2}$$

or, for $v = 0.05 C_0$ and $\theta = 135^\circ$, $\epsilon_v = 0.01$.

In summary, the effects of refraction produce a new Doppler expression Equation (16A) valid for $v/C_0 \ll 1$, $\Delta C/C_0 \ll 1$ and $\Delta f/f_0 \ll 1$.

This expression is valid to second order in these three small quantities. Equation (16A) represents a fractional correction in the measured wind

$\epsilon_v = \Delta v/v$, equal to the measured fractional bandwidth, i.e.,

$$\epsilon_v = \Delta f/f_0 .$$

Conversely, the usual Doppler formula, Equation (3), is valid to this order of accuracy. Normally, we observe $\Delta f/f_0 < 0.04$, and hence our winds determined from Equation (3) are in error by 4%. The change in position of scattering volume appears from our calculations to be less than the original scattering volume and hence is negligible. The change in the angle of Doppler wind resolution is given by Equation (25A) and produces an additional 1.0% error in our wind estimate, for the assumed worst case conditions,

$$v = 0.05 C_0, \Delta C/C_0 = 0.05 .$$

REFERENCE

Georges, T. M. (1971), A program for calculating three-dimensional acoustic-gravity ray paths in the atmosphere, NOAA Tech. Rept. ERL 212-WPL16.

Reprinted with permission from Boundary Layer Meteorology, Vol. 4,
133-153, 1973.

ACOUSTIC ECHO-SOUNDING TECHNIQUES AND THEIR APPLICATION TO GRAVITY-WAVE, TURBULENCE, AND STABILITY STUDIES

D. W. BERAN, W. H. HOOKE, and S. F. CLIFFORD

*Wave Propagation Laboratory, Environmental Research Laboratories,
National Oceanic and Atmospheric Administration, Boulder, Colo. 80302, U.S.A.*

(Received 8 August, 1972)

Abstract. This paper is a brief summary of recent experimental studies conducted by the WPL staff in order to: (a) compare acoustic echo strengths with those predicted from measured turbulence intensities and scatter theory; (b) develop optimum experimental geometries for Doppler work, and (c) use the acoustic echo-sounder as a quantitative tool in studies of gravity wave dynamics in, and immediately above, the stable planetary boundary layer. We find that the observed acoustic echo strengths are roughly an order of magnitude greater than those predicted theoretically. This discrepancy might be in part due to partial reflection although the comparison is somewhat clouded by uncertainties in our knowledge of the equipment characteristics, propagation losses, etc. Comparisons between Doppler and *in situ* wind measurements give confidence in the Doppler results, but further experimentation and comparisons are needed. Preliminary use of acoustic Doppler data in a case study of gravity-wave dynamics in the planetary boundary layer has yielded boundary-layer wind speed and direction profiles which give insight into the mechanisms responsible for the wave generation. The Doppler data yield estimates of the wave associated momentum fluxes (\sim a few dyn cm^{-2}) as well. The results derived from the acoustic techniques are quite encouraging, but thus far remain unsubstantiated by independent wind and flux measurements.

1. Introduction

From the start, acoustic echo-sounder facsimile records of boundary-layer turbulent structure have provided valuable qualitative insights into the nature of physical processes at work in the planetary boundary layer. With the aid of such records, it is often a trivial matter to visualize the structure and dynamics of regularly occurring, characteristic features of the boundary layer such as wave generation by shear-flow instability and thermal plume development, and to understand, often for the first time, how these events manifest themselves on conventional, *in situ*, measurements.

Of potentially greater importance to the development of our understanding of gravity waves, turbulence and atmospheric stability, however, is the fact that the amplitudes and the frequency spectra of the returned acoustic echoes contain quantitative information. In particular, the echoes hold forth the promise of remote measurement of boundary-layer wind profiles as well as profiles of the turbulence intensity (Little, 1969). In principle, such measurements would provide data on the possible role of the boundary-layer wind shears responsible for gravity wave generation, the wave-associated momentum transport, wave breaking and the concomitant production of turbulence, and the turbulent energy dissipation, for example.

Whether such quantitative observations can, in fact, be usefully made in practice

depends upon the spatial and temporal resolving power of the acoustic systems, as well as their sensitivity and accuracy. These system characteristics are strongly coupled, so that in most cases the improvement of system performance in any one respect results in deterioration of system performance in others. However, just which system qualities are most desirable for boundary-layer work, and how serious a limitation these tradeoffs will prove to be, remain unknown. Thus, more research is needed in order to realize most effectively the potential of acoustic echo-sounding for atmospheric studies. We need to develop our understanding of the scattering and partial reflection mechanisms producing the observed acoustic echo-returns. The scattering theory (see review by Little (1969)) applies only to scattering from volumes of locally homogeneous and isotropic turbulence many times larger than the outer scale. We need to extend this theory so that it describes the scatter from the much smaller volumes of (possibly) inhomogeneous turbulence occurring in the presence of strong background temperature and wind gradients. We need to develop optimal equipment configurations for the Doppler velocity determinations, and to perform extensive calibration of this equipment with respect to conventional *in situ* measurements. And finally, we must use the acoustic echo-sounder in atmospheric wave and turbulence studies, in order to judge accurately its effectiveness in such work, and to learn how to improve its performance. Quite obviously, these are major theoretical and experimental problems which by no means have been solved; here we shall simply summarize recent progress made by the WPL staff in each of these areas.

2. Observed Acoustic Echo Strengths Compared with Theoretical Predictions

We shall begin by comparing the observed strength of the acoustic echo returns with those predicted from *in situ* measurements of the temperature structure constant and the theory of acoustic-wave scatter in homogeneous, isotropic turbulent media as developed by Kallistratova (1961), Monin (1962), and Tatarski (1971). Details of the scatter theory, the experimental configuration, and the data comparisons are to be described in a paper that is now in preparation; only a few salient points will be discussed here. In the experimental comparisons, the acoustic echo power P_r is related to the transmitted power P by the so-called radar equation

$$\frac{P_r}{P} = \frac{\sigma c \tau}{2} A R^{-2} L, \quad (1)$$

where σ is the scattering cross section, c is the speed of sound, τ is the pulse width, R is the range, A is the antenna area, and L is a factor containing the equipment efficiencies, antenna gain and the atmospheric absorption (a function of temperature, humidity, carrier frequency, and range). According to Little (1969), $\sigma(\theta)$, the scattered power per unit volume per unit incident flux per unit solid angle at the angle θ from the initial propagation direction, is given by the formula

$$\sigma(\theta) = 0.03k^{1/3} \cos^2 \theta \left[\frac{C_v^2}{c^2} \cos^2 \frac{\theta}{2} + 0.13 \frac{C_T^2}{T^2} \right] \left(\sin \frac{\theta}{2} \right)^{-11/3}, \quad (2)$$

applicable to homogeneous, isotropic turbulence. Here k is the angular wave number and T is the temperature; C_v and C_T are the structure constants for the wind and the temperature, respectively, defined by

$$C_v^2 \equiv [\mathbf{v}(\mathbf{r}) - \mathbf{v}(\mathbf{r} + \mathbf{q})]^2 \varrho^{-2/3}, \quad C_T^2 \equiv [T(\mathbf{r}) - T(\mathbf{r} + \mathbf{q})]^2 \varrho^{-2/3}, \quad (3)$$

where \mathbf{r} is a position vector and \mathbf{q} is the separation vector. In the experiment, the backscatter ($\theta = 180^\circ$) power returned from a roughly 3-m height interval centered at a fixed height of 95 m was measured, so that the echo power P , given by Equations (1) and (2) depended only upon C_T^2 , and could be compared with a direct measurement of C_T^2 made at the same height by fast-response differential temperature probes mounted on a tower some 230 m distant. These probes were AC coupled to the recording instruments so that any contributions to the measured C_T from the background temperature gradients were effectively removed. The absorption contained in the factor L of Equation (1) was computed using temperature and humidity height profiles measured by a movable instrument carriage on the tower. Because these profiles were taken only once per hour, the absorption of sound remains a source of uncertainty in the comparison. The equipment efficiencies, also included in the L term, were not accurately known and may also have contributed to errors in the calculation of C_T^2 .

The scatter theory cited above does not include the effects of the statistical inhomogeneity and anisotropy, or the effects of background temperature gradients. One might therefore be prepared *a priori* to find serious discrepancies in the experimental comparison, and this has indeed proven to be the case. The many hours of data available were found to contain a few intervals during which the acoustic and *in situ* measurements of C_T^2 agreed rather closely, but there were many more hours when the acoustic sounder estimates were consistently higher than those from the tower sensor, and only a few occasions when the reverse was true. When we confine our attention, however, to those intervals during which the mean wind direction was from the sounder to the tower, so that the sensors tended to interrogate the same volume, and to those intervals during which the variance of wind speed remained small relative to the mean, so that the assumption of stationarity applies, we find, as shown in Figure 1, that the sounder estimates are rather consistently higher than the tower estimates. The data have been low-pass filtered to remove the contribution from spatial wavelengths shorter than the distance between the two sensors. There appears to be a marked correlation between the two records, but they are different in magnitude by about 10–15 dB.

At present we are investigating various possible explanations of the results. Naturally, one likely possibility is that the acoustic echo returns may arise in large part from partial reflection of the acoustic pulses as they propagate in the background tempera-

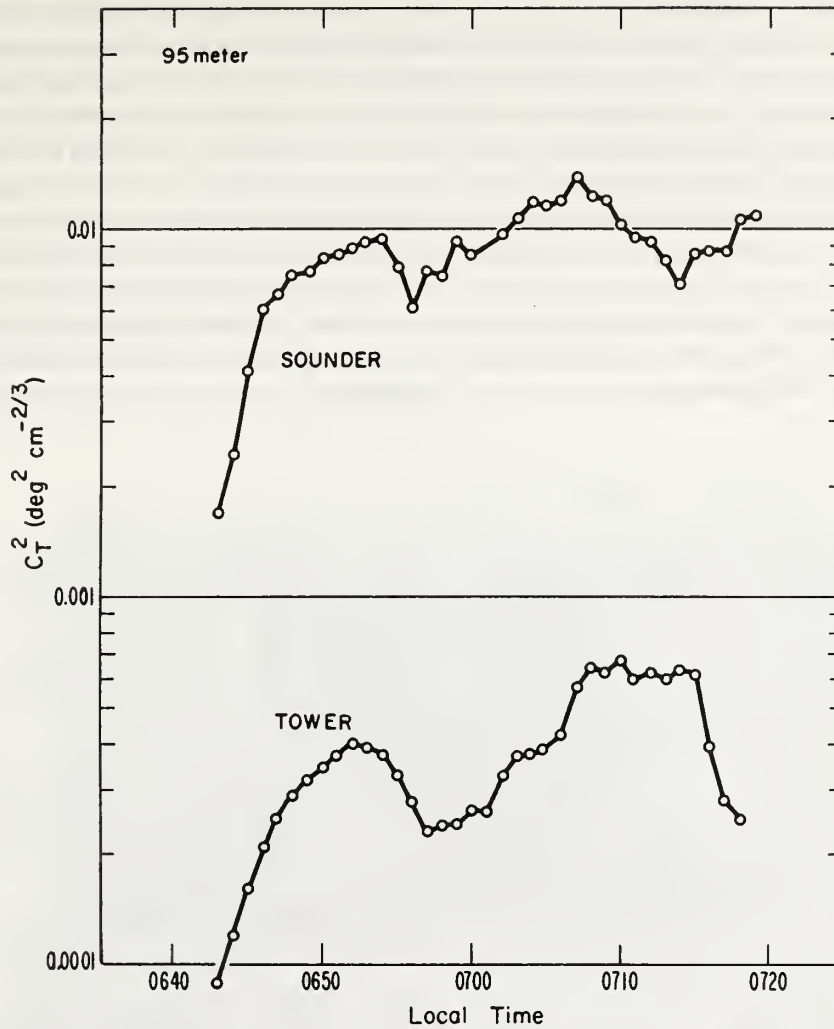


Fig. 1. Comparison of C_T^2 measured by an *in situ* sensor and by a vertically pointing acoustic echo sounder. The sampling volumes were at equal heights above the ground, but were separated by about 230 m horizontally.

ture and wind structure of the atmosphere. This is a problem as old as wave propagation itself; it has been treated in the clear-air EM radar case by authors such as Atlas (1964), and Ottersten (1970).

Several methods would appear to be available for distinguishing partial reflection in this sense from scatter by turbulence in the medium. We could compare the frequency dependence of the observed echo return with that predicted by scatter theory (a relatively weak $k^{1/3}$ dependence) and with that predicted from partial reflections (sensitive to details of the profile, but in general terms a rather strong k^{-2} dependence).

A limited amount of such data is already available, but as yet it has not been analyzed. Figure 2 shows two acoustic sounder facsimile records taken last winter in Alaska as part of a study of ice fog inversions run jointly with the Geophysical Institute of the University of Alaska and supported by the National Science Foundation. The lower record was made using a sounder operating at a constant frequency of 2000 Hz. The large variation in the intensity of the signal return with frequency (see upper record) is primarily due to the complicated dependence of acoustic absorption on the carrier frequency. The effect of this absorption will have to be removed from the data of Figure 2 before the validity of the partial reflection approach can be confirmed or rejected by this means. Since the frequency dependence of the absorption is likely to be quite considerable (in fact, it is the basis for theoretical hopes that acoustic echo-sounding may provide boundary-layer temperature and humidity

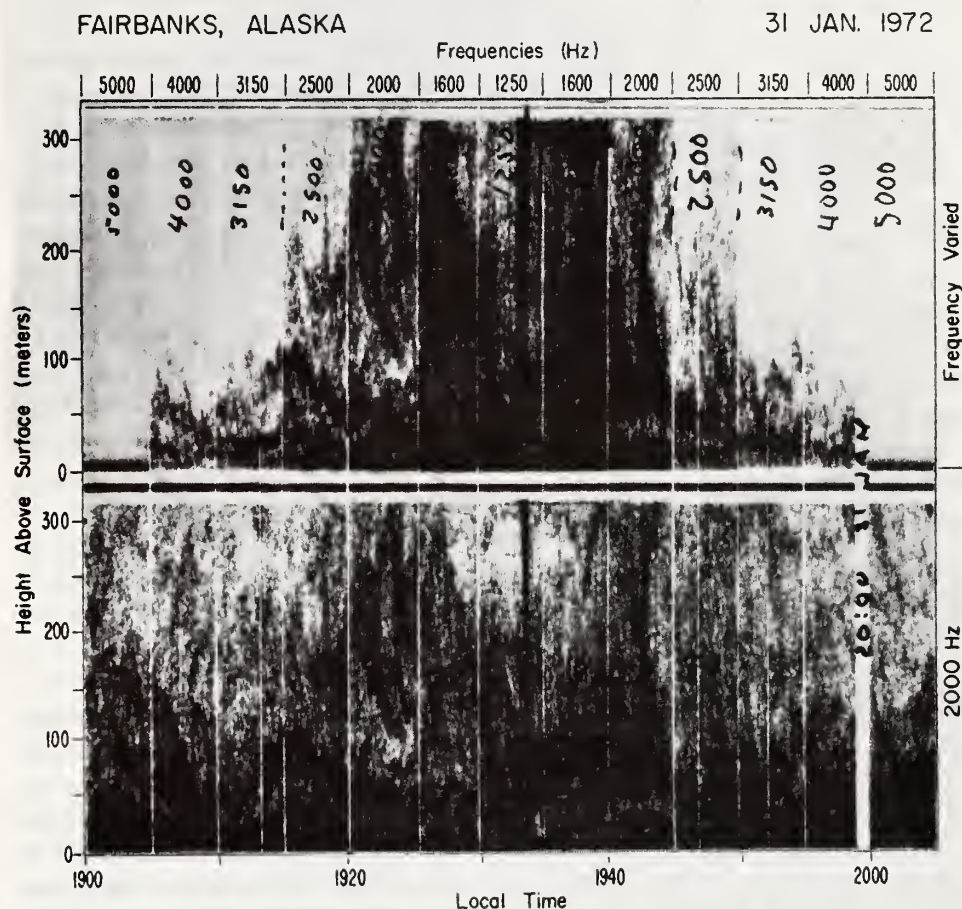


Fig. 2. Acoustic echo-sounder records showing the change in echo intensity with a change in carrier frequency. The frequencies used to produce the upper half of the picture are shown along the top. The lower portion of the figure is the echo return from a constant frequency of 2000 Hz.

profiles (Little, 1969; Gething and Jenssen, 1971)), it may completely obscure the frequency dependence resulting from the scatter or reflection mechanisms.

Alternatively we could assume that the refractive index gradients produced by the mean boundary-layer temperature and wind structures are vertical, so that the strength of the partial reflection echo should fall off rapidly as we steer the acoustic beam from the vertical to off-vertical angles. There is a limited amount of qualitative data of this type available as well. Figure 3 shows two acoustic echo facsimile records, one made using a vertical sounder beam, the other using a beam inclined at an angle of $35^{\circ}9'$ from the vertical.

The two records, in general, show the same features, although those sensed by the tilted antenna appear at correspondingly greater ranges and have greater apparent thickness. (The scales on the left side of the figure compensate for this difference and give the height above the surface). There does not seem to be any marked trend

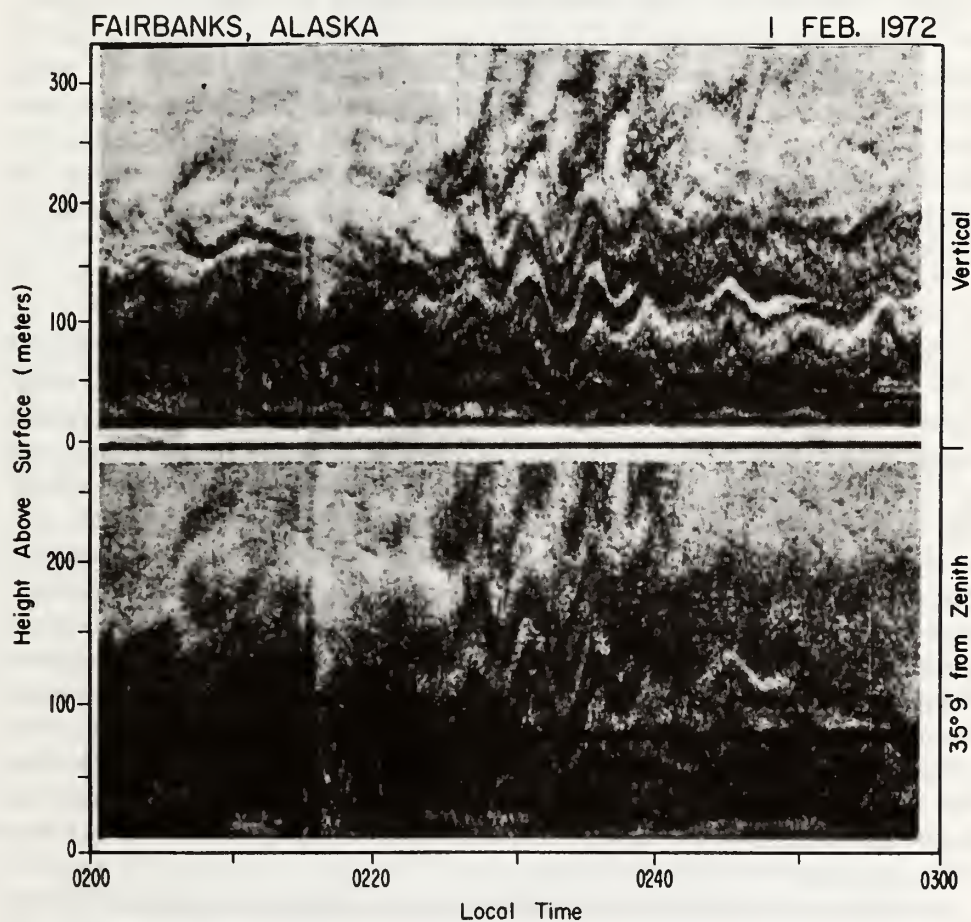


Fig. 3. Acoustic echo-sounder records from a vertically pointing antenna (top) and an inclined antenna (bottom).

favoring echo returns from the vertical direction (top record) with the possible exception of the thin layer between 0210 and 0215 at a height of 170 m. Nevertheless, mere visual evidence of this type is inconclusive and quantitative comparisons which take into account the distortion of the radiation pattern with changes in antenna inclination, etc., remain to be performed.

As a final possibility, we could measure the atmospheric wind and temperature profiles directly, using carriage data from the instrumented tower, and calculate the associated refractive-index profiles. Making such measurements with a resolution and accuracy sufficient to be definitive may prove impracticable, however, since the most important partial reflections are produced by sharp gradients occurring on scales small compared to the probing wavelength. Further theoretical and experimental studies of partial reflection mechanisms and their bearing on the observed strength of the acoustic echo returns are currently underway.

A second factor, possibly leading to an overestimate of C_T^2 by the acoustic echo-sounder, is the small size of the scattering volume used in the experiment. As pointed out, for example, by Tatarski (1971), there is, in consequence, a contribution to the scatter arising from spectral components of the turbulence for which the Bragg condition does not hold exactly. Preliminary estimates suggest, however, that these contributions are not sufficiently large to account for the observed discrepancy between theory and the experiment. Errors in determining the beam shape, the equipment parameters, and atmospheric absorption may also account for some of the discrepancy.

3. Doppler Winds vs. *In-Situ* Measurements

We now turn to a brief description of an experiment performed in the summer of 1971 using a three-antenna Doppler system designed to measure the three vector components of the boundary-layer wind at a single fixed level. The measurements were compared with those from an anemometer made at roughly the same level using an NCAR tethered-kytoon system known as the Boundary Layer Profiler (BLP). The BLP measured only the total wind speed and not its direction; the only data available for a direction comparison came from a wind vane atop a 15-m tower. Our consideration of these results will be brief, since they have been presented elsewhere (Beran and Clifford, 1972) and since the comparisons were limited to convectively unstable conditions as part of a thermal plume study, of peripheral interest at best to this conference. Nevertheless, the wind measurements constitute the only calibration or comparison to date between the Doppler technique and wind measurements by more conventional means. The data nicely illustrate the difficulties and subtleties involved in such comparisons, and they serve as well to indicate the degree of confidence we may have in the acoustic echo-sounding wind *profiles* obtained since, and discussed in the next section.

A schematic of the experimental geometry and the antenna configuration used in the experiments described here and in the next section is shown in Figure 4. One of the three antennas was directed vertically. The other two were located along roughly

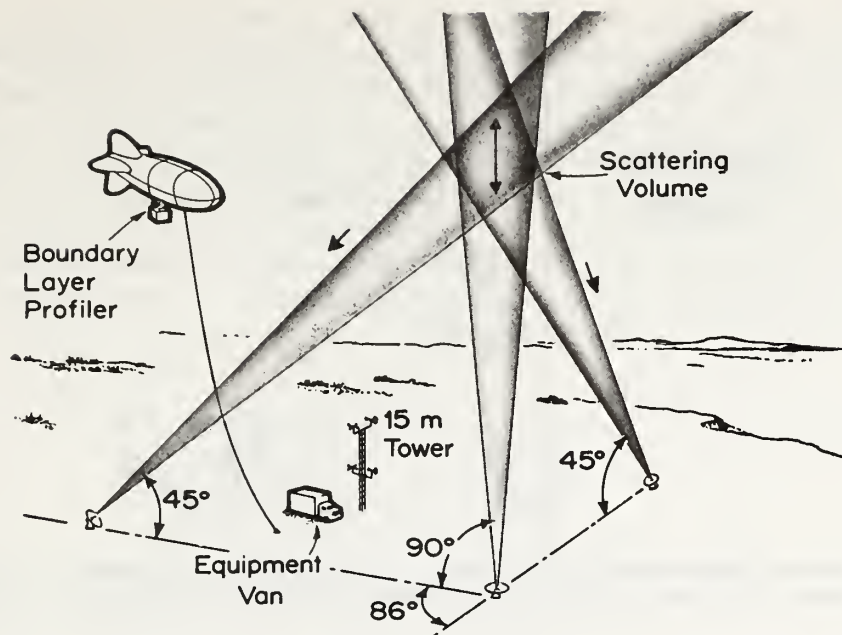


Fig. 4. Experimental antenna configuration used to measure winds from the acoustic Doppler shift.

orthogonal axes intersecting the first; they were tilted so that the three beams intersected at a height of from 150–200 m (depending upon the antenna spacing, which was varied from 150–200 m). Only the vertical antenna was pulsed. The echo return from the common volume was recorded using all three antennas, so that the three components of the wind could be measured using the standard Doppler Equation

$$V \cos \beta = \frac{c}{2 \sin \theta} \left[\frac{\Delta f}{f_0} \right] \quad (4)$$

(see Figure 5).

Here f_0 is the transmitter frequency and Δf is the frequency shift of the acoustic echo return; V is the magnitude of the wind vector and β is the angle between the velocity vector and the difference of the transmitted and scattered wave vectors. In this experiment it was assumed that refraction of the acoustic pulses could be ignored; a recent analysis by Georges and Clifford (1972) of such effects suggests that they are likely to be small in the boundary-layer application. Beran and Clifford (1972) computed the spatial and velocity resolutions of the system; it was found to have a scattering volume ≈ 30 m on a side and a velocity resolution (obtained partially at the expense of the spatial resolution) $\approx \pm 0.15 \text{ m s}^{-1}$.

Figure 6 shows a comparison between Doppler and *in situ* measurements of wind speed and direction for an eight-minute interval during the course of the experiment. The Doppler records have been lagged 48 s; this lag corresponds to the point at

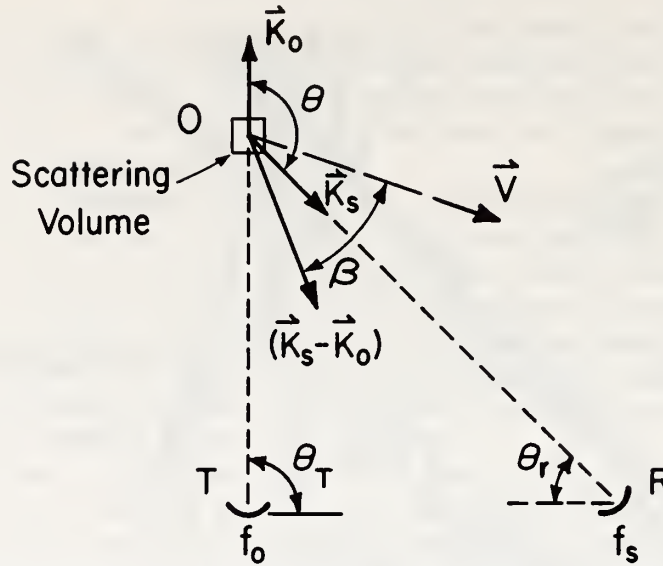


Fig. 5. Schematic diagram showing the orientation of wave vectors from a transmitter, T, and a receiver, R. The vector $(\vec{K}_s - \vec{K}_0)$ represents the Doppler shift produced by a wind V.

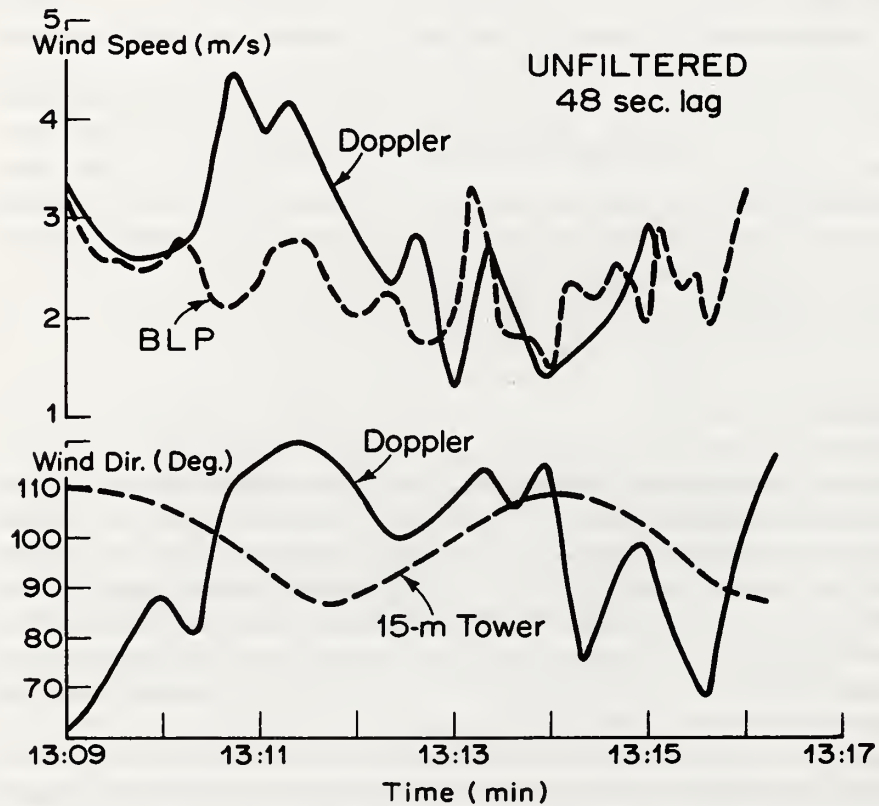


Fig. 6. Comparison of wind speed measured by the Doppler technique and a kytoon-mounted anemometer (BLP) (top). The lower traces show the Doppler wind direction at a height of 200 m compared with those sensed on a tower at 15 m.

which maximum cross-correlation between the two sets of wind data occurred, and it compensates for the spacing between the BLP and Doppler sampling volumes. The correspondence between the two records appears to be excellent. What differences there are can be attributed to the fact that the sounder and BLP were not sampling the same volume at the same time, and to changes in the wind speed which caused the height and distance from the sampling volume to vary. Low-pass filtering was used to remove spectral wavelengths shorter than the separation distance between the Doppler and BLP sampling volumes. A total of 30 min of data that have been low-pass filtered with a time constant of 2 min is shown in Figure 7, a scatter diagram of

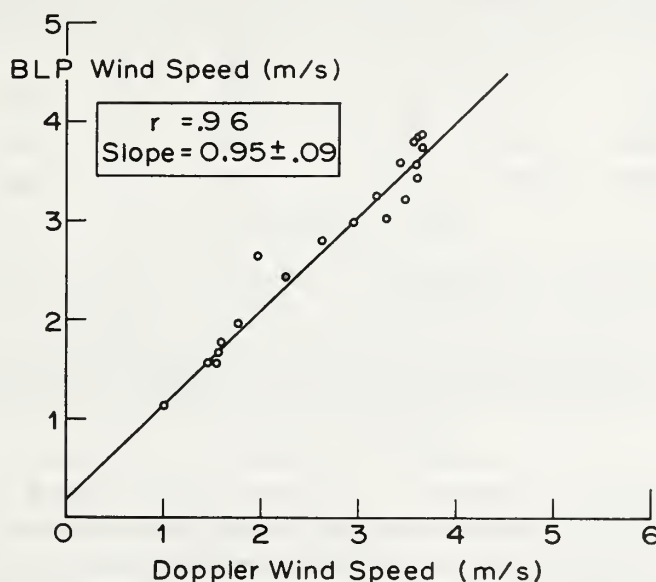


Fig. 7. Scatter diagram of winds measured by an *in situ* anemometer (BLP) and the acoustic Doppler technique.

Doppler vs. BLP winds. Again it can be seen that there is good agreement between the wind speeds measured by the two techniques. The non-zero y-intercept of the straight-line fit results from the 0.5 m s^{-1} start speed of the BLP anemometer. These biased high values were averaged in the two-minute means causing all low BLP winds to appear too high.

4. Gravity-Wave Studies

In the course of the acoustic echo-sounder equipment development and testing, we have begun to evolve procedures for the observation and study of gravity-wave dynamics in the planetary boundary layer. The acoustic echo-sounder facsimile records are useful in such studies since they reveal the wave motions rather clearly as undulations in the strata of strong echo returns (Figure 8). Indeed, there is now some theoretical and experimental evidence to suggest that these strata are themselves

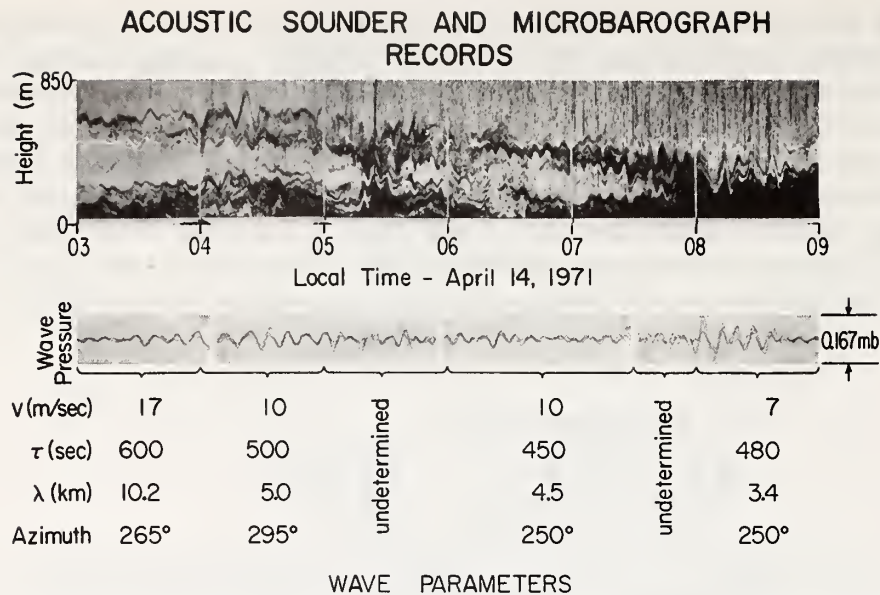


Fig. 8. Atmospheric gravity waves revealed by the acoustic echo sonder as undulations in the strata of strong echo returns in the stable planetary boundary layer. The white line superimposed on the facsimile record is the pressure trace from a microbarograph located roughly 800m from the sonder. The good correspondence between the two records is obvious. The microbarograph was part of a four-element array; the four pressure traces, superimposed and time shifted to provide maximum cross-correlation, are also shown. The wave parameters thus deduced are indicated in the table.

produced by gravity-wave encounters with the stable planetary boundary layer (Gossard *et al.*, 1971). Nevertheless, the facsimile records alone give little quantitative information other than the wave period and a somewhat indirect measure of wave amplitude (the vertical displacement of the strata). They yield no information on wavelength and phase velocity, the background temperature and wind structure in which the waves may be ducted, and the wave-associated momentum and energy transports, all of which must be known if the role of the waves in boundary-layer dynamics is to be properly understood.

To obtain at least some of this missing information, we have supplemented the facsimile records with *in situ* measurements of various kinds. One approach, for example, has been simply to use acoustic echo-sounding facsimile records to supplement the conventional micrometeorological experiments employing towers instrumented with anemometers and temperature sensors to measure the terms in the boundary-layer turbulent energy budget. The facsimile records can then be used to select the events for analysis and to show what boundary-layer features are responsible for the differences in the turbulence intensity seen at the different instrument levels and times. This is the kind of approach used with great effect by Emmanuel *et al.* (1973) and Bean *et al.* (1973), for example.

In addition, we have begun to use the acoustic echo-sounder equipment in conjunc-

tion with microbarograph arrays (Hooke *et al.*, 1972). These instruments which detect and measure small-amplitude pressure fluctuations occurring with periods of a few seconds to several tens of minutes, have been used for years to detect the acoustic signals from explosions, severe weather, the aurora, and other natural sources. The arrays provide data on the wave amplitude, wave period, horizontal phase speed and direction of propagation, and the horizontal wavelength (e.g., Cook, 1962, 1969; Cook and Young, 1962). In most microbarograph work, interest has focused on the acoustic signals, while the pressure fluctuations associated with gravity waves have been regarded as noise to be eliminated by any means possible. The latter tend to have a much larger amplitude, however, so that they often appear quite clearly on the records despite considerable filtering.

A comparison between such microbarograph records and acoustic echo-sounding facsimile records taken nearby shows rather convincingly that the microbarographs and the sounder can detect the same waves (See Figure 8). Superimposed on the sounder record of this figure is a microbarograph pressure trace recorded some 800 m away. The pressure fluctuations and the short-period undulations in the echo strata exhibit an excellent correspondence which persists for over six hours. Below the acoustic echo-sounder record, we show the four pressure traces from the microbarograph array (roughly 1.8 km on a side – the geometry of the experiment is shown in Figure 1 of Hooke *et al.* (1972)). These have been time-shifted relative to one another so as to provide maximum cross-correlation. The wave parameters deduced from these time-shifts are shown in the table at the bottom of Figure 8. There were two time intervals during which it proved impossible to determine a single time-shift providing good cross-correlations, implying that either (a) the wave propagation was quite dispersive, (b) the wave parameters were changing very rapidly, or (c) there was, in fact, no wave motion present during these intervals. It is interesting to note the chaotic appearance of the facsimile records during these intervals.

It turns out that both the acoustic echo-sounder and the microbarograph array are able to detect gravity-wave motions present in elevated inversions, even during intervals when the boundary layer itself is convectively unstable. This can be seen in Figure 9, which shows data taken later during the morning of April 14, 1971. Here the acoustic echo-sounder reveals that at low levels there is a great deal of convective plume activity of the type observed and discussed by McAllister *et al.* (1969), Beran *et al.* (1971) and Hall *et al.* (1971). This plume activity manifests itself on the microbarograph records as pressure fluctuations of rather high frequency which are essentially uncorrelated over the array. In addition to these pressure fluctuations, there are pressure fluctuations over a range of very low frequencies that are rather well correlated over the array, all having the horizontal phase speed and direction indicated in the Table. In addition, they seem to correlate well with the undulations in the strata of the inversion layer capping the thermal plume activity. It is of interest to note the apparent interaction between the waves in the inversion and the underlying thermal plume activity, as has been observed by other authors (Gossard *et al.* (1971)). Whether the waves are generated by the penetrative convection

ACOUSTIC SOUNDER AND MICROBAROGRAPH RECORDS

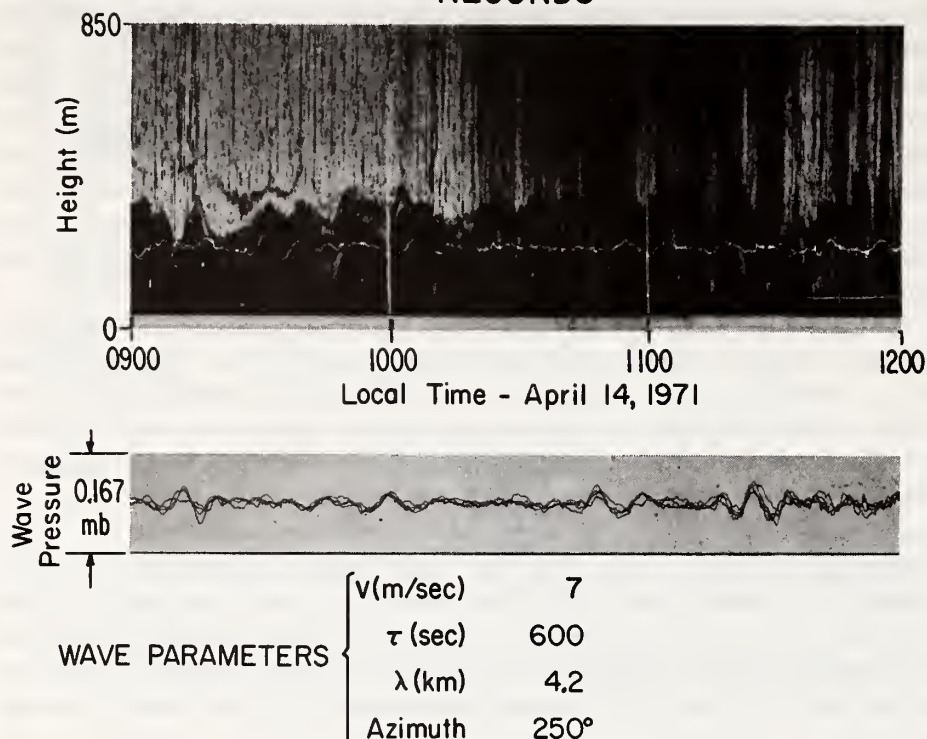


Fig. 9. Observations of wave structure in an elevated inversion just above a convectively unstable boundary layer. The acoustic echo-sounder facsimile record shows the thermal plume structure characteristic of the unstable boundary layer, with the stratified structure of the elevated inversion overlying it. Superimposed on the facsimile record is the pressure trace from a microbarograph 800m distant from the sounder. Some degree of correspondence is evident. Also shown are the pressure traces from the four microbarographs of the array superimposed and time-shifted to provide maximum cross-correlation, and the wave parameters deduced therefrom.

process described by Townsend (1966, 1968) and appearing as well in numerical boundary-layer models (Deardorff, 1969) or whether the gravity waves somehow control the thermal convection, is at present impossible to say. Further studies of this interaction are currently underway.

We carried the microbarograph-sounder studies one step further at Haswell, Colorado, in the following autumn, by using not only a ground-based microbarograph array, but also a microbarograph atop the 150-m tower, in order to study gravity waves generated by shear instability in the planetary boundary layer. This type of wave generation had been studied earlier at Haswell, with results reported by Emmanuel *et al.* (1972) and Emmanuel (1973). Together with a bivane anemometer atop the tower, the microbarograph provides direct data on the micro-scale wave phase velocity V_p (measured relative to the moving medium) given by the so-called impedance

relation (Gossard and Munk, 1954)

$$V_p = \frac{\Delta p}{\rho_0 \Delta V_x}, \quad (5)$$

where Δp is the wave-associated pressure perturbation, ΔV_x is the wave-associated horizontal velocity perturbation, and ρ_0 is the background atmospheric density. The microbarograph and anemometer also measure the vertical wave energy flux, which is given by

$$E = \langle \Delta p \Delta V_z \rangle, \quad (6)$$

where ΔV_z is the wave-associated vertical velocity perturbation. In the one event studied in detail so far (Figure 10), we have determined that the wave phase velocity is indeed equal to the wind velocity in the middle of the shear zone, as assumed by Emmanuel and his co-workers in their analyses, and we have measured a rather considerable vertical energy flux, $\sim 800 \text{ erg cm}^{-2} \text{ s}^{-1}$. The results are discussed in more detail in a separate paper (Hooke *et al.*, 1973).

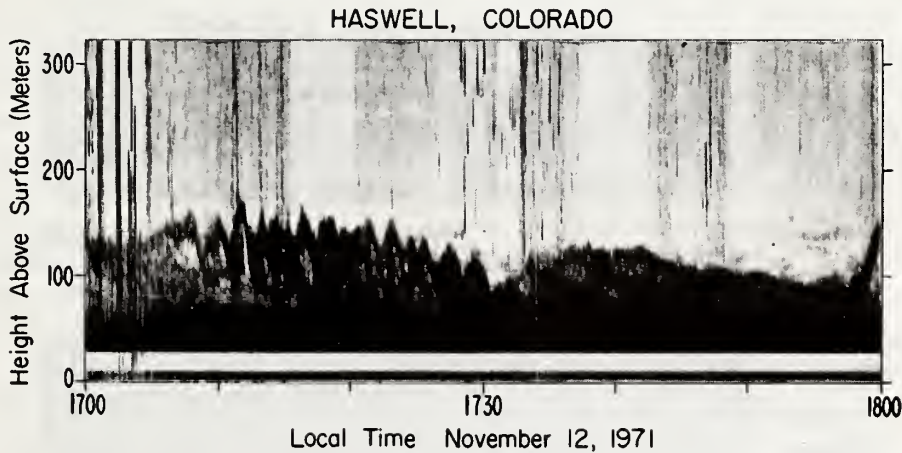
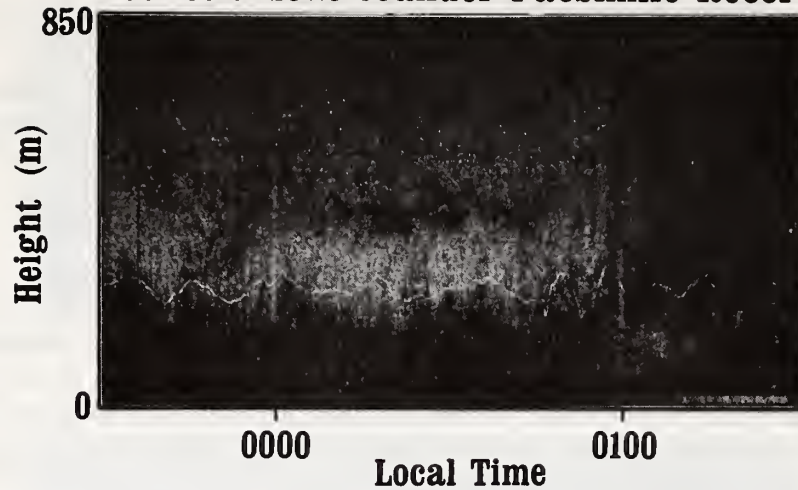


Fig. 10. Acoustic echo-sounder facsimile record showing the breaking wave structure characteristic of wave generation by shear instability in the boundary-layer shear flow. This particular event is discussed in detail by Hooke *et al.* (1973).

In the studies described above, the acoustic echo-sounder has played only a supporting role, aiding in the selection of events for analysis and in the interpretation of measurements made using conventional sensors. In other experiments, however, the Doppler capabilities of the technique have been utilized; for example, Beran *et al.* (1971) have used acoustic Doppler to measure the vertical fields within thermal plumes and breaking wave structures. In addition, we now have about 90 min of Doppler data taken during stable conditions using a three-antenna acoustic echo-sounding system designed to yield height profiles of the three vector wind components.

TABLE MOUNTAIN AUGUST 19, 1971

Acoustic Echo-Sounder Facsimile Record



Microbarograph Records

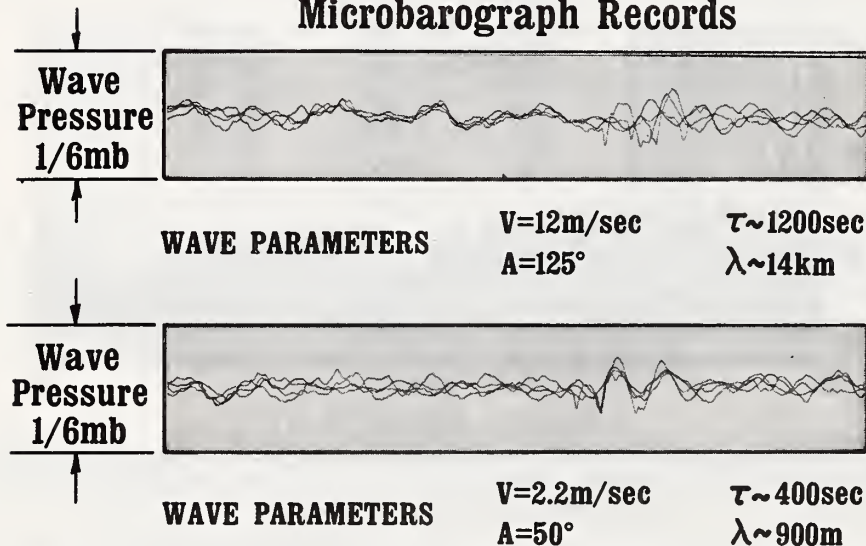


Fig. 11. Acoustic echo-sounder facsimile record and microbarograph records for the early morning hours of August 19, 1971 at Table Mountain. Superimposed on the facsimile record is the pressure trace from the microbarograph nearest the sounder, to indicate the degree of correspondence. Immediately below the facsimile record, the four microbarograph records have been superimposed and time-shifted to exhibit maximum cross-correlation for the long-period wave evident during the interval between 0000 and 0040 LT; and for the short-period wave prominent after roughly 0045 LT. The wave parameters thus deduced are shown for each wave. While it appears that the short-period fluctuations are correlated only for two cycles, slight time shifts markedly improve the apparent correlation after this time, while still leading to the conclusion that the wave phase velocity is $\sim 2\text{m s}^{-1}$ from the northeast. The microbarograph sensitivity is dependent upon frequency and the frequency difference between the two waves is considerable; for this reason the pressure amplitude scale is indicated as approximate.

The data were recorded during the early morning of August 19, 1971. As might be expected, this 90-min interval did not happen to be as interesting from the dynamical standpoint as a number of other periods for which the Doppler data are unavailable, but there did exist a certain amount of wave activity throughout the interval, and in any event it is instructive to consider the kind of insight the Doppler data gave.

The Doppler system was operated in this experiment in the same configuration as described in Section 3, except that in this instance, all three antennas were operated in the active monostatic mode, at different frequencies. The signals were gated at intervals along the respective beams, and the Doppler-shifted frequencies were extracted from each of the three for equal heights above the surface. The three radial wind components thus measured are in the same volume only at the height of intersection of the beams (200 m), but provided there exists horizontal homogeneity over a distance the order of the antenna spacing and over averaging times the order of one minute, the data yield height profiles of the wind speed and direction from roughly 70 m (a lower cutoff determined by antenna ringing, ground clutter, etc.) to 500 m (the boundary-layer thickness).

Figure 11 shows the facsimile record from the vertically-oriented antenna for the night of August 18–19, 1971. The record is unfortunately not so clear as some; nevertheless it shows the usual laminated structure characteristic of the stable planetary boundary layer, and wave-associated undulations in the strata of strong echo returns. Of particular interest here is a change in the character of the record beginning at about 0045 LT. This change manifests itself as an increase of the general intensity of the echo returns as well as a change in the appearance of the wave motions, and this is borne out by the microbarograph records taken nearby. During the first half of the observing interval, the dominant wave motion is of relatively long period (~ 20 min) and the wave is propagating across the array from the southeast, with a rather high phase speed ($\sim 12 \text{ m s}^{-1}$), as shown in the lower half of Figure 11. There is some visual evidence that this wave motion may well persist throughout the remainder of the observing interval, from 0045–0140, but during this latter interval there is another wave motion present as well; this has considerably shorter period (~ 7 min) and propagates with small phase speed ($\sim 2 \text{ m s}^{-1}$) from the northeast.

Figure 12 shows height profiles of wind speed and direction computed from 10-min averages (120 pulses) of the Doppler shifts at ten different heights between 73 and 470 m. The profiles show evidence of a low-level wind maximum. The boundary-layer wind-direction profiles change significantly at about 0045 LT. The upper-level winds become more easterly while the lower-level winds shift from northerly to westerly. As a result the directional shear is increased considerably after 0045 LT, the shear magnitude reaching $3 \times 10^{-2} \text{ s}^{-1}$ in the vicinity of 300 m. This is a large value, perhaps sufficiently large to result in dynamical instability, in which case it would seem reasonable to ascribe the source of the small-scale waves appearing on the facsimile and microbarograph records at this time to this shear.

Figure 13 shows the isotach contours (contours of constant wind speed), as derived from the three-minute averages of the Doppler data, superimposed on the facsimile

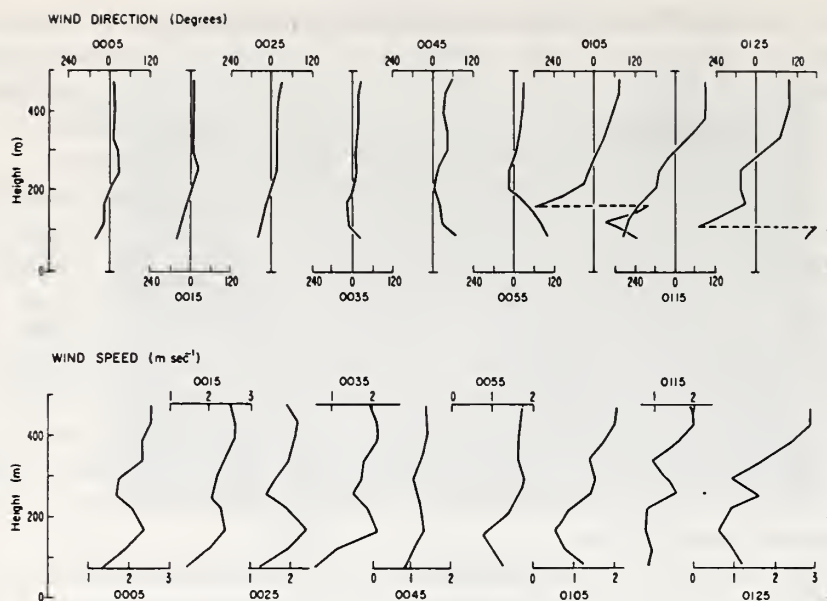


Fig. 12. 10-min averages of the vertical profiles of wind speed (lower half) and wind direction (upper half) as measured by the acoustic Doppler technique. The time shown on each graph refers to the central time of the 10-min average.

record. In general, the undulations in these contours follow even the higher frequency undulations of the strata, seen in the facsimile record, rather closely.

Encouraged by this agreement, we decided, as an exercise, to estimate the boundary-layer momentum flux in the spectral region between roughly 1 min and 20 min period during this one and one-half hour interval. After removing long-period trends, we computed the vertical fluxes of zonal (x) and meridional (y) momentum from the formulas

$$M_x = \frac{\rho_0}{10} \sum_{i=1}^{10} (v_x - \bar{v}_x) (v_z - \bar{v}_z),$$

$$M_y = \frac{\rho_0}{10} \sum_{i=1}^{10} (v_y - \bar{v}_y) (v_z - \bar{v}_z),$$

at 10-min intervals, for each of the ten heights considered. Because the data at heights away from the beam intersections are subject to some uncertainty, and because the momentum fluxes appeared to be largest at the 250-, 294- and 338-m levels, we concentrated our attention on the average of the fluxes through these three levels, plotted in Figure 14. The results indicate a rather large flux (3 dyn cm^{-2}) of southeasterly momentum upwards throughout the early part of the observing interval. We

TABLE MOUNTAIN COLORADO

19 August 1971

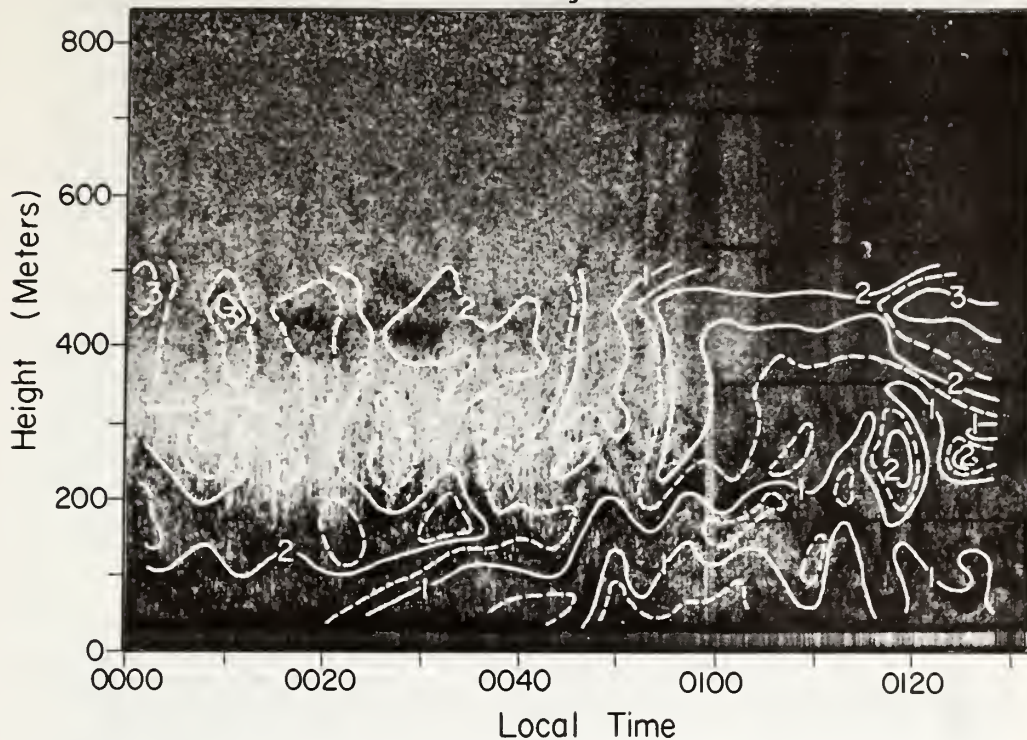


Fig. 13. The isotach field of the total horizontal wind component derived from the acoustic Doppler measurements superimposed on the facsimile record for the same time period. Note the close agreement between the wave motions shown by the facsimile record and the fluctuations in the wind field.

find it difficult to attribute a large flux in this direction to anything other than the wave observed propagating from the Southeast. The data filtering would cause this flux measurement to be something of an underestimate. Such a large flux implies that the wave is either imperfectly ducted, so that some energy and momentum are free to leak upwards, or that the interaction of the wave with the orography of the site is causing an upward energy-momentum propagation. The easterly component of the momentum flux decreases considerably during the second half of the observing interval; this could be explained if the wave generated by shear instability during the latter half of the observing interval produced a downwards flux of northeasterly momentum of the order of 1 dyn cm^{-2} or so. This would appear to be consistent with current ideas of the momentum transport occurring during such events.

It should be mentioned that the wind speeds and particularly the wind directions measured here are subject to some uncertainty. In the Doppler data processing, we have included only signals of a strength above a certain cutoff value, chosen somewhat subjectively; the horizontal wind directions subsequently determined turn out to be

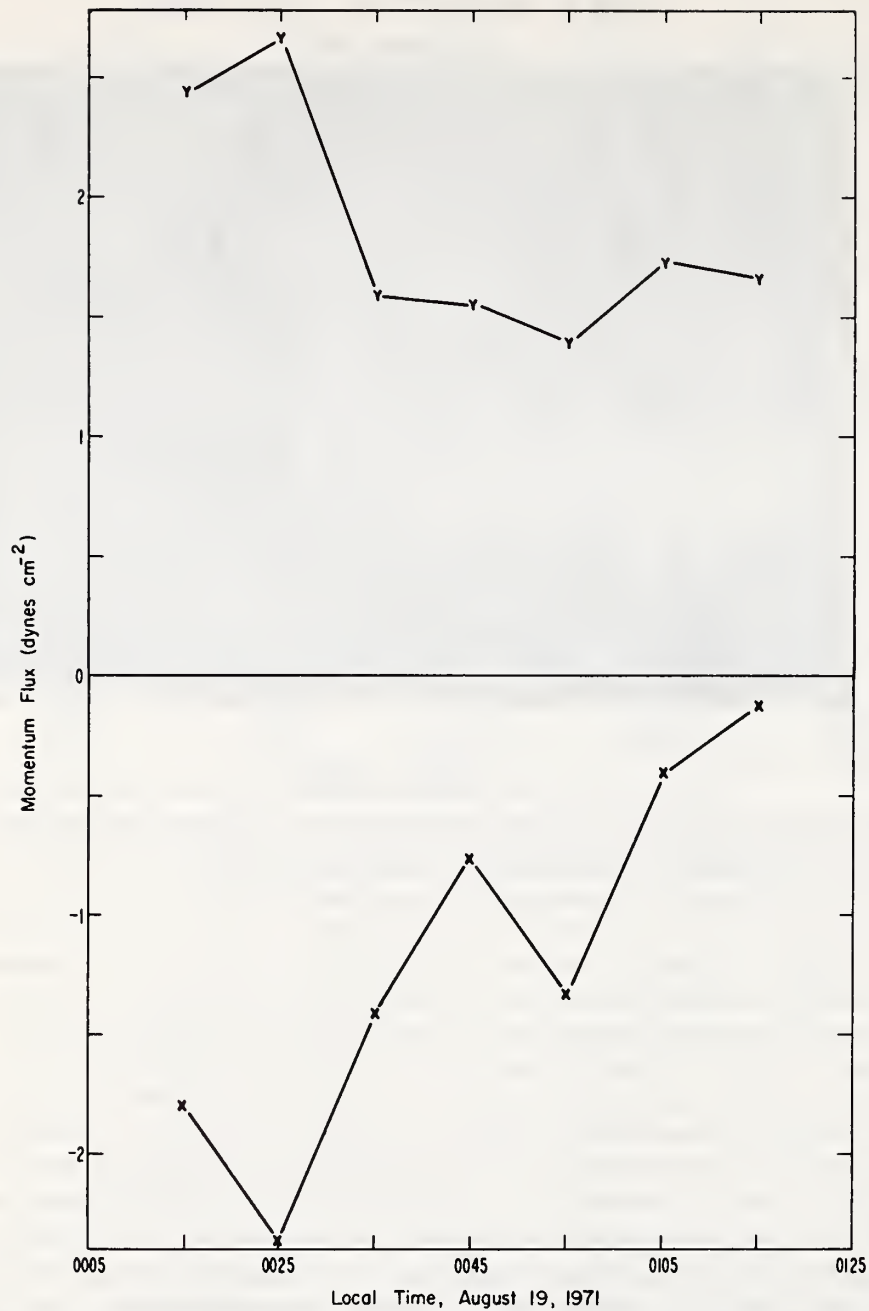


Fig. 14. The vertical fluxes of zonal (x) and meridional (y) momentum as derived from the acoustic Doppler measurements. Positive values correspond to upward fluxes of eastward- and northward-directed momentum, respectively (or equivalently, to downward fluxes of westward- and southward-directed momentum).

sensitive to the level of this cutoff. For this reason, we cannot claim to have estimated the momentum fluxes to within better than a factor of two or so. Improvements in the methods of data acquisition and processing should eliminate this uncertainty in future experiments.

Nevertheless, it is encouraging to see that the Doppler data, the facsimile record, and the microbarograph data appear to give a reasonably consistent picture of the boundary-layer dynamics during this one and one-half hour period. We are optimistic about the usefulness of quantitative acoustic echo-sounder data in future studies of gravity-wave dynamics in the stable boundary layer.

Acknowledgments

G. E. Greene, J. W. Wescott, and B. C. Willmarth aided significantly in the data acquisition. M. Ackley and W. D. Neff assisted with the computer processing of the Doppler data. Dr H. Baynton and R. McBeth kindly contributed the use of the NCAR Boundary Layer Profiler as well as considerable time and effort. We also acknowledge the many helpful comments of Drs F. F. Hall, E. Gossard, and B. Bean during the preparation of this manuscript.

References

- Atlas, D.: 1964, 'Advances in Radar Meteorology', *Advan. Geophys.* **10**, 317.
- Bean, B., Frisch, A. S., McAllister L. G., and Pollard, J. R.: 1973, 'Planetary Boundary-Layer Turbulence Studies from Acoustic Echo Sounder and In-situ Measurements', *Boundary-Layer Meteorol.*, in this issue, p. 449.
- Beran, D. W. and Clifford, S. F.: 1972, 'Acoustic Doppler Measurements of the Total Wind Vector', *Proc. of AMS Second Symp. on Meteorol. Obs. and Inst.*, San Diego, Calif., 100-109.
- Beran, D. W., Little, C. G., and Willmarth, B. C.: 1971, 'Acoustic Doppler Measurements of Vertical Velocities in the Atmosphere', *Nature* **230**, 160-162.
- Cook, R. K.: 1962, 'Strange Sounds in the Atmosphere. Part I', *Sound* **1**, 12-16.
- Cook, R. K.: 1969, '*Atmospheric Sound Propagation*', Final Report, Panel on Remote Atmospheric Probing of the Committee on Atm. Sc. NAS-NRC, 633-669.
- Cook, R. K. and Young, J. M.: 1962, 'Strange Sounds in the Atmosphere. Part II', *Sound* **1**, 25-33.
- Deardorff, J. W.: 1969, 'Numerical Study of Heat Transport by Internal Gravity Waves Above a Growing Unstable Layer', *Phys. Fluids*, Supplement II, High Speed Computing in Fluid Dynamics, II 184-II 194.
- Emmanuel, C. B.: 1973, 'Richardson Number Profile Through Shear-Instability Wave Regions Observed in the Lower Planetary Boundary Layer', *Boundary-Layer Meteorol.*, in press.
- Emmanuel, C. B., Bean, B. R., McAllister, L. G., and Pollard, J. R.: 1972, 'Observations of Helmholtz Waves in the Lower Atmosphere With an Acoustic Sounder', *J. Atmospheric Sci.* **29**, 886-892.
- Georges, T. M. and Clifford, S. F.: 1972, 'Acoustic Sounding in a Refracting Atmosphere', *J. Acoust. Soc. Amer.* (in press).
- Gething, J. T. and Jenssen, D.: 1971, 'Remote Measurement of Temperature and Humidity by Means of Acoustic Echo Sounding', *Nature*, **231**, 198-200.
- Gossard, E. E. and Munk, W.: 1954, 'On Gravity Waves in Atmosphere', *J. Meteorol.* **11**, 4, 246-269.
- Gossard, E. E., Jensen, D. R., and Richter, J. H.: 1971, 'An Analytical Study of Tropospheric Structure as Seen by High-Resolution Radar', *J. Atmospheric Sci.* **28**, 794-807.
- Hall, F. F., Jr., J. W. Wescott, and W. R. Simmons: 1971, 'Acoustic Echo Sounding of Atmospheric Thermal and Wind Structure', *Proc. of 7th Int. Symp. on Remote Sensing of Environ.*, Univ. of Mich., 1715-1732.

- Hooke, W. H., Young, J. M., and Beran, D. W.: 1972a, 'Atmospheric Waves Observed in the Planetary Boundary Layer Using an Acoustic Sounder and Microbarograph Array', *Boundary-Layer Meteorol* **2**, 371-380.
- Hooke, W. H., Hall, F. F., and Gossard, E. E.: 1973, 'Observed Generation of an Atmospheric Gravity Wave by Shear Instability in the Mean Flow of the Planetary Boundary Layer', *Boundary-Layer Meteorol.*, in press.
- Kallistratova, M. A.: 1961, 'Experimental Investigation of Sound Wave Scattering in the Atmosphere', *Trudy Inst. Fiz. Atmos., Atmos. Turbulentnost* **4**, 203-256.
- Little, C. G.: 1969, 'Acoustic Methods for the Remote Probing of the Lower Atmosphere', *Proc. IEEE* **57**, 571-578.
- McAllister, L. G., Pollard, J. R., Mahoney, A. R., and Shaw, P. J. R.: 1969, 'Acoustic Sounding - A New Approach to the Study of Atmospheric Structure', *Proc. IEEE* **57**, 579-587.
- Monin, A. S.: 1962, 'Characteristics of the Scattering of Sound in a Turbulent Atmosphere', *Akust. Zh.* **7**, 457-461 (*Sov. Phys. Acoust.* **7**, 370-373).
- Ottersten, H.: 1970, 'Radar Angles and Their Relationship to Meteorological Factors', *Final Report FOA, Res. Inst. of Nat. Def. Sweden* **4**, 1-33.
- Tatarski, V. I.: 1971, 'The Effects of the Turbulent Atmosphere on Wave Propagation', (Israel Prog. for Sci. Transl.) NOAA TT 68-50464, 471 pp.
- Townsend, A. A.: 1966, 'Internal Waves Produced by a Convective Layer', *J. Fluid Mech.* **24**, 307-319.
- Townsend, A. A.: 1968, 'Excitation of Internal Waves in a Stably-Stratified Atmosphere With Considerable Wind Shear', *J. Fluid Mech.* **32**, 145-171.

Reprinted from the Proceedings of Symposium in Air Pollution,
Turbulence and Diffusion, December 7-10, 1971, 66-72, March 1972.

APPLICATION OF AN ACOUSTIC SOUNDER TO AIR POLLUTION MONITORING

D. W. Beran, F. F. Hall, Jr., J. W. Wescott, W. D. Neff*

Wave Propagation Laboratory
NOAA, Environmental Research Labs.
Boulder, Colorado

INTRODUCTION

Control measures for air pollution in most large cities, are more in the nature of an effort to lessen the pain, rather than to cure the patient. In this unhappy state, the role of monitoring devices, which make possible some prediction of hazardous conditions, becomes even more important.

Effective monitoring requires instruments which provide information on the concentration of both gaseous and particulate matter, and instruments for monitoring meteorological conditions which control the dissipation of the noxious elements. This paper concentrates on a relatively new device, the Acoustic Echo Sounder, which is particularly well suited for the task of monitoring those meteorological parameters required for making intelligent decisions concerning the degree of hazard during a particular event.

It is common knowledge that the low level temperature structure is a prime factor in the creation of air pollution events. Severe problems are associated with the low level capping inversion off the coast of California and the Los Angeles basin, an area where quantities of polluted air can be trapped under the advected inversion. While Los Angeles may claim pride of place for these conditions, it is not, unfortunately, unique and many other cities can be found where similar topography - temperature structure interaction leads to severe pollution conditions.

While the temperature lapse rate is of prime concern in air pollution meteorology, secondary, and at times equally important, effects can be attributed to the wind pattern over a city. Clearly, wind direction plays an important role in determining the path pollutants will take after emission. In addition, the strength of the wind is important in determining how rapidly effluents will be carried away; a necessary input when determining if a given emission rate will produce critical concentration levels over a region. Other meteorological parameters, such as the presence of humidity and solar radiation, (both of which induce chemical reactions of certain pollutants) are important, but to a lesser degree.

A monitoring system which could provide a continuous detailed picture of the wind and temperature structure in the lowest 1 km over a city would be of much more value than the in situ meteorological sensors presently used. In general, most forecasters must rely on instrumentation designed to sample the larger synoptic scale, and as such, provide continual data only on surface parameters, upper air soundings being made, at most, four times daily. In addition, aviation requirements have often dictated the location of these sensors, a situation not necessarily in the best interests of the urban meteorologist.

It is suggested that the acoustic sounder is a device which could collect continuous mesoscale measurements in critical regions at a cost significantly below other proposed methods. The remainder of this paper will present a brief discussion of the theory of acoustic sounding followed by the results from recent field tests which demonstrate the potential of the device for measuring wind and temperature structure. In addition, problems relating to operating in the urban environment under all types of conditions will be covered.

THE ACOUSTIC ECHO SOUNDER

The acoustic echo sounder is, in principle, not unlike Sonar. A sound wave is transmitted into the medium to be interrogated, the atmosphere. Turbulent wind and temperature fluctuations scatter some of this wave energy, a part of which can then be collected at a receiver. This process is described by the radar equation

$$P_r = P_t \sigma \frac{c\tau}{2} \frac{A^2}{R^2} L, \quad (1)$$

*Assigned to NOAA/ERL from the NOAA Commissioned Officer Corps.

where the acoustic power returned P_r , is a function of the power transmitted, P_t , the speed of sound, C ; the length of pulse, τ ; the area of the receiving antenna, A ; the range to the area where the return is generated, R ; the losses, L due to absorption and equipment efficiencies, and, finally, the scattering cross section, σ . Theoretical work^{2,3} has established the relationship of the scattering cross section per unit volume, σ , to the turbulence parameters. The final form of the scattering equation is,

$$\sigma(\theta) = 0.03k^{1/3} \cos^2 \theta \left[\frac{C_v^2}{C^2} \cos^2 \frac{\theta}{2} + 0.13 \frac{C_t^2}{T^2} \right] \left(\sin \frac{\theta}{2} \right)^{-\frac{11}{3}}, \quad (2)$$

where $\sigma(\theta)$ is the scattered power, per unit volume, per unit incident flux, per unit solid angle at an angle, θ , from the initial direction of propagation. The wave number of the acoustic wave is represented by $k = 2\pi/\lambda$; C and T are the mean speed of sound and temperature in the scattering volume and C_v^2 and C_t^2 are the structure constants for velocity fluctuation and temperature fluctuations respectively.

The potential of acoustic echo sounding, first analyzed by C. G. Little⁴, has been demonstrated by the work of several investigators^{5,6,7} concentrating mainly on vertically pointing monostatic (colocated transmitter and receiver) systems. This early work clearly showed one of the possible roles that the acoustic echo sounder might play in air pollution monitoring⁸. One of these records made by the repeating traces of a facsimile recorder, synchronized with the pulses from the sounder is shown in Figure 1. This type of record gives a height time cross section of the low level

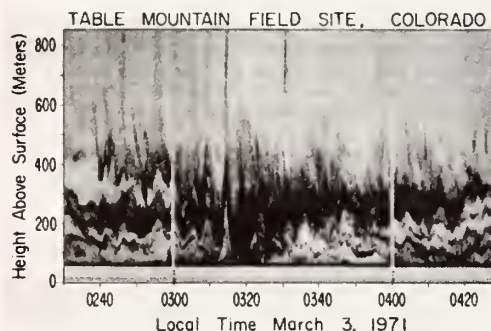


Figure 1 - Acoustic sounder record taken under stable conditions.

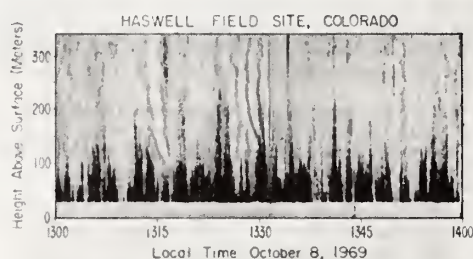


Figure 2 - Acoustic sounder record taken under unstable conditions.

boundary layer structure. Absolute temperature and gradients cannot be directly determined from this type of presentation, but the known interaction of C_t with various stability parameters i.e., temperature gradient and Richardson's number does make it possible to derive a qualitative assessment of the low level temperature structure. For example, regions which are dark (i.e. showing strong echoes) can, in general, be associated with either stable or unstable lapse rates and white areas are produced where conditions are neutral.

It is then logical to ask, how stable regions can be distinguished from those which are unstable? Here, experience has shown that distinctive patterns are associated with the two stability regimes. When acoustic returns are generated in a stable region, the pattern will be horizontally stratified, usually with a wave structure superimposed on the layers. Conversely, when unstable conditions are present, the record will contain predominantly vertically oriented structure. Figure 1 is an example of the return from a stable atmosphere. This can be compared with an unstable case shown in Figure 2. During the morning transition periods, when surface heating after sunrise starts to lift an inversion surface, both patterns can be observed during the same time period. An example of this is shown in Figure 3 where the quasi-horizontal dark region is associated with the remains of the surface based nocturnal inversion. This layer is progressively lifted as the low level lapse rate becomes more unstable. Later the unstable lapse rate predominates, and all remnants of the inversion layer are gone.

Where a particular application requires only that the presence and depth of an inversion are known, this type of system, consisting of a single monostatic antenna and receiver, would suffice. As indicated earlier, however, the wind structure under the inversion is also a major concern. The acoustic echo sounder can be used to provide this type of information through a slightly more complex configuration.

A component of the total wind can be sensed by analyzing the Doppler shift of the returned signal at a single receiver. For monostatic configurations, this component is directed along the axis of the beam and for bistatic systems, the component is along the bisector of the angle formed by the intersections of the two beams. Recent work^{9,10,11} has tested many different configurations and assessed the accuracy with which the wind can be measured with the Doppler technique. The most recent of these experiments used three antennas, one pointing vertically and the other two positioned along orthogonal axes through the first, and tilted in such a way that the three beams intersected at some height above the ground (see Figure 4). In tests with this configuration, the wind measured by

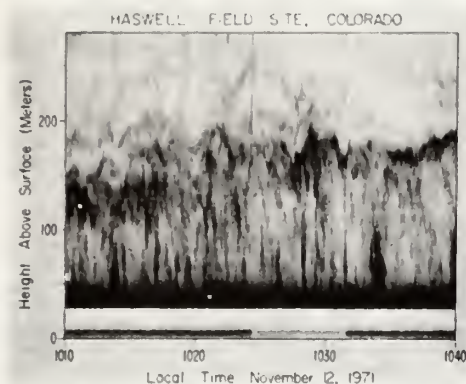


Figure 3 - Acoustic sounder record taken during the transition from stable to unstable conditions. The stable layer is associated with the upper portion of the dark areas: Unstable conditions are forming vertical convective elements below the stable layer.

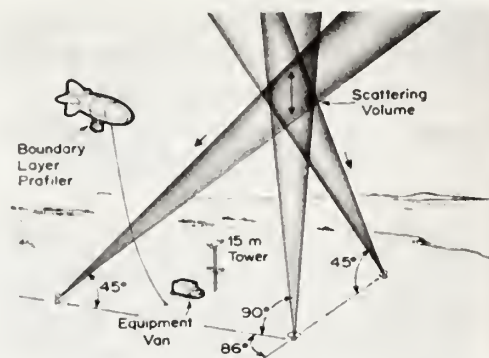


Figure 4 - Antenna configuration used to measure total wind vector.

the Doppler system was compared with that measured by a Boundary Layer Profiler (BLP), a kite-mounted anemometer supplied by the field facilities group of NCAR. Results of this comparison are given in the scatter diagram shown in Figure 5. For comparable 30 minute samples, the average value for the Doppler method was 2.33 m/s and that for the BLP was 2.43 m/s. The observed very close agreement indicates the ability of the acoustic Doppler to measure the total wind vector at any height within range of the system.

By using the same configuration as that shown in Figure 4, but with all three systems operating in the monostatic mode, it is possible to measure a vertical profile of the total wind vector. This is done by gating the signal from each of the systems at distances which correspond to the same height above the terrain. The components measured at each of the three gates at a given level are then averaged for periods of the order of 1 or 2 minutes. The resulting components are then resolved into the total wind vector at that height. (The averaging process, assuming Taylor's Hypotheses is valid, minimizes the error that might be produced because of the spatial separation of volumes along the beams away from the point of intersection.) An example of winds measured in this way is shown in Figure 6, a height time section of the horizontal isotachs derived from the total wind vector at ten elevations.

Where absolute temperature information is required, it is at least conceptually feasible to use the wind information and boundary layer theory to calculate the temperature gradient. Greater refinements might also be possible if the measured intensity of C^2 and C_t^2 , the structure constant for wind and temperature fluctuations are incorporated. These parameters and the measured wind profile can be combined through empirical boundary layer expressions of stability to estimate lapse rates between very unstable and neutral, and very stable and neutral. These concepts show promise, but have not yet been field tested.

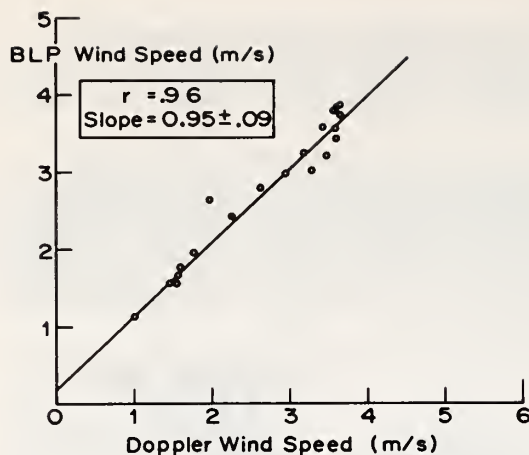


Figure 5 - Scatter diagram of winds measured by Doppler (DOP) and Boundary Layer Profiler Anemometer (BLP).

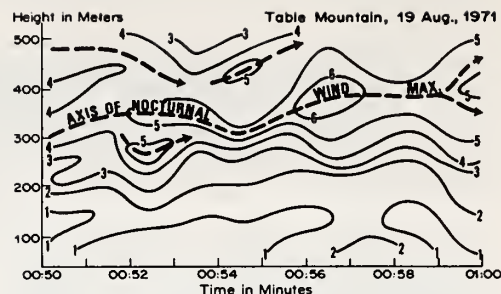


Figure 6 - Isotachs of horizontal wind derived from acoustic Doppler measurements.

A second approach, also untested, would use the dependence of sound absorption on the frequency of the carrier wave and on temperature and humidity. If it can be assumed that all absorption is due to the classical and molecular portions of the attenuation coefficient, this method should work well, and would require only that 2 or 3 separate frequencies be generated; the difference in signal strength at each frequency is used to derive the temperature and humidity profiles. The assumption of no excess absorption (i.e. that due to processes other than molecular or classical) may prove to be limiting^{12,13} and more information on the nature of the attenuation is needed before the method can be demonstrated.

MONITORING DURING AN AIR POLLUTION EVENT

Our best example, to date, of the potential of an acoustic sounder for monitoring meteorological structure during an air pollution event was obtained during April of 1971. The acoustic sounder was located at Table Mountain, a field site some 50 km northwest of downtown Denver. It was being operated on a round-the-clock basis in a monostatic mode with the antenna pointed vertically.

Fortuitously, the sounder recorded the low level pattern of C_T^2 , indicative of the temperature structure on the 13th and 14th of April, a period when effluent concentrations in Denver reached the "pollution alert" level. The 24 hour long acoustic record for this period is shown in Figure 7.

TABLE MOUNTAIN, COLORADO
April 13-14, 1971

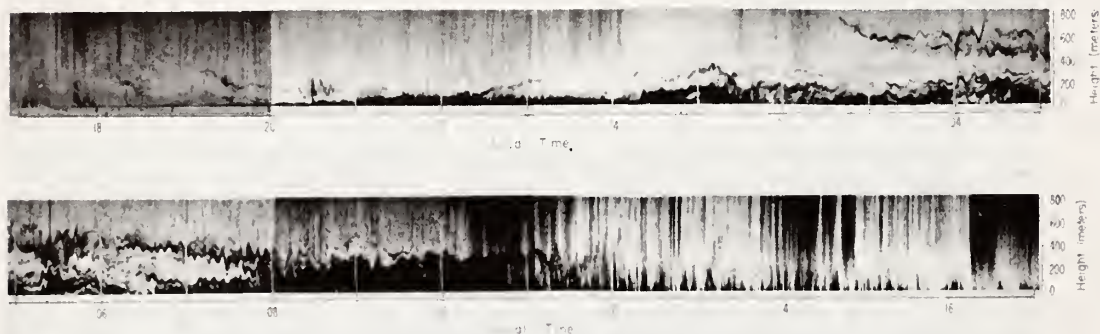


Figure 7 - Acoustic sounder record showing the evolution of the boundary layer structure before, during and after an air pollution alert.

The late afternoon portion, 1700 to 2000 (local time) on the 13th, shows the typical pattern which occurs after thermal plume activity has subsided and the lapse rate is near neutral. Following 2000, we see evidence of a surface based radiation inversion starting to form and deepen. This process continues throughout the nocturnal hours. Other layered structure, probably the result of advected inversion layers, also appear throughout the night. These layers all show the typically horizontally stratified structure with a variety of wave modes superimposed. Of particular interest is the subsiding layer which appears at about 800 meters shortly before 0300 on the 14th. This layer continues to descend until just before 0800 where it merges with the other lower layers and a very strong surface based inversion results. Shortly after this time, surface heating begins to have an effect and the lower regions start to take on the vertically oriented structure indicative of convective activity. This process tends to lift and intensify the capping inversion which was responsible for the air pollution alert. By 1200 on the 14th, the convective activity has destroyed the inversion layer and deep mixing has started. Two hours later at 1400, the air pollution alert was cancelled in Denver.

The temperature structure during this period was recorded by conventional radiosonde soundings at Denver's Stapleton Airport. The temperature, T , and dew point, T_d , profiles for 1700 LT on the 13th, and 0500 LT on the 14th are shown in Figure 8.

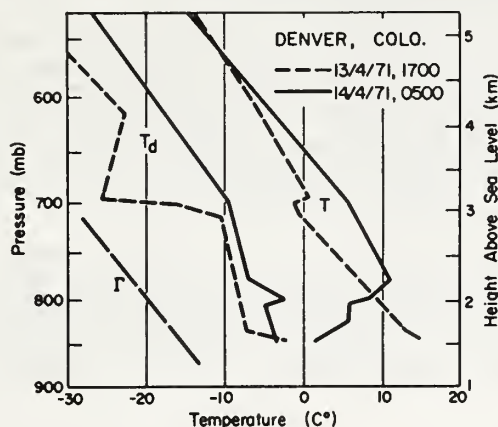


Figure 8 - Denver radiosonde records corresponding to the record shown in Figure 7.

The temperature and dew point profiles taken at 1700 LT on 13 April, 1971 show the typical subsidence inversion associated with a large high pressure region. These profiles, shown as dashed lines in Figure 8, were taken near the beginning of the record shown in Figure 7. The second set of profiles (solid lines) were taken at 0500 on the 14th, near the right side of the top portion of the 24 hour record. Looking at the radiosonde records alone, one can only speculate that the elevated inversion, near 3.3 km above sea level (1700 meters above the ground) at 1700 on the 13th had lowered and helped to intensify the inversion at 2.4 km on the 14th. The acoustic sounder record, on the other hand, clearly shows this evolution with the subsidence inversion entering the picture just before 0300 and lowering to about 600 meters above the ground. It is difficult to make a direct comparison of the inversion height at the two locations in question. However, the difference of less than 200 meters at 0500 LT appears very good despite such factors as the variation in surface elevations, local flow patterns and ground cover.

While this record does not tell the entire story, i.e., the concentration level of pollutants and the low level winds are absent, it is a simple matter to trace the events, even with data taken at a point far removed from downtown Denver. Using only this basic type of display, the air pollution meteorologist would have far more information than the present four per day temperature soundings provide.

Before placing an acoustic sounder in the urban environment, it is important to address certain practical questions relating to the ambient background noise in a city. The issue is really two sided; 1) can the sounder be successfully operated in the high noise environment of an urban area, and 2) will the operation of the sounder in this environment prove to be an annoyance to the inhabitants?

The first problem has been extensively analyzed with the conclusion reached that proper side-lobe suppression can be achieved by shielding the antennas¹⁴. It is also interesting to note that acoustic systems designed for other purposes, but essentially operating on the same basic principle, are now being successfully used in the extremely high noise environment of major airports.

Solution of the first part of this problem also eliminates the worst aspect of the second part, the annoyance factor. As most of the sound which might bother people is transmitted in the side-lobe of the antenna, shielding for sidelobe suppression will also greatly reduce the annoyance factor.

CONCLUSIONS

While full scale testing in an urban environment remains to be completed, the results to date clearly indicate the potential of an acoustic sounder as a monitor of important meteorological parameters that contribute to undesirable air pollution situations. At present it appears that the worst effect of a high noise environment on the operation of a sounder will be periodic losses of record, a factor which can be significantly reduced by improved anechoic shielding and proper selection of operating frequencies. In the unlikely event that as much as half of the record is lost, the amount of usable information would still be orders of magnitude greater than is available from conventional measuring techniques. This point is well amplified by comparing the information in Figures 6 and 7 of the previous section.

The importance of knowing the low level winds associated with an inversion also suggests that the Doppler capability should be incorporated into any operational system. The alternative would be to produce a backlog of acoustic records taken under various types of boundary layer structure and then use a pattern recognition technique to relate the observed records to conditions which might produce hazardous air pollution events. The Doppler capability would require slightly more complex equipment, but the additional information would seem to be worth the extra investment. Analog techniques, now under development, will allow rapid extraction of the Doppler shift at predetermined intervals above the ground. This information can then be converted into a real time display of the wind profile, updated every two or three minutes.

The number and location of monitoring stations in an urban environment must be a function of such factors as, the local terrain, the pattern of residential vs. commercial zoning, and the meso-scale climatology of the city, each case being analyzed individually. If, for example, convergence into the urban heat island is a factor, stations could be placed at strategic locations around the perimeter of a city and the rate of inflow monitored continuously. In the final analysis, especially when compared with other types of remote sensors, the inexpensive acoustic sounder, combining its wind and temperature measuring capability, seems well suited to the task of monitoring the mesoscale urban environment.

REFERENCES

1. Tatarski, V. I. (1961), Wave Propagation in a Turbulent Medium (R. A. Silverman, transl.) New York: McGraw-Hill, 1961.
2. Kallistratova, M. A. (1961), Experimental investigation of sound wave scattering in the atmosphere, Trudy Inst. Fiz. Atmos. Atmos. Turbulentnost, 4, pp. 203-256.
3. Monin, A. S. (1962), Characteristics of the scattering of sound in a turbulent atmosphere, Akust. Zh., 7, pp. 457-461, (Sov. Phys - Acoust. 7, pp. 370-373).
4. Little, C. G. (1969), Acoustic methods for the remote probing of the lower atmosphere. Proc. of the IEEE, 57, pp. 571-578.
5. McAllister, L. G., J. R. Pollard, A. R. Mahoney, and P.J.R. Shaw (1969), Acoustic sounding - a new approach to the study of atmospheric structure. Proc. IEEE, 57, pp. 579-587.
6. Beran, D. W. (1970), Project EAR (Environmental Acoustic Research) Vol. I, Univ. of Melbourne, Meteorology Dept. Pub. No. 15.
7. Wescott, J. W., W. R. Simmons, and C. G. Little (1970), Acoustic echo sounding measurements of temperature and wind fluctuations, ESSA Tech. Memo. ERLTM-WPL-5.
8. Beran, D. W., G. H. Clark, and U. Radok (1969), Meteorological aspects of air pollution in the Geelong region, Proceedings of the Third Clean Air Conference, Sydney, Australia, May 1969.
9. Beran, D. W., C. G. Little, and B. C. Willmarth (1971), Acoustic Doppler measurements of vertical velocities in the atmosphere, Nature, 230, pp. 160-162.

10. Beran, D. W., and B. C. Willmarth (1971), Doppler winds from a bistatic acoustic sounder, Proc. Seventh Int. Symp. on Remote Sensing of the Environment, Univ. of Mich., Ann Arbor, Vol. III, pp. 1699-1714.
11. Beran, D. W., and S. F. Clifford (1972), Acoustic Doppler measurements of the total wind vector, Proc. of American Met. Soc. Second Symp. on Met. Observations and Inst. To be held in San Diego, Calif. March 1972.
12. Delsasso, L. P., and R. W. Leonard (1953), The attenuation of sound in the atmosphere, Rept. for USAF Cont. W-28-099-AC-228.
13. Beran, D. W., R. M. Reynolds, and J. T. Gething (1970), Sound attenuation in the free atmosphere, Project EAR Rept. No. 5, Publ. No. 17, Univ. of Melbourne, Dept. of Meteorology.
14. Simmons, W. R., J. W. Wescott, and F. F. Hall (1971), Acoustic echo sounding as related to air pollution in urban environments, NOAA Tech. Rept. ERL 216-WPL 17.

A FEASIBILITY STUDY FOR THE REMOTE MEASUREMENT OF UNDERWATER
CURRENTS USING ACOUSTIC DOPPLER TECHNIQUES

C. B. Emmanuel and P. A. Mandics

ABSTRACT

A need exists for the remote measurement of water currents in the estuarine, coastal, and open ocean environments. Conventional rotor-type current measuring devices have been found, at best, to be of limited use in measurements requiring high temporal and spatial resolution. Remote sensing techniques, however, such as the measurement of the Doppler shift of acoustic waves scattered by irregularities embedded in water, offer an attractive alternative.

Based on available information on the concentration and size distribution of scatterers, an attempt is made to estimate the scattering cross section for some typical scatterers. In particular, the scattering characteristics of suspended particulate and organic matter, gas bubbles, and temperature and current velocity fluctuations are examined. The effects of transmission losses and ambient noise on the signal-to-noise ratio of the returned signal are evaluated. The results are used to ascertain the feasibility of acoustic Doppler techniques to measure water currents for ranges of up to 100 m with a varying pulse length resolution of 0.3 to 3 m. This resolution and additional noise considerations necessitate the use of frequencies of the order of several hundred kHz.

It is shown that a pulse Doppler current measuring system is feasible. As an example, for 100 W transmitted (electrical) power, reasonably strong scattering (scattering cross section per unit volume per unit solid angle $d\sigma/d\Omega = 10^{-13} \text{ cm}^{-1}$), and a pulse length $c\tau/2 = 3.05 \text{ m}$, it is possible to detect returns from a distance of 100 m with a 14 dB signal-to-noise ratio. Some aspects of the problem need more careful examination and, consequently, the system described may not represent an optimum design; nevertheless, this preliminary investigation lays the groundwork for future efforts in that direction.

Key Words: Estuarine environment, acoustic scattering, Doppler shift, turbulence, remote current measurements.

Reprinted with permission from *Reviews of Geophysics and Space Physics*, Vol. 11, No. 3, 571-594, August 1973.

Infrasound from Convective Storms: Examining the Evidence

T. M. GEORGES

*Wave Propagation Laboratory
NOAA Environmental Research Laboratories
Boulder, Colorado 80302*

Two kinds of waves, infrasonic pressure fluctuations recorded on the ground and certain wavelike fluctuations in ionospheric phase height recorded by ground-based radio sounders, have been independently associated with some severe convective storms. When we compare their phenomenologies, such a remarkable similarity emerges that it is hard to avoid the conclusion that both waves are different manifestations, in different parts of the acoustic spectrum, of the same emission mechanism. We tabulate the constraints each observation imposes on possible source models and estimate the average acoustic power required. A case study of one storm observed with both techniques reinforces the hypothesis of a common emission mechanism.

1. INTRODUCTION

Substantial evidence is accumulating that some (as yet unidentified) process associated with certain severe convective storms radiates subaudible acoustic waves that are detected at great distances. In this paper, the first in a series about infrasound from convective storms, we review and critically evaluate this evidence.

The levels of emitted power that the observations suggest are probably not great enough to represent an important part of a convective storm's energy budget. Yet the emissions are interesting from at least two other points of view: The very elusiveness of the emission mechanism suggests that its discovery might also reveal something new about the dynamics of certain severe convective storms. Interest also arises from the emissions' potential value in severe-storm detection and diagnosis.

One reason that such a review now seems appropriate is that the bulk of the evidence is scattered about in obscure or inaccessible places, mainly in unpublished reports and conference proceedings; indeed, some of the evidence resides only in the minds of a few researchers. As we shall see, two diverse kinds of measurement form the evidence, so it is understandable that researchers familiar with one may not fully appreciate the other. We find that, as a result, many workers in the field are not fully aware of what has already been done.

Another reason for this review is to lay the groundwork for further progress on the problem by, in effect, defining the problem as precisely as possible. Without such groundwork, it makes little sense to attempt a synthesis of realistic models of the emitting mechanism.

Sections 2 and 3 of this paper examine the two ways the waves have been observed: In one, ground level atmospheric pressure fluctuations are recorded with arrays of sensitive microbarographs; in the other, certain wavelike fluctuations in ionospheric electron concentration (200–300 km above the ground) are detected with ground-based radio sounders. Although the phenomenologies of the two kinds of waves are very similar, it is not yet certain that both waves can be traced to a common emission mechanism. One goal of this paper is to reinforce the evidence favoring a common mechanism.

In addition to summarizing the present knowledge about each wave type, each section also dwells briefly on the observing techniques themselves. This is to minimize misunderstanding about what is actually being observed and to call attention to sources of error and observational bias that are built into the methods themselves. To provide energy limits for possible source models we then make some elementary energy estimates based on observed wave intensities.

Section 4 compares and contrasts the two kinds of observations, focusing attention on those properties of the emissions on which the two observations apparently disagree. The constraints imposed by the observations on possible source models should then be clear. Section 5 is a case study of one storm during which both types of observations were made. Certain common features emerge that apparently have not been recognized before.

2. IONOSPHERIC EFFECTS

a. History. The history of ionospheric radio has recorded numerous attempts to associate fluctuations in different properties of ionospheric radio transmissions with tropospheric weather events. *Davies and Jones [1972c]* review early work. Most of the published associations are reports of isolated coincidences in time and duration between certain weather events (the passage of a hurricane, a squall line, or an electrical storm) and fluctuations of some ionospheric observable, such as *F* layer critical frequency, the appearance of sporadic *E* layers, or a change in radio absorption by the *D* layer [cf., *Rastogi, 1962*]. Some early attempts to associate thunderstorms with ionospheric activity invoked direct electrostatic coupling between lower and upper atmosphere [cf., *Wilson, 1925*]. Others supposed that synoptic-scale pressure fluctuations are communicated to ionospheric heights and alter electron concentration by means of neutral-density changes [*Bauer, 1958*].

Although not denying that any of the proposed coupling mechanisms exist, I feel it is fair to say that until 1967 no conclusive or consistently repeatable causal relationships between ionospheric events and tropospheric weather emerged from these studies.

In 1966, during a study of wavelike ionospheric motions revealed by HF-CW (high-frequency, continuous-wave) Doppler soundings at Boulder, certain nearly monochromatic oscillations, with a characteristic period always near 3 min and durations of several hours, began to emerge as a distinct type of event. The oscillations are distinguished from the ionospheric 'background' mainly by their monochromatic appearance but also by their short periods, in contrast to the

longer periods and irregular appearance of most background fluctuations. One particularly clear example of such an event was recorded on two radio sounding frequencies at Boulder, Colorado, on November 11, 1965. A picture of the Doppler record of this event has been published by *Georges* [1967a]. A relative phase lag in the oscillations corresponding to the sounding from the greater height permitted an estimate of vertical travel time between the two heights sounded. The phase lag corresponded to a sonic travel speed at ionospheric heights. Because 3-min acoustic waves could theoretically exist there without excessive attenuation, the oscillations were tentatively identified as manifestations of acoustic waves interacting with *F* layer ionization [*Georges*, 1967a]. No known association with other geophysical events then pointed to a source, though infrasonic pressure waves with about a 30-sec period were noted at Boulder at the same time. The infrasound had the high horizontal trace speed that is sometimes associated with nearby sources. No severe-weather event was found in the vicinity, although weather-radar data were not available for that time. (Although these ionospheric waves typify waves that were later associated with severe weather, this particular event is singularly mysterious because of the apparent absence of nearby storms and because it appeared in late fall.)

During 1966–1967, similar waves were frequently seen on the records of a new spatial array of Doppler sounders centered at Little Rock, Arkansas [*Georges*, 1967b]. The availability of Doppler soundings spread over a wide geographical area and the variations of wave intensity among the sounding paths revealed that the 3-min ionospheric waves were always geographically confined within an area only a few hundred kilometers in diameter. A source of a global nature, e.g., solar or geomagnetic, was thus unlikely, as was the propagation of the waves over long horizontal distances.

Pierce and Coroniti [1966] suggested on theoretical grounds that buoyancy oscillations in convective storms should emit acoustic-gravity-wave energy near the Brunt-Väisälä frequency. This prompted an investigation of the possibility that the 3-min waves were ionospheric manifestations of acoustic-gravity waves from severe convective storms, even though the periods of waves from buoyancy oscillations were not expected to be as short as 3 min. Surface weather and radar summary charts revealed that significant convective storm activity was indeed frequently nearby during the ionospheric events in question. A more careful analysis comparing the relative strengths of the ionospheric waves among the spaced-sounder records revealed an inverse relationship to the distance of the sounding path from a nearby storm. The times of onset and cessation of the ionospheric waves often coincided remarkably well with the appearance on weather-radar charts of nearby thunderstorms with cloud tops over 40,000 ft [*Georges*, 1967b]. About a dozen case studies confirmed such a detailed spatial and temporal relationship. In addition, a contingency table derived from a year of continuous sounding formed convincing statistical evidence for an association between certain convective storms and the 3-min ionospheric waves [*Georges*, 1968a, 1968b]. A model based on atmospheric filtering by refraction, absorption, and acoustic cutoff effects was advanced to explain the narrow spectrum observed, the localized geographic effects of the waves, and the fact that the waves appear

mainly at night [Georges, 1968a]. The exact emitting mechanism remained unspecified, however.

Detert [1969] carried out a similar spaced-path Doppler sounding experiment during 1967–1968 at Huntsville, Alabama, and confirmed the presence of 3-min oscillations during several severe local storms.

Baker and Davies [1969] and *Davies and Jones* [1971, 1972a] have used Doppler observations over various oblique and steep-incidence paths to further refine the evidence for the association. In particular, they showed that the spectrum of the waves usually exhibits a double-peaked 'fine structure,' and they used a closely spaced sounder array to verify that horizontal trace speeds are also appropriate to acoustic waves. By measuring wave travel direction they were able to 'trace back' the acoustic energy to the troposphere and identify the apparent source storms on radar maps and on radarscope photographs.

b. Summary of observations. What we have learned about the ionospheric effects of severe storms from the observations just cited can now be distilled as follows:

1. The ionospheric oscillations are consistently seen only on HF-CW Doppler soundings of the *F* layer.

2. They are seen almost exclusively in the early evening; occasional appearances at other times are usually much weaker. Some instances of abrupt cessation at sunrise have been recorded, even in the presence of continuing storm activity. Increased acoustic defocusing at the base of the thermosphere has been suggested as a reason for the absence of daytime effects [Georges, 1968a].

3. Seasonal occurrence maximizes during midsummer for soundings on the Kansas-Nebraska border, shifts to early summer for the Oklahoma location, and to late spring at the Arkansas location.

4. Storm-associated waves are so identified by their characteristic wave form. Most of the 2- to 5-min ionospheric oscillations can be associated with nearby convective storms; however, many instances are found when apparently suitable storms produce no observable ionospheric effects.

5. The oscillations typically persist for 3 or 4 hours and often recur on several successive evenings.

6. Wave amplitudes are greater than 1 Hz (Doppler shift) for the largest events but are typically between 0.1 and 1.0 Hz. Those smaller than 0.1 Hz are difficult to detect in the 'noise' of other ionospheric fluctuations.

7. Appearance of the oscillations on Doppler records is that of a nearly monochromatic sinusoidal wave train, always with an apparent period between 2 and 5 min and often having a 'beaded' or amplitude-modulated appearance.

8. Accordingly, spectral analysis of the oscillations consistently reveals the presence of a sharp, dual-peaked spectrum; one peak is always close to a 4.5-min period, whereas the second peak is near 3.5 min and has a slightly larger variance from event to event. The apparent bandwidth of an individual spectral peak is of the order of 1 mHz for a typical event.

9. Unambiguous azimuth determinations are possible only if the horizontal spacing of the sounding points is less than about 50 km.

10. Only a few determinations of horizontal wave travel directions have been possible. When these waves are traced back to storm activity indicated by weather radars, time variations in azimuth tend to follow storm activity.

11. A few azimuth determinations using spaced soundings show that the apparent source direction often shifts abruptly, evidently in response to the death of one emitter and the birth of another nearby.

12. Horizontal trace speeds vary from about sonic to almost 3 km/sec, whereas vertical trace speeds measured with multifrequency soundings are typically 500 to 600 m/sec and are directed upward. The waves thus travel essentially vertically upward.

13. Ionospheric effects are typically visible up to about 300 km from the source storms. Waves from more distant storms, if seen, are usually very weak.

14. The ionospheric oscillations are almost always associated with nearby (within about 300 km) thunderstorm cells with radar-indicated tops over 40,000 ft.

15. No preference for tornadic storms is evident in the ionospheric waves, although some of the identified source storms have produced tornadoes.

16. All significant observations of severe-weather ionospheric waves have been roughly in the central United States (Boulder, Colorado, to Huntsville, Alabama; Urbana, Illinois, to Little Rock, Arkansas). Magnitudes of Doppler effects show a slight tendency to be highest near midcontinent. Some unpublished Doppler sounds in Florida [Davies and Jones, 1972c] have failed to reveal clear ionospheric effects associated with the frequent thunderstorm activity there. However, more negative results of this kind are required before conclusive statements about geographic localization can be made.

17. Ionospheric oscillations are observed more often when the assumed thunderstorm source is to the north (northern hemisphere) of the ionospheric observation point than when it is to the south. This directional filtering effect is apparently associated with the way the waves move the ionization under the influence of the geomagnetic field (see section 2d).

18. Among the various observers, at least 60 ionospheric events have now been associated with severe convective storms. Most of these associations have been based on the spatial and temporal coincidence arguments given earlier, rather than on measurements that permit tracing back a wave to a source.

c. Doppler sounding: Method and biases. The CW Doppler ionospheric sounding technique was invented by Watts and Davies [1959] to monitor the frequency fluctuations of HF radio waves caused by ionospheric motions. The essential features of the technique are as follows: A transmitting station emits a continuous, unmodulated, high-frequency radio wave that reflects from the ionosphere and is detected at a receiving station that may be thousands of kilometers away or only far enough away to prevent receiver domination by direct 'ground wave.' The transmitter frequency is so stable that any frequency deviations or spreading observed at the receiver can be attributed to propagation effects. After appropriate heterodyning and frequency multiplication, the frequency fluctuations are usually processed and displayed in a fre-

quency versus time format by an audio spectrograph. This kind of processing (as opposed to phase-detecting schemes) preserves the identities of the multiple-frequency components that represent separate propagation paths with different Doppler shifts. The special case of sounding over steep (nearly vertical) paths permits monitoring vertical ionospheric motions nearly directly overhead. This method is usually employed in studies of severe-weather effects. Sounding from geographically spaced locations and on different radio frequencies can indicate motions at spaced locations in the ionosphere. Frequency shifts as small as 0.1 Hz are detectable. Readers interested in the details of the technique, the interpretation of the measurements, and examples of applications should also see the papers by *Davies et al.* [1962], *Davies and Baker* [1966], *Chan and Villard* [1962], and *Georges* [1967b] and the references they cite.

What the Doppler sounding technique actually measures, then, is fluctuations in received radio frequency. The chain of reasoning that allows us to infer properties of neutral atmospheric waves from these frequency fluctuations contains a number of assumptions about the way atmospheric waves interact with ionization and about the way ionization density changes induce Doppler shifts. Each assumption represents, in effect, a simplified model of that step in the process. Anyone who interprets the measurements ought to be aware of the kinds and magnitudes of errors that the use of such models can introduce. But a complete analysis of these errors would take up too much space here and is a more suitable topic for a specialized report [cf. *Davies and Jones*, 1972c; *Jones*, 1969]. Here only features of the models that can cause errors will be listed:

1. Although Doppler shifts can be caused by temporal variations in radio refractive index all along the sounding path and by motions of the height where the radio wave reflects, only motions of the latter type are usually considered. Such a model is called a specular-reflector model. For wave-induced fluctuations, the errors this model introduces are small but may not be negligible in precise measurements [*Georges*, 1967b].
2. The shape and motions of the reflecting boundary are taken to be those of a particular constant electron density surface. That value of electron density depends on the radio wave frequency and the transmitter-receiver geometry.
3. For steep sounding paths, the reflecting surface is where the electron plasma frequency equals the radio wave frequency (possibly plus a constant correction factor to account for magnetoionic effects).
4. Steep sounding paths are essentially straight lines; that is, ray deviations are not important. *Davies and Jones* [1972c] have estimated refractive corrections, however.
5. The ambient electron density distribution is assumed to be horizontally stratified. Horizontal gradients thus introduce errors in determinations of acoustic-wave-vector magnitude and direction from spaced-path soundings.
6. Electron density perturbations are supposed to be of sufficiently large horizontal scale that the reflecting surface remains essentially plane and horizontal. Therefore Doppler shifts indicate only vertical motions of the surface. (Smaller-scale ripples are known to appear on isodensity surfaces, but they

present a characteristic Doppler signature that is easily recognized and interpreted accordingly [cf. *Davies and Jones, 1972b*]. The waves we are interested in appear not to be of this type; that is, they do not cause significant curvature of the isodensity surfaces.)

7. To calculate their interaction with *F* region ionization, the atmospheric waves are considered to be plane compression waves. This is not really true because (1) the wave fronts have a finite radius of curvature, and (2) air parcel orbits are elliptical (slightly transverse) for waves near the acoustic cutoff frequency.

8. The acoustic waves move electrons by collisional interaction, and the electrons oscillate in phase with the neutral wave with a velocity equal to the component of wave-associated neutral-air velocity along the direction of the geomagnetic field [*Georges, 1968b*]. Wave-induced perturbations of the photochemical balance are normally neglected because they are almost certainly unimportant for the short wave periods and ionospheric heights of interest [*Hooke, 1968*].

9. Again, because the waves of interest are so long that the electron density gradients they cause are smaller than the height gradients of ambient electron density, the vertical motion of the constant electron density surfaces is nearly the same as vertical electron velocity. To be perfectly rigorous, however, estimates of motions of the reflecting height should include the total wave-induced density perturbations, especially when reflection is from near the *F* layer peak.

10. Serious errors in estimating the radio reflection height can occur if the identities of the magnetoionic modes (ordinary or extraordinary) present are misjudged. Measuring acoustic velocities requires accurate knowledge of the locations of the ionospheric reflection points.

To measure spatial properties of the waves it is necessary to sound the ionosphere at different heights and at geographically separate locations. Interpreting spaced-path soundings means making some simplifying assumptions about the relative locations of the points in the ionosphere being probed and how these points may vary with wave passage. These assumptions determine, among other things, the method to use in deriving velocities from spaced-sensor data (e.g., visual overlay and cross correlation), and they are discussed by *Jones [1969]* and *Davies and Jones [1972c]*.

The combined effect of all these simplifications should not cause order of magnitude errors in estimates of neutral-wave amplitude and should permit rough estimates of other wave parameters. But those who contemplate more precise interpretation of Doppler soundings definitely need to contend with these sources of error.

Quite apart from errors that arise from using simplified models to interpret the measurements, several observational biases are built into the Doppler sounding technique. Some arise from atmospheric filtering of the waves that reach ionospheric heights and move the ionization; others arise from the velocity-sensing nature of Doppler measurements. We need to understand these biases so

that we won't expect Doppler sounding to respond to waves beyond its capabilities.

The 'atmospheric filtering' that operates on acoustic waves reaching ionospheric heights is only vaguely understood at this time. *Georges* [1968a] suggested a simple filtering model involving absorption and acoustic cutoff effects, but this model leaves several observed wave properties unexplained. *Jones* [1970] proposed a filtering mechanism based on strong coupling between acoustic-gravity modes, but objections can be raised to treating nearly vertical propagation from a wave guide mode viewpoint. A detailed discussion of this topic will be reserved for a later paper.

Because Doppler sounders are inherently velocity-measuring devices the technique is naturally biased in favor of higher-frequency motions. For example, 3-min oscillations in reflecting-layer height would cause fluctuations in Doppler shift with an amplitude 10 times greater than if the same height oscillations had a 30-min period. On the other hand, short-period wavelike ionospheric motions tend to be of smaller amplitude; therefore Doppler measurements tend to equalize the observed effects of different wave periods.

d. Estimating source power. The ionospheric Doppler measurements permit an estimate of the average acoustic power radiated by the severe-weather source. To make such an estimate we construct the following model: A source of spherical, monochromatic acoustic waves exists near the ground. In propagating upward, only a portion of this wave within a narrow cone (30° – 45° from vertical) penetrates into the thermosphere; the rest is refracted back to earth by the large temperature gradient near 100-km height. The portion of the wave reaching ionospheric heights nearly above the source is not refracted very much, and the vertically traveling wave remains essentially spherical.

The neutral acoustic wave moves ionization by collisional interaction between neutral molecules and free electrons. In the presence of the earth's magnetic field, only the component of the wave-associated air velocity parallel to the field is communicated to the ionization. The mean time between collisions is short enough that, for the wave frequencies of interest here, the ionization moves in phase with the neutral wave.

In the measurement of Doppler shifts of steep-incidence radio waves, only the vertical component of ionization motion is of interest (see section 2c). We can then write a formula relating the vertical ionization speed U_{ez} to the wave-associated neutral-air velocity U , assuming that the wave travels vertically:

$$U_{ez} = U \sin^2 I \quad (1)$$

where I is the inclination of the local magnetic field [*Georges*, 1968c]. For rough estimates applicable to midlatitudes and higher, we can neglect the $\sin^2 I$ factor.

Now we have a simple model connecting the neutral-wave amplitude to vertical oscillations of the reflecting layer, which in turn can be simply related to the induced radio Doppler shift. Mathematically, we can now write

$$-\frac{c_0}{f_0} \Delta f = \frac{dP}{dt} \cong \frac{2 dh}{dt} \cong 2U_{ez} \cong 2U \quad (2)$$

where c_0 is the free-space speed of light, f_0 is the transmitted radio frequency, Δf is the Doppler shift, P is the radio phase path, and h is the radio reflection height. Equating (dP/dt) to $2(dh/dt)$ involves the assumption of specular reflection mentioned earlier.

As an illustration, we calculate the velocity amplitude U of an acoustic wave required to give a 1-Hz (amplitude) Doppler shift to a 5-MHz radio wave:

$$U = (c_0/2f_0)\Delta f = 30 \quad \text{m/sec} \quad (3)$$

To estimate the corresponding source power, we calculate the average power-flux density W :

$$W = \frac{1}{2}\rho_0 C U^2 \quad (4)$$

where ρ_0 is the ambient air density, and C is the ambient sound speed. In MKS units, W is in watts per square meter. Substituting U from (2) into (4), we write an approximate formula for acoustic power-flux density in terms of the amplitude of Doppler shift fluctuations [Davies and Jones, 1972c]:

$$W \simeq (\rho_0 C c_0^2/8)(\Delta f/f_0)^2 \quad (5)$$

where the values of ρ_0 and C refer to the ionospheric height h being probed. The emitted source power is estimated by integrating W over a hemisphere of radius h :

$$P = 2\pi h^2 W = \frac{\pi \rho_0 C c_0^2 h^2}{4} \left(\frac{\Delta f}{f_0} \right)^2 \quad (6)$$

This formula neglects acoustic absorption. Using the same values of f and Δf and assuming atmospheric parameters appropriate to a height of 200 km, we get an emitted acoustic radiated power of about $2.8 \times 10^7 W$. The numerical values we have used represent typical conditions under which severe-weather Doppler effects have been observed, so that our estimate of source power should be realistic. Including absorption would raise this estimate, however. Davies and Jones [1972c], who use slightly different numbers, estimate $5 \times 10^7 W$.

3. INFRASONIC PRESSURE FLUCTUATIONS

a. History. Infrasonic pressure waves were studied as early as 1888, when signals from the explosion of Krakatoa were detected all over the world (see the bibliographies by Pierce and Posey [1970] and Thomas et al. [1971]). Now many different kinds of natural infrasound are known. Each is identified by its particular combination of wave observables: wave amplitude, wave period, duration, horizontal trace velocity (speed and direction), spatial and frequency coherence, and coincidence with other geophysical events. Cook [1969], Cook and Young [1962], and Georges and Young [1972] review our knowledge about at least nine different kinds of natural infrasound that are now distinguished. We want to focus our attention on just one species in the atmospheric wave 'zoo': a class of wave that has been called 'severe-weather infrasound.'

The history of the discovery of severe-weather infrasound is clouded by an almost complete absence of early published results. A few unpublished internal reports and records of oral conference presentations indicate that as early as 1960 the NOAA (then National Bureau of Standards) Geoacoustics Group had found a connection between certain pressure waves and distant tornadic storms. *Cook and Young* [1962] briefly reported the reception of a certain kind of infrasound at Washington, D.C., during eight time intervals when tornadoes were reported in the midwest within 5° of the azimuth of infrasound arrival. No further reports were published until 1966, when *Goerke and Woodward* [1966] reported tracking a nearby severe (nontornadic) storm from Boulder, Colorado, using infrasound of about 20- to 25-sec period. Although no triangulation was possible from a single array of microbarographs, the change in the waves' direction of arrival during this storm appeared to coincide with the motion of the storm's leading edge of maximum convective activity. *Bowman* [1968] reported observations of long-period 'subsound' (internal gravity waves) associated with severe hailstorms, but these are not the essentially acoustic waves of interest here. We shall return to them briefly later. *Bowman and Bedard* [1971] published a comprehensive report on both infrasound and 'subsound' from severe weather, in which they reviewed the published and unpublished history of severe-weather waves. They reported an apparent connection between observed wave period and hail size, and they demonstrated a spatial and temporal coincidence between radar-located storm activity and wave origin determined by triangulation from up to four microbarograph arrays. They also showed a similarity between seasonal and diurnal wave-occurrence statistics and those of severe storms in the midwest and suggested that the direction of upper-atmosphere winds plays an important role in determining wave observability.

Curiously, I have not found any published reports of severe-weather infrasound by anyone outside the NOAA Geoacoustics Group.

b. Summary of observations. Because no distinguishing wave form characteristics identify severe-weather infrasound, it is more difficult than for the ionospheric events discussed in section 2 to define the criteria by which one identifies a given infrasound signature as being of the severe-weather type. In practice, severe-weather waves are tentatively screened simply by eliminating all other identifiable wave types. In retrospect, this turns out to be a sensible process, because during spring and summer, severe-weather infrasound is observed much more frequently than any other type. However, experience has shown that the relative frequency of 'mistaken identities,' though still small, is larger for severe-weather infrasound than for ionospheric Doppler signatures, unless independent corroborative evidence is sought from meteorological data. After such corroborative evidence was obtained for a large number of wave events, the identification and selection criteria were reinforced and refined, and the selection process became more reliable.

As a result of this process, what we now know about severe-weather infrasound can be distilled as follows:

1. Severe-weather infrasound is detected with microbarograph arrays whose sensors are spaced from 3 to 10 km apart and are tuned to accept signals

primarily within the 1- to 60-sec (wave period) band.

2. The waves are observed most frequently during early evening.
3. Seasonal dependence maximizes during midsummer at Boulder but in late spring at Washington, D.C. (see item 17).
4. Storm-associated waves are so identified when their arrival direction coincides within 3° with a radar-indicated storm with at least 40,000-foot tops occurring at the same time. On the other hand, many apparently suitable storms produce no observable infrasound. This implies the existence of some unknown additional condition that must be satisfied before emissions occur.
5. Events can last several hours, i.e., much longer than the lifetime of a single convection cell. Mean duration is about two hours. Occasionally very short duration events are recorded, but their apparent brevity is often caused by increases in local background noise at the sensors.
6. The amplitude distribution of several hundred events recorded at Boulder has a median at $0.6 \mu\text{bar}$ and 10 and 90 percentile values of 1.25 and $0.3 \mu\text{bar}$.
7. Observed wave periods range between extremes of about 6–300 sec, with 12–60 sec being 'typical.'
8. Frequency spectra are generally broad but occasionally exhibit sharp peaks. No characteristic wave frequencies or frequency-time patterns are yet evident. There is some evidence linking longer-period waves with larger, more severe storms, especially those producing hail.
9. Spatial coherence is usually as high as for waves from point sources, often permitting azimuth-of-arrival determinations to within about 3° .
10. Changes in azimuth of wave arrival often coincide with the motion of storm systems indicated by weather radars.
11. Azimuth of arrival often shifts abruptly during an event. Occasionally waves from two locations in a storm system appear simultaneously, one diminishing in strength while a second is increasing. The waves are apparently generated within regions having dimensions much smaller than those of storm groupings indicated on weather radars. Such groupings typically subtend 20° or more at the sensors.
12. Horizontal trace speeds are always nearly sonic or slightly greater. During observations of waves attributable to nearby storms (within about 100 km), horizontal trace speeds appear to increase with the storm's approach, suggesting an increase in vertical arrival angle, but the waves still travel essentially horizontally.
13. Some storms over 1500 km from the sensors have been identified as sources by triangulation and tracking from several observatories.
14. A strong correlation apparently exists between wave events and the appearance on weather radars of strong convective storm echoes whose indicated tops penetrate the tropopause.
15. Although a relatively large fraction of the waves have been associated with tornado-spawning storms, many of the waves appear to come from non-tornadic storms.
16. With the exception of 'local' storms, i.e., those within about 100 km of an observatory, severe-weather infrasound observed at both Boulder, Colo-

rado, and Washington, D.C., appears to come almost exclusively from the central United States. In particular, apparently none is ever observed from the direction of Florida, where thunderstorm frequency is high [*U.S. Department of Commerce*, 1970].

17. The different seasonal dependence at different observatories suggests that upper-atmosphere winds exert a strong directional filtering effect on wave propagation to long distances.

18. Well over 100 instances of severe-weather infrasound have so far been associated with independently observed storm activity. The sparsity of published data makes the actual number uncertain, however, and it may be much higher.

c. Other severe-weather waves. To avoid confusion with the waves whose properties have just been outlined, the existence of at least two other distinct kinds of storm-associated waves must be mentioned here. The first is a class of long-period (greater than about 5 min) slow-speed (much less than sonic) waves that *Donn et al.* [1954] and *Bowman and Bedard* [1971] have associated with the passage of weather fronts, squall lines, and nearby convective activity. Some of these waves appear to be closely related to the pressure jumps recorded on ordinary barographs [*Williams*, 1953], while others are more oscillatory and display properties of atmospheric internal gravity waves. It is worth repeating some of the details of *Donn's* wave observations because they might be related to severe-weather infrasound:

1. Pressure jumps frequently precede (by as much as 1 hour) the passage of a squall (a line of convective storms accompanying cold-front passage), but only when unstable atmospheric conditions exist ahead of the cold front. Pressure jumps observed under stable conditions are not followed by squalls. The pressure jumps are probably manifestations of waves or pressure surges aloft and force convection only when they pass through a zone of latent instability.

2. Short-period (~ 1 min) fluctuations often cease during frontal passage (when longer-period fluctuations appear) and then resume after the front has passed. These fluctuations appear to be related to the diurnal variations in cloud cover and usually disappear at night. They are interpreted as pressure oscillations of low-level turbulence or convection phenomena dependent on solar heating of the surface.

3. Medium-period (6 to 7 min) waves very frequently follow the passage of cold fronts in the evening. These are thought to be gravity waves on the frontal surface aloft, which are triggered by small but sudden pressure changes following sunset.

4. Strong, full-wave oscillations with periods of about 20 min frequently accompany thunderstorm passage. These are interpreted as marking the convection pattern of thunderstorm cells, namely, a sharp downdraft followed by an updraft and a weaker downdraft.

As these observations illustrate, it is important to distinguish between pressure fluctuations that may be generated by convective activity and those

that may precede (and even play a role in causing) such activity. *Williams and Hori* [1970] have developed a possibly relevant model for the formation of hydraulic jumps in the atmosphere, and they cite previous attempts to construct hydraulic analogues of squall lines.

The second class of storm-associated waves is generally known as 'microbaroms,' because they are closely related to a class of seismic waves called 'microseisms.' Both microbaroms and microseisms come from the vicinity of storms at sea and appear to be directly related to each other and to sea state. Current models for microbarom generation invoke selective coupling between sea waves and atmospheric waves [*Donn and Posmentier*, 1968]. Distinguishing characteristics of microbaroms are their low spatial coherence and high frequency coherence. The pressure signatures are virtually monochromatic in appearance and always have wave periods very near 5–7 sec. Microbarom amplitudes are usually less than 1 μ bar.

In practice, once the distinguishing characteristics of these two wave types are recognized, neither is likely to be confused with the acoustic waves from convective storms.

d. Pressure sensing: Method and biases. Direct measurements of the pressure fluctuations associated with infrasonic waves are considerably more straightforward than indirect wave sensing by means of ionization 'tracers' of the wave motions. We therefore expect fewer sources of error and observational bias in their interpretation. *Cook and Bedard* [1971] and *Georges and Young* [1972] review the essentials of microbarometric pressure measurements.

Probably the most important source of bias in microbarograph systems is the spatial and temporal filtering that each observer builds into his sensing and processing systems. No standards have become widely accepted, so that most observatories operate systems that respond in their own unique way to the atmospheric wave spectrum. This inhibits intercomparison of data.

Another important bias in surface-pressure measurements is imposed by the level of so-called background noise produced by local (nonpropagating) pressure fluctuations. On the average, the frequency dependence of this noise sets an f^{-2} lower bound on detectable signals (cf. *Kimball and Lemon* [1970] and references they cite). Thus, for example, waves with an essentially uniform power spectral density over a broad band may be above noise level only in some high-frequency portion of that band. It should be noted, however, that the absolute noise level is highly variable with time and location. Even under optimum noise conditions, signal to noise ratios for severe-weather infrasound are typically less than 1.

e. Estimating source power. Estimates of source power from microbarograph measurements are not complicated by the interaction between the waves and a tracer, e.g., ionization, but are hindered by complicated propagation effects and the fact that sources at many distances have been identified. As long as we are interested only in wave energy, we can regard the refraction and trapping of acoustic waves below the thermosphere as a process that essentially converts a spherical wave into a cylindrical wave for distances greater than a few hundred kilometers. The height of the cylindrical wave guide h is about

100 km, and we assume that acoustic energy is distributed uniformly between the bottom and top of the guide. The radiated power P in terms of the measured power-flux density W at a horizontal distance r is thus

$$P = 2\pi rhW \quad (7)$$

A pressure wave of amplitude p has an average power-flux density of

$$W = \frac{1}{2}(p^2/\rho_0 C) \quad (8)$$

In section 3b we said that the median observed wave amplitude is 0.6 μ bar, or 0.06 N/m². No dependence of wave amplitude on source distance has emerged from observations, so that the best we can do is assign the 0.6 μ bar value to some mean source distance. A tentative estimate of 500 km is suggested by inspection of a sample of wave events whose sources have been identified with some certainty. This gives a value of $2.3 \times 10^7 W$ average radiated power, which compares favorably with the $2.8 \times 10^7 W$ estimated from ionospheric soundings.

4. CONTRASTS AND SIMILARITIES

The points enumerated under 'Summary of Observations' in sections 2b and 3b are arranged to permit direct comparison of corresponding numbers for the two forms of observation. The reader is encouraged to now go back and read the two lists 'in parallel.'

The similarity of the circumstances under which both kinds of waves are seen is so striking that it is hard to avoid the conclusion that they have a common source mechanism. Still, only a few examples have been recorded where both wave types were seen simultaneously and where both could be identified with the same storm system.

A minor discrepancy exists in the distances at which the two kinds of waves are detected. The ionospheric waves seldom appear more than 300 km from the source, whereas surface pressure waves are seen as far as 1500 km away. This discrepancy is rather easily explained in terms of a model for acoustic refraction at the base of the thermosphere, and it will be discussed in more detail in a later paper on propagation effects.

The only serious discrepancy appears to be in the wave spectrum seen with the two techniques. A narrow band, double-peaked spectrum, always near 2- to 5-min period, appears in the ionosphere, whereas a broad band, highly variable spectrum of wave periods in the tens of seconds characterizes the surface pressure fluctuations. The most obvious explanation of this difference is that the emissions are essentially broad band and that propagation and observational effects filter differently the waves detected by the two different sensors. In one test of this assumption, *Davies and Jones [1972c]* attempted unsuccessfully to detect the 2- to 5-min waves on a single microbarograph during their 1970 experiment in Oklahoma. This result is inconclusive, however, because the microbarograph bandwidth they used passed waves with periods as long as 30 min or more, whose large amplitudes (over 100 μ bar) could easily

mask short-period fluctuations of microbar amplitude. Furthermore, a single microbarograph is unable to distinguish propagating waves from local, non-propagating pressure fluctuations.

The source power estimates in the previous two sections seem, on the surface, to indicate agreement, until it becomes evident that the two estimates refer to different parts of the atmospheric wave spectrum and to different bandwidths. Is the apparent agreement, then, only fortuitous? Since both source power estimates were made from typical amplitude measurements of band-limited signals, the power estimates refer to the total power in the respective bands. Let typical bandwidths for the ionospheric waves be between 3- and 4-min period, or 1.38 mHz, and for the surface infrasound, 10–30 sec (67 mHz). Then the average power spectral densities for the respective waves are 2.03×10^7 W/mHz and 3.5×10^5 W/mHz.

In the light of what we now know, it seems reasonable to form a set of hypotheses about the nature of the emitting mechanism from which alternative models of the source can be constructed. Until we find evidence to the contrary, let us tentatively assume the following:

1. The ionospheric and surface pressure waves are just different manifestations of the same emissions.
2. The emission mechanism is essentially broad band, and its spectrum may vary considerably from event to event.
3. The difference between the observed wave spectra on the ground and in the ionosphere is caused by the interplay of several filtering mechanisms that involve both propagation effects and those of background noise on the sensors.

Figure 1 illustrates this last hypothesis in a purely schematic and qualitative way. The shaded areas indicate the portions of the source spectrum observable (above noise level) on the ground (right) and in the ionosphere (left). This picture also explains why it is difficult to detect 3-min waves on microbarographs even though they may be as strongly emitted as 10-sec waves. More careful measurements of the power spectral density distributions of both wave types should permit more accurate estimates of the source spectrum shape.

When the power spectral density calculations made earlier are considered in the light of such a model, much larger estimates for total source power emerge. The estimates of power spectral density for both bands suggest that the actual emission spectrum is at least two decades wide and peaks nearer 3-min period than tens of seconds. If a total of 5×10^7 W is visible only through the 4- to 5-min and the 10- to 30-sec windows, it is not unreasonable to suppose that an order of magnitude more energy is emitted over some much broader band. A broad band source candidate would thus have to predict emissions of the order of 10^8 to 10^9 W.

Our early assertion that the emissions probably do not represent a significant portion of a convective storm's energy budget can now be made more quantitative. A rough estimate (at least a lower bound) for a severe storm's

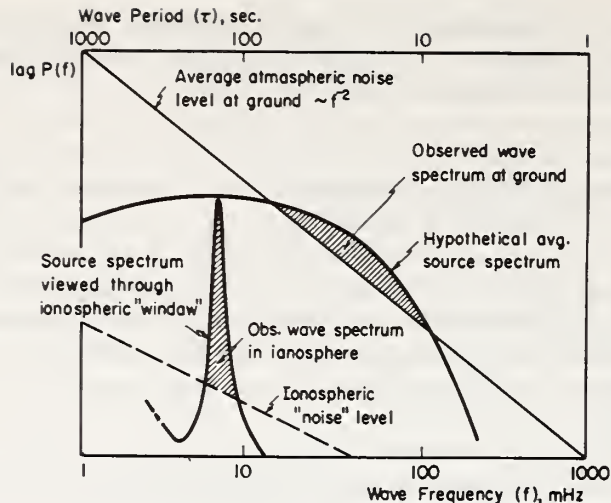


Fig. 1. Sketch of a hypothetical broad band source spectrum showing how different portions (shaded) might be visible on the ground and in the ionosphere in the presence of ambient noise levels and atmospheric filtering.

total energy can be obtained from the total kinetic energy in the updraft current. Assume an updraft with a 10-km diameter, a 5-km height, and a mean updraft speed of 10 m/sec [Newton, 1967]. Its total kinetic energy is about 2.3×10^{13} joules. Taking a cell lifetime of 1000 sec (the time for the energy to be converted into other forms) gives an average energy conversion rate of about 2.8×10^{10} W, compared with our estimated 10^8 to 10^9 W acoustic radiated power. Also an elementary estimate shows that a storm's kinetic energy is probably 2 orders of magnitude less than that released by condensation of water vapor. The imprecision inherent in both of these estimates of acoustic and storm-associated power allows only a small possibility for the acoustic radiation to be energetically significant.

5. A CASE STUDY OF A STORM OBSERVED WITH BOTH TECHNIQUES

Finally, in this review of present knowledge about severe-weather infrasound, we examine the details of one instance of simultaneous recordings of both the ionospheric waves and surface pressure waves from severe weather. Both waves apparently originated in the western Oklahoma storm system of June 27–28, 1969, whose ionospheric effects Davies and Jones [1971] studied. The reader should study Figures 7 and 8 of that paper, which reproduce the Oklahoma City Doppler record and associated weather-radar charts.

Broad band infrasound with dominant periods between 20 and 40 sec was recorded on the Boulder array of four microbarographs during the same interval. Its arrival azimuth, mainly between 125° and 130° , coincided with the direction of the Oklahoma storm system about 750 km away. We processed this infra-

sound on the NOAA analogue correlator [Brown, 1959] to produce the azimuth-time display of Figure 2. 'Altitude' in this three-dimensional representation is an estimate of signal to noise ratio calculated automatically by the correlator, which used the definition $S/N = R/(1 - R)$, where R is the broad band coherence of the wave over the microbarograph array. Background noise level remained relatively constant during the period, so that fluctuations in S/N presumably reflect fluctuations in the strength of the received acoustic wave. The shape of the pattern is of course smoothed in azimuth by the antenna pattern of the microbarograph array and in time by a 10-min integration window. Also, the display has been truncated below $S/N = 0.3$ to emphasize the features of the more coherent wave arrivals. The value 0.3 is somewhat arbitrary but is roughly the value above which experience has shown reliable wave measurements can be made.

Evidently, the 'signal' is composed of a sequence of pulsations, each about 20 min in duration, arriving mainly from between 125° and 130° but differing slightly in azimuth. The mean interval between the indicated pulsations is 20.3 min, with a standard deviation of 4.6 min. Measurements of dominant wave period and apparent direction of arrival during each individual pulsation are indicated at the top of Figure 2.

Such pulsations of severe-weather infrasound have not been mentioned heretofore; they apparently have not been noticed because low signal to noise ratios require the sort of processing displayed here to reveal the waves' structural details. Similar pulsations, in fact of similar duration, are of course a well-known feature of the ionospheric waves (see section 2b, items 7 and 8). However, in analysis of the pulsations, emphasis has been placed on their properties in the frequency domain. Using the nominal values of 3.5 and 4.5 min that Davies and Jones [1971] give for the peaks of the spectral fine structure, we calculate a nominal duration of each modulation cycle of 15.75 min. Small departures from the nominal values yield large changes in the modulation period; for example, 3.7 and 4.5 min give a 20.8-min envelope.

The existence of pulsations in both wave observations immediately prompts a detailed comparison of their time histories during this storm. To make the comparison we plot on the same time axis the S/N computed for the infrasound arriving at Boulder along with the amplitude of the Oklahoma City Doppler fluctuations scaled from Figure 7 of Davies and Jones's [1971] paper. We expect a time shift between wave arrivals at the two sensing locations, so that we can shift the two traces somewhat along the time axis for optimum fit. Figure 3 shows the two records adjusted for best visual correlation; the Boulder infrasound record has been advanced 21 min relative to the time scale and to the Doppler amplitude record. A 21-min shift is reasonably close to estimates of the difference in acoustic propagation time calculated with standard-atmosphere winds and temperatures.

Continuous beam steering in azimuth was employed in constructing the Boulder S/N trace; this maximizes overall coherence in case azimuth of wave arrival varies during the interval. In this case, the trace is essentially the same as the 125° trace of Figure 2, because azimuth changes were small.

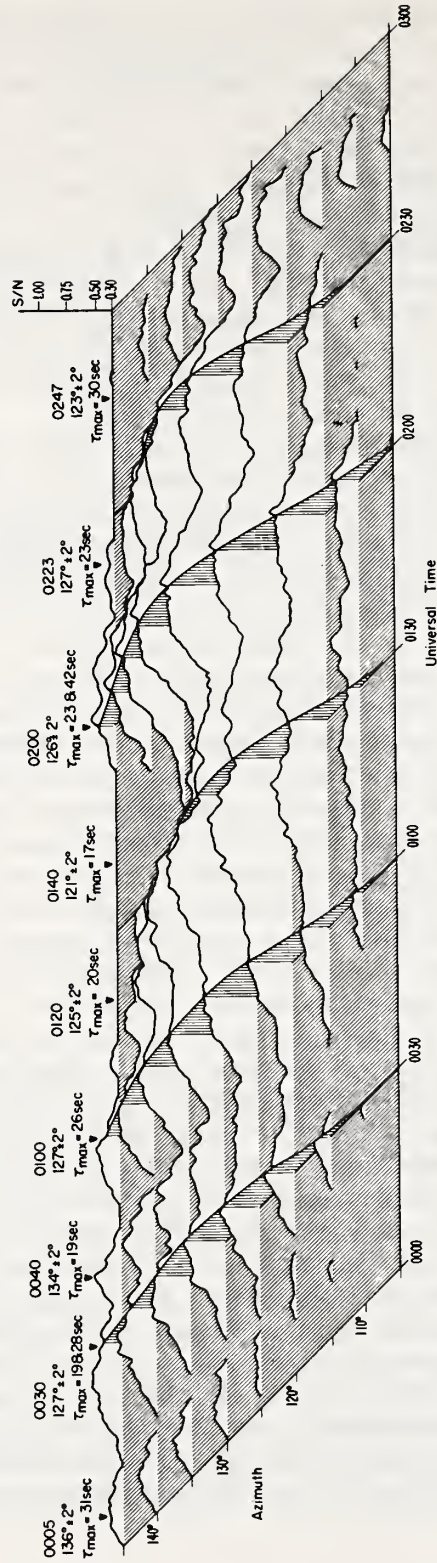


Fig. 2. A three-dimensional representation of the strength of severe-weather infrasound in the azimuth-time plane as received at Boulder, Colorado, on June 28, 1969. Individual 'pulsations' are identified by the azimuth and spectral notations at the top of the figure.

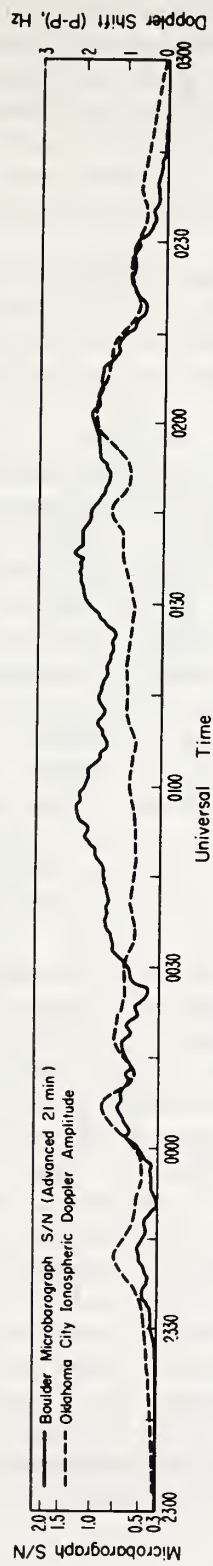


Fig. 3. A comparison of the time histories of infrasound from the June 28 storm as recorded in the ionospheric fluctuations over Oklahoma City with infrasound from the same storm recorded on the Boulder microbarograph array.

We feel that the fit, though far from perfect, is remarkable in view of the numerous propagation effects that could cause different amplitude scintillations over the widely different propagation paths. Coincidence of total event duration is also notable. Correlation appears to be best near the beginning and end of the event but poorer in the middle, when the ionospheric oscillations exhibit a less regular appearance. Similar correlations have been found between the other three ionospheric events studied by *Davies and Jones* [1971] and infrasound recorded at Boulder.

This result suggests that the same modulation or pulsations visible on the ionospheric waves are also characteristic of infrasound detected on the ground. If so, it is the modulation envelope, not the 3.5- and 4.5-min spectral components of the ionospheric waves, that may be characteristic of the wave source mechanism.

The appearance of the same modulation on both wave types strongly argues against any explanation of the spectral 'fine structure' of the ionospheric waves based on propagation filtering. The basic question that remains, however, is why the 'carrier' frequencies differ so much in the two cases. Propagation effects still seem the most likely explanation of this anomaly.

The 20-min pulsation interval strongly suggests a relationship with the observed 15- to 20-min interval between successive emergences of individual cumulus towers in multicellular storms (cf. *Anderson* [1960] and references he cites). It is thus tempting to explain the observed pulsations as the sequential radiation from individual convective cells within a storm complex. If, for example, the emission mechanism is aerodynamic, one might expect each cell to radiate most strongly during its period of most rapid growth when updraft currents are strongest. The observed changes in azimuth and spectral content between pulsations lend support to this idea. What remains, of course, is to identify the pulsations observationally with the birth and death of individual convection cells.

To find out if any specific details of a storm's development could be associated with the acoustic radiation, we examined the sequence of radarscope photographs made at the Oklahoma City weather radar during the June 28, 1969, storm. Figure 4 plots the principal storm tracks on an outline of Oklahoma that also contains a scale showing azimuth from Boulder. A puzzling feature of this storm complex is the appearance between 2330 and 0330 hours of a virtually stationary storm echo, while several other storm echoes simultaneously appeared to move rapidly toward the northeast. Some of the moving storms (those labeled B and C in Figure 4) apparently merged with the stationary storm at about 0200; another (labeled D) apparently split from the stationary storm at about 0000 hours, then moved rapidly northeastward. Most of the acoustic radiation observed at Boulder appears to come from between 124° and 130° , the azimuth of the stationary storm, and between about 0030 and 0230 hours (corrected for propagation time). Some arrivals outside of this azimuth range are indicated on Figure 2, and they may be associated with the moving storms, but we associate less confidence with those measurements because of their lower signal to noise ratios. The National Weather Service

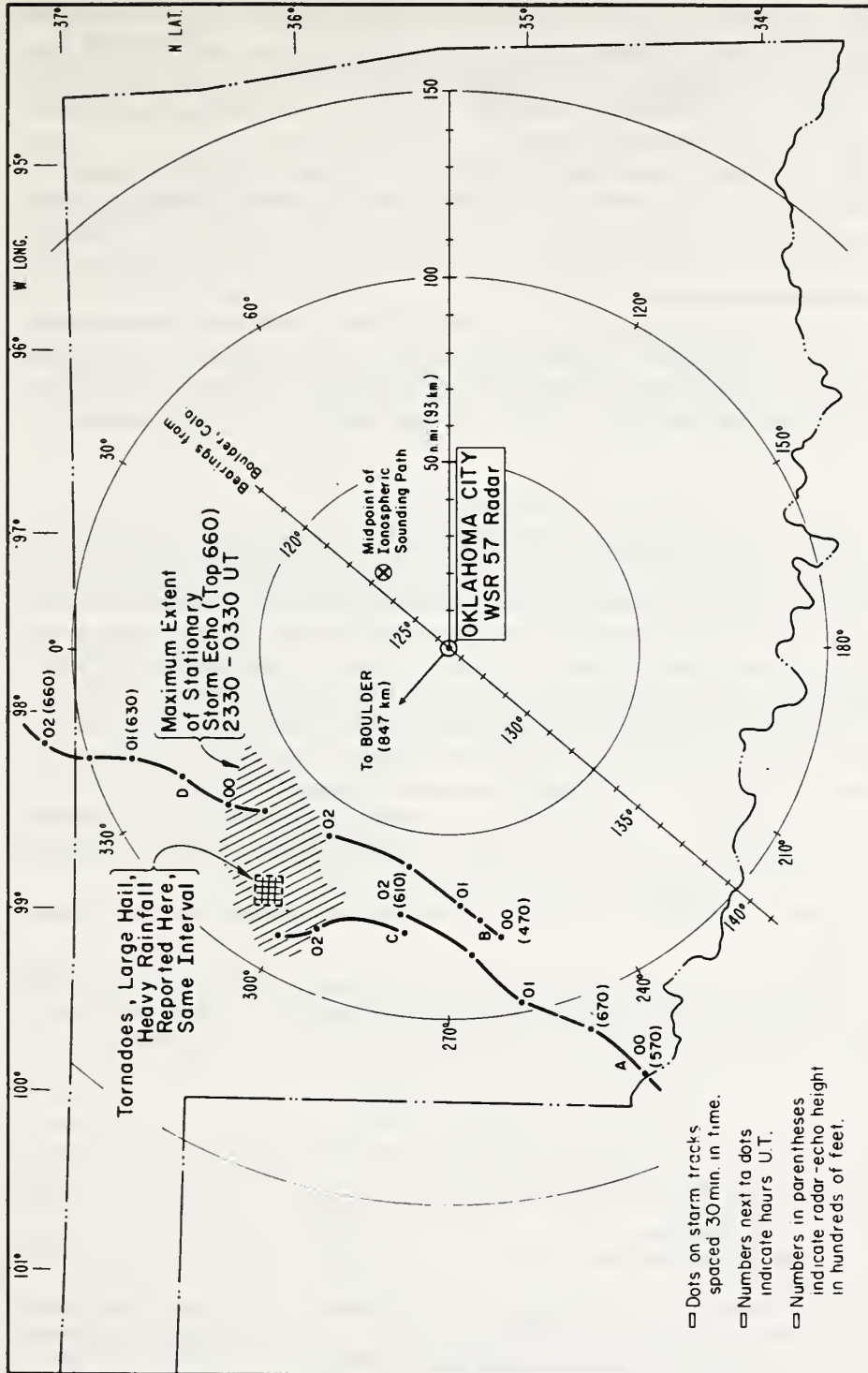


Fig. 4. Storm tracks indicated on Oklahoma City radar, June 28, 1969. This storm complex featured several cells apparently moving to the north-east while another storm remained virtually stationary, producing tornadoes, large hail, and heavy rainfall. Infrasound arrived at Boulder principally from 125° to 128° during the interval.

reported hail as large as $1\frac{3}{4}$ inches, up to 5 inches of rainfall, and two tornadoes associated with the stationary storm, but no severe weather was reported from the nearby moving storms, even though some of their echo heights were well above 40,000 ft. Evidently, infrasound is closely associated with a storm's severity, as judged in human terms.

This case study shows that we need to know more evolutionary details of the emitting storms than seem to be available from conventional weather radars. For example, it would be useful to identify the birth and death of individual convection cells for comparison with the acoustic pulsations. Doppler radars may be suited to this purpose.

An alternative explanation of the acoustic pulsations might be formulated in terms of propagation scintillations, where the atmospheric irregularities producing the scintillations are composed mainly of internal atmospheric gravity waves. This suggestion will be examined quantitatively in a future paper.

6. WHAT NEXT?

Research on this problem can now proceed in at least three useful directions. First, the several proposed source models should be refined and examined more closely to see if they survive the constraints imposed by existing knowledge about the waves. Each surviving model should predict distinct consequences that can be tested observationally. Second, an observational program should be mounted to refine the spatial and temporal relationships between both wave types and storm observables. In particular, such a program should test the predictions of the alternative source models. Third, because it is already clear that several 'atmospheric filtering' mechanisms obscure the true nature of the source, we should try to understand how propagation effects color the observations. In particular, refraction, ducting, dissipation, and possibly nonlinear effects need to be examined.

The papers that follow in this series will report on attempts to carry through such a plan.

Acknowledgment. I have drawn heavily on the collective experience of the NOAA Geoacoustics Group in preparing this paper. From data processing, through many informative discussions, to revisions of the manuscript, their help has been indispensable.

REFERENCES

- Anderson, C. E., A study of the pulsating growth of cumulus clouds, *Geophys. Res. Pap.* 72, Air Force Cambridge Res. Lab., Bedford, Mass., 1960.
- Baker, D. M., and K. Davies, F2-region acoustic waves from severe weather, *J. Atmos. Terr. Phys.*, 31, 1345-1352, 1969.
- Bauer, S. J., An apparent ionospheric response to the passage of hurricanes, *J. Geophys. Res.*, 63, 265-269, 1958.
- Bowman, H. S., Subsonic waves and severe weather phenomena, in *Acoustic-Gravity Waves in the Atmosphere—Symposium Proceedings*, edited by T. M. Georges, pp. 215-222, U.S. Government Printing Office, Washington, D.C., 1968.
- Bowman, H. S., and A. J. Bedard, Observations of infrasound and subsonic pressure disturbances related to severe weather, *Geophys. J. Roy. Astron. Soc.*, 26, 215-242, 1971.

- Brown, R. F., Jr., An automatic multichannel correlator, *J. Res. Nat. Bur. Stand., Sect. C*, **67**, 33-38, 1959.
- Chan, K. L., and O. G. Villard, Observation of large-scale traveling ionospheric disturbances by spaced-path high-frequency instantaneous-frequency measurements, *J. Geophys. Res.*, **67**, 973-988, 1962.
- Cook, R. K., *Atmospheric Exploration by Remote Probes*, vol. 2, *Atmospheric Sound Propagation*, pp. 658-662, National Academy of Sciences, Washington, D.C., 1969.
- Cook, R. K., and A. J. Bedard, On the measurement of infrasound, *Geophys. J. Roy. Astron. Soc.*, **26**, 5-12, 1971.
- Cook, R. K., and J. M. Young, Strange sounds in the atmosphere, **2**, *Sound Its Uses Contr.*, **1**, 25-33, 1962.
- Davies, K., and D. M. Baker, On frequency variations of ionospherically propagated HF radio signals, *Radio Science*, **1**, 545-556, 1966.
- Davies, K., and J. E. Jones, Ionospheric disturbances in the F2 region associated with severe thunderstorms, *J. Atmos. Sci.*, **28**, 254-262, 1971.
- Davies, K., and J. E. Jones, Infrasound in the ionosphere generated by severe thunderstorms, *J. Acoust. Soc. Amer.*, **52**, 1087-1090, 1972a.
- Davies, K., and J. E. Jones, Evidence for waves and winds in the ionospheric F2 region, *Space Res.*, **12**, 1149-1156, 1972b.
- Davies, K., and J. E. Jones, Ionospheric disturbances produced by severe thunderstorms, *Prof. Pap. 6*, Nat. Oceanic Atmos. Admin., Boulder, Colo., 1972c.
- Davies, K., J. M. Watts, and D. H. Zacharisen, A study of F2 layer effects as observed with a Doppler technique, *J. Geophys. Res.*, **67**, 601-609, 1962.
- Detert, D. G., A study of the coupling of acoustic energy from the troposphere to the ionosphere, final report to Marshall Space Flight Center, NASA, Avco Corp., Wilmington, Mass., Feb. 15, 1969.
- Donn, W. L., and E. Posmentier, Infrasonic waves from natural and artificial sources, in *Acoustic-Gravity Waves in the Atmosphere—Symposium Proceedings*, edited by T. M. Georges, pp. 195-208, U.S. Government Printing Office, Washington, D.C., 1968.
- Donn, W. L., R. Rommer, F. Press, and M. Ewing, Atmospheric oscillations and related synoptic patterns, *Bull. Amer. Meteorol. Soc.*, **35**, 301-309, 1954.
- Georges, T. M., Evidence for the influence of atmospheric waves on ionospheric motions, *J. Geophys. Res.*, **72**, 422-425, 1967a.
- Georges, T. M., Ionospheric effects of atmospheric waves, *Tech. Rep. IER 57-ITSA 54*, ESSA, U.S. Government Printing Office, Washington, D.C., 1976b.
- Georges, T. M., HF Doppler studies of traveling ionospheric irregularities, *J. Atmos. Terr. Phys.*, **30**, 735-746, 1968a.
- Georges, T. M., Short-period ionospheric oscillations associated with severe weather, in *Acoustic-Gravity Waves in the Atmosphere—Symposium Proceedings*, edited by T. M. Georges, pp. 171-178, U.S. Government Printing Office, Washington, D.C., 1968b.
- Georges, T. M., Collisional interaction of atmospheric waves with the ionospheric F region, in *Acoustic-Gravity Waves in the Atmosphere—Symposium Proceedings*, edited by T. M. Georges, pp. 377-380, U.S. Government Printing Office, Washington, D.C., 1968c.
- Georges, T. M., and J. M. Young, Passive sensing of natural acoustic-gravity waves at the earth's surface, in *Remote Sensing of the Troposphere*, edited by V. E. Derr, U.S. Government Printing Office, Washington, D.C., 1972.
- Goerke, V. H., and M. W. Woodward, Infrasonic observations of a severe weather system, *Mon. Weather Rev.*, **94**, 395, 1966.
- Hooke, W. H., Ionospheric irregularities produced by internal atmospheric gravity waves, *J. Atmos. Terr. Phys.*, **30**, 795-823, 1968.
- Jones, J. E., Observation of traveling ionospheric disturbances by the Doppler technique with spaced transmitters, *Tech. Rep. ERL 142-SDL 11*, ESSA, U.S. Government Printing Office, Washington, D.C., 1969.
- Jones, W. L., A theory for quasi-periodic oscillations observed in the ionosphere, *J. Atmos. Terr. Phys.*, **32**, 1555-1566, 1970.

- Kimball, B. A., and E. R. Lemon, Spectra of air pressure fluctuations at the soil surface, *J. Geophys. Res.*, **75**, 6771-6777, 1970.
- Newton, C. W., Severe convective storms, *Advan. Geophys.*, **12**, 257-308, 1967.
- Pierce, A. D., and S. C. Coroniti, A mechanism for the generation of acoustic-gravity waves during thunderstorm formation, *Nature*, **210**, 1209-1210, 1966.
- Pierce, A. D., and J. W. Posey, Theoretical prediction of acoustic-gravity pressure wave-forms generated by large explosions in the atmosphere, final report to Air Force Cambridge Res. Lab., Dep. of Mech. Eng., Mass. Inst. of Technol., Cambridge, Mass., 1970.
- Rastogi, R. G., Thunderstorms and sporadic-E layer ionization over Ottawa, Canada, *J. Atmos. Terr. Phys.*, **24**, 533-540, 1962.
- Thomas, J. E., A. D. Pierce, E. A. Flinn, and L. B. Craine, Bibliography on infrasonic waves, *Geophys. J. Roy. Astron. Soc.*, **26**, 399-425, 1971.
- U.S. Department of Commerce, *Lightning*, NOAA/PI 70005, 4 pp., U.S. Government Printing Office, Washington, D.C., 1970.
- Watts, J. M., and K. Davies, Rapid frequency analysis of fading radio signals, *J. Geophys. Res.*, **65**, 2295-2301, 1959.
- Williams, D. T., Pressure wave observations in the central midwest, 1952, *Mon. Weather Rev.*, **81**, 278-289, 1953.
- Williams, R. T., and A. M. Hori, Formation of hydraulic jumps in a rotating system, *J. Geophys. Res.*, **75**, 2813-2821, 1970.
- Wilson, C. T. R., The electric field of a thundercloud and some of its effects, *Proc. Phys. Soc. London*, **37**, 32D-37D, 1925.

(Received February 20, 1973; revised April 30, 1973.)

Reprinted from the Proceedings of the Eighth Conference on Severe Local Storms, October 15-17, 1973.

INFRAOUND FROM SEVERE STORMS

T. M. Georges

Wave Propagation Laboratory
NOAA, Environmental Research Laboratories
Boulder, Colorado 80302

1. INTRODUCTION

Infrasound is the name given to a class of acoustic waves whose frequencies are subaudible but which travel through the atmosphere at essentially the local speed of sound. A long-period limit therefore exists at the atmosphere's acoustic-cutoff period, about 4 minutes in the troposphere.

Many kinds of natural infrasound have now been classified, but adequate models of natural source mechanisms exist for only a few. Georges and Young (1972) review techniques for observing infrasound with arrays of microbarographs as well as present knowledge about at least nine different kinds of natural infrasound.

It has been known for over a decade that certain convective storms emit infrasound powerful enough to be detected over 1500 km away. These waves typically have amplitudes of about 1 microbar and periods between 10 and 40 sec. More recently, a connection has been found between certain severe storms and a particular class of wavelike oscillations in the ionospheric F region, 200 to 300 km above the ground. These waves are observed with ground-based radio-echo sounders and have periods between 2 and 5 minutes. I have recently reviewed elsewhere (Georges, 1973) the history and phenomenology of both of these manifestations of severe-weather infrasound.

The purpose of this paper is to report briefly some results of recent observations that may interest those who study severe storms and also those responsible for forecasting their behavior.

2. OBSERVATIONS

As part of an effort to find the emitting mechanism, we examined the details of infrasound received at Boulder, Colorado, during the 1972 storm season. Some 146 distinct wave 'events' were logged during June, July and August (a slightly larger number would have resulted from a stricter definition of 'event', since a few intervals studied evidently contained multiple arrivals.)

With the aid of weather-radar charts, severe-storm reports and other relevant geophysical data, we screened and classified each of the 146 events according to its most probable origin. Figure 1 shows the classification scheme used and the number of events falling

into each category.

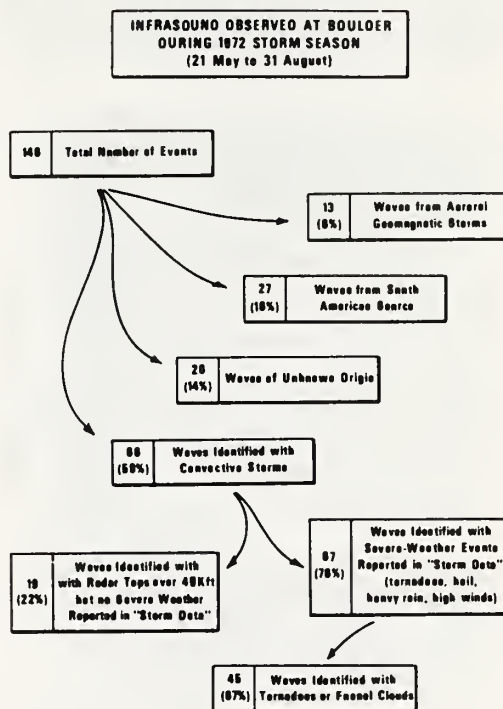


Figure 1. Classification of infrasound received at Boulder, Colorado, during the 1972 observing period (21 May through 31 August). Each percentage figure refers to the number in the respective "parent" boxes.

Events were classified as storm-associated when a time coincidence between wave arrival and storm activity existed (accounting for acoustic propagation time), and when the direction of wave arrival coincided within 2 degrees with the location of storm activity. With these rather stringent criteria we expect few 'mistaken

identities.' In some cases, triangulation from other infrasound observatories provided additional confirmation.

About 86 (59%) of the events appear to be connected with convective-storm activity, mainly in the Midwest. Of those, we identify 67 (78%) with storms that produced effects usually denoted by the term 'severe weather', that is, large hail, heavy rainfall, high local winds or tornadoes. The remaining 19 storm-associated waves were so identified because of apparent coincidence with storms indicated only on weather radars, but whose tops exceed 40,000 ft. It seems likely that many of these detected storms produced severe effects that were simply not reported for some reason.

A breakdown of severe-storm sources by state is shown in figure 2. (The total adds up to more than 86 because of storms that overlap states.)

If we adopt the point of view of storm detection or warning, the remaining 60 (41%) events that we could not associate with storm activity might be called 'false alarms.' However, virtually all of the false alarms appear to exhibit some property that permits them to be distinguished from storm-associated waves after detailed analysis of wave properties. In particular, most of the false alarms (such as the two specifically mentioned in figure 1) could be identified without the need to consult independent weather records by a sensor network that permitted source location. Also, because of the long distances at which severe-storm infrasound can be detected, it is reasonable to think of a network of two or three sensor arrays that could identify, locate and possibly track most of the emitting storms between the Mississippi and the Rockies.

To test this idea, we have recently deployed two additional microbarograph arrays at Rapid City, South Dakota, and near Albuquerque, New Mexico, to supplement the Boulder observatory for observations during the 1973 season. The three triangles on the map of figure 2 indicate the locations of the three observatories. No results of this test are available at this writing, however.

Results of further statistical breakdown of the 1972 observations are shown in figure 3. Part (a) shows the distribution of observations of severe-weather infrasound by hour of the day, during the 3-month observing period. The waves clearly tend to occur in late afternoon or early evening, just as do severe thunderstorms in the Midwest. Part (b) shows the number of hours each calendar day, during which severe-weather infrasound was observed. This plot is smoothed by a 5-day running average. No attempt has yet been made to associate this pattern with any synoptic-scale weather trends. Waves begin to appear in Boulder in mid-May, rather than in March or April when severe storms begin in the Midwest,

because east-to-west infrasound propagation is inhibited by prevailing mesospheric winds before they reverse direction from eastward to westward around mid-May. Wave observations in Washington, D.C., exhibit a complementary behavior. Part (c) is a histogram showing the distribution of wave-event duration. The mean duration is about 2 hours.



Figure 2. Distribution by state of sources of severe-weather infrasound during the 1972 observing period, also showing the locations of three observatories for the 1973 season.

It is significant that 45 of the 86 storm-associated waves have been identified with storms that produced documented tornadoes or funnel clouds. Furthermore, over two-thirds of the emitting storms were in Texas, Oklahoma, Kansas, Nebraska or South Dakota, notorious as 'tornado alley.' The fact that tornadic storms represent a large fraction (over half) of the emitting storms, but a small fraction of all storms, suggests that the emitting mechanism may be tornado-related. Yet a significant fraction of the emitters evidently produced no reported tornadoes. It is thus tempting to seek an explanation in terms of the intense concentrations of vorticity that seem to be present in some storms, some but not all of which grow into tornadoes. Work is presently underway on theoretical source models for the production of infrasound by vortices.

Perhaps the most interesting and potentially useful feature of the emissions is an apparent tendency to occur in the early stages of storms that later produce the severest effects. In one closely studied case, a storm on 27-28 June 1969 in western Oklahoma emitted infrasound that was monitored in Boulder between about 00-03 hours (U.T.). After accounting for acoustic-propagation time, the beginning of the emissions is estimated to be 30 to 45 min earlier, or at 2315 to 2330 on the 27th. The NOAA publication 'Storm Data' for June 1969 reports a tornado, up to 5 inches of rainfall and 1-3/4 inch hail in the emitting area between 00 and 0445 U.T., and, in particular, one tornado at 0157 U.T. Furthermore,

the emissions appeared to come from the area reporting the severe effects and not from other nearby storms with echo tops up to 66,000 ft. Further details of the emissions from this storm are reported in the review paper cited earlier (Georges, 1973).

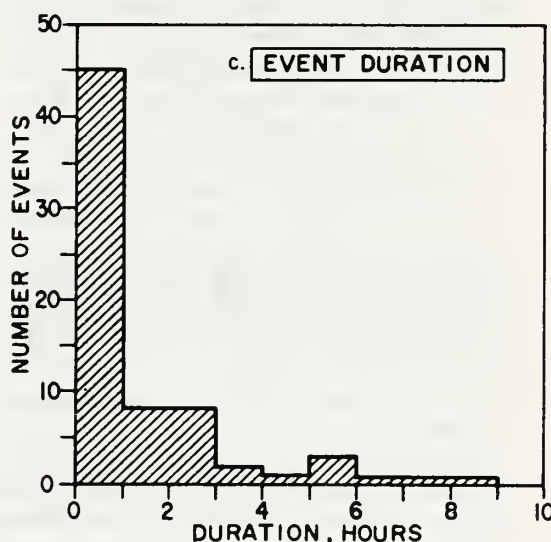
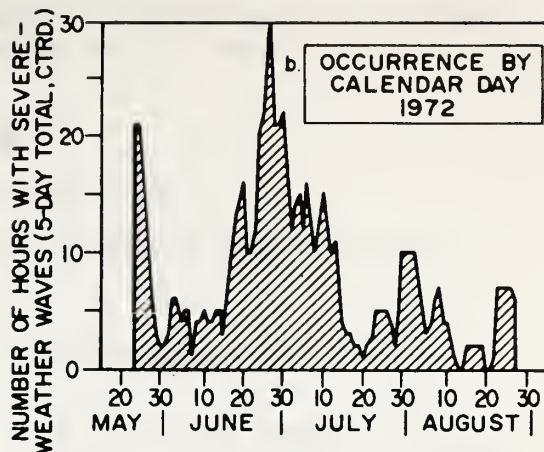
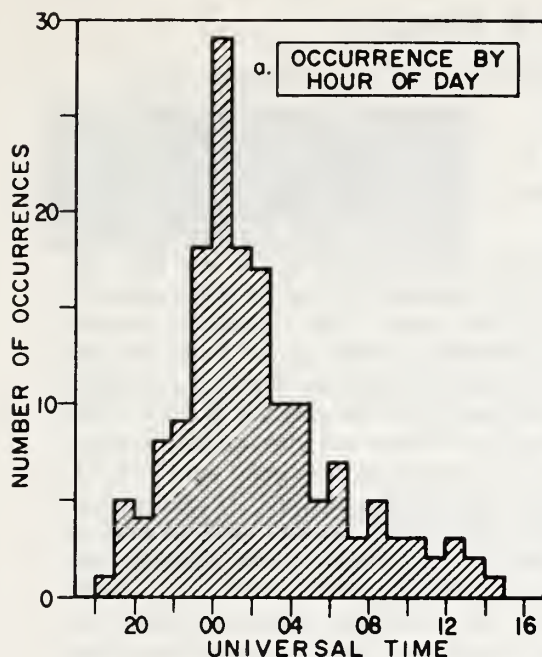


Figure 3. Statistical breakdown of 86 severe-storm-infrasound events according to (a) time of day, (b) day of year, and (c) event duration.

Work is continuing toward refining and testing various source models and toward assessing the ultimate usefulness of infrasound for severe-storm identification and warning purposes. It seems reasonable to assume that much of the loss of life and social disruption wrought by severe thunderstorms may ultimately be preventable, either through timely warnings that permit the public to take shelter, or through storm-modification techniques. In either case, a key problem, clearly, is to refine our abilities to identify the potentially dangerous storms in their earliest stages. Infrasound is just one of several new 'remote-sensing' tools being applied to this task.

References

- Georges, T. M. and J. M. Young, Passive sensing of natural acoustic-gravity waves at the earth's surface, Remote Sensing of the Troposphere, V. E. Derr, Ed., U.S. Govt. Printing Off., Washington, D.C. 1972.
- Georges, T. M., Infrasound from convective storms: examining the evidence, Reviews of Geophysics, August, 1973.

Reply

E. E. GOSSARD¹ AND J. H. RICHTER

Radio Physics Division, Naval Electronics Laboratory Center, San Diego, California 92152

D. ATLAS

Department of the Geophysical Sciences, University of Chicago, Chicago, Illinois 60637

As stated by Baker, *Murrow and Henry* [1965] conclude that the rms apparent velocity fluctuations due to the self-induced motion of balloons depends on terminal velocity of the balloons. The actual ascent rate of the Gossard, Richter, Atlas (GRA) balloon is shown in Figure 1. The ascent rate was deliberately chosen to be as small as possible. In the region above the inversion layer, where the GRA oscillations are most pronounced, it is seen that the ascent rate is less than that of any of the balloon systems tested by Murrow and Henry and about half that assumed by Baker. Thus the balloon self-induced velocity fluctuation should be about half that deduced by Baker. However, the self-induced fluctuation so deduced would still be of the same general magnitude as that observed by GRA.

We believe the following are convincing arguments for the physical reality of the fluctuations in velocity discussed by GRA [1970] and *Hines* [1970]:

1. Instead of being proportional to balloon ascent rate, as are the self-induced oscillations of Murrow and Henry, the GRA oscillations are greatest above 400 meters where the ascent rate is least, as shown by Figure 1.

2. Murrow and Henry state that 'these oscillations are not simple sinusoidal motion and are not limited to a single plane,' and their figures testify to the inherent randomness of the self-induced motions. An impressive feature of the GRA oscillations is their sinusoidal character

(actually more apparent in the raw data plot than the drawing produced by the illustrator).

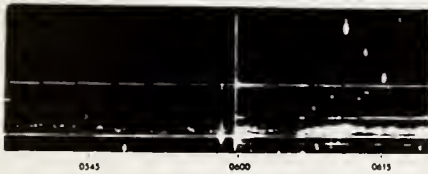
3. There seems to be a consistent relationship between the GRA type of fluctuation and the atmospheric structure. Figure 2 is included to emphasize that the sounding in GRA is not unique and to point out characteristic similarities. The observation techniques were very different. The sounding in GRA was obtained by optical (theodolite) tracking with readings at 10-sec intervals. Figure 2 was obtained with standard GMD equipment which automatically tracks the transmitted signal and reads out automatically and digitally every 6 sec. As in the GRA sounding, the oscillations are roughly sinusoidal and appear above and within the temperature inversion but cease at the top of the radar echo. Fairly small, more-or-less random velocity fluctuations reminiscent of the Murrow and Henry oscillations appear in all balloon soundings, but the characteristic structure of Figure 2 and GRA Figure 14 is only seen occasionally (3 cases out of approximately 20 observations), and in all cases the radar reveals a similar relation to atmospheric structure.

4. Figure 2 shows that the oscillations appear also in humidity and temperature within the inversion layer. They are most pronounced in humidity, probably because of the fast response of the carbon humidity element. If self-induced displacement of the balloon were to account for the variations in relative humidity, vertical displacements of 70 meters would be required during a mean height change of approximately 140 meters. No fluctuations even close to this magnitude are indicated by the pressure height calculations, and it is much more reasonable to assume the humidity fluctuations

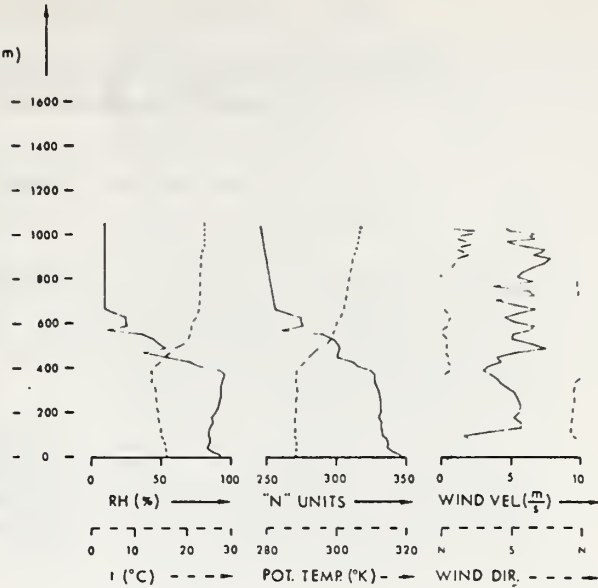
¹ Now at Wave Propagation Laboratory, Environmental Research Laboratories, NOAA, Boulder, Colorado 80302.

DATE: 24 JUNE 1970

RADIOSONDE RELEASE TIME: 0559



→ PACIFIC STANDARD TIME



SIMULTANEOUS RADAR AND RADIOSONDE SOUNDINGS

LOCATION: 32°42' N. LAT., 117° 15' W LONG., 31 m ABOVE MSL.

Fig. 1. Ascent rate.

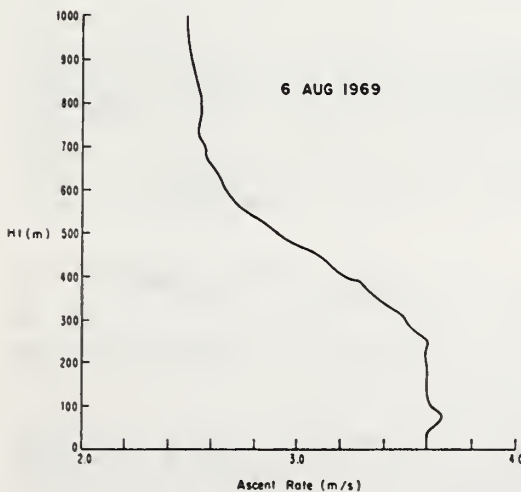


Fig. 2. Simultaneous radar and radiosonde soundings.

are caused by wave motion perturbing the atmospheric region of the large humidity gradient.

We recognize the importance of Baker's suggestion and urge definitive experiments to resolve the issue. We believe that experiments of major importance can now be carried out combining the new class of radar and acoustic sounders with special wind profile measurements. We suggest optical tracking of smoke, trails from rockets or smoke bombs, or perhaps tracking of Jimspheres.

REFERENCES

- Gossard, E. E., J. H. Richter, and D. Atlas, Internal waves in the atmosphere from high resolution radar measurements, *J. Geophys. Res.*, 75, 3523-3536, 1970.
- Hines, C. O., Comments on paper by E. E. Gossard, J. H. Richter, and D. Atlas, 'Internal waves in the atmosphere from high resolution radar measurements,' *J. Geophys. Res.*, 75, 5956-5959, 1970.
- Murrow, H. N., and R. M. Henry, Self-induced balloon motions, *J. Appl. Meteorol.*, 4, 131-138, 1965.

(Received October 27, 1971.)

On the Detectability of Fog, Cloud, Rain and Snow by Acoustic Echo-Sounding Methods

C. GORDON LITTLE

Environmental Research Laboratories, NOAA, Boulder, Colo. 80302

(Manuscript received 19 August 1971, in revised form 17 January 1972)

The scatter of sound waves by fog, cloud, rain and snow particles is analyzed for the Rayleigh case (i.e., $D \ll \lambda$). It is shown that relatively standard acoustic echo-sounding equipment should obtain strong echoes (about 49 dB above noise at 300 m range) during heavy snow conditions. Rain at 300 m range would produce echoes varying from about 23 dB to about (58- I) dB above noise for conditions ranging from drizzle (1 mm hr⁻¹) to heavy rain (25 mm hr⁻¹), the parameter I being used to denote the increase in noise level in dB due to precipitation noise. Fogs and clouds with $Z \geq 5 \times 10^{-2}$ mm⁶ m⁻³ would be detectable out to 300 m range on the standard system.

Acoustic energy scattered from naturally occurring velocity and temperature fluctuations in the boundary layer of the atmosphere will tend to mask the hydrometeor echoes. Three methods of distinguishing hydrometeor echoes from those resulting from irregular velocity and temperature fields are suggested. An optimum experimental configuration to study hydrometeor echoes is proposed.

The fluctuation in acoustic refractive index created by the turbulent wakes of precipitating hydrometeors has also been investigated theoretically; it is concluded that the wakes are too weak to be detected in the presence of the normal spectra of variability of the atmospheric boundary layer.

1. Introduction

The scatter of acoustic waves by atmospheric turbulence and temperature inhomogeneities has been studied, both experimentally and theoretically, by a number of authors [see Little (1969) for a review of this work]. The current paper turns to the theory of the detectability of hydrometeors by direct acoustic echo-sounding methods. Rayleigh's early result on the scattering cross section of small spherical particles is used to compute the expected signal-to-noise ratios for given hydrometeor and acoustic echo-sounder conditions. Since any hydrometeor echoes must be detected in the presence of echoes from the irregular velocity and temperature fields of the boundary layer of the atmosphere, methods for identifying the hydrometeor echo component are proposed.

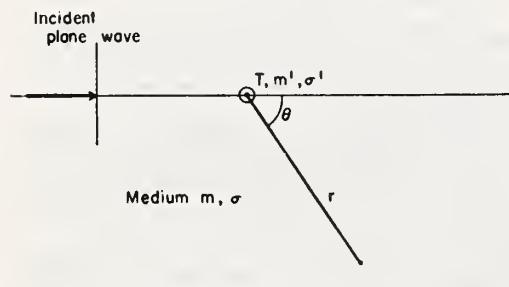


FIG. 1. The scattering of a plane acoustic wave by a small sphere.

The problem of the acoustical effects of the wakes produced by precipitating hydrometeors is discussed briefly.

2. The scatter of sound waves by small spherical particles

The scatter of sound waves by a spherical particle whose diameter is small compared with the acoustic wavelength was originally discussed by Rayleigh in 1872.

For the case (see Fig. 1) in which a plane wave of wavelength λ , propagating through a medium of bulk modulus m and density σ , is incident upon a small sphere of volume T , bulk modulus m' , and density σ' , he showed that the amplitude of the scattered wave at a point a distance r from the sphere at an angle θ relative to the direction of propagation of the plane wave, is given by (dropping the time-dependent term)

$$\psi_s = \psi_i \left[\frac{\pi T}{\lambda^2 r} \left[\frac{m' - m}{m'} - \frac{3(\sigma' - \sigma)}{\sigma + 2\sigma'} \cos \theta \right] \right], \quad (1)$$

where ψ_i is the amplitude of the incident plane wave¹ (Rayleigh, Vol. 2, p. 284).

¹ This equation differs from Rayleigh's by the use of the negative sign in the bracket; this is necessary because I have followed the current practice of measuring scatter angles from the forward propagation direction, instead of from the opposite direction.

Hence, the scattered power flux is proportional to

$$(\psi_s)^2 = \frac{\psi_i^2 \pi^2 T^2}{\lambda^4 r^2} \left[\frac{m' - m}{m'} - \frac{3(\sigma' - \sigma)}{\sigma + 2\sigma'} \cos\theta \right]^2 \quad (2)$$

Note that the intensity shows the standard Rayleigh λ^{-4} dependence of the scattered energy, characteristic of scatter at wavelengths large compared with the diameter of the scatterers.

In modern meteorological radar parlance the scattering efficiency of a single target is expressed in terms of its radar cross section α , defined by

$$P_s = \alpha \frac{P_i}{4\pi r^2} \quad (3)$$

where P_i is the power flux in the beam incident upon the target, and P_s the scattered power flux at range r . It will be seen that α is that area which, normal to an incident flux P_i , and re-radiating the intercepted flux isotropically, would produce the observed scattered power flux P_s .

Using (3) in (2) we have

$$\alpha = \frac{4\pi r^2 P_s}{P_i} = \frac{4\pi^3 T^2}{\lambda^4} \left[\frac{m' - m}{m'} - \frac{3(\sigma' - \sigma)}{\sigma + 2\sigma'} \cos\theta \right]^2$$

Substituting

$$T = \frac{\pi D^3}{6},$$

where D is the diameter of the sphere, we have

$$\alpha = \frac{\pi^5 D^6}{9\lambda^4} \left[\frac{m' - m}{m'} - \frac{3(\sigma' - \sigma)}{\sigma + 2\sigma'} \cos\theta \right]^2$$

For the case of water or ice spheres in air, the bulk modulus m' of the drop is very large compared with that of the air, m , and similarly, $\sigma' \gg \sigma$. Using these facts

$$\alpha = \frac{\pi^5 D^6}{9\lambda^4} [1 - \frac{3}{2} \cos\theta]^2 \quad (4)$$

As discussed by Lamb (1932), the two terms within the brackets represent two types of disturbance which have different polar diagrams. In the absence of the drop, the space which it occupies would be filled alternately with condensations and rarefactions of the air due to the incident acoustic wave. The presence of the drop inhibits these density variations. The resultant scattered wave at a distance is just that which would be caused in an otherwise uniform medium by a periodic variation in the volume of the obstacle sufficient to compensate for the above variations in density. This alternate dilation and contraction would act as a monopole source, and would radiate isotropically.

Superimposed on this field is a second scattered wave component due to the immobility of the obstacle. If the obstacle had the same inertia (i.e., density) as the air, and was freely movable, it would participate in the longitudinal oscillations of the sound wave, swaying to and fro in response to the wave. Because the obstacle has much greater density, it behaves as if it were fixed. The resultant scattered component at a distance is just that which would be produced if the obstacle were to oscillate to and fro in a straight line, with a motion equal and opposite to that of the air particles in the undisturbed wave. This component is therefore equivalent to a dipole source, i.e., it has a $\cos\theta$ amplitude polar diagram with nulls at $\theta = 90^\circ$, and changes phase between the forward and backward hemisphere.

The amplitudes of these two scattered waves are in the ratio $1:(-1.5 \cos\theta)$. They are in phase in the rearward hemisphere and out of phase in the forward hemisphere; as a result more power is scattered into the rearward than into the forward hemisphere. At an angle $\theta = \cos^{-1}(\frac{2}{3}) = 48.2^\circ$, the two scattered components are equal in magnitude and opposite in phase, and therefore exactly cancel each other.

The above discussion has ignored the effects which the hydrometeors may have on the absorption of acoustic waves. The absorption effects fall into three categories: absorption in the interior of the hydrometeor; excitation of mechanical oscillations of the hydrometeor; and absorption associated with momentum, energy and mass exchange between the moist air and the hydrometeor.

Taking first the absorption in the interior of the hydrometeor, it is known (Vigoreux and Hersey, 1962; Westphal, 1965) that the attenuation of sound in water and ice is low. In addition, the discontinuity in acoustic impedance at the air-water or air-ice interface is large, and therefore very little energy is transmitted into the medium. (For a plane wave incident normally onto a plane water surface, only about 1 part in 1000 of the incident energy is transmitted into the water; the amount transmitted will be even less for ice, or for angles of incidence other than normal.) For these reasons, we may ignore the absorption of sound in the interior of water or ice spheres.

A second possibility, the transfer of acoustic energy into mechanical oscillation of liquid (or solid) drops, can also be seen to be negligible. Such a transfer of energy will proceed with maximum efficiency only if the frequency of the acoustic wave is resonant with the natural frequency of oscillation of the drop, and if the wavelength of the acoustic wave is "resonant" (i.e., equal to) the diameter of the drop. Fig. 2 shows that for the range of drop sizes and acoustic frequencies appropriate to acoustic echo sounding of hydrometeors, these two conditions cannot be fulfilled simultaneously.

The extra absorption produced by the presence of small fog particles has been investigated both theo-

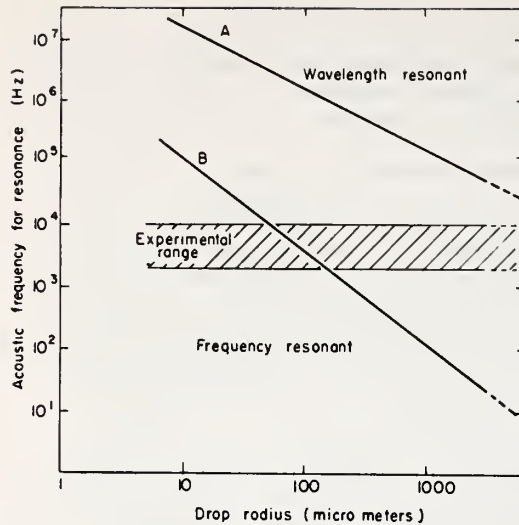


FIG. 2. Spatial and frequency resonance conditions for resonant interaction between acoustic waves and mechanical oscillation of a water drop, as a function of drop radius. Line A gives the wavelength resonance condition, $\lambda = D$; line B the mechanical resonance condition, $f = (8F/3\pi m)^{1/2}$ [Lamb, 1932], relating the acoustic frequency f to the surface tension F and mass m of the drop.

retically and experimentally by Cole and Dobbins (1970, 1971), whose theoretical work included the effects of momentum, energy and mass transfer between the droplet and the moist air. Their work shows that, at the high audio frequencies appropriate to acoustic echo-sounding of hydrometeors, the extra absorption produced by the presence of fog particles is small compared with that already existing in the moist air, being largest in the case of dense fogs of small particles (diameter $\sim 5 \mu\text{m}$). For a given liquid water content per cubic meter of air, the excess absorption decreases rapidly with increasing droplet size, and would be insignificant for medium and heavy rainfall conditions.

The effect of snowflakes upon the attenuation of acoustic waves is not known. Their large surface areas will enhance the effects of viscosity, and it is possible that significant absorption might occur along the acoustic propagation path. However, the true scattering cross section could presumably be obtained by measuring the hydrometeor scattering cross section as a function of height and extrapolating the observed values to zero range.

For backscatter, $\theta = 180^\circ$, Eq. (4) reduces to

$$\alpha_{180} = \frac{25\pi^5 D^6}{36\lambda^4}.$$

The above equation relates to the scattering cross section of a single drop. Under conditions of fog or precipitation, there will be many drops within the pulse

volume of an acoustic echo-sounder. Assuming that the drops scatter independently of each other, the total scattering cross section of the particles within the pulse volume V will be given by

$$\alpha_{\text{total}} = \frac{25\pi^5}{36\lambda^4} \sum_v D^6.$$

The acoustic reflectivity η , i.e., the backward-scattering cross section per unit volume of the region, will be given by

$$\eta = \frac{25\pi^5}{36\lambda^4 V} \sum_v D^6. \quad (5)$$

Eq. (5) can be compared with the corresponding expression for the Rayleigh scatter of electromagnetic waves incident upon small spheres (see, for example, Atlas, 1964)

$$\eta = \frac{\pi^6}{\lambda^4 V} \sum_v D^6 |K|^2, \quad (6)$$

where $|K|^2 = |(m^2 - 1)/(m^2 + 2)|^2$ and $m = n_1 - in_2$, i.e., m is the complex refractive index of the spherical target. (In the acoustic case $|K|^2$ is replaced by

$$\frac{1}{9} \left[\frac{m' - m}{m'} + \frac{3(\sigma' - \sigma)^2}{\sigma + 2\sigma'} \right] = \frac{25}{36}$$

for the case $\theta = 180^\circ$, $m' \gg m$ and $\sigma' \gg \sigma$.)

Since $|K|^2$ is of the order 0.9 for water and 0.2 for ice, we see that the acoustic reflectivities of small spherical liquid or ice particles are respectively about 0.77 and 3.5 times the corresponding microwave reflectivities.

Eqs. (5) and (6) are appropriately applied to small spherical raindrops or hailstones. For snowflakes, it might seem necessary to use values of D , σ' and m' appropriate to the size, shape and densities of the snowflakes. By analogy with the radio case (Atlas, 1964) we may use the value of m' and σ' corresponding to solid ice, providing that we use the corresponding value of D , i.e., the diameter of the (solid) ice sphere of mass equal to snowflake. This argument, of course, requires that the snowflake dimensions remain small compared with the wavelength.

For a given echo-sounder, λ is usually constant and the reflectivity of a region of precipitation is proportional to $\sum_v D^6$. In meteorological radar, it is conventional to write $(1/V) \sum_v D^6 = Z$, where Z is termed the reflectivity factor, and is a function only of the number and size of the particles per unit volume. Note that both the acoustic and the radiowave reflectivities are proportional to Z ; hence, the numerous published measurements of Z obtained with meteorological radars can be used immediately in estimating the acoustic reflectivities of fog and precipitation. In particular,

the empirical relationships between Z and M (the liquid water content per unit volume of air) or between Z and R (the precipitation rate) found using meteorological radars will also be directly applicable to acoustic echo-sounders.

The experimentally determined relationships between Z , M and R show considerable spread, as might be expected from the known variability in size distribution of precipitating particles (Mason, 1957). Nevertheless, experience has shown that the following empirical relationships typically predict Z to within about a factor of two (Atlas, 1964):

$$\text{For rain, } Z = 200R^{1.6}, \quad (7)$$

$$\text{For snow, } Z = 1000R^{1.6}, \quad (8)$$

where Z is in $\text{mm}^6 \text{m}^{-3}$ and R in mm hr^{-1} .

3. The detectability of backscattered signals from hydrometeors

a. The radar equation

For a diffuse target which completely fills the antenna beam, the received echo power available at the receiver input terminals can be shown to be given by

$$P_r = \left[\frac{0.76 \cdot P_t \cdot \gamma_t \cdot \gamma_r \cdot L \cdot c \tau \cdot A_e}{16\pi} \right] \frac{\eta}{R^2} = S \frac{\eta}{R^2}, \quad (9)$$

where the constants and the echo-sounder parameters grouped in the square bracket are denoted by S , and where:

- P_t input electrical power to transmitting transducer
- γ_t efficiency of conversion of electrical power to acoustic power in the transmitting transducer
- γ_r efficiency of conversion of acoustic power to electrical power in the receiving transducer
- L loss factor to allow for any attenuation in the two-way round trip path to the scattering region
- C velocity of sound
- τ pulse length
- η radar reflectivity of diffuse target
- λ acoustic wavelength
- R range of scattering region
- A_e effective collecting area of antenna to a point source on the axis of the antenna beam ($G_0 \lambda^2 / 4\pi$)
- G_0 power gain of antenna, in direction of maximum gain, over isotropic radiator

b. Predicted signal-to-noise ratios

Eq. (9) shows that the echo strengths can be predicted for various hydrometeor conditions, if one assumes appropriate values for each of the parameters shown. These echoes must, however, be detected in the presence of background noise. The critical factor de-

TABLE 1. Assumed parameters of the acoustic echo sounder.

| |
|-------------------------------------------------|
| $P_t = 40 \text{ W}$ |
| $\gamma_t = \gamma_r = 0.2$ |
| $C = 340 \text{ m sec}^{-1}$ |
| $\tau = 10^{-1} \text{ sec}$ |
| $A_e = 1 \text{ m}^2$ |
| $B = 10 \text{ Hz}^*$ |
| $\lambda = 6.8 \text{ cm } (f = 5 \text{ kHz})$ |
| $N = 10 \text{ dB}$ |
| $R = 300 \text{ m}$ |

* This bandwidth is the minimum appropriate bandwidth for a pulse length of 10^{-1} sec, and would be applicable only under conditions of negligible Doppler broadening (for example, cloud and fog particles viewed vertically). Under other conditions, receiving bandwidths of up to perhaps 300 Hz might be required to receive the Doppler-shifted and or Doppler-broadened signal. Such bandwidths would degrade the signal-to-noise ratio by up to 30:1 (i.e., $\leq 15 \text{ dB}$) relative to the values shown in Table 2.

termining the detectability of echoes is the signal-to-noise ratio X , usually expressed in decibels (dB), i.e.,

$$X(\text{dB}) = 10 \log_{10} \frac{\text{signal power}}{\text{system noise power}}.$$

The system noise power is given by $NkTB$, where N is the effective system noise figure, K Boltzmann's constant, T the ambient temperature (assumed to be 293K) and B the receiver bandwidth. Using this fact, we have

$$X = 10 \log_{10} \left[S \left(\frac{\eta}{R^2} \right) \frac{1}{NkTB} \right]. \quad (10)$$

The signal-to-noise ratios have been calculated, using Eq. (10) and appropriate values of echo sounder and hydrometeorological conditions, as indicated in Tables 1 and 2.

From Table 2 we see that clouds and fogs would give detectable echoes only at the higher Z values, specifically, for $Z > 5 \times 10^{-2} \text{ mm}^6 \text{m}^{-3}$. However, the parameters of the sounder have deliberately been chosen conservatively, and it should be practicable to increase the signal-to-noise ratios by from 10–20 dB by such

TABLE 2. Predicted signal-to-noise ratios for various hydrometeor conditions, at a range of 300 m.

| Hydrometeor condition | Precipitation rate (mm hr ⁻¹) | Z (mm ⁶ m ⁻³) | L^* (dB) | Signal/noise (dB) |
|-----------------------|-------------------------------------------|----------------------------------------|------------|-------------------|
| Cloud | — | 10^{-3} to 1 | 10 | -17 to +13 |
| Fog | — | 10^{-3} to 1 | 10 | -7 to +13 |
| Drizzle | 1 | 10^1 | 10 | 23 |
| Light rain | 1 | 2×10^2 | 10 | (36–X) |
| Heavy rain | 25 | 3.3×10^4 | 10 | (58–Y) |
| Light snow | 1 | 10^3 | 20 | 33 |
| Heavy snow | 10 | 4×10^4 | 20 | 49 |

* The round-trip attenuation values L were chosen to be consistent with the acoustic frequency, the echo range, and the precipitation conditions.

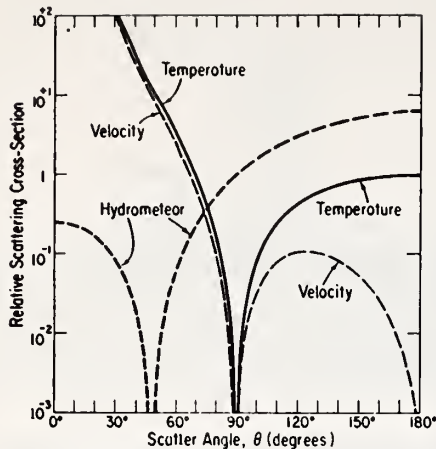


FIG. 3. Angular dependence of the acoustic scattering cross section for small hydrometeors ($D \ll \lambda$), and for the Kolmogorov spectra of velocity and temperature fluctuations.

steps as increased radiated power, increased pulse length, decreased receiver bandwidth, increased transducer efficiency, increased antenna size, etc. In this case, echoes of detectable strength (i.e., $X \geq 0$) should be obtainable to 300 m range in almost all fog and cloud conditions.

Table 2 also shows that the proposed sounder would give strong (~ 23 dB) to very strong (58 dB) echoes under conditions of precipitation. Thus, a light drizzle (1 mm hr^{-1}) would give a signal-to-noise ratio of ~ 23 dB, a light snow ~ 33 dB, and a heavy snow ~ 49 dB. It is, however, important to note that the increase of noise level during light-to-heavy rainfall conditions would reduce the signal-to-noise level by an unknown amount. This reduction would, of course, be a strong function of the design of the antenna (especially its sensitivity to precipitation noise) and would depend upon rainfall conditions (precipitation rate and drop-size distribution). The corresponding signal-to-noise values expected for light and heavy rain should therefore be written as $(36-X)$ dB and $(58-Y)$ dB, where X and Y represent the unknown degradation of the noise levels by the rain. Studies should be made of the magnitude of this degradation, though appropriate shielding of the antenna against direct impact by the raindrops, plus careful control of the antenna side lobes and electronic filtering techniques should give values of X and Y considerably smaller than 36 and 58 dB, respectively, thereby permitting detection of the hydrometer echo.

The above estimates of signal-to-noise ratio are based on a scatter angle of 180° , i.e., co-located transmitter and receiver. For bistatic systems, it is necessary to correct for the $[1 - (\frac{3}{2}) \cos \theta]^2$ change in scattering cross section of the individual scatterers, as well as for the change in the scattering volume, i.e., the change in the

volume of the atmosphere which contributes echoes simultaneously to the receiver.

4. Distinguishing the hydrometeor echoes

Several authors, notably McAllister *et al.* (1969), have shown that acoustic echoes can readily be obtained from the naturally occurring small-scale turbulence and temperature inhomogeneities in the boundary layer of the atmosphere. The echo strengths obtained are comparable to or greater than those computed above for hydrometeors (Little, 1969; Derr and Little, 1970), and the problem of distinguishing the hydrometeor echoes from the atmospheric echo is therefore a significant one.

The above analysis has concerned itself only with the amplitude of the scattered signal. Three other characteristics of the scattered signal may, however, be used to distinguish between the hydrometeor and atmospheric echoes. These are the different scatter-angle dependence, the different wavelength dependence, and the different Doppler shifts, to be expected for scattered signals of the two types.

a. The scatter-angle dependence of acoustic echoes

As shown by several authors (e.g., Monin, 1961), the scattering cross section of atmospheric inhomogeneities is a strong function of scatter angle. In the case of a Kolmogorov spectrum of turbulence in a region containing temperature and velocity fluctuations, the scattering cross section per unit volume is given by

$$\eta(\theta) = 0.30k^3 \cos^2 \theta \left[\frac{C_v^2}{C^2} \cos^2 \frac{\theta}{2} + 0.13 \frac{C_T^2}{T^2} \right] \times \left(\sin \frac{\theta}{2} \right)^{-11/3}, \quad (11)$$

where $k = 2\pi/\lambda$, λ is the acoustic wavelength, and C_v and C_T are the structure constants defining the intensity of the small-scale velocity and temperature fluctuations, respectively. The $\cos^2 \theta$ term preceding the bracket means that the scattering cross section will be zero for $\theta = 90^\circ$, i.e., that no echo will be obtained from either the velocity field or the temperature field if the transmitter beam and receiver beam intercept at 90° . The $\cos^2(\theta/2)$ term inside the bracket multiplies only the velocity fluctuations and results in zero cross section at $\theta = 180^\circ$, i.e., no echoes from the velocity fluctuations will be observed in the direct backscatter direction. The $(\sin \theta/2)^{-11/3}$ multiplies both the velocity and the temperature fluctuations, and shows that the scattered power is, in fact, mostly concentrated into the forward hemisphere.

As discussed earlier, the scatter of sound by small hydrometeors shows a null at $\theta \approx 48.2^\circ$, and most of the scattered power is scattered into the backward hemisphere. The scatter-angle dependences for hydro-

meteors, velocity fluctuations and temperature fluctuations are shown in Fig. 3. It is important to note that measurements of radar reflectivity η at three sufficiently widely-spaced scatter angles will permit the separate identification of each component of the total reflectivity, since we obtain three equations with only three unknowns. A suitable selection of scatter angles would be $\theta = 90^\circ$ (for which $\eta_v = \eta_T = 0$, i.e., the scatter cross sections due to velocity fluctuations and temperature fluctuations are both equal to zero); $\theta = 180^\circ$ (for which $\eta_v = 0$) and $\theta = 48.2^\circ$ (for which η_H , the scattering cross section per unit volume due to hydrometeors, is equal to zero). Thus, the echo power for $\theta = 90^\circ$ is given by

$$P_{90} = A(\eta_{T90} + \eta_{v90} + \eta_{H90}) = A\eta_{H90} = \frac{4A\eta_{H180}}{25}.$$

For $\theta = 180^\circ$, we may write

$$P_{180} = B(\eta_{T180} + \eta_{v180} + \eta_{H180}) = B(\eta_{T180} + \eta_{H180}),$$

$$= B\left(\eta_{T180} + \frac{25P_{90}}{4A}\right);$$

therefore,

$$\eta_{T180} = \frac{P_{180}}{B} - \frac{25P_{90}}{4A}.$$

For $\theta = 48.2^\circ$, we may write

$$P_{48.2} = C(\eta_{T48.2} + \eta_{v48.2} + \eta_{H48.2}) = C(\eta_{T48.2} + \eta_{v48.2}),$$

$$= C(\gamma\eta_{T180} + \eta_{v48.2});$$

therefore,

$$\eta_{v48.2} = \frac{P_{48.2}}{C} - \gamma\left(\frac{P_{180}}{B} - \frac{25P_{90}}{4A}\right).$$

In the above equations, A , B and C are constants determined from the known parameters of the sounding system, and

$$\gamma = \frac{\left[\frac{\cos^2\theta}{\left(\sin\frac{\theta}{2}\right)^{11/3}}\right]_{\theta=48.2^\circ}}{\left[\frac{\cos^2\theta}{\left(\sin\frac{\theta}{2}\right)^{11/3}}\right]_{\theta=180^\circ}} = 11.9.$$

In using this approach, it should be recognized that practical systems will use antenna beamwidths up to several degrees wide, and therefore will not attain the complete 90° , 48.2° and 180° nulls discussed above. However, it can be shown that more than 30 dB of suppression of the unwanted component will be obtained, provided that beamwidths of less than 4° between half-power points are used. This implies the use of antenna apertures of the order 15λ in diameter, or about 1 m for a typical hydrometeor echo-sounding frequency.

b. Multi-wavelength method of identifying hydrometeor echoes

As shown by Eqs. (4) and (11), a very strong difference exists between the wavelength dependence of the scattering cross sections of hydrometeors and a Kolmogorov spectrum of velocity and temperature irregularities. The hydrometeors would be expected to show the standard Rayleigh λ^{-4} dependence and a Kolmogorov spectrum of irregularities a λ^{-1} dependence.

This difference could therefore be used to differentiate between the hydrometeor and atmospheric components of the echoes. (This method has been used successfully in radar meteorology, where the same wavelength dependences occur.) Thus, neglecting changes in absorption, atmospheric echoes should increase in strength by 1 dB octave increase in frequency; for hydrometeors, the change would be +12 dB, assuming that the hydrometeors are still small compared with the wavelength.

One difficulty with this method is that any frequency-dependent attenuation of the acoustic waves by the intervening atmosphere would modify the observed frequency dependence of the echoes. The magnitude of this effect would, of course, be dependent upon range, and it would therefore be desirable to measure the frequency dependence as a function of range, and then to determine the true frequency dependence by extrapolating to zero range.

c. The Doppler method of identifying hydrometeor echoes

In the general bistatic case, acoustic echoes from either hydrometeors or irregularities in the acoustic refractive index of the atmosphere will show a Doppler shift in the observed frequency of the echo given by

$$\Delta f = \left(\frac{V_T}{\lambda} + \frac{V_R}{\lambda}\right),$$

where V_T is the component of the velocity of the scatterers in the direction of the transmitter and V_R the component of this velocity toward the receiver. In the special case of collocated transmitter and receiver this reduces to

$$\Delta f = \frac{2V_T}{\lambda}.$$

Since the vertical velocities of snowflakes and rain are of the order 1 and 5 m sec⁻¹, respectively, a vertically directed 5-kHz ($\lambda = 6.8$ cm) acoustic sounder would see precipitating hydrometeor echoes Doppler-shifted by about 30 and 150 Hz, respectively, relative to the atmospheric echoes. These Doppler shifts, though somewhat masked by the 100-Hz bandwidth of the millisecond transmitted pulses, should be readily detected, and could be used to confirm that echoes were being detected from hydrometeors.

Increased frequency (and therefore velocity) resolution could be obtained by using a continuous wave bistatic system, preferably with $\theta = 90^\circ$, since this would serve to suppress the non-hydrometeor echoes. Assuming that the two beams intersect above the mid-point between the transmitter and the receiver, only the vertical component of velocity will be measured. Such a continuous wave system would have several important advantages, including 1) suppression of unwanted atmospheric echoes; 2) continuous, rather than pulse, measurements of echo spectrum; 3) greatly increased Doppler resolution, because of the reduced transmitted bandwidth; and 4) reduced noise level, because of reduced receiver bandwidth.

Such an experimental configuration would, of course, require careful attention to the side lobe structure of the antennas, in order to limit the strength of the signal leaking direct from the transmitting antenna into the receiving antenna. In addition, this method would not be applicable to fogs or clouds in which the terminal velocities of the particles are too small to be resolved by Doppler techniques.

5. On the possibility of acoustic echoes from the turbulent wakes created by precipitating hydrometeors

A precipitating hydrometeor will produce small-scale local fluctuations in the velocity, temperature and humidity of the air in its wake. Since the phase velocity of sound is sensitive to each of these parameters (see, for example, Little, 1969), the localized eddies in the wake will serve as refractive index fluctuations for acoustic waves. It is therefore possible that, in addition to the direct acoustic body echo, echoes will be obtained from the turbulent wakes of precipitating hydrometeors.

Once terminal velocity is reached, energy balance requires that the loss of gravitational energy by the falling hydrometeor be equal to the gain of kinetic energy by the atmosphere. (Other energy exchange mechanisms, such as by the radiation of acoustic waves, are believed to be negligible.) In the absence of other sources of turbulence, the turbulent kinetic energy density of the atmosphere will increase with time until the rate of loss of turbulent kinetic energy by viscous dissipation is equal to the rate of input of kinetic energy by the precipitation. Once this equilibrium is reached, the rate of gain of turbulent kinetic energy E per unit mass of air and the energy dissipation rate ϵ per unit mass are related by

$$\frac{dE}{dt} = \epsilon = \frac{Qg}{\rho},$$

where Q is the precipitation rate in grams per unit area per unit time, g the acceleration due to gravity, and ρ the density of air.

Substituting $\rho = 1.2 \times 10^{-3} \text{ gm cm}^{-3}$, $g = 981 \text{ cm sec}^{-2}$, $Q = 2.8 \times 10^{-4} \text{ gm cm}^{-2} \text{ sec}^{-1}$ (equivalent to a rainfall rate of 10 mm hr^{-1}), we have

$$\epsilon = 230 \text{ ergs gm}^{-1} \text{ sec}^{-1}.$$

This dissipation rate is to be compared with a median value of approximately $100 \text{ ergs gm}^{-1} \text{ sec}^{-1}$ reported for 50 daytime measurements in the lowest 1 km of the atmosphere by Taylor (in press), whose results also indicate that the above energy dissipation rate due to a 10 mm hr^{-1} precipitation rate exceeds all but about 10% of his values. Thus, we see that the energy dissipation rates are quite large, and conceivably might be associated with significant acoustic refractive index fluctuations.

In order that these refractive index fluctuations be significant in the context of acoustic echo sounding, it is necessary, however, that they have appreciable intensity at the appropriate spatial size. An acoustic echo sounder "interrogates" the atmosphere at a specific spatial size $L = \lambda/2 \sin(\theta/2)$, where λ is the operating wavelength and θ the scatter angle. For $\theta > 30^\circ$ (true for all monostatic systems and almost all bistatic systems) $\lambda/2 < L < 2\lambda$, and we see that L is of the order λ . Initially, the energy input by the drops takes place in the form of eddies up to about the drop diameter in size. Although the turbulent wake grows in size with distance behind the drop, calculations based on the theory of axisymmetric wakes shows that the kinetic energy of the λ -size eddies is, in fact, very small, because most of the energy is dissipated by viscosity before the wake has time to grow. Calculations, to be published in a planned NOAA Technical Report, show that the intensity of the 5-cm scale velocity fluctuations produced by a medium rainfall rate ($R = 10 \text{ mm hr}^{-1}$) is some two orders of magnitude smaller than the median values for the boundary layer reported by Taylor. Similarly, the temperature and humidity fluctuations produced by heat conduction or evaporation from the drop can be shown to be too small to be detected in the real atmosphere, though possibly detectable in still air.

One further possibility should be considered. The turbulent kinetic energy introduced into the atmosphere by precipitation will act upon any pre-existing sharp gradients in wind, temperature or humidity in such a way as to reduce these gradients, and hence to modify the internal structure of the atmosphere as seen by the acoustic echo sounder. It is therefore suggested that acoustic echo-sounding records be examined for such effects.

6. Summary and conclusions

Computations have been made of the expected intensity of acoustic echoes under various hydrometeor conditions. Using a standard low power echo-sounding system, clouds and fogs would give detectable echoes

at 300 m range, at least for the higher Z values. Other hydrometeor conditions ranging from drizzle to heavy rain or snow would result in echoes ranging from about 23 to about 58 dB above noise. Signal-to-noise estimates for other system parameters can readily be made using Eqs. (5)–(10).

In any experimental testing of the above predictions, the problem of differentiating between echoes of hydrometeor and (gaseous) atmospheric origin will arise. It is shown that at least three different techniques, based respectively on differences in the scatter-angle dependence, the wavelength dependence, and the Doppler spectra of the echoes, may be used to identify the hydrometeor component.

The optimum experimental configuration for the study of hydrometeor echoes would appear to be a multi-wavelength, bistatic, continuous wave system with a scatter angle of 90° , thereby minimizing the atmospheric echoes. Such a configuration, with the two antenna beams intersecting above the midpoint between the transmitter and the receiver, would give the distribution of vertical fall velocities of the hydrometeors, weighted by D^6 , where D is the diameter of the drops. Since for rain the terminal velocities are known as a function of drop diameter, the measurement of Doppler spectrum could be used to estimate the distribution of drops in size. Note that the Doppler shift of the atmospheric echo could be used to measure the vertical velocity of the air through which the precipitation is falling.

Acoustic techniques do not appear to have significant advantages over existing radar techniques for the study of hydrometeors, except perhaps in range resolution. The chief value of this analysis probably lies in the identification of the main features of acoustic echoes from hydrometeors. Acoustic sensing of hydrometeors

is likely to be limited to a range of several hundred meters, because of the enhanced atmospheric absorption which occurs at the high frequencies required to achieve reasonably large hydrometeor scattering cross sections.

Acknowledgments. This paper was prepared while on temporary assignment with the Division of Atmospheric Physics, CSIRO, Aspendale, Victoria, Australia. I am indebted to its Chief, Dr. C. H. B. Priestley, and to the staff of the Division, for the many courtesies extended to me during my stay.

REFERENCES

- Atlas, D., 1964: Advances in radar meteorology. *Advances in Geophysics*, Vol. 10, New York, Academic Press, 317–478.
- Cole, J. E., and P. A. Dobbins, 1970: Propagation of sound through atmospheric fog. *J. Atmos. Sci.*, **27**, 426–434.
- , and —, 1971: Measurements of the attenuation of sound by a warm air fog. *J. Atmos. Sci.*, **28**, 202–209.
- Derr, V. E., and C. G. Little, 1970: A comparison of remote sensing of the clear atmosphere by optical, radio and acoustic radar techniques. *Appl. Opt.*, **9**, 1976–1991.
- Evans, J. V., 1969: Theory and practice of ionosphere study by Thomson scatter radar. *Proc. IEEE*, **57**, 496–530.
- Lamb, H., 1932: *Hydrodynamics*, 6th ed. Cambridge University Press, 738 pp.
- Little, C. G., 1969: Acoustic methods for the remote probing of the lower atmosphere. *Proc. IEEE*, **57**, 571–578.
- McAllister, L. G., J. R. Pollard, A. R. Mahoney and P. J. R. Shaw, 1969: Acoustic sounding—A new approach to the study of atmospheric structure. *Proc. IEEE*, **57**, 579–587.
- Monin, A. S., 1961: Characteristics of the scattering of sound in a turbulent atmosphere. *Akust. Zh.*, **7**, 457–461.
- Mason, B. J., 1957: *The Physics of Clouds*. Oxford, Clarendon Press, 481 pp.
- Rayleigh, J. W. S., 1872: *The Theory of Sound*, 2nd ed. Reprinted by Dover Publications Inc., New York, 1945.
- Vigoureux, P., and J. B. Hersey, 1962: *The Sea*, Vol. 1. New York, Wiley, 476–497.
- Westphal, J. A., 1965: *In situ* acoustic attenuation measurements in glacial ice. *J. Geophys. Res.*, **70**, 1849–1853.

Reprinted with permission from the IEEE Transactions on Antennas and Propagation AP-20, No. 1, 2-10, January 1972.

First-Order Theory and Analysis of MF/HF/VHF Scatter from the Sea

DONALD E. BARRICK, MEMBER, IEEE

Abstract—Scatter from the sea near grazing from MF through VHF is analyzed in this paper. Results based on the compensation theorem show that the dependence upon the grazing angles, as well as upon frequency, range, and the effective surface impedance, can be removed for vertical polarization as the familiar "Norton attenuation factors." Time variation of the surface is included, and results are derived for both the average received power and its spectral density. The first-order dispersion relationship for gravity waves is used to show that the received spectrum from a patch of sea consists of two discrete Doppler shifts above and below the carrier, predictable from simple Bragg diffraction considerations. Using the Phillips wind-wave model as an upper limit for wave heights, estimates for σ^0 (radar cross section per unit area) of -17 dB are obtained near grazing. Both the magnitude of $\sigma_{\text{v},0}^0$ predicted from theory and the nature of the received spectrum are compared with measurements, and the agreement supports the theory on both counts. Finally, the use of MF/HF radars for measuring sea state is suggested and discussed.

I. INTRODUCTION

SEA ECHO at frequencies below VHF has been observed by radars since World War II. Crombie [1] in 1955 appears to have been the first to correctly deduce the physical mechanism producing sea scatter. Based upon HF experimental observations of the backscatter Doppler spectrum, he noted that the discrete frequency shifts of the sea echo above and below the carrier corresponded

uniquely with the shifts that would be produced by ocean waves moving toward and away from the radar having lengths precisely one half the radio wavelength. Hence the mechanism was seen to be "Bragg scatter," the same phenomenon responsible for scatter of X-rays in crystals and light rays from diffraction gratings and holograms.

Quantitative theoretical analyses of the scatter problem lagged these experimental deductions by several years. Peake [2] appears to have been the first to reduce the classic boundary perturbation theory of Rice [3] to σ^0 , the normalized scattering cross section per unit area for a slightly rough surface. Barrick and Peake [4] noted that this result, when interpreted, shows that scatter is produced via the Bragg mechanism, in agreement with Crombie's deductions. No attempt was made at that time to apply the theory to the sea, which was a unique wave height spectrum¹ and spatial-temporal wavenumber dispersion relationship. Thus in this paper we include the

¹ Guinard and Daley [5] have employed the "slightly rough" model derived from perturbation analysis, along with a Phillips wave height spectrum, to explain the diffuse component in microwave scatter from the sea. Since the ocean surface is "composite" at those frequencies and thus more difficult to analyze, a rigorous mathematical justification of this result is not possible. Their empirical comparisons, however, leave little doubt that this simple model is reasonably valid even at microwave frequencies, so long as one is not too close to the specular direction or to grazing. Those results along with the spectral measurements of Wright [6] and Bass *et al.* [7], show that the Bragg effect also produces scatter above VHF; this paper concentrates on analysis and comparisons below VHF, where more rigorous mathematical justification and interpretation is possible.

Manuscript received February 3, 1971; revised July 14, 1971.

The author is with Columbus Laboratories, Battelle Memorial Institute, Columbus, Ohio 43201.

temporal motion of the sea surface and derive a result for the average received signal spectrum, as well as σ^0 . Furthermore, we analyze in detail the region near-grazing incidence for vertical polarization and show how the behavior of backscatter varies with grazing angle for frequencies below 100 MHz. Using the Phillips ocean wave height spectrum in the model, the predicted results are compared with HF measurements, both with regard to the signal spectrum and σ^0 . Limitations of the first-order theory are pointed out. Finally, the exciting possibility of using MF/HF radars to measure sea state is discussed in light of the theory.

Many previous theoretical analyses of rough surface scatter were based upon the Kirchhoff (or physical optics) integral approach (see Beckmann and Spizzichino [8], or Ruck *et al.* [9]). While the physical optics approach leads to Bragg scatter also (e.g., Parkins [10] derives the received spectrum of acoustic signals scattered from the sea surface with this approach), polarization dependence and near-grazing behavior is lost with that technique. Measurements, however, show that σ_{ee}^0 for near-grazing backscatter is considerably greater than $\sigma_{\lambda\lambda}^0$, which is in agreement with results derived from the perturbation theory. In addition, the radius of curvature of the surface need not be much greater than wavelength in the perturbation theory, as it must with physical optics.

The Rice boundary perturbation approach employs the following restrictions: 1) the height of the surface must be small in terms of radio wavelength, 2) surface slopes must be small, and 3) the impedance of the surface medium must be small in terms of the free-space wave impedance. These conditions are all satisfied by the sea below mid-VHF; the upper limit on frequency in terms of sea state will be examined in Section VI.

II. RERADIATION TO A POINT ABOVE AN IMPERFECT SURFACE

In this section we analyze the problem of scatter from the imperfectly conducting rough sea in a manner different from conventional treatments [2], [4]. We are not concerned in this section with the interaction and scatter mechanism; that will be treated in the next section. Rather, we consider separately an elemental patch of sea dS' as shown in Fig. 1. Energy is incident upon this patch from an arbitrary angle and is reradiated (or scattered) from the patch due to the roughness. The size of the patch is to be small with respect to the distance R_0 to the scattering point, but large with respect to λ the radio wavelength. Thus if the patch were reradiating in the absence of the surrounding imperfect surface, the field at the observation point would diverge as $1/R_0$. The same would be true if the surrounding surface were a perfectly conducting smooth plane, with an additional factor of 2 to account for the image.

In including the effects of imperfect conductivity and roughness of the sea surrounding dS' , we assume 1) that the mean surface near dS' is planar, and 2) that an effective impedance $\bar{\Delta}$ can be assigned to the surface to account

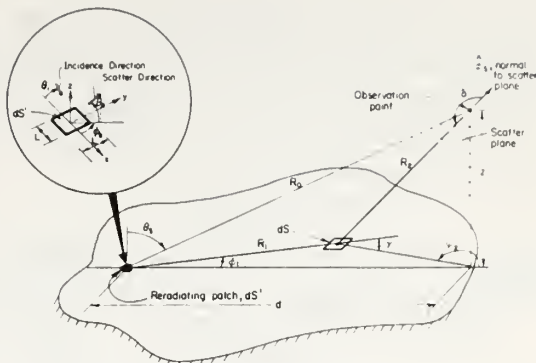


Fig. 1. Geometry for reradiation (scatter) from patch dS' used with compensation theorem.

for both its finite conductivity and roughness. The concept of normalized surface impedance was popularized by Wait [11]; this quantity is normalized with respect to the wave impedance of free space $(\mu_0/\epsilon_0)^{1/2}$ and is a function of the radiation angle θ_s , as well as the surface parameters. We intend to employ the “compensation theorem” attributed to Monteath [12] and applied by King [13] to the problem of radiation from a dipole above an imperfect half space. In fact, the analysis here parallels that of King; the scattering behavior of the reradiating patch can in reality be modeled by a collection dipoles.

We are interested here only in the vertically polarized scattered far-field component; this can be easiest obtained by employing H_φ the azimuthal magnetic field. King shows in [13, eqs. (6) and (7)] that an integral equation in H_φ can be obtained from the compensation theorem as follows:

$$H_{\varphi s'} = H_{\varphi s} + \frac{ik_0}{2\pi} \int_s \bar{\Delta} H_{\varphi s'} \left(\frac{\exp(ik_0 R_2)}{R_2} \right) \sin \delta \cos \gamma dS \quad (1)$$

where the indicated angles are shown in Fig. 1. Here H_0^* is called the "unperturbed" H field at the observation point, and $H_0^{*'} is the "perturbed" H field. The integration takes place at dS , a distance R_1 from the reradiating point; at this point, the effective surface impedance is described by $\bar{\Delta}$. The time dependence $\exp(-i\omega t)$ is assumed here.$

The perturbed field here denotes the unknown quantity we are seeking, whose nature depends upon the surface over which it propagates. The unperturbed solution H_0^* is presumed known and can be selected so as to simplify solution of the integral equation in H_0^* . Following King, we select for H_0^* the far-zone field reradiated from the surface patch dS' when the remainder of the surface is smooth and perfectly conducting (i.e., $\bar{\Delta} = 0$); for now we write it as

$$H_{\varphi^*} = \frac{ik_0 L^2 \exp(ik_0 R_0)}{2\pi R_0} G_{\varphi^*}^c \quad (2)$$

where G_φ is a quantity to be determined in the next section. The preceding equation places in evidence the $1/R_0$ dependence of the field above the perfectly conducting smooth plane.

Following King [13], we define the perturbed field as equal to the unperturbed field times an unknown slowly varying attenuation function, i.e.,

$$H_\varphi' = H_\varphi F(d, z, \bar{\Delta}).$$

Then (1) can be rewritten as an integral equation in F , obtaining

$$F(d, z, \bar{\Delta}) = 1 + \frac{ik_0 R_0 \exp(-ik_0 R_0)}{2\pi G_\varphi(0)} \cdot \int_{\bar{\Delta}} \bar{\Delta} G_\varphi(\varphi_1) \left(\frac{\exp[ik_0(R_1 + R_2)]}{R_1 R_2} \right) \cdot F(R_1, 0, \bar{\Delta}) \cdot \sin \delta \cos \gamma dS \quad (3)$$

where $G_\varphi(0)$ is G_φ evaluated at the observation point (θ_s, φ_s) , while $G_\varphi(\varphi_1)$ is G_φ evaluated at the integration point $(\pi/2, \varphi_s + \varphi_1)$.

We now note for highly conducting surface where $|\bar{\Delta}| \ll 1$, that F is close to unity and the preceding integral is nearly zero. It is only when the observation point is near the surface (i.e., $\pi/2 - \theta_s \simeq z/d \ll 1$) that the incident and reflected waves cancel, and only the surface wave remains. Therefore, the integral term in (3) is important for θ_s very near $\pi/2$, typically within 1° of grazing for seawater at HF. In this region near the Brewster angle $\bar{\Delta}$ and $G_\varphi(\varphi_1)$ appearing in the integrand are nearly constant over the important region near the baseline where $\varphi_1 \simeq 0$ and $\theta_s \simeq \pi/2$. By the same reasoning, $\sin \delta \simeq 1$, and $\cos \gamma \simeq 1$, so that the integral equation simplifies to

$$F(d, z, \bar{\Delta}) \simeq 1 + \frac{ik_0 R_0 \exp(-ik_0 R_0)}{2\pi} \bar{\Delta} \cdot \int F(R_1, 0, \bar{\Delta}) \left(\frac{\exp[ik_0(R_1 + R_2)]}{R_1 R_2} \right) dS. \quad (4)$$

The solution to (4) is straightforward and is performed by King [13], [14]; the details will not be repeated here. He employs an elliptic coordinate system as a basis for the surface integral; he performs a stationary phase integration in the φ_1 direction, and the result reduces to an inhomogeneous Volterra integral equation of the second kind. This is then solved by Laplace transform techniques, and $F(d, z, \bar{\Delta})$ is shown to be identically the "Norton attenuation factor" of ground wave theory. The only approximation (other than the far-zone assumption) on which solution of (1) is based is that [13] $|\bar{\Delta}| \ll 1$, where $\bar{\Delta}_r$ is the real part of $\bar{\Delta}$.

Thus in this section we have shown that a patch of sea reradiating (or scattering) vertically polarized electromagnetic energy over an imperfect surface does so in a manner identical to a vertical dipole located on the same plane. Within the restrictions of the analysis, therefore,

one merely solves the problem of scatter of vertically polarized waves by a perfectly conducting sea and multiplies by F , the Norton attenuation factor, to account for propagation near grazing from the patch dS' to the observation point. A similar factor must be used to account for propagation from the transmitter to the scattering patch if this path is near grazing also.

III. SCATTER FROM A MOVING SLIGHTLY ROUGH SURFACE

In the preceding section it was shown possible to express the scattered field from a patch of sea in terms of the Norton attenuation factor F times the unperturbed scattered field. This unperturbed field is to be determined in this section. It is the field scattered from the patch with the sea treated as a perfect conducting surface; the effect of finite conductivity is already accounted for in F . Below VHF the sea is "slightly rough," satisfying the restrictions mentioned in the Introduction for applicability of the boundary perturbation approach.

The first-order solution for scatter from a *stationary* random perfectly conducting surface using this approach is well-known [2], [4], [9]. We intend to extend this analysis to the case of a *moving* perfectly conducting surface, so that the temporal spectrum of the scattered signal can be obtained. We concentrate on only the vertical polarization states, since near-grazing propagation over the highly conducting sea at these frequencies is much larger for vertical than for horizontal. However, we will provide answers for the other linear polarization combinations also.

The inclusion of time as an independent variable in the description of the random surface height ζ is readily accomplished by a Fourier series expansion over time as well as space:

$$\zeta(x, y, t) = \sum_{m, n, l=-\infty}^{\infty} P(m, n, l) \exp\{ia(mx + ny) - i\omega t\} \quad (5)$$

where $a = 2\pi/L$ and $\omega = 2\pi/T$; L and T being defined as the spatial (both x and y) and temporal period of the surface. $P(m, n, l)$ is the coefficient of the m, n, l th Fourier component, with P being zero for $m = n = 0$ (i.e., the coordinate system is chosen so that the x - y plane is the mean surface). The minus sign before the time argument places in evidence the expected traveling nature of ocean waves, i.e., a wave with $+am$ and $+wl$ wavenumbers in the $+x$ direction.

Following Rice [3] we define an average spatial-temporal spectrum $W(p, q, \omega)$ of the surface height in terms of the Fourier coefficients as

$$W(p, q, \omega) = \frac{1}{\pi^3} \iiint_{-\infty}^{\infty} \langle \zeta(x_1, y_1, t_1) \zeta(x_2, y_2, t_2) \rangle \cdot \exp(ip\tau_x + iq\tau_y - i\omega\tau) d\tau_x d\tau_y d\tau \\ = \frac{L^2 T}{\pi^3} \langle P(m, n, l) P(-m, -n, -l) \rangle \quad (6)$$

where $\langle P(m_1, n_1, l_1) P(m_2, n_2, l_2) \rangle$ is zero when $m_2 \neq -m_1$, $n_2 \neq -n_1$, and $l_2 \neq -l_1$ because the Fourier coefficients are uncorrelated. Also, $p = am$, $q = an$, $\omega = wl$, $\tau_x = x_2 - x_1$, $\tau_y = y_2 - y_1$, and $\tau = t_2 - t_1$ in (6). The angular braces $\langle \cdot \rangle$ denote a statistical ensemble average. Also, $\langle P(m, n, l) \rangle = 0$, for all m, n, l .

The total fields above the surface (see Fig. 1 inset for scatter geometry) are represented by plane-wave (eigenfunction) expansions of the same form as (5)

$$E_x = \frac{b(\nu, 0)}{k_0} [E(\nu, 0, 0; z) - E(-\nu, 0, 0; z)] + \sum_{m, n, l=-\infty}^{\infty} A_{mn} E(m + \nu, n, l; z) \quad (7a)$$

$$E_y = \sum_{m, n, l=-\infty}^{\infty} B_{mn} E(m + \nu, n, l; z) \quad (7b)$$

$$E_z = \frac{a\nu}{k_0} [E(\nu, 0, 0; z) + E(-\nu, 0, 0; z)] + \sum_{m, n, l=-\infty}^{\infty} C_{mn} E(m + \nu, n, l; z) \quad (7c)$$

where

$$E(m + \nu, n, l, z) = 2E_0 \exp \{ ia(m + \nu)x + iany + ib(m + \nu, n)z - i(wl + \omega_0)t \}$$

and

$$b(m + \nu, n) = [k_0^2 - a^2(m + \nu)^2 - a^2n^2]^{1/2}.$$

Here $\nu = k_0 \sin \theta_i / a$, and the two terms in square brackets in (7a) and (7c) are the incident and reflected plane waves from the perfectly conducting surface in the absence of roughness. The incident electric field strength E_0 is normalized such that the total vertical component at the surface for incident propagation near grazing is $2E_0$.

The solution for the unknown scattered field coefficients A_{mn} , etc., is straightforward. In fact, these coefficients are identical to the first-order coefficients A_{mn} , etc., derived by Rice in [3, eq. (4.2)] with three notation differences: 1) his $m - \nu$ is our m ; 2) his i is our $-i$ because of a difference in sign in our time conventions; 3) our A_{mn} , etc., are directly proportional to $P(m, n, l)$, whereas his are proportional to $P(m, n)$; the factors of proportionality however, are the same.

It is now necessary to relate the modal fields scattered by an infinite periodic random surface to the field scattered by a finite patch of area dS' of such a surface. This is again straightforward and can follow the geometrical arguments of Peake [2] and Barrick and Peake [15] or a Kirchhoff-type transformation of Barrick [16]; the reader is referred to these treatments. Basically, the result shows that the field strength falls off as $1/R_0$, as it should, and relates the modal field wavenumbers $a(m - \nu)$, an , and $b(m + \nu, n)$ to the scattered field direction cosines $\sin \theta_s \cos \varphi_s$, $\sin \theta_s \sin \varphi_s$, and $\cos \theta_s$.

The average scattered power correlation function at two different times is then computed, i.e.,

$$\langle E_s^*(R_0, t_1) E_s^{**}(R_0, t_2) \rangle \equiv R^*(\tau)$$

where $\tau = t_2 - t_1$. The Fourier transform of this then gives the average scattered signal spectrum in terms of $W(p, q, \omega)$ as defined in (6). Details can be found in Barrick [16].

IV. AVERAGE SCATTER CROSS SECTIONS AND THE RADAR RANGE EQUATION

The average scattered signal power density spectrum can now be converted to $\sigma_{vs}(\omega)$ the average scatter cross section per unit area per rad/s bandwidth; its integral is the familiar σ_{vs}^0 , i.e., $\sigma^0 = 1/2 \int_{-\infty}^{\infty} \sigma(\omega) d\omega$, which is

$$\left. \sigma_{vs}(\omega) \right\} = 4\pi k_0 (\sin \theta_i \sin \theta_s - \cos \varphi_s)^2 \times \begin{cases} W[k_0(\sin \theta_s \cos \varphi_s - \sin \theta_i), \\ k_0 \sin \theta_s \sin \varphi_s, \omega - \omega_0] \end{cases} \quad (8a)$$

$$\times \begin{cases} W[k_0(\sin \theta_s \cos \varphi_s - \sin \theta_i), \\ k_0 \sin \theta_s \sin \varphi_s] \end{cases} \quad (8b)$$

where the spatial spectrum $W[p, q]$ is obtained from $W[p, q, \omega]$ by integration over ω and division by 2. Both spectra have the wavenumbers p, q , replaced by $k_0(\sin \theta_s \cos \varphi_s - \sin \theta_i)$, $k_0 \sin \theta_s \sin \varphi_s$. The latter are precisely the wavenumbers required of a diffraction grating which is to scatter a wave incident from θ_i into a direction θ_s, φ_s . Hence the theory shows that the ocean surface produces scatter by the simple Bragg mechanism, which confirms the experimental deductions of Crombie [1].

Although they are not of interest in this paper, the other three cross section spectra for a perfectly conducting surface $\sigma_{vh}(\omega)$, $\sigma_{hv}(\omega)$, and $\sigma_{hh}(\omega)$ are obtained by replacing the factor $(\sin \theta_i \sin \theta_s - \cos \varphi_s)^2$ in (8a) by $(\cos \theta_i \sin \varphi_s)^2$, $(\cos \theta_s \sin \varphi_s)^2$, and $(\cos \theta_i \cos \theta_s \cos \varphi_s)^2$, respectively. The same substitution is made in (8b) also. Thus the dependence upon the nature of the roughness is the same for any polarization state; it is contained in the surface height spatial-temporal spectrum.

The average power energy density and power received in a bistatic radar system, $dP_R(\omega)$ and dP_R , from a patch of sea dS' located at distances R_T and R_R from the transmitter and receiver can now be written

$$\left. \frac{dP_R(\omega)}{dP_R} \right\} = \frac{P_T G_T^0 G_R^0 \lambda^2}{(4\pi)^3 R_T^2 R_R^2} F_T^2 F_R^2 dS' \times \begin{cases} \sigma_{vs}(\omega), & \text{W/rad/s} \quad (9a) \\ \sigma_{vs}^0, & \text{W} \quad (9b) \end{cases}$$

where P_T is the average transmitted power and G_T^0 and G_R^0 are the transmitting and receiving antenna gains (defined with respect to free space) in the direction of the patch. The quantities F_T^2 and F_R^2 are the Norton attenuation factors. The use of F_R^2 was justified in Section II to account for the imperfect nature of the surface medium

in the analysis of propagation from the patch dS' . It of course has significance here only for scattered vertical polarization, and is a function of range R_R to the receiver. A similar and even more obvious use of the compensation theorem shows that F_T^2 accounts for propagation of a vertically polarized field from the transmitter to the patch.

The Norton attenuation factor (e.g., F_R) appearing in the preceding equation is a function of the effective surface impedance $\bar{\Delta}$, of range R_R , and finally of the height of the receiver above the surface. Hence it contains the "dependence upon grazing angle" produced by the finite conductivity of the surface medium. It is normalized, and approaches unity as $R_R \rightarrow 0$ and for sufficiently small $\bar{\Delta}$. In this limit, one has in (9) the conventional radar range equation above a perfectly conducting flat plane. While F_R was defined for a "flat" surface, the definition can be extended to a "spherical" surface, in which case F_R is found, for example, from a residue series [11] when the observation point is distant and below the horizon.

One must be cautious in the definition of σ^0 . Had one defined σ^0 in terms of $2E_0$ the total near-grazing field, rather than the *incident* field, the factor of 4 appearing in (8) would be missing; this alternate definition [8] might be considered more appropriate for ground-wave propagation. On the other hand, others include factors of 4 in the antenna gains by measuring their efficiencies in the presence of the highly conducting ground rather than in terms of their equivalent gains in free space. The reasoning behind the definition appearing in (8) and (9) is that propagation effects (i.e., the factors of 4, as well as F_R and F_T) due to the medium are clearly separated from the parameters describing the transmitter (G_R^0), the scatterer (σ^0), and the receiver (G_R^0). Because of widespread differences, however, reported values of σ^0 can vary by as much as 16 merely due to the definition employed.

V. FIRST-ORDER OCEAN WAVES AND THE PHILLIPS MODEL

It has been shown that Bragg scatter from the larger gravity waves (longer than 1 m) produces the return at HF. Such gravity waves have a unique first-order dispersion relationship. The latter makes it possible to relate the spatial-temporal height spectrum $W(p, q, \omega)$ to the simpler spatial spectrum $W(p, q)$. Stated simply, deep-water gravity waves of length L travel at a given phase velocity $v_w = (gL/2\pi)^{1/2}$, where $g \approx 9.81 \text{ m/s}^2$ is the acceleration of gravity. This first-order velocity expression provides the dispersion relationship between the temporal and spatial wavenumbers of gravity waves:

$$\omega_g = +[g(p^2 + q^2)^{1/2}]^{1/2} = +[g(a^2 m^2 + a^2 n^2)^{1/2}]^{1/2}. \quad (10)$$

Thus the more general (5) for the height of a moving random surface reduces to the following in the case of ocean waves moving into the $+x$ half space:

$$\zeta(x, y, t) = \sum_{m, n=-\infty}^{\infty} P_+(m, n) \cdot \exp[iamx + iany - i \operatorname{sgn}(m) \omega_g t] \quad (11)$$

where $\operatorname{sgn}(m)$ is ± 1 , for $m \pm$. A similar expression holds for ocean waves moving into the $-x$ half space, with P_+ replaced by P_- and a plus sign in front of the last term of the exponential. Thus two sets of coefficients P_+ and P_- are called for, depending upon the strengths of the various Fourier components moving in the $+x/-x$ directions. Using (6) we can determine $W(p, q, \omega)$ from (11) by multiplying $\zeta(x_1, y_1, t_1)$ by $\zeta^*(x_2, y_2, t_2)$, averaging, and taking the Fourier transform. We then obtain

$$W(p, q, \omega) = 2W_+(p, q) \delta(\omega + \operatorname{sgn}(p) \omega_g) + 2W_-(p, q) \delta(\omega - \operatorname{sgn}(p) \omega_g) \quad (12)$$

where $W_{\pm}(p, q) = \langle |P_{\pm}(m, n)|^2 \rangle L^2 / \pi^2$ and $\delta(x)$ is the impulse function of argument x .

Equation (12) simply means that for a given set of spatial wavenumbers p, q , only one temporal wavenumber ω_g is possible, as given by (10). When (12) is substituted into (8a), we see that the signal scattered from an infinitesimal patch of ocean dS' occurs at two unique Doppler shifts from the carrier, as represented by the impulse functions. The shifts are determined from substituting the arguments appearing in place of p, q in (8a) into (10) to obtain

$$\omega_g = +(gk_0)^{1/2} [\sin^2 \theta_s - 2 \sin \theta_s \sin \theta_i \cos \varphi_s + \sin^2 \theta_i]^{1/4}. \quad (13)$$

This Doppler shift corresponds to a velocity for those ocean waves having the proper length for Bragg scatter. The shift is zero for forward scatter where $\theta_s = \theta_i$ and $\varphi_s = 0$. It is largest for backscatter at grazing, where $\theta_s = \theta_i = \pi/2$, $\varphi_s = \pi$; here $\omega_g = +(2kg_0)^{1/2}$, and the length of the ocean waves responsible for scatter is the shortest, i.e., $L = \lambda/2$.

In order to obtain a rough feeling for the magnitude of ocean wave scatter, we employ a semiempirical model for $W(p, q)$ proposed by Phillips [17] and Munk and Nierenberg [18]. This model relates the roughness height to the wind blowing across the water. The model neglects swell, that is, waves due to storms in other areas which propagate to the region of interest. In addition, the model assumes that the winds have been blowing for a sufficient time that the ocean waves are fully developed. This time period may exceed 20 h for the longer ocean waves. Based on neglect of possible swell, the model has the form

$$W(p, q) = \frac{2 \times 10^{-2}}{\pi(p^2 + q^2)^2} \text{ m}^4 \quad (14)$$

where the spectrum is assumed to be identically zero when $(p^2 + q^2)^{1/2} < g/U^2$ (U = wind velocity in m/s) and also in the half space of the p - q plane from which the wind is blowing. The dimensionless constant 2×10^{-2} has been estimated as high as 4×10^{-2} by some [17]. The preceding spectrum is semiisotropic rather than highly directional; wave slope measurements by Cox and Munk [19] lead them to believe that a highly directional spectrum is difficult to justify [18].

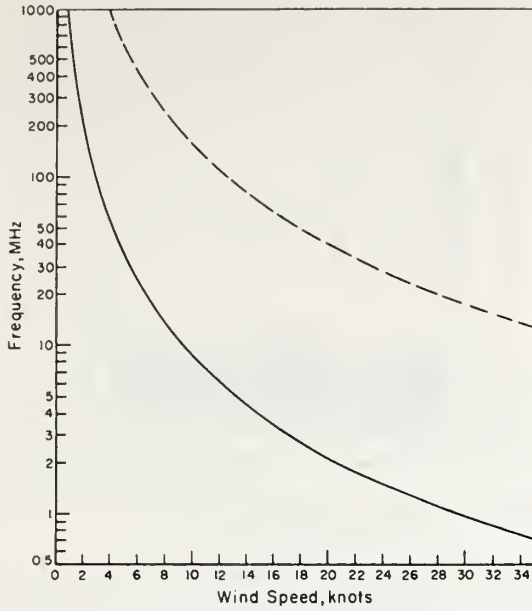


Fig. 2. Solid curve gives frequency necessary to observe lower end (cutoff) of gravity wave spectrum versus frequency for near-grazing backscatter. Dashed curve gives frequency limit where slightly rough surface model fails for given wind speed.

We now introduce the Phillips spectrum into (8), but restrict our attention to the case where both the transmitter and receiver are near the surface, i.e., $\theta_s, \theta_i \rightarrow \pi/2$. We then obtain

$$\sigma(\omega) = 4 \times 10^{-2} \left[f_+ \delta \left(\omega - \omega_0 + \left(2gk_0 \sin \left(\frac{\varphi_s}{2} \right) \right)^{1/2} \right) + f_- \delta \left(\omega - \omega_0 - \left(2gk_0 \sin \left(\frac{\varphi_s}{2} \right) \right)^{1/2} \right) \right] \quad (15)$$

$$\sigma^0 = 0.02 = -17 \text{ dB} \quad (16)$$

where f_+ and f_- represent the fraction of spectral energy in the forward-moving (+x) and backward-moving (-x) ocean waves, with $f_+ + f_- = 1$.

Section VII compares the preceding prediction for $\sigma_{\epsilon\epsilon}^0$ of -17 dB with measurements. It should be noted that the Phillips model predicts no dependence of $\sigma_{\epsilon\epsilon}^0$ on frequency, assuming that the sea is fully developed with $U^2 > g/(p^2 + q^2)^{1/2}$; for wind speeds below this limit $\sigma_{\epsilon\epsilon}^0$ is predicted to be zero. Obviously this abrupt cutoff is not physically realized in nature due to swell and incomplete wind development. We plot in Fig. 2 the idealized lower wind cutoff of near-grazing backscatter with frequency, nonetheless, to obtain a feel for the frequencies necessary to observe the lower end of the gravity wave spectrum. Also shown is the frequency at which the height requirement for the slightly rough surface analysis fails (i.e.,

where $k_0^2 \langle \zeta^2 \rangle = 0.2$) versus wind speed; for the Phillips spectrum, $\langle \zeta^2 \rangle = (10^{-2}/4) \times U^4/g^2$. The slope requirement is always satisfied, even when the sea is fully developed, or saturated; higher winds cause breaking and dissipation of wave energy at a saturated wavenumber, hence maintaining the Phillips value as an upper limit.

VI. NEAR-GRAZING BEHAVIOR

Equation (9b) for the received power (the radar range equation) exhibits a dependence with grazing angle as contained explicitly in the factors $F_T^2 F_R^2 \sigma_{\epsilon\epsilon}^0$. The factor $\sigma_{\epsilon\epsilon}^0$ alone, however, is nearly a constant near grazing ($\theta_s, \theta_i \simeq \pi/2$), as can be seen from (8b) and (16). Hence any decrease near grazing due to the imperfect nature of the surface is contained in the Norton attenuation factors F_T^2, F_R^2 .

One might have alternately defined the scatter cross section per unit area directly from the radar range equation as $\sigma_{\epsilon\epsilon}^{0'} = F_T^2 F_R^2 \sigma_{\epsilon\epsilon}^0$ (give or take a factor of 16, depending upon how the antenna gains are normalized). This $\sigma_{\epsilon\epsilon}^{0'}$, which might be a more logical definition for an experimentalist reducing his data, will obviously depend upon the surface impedance and grazing angle. However, this dependence will not be simple; furthermore, $\sigma_{\epsilon\epsilon}^{0'}$ will also depend upon the ranges R_T and R_R to the scatterer patch.

In order to study the dependence of $\sigma_{\epsilon\epsilon}^{0'}$ upon grazing angle for the sea, we specialize to backscatter, where $\varphi_s = \pi$ and $F_R = F_T$. Then $\sigma_{\epsilon\epsilon}^{0'} = F_R^4 \sigma_{\epsilon\epsilon}^0$. We consider also a spherical earth; therefore, F_R does not have a simple closed form, especially for short ranges and near the penumbra. To evaluate F_R , we employ a computer program developed at ITS [20]. The value Δ employed to describe the imperfect nature of the sea surface contains both Δ , the wave impedance of ocean water ($\epsilon = 81\epsilon_0$, $\sigma = 4 \text{ mho/m}$), as well as the increase due to roughness (see Barrick [21] for a treatment of the latter effect).

Fig. 3 shows the predicted dependence of $\sigma_{\epsilon\epsilon}^{0'}$ on grazing angle over the sea at 10 and 100 MHz using the Phillips spectrum (14) in (8b). The cutoff criterion for this model implies that σ^0 should follow these curves up to a grazing angle α given by $\cos^{-1}[\lambda g/4\pi U^2]$; the backscatter should drop to zero for directions closer to normal than this "cutoff" angle. The angular region near grazing is shown enhanced by a logarithmic abscissa scale; in addition, we display the predicted dependence *beyond the horizon*, i.e., when dS' is in the earth's shadow of the radar. Also shown are σ_{hh}^0 the horizontal cross section.

The figures show that near grazing, sea scatter for vertical polarization is strongly dependent upon frequency. At MF and HF it is possible to obtain sea clutter echo from below the horizon for moderate ranges. At VHF, however, the Norton attenuation factor decreases so rapidly near grazing that one could expect below-the-horizon clutter only from very short ranges (less than 10 km).

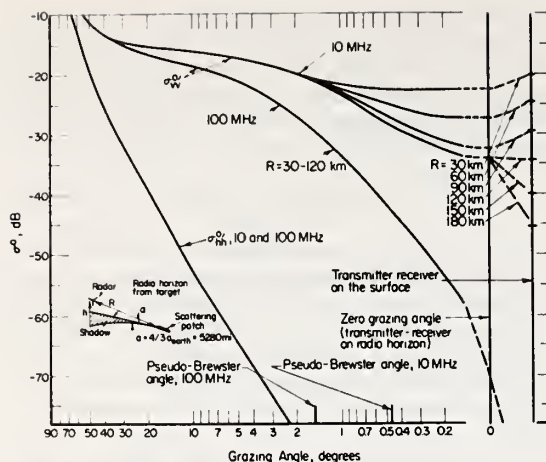


Fig. 3. Dependence of received backscatter power on grazing angle (including Norton attenuation factors in $\sigma_{w,0}$) for Phillips wind-wave spectrum.

VII. COMPARISON WITH MEASUREMENTS

While many persons have observed near-grazing sea clutter at HF and VHF, few have taken the effort to calibrate their radar parameters so as to permit determination of σ^0 . One recent experiment at 10.087 MHz was performed by Headrick of the Naval Research Laboratory (NRL) [22], in which he obtained estimates of $\sigma_{w,0}$. In this experiment, two vertical monopoles were located near Annapolis, Md., on the upper Chesapeake Bay in a monostatic radar configuration. Spectral processing permitted separation of water-wave scatter from stationary ground clutter echoes. A coded signal format permitted a 20-nmi range resolution cell. The Norton attenuation factor F_R was calculated for four different range cells on the bay using the pertinent water conductivity (i.e., $\sigma \approx 2$ mho/m).

Data were recorded and processed on February 4, 1969, a day on which a moderate wind was blowing from the north. Waves receding from the radar were observed to be stronger due to the wind, and water waves of the Bragg scatter length (15 m in this case) were estimated to be fully developed. The averaged received power was processed at four ranges down the bay: 45, 55, 67, and 75 nmi. Propagation to all of these points was via ground wave *since they were all below the radio horizon*. The area within each resolution cell dS' was estimated from maps of the bay. When cast in the form of (9b) with the attenuation factors removed, $\sigma_{w,0}$ was measured to be -17 dB at all four ranges.²

The fact that the water surface in this case was fairly rough means that the backscatter might have been expected to approach the Phillips wind-wave estimate from (16) as an upper limit. The agreement between measured

² Headrick reports the actual antenna gains rather than the free-space gains. Hence his reported values of -29 dB correspond to $\sigma_{w,0}$ of -17 dB by our definition.

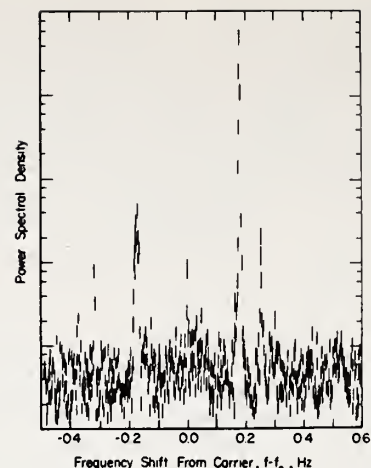


Fig. 4. Measured ocean backscatter signal spectrum at 2.9 MHz (after Crombie, *et al.* [21]).

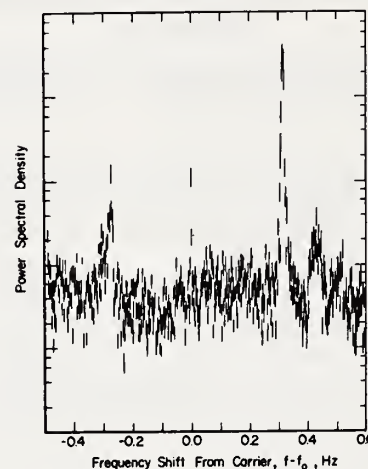


Fig. 5. Measured ocean backscatter signal spectrum at 8.37 MHz (after Crombie, *et al.* [21]).

and predicted values of $\sigma_{w,0}$ not only lends credence to the theory, but confirms the oceanographic estimate of the "Phillips saturation constant" of 2×10^{-2} used in (14).

As further evidence of the validity of the first-order theory for ocean-wave scatter, we cite recent HF measurements by Crombie *et al.* [23] from Barbados Island in the West Indies. Again the antennas were located near the water so that propagation to ranges beyond the horizon was via ground wave. In this case, absolute estimates of σ^0 were not reported, but very accurate digital processing permitted detailed resolution of the received signal spectrum. Backscatter was received with broad-band vertical monopole antennas from the half space toward the east.

Shown in Figs. 4 and 5 are the received power spectra measured simultaneously on August 15, 1969 at 2.9 and

8.37 MHz from the range cell at 45 km. The processor permitted 0.002-Hz resolution; coherent processing at an offset of 0.5 Hz (removed in the figures) permits both negative and positive shifts about the carrier to be observed. The first-order peaks (corresponding to our impulse functions of (12)) occur at ± 0.174 Hz from the carrier at 2.90 MHz and at ± 0.296 Hz at 8.37 MHz. The relative strength of the positive spike over the negative spike at both frequencies agrees with the dominant wind direction in this area; trade winds from the east should excite west-moving water waves, producing a positive Doppler shift.

Lesser spikes in the records at 0.0 Hz, $+0.25$ Hz (in Fig. 4) and $+0.42$ Hz (in Fig. 5) are attributed by Crombie as due to nonlinearities in both the water-wave equations and scattering process. Section VI estimated the spatial-temporal spectrum based upon a linear hydrodynamic theory of water waves and the first-order terms in the perturbation analysis.

VIII. DISCUSSION AND CONCLUSIONS

This paper set forth a simple closed-form result for both σ^0 and the average scattered signal spectrum from a moving sea surface, based upon a straightforward first-order hydrodynamic and electromagnetic analysis. The discrete Bragg-produced Doppler shifts [1], [23], observed experimentally manifest themselves in the impulse spectral functions contained in our result. Our quantitative estimates for σ_{cr}^0 of -17 dB are shown to agree with measurements also. Limits on the mathematical validity of the boundary perturbation approach are derived in terms of frequency and sea state.

We showed that the effect of incidence or scatter of vertically polarized waves near grazing could be separated from σ^0 as the Norton attenuation factors. These factors are not only functions of the effective surface impedance, frequency, and the propagation angles, but also of range. These factors can also conveniently account for sea scatter below the horizon, where concepts of incidence and scattering angles no longer have meaning. It appears more sound to separate these propagation factors from the radar scattering cross section, as we are suggesting in this paper, for two reasons: 1) their interpretation is clear and their origin is unrelated to the mechanism producing scatter, and 2) σ_{cr}^0 then approaches a more universal constant value near grazing, independent of range to the scattering patch.

Several have suggested earlier (Crombie [1], Ward [24], etc.) that MF/HF radars should prove to be extremely useful tools for remote sensing of sea state. With the analysis presented in this paper, we have provided a quantitative link between the radar observables and the ocean-wave height spectrum which will be essential in the implementation of such ocean-wave sensors. Furthermore, the simple Bragg-scatter interpretation of the interaction process confirmed by the theory should permit the design of a variety of bistatic (Barrick [16], Peterson *et al.* [25]) as well as backscatter experiments for the monitoring of ocean waves.

For example, a ship equipped with a broad-band omnidirectional vertical monopole could serve as a backscatter radar.³ The average scattered power from a circular range cell at a given radio wavenumber k_0 will be directly proportional to the ocean-wave height spectrum evaluated at spatial wavenumber $2k_0$. By sweeping frequency from about 1 to 20 MHz, the significant portion of the lower end of the gravity wave spectrum can be measured. Furthermore, directionality of ocean-wave movement can be ascertained because the ship's velocity imposes a unique Doppler bias on the first-order sea-scatter shifts versus bearing from the ship heading. Such a technique, employing the quantitative model set forth in this paper, could prove to be a useful tool for detailed oceanographic studies of directional wave height spectra.

REFERENCES

- [1] D. D. Crombie, "Doppler spectrum of sea echo at 13.56 Mc/s," *Nature*, vol. 175, pp. 681-682, 1955.
- [2] W. H. Peake, "Theory of radar return from terrain," in *1959 IRE Int. Conv. Rec.*, vol. 7, pt. 1, pp. 27-41.
- [3] S. O. Rice, "Reflection of electromagnetic waves from slightly rough surfaces," in *Theory of Electromagnetic Waves*, M. Kline, Ed., New York: Interscience, pp. 351-378.
- [4] D. E. Barrick and W. H. Peake, "A review of scattering from surfaces with different roughness scales," *Radio Sci.*, vol. 3, pp. 865-868, 1968.
- [5] N. W. Guinard and J. C. Daley, "An experimental study of a sea clutter model," *Proc. IEEE*, vol. 58, pp. 543-550, Apr. 1970.
- [6] J. W. Wright, "A new model for sea clutter," *IEEE Trans. Antennas Propagat.*, vol. AP-16, pp. 217-223, Mar. 1968.
- [7] F. G. Bass, I. M. Fuks, A. I. Kalmykov, I. E. Ostrovsky, and A. D. Rosenberg, "Very high frequency radiowave scattering by a disturbed sea surface—parts I and II," *IEEE Trans. Antennas Propagat.*, vol. AP-16, pp. 554-568, Sept. 1968.
- [8] P. Beckmann and A. Spizzichino, *The Scattering of Electromagnetic Waves from Rough Surfaces*. New York: Macmillan, 1963, p. 503.
- [9] G. T. Ruck, D. E. Barrick, W. D. Stuart, and C. K. Krichbaum, *Radar Cross Section Handbook*, vol. 2. New York: Plenum, 1970, ch. 9.
- [10] B. E. Parkins, "Coherence of acoustic signals reradiated from the time-varying surface of the ocean," *J. Acoust. Soc. Amer.*, vol. 45, pp. 119-123, 1969.
- [11] J. R. Wait, "Electromagnetic surface waves," in *Advances in Radio Research*, vol. 1, J. A. Saxton, Ed., New York: Academic Press, 1964, pp. 157-217.
- [12] G. D. Monteath, "Application of the compensation theorem to certain radiation and propagation problems," *Proc. Inst. Elec. Eng.*, vol. 98, pp. 23-30, 1951.
- [13] R. J. King, "Electromagnetic wave propagation over a constant impedance plane," *Radio Sci.*, vol. 4, pp. 255-268, 1969.
- [14] —, "An introduction to electromagnetic surface wave propagation," *IEEE Trans. Educ.*, vol. E-11, pp. 59-61, Mar. 1968.
- [15] D. E. Barrick and W. H. Peake, "Scattering from surfaces with different roughness scales: analysis and interpretation," Battelle Memorial Inst., Columbus, Ohio, Res. Rep. BAT-197-10-3, ASTIA Doc. AD662751; also ElectroScience Lab., Ohio State Univ., Columbus, Tech. Rep. 1388-26, N67-39091, 1967.
- [16] D. E. Barrick, "The interaction of HF/VHF radio waves with the sea surface and its implications," in *AGARD Conf. Proc. Electromagnetics of the Sea* (no. 77), available from Clearinghouse for Federal Scientific and Technical Information, Springfield, Va., accession no. AD716305, 1970.
- [17] O. M. Phillips, *Dynamics of the Upper Ocean*. London: Cambridge Univ. Press, 1966, pp. 109-139.
- [18] W. H. Munk and W. A. Nierenberg, "High frequency radar sea return and the Phillips saturation constant," *Nature*, vol. 224, p. 1285, 1969.

³This shipboard system was conceived jointly at a Scripps Institution of Oceanography Symposium, November 15, 1969, with Dr. W. H. Munk and Dr. R. M. Stewart of Scripps, Dr. A. M. Peterson, Dr. G. L. Tyler, and Dr. C. C. Teague of Stanford University, Dr. D. D. Crombie of ITS, and this author; their contributions are greatly acknowledged.

- [19] C. Cox and W. H. Munk, "Measurement of the roughness of the sea surface from photographs of the sun's glitter," *J. Opt. Soc. Amer.*, vol. 44, pp. 838-850, 1954.
- [20] L. A. Berry and M. E. Chrisman, "A Fortran program for calculation of ground wave propagation over homogeneous spherical earth for dipole antennas," Nat. Bur. Stand., Boulder, Colo., Rep. 9178, 1966.
- [21] D. E. Barrick, "Theory of HF VHF propagation across the rough sea—parts I and II," *Radio Sci.*, vol. 6, pp. 517-533, 1971.
- [22] J. M. Headrick, private communication, Nav. Res. Lab., Washington, D. C., 1970.
- [23] D. D. Crombie, J. M. Watts, and W. M. Berry, "Spectral characteristics of HF ground wave signals backscattered from the sea," in *AGARD Conf. Proc. Electromagnetics of the Sea* (no. 77), available from Clearinghouse for Federal Scientific and Technical Information, Springfield, Va., Accession no. AD716305, 1970.
- [24] J. F. Ward, "Power spectra from ocean movements measured remotely by ionospheric radio backscatter," *Nature*, vol. 223, pp. 1375-1380, 1969.
- [25] A. M. Peterson, C. C. Teague, and G. L. Tyler, "Bistatic radar observation of long-period directional ocean-wave spectra with LORAN A," *Science*, vol. 170, pp. 158-161, 1970.

The Use of Skywave Radar for Remote Sensing of Sea States

DONALD E. BARRICK

Introduction

A semidiurnal knowledge of sea state over the oceans would be quite useful and desirable for several applications. Maritime shipping — as well as naval vessels — chart their courses based upon the seas ahead of them. Since ocean waves are produced by the winds, a knowledge of waveheights and directions can be used to infer the average wind conditions near the surface for the prior 6-to-24 hour period; a grid of such oceanic surface wind velocities is an essential input to global meteorological prediction programs. Finally, a knowledge of waveheights, lengths, and propagation directions in storm areas thousands of miles offshore can provide quite accurate extrapolations as to where and when these high waves will reach other areas, and in particular allow adequate warning to coastal areas likely to be damaged by the waves.

At present, weather maps are prepared and available every six hours; these show wind and wave strength/direction data only at a few scattered points over the oceans. These points originate from ships in the area which have radioed this information back to shore. These reported waveheights are "eyeball" estimates made from the bridge of the ship, and consequently one notes a considerable variance in the numbers for a given area. In addition, there are always vast expanses of ocean (probably approaching 80

percent) in which there are no reported sea/wind data.

Various in-situ techniques exist for measuring waveheights, such as buoys and wavestaffs. Aircraft equipped to do Stilwell photography (Stilwell, 1969) or multi-course laser profilometry (Olsen and Adams, 1970) of the sea surface can obtain estimates of the waveheight directional spectrum during good visibility. Such aircraft techniques are complex and expensive — hardly suited to regular routine monitoring of sea state on a wide scale. Short-pulse satellite radar altimeters, to be implemented in 1973 on the NASA GEOS-C and Skylab satellites, can provide estimates of waveheights at the suborbital point, but one cannot determine wave direction with this instrument. Other HF sensor combinations, including buoys, ships, and satellites (Barrick, 1972b), can yield the waveheight directional spectrum in a localized area near the ocean station (e.g., out to perhaps 100 nmi from the device); these techniques should prove useful in particular regions of interest (e.g., near straits, islands, etc.). For a constant surveillance of large ocean areas, however, the large number of required stations makes utilization of these techniques less attractive.

The use of shore-based HF radars which propagate via ionospheric reflections (i.e., "skywave" radars) appears to be an ideal solution to the problem of wide-area routine

sea-state monitoring (see Figure 1). For example, a single backscatter radar located, say, in Kentucky, could observe sea scatter over the entire Atlantic coast out to about 1,200 nmi. While radial and azimuthal resolutions of the order of two-to-three nmi have been demonstrated with skywave radars, resolutions no higher than 20 nmi would likely be required for this application. Sea scatter propagated via the ionosphere has been observed many times (e.g., Tveten, 1967; Ward, 1969; Curley *et al.*, 1972; Barnum, 1971). The problem, therefore, in bringing this technique to fruition lies in establishing and verifying the relationship between the observed sea-scatter signal spectrum and the ocean-wave directional spectrum. Preliminary theoretical analyses and empirical interpretations of measured data indicate that progress is rapidly being made toward resolving this problem.

Physical Interpretation of Scatter

Crombie (1955) appears to have been the first to

explain the origin of HF sea scatter, based upon his near-grazing radar observations. The dominant contribution to the echo at MF/HF arises from those ocean waves exactly one-half the radar wavelength advancing and receding radially from the radar. Since these deepwater ocean waves have a phase velocity, v , which varies with the square-root of their length (i.e., $v = \sqrt{gL/2\pi}$, where g is the acceleration of gravity), one observes this dominant (or "first-order") sea echo of a unique Doppler shift, $\Delta f = \pm \sqrt{g/\pi\lambda}$, where λ is the radar wavelength. This rather unusual variation of Doppler shift with the square-root of the carrier frequency – rather than in direct proportion to it – provides convincing proof of the validity of the above "diffraction grating" explanation of scatter. Figure 2 exemplifies a non-ionospherically propagated spectral record of sea backscatter at 8.37 MHz as observed by Crombie (1971). Analysis (Barrick, 1972a) has shown that the strength of the first-order echo at these Doppler shifts is proportional to the height of those ocean waves present having the required length and direction.

SKYWAVE SEA SCATTER

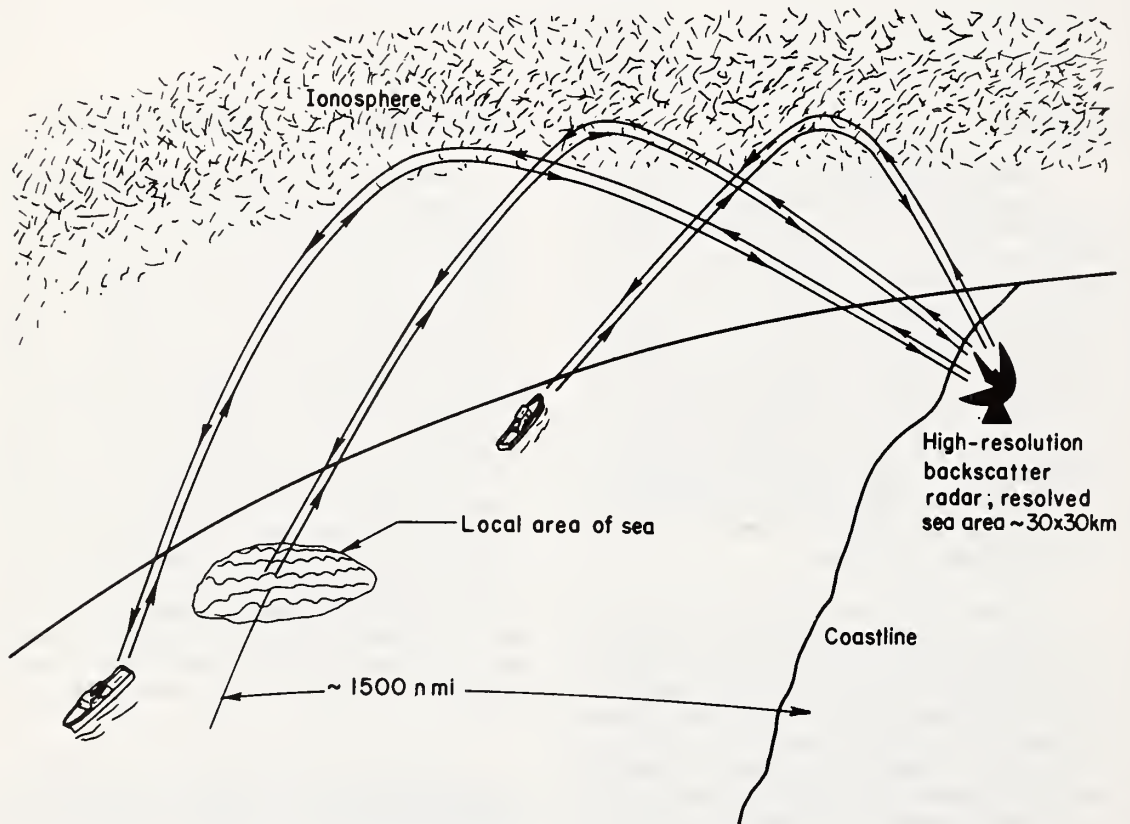


Figure 1. Typical Sky-Wave Sea-Scatter Geometry.

To measure the ocean-waveheight spectrum using first-order scatter, one must sweep the carrier frequency over the MF and lower HF regions, so that the important long-wavelength end of the ocean spectrum is observed. However, this frequency region is not well matched to the ionospheric propagation channel; the upper HF region (i.e., above 10 MHz) gives greater ionospheric radar area coverage with less signal attenuation. Hence attempts are being made to interpret the "second-order" sea scatter signal spectrum and relate it to sea state.

Hasselmann (1971) and Barrick (1971) proposed that the second-order Doppler return at a higher HF frequency bears a definite relationship to the waveheight directional spectrum. The analysis (Barrick, 1972b) shows that this return is produced by a double first-order interaction process. Both twice-scattered electromagnetic return and also the once-scattered return from two nonlinearly interacting ocean waves account for this echo. Figure 3 is a prediction of this Doppler return and its dependence upon sea state at 10 MHz. Assumed here is a Phillips waveheight

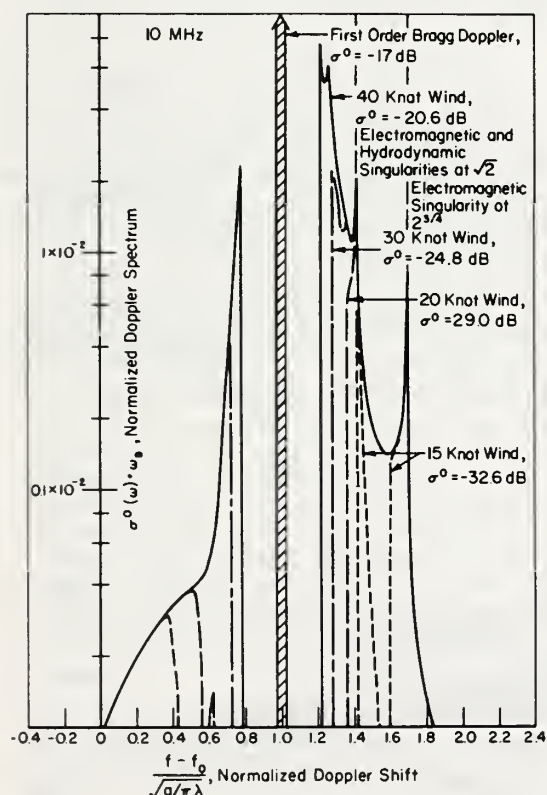


Figure 2. Measured Ocean Backscatter Signal Spectrum at 8.37 MHz Via Ground-Wave Propagation (after Crombie, 1971).

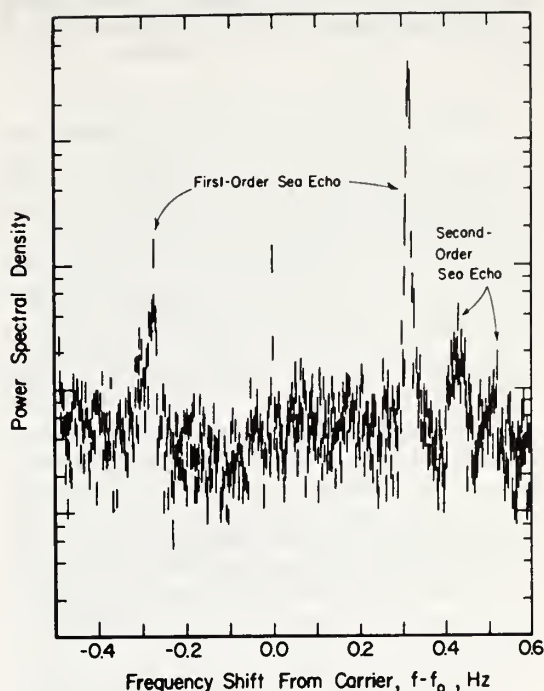


Figure 3. Predicted Ocean Backscatter Signal Spectrum at 10 MHz for Phillips Semi-Isotropic Waveheight Spectrum.

directional spectrum for fully developed seas; the lower cutoff for this spectrum corresponds to waves whose length is great enough to allow them to keep up with the wind. The radar propagation direction in this example is assumed to be into the wind. The appearance of the second-order return is somewhat different for the crosswind case (see Barrick 1972b). The theory shows that in general the height and proximity of the second-order peaks to the first-order line is a direct indicator of sea state. Further theoretical effort and experimental verification are required to solve the inverse problem — predicting the sea waveheight directional spectrum with confidence from the Doppler signal spectrum at a single HF carrier frequency.

Ionospheric Complications

While it is the ionosphere which holds out the prospect of sea-state monitoring at great distances, the ionosphere also injects complications and limitations on such a system. These problems must be understood in order to operate such a system effectively. Great strides have been made over the past decade in dealing with the vagaries

of the ionosphere in the operation of skywave radars. This extensive research has eliminated most of the major unknowns, and has yielded diagnostic techniques and computerized models for forecasting ionospheric propagation conditions. An excellent review of the current state of the art in ionospheric research was published by Croft (1972).

The first problem in the use of the ionosphere is the variation in frequency required to transmit to a given range as the ionosphere undergoes its diurnal and seasonal cycles. The system must be capable of transmitting over several octaves (e.g., from 6-to-30 MHz). One normally selects the frequency to use by making a backscatter ionogram, finding the MUF (maximum usable frequency) which will propagate to the desired range, and then operating at a frequency about 80-to-90 percent of this value. Much about propagation conditions can be learned from such a backscatter ionogram; it can also be used as an input to ray-tracing programs presently available. Figure 4 shows an example of a typical ionospheric ray trace, including the effects of the antenna pattern (Curley *et al.*, 1972). Such programs permit one to deduce from the observed time delay the great circle range to the ground point being observed. The ionogram and ray-tracing programs will often indicate complications, such as multiple moding (i.e., reflections from different layers simultaneously) and sporadic-E reflections.

Other complicating ionospheric effects will inevitably degrade the echo to some extent. To illustrate these effects, refer to Figure 5; this is a record of skywave backscatter from the North Atlantic made at the Naval Research Laboratory facility on the Chesapeake Bay at 17.5 MHz. The range (~1000 nmi) and azimuth were such that the return includes both sea scatter and land echo from Newfoundland. Two consecutive range cells are shown for comparison. The spectral processing resolution was better than 0.01 Hz. Ionospheric motions produce two effects: an overall Doppler shift and spectral smearing. The overall

shift can be deduced by measuring the position of the land echo from the carrier frequency. In Figure 5, this shift is barely noticeable, but at sunrise and sunset when the ionospheric layers are descending and ascending vertically, this shift can be as much as 0.1 Hz. Smearing is noticeable in this record, however. The land echo, which should be no wider than 0.01 Hz due to the processing resolution, is rather of the order of 0.05 Hz. The first-order Bragg lines, nonetheless, are unmistakable. There is without question some second-order return at negative Dopplers beyond $-f_B$. The overall picture agrees qualitatively with expectations; winds of about 20 knots were blowing toward the Northeast, producing dominant waves moving away from the radar.

One of the primary difficulties with skywave radars is not encountered in this application: that of system calibration. Since ionospheric attenuation is unknown at any time, one has no way of determining the radar cross section of the scatterer without the use of a known standard target (or calibrator) in the area of interest. Here, however, it is the strength and position of the second-order echo *with respect to the first-order return* which is related to sea state. Since both propagate via the same ionospheric path, unknown propagation losses do not impede the interpretation of the results.

Figure 5 is a relatively "clean" skywave record. Occasionally ionospheric multimoding, Faraday rotation, sporadic E, and other complications will produce such a multiplicity of echoes that interpretation is impossible. Such conditions, however, will seldom exist beyond a few hours. Since sea-state conditions do not change much over a six-hour period or so, one can afford to wait until the skywave signal becomes cleaner.

As emphasized earlier, much about ionospheric propagation is presently known. However, one cannot outline a simple operational procedure which will work at all times and ranges. Experience, adaptability, and patience are

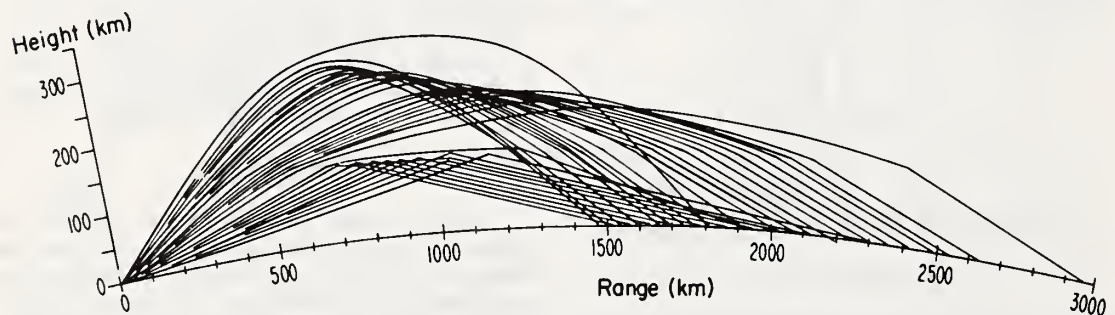


Figure 4. Typical Trace of Rays Through the Ionosphere, Including Pattern.

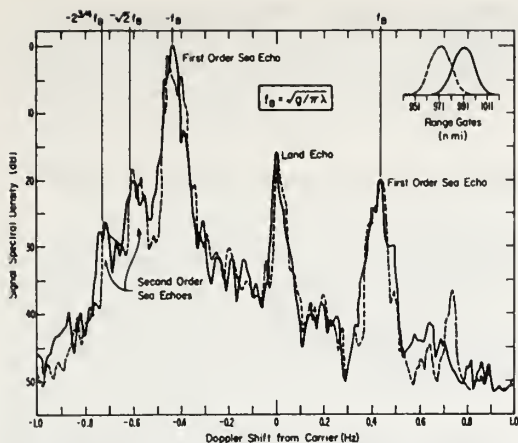


Figure 5. Measured Backscatter Signal Spectrum at 17.5 MHz via Skywave Propagation.

prerequisites in the successful operation of a skywave radar. Since minutes and hours are not critical for sea-state monitoring, the system should prove to be entirely adequate for this application.

Conclusions

Skywave radar — in conjunction with the second-order sea Doppler echo — appears to be the ideal tool for remotely sensing sea state from land out to great distances. Further research should be done relating the second-order echo to the sea waveheight spectrum;¹ this is best tested using nonionospheric propagation. Statistics on skywave sea backscatter should then be gathered to assess the utility of the technique and to aid in the eventual design and operation of the system.

A final advantage to this HF system is the inherent potential for communication/lifesaving with ships and personnel in the area. Ships within radar range can be informed of sea conditions ahead of them by the same HF transmitter used for sea state monitoring. These vessels can be tracked — either via their echo or aided by an active repeater — to permit dispatch of assistance in case of peril. Finally, personnel in distress equipped with low-power HF beacons — either aboard small craft or lifeboats — could be located in relatively short order by the radar receiver.

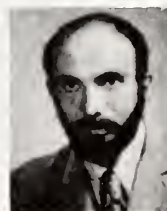
Footnote

¹Even in the absence of this relationship, Curley *et al.* (1972) have already demonstrated considerable success in predicting oceanic wind and wave conditions strictly on the basis of empirical deductions from skywave sea echo records over the Atlantic.

References

- Barnum, J. R. 1971. Private communication.
- Barrick, D. E. 1971. *Dependence of Second-Order Sidebands in HF Sea Echo upon Sea State*, G-AP International Symposium Digest, IEEE, Sept. 1971, 194-197.
- Barrick, D. E. 1972a. *First-Order Theory and Analysis of MF/HF/VHF Scatter from the Sea*, IEEE Trans. Ant. Prop., AP-20, 2-10.
- Barrick, D. E. 1972b. *Remote Sensing of Sea State by Radar*, Chapter 12 in *Remote Sensing of the Troposphere*, V. E. Derr, Ed., U.S. Government Printing Office, Washington, D.C.
- Croft, T. A. 1972. *Sky-Wave Backscatter: A Means for Observing Our Environment at Great Distances*, Rev. Geophys. and Space Phys., 10, 73-155.
- Crombie, D. C. 1955. *Doppler Spectrum of Sea Echo at 13.56 Mc/s*, Nature, 175, 681-682.
- Crombie, D. D. 1971. *Backscatter of HF Radio Waves from the Sea*, Chapter 4 in *Electromagnetic Probing in Geophysics*, J. R. Wait, Ed., The Golem Press, Boulder, Colorado.
- Curley, S. R., J. Headrick, J. Ahearn, and J. Ferrel. 1972. *Sea-Air Interaction Determinations from Remote (OTH) Radar Measurements of Ocean Wave Spectra*, IEEE Internat. Conference on Engineering in the Ocean Environment, Newport, R.I., Sept. 1972.
- Hasselmann, K. 1971. *Determination of Ocean Wave Spectra from Doppler Radio Return from the Sea Surface*, Nature Physical Science, 229, 16-17.
- Olsen, W. S., and R. M. Adams. 1970. *A Laser Profilometer*, Journal Geophysical Research, 75, 2185-2187.
- Stilwell, D., Jr. 1969. *Directional Energy Spectra of the Sea from Photographs*, Journal Geophysical Research, 74, 1974-1986.
- Tveten, L. H. 1967. *Ionospherically Propagated Sea Scatter*, Science, 157, 1302-1304.
- Ward, J. F. 1969. *Power Spectra from Ocean Movements Measured Remotely by Ionospheric Radio Backscatter*, Nature, 223, 1325-1330.

DONALD E. BARRICK is currently Project Leader of the Wave Propagation Laboratory Program in Radar Remote Sensing of Sea State. He was formerly a Fellow with Battelle's Columbus Laboratories and an Adjunct Assistant Professor of Electrical Engineering at the Ohio State University. At Battelle he directed programs in radar research and analysis, and is coauthor of the *Radar Cross Section Handbook*. He received his B.S.E., M.Sc., and Ph.D degrees in electrical engineering at the Ohio State University.



Reprinted from the Proceedings of IEEE, Ocean '73, 191-197,
September 1973

INTERPRETATION AND APPLICATION OF SECOND-ORDER HF SEA-ECHO DOPPLER SPECTRUM

D. E. Barrick and E. R. Westwater

National Oceanic and Atmospheric Administration
Wave Propagation Laboratory/ERL
Boulder, Colorado 80302

ABSTRACT

The purpose of the present research is to demonstrate that sea state--as expressed via the waveheight directional spectrum--can be determined with a long-range sky-wave HF radar system by a proper interpretation of the higher-order signal-echo Doppler spectrum. Sea-echo spectra measured at many HF frequencies in an experimental surface-wave radar system agree with theoretical predictions to first and second order, indicating that gross initial estimates of the waveheight directional spectrum can be obtained quickly from inspection of the radar records. Those initial estimates--along with an understanding of the general behavior of the integrand--will permit the numerical inversion of an integral equation for second-order scatter to obtain a considerably more refined calculation of the waveheight directional spectrum. Such techniques should prove useful in a future operational system for the routine monitoring of sea conditions out to 1500 nmi from the U.S. coasts.

INTRODUCTION

There is considerable effort underway at present to apply HF sky-wave radars (using an ionospheric reflection during propagation) to the problem of remotely sensing sea state. Besides NOAA's Wave Propagation Laboratory (WPL)*, NRL is conducting sky-wave experiments on this concept looking into the mid-to-North Atlantic [1], and the James Cook University at Townsville, Australia is doing likewise looking in the South Pacific and Indian Oceans [2]. All of these experiments are examining the Doppler signal spectrum of the HF echo back-scattered from the sea and attempting to relate its characteristics to the significant descrip-

tors of sea state. The sky-wave radar offers the exciting prospect of coverage out to 2000 nmi from the land-based site; however, one is normally restricted to operating near a frequency dictated by the desired range, time of day, and peculiar ionospheric conditions. Therefore, all deductions about sea state must be obtained from an average Doppler spectrum made essentially at a single frequency and a given azimuthal look angle, since it is not possible to vary these parameters at will. Hence it is quite important to analyze and verify the angle/frequency/sea-state dependencies of the echo spectrum in order to ascertain the utility and accuracy of the sky-wave technique.

A theoretical model has been developed relating the Doppler signal spectrum of the sea echo to the waveheight directional spectrum. The model exhibits a second-order nonlinearity, in that the signal Doppler spectrum is equal to an integral containing the waveheight directional spectrum as a factor twice. Since the waveheight directional spectrum is the unknown, or desired, quantity and the Doppler spectrum is the known, or measurable, quantity, one has in effect an integral equation which must be inverted. It would of course be most desirable to numerically invert this equation automatically in any operational sky-wave system to produce an estimate of the ocean waveheight directional spectrum. The alternative to such an inversion scheme is a "pattern recognition" process, whereby many echo Doppler spectra are computed for various waveheight spectrum models and radar parameters. The operator then searches for the echo Doppler spectrum which best matches what he is currently observing, and thusly deduces the nature of the sea waveheight directional spectrum. In doing so, the operator will begin to subconsciously employ certain features of the echo spectrum which appear to be the more sensitive indicators of the sea spectrum. Once these echo features are identified, of course, a computer could just as easily do the pattern comparison.

Of the two techniques (integral inversion and pattern recognition), the integral inversion is more technically thorough and satisfying. Both techniques are being studied at WPL and are being tested with the theory against measurements of HF sea echo made from a surface-wave radar. Surface-wave measurements have been used up to this point in preference to sky-wave measurements because

*It is presently planned that NOAA/WPL will join with the Institute for Telecommunication Sciences (ITS) and the Naval Research Laboratory (NRL) in a joint sky-wave experiment on San Clemente Island looking into the North Pacific.

such signals are more free of time-varying propagation distortions. Once the two techniques have been verified against surface-wave echo signals, a sky-wave research facility will be implemented to ascertain the ultimate accuracy of such a system in the presence of diurnal and seasonal ionospheric distortions.

EXPERIMENTAL FACILITY

A series of HF surface-wave measurements of sea echo were undertaken in a joint experiment between NOAA/WPL, NRL, and ITS on San Clemente Island off California. Between 1 November 1972 and 30 April, 1973, approximately 25 hours of sea-echo Doppler spectra were gathered. The facility is located on the Northwest side of the island and looks Westward into the Pacific. It is capable of transmitting any number of frequencies (up to 100) simultaneously from 2 to 25 MHz in a pulse-to-pulse progression--and processing the returns on each frequency coherently. Pulswidths available are 20, 50, and 100 μ s with a 200 pulse-per-second repetition rate. The sea echo from several range gates can be processed simultaneously; to provide adequate signal-to-noise ratio, the echoes at 22.5, 30, and 37.5 km from the radar were found to be optimal, and hence most sea echo data were recorded at these ranges.

The transmitter provided an output power of 75 kW peak. The transmitting antenna was a twin-bay log-periodic monopole array producing vertical polarization; with a gain of 14 dB, it provided a beamwidth of 60° centered on 255° T. An 850-foot receiving array parallel to the beach was capable of forming two simultaneous beams at 240° and 270°, with elements switched in and out automatically vs frequency so that the beamwidth did not vary drastically over the decade frequency range; as a result, the beamwidth was about 15° at 3 MHz and 7° at 24 MHz. Data were processed and recorded digitally on magnetic tape--both in raw IF form and as 200-second coherent spectra.

A Datawell Waverider buoy was also moored in the scattering area. This device provided both sea significant waveheight and nondirectional waveheight spectra. The buoy output was confirmed and supplemented by wave hindcast tables prepared by IBM, Inc.; these data indicated wave direction and also listed the height, period, and direction of any swell present.

SECOND-ORDER THEORY

First-order theory [3,4] in which scatter from the surface is derived via a boundary-conditional treatment (assuming (i) small sea heights in terms of radar wavelengths and (ii) small slopes), shows that the average, vertically polarized, Doppler signal spectrum for surface-wave sea backscatter, $\sigma_{VV}(\eta)$, is directly proportional to the waveheight directional spatial spectrum $S(\kappa_x, \kappa_y)$. Furthermore, the Doppler shift always occurs at two discrete frequencies, caused by waves precisely one-half the

radar wavelength moving toward and away from the radar. This is the "Bragg-scatter" mechanism and may be expressed quantitatively as

$$(1) \quad \sigma_{VV}^{(1)}(\eta) = 2^7 \pi k_0^4 [S_+(2k_0, 0) \delta(\eta - \omega_+) + S_-(-2k_0, 0) \delta(\eta - \omega_-)],$$

where $\eta = \omega - \omega_0$ is the Doppler shift (rad/s), ω_0 is the radian carrier frequency, $k_0 = \omega_0/c$ is the radar wavenumber, c is the free-space radio propagation velocity, and $\omega_{\pm} = \pm \sqrt{2gk_0}$. The $\delta(x)$ is the Dirac-delta function of argument x . The square-root relationship merely expresses the first-order dispersion equation for deep-water surface waves under the influence of gravity with a vertical accelerational constant g . The $+$ notation is used to denote those portions of the wave spectrum moving toward (positive) and away from (negative) the radar. In the above equation, the x -direction is assumed to coincide with the radar line of sight.

Unfortunately, at the upper HF frequencies (6-30 MHz) at which a sky-wave radar is forced to operate, the sea spectrum $S(2k_0, 0)$ usually always has the same constant magnitude, independent of "sea state"; it is hence said to be saturated, following an inverse fourth-power wavenumber law typical of this equilibrium region. Thus the dominant "spike"--as expressed in the delta function above--is saturated in its magnitude, and hence insensitive to the lower "sea state" end of the gravity-wave spectrum. In this frequency region, investigators have observed the presence of an appreciable higher-order Doppler continuum on their measured records, in addition to the prominent first-order spikes. This higher-order echo appears to fluctuate more significantly with waveheight and direction. Therefore, the theory was extended to second-order in an attempt to predict and interpret the higher-order observed signals. Two contributions to this echo were found: (1) second-order "hydrodynamic" contributions due to the small nonlinear terms in the boundary conditions at the free water surface and (ii) second-order "electromagnetic" contributions due to the previously neglected higher-order terms of the boundary perturbational scatter theory. The result of this analysis [5] is

$$(2) \quad \sigma_{VV}^{(2)}(\eta) = 2^7 \pi k_0^4 \int_{-\infty}^{\infty} \int_{-\infty}^{\infty} |\Gamma_H + \Gamma_{EM}|^2 \times \\ \times S(\kappa_1 x \kappa_1 y) S(\kappa_2 x \kappa_2 y) \times \\ \times \delta(\eta - \omega_1 - \omega_2) dp dq,$$

where $\vec{\kappa}_1 = (p - k_0)\hat{x} + q\hat{y}$; $\vec{\kappa}_2 = -(p + k_0)\hat{x} - q\hat{y}$; $\kappa_1 = |\vec{\kappa}_1|$; $\kappa_2 = |\vec{\kappa}_2|$; $\omega_1 = \text{sgn}(\kappa_1) \sqrt{g\kappa_1}$; $\omega_2 = \text{sgn}(\kappa_2) \sqrt{g\kappa_2}$. The convention $\text{sgn}(x)$ represents the factor ± 1 depending upon whether x is $+$. The Γ 's are the contributions due to the hydrodynamic and

electromagnetic second-order processes described above, and are

$$\vec{r}_H = -\frac{i}{2} \left[\kappa_1 + \kappa_2 - (g/\omega_1 \omega_2) (\kappa_1 \kappa_2 - \kappa_1 \cdot \kappa_2) \left(\frac{\omega_1^2 + \omega_2^2}{\omega_1^2 - \omega_2^2} \right) \right]$$

$$\vec{r}_{EM} = \frac{1}{2} (\kappa_{1x} \kappa_{2x} - 2\vec{\kappa}_1 \cdot \vec{\kappa}_2) / (\sqrt{\kappa_1 \cdot \kappa_2} + k_0 \Delta),$$

where Δ is the normalized effective wave impedance of the rough sea surface, and ω_+ is defined following Eq. (1).

The interpretation of the above equation clearly indicates a second-order "Bragg" interaction process as the mechanism responsible for the scatter. The scattered radio wavenumber, $-\kappa_0 \hat{x}$, is equal to $\kappa_1 + \kappa_2 + k_0 \hat{x}$, where the last term is the incident radio wavenumber. The frequency of the scattered radiation, ω , is equal to $\omega_1 + \omega_2 + \omega_0$, as implied in the argument of the δ -function. Thus two moving ocean waves of wavenumbers κ_1 and κ_2 (with corresponding temporal frequencies ω_1 and ω_2) are interacting to produce the second-order scattered signal. The presence of the δ -function permits one of the integrations to be executed in closed form (after appropriate transformations), with a single integration remaining. If one assumes a form for the waveheight spectrum, $S(\kappa_x, \kappa_y)$, this integration must generally be done numerically. On the other hand, if one wants to determine the waveheight spectrum, $S(\kappa_x, \kappa_y)$, from the second-order Doppler signal spectrum, $\sigma_{VV}^{(2)}(\eta)$, one must "invert" the resulting integral. As mentioned previously, the inversion process is nonlinear in the sense that the desired waveheight spectrum appears as a factor twice in the integrand.

COMPARISON OF THEORY AND EXPERIMENT

As a preliminary check on the theory, we selected measurements from 4 December 1972, a day during which the sea was fully developed by a 25 knot wind blowing predominantly toward the radar. Fig. 1 is the non-directional waveheight spectrum measured by the Waverider buoy, along with the Phillips spectrum model we employed in Eqs. (1) and (2) to represent the sea. Hindcast calculations for that time showed that the wind-driven sea was from approximately 290°T (about 20° from the 270° centerline), and had a significant waveheight of about 8 feet. In addition, the hindcasts revealed a swell of 14 seconds period from 255°T with a significant waveheight of 3.5 feet. This swell is clearly evident in the buoy spectrum of Fig. 1 at 0.07 Hz, but was not taken into account in the theoretical model.

Because little is known about the angular patterns of waveheight spectra, we selected two patterns for use in the idealized Phillips model of Fig. 1. One is the semi-isotropic pattern suggested by Phillips [6], in which the waves of a

given wavenumber are assumed to be moving in all directions with equal height into the half-space into which the wind is blowing. The other is a cosine-squared directional pattern about the mean

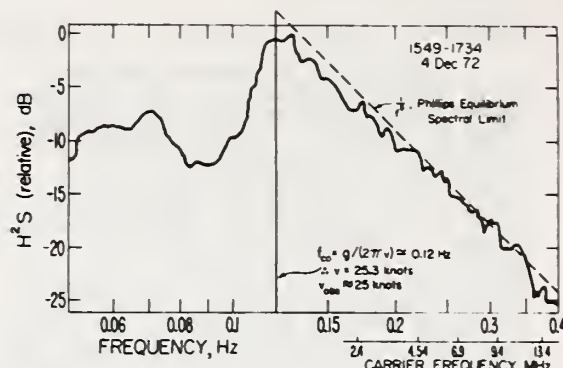


Figure 1. Measured nondirectional waveheight in scattering area off San Clemente Island. Theoretical Phillips model shown as triangle. Scale at bottom gives ocean wave frequency directly observed by radar carrier frequency, according to first-order Bragg scatter mechanism.

wind direction. In both cases the energy under the wave spectra are kept the same so that they produce the same significant waveheight. Also it was assumed that the sea was symmetric about 270°--the right radar beam--rather than the actual 290°, for convenience of calculation.

Figs. 2, 3, and 4 are comparisons of the measured Doppler spectra and the theoretical using the models described above in Eqs. (1) and (2). While data were recorded at ten frequencies between 2.41 and 24 MHz, only those at 4.54, 9.4, and 17.4 MHz are shown here for lack of space. The measured spectra have 0.005 Hz Doppler resolution, corresponding to 200-second Fourier transforms. Nine such power spectra were incoherently averaged, for a total of one-half hour. The measurements were taken on the 20 μ s pulse width at 22.5 km range. Both the theoretical and experimental data were normalized to the first-order echo positions (occurring at unity) and smoothed using a Gaussian smoothing function with a half-power width of .087 times the first-order echo Doppler ($\sqrt{2k_0 g}$ rad/s). The smoothing ensured that the theoretical and experimental data would have the same first-order peak widths. Since the first-order peaks are assumed to be saturated,* their heights are used as

*The scale at the bottom of Fig. 1 shows the positions at which a given carrier frequency observes the sea spectrum in the first-order interaction. Above 2.5 MHz, the first-order interaction occurs in the f^{-5} equilibrium region, satisfying the assumption of saturation.

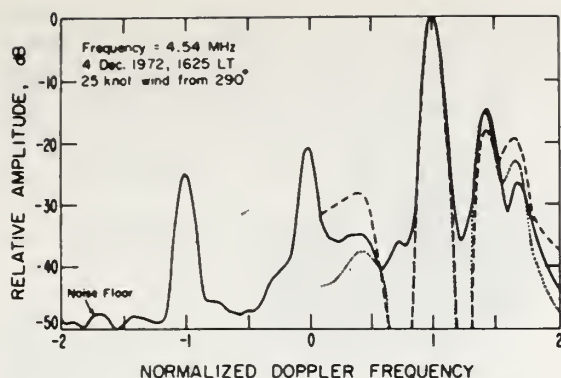


Figure 2. Measured smoothed backscatter Doppler spectrum (solid line) off San Clemente Island at 4.54 MHz on 4 Dec 1972. Also shown (only on dominant positive Doppler side) are theoretical predictions using Phillips spectrum with semi-isotropic (dash) and cosine-squared (dot) directionalities.

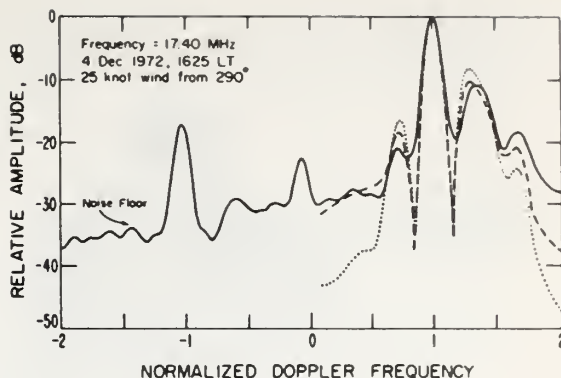


Figure 4. Measured smoothed backscatter Doppler spectrum (solid line) off San Clemente Island at 17.40 MHz on 4 Dec 1972. Also shown (only on dominant positive Doppler side) are theoretical predictions using Phillips spectrum with semi-isotropic (dash) and cosine-squared (dot) directionalities.

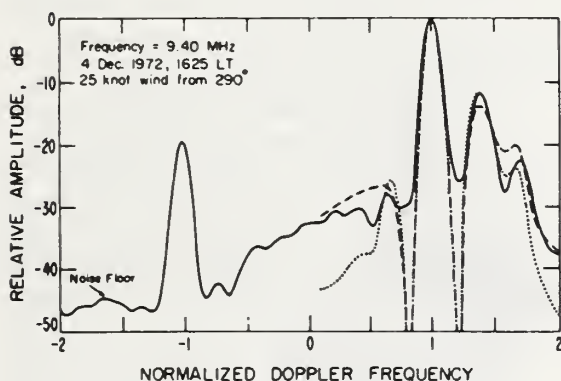


Figure 3. Measured smoothed backscatter Doppler spectrum (solid line) off San Clemente Island at 9.40 MHz on 4 Dec 1972. Also shown (only on dominant positive Doppler side) are theoretical predictions using Phillips spectrum with semi-isotropic (dash) and cosine-squared (dot) directionalities.

the amplitude normalization between theory and experiment in Figs. 2, 3, and 4. The agreement is quite good; the implication of the comparison will be discussed in the subsequent sections.

APPROACH TOWARD INTEGRAL INVERSION

In any attempt to invert an integral equation such as Eq. (2), one should understand the typical behavior of the unknown function in the integrand for parameter values representative of sky-wave radar operation. To obtain such an understanding, the semi-isotropic and cosine-squared directional waveheight spectrum models discussed in the above section are shown three-dimensionally in Figs. 5(a) and 6(a). These spectra are normalized in amplitude; also, the spatial wavenumbers are normalized, the latter being divided by the cutoff wavenumber, $\kappa_{co} = g/U^2$ where U is the wind speed. Thus the p, q -axes become u, v , where $u = p/\kappa_{co}$, $v = q/\kappa_{co}$. The wind/wave direction is the x -direction, corresponding to the u -axis in a normalized wavenumber space. As mentioned previously, the spectra follow an inverse fourth-power wavenumber dependence in the equilibrium region, and drop abruptly to zero below the cutoff wavenumber (with this normalization, for $\sqrt{u^2 + v^2} < 1$).

In Figs. 5(b) and 6(b) are shown the normalized product functionals $S(\kappa_{1x}, \kappa_{1y})S(\kappa_{2x}, \kappa_{2y})$, plotted in $u = p/\kappa_{co}$, $v = q/\kappa_{co}$ space. They are plotted for a value of radar wavenumber-to-cutoff wavenumber (κ_0/κ_{co}) of 5; this is typical of sky-wave radar operation, and would correspond to a carrier frequency of 18 MHz scattering from a sea fully developed by 22 knot winds. The surface plots are shown only for $u < 0$ because they are symmetric about $u=0$. The appearance of the product functional is that of the single spectrum, but

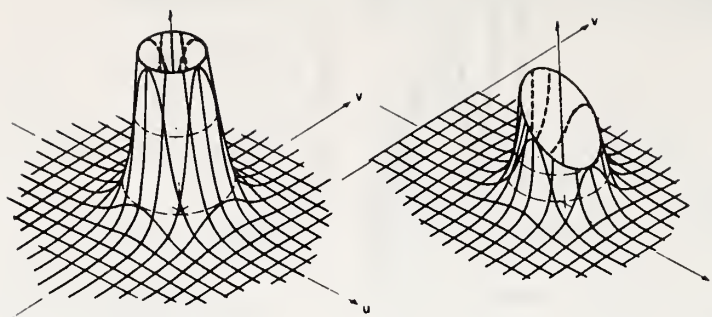


Figure 5. Isometric views of normalized semi-isotropic Phillips wave-height spectrum model; plotted singly in (a) as a function of spatial wavenumbers, $S(u,v)$; plotted in (b) as product appearing in integrand of Eq. (2) vs spatial wavenumbers, $S(u+5,v)S(u-5,v)$.

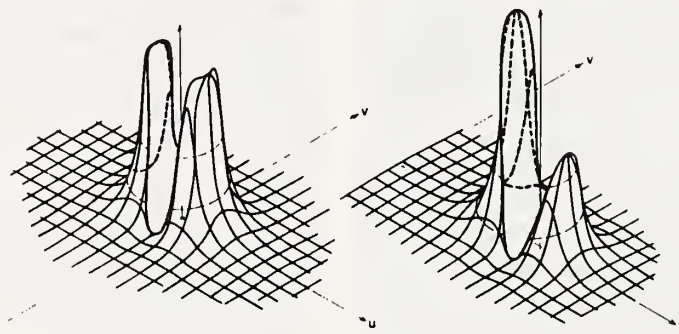


Figure 6. Isometric views of normalized cosine-squared Phillips wave-height spectrum model; plotted singly in (a) as a function of spatial wavenumbers, $S(u,v)$; plotted in (b) as product appearing in integrand of Eq. (2) vs spatial wavenumbers, $S(u+5,v)S(u-5,v)$.

shifted out to a new position at $k_0/\kappa_{CO}=5$, and monotonically weighted by the $[(u+5)^2+v^2]^{-2}-(u+5)^{-4}$ value of the other spectrum. Note that all of the significant volume in these product spectra occur within a radius of about 2.5 from the spectrum center. The normalized Doppler shifts implied by the δ -function in Eq. (2) which fall within this circle of importance lie in the region $.55 < \eta/\omega_B < 1.5$.

Hence Figs. 5 and 6 reveal two important facts relevant to the inversion of Eq. (2):

(1) In the regime of most interest to sky-wave radar, it may be possible to "linearize" the nonlinear product functional, since one of the spectrum factors has the effect of monotonically weighting the other spectrum factor in a known manner in the region where the latter factor is important. Thus one of the factors should be replaceable by a tilted surface (to the first order) whose slope and height are constants. This then leaves only one directional waveheight spectrum in the integrand whose shape must be determined.

(2) The normalized Doppler frequencies at which significant echo energy will appear in the second-order analysis are those intersecting the circle of radius ~ 2.5 centered at $u_0=k_0/\kappa_{CO}$ ($=5$ here). This is somewhat confirmed by Fig. 4, which shows that the best agreement between measurement and first and second-order theory occurs for normalized frequencies between about 0.55 and 1.5.

A brief discussion will be undertaken here on the integral inversion techniques being developed at WPL. Consider Eq. (2) to be the integral equation in which the waveheight spectrum $S(\kappa_x, \kappa_y)$ is to be determined from measurements of $\sigma_{VV}^{(2)}(\eta)$. Since a nonlinear integral equation such as (2) does not, in general, possess globally unique solutions, additional information is required to extract meaningful results. However, since both theory and previous direct measurements can provide a physically reasonable first estimate of $S(\kappa_x, \kappa_y)$, locally unique and meaningful solutions can be obtained by iterating a linearized version of the original equation. For example, one of two situations will be obvious from initial examination of a measured Doppler signal spectrum: (i) the second-order echo is sufficiently strong as to suggest a large value of k_0/κ_{CO} (e.g., greater than 2); (ii) the second-order echo is weak, suggesting $k_0/\kappa_{CO} < 2$. In the first case, the approximation suggested in Section (1) of the preceding paragraph is applicable; the integral is linearized by representing one of the two waveheight spectrum factors by a plane with two unknown constants. These constants--along with the remaining waveheight spectrum--can be determined by standard linear integral equation techniques.

The second situation, resulting at lower HF frequencies and for lower sea states, is more difficult, for there the integral equation remains nonlinear because the linearization of one of the S-factors is not possible. In this case, a differ-

ent linearization of the problem is accomplished by perturbations about a previous estimate, and this leads directly to an equation of the general form

$$(3) \quad \delta\sigma_{VV}^{(2)}(\eta) = \int K(\eta, \zeta) \delta S(\kappa_x(\zeta), \kappa_y(\zeta)) d\zeta,$$

where $\delta\sigma_{VV}^{(2)}$ is the difference between measured and calculated values of the spectrum, δS is the difference between true and previous estimate of the waveheight spectrum, and K is the known kernel.

A fundamental difficulty in solving (3) arises because measurements of $\sigma_{VV}^{(2)}$ contain noise which is uncorrelated with $S(\kappa_x, \kappa_y)$. Thus any attempt to satisfy (3) will be ultimately limited in accuracy by the noise level [7]. Our first attempt on the solution of (3) is underway at present, and is employing the Bacchus-Gilbert algorithm [8]. This inversion technique forms estimates of $S(\kappa_x, \kappa_y)$ from a linear combination of measurements with known noise level. A trade-off curve allows a comparison between resolution of S and error in S due to propagation of measurement errors. Thus this technique yields, at a given point, κ_x, κ_y , an estimate of S , its associated error variance, and its accuracy. Other stable algorithms (such as the Phillips-Twomey, the Landweber iteration, and statistical inversion) which are available at WPL will be used if the Bacchus-Gilbert method yields questionable results.

CONCLUSIONS

The results of a series of surface-wave measurements--backed by a theoretical model for first and second-order sea scatter--indicate that it will be possible to interpret the Doppler spectrum of sky-wave sea echo in terms of the waveheight directional spectrum. While a pattern recognition procedure of correlating an observed Doppler spectrum with a model of the directional sea spectrum is certainly possible, dominant emphasis at WPL is being given to numerical inversion of the echo spectrum to obtain the sea waveheight spectrum. Since previous correlations of echo spectra and waveheight spectra have thus far proved successful, the fairly close initial estimates required for the convergence of our integral equation inversion techniques seem assured. Thus it appears that the accuracy of the numerical inversion technique will ultimately be limited by "noise". This noise in an operational system will include external atmospheric noise, ionospheric spectral distortions and multi-path, and sea scatter of higher order than second. A sky-wave experimental program is to be undertaken shortly to determine the ultimate accuracy of an operational system. An important consideration which mitigates the accuracy requirements of a single observation is the fact that the sea state normally does not change significantly in a 6-hour period; during this time, a number of

observations of the same sea area can be made over a two or three octave frequency range, as ionospheric propagation conditions vary through their diurnal cycle. Such (essentially) independent observations--based upon a validated theoretical model--will certainly increase the accuracy of the sea state deductions possible with an operational system.

REFERENCES

- [1] S. R. Curley, J. M. Headrick, and J. L. Ahearn, "Determination of ocean surface conditions by long range radar reflections," paper presented at OHD Technical Review Meeting, U. S. Air Force Academy, 2-3 May 1973; appears in Conference Proceedings.
- [2] J. F. Ward, "Coherent-radar, ocean backscatter at high frequencies," submitted to *Nature Physical Science*, 1973.
- [3] D. E. Barrick, "First-order theory and analysis of MF/HF/VHF scatter from the sea," *IEEE Trans. Ant. Prop.*, vol. AP-20, pp. 2-10, 1972.
- [4] D. D. Crombie, "Backscatter of HF radio waves from the sea," from *Electromagnetic Probing in Geophysics*, ed. J. R. Wait, Boulder, Colo.: The Golem Press, pp. 131-162, 1971.
- [5] D. E. Barrick, "Remote sensing of sea state by radar," from *Remote Sensing of the Troposphere*, ed. V. E. Derr, Washington, D. C.: U. S. Government Printing Office, Chapter 12, 1972.
- [6] O. M. Phillips, *Dynamics of the Upper Ocean*, London: Cambridge at the University Press, pp. 109-139, 1966.
- [7] E. R. Westwater, and O. N. Strand, "Inversion techniques," from *Remote Sensing of the Troposphere*, ed. V. E. Derr, Washington, D. C.: U. S. Government Printing Office, Chapter 16, 1972.
- [8] Backus, G. F., and J. F. Gilbert, "Uniqueness in the inversion of inaccurate grass earth data," *Philosophical Transactions of the Royal Society of London*, Vol. 266, pp. 123-192, 1970.

Reprinted with permission from IEEE Transactions on Aerospace and Electronic Systems AES-8, No. 6, 743-750, November 1972.

Measurement of Distributed Targets With the Random Signal Radar

RUSSELL B. CHADWICK, Member, IEEE
Institute for Telecommunication Sciences
Boulder, Colo. 80302

GEORGE R. COOPER, Fellow, IEEE
Purdue University
Lafayette, Ind.

Abstract

A model of a distributed target as a collection of independent, Poisson distributed point scatterers or scattering centers in a range-velocity target space is introduced and is characterized by a deterministic function called the "scatterer density function." This function is the density of the point scatterers in the range-velocity space and can be estimated in a relatively straightforward manner by any radar having adequate resolution in both range and velocity and no ambiguities in the region occupied by the distributed target. The use of the random signal radar with a correlator receiver is considered here and the statistical properties of the correlator output, when the return signal is from a distributed target, are derived. It is shown that the spectral density is simply related to the scatterer density function.

The technique is illustrated by an example in which the target is a tornado modeled as a cylinder with constant angular velocity. The example suggests that it is possible to remotely estimate the radar cross section per unit volume as a function of distance from the center of the tornado.

Manuscript received March 19, 1971.

This paper is based upon a Doctoral thesis submitted to the faculty of Purdue University, Lafayette, Ind., by R. B. Chadwick. The work was supported by the U.S. Army Electronics Command, Fort Monmouth, N.J., under Contract DAA B07-67-C-0409 and by the U.S. Naval Avionics Facility, Indianapolis, Ind., under Contract N00 163-68-C-0106.

I. Introduction

Four important properties of any radar target are range, velocity, azimuth angle, and elevation (or depression) angle. The target can be considered as a point scatterer or collection of point scatterers in this four-dimensional space. If the radar can resolve each scattering point from all nearby scatterers in any of the four dimensions, the target is said to be "discrete." If, however, the radar cannot resolve any scattering point from nearby scatterers in any dimension of the space, it is a "distributed" target. There are also mixed targets which have a discrete component and a distributed component, and this is the situation that most often occurs.

The class of distributed targets can be further subdivided according to scatterer motion. If there is no relative motion between the scatterers that make up the distributed target, it is a rigid target. If the scatterers have relative motion, the target is nonrigid. Again, there are also targets that have both a rigid component and a non-rigid component.

The main concern here is the study of nonrigid, distributed targets in a two-dimensional target space. The two dimensions are range and velocity; all scattering points of interest are assumed to be in the antenna beam at the same time.

An appropriate waveform selection criteria for the study of distributed targets is based on the ambiguity function of the waveform. Since the distributed target will fill a large portion of the target space, the ambiguity function should have only one main peak. Also, since the objective is to determine how the target is distributed in the range-velocity target space, the main peak of the ambiguity function should be narrow in both dimensions. These two requirements imply that the ambiguity function should be a "thumbtack" ambiguity function. Cooper and Purdy [5] have derived the ambiguity function of a nondeterministic or stochastic signal. They show that this ambiguity function has a narrow central peak and a low, broad pedestal. Thus, a random waveform should be a good choice to study distributed targets.

The theory and application of the random signal radar have been documented elsewhere [3]-[5], [7] and will not be repeated here. The unique feature of this type of radar is that the transmitted signal is a purely random, nondeterministic signal having a known correlation function. In practice, this signal may be derived from the shot noise of a traveling wave tube. Also, the signal may be pulsed, as described in [9], in order to use the same antenna to transmit and receive. However, for convenience in this analytical study, the transmitted signal is assumed to be stationary, wide-band, Gaussian noise. If there is a single point target at range r at the time $t = 0$, moving with constant radial velocity v , then the time delay τ corresponding to range r , and the delay rate α , associated with a signal returned from this target, are given by

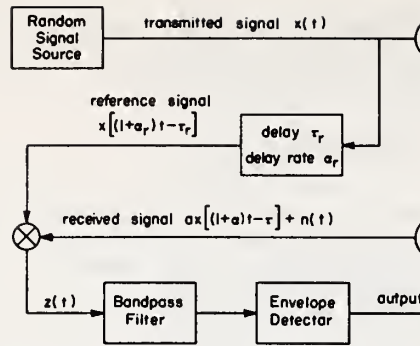


Fig. 1. Block diagram of the random-signal radar.

$$\tau = \frac{2r}{c}$$

$$\alpha = \frac{2v}{c - v} \approx \frac{2v}{c}$$

where c is the velocity of electromagnetic propagation. If the transmitted signal is designated as $x(t)$, the received signal from the single point target is $a(\tau)x[(1 + \alpha)t - \tau]$, where the attenuation coefficient $a(\tau)$ is real and between zero and one. This received signal plus receiver noise is cross correlated with a suitable reference signal, as shown in Fig. 1. The correlator output $z(t)$ may be considered to be the sum of its expected value and zero mean noise. The expected value of $z(t)$, which is the desired correlator output, is

$$E\{z(t)\} = E \left\{ a(\tau)x[(1 + \alpha)t - \tau] + n(t) \right. \\ \left. \cdot x[(1 + \alpha_r)t - \tau_r] \right\}$$

or, since $n(t)$ is zero mean and independent of $x(t)$,

$$E\{z(t)\} = \overline{a(\tau)} R_x[(\alpha_r - \alpha)t - (\tau_r - \tau)].$$

Since this is the autocorrelation function of a bandpass random process, it can be written in terms of a slowly varying envelope and a center frequency as

$$E\{z(t)\} = \overline{a(\tau)} R_c[(\alpha_r - \alpha)t - (\tau_r - \tau)] \\ \cdot \cos \omega_c[(\alpha_r - \alpha)t - (\tau_r - \tau)]. \quad (1)$$

A sketch of (1) is shown in Fig. 2. The radian frequency of the output is

$$\omega = \omega_c(\alpha_r - \alpha)$$

and the time at which the peak occurs is

$$t_p = \frac{\tau_r - \tau}{\alpha_r - \alpha}$$

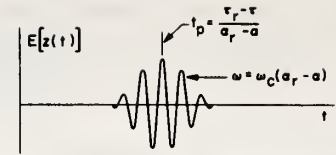


Fig. 2. Expected correlator output.

It is clear that the ability to resolve targets that are slightly separated in velocity depends on the bandwidth of the bandpass filter that follows the multiplier. Filters with narrower bandwidths will result in better velocity resolution. Also, the ability to resolve targets that are slightly separated in range depends on the width of the correlation function shown in Fig. 2. This width is inversely proportional to the bandwidth of the transmitted signal. The important thing is that the bandwidth of the transmitted signal and the bandwidth of the filter can be controlled independently. Thus, it is possible to simultaneously control the resolution in both range and velocity.

Another advantage of the random signal radar is that the signal is not periodic and, hence, there are no range ambiguities. The problem of ambiguous returns is a severe limitation on the use of pulse-Doppler radars to study widely distributed targets. The problem is due to the fact that the maximum unambiguous range and maximum unambiguous velocity are inversely related; in fact, their product is a constant. There is no such limitation for the random signal radar; since it has no range ambiguities, it can usually be operated in a mode that places the velocity ambiguities outside the region of interest.

The random signal radar receiver and correlator can be realized as a digital system [4], [7]. There are no severe limitations on the bandwidth or center frequency of the transmitted signal. Thus, the technique can also be employed with an acoustical or optical system.

II. Model of a Distributed Random Target

A random target is one that is a member of a target ensemble, each member of the ensemble being equally likely to occur. The target is assumed to be a collection of scattering centers or point scatterers, and the randomness of the target comes about because the number of point scatterers and their exact location in two-dimensional target space changes from one member of the ensemble to another. Also, the attenuation coefficients for each scatterer are random variables.

It is unlikely that a radar can determine the number of scatterers, along with the range and velocity of each, when this number is large. Even if this could be done, it would be of little value because only one member of the ensemble has been observed. Hence, rather than attempt to measure characteristics of one member of the ensemble,

it seems more reasonable to measure something that is characteristic of the whole ensemble.

Let $\Delta\tau\Delta\alpha$ denote a small area, smaller than a resolution cell, of the two-dimensional target space located around the τ, α point. This notation indicates not only the size of the small area, but also its location. Let $N|\Delta\tau\Delta\alpha$ be a random variable that is equal to the number of scatterers in the area $\Delta\tau\Delta\alpha$. The scatterer density function is defined as,

$$\rho(\alpha, \tau) = \frac{E[N|\Delta\tau\Delta\alpha]}{\Delta\tau\Delta\alpha} \quad (2)$$

and is a deterministic, nonrandom function that characterizes how the target is distributed in range-velocity space. The central problem considered here is how to estimate $\rho(\alpha, \tau)$ from the return radar signal.

There are two assumptions that must be made. First, the point scatterers are assumed to follow a Poisson distribution in the target space; i.e., in any small area $\Delta\tau\Delta\alpha$, the number of point scatterers $N|\Delta\tau\Delta\alpha$ is a random variable that is Poisson distributed [8, p. 378]. The second assumption is that the returns from the individual scatterers are independent of each other; i.e., the total power is the sum of the individual powers. This means that one (or both) of the following two conditions must be met. First, any two scatterers may be further apart (in range) than the correlation distance of the radar signal, and/or second, the scatterers are not fastened together. Close scatterers that have relative motion, such as raindrops, can still be independent. The assumption of independence is quite realistic for the types of targets considered here.

III. Description of Correlator Output

As shown in Section I, a single scatterer at τ, α in the target space causes a signal at the correlator output given by

$$u(t) = a(\tau)x[(1 + \alpha)t - \tau]x[(1 + \alpha_r)t - \tau_r] \quad (3)$$

where $a(\tau)$ is a random attenuation coefficient and is dependent upon range. Define $\Delta_z(t)$ as the component in the correlator output due to N scatterers in $\Delta\tau\Delta\alpha$. Thus, $\Delta_z(t)$ will be a sum of N terms, each having the form of (3). There is also a component at the correlator output due to receiver noise. This component is given by

$$z_n(t) = n(t)x[(1 + \alpha_r)t - \tau_r]. \quad (4)$$

Hence, the total output of the correlator is given by

$$z(t) = y(t) + z_n(t) \quad (5)$$

where

$$y(t) = \sum \Delta_z(t)$$

and the summation is over all the small $\Delta\tau\Delta\alpha$ areas.

Using the assumptions made above and the approach in either [2] or [8], the n th-order characteristic function of $y(t)$ can be shown to be

$$F_y[i\omega_1, \dots, i\omega_n] = \exp \left\{ \iint \rho(\alpha, \tau) \cdot E_{x,a} \left[\exp \left(i \sum_{l=1}^n \omega_l u(t_l) \right) - 1 \right] d\tau d\alpha \right\} \quad (6)$$

where $E_{x,a}[\cdot]$ denotes an expectation over the transmitted signal and the attenuation coefficients. This n th-order characteristic function is a complete statistical description of the signal component of the correlator output. Any of the moments of the correlator output can be found by using this characteristic function.

The correlator output is given by (5) as

$$z(t) = y(t) + z_n(t)$$

where the n th-order characteristic function of $y(t)$ is given by (6) and $z_n(t)$ is given by (4). The expected value of $z(t)$ is the sum of the expected values of $y(t)$ and $z_n(t)$, and since the receiver noise is independent of the transmitted signal and both are zero mean, the expected value of $z_n(t)$ is zero. The expected value of $y(t)$ can be found by differentiating the first-order characteristic function of $y(t)$, which leads to

$$E[y(t)] = \iint \rho(\alpha, \tau) E_{x,a}[u(t)] d\tau d\alpha$$

where $u(t)$ is given by (3). The expected value of the product of reference and received signals is just the autocorrelation function of the transmitted signal. Therefore,

$$E[z(t)] = \iint \rho(\alpha, \tau) \overline{a(\tau)} R_x[(\alpha_r - \alpha)t - (\tau_r - \tau)] d\tau d\alpha$$

where $a(\tau)$ indicates the mean attenuation coefficient at delay τ . It can be seen easily from (2) that, for a deterministic point target at α_0, τ_0 , the scatterer density function is given by an impulse

$$\rho(\alpha, \tau) = \delta(\alpha - \alpha_0, \tau - \tau_0).$$

Hence, for a deterministic point target, the expected output of the correlator is

$$E[z(t)] = \overline{a(\tau_0)} R_x[(\alpha_r - \alpha_0)t - (\tau_r - \tau_0)]$$

which is the same output as derived in Section I.

It is important to note that if $\rho(\alpha, \tau)$ is a slowly varying function compared to $R_x[(\alpha_r - \alpha_0)t - (\tau_r - \tau_0)]$, the expected output (as a function of time) is zero at any time. In the usual mode of operation, $R_x[\cdot]$ is a bandpass function, as in Fig. 2, and, hence, the expected value of the output is zero. This implies that first-order statistics are of little value when dealing with random distributed targets.

The next step is to find the autocorrelation function of

the correlator output. Since the receiver noise is zero mean and independent of the transmitted signal, the autocorrelation of $z(t)$ is given by

$$R_z(t_1, t_2) = R_y(t_1, t_2) + R_{z_n}(t_1, t_2). \quad (7)$$

At this point, it is convenient to assume that the transmitted signal and the receiver noise are Gaussian random processes. Then, using the fourth product moment, and noting that $\alpha_r \ll 1$,

$$R_{z_n}(t_1, t_2) = R_x(t_1 - t_2)R_n(t_1 - t_2).$$

The autocorrelation function of $y(t)$ can be found by differentiation of the second-order characteristic function. Performing the differentiations and assuming that $\rho(\alpha, \tau)$ is slowly varying,

$$E[y(t_1)y(t_2)] = \iint \rho(\alpha, \tau) E_{x,n}[u(t_1)u(t_2)] d\tau d\alpha. \quad (8)$$

Use of (3) and the fourth product moment gives

$$\begin{aligned} E_{x,n}[u(t_1)u(t_2)] &= \overline{a^2(\tau)} R_x[(1 + \alpha_r)(t_1 - t_2)] \\ &\quad R_x[(1 + \alpha)(t_1 - t_2)] \\ &\quad + \overline{a^2(\tau)} R_x[(\alpha_r - \alpha)t_1 - (\tau_r - \tau)] \\ &\quad R_x[(\alpha_r - \alpha)t_2 - (\tau_r - \tau)] \\ &\quad + \overline{a^2(\tau)} R_x[(1 + \alpha_r)t_1 - (1 + \alpha)t_2 - (\tau_r - \tau)] \\ &\quad R_x[(1 + \alpha_r)t_2 - (1 + \alpha)t_1 - (\tau_r - \tau)] \end{aligned}$$

where $\overline{a^2(\tau)}$ indicates the mean-square value of the attenuation coefficient. This mean-square value is a function of delay. Substitution of this equation into (8) yields three integrals. Considering the third integral first, writing the correlation functions as in (1) and combining the cosine terms gives

$$\begin{aligned} I_3 &= \iint \overline{a^2(\tau)} \rho(\alpha, \tau) \\ &\quad \cdot R_c[(1 + \alpha_r)t_1 - (1 + \alpha)t_2 - (\tau_r - \tau)] \\ &\quad \cdot R_c[(1 + \alpha_r)t_2 - (1 + \alpha)t_1 - (\tau_r - \tau)] \\ &\quad \cdot \left\{ \frac{1}{2} \cos \omega_c [(\alpha_r - \alpha)(t_1 + t_2) - 2(\tau_r - \tau)] \right. \\ &\quad \left. + \frac{1}{2} \cos \omega_c [(2 + \alpha_r + \alpha)(t_1 - t_2)] \right\} d\tau d\alpha. \end{aligned}$$

When the first of these two terms is integrated over τ , the result is essentially zero, since $\omega_c \tau$ goes through many periods in the width of $R_c[\cdot]$. The second term is a high-frequency term that will be filtered out and can be neglected. Therefore, the remaining terms of (8) become

$$\begin{aligned} E[y(t_1)y(t_2)] &= \iint \rho(\alpha, \tau) \\ &\quad \cdot \{ \overline{a^2(\tau)} R_x[(1 + \alpha_r)(t_1 - t_2)] R_x[(1 + \alpha)(t_1 - t_2)] \\ &\quad + \overline{a^2(\tau)} R_x[(\alpha_r - \alpha)t_1 - (\tau_r - \tau)] \\ &\quad \cdot R_x[(\alpha_r - \alpha)t_2 - (\tau_r - \tau)] \} d\tau d\alpha. \end{aligned}$$

Noting that $\alpha_r \ll 1$, and that $\alpha \ll 1$ over the significant region of the integral, and using (7), gives

$$\begin{aligned} R_z[t_1, t_2] &= \iint \rho(\alpha, \tau) \{ \overline{a^2(\tau)} R_x[t_1 - t_2] R_x[t_1 - t_2] \\ &\quad + \overline{a^2(\tau)} R_x[(\alpha_r - \alpha)t_1 - (\tau_r - \tau)] \\ &\quad \cdot R_x[(\alpha_r - \alpha)t_2 - (\tau_r - \tau)] \\ &\quad + R_x[t_1 - t_2] R_n[t_1 - t_2] \}. \end{aligned}$$

The received power from ranges other than the range of interest (uncorrelated clutter power) is approximately given by

$$P_c = \iint P_T \overline{a^2(\tau)} \rho(\alpha, \tau) d\tau d\alpha$$

from the definitions of $a(\tau)$ and $\rho(\alpha, \tau)$, where P_T is the transmitted power. Therefore, the autocorrelation function of the correlator output is

$$\begin{aligned} R_z[t_1, t_2] &= R_x[t_1 - t_2] R_n[t_1 - t_2] \\ &\quad + \frac{P_c}{P_T} R_x^2[t_1 - t_2] \\ &\quad + \iint \overline{a^2(\tau)} \rho(\alpha, \tau) R_x[(\alpha_r - \alpha)t_1 - (\tau_r - \tau)] \\ &\quad R_x[(\alpha_r - \alpha)t_2 - (\tau_r - \tau)] d\tau d\alpha. \quad (9) \end{aligned}$$

The first term in (9) is due to the receiver noise; the second term is due to the uncorrelated clutter; and the third term is due to the correlated clutter. Note that even though the transmitted signal is stationary, the component in the output due to the correlated clutter is nonstationary, while the other two components are stationary.

IV. Spectral Density of Correlator Output

The fact that the correlator output can be nonstationary causes difficulties when attempting to evaluate the spectral density. If nothing is changing with time, including the reference delay, the correlator output can be considered stationary. The case where the reference delay is scanning relatively slowly approximates the situation where the correlator output is stationary. In this section, the spectral density of the correlator output

is related to the scatterer density function.

In Section III the autocorrelation function of the correlator output was shown to be composed of the three terms in (9). Since two of these, the receiver noise component and the uncorrelated clutter component, readily combine, the spectral density of the correlator output is a combination of two terms and may be written as

$$S_z(\omega) = S_1(\omega) + S_2(\omega). \quad (10)$$

The first term, $S_1(\omega)$, is the component due to receiver noise and uncorrelated clutter, while $S_2(\omega)$ is due to the correlated clutter.

The two terms in (10) can be found by taking Fourier transforms of the appropriate terms in (9). The component due to the receiver noise and the uncorrelated clutter is given by

$$S_1(\omega) = \mathcal{F}\{R_x(t_1 - t_2)R_n(t_1 - t_2) + \frac{P_c}{P_T} R_x(t_1 - t_2) R_x(t_1 - t_2)\}$$

where the Fourier transform is, with respect to the time difference, $t_1 - t_2$. Evaluation of this transform gives

$$S_1(\omega) = \frac{1}{2\pi} \left\{ S_x(\omega) * S_n(\omega) + \frac{P_c}{P_T} S_x(\omega) * S_x(\omega) \right\} \quad (11)$$

where * implies convolution in the frequency domain. Since $x(t)$ and $n(t)$ are wide-band signals, the convolution operations in (11) will result in wide-band signals with nonzero spectral density at $\omega = 0$. Since the signals of interest are relatively low frequency, $S_1(\omega)$ can be assumed white. If the receiver noise is white with spectral density N_0 and the reference signal is band-limited white noise with spectral density X_0 , and bandwidth B (hertz), then $S_1(0)$ is

$$S_1(0) = 2N_0X_0B + \frac{P_c}{P_T} 2X_0^2B$$

or

$$S_1(0) = P_T N_0 + P_c X_0 \quad (12)$$

where P_T is the reference signal power and is assumed to be identical to the transmitted signal power, as shown in Fig. 1. The actual power of the reference signal does not affect the signal-to-noise ratios in any way, so this assumption is simply a matter of convenience.

Next, the spectral density of the contribution due to the correlated clutter must be determined. Let the autocorrelation function of this contribution be $R_2[t_1, t_2]$. From (9),

$$R_2[t_1, t_2] = \iint \overline{a^2(\tau)} \rho(x, \tau) R_c[(x_r - x)t_1 - (\tau_r - \tau)] \cdot R_c[(x_r - x)t_2 - (\tau_r - \tau)]$$

$$\cdot \cos \omega_c[(x_r - x)t_1 - (\tau_r - \tau)]$$

$$\cos \omega_c[(x_r - x)t_2 - (\tau_r - \tau)] d\tau dx.$$

The cosine product can be expanded as a sum of cosines, one of which has τ in its argument. When this is integrated over τ , the result will be small and can be neglected. The second cosine term is not a function of τ , and the autocorrelation function of the correlated clutter can be written as

$$R_2[t_1, t_2] = \int \cos \omega_c(x_r - x)(t_1 - t_2)$$

$$\cdot \int \frac{1}{2} \overline{a^2(\tau)} \rho(x, \tau)$$

$$\cdot R_c[(x_r - x)t_1 - (\tau_r - \tau)]$$

$$\cdot R_c[(x_r - x)t_2 - (\tau_r - \tau)] d\tau dx.$$

The autocorrelation functions are typically quite narrow. Therefore, the τ integral will take on an appreciable value only when the two autocorrelation functions are at the same point. Suppose this point is determined by time t_0 ; then the slowly varying scatterer density function can be taken outside the integral and evaluated at $\tau_0 = \tau_r - x_r t_0$. If this approximation is made only in the τ integral, the result is

$$R_2[t_1, t_2] = \int \frac{1}{2} \overline{a^2(\tau_0)} \rho(x, \tau_0) \cos \omega_c(x_r - x)(t_1 - t_2) \cdot \int R_c^2[(x_r - x)t_0 - (\tau_r - \tau)] d\tau dx. \quad (13)$$

A common definition of bandwidth is

$$B = \frac{P_T^2}{\int R_c^2(\tau) d\tau}.$$

Therefore,

$$\int R_c^2[(x_r - x)t_0 - (\tau_r - \tau)] d\tau = \frac{P_T^2}{B}.$$

This can then be substituted into (13):

$$R_2[t_1, t_2] = \frac{P_T^2}{B} \int \frac{1}{2} \overline{a^2(\tau_0)} \rho(x, \tau_0) \cdot \cos \omega_c(x_r - x)(t_1 - t_2) dx. \quad (14)$$

The spectral density of the correlated clutter can be found by taking the Fourier transform of (14) with respect to $t_1 - t_2$. When this is done, (14) becomes

$$S_2(\omega) = \frac{\pi P_T X_0}{\omega_c} \left\{ \overline{a^2(\tau_0)} \rho \left(x_r + \frac{\omega - \omega_0}{\omega_c}, \tau_0 \right) + \overline{a^2(\tau_0)} \rho \left(x_r - \frac{\omega - \omega_0}{\omega_c}, \tau_0 \right) \right\} \quad (15)$$

where ω_0 is a frequency offset (see [4]) introduced in the local oscillator. For the types of targets considered here, the frequency offset can be chosen larger than the largest Doppler frequency, and this results in one of the terms of (15) being zero, so that the spectral density due to correlated clutter becomes

$$S_2(\omega) = \frac{\pi P_T X_0}{\omega_c} \overline{a^2(\tau_0)} \rho \left(\alpha_r + \frac{\omega - \omega_0}{\omega_c}, \tau_0 \right). \quad (16)$$

Hence, using (10), (12), and (16), the spectral density at the output of the correlator is

$$S_z(\omega) = P_T N_0 + P_c X_0 + \frac{\pi X_0}{\omega_c} P_T \overline{a^2(\tau_0)} \rho \left(\alpha_r + \frac{\omega - \omega_0}{\omega_c}, \tau_0 \right). \quad (17)$$

Equation (17) is the two-sided spectral density of the correlator output. It is convenient to express this spectral density in the one-sided form as

$$S_z(f) = 2P_T N_0 + 2P_c X_0 + \frac{P_T X_0}{f_c} \overline{a^2(\tau_0)} \rho \left(\alpha_r + \frac{f - f_0}{f_c}, \tau_0 \right). \quad (18)$$

The value of reference delay at the "current" time, t_0 , is denoted by τ_0 and is equal to $\tau_r - \alpha_r t_0$.

It has been tacitly assumed that during the time that it takes to find the spectral density at the output of the correlator, the signal can be considered stationary. This will be the case when the reference delay rate is small.

V. Example of Tornado Detection

One of the most interesting and important types of distributed targets is that of weather formations. These include thunderstorms, tornados, and clear air turbulence. There has been a great deal of work done in the study of severe storms by radar [1]. However, most of this work has been done using pulse radars that give no indication of target velocities, and only recently has there been interest in using Doppler radars for the study of weather phenomena [6]. Most of the radars used have been pulse-Doppler radars, and these have some disadvantages. In the first place, the range cell is equal to the length of the pulse, so it is difficult to achieve extremely good resolution in range with adequate power and velocity resolution. For this reason, the fine-scale structure of meteorological phenomena has been largely uninvestigated. Second, as pointed out in Section I, the problem of ambiguous returns is a severe limitation of the use of pulse-Doppler radars to study widely distributed targets. Since the random signal radar has no range ambiguities, it is usually possible to operate with a pulse rate such that the ambiguous returns in Doppler are of no concern. This property means that the random signal radar can mea-

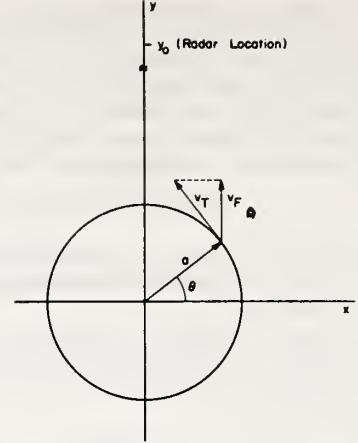


Fig. 3. Tornado geometry.

sure very wide Doppler spectra. Pulse-Doppler radars would encounter range ambiguities in making the same measurement.

Consider a tornado to be a mass of air and scatterers turning with an angular velocity Ω . This is an adequate model if the region where there is wind shear has small radar cross section. Let (r, θ) be polar coordinates and (x, y) be Cartesian coordinates, both centered at the center of the tornado, as shown in Fig. 3. Let $\eta(r)$ be the radar cross section per unit volume of the tornado. Assume that the radar is located on the positive y axis, at $y = y_0$, and that y_0 is such that the tornado is in the far field of the antenna. Also, assume that all parts of the tornado are illuminated equally. Denote the tangential velocity of any point in the tornado by V_T . Thus, $V_T \cos \theta$ is the Doppler producing velocity of this point. Denote this Doppler producing component by V_F . Thus,

$$V_F = r\Omega \cos \theta = x\Omega \quad (19)$$

and

$$\alpha = \frac{2V_F}{c} = \frac{2x\Omega}{c}. \quad (20)$$

Since the tornado is in the far field of the antenna, time delay is related only to the y variable. The time delay for any point is given by

$$\tau = \frac{2(y_0 - y)}{c}. \quad (21)$$

Equations (20) and (21) will be used to determine the relationship between the scatterer density function and the radar cross section per unit volume by examining the output spectral density.

Let $\delta x \delta y$ be a small area in the x, y plane, and let $\delta \tau \delta \alpha$ be a small area in the τ, α plane. These relations follow from (20) and (21):

$$x = \frac{c\alpha}{2\Omega}; \quad \delta x = \frac{c}{2\Omega} \delta\alpha$$

$$y = y_0 - \frac{c\tau}{2}; \quad \delta y = \frac{c}{2} \delta\tau. \quad (22)$$

Let P_1 be the power returned from the volume that has $\delta x \delta y$ as a base and a height H , the height of the tornado. The radar equation gives (for the transmitter power of P_T)

$$P_1 = \frac{P_T G^2 \lambda^2 H}{(4\pi)^3 (y_0 - y)^4} \eta (\sqrt{\lambda^2 + y^2}) \delta x \delta y \quad (23)$$

where G is the one-way antenna power gain. Note that since the tornado is in the far field of the antenna, $y_0 \gg y$ for any y in the tornado. Equation (23) can be converted into the power returned from a small area of the τ, α plane by using (22). Thus,

$$P_1 = \frac{P_T G^2 \lambda^2 H}{(4\pi)^3 y_0^4} \eta \left(\sqrt{\left(\frac{c\alpha}{2\Omega}\right)^2 + \left(y_0 - \frac{c\tau}{2}\right)^2} \right) \frac{c^2}{4\Omega} \delta\alpha \delta\tau.$$

This same power can be written using the scatterer density function, and is

$$P_1 = P_T \overline{a^2(\tau)} \rho(\alpha, \tau) \delta\alpha \delta\tau.$$

Therefore,

$$\overline{a^2(\tau)} \rho(\alpha, \tau) = \frac{G^2 \lambda^2 c^2 H}{4(4\pi)^3 y_0^4 \Omega} \eta \left(\sqrt{\left(\frac{c\alpha}{2\Omega}\right)^2 + \left(y_0 - \frac{c\tau}{2}\right)^2} \right).$$

If τ is adjusted so that the range cell is in the center of the tornado, i.e., $\tau = 2y_0/c = \tau_0$, then

$$\overline{a^2(\tau_0)} \rho(\alpha, \tau_0) = \frac{G^2 \lambda^2 c^2 H}{4(4\pi)^3 y_0^4 \Omega} \eta \left(\left| \frac{c\alpha}{2\Omega} \right| \right). \quad (24)$$

The spectral density of the correlator output is obtained by substituting (24) into (18).

If there is no range sweep, i.e., if $\alpha_r = 0$, then

$$S_z(f) = 2P_T N_0 + 2P_T X_0 + P_T \frac{G^2 \lambda^3 c H X_0}{4(4\pi)^3 y_0^4 \Omega} \eta \left(\left| \frac{\lambda}{2\Omega} f - f_0 \right| \right).$$

This spectral density can then be estimated with a bank of filters or with a spectrum analyzer. This would not only aid in detecting these types of targets, but would also allow their structure to be studied and more clearly understood.

An example relating the scatterer density function to conventional radar terms when the velocity information is not desired is given in [3].

TABLE I
Tornado Parameters

| Parameters | Value |
|-----------------------------|-----------------------|
| average transmitted power | 10 ³ watts |
| bandwidth | 15 MHz |
| wavelength | 3 cm |
| effective noise temperature | 2000° K |
| vertical beamwidth | 0.1 rad |
| horizontal beamwidth | 0.05 rad |

TABLE II
Radar Parameters

| Parameters | Value |
|-------------------------------------|----------------------------------|
| radar cross section per unit volume | 10 ⁻⁷ m ⁻¹ |
| radius of tornado | 100 meter |
| angular velocity of tornado | 1 rad/sec |
| range to tornado | 20 km |
| height of tornado | 1 km |

Assume that an isolated tornado has a constant radar cross section per unit volume extending over a radius r_0 . Assume, further, that the tornado has parameters as given in Table I. Also, assume that the radar has parameters as given in Table II.

The spectral density of the correlator output can be estimated with a bank of 14 bandpass filters, each with a bandwidth of 1000 Hz. Each bandpass filter is followed by a square-law envelope detector, which, in turn, is followed by a low-pass filter with a 10-Hz bandwidth. The signal-to-noise ratio at the output of each branch, for the parameters in Tables I and II, is 132 or 21 dB.

VI. Conclusions

It appears feasible to measure the attenuation coefficient-scatterer density function product, $a^2(\tau) \rho(\alpha, \tau)$, with the random signal radar. A possible application of this technique to the detection of tornados has been discussed. There are numerous other meteorological applications, including precipitation studies and clear air turbulence (CAT) detection. The detection of hazardous CAT with a random signal radar mounted onboard the aircraft is particularly attractive since there would be no mutual interference with similar radars onboard other aircraft.

Another possible application is a high resolution radar study of the sea surface. It is well known that sea return for a vertically downward pointing radar is mainly due to specular points on the surface. Information on how these points are distributed in range and velocity, i.e., the scatterer density function, would be immensely valuable to

oceanographers. The high resolution attainable (20 cm or less) would allow an accurate and direct measurement of wave height (see [3]).

The technique outlined here might also be useful in certain situations in the atmosphere. This could aid in an understanding of the motion of such pollutants, as well as serve as a particulate density monitor.

References

- [1] D. Atlas, "Radar analysis of severe storms," *Meteorol. Mono.*, vol. 5, no. 27, September 1963.
- [2] R. B. Chadwick, "Use of random signals to study distributed radar targets," Ph.D. thesis, Purdue University, Lafayette, Ind., August 1970.
- [3] R. B. Chadwick and G. R. Cooper, "Measurement of ocean wave heights with the random signal radar," *IEEE Trans. Geoscience Electronics*, vol. GE-9, October 1971.
- [4] G. R. Cooper and C. D. McGillem, "Random signal radar," Purdue University, Lafayette, Ind., Tech. Rept. TR-EE67-11, June 1967.
- [5] G. R. Cooper and R. J. Purdy, "Detection, resolution and accuracy in the random signal radar," Purdue University, Lafayette, Ind., Tech. Rept. TR-EE68-16, August 1968.
- [6] R. M. Lhermitte, "Application of pulse Doppler radar techniques to meteorology," *Bull. Am. Meteorol. Soc.*, vol. 49, no. 9, September 1966.
- [7] C. D. McGillem, G. R. Cooper, and W. B. Waltman, "Use of wide-band stochastic signals for measuring range and velocity," 1969 *EASCON Rec.*
- [8] D. Middleton, "A statistical theory of reverberation and similar first-order scattered fields, Part I," *IEEE Trans. Information Theory*, vol. IT-13, July 1967.
- [9] R. B. Chadwick and G. R. Cooper, "A clutter reduction technique for coded radars," *IEEE Trans. Aerospace and Electronic Systems* (to be submitted).



Russell B. Chadwick (S' 63—M' 70) was born in Cody, Wyo., on June 4, 1942. He received the B.S. degree from the Montana State University, Bozeman, in 1964, the M.S. degree from the University of Wyoming, Laramie, in 1966, and the Ph.D. degree from Purdue University, Lafayette, Ind., in 1970, all in electrical engineering.

He has been employed in an engineering capacity by the Power Division of the U.S. Bureau of Reclamation and by the Natural Resource Research Institute, Laramie. From 1966 to 1970 he was an Instructor at Purdue University. He is currently with the Institute for Telecommunication Sciences in Boulder, Colo., where he is engaged in work involving satellite communications and multiple-access systems, and channel sounding for high data rate communications. He has also been closely involved in sensing of atmospheric refractive index structure with the FM-CW radar, and he is teaching a graduate level course on remote probing at the University of Colorado.

Dr. Chadwick is a member of Sigma Xi and Eta Kappa Nu. He is on the IEEE Communications Society Committee on Education.



George R. Cooper (A'44—M'44—F'69) was born in Connorsville, Ind., on November 29, 1921. His undergraduate and graduate training were at Purdue University, Lafayette, Ind., where he received the Ph.D. degree in electrical engineering in 1949.

Since 1943 he has been on the staff of Purdue University, where he is currently Professor of Electrical Engineering. He was Assistant Head for Graduate Study in the School of Electrical Engineering from 1965 to 1969. His teaching and research have been in the areas of radar, statistical communication theory, estimation theory, and systems analysis. He has had extensive consulting experience in the areas of active and passive radar systems, adaptive control systems, signal design, multiple-access communication systems, seismic data analysis, interference prediction, and electromagnetic compatibility.

Dr. Cooper is a member of Tau Beta Pi, Eta Kappa Nu, Sigma Xi, Sigma Pi Sigma, and the ASEE. He is a member of the Board of Governors of the IEEE Communications Society, and Chairman of the Education Committee of that Society. He is also a past member of the Administrative Committee of the IEEE Information Theory Group, and past Chairman of the Chicago Area Chapter of the Information Theory Group.

Reprinted from the Proceedings of Conference on Propagation of Radio Waves at Frequencies above 10 GHz, London, April 10-13, 1973.

CORRECTION OF ELECTRICAL PATH LENGTH BY PASSIVE MICROWAVE RADIOMETRY

M.T. Decker, F.O. Guiraud and E.R. Westwater

INTRODUCTION

Sophisticated missile and space tracking systems require accurate methods of correcting for the atmospheric contribution to electrical path length along slant paths through the atmosphere. Similar problems arise in correcting for atmosphere-induced differential time delays in radio astronomical observations using long-baseline interferometry. Currently used correction techniques depend on limited meteorological information from surface or radiosonde observations, and generally require the assumption of horizontal stratification of atmospheric variables. This paper describes an experimental evaluation of a technique for determining the highly variable wet component of integrated refractivity by passive emission measurements near the 22.235 GHz water vapor absorption line. This technique determines the most variable component of the required correction and, since the measurement can be made in any desired direction, does not require an assumption of atmospheric stratification.

The radiometric technique for obtaining the wet component of range correction has been described by Menius, et al. (1964) and Westwater (1967). These authors show that the total absorption of atmospheric water vapor near the 22.235 GHz absorption line can be directly related to the integral of the wet component of refractivity, and the absorption can be determined from passive observations of thermal emission at that frequency.

Because of atmospheric refraction, a tracking system observes an apparent range equal to $\int_0^s n ds$, where n is the refractive index of the atmosphere, ds is an increment of path length, and the integration extends from the observer to the tracked object. Neglecting bending, the range error is then $\int (n-1) ds = 10^{-6} \int N ds$, where N is refractivity as usually defined ($N \equiv (n-1) 10^6$). The refractivity may be separated into a dry (and predictable) component and a highly variable wet component resulting in a residual refraction correction that depends mainly on the water vapor term, $\int N_w ds$. In general there is no simple relation between this term and the wet component of integrated absorption, $\int \alpha_w ds$, where α_w is the water vapor absorption coefficient. However, it is possible to find a frequency near the water vapor absorption line where the two integrals are very nearly proportional over the range of temperature, pressure, and water vapor density normally encountered in the troposphere, and we can write

$$\int_0^\infty \alpha_w ds = g(\nu_1) \int_0^\infty N_w ds, \quad (1)$$

where ν_1 is an optimum frequency and $g(\nu_1)$ is the known constant of proportionality. On the basis of Westwater's (1967) analysis we have chosen 20.6 GHz for our experiments. The total integrated absorption $\int \alpha ds$ can be accurately determined from sky brightness measurements. The radiative transfer equation is written

$$T_b = \int_0^\infty T \alpha e^{-\int_0^s \alpha ds'} ds, \quad (2)$$

The authors are with the National Oceanic and Atmospheric Administration, Environmental Research Laboratories, Boulder, Colorado, U. S. A.

where T_b is the sky brightness temperature and T is the temperature of the medium. A "mean radiating temperature," T_m , can be estimated for T , and the integration in (2) performed to give

$$\int_0^\infty \alpha ds = -\ln \left(1 - \frac{T_b}{T_m} \right) \quad (3)$$

The total integrated absorption at 20.6 GHz consists of a small dry component τ_d , and a larger more variable wet component. An estimate of τ_d is subtracted from (3) which is then combined with (1) to give

$$\int_0^\infty N_w ds = \frac{1}{g(v_1)} \left[-\ln \left(1 - \frac{T_b}{T_m} \right) - \tau_d \right] \quad (4)$$

This is the basic equation used to convert radiometric observations of T_b to range correction $\int N_w ds$. The quantities $g(v_1)$, T_m and τ_d are determined from climatological and surface meteorological data.

The objective of the experimental program was to verify the relationship between $\int N_w ds$ and T_b as predicted by (4). The first method is to measure independently the fluctuations of the two sides of (4) and to compute the correlation between them. This method does not require an absolute measure of $\int N_w ds$, obviates the need for estimation of $g(v_1)$, and greatly reduces the accuracy requirements on the other quantities on the right hand side of (4). Second, in one of the experimental periods an attempt was made to measure the absolute values of the quantities in (4) as a function of time.

INSTRUMENTATION AND OBSERVATION

Experiments of two-week duration were conducted in 1968 and 1971, and three general categories of measurements were made. These are phase of arrival of signals propagated over a fixed path, thermal radiation from the atmosphere at 20.6 GHz, and various surface and airborne meteorological measurements.

The fluctuations of $\int N ds$ are measured by observing the variations in phase of a microwave (10 GHz) signal propagated over a fixed test path. This test path is chosen so that the upper terminal is above as much of the atmospheric water vapor as possible, and hence a sea level-to-mountain top path in the Hawaiian Islands was used. The 64-km path extends from a height of 30 m above sea level at Upolu Point at the northern tip of the island of Hawaii to the top of the mountain Haleakala on the island of Maui at an altitude of 3048 m, resulting in an elevation angle of 2.49° as seen from Upolu Point. The path is almost completely over water and the steep slope of Haleakala provides a path with no obstructions. In general, approximately 90 percent of the atmospheric water vapor was below the mountain top.

During the 1971 period a series of path length measurements were made using the optical spectrum where the effect of water vapor on apparent path length is quite small. This, together with simultaneous measurements of temperature by aircraft flights along the path, allowed an independent measure of the geometric path length. The fixed geometric path length together with the measured electrical path length at the microwave frequency then gives an absolute value of $\int N ds$ to be used in comparison with the radiometrically derived values.

Thermal radiation from the atmosphere (in terms of sky brightness temperature T_b) was measured with a Dicke radiometer and a 1.2-m aperture antenna located at Upolu Point (Guiraud, et al., 1971). It was not possible to direct the antenna along the same path used for phase measurements since thermal radiation from the mountain itself would influence the results. The antenna was pointed in a fixed direction for most of the recording

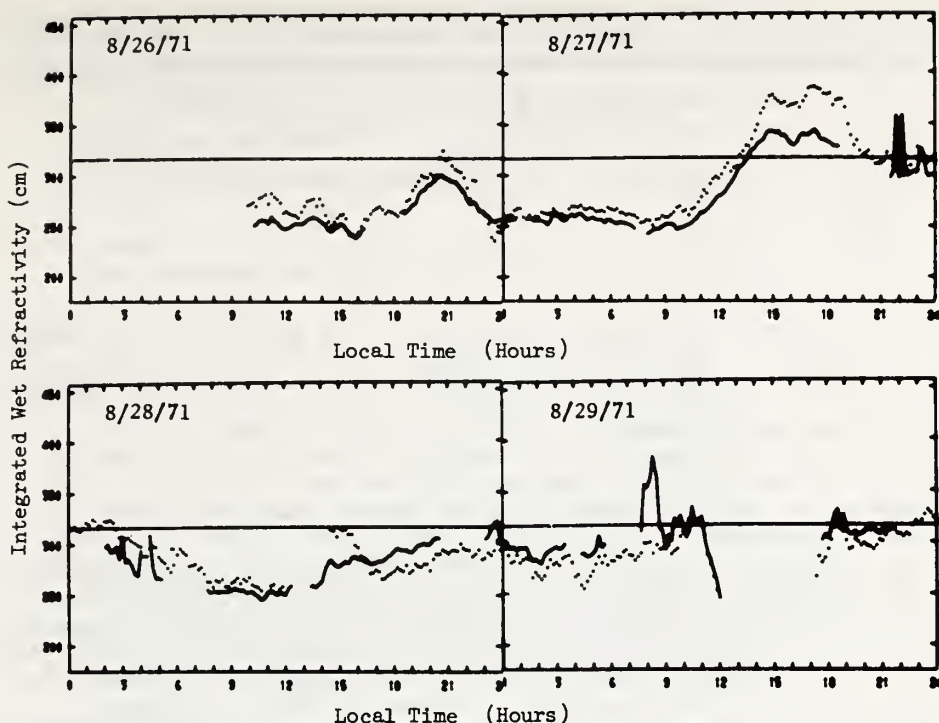


Fig. 1. Comparison of integrated wet refractivity derived from path length measurements (dots) and from radiometric measurements (solid curve).

period, with short interruptions for observation of sky brightness as a function of elevation angle. In the 1968 experiment the antenna was pointed at an elevation angle of 7.5° where the greatest variation of T_b normally occurs, and at an azimuth 15° west of the bearing to Haleakala in order to minimize the influence of clouds. This pointing direction was changed in the 1971 experiment to an elevation angle of 3.3° on the bearing to Haleakala. Details of the radiometric instrumentation and the conversion of a power measurement at the antenna input terminals to the sky brightness temperature are given by Guiraud, et al., (1971).

Meteorological data consisted of surface temperature, pressure, and humidity measurements, radiosonde releases, and time-lapse photographs and operator comments on cloud and weather conditions. Radiosondes were released at 3-hour intervals in the 1968 period, while in 1971 the releases were on an irregular schedule of approximately 3 per day. Meteorological data were used primarily for determination of constants required in (4), and in the conversion to brightness temperature mentioned above.

RESULTS AND CONCLUSIONS

An example of the comparison of the absolute values of the integrated wet refractivity derived from path length measurements and from radiometric measurements is shown in Figure 1, where data from the first four days of the 1971 recording period are shown. As mentioned earlier, the integrated refractivity $\int N_{ds}$ is taken to be the difference between the electrical

Table 1. Cross correlation between microwave range fluctuations and sky brightness temperature during two-week recording periods in 1968 and 1971.

| Year | Clear and nearly clear skies | | All data | |
|------|------------------------------|------------------|-------------|------------------|
| | Correlation | Number of points | Correlation | Number of points |
| 1968 | 0.76 | 337 | 0.70 | 546 |
| 1971 | 0.90 | 547 | 0.86 | 1241 |

path length measured at microwave frequencies and the geometrical path length. The dry component of this integral is estimated from meteorological data and the remainder is assumed to be the contribution of water vapor. This quantity is plotted as the dotted curve in Figure 1. The solid curve is derived from the sky brightness T_b using (4). In this equation a constant value of $g(\nu_1)$ derived from radiosonde data is used for the entire recording period. The values for mean radiating temperature T_m , and total dry absorption τ_d are derived from surface meteorological data taken at the time of range and radiometric measurements. Two adjustments must be made to the data to allow a direct comparison with the path-length measurements. First, an adjustment for the difference in elevation angle is made by using the geometry of a curved earth and the average bending of radio rays at the appropriate elevation angles. Second, since the radiometer observes the line integral of water vapor through the entire atmosphere, the integral derived from (4) is reduced by the average fraction of total water vapor below the 3048-m level as indicated by radiosonde data. All available data are plotted including periods during which clouds were present. The effect of clouds on the radiometric data can be seen clearly at about 2200 hours on 27 August 1971. For the entire two-week period, the means of the two curves differ by 12.4 cm, with nearly equal standard deviations of 46.9 and 49.8 cm for the dotted and solid curves respectively. While an error analysis is not presented here, the difference of means is well within the expected range, and shows that the path length as measured by the microwave and optical techniques differs by less than 2 parts per million.

Correlation coefficients were computed for variations in microwave range and corresponding sky brightness temperatures at the fixed pointing direction over each of the two recording periods. These results are summarized in Table 1. Pairs of points are taken at 30-minute intervals in the 1968 data and at 10-minute intervals in 1971. In each case the correlations are computed for all data and for the subset for which the operator classified the sky as clear or nearly clear. In addition, correlations were computed for the individual days of the recording period and these ranged from -0.24 to 0.93 in 1968 and from 0.24 to 0.94 in 1971 when all data were included regardless of the presence or absence of clouds. Correlations were also computed from data recorded during observation of sky brightness as a function of elevation angle. These results are given in Table 2, where it is noted that the maximum correlations occur at elevation angles comparable to that of the fixed path from sea level to mountain top.

These data show a significant improvement in correlation as the phase propagation path and emission path become closer together. This indicates that the water vapor distribution departs significantly from horizontal stratification. We conclude that when range measurements must traverse a

Table 2. Cross correlation between microwave range fluctuations at 2.5° elevation angle and sky brightness temperature at various elevation angles. Each coefficient is computed from 74 points for the 1968 data and 52 points for the 1971 data.

| Elevation Angle (degrees) | Correlation Coefficient | |
|------------------------------|-------------------------|------|
| | 1968 | 1971 |
| 1.0 | - | .78 |
| 2.5 | - | .91 |
| 2.8 | .76 | - |
| 3.3 | - | .92 |
| 4.5 | .78 | .91 |
| 7.5 | .77 | .88 |
| 11.2 | .75 | .85 |
| 22.5 | .71 | .86 |
| 90.0 | .67 | .85 |

large portion of the atmosphere, refractivity corrections derived from the radiometric technique provide an appreciable improvement in accuracy as compared to a method based on radiosonde measurements. It is also evident that cloud effects in some cases are serious, and we are currently evaluating a dual frequency method for correcting these errors.

ACKNOWLEDGEMENTS

We express our thanks to the EHF-Optical Wave Propagation Group of the Institute for Telecommunication Sciences who were responsible for obtaining the electrical range data reported here. This work was partially funded by the U. S. Air Force Electronic Systems Division and the U. S. Army SAFEGUARD Systems Command.

REFERENCES

- Guiraud, F. O., M. T. Decker, and E. R. Westwater (1971), Experimental investigation of the correction of electrical range errors by passive microwave radiometry, NOAA Tech. Rept. ERL-221-WPL 19.
- Menius, A. C., C. F. Martin, W. M. Layson, and R. S. Flagg (1964), Tropospheric refraction corrections using a microwave radiometer, Pan American Airways Technical Staff Technical Memo No. 19, ETV-TM-64-12.
- Westwater, E. R. (1967), An analysis of the correction of range errors due to atmospheric refraction by microwave radiometric techniques, ESSA Tech. Rept. No. IER 30-ITSA 30.

Reprinted from the Proceedings of Conference at U.S. Air Force Academy,
Colorado Springs, May 2-3, 1973.

SOME FEATURES OF SEA ECHO AT HF (U)

J. M. Headrick

Naval Research Laboratory
Washington, D.C.

D. E. Barrick J. B. Snider

National Oceanic and Atmospheric Administration
Boulder, Colorado

ABSTRACT (U)

(U) Examples of the HF groundwave radar sea echo obtained in the NONESUCH program have been examined. The dominant resonant line served as a constant-amplitude target within ± 3 dB when the sea was fully developed. The higher-order response is shown for the first time to contain a measure of sea state.

I INTRODUCTION (U)

(U) Preliminary examination of data taken in the NONESUCH program provides evidence of the utility of sea echo for radar calibration and sea-state sensing.

(U) As to calibration, it has been noticed for some time in skywave work at the higher frequencies that the sea echo--appropriately averaged--possesses a fairly constant scattering coefficient, σ^0 , and that the value

(U)

of σ^0 is approximately -17 dB. In a large number of groundwave operations on the Chesapeake Bay, σ^0 was found to increase with roughness to a limiting value of -29 dB.* Barrick¹ has provided a first-order theory that supports these observed values of σ^0 .

(U) In sea-state sensing the promise of using the HF sea echo has existed since Crombie² first noticed the resonant nature of the scattering. Unfortunately, the very quality that makes the dominant sea echo a good calibration target--that is, saturation in amplitude of the first-order scatter at higher HF--tends to defeat its use for roughness determination. The higher-order scatter, however, can provide a means for roughness determination.

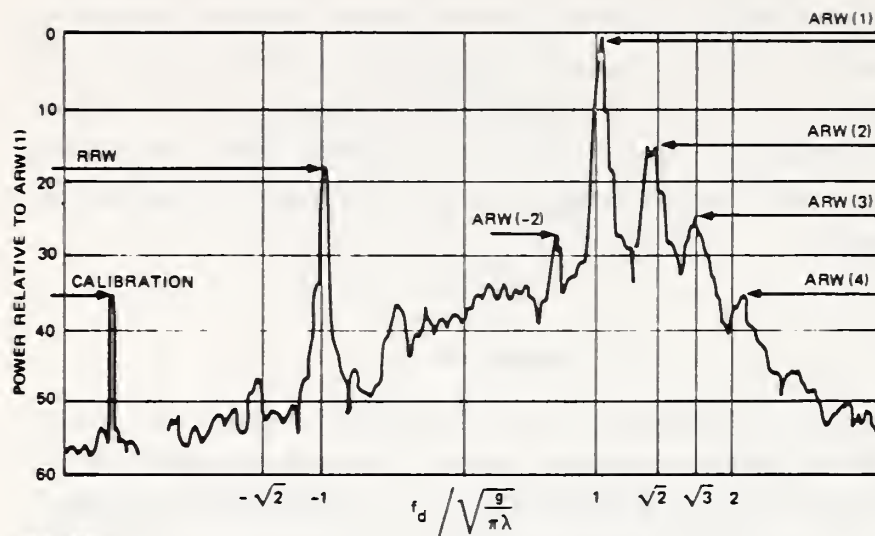
II DESCRIPTION (U)

(U) The equipment used has been described elsewhere.³ The form of data studied is shown in Figures 1 and 2. These are range-gated echo-power-versus-Doppler records of the sea echo. The 13.4-MHz median frequency of Figure 1 is used as a comparison standard in this paper; Doppler frequency in that figure is normalized to the resonant, first-order shift of $\sqrt{g/\pi\lambda}$, where $g = 9.81 \text{ m/s}^2$, and λ is the radar wavelength ($\sqrt{g/\pi\lambda} = 0.3735 \text{ Hz}$ at 13.4 MHz).

A. Radar Calibration (U)

(U) Some observations made on 4 and 7 December 1972 were used in an effort to confirm the measured values of transmit and receive antenna

* (U) In reality these two values of σ^0 are fundamentally identical. It is common that in skywave radars a factor of 12 dB accounting for the ionospheric reflection is absorbed in the target cross section.



UNCLASSIFIED

FIGURE 1 A TYPICAL AVERAGED DOPPLER SPECTRUM OF THE SEA ECHO AT 13.4 MHz, 1530-1600 GMT, 4 DECEMBER 1972. Some of the distinct responses are given identifiers. ARW denotes approach resonant wave; RRW denotes recede resonant wave. The amplitude and position of these responses are a function of sea state and radar frequency. (U)

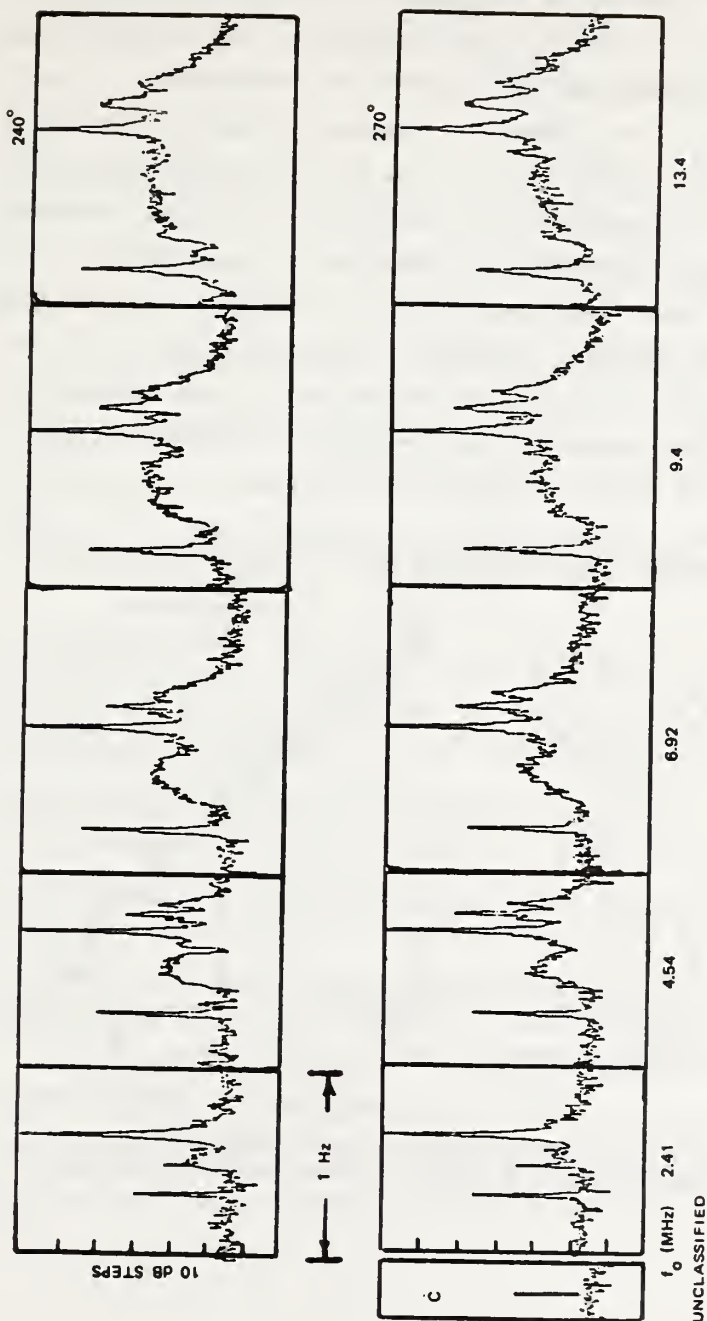


FIGURE 2 SIMULTANEOUS DOPPLER RECORDS OF THE SEA ECHO AT FIVE FREQUENCIES. The coherent bandwidth was about 0.01 Hz and averaging was about 30 min. The range gate was 7.5 km deep, the beamwidths were approximately 15°, the two receiver beam centers were displaced 30° at 240° and 270° bearings, and the range was 22.5 km. The difference between the RRW and ARW amplitude is greater on the 270° bearing because the sea is more nearly from that direction. The higher-order echoes between the ARW and RRW and those external to the ARW grow with increasing frequency. (U)

(U)

gains. Enough separate measurements were made to give credibility to the method of using the sea echo as a calibrator. The basic assumption was that the average first-order energy backscattered by the approach resonant wave, ARW1, could be described by a radar clutter coefficient, σ^0 of -29 dB. Implicitly it was assumed that the sea was fully developed at the frequencies used. Figures 3 and 4 give the sea-spectrum descriptions used, as measured by a nondirectional wave-height buoy in the scattering area. The f^{-5} frequency dependence of these spectra agree with the Phillips model for fully developed seas in the saturated--or equilibrium--region. The cutoff and energy under the measured curves agree with the observed wind and wave conditions for the two days. It was necessary to take into account the increase in groundwave path loss due to roughness.⁴ Since not all of the first-order scatter was contained in a constant

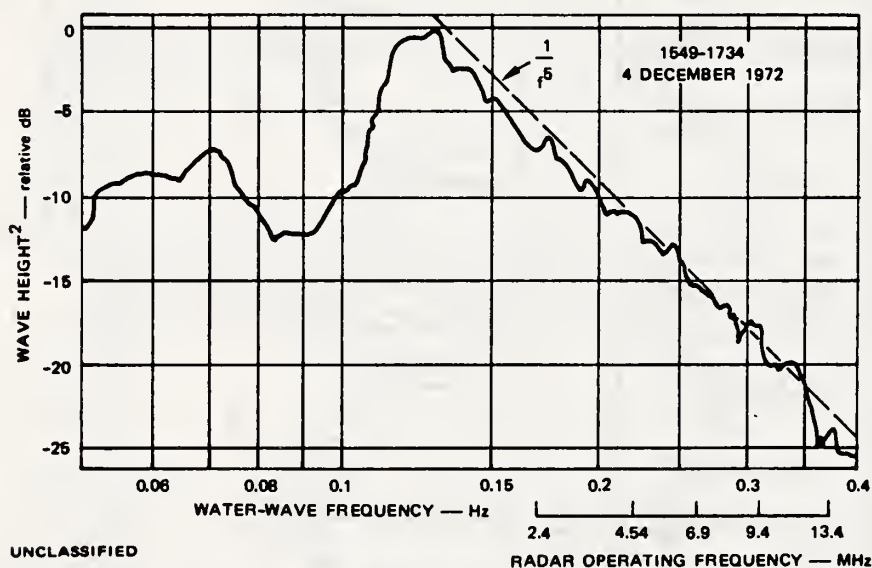


FIGURE 3 THE OCEAN-WAVE SPECTRA DERIVED FROM A WAVERIDER BUOY.
The sea appears to be fully developed for a 25-knot wind radial to the radar. (U)

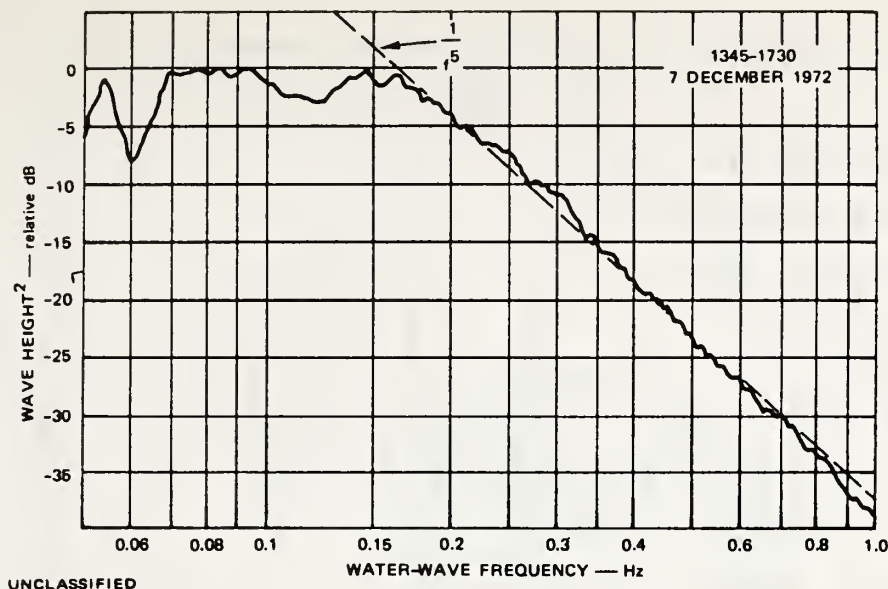
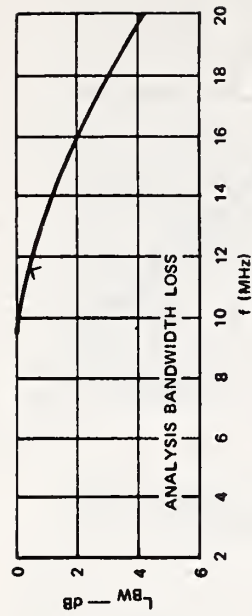


FIGURE 4 THE OCEAN WAVE SPECTRUM DERIVED FROM A WAVERIDER BUOY.
The sea was estimated to be that developed by a 20-knot radial wind. (U)

(U)

bandwidth at the higher frequencies, it was necessary to include a bandwidth loss; this loss merely reflects the fact that as higher-order processes broaden the first-order line, its peak will decrease in order to maintain the constant $\sigma^0 = -29$ dB energy under the curve. Figure 5 shows the loss curves used and the radar equation. Using the first form of the radar equation, the transmit-receive antenna gain product, $G_t G_r$, was computed for the measurements and analyses made on 4 and 7 December 1972. Figure 6 gives the results. Using the sea as a calibrated target does confirm the antenna gains. The spread in points at the lower frequencies may be due to inaccurate assumptions in our sea description. However, the spread of points at 13.4 MHz is a true index of variations in results, and all points are within ± 3 dB. The path losses are so insensitive to sea state at the higher frequencies that use of the correct roughness



$$G_T G_R = \frac{(4\pi)^3 R^4 P_R}{a_C \lambda^2 P_T} \times L_{GW} L_{BW}$$

$$a_C = \sigma^p A = \frac{(4\pi)^3 R^4 P_R}{G_T G_R \lambda^2 P_T} \times L_{GW} L_{BW}$$

$$L_{GW} = \frac{G_T G_R \lambda^2 P_T a_C}{(4\pi)^3 R^4 P_R L_{BW}}$$

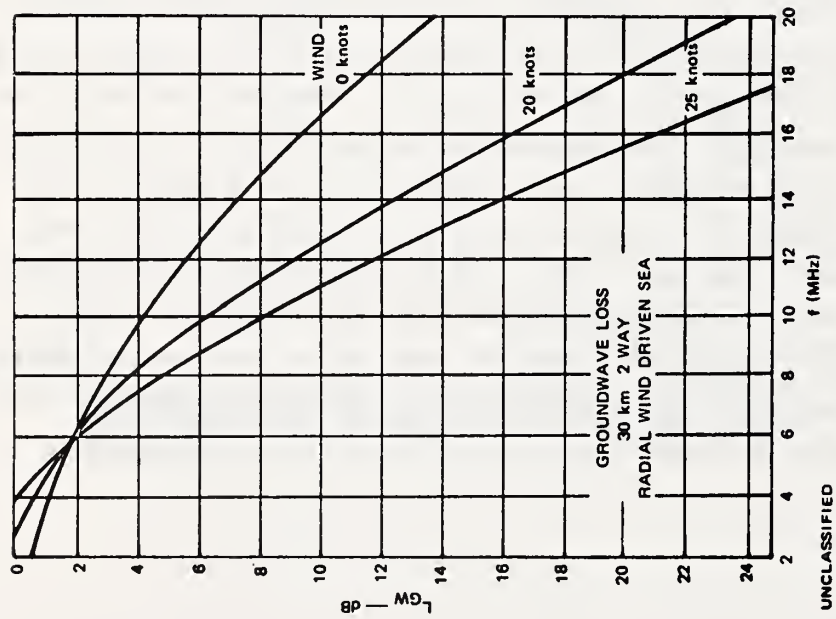


FIGURE 5 THE RADAR EQUATION, AND THE LOSS DESCRIPTIONS vs. FREQUENCY (U)

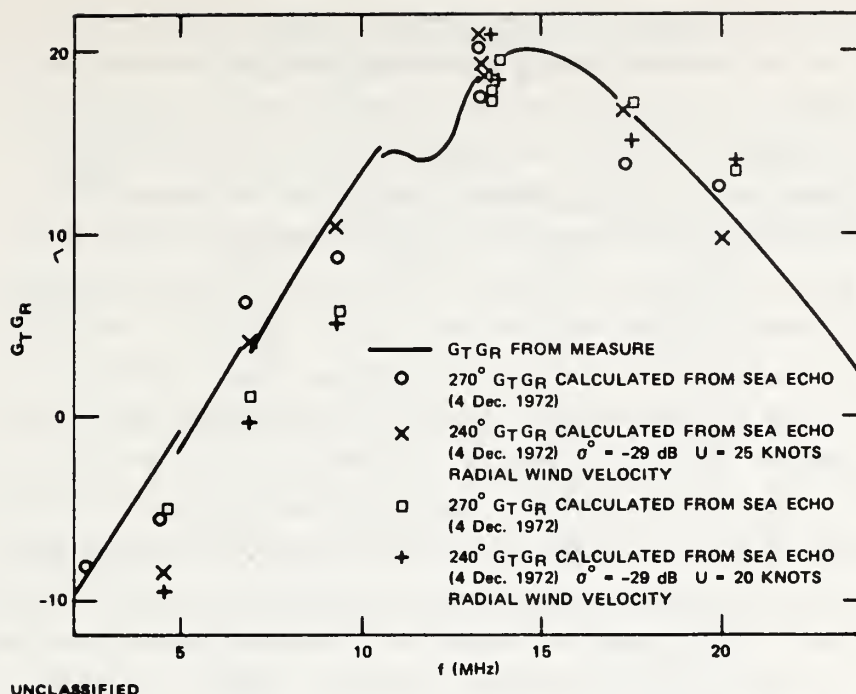


FIGURE 6 TRANSMIT-RECEIVE ANTENNA GAIN PRODUCT. The solid line is derived from independent gain measurements made on the two antennas. The plotted points were calculated using the ARW(1) amplitude and $\sigma^0 = -29$ dB. (U)

(U)

description is critical. However, once a groundwave radar is well calibrated, the sea echo can be interpreted to give path loss, and therefore the roughness.*

B. Sea-State and Surface-Wind Measures (U)

(U) A number of investigators have considered methods for deriving sea state from the sea-echo. Barrick⁶ has discussed much of this work,

* (U) Differences in the atmospheric refractive index from the assumed $4/3$ earth radius factor could corrupt this method of measurement, if they are indeed important at HF. Evidence is⁵ that such atmospheric anomalies do influence groundwave data, but only at frequencies higher than about 12 MHz.

(U)

and Long and Trizna⁷ provide a recent example. Here we are going to examine the data taken on 4 and 7 December 1972, and try to expose the better methods for determining the sea roughness from the radar echo. A comparison between Figures 1 and 2 and Barrick's results considering second-order scatter⁸ strongly suggests that second- and third-order scatter provide the spread echoes and distinct peaks seen in the experimental data. Considering this theory, it is natural to present predicted curves in terms of dimensionless parameter γ , [$\gamma = gc/(4\pi fU^2)$] which is inversely proportional to wind speed squared times radar frequency.* Figure 7 shows smoothed versions of seven radar-echo spectra from 4 December, parametric in operating frequency and normalized to the amplitude of ARW(1). Table 1 indicates how these seven curves--measured at different frequencies but at one wind speed--can be reinterpreted to show the spectra produced by different radial wind-driven seas but at a single frequency of 13.4 MHz. Figure 8 shows the theoretically predicted spectra (positive Doppler side only) for the same seven parameters, γ , based on using a semi-isotropic Phillips wave-height spectrum for fully developed seas. These theoretically calculated spectra⁸ include both hydrodynamic and electromagnetic effects, but only of second-order (i.e., produced by two sets of ocean waves satisfying a double-interaction Bragg resonant relationship)

(U) Comparison of measured (Figure 7) and predicted (Figure 8) spectra shows that the amplitude and area under ARW(2) and ARW(-2)[†] are indicators of sea state, and so possibly to a lesser extent are the positions

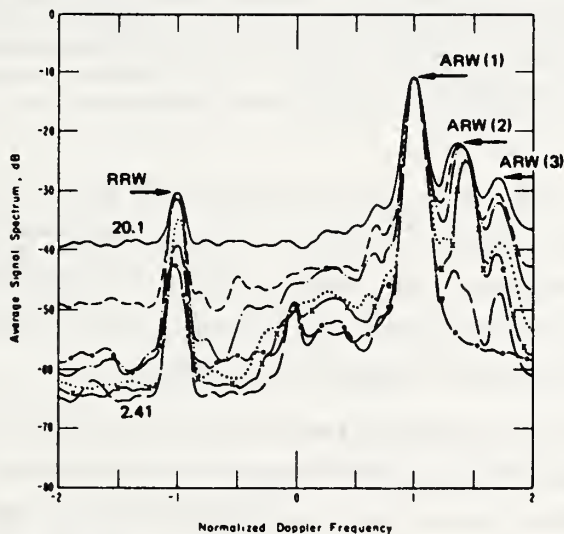
* (U) When the parameter γ is unity and less, the first-order resonant echo, ARW(1), reaches and remains at its saturated value, corresponding to $\sigma^0 \approx -29\text{dB}$, according to the theory. Thus, as is shown at the bottom of Figure 3, the first-order echo ARW(1) is saturated even at the lowest frequency of 2.4 MHz in 25-knot seas.

[†] (U) The peaks labeled ARW are defined in Figure 1; those carrying the numbers ± 2 refer to second-order echoes.

Table 1

(U) PARAMETRIC INTERDEPENDENCE BETWEEN
CARRIER FREQUENCY AND WIND SPEED (U)

| Channel | Parameter γ | Actual | | Scaled | |
|---------|--------------------|---------|-----------|---------|-----------|
| | | f (MHz) | U (knots) | f (MHz) | U (knots) |
| 1 | 0.59 | 2.41 | 25 | 13.4 | 11 |
| 2 | 0.31 | 4.54 | 25 | 13.4 | 15 |
| 3 | 0.20 | 6.8 | 25 | 13.4 | 18 |
| 4 | 0.15 | 9.4 | 25 | 13.4 | 21 |
| 5 | 0.11 | 13.4 | 25 | 13.4 | 25 |
| 6 | 0.08 | 17.4 | 25 | 13.4 | 29 |
| 7 | 0.07 | 20.1 | 25 | 13.4 | 31 |



UNCLASSIFIED

FIGURE 7 MEASURED AMPLITUDE-VS.-NORMALIZED-DOPPLER SPECTRA FROM A 22.5-km RANGE GATE ON 4 DECEMBER 1972, WHERE THE DOPPLER NORMALIZATION IS TO THE FIRST-ORDER RESONANT LINE AT $f_B = \sqrt{g/\pi\lambda}$ Hz. This is a smoothed sketch made from data similar to those shown in Figures 1 and 2, where the smoothing width is also normalized here to be $0.087 f_B$ Hz. (U)

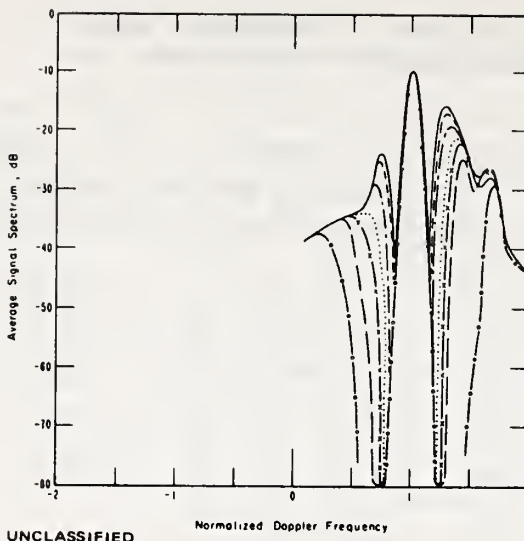


FIGURE 8 THEORETICAL AMPLITUDE-vs.-NORMALIZED-DOPPLER SPECTRA USING PHILLIPS SEMI-ISOTROPIC SPECTRUM FOR PROPAGATION IN UPWIND DIRECTION. Curves are for a 25-knot radial wind and the frequencies listed in the measured spectra of Figure 7. Only the dominant, positive-Doppler side is shown, smoothed in the same normalized manner as in Figure 7. (U)

(U)

of the peaks. While the nature of ARW(2) and ARW(-2) is reasonably well explained by the theory, ARW(3) is not always in agreement with theory and ARW(4) is not predicted by the theory at all. This means that these peaks are of higher order than second, and the theory must be extended to third and possibly fourth order to explain these peaks.

(U) The theory indicates that the second-order peaks ARW(2) and ARW(-2) are sensitive in magnitude, energy, and position not only to the heights of the ocean waves, but to their dominant travel directions with respect to the radar line of sight. Thus, for example, seas that are moving predominantly across the line of sight should produce a much diminished ARW(2) compared to ARW(-2), and the dominant second-order spectral energy should appear symmetrically distributed between ARW1 and RRW1. Limited experimental evidence examined so far from NONESUCH for crosswind seas supports this predicted behavior. Many more NONESUCH records re-

(U)

main to be analyzed in detail, and these should provide a valid comparison of theory with measured results.

III CONCLUSIONS (U)

(U) Many useful applications related to HF sea scatter can be projected from the knowledge and interpretation being gained from experiment and theory. It is shown that first-order sea echo can serve as an excellent calibrator for HF radar systems, providing, for example, a measure of path loss when all other radar system parameters are known. In a skywave radar, such calibration is necessary for determination of system sensitivity and thus the instantaneous probability of detection. In a groundwave radar, a knowledge of path loss in itself can be used to infer sea state.⁴ Further analysis of measured data will yield the variance of first-order σ^0 and the amount of time the sea echo is saturated versus frequency; these two factors will indicate in a more quantitative manner the precise accuracy of first-order sea echo as a calibrator.

(U) The determination of sea state from the higher-order characteristic of the sea echo appears as a very promising and exciting possibility. Since some characteristic of the higher-order echo is to be compared with the first-order echo, the technique is self-calibrating because all forms of sea echo traverse the same path and thus undergo the same path loss. This is particularly important for long-range skywave radar sensing of sea state. The selection of the best indicators within the radar records will depend somewhat upon the task. For example, spectral data collected with a skywave radar often suffers in its crispness due to multipath, and this can make measurement--indeed the very identification--of higher-order peaks difficult. Thus some measure of the area of energy under the higher-order spectrum--compared with the first-order resonant peak--could prove optimum for skywave systems. Curley et al.⁸ use an empirical technique

(U)

for interpreting skywave sea echo that in part is related to the shape and area of the spectral energy between the two first-order lines; their success suggests that some variant of this technique may be optimum for skywave data. This whole question of how to best "invert" the radar Doppler-signal spectrum to extract the dominant parameters of the ocean wave-height directional spectrum is receiving considerable attention. Inversion techniques are being tested first against the recorded NONESUCH groundwave data, and later will be tried against skywave sea echo.

REFERENCES (U)

1. D. E. Barrick, "First Order Theory and Analysis of MF/HF/VHF Scatter from the Sea," IEEE Trans. Prop., Vol. AP-20, pp 2-10 (1972), UNCLASSIFIED.
2. D. C. Crombie, "Doppler Spectrum of the Sea Echo at 13.56 Mc/s," Nature, Vol. 175, pp. 681-682 (1955), UNCLASSIFIED.
3. R. W. Bogle, L. S. Wagner, L. H. Tveten, W. M. Beery, and J. M. Watts, (Title classified), these Proceedings.
4. D. E. Barrick, "Theory of HF and VHF Propagation Across the Rough Sea, 2, Application to HF and VHF Propagation Above the Sea," Radio Science, Vol. 6, pp. 527-533 (May 1971), UNCLASSIFIED.
5. L. C. Edwards, "Project MAY BELL, SEAMEWS System Study A and Propagation Experiment (U)," Final Technical Report, Contract N00014-71-C-0440, Raytheon Company, Sudbury, Mass. (July 31, 1972), SECRET.
6. D. E. Barrick, "Remote Sensing of Sea State by Radar," Chapter 12 of Remote Sensing of the Troposphere, V. E. Derr, ed. (U.S. Government Printing Office, Washington, D.C., August 1972), UNCLASSIFIED.
7. A. E. Long and D. B. Trizna, "Measurements and Preliminary Interpretation of HF Doppler Spectra From the Sea Echo of an Atlantic Storm," NRL Report 7456, Naval Research Laboratory, Washington, D.C. (September 14, 1972), UNCLASSIFIED.
8. S. R. Curley, J. M. Headrick, and J. L. Ahearn, "Determination of Ocean Surface Conditions by Long-Range Radar Reflections (U), these Proceedings.

Reprinted from the 15th Radar Meteorology Conference,
October 10-12, 1972, 309-314, 1972.

DUAL-DOPPLER RADAR OBSERVATIONS OF CIRCULATION IN SNOW CONDITIONS

L. Jay Miller

NOAA Research Laboratories
Boulder, Colorado

1. INTRODUCTION

Unambiguous observation of three-dimensional particle motion requires simultaneous measurement at the same point in space of radial velocity components provided by three Doppler radars having noncollinear beams. Nevertheless, dual radar methods can still provide significant information on the detailed structure of atmospheric motion. One such dual radar method, COPLAN (coordinated coplanar) scanning, proposed by Lhermitte and Miller (1970) simplifies the data analysis and relaxes the stationarity assumptions.

Conventional radar methods (PPI scanning) require the completion of a three-dimensional sequence of azimuth and elevation angle scans before the measured radial velocity fields can be expressed in a common coordinate system. The particle motion field, therefore, must be assumed stationary for this total scan time. However, in COPLAN scanning data to be combined for a two-dimensional motion field is acquired in a common coordinate system so that stationarity is necessary only for the scan time of this restricted region. The advantage is a better assessment of the true stationarity of the three-dimensional motion field since short-duration samples (data in a single plane) are obtained at relatively long intervals. Moreover, interpolation procedures are now two-dimensional rather than three-dimensional. This simplification of the data analysis leads to a significant savings in the analysis of the large volume of data that a Doppler radar can provide.

The method requires that data from two radars be separately evaluated for radial velocity estimates at grid points in the plane defined by the axes of the radar beams. These two radial velocity fields are then combined providing an unambiguous two-dimensional particle motion field. If the particle terminal fall velocity can be assessed, two-dimensional air motion is obtained by subtracting the fall velocity contribution from the particle motion. The third orthogonal component of air motion normal to the plane is estimated using the equation of continuity.

This paper defines the COPLAN coordinate system conventions and derives expressions for the air motion components in the plane. Results obtained by this method applied to the observation of circulation in snow conditions are also presented.

2. COORDINATE SYSTEM AND COPLAN SOLUTIONS

For COPLAN analysis the appropriate coordinate system is a circular cylindrical system with the axis of the cylinder along the radar baseline. From figure 1 the transformation relations are

$$\rho = \sqrt{x^2 + z^2} \quad , \quad (1)$$

$$s = y \quad , \quad (2)$$

$$\alpha = \tan^{-1} (z/x) \quad , \quad (3)$$

where α is the plane tilt angle measured from the positive x direction, $0 \leq \alpha \leq \pi$, ρ is the perpendicular distance from the baseline in the plane, $0 \leq \rho < \infty$, and s is the distance along the baseline, $-\infty < s < \infty$. The xy -plane defines the horizontal, $z = 0$, plane. The $\alpha = 0^\circ$ and $\alpha = 180^\circ$ half-planes, respectively, are the horizontal planes for positive and negative x .

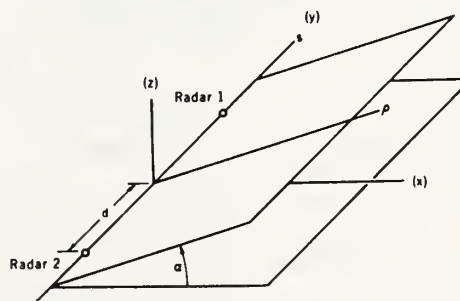


Fig. 1. COPLAN coordinate system.

The mean radial velocity derived from the Doppler velocity spectrum is, for a radar located at the origin,

$$\bar{V}_r(\rho, s) = \frac{1}{r} \left(\rho \bar{u}_\rho + s \bar{u}_s \right), \quad (4)$$

where the radar slant range $r = \sqrt{\rho^2 + s^2}$. The two orthogonal components of mean particle motion \bar{u}_ρ and \bar{u}_s are, respectively, perpendicular and parallel to the baseline and lie in the plane. Note that the component \bar{u}_α normal to the plane does not contribute to the mean radial velocity. Therefore, resolution of two-dimensional unambiguous particle motion in the plane is realized from the solution of two expressions analogous to (4).

Observation at the same point in the plane of two mean radial velocity estimates, \bar{V}_1 and \bar{V}_2 provided by radars 1 and 2 located respectively at (0, d) and (0, -d) leads to

$$\bar{u}_\rho(\rho, s) = \frac{r_1 \bar{V}_1(s+d) - r_2 \bar{V}_2(s-d)}{2dp}, \quad (5)$$

$$\bar{u}_s(\rho, s) = \frac{r_2 \bar{V}_2 - r_1 \bar{V}_1}{2d}, \quad (6)$$

with $r_1 = \sqrt{\rho^2 + (s-d)^2}$ and $r_2 = \sqrt{\rho^2 + (s+d)^2}$. Subtracting the contribution from the mean terminal velocity \bar{V}_t from (5), the mean air motion components in the plane become

$$\bar{u}_{\rho a} = \bar{u}_\rho - \bar{V}_t \sin \alpha, \quad (7)$$

$$\bar{u}_{sa} = \bar{u}_s. \quad (8)$$

It should be noted that the component \bar{u}_{sa} parallel to the baseline is completely determined by the radar measurements. This has also been shown by Armijo (1969) in the derivation of three-dimensional wind fields and by Lhermitte and Miller (1970).

Estimates of the mean air motion component $\bar{u}_{\alpha a}$ normal to the plane are obtained from the equation of continuity. Divergence in cylindrical coordinates is given by

$$\text{div } \bar{V}_a = \frac{1}{\rho} \frac{\partial}{\partial \rho} \left(\rho \bar{u}_{\rho a} \right) + \frac{1}{\rho} \frac{\partial \bar{u}_{\alpha a}}{\partial \alpha} + \frac{\partial \bar{u}_{sa}}{\partial s}, \quad (9)$$

where \bar{V}_a is the total vector air motion. Given

the time coincident fields $\bar{u}_\alpha(\rho, s)$ and $\bar{u}_{\alpha a}(\rho, s)$ at tilt angles α_i ($i=0, 1, 2, \dots, h$), $\bar{u}_{\alpha a}(\alpha_{i+1})$ becomes, with the assumption of incompressibility,

$$\bar{u}_{\alpha a}(\alpha_{i+1}) = \bar{u}_{\alpha a}(\alpha_i) - \int_{\alpha_i}^{\alpha_{i+1}} \left[\rho \frac{\partial \bar{u}_{sa}}{\partial s} + \frac{\partial}{\partial \rho} (\rho \bar{u}_{\rho a}) \right] d\alpha, \quad (10)$$

where $\alpha_i < \alpha_{i+1}$. If α_0 corresponds to the surface of the earth, the boundary condition is $\bar{u}_{\alpha a}(\alpha_0) = 0$. The transformations to air motion components in rectangular coordinates are then

$$\bar{u} = \bar{u}_{\rho a} \cos \alpha - \bar{u}_{\alpha a} \sin \alpha, \quad (11)$$

$$\bar{v} = \bar{u}_{sa}, \quad (12)$$

$$\bar{w} = \bar{u}_{\rho a} \sin \alpha + \bar{u}_{\alpha a} \cos \alpha, \quad (13)$$

where \bar{w} is the mean vertical component of air motion and the horizontal mean components \bar{u} and \bar{v} are, respectively, perpendicular and parallel to the baseline.

3. COPLAN IMPLEMENTATION AND RADAR CHARACTERISTICS

As the radar beam moves in azimuth the elevation angle θ is changed according to the relation (Lhermitte and Miller, 1970)

$$\tan \theta = \tan \alpha \sin (\beta - \beta_0), \quad (14)$$

where β is the azimuth angle measured clockwise from true north and β_0 is the azimuth angle of the baseline. For angles less than 10° , the tangent is approximately equal to the angle ($< 1\%$ error) so that

$$\theta \approx \alpha \sin (\beta - \beta_0). \quad (15)$$

The plane angle for antenna steering is restricted to $0 \leq \alpha \leq \pi/2$. Thus, the absolute value of the sine of the azimuth angle $(\beta - \beta_0)$ relative to the baseline is required to provide correct elevation angle information on both sides of the baseline.

The two radar systems digitally record the complex phase-coherent (in-phase and quadrature) signal outputs of the phase demodulator. Recorded time series are processed for the Doppler velocity spectrum using the fast-Fourier transform algorithm. The complex signal representation sampled at the pulse repetition rate permits an unambiguous velocity range of $\pm 15.7 \text{ m sec}^{-1}$. Data is acquired simultaneously at 4 range gates

during a signal dwell time of 262 msec (512 complex samples per range gate). As the antennas rotate (~ 1 -2 degrees per sec depending on the azimuth sector size) with the beams in a common plane, the 4 gates are successively positioned in 6 non-overlapping range intervals. This range positioning generates 24 gates equally spaced in range but slightly skewed in azimuth. At the boundary of the azimuth sector (16 beams), the antennas reverse scan direction, step to a new plane, and the entire process is repeated. The scanning time for a plane is 32.6 seconds.

Both radars are pulsed X-band Doppler radars with the following characteristics:

| | |
|-----------------------------------|---------------------------------------|
| Operating frequency | 9.31 GHz |
| Peak power | { 2.5 kW (Radar 1) 16 kW (Radar 2) |
| Minimum detectable signal | -103 dbm |
| Pulse repetition rate | 1953 Hz |
| Pulse width | 0.4 μ sec |
| Dynamic range | 53 db |
| Beam width (half-power estimated) | 0.7° |
| Antenna scan rate | 0-3 rpm (continuously variable) |
| Polarization | Horizontal |

4. EXPERIMENT AND RESULTS

Two Doppler radars with COPLAN scanning capabilities were operated east of the Rocky Mountains during the winter of 1971-72. The geometry for results presented here is shown in figure 2. Radar 1 was located 8 miles northeast of Boulder, Colorado. Since the radars were not at exactly the same height, the beam axes scanned in two planes which were parallel and separated by the difference in the two heights. This effect can be neglected for differences comparable to the linear extent of the beams at the ranges involved.

Data was acquired on January 3, 1972, from 1130 MST to 1145 MST in nine planes from 0° to 8° at 1° tilt angle steps. The 1500 Z (0800 MST) surface map showed a polar front located in southern Colorado. Also, there was a low pressure center in west-central New Mexico. Light steady snow fell uniformly over the scanning region as indicated by relative reflectivity measurements (< 2 dbz change).

Two radial velocity fields, \bar{V}_1 and \bar{V}_2 , obtained from the Doppler measurements were linearly interpolated to arrive at solutions to (5) and (6). A computed horizontal wind field having a spatial resolution of 300 meters (comparable to the scanning resolution) is shown in figure 3. This horizontal wind field appears to be nearly uniform.

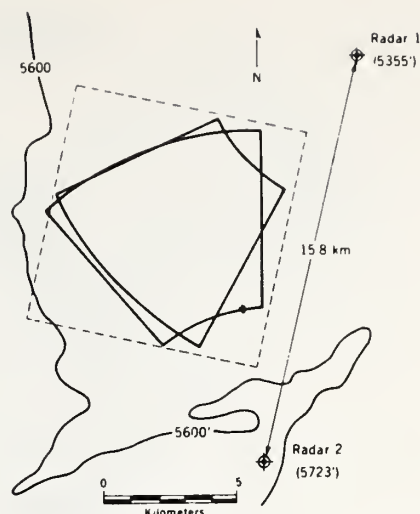


Fig. 2. Plan view of overlapping scanning region and radar locations. Radar heights are feet above mean sea level. The baseline is oriented at an angle of 14.6° from the true north. The 5600' MSL height contour is shown to delineate the foothills of the Rocky Mountains.

A given wind component can be expressed as a mean plus a fluctuating component so that

$$u_{pa}(\rho, s) = \bar{u}_{pa} + u'_{pa}(\rho, s), \quad (16)$$

$$u_{sa}(\rho, s) = \bar{u}_{sa} + u'_{sa}(\rho, s), \quad (17)$$

where the prime denotes the fluctuating component. The averages here apply to the entire scanned region rather than to the pulse volume previously associated with the mean of the Doppler velocity spectrum. Subtraction of the spatial averages, \bar{u}_{pa} and \bar{u}_{sa} , from (16) and (17) results in a field of spatial fluctuations from the mean flow.

This so-called eddy flow field for the horizontal plane is shown in figure 4. The mean wind is from 14.8° true at 5.5 msec⁻¹. Clearly there is a well organized smaller scale (2 km) flow superimposed on the larger scale (8 km) mean flow.

Streamlines for the horizontal eddy flow are shown in figure 5. Also indicated are four apparent vortex centers. The area where no streamlines have been drawn (nearly zero fluctuation velocities) is a region of weak (10^{-4} sec⁻¹) divergence. This is divergence estimated by finite differences on a scale of 300 meters.

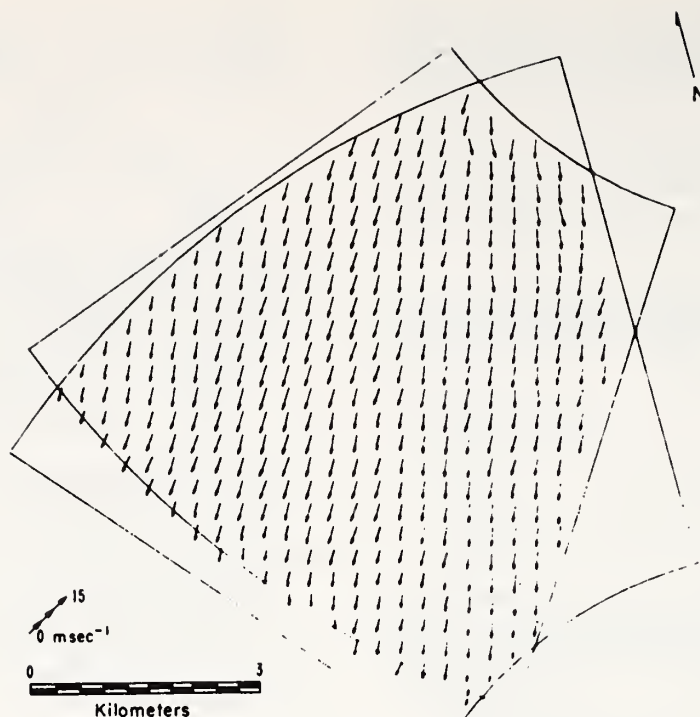


Fig. 3. Horizontal ($\alpha = 0^\circ$ plane) vector wind field derived from data taken on January 3, 1972. Vectors are drawn from the field points in the direction of flow. Field points are separated by 300 meters.

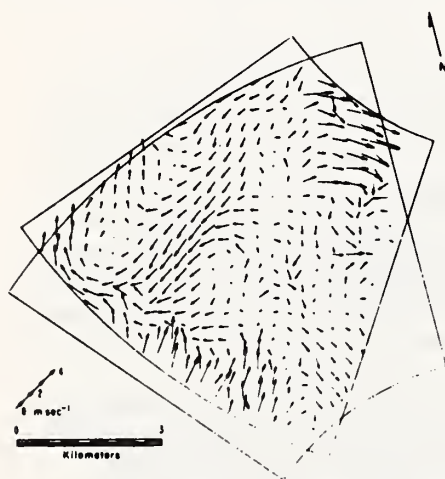


Fig. 4. Eddy flow field for the horizontal wind field of figure 3. The mean flow is from 14.8° at 5.5 m sec^{-1} as derived from the spatial averages of the u_{pa} and u_{sa} components.



Fig. 5. Streamlines for the horizontal eddy flow field of figure 4. Four vortex centers are also shown.

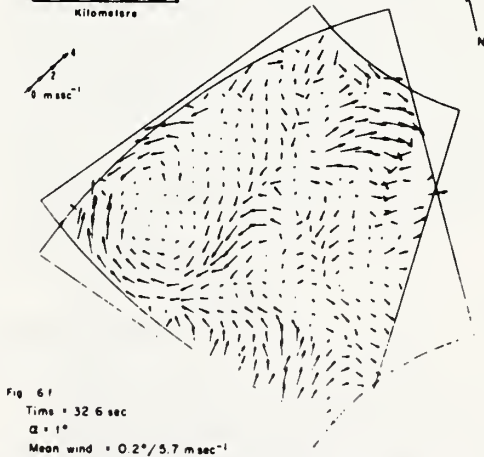
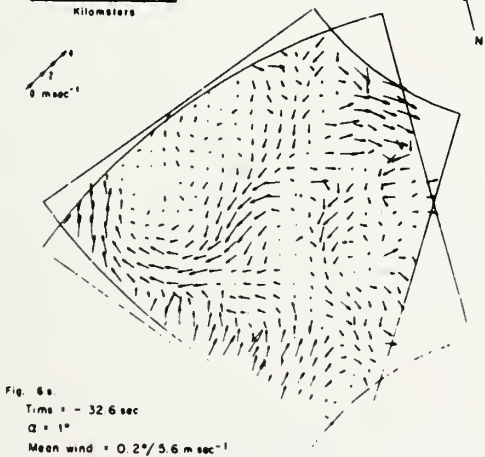
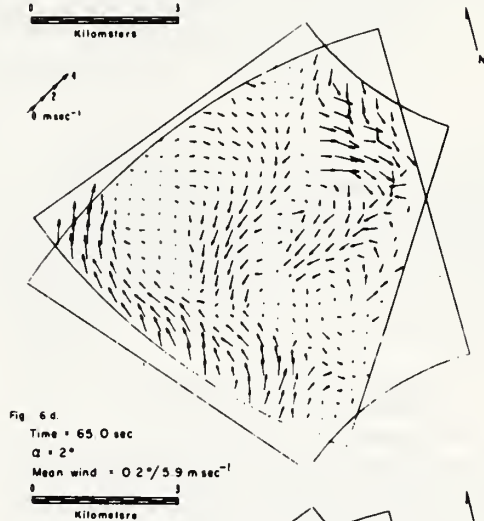
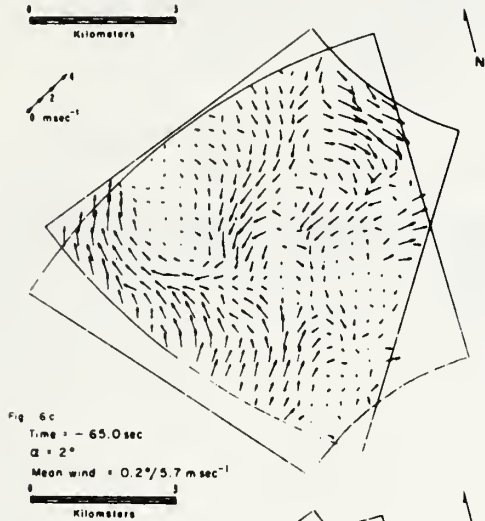
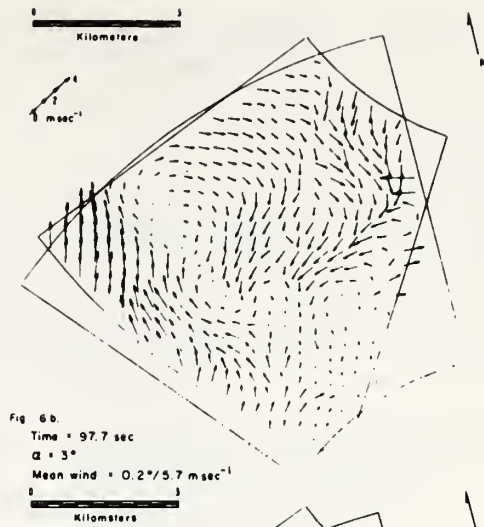
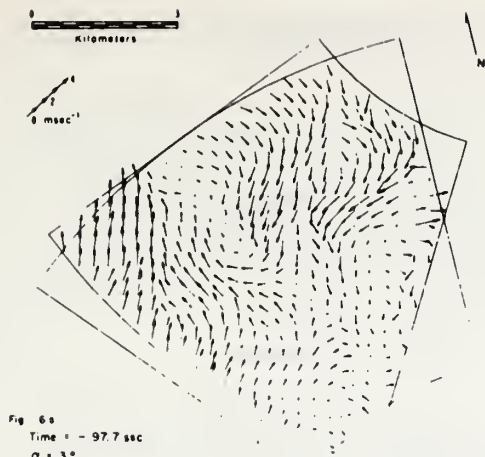


Fig. 6a-f. Two-dimensional eddy flow field for 1° , 2° , and 3° planes at times relative to the horizontal fields of figures 3, 4, and 5. Results are presented at different tilt angles and different times thereby showing the spatial and temporal behavior of the detailed circulation in snow.

Temporal and spatial behavior of the eddy flow is evidenced by figures 6a-f. Comparison of the field in a plane at two different times indicates that the eddies are advecting relatively unchanged with the mean flow. Note the spatial continuity of the eddy flow pattern as the tilt angle is increased. However, there are also some distinct changes in the flow. In particular, the northwest quadrant of the 1° plane (figure 6e) has a small vortex center (not shown in figure 5) which has changed to an easterly flow in the 3° plane (figure 6b). If COPLAN scanning had not been used, three-dimensional interpolation of radial velocity estimates taken several minutes apart would have averaged out much of the detailed motion. The random deviations of the eddy flow are attributable to experimental error.

The variance of the mean radial velocity estimate derived from the Doppler spectrum is (Lhermitte and Miller, 1970), neglecting noise,

$$\sigma_{\bar{V}}^2 \approx \frac{\lambda^2 \sigma_V^2}{4T} \quad (18)$$

where λ is the wavelength, σ_V^2 is the Doppler spectral variance, and T is the signal dwell time. Using (18) to estimate the error in the \bar{u}_p and \bar{u}_s components in (5) and (6) leads to an uncertainty of $\pm 9 \text{ cm sec}^{-1}$ for an average spectral standard deviation of $\sigma_V \approx 30 \text{ cm sec}^{-1}$. The terminal fall velocity ($\bar{V}_t \approx 1 \text{ m sec}^{-1}$ for snow) contribution in (7) of 6 cm sec^{-1} ($\alpha = 3^\circ$) can therefore be neglected. The particle motion fields of figures 6a-f are then the eddy flow fields of the air.

5. SUMMARY AND CONCLUSIONS

This paper has presented the COPLAN scanning and data analysis technique. The preliminary results obtained in snow conditions have been used as a vehicle to demonstrate the potential of this method applied to dual-Doppler observations of atmospheric motion. When the fall velocity contribution can be assessed, the technique gives the detailed spatial and temporal variability of the air motion. Further studies using the COPLAN method in snow conditions or for artificially introduced motion tracers with a known fall velocity can lead to a better understanding of the turbulence processes in the boundary layer.

Application of the COPLAN method to storms where the fall velocity may not be known a priori must include this measurement before the true air motion is obtained. However, since the fall velocity contributes to only one of the air motion components, areas of flow having strong gradients of \bar{V}_t will appear as regions of significant departure from the larger scale mean flow. These perturbations of the particle motion in the plane are then a qualitative means of determining changes in \bar{V}_t associated with changes in the drop

sizes. This flow pattern recognition coupled with reflectivity measurements needs to be investigated more fully.

Compared to conventional radar scanning methods, COPLAN scanning provides a more systematic means of acquiring dual-Doppler radar measurements of storm circulation. Short-duration samples in a single plane obtained at relatively long intervals lead to a better assessment of the storm's true temporal variability. Furthermore, interpolation techniques are two-dimensional rather than three-dimensional thereby simplifying the data analysis.

6. ACKNOWLEDGEMENTS

The author is indebted to Mr. R. G. Strauch for his critical review of the manuscript. Mr. Strauch and Mr. H. Frank assisted in the operation of the radars. Mr. F. Merrem helped in the Doppler spectral analysis. Mrs. B. Patterson typed the manuscript.

7. REFERENCES

- Armijo, L., 1969: A theory for the determination of wind and precipitation velocities with Doppler radars, *J. Atmos. Sc.* **26**, 570-573.
- Lhermitte, R. M. and L. J. Miller, 1970: Doppler radar methodology for the observation of convective storms, *Proc. 14th Radar Meteorol. Conf.*, 133-138.

Ground-Based Sensing of Temperature Profiles from Angular and Multi-Spectral Microwave Emission Measurements

J. B. SNIDER

Wave Propagation Laboratory NO.14, Boulder, Colo. 80302

(Manuscript received 8 February 1972, in revised form 15 June 1972)

ABSTRACT

The use of angular-scan and multi-spectral techniques for inferring temperature profiles from ground-based radiometric observations of emission by atmospheric oxygen is discussed. A recently developed multi-frequency radiometer used to evaluate, experimentally, the two techniques is described. Temperature profiles inferred from emission measurements are compared to radiosonde profiles recorded simultaneously with the radiometric data. It is concluded that a combination of angular-scan and multi-spectral input data yields a more accurate profile recovery than other sets of input data.

1. Introduction

The application of ground-based radiometric measurements of emission from atmospheric oxygen to the problem of estimating the variation of temperature with height has been discussed in the recent literature (Westwater, 1972; Hosler and Lemmons, 1972; Staelin, 1969). The majority of the reported ground-based measurement systems has determined temperature profiles by mathematical inversion of single-frequency measurements of brightness temperature as a function of elevation angle. An alternate technique consists of inverting observations of brightness temperature as a function of frequency at either a fixed or variable elevation angle. This second technique has received relatively little attention.

An obvious advantage in favor of the first, or angular scan method, is that the instrumentation is fairly simple, consisting of a single-frequency radiometer with an antenna that is steerable in elevation. However, conversion of antenna temperature to brightness temperature may be complicated and subject to error since the stray radiation into antenna back and side lobes changes with elevation angle. In the second, or multi-spectral method, the antenna is not moved with the result that stray radiation is relatively constant, thus simplifying the determination of brightness temperature.

In principle, the multi-spectral system offers the advantage that a profile can be measured in a time period set mainly by the radiometer time constant. With present radiometer sensitivities, the angular scan method requires of the order of 15-30 min to complete a temperature profile measurement. The major disadvantage of the multi-spectral system is that the instrumentation is complicated and relatively expensive.

This paper describes instrumentation developed to permit experimental evaluation of both techniques and presents the results of an experiment performed to compare quantitatively the relative merits of the two techniques.

2. Theory

In this section we briefly consider the theory of the estimation of temperature profiles from measurements of microwave emission by oxygen. Emission by oxygen is utilized because this gas is well-mixed in the atmosphere and its absorptive properties in the microwave region are reasonably well understood. Absorption of electromagnetic energy by O_2 occurs in a series of resonant lines centered at 60 GHz and in a single line near 118 GHz; here we consider only the 60-GHz absorption complex. At the earth's surface the individual absorption lines merge into an absorption continuum due to pressure broadening and a ground-based radiometer observes a smooth variation of brightness with frequency. The brightness temperature T_b , measured at frequency ν and elevation angle θ , is given by Meeks and Lilley (1963) as

$$T_b(\nu, \theta) = T_b^{\text{ext}}(\nu, \theta) \exp\left(-\int_0^\infty \alpha_\nu \csc\theta dh'\right) + \int_0^\infty T(h) \alpha_\nu \left[\exp\left(-\int_0^h \alpha_\nu \csc\theta dh'\right)\right] \csc\theta dh, \quad (1)$$

where T_b^{ext} is the brightness temperature caused by a source external to the earth's atmosphere, $T(h)$ the absolute temperature as a function of height h above the earth's surface, and α_ν the absorption coefficient at frequency ν . Here we assume that the absorption is a

function of oxygen, water vapor, temperature and pressure only, and that scattering is negligible; these assumptions are valid except when clouds or precipitation are present. The problem at hand is to estimate the quantity, $T(h)$, from measurements of the quantity, $T_b(\nu, \theta)$.

Study of (1) shows that input data may be generated in three ways:

- 1) Angular scan, i.e., measurements of T_b at a given frequency vs elevation angle.
- 2) Multi-spectral, i.e., measurements of T_b vs frequency at a fixed elevation angle.
- 3) A combination of angular-scan and multi-spectral techniques.

The method employed to invert the radiative transfer equation (1) has been described in detail by Westwater (1972) and will only be briefly described here. The method involves replacing (1) with a Fredholm integral equation of the first kind. The Fredholm equation is then solved by means of a statistical estimation technique that yields estimates of the atmospheric temperature structure based upon *a priori* knowledge of the temperature, pressure and humidity statistics for the particular measurement location and the given set of brightness temperature measurements. The solution is the set of atmospheric temperature vs height values that results in the minimum expected mean square error at each altitude of interest. Inclusion of the *a priori* statistical information in addition to the brightness observations allows one to estimate the temperature profile at an arbitrarily large number of altitudes from a given set of measurements. Although each of these

estimates is computationally distinct, the information at adjacent points is, of course, highly correlated.

3. Multi-frequency radiometer

We now describe the instrument developed to compare the relative usefulness of the methods described above in making accurate estimates of atmospheric temperature profiles. Major objectives in the design of the radiometer were capability of operation in both angular-scan and multi-spectral modes, simultaneous operation on three or four frequencies from a common antenna, high angular resolution in the antenna system, good spectral resolution, and the greatest possible sensitivity consistent with the other design goals.

A block diagram of the final radiometer design is given in Fig. 1. The basic system is the well-known Dicke radiometer in which the receiver is switched between the antenna and a temperature-controlled reference termination. In the present system, the Dicke switch (modulator) is a rotating vane attenuator that alternately transmits and absorbs the energy from the antenna. The components located between the antenna and rotary modulator serve the following functions. During calibration the radiometer is connected to one of the temperature-controlled terminations through the waveguide switch to establish a known temperature reference. (At 0° elevation angle and in the 60-GHz spectral region, the atmosphere is essentially a black-body having an effective temperature very nearly equal to the surface temperature; hence, atmospheric emission may also be used as a calibration point.) Incremental calibration of the radiometer output is accomplished by injecting noise from the gas discharge noise source into

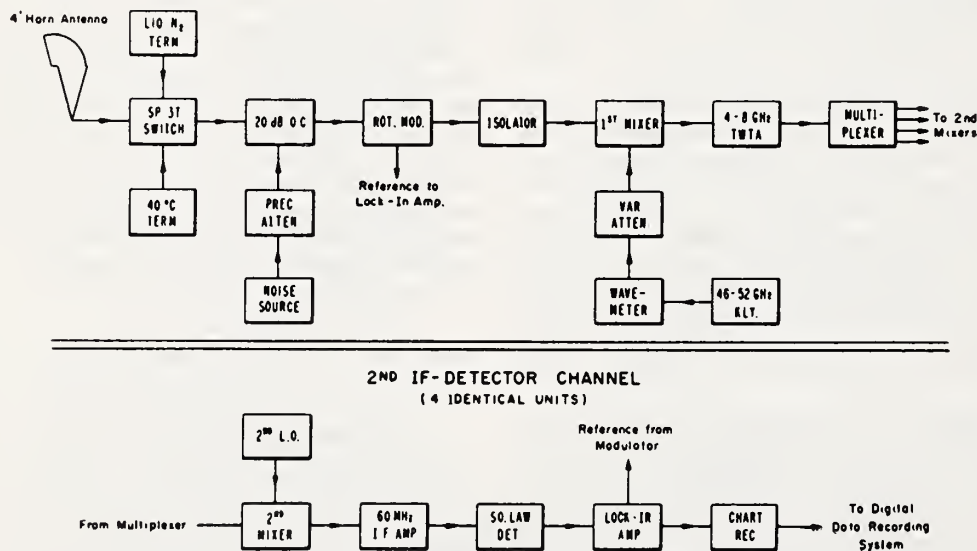


FIG. 1. Block diagram of multi-frequency radiometer.



FIG. 2. Multi-frequency radiometer installed in elevation over azimuth antenna mount.

the signal channel via the precision attenuator and auxiliary arm of the directional coupler. During measurements, the antenna is connected to the radiometer and noise is injected into the signal channel to allow operation in a "semi-balanced" condition. Since a true balance cannot be obtained at more than a single frequency, an appropriate amount of noise is injected to obtain an approximate balance at all frequencies.

The first mixer translates a 4-GHz band of frequencies in the 50-GHz region to a 4–8 GHz intermediate frequency. After a stage of amplification, separation into four individual channels takes place in a strip-line multiplexer; center frequencies are 4.5, 5.5, 6.5 and 7.5 GHz. A second conversion to a 60-MHz center frequency follows the multiplexer; the noise bandwidth of the 60-MHz i.f. amplifiers is approximately 30 MHz to achieve a fair degree of spectral resolution. Following the second i.f. amplifiers are four identical stages of video detection, synchronous detection using a lock-in amplifier, and analog output recording.

All components before the lock-in amplifiers are located in an equipment enclosure mounted at the antenna. The waveguide compartment is heated to

maintain the ambient temperature reasonably constant. Since ohmic losses in the waveguides generate noise, waveguide temperatures are measured by thermistor probes located at several points and remotely recorded for subsequent use in computing the antenna temperature.

A summary of the essential radiometer characteristics is presented in Table 1.

The radiometer enclosure and its 1.2 m conical horn antenna are mounted in an elevation over azimuth antenna mount which provides the capability of angular scan operation (see Fig. 2). The antenna position is read out remotely at the data recording position. A relatively large antenna aperture was employed to obtain the high angular resolution mentioned earlier, while the conical horn configuration was selected to minimize stray radiation into the back and side lobes and thereby simplify the conversion of antenna temperature to brightness temperature.

The measured antenna power patterns in the region of the main beam are shown in Figs. 3a and 3b for longitudinal and transverse polarization. The antenna feed is arranged so that the power pattern in the vertical plane corresponds to Fig. 3a; thus, radiation from the ground is reduced because of the less intense side lobes.

We now consider the method used to convert radiometric measurements of antenna temperature to brightness temperature required as input data to invert (1). For any elevation angle θ , the antenna temperature T_a is the weighted average of the brightness temperature distribution surrounding the antenna, i.e.,

$$T_a(\theta) = \frac{1}{4\pi} \int_{4\pi} G(\Omega) T_b(\Omega) d\Omega, \quad (2)$$

where $G(\Omega)$ is the antenna gain as a function of angle, $T_b(\Omega)$ the brightness temperature distribution, and $d\Omega$ the elemental solid angle. Eq. (2) can be rewritten as the sum of an integral over the main beam region, e.g., between the first nulls in the pattern, plus an integral over the remainder of the power pattern. Performing this modification and solving for the brightness temperature integrated over the main beam, T_{bm} , we obtain

$$T_{bm}(\theta) = T_a(\theta) - \int_{\text{remainder}} G(\Omega) T_b(\Omega) \frac{d\Omega}{4\pi}. \quad (3)$$

For this antenna system, the main beam efficiency, i.e., the percent of the total antenna power contained in the

TABLE 1. Multi-frequency radiometer characteristics.

| | |
|-------------------------|-------------------------------------------------------------|
| Operating frequency | 52.5, 53.5, 54.5, 55.5 GHz |
| Antenna characteristics | 1.2 m diameter conical horn, 3 dB beamwidth 0.3° |
| Receiver type | Dicke switching radiometer, dual-conversion superheterodyne |
| Sensitivity | ~1K for 60 sec-integration time |

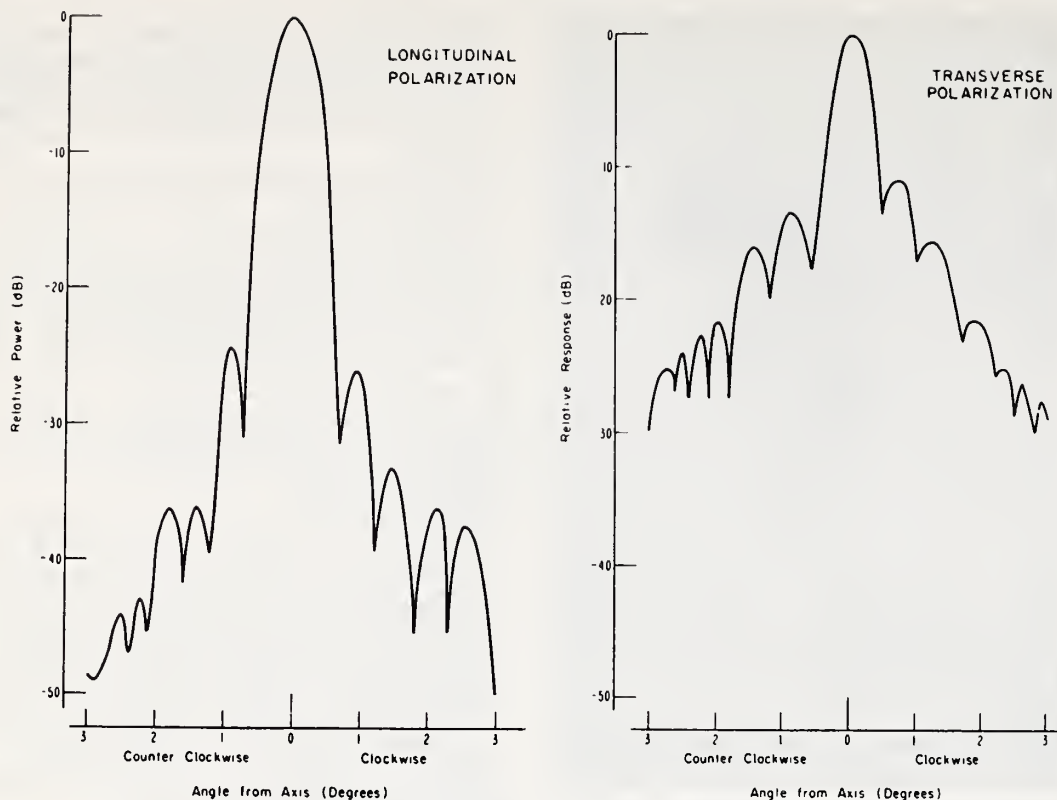


FIG. 3. Power pattern for 1.2 m conical horn antenna, 54 GHz: longitudinal polarization, a., transverse, b.

main beam, is sufficiently high that the last integral in (3) is insensitive to the range of brightness temperature profiles encountered in Colorado. As a result, it is possible to make use of a simple conversion factor to obtain brightness temperature from antenna temperature. Curves of this factor, the quantity $(T_{bm} - T_a)$, vs antenna elevation are shown in Fig. 4; the curves were computed by numerically integrating (2) using the measured antenna power pattern and the mean brightness temperature profile for April. The latter profile was computed using 5-year mean Denver radiosonde data and appropriate absorption coefficients in (1).

4. Description of experiment

During April 1971, an experiment was conducted near Boulder, primarily to evaluate the performance of several radiometric systems in yielding atmospheric temperature profiles. However, as the planning for the experiment evolved, it became clear that additional sensors could not only benefit from, but supplement the basic objectives of the main experiment. As a result, the final scope of the program greatly exceeded the original plan. The list of participants along with their respective measurements follows:

| Participant | Equipment |
|------------------------------------------|-----------------------------------------------------------------------------------------------------------------------------------------------------------------------------------------------------------------------------------------------|
| Air Pollution Control Office | 54.5 GHz radiometer, angle-scan mode |
| Sperry Rand Corporation | 54.5 GHz radiometer, angle-scan mode |
| Wave Propagation Laboratory, NOAA | Four-frequency radiometer, angle-scan and multi-spectral modes Acoustic sounder Infra-sound array Lidar Infrared radiometer Radiosonde data Aircraft temperature measurements Surface T , RH , P , sky photographs |
| National Center for Atmospheric Research | Boundary layer profiler (tethered balloon with radiosonde) |

Data were recorded three times daily beginning at 0400, 0900 and 1500 during a one-week period in April 1971. These observation times were selected in order to acquire data for a variety of profiles. The radiometric observations were made at a series of 10 discrete antenna elevation angles ranging from 0° to 90° ; a complete run required about 1 hr. During the radiometer measurements, a radiosonde was released and data were recorded to an altitude of about 10 km; the aircraft also recorded temperature-height variations to an altitude of 3 km. Prior to and following recording of the radiosonde data, the boundary layer profiler made

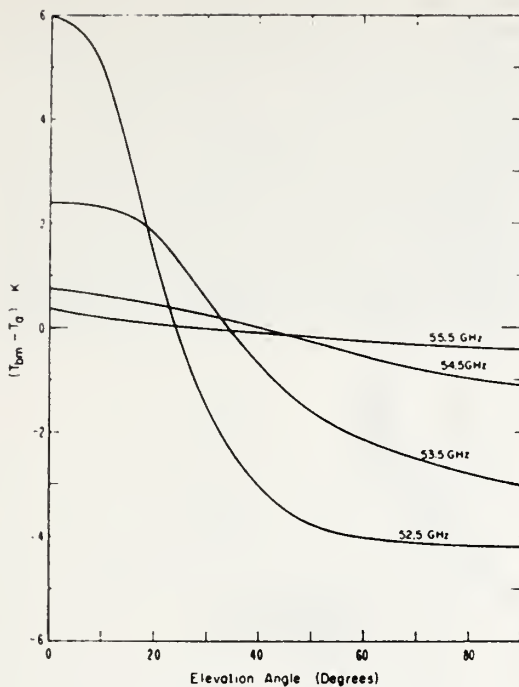


FIG. 4. Antenna-temperature-to-brightness-temperature conversion factor.

a sounding from the surface to about 500 m and back to the surface. In addition to these supporting data, sky photographs were made at each antenna elevation angle so that possible contamination of data by clouds could be detected.

5. Measurement results

In the remainder of this paper, we shall limit our discussion to recovery of temperature profiles from radiometric data obtained with the WPL multi-frequency radiometer. We shall consider our experimental results from two viewpoints: (i) What is the optimum set of input data?, and (ii) What are the relative effects of different statistics upon the final inversion result?

The statistical inversion technique can also be used as a tool to study achievable accuracy in profile retrieval as a function of number and kind of altitude weighting functions, radiometer noise levels, and *a priori* knowledge of temperature statistics (Westwater and Strand, 1968). This technique evaluates effective numbers of independent data in terms of reduction of variance of the original temperature statistics, i.e., the addition of redundant measurements reduces the variance only slightly. An optimum set of measurement ordinates is that which maximizes the reduction in variance. We then apply this criterion to evaluate various kinds of measurement possibilities.

The theoretical accumulated standard deviation of the estimated difference in inferred and actual (measured) temperature profiles are shown in Figs. 5 and 6; the two figures illustrate the effects of using different statistics as well as different sets of input data. The instrumental noise level is also taken into account. Fig. 5 is based upon the 5-year mean all-month radiosonde data for Denver, while Fig. 6 is calculated using the 5-year mean April radiosonde data. The various curves are plotted for different sets of input data; the symbol for a particular set is shown in the legend. Combinations 1A, 1, and 2 refer to the multi-spectral input data combinations listed in Table 2. Combinations 1A and 1 are equivalent except that 1A is computed for a simulated measurement accuracy (noise level) of 0.1K while combination 1 is based upon the actual noise levels determined by the observed differences between radiometric measurements and the brightness temperature calculated from radiosonde information. Angle scan designations are simply measurements of brightness temperature vs elevation angle at the frequency indicated. The curve labeled *a priori* is the theoretical accuracy in the estimated profile that would be obtained if only the long-term statistics and the surface temperature were known. In all the results presented here, the measured surface temperature is used as a constraint. The theoretical curves for spectral combinations 1 and 4 are nearly identical; the curves for combination 4 have been omitted from Figs. 5 and 6 for clarity.

Several important points are brought out in Figs. 5 and 6. First, it is clear that spectral combination 1 results in the smallest standard deviation over the full 10-km height interval (remembering that combination 1A is based on a hypothetical 0.1K noise level). Second, the total mean square error per point in the angular scan mode is about the same at both 53.5 and 54.5 GHz and is smaller than for multi-spectral measurements at a fixed elevation angle, i.e., combination 2. Thus, we

TABLE 2. Explanation of spectral combinations employed to estimate temperature profiles.

| Combina- tion | Input data Elevation angle (deg) | Frequency (GHz) |
|------------------|----------------------------------------|---------------------------|
| 1 | 5 | 54.5, 55.5 |
| | 10 | 54.5, 55.5 |
| | 15 | 54.5, 55.5 |
| | 30 | 53.5, 54.5, 55.5 |
| | 60 | 52.5, 53.5, 54.5 |
| | 90 | 52.5, 53.5, 54.5 |
| 2 | 90 | 52.5, 53.5, 54.5, 55.5 |
| 4 | 5 | 53.5, 54.5 |
| | 10 | at all angles |
| | 15 | |
| | 20 | |
| | 30 | |
| | 60 | |
| | 90 | |

reach the not surprising conclusion that a combination of angular scan and multi-spectral input data yields a better inversion result than either set of input data alone. However, it is somewhat surprising that a fairly large reduction in measurement error (from $\sim 2.5\text{K}$ to 0.1K) does not result in a substantial decrease in total mean square error for combination 1. This result may indicate that multi-spectral angular scan measurements need not be extremely accurate to give good inversion results except during serious departures from horizontal stratification.

The rather poor performance of the multi-spectral inversion method may be partly due to measurement error. However, the main reason is believed to be the

smaller number of input measurements in the multi-spectral case. It is also possible that a more optimum selection of frequencies would result in a smaller difference between inferred and actual profiles.

As for the comparative merits of the statistics used to invert the data, it appears that all-month and April statistics produce comparable results over the first 3 or 4 km for all input data combinations. Above 4 km, use of April statistics results in a slightly smaller error when angular scanning or spectral combination is used. Attempts were made to improve the accuracy of the estimated profile by employing *a priori* data corresponding closely in time with the radiometric measurements. Of the available long-term statistical data, a time

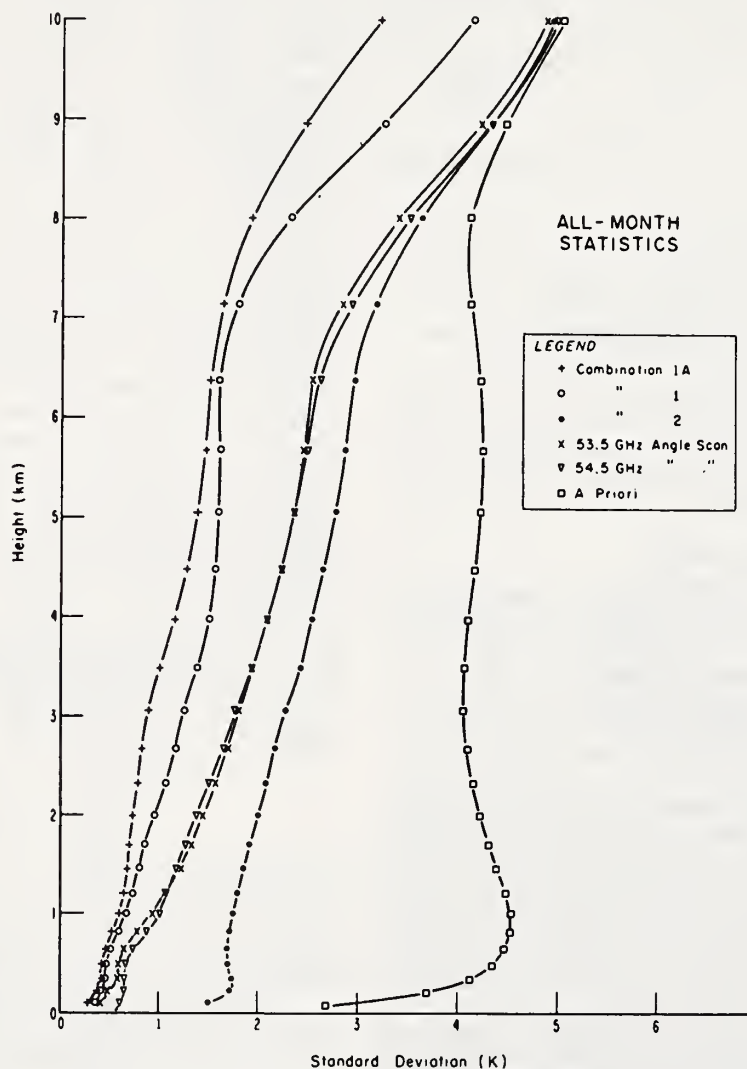


FIG. 5. Theoretical accuracy of estimated profile using all-month statistics.

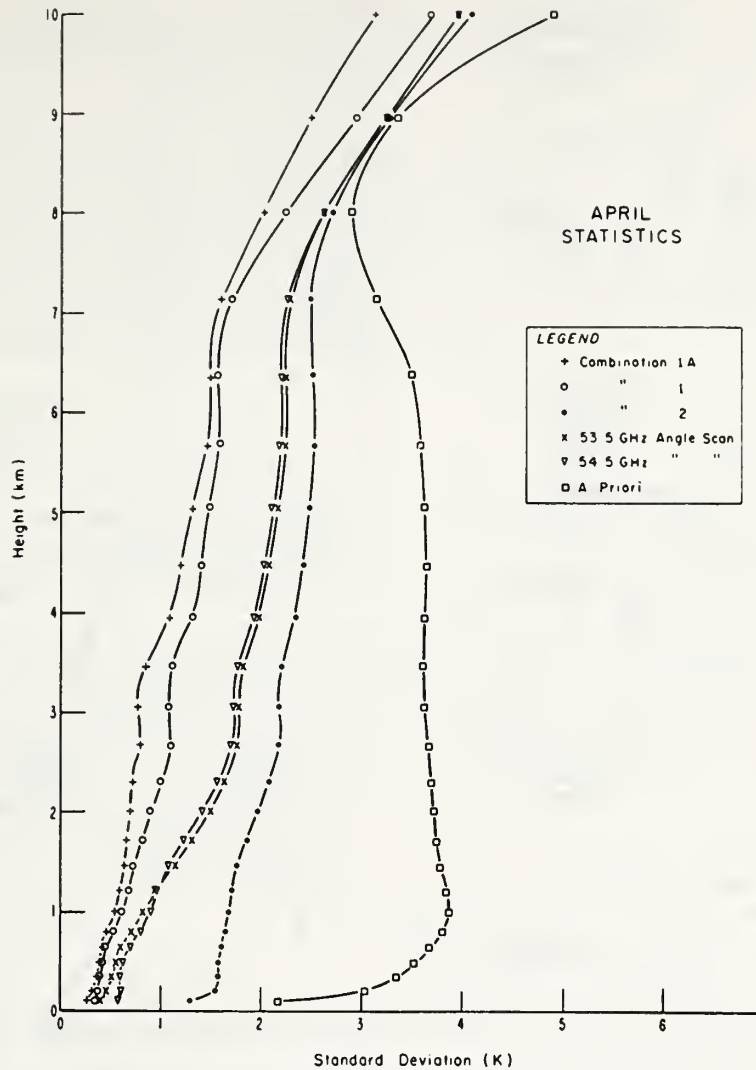


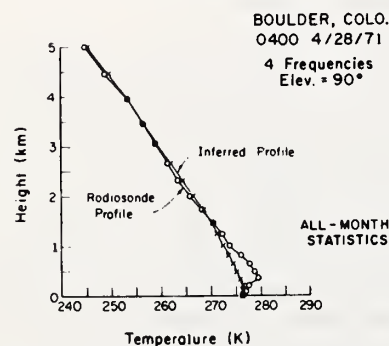
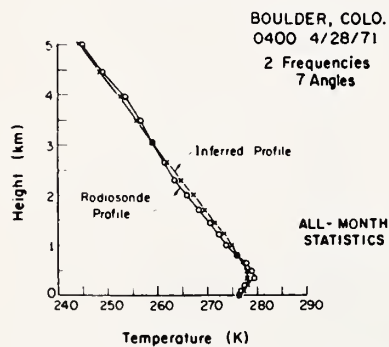
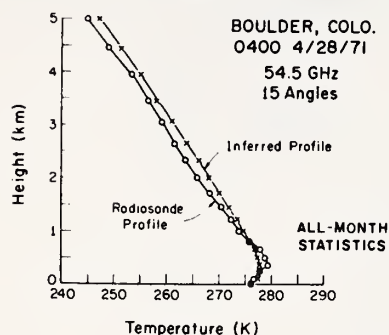
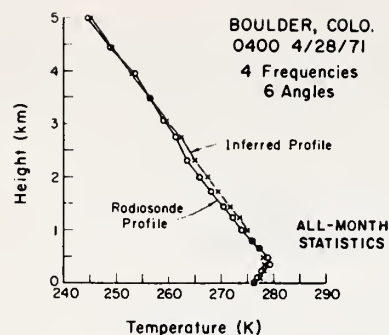
FIG. 6. Theoretical accuracy of estimated profile using April statistics.

correspondence occurred for only the 0400 measurements, a total of three samples. No significant improvement in the mean square difference between estimated and radiosonde profiles resulted from this procedure.

We shall now compare the measured and inferred profiles for a few samples. Fig. 7 is an example of a profile containing a surface-based temperature inversion. The curves are the profile measured by the radiosonde and the profile inferred from the radiometric data; inversion results are shown for four different combinations of input data. All sets of data, except for spectral combination 2, show the presence of the temperature inversion. Although the maximum temperature is slightly underestimated in this example, the height of

the maximum is fairly well defined. As predicted by theory, spectral combination 1 gives the best overall agreement with the radiosonde profile. Note that combination number 4, for which a theoretical curve is not shown, results in agreement comparable to that obtained with combination 1 and the angular scan at 54.5 GHz. This trend was observed consistently in all the samples considered in this study which suggests that a two-frequency radiometer operated in the angular scan mode yields results comparable in accuracy with those obtainable with a four-frequency device. However, it does not necessarily follow that this behavior would be true for all geographic areas.

Figs. 8-10 show inversion results for three other



samples using spectral combination 1 to illustrate recovery of several different types of profiles. The radiosonde data in Fig. 8 show an elevated temperature inversion at about 500 m; the inversion is also seen in the aircraft and boundary layer profile recordings. The inferred profile does not detect the intensity of the elevated inversion although there is a change in the estimated profile lapse rate in the vicinity of the temperature inversion. This inability to detect the intensity and mixing depth of elevated temperature inversions has been observed in angular scan measurements (Westwater, 1971). In both instances, it is believed that the temperature structure is smoothed out because of integration effects and/or overlapping of weighting

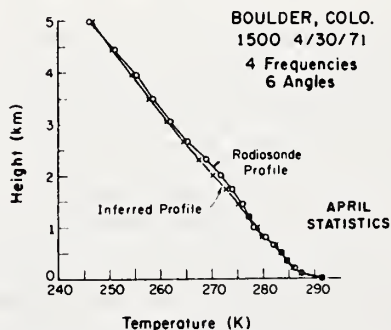
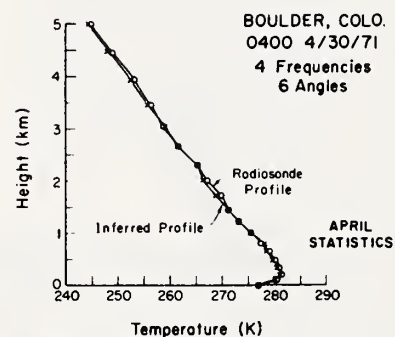
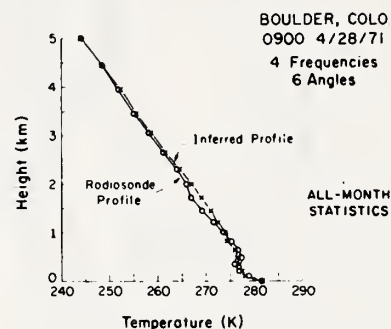


FIG. 7. Inferred and measured temperature profiles using four combinations of input data.

FIGS. 8-10. Inferred and measured temperature profiles using combinations of angle scan and multi-spectral input data.

TABLE 3. Summary of profile recovery for various combinations of input data using all-month statistics. Tabulated quantity is the rms difference between inferred and radiosonde temperatures for nine profiles. Quantities in parentheses are maximum observed differences in the entire set of nine samples.

| Height (km) | Spectral combination 1 | Spectral combination 2 | Spectral combination 4 | 53.5 GHz angular scan | 54.5 GHz angular scan | <i>A priori</i> |
|----------------------------------------------|---------------------------|---------------------------|---------------------------|--------------------------|--------------------------|---------------------|
| 0 | 0 | 0 | 0 | 0 | 0 | 0 |
| 0.105 | 0.37 (+0.70, -0.23) | 1.50 (+3.46, -1.94) | 0.29 (+0.61, -0.15) | 0.64 (+1.73, -0.24) | 0.31 (+0.51, -0.14) | 2.25 (+2.46, -4.00) |
| 0.221 | 0.40 (+0.75, -0.23) | 1.82 (+3.91, -2.40) | 0.22 (+0.53, -0.18) | 0.25 (+0.47, -0.13) | 0.26 (+0.41, -0.17) | 2.81 (+2.96, -4.71) |
| 0.350 | 0.49 (+0.73, -1.07) | 2.24 (+4.02, -4.58) | 0.56 (+0.63, -1.34) | 0.59 (+0.82, -1.27) | 0.61 (+0.52, -1.54) | 3.08 (+3.17, -4.95) |
| 0.491 | 0.52 (+0.20, -1.16) | 1.85 (+1.60, -3.52) | 0.61 (+0.22, -1.27) | 0.56 (+0.20, -1.16) | 0.76 (-0.11, -1.53) | 2.78 (+3.27, -4.95) |
| 1.013 | 0.71 (+1.36, -0.86) | 1.36 (+1.90, -1.66) | 0.67 (+1.20, -0.76) | 0.67 (+1.08, -0.27) | 0.53 (+1.04, -0.92) | 2.99 (+1.89, -5.81) |
| 1.458 | 0.90 (+1.78, -0.85) | 1.21 (+2.82, -1.07) | 0.77 (+1.59, -0.67) | 0.76 (+1.34, -0.66) | 1.09 (+1.97, -1.58) | 2.88 (+0.82, -4.26) |
| 2.001 | 0.90 (+1.55, -1.50) | 1.04 (+1.77, -0.87) | 1.05 (+1.26, -1.30) | 0.98 (+1.90, -0.81) | 1.35 (+2.41, -1.80) | 3.13 (+0.63, -4.97) |
| 2.665 | 0.51 (+0.86, -0.72) | 1.12 (+1.69, -0.28) | 0.38 (+0.42, -0.60) | 1.09 (+1.64, -0.77) | 1.30 (+2.21, -0.53) | 3.37 (-0.54, -5.22) |
| 3.050 | 0.50 (+0.68, -0.58) | 1.29 (+2.06, -0.27) | 0.41 (+0.69, -0.77) | 0.99 (+1.65, -0.47) | 1.39 (+2.06, -0.67) | 3.51 (-0.78, -5.61) |
| 3.946 | 0.62 (+0.67, -1.18) | 1.40 (+2.10, -0.32) | 0.58 (+0.65, -1.14) | 1.18 (+1.92, -1.20) | 1.41 (+2.05, -0.46) | 3.62 (-0.33, -5.54) |
| 5.040 | 0.72 (+1.71, -0.25) | 2.08 (+3.67, +0.15) | 0.82 (+1.45, -0.84) | 1.90 (+3.52, -0.98) | 0.88 (+2.49, -0.04) | 4.39 (-0.94, -7.63) |
| Nine profile average of 19 points to 5.04 km | | | | | | |
| | 0.59 | 1.44 | 0.52 | 0.84 | 1.01 | 2.81 |

functions. In principle, the multi-spectral approach should be more successful in recovering elevated inversions if the frequencies of operation are chosen so as to cause the weighting function to give more information in the vicinity of the elevated inversion. It is clear that the optimum frequency problem should receive additional study.

Tables 3 and 4 contain a detailed summary of the relative accuracy of temperature profile recovery using the various combinations of input data and all-month and April statistics, respectively. The values tabulated are the rms difference between estimated and radiosonde temperature profiles for the nine samples recorded during the one-week measurement period. The numbers in parentheses are the extreme differences between the two types of measurements; a positive value indicates that the inferred temperature is greater than the radiosonde temperature.

6. Conclusions

Based upon the very limited sample available for this study, it is concluded that a combination of angular

scan and multi-spectral input data produces more accurate inferred profiles than do other input data combinations. It further appears that the angular scan method is superior to multi-spectral techniques especially when detecting surface based temperature inversions. However, the possibility exists that a more optimum selection of frequencies would result in improved accuracy for the multi-spectral method. It should also be remembered that the rapidity of making measurements in the multi-spectral mode may offset the reduced accuracy obtainable. For the measurements reported here, a two-frequency angular scan combination yields results nearly as good as obtained with the four-frequency angular scan combination. The implication regarding simplification of equipment is obvious; thus, the extent to which this result applies to other geographic areas should be carefully evaluated. The accuracy of the inferred profile is not very sensitive to the particular set of *a priori* statistics used; however, it should be stressed that this situation may be the result of the small sample size.

TABLE 4. Summary of profile recovery for various combinations of input data using April statistics. Tabulated quantity is the rms difference between inferred and radiosonde temperatures for nine profiles. Quantities in parentheses are maximum observed differences in the entire set of nine samples.

| Height (km) | Spectral combination 1 | Spectral combination 2 | Spectral combination 4 | 53.5 GHz angular scan | 54.5 GHz angular scan | <i>A priori</i> |
|--------------------------------------------|---------------------------|---------------------------|---------------------------|--------------------------|--------------------------|---------------------|
| 0 | 0 | 0 | 0 | 0 | 0 | 0 |
| 0.105 | 0.39 (+0.78, -0.39) | 1.50 (+3.55, -1.73) | 0.31 (+0.67, -0.19) | 0.22 (+0.39, -0.24) | 0.46 (+0.94, -0.20) | 1.87 (+2.28, -3.68) |
| 0.221 | 0.31 (+0.77, -0.23) | 1.79 (+4.06, -2.06) | 0.23 (+0.52, -0.18) | 0.22 (+0.41, -0.20) | 0.30 (+0.46, -0.40) | 2.25 (+2.85, -4.25) |
| 0.350 | 0.52 (+0.76, -1.15) | 2.22 (+4.17, -3.63) | 0.59 (+0.66, -1.42) | 0.61 (+0.85, -1.42) | 0.62 (+0.76, -1.52) | 2.77 (+3.19, -4.37) |
| 0.491 | 0.56 (+0.25, -1.21) | 1.82 (+1.65, -3.60) | 0.66 (+0.17, -1.30) | 0.63 (+0.16, -1.23) | 0.69 (+0.04, -1.37) | 2.21 (+3.51, -2.82) |
| 1.013 | 0.63 (+1.34, -0.71) | 1.40 (+1.82, -1.82) | 0.59 (+1.13, -0.69) | 0.63 (+1.01, -0.36) | 0.57 (+1.28, -0.36) | 2.00 (+2.50, -3.45) |
| 1.458 | 0.83 (+1.53, -0.86) | 1.21 (+2.56, -1.42) | 0.70 (+1.37, -0.71) | 0.68 (+1.17, -0.70) | 0.54 (+1.54, -1.52) | 1.69 (+1.68, -2.82) |
| 2.001 | 0.87 (+1.60, -1.22) | 1.08 (+1.47, -1.45) | 0.66 (+1.23, -1.02) | 0.93 (+1.85, -0.77) | 1.36 (+2.54, -1.80) | 1.85 (+1.66, -2.96) |
| 2.665 | 0.51 (+1.00, -0.54) | 0.85 (+1.25, -1.07) | 0.39 (+0.51, -0.67) | 0.94 (+1.61, -1.00) | 1.25 (+2.26, -0.94) | 1.82 (+0.55, -3.11) |
| 3.050 | 0.48 (+0.78, -0.64) | 0.96 (+1.52, -1.28) | 0.42 (+0.53, -0.89) | 0.89 (+1.52, -0.83) | 1.25 (+2.12, -1.00) | 1.89 (+0.41, -3.39) |
| 3.946 | 0.51 (+0.60, -1.07) | 1.03 (+1.54, -0.96) | 0.54 (+0.56, -0.93) | 1.04 (+1.70, -1.11) | 1.14 (+1.41, -1.00) | 1.95 (+0.89, -3.42) |
| 5.040 | 0.58 (+1.23, -0.59) | 1.24 (+1.19, -0.79) | 0.72 (+1.11, -1.01) | 1.53 (+2.99, -1.35) | 1.11 (+1.53, -0.53) | 2.25 (+0.66, -3.50) |
| Nine-point average of 19 points to 5.04 km | | | | | | |
| | 0.54 | 1.26 | 0.49 | 0.74 | 0.87 | 1.82 |

REFERENCES

- Hosler, C. R., and T. J. Lemmons, 1972: Radiometric measurements of temperature profiles in the planetary boundary layer. *J. Appl. Meteor.*, **11**, 341-348.
- Meeks, M. L., and A. E. Lilley 1963: The microwave spectrum of oxygen in the earth's atmosphere. *J. Geophys. Res.*, **68**, 1683-1703.
- Staelin, D. H., 1969: Passive remote sensing at microwave wavelengths, *Proc. IEEE*, **57**, 427-439.
- Westwater, E. R., 1971: Microwave determination of low altitude temperature profiles. *Proc. 7th Intern. Symp. Remote Sensing of Environment*, Ann Arbor, Mich., 17-21 May, 585-594.
- , 1972: Ground-based determination of low altitude temperature profiles by microwaves. *Mon. Wea. Rev.*, **100**, 15-28.
- , and Otto Neall Strand, 1968: Statistical information content of radiation measurements used in indirect sensing. *J. Atmos. Sci.*, **25**, 750-758.

Reprinted from the Proceedings of Symposium on Air Pollution,
Turbulence and Diffusion, March 1972.

RECENT RESULTS IN GROUND-BASED SENSING
OF ATMOSPHERIC TEMPERATURE PROFILES

J. B. Snider

Wave Propagation Laboratory
Environmental Research Laboratories
National Oceanic and Atmospheric Administration
Boulder, Colorado 80302

INTRODUCTION

The application of ground-based radiometric measurements of emission from atmospheric oxygen to the problem of estimating the variation of temperature with height has been discussed in recent literature.⁽¹⁻³⁾ In the majority of measurements reported, temperature profiles have been determined by inverting single frequency measurements of brightness temperature as a function of elevation angle. An alternate technique consists of inverting observations of brightness temperature as a function of frequency at either a fixed or variable elevation angle. The second technique has received relatively little attention.

An obvious advantage in favor of the first, or angular scan method, is that the instrumentation is fairly simple, consisting of a single frequency radiometer with an antenna that is steerable in elevation; however, conversion of antenna to brightness temperature may be complicated and subject to error since the stray radiation into antenna back and side lobes changes with elevation angle. In the second, or multi-spectral method, the antenna is not moved with the result that stray radiation is relatively constant thus simplifying the determination of brightness temperature.

In principle, the multi-spectral system offers the advantage that a profile can be measured in a time period set mainly by the radiometer time constant. With present radiometer sensitivities, the angular scan method requires 15 to 30 minutes to complete a temperature profile measurement. The major disadvantage of the multi-spectral system is that the instrumentation is complicated and relatively expensive.

This paper describes instrumentation developed to permit experimental evaluation of both techniques and presents the results of an experiment performed to compare quantitatively the relative merits of the two techniques.

THEORY

In this section we briefly consider the theory of the estimation of temperature profiles from measurements of microwave emission by oxygen. Emission by oxygen is utilized because this gas is well-mixed in the atmosphere and its absorptive properties in the microwave region are reasonably well understood. Absorption of electromagnetic energy by O_2 occurs in a series of resonant lines centered at 60 GHz and in a single line near 118 GHz; here we consider only the 60 GHz absorption complex. At the earth's surface the individual absorption lines merge into an absorption continuum due to pressure broadening and a ground-based radiometer observes a smooth variation of brightness with frequency. The brightness temperature, T_b , measured at frequency, ν , and elevation angle, θ , is given by⁽⁴⁾

$$T_b(\nu, \theta) = T_b^{\text{ext}}(\nu, \theta) \exp\left(-\int_0^\infty \alpha_\nu \csc \theta \, dh\right) + \int_0^\infty T(h) \alpha_\nu \left[\exp\left(-\int_0^h \alpha_\nu \csc \theta \, dh'\right)\right] \csc \theta \, dh \quad (1)$$

where T_b^{ext} = brightness temperature caused by a source external to the earth's atmosphere,

$T(h)$ = absolute temperature as a function of height, h , above the earth's surface, and

α_ν = absorption coefficient at frequency ν .

Here we assume that the absorption is a function of oxygen, water vapor, temperature, and pressure only and that scattering is negligible; these assumptions are valid except when clouds or precipitation is present. The problem at hand is to estimate the quantity, $T(h)$, from measurements of the quantity, $T_b(\nu, \theta)$.

Study of (1) shows that input data may be generated in three ways:

1. Angular scan, i.e., measurements of T_b at a given frequency versus elevation angle,
2. Multi-spectral, i.e., measurements of T_b versus frequency at a fixed elevation angle,
- and 3. A combination of angular-scan and multi-spectral techniques.

The method employed to invert the radiative transfer equation (1) has been described in detail by Westwater⁽¹⁾ and will only be briefly described here. The method involves replacing (1) with a Fredholm integral equation of the first kind. The Fredholm equation is then solved by means of a statistical estimation technique that yields estimates of the atmospheric temperature structure based upon a priori knowledge of the temperature, pressure, and humidity statistics for the particular measurement location and the given set of brightness temperature measurements. The solution is the set of atmospheric temperature versus height values that results in the minimum departure (in a least-squares sense) from the expected value.

MULTI-FREQUENCY RADIOMETER

We now describe the instrument developed to compare the relative usefulness of the methods described above in making accurate estimates of atmospheric temperature profiles. Major objectives in the design of the radiometer were capability of operation in both angular-scan and multi-spectral modes, simultaneous operation on 3 or 4 frequencies from a common antenna, high angular resolution in the antenna system, good spectral resolution, and the greatest possible sensitivity consistent with the other design goals.

A block diagram of the final radiometer design is given in Figure 1. The basic system is the well known Dicke radiometer in which the receiver is switched between the antenna and a temperature-controlled reference termination. In the present system, the Dicke switch (modulator) is a rotating vane attenuator that alternately transmits and absorbs the energy from the antenna. The components located between the antenna and rotary modulator serve the following functions: during calibration the radiometer is connected to one of the temperature controlled terminations through the waveguide switch to establish a known temperature reference. (At 0° elevation angle and in the 60 GHz spectral region the atmosphere is essentially a blackbody having an effective temperature very nearly equal to the surface temperature; hence, atmospheric emission may also be used as a calibration reference point.) Incremental calibration of the radiometer output is accomplished by injecting noise from the gas discharge noise source into the signal channel via the precision attenuator and auxiliary arm of the directional coupler. During measurements, the

antenna is connected to the radiometer and noise is injected into the signal channel to allow operation in a "semi-balanced" condition. Since a true balance cannot be obtained at more than a single frequency, an appropriate amount of noise is injected to obtain an approximate balance at all frequencies.

The first mixer translates a 4 GHz band of frequencies in the 50 GHz region to a 4-8 GHz first intermediate frequency. After a stage of amplification, separation into four individual channels takes place in a strip-line multiplexer; center frequencies are 4.5, 5.5, 6.5, and 7.5 GHz. A second conversion to a 60 MHz center frequency follows the multiplexer; the noise bandwidth of the 60 MHz IF amplifiers is approximately 30 MHz to achieve a fair degree of spectral resolution. Following the second IF amplifiers are four identical stages of video detection, synchronous detection using a lock-in amplifier, and analog output recording.

All components before the lock-in amplifiers are located in an equipment enclosure mounted at the antenna. The waveguide compartment is heated to maintain the ambient temperature reasonably constant. Since ohmic losses in the waveguides generate noise, waveguide temperatures are measured by thermistor probes located at several points and remotely recorded for subsequent use in computing the antenna temperature.

The radiometer enclosure and its 1.2 m diameter conical horn antenna are installed on an elevation over azimuth antenna mount which provides the capability of angular scan operation. The antenna position is read out remotely at the data recording position. A relatively large antenna aperture was employed to obtain the high angular resolution mentioned earlier, while the conical horn configuration was selected to minimize stray radiation into the back and side lobes and thereby simplify the conversion of antenna temperature to brightness temperature.

A summary of the essential radiometer characteristics is presented in Table 1.

Table 1. Multi-frequency radiometer characteristics

| | |
|-------------------------|-----------------------------------------------------------------|
| Operating frequency | - 52.5, 53.5, 54.5, 55.5 GHz |
| Antenna characteristics | - 1.2 meter diameter conical horn, 3 dB beamwidth 0.3° |
| Receiver type | - Dicke switching radiometer, dual-conversion superheterodyne |
| | 1st IF: 4 to 8 GHz |
| | 2nd IF: 60 MHz center frequency, noise bandwidth approx. 30 MHz |
| Sensitivity | - Approx. 1K for 60 s integration time |

TABLE MOUNTAIN EXPERIMENT

During April 1971, an experiment was conducted at Table Mountain near Boulder, Colorado, primarily to evaluate the performance of several radiometric systems in yielding atmospheric temperature profiles; however, as the planning for the experiment evolved, it became clear that additional sensors could not only benefit from but supplement the basic objectives of the main experiment. As a result, the final scope of the program greatly exceeded the original plan. The list of participants along with their respective measurements follows:

| <u>Participant</u> | <u>Equipment</u> |
|------------------------------------------|-------------------------------------------------------------|
| Air Pollution Control Office | 54.5 GHz radiometer, angle-scan mode |
| Sperry Rand Corporation | 54.5 GHz radiometer, angle-scan mode |
| Wave Propagation Laboratory, NOAA | 4-frequency radiometer, angle-scan and multi-spectral modes |
| | Acoustic sounder |
| | Infra-sound array |
| | Lidar |
| | Infrared radiometer |
| | Radiosonde data |
| | Aircraft temperature measurements |
| | Surface T, RH, P, Sky photographs |
| National Center for Atmospheric Research | Boundary layer profiler (tethered balloon with radiosonde) |

In the remainder of this paper, we shall limit our discussion to the WPL radiometric observations to provide temperature profiles and a comparison of the inversion results with the temperature profiles measured by the radiosondes.

Data were recorded three times daily beginning at 0400, 0900, and 1500 during a one-week period in April 1971. These observation times were selected in order to acquire data for a variety of profiles. The radiometric observations were made at a series of 10 discrete antenna elevation angles ranging from 0° to 90° ; a complete run required about one hour. During the radiometer measurements, a radiosonde was released and data were recorded to an altitude of about 10 km; the aircraft also recorded temperature-height variations to an altitude of 3 km. Before and after recording of the radiosonde data, the boundary layer profiler made a sounding from the surface to about 500 meters and back to the surface. In addition to these supporting data, sky photographs were made at each antenna elevation angle so that possible contamination of data by clouds could be detected.

The majority of measurements recorded showed lapse temperature profiles; however, 3 temperature inversions were present. We shall now examine a few sets of data from two viewpoints:

1. What is the optimum set of input data?, and
2. What are the relative effects of different statistics upon the final inversion result?

INVERSION RESULTS

The theoretical accumulated standard deviation of the estimated difference in inferred and actual (measured) temperature profiles is shown in Figures 2 and 3; the two figures illustrate the effects of using different statistics as well as different sets of input data. Figure 2 is based upon the 5 year mean all month radiosonde data for Denver, Colorado, while Figure 3 is calculated using the 5 year mean April radiosonde data. The various curves are plotted for different sets of input data; the symbol for a particular set is shown in the legend. Combinations 1A, 1, and 2 refer to the multi-spectral input data combinations listed in Table 2. Combinations 1A and 1 are equivalent except that 1A is computed for a simulated measurement accuracy of 0.1K while combination 1 is based upon the actual observed differences between radiometric measurements and the brightness temperature calculated from radiosonde information. Angle scan designations are simply measurements of brightness temperature versus elevation angle at the frequency indicated.

The curve labeled a priori is the theoretical inversion accuracy that would be obtained if only the long-term statistics and the surface temperature were known. In all the results presented here, the measured surface temperature is used as a constraint. The theoretical curves for spectral combinations 1 and 4 are nearly identical; the curves for combination 4 have been omitted from Figures 2 and 3 for clarity.

Table 2. Explanation of spectral combinations employed to estimate temperature profiles

| Combination No. | Input Data | |
|-----------------|-----------------------|------------------------|
| | Elevation Angle (deg) | Frequency (GHz) |
| 1 | 5 | 54.5, 55.5 |
| | 10 | 54.5, 55.5 |
| | 15 | 54.5, 55.5 |
| | 30 | 53.5, 54.5, 55.5 |
| | 60 | 52.5, 53.5, 54.5 |
| | 90 | 52.5, 53.5, 54.5 |
| 2 | 90 | 52.5, 53.5, 54.5, 55.5 |
| 3 | 60 | 52.5, 53.5, 54.5, 55.5 |
| 4 | 5 | 53.5, 54.5 |
| | 10 | at all angles |
| | 15 | |
| | 20 | |
| | 30 | |
| | 60 | |
| | 90 | |

Several important points are brought out in Figures 2 and 3. First, it is clear that spectral combination 1 results in the smallest standard deviation over the full 10 km height interval. Second, the accumulated error in the angular scan mode is about the same at both 53.5 and 54.5 GHz and is smaller than for multi-spectral measurements at a fixed elevation angle, i.e., combination 2. Thus we reach the not surprising conclusion that a combination of angular scan and multi-spectral input data yields a better inversion result than either set of input data alone. It is somewhat surprising that a fairly large reduction in measurement error (from approx. 2.5K to 0.1K) does not result in a substantial decrease in accumulated error for combination 1. This result may indicate that multi-spectral angular scan measurements need not be extremely accurate to give good inversion results except during serious departures from horizontal stratification.

The rather poor performance of the multi-spectral inversion method may be partly caused by measurement error; however, the main reason is believed to be the smaller number of input measurements in the multi-spectral case. It is also possible that a more optimum selection of frequencies would result in a smaller difference between inferred and actual profiles.

As for the comparative merits of the statistics used to invert the data, it appears that all-month and April statistics produce comparable results over the first 3 or 4 km for all input

combinations. Above 4 km, use of April statistics results in a slightly smaller error when angular scanning or spectral combination is used. Thus, for this rather limited sample at least, the inversion result is rather insensitive to the statistics employed.

We shall now examine some of the actual inversion results and compare the measured and inferred profiles for a few samples. Figure 4 is an example of a profile containing a surface based temperature inversion. The curves are the profile measured by the radiosonde and the profile inferred from the radiometric data; inversion results are shown for four different combinations of input data. All sets of data, except for spectral combination 2, show the presence of the temperature inversion. Although the magnitude of the inversion is slightly underestimated in this example, the height of inflection is fairly well defined. As predicted by theory, spectral combination 1 gives the best overall agreement with the radiosonde profile. Note that combination number 4, for which a theoretical curve is not shown, results in agreement comparable to that obtained with combination 1 and the angular scans at both frequencies. This trend was observed consistently in all the samples considered in this study which suggests that a two-frequency radiometer operated in the angular scan mode yields results comparable in accuracy with those obtainable with a 4-frequency device; however, it does not necessarily follow that this behavior would be true for all geographic areas.

Figures 5 through 7 show inversion results for three other samples using spectral combination 1 and April statistics to illustrate recovery of several different types of profiles. The radiosonde data in Figure 5 show an elevated temperature inversion at about 500 m altitude: the inversion is also seen in the aircraft and boundary layer profile recordings. The inferred profile does not detect the intensity of the elevated inversion although there is a change in the estimated profile lapse rate in the vicinity of the temperature inversion. This inability to detect elevated temperature inversions has also been observed in angular scan measurements.⁽³⁾ In both instances, it is believed that the temperature structure is smoothed out because of integration effects and/or overlapping of weighting functions. In principle, the multi-spectral approach should be more successful in recovering elevated inversions if the frequencies of operation are chosen so as to cause the weighting function to give more information in the vicinity of the elevated inversion. It is clear that the optimum frequency problem should receive additional study.

CONCLUSIONS

Based upon the very limited sample available for this study, it is concluded that a combination of angular scan and multi-spectral input data produces more accurate inferred profiles than do other input data combinations. It further appears that the angular scan method is superior to multi-spectral techniques especially when detecting surface based temperature inversions. However, the possibility exists that a more optimum selection of frequencies would result in improved accuracy for the multi-spectral method. For the measurements reported here, a 2 frequency-angular scan combination yields results nearly as good as those obtained with the 4 frequency angular scan combination. The implication regarding simplification of equipment is obvious; thus, the extent to which this result applies to other geographic areas should be carefully evaluated.

REFERENCES

1. Westwater, E. R. (1970): Ground-based determination of temperature profiles by microwaves, Ph.D. Thesis, Dept. of Physics, University of Colorado, Boulder, Colorado, 121pp.
2. Steelin, D. H. (1969): Passive remote sensing at microwave wavelengths, Proceedings of the IEEE 57, No. 4, 427-439.
3. Westwater, E. R. (1971): Microwave determination of low altitude temperature profiles, Proceedings of 7th International Symposium on Remote Sensing of Environment, Ann Arbor, Michigan, May 17-21, 1971.
4. Meeks, M. L., and A. E. Lilley (1963): The microwave spectrum of oxygen in the earth's atmosphere, J. Geophys. Res. 68, No. 6, 1683-1703.

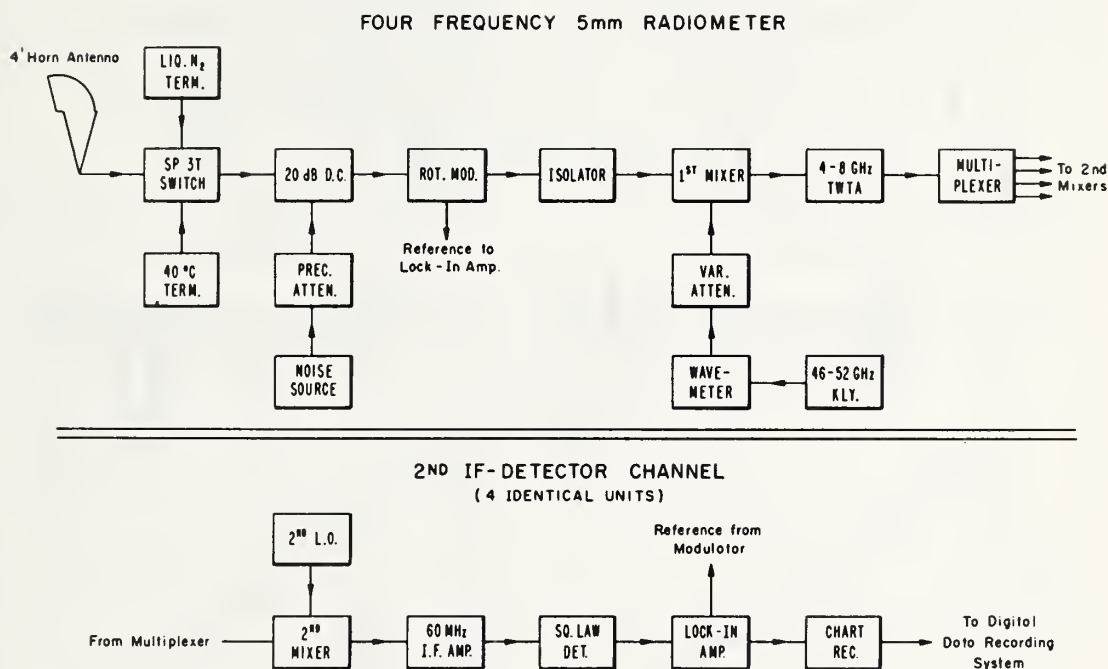


Figure 1. Block diagram of multi-frequency radiometer.

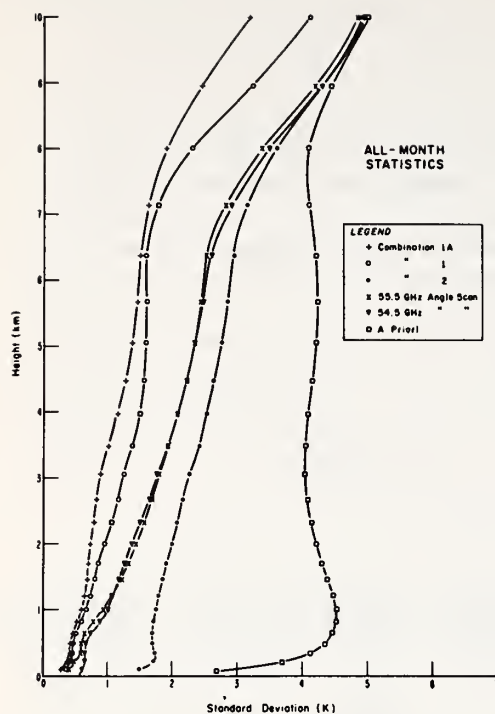


Figure 2. Theoretical accumulated standard deviation of estimated profile using all-month statistics.

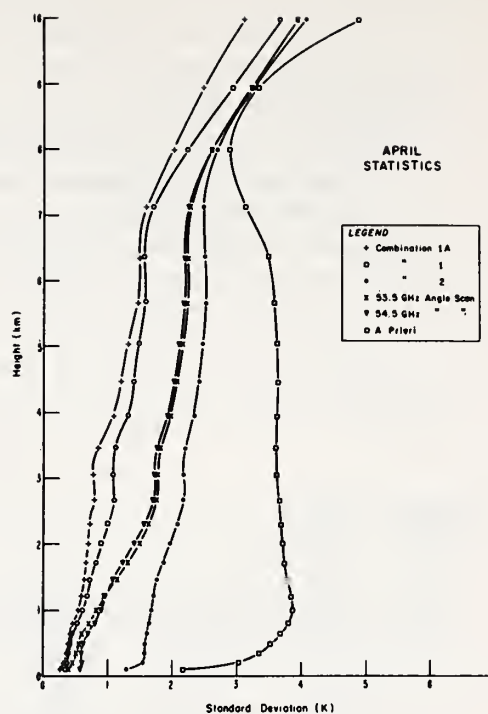


Figure 3. Theoretical accumulated standard deviation of estimated profile using April statistics.

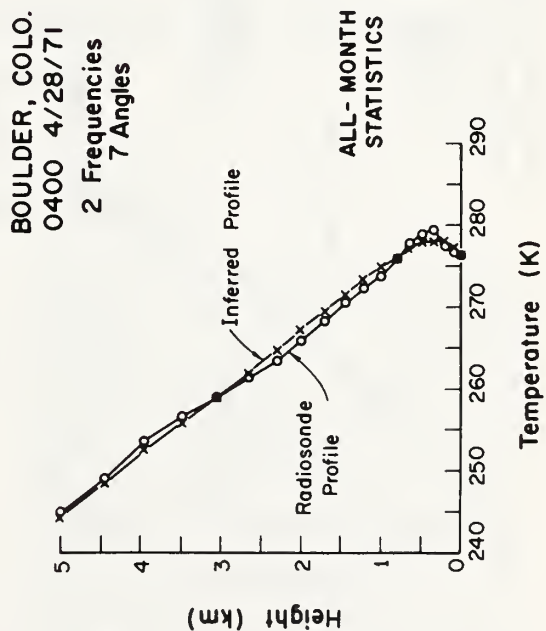
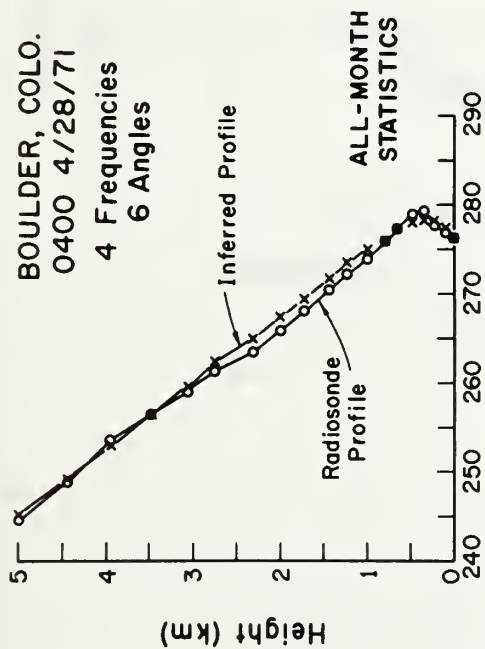
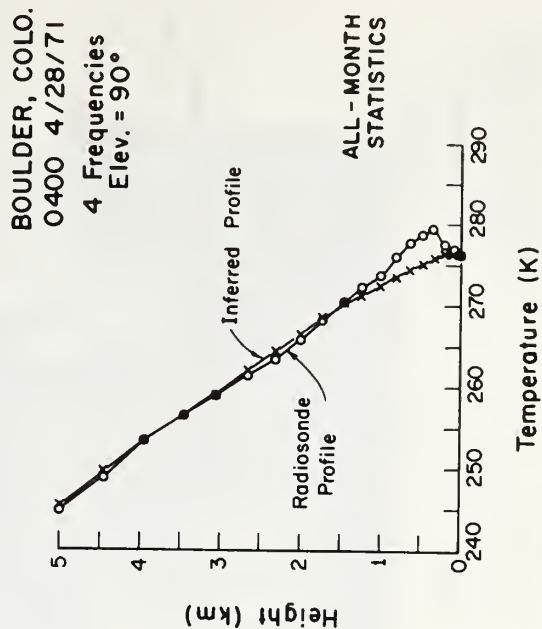
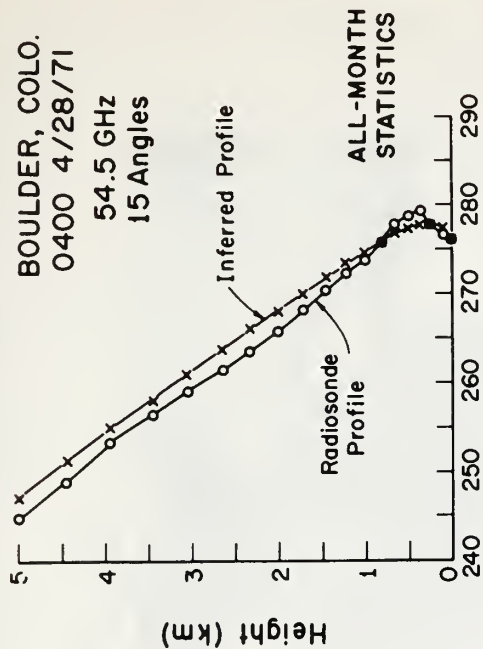
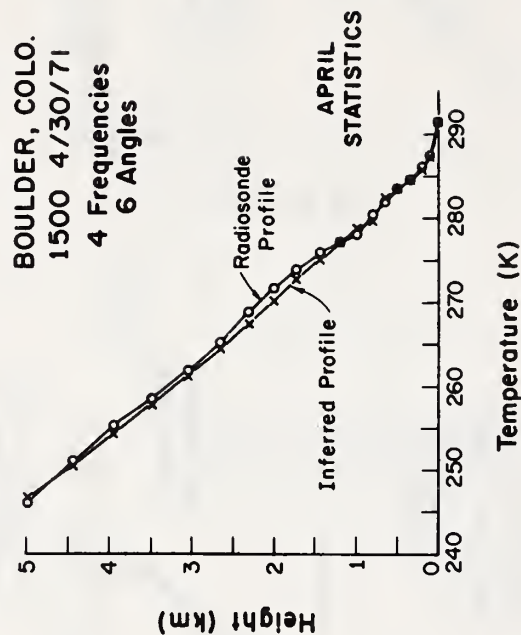
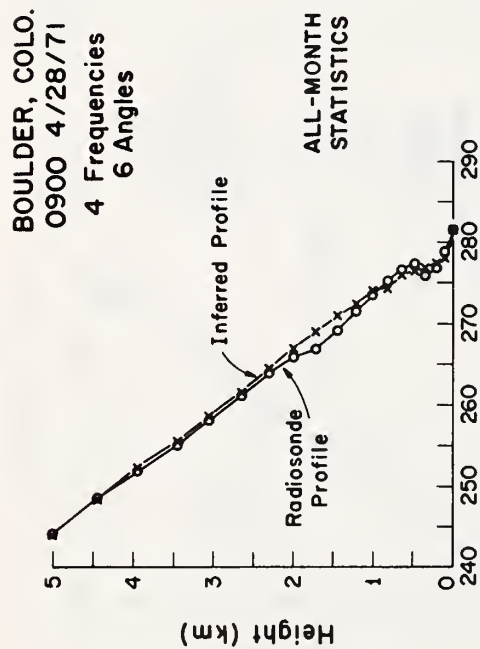
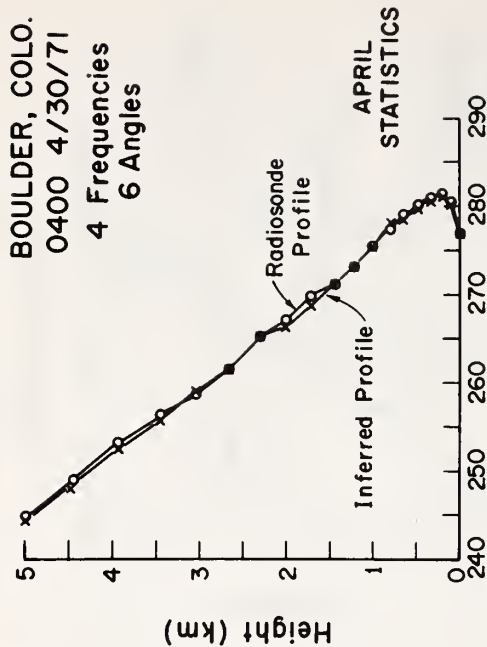


Figure 4. Inferred and measured temperature profiles using four different combinations of input data.



Figures 5, 6, 7. Inferred and measured temperature profiles using combination of angle-scan and multi-spectral input data.



An Electromagnetic Technique for Tornado Detection

W. L. TAYLOR, *Environmental Research Laboratories,
NOAA, Boulder, Colorado*

A STUDY has been conducted during the past few years by the Wave Propagation Laboratory of the Environmental Research Laboratories of the National Oceanic and Atmospheric Administration to find an electromagnetic signature suitable for tornado detection. The initial experimental phase of this work showed that most tornadic storms have major radio-frequency electrical activity associated with them. The parameter most suitable for use as a radio-frequency signature of tornadic activity was the number of bursts, per unit time, of high impulse rates as measured at frequencies in the range 1 MHz to 100 MHz. These electromagnetic impulses seem to be radiated from lightning discharge processes within the parent cloud producing the tornado. It was also found, however, that a few severe storms, as well as some local nonsevere storms, produced burst rates comparable to those associated with tornadic storms.

To test the feasibility of this electromag-

netic technique of tornado detection, fifteen observational units were operated within or near "tornado alley" between 15 March and 15 September 1972. Each unit continuously recorded the number of bursts per minute of high impulse rates at a frequency of 3.16 MHz. Two amplitude threshold levels corresponding to nominal impulse field strengths expected at distances less than about 15 nautical miles and less than about 30 n mi were employed to give an approximate indication of range.

A column of four color-coded lights for each range was located on the front panel of the equipment cabinet. The different colors served as indicators of the observed burst rates at the two threshold levels. To be counted as a burst, the received 3.16 MHz signals were required not only to exceed the range threshold but also to contain more than 50 impulses at rates exceeding 500 per second. The different lights were used to indicate when the burst rate exceeded three per

minute, 10 per minute, 20 per minute, and 30 per minute. A multichannel event recorder produced a paper chart record of the equipment responses.

Analyses of these data revealed there were 542 electromagnetic equipment responses during the season. These responses were correlated with the Severe Weather Reports from the National Severe Storms Forecast Center in Kansas City. A total of 41 tornadoes, 30 funnel clouds, 54 hail storms, 60 wind storms, and 507 thunderstorms was reported within a range of 30 n mi from the 15 recording units during the observational period. The correlation of equipment responses with the various reported storm conditions indicated that nonsevere thunderstorms produced an average burst rate of about three per minute, severe storms related to wind or hail damage resulted in about 10 bursts per minute, severe storms associated with funnel clouds produced about 13 per minute, and severe storms that produced tornadoes attained an average of about 20 bursts per minute.

The degree of success of this technique for tornado detection was measured by presuming that a burst rate exceeding 20 per minute was indicative of tornado activity. Based on this presumption, it was found that 73% of the tornadoes would have been warned for, 40% of the funnels would have been indicated as tornadic, 27% of the hail and wind storms would have been classified as tornadic, and only 6.5% of the thunderstorms would have produced false alarms. These percentage values are rather impressive until we remember there are many more nonsevere thunderstorms than there are tornadic storms. Thus, if tornadic conditions were warned for each time a burst rate exceeds 20 per minute, there would actually have been tornadoes or funnel clouds present during only about 25% of the warnings.

It should be realized that these results were obtained using only the responses of the electromagnetic detection equipment and without taking advantage of any other available information. This technique should not be considered as an independent tornado detector on an operational basis, but rather as an aid in warning of tornadoes in conjunction with radar and other information.

Based on the success of these 1972 tests, an operational evaluation of the technique will be undertaken during the 1973 tornado season at a selected number of National Weather Service Offices. In addition, directional capability is being developed and will be available in a new generation of detection equipment in the near future. The addition of direction of arrival to the burst rate measurement is expected to greatly reduce the false alarms caused by the additive effect of numerous nontornadic sources simultaneously occurring within range of the equipment. The indication of direction will also aid the local personnel to track electrically-active storm regions and to relate these with the radar returns.

Reprinted with permission from Journal of Geophysical Research
Vol. 78, No. 36, 8761-8777, December 1973

Electromagnetic Radiation from Severe Storms in Oklahoma during April 29-30, 1970

WILLIAM L. TAYLOR

*National Oceanic and Atmospheric Administration
Environmental Research Laboratories, Wave Propagation Laboratory
Boulder, Colorado 80502*

The results of observing the radiation from lightning discharge processes indicated that major radio frequency electrical activity was associated with the tornado-producing severe storms that struck Oklahoma City during this period. Rates of occurrence of atmospherics at frequencies from 10 kHz to above 3 MHz were observed by using short time constant circuits to preserve the burst nature of the received impulse signals. It is suggested that the parameter most indicative of tornadic activity is the number of bursts of high atmospherics rates at frequencies above about 1 MHz.

A project to search for possible electromagnetic signatures suitable for tornado detection was initiated in 1969 by the Institute for Telecommunication Sciences of the Environmental Science Services Administration. This project was subsequently assigned to the Wave Propagation Laboratory in the Environmental Research Laboratories of the National Oceanic and Atmospheric Administration. This paper summarizes the electromagnetic observations conducted during April 29 and 30, 1970, and includes an interpretation of the recorded data.

The concentration of energy within the relatively small volume of a tornado has been the subject of much investigation for more than a century, but this concentration has not been explained in terms of the energy budget. The power required to drive a tornado vortex has been estimated to exceed 10^8 kw [Vonnegut, 1960], yet this is small in comparison with the energy available in a single thunderstorm cell, which may exceed 10^9 kw [Braham, 1952]. Various theories have been proposed over the years that suggest that a tornado may be produced by the concentration of kinetic energy resulting from the conservation of angular momentum through some not yet understood mechanism associated with the intense electrical activity often observed during severe storms.

Many eyewitness accounts of unusual electrical activity in and around tornados have been reported during the last 20 or 30 years. Jones

[1950] gives accounts of lightning and thunder during a tornado being decidedly different from that during ordinary thunderstorms, for example, the presence of St. Elmo's fire in the vicinity of a tornado funnel and the rapid occurrence of 'one stroke right after another' at the base of a cloud just ahead of the funnel. Jones [1965] also reported nighttime observations of approximately circular patches of flashing pale blue illumination originating from within severe storms. Vonnegut [1960] references some observations that are indicative of intense electrical discharges near and within the funnel.

Jones [1959] reported that the atmospherics rate in the 10-kHz region of the spectrum increased as the intensity of a thunderstorm increased but decreased to a relatively small value prior to a tornado formation. However, the atmospherics rate at 150 kHz greatly increased during the formation of a tornado. More recently, the effects observed on television sets tuned to channel 2 (54 MHz) have been reported by Waite and Weller [1969] and by Biggs and Waite [1970].

The electrical charges within a thunderstorm cloud are usually dispersed throughout the cloud and discharged to the earth by the discrete current surges of lightning strokes. Electromagnetic fields radiated during lightning strokes, called atmospherics, contain frequency components extending from a few hertz to many megahertz. Reviews of the complex structure

of these fields are given by *Horner* [1964], *Oetzel and Pierce* [1969], and *Taylor* [1972]. The responses of receivers tuned to frequencies less than about 30 kHz are discrete and are easily associated with return strokes in a cloud-to-ground discharge. As observing frequency increases, the number of responses increases to several thousand at frequencies above 10 MHz and results from the high rate of electromagnetic impulses radiated from various intracloud processes during the lightning discharge.

If appreciable electric currents do flow either within or in close association with the tornado funnel, as is indicated by *Brook* [1967], and are widely distributed within the parent storm cloud, the process might well tend to be almost continuous in the form of corona sparks or a gaseous glow. This would tend to reduce the energy radiated at lower frequencies from return strokes and increase the energy partitioned into higher frequencies from short-distance rapid occurrence dispersive processes within the cloud.

Recent works of *Silberg* [1965], *Stanford et al.* [1971], and *Taylor* [1972] show that enhancements in impulse counting rates occur at times of reported tornados and that high-frequency receivers are better monitors than receivers tuned to the lower portion of the radio spectrum. But the tornado vortex may not be the source of these impulses, for *Scouten et al.* [1972] suggest that a general intense electrification of the parent thunderstorm may produce the observed increase in activity.

The present paper is concerned with the selection of electromagnetic parameters that are practical to monitor and have a high probability of being sensitive indicators of tornadic conditions.

INSTRUMENTATION

The initial work in May 1969 using a mobile van operating in central Oklahoma consisted of intermittent observations of the resonant circuit responses at six frequencies in the 10- to 500-kHz region using single-stage filters with 1-kHz bandwidths. The analysis of these initial data showed that new equipment having greater dynamic range and wider bandwidth filters and extending to much higher frequencies would be required to define properly the character-

istics of radio frequency electromagnetic radiation from severe storms.

The design of equipment for the observation of electromagnetic signals from lightning discharge processes was dictated in part by the results from the 1969 observations, the cost of the instrumentation, and the need to record some parameter closely associated with thunderstorm activity. To record and analyze the amplitude responses of several resonant circuits for individual impulses would require elaborate and expensive equipment. It was decided to observe the rate of occurrence of atmospherics, which would be represented by the average number of resonant circuit responses exceeding certain amplitude levels per unit of time.

Two vertical monopole antennas with associated gain controls and amplifiers were used to cover the frequency band from 10 kHz to 3.16 MHz. Each antenna was 0.63 cm in diameter and 1 meter in length and had a 15-cm hemispherical corona cap at the top and an antenna coupler at the base. The corona cap greatly reduced the occurrence of corona on the antenna. It added only 3 pF to the antenna capacity of 15 pF and did not otherwise affect the antenna response. The antenna coupler was secured to a 4-foot-square aluminum base, and the whole unit was enclosed in a plexiglass dome. The low-frequency system band pass (3-db reduction in response) from antenna input to the distribution amplifier output extended from 2 kHz to 600 kHz. Band pass of the high-frequency system was from 300 kHz to 5 MHz.

Calibrations were performed by inserting rectangular pulses into the antenna coupler through a dummy antenna equivalent to the antenna capacity. The amplitude of the pulses was adjusted to be equivalent to that of the desired free space field. The length of the pulses was adjusted to produce the same Fourier spectrum amplitude at a particular frequency, and thus the same tuned circuit response, as would be obtained from a single voltage step function of the desired amplitude. The amplitude responses of all the tuned circuits were the same, since the decrease in spectral amplitude of the pulse was just compensated by the increase in bandwidth as the channel frequency increased. The actual pulse used had a rise time of about 0.05 μ sec, which caused the pulse spectrum to

change from 6 db per octave to 12 db per octave at a frequency of about 5 MHz.

After the threshold levels were adjusted, each recorder response was calibrated for atmospheric rates by using rectangular pulses of the proper amplitude and pulse length for each channel. Atmospheric rates were calibrated each decade starting with 5 pulses/sec for 10 kHz, 100 kHz, and 1 MHz and starting with 1.6 pulses/sec for 31.6 kHz, 316 kHz, and 3.16 MHz. The maximum rate to which a set of channels could respond was limited by the bandwidth.

Thirty channels of atmospheric rate data were available for presentation. Observation frequencies were 10 kHz, 31.6 kHz, 100 kHz, 316 kHz, 1 MHz, and 3.16 MHz with five amplitude threshold levels for each frequency. These levels corresponded to electromagnetic fields at the antenna of 0.316, 1.0, 3.16, 10.0, and 31.6 v/m, which are -10 db, 0 db, 10 db, 20 db, and 30 db, respectively, relative to 1.0 v/m. Integration time constants were inversely proportional to frequency, varying from 1.0 seconds at 10 kHz to a minimum of 0.01 seconds at 1.0 and 3.16 MHz. All of the atmospheric rate data were recorded on FM magnetic tapes. These tapes were played back and the data transcribed onto paper charts. Reproductions from the paper charts were cut into narrow strips, aligned in time, and presented in a single figure for a particular selection of data to assist the eye in following related events. Although other frequencies and other channels of data were obtained, these will not be presented here.

A simplified block diagram and the associated circuit responses for the atmospheric rate equipment are shown in Figure 1. A transient signal radiated from a lightning discharge process arrived at the antenna. The transient passed through a high-input impedance antenna coupler, which in turn drove the transient through about 70 meters of coaxial cable to the main equipment van. It was then distributed to the appropriate single stage tuned circuits, which were resonant at the desired frequencies. The bandwidth of each tuned circuit was 10% of its center frequency. The response signal was presented to a logarithmic amplifier and then rectified and smoothed. Five trigger circuits were individually adjusted to activate a one-

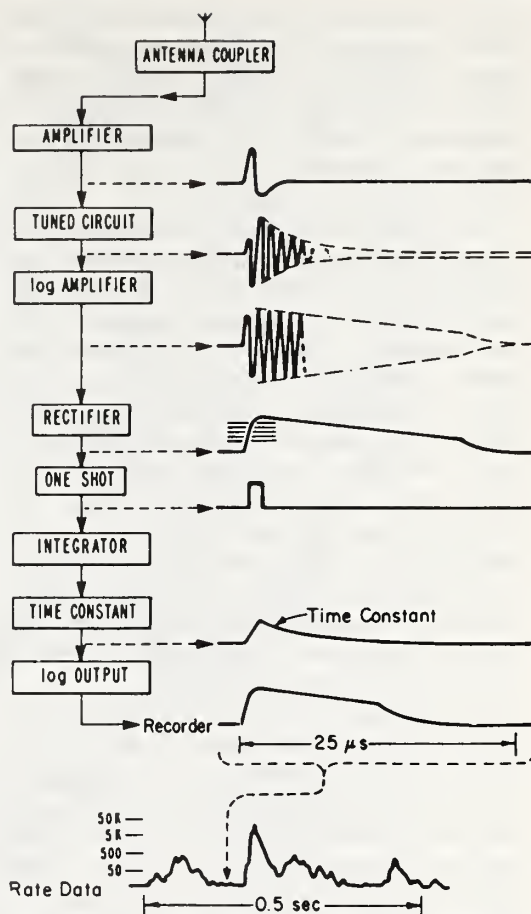


Fig. 1. Simplified block diagram and circuit responses for atmospheric rate equipment.

shot multivibrator each time the signal exceeded a predetermined level. The output of each one-shot was integrated with a suitable time constant and presented to a data recorder through a logarithmic output driver.

The 25- μ sec time base for the circuit responses in Figure 1 is appropriate for a 1-MHz channel. A single transient is hardly recognizable in the atmospheric rate data sample shown, which was for a 0.01-sec integration time constant. Overall measured response time to 90% of the actual atmospheric rate was about twice the time constant. The recorded atmospheric rate for a very short duration burst of impulses would be less than the actual rate. Very few bursts are less than 20 msec, however, and therefore the indicated rates should be reasonably accurate. The atmospheric rate data

can be interpreted as the running average number of atmospherics producing tuned circuit responses exceeding a selected amplitude threshold. A burst is defined as a group or packet of atmospherics that arrive at relatively high rates and have a duration usually greater than 0.1 sec but less than 1.0 sec.

The direction of arrival of atmospherics was obtained from two orthogonally positioned loop antennas in the vertical plane combined with the vertical electric antenna for sense. Each loop consisted of 16 turns on a 0.7-meter-square frame covered by an electrostatic shield. This was a relatively wide band directional unit in which the frequency response extended from 2 kHz to 600 kHz. A cathode ray tube of an oscilloscope was used to indicate the directions, and a 35-mm camera was used to record the cathode ray tube display. The camera was operated intermittently in an open shutter strip-film mode at a rate of one time exposure frame each second or was operated so that time exposures of several minutes were obtained.

Loop antennas respond to both the vertical and the horizontal component of signals. It is the horizontal component that causes what is referred to as polarization error in a crossed-loop direction-finding unit. The error in the indicated direction will be a function of the polarization of the source and the angle of elevation as viewed from the loops. The polarization of the source (i.e., the ratio of horizontal to vertical orientation of the discharge current moments) may become very large in severe storms, as was indicated recently by *Shanmugam and Pybus* [1971]. Angle of elevation is determined by range and height. The height can be appreciable, as is shown by *Atlas* [1959] and *Taylor* [1969], but only a small percentage of lightning discharges are likely to exceed a height of 10 km. At very close ranges of about 10 km or less, where the angle of elevation is large, directional errors become very large, and crossed-loop direction-finding systems become essentially useless. But azimuthal error decreases very rapidly as distance increases. For 30-km range the error is not likely to exceed 10° for a source polarization ratio of 1 and a height of 5 km. The error for 50-km range will be less than 5° , which is approximately the azimuthal spread in direction expected from many discharge processes observed from this

range. If the whole discharge containing random polarization of current moments is observed, then the polarization error of the crossed loops will produce a random distribution in indicated direction around the true azimuth to the source. Thus a discharge at 30-km range will produce a distribution in the indicated azimuth to each element of the discharge and may result in a direction pattern that is 20° wide. However, the center of the distribution should give the true azimuth to the center part of the discharge, provided there is no preferred orientation of the current moment polarizations. Other directional errors resulting from loop construction, local site conditions, and scaling techniques are estimated to be less than 2° .

OBSERVATIONS AND ANALYSES

The recording equipment was located in a large van near the National Severe Storms Laboratory (NSSL) at Norman, Oklahoma. Thunderstorm areas were tracked by associating the observations of atmospherics activity from the direction of arrival display with precipitation echoes from WSR-57 weather radar operated by NSSL. Data recording was started when thunderstorm activity began to either grow within or move into the general Oklahoma area, and the recording ended when the thunderstorms began to dissipate or move outside a range of about 100 km.

During the 1970 spring tornado season in Oklahoma, 93 hours of observations were recorded during 13 periods of thunderstorm activity in April and May. The data presented in this paper include only those obtained during an observation period totaling $13\frac{1}{2}$ hours beginning at 1900 GMT on April 29 and ending at 0830 on April 30, 1970.

Thunderstorms began to build by 1500 GMT on April 29 and were numerous in central Oklahoma by 1800 GMT, although atmospherics activity was very low at that time. Movement of the thunderstorms during all of the observations was toward the northeast at about 75 km/hr. Tracings of the NSSL radar echoes are presented in Figure 2 to give an overall qualitative view of the weather picture during the main period of thunderstorm activity. The complexity of the weather as indicated by these radar tracings is obvious as one follows the movement of the many storm areas and the

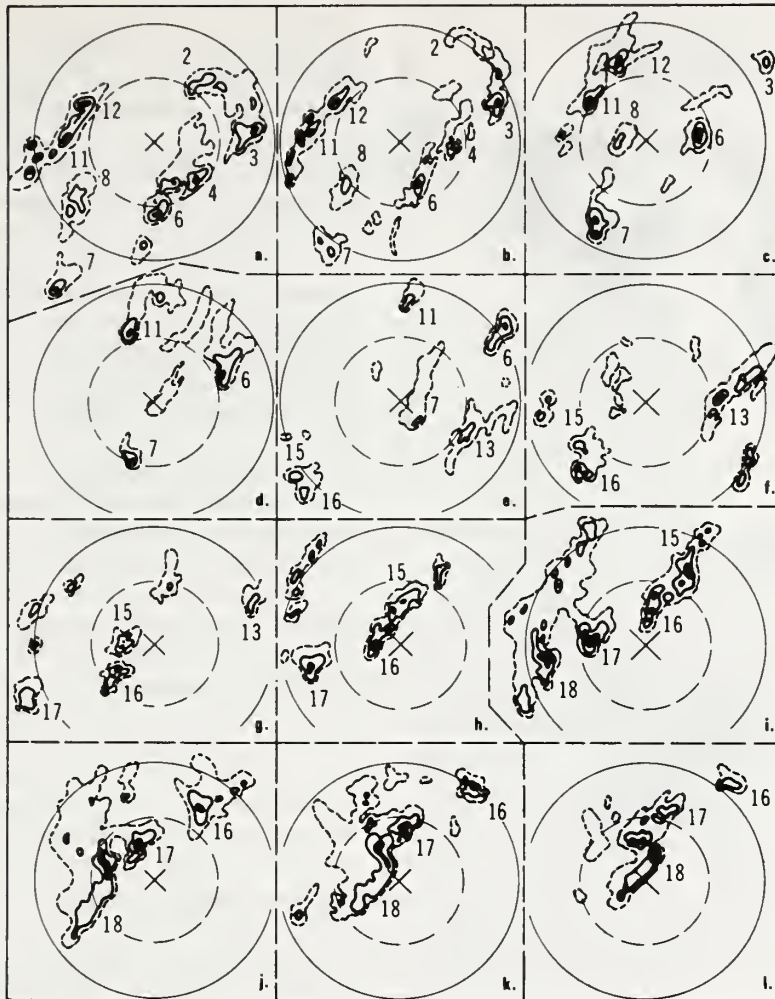


Fig. 2. Qualitative radar tracings for April 29–30, 1970. Inner circle is 100-km range; outer circle is 185-km range. Approximate times of the radar frame from which the tracings were made are (a) 2230 GMT, (b) 2300 GMT, (c) 0000 GMT, (d) 0100 GMT, (e) 0200 GMT, (f) 0300 GMT, (g) 0400 GMT, (h) 0500 GMT, (i) 0600 GMT, (j) 0700 GMT, (k) 0730 GMT, (l) 0745 GMT. NSSL is at the cross in the center of the circles, north is up, and east is to the right.

changes in shape and intensity of each area as a function of time. Storm areas that will be referred to later in the text are numbered to aid in their identification and in following the movement of these particular echoes.

An example of weather radar precipitation areas and of the corresponding atmospheric direction of arrival display is shown in Figure 3. Range from the center of the radar frame is given as 93 and 185 km. The darkest portions represent locations of heaviest precipitation. The approximately circular radar echo area in

the center of the frame resulted from ground clutter. The length of each trace from the center of the direction of arrival display is proportional to the atmospheric pulse amplitude. The darkest parts of the display indicate directions to the most active thunderstorms. Number designations are shown to assist in identifying some of the thunderstorm areas with the corresponding direction of arrival of atmospherics. The radar frame shown in Figure 3 is for the same time as the radar tracing presented in Figure 2a.

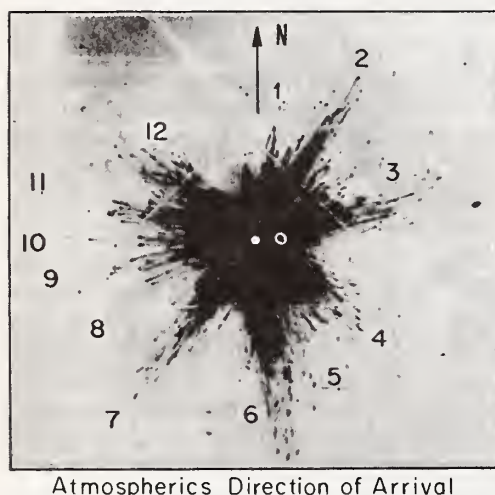
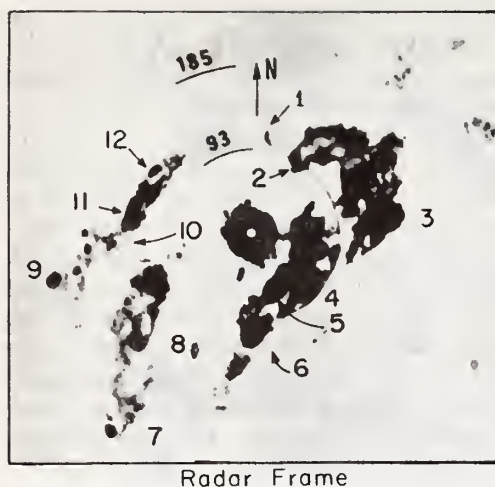


Fig. 3. Examples of radar and direction of arrival for April 29, 1970, at 2230 GMT.

Thunderstorm areas 2, 3, 6, and 7 are distinctive on the direction of arrival display and readily located on the radar frame in Figure 3. Some of the other indicated precipitation areas and directional displays are not as easily related. The large precipitation area between storms 2 and 3 produced few large atmospherics, as was the situation with storms 3 and 4. Storm 8 produced no large atmospherics. Widespread atmospherics activity from storm areas 9, 10, 11, and 12 was indicated. Area 1 produced a recognizable number of atmospherics.

The electrical activity of the thunderstorms shown in Figure 3 was very low when com-

pared with the activity observed during severe storm conditions. Although the atmospheric direction of arrival display seems to indicate a large number of atmospherics from the various storms, this presentation resulted from a time exposure of 18 min. The thunderstorms moved a considerable distance during this period, and thus a large change in direction of arrival for some storms resulted. The greatest change in direction would be noticed for those storms located perpendicular to the direction of storm movement (i.e., storms 4 and 12), and the least change in direction would be for storms located along the line of movement (i.e., storms 2 and 7).

Exposure times were adjusted to compensate partly for variations in storm activity. As will be shown later, a time exposure of only 1 sec was sufficient for obtaining directional information from some very active severe storms. Photographic records were not made, unfortunately, in a consistent manner during these observations. Also the quality of some records was often poor because of distortion of the large amplitude atmospherics caused by limitations in the amplifier circuits, an intermittent light leak in the camera, and elliptical or loopy directional traces produced from nearby horizontal lightning channels. Therefore no further examples of long time exposure direction of arrival data will be presented.

Two examples of atmospherics rate data for an approximate 2-min period each are shown in Figures 4 and 5. Each channel is aligned in time and arranged with the 5 channels of 10-kHz rates at the top, channels 6–10 for 31.6 kHz next, etc. The frequency for each group of channels is indicated in a column on the far left of the figure. The threshold in volts per meter, which is the amplitude level the atmospherics must exceed before activating the counting circuits in each channel, is presented in the second column on the left for the odd-numbered channels and in the far right column for the even-numbered channels. Thus the lower frequencies are nearer the top, the threshold level increasing from top to bottom within each frequency. The data format is rate versus time, the atmospherics rates on an approximate logarithmic scale being presented just to the left of the data for odd-numbered channels and just to the right of the data for even-numbered channels. At-

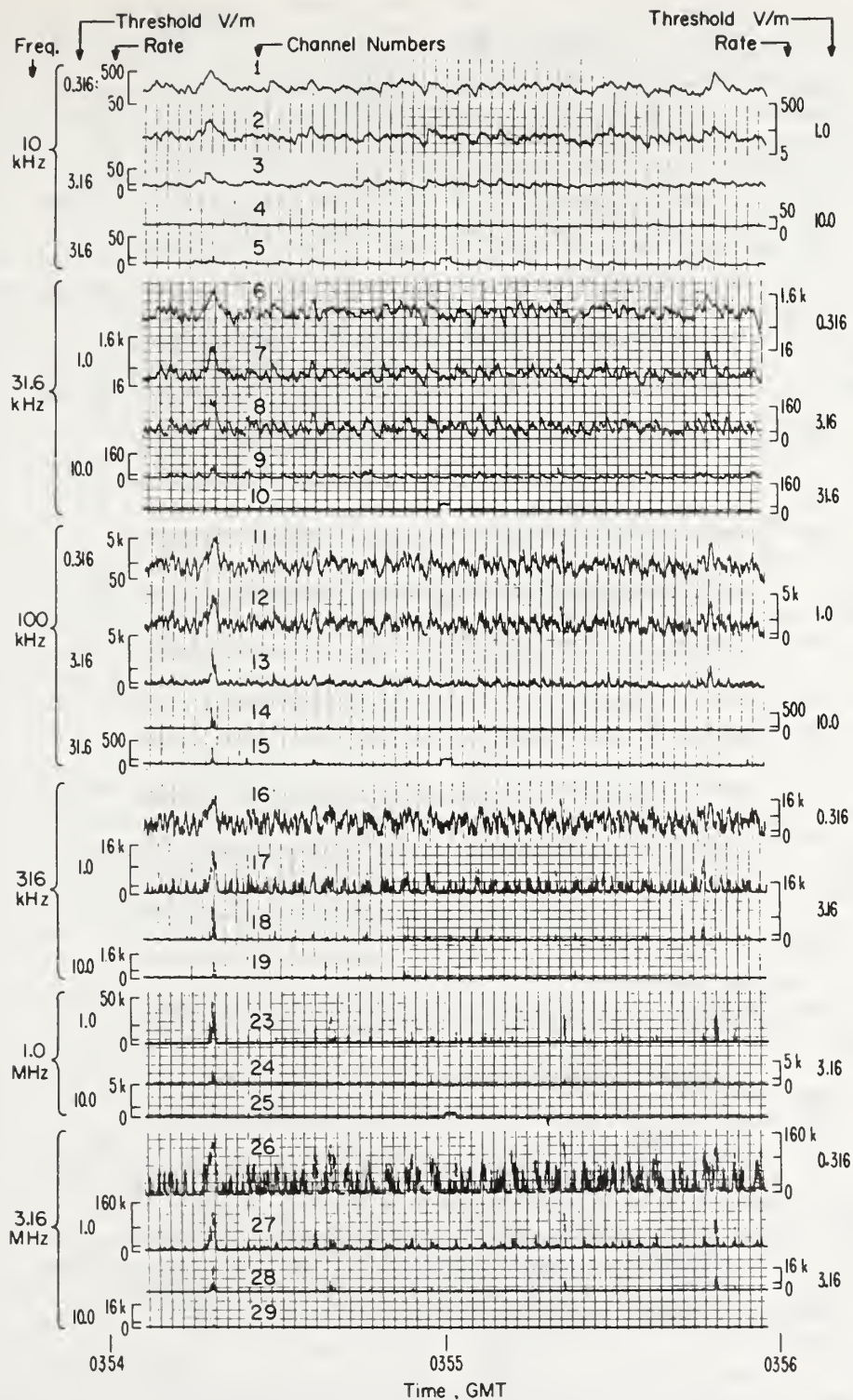


Fig. 4. Example of atmospheric rate data for low activity.

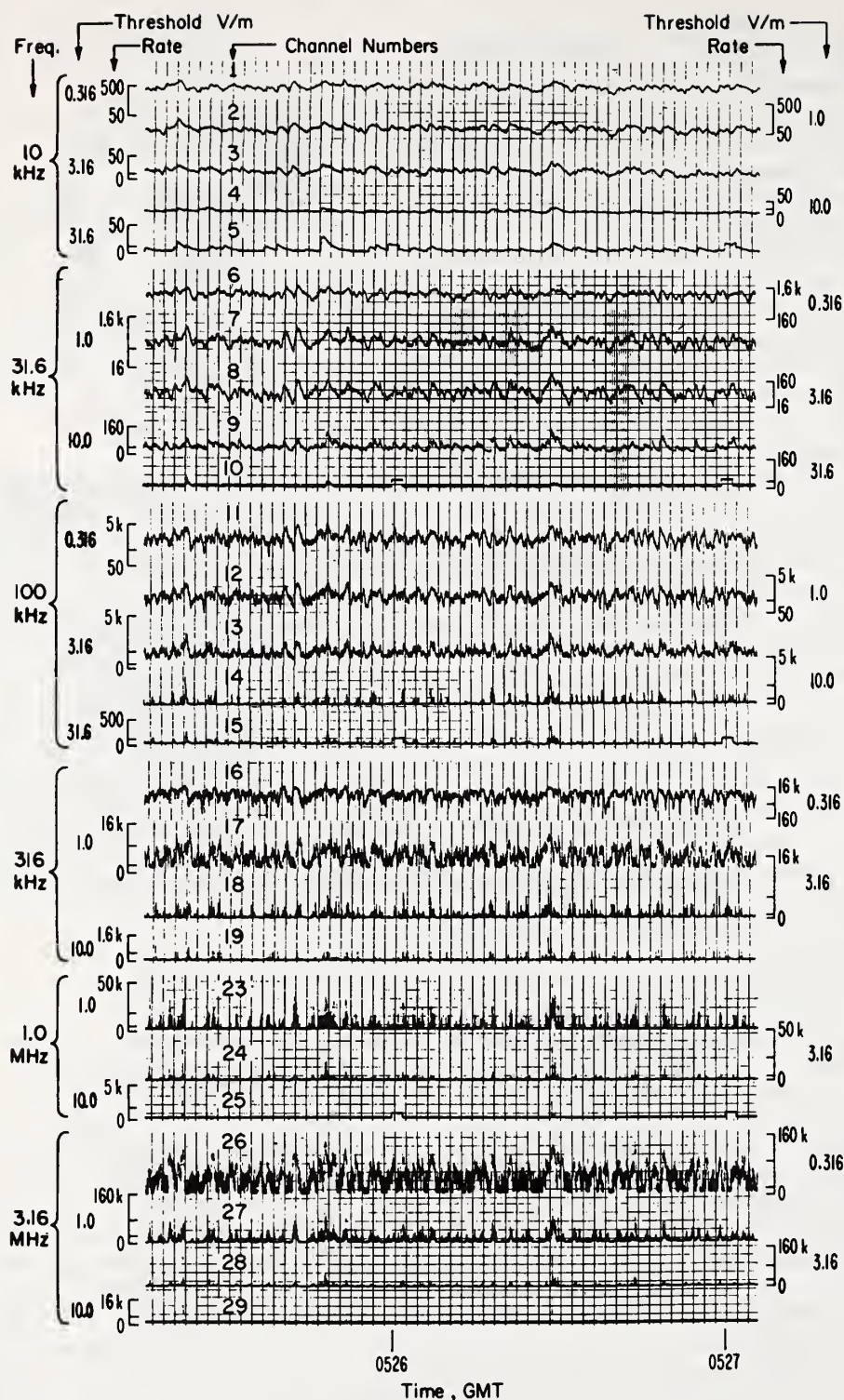


Fig. 5. Example of atmospheric rate data for high activity.

mospherics were calibrated each decade beginning at either 1.6 or 5.0 impulses per second. For example, channel 17 is the second channel of the 316-kHz group. This is an odd-numbered channel for which the threshold level of 1.0 v/m is found on the left together with a rate scale that extends from 0 to 16k per second, where k denotes thousands. The two other marks on the rate scale are for 160 and 1.6k impulses per second. When a zero rate is indicated, the rate varies approximately linearly between zero and the first rate mark and logarithmically thereafter. Indicated rates are shown in decades, and the marks indicate rates counted down from the highest rate. Small rate values not marked are identical with zero. Greenwich mean time is shown along the bottom, the vertical grid lines being separated by about 2 sec. Time marks are shown as square pulses on channels 5, 10, 15, and 25.

The data shown in Figure 4 are representative of relatively low levels of atmospherics activity seemingly characteristic of nonsevere thunderstorms. Figure 5 data, however, are representative of relatively high levels of activity observed from the more intense storms. The overall responses of the 10- and 31.6-kHz channels were very similar when these two figures were compared. Differences were beginning to show in a comparison of the 100-kHz channels and became substantial in a comparison of data channels for frequencies equal to or greater than 316 kHz.

The general characteristic of the atmospherics rate data at a given frequency will be at least in part a function of the threshold level. The lower threshold levels (e.g., channels 1, 6, 11) will be exceeded not only by the small lightning discharges from nearby sources but also by the large lightning discharges from very distant sources. This situation produces very high atmospherics rates, which tend to mask the variation in discharge rates from nearby storms. Very high threshold levels (e.g., channels 5, 10, 15) will be exceeded only by the large lightning discharges from local sources, the result being only a few occurrences of very low atmospherics rates.

To obtain a measure of the electrical activity of a storm, the average number of bursts of atmospherics per minute obtained from a 5-min sample of data was calculated for data chan-

nels 18, 23, and 27. These represented frequencies 316 kHz, 1.0 MHz, and 3.16 MHz, respectively, at threshold levels of 3.16, 1.0, and 1.0 v/m. These levels were chosen as representing the amplitude of atmospherics expected from thunderstorms at ranges less than 100 km and approximately compensate for some of the propagation losses expected at the 1- and 3.16-MHz frequencies. Bursts were counted only if the atmospherics rates exceeded the observing frequency in kilohertz. The average values of the burst rates computed each 30 min during the period from 2100 GMT, April 29, to 0830 GMT, April 30, for the selected data channels were connected by a smooth curve and shown in the upper portion of Figure 6. Three major periods of high electrical activity as manifested by these burst rates are indicated near 0000, 0500, and 0715 GMT. The ranges to the major thunderstorms previously identified by numbers in Figure 2 are shown as a function of time in the lower portion of Figure 6. Range curves from storms 6, 15, 16, 17, and 18 are shown heavier to indicate that these storms were identified by the direction of arrival measurements as being major sources of atmospherics. Range was measured from NSSL to the center of the heaviest precipitation in each thunderstorm by means of the radar data. As can be seen from Figure 2, radar echoes often extend out 30–40 km or more from the center of large storms. It is not difficult to see that, although no storm center passed over NSSL, the outside parts of many storms were much nearer than is indicated in Figure 6, and indeed, on several occasions, precipitation and lightning discharges in the vicinity of the recording equipment were experienced.

By reference to the presentations in Figures 2 and 6, the relationships between weather conditions and observed burst rates can easily be inferred. Storms 2, 3, and 4 passed east of NSSL between 2100 and 2300 GMT but were electrically inactive. To the west, storms 11 and 12 moved by between 2200 and 0100 GMT and were likewise inactive in the production of atmospherics. Storm 6 began to grow, as was indicated by radar, at about 2200 GMT and reached a maximum around 0000 GMT. This was the most active single storm area at 2230 GMT, as is shown in Figure 3. The burst rate

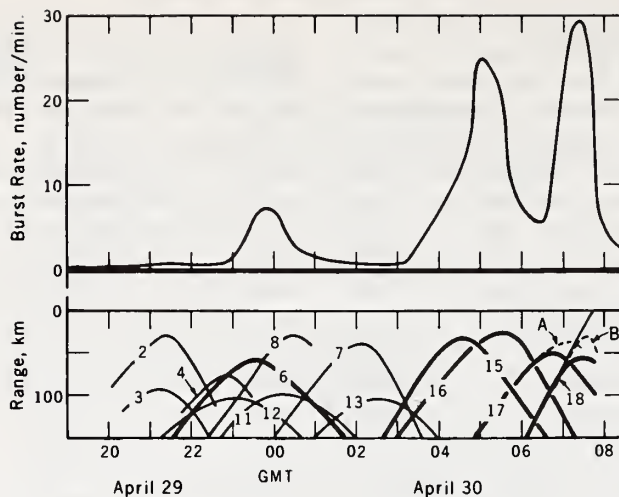


Fig. 6. Observed average burst rate and range to major thunderstorms.

for storm 6 was very low, however, until about 2330 GMT and then reached a maximum value of about 7 per minute at 0000 GMT. By this time it was moving away from NSSL and began to decrease slowly in both size and intensity.

Storm 8 never showed any electrical activity and passed just west of NSSL at about 0030 GMT before completely dissipating. Atmospheric activity from storm 7, although it was never very great, steadily decreased as the center moved to the east of NSSL, and radar echoes were no longer observed after about 0300 GMT. Radar showed that storm 13 began before 0100 GMT and continued to grow as it passed out of the range of interest, but only very low electrical activity was observed.

Storms 15 and 16 began as a single storm but separated into two areas by 0300 GMT. As this storm complex separated, the individual storm areas grew rapidly in size and intensity, as was indicated by radar. The burst rate began to increase when storm 15 moved inside the 100-km range. By 0355 GMT, the time of the example of low burst rates given in Figure 4, the burst rate had reached about 6 per minute. The center of storm 15 at this time was located due west of NSSL at a range of 45 km.

A large burst, typical of a ground discharge, is shown just to the left of the column of channel numbers in Figure 4. The duration of this burst was about 1 sec for the lower threshold levels. It is interesting to note that at these

lower thresholds the atmospheric rates are approximately proportional to the observing frequency. Thus for this particular example the atmospheric rates vary as 50 times the frequency in kilohertz, changing from about 500 per second for 10-kHz channel 1 to about 160k per second for 3.16-MHz channel 26. Most of the small-rate bursts are evidently from small intracloud discharge processes not usually regarded as primary discharges.

The rates obtained from the large-burst example shown in Figure 4 do not seem to be seriously limited by the bandwidth. The single tuned resonant circuits and associated equipment could respond to atmospheric rates of 100 times the frequency in kilohertz provided the amplitude of the largest atmospheric in the burst did not exceed 4 times the threshold level. (The instantaneous response of the resonant circuit must decay below the threshold level before the next atmospheric. Actually, the largest amplitude atmospheric can be 16 times the threshold level before limiting the counting rate to below 50 times the frequency.)

Atmospherics from storm 16 began to contribute to the burst rates after 0400 GMT. The burst rates continued to increase until a maximum of about 25 bursts per minute was reached at 0500 GMT, when both storms 15 and 16 were at about 40-km range and each was contributing equally to the received atmospheric. At 0526 GMT, storm 16 was at its closest approach at a range of 25 km, while storm 15

had moved away to a range of 70 km. Examination of the direction of arrival data indicated that storm 15 reached maximum activity near 0455 GMT, storm 16 attained maximum activity around 0515 GMT, and at 0526 GMT storm 16 was contributing about 65% of the total received atmospherics activity.

The atmospherics rate data around 0526 GMT, representative of a relatively high level of electrical activity from primarily a single storm area, can be seen by referring again to Figure 5. The average burst rate computed from channels 18, 23, and 27 was about 22 per minute. By 0600 GMT the range to storm 16 had increased to about 40 km, but the average burst rate had decreased to one third of its previous value as the storm rapidly declined in electrical activity.

Storm 17 moved toward NSSL from the WSW and reached a minimum range of 50 km at 0645 GMT. A hooked radar echo formed on the southwest edge of this storm and was associated with a long path of damage through the northwest and northern extremities of Oklahoma City. The damage was scattered and broken along the path but was believed to be tornadic in nature. The location of this tornadic disturbance relative to the radar echoes is shown in Figures 7*a* and 8*a* at the tip of the arrows marked 1. These radar displays were from a system that provided intensity contours in a sequence of shades, dim, bright, dark, dim, bright, and dark, in ascending received echo power [Sirmans *et al.*, 1970]. The range to this area of the storm producing the damage is shown in the lower part of Figure 6 as the dashed line A.

Storm 18 moved along a path almost identical to storm 17 but much faster, sustaining an average speed of about 100 km/hr. The closest approach of the center of maximum radar echo intensity was at 0730 GMT at a range of 55 km. The central part of the storm 18 complex tended to rotate counterclockwise around the most intense radar echo. The southern part of this reached the NSSL facilities at about 0745 GMT and disrupted the ac power, and so further radar observations were prevented. Range to the leading edge of this region of storm 18 is shown in Figure 6 as the solid line branching off from the range curve for storm 18 at 0700 GMT and reaching zero

range at about 0745 GMT. A path of tornadic damage was produced in the western and northern parts of Oklahoma City associated with the rapidly moving central part of storm 18, as is indicated by the tip of arrows marked 2 in Figures 7*a* and 8*a*. This tornado was generally at treetop heights and only occasionally reached ground level. Range to the tornado is shown in Figure 6 as the dashed line B.

It is difficult to interpret properly the burst rate data observed after about 0630 GMT because of the complexities associated with storms 17 and 18. Figure 7*a* shows the radar data for 0703 GMT. Figures 7*b*, *c*, and *d* show the atmospherics direction of arrival during three consecutive 1-sec time exposures. These three exposures are similar to the directional data previously presented but are for a time period of only 1 sec each, compared with several minutes for the other data. The camera shutter was open continuously, and the film was advanced between frames at a transport speed of 25 cm/sec, which required only a small fraction of a second.

Atmospherics activity as indicated by the 1-sec direction of arrival frames tended to be more persistent from the directions of about 305° and 350°, as indicated by the arrows in Figures 7*b*, *c*, and *d*. These directions are marked on Figure 7*a* and approximately pass through the stronger radar echoes of storms 17 and 18 as indicated by the placement of their identifying numbers. Note that there are relatively few atmospherics from either the direction of tornado 1 (335° at 41 km) or the direction of the genesis of tornado 2 (265° at 55 km).

The radar echoes for 0730 are shown in Figure 8*a*, and three consecutive 1-sec direction of arrival displays are shown in Figures 8*b*, *c*, and *d*. The directions to the various parts of storms 17 and 18 shifted in respect to their relative movements. The primary direction from which most atmospherics arrived was about 335°; the secondary direction from which a substantial but smaller number arrived was about 5°. These directions are shown in Figure 8*a* and indicated by arrows in Figures 8*b*, *c*, and *d*. Most of the atmospherics still seemed to come from the general directions of the stronger radar echoes, although at this time there was no way to distinguish the possible

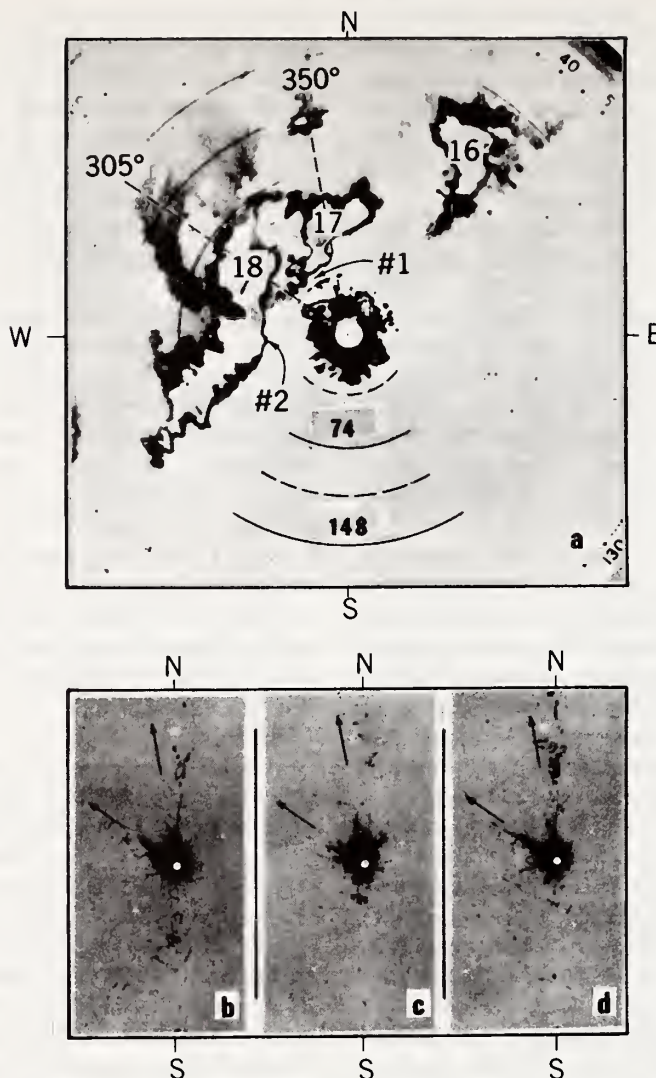


Fig. 7. Radar echoes and atmospheric direction of arrival at 0703 GMT, April 30, 1970: (a) radar frame NSSL 0930, (b) directional display at 0703:01 GMT, (c) directional display at 0703:02 GMT, (d) directional display at 0703:03 GMT.

atmospherics directly associated with the tornados from those generated near the main storm centers. The directions to the remains of tornado 1 (6° at 43 km), which had dissipated by this time, and to tornado 2 (340° at 31 km) were along almost the same bearings as storms 17 and 18, respectively.

The average burst rates did show a rapid increase prior to 0700 GMT, about the time tornado 1 was west of Oklahoma City but before tornado 2 formed. Estimates of electrical

activity based on the 1-sec directional displays, of which Figures 7b, c, and d are a part, indicated that perhaps 40% of the atmospheric originated from storm 17 whereas 60% came from storm 18. At 0700 GMT the average burst rate was 23 per minute, about the same as that for 0526, shown in Figure 5.

A maximum average burst rate of about 30 bursts per minute was observed at 0723. Tornado 1 had probably dissipated by this time, and tornado 2 had formed and was moving

into the western edge of Oklahoma City. The 1-sec directional displays, of which Figures 8b, c, and d are a part, indicated that the average burst rate of 28 per minute observed at 0730 GMT resulted almost entirely (80–90%) from atmospherics that originated from storm 18. An example of the atmospherics rate data is not presented because of a malfunction of a tape recorder during this period that eliminated channels 11 through 16. Otherwise, the data obtained during tornado 2 were similar to those

shown in Figure 5 but had about $\frac{1}{3}$ more bursts on each data channel.

Average burst rates decreased very rapidly after 0730 GMT, and there were only about 5 per minute at 0800 GMT. At 0830 GMT, only 2 or 3 bursts per minute were observed, and the observations were terminated. Although no radar records were made after about 0745 GMT because of ac power outage, atmospherics observations continued through the use of auxiliary power until it was obvious from the

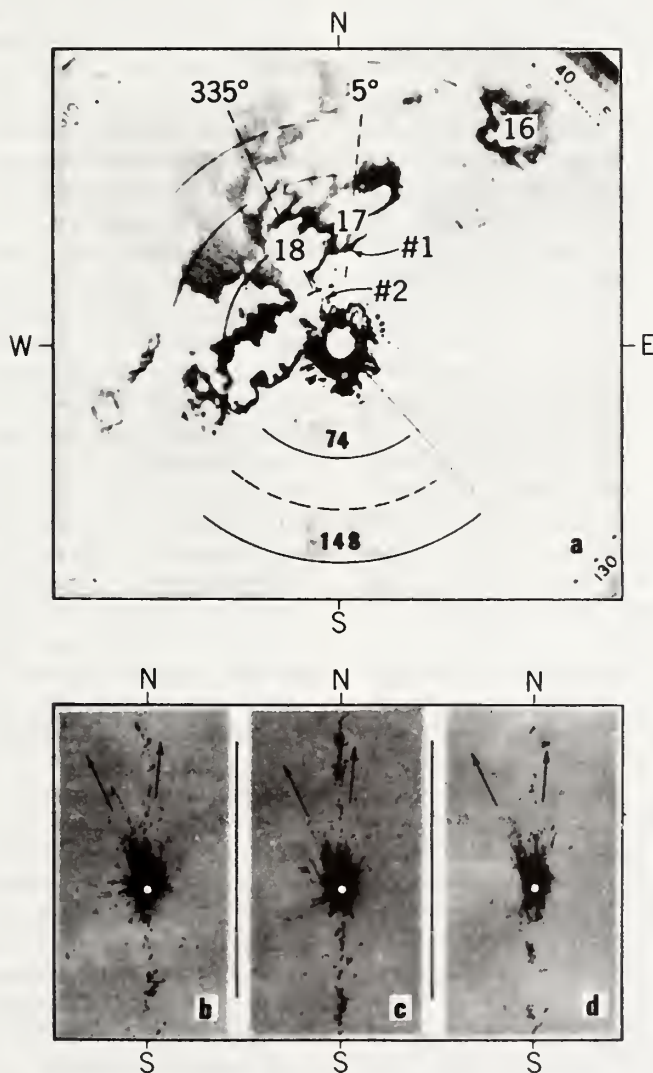


Fig. 8. Radar echoes and atmospherics direction of arrival at 0730 GMT, April 30, 1970: (a) radar frame NSSL 1012, (b) directional display at 0730:01 GMT, (c) directional display at 0730:02 GMT, (d) directional display at 0730:03 GMT.

observed burst rates that severe storm activity had moved out of the area.

DISCUSSION

The study of electrical activity associated with thunderstorms is made more difficult by the complexities of the weather. Especially during periods of severe weather conditions, many active storm areas may be within observational range at a time of particular interest. The radar tracing in Figure 2 and the range curves in the lower portion of Figure 6 testify to the complex nature of the thunderstorm conditions experienced during the period from about 2000 GMT, April 29, to 0800 GMT, April 30, 1970.

Most atmospherics seem to have radiated from sources closely associated with radar echoes of high intensity (i.e., high radar reflectivity), as is clearly indicated in Figure 3, from which atmospherics arriving from the various directions could be used to identify the thunderstorm areas indicated by radar from which they originated. Kinzer [1972] has found a close relationship between the locations of return strokes obtained from atmospheric wave forms and radar reflectivity values. Figures 7 and 8 substantiate this by showing that most atmospherics were arriving from the directions of the more intense storm centers indicated by the positions of the identifying numbers. Although the atmospherics rate data, from which the average burst rates were computed, were obtained from omnidirectional antennas, the relative activity level of the storm areas were estimated from the direction of arrival displays.

Most thunderstorms produced relatively low burst rate levels in all frequency bands. It should be realized, of course, that observed burst rates are functions of frequency, threshold level, and atmospherics rates, as well as thunderstorm activity and distance. The burst rates generally increased on all frequency channels as each observed thunderstorm grew in electrical activity. However, at some level of activity an apparent limit was reached in burst rates at the lower frequencies, whereas the burst rates at the higher frequencies continued to increase. For this reason, only the burst rates for the three higher frequencies (316 kHz, 1 MHz, and 3.16 MHz) were used for computing the average burst rates. It should be

mentioned, however, that the change in burst rates between nonsevere thunderstorm conditions and tornadic conditions was only about half as great at 316 kHz as it was at the other higher frequencies. This suggests that observations at frequencies of 1 MHz and higher would be better indicators of severe storms in general and of tornadic activity in particular. Other workers have recently arrived at similar conclusions. Hughes and Pybus [1970] studied severe storms in the frequency range of 10 kHz to 250 kHz and found that atmospheric rates were associated with a storm's convective processes and that the higher frequencies seemed to be better indicators of severe storm activity. Stanford *et al.* [1971] reported on observations of atmospheric rates at various frequencies from 670 kHz to 144 MHz and concluded that frequencies above about 1 MHz were more indicative of tornadic activity than lower frequencies.

No detailed analysis of the present data has been made as yet to measure the spectral distribution of the received signals as a function of frequency for different levels of storm activity. Preliminary examination of representative portions of the data, however, has given an indication of how the relative spectral amplitudes change with frequency. As can be seen from inspecting the large isolated burst shown in Figure 4, there is close agreement in equipment response characteristics between the corresponding threshold levels for all frequencies. This implies that the discharge processes associated with this burst tended to produce amplitude responses of the 10% bandwidth circuits that were independent of frequency. If the bandwidth was assumed to be adequate to resolve essentially all of the individual atmospherics so that a linear scale factor with bandwidth could be used, then the spectral amplitude of signals radiated from this low-activity storm was inversely proportional to frequency over the range from 10 kHz to 3.16 MHz. Since the atmospherics rate, and consequently the total number of impulses, was proportional to frequency for this example, the distribution of energy for the complete discharge was inversely proportional to frequency.

In a similar manner, other periods were examined, and it was found that more energy was partitioned into the higher frequencies than

was found at lower frequencies as storm activity increased. The observations taken during the reported periods of the tornados showed an apparent increase in amplitude as well as in total number of impulses. For the times when tornados were reported the spectral amplitude tended to decrease less rapidly than an inverse frequency relationship, and the total number of impulses increased more rapidly than the first power of frequency as the observational frequency increased. The resultant estimated distribution of energy was approximately independent of frequency within the frequency bands dealt with here. Similar findings were reported by *Silberg* [1965] in a study of Oklahoma tornados.

To summarize the results obtained from the storms that produced an enhanced burst rate, storm 6 was a relatively active thunderstorm that produced a maximum average burst rate of 7 per minute. Storms 15 and 16 were very intense thunderstorms, but, because no major damage reports were associated with them, they were not classified as severe storms by the National Severe Storms Forecast Center in Kansas City, Missouri. If the number of bursts received during the passage of these two storms was assigned to each storm area as indicated by the direction of arrival displays, then the maximum average burst rate for either storm area would have been less than 15 per minute.

Storms 17 and 18 were both classified as severe storms, and each was responsible for numerous reports of hail, damaging wind, and tornados. Storm 18 was the more electrically active of the pair. After partitioning the burst rates according to their sources from the atmospherics directional displays, the average burst rate from storm 18 would have been at least 23 per minute. It should be noted that any correction for burst rates dependent on distance to the source would produce a greater difference in observed burst rates between storms 16 and 18. The main part of storm 16 produced 15 bursts per minute at a range of 25 km, whereas storm 18 produced 23 bursts per minute at a range of 55 km.

The general characteristic of the atmospherics rate data during nonsevere or normal thunderstorm conditions was a few short-duration bursts of low rates with occasional long-duration bursts of very high rates as shown in

Figure 4. The number of both short- and long-duration bursts increased during periods of moderately high levels of thunderstorm activity, as is shown in Figure 5. During periods of reported tornadic conditions, many more short-duration bursts of relatively high rates were produced that resulted in an enhanced background of almost continuous bursts with few individual or isolated long-duration bursts.

The burst rate data obtained indicate that low burst rates of less than 10 per minute represent general thunderstorm conditions. Medium burst rates between 10 and 20 per minute represent very active thunderstorms with possible severe storm conditions. High burst rates of 20 per minute or greater are indicative of severe storm activity with possible tornados.

It is believed that the severe storms with the accompanying tornados discussed here are similar in electrical characteristics to most other tornadic storms. However, in keeping with the whole history of radio and visual observations of tornados, it is reasonable to assume that most tornadic storms, but not all, would have major radio frequency electrical activity associated with them. Conversely, a few severe storms, and a few nonsevere storms as well, may have electrical activity comparable to that of tornadic storms. *Stanford et al.* [1971] reported increases in pulse rates that were closely associated in time with reported tornados but also found increased pulse rates during periods of no reported tornados. *Lind et al.* [1972] showed that, whereas some reported tornados can be associated with a sharp increase in pulse rates, others can be associated with only a gradual buildup and decay in pulse rates, and still a few others may occur during periods of no unusual enhancements of radio noise.

Since high burst rates were not limited only to the storms that produced tornados (or at least to the times when tornados were reported present), it seems logical to assume that a tornado is not the source of the observed radio energy. This assumption is further substantiated by Figure 7 and the related discussion, which clearly showed that the atmospherics were not coming from the directions of either tornado 1 or the genesis of tornado 2. *Scouten et al.* [1972] in analyzing the 150-kHz direction of arrival data obtained when a tornado

was 42 km from the receiving site found that atmospherics were arriving from a very wide azimuthal sector that included the direction to the tornado. They reasoned that the atmospherics did not originate from the tornado or other isolated region of the storm but instead represented a general intense electrification of the entire storm system associated with the tornado. It is therefore logical to conclude that the tornado funnel or the storm cloud in close proximity to the funnel may be the primary source of atmospherics for some tornados but perhaps not for most.

The source of the radio energy associated with tornados evidently remains primarily with the parent cloud. Since the observations at 1 MHz and higher frequencies seem to be the most sensitive to the enhancement of atmospherics indicative of tornadic activity, it is suggested that the intracloud discharge processes are the primary signal sources. These intracloud processes are most likely located near regions of strong turbulence and at heights above the freezing level, which is at 5 km or so during the thunderstorm season in the Great Plains area of the United States.

There are many questions still unanswered concerning the electrical identification of tornado and other severe storm characteristics. The results of this present work indicate that the number of bursts of high atmospheric rates at frequencies above about 1 MHz is very closely related to tornadic activity. It now seems feasible to design a monitoring system using the burst rate parameter to warn of probable tornadic conditions within 100 km of a receiving site.

Acknowledgments. I wish to thank H. Burdick for much of the equipment design and construction and for assisting with the observations and also to thank the many individuals in the NSSL who helped in support of this work, especially Edwin Kessler, Gilbert Kinzer, and J. T. Lee.

The observations for this work could not have been completed successfully without the extra financial support received from NSSL.

REFERENCES

- Atlas, D., Radar echoes and atmospherics in vertical cross section, *Recent Advances in Atmospheric Electricity*, pp. 441-459, Pergamon, New York, 1959.
- Biggs, W. G., and P. J. Waite, Can TV really detect tornadoes?, *Weatherwise*, 23(3), 120-124, 1970.
- Braham, R. R., Jr., The water and energy budgets of the thunderstorm and their relation to thunderstorm development, *J. Meteorol.*, 9, 227-242, 1952.
- Brook, M., Electric currents accompanying tornado activity, *Science*, 157(3795), 1434-1436, 1967.
- Horner, F., Radio noise from thunderstorms, *Advances in Radio Research*, vol. 2, pp. 121-204, Academic, New York, 1964.
- Hughes, W. L., and E. J. Pybus, Severe storm sferics-stroke rate, paper presented at 14th Radar Meteorology Conference, Amer. Meteorol. Soc., Boston, Mass., Nov. 17-20, 1970.
- Jones, H. L., The identification and tracking of tornadoes, paper presented at a meeting of the International Scientific Radio Union (URSI), Commission 4, Washington, D.C., April 18, 1950.
- Jones, H. L., The identification of lightning discharges by sferic characteristics, *Recent Advances in Atmospheric Electricity*, pp. 543-556, Pergamon, New York, 1959.
- Jones, H. L., The tornado pulse generator, *Weatherwise*, 18(2), 78-80, 1965.
- Kinzer, G. D., Cloud-to-ground lightning versus radar reflectivity in Oklahoma thunderstorms, *NOAA Tech. Memo., ERL NSSL-59*, Nat. Tech. Inform. Serv., Springfield, Va., 1972.
- Lind, M. A., J. S. Hartman, E. S. Takle, and J. L. Stanford, Radio noise studies of several severe weather events in Iowa in 1971, *J. Atmos. Sci.*, 29(6), 1220-1223, 1972.
- Oetzel, G. N., and E. T. Pierce, Radio emissions from close lightning, *Planetary Electrodynamics*, vol. 1, pp. 543-569, Gordon and Breach, New York, 1969.
- Scouten, D. C., D. T. Stephenson, and W. G. Biggs, A sferic rate azimuth-profile of the 1955 Blackwell, Oklahoma, tornado, *J. Atmos. Sci.*, 29(5), 929-936, 1972.
- Shanmugam, K., and E. J. Pybus, A note on the electrical characteristics of locally severe storms, paper presented at 7th Conference on Severe Local Storms, Amer. Meteorol. Soc., Boston, Mass., Oct. 5-7, 1971.
- Silberg, P. A., Passive electrical measurements from three Oklahoma tornadoes, *Proc. IEEE*, 53(9), 1197-1204, 1965.
- Sirmans, D., W. L. Watts, and J. H. Horwedel, Weather radar signal processing and recording at the National Severe Storms Laboratory, *IEEE Trans. Geosci. Electron.*, GE-8(2), 88-94, 1970.
- Stanford, J. L., M. A. Lind, and G. S. Takle, Electromagnetic noise studies of severe convective storms in Iowa: The 1970 storm season, *J. Atmos. Sci.*, 28(3), 436-448, 1971.
- Taylor, W. L., Determining lightning stroke height from ionospheric components of atmospheric

- waveforms, *J. Atmos. Terr. Phys.*, *31*, 983-990, 1969.
- Taylor, W. L., Atmospherics and severe storms. *Remote Sensing of the Troposphere*, edited by V. E. Derr, chapter 17, U.S. Government Printing Office, Washington, D.C., 1972.
- Vonnegut, B., Electrical theory of tornadoes, *J. Geophys. Res.*, *65*(1), 203-212, 1960.
- Waite, P. J., and N. Weller, The Weller method: Tornado detection by television, paper presented at 6th Conference on Severe Local Storms, Amer. Meteorol. Soc., Boston, Mass., April 8-10, 1969.

(Received April 25, 1973;
revised August 13, 1973.)

Reprinted from the Eighth Conference on Severe Local Storms,
October 15-17, 1973.

EVALUATION OF AN ELECTROMAGNETIC TORNADO-DETECTION TECHNIQUE

William L. Taylor

NOAA - ERL
Wave Propagation Laboratory
Boulder, Colorado

1. INTRODUCTION

This is a progress report on recent efforts to find an electromagnetic signature that could be used for detecting nearby tornadoes. The previous works of Stanford, et al. (1971), Hughes and Pybus (1970), Jones (1965), Vonnegut (1960), and many other reports of radio and visual observations of tornadoes, generally conclude that most tornadic storms have a high level of electrical activity associated with them. Taylor (1972 and 1973a) began searching for an electromagnetic signature suitable for detecting tornadoes by observing the radiation from lightning-discharge processes in the frequency band from 10 kHz to 137 MHz. In the 1967-71 tornado seasons during periods when severe weather was expected, observations were made near Norman, Oklahoma in cooperation with the National Severe Storms Laboratory. A total of 267 hours of data were recorded. Sferic activity from 39 severe storms was observed, of which 18 developed tornadoes or funnel clouds within a distance of 100 km from a recording site.

Previous work of Taylor (1971) indicated that: a) No one-to-one correspondence would be found between observed electrical emissions of thunderstorms and reported weather conditions. b) The general characteristic of the signals observed during nonsevere storm conditions was that of a few short-duration bursts of low sferic rates with occasional long duration bursts of high sferic rates produced by discrete discharges. c) Tornadic storms typically showed enhanced sferic activity, with many bursts of high sferic rates, presumably associated with very rapidly occurring discharge processes in the storm (Taylor, 1973b). d) This enhancement in burst rate was not generally apparent at lower frequencies (below about 300 kHz) but was easily recognized at frequencies above 1 or 2 MHz.

2. INSTRUMENTATION AND OBSERVATION

For observations during the 1972 tornado season, a technique was developed to measure the electrical activity of thunderstorms as indicated by the sferics "burst rate." The burst rate is the number of groups or clusters of large-amplitude sferics occurring during a one-minute period. The signal from a 1 meter long vertical monopole antenna was applied to a single-stage tuned-radio-frequency (TRF) circuit with a center frequency of 3.16 MHz and a bandwidth of 10 percent. The operating frequency was selected from the wide range above 1 or 2 MHz that was earlier found to be suitable for detecting tornadic signatures. (Taylor, 1973a). The specific value of 3.16 MHz was based on the availability of equipment from those earlier tests.

A bandwidth of at least 10 percent was needed to process the received sferics that often exceeded rates of 10^5 per second.

Two amplitude threshold levels - 5 V/m and 2 V/m - were used, corresponding to nominal ranges of 30 km and 70 km for typical sferics. To be counted as a "burst," the received signals were required not only to exceed an amplitude threshold level, but also to exceed a rate of 500 per second for a time period greater than 0.1 second. The burst rate was sensed continuously for each threshold level and presented to a multi-channel event recorder to show when the burst rate exceeded 3, 10, 20, and 30 per minute. These 8 channels of data plus an additional channel for time marks constituted the information available from each tornado-detector unit.

To provide a statistically meaningful sample, fifteen detector units were constructed and installed at locations indicated in Figure 1. The radius of each circle corresponds approximately to their nominal 70 km range. Operation of the three units shown in Louisiana and Mississippi was terminated at the end of May and these units were moved to locations shown in Nebraska, Iowa, and Illinois to follow the expected northerly progression of tornadic activity during the season. Except for slight overlapping of coverage area for the units in the Oklahoma region, all other units were distributed as uniformly as possible over the part of the United States subject to high tornado activity.

Installation of the detector units began in February 1972 in the southern region and all units were operational by March 15. Some units were deactivated about the end of August, and all units were turned off by September 18. During this one season of continuous operation, the 15 units logged a total of over 66,000 operational hours and experienced about 3,000 hours of outages (< 4.5%) due to interference and equipment malfunction.

3. ANALYSIS AND RESULTS

The reports of weather conditions compiled by the National Severe Storms Forecast Center in Kansas City were used to determine the periods when thunderstorms or other manifestations of severe weather were observed within 70 km of each detector. The maximum burst rate observed during each period was tabulated, corresponding to the particular category of storm activity, i.e., thunderstorm, large hail, damaging wind, funnel clouds and tornadoes. If more than one weather condition was reported during the same

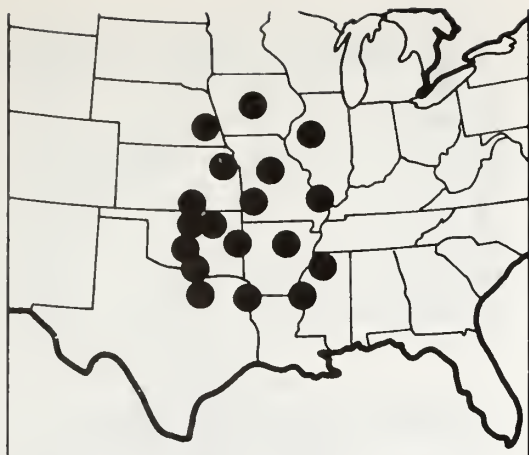


Figure 1. Location of tornado-detection units during 1972.

period then the observed burst rate was assigned to the more severe category. This selection was made with first preference given to tornadoes, then funnels, windstorms, hailstorms, and finally nonsevere thunderstorms. The averaged maximum burst rates in each weather category are presented in Figure 2 for the three range intervals indicated.

Three sets of blocks are shown in this figure. The broad-striped blocks show average burst rates of the sensitive, far-range equipment channel operating at the 2 V/m threshold and for all reported weather activity within a range of 70 km. The narrow-striped blocks represent the same equipment channel as the broad-striped blocks but only show average burst rates during reported weather activity at ranges greater than 30 km and less than 70 km, and do not include any reported nonsevere thunderstorms. The dotted blocks show average burst rates of the insensitive, near-range equipment channels operating at the 5 V/m threshold level and for all reported weather activity within a range of 30 km.

Figure 2 indicates that nonsevere thunderstorms, as expected, show the lowest burst rate, with hail, wind, and funnel clouds showing a general increase in burst rates. Responses associated with tornadoes show a definite enhanced average burst rate relative to the other reported severe storms for all observing ranges. The average burst rates for each weather category in the 30-70 km range show about one burst per minute greater than the average burst rate for the corresponding weather category in the 0-30 km range. This probably resulted from relatively nearby storms producing infrequent bursts of sferics that were of sufficient amplitude to exceed the 2 V/m threshold level but not the 5 V/m threshold level. The

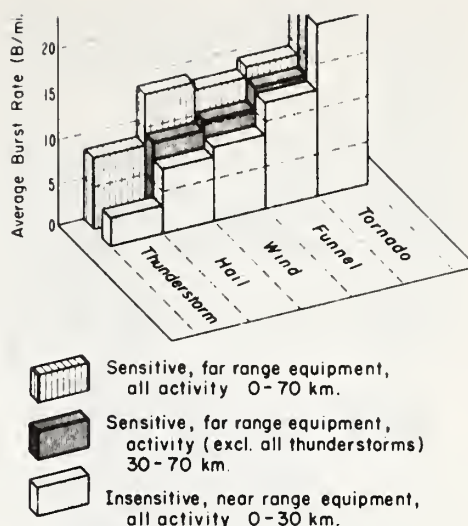


Figure 2. Average burst rates for various reported weather conditions within certain ranges and for two threshold levels.

average burst rates for the 0-70 range compared with corresponding burst rates for the 0-30 km range show about 6 more bursts per minute for thunderstorm, hail and wind categories and only about 2 more bursts per minute for funnel and tornado categories. The relatively large differences of about 2-to-1 in average burst rates for the thunderstorm, hail and wind categories between the 0-70 km and 0-30 km range indicate that observed burst rates for these weather categories are strongly dependent on threshold level and range. The average burst rates for funnels and tornadoes only differed by factors of about 1.2-to-1 which indicate that burst rates observed from these weather conditions are not greatly influenced by threshold level and range.

The probability distributions of the burst rates obtained at the 5 V/m threshold for the various reported weather conditions within a range of 30 km of the observation sites are shown in Figure 3. These curves clearly show that tornadoes tend to be associated with burst rates considerably higher than the nearest competitor - the funnel cloud. While the burst rate for half of the tornadoes exceeded 27 per minute, 50 - percentile burst rates for the hail, wind and funnel categories of severe weather varied between about 9 and 18. Some of the high burst rates apparently associated with nonsevere thunderstorms (3.5 percent exceeding a burst rate of 30 per minute) may actually have resulted from unreported tornado activity within range of the equipment.

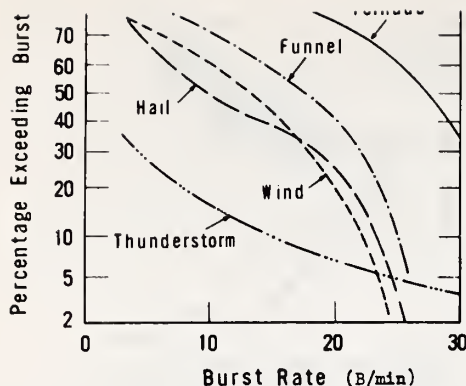


Figure 3. Probability distributions of burst rates from the 5 V/m threshold responses for reported weather conditions within 0-30 km range.

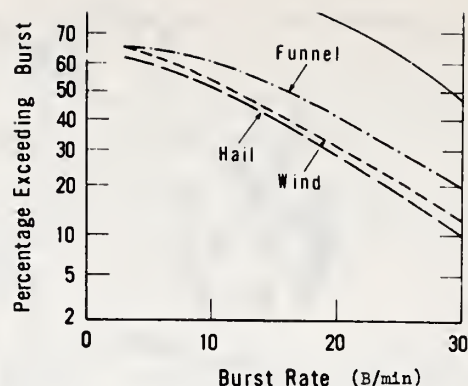


Figure 4. Probability distributions of burst rates from the 2 V/m threshold responses for reported weather conditions within 30-70 km range.

Figure 4 shows the probability distribution of the burst rates from sources of ranges greater than 30 km and less than 70 km obtained with the 2 V/m threshold responses. Fifty percent of the tornadoes resulted in an observed burst rate in excess of 29 per minute, while severe storms associated with hail, wind and funnel clouds caused 50-percent burst rates between about 11 and 16 per minute. No thunderstorm responses are included in this group of data because of the recognized difficulty of obtaining accurate reports of thunderstorms in rural areas far removed from the observing units and the National Weather Service Offices.

Presuming that a burst rate exceeding 20 per minute was indicative of tornado activity, then 73 percent of the tornadoes would have been "detected" as indicated in Figures 3 and 4. Table I summarizes the results of using a 20 burst-per-minute rate and a 5 V/m threshold as a tornado warning level for reported weather activity within a 30 km range of the detector units. Note that although only 6.5 percent of the thunderstorms produce a burst rate greater than 20 per minute, there were so many more thunderstorms than reported periods of severe storms that over half of the warnings would have resulted from the local nonsevere thunderstorms. This table shows, however, that each time the warning level was reached, there was about one chance in five that a tornado was present, about one chance in four that either a tornado or funnel cloud was present, and slightly less than one chance in two that some form of severe weather was in existence within 30 km at the time. There were no observed burst rates greater than 20 per minute without at least thunderstorm activity reported. A summary of the 2 V/m responses to the 30-70 km weather

TABLE I

Summary of 1972 results for the 30 km range using the equipment with a 5 V/m threshold.

| Weather Condition < 30 km | Number Observed | No. With Burst Rates > 20/min | % With Burst Rates > 20/min |
|---------------------------|-----------------|-------------------------------|-----------------------------|
| Tornado | 15 | 11 | 73 |
| Funnel* | 10 | 4 | 40 |
| Wind† | 20 | 4 | 20 |
| Hail† | 23 | 6 | 26 |
| Thunderstorm† | 507 | 33 | 6.5 |
| Totals | 575 | 58 | |

*May have been a tornado, but was not observed to touch ground.

†May have had tornado activity, though none was reported.

activity, as could be envisioned by comparing the corresponding curves in Figures 3 and 4 at a burst rate of 20 per minute, would be very similar to that presented in Table I.

the observation units described here was to determine the feasibility of using burst-rate measurements to supplement existing National Weather Service capabilities for warning of tornadic conditions. It was found that most, but not all, tornadic conditions were associated with high burst rates, but a few severe storms, as well as some nonsevere thunderstorms also have burst rates comparable to those associated with tornadic storms. Of course, some of these storms may have been tornadic while beyond the nominal 70 km monitoring range prior to or after the equipment responses. Also, because of the problems and limitations of weather observations, particularly in sparsely populated areas, some unreported tornadic activity may have been present during some of the equipment responses associated with other weather categories.

Operational evaluation tests of these tornado detectors will be conducted during 1973 by a number of National Weather Service Offices to appraise the usefulness of this technique in assisting the local NWS personnel in recognizing tornadic conditions. A recognized limitation of the present detector is that it does not indicate the direction from which the electromagnetic signals arrive, and therefore does not help the local personnel to track electrically active storm regions. This omnidirectional characteristic also results in a relatively large number of false alarms caused by the additive effect of numerous nontornadic sources occurring within the response range of the equipment. Directional capabilities will be included in a second-generation tornado detector that will be operational by the spring of 1974; it is hoped that the false-alarm rate and the failure-to-alarm rate will both be markedly reduced by the addition of this direction-finding capability.

forecast Center for their assistance and cooperation, and the many people at each detector unit location without whose help this work could not have been completed.

6. REFERENCES

- Jones, H. L., 1965: The tornado pulse generator. Weatherwise, 18, No. 2, 78-80.
- Hughes, W. L. and E. J. Pybus, 1970: Severe storm sferics - stroke rate. Proc. 14th Radar Meteor. Conf., Tucson, AZ., 315-318.
- Stanford, J. L., M. A. Lind, and G. S. Takle, 1971: Electromagnetic noise studies of severe convective storms. J. Atmos. Sci., 28, 436-448.
- Taylor, W. L., 1971: Review of electromagnetic radiation data from severe storms in Oklahoma during April 1970. NOAA Tech. Memo. ERL WPL-6, 80 pp.
- Taylor, W. L., 1972: Atmospherics and severe storms, Chapter 17 of Remote Sensing of the Troposphere, V. E. Derr, Editor, Superintendent of Documents, U. S. Gov't Printing Office, Washington, D. C. 20402.
- Taylor, W. L., 1973a: The search for electromagnetic radiation indicative of tornadic activity. Submitted for publication.
- Taylor, W. L., 1973b: Electromagnetic radiation from severe storms in Oklahoma during April 29-30, 1970. Submitted for publication.
- Vonnegut, B., 1960: Electrical theory of tornadoes. J. Geophys. Res. 65, No. 1, 203-212.

Ground-Based Determination of Low Altitude Temperature Profiles by Microwaves

ED R. WESTWATER—*Environmental Research Laboratories, NOAA, Boulder, Colo., and
Department of Physics, University of Colorado, Boulder, Colo.*

ABSTRACT—Vertical temperature profiles of the lower atmosphere are determined from clear air ground-based measurements of microwave thermal emission by oxygen. Angular emission data from two diverse meteorological locations are mathematically inverted by statistical techniques to recover the vertical profiles. Inversion of 52.5 GHz data, gathered at Upolu Point, Hawaii, Hawaii, resulted in an average root-mean-square (rms) difference of 1.27°K between inverted and radiosonde measured profiles from 0 to 10 km. Pressure and humidity profiles are simultaneously estimated from the data; numerical integration of the inverted humidity profiles results in a determination of total vertical water content with a relative accuracy of about 10 percent. Radiometer emission data at 54.0, 54.5, and 55.0 GHz, taken at Salt Lake City, Utah, are inverted with resulting average rms differences of 1.17°K over the

height interval from 0 to 6.4 km. A priori temperature variance, corresponding to known surface conditions, is reduced by a factor of 8 to 1. Ground-based thermal inversions are successfully recovered. For both locations, the rms accuracies agree well with predictions based on the theory of statistical estimation.

The statistical inversion equations of Rodgers, and Strand and Westwater are extended for the purpose of inferring profiles from spectrally contaminated radiation measurements. The equations require auto- and cross-covariance matrices of all meteorological variables that contribute to the emission. The general linear estimation equations of Deutsch are applied to a linear approximation to the radiative transfer equation to derive the inversion equations. An analysis of the linearization errors is given.

1. INTRODUCTION

The remote sensing of low altitude vertical temperature profiles is of great interest in studies of air pollution. Previous theoretical results have indicated that passive ground-based microwave measurements of thermal emission by oxygen can provide significant information on the temperature structure up to about 2 or 3 km under clear atmospheric conditions (Westwater and Strand 1968, Mount et al. 1968).

Temperature profiles have been recovered from radiometric data by using a variety of mathematical techniques (Chahine 1970, Smith et al. 1970, Wark 1970). The technique presented here utilizes statistical characteristics of atmospheric variables contributing to the observed emission for the construction of a physically significant solution to the inverse problem of radiative transfer. This method retains features of the earlier statistical inversion techniques of Rodgers (1966) and Strand and Westwater (1968) but also permits the effect of background atmospheric noise (such as that from water vapor fluctuations) to be estimated.

The inversion equations are applied to single-frequency radiometer scan data, and the results are compared with concurrent radiosonde measurements. The data were taken at two diverse meteorological locations:

1. Upolu Point, Hawaii, Hawaii. Angular measurements at 52.5 GHz are used to derive temperature profiles with a root-mean-square (rms) error of 1.25°K over a 10-km height interval. The brightness spectrum is shown to be substantially affected by water vapor at the higher elevation angles. The integrated vertical water content was also determined from the radiometric data and compared

with water content derived from radiosonde measurements to about 10 percent.

2. Salt Lake City, Utah. Discrete angular data at 54.0, 54.5, and 55.0 GHz are used to derive temperature profiles with an rms accuracy of about 0.5°K up to 2 km. Both lapse and ground-based inversion profiles are encountered and successfully recovered.

2. INVERSION METHOD

The problem of remotely inferring temperature profiles from radiation measurements can be regarded as a problem in statistical estimation (Rodgers 1966, Strand and Westwater 1968). A related problem of filtering a signal from noise was solved by Foster (1961). If the contributions to brightness temperature fluctuations caused by temperature fluctuations are regarded as the desired signal, then all other contributions to this signal may be considered as noise. This noise may arise from instrumental noise or from effects of atmospheric origin, such as pressure, water vapor, or clouds. If the a priori statistical behavior of the signal and the noise is known, this knowledge can be used to construct a filter or an optimum estimator using the minimum expected mean square error criterion of Wiener (1949). The linear method for achieving the minimum variance estimator from past data will be presented below by extending the equations of Foster (1961), Rodgers (1966), and Strand and Westwater (1968) to those equations applicable when the contaminating noise is correlated with the desired signal. In addition, the effective noise level of background fluctuations is determined and the reduction of this noise using surface constraints is discussed.

Statistical inversion techniques attempt to derive atmospheric profiles by using radiation measurements to form statistical estimates. This is a specific example of a general problem in statistical estimation, that of estimating one vector quantity from measurements of another. The linear solution of this general problem is outlined below, following Deutsch (1965).

Consider two (column) vectors, \mathbf{x} and \mathbf{y} , the components of which are random variables. For our purposes, \mathbf{y} can be regarded as a vector representing an atmospheric profile and \mathbf{x} as a vector of measurements. If the dimensions of \mathbf{x} and \mathbf{y} are n and m , respectively, then the quantities are described by a $(n+m)$ -dimensional joint probability distribution. Let $E\{\}$ be the expected value operator over this distribution. Denote the mean, or average, of any vector \mathbf{x} by $\langle \mathbf{x} \rangle \equiv E\{\mathbf{x}\}$ and the departure of \mathbf{x} from its mean by $\mathbf{x}' \equiv \mathbf{x} - \langle \mathbf{x} \rangle$. In the following, we will consistently use primes on statistical quantities to denote departures from average values. Deutsch shows that \mathbf{y}' may be estimated as a linear function of \mathbf{x}' by the minimum variance estimator, $\hat{\mathbf{y}}'$ where

$$\hat{\mathbf{y}}' = S_{yx} S_x^{-1} \mathbf{x}', \quad (1)$$

$$S_{yx} \equiv E\{\mathbf{y}' \mathbf{x}'^*\}, \quad (2)$$

and

$$S_x \equiv E\{\mathbf{x}' \mathbf{x}'^*\}. \quad (3)$$

The superscript * means matrix transposition, and the standard statistical notation of designating estimators by the superscript ^ has been followed. The i, j element of the $m \times n$ matrix S_{yx} is the cross-covariance of y_i and x_j ; similarly, the i, j element of the $n \times n$ matrix S_x is the autocovariance of x_i and x_j . The determination of the above matrices, which are defined with respect to an ensemble average over an infinite population, usually requires averaging over a finite sample.

The equations outlined above may be applied to the inversion problem in several different ways depending on the data at one's disposal. The most direct application occurs by correlating a representative sample of simultaneous direct measurements of both the vertical temperature profile and either spectral or angular measurements of brightness. The coefficient matrix relating the vector representation of the temperature profile, \mathbf{T} , to the vector of measurements, \mathbf{T}_b , is determined simply by linear regression. This technique has been discussed recently by Smith et al. (1970).

When the absorption and emission characteristics are known as a function of meteorological parameters, the "pseudo-regression" coefficients, $S_{T,T}, S_{T,T}^{-1}$, may be approximated by calculations taken over a representative history of meteorological data. The noise levels associated with brightness temperature measurements are also assumed known. This method was not used here because of the prohibitive number of calculations required to evaluate $S_{T,T}, S_{T,T}^{-1}$. In addition, the strict use of correlation tends to obscure the magnitude of the causes of the brightness fluctuations and their relation to profile fluctuations.

The procedure used here directly relates a linear approximation of the brightness equation to the desired profile fluctuations using eq (1), (2), and (3). In addition to reducing the number of brightness calculations to one, namely the brightness of the average profile, this procedure has the advantage of explicitly showing the separate contributions to the variance of the brightness fluctuations by each of the atmospheric parameters.

The monochromatic brightness at an initial elevation angle, θ , is given by

$$T_b(\theta) = \int_0^\infty dh T \alpha \csc \theta e^{-\int_0^h \alpha \csc \theta} \quad (4)$$

where h is height, and the absorption coefficient, α , is a function of temperature, T , pressure, p , and relative humidity, r (Staelin 1969). Because of atmospheric refraction and earth curvature, the local elevation angle along a ray path is a (usually weak) function of height and refractive index profile. By expanding the integrand of eq (4) in a Taylor series about the mean profiles of T , p , and r , and then averaging over their joint distribution, it is seen that, to the second order, the average brightness at a fixed initial elevation is the brightness of the average profile:

$$\langle T_b(\theta) \rangle = \int_0^\infty dh \langle T \rangle \langle \alpha \rangle \langle \csc \theta \rangle e^{-\int_0^h \langle \alpha \rangle \langle \csc \theta \rangle} \quad (5)$$

In eq (5), the ensemble average of $\csc \theta$ has been indicated because of the dependence of refractive bending on profile variations. The linear terms in the Taylor expansion are

$$T_b(\theta) \equiv T_b(\theta) - \langle T_b(\theta) \rangle = \int_0^\infty dh [I_T(\theta, h) T'(h) + I_p(\theta, h) p'(h) + I_r(\theta, h) r'(h)] \quad (6a)$$

where $T'(h) \equiv T(h) - \langle T(h) \rangle$, etc., and

$$I_T(\theta, h) = \frac{\partial}{\partial T(h)} \left(T \alpha \csc \theta e^{-\int_0^h \alpha \csc \theta} \right) \Big|_{\text{mean profile}}, \quad (6b)$$

$$I_p(\theta, h) = \langle T(h) \rangle \frac{\partial}{\partial p(h)} \left(\alpha \csc \theta e^{-\int_0^h \alpha \csc \theta} \right) \Big|_{\text{mean profile}}, \quad (6c)$$

and

$$I_r(\theta, h) = \langle T(h) \rangle \frac{\partial}{\partial r(h)} \left(\alpha \csc \theta e^{-\int_0^h \alpha \csc \theta} \right) \Big|_{\text{mean profile}} \quad (6d)$$

The coefficient $I_T(\theta, h)$ reduces to the usual definition of the temperature weighting function, as given, for example, by Meeks and Lilley (1963), when the temperature dependence of the absorption coefficient is neglected. In practice, the above integrals cannot be evaluated analytically and must be reduced to computational form. Introducing a suitable quadrature approximation involv-

ing m points on the profile leads to the matrix equation

$$\mathbf{T}'_b = A_T \mathbf{T}' + A_p \mathbf{p}' + A_r \mathbf{r}'. \quad (7)$$

In eq (7), each component of the $n \times 1$ vector \mathbf{T}'_b is the departure of the brightness temperature from its average at the chosen set of discrete elevation angles, each component of the $m \times 1$ vectors \mathbf{T}' , \mathbf{p}' , and \mathbf{r}' is the departure of the profile from its average at each quadrature height, and the i, j element of the $n \times m$ matrix A_T , say, is the derivative of the i th brightness with respect to the temperature at the j th level. The average accuracy of the linear approximation is a function of second and higher order derivatives of the integrand of eq (4) and of the distribution of T , p , and r . To the second order, the mean square error in the linear approximation of a function, $f(x)$, of a random variable, x , is

$$\frac{d^2 f(\langle x \rangle)}{dx^2} \frac{\sigma_x^2}{2}$$

and, hence, will be small if either the variance, σ_x^2 , or the second derivative is small. The accuracy of the approximations used here are evaluated numerically in sections 5 and 6.

Any brightness temperature measurement will be in error by an amount ϵ , where ϵ is a random variable that is uncorrelated with atmospheric fluctuations. These errors will be caused by receiver noise fluctuations, antenna side lobes, lossy wave guides, etc. It is assumed that any bias present in the measurement can be removed experimentally so that ϵ has zero mean. In the linear approximation, we may express the measured brightness, $\mathbf{T}'_b(m)$ (relative to its mean), as the sum of the atmospheric contribution, \mathbf{T}'_b , and an $m \times 1$ error vector ϵ as

$$\mathbf{T}'_b(m) = \mathbf{T}'_b + \epsilon \quad (8)$$

and

$$\mathbf{T}'_b(m) = A_T \mathbf{T}' + A_p \mathbf{p}' + A_r \mathbf{r}' + \epsilon. \quad (9)$$

To derive a temperature profile \mathbf{T}' from measurements $\mathbf{T}'_b(m)$ by eq (1) requires the autocovariance matrix of the brightness, $S_{T_b(m)}$ and the cross-covariance matrix between the temperature and the brightness, $S_{T, T_b(m)}$. Under the above assumptions, these matrices may be straightforwardly evaluated using eq (2), (3), and (9) to yield

$$S_{T_b(m)} = A_T S_T A_T^* + A_T S_{Tp} A_p^* + \dots + A_r S_{rp} A_p^* + A_p S_p A_p^* + S_\epsilon \quad (10)$$

and

$$S_{T, T_b(m)} = S_T A_T^* + S_{Tp} A_p^* + S_{Tr} A_r^*. \quad (11)$$

Equation (10) relates the variance in measured atmospheric brightness to the variance at each of the points on the profiles of the temperature, pressure, and humidity and instrumental noise; the matrix $S_{T, T_b(m)}$ expresses the degree of correlation between temperature fluctuations and brightness measurements. The random vectors \mathbf{p}' , \mathbf{r}' , and ϵ may also be estimated by

equations identical in form to eq (9) and (10). Two special cases of the above equations may be noted. First, if A_p and A_r are negligible, that is, if the spectral region or meteorological conditions are such that pressure and water vapor effects are small, then the above equations reduce to those of Rodgers (1966) and Strand and Westwater (1968):

$$S_{T_b(m)} = A_T S_T A_T^* + S_\epsilon, \quad (12)$$

and

$$S_{T, T_b(m)} = S_T A_T^*. \quad (13)$$

Second, if the cross-covariance matrices between temperature and the other two atmospheric parameters are negligibly small, then we again get eq (13), but

$$S_{T_b(m)} = A_T S_T A_T^* + S_\epsilon^{(e)} \quad (14)$$

where

$$S_\epsilon^{(e)} = S_\epsilon + A_p S_p A_p^* + A_p S_{pr} A_r^* + A_r S_{rp} A_p^* + A_r S_r A_r^*. \quad (15)$$

This explicitly shows that atmospheric fluctuations that are uncorrelated with temperature fluctuations have the same effect as instrumental noise. It also implies that if the "effective" noise level, $S_\epsilon^{(e)}$, is dominated by background fluctuations of atmospheric origin, then very little improvement in inversion results can be achieved by lowering of instrumental noise levels alone.

The linear eq (6) were expressed with temperature, pressure, and humidity as functions of height. It would also be possible to express the equations in terms of temperature and humidity as a function of pressure by using the hydrostatic equation. For ground-based applications, the greatest difficulty with this approach is the construction of various averages appropriate to the variable surface pressure.

When ground-based remote measurements are made, they can frequently be supplemented with direct measurements of surface values of the parameter(s) to be inferred. For example, surface measurements of temperature, pressure, and relative humidity can easily be taken. The value of the surface temperature can then be used as an exact mathematical constraint on the solution of the integral equation. When statistical inversion methods are used, the laws of conditional probability allow the use of additional statistical constraints that modify the estimate of the function at each point of the profile. These constraints frequently considerably reduce the a priori variance of the temperature profile. In addition, the pressure and humidity constraints reduce the effective noise level, $S_\epsilon^{(e)}$. In particular, since pressure fluctuations tend to be highly correlated over broad height intervals, the pressure constraint considerably reduces the effective noise from this component.

As in the unconstrained case, we may apply eq (1), (2), and (3) to the inversion problem if:

1. We restrict the expected value operator to range over the conditional distribution of given surface parameters, and
2. We transform the original data vector $\mathbf{T}'_b(m)$ to one that has zero mean with respect to the conditional distribution.

Requirement (1) may be imposed, under the assumption of normality, by applying a standard statistical method using conditional probability to modify each of the covariance matrices occurring in eq (10). The rather cumbersome details of this technique are described by Graybill (1961).

An alternate method of incorporating surface measurements is to adjoin the vector of constraints to the vector of brightness measurements to form a "generalized" data vector. Equations (1), (2), and (3) can then be applied directly using the unconstrained distribution.

The transformation of the measured brightness to a quantity that has zero mean with respect to the conditional distribution is achieved by taking the conditional average of eq (9) and subtracting the result from the measured brightness. The mean brightness, conditional upon fixed surface conditions, is related to the ensemble averaged brightness $\langle T_b \rangle$ by

$$\langle T_b | C \rangle = \langle T_b \rangle + A_T (\langle T | C \rangle - \langle T \rangle) + A_p (\langle p | C \rangle - \langle p \rangle) + A_r (\langle r | C \rangle - \langle r \rangle). \quad (16)$$

Above, C refers to the triplet of fixed surface constraints, T_b, p_b , and r_b and the notation $\langle V | C \rangle$ designates the conditional average of the vector V , given C . In section 5, results of inversions are given using both constrained and unconstrained statistical methods.

Although we have presented only linear techniques above, the extension of the statistical method to iterative analysis is straightforward. To apply iterative analysis, each component of the temperature, pressure, and humidity profiles is estimated by the appropriate application of eq (1). These estimates are then used to correct the weighting functions at each stage of the iteration process. The necessity of recorrecting the weighting functions by iteration depends on the experimental noise level: if the linearization errors are larger than the noise levels, then iteration can improve solution accuracy. However, it is not clear that a linearized iterative technique is preferable to the general eq (1) since one of the prime motivators of the linearization technique was to avoid excessive computer calculation. If the system of equations is strongly nonlinear, the use of nonlinear noniterative estimation involving higher order moments of the profile distribution is possible (Staelin 1969). As stated by Swerling (1966), linear estimates are optimum (of all estimates, linear or not) if all quantities are multivariate Gaussian and if the measurement fluctuations are linearly related to the profile fluctuations.

3. WEIGHTING FUNCTIONS

The brightness temperature at frequency ν and elevation angle θ is a weighted average of the temperature distribution over some spatial region. For a stratified atmosphere, the weighted height average is determined by the temperature weighting function given by eq (6b). As a typical example of microwave ground-based temperature weighting functions, figure 1 shows monochromatic

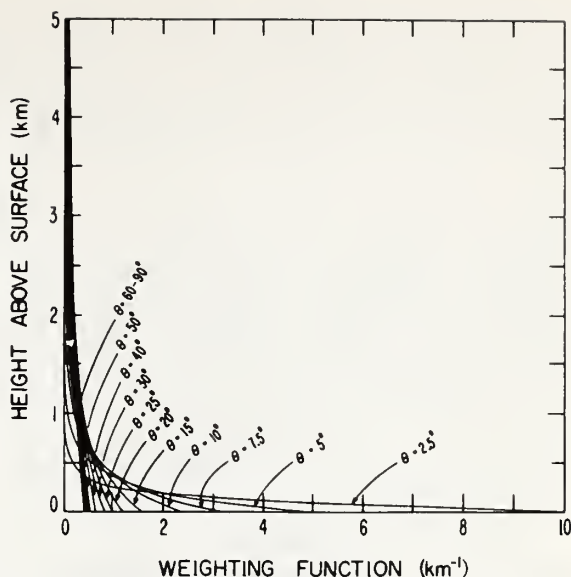


FIGURE 1.—Temperature weighting functions at 54.0 GHz for angular probing. August values are for Salt Lake City, Utah.

weighting functions at 54.0 GHz for discrete elevation angles. These calculations are for the August monthly average profiles of temperature, pressure and relative humidity at Salt Lake City, Utah. The oxygen absorption coefficient is determined using the Van Vleck-Weisskopf (1945) line shape with line width parameters of Carter et al. (1968). The small water vapor contribution was calculated using the same line shape, but with line parameters determined by Westwater (1967). As is evident from the figure, very narrow height resolution is obtained near the surface, but this resolution degrades rapidly with altitude. The corresponding transmission curves for this location and frequency are shown in figure 2.

4. ANALYSIS AND INVERSION OF HAWAIIAN RADIOMETER DATA

The ultimate test of a remote sensing technique is its performance in a field operation. In this and the following section, we derive temperature profiles from microwave radiometer data and compare the results with theoretical predictions and with independent direct temperature measurements. The sequential analysis procedure that we follow is to (1) compare radiometer measurements and brightness calculations to determine effective measurement noise levels; (2) perform theoretical calculations of expected accuracies in inversion results using the noise levels determined in (1); (3) invert the data using the method of section 3; and (4) compare inverted and directly measured profiles.

The Hawaiian data were taken at Upolu Point, Hawaii, Hawaii, during two 2-week periods in April and July—

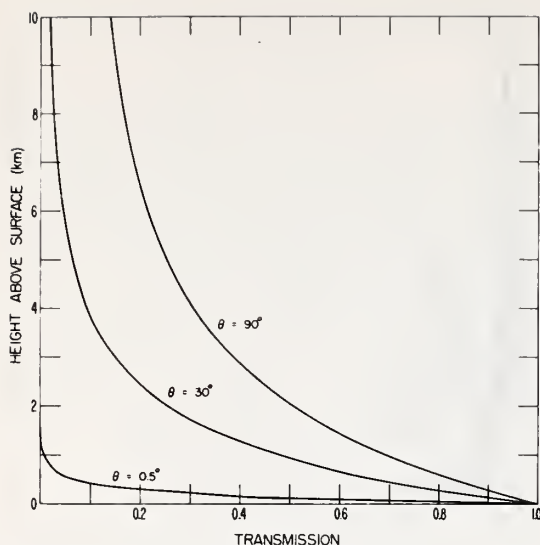


FIGURE 2.—August atmospheric transmission at 54.0 GHz for Salt Lake City, Utah.

August 1968. Thermal emission measurements at 52.5 GHz were made with a microwave radiometer designed and constructed by Jack B. Snider of National Oceanic and Atmospheric Administration (NOAA) Environmental Research Laboratories. Radiosonde observations of temperature, pressure, and relative humidity were taken at 3-hr intervals and covered the height range from the surface to 10 km. Emission measurements at a set of nine fixed elevation angles were taken at 3-hr intervals to coincide with the onsite radiosonde release; the angles were chosen to divide the cosecant into equal increments between the lowest (5.25°) and the highest (90°) elevation angles used.

The data were supplied to the author in the form of antenna temperature versus elevation angle. Before these data could be used for inversion, a study of the bandwidth integration and antenna effects was necessary. The radiometer was a double sideband Dicke type. In this type of receiver, the weak radio frequency signal, ν_{RF} , incident on the antenna is mixed with a strong local-oscillator signal, ν_o , to produce an output power on an intermediate frequency, ν_{IF} . In a double sideband receiver, both the signal frequency $\nu_{RF} = \nu_o + \nu_{IF}$ and the image frequency $\nu'_{RF} = \nu_o - \nu_{IF}$, can be received and amplified at the intermediate frequency ν_{IF} . The predetection bandwidth $\Delta\nu$ is usually determined by the IF amplifier. The effective bandwidth filter function is indicated schematically in the lower left portion of figure 3. To determine the effect of this bandwidth integration on the brightness temperature and on the profile weighting functions defined by eq (6), numerical calculations were performed assuming Gaussian bandwidths and the radiometer parameters given in figure 3. A seven point Gauss-hermite quadrature was used in integrating each side of the band. Integrating

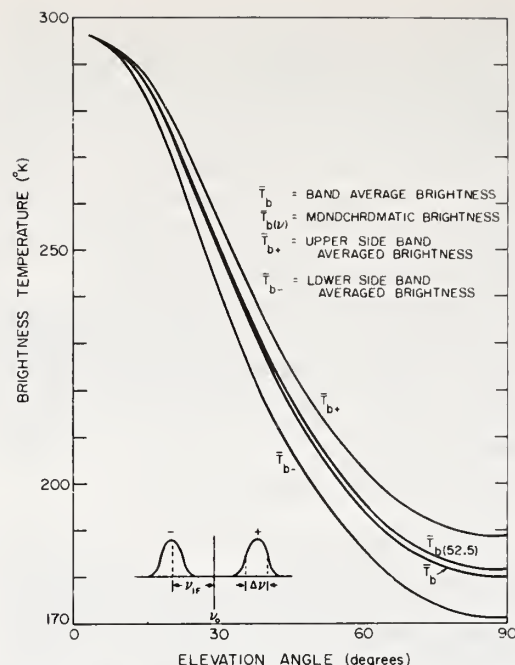


FIGURE 3.—Band averaged brightness for a double side band radiometer for the mean atmosphere at Upolu Point, Hawaii, Hawaii ($\nu_o = 52.5$ GHz, $\nu_{IF} = 160$ MHz, $\Delta\nu = 40$ MHz).

the brightness of the mean Hawaiian atmosphere during the period of observation resulted in a maximum difference of about 1.5°K; the complete results are shown in the figure. To test the sensitivity of these results to profile variations, bandwidth calculations for two extreme profiles were performed; again, the differences between integrated and monochromatic brightness were the same to within about 0.02°K. Thus, for the frequency characteristics of this radiometer, and if departures from the mean brightness are used, we may make the approximation of replacing double sideband averages by the value at the center frequency.

The antenna used in collecting the emission data was a 4-ft Cassegrain-type parabolic dish with a half-power main beam width of about 0.2°. Any antenna measures a weighted brightness distribution over a sphere; for a narrow beam antenna with low side lobes, the antenna and brightness temperature are approximately equal. For the antenna described above, such was not the situation as is evident from figure 4 which shows the average of 84 antenna temperature measurements versus the band average brightness calculated for the average profile during the same period. Included in the average of T_A were some data taken in the presence of clouds. Clouds showed little effect, however, except during periods of rain and heavy overcast, periods which were excluded from the average. The standard method of converting T_A to T_b

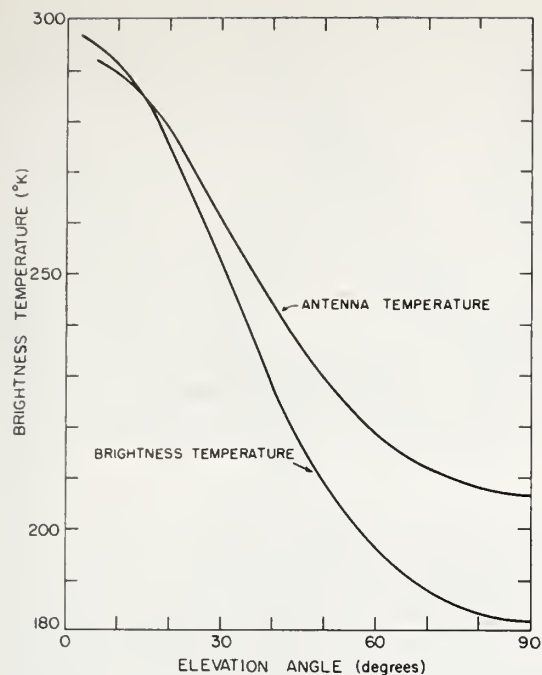


FIGURE 4.—Average antenna and brightness temperature for Upolu Point, Hawaii, Hawaii, July–August 1968 ($\nu = 52.5$ GHz).

requires convolution of a known gain pattern with a background brightness model to estimate the stray contribution to T_A from outside the main beam. The stray contribution is then subtracted from T_A to get T_b . For the dish antenna used in Hawaii, the gain pattern was known only for a few degrees surrounding the main beam, and the above method could not be used. A statistical technique of estimating T_b from T_A will be described below. The equation relating the two, namely,

$$T_A(\theta, \varphi) = \frac{1}{4\pi} \int_{\Omega} G(\theta, \varphi; \theta', \varphi') T_b(\theta', \varphi') d\Omega' \quad (17)$$

where θ and φ are elevation and azimuth in polar coordinates, and $d\Omega$ is an element of solid angle, is similar in form to an integral equation of the first kind. If noiseless measurements of $T_A(\theta, \varphi)$ were made for all (θ, φ) and if the antenna gain function, $G(\theta, \varphi; \theta', \varphi')$, were known, then in principle (eq 17) could be inverted to determine $T_b(\theta, \varphi)$, at least for gain functions with good angular resolution. In practice, only a finite number of imperfect measurements are available. However, in a manner similar to the technique used in the statistical inversion of the transfer equation, the antenna temperature measurements may be used as estimators of the desired brightness temperatures; thus

$$\hat{T}_b(\theta) = \sum_i C_i(\theta) T_{A_i} \quad (18)$$

TABLE 1.—Measurement noise level

| $\sigma_{T_b} (^{\circ}\text{K})$ | Elevation angle (degrees) | | | | | | | | |
|-----------------------------------|---------------------------|-------|--------|------|--------|-------|--------|------|--------|
| | 5.625 | 11.25 | 16.875 | 22.5 | 28.125 | 33.75 | 39.375 | 45.0 | 50.625 |
| | 0.76 | 0.76 | 0.59 | 0.63 | 0.76 | 0.71 | 0.61 | 0.82 | 0.73 |

where the summation extends over the number of observed antenna temperatures, T_{A_i} . Physically, it is reasonable to assume that T_b could be approximated by a weighted sum of well-chosen antenna temperatures since T_A is a weighted average of T_b . The coefficients, $C_i(\theta)$, could be determined by the least-squares criterion if a simultaneous collection of correct brightness temperatures and corresponding antenna temperatures were available over a representative ensemble of atmospheric (and surface) conditions. In this way, measurements of surface emission could be used to improve estimates of sky brightness. Assuming the correctness of the analytical absorption equations, the "correct" brightness can be approximated by calculations based upon onsite radiosonde observations. The correctness of the absorption equations may be (and were) independently checked by other methods such as comparison of attenuation calculations based on radiosonde observations with zenith attenuation measurements. To apply this technique to the Hawaiian data, 25 radiometer-radiosonde profile pairs were selected at random and excluded from the 84 original data pairs for later use in inversion. The weighting coefficients, $C_i(\theta)$, were determined by least squares over the remaining data. The results of using the $C_i(\theta)$ to predict the original 25 brightness temperatures are shown in table 1. The average standard deviation per angle was 0.72°K . This is about an order of magnitude greater than the theoretical receiver sensitivity, which was 0.13°K for the $2\frac{1}{2}$ -min averaging time.

An important point in the development of the inversion method derived in section 2 is the assumption that brightness fluctuations may be linearly related to profile fluctuations. In the microwave region, where the Planck function is a linear function of temperature, linearity requires fluctuations in the kernel (derivative of the transmissivity) to be linearly related to profile fluctuations. The accuracy of the linear approximation was evaluated exactly at 52.5 GHz for all 25 profiles used in inversion and at 54.5 GHz for two extreme profiles. For the lower frequency, where the emission is strongly affected by water vapor fluctuations, the rms linearization error at zenith elevation was 0.36°K ; the error at $\theta = 5.25^{\circ}$ was 0.07°K . It was also noticed that the zenith linearization error had an average bias of -0.25°K . At 54.5 GHz, where the variance of the weighting function is much less, the maximum linearization errors were less than 0.1°K .

The linear model developed in section 2 can be applied to the determination of the atmospheric contributions to ground-based observations of brightness fluctuations. At low elevation angles, where the radiometer is viewing the optically opaque portion of the atmosphere, intensity

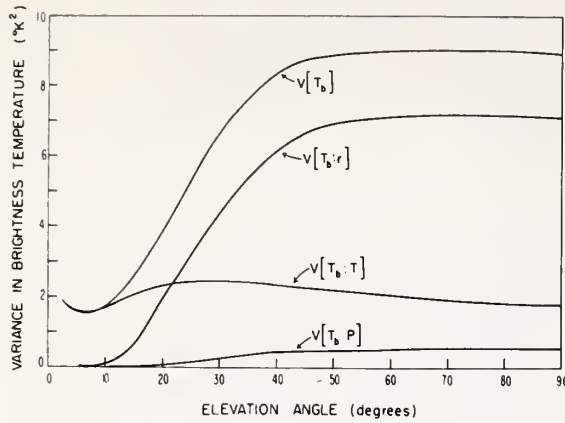


FIGURE 5.—Relative contribution to fluctuations in brightness temperature at Upolu Point, Hawaii, Hawaii, for April and July-August ($\nu=52.5$ GHz, T is temperature, r is relative humidity, p is pressure).

fluctuations are caused primarily by temperature fluctuations; for higher angles, where the optical depth is less, fluctuations in optical depth may add a component to the observed intensity fluctuations. The quantitative description of the relative contributions to the atmospheric brightness fluctuations is

$$S_{T_i} = A_T S_{T_i} A_T^* + A_T S_{T_p} A_p^* + \dots + A_T S_{T_r} A_r^* + A_p S_p A_p^* \quad (19)$$

The diagonal elements of S_{T_i} are the variances of atmospheric brightness at the chosen set of angles; the off-diagonal elements represent the covariances between brightness temperatures at different angles. The brightness variance at the i th angle due to the integrated effect of temperature fluctuations, say, is the i th diagonal element of $A_T S_{T_i} A_T^*$. Figure 5 shows the diagonal elements of the various matrices as a function of elevation angle for the April-July-August Hawaiian ensemble. In the notation used here, $V[T_b; T]$ is the contribution to the variance of T_b due to fluctuations in temperature alone; $V[T_b]$ is the total variance of T_b . The correlation effects between the three parameters p , T , and r are small as shown by approximate equality of the sum of the three partial variances and the total variance $V[T_b]$. The surprising feature demonstrated by this figure is the large contribution to the variance at the higher elevation angles by the moisture fluctuations. The water vapor contribution to the average brightness is large because of the large amount of water contained in the narrow height interval from the surface to the base of the trade wind inversion. The water vapor variance is particularly large for this ensemble because of the contrast between the normal trade wind pattern that was present in much of the July-August data and the 2-week period in April when the trade wind pattern was interrupted by the so-called kona winds. For this period, in which the trade

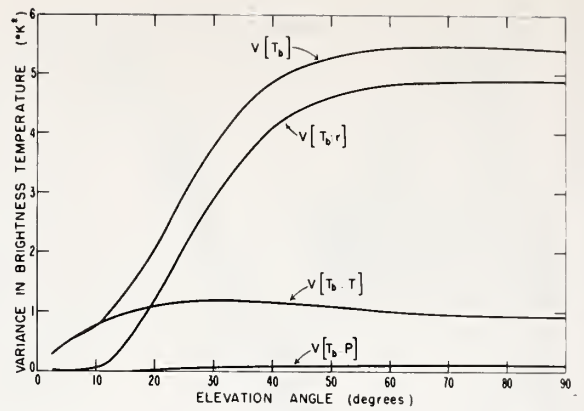


FIGURE 6.—Same as figure 5 except constrained surface conditions.

wind inversion was absent, the water vapor was distributed to much higher altitudes.

As discussed in section 2, atmospheric fluctuations that are uncorrelated with the temperature have the same effect on the inversion process as instrumental noise. Thus, figure 5 shows that for the higher elevation angles, the effective signal to noise ratio is less than unity. The obvious way to reduce this noise level would, of course, be to measure the emission around the 22.235 GHz water vapor line. Because a radiometer at this frequency was not available, only surface constraints were available to reduce the noise level. Figure 6 shows the resulting contributions to the variance in brightness for fixed surface conditions. Since the variance in moisture distribution was primarily related to the presence or absence of the trade wind inversion, the surface constraints do little to affect this component of variance. As is evident from the figures for both constrained and unconstrained distributions, the pressure effect is small. The fractional reduction of the pressure contribution by surface constraints is substantial, here and in general, because pressure distributions tend to be highly correlated. Meteorological conditions where pressure fluctuations can contribute 1 to 2 $(°K)^2$ to the zenith brightness variance are not uncommon.

Statistical techniques can be used to predict the accuracy that can be achieved by inverting indirect measurements (Westwater and Strand 1968). This accuracy is a function of the statistical characteristics of the vertical temperature structure, the shape of the weighting functions, the measurement noise level, and the number of measurements used. The accuracies expected for Hawaiian statistics constrained to surface conditions and experimental noise levels determined for various sets of the 52.5 GHz radiometer data are shown in figure 7. Here, the curve labeled σ_T shows the a priori standard deviation in temperature as a function of height. The residual standard errors of estimate to be expected after inverting measurements with the three noise levels (average per angle for nine angles), are also plotted as a function of height. Thus,

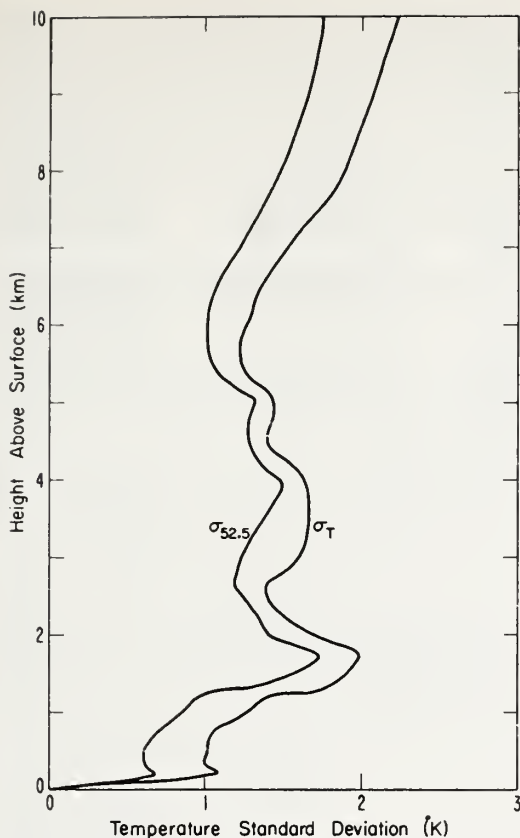


FIGURE 7.—Theoretical resolution in standard deviation of Upolu Point, Hawaii, Hawaii, temperature profiles (constrained to surface conditions) by inversion of 52.5 GHz radiometer data. (Nine angles, $\sigma_r = 0.72^\circ\text{K}$.)

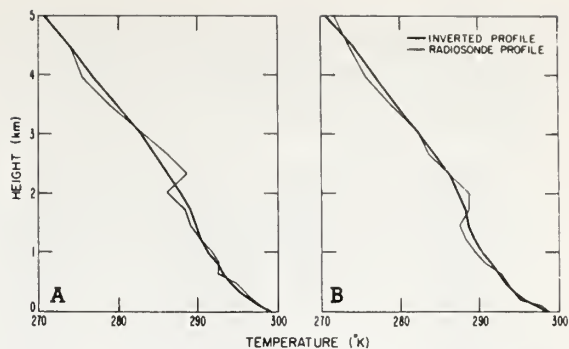


FIGURE 8.—Upolu Point, Hawaii, Hawaii, temperature profile derived from radiometer measurements at 52.5 GHz using constrained statistics for (A) 1700 hst, July 23, and (B) 0003 hst, July 28.

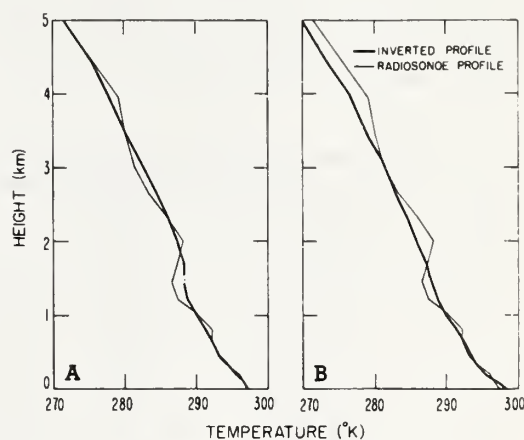


FIGURE 9.—Upolu Point temperature profile derived from radiometer measurements at 52.5 GHz for 0606 hst, July 28, using (A) constrained statistics and (B) unconstrained statistics.

the average accuracy expected from inversion with measurements of the assumed accuracies is about 1°K rms error. The intersection of the residual error curves occurs because of correlation of angular measurement errors.

The statistical inversions of the previously described 25 sets of angular brightness temperature measurements were performed using both constrained and unconstrained statistics. These profiles were excluded from the statistical ensemble used in constructing the relevant covariance matrices. Figure 8 shows typical inversion results. In both cases, the inverted profile is a smoothed version of the original, with a smoothing that is commensurate with the effective noise levels. Note that the trade wind inversion at 2 km is smoothed out; the average rms deviation per point is around 1°K , a figure not out of line with theoretical predictions. The effect of using constrained methods is shown in figure 9 where constrained and unconstrained inversions are compared for the same profile. Using constrained statistics lowers the effective noise level and

allows some of the higher frequency spacial components to be present in the solution.

The summary of constrained inversion results is shown in table 2. The tabulated quantities represent average rms errors between the inverted profile and the radiosonde profile at each quadrature height. The indicated 90-percent confidence limits were determined using the χ^2 -test with 25 degrees of freedom. The improvement over a priori statistics is evident as shown, with the exception of the 2.00-km level. The statistics there reflect that the trade wind inversion is being smoothed out in the solution. The improvement over the original statistics is not particularly large because (1) their variance is small and further reduction is difficult, (2) the vertical profiles have poor autocorrelation (Westwater 1970), and (3) the contaminating effect of water vapor gives rise to large effective noise levels at the higher elevation angles. The average rms

TABLE 2.—Summary of Hawaiian constrained inversion results ($\nu=52.5$ GHz, 9 angles). Data are based on 25 profiles at 90-percent confidence intervals. T is radiasande temperature profile, \hat{T} is inverted temperature profile, \bar{T} is constrained mean profile.

| Height (km) | $\frac{1}{25} \sum (T-\bar{T})^2$ | $\frac{1}{25} \sum (T-\hat{T})^2$ | $\sqrt{\frac{1}{25} \sum (T-\bar{T})^2}$ | $\sqrt{\frac{1}{25} \sum (T-\hat{T})^2}$ |
|-------------------------------|-----------------------------------|-----------------------------------|------------------------------------------|------------------------------------------|
| | (°K) ² | (°K) ² | (°K) | (°K) |
| 0.000 | 0.000 | 0.000 | 0.000 | 0.000 |
| 0.350 | 0.52 (0.35, 0.88) | 0.37 (0.25, 0.63) | 0.72 (0.59, 0.94) | 0.61 (0.49, 0.80) |
| 0.648 | 0.62 (0.41, 1.06) | 0.44 (0.29, 0.75) | 0.79 (0.64, 1.03) | 0.66 (0.54, 1.02) |
| 1.013 | 2.50 (1.66, 4.27) | 2.22 (1.47, 3.80) | 1.58 (1.30, 2.10) | 1.49 (1.15, 1.46) |
| 1.458 | 4.01 (2.66, 6.86) | 3.28 (2.17, 5.60) | 2.00 (1.64, 2.63) | 1.81 (1.29, 2.38) |
| 2.001 | 4.01 (2.66, 6.86) | 3.96 (2.63, 6.77) | 2.00 (1.64, 2.63) | 1.99 (1.63, 2.60) |
| 3.050 | 1.29 (0.85, 2.21) | 0.75 (0.50, 1.28) | 1.13 (0.93, 1.50) | 0.87 (0.71, 1.14) |
| 3.946 | 3.41 (2.26, 5.83) | 2.72 (1.80, 4.65) | 1.85 (1.51, 2.42) | 1.65 (1.35, 2.16) |
| 5.040 | 1.27 (0.84, 2.17) | 1.14 (0.76, 1.95) | 1.17 (0.92, 1.48) | 1.07 (0.88, 1.40) |
| 6.376 | 1.61 (1.06, 2.75) | 1.20 (0.79, 2.05) | 1.27 (1.03, 1.67) | 1.09 (0.89, 1.44) |
| 8.008 | 2.40 (1.59, 4.10) | 1.67 (1.11, 1.90) | 1.55 (1.27, 2.02) | 1.29 (1.06, 1.39) |
| 10.000 | 3.90 (2.59, 6.67) | 1.89 (1.25, 3.23) | 1.98 (1.62, 2.60) | 1.38 (1.13, 1.80) |
| Average of 25 points to 10 km | | | | |
| | 2.002 | 1.604 | 1.414 | 1.265 |

TABLE 3.—Comparison of experimental versus theoretical accuracies in inversion ($\nu = 52.5$ GHz, 9 angles). Data are based on 25 profiles at 90-percent confidence intervals. T , \bar{T} , and \hat{T} have the meanings given in table 2.

| Height (km) | $\sigma(T-\bar{T})$ | $\sqrt{\frac{1}{25} \sum (T-\bar{T})^2}$ | $\sigma(T-\hat{T})$ | $\sqrt{\frac{1}{25} \sum (T-\hat{T})^2}$ |
|-------------------------------|---------------------|------------------------------------------|---------------------|------------------------------------------|
| | (°K) | (°K) | (°K) | (°K) |
| 0.000 | 0.000 | 0.000 | 0.000 | 0.000 |
| 0.350 | 0.99 | 0.72 (0.59, 0.94) | 0.61 | 0.61 (0.49, 0.80) |
| 0.648 | 1.04 | 0.79 (0.64, 1.03) | 0.66 | 0.66 (0.54, 1.02) |
| 1.013 | 1.30 | 1.58 (1.30, 2.10) | 0.89 | 1.49 (1.15, 1.46) |
| 1.458 | 1.89 | 2.00 (1.64, 2.63) | 1.54 | 1.81 (1.21, 2.38) |
| 2.001 | 1.68 | 2.00 (1.64, 2.63) | 1.40 | 1.99 (1.63, 2.60) |
| 3.050 | 1.64 | 1.13 (0.93, 1.50) | 1.24 | 0.87 (0.71, 1.14) |
| 3.946 | 1.64 | 1.85 (1.51, 2.42) | 1.50 | 1.65 (1.35, 2.16) |
| 5.040 | 1.44 | 1.17 (0.92, 1.48) | 1.33 | 1.07 (0.88, 1.40) |
| 6.376 | 1.34 | 1.27 (1.03, 1.67) | 1.05 | 1.09 (0.89, 1.44) |
| 8.008 | 1.90 | 1.55 (1.27, 2.02) | 1.50 | 1.29 (1.06, 1.39) |
| 10.000 | 2.19 | 1.98 (1.62, 2.60) | 1.76 | 1.38 (1.13, 1.80) |
| Average of 25 points to 10 km | | | | |
| | 1.49 | 1.42 | 1.20 | 1.27 |

accuracy to 10 km is 1.27°K as compared with an accuracy of 1.42°K achieved by using only constrained statistics.

As mentioned above, the theory of statistical estimation allows prediction of the accuracies to be achieved by inversion. In table 3, a comparison of theoretical predictions versus experimental results are shown. The theoretical values represent square roots of the diagonal elements of the appropriate covariance matrices; the solution covariance matrix was calculated using the effective noise level, $S_e^{(e)}$ given by eq (15), a procedure that neglects the correlation effects between temperature and the other variables. As is evident from inspection, the numbers usually agree within the 90-percent confidence limits.

The inversion equations developed in section 2 can be used to estimate each component contributing to the measured brightness fluctuations. This includes, in addition to temperature, the pressure, relative humidity, and experimental error components. The 25 measurements described above, when inverted for pressure and relative humidity profiles, allowed a reduction in average rms error per point (constrained surface conditions) from 0.78 to 0.62 mb in pressure and 1.57 to 1.35 gm⁻³ in absolute humidity. The absolute humidity inversions were achieved by linearly inverting the temperature and relative humidity profiles and then combining these to form the absolute humidity. In addition to profile estimation, the

point estimates of absolute humidity were integrated with respect to height to form estimates of the total vertical water content. The water content, as determined by numerically integrating the 25 radiosonde soundings, averaged $2.85 \text{ g}\cdot\text{cm}^{-2}$ with a range of $1.95\text{--}4.18 \text{ g}\cdot\text{cm}^{-2}$. The rms deviation between radiometrically inferred and radiosonde measured water content was $0.21 \text{ g}\cdot\text{cm}^{-2}$ and corresponded to a correlation coefficient of 0.92. This was an improvement over constrained statistics by about 6 to 1.

5. ANALYSIS AND INVERSION OF SALT LAKE CITY RADIOMETER DATA

The application of microwave radiometry to remote probing of low altitude temperature profiles is being investigated experimentally by Sperry Rand Corporation (Mount et al. 1968). To further test statistical inversion techniques on microwave data, we procured data from one of their field tests. The analysis and inversion of these data are discussed in this section.

The data were taken at Salt Lake City, Utah, on Aug. 15 and 16, 1968, during clear daytime conditions. Null balance radiometer measurements of thermal emission at discrete elevation angles ranging from horizontal to zenith were taken at 54.0, 54.5, and 55.0 GHz. The radiometer measurements had been reduced to brightness temperature by Sperry Rand and were supplied to the author in this form. Supplementing the radiometer data were onsite radiosonde soundings of height, pressure and temperature extending to 400 mb or approximately 6 km above the surface; the meteorological package did not have a humidity sensor. Nine radiometer runs and six balloon soundings were taken.

As will be seen, for the 54–55 GHz frequency interval, theoretical calculations show that detailed information about the temperature structure above 3 or 4 km would be difficult to obtain by inversion of radiometer data. Nevertheless, at high elevation angles the radiometer can detect gross changes in atmospheric structure above 6 km. Calculations of vertical brightness using the Salt Lake City mean atmosphere indicated that a $10^{\circ}\text{--}30^{\circ}\text{K}$ contribution would arrive at the ground from the thermal emission above 6 km (the transmissivity from 0 to 6 km was 0.23 at 54 GHz). Since meteorological coordinates were not available above 6 km from the onsite soundings, the August mean profiles of temperature, pressure, and humidity were used above the termination point for the brightness calculations described below. Changing the upper level profile from the Salt Lake City August mean to a standard atmosphere resulted in a 3°K change at 54 GHz, a 0.5°K change at 54.5 GHz, and a negligible change at 55 GHz, so that at least one of the channels was sensitive to gross changes in the atmosphere above 400 mb.

The humidity up to 6 km was estimated from the radiosonde observations at the Salt Lake City airport, roughly one mile away from the radiometer field site. At the surface, the absolute humidity was about 4 gm^{-3} . Calculations of wet and dry absorption indicated that the relative

water vapor contribution was small at these frequencies. This contrast to the absorption at 52.5 GHz at Hawaii occurs because (1) the water content of Salt Lake City was nearly a factor of three less, and (2) the dry absorption was from three to five times greater, depending on the frequency.

Before attempting to recover temperature profiles from the radiometer data described above, comparisons of measured brightness with brightness calculations based on radiosondes were made. The oxygen line shape parameters of Carter et al. (1968) can be used with confidence here since they were derived from measurements at frequencies almost coincident with the 54.0-, 54.5-, and 55.0-GHz channels. Initial calculations showed an almost constant difference of about 5°K between measurements and calculations of angular brightness. A bias correction, approximately equal to the difference between the ambient surface temperature and the horizontal brightness, removed the major portion of this error. Theoretically, at the highly absorbing frequencies used here, the horizontal brightness is nearly equal to ambient temperature so the magnitude of the correction was reasonable. Using 12 pieces of data at 54 GHz, 18 at 54.5 GHz, and 48 at 55 GHz, a single bias correction was determined for each frequency by least-squares comparison of calculated versus measured brightness. The resulting standard deviations between measured and calculated brightness were 1.47° , 1.28° , and 0.58°K at 54.0, 54.5, and 55.0 GHz, respectively. When the same procedure was applied to half of the above data sample, neither the bias corrections nor the standard deviations changed appreciably from the above values. The results of the calculations and measurements are shown in figure 10. The calculated average brightness temperatures at the corresponding frequency are shown in each graph for comparison and, in addition, the mean brightness calculations are shown separately in figure 11. There is reasonable agreement between measurements and calculations for all of the nine profiles. Note that the largest deviation at $\nu=54.0$ GHz, radiometer time 2000–2020 MDT, August 16 (0200–0220 GMT, August 17), and radiosonde time 1747 MDT (2347 GMT), August 16, occurs when there is about a 2-hr time interval between radiometer and radiosonde observations.

The absence of the bandwidth correction in the above calculations should be noted. The radiometer was a double sideband type with an intermediate frequency of 157.5 MHz and an equivalent rectangular bandwidth of 160 MHz. The filter function was unknown, but calculations assuming a rectangular filter indicated a maximum deviation from linearity of about 1°K at 54 GHz and a negligible effect at 55 GHz. As indicated previously, when departures from averages are considered, the dependence on bandwidth is considerably reduced. The bandwidth effect becomes much more important at lower pressures where resonant line structure is resolved.

The theoretical variance in brightness temperature as a function of elevation angle at each of the three operating

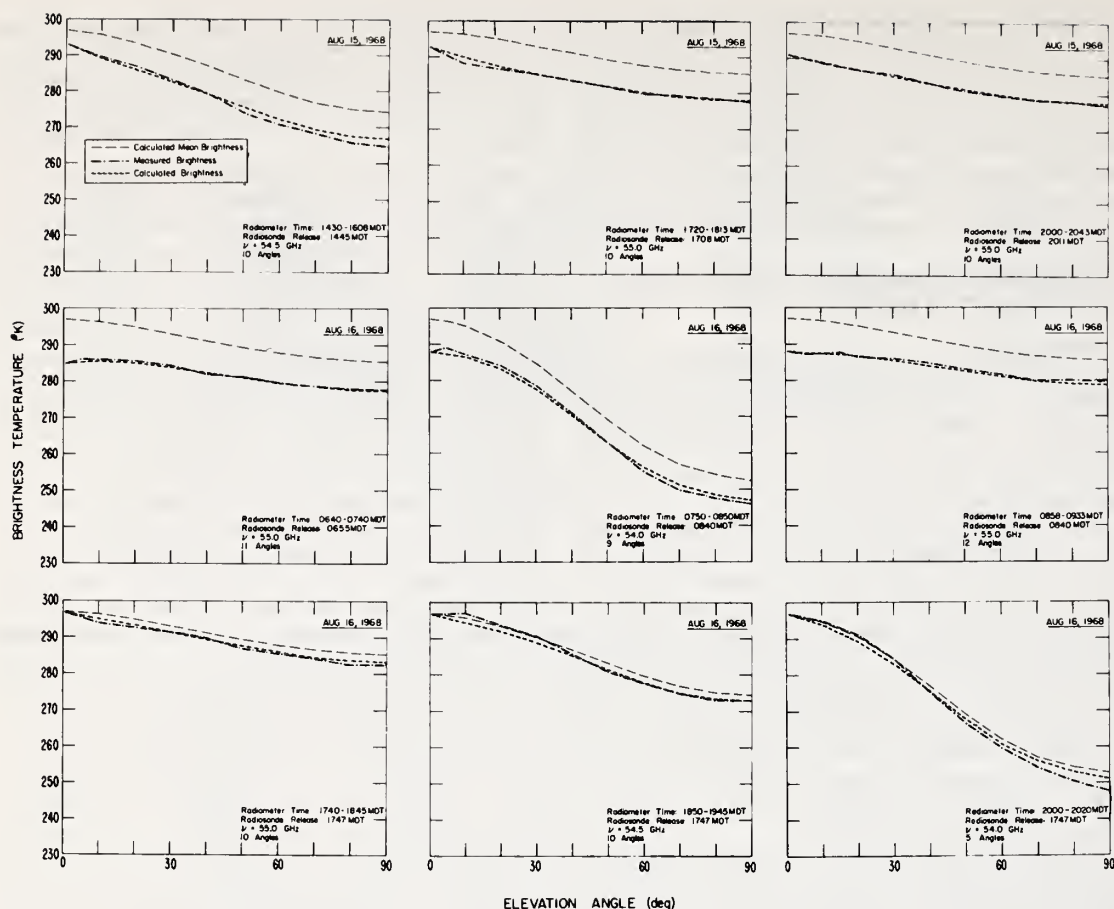


FIGURE 10.—Comparison of measured and calculated brightness temperatures at Salt Lake City, Utah.

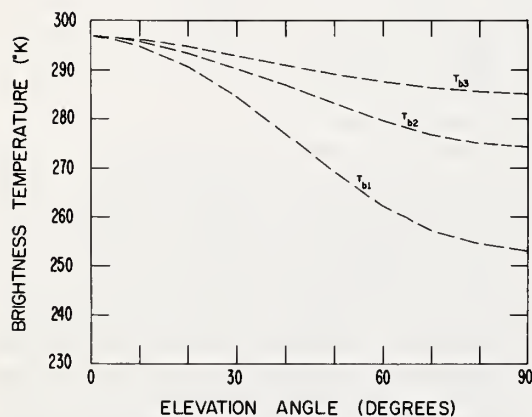


FIGURE 11.—Calculated brightness temperatures at Salt Lake City, Utah ($T_{b1}=54.0$ GHz, $T_{b2}=54.5$ GHz, $T_{b3}=55.0$ GHz).

frequencies was calculated for the Salt Lake City August statistics. The relevant covariance matrices were calculated from a carefully edited ensemble of 5 yr of twice per day radiosonde soundings (287 profiles). In contrast to the variance calculations at 52.5 GHz for Hawaiian climatology, the humidity and pressure fluctuations yielded a contribution to total variance that was 100 to 1 less than that due to temperature fluctuations. The results are shown in figures 12 and 13 for unconstrained and constrained surface conditions, respectively. Note the large variance in the unconstrained case at low elevation angles, reflecting the large dependence on the highly variable surface temperature. Although the imposition of surface constraints considerably lowers the total variance, the resulting signal-to-noise ratio (of variances) is around 25 to 1 for a noise level of 0.5° K.

Following the method described above, the accuracies to be expected from inverting angular measurements at 54.0,

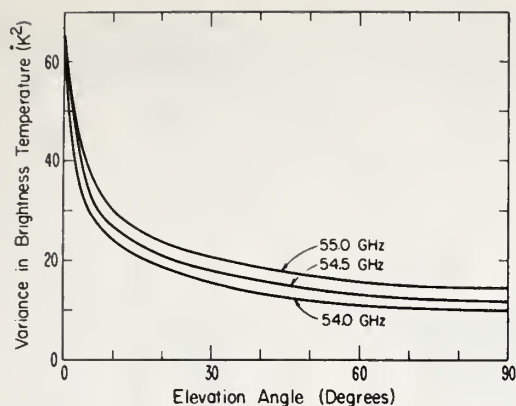


FIGURE 12.—Calculated unconstrained variance in brightness temperature at Salt Lake City, Utah, in August.

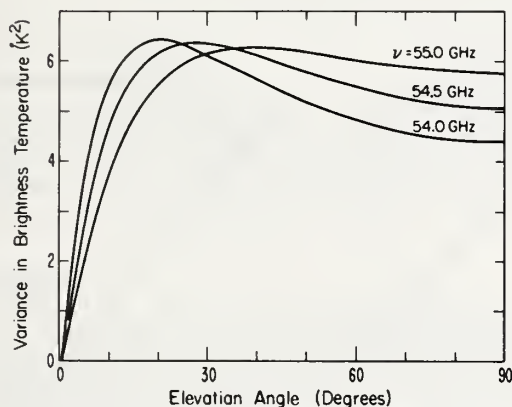


FIGURE 13.—Calculated variance in brightness temperature for constrained surface conditions at Salt Lake City, Utah, in August.

54.5, and 55.0 GHz were calculated. The results, as determined using the Salt Lake City August temperature covariance matrix appropriate to given surface conditions and the effective noise levels determined by comparing measured and calculated brightness, are shown in figure 14. As expected, both the magnitude and the height distribution of the temperature variance are radically different from the Hawaiian ensemble shown previously. A substantial reduction in variance is predicted below 3 km but expected results approach the statistics above this height.

The mathematical inversions of the data described above were achieved by the same techniques that were applied to the Hawaiian ensemble. Pressure and humidity covariance matrices were used in the inversion although

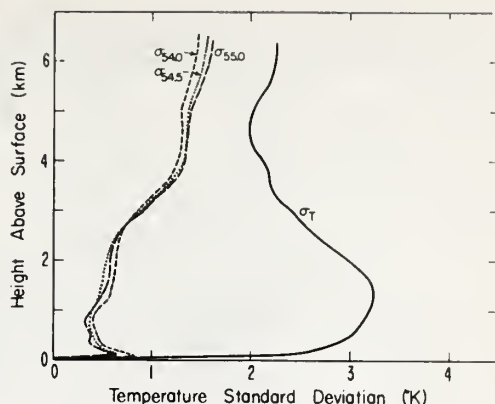


FIGURE 14.—Theoretical reduction in standard deviation of temperature profiles by inversion of microwave radiometer data at Salt Lake City, Utah, in August, using constrained statistics [σ (54.0 GHz), 5 angles, $\sigma_e = 1.5^\circ\text{K}$; σ (54.5 GHz), 10 angles, $\sigma_e = 1.3^\circ\text{K}$; σ (55.0 GHz), 10 angles, $\sigma_e = 0.6^\circ\text{K}$].

their effect was small. All results shown in figure 15 used covariance matrices appropriate to constrained surface conditions, although strictly speaking the statistics were non-Gaussian (Westwater 1970). Several features of the figures should be noted. First, all inversions of lapse profiles are almost coincident with the radiosonde profiles. This is not simply reproducing the mean, because several of the conditional averages show ground-based thermal inversions occur their features are clearly defined. The structure of the elevated isothermal layer occurring at 1445 mDT (2045 GMT) on August 15 is smoothed out. The 3°K maximum difference on the $\nu = 55.0$ -GHz inversion on the August 16, 0840 mDT (1440 GMT) sounding occurs around 4.0 km, well out of the range of this strongly absorbing channel. This is slightly above two standard deviations of the theoretical predictions given previously. Note that the preceding radiometer run at 54.0 GHz at 0750–0850 mDT (1350–1450 GMT), for the same temperature profile, corrects the above errors which suggests that, even with an angular scheme, multispectral measurements can complement each other. These two adjacent radiometer runs also show consistency in indicating a surface-based isothermal layer that the radiosonde does not show. This could result from antenna side lobe effects or from smoothing due to inadequate height resolution.

The inversion results are summarized in table 4. Here, the rms differences between the inverted and the radiosonde profiles are given at selected heights. In addition, the rms differences between the radiosonde soundings and the mean profile, adjusted to the same surface conditions, are shown, so that an indication of the amount of improvement over past statistics can be seen by inspection. Except

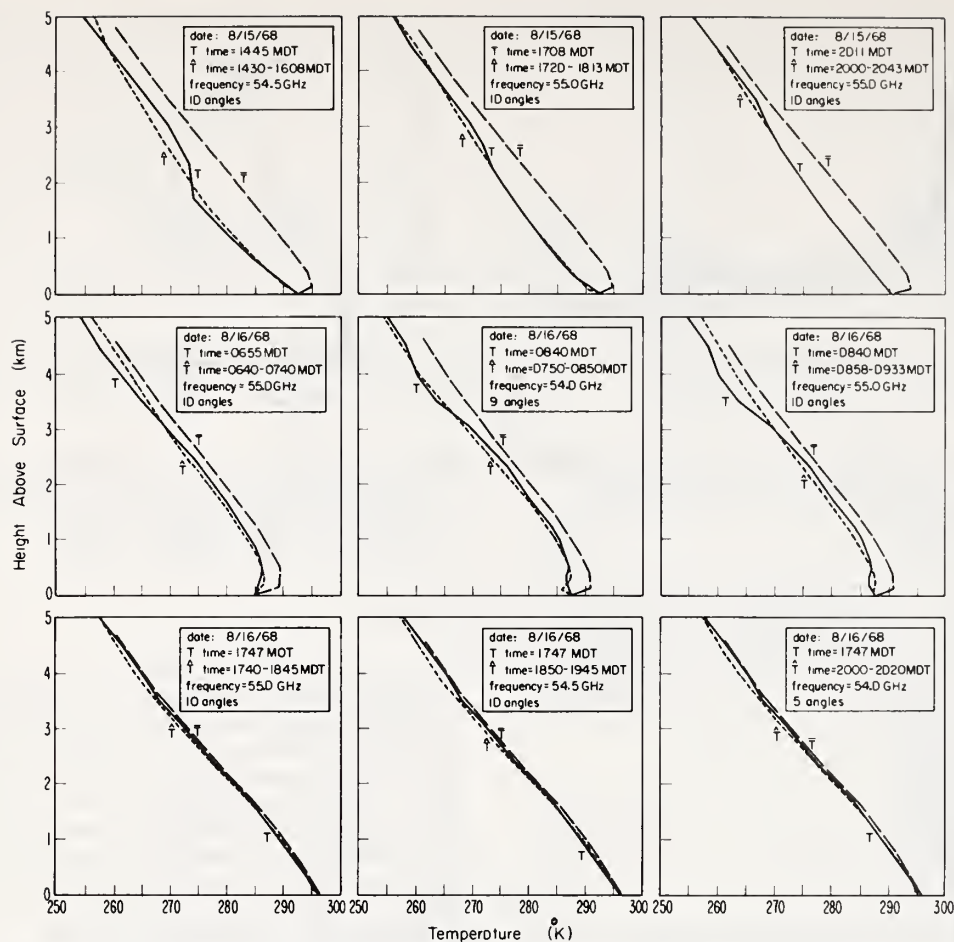


FIGURE 15.—Comparison of inverted and radiosonde temperature profiles at Salt Lake City, Utah. \bar{T} is the constrained mean temperature T is the radiosonde measured profile, \hat{T} is the radiometrically determined profile.

for the 0.105-km level, these inversions give substantial improvement over pure statistics below 3 km. The average improvement in variance was about 25 to 1 over this height interval. As indicated in figure 14, this improvement is expected to diminish rapidly above 3 km for all channels. The resulting rms errors for all three channels show excellent agreement with theory. Note, however, that the numbers represent rms differences and are not errors in inversion unless the radiosonde measures the "true" profile exactly.

6. SUMMARY AND CONCLUSIONS

The technique described here shows promise as a tool for determining low altitude temperature profiles. Microwave angular emission measurements taken at two loca-

tions (during cloudless conditions) were used to recover low altitude profiles with a rms accuracy of about 1°K . Lapse rate and ground-based inversion profiles were successfully inferred, but the details of the Hawaiian trade wind inversion were smoothed out. The accuracies of the inferred profiles agree well with predictions based on the theory of statistical estimation.

Further experimental and theoretical work is necessary to determine the limitations and extension of this technique, particularly in the presence of clouds. Additional refinements in equipment include the use of an antenna with better angular resolution and a radiometer with a multifrequency capacity. A four-channel radiometer developed by the Wave Propagation Laboratory of NOAA will soon be in operation.

TABLE 4.—Comparison of inverted and radiosonde temperature profiles, Salt Lake City, Utah, Aug. 15 and 16, 1968. T , \hat{T} , and \bar{T} have the meanings given in table 2.

| Height (km) | $\nu=54.0$ GHz $\sigma_s=1.5^\circ\text{K}$ 2 profiles | | $\nu=54.5$ GHz $\sigma_s=1.3^\circ\text{K}$ 2 profiles | | $\nu=55.0$ GHz $\sigma_s=0.8^\circ\text{K}$ 5 profiles | |
|--------------------------------|--------------------------------------------------------------|----------------------|--------------------------------------------------------------|----------------------|--------------------------------------------------------------|----------------------|
| | $\sigma(\bar{T}-T)$ | $\sigma(\hat{T}-T)$ | $\sigma(\bar{T}-T)$ | $\sigma(\hat{T}-T)$ | $\sigma(\bar{T}-T)$ | $\sigma(\hat{T}-T)$ |
| | ($^\circ\text{K}$) | ($^\circ\text{K}$) | ($^\circ\text{K}$) | ($^\circ\text{K}$) | ($^\circ\text{K}$) | ($^\circ\text{K}$) |
| 0.00 | 0.00 | 0.00 | 0.00 | 0.00 | 0.00 | 0.00 |
| 0.105 | 0.71 | 0.93 | 1.16 | 0.37 | 0.92 | 0.47 |
| 0.221 | 1.07 | 0.37 | 1.99 | 0.35 | 1.70 | 0.82 |
| 0.350 | 1.11 | 0.69 | 2.76 | 0.32 | 2.38 | 0.50 |
| 0.491 | 1.48 | 0.21 | 3.39 | 0.26 | 2.72 | 0.22 |
| 1.013 | 2.75 | 0.60 | 4.51 | 0.59 | 3.60 | 0.68 |
| 1.458 | 2.98 | 0.48 | 4.96 | 0.86 | 3.82 | 0.65 |
| 2.001 | 3.24 | 0.66 | 3.71 | 0.37 | 3.93 | 0.70 |
| 2.665 | 3.46 | 1.08 | 1.64 | 1.67 | 3.58 | 0.62 |
| 3.050 | 3.06 | 0.89 | 1.55 | 1.93 | 3.24 | 0.66 |
| 3.946 | 1.78 | 1.08 | 1.54 | 1.37 | 2.69 | 1.62 |
| 5.040 | 2.98 | 0.50 | 1.87 | 1.48 | 3.11 | 1.39 |
| Average of 20 points to 6.4 km | | | | | | |
| | 2.71 | 0.83 | 3.16 | 1.21 | 3.24 | 0.88 |

ACKNOWLEDGMENTS

The author thanks J. London and M. Mizushima of the University of Colorado for many stimulating discussions of this work. Martin T. Decker offered many worthwhile suggestions on the manuscript. The research was supported in part by the Air Pollution Control Office of the Environmental Protection Agency.

REFERENCES

- Carter, C. J., Mitchell, R. L., and Reber, E. E., "Oxygen Absorption Measurements in the Lower Atmosphere," *Journal of Geophysical Research*, Vol. 73, No. 10, May 15, 1968, pp. 3113-3120.
- Chahine, Moustafa T., "Inverse Problems in Radiative Transfer: Determination of Atmospheric Parameters," *Journal of the Atmospheric Sciences*, Vol. 27, No. 6, Sept. 1970, pp. 960-967.
- Deutsch, R., *Estimation Theory*, Prentice-Hall Publishing Co., Inc., Englewood Cliffs, N.J., 1965, 269 pp. (see p. 59).
- Foster, Manus, "An application of the Wiener-Kolmogoroff Smoothing Theory to Matrix Inversion," *Journal of the Society for Industrial and Applied Mathematics*, Vol. 9, No. 3, Philadelphia, Pa., Sept. 1961, pp. 387-392.
- Graybill, Franklin A., *An Introduction to Linear Statistical Models*, Vol. I, McGraw-Hill Series in Probability and Statistics, McGraw-Hill Book Co., Inc., New York, N.Y., 1961, 463 pp. (see pp. 62-63).
- Meeks, M. L. and Lilley, A. E., "The Microwave Spectrum of Oxygen in the Earth's Atmosphere," *Journal of Geophysical Research*, Vol. 68, No. 6, Mar. 15, 1963, pp. 1683-1703.
- Mount, W. D., Anway, A. C., Wick, C. V., and Maloy, C. M., "Capabilities of Millimeter Wave Radiometers for Remotely Measuring Temperature Profiles Pertinent to Air Pollution," *Final Report*, Contract No. PH 86-67-76, Sperry Rand Research Center, Sudbury, Mass., Feb. 1968, 53 pp.
- Rodgers, C. D., "Satellite Infrared Radiometer—A Discussion of Inversion Results," *Memorandum No. 66.13*, Clarendon Laboratory, Oxford University, England, Sept. 1966, 31 pp.
- Smith, W. L., Woolf, H. M., and Jacob, W. J., "A Regression Method for Obtaining Real-Time Temperature and Geopotential Height Profiles From Satellite Spectrometer Measurements and Its Application to Nimbus 3 'SIRS' Observations," *Monthly Weather Review*, Vol. 98, No. 8, Aug. 1970, pp. 582-603.
- Staelin, D. H., "Passive Remote Sensing at Microwave Wavelengths," *Proceedings of the IEEE*, Vol. 57, No. 4, Apr. 1969, pp. 427-439.
- Strand, Otto Neall, and Westwater, Ed R., "Minimum RMS Estimation of the Numerical Solution of a Fredholm Integral Equation of the First Kind," *SIAM Journal of Numerical Analysis*, Vol. 5, No. 2, Society for Industrial and Applied Mathematics, Philadelphia, Pa., June 1968, pp. 287-295.
- Swirling, P., "Topics in Generalized Least Squares Signal Estimation," *Journal of the Society for Industrial and Applied Mathematics*, Vol. 14, No. 5, Philadelphia, Pa., Sept. 1966, pp. 998-1031.
- Van Vleck, J. H., and Weisskopf, V. F., "On the Shape of Collision Broadened Lines," *Reviews of Modern Physics*, Vol. 17, No. 2-3, American Institute of Physics, Inc. New York, N.Y., Apr.-July 1945, p. 227.
- Wark, D. Q., "SIRS: An Experiment to Measure the Free Air Temperature From a Satellite," *Applied Optics*, Vol. 9, No. 8, Aug. 1970, pp. 1761-1766.
- Westwater, Ed R., "An Analysis of the Correction of Range Errors Due to Atmospheric Refraction by Microwave Radiometric Techniques," *ESSA Technical Report IER 30-ITSA 30*, Institute for Telecommunication Sciences and Aeronomy, Boulder, Colo., Mar. 1967, 69 pp.
- Westwater, Ed R., "Ground-Based Determination of Temperature Profiles by Microwaves," Ph. D. thesis, University of Colorado, Boulder, Sept. 1970, 121 pp.
- Westwater, Ed R., and Strand, Otto Neall, "Statistical Information Content of Radiation Measurements Used in Indirect Sensing," *Journal of the Atmospheric Sciences*, Vol. 25, No. 5, Sept. 1968, pp. 750-758.
- Wiener, N., *Extrapolation, Interpolation, and Smoothing of Stationary Time Series*, John Wiley & Sons, Inc., New York, N.Y., 1949, 163 pp. (see chapter II).

[Received April 5, 1971; revised July 6, 1971]

MICROWAVE EMISSION FROM CLOUDS

Ed R. Westwater

Calculations of microwave thermal emission to space from Rayleigh attenuating clouds are given. The emission and attenuation from ice, water, and two-component ice-water spheres are calculated for tropical, arctic, and standard atmospheres with stratiform clouds and thunderstorm liquid water distributions. The effect of clouds on temperature weighting functions is considered. Cumulative distributions of measured attenuation at 15.25, 31.65, and 52.50 GHz are presented. The Rayleigh attenuation from two-component spheres is discussed in detail.

THE SIZE SPECTRUM DETERMINATION OF SPHERICAL AEROSOLS BY LIGHT SCATTERING
PART I: METHOD

Ariel Cohen
Wave Propagation Laboratory
Environmental Research Laboratories
National Oceanic and Atmospheric Administration
Boulder, Colorado 80302

INTRODUCTION

The scattering functions for spherical particles with size parameters $\alpha = 2\pi r/\lambda |S|$ are given by the Mie theory.^(1,2) The theory shows that unless the scattering medium is composed of mono-dispersed particles, the fluctuation of the scattering intensities with the variation of either the incident wavelength or with the radius of the particles cannot be easily predicted.⁽³⁾ The usual method to overcome this difficulty is to assume an experimentally-based size spectrum function (such as the Junge distribution) with, normally, two parameters.⁽⁴⁾ These parameters are then calculated from the behavior of the scattering or the extinction of light as a function of wavelength by the examined particles.⁽⁵⁾ Polarization properties of the scattered light as compared with the degree of polarization of the incident light can also be used for the size spectrum definition but their use requires certain assumptions, among others - the number densities - and usually does not have a unique solution.⁽⁶⁾

In this article a method will be described for the determination of the size spectrum of spherical particles with a distribution of indices of refraction, which are present in an atmospheric volume containing aerosol particles (possibly both spherical and unspherical) of unknown nature *a priori* based on the properties of the scattering intensity as a function of α . The method does not require any assumption on the size spectrum function, nor does it demand any knowledge of the type (refractive index) of the scattering spheres.

Method

The scattering intensity of unpolarized light by a spherical particle having a size parameter $\alpha = 2\pi r/\lambda$ and a known index of refraction $n = f(\lambda)$ can be calculated by the use of Mie scattering functions.⁽²⁾ For this calculation, the polarized component (I_{11}) of the scattered light at $\theta = 90^\circ$ by a water droplet normal to the scattering plane, was chosen as an example (see Figure 1). In Table I a series of α_i values is given for which $I_{11,i}$ have maximal values. A corresponding series of α_i values for which $I_{11,i}$ have minimal values can also be given (13 pairs of minimal and maximal values are given in Table II).

Let us now assume that the relative number densities ($\rho_1^{(n)}$; $\rho_2^{(n)}$) of spherical particles having radii r_1 ; r_2 and refractive index n (out of many other particles) may be defined by measuring the dependence of $I_{11}(\theta = 90^\circ)$ on λ (wavelength). The method suggested here is as follows: each $\alpha_i^{(n)}$ determines two values $\lambda_i^{(n)}(r_1)$; $\lambda_i^{(n)}(r_2)$, for the above mentioned spheres:

$$\lambda_i^{(n)}(r_1) = 2\pi r_1 / \alpha_i^{(n)}; \lambda_i^{(n)}(r_2) = 2\pi r_2 / \alpha_i^{(n)}$$

We now measure the scattering intensities of the sample as a continuous function of wavelength, and, thus for each of the above calculated $\lambda_i^{(n)}$, the measured intensity $I_{11}^{(n)}(\lambda_i^{(n)}[r])$ is found. (In this work, the measured intensities are divided by λ_i^2 , see Example.)

If we define:

$$A_n(r) = \sum_{i=1}^N I_n^{(n)}(\lambda_i^{(n)}(r)) - \sum_{i=1}^N I_n^{(n)}(\lambda_i'^{(n)}(r)) \quad (1)$$

$$A_n(r_1) = \sum I_n^{(n)}(\lambda_i^{(n)}(r_1)) - \sum I_n^{(n)}(\lambda_i'^{(n)}(r_1)) \quad (1a)$$

$$A_n(r_2) = \sum I_n^{(n)}(\lambda_i^{(n)}(r_2)) - \sum I_n^{(n)}(\lambda_i'^{(n)}(r_2)) \quad (1b)$$

(where N is the chosen number of the $\alpha_i^{(n)}$ and $\alpha_i'^{(n)}$ values* for which the theoretical $I_{11}(\alpha)$ have maximum [and minimum] values), then $A_n(r_1)/A_n(r_2) = \rho_1^{(n)}/\rho_2^{(n)}$ with an increased accuracy with the increasing of N . The function $A_n(r)$ is therefore, proportional to the size spectrum of the particles with refractive index n , acting as a filter with 100 percent transmission for one particle and almost zero percent transmission for any other particle.

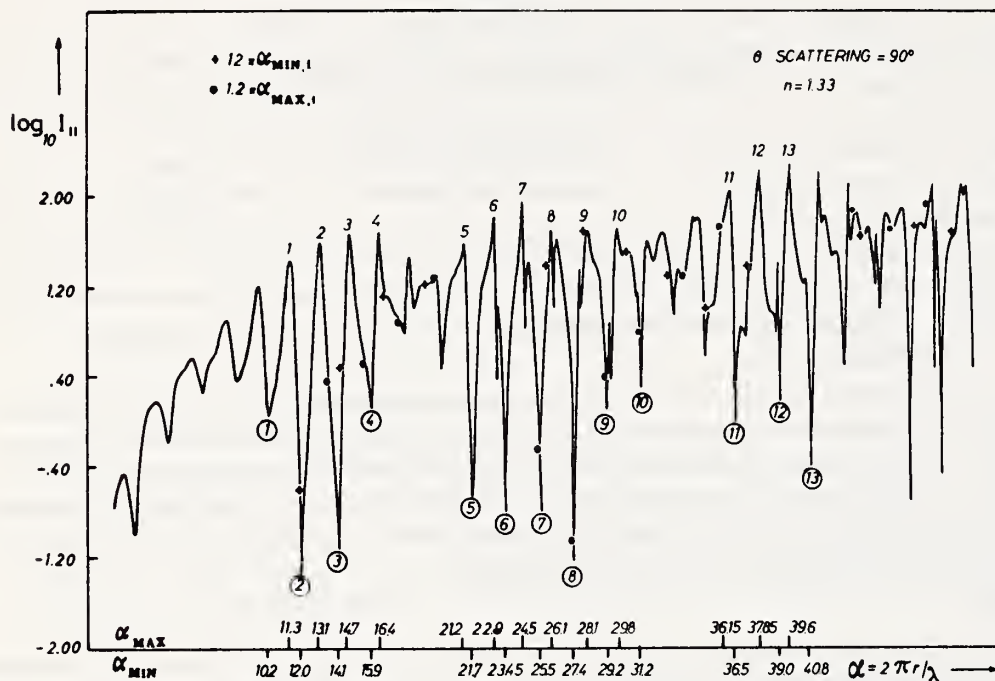


Fig. 1. Computer plotting of $\log_{10} I_{11}$ (I_{11} = the polarized light, normal to the scattering plane), as a function of α . The α for 13 of the maximum values of I_{11} are noted on the abscissa. Dots and plus signs on the graph correspond to the above α values multiplied by 1.2. It can be seen that their ordinate values are "random" with respect to the maxima and minima of the curve.

To prove this assertion, one has to check the contribution of any other particle in the two summations appearing in the definition of $A_n(r)$ (Equation 1) and to show that it can be approached to zero. For example, the contribution of the particles having radius r_2 in Equation 1a, depends on the $\alpha_i^{(n)}(r_2)$ values corresponding to the $\lambda_i^{(n)}(r_1)$ and $\lambda_i'^{(n)}(r_1)$:

*Within a range defined by the measuring system, i.e. if the measurements can be made only in the visible range, the α_i values are limited: $2\pi r_j/0.7 \leq \alpha_i \leq 2\pi r_j/0.4$ (r_j is the radius of the sphere, the number density of which is to be defined).

$$a_1^{(n)}(r_2) = 2\pi r_2 / \lambda_1^{(n)}(r_1) = (r_2/r_1) \times a_{\text{MAX},1}^{(n)} \quad (2a)$$

$$a_1^{(n)}(r_2) = (r_2/r_1) \times a_{\text{MIN},1}^{(n)} \quad (2b)$$

It can be seen from Table I, that the ratio $a_{i,\text{MAX}}^{(n)} / a_{i+1,\text{MAX}}^{(n)}$ is not constant. Nor is the ratio of $a_{i,\text{MAX}}^{(n)} / a_{i+j,\text{MAX}}^{(n)}$, for any 'j'.

It follows that the particles with radii r_2 contribute to the first summation of Equation 1a, practically random values in respect to the appearance of maxima and minima in Figure 1. Since the same effect of "randomization" appears in the second summation in Equation 1a, the summations** for the r_2 particles can be approached to the same value

$$\begin{aligned} A_n(r_1) &= \underbrace{\sum_i I_{n,r_1}^{(n)}(\lambda_i(r_1)) - \sum_i I_{n,r_1}^{(n)}(\lambda'_i(r_1))}_{\text{Contribution of particle having radius } r_1} + \underbrace{\sum_i I_{n,r_2}^{(n)}(\lambda_i(r_1)) - \sum_i I_{n,r_2}^{(n)}(\lambda'_i(r_1))}_{\text{Contribution of particle having radius } r_2} \\ &\approx \sum_i I_{n,r_1}^{(n)}(\lambda_i(r_1)) - \sum_i I_{n,r_1}^{(n)}(\lambda'_i(r_1)) \approx \sum_{\text{MAX},r_1} - \sum_{\text{MIN},r_1} \end{aligned} \quad (3)$$

(see example, Section III). In the case that N (- the number of maxima and minima values), derived from Figure 1, is not sufficient in order to achieve a desired accuracy, this number can be approximately doubled by repeating the experiment at a different scattering angle or at a different polarization angle; or even by extinction measurements.

Now:

$$\begin{aligned} \sum_{\text{MAX},r_1} - \sum_{\text{MIN},r_1} &= \\ V \times \rho_1 \times (\sum_{\text{MAX},r_1} - \sum_{\text{MIN},r_1})_{\text{per one particle}} \end{aligned} \quad (4)$$

where V is the scattering volume.

Also, we surely have:

$$\begin{aligned} (\sum_{\text{MAX},r_1} - \sum_{\text{MIN},r_1})_{\text{per one particle}} &= F \times \sum_i (I_{n,1}(\alpha_{\text{MAX},1}) - I_{n,1}(\alpha_{\text{MIN},1})) \\ \frac{1}{N} F \times \sum &= F \times \text{Constant} \end{aligned} \quad (5)$$

where $I_{n,1}(\alpha)$ is the theoretical (relative) Mie scattering intensity and F is a factor of the specific experimental system for rationalizing the units of intensity.

By elimination between (4) and (5), and substitution into (3), we get:

$$A_n(r_1) = V \times \rho_1 \times F \times \sum \rightarrow \rho_1 = A_n(r_1) / (V \times F \times \sum) \quad (6)$$

or dropping the index 1, we get

$$\rho_r = A_n(r) / (V \times F \times \sum) \quad (6a)$$

If the incident light intensity I_0 , is a function of the wavelength so that $I_0 = \int_0^\infty f(\lambda) d\lambda$ one would have to weigh the $I_{n,1}^{(n)}(\lambda)$ values (appearing in Equation 1) by the factors $f(\lambda)$

Example

To illustrate the method, let us assume that we have a sample of molecular air containing spherical water particles of only two sizes $r_1 = 2.0 \mu\text{m}$ and $r_2 = 2.4 \mu\text{m}$. In Table III, the

**Each recorded scattering intensity at a specific wavelength ($I_{n,1}(\lambda_1)$) is the summation of the scattering intensities of the individual particles having radii r_1 and r_2 :

$$A_n(r_k) = \sum_i \sum_j (I_{r_j}(\lambda_i) - I_{r_j}(\lambda'_i))$$

corresponding λ_i and λ_i' values are listed for the calculation of $A(r_1)$ and $A(r_2)$, respectively. Since $I(\alpha = 2\pi r_1/\lambda_1)/\lambda_1^2 = I(\alpha = 2\pi r_2/\lambda_2)/\lambda_2^2$ when $r_1/\lambda_1 = r_2/\lambda_2$, the experimental values are assumed to be divided by λ^2 (see Figure 2a, b). This is done to permit the use of one set of $I = f(\alpha)$ values for all wavelengths and radii of particles. 13 maxima and 13 minima were chosen for both the calculation of $A(r_1)$ and $A(r_2)$; $A(r)$ was calculated for a single particle. It can be seen from Table II that the contribution of the particle with radius $r_2 (= 2.4 \mu\text{m})$ in the value of $A(r_1 = 2.0 \mu\text{m})$ is less than two percent.

The same calculations for the contribution of the particle with radius $r_1 (= 2.0 \mu\text{m})$ in the value of $A(r_2 = 2.4 \mu\text{m})$ show that it is less than 1.3 percent.

The first contribution was calculated for

$$\alpha_i = \frac{2.4}{2.0} \alpha_{\text{MAX},i} ; \alpha_i' = \frac{2.4}{2.0} \alpha_{\text{MIN},i}' ,$$

and the second for

$$\alpha_i = \frac{2.0}{2.4} \alpha_{\text{MAX},i} ; \alpha_i' = \frac{2.0}{2.4} \alpha_{\text{MIN},i}' .$$

Figure 2a.

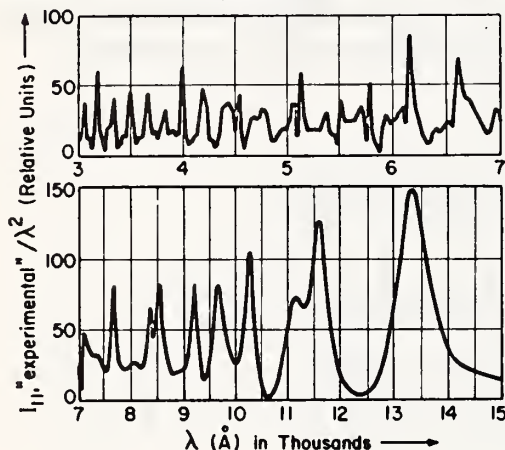
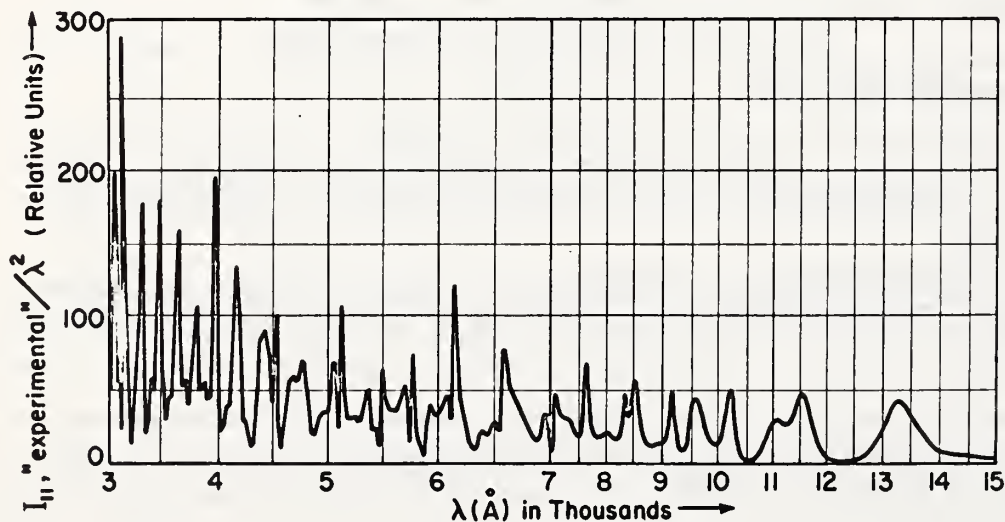


Figure 2. The expected 90° scattering intensities measured as a function of wavelength ($3000 \text{ Å} \leq \lambda \leq 15000 \text{ Å}$) of the component normal to the scattering plane, by a sample including water droplet particles having radii $r_1 = 2.0 \mu\text{m}$ and $r_2 = 2.4 \mu\text{m}$ (2a). In Figure 2b all "measured" values are multiplied by $(7000/\lambda)^2$.

Figure 2b.



| i | $\alpha_{MAX,i}$ | $\log I_{11}$ | 1.2α | $1.2^{-1} \alpha$ | i | $\alpha_{MAX,i}$ | $\log I_{11}$ | 1.2α | $1.2^{-1} \alpha$ |
|----|------------------|---------------|--------------|-------------------|----|------------------|---------------|--------------|-------------------|
| 1 | 2.0 | -.456 | 2.4 | 1.7 | 26 | 32.4 | 1.675 | 38.9 | 27.0 |
| 2 | 3.8 | .177 | 4.6 | 3.2 | 27 | 33.2 | 1.345 | 39.8 | 27.7 |
| 3 | 5.9 | .599 | 7.1 | 4.9 | 28 | 34.1 | 1.818 | 40.9 | 28.4 |
| 4 | 7.8 | .904 | 9.4 | 6.5 | 29 | 34.4 | 1.798 | 41.3 | 28.7 |
| 5 | 9.6 | 1.202 | 11.5 | 8.0 | 30 | 36.2* | 2.047 | 43.4 | 30.2 |
| 6 | 11.3 | 1.428 | 13.6 | 9.4 | 31 | 37.3 | 1.389 | 44.8 | 31.1 |
| 7 | 13.1* | 1.583 | 15.7 | 10.9 | 32 | 37.9* | 2.224 | 45.5 | 31.6 |
| 8 | 14.7* | 1.665 | 17.6 | 12.3 | 33 | 38.9 | 1.396 | 46.7 | 32.4 |
| 9 | 16.4* | 1.673 | 19.7 | 13.7 | 34 | 39.6* | 2.290 | 47.5 | 33.0 |
| 10 | 18.1 | 1.467 | 21.7 | 15.1 | 35 | 40.5 | 1.291 | 48.6 | 33.8 |
| 11 | 18.8 | 1.219 | 22.6 | 15.7 | 36 | 41.2 | 2.209 | 49.4 | 34.3 |
| 12 | 19.6 | 1.296 | 23.5 | 16.3 | 37 | 41.6 | 1.814 | 49.9 | 34.7 |
| 13 | 21.2* | 1.579 | 25.4 | 17.7 | 38 | 42.1 | 1.500 | 50.5 | 35.1 |
| 14 | 22.9* | 1.844 | 27.5 | 19.1 | 39 | 42.9 | 2.114 | 51.5 | 35.8 |
| 15 | 23.1 | 1.026 | 27.7 | 19.3 | 40 | 43.3 | 1.888 | 52.0 | 36.1 |
| 16 | 24.5* | 1.964 | 29.4 | 20.4 | 41 | 44.0 | 1.708 | 52.8 | 36.7 |
| 17 | 24.8 | 1.418 | 29.8 | 20.7 | 42 | 44.5 | 1.662 | 53.4 | 37.1 |
| 18 | 26.1* | 1.794 | 31.3 | 21.8 | 43 | 45.1 | 1.851 | 54.1 | 37.6 |
| 19 | 26.4 | 1.631 | 31.7 | 22.0 | 44 | 45.9 | 1.887 | 55.1 | 38.3 |
| 20 | 27.7 | 1.362 | 33.2 | 23.1 | 45 | 46.9 | 1.753 | 56.3 | 39.1 |
| 21 | 28.1* | 1.710 | 33.7 | 23.4 | 46 | 47.7 | 2.115 | 57.2 | 39.8 |
| 22 | 29.8* | 1.702 | 35.8 | 24.8 | 47 | 47.9 | 1.785 | 57.5 | 39.9 |
| 23 | 30.5 | 1.532 | 36.6 | 25.4 | 48 | 49.3 | 2.119 | 59.2 | 41.1 |
| 24 | 31.0 | 1.140 | 37.2 | 25.8 | 49 | 49.6 | 2.087 | 59.5 | 41.3 |
| 25 | 31.5 | 1.601 | 37.8 | 26.3 | | | | | |

Table I. Maxima of scattering function I_{11} , as a function of size parameter α (θ scattering = 90° , $n = 1.33$).

*(see Figure I and Table II)

| | α_{MAX} | $I(\alpha_{MAX})$ | $I(1.2\alpha_{MAX})$ | α_{MIN} | $I(\alpha_{MIN})$ | $I(1.2\alpha_{MIN})$ |
|----------------|----------------|-------------------|----------------------|----------------|-------------------|----------------------|
| 1 | 11.3 | 26.4 | 2.3 | 10.2 | 1.09 | 0.24 |
| 2 | 13.1 | 38.4 | 3.2 | 12.0 | 0.04 | 3.02 |
| 3 | 14.7 | 46.0 | 7.7 | 14.1 | 0.07 | 12.8 |
| 4 | 16.4 | 47.0 | 18.4 | 15.9 | 1.25 | 16.5 |
| 5 | 21.2 | 37.8 | 0.57 | 21.7 | 0.21 | 23.7 |
| 6 | 22.9 | 70.0 | 0.087 | 23.45 | 0.15 | 47.0 |
| 7 | 24.5 | 94.2 | 2.5 | 25.5 | 0.16 | 31.6 |
| 8 | 26.1 | 58.3 | 6.2 | 27.4 | 0.06 | 19.0 |
| 9 | 28.1 | 52.4 | 19.7 | 29.2 | 1.27 | 9.9 |
| 10 | 29.8 | 50.6 | 52.4 | 31.2 | 1.95 | 23.7 |
| 11 | 36.15 | 114.3 | 70.0 | 36.5 | 1.00 | 43.7 |
| 12 | 37.85 | 172.6 | 52.4 | 39.0 | 1.51 | 54.3 |
| 13 | 39.6 | 199.5 | 80.9 | 40.8 | 0.40 | 47.0 |
| $\Sigma I_1 =$ | | 1007.5 | 316.4 | $\Sigma I_1 =$ | 9.16 | 332.4 |

$$\Sigma I_1(\alpha_{MAX}) - \Sigma I_1(\alpha_{MIN}) = 998.3 \approx \Sigma I_1(\alpha_{MAX}) \equiv A$$

$$\Sigma I_1(1.2 \alpha_{MAX}) - \Sigma I_1(1.2 \alpha_{MIN}) = 16.0 \equiv a \ll A$$

Table II. Demonstration of the validity of the assertion that $A(r_1) \approx \Sigma_{MAX, r_1} - \Sigma_{MIN, r_1}$ (Equation 3) for 2 water droplets of radii $r_2/r_1 = 1.2$ with a randomly chosen set of 13 pairs of α_{MAX} , α_{MIN} . (I_{11} - relative units)

This example indicates that for a sample of water particles with the above mentioned sizes having a size distribution varying within one order of magnitude, 13 maxima and 13 minima are sufficient for determining the size distribution to a high degree of accuracy. When the size distribution covers a variation of more than one order of magnitude, the more maxima and minima values, the better precision is achieved.

$I_{11}(\alpha)$, with $\alpha_{MAX,i}$ and $\alpha_{MIN,i}$, were calculated on the CDC 6400 computer, at the Hebrew University of Jerusalem.

Conclusions

The method described above requires, in principle, only experimental facilities of recording (preferably, by means of a multi-channel recorder) scattering (or extinction) intensities as a function of wavelengths. It can be seen from Table III, that for water droplets with radii varying

| | | | | | | | | | | | | | |
|---------------------------------------------|-------|-------|-------|------|------|------|------|------|------|------|------|------|------|
| (2.0 μm) $\lambda_{MAX,i}$ Å | 11120 | 9590 | 8550 | 7660 | 5930 | 5490 | 5130 | 4820 | 4470 | 4220 | 3470 | 3320 | 3170 |
| (2.4 μm) $\lambda_{MAX,i}$ Å | 13340 | 11510 | 10260 | 9200 | 7110 | 6580 | 6160 | 5780 | 5370 | 5060 | 4160 | 3980 | 3810 |
| (2.0 μm) $\lambda_{MIN,i}$ Å | 12320 | 10470 | 8910 | 7900 | 5790 | 5360 | 4930 | 4590 | 4300 | 4030 | 3440 | 3220 | 3080 |
| (2.4 μm) $\lambda_{MIN,i}$ Å | 14780 | 12570 | 10700 | 9480 | 6950 | 6430 | 5910 | 5500 | 5160 | 4830 | 4130 | 3870 | 3700 |

Table III. Wavelengths used in the determination of the number densities of water droplets of radii 2.0 μm and 2.4 μm .

Note: Since any random size distribution may be divided into sets of two radii each (r_{i1}, r_{i2}) so that $r_{i1}/r_{i2} = 1.2$, the respective λ values appearing above multiplied by the factor ($r_{i1}/2.4$) can be used for the determination of the number densities of any random sample. In case of the available apparatus not covering the required range of λ values, see Conclusions.

between 1.0 μm and 5.0 μm , the α_{MAX} and α_{MIN} values, given as an example in this work (Figure 1, Table II) correspond to wavelengths near and within the visual range. Since the experimental methods of wavelength-scanning are limited, it is suggested that other α_{MAX} and α_{MIN} values be selected (not appearing in Figure 1) rather than change the wavelength range for droplets with radii > 5.0 μm . The only requirement on the selection of these α values is that the Mie scattering intensities corresponding to the $\alpha_{MAX,i}$ or $\alpha_{MIN,i}$ should not vary by more than an order of magnitude (preferably much less).

The required accuracy in the definition of the scattering angle, for this purpose, was calculated to be within ± 0.2 degrees.

It would be well to note that since no theoretical limitations are imposed on the accuracy in calculating the values α_{MAX} and α_{MIN} , it is always possible to calculate these values to an accuracy compatible with the wavelength resolution of the experimental system.

ACKNOWLEDGEMENT

I wish to thank Professor J. Neumann and Professor Y. Gallily of the Department of Meteorology of the Hebrew University, Jerusalem, and Dr. Vernon E. Derr of the Wave Propagation Laboratory, ERL, NOAA, Boulder, Colorado, for their helpful discussions, Mr. M. Graber for assisting with the computer analysis, and Mr. M. Berman for his assistance.

This research was completed while the author held a National Research Council Postdoctoral Research Associateship supported by the National Oceanic and Atmospheric Administration.

References

1. G. Mie, Ann. Phys., 25, 377 (1908).
2. H. C. van de Hulst, Light Scattering by Small Particles (Wiley, New York, 1957).
3. A. Cohen, Tellus XXI, 5 (1969).
4. C. Junge, J. Meteorology 12, 13 (1955).
5. G. Yamamoto and T. Masayuhi, Appl. Opt. 8, 447 (1969).
6. A. Cohen, M. Graber and J. Neumann, The Effect of Double-Scattering by Water Droplet Clouds on the Polarization of Laser Pulses. Presented at the International Conference on Meteorology, IMS-AMS, Nov. 30 - Dec. 4, (1970).

Measurement of Mie Scattering Intensities from Monodispersed Spherical Particles as a Function of Wavelength

A. Cohen, V. E. Derr, G. T. McNice, and R. E. Cupp

Mie scattering intensities as a function of the size parameter are measured by use of a tunable dye laser and monodispersed spherical particles. The experimental results are compared with the Mie single scattering theory; a discrepancy in the exact position of the maxima and minima was detected. Agreement between experiment and theory was improved by applying a correction to the manufacturer's index of refraction function for the particles.

The scattering intensity functions for spherical particles having radii r , greater than the scattering wavelength λ , were developed by G. Mie.¹ Theoretical calculations of Mie scattering (MS) intensity values as a function of wavelength have been carried out by several authors either for monodispersed particles or a distribution of particle sizes.²⁻⁴ Since scattering intensities may vary by more than one order of magnitude with a change of 2-5° in the scattering angle or 3-5 nm in the scattering wavelength, it was not until the development of the laser that high resolution measurements of scattering intensities (with respect to scattering angle or wavelength) could be performed with facility. Angular dependence of the MS functions was then measured,⁵⁻⁷ providing the first experimental verification of the exact Mie theory of scattering from spheres. The MS intensities as a function of the size parameter $\alpha = 2\pi r/\lambda$ for a fixed scattering angle have not been measured by other workers, mainly because of the discrete monochromatic characteristics of the first generation of lasers.

Here we present MS measurements as a function of the wavelength generated by a tunable dye laser. (MS intensity measurements as a function of the particle's radius were carried out previously by one of us,⁸ but they involve the assumption that the equations for particle growth by condensation are well known.)

The MS intensities were measured for a constant

scattering angle and for three samples of monodispersed diluted particles suspended in distilled water. The experimental arrangement is shown in Fig. 1. The laser was a flashlamp pumped dye laser with the following characteristics:

Active medium, calcein blue in water; output energy, 10^{-3} J/pulse; pulse rate, 4 sec⁻¹; wavelength, 438-472 nm; line width, <0.2 nm; pulse width, 0.5 μ sec; beam size, 1 mm; polarization, unpolarized.

The output of the laser was directed through a diverging lens and a beam splitter into a glass cell containing 1.305- μ m, 2.051- μ m, or 2.956- μ m latex spheres in distilled water. The lens improved signal statistics by expanding the beam to include more scatterers. Light scattered from the cell was apertured to define a 0.5° beam and detected by a RCA 1P28A photomultiplier at a scattering angle of 90.0 \pm 0.3°.

The light removed from the main beam by the beam splitter was directed to a second RCA 1P28A photomultiplier to provide a reference signal. The outputs of both photomultipliers were sampled at the peak of the laser pulse, then integrated, and finally directed to an analog divider, where the signal from the sample cell was divided by the reference signal, thus removing most of the effects of variations in laser output power and spectral response of the photomultipliers. The output of the analog divider was recorded on a strip-chart recorder, and the laser wavelength was calibrated against a mercury spectrum in a Bausch and Lomb 1.5-m grating spectrograph.

The experimental results of the MS as a function of wavelength are shown in Fig. 2. The particles were polyvinyl toluene latex (obtained from the Dow

All the authors were with NOAA Environmental Research Laboratories, Boulder, Colorado 80302, when this work was done; A. Cohen has now returned to the Department of Atmospheric Sciences, Hebrew University of Jerusalem, Jerusalem, Israel.

Received 5 June 1972.

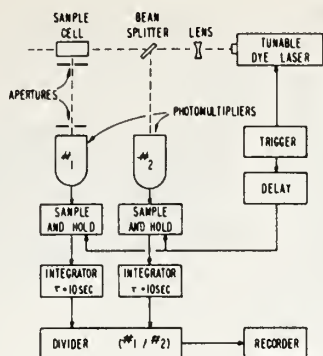


Fig. 1. Schematic diagram of the experimental arrangement.

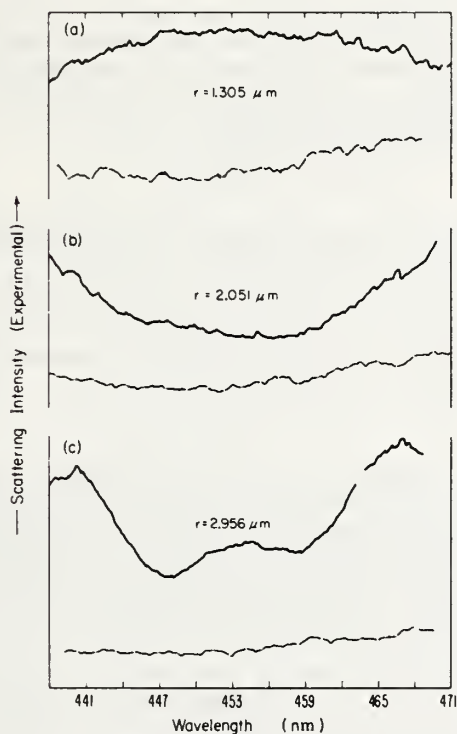


Fig. 2. Measured 90° scattering intensities as a function of wavelength for $438 \text{ nm} \leq \lambda \leq 471 \text{ nm}$. The solid curves are examples of a series of repeating curves for each particle size: (a) $1.305 \mu\text{m}$; (b) $2.051 \mu\text{m}$; (c) $2.956 \mu\text{m}$. The dashed curves are reference curves obtained by replacing the monodispersed spheres with a white, diffuse target.

Chemical Company), the refractive index of which (relative to water) was assumed to be 1.18 for room temperature and the above-mentioned scattering wavelengths. The value of 1.18 was derived from the refractive index relative to air as measured by the manufacturers of the particles.

In Fig. 3(a), the theoretical MS curve is presented as a function of the size parameter α (in incremental steps of $\Delta\alpha = 0.1$) for the scattering angle: $\theta = 90.0^\circ$ and relative index of refraction $n = 1.181 - 0.0i$. Figure 3(b)–(d) are subsections of Fig. 3(a), corresponding to the size-parameter ranges defined by the radii of the particles and the wavelengths of the experiments. The incremental steps used in the calcu-

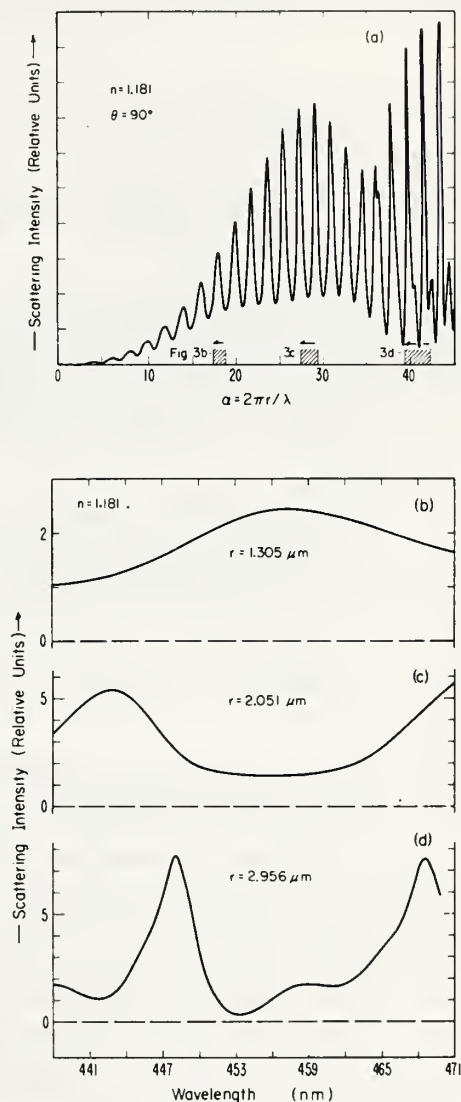


Fig. 3. Theoretical 90° scattering intensities for spherical particles having a refractive index of $n = 1.81 - 0.0i$. (a) $0.0 \leq 2\pi r/\lambda \leq 45.0$. (b) $r = 1.305 \mu\text{m}$ and $438 \text{ nm} \leq \lambda \leq 471 \text{ nm}$ ($17.4 \leq 2\pi r/\lambda \leq 18.7$). (c) $r = 2.051 \mu\text{m}$ and $438 \text{ nm} \leq \lambda \leq 471 \text{ nm}$ ($27.3 \leq 2\pi r/\lambda \leq 29.4$). (d) $r = 2.956 \mu\text{m}$ and $438 \text{ nm} \leq \lambda \leq 471 \text{ nm}$ ($39.4 \leq 2\pi r/\lambda \leq 42.4$).

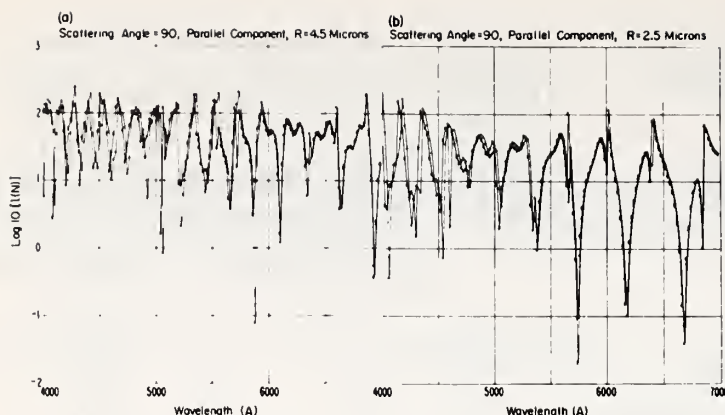


Fig. 4. The log of the scattering intensities of the component normal to the scattering plane as a function of wavelength; the scattering angle $\theta = 90^\circ$, $m = 1.33$; \circ , $m = m(\lambda)$. (a) R (= radius of scattering sphere) = 4.5 μ ; (b) $R = 2.5 \mu$.

lation of the last three curves were $\Delta\lambda = 0.2$ nm, and the scattering values were averaged over 0.6° , centered at a scattering angle of $\theta = 90^\circ$.

Agreement between experimental measurements and theory proves the feasibility of the method to provide an experimental determination of the MS intensities as a function of wavelength. The small shifts in the theoretical positions of the maxima and minima (with respect to wavelength), as compared to the experimental results, are believed to be caused by the use of a constant refractive index for the theoretical calculations.

In order to illustrate the dependence of the MS intensities on small variations of the relative index of refraction we calculated the 90° scattering intensity of the visible light by monodispersed water droplets, once by assuming that the refractive index is constant, i.e., $m = 1.33$, and once by substituting the exact values of m as a function of wavelength (see Fig. 4.).

The main characteristics of the computational results, for a scattering angle $\theta = 90^\circ$, can be summarized as follows:

Let I_1 ($\alpha = 2\pi r_0/\lambda$, $\beta = \alpha m_0$) be the MS intensity value calculated as a function of the wavelength λ , where m_0 is a constant index of refraction, and let I_2 [$\alpha = 2\pi r_0/\lambda$, $\beta = \alpha m(\lambda)$] be the MS intensity value for the exact index of refraction; then in the visible range for each value of I_1 there is a corresponding equal value of I_2 calculated for a slightly different α value. The more the deviation of $m(\lambda)$ from m_0 , the larger the difference in the α values. As a consequence, if a constant index of refraction m_0 is used for the theoretical determination of the MS for monodispersed particles as a function of α , the positions of the maxima and minima values in the calculations will be shifted (in respect to the wavelength) in correspondence with the deviation of m_0 from the exact refractive index of the particles.

In the comparison of Figs. 2(c) and 3(d), it can be seen that one of the calculated maxima for $m \approx 1.18$ appears at $\lambda \approx 448$ nm while the corresponding (in respect to the general shape of the intensity func-

tion) measured maximum was recorded at $\lambda \approx 441$ nm. The second calculated and measured maxima are centered at $\lambda \approx 458$ nm and $\lambda \approx$ nm, respectively. These two deviations can be corrected by associating with the monodispersed particles an index of refraction obeying the equation

$$m(\lambda) = 1.161 + (\lambda - 440) \times 10^{-4}/1.5 \quad (1)$$

where $440 \text{ nm} \leq \lambda \leq 471 \text{ nm}$. The results are shown in Fig. 5.

In order to verify whether the linear approximation suggested by Eq. (1) is the only (within a certain degree of accuracy) solution for the refractive index as a function of wavelength, we examined the following other possible solutions:

$$(a) m(\lambda) = \text{const.} \neq 1.181.$$

In doing so, i.e., in trying to fit another constant value for the refractive index, we shifted the positions of all maxima and minima but almost no change in their mutual separation was achieved. The introduction of an absorption coefficient [$m(\lambda) = 1.181 - 0.1i$] partially smothered out the maxima and minima without shifting from the wavelengths in Fig. 3.

(b) Associate the three maxima of Fig. 2(c) to another similar group of maxima in Fig. 3(a), i.e., suggest much larger deviations of the refractive index for the whole wavelength range in comparison with those defined by Fig. 3.

The extrapolation of Fig. 3 was used to estimate the required index of refraction m ($\lambda = 467$) for shifting the theoretical maximum at $\lambda \approx 448$ nm [Fig. 3(d)] to the measured maximum at $\lambda \approx 467$ nm.

$$m(\lambda = 467) \approx 1.24$$

The same deviation in the index of refraction was then applied to Fig. 3(b)-(c) and on the basis of the disagreement between the corresponding measured

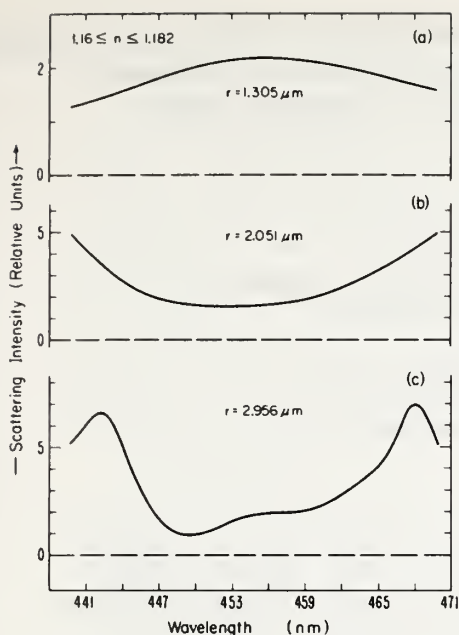


Fig. 5. Theoretical 90° scattering intensities for spherical particles having a refractive index of $n = 1.16 + (\lambda - 440) \times 10^{-4}/1.5$. (a) $r = 1.305 \mu\text{m}$; (b) $r = 2.051 \mu\text{m}$; (c) $r = 2.956 \mu\text{m}$.

curves in Fig. 2(a) and (b) this second possibility was eliminated.

Since only a few data points were used to derive the wavelength dependence of the refractive index [Eq. (1)], only a linear function for $m(\lambda)$ was checked. Due to the good agreement achieved between the three curves of Figs. 2(a)–(c) and 4(a)–(c), no effort was made to find an even better fit than Eq. (1). It would be well to note that the variation of the refractive index of distilled water in the discussed wavelength range does not explain the above-mentioned shifts when a constant refractive index is assumed for the spherical particles.

The main advantages of the experimental determination of the MS intensities as a function of wavelength can be summarized in the following way:

(1) A continuous curve of MS vs α rather than a series of MS values for certain α values can be obtained.

(2) A scattering value for a defined spectral line width is being measured.

(3) Accurate scattering values involving no assumptions on the refractive index of the particles are being recorded.

(4) The refractive index as a function of wavelength can be studied and determined for various types of aerosols, thus permitting a higher accuracy and reliability in the inversion procedure of MS data into the size distribution of a sample of particles.

The results of this experiment, and Blau's results, indicate that for most practical uses the MS theory provides an accurate scattering curve for real spherical particles.

On the other hand, the agreement between the data and the MS theory proves the capabilities of this experimental system for the laboratory measurement of scattering as a function of wavelength of complex nonspherical atmospheric particles for which no theory exists.

The research was accomplished while one of the authors (A.C.) held a National Research Council Postdoctoral Resident Research Associateship supported by the National Oceanic and Atmospheric Administration.

References

1. G. Mie, *Ann. Physik* 25, 377 (1908).
2. H. C. van der Hulst, *Light Scattering by Small Particles* (Wiley, New York, 1957).
3. A. Penndorf, *J. Opt. Soc. Am.* 52, 4 (1962).
4. D. Diermendjian, *Electromagnetic Scattering of Spherical Polydispersions* (American Elsevier, New York, 1969).
5. G. C. Sherman, F. S. Harris, Jr., and F. L. Morse, Jr., *Appl. Opt.* 7, 421 (1968).
6. H. H. Blau, Jr., D. J. McCleese, and D. Watson, *Appl. Opt.* 9, 2522 (1970).
7. A. I. Carswell, *Appl. Opt.* 11, 1611 (1972).
8. A. Cohen, *Tellus* 21, 736 (1969).

Reprinted from the Proceedings of Workshops on Research Problems
in Air and Water Pollution, University of Colorado,
August 3-15, 1970, 309-321, February 1972

RESEARCH PROBLEMS IN THE USE OF LIDAR IN
ANTI-POLLUTION STUDIES

V. E. Derr
ESSA Research Laboratories
Boulder, Colorado

Introduction

The purpose of this workshop is to present discussions of the research problems remaining in the understanding, measurement and control of air and water pollution. These research problems can then be studied where appropriate knowledge and facilities exist.

One of the earliest uses of lidar was in the determination of the presence of aerosols, but it also has direct application to the specific task of remote detection and measurement of gaseous pollutants when Raman scattering and fluorescence are employed. These radiative interactions produce an output at a frequency that differs from the irradiating frequency. The frequency of the scattered radiation is usually uniquely related to the scattering molecule, allowing identification. Thus lidar can be used in the remote measurement of water profiles by Raman scattering, and also in the remote measurement of wind profiles by the use of Mie scattering. Wind and water vapor profiles are important in the prediction of weather conditions leading to pollution trapping or dissemination conditions. The use of lidar in the measurement of aerosols, smoke stack constituents, humidity profiles, and wind velocities will be discussed, and the limitations of present systems that are potentially removable through research will be pointed out. More detailed consideration of the use of lasers may be found in references 1, 2, and 3, with extensive literature references in reference 1.

Use of lidar in aerosol determination and wind sensing

Atmospheric aerosols scatter laser radiation so strongly that the location of aerosol layers is only prevented when the attenuation due to atmospheric loading is very high. Indeed aerosols have been detected above 90 km by lidar. However important limitations occur in the interpretation of lidar signals from aerosols since the information received is usually not sufficient to allow the determination of an unknown distribution of sizes and shapes by solution of the radar equation. Since the product of the backscattering coefficient and the attenuation factor occur in the system equation (Reference 1) they cannot be separately determined by examining the Mie scattering alone, at a single frequency.

Two additional pieces of information aid in distinguishing between molecular and aerosol scattering, the specifically molecular information inherent in Raman scattering, and the Doppler spectrum of the on-frequency backscattering. The latter method depends on the difference in the Doppler spectrum of air molecules and the much heavier and, on the average, slower, aerosol particles. With this information, the knowledge of the presence and opacity of atmospheric aerosol layers can be supplemented by further details of the nature of the aerosols, reducing the requirements on the specifications of the atmosphere model, although it appears that some limitations on the possible aerosol constitution will always have to be assumed. In practice, this is probably not a serious limitation since aerosols are very frequently of known origin, and their distributions are often known by prior observation within broad limits.

In the real atmosphere, passive additives that are carried along by the prevailing wind are inhomogeneous. To the extent that the structure of the turbulent eddies persists as they travel with the wind, they can be observed at two points separated by a known distance. Even in strong mixing conditions, the eddy structure remains recognizable over useful distances. Thus, by a pattern recognition process, such as cross correlation, we can compare the signals at two points in the wind stream, determining velocity from the passage time of eddies (Reference 1)

Active and passive correlation methods have been effective in wind tunnels. Passive methods have been used in the field, but their signal-to-noise ratio is unfavorable (Reference 3). Active wind sensing methods using lasers to illuminate the atmosphere have been used by V.E. Derr and R.G. Strauch at ESSA Research Laboratories. Fig. 1 shows a simple scheme used to test the method. (It is too cumbersome to use in practice, since the wind direction changes frequently.) A coaxial transmitter and receiver (or closely coupled parallel axes) may be used as in Fig. 2. The beam is conically scanned at so rapid a rate that no turbulence crosses the cone unilluminated, and with sufficiently high pulse repetition frequency that the turbulent spectra is sampled. The cone may be divided into elements and cross correlation between elements may be used to detect the drift of turbulence across the cone, while the height is determined by ranging. The data rate is high and would require special purpose data processing equipment, especially if off-frequency backscattering is also examined by a scanning monochromator. (The later device would allow the simultaneous determination of water vapor profiles by Raman backscattering as described below.)

Fig. 1 shows a typical output of two laser illuminated cells of the atmosphere examined by two telescopes. The output of receiver B is delayed by an average of one second with respect to receiver A. Parts of the record require a cross correlation analysis to determine wind speed, but large fluctuations which allow determination of wind velocity from visual examination of the record occur with great frequency when the wind is steady. The record above was taken under light, variable wind conditions, from 0 to 10 mph in the configuration shown in Fig. 1.

Research areas in aerosol and wind determination

The determination of the presence of aerosols is easily done by present lidar systems to great altitudes. The major problems remaining are the determination of size and shape distributions and the determination of composition by remote means. Better statistics of atmospheric aerosol composition are required in order to set limitations on possible distributions in nature. The size and shape distribution can be partially determined by the scattered

curves. The graph has been computed for one pulse; the lidar is capable of 100 pulses per second. Integration times of several hundred seconds are not unreasonable in applications. The transmitter characteristics shown are those of a commercially available pulsed nitrogen laser; the receiver has very modest dimensions, and could be improved. The cross sections listed are estimated for the graph and should not be construed as accurate to closer than an order of magnitude.

Water vapor in the atmosphere has been detected and a humidity profile determined to several thousand meters with ruby laser systems by a few minutes integration, and this could also be done with the system described above. With such a system only short ranges may be achieved in daylight because of the sky background. Of course the receiver may be improved by a larger collector; this helps only a little since when background limited, the increase in signal is partially offset. The increase in SNR would be a factor of the square root of the collector area increase, or by the increase in linear dimensions. A significant increase in SNR could be obtained by operating in the spectral region below 2900 Å, where the strong solar absorption by stratospheric ozone lowers the background noise to a level below that of the best detectors. At short range, pollutants such as SO₂ have been detected by Raman lidar, as well as impurities in water.

Research areas in Raman and fluorescent lidar

The use of backscattered off-frequency radiation has important potential uses in remote identification of atmospheric, oceanic and terrestrial constituents, in the study of atmospheric statistics, in cloud height and wind velocity measurement and in precise measurement of the ratios of atmospheric constituents². Some of these, such as the measurement of humidity profiles, have essentially been proven. The extension of the method to other problems depends very strongly on the results in achieved in research areas relating to the components, and the basic spectroscopic properties of the atmosphere.

For tropospheric use, transmitters in the ultraviolet below 2900 Å would be preferable because the intensity of Raman scattering is generally proportional to the fourth

signal amplitude recorded as a function of frequency; thus the development of lasers tunable over wide frequency ranges is important. The most likely approaches appear to be in dye lasers and in parametric devices.

Thus far, insufficient attention has been given to the depolarization effects of Mie particles and both theoretical and experimental investigations are needed here. The composition can be obtained only by off-frequency backscattering and probably only by either Raman scattering or fluorescence. The field of shifted frequency scattering from aerosols has not received very much attention and may be very fruitful. It has been noted by researchers that an ultraviolet laser does produce strong fluorescence in some dust particles and not in others; also some insects are observed to fluoresce strongly.

Further, the use of Doppler lidar methods for wind measurement should be explored. These have been used at short ranges. They require the development of highly stable, high power lasers, but may be eventually the best method of wind velocity measurement. The Doppler method is limited to the measurement of radial components while correlation methods measure transverse components.

Raman and fluorescent scattering in laser ranging

In addition to the radiation scattered by atmospheric constituents at the frequency of the lidar transmitter, frequency-displaced signals are also received, either from Raman scattering or fluorescence. As mentioned above, the spectral frequency of the Raman or fluorescence signal is specific to the molecules interacting with the lidar radiation and is a means of identification, unlike Rayleigh or Mie scattering. Specific cases of Raman scattering by atmospheric constituents are summarized in Fig. 3. The number of signal photons received is shown as a function of range. Sky background noise appears on the same ordinate scale. The rms values of the sky noise are the most significant, in the absence of saturation, since the average level can be suppressed. The right side shows the detector dark noise from some selected photomultipliers. The graph can be used to determine the SNR of any gas with the same backscattering cross section as N_2 by reference to the ppm

power of the frequency of the irradiating source, and solar background noise is largely eliminated by the strong absorption by ozone in the upper atmosphere. The wavelength chosen must be short of the oxygen absorption beginning at 1800 Å. The development of suitable lasers in the 2000 Å to 2900 Å range would have important consequences in pollution measurement.

At this time field-worthy laser transmitters below 2900 Å are unavailable. The closest to realization is the quadrupled neodymium laser near 2650 Å, but the efficiency is low and the adjustment is tedious. Ideally, a tunable pulsed laser below 2900 Å with 10^6 W peak power, 10 ns pulse width, and 1000 pulses per second, could perform most of the tasks outlined above; no such equipment is in the field at present. Probably pulsed gas lasers offer the most likely future possibility. An additional important factor in a laser transmitter is the brightness of beam divergence. Indeed the greatest single source of loss in lidar systems is usually found in the mismatch of transmitter and receiver apertures. Greater brightness is always an advantage; a beam with no greater divergence than 2 mr is a good design goal. Finally, the laser output should be free of fluorescence or any radiation other than the laser output.

The optics of the receiver must be treated for high reflectivity (mirrors) or transmission (lenses) in the ultraviolet. The techniques of interference filters could be applied here. There is an additional problem observed by workers in the field, - almost everything fluoresces under short ultraviolet radiation. Lenses, filters, windows, the dust of the atmosphere, black paint and water droplets all fluoresce. At present very pure quartz is one of the few materials which can be used. The problem can be alleviated by a judicious placement of the components of the optical train, but new non-fluorescing materials of optical quality would be very welcome. It has been observed that some plastics fluoresce much less than other materials and purification of them might be profitable.

The use of wavelengths below 2900 Å requires a careful measurement of the attenuation coefficient of the atmosphere in the wavelength range 2000-3000 Å and a distance up to 10 km. Further, more exact measurements of solar

absorption in this part of the spectrum are necessary in order to determine system range capability.

Until recently, the manufacturers of photomultipliers have paid very little attention to the needs of lidar systems; the principal developments in phototubes have accommodated the nuclear scintillation counting art. Phototubes of higher quantum efficiency, solar blind, with high gain and rise times of a few nanoseconds are needed. The cathode should be solid, for high efficiency, the envelope should be of ultraviolet transmitting material, and the gain should be at least 10^8 . The tube should be end-on so that a low silhouette can be obtained in use at the Coudé focus. The tube base should be left off so resistors and a small transistorized preamplifier can be soldered directly to the leads. The effective sensitive area should not be less than an inch in diameter to prevent vignetting the field. The dark count, uncooled, should not be more than 100 per second.

Although improvements in system components can be expected to increase the effectiveness of lidar in pollution measurement, it will probably be limited to lower atmospheric uses for constituents with the presently known cross sections. Even the use of the highest lidar frequency available will not substantially change this estimate. It is necessary to examine to what extent we may hope for larger cross sections. Aside from the fourth power frequency dependence of cross sections, there is a dependence on resonance denominators.

The intensity of Raman lines, when the molecule makes a transition from state m to state n , is given by

$$I = \frac{2^7 \pi^6}{3^2 c^4} I_0 (\nu_0 - |\nu_{mn}|)^4 \sum_{\rho \sigma} |\alpha_{\rho \sigma, mn}|^2,$$

where $\alpha_{\rho \sigma, mn}$ is the $\rho \sigma (=X, Y, Z)$ component of the scattering dyadic

$$\alpha_{mn} = \frac{1}{h} \sum_r \frac{\vec{\mu}_{rn} \vec{\mu}_{mr}}{\nu_{rm} - \nu_0 + i\gamma_r} + \frac{\vec{\mu}_{mr} \vec{\mu}_{rn}}{\nu_{rn} + \nu_0 + i\gamma_r}.$$

Here c is the velocity of light, h is Planck's constant, I_0 is the incident plane-polarized intensity of frequency ν_0 , r is an intermediate state, and $\vec{\mu}_{rn}$ and $\vec{\mu}_{mr}$ are the transition moments of the dipole moment operator μ , and γ_r is the damping constant of state r . When the denominators of α are not small, it can be seen that the intensity varies as the fourth power of the output frequency, making higher frequency lasers advantageous.

When the incident radiation is at a frequency close to any of the transition frequencies, ν_{rm} , the scattered intensity can be greatly increased. Although few experiments have been performed on gases, other than alkali metal vapors, experiments on liquids have indicated several orders of magnitude increase in intensity for resonance Raman scattering. If such increases could be obtained in gases or aerosols the range-sensitivity product of lidars could be greatly increased and their utility in pollutant measurement and atmospheric studies magnified. The problem of the nature of the transition in resonance effects must be examined to determine whether the process remains essentially one of scattering or becomes more like a fluorescence. In the latter case, at atmospheric pressure, the effect would be at least partially quenched by collisions and the intensity increase could only be found high in the atmosphere.

Conclusions

Lidar is presently a useful device at short ranges for pollutant measurement, humidity profile determination and wind sensing. The optimization that can be achieved by research on the problems listed above will probably extend its useful range to the whole troposphere, and to greater distances if resonance effects can be found.

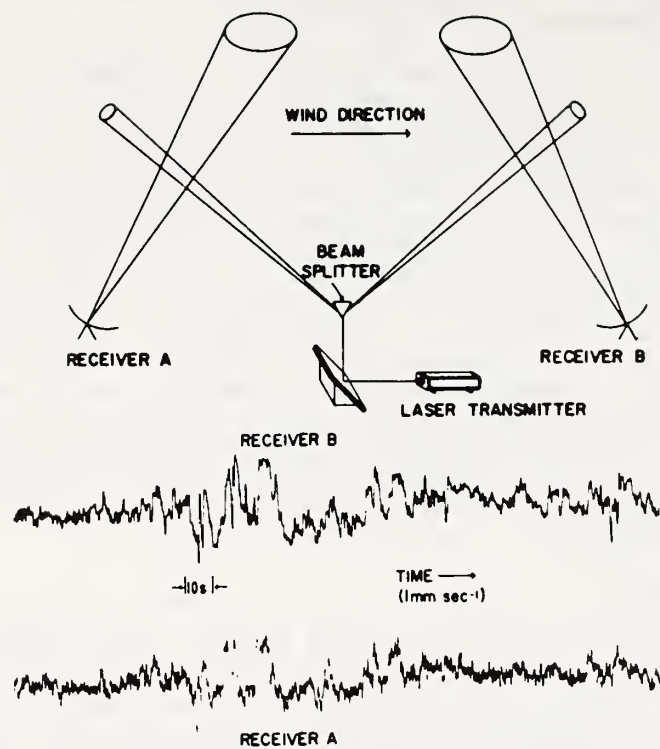


Figure 1

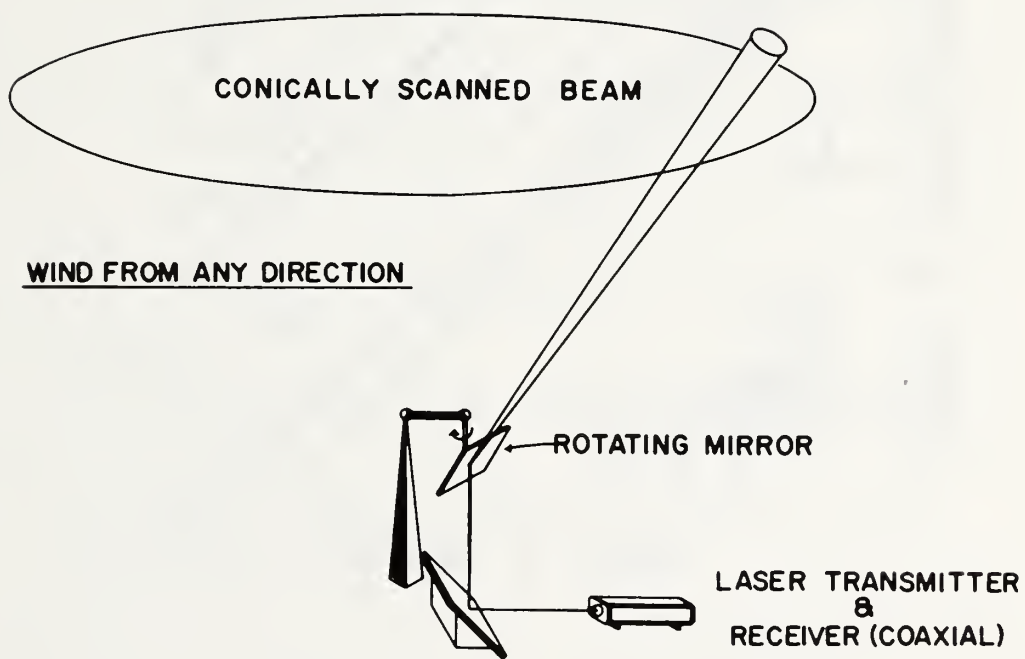


Figure 2

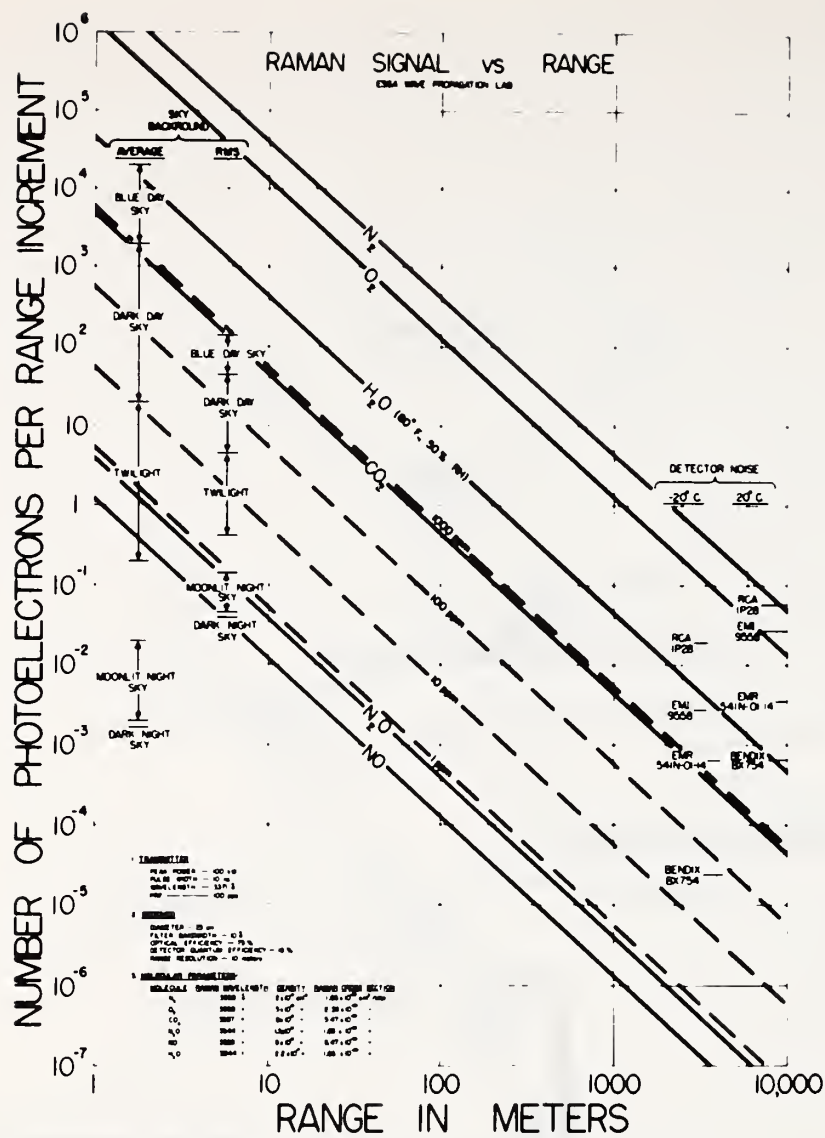


Figure 3

REFERENCES

1. Derr, V.E. and C.G. Little, "A comparison of remote sensing of the clear atmosphere by optical, radio and acoustic radar techniques," Appl. Opt. 9, 1976, (Sept. 1970).
2. Schwiesow, R.L. and V.E. Derr, "A Raman scattering method for precise measurement of atmospheric oxygen balance," J. Geophys. Res., 75, No. 9, 1629, (March 20, 1970).
3. Krause, F.R., V.E. Derr, et al., "Remote probing of wind and turbulence through cross-correlation of passive signals," Proc. of the Sixth International Symposium on Remote Sensing of the Environment, Vol II, 327, (Oct. 1969).

320

Derr

LEGEND

FIGURES

1. Wind velocity measurement configuration and typical signals
2. Conical scan configuration for wind sensing
3. Raman signal vs. range

Two-Laser Optical Distance-Measuring Instrument that Corrects for the Atmospheric Index of Refraction

K. B. Earnshaw and E. Norman Hernandez

The Wave Propagation Laboratory of the Environmental Research Laboratories of the National Oceanic and Atmospheric Administration has been engaged in the development of dual-wavelength, optical distance-measuring instruments. Recently a new generation of this type of high-accuracy instrument has been completed. Preliminary testing of the new instrument indicates that the original goal of the project, accuracy of better than one part in a million over distances of 5-10 km using averaging times of less than 1 min, is being met. This paper describes the instrument and preliminary test results.

Introduction

There are many papers¹⁻⁴ describing electromagnetic techniques for making precise geodetic distance measurements. Reference 2 gives a list of the most pertinent references. Two promising techniques of distance measuring involve measuring the transit time of either microwave or optical waves over a path.⁴ In either case, the significant limitation to the accuracy of measurement is the estimation of the velocity of the electromagnetic wave over the path. Because the speed of light is about 33 μsec for 10 km, purely pulse techniques require unreasonably accurate time measurements; the transit time must be accurate to psec to measure the distance to 1 part in a million. A more promising technique involves measuring the phase shift of the electromagnetic wave due to the atmospheric path. An immediate compromise is realized; for a fixed phase resolution the higher the frequency, the higher the inherent accuracy. It appears, at present, that the optimum frequencies for precise distance measuring (of the order of 1 part per million or better) are in the microwave range.⁴ Direct use of microwaves proves to have several drawbacks. A more reasonable approach utilizes microwave-modulated light beams. The advantages of such systems are well documented.⁷

The use of a microwave-modulated optical system requires an accurate estimation of the average group index of refraction over the propagation path. Several techniques are presently being used: (a) several meteorological sensors are placed along the path; (b)

an airplane equipped with sensors is flown over the path; and (c) long time averages are used to average out the meteorological fluctuations. None of these techniques is very satisfactory, and there are some situations in which none is possible, for example, using technique (b) at night in mountainous terrain.

Since the group index of refraction, n , is a function of wavelength, the use of two different optical light sources makes it possible to correct an optical pathlength measurement for n .^{8,9} The atmosphere increases the transit time for optical beams by about 300 parts in a million at sea level. The difference in transit time for 6328 Å and 4416 Å is about 15 parts in a million. By measuring each optical pathlength to 5 parts in 100 million the true length can be corrected to 1 part in a million.

It has been shown that the most serious noninstrumental source of error is due to incorrectly estimating the relative humidity over the path.¹⁰ This error is small for most conditions, an error of 50% relative humidity at 15°C being required to produce an error of 1 part in a million.

This paper presents a two-laser, microwave-modulated, distance-measuring instrument that corrects for the index of refraction (see Fig. 1). By measuring the optical pathlength for blue and red the instrument cancels the first-order effects of temperature fluctuation along the propagation path on the index of refraction. This instrument has been built and is being tested over a 5.9-km path. The preliminary tests indicate that the instrument can correct a distance measurement to better than 1 part in a million.

System Operation

The system operation of our instrument is shown in Fig. 2. We use a nulling technique to measure the atmospheric dispersion and, as a consequence, avoid a number of internal systematic errors. The basis of

Both authors were with NOAA Environmental Research Laboratories, Boulder, Colorado 80302, when this work was done; E. Norman Hernandez is now with the University of Washington, Seattle, Washington 98105.

Received 5 August 1971.

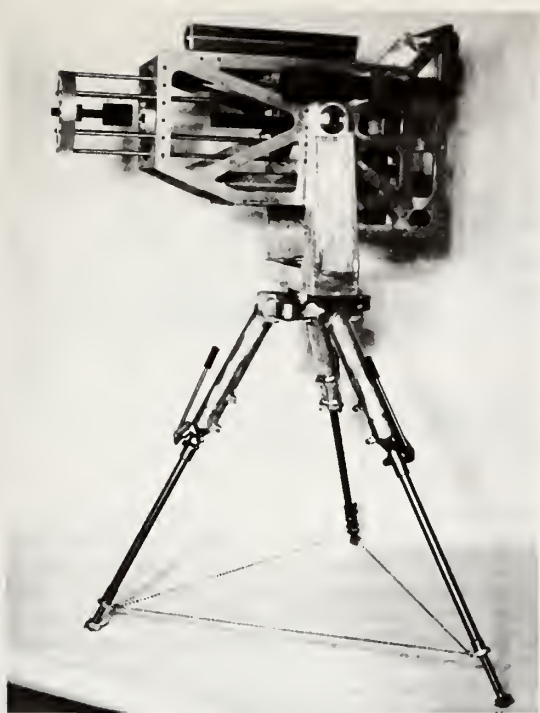


Fig. 1. Two-laser, microwave-modulated distance-measuring instrument.

operation is as follows. Two laser beams, red at 6329.9 Å (vacuum wavelength) and blue at 4416.8 Å, are blended by a Wollaston prism and passed through a KH_2PO_4 (KDP) crystal modulator. The modulator changes the phases of the optical beams at a microwave frequency, approximately 2.7 GHz.¹¹ The light is then propagated over a path to be measured, reflected from a polarization-preserving telescope, and returned over the path to the modulator.

The modulator then either adds to or subtracts from the polarization of the optical beams. If, for example, the modulator is 180° out of phase with the returning polarized light, the light that has passed through the modulator twice will have no polarization. If it is in phase, the twice-modulated light has twice the depth of polarization as the once-modulated light.

By changing the frequency of modulation, exactly an odd number of half wavelengths (of the microwave frequency) of modulation can be made to occur over the optical path. This will cause a null condition (i.e., no polarization) on the horizontal polarization of the received light. In practice one must change continually the microwave frequency because the atmosphere is continually changing, and, as a consequence, the optical pathlength is continually changing.

To accomplish the nulling operation the output of the signal photomultiplier (PM) tubes and noise PM tubes are combined in the noise-canceling circuits to produce

a pulse-duration modulated signal. This signal is the input to the digital servo system. The digital servo computes an estimate of the correct nulling frequency based on the previously computed frequency and the output of the noise canceling circuits. This value is converted to a voltage via a digital-to-analog converter and is then used to control the frequency of the voltage controlled crystal oscillator (VCXO). The VCXO outputs are amplified and multiplied to approximately 6 W at 2.8 GHz and used to drive the KDP modulator.

This entire operation is alternated for the blue light and then for the red light 500 times/sec.

Light sources of high spectral radiance are important, because a narrow band of wavelengths can be used with a reasonable amount of light focused onto and returned from a distant retroreflector in spite of the loss due to atmospheric absorption and scatter. High spectral radiance is also important for correct operation of currently available microwave light modulators, since a beam only 3 mm or 4 mm in diameter and having a divergence less than $\frac{1}{2}^\circ$ can be accepted. In general, the amount of optical power needed for a particular distance-measuring system depends on the modulation index, the amount of atmospheric absorption and scatter, and the diameter of the transmitting and receiving optics.

The present instrument uses a helium-neon cw laser operating at a vacuum wavelength of 6329.9 Å as a red light source, producing approximately 7.0 mW of radiant power in a beam having a divergence of 6 mrad. A helium-cadmium cw laser, radiating approximately 15 mW of radiant power centered on a vacuum wavelength of 4416.8 Å, is used as the blue light source.

Optical System

The beams of light from the two sources are joined into a common, vertically polarized beam, passed through the polarization modulator, and transmitted to a distant retroreflector (Fig. 3). After returning from the retroreflector and back through the modulator, the

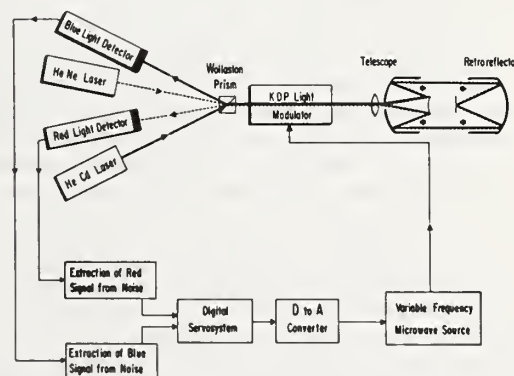


Fig. 2. Block diagram of two-laser distance-measuring instrument.

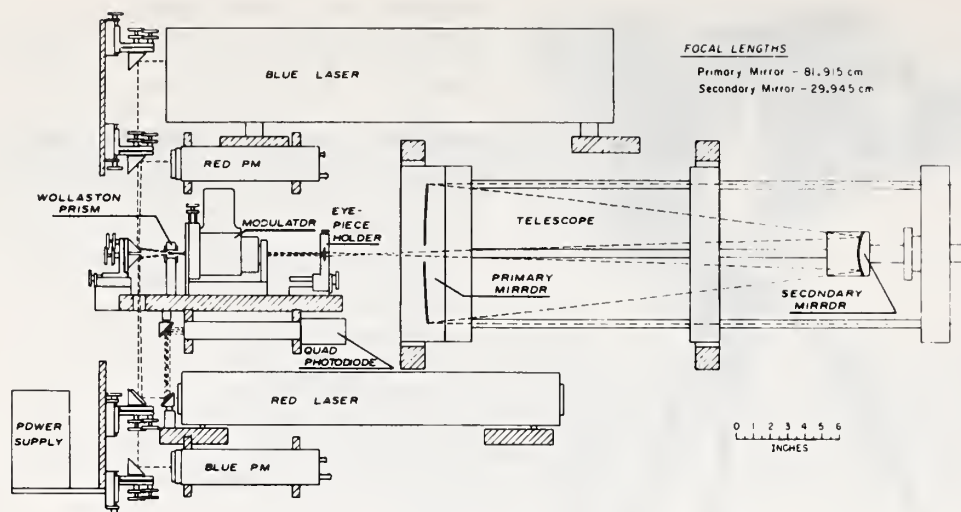


Fig. 3. Scale drawing of instrument head.

beam is analyzed for horizontally polarized light, separated into two beams of the two colors, and detected by photomultipliers. A single optical element (a 12° Wollaston prism) performs the combined functions of polarizing and analyzing the light and of joining and separating the two colors. Vertically polarized fractions of the two colored beams are superimposed by the Wollaston when the correct angle of incidence is used for each color. To make the system more compact the red beam is folded by reflecting it from a mirror placed close to the blue beam. Horizontally polarized light from the two light sources is deflected out of the transmitted beam and not used.

The two-color beam passes through the modulator to a simple double convex quartz lens that serves as a telescope eyepiece. Because the slight divergence of the blue light can be adjusted to compensate exactly for the chromatic aberration of the lens, both colors are brought to a sharp focus at the focal point of a Cassegrainian telescope to produce a 20-cm collimated beam. (A Cassegrainian telescope is used to preserve the polarization of the light beam.) This beam is transmitted to the cat's eye retroreflector (a 20-cm telescope with a plane mirror at its focal point), where it is reflected back through the optical system to emerge from the modulator. On returning through the Wollaston prism, the light is resolved into horizontally and vertically polarized components. The horizontal components, which are maximum when the modulation adds, are separated by color and directed respectively to the photomultiplier detectors for red and blue light.

Since polarization modulation is used, care must be exercised to prevent polarization caused by reflection from any optical component. The mirrors in the two telescopes have relatively long focal lengths (1 m or more) so that all reflection angles (except total internal reflection) will be less than 15%.

Because a common optical system is used for both the transmitted and received light, it is important that reflections from the various optical elements do not return to the photomultiplier tubes. Although coated optics are used throughout, some reflections still occur, and these can be large compared with light returning from the distant reflector. Each optical component is therefore angled slightly to prevent spurious reflected beams from reaching the photomultipliers.

Microwave System

The microwave system provides the light modulator with enough power to produce the maximum possible modulation index at a stable, accurately measured frequency (see Fig. 4). Since the modulator gives a peak retardation of only 0.06 rad at its maximum average power rating of 1 W, higher power pulses at a low duty cycle are desirable to obtain a reasonably large percentage of modulation. The modulation pulses must be long compared with the time required for light to travel over the measurement path, and the pulse repetition rate must be high compared with the fluctuations in atmospheric density. Since atmospheric fluctuations have a power spectrum extending from very low frequencies up to about 500 Hz, the system is designed to deliver 6 W at a 10% duty cycle at pulse repetition frequencies of 1000 Hz (for distances up to 8 km).

To ensure a stable frequency that can be measured accurately, the microwave power source is operated continuously. This source, a voltage-controlled crystal oscillator (VCXO), is amplified with a solid state microwave system. The power to the modulator is supplied through a microwave switch driven at the desired pulse repetition rate. A sample of the signal pulse reflected

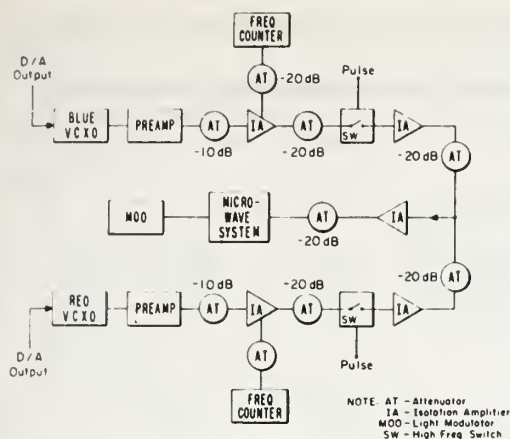


Fig. 4. VCXO and microwave system.

back from the light modulator is used to tune the modulator cavity to resonance.

To track fluctuations in the optical pathlength, a digital servo-control circuit locks the microwave modulation frequency to the optical pathlength so that the path always remains a half-integral number of modulation wavelengths. This is done as follows: The average light intensity at either photomultiplier varies sinusoidally with pathlength and with modulation frequency, maxima occurring when the transit time is an integral number of modulation periods and minima when it is a half-integral number. If the modulation frequency is set at one of the minimum-intensity points, which we call f_0 , any change in frequency will increase the photomultiplier output signal. Frequencies that are symmetrical about f_0 , which we denote by $f_0 \pm \delta f$, will give larger but identical signals. In particular, if the frequency of the microwave oscillator is square-wave modulated at a 500-Hz rate with peak deviation δf about f_0 , the photomultiplier output will be larger but will still be constant because both halves of the square-wave cycle give the same output. If the mean frequency f_c of the square wave differs from f_0 , however, the two halves of the cycle will give different outputs, and hence the photomultiplier signal will also be square-wave modulated at 500 Hz. By comparing the photomultiplier output at $f_c + \delta f$ and at $f_c - \delta f$ the digital controller estimates a new f_c . In practice the digital controller is continually changing f_c , attempting to keep the photomultiplier outputs at $f_c + \delta f$ and $f_c - \delta f$ equal.

A counter that determines the average modulation frequency during each counting period, normally 1 sec or 10 sec, averages the pathlength fluctuations. Thus the instrument is self-balancing, a convenience during periods when the optical path is systematically changing.

Digital Servosystem (Subsystem)

The digital servosystem (DS) in Fig. 2 is a special purpose digital computer designed and built specifically

to provide computations, timing pulses, feedback information, and noise computations necessary for a distance measurement.

For general timing and control the DS provides both the necessary pulses to turn the KDP modulator on and off (variable pulsewidth and transit time) and the necessary pulses to operate the noise canceling networks.

As explained previously, a certain frequency is required to null the PM tube output for either the red or the blue channel. To detect whether the chosen frequency (f) is too high or too low the DS varies the frequency (a value equal to δf) from slightly above to slightly below the chosen frequency. This generates an error signal that is used by the DS to make a best estimate for the next chosen frequency.

Distance Measuring

An actual distance measurement is made by utilizing the following equations: red apparent length,

$$n_R^o L = (N_R \lambda_0 / 2) - k_R, \quad (1)$$

and blue apparent length,

$$n_B^o L = (N_B \lambda_0 / 2) - k_B, \quad (2)$$

where

L is the true length;
 n_R^o, n_B^o are the group indices of refraction for red and blue light;
 N_R, N_B are the number of modulation wavelengths along the path for red and blue light;
 λ_0 is the modulation wavelength in vacuum;
 k_R, k_B are the corrections for optical components in the red and blue light beams.

One way to determine the last two quantities is to measure carefully the thickness of each optical element in the optical paths, multiply each thickness by the appropriate group index of refraction, and add the individual apparent lengths for red and blue light to obtain the total apparent lengths caused by the optical components.

A more practical way involves an experiment. Three points on a straight line (A, B, C) are measured in the following manner. The distances (A, B), (B, C), and (A, C) are separately measured. The discrepancy between (A, C) and (A, B) + (B, C) is the total additional path added by the optics.

We calculate the geometrical distance by using the difference in apparent pathlengths to correct either the red or blue apparent length for the apparent extra length caused by the atmosphere. The corrected length is thus given by

$$L = n_B^o L - A_B(n_B^o L - n_R^o L) \quad (3)$$

or

$$L = n_R^o L - A_R(n_R^o L - n_B^o L), \quad (4)$$

where

$$A_R = (n_R^o - 1)/(n_B^o - n_R^o) \quad (5)$$

and

$$A_B = (n_B^o - 1)/(n_B^o - n_R^o) = A_R + 1. \quad (6)$$

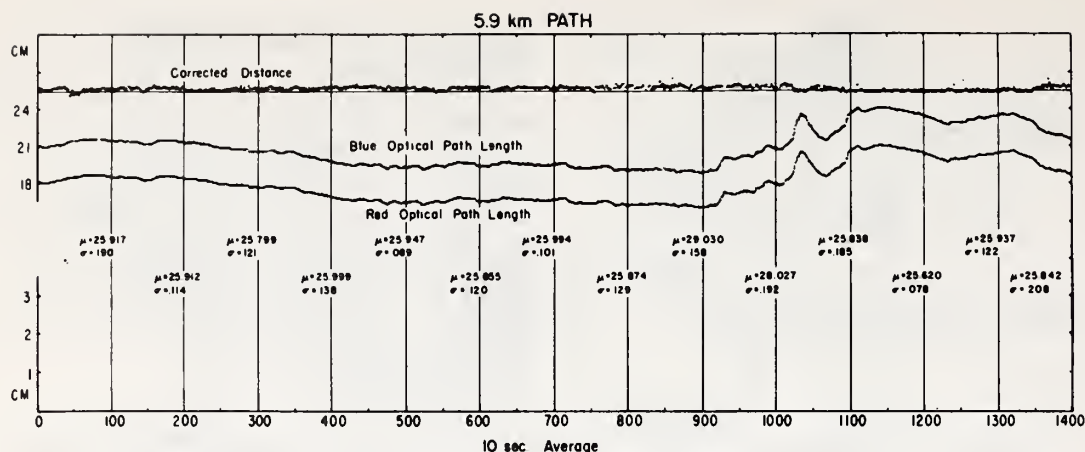


Fig. 5. Typical data for summer 1971.

In a dry atmosphere of standard composition the correction factors A_B or A_R depend only on the two optical wavelengths and are known to high accuracy.¹⁰ However, water vapor changes the composition of the atmosphere and therefore changes the values of A necessary for the true correction of distances. Fortunately, the dependence of A on water vapor pressure is small so that very accurate values of relative humidity and temperature are not needed. For example, when measured temperatures and relative humidity are in error by 5°C and 10%, respectively, the error in calculated distance will be less than 5×10^{-7} .

Results of Field Testing

The instrument was tested during spring and summer 1971 over a 5.9-km path just north of Boulder, Colorado. It operated continuously over a period of many hours proving the basic reliability of the design. We decided to investigate two particular points with this experiment. The first was to determine the maximum optical pathlength fluctuation for the red and blue channels. The second was to determine whether the two-color system corrected for the dispersion over the propagation path during a period of time when the optical pathlength was changing by a large amount.

Figure 5 shows data taken on a typical day. The second curve is the blue optical pathlength, the third curve is the red optical pathlength, and the top curve is the corrected pathlength computed from the bottom two curves. To show the small scale fluctuation each curve has been normalized by subtracting from each curve its average value. The three curves are artificially separated to avoid confusion, and the corrected distance curve is scaled by a factor of 3.

Each point represents a 10-sec averaged distance measurement. Every 100 points (corresponding to a period of time of 1000 sec or approximately 17 min) the mean

and variance for the correct curve are given in centimeters. The total curve represents approximately 4 h of data (1400 points at 10 sec each).

The plot in Fig. 5 is typical of the data taken in summer 1971. During the approximate 4 h covered by the figure, the optical pathlength changed over 20 mm on the 5.9-km path. This corresponds to an average temperature change along the propagation path of approximately 3°C. During this period the average corrected distance (averaging 100 points at a time) ranged from 25.799 cm to 26.030 cm, a maximum change of 2.31 mm. This corresponds to 3.9 parts in 10 million over the 5.9-km path, considerably better than the original goal.

Conclusions

The present version of the two-color distance-measuring instrument is still undergoing tests and modifications. At present, the instrument is making primary measurements (10-sec averages) over a 5.9-km path, that have a standard deviation of less than 4 parts in 10 million. By averaging over several hours the instrument can easily obtain accuracies approaching 1 part in 10 million. Recent tests indicate that an improvement in the optical pathlength measurements can be obtained easily by using presently available high-stability intermediate frequency sources. With this simple improvement we expect that the maximum peak-to-peak fluctuations of corrected distances using 10-sec averages will be less than 2 parts in 10 million.

We gratefully acknowledge the help of K. B. Moran, G. M. Bouricius, R. Dickerson, and D. Vance in building and testing this instrument. We also wish to thank J. C. Owens (Eastman Kodak Research Laboratories, Rochester, New York) and P. Bender (JILA/NBS, Boulder, Colorado) for their many helpful and stimulating discussions and for their initial efforts in the

development of two-color distance measuring instruments.

This work was partially supported by AFCL under project order Y69-829 and by NASA under project order W12, 929.

References

1. K. B. Earnshaw and J. C. Owens, *IEEE J. Quantum Electron.* **QE-3**, 11 (1967).
2. L. E. Wood, *EOS Trans. Am. Geophys. Union* **52**, 17 (1971).
3. L. E. Wood and M. C. Thompson, Jr., "Differential Phase Techniques for Measuring Atmospheric Refractivity," *Proc. of Electro Optic Systems Design Conference*, September 1970, pp. 921-926.
4. P. L. Bender, *Proc. IEEE* **55**, 1039 (1967).
5. B. R. Bean and E. J. Dutton, "The Radio Refractive Index of Air," in *Radio Meteorology*, NBS Monograph (U.S. Government Printing Office, Washington, D.C., 1966).
6. M. C. Thompson, Jr., "The Effects of Propagation on Measurements of Distance, Angle-of-Arrival, and Doppler Effect in Ground-to-Ground Systems," presented at XV General Assembly of URSI, Munich, September 1966; in *Prog. Radio Sci.* **1**, 579 (1966).
7. K. D. Froome and R. H. Bradsell, *J. Sci. Instrum.* **38**, 458 (1961).
8. M. T. Prilepin, "Light-Modulating Method for Determining the Average Index of Refraction of Air Along a Line," *Trans. Institute of Geodesy, Aeronomy, and Cartography (U.S.S.R.)* No. 114, 127 (1957).
9. P. L. Bender and J. C. Owens, *J. Geophys. Res.* **70**, 2461 (1965).
10. J. C. Owens, *Appl. Opt.* **6**, 51 (1957).
11. I. P. Kaminow and E. H. Turner, *Appl. Opt.* **5**, 1612 (1966).

New heights for atmospheric optics

Remote sensing and pollution monitoring may overshadow "classical" investigations.

OVER THE PAST TEN YEARS, the impetus for much of the work in atmospheric optics has been from defense and space funds. While such support will continue at a reduced level in the future, there is no doubt that the importance of atmospheric optics in remote sensing, as related to environmental problems, will increase.

In atmospheric spectrometry, the transmission characteristics of the permanent atmospheric gases are reasonably well understood. The intensive efforts to map accurately the water vapor spectrum in the infrared have resulted in an accumulation of line strength and position data sufficient to solve most existing or contemplated transmission problems.

However, much remains to be done in understanding the spectra of typical constituents of atmospheric pollution. Even such a common pollutant gas as SO_2 requires fur-

ther spectral studies before the present level of understanding for CO_2 is reached. Similarly, spectra of hydrocarbons over long absorption paths in the infrared will require much future study to allow reliable quantitative detection using long path absorption measurements. The Raman spectral characteristics of such gases may also prove important in pollution monitoring, and the search for resonance enhancement of scattering cross sections must certainly continue for some time to determine more completely the feasibility of laser-Raman detection techniques.

Since the appearance of the laser, a number of studies of the propagation of coherent radiation in the atmosphere have been sponsored. The discovery of scintillation saturation effects and the mapping of the

refractive index power spectrum of the turbulent atmosphere over horizontal paths has occupied the time of a number of investigators. An ability to sense the integrated wind field across the path of a laser beam by time-lag correlation techniques, based upon an improved understanding of scintillation, has already been proven feasible at NOAA.

Coherent propagation effects

Some of this effort to understand coherent propagation effects will certainly continue, especially for vertical paths simulating optical communication links to space. Additional effort will be required to predict reliably propagation characteristics of high power laser beams through the atmosphere. The possible evolution of chemical lasers at wavelengths other than $10.6\text{ }\mu\text{m}$ may call for a number of additional

basic contributions to propagation theory, absorption, beam steering, and beam blowup, in the future.

Monitoring industrial haze

Studies of two dimensional contrast transfer must continue, to be able to predict more accurately the performance of imaging systems operating through the atmosphere. The relative importance of angular scintillation and atmospheric path radiance in reducing contrast in small scale detail in aerial photography and satellite remote sensing will continue to be of importance as imagery techniques acquire even further maturity and sophistication in interpretation. More field measurements are needed of path luminance functions for a variety of atmospheric turbidity and earth surface reflectance characteristics to supplement the measurements made

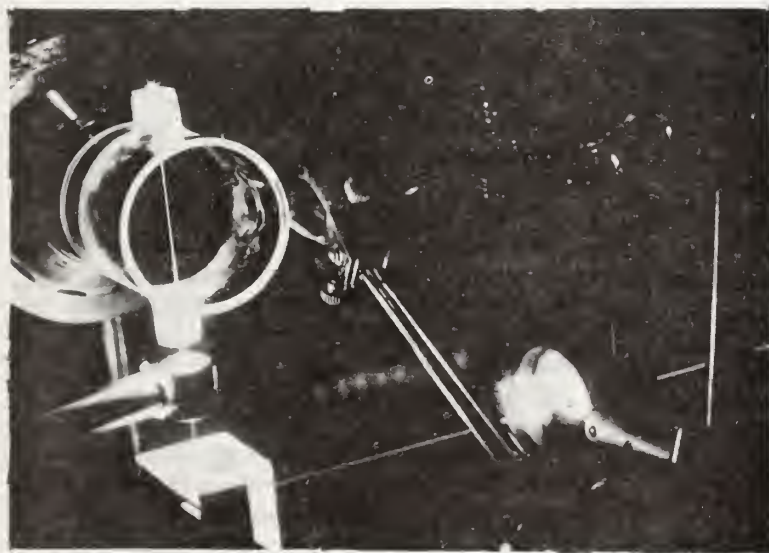
several years ago at the Visibility Laboratory of UCSD.

With the increasing importance of monitoring industrially produced turbidity and in understanding the climatic effects of haze, better knowledge is required of the optical constants of aerosols. Both the real and imaginary refractive indices must be better known and scattering dependence on non-spherical shape effects understood. Although the present consensus seems to be that industrial hazes must lead to climatic cooling, more studies of the infrared optical properties of hazes are needed. The magnitude of the increased albedo expected from haze requires better understanding.

Measuring cloud effects

Significant improvements in the calculation of multiple scattering in clouds through Monte Carlo techniques are now available, and must be applied to radiative transfer problems in the real atmosphere to model more accurately the effects of haze and clouds in the overall earth heat budget. The properties of stratospheric aerosols, both naturally occurring and those which may be introduced by a significant population of commercial SSTs, must be better understood. Accurate remote measuring techniques should be developed to monitor such aerosols and their possible effects on stratospheric heat and chemical balance.

Finally, it is hoped that a future trend in computer studies of "classical" investigations in atmospheric optics—formations of halos, coronas, and rainbows—will continue to see some support, both for the pure enjoyment obtained from a better understanding of the optics of such phenomena, and in the hope of making available other methods for monitoring particle shape and size distributions in clouds. □



Laboratory studies of scattering by atmospheric gases are part of current research in atmospheric optics. Here, a quartz cell containing NO_2 is illuminated by an argon ion laser at 488 nm. The incident beam from the right passes through a prism and a 5 cm focal length lens and then vertically through the cell. The bright (orange) vertical scattering filament in the cell is imaged by the $f/1.5$ lens behind the cell onto the slit of a double monochromator behind the lens. Quantitative measurements of scattering cross section and depolarization ratio are made with the apparatus. Figures on a counter, part of the digital data acquisition system, can be seen in the background.

Freeman F. Hall
Wave Propagation Laboratory
NOAA Environmental Research
Laboratories

Field Tests of a Two-Laser (4416 A and 6328 A) Optical Distance-Measuring Instrument Correcting for the Atmospheric Index of Refraction

E. N. HERNANDEZ¹ AND K. B. EARNSHAW

Environmental Research Laboratory, NOAA, Boulder, Colorado 80302

The most recent version of a microwave-modulated two-laser distance-measuring instrument has completed several months of field tests. This instrument was operated almost continuously for about a month over a 5.9-km base line just north of Boulder, Colorado. During the tests the optical path lengths for red and blue varied over 3 cm for the base line, and the corrected distance typically has a σ of <3 mm. The preliminary results of these tests clearly show that this type of instrument can correct a distance measurement taken in 10 sec to better than five parts in 10 million.

A recent review article [Wood, 1971] cites many papers that describe various electromagnetic techniques for making precise geodetic distance measurements. The major limitation to the precision of these measurements is the difficulty in estimating the average index of refraction along the base line for the particular frequency of electromagnetic energy being used [Owens, 1971]. Bender and Owens [1965] noted the advantages of using two optical frequencies to correct for the index of refraction. Such a two-color instrument has been described previously by the authors [Earnshaw and Hernandez, 1972].

This particular instrument incorporates two lasers (4416 A HeCd and 6328 A HeNe) that are polarization modulated at approximately 2.7 GHz. By measuring the optical path length $n_o D$ for each color, where n_o is the group index of refraction for the particular color and D is the true distance, the index of refraction for the atmospheric path can be corrected to first order for temperature fluctuations.

The distance is determined by measuring D_R and D_B , the optical path length for the red and blue lights, respectively, and is given by

$$D = D_R - A_R(D_B - D_R) + B_R + A_R(B_B - B_R) \quad (1)$$

where

$$A_R = (n_R - 1)/(n_B - n_R) \quad (2)$$

and where B_R and B_B are the extra optical path lengths for red and blue added by the lens, the modulator, and the folded path inside the instrument, C is the vacuum velocity of light, and n_R and n_B are the group indices of refraction for the modulated red and blue lights. Earnshaw and Hernandez [1972] discuss the steps necessary to determine the constants B_R and B_B . A simple experiment of measuring the points A , B , and C in a straight line will be sufficient. The distance $(A, B) + (B, C) - (A, C)$ will be the extra path length due to the optics.

To first order, A_R is independent of temperature. This relative insensitivity to temperature fluctuations is exploited to produce a highly accurate correction. A polynomial approximation for n_R or n_B is given by [Owens, 1967]

$$(n_R - 1)10^8 = \frac{P_D}{T} (1 + P_0 B_1) C_1 + \frac{P_W}{T} (1 + P_W B_2) C_2 \quad (3)$$

where P_D is the partial pressure of dry air, P_W is the partial pressure of the water vapor in millibars, T is the temperature in degrees

¹ Now holding joint appointments in the Applied Physics Laboratory, the Electrical Engineering Department, and the Geophysics Program, University of Washington, Seattle, Washington 98195.

Kelvin, B_1 and B_2 are functions of T^{-1} and T^{-2} , and C_1 and C_2 are functions only of the wavelength of the red light. For the colors chosen (4413 Å and 6328 Å), A is approximately 20; thus the determination of the optical path length must be better than that of the desired corrected distance measurement by a factor of 20.

EXPERIMENT

The instrument (Figure 1) was housed in a 16-foot travel trailer parked on Table Mountain, ~12 km north of Boulder, Colorado. The base line was established across a valley between Table Mountain and a point ~5.1 km south of Table Mountain. A polarization-preserving 8-inch-diameter Cassegrainian telescope served as a retroreflector. The retroreflector, housed in a small shack, was plumbed over a bench mark located across a valley ~5.9 km south of Table Mountain. The instrument rested on the ground through holes in the trailer and thus was effectively isolated from the trailer.

The combined red and blue laser beams were propagated over the ~5.9-km path to the retroreflector and back to the instrument. The electrooptic crystal (KDP) modulators of the instrument acted as the transmitter and receiver. Since B_R and B_B affect the measured distance only by an additive constant, no attempts were made to determine their values experimentally.

A major objective of the experiment was to determine how well the two-color system could correct for the index of refraction. We believed that measuring a fixed base line under widely varying atmospheric conditions would provide the answer. The instrument was operated almost continuously for over a month on the 5.9-km base line.

Initially, we attempted to record data 24 hours a day but found this was impractical because of the large amount of data produced and our limited data-logging system. (An optical path length measurement for red and blue every 10 sec yielded 17,280 six-digit numbers each day. Each digit was hand punched to produce paper tape input for the computer.) The amount of data taken was soon limited by our ability to process it. The instrument was allowed to operate continuously, but most of the time no data were recorded.



Fig. 1. The two-laser optical distance-measuring instrument.

Since the instrument operated exceptionally well during the more difficult daylight hours (nighttime conditions generally improve the signal-to-noise ratio and range) and since we were interested in the performance of the instrument under adverse conditions, our schedule was quickly reduced to recording data from approximately 10:00 A.M. to 6:00 P.M. on weekdays.

DATA

Figures 2-6 show typical data from the experiment. Each graph contains three curves, correct distance, blue optical path length, and red optical path length, and each curve contains 1400 points. The optical path lengths for red D_R and blue D_B were measured every 10 sec, and the corrected distance D was computed later from (1). Each curve is normalized by subtracting its respective average value. The three curves are then artificially separated for clarity. The optical path length curves are

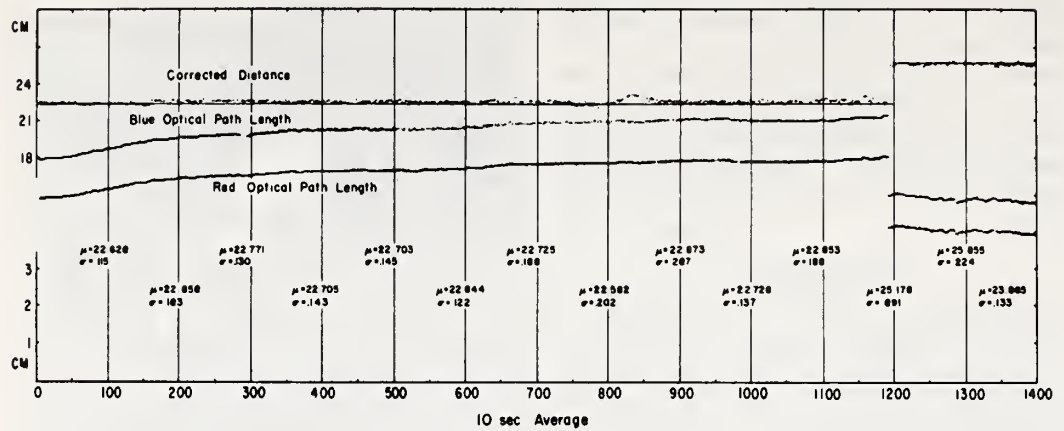


Fig. 2. The step jump at point 1200 corresponds to an approximate 1-inch increase in the base line achieved by moving the retroreflector.

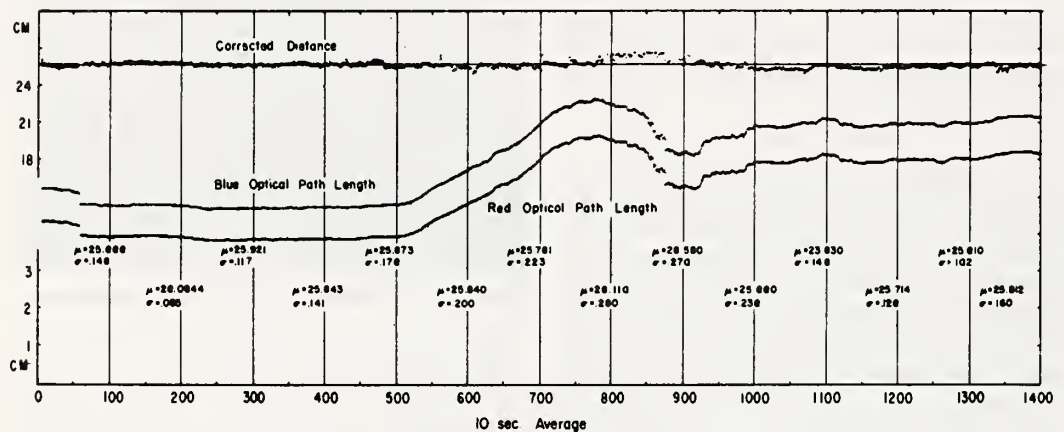


Fig. 3. An example of poor data during a period of time in which the optical path lengths are rapidly changing.

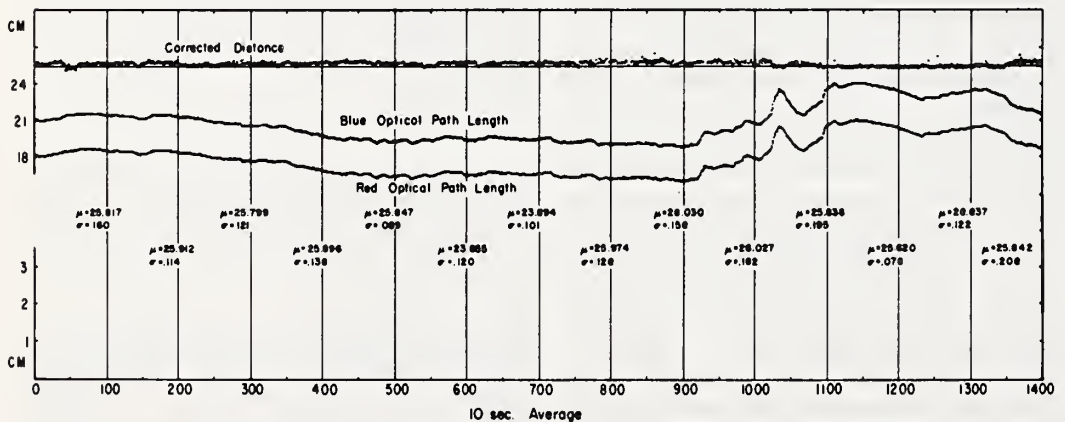


Fig. 4. An example of good data during a period of time in which the optical path lengths are rapidly changing.

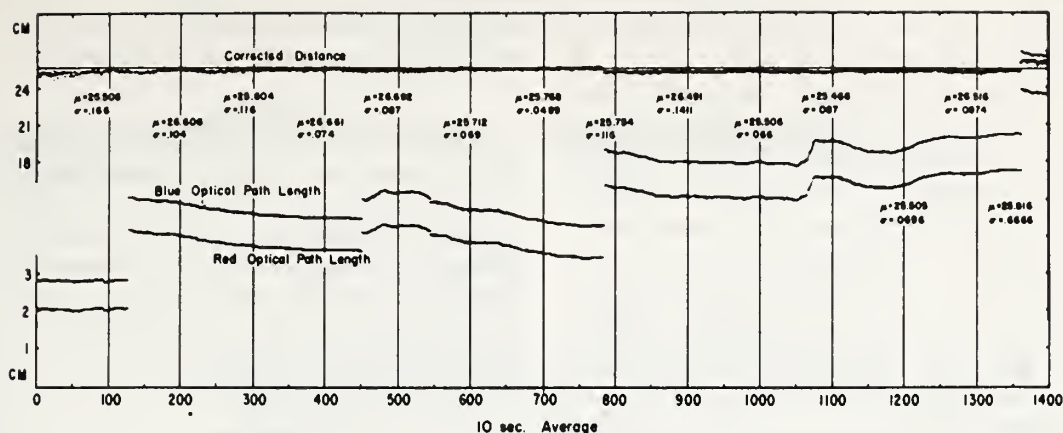


Fig. 5. A decrease in base line of 0.1 inch produced the change at point 780, and an increase of 0.2 inch produced the change at point 1360.

scaled at 1 cm per division, and the corrected distance is scaled at 3 cm per division. The right-hand vertical axis is identical to the left-hand vertical axis. At every 100 points a vertical line is drawn for reference, and the mean μ and variance σ are computed for that block of 100 points. Here μ and σ are given in centimeters. Since 0.59 mm represents approximately one part in 10 million for this particular path (base line, ~ 5.9 km), the variances for each 100-point section range from approximately one part in 10^7 to five parts in 10^7 .

During certain periods of time (Figure 4, points 300-900), σ remains around two parts in 10^7 , even though μ is slowly increasing from 25.799 to 26.030 (approximately four parts in 10^7).

This type of drift could be attributed to many things, including (1) drift in the base line length, (2) tilting of the fiducial points of the instrument and/or the retroreflector, (3) drift in the additional optical path added by the optics of the instrument, (4) drift in the effective center of modulation, and (5) unexpected effects of atmospheric variables such as pressure, water vapor, and temperature.

The problem with these sources of drift is that each is difficult to isolate and study. We are convinced that the drifts we observed were not due to items 3 and 4, although some drifts were clearly caused by item 2. At present the Environmental Research Laboratory is improving the base line to minimize item 1. The only easy way to check item 5 in the open atmos-

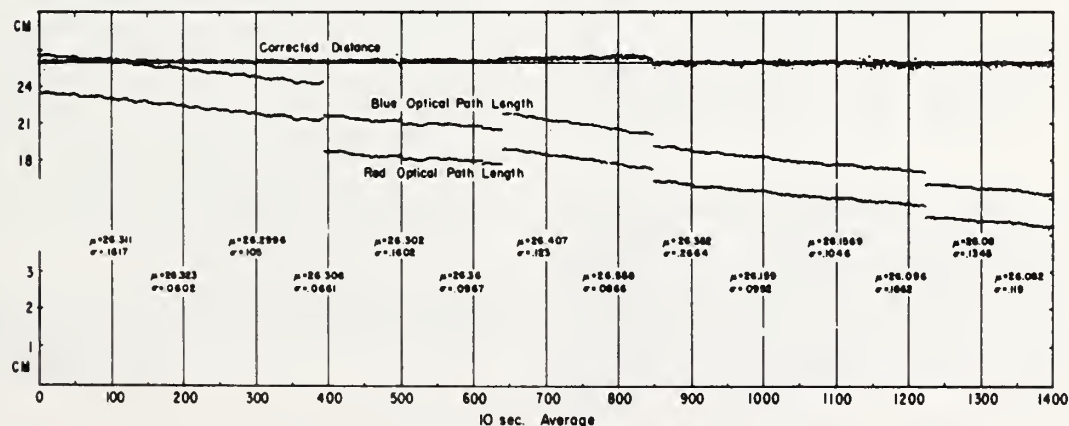


Fig. 6. Continuation of Figure 5.

phere is to take adequate data over widely varying atmospheric conditions.

We wanted to measure the base line over widely varying temperature conditions, but, to do this, we needed a front of radically different air temperature. Unfortunately, the usually changeable Colorado weather became stable, and no such front appeared. In fact, the temperature at ~ 1 m above the ground at the transmitter side varied about 13°C throughout the data runs, and, as the data indicate, the average temperature varied about 6°C over the propagation path.

The step discontinuity on the corrected-distance curves in Figures 2 and 5 corresponds to the exact distance by which the far retro-reflector was moved. This movement was accomplished by mounting a machinist's table between the tripod and the retroreflector. With care, movements of the retroreflector in 0.1-mm increments were reasonable. In Figures 2 and 5 the discontinuities occurred within a few seconds. The discontinuities in the optical path lengths in Figures 2 and 5 are arbitrary offsets in the path lengths due to losing the total fringe numbers. Figure 5 shows data with optical path length discontinuities. These jumps occurred during a period of optical path length

change when no data were taken. The corrected path length is constant during these periods.

CONCLUSION

A two-laser microwave-modulated distance-measuring instrument has been tested over a 5.9-km atmospheric path. These tests show that by using two colors the atmospheric index of refraction can be corrected for temperature fluctuations sufficiently well to provide a corrected distance measurement in better than five parts in 10 million. Under some conditions, two parts in 10 million may be achieved.

REFERENCES

- Bender, P. L., and J. C. Owens, Correction of optical distance measurements for the fluctuating atmospheric index of refraction, *J. Geophys. Res.*, **70**, 2461, 1965.
- Earnshaw, K. B., and E. N. Hernandez, Two-laser optical distance measuring instrument that corrects for the atmospheric index of refraction, *Appl. Opt.*, **11**, 749-754, 1972.
- Owens, J. C., Optical refractive index of air: Dependence on pressure, temperature and composition, *Appl. Opt.*, **6**, 51-59, 1967.
- Owens, J. C., Laser applications in meteorology and geology, in *Laser Applications*, edited by M. Ross, pp. 61-131, Academic, New York, 1971.
- Wood, L. E., Recent progress in electronic surveying, *Eos Trans. AGU*, **52**, IUGG 17, 1971.

(Received March 2, 1972;
revised August 30, 1972.)

Use of Scintillations to Measure Average Wind Across a Light Beam

R. S. Lawrence, G. R. Ochs, and S. F. Clifford

We report the successful construction and testing of an optical wind sensor that uses the motion of the scintillation pattern to measure the transverse component of wind blowing across a laser beam. As is done for measuring ionospheric and interplanetary winds, we use a correlation method. However, in our application, the slope at zero lag of the time-lagged correlogram proves to be more useful than the more commonly used delay to the peak. The reason is that, in the atmosphere, irregularities are distributed along the entire propagation path. We use a detector spacing of 0.33 of the diameter of the first Fresnel zone to obtain a nearly uniform weighting function along the path, though the center of the path is still more effective than the ends. The sensor has been used extensively over 1-km and 15-km paths, and field tests of various applications are planned.

Introduction

A casual glance at the optical scintillation pattern produced by atmospheric turbulence shows that it drifts with the transverse wind. If this drift can be interpreted quantitatively as representing the average wind velocity across the light beam, a number of promising applications appear for which conventional anemometers are poorly suited, either because the desired location is inaccessible or because widely separated point measurements are a poor substitute for a true spatial average. For example, it is the wind immediately above the runway that is of interest to an airplane pilot, not the wind at some nearby point where it is practical to install an anemometer. Similarly, the drift of air pollutants down a valley depends on the average wind, which may be very different from the readings of a few anemometers placed near the floor of the valley. We report here the successful construction and testing of such an optical wind sensor, whose principal elements appear in Fig. 1, and describe the problems and limitations involved in its performance.

Measurements of scintillation drift, at radio frequencies, have long been used to measure winds in the ionosphere.^{1,2} In that application the turbulence producing the scintillations tends to be concentrated in a single portion of the propagation path. This effect minimizes the random decay of the scintillation pattern and so simplifies the interpretation. More recently, radio-star scintillations have been used to infer the speed of the interplanetary solar wind.³ Here

again the diffracting irregularities tend to be concentrated (near the point of closest approach to the sun). In addition, the illuminating radiation is a plane wave rather than a diverging spherical one, and both these factors tend to reduce the random decay of the pattern. The formal inversion of the equations relating the wind velocity and turbulence profiles for an extended medium to the covariance function of the scintillations of a plane wave has been published by Peskoff,⁴ using a suggestion by Lee and Harp⁵ that permitted linearization of the integral equation. No test was made of the stability, resolution, or sensitivity of this solution with real, noisy observations made through the actual atmosphere. Shen⁶ developed a numerical inversion scheme for the spherical-wave covariance function, using the correlation and slope at zero lag to deduce the turbulence and wind profiles from scintillations observed over a 28-km microwave link. He concluded that an averaged wind could be determined and included data that did show that winds of the proper sign and reasonable magnitude could be deduced.

We shall demonstrate a modification of previous methods, one that measures, with a real-time, on-line indicator, the average wind across a laser beam and successfully allows for the use of diverging waves and a turbulent medium extending along the entire path.

Theory

A photograph of the laser scintillation pattern reveals many different areas of light and dark. The sizes of these areas are determined by the diffraction of the incident beam resulting from irregularities in the temperature of the atmosphere at various positions along the propagation path. At each position, the diffraction process selects a most effective scale of irregularity, or eddy, whose size is sufficient to cause a half-wavelength difference in pathlength to the receiver for two

The authors are with the National Oceanic & Atmospheric Administration, Environmental Research Laboratories, Boulder, Colorado 80302.

Received 11 June 1971.

CLEA paper 2.3.

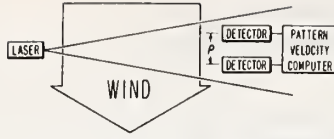


Fig. 1. The general arrangement used to measure the average component of the wind, across a laser beam, parallel to the (usually horizontal) spacing of two detectors.

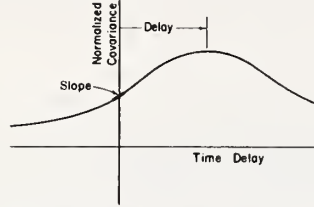


Fig. 2. A schematic diagram of the normalized covariance function, showing the delay to the peak and the slope at zero time lag. While the former is frequently used to measure pattern drift velocities, the latter is more suitable in the optical case where the pattern decays rapidly.

extreme rays passing through its edges. The diffractive effects of this particular eddy dominate over those of other eddies at the same location.

If a diverging laser beam is effectively a point source, geometric magnification increases the size of the received eddy image by the factor L/z , where z is the position along a beam of length L . The image drift rate at the receiver caused by the local eddy drift velocity $v(z)$, depending on the wind at position z , is also increased by the same factor. Therefore, the received optical disturbance is larger and moves faster than the eddy that produced it. Since different portions of the path contribute to the total scintillation pattern, that pattern will be continuously evolving because of the relative speeds of the different-sized features it contains. The pattern will change even under the ideal circumstance of uniform wind and unchanging turbulent conditions along the entire path. Nonuniformities in the wind or in the strength of turbulence will increase the rate of decay.

These ideas are compactly expressed in the two-dimensional time-lagged covariance function of the intensity (or irradiance) fluctuations. In practice, it is more convenient to use the covariance of the logarithm of the intensity or, equivalently, the log-amplitude χ , since the logarithm of intensity is normally distributed and so allows the use of a polarity-coincidence correlator. From the spatial covariance function of the log-amplitude given by Lee and Harp,⁵ we may derive the time-lagged covariance via Taylor's hypothesis and the additional assumption that different portions of the path produce effects in the received

scintillation pattern that are uncorrelated.⁷ Taylor's hypothesis implies that eddies do not change significantly during the time they drift through the beam. This is not strictly true, since they tend to decay with lifetimes proportional to their sizes, and so produce time changes in the pattern that appear as additional random velocity components. Although we use Taylor's hypothesis in the following derivation, we shall discuss later the implications of eddy decay.

The time-lagged covariance of the log-amplitude fluctuations is

$$C_{\chi}(\rho, \tau) = 4\pi^2 k^2 \int_0^L dz \int_0^\infty dK K \Phi_n(K, z) \times \sin^2[K^2 z(L - z)/(2kL)] J_0[K|\rho z/L - v(z)\tau|]. \quad (1)$$

This equation applies for a spherical wave of wavelength $\lambda = 2\pi/k$ propagating along the z direction to $z = L$ through two-dimensionally isotropic turbulence described by some refractivity spectrum $\Phi_n(K, z)$, a function of position and of two-dimensional spatial wavenumber K . The turbulence is drifting with a velocity $v(z)$ perpendicular to the propagation direction and we calculate the covariance function at two points in the scintillation pattern separated by a displacement ρ . The wind velocity parallel to the propagation path has a negligible effect.

The additional assumption of local homogeneity permits us to write $\Phi_n(K, z)$ in terms of the Kolmogorov spectrum. Then, the path may be partitioned into segments within which the $K^{-1/3}$ turbulence spectrum prevails over some well-defined scale region, $1/L_0 < K < 1/l_0$, where L_0 and l_0 are, respectively, the outer and inner scales of turbulence.⁸ A new value of the refractive turbulence structure parameter C_n^2 is assumed for each L_0 -sized segment. This generates a spectrum that is a function of position and has the form

$$\Phi_n(K, z) = 0.033 C_n^2(z) K^{-1/3}. \quad (2)$$

Substituting Eq. (2) into Eq. (1) and assuming horizontal ρ and v , Eq. (1) becomes

$$C_{\chi}(\rho, \tau) = 0.132 \pi^2 k^2 \int_0^L dz C_n^2(z) \int_0^\infty dK K^{-5/3} \times \sin^2[K^2 z(L - z)/(2kL)] J_0[K|\rho z/L - v(z)\tau|] \quad (3)$$

for $l_0 \ll (\lambda L)^{1/3} \ll L_0$.

Equation (3), normalized to the spherical-wave log-amplitude variance $\langle \chi^2 \rangle$ ($\langle \chi \rangle = 0$) in order to make it insensitive to changes in the level of C_n^2 occurring simultaneously along the entire path, provides a direct statistical measure of both the spatial and temporal characteristics of the amplitude scintillation pattern. Writing $\langle \chi^2 \rangle$ as

$$\langle \chi^2 \rangle = C_{\chi}(0, 0) = 0.728 k^{3/6} L^{-1/3} \int_0^L dz C_n^2(z) [z(L - z)]^{1/3} \quad (4)$$

and dividing into Eq. (3), we obtain

$$C_{\chi N}(\rho, \tau) = 2.33 (kL)^{3/6} \frac{\int_0^L dz C_n^2(z) \int_0^\infty dK K^{-5/3} \sin^2[K^2 z(L - z)/(2kL)] J_0[K|\rho z/L - v(z)\tau|]}{\int_0^L dz C_n^2(z) [z(L - z)]^{1/3}} \quad (5)$$

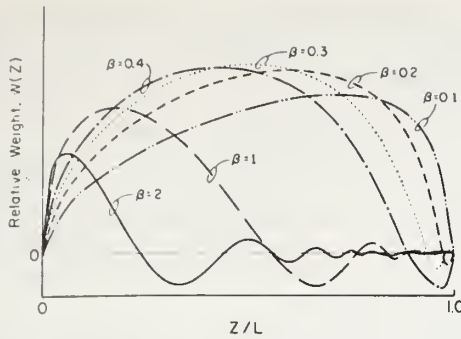


Fig. 3. The relative weights of the different portions of the path in determining the optically measured wind. The parameter $\beta = \rho(\lambda L)^{-1}$ is the separation of the sensors. These curves are calculated for point sensors; the finite area of a real sensor will tend to remove the negative weights near the receiver.

Equation (5) is the desired normalized time-lagged covariance function, a function of the wind and turbulence profiles along the path, from which we intend to derive information about the path average of $v(z)$. This function is shown schematically in Fig. 2. Clearly the location of the maximum value of C_{xN} depends on the wind velocity. Maximizing by either varying the spacing at a fixed time lag or varying the lag for a fixed spacing yields some sort of a weighted average wind measurement. However, as we shall show, these methods give averaged winds that depend on the wind profile, yielding different results for different assumed profiles with the same average. Maximizing by varying spacing has the further disadvantage of being cumbersome and impractical, although in the presence of eddy decay, it gives a more nearly correct value for the average wind.⁹ The time lag to the peak gives a wind reading that is systematically high, especially at low wind velocities when eddy decay is most important. Eddy decay inhibits the contributions of the slowly moving features in the pattern because, after a long lag, the pattern passing the second sensor scarcely resembles that which passed the first sensor, and the correlation is reduced. Further, the variations in C_n^2 and the relative motions in the pattern, due to both the variable wind along the path and the geometrical magnification mentioned above, cause severe distortions in the measured average. In summary, the location of the peak covariance is a technique best suited to measuring velocities in cases where the pattern structure drifts without much evolution.

A method that avoids the problems of pattern decay is the measurement of the slope of the covariance function at zero time lag, since that measurement involves comparing features at nearly the same instant (see Fig. 2). As we shall see, the slope gives a time-weighted average, producing a correct result for all profile realizations with the same average wind. It is also relatively insensitive to physically reasonable variations in C_n^2 (i.e., the strength of refractive-index turbulence) along the path.

Differentiating Eq. (5) with respect to τ and setting $\tau = 0$, we obtain¹⁰

$$M_N = \int_0^L dz C_n^2(z) v(z) W(z) / \int_0^L dz C_n^2(z) [z(L-z)]^{1/2} \quad (6)$$

where $W(z)$ is the path-weighting function for the slope given by

$$W(z) = 2.33(kL)^{1/2}$$

$$\int_0^\infty dK K^{-3/2} \sin^2\{K^2 z(L-z)/(2kL)\} J_1(K\rho z/L). \quad (7)$$

Equation (7), plotted in Fig. 3, shows the relative weights of different portions of the path in computing the average. Note how the weighting function varies for different spacings. For our wind measuring system we chose $\beta \equiv \rho(\lambda L)^{-1} = 0.33$, which gives the most nearly uniform weighting. The negative weights shown in the figure will not occur in practice. Equation (7) is the expression for the wind weighting function using point sensors. A similar result for finite apertures would remove the negative weighting for the last portion of the path by averaging over pattern scales smaller than the aperture and would bias the average slightly toward the transmitting end of the path.

Figure 4 illustrates numerical calculations that demonstrate the superiority of the slope method over using the time delay to the peak of the covariance function. The wind velocity was assumed to vary along the path as shown in the inset, the amplitude of the variation being described by the parameter a . The average wind is the same in all cases. The figure shows clearly that while the delay to the peak of the curve varies with the nonuniformity of the wind, the slope at zero delay remains constant, reflecting the constant mean value of the wind. Other calculations show that the slope method, as distinct from the time-

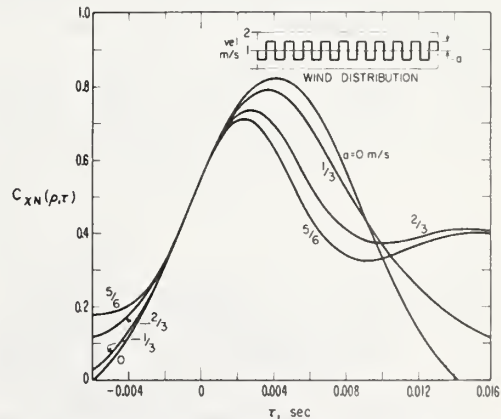


Fig. 4. Time-lagged covariance functions calculated for a 1-km path and $\beta = 0.33$, using the irregular wind distribution shown in the inset. Notice that the delay to the peak depends on the variability a of the wind, while the slope at zero lag does not.

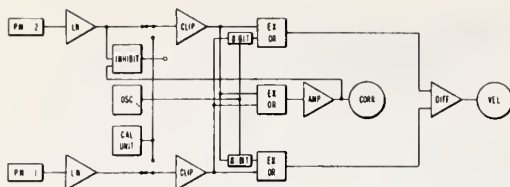


Fig. 5. A block diagram of the pattern-velocity computer used to measure the slope of the normalized covariance function at zero time lag.

delay method, is unaffected by the symmetrical contribution made by vertical winds, i.e., by the component of transverse wind perpendicular to the line joining the sensors.

Implementation

The prototype system developed for the measurement of mean wind flow is compact and fairly simple. It consists of a low-power laser, two receivers, and a small computer to provide a real-time readout of wind velocity.

The laser transmitter consists of a mount having a sighting telescope and a 3-mW He-Ne laser operating single-mode. Since changing vertical temperature gradients from day to night, even 50 m or so above the ground, may deflect the beam as much as $4 \mu\text{rad}/100 \text{ m}$ in the vertical direction, we use a cylindrical lens to expand the beam vertically. In this way we are able to keep the receivers illuminated sufficiently over a 15-km path without resorting to servocontrolled pointing.

Photomultipliers are used to measure the irradiance upon two horizontally spaced circular apertures whose diameter is only slightly less than the center-to-center spacing $\beta = \rho(\lambda L)^{-1}$. The angular field of view of each aperture is restricted to 3 mrad, a value sufficient to include rapid angular fluctuations as well as diurnal angle-of-arrival changes in the wavefront. The background light levels are further reduced by the use of $10\text{-}\text{\AA}$ interference filters.

A real-time readout of wind velocity is obtained with a small computer that we have designed for this purpose. We wish to measure the slope, at zero delay, of the normalized time-lagged covariance of the logarithm of the fluctuating signals. To accomplish this, the computer measures the normalized covariance a small time lag on either side of zero delay. The magnitude of the difference is then a measure of the slope at zero delay.

The system is shown in Fig. 5. First, we obtain the logarithms of the received signals. From the logarithmic converters, the signals pass through clipping circuits that determine the signs of the signals relative to their means. This sign information is fed to *exclusive or* (EXOR) circuits that determine the fraction of time that the signs of the signals are alike. The combination of clippers and any of the EXOR circuits forms a one-bit correlator that computes

the normalized covariance of input signals having a Gaussian amplitude distribution.¹¹ Since the optical signal irradiance fluctuations are log-normally distributed, this condition is satisfied by taking the logarithm.

The eight-bit shift registers delay signal 1 relative to 2 in the upper EXOR circuit and signal 2 relative to 1 in the lower EXOR circuit. The delay, less than a millisecond, is sufficiently small so that the covariance measurements are made over a nearly linear portion of the covariance function, up to the highest expected wind velocity. The computer output is the difference of the upper and lower EXOR circuits, calibrated in terms of wind velocity.

Several auxiliary circuits improve the practical operation of the system. The center EXOR circuit measures the normalized covariance at zero delay. This quantity is useful as a check on the theoretically expected value for a given pathlength and sensor separation. In the present system, it is used as one input to an inhibit circuit. If the laser beam is obscured, that circuit detects either an excessively low signal or a low normalized covariance. The dual test is necessary for the following reasons. If the laser signal is lost in the daytime, the covariance will go to zero, since the noise in the detectors generated by background light is uncorrelated. However, the ambient background light may be intense enough to prevent low-signal turnoff. If the laser signal is lost at night, the low-signal test is effective even though the covariance may still be appreciable because of stray correlated pickup in the absence of other signals.

A known slope may be inserted into the computer by means of the calibration unit. The unit consists of a generator of variable frequency having two square-wave outputs differing in phase by 90° . The expected normalized covariance of these two signals is a triangular waveform with zero covariance at zero delay. The slope of the covariance at zero delay is four times the square-wave frequency, the sign being determined

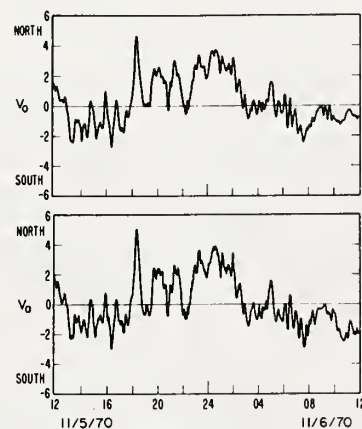


Fig. 6. A 24-h comparison between the optically measured wind (upper curve) and the mean of seven propeller-type anemometer spaced evenly along the 1-km test path.

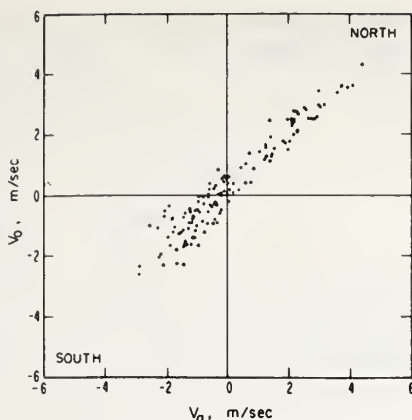


Fig. 7. A scatter diagram of individual 10-min readings taken from Fig. 6. Most of the variation seems to result from failure of the anemometers to measure a true average.

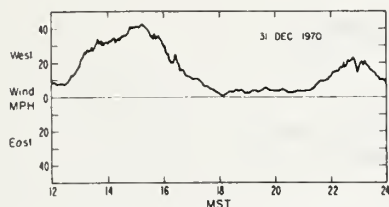


Fig. 8. A 12-h sample of the average wind measured optically across a 15-km path passing over Boulder, Colorado.

by which signal is leading. A more detailed discussion of the calibration procedure as well as other aspects of the computer may be found in Ref. 12.

In order to verify the wind measurement, we tested the system over a 1-km east-west path instrumented with seven propeller anemometers fixed in position to read the wind component normal to the path. The optical receiver spacing was 0.8 cm, about one third of a Fresnel zone for the path, i.e., $\rho = 0.33(\lambda L)^{1/2}$, giving a nearly symmetrical weighting of wind velocity with respect to the center of the path.

A comparison of the wind velocity v_a normal to the optical path as determined by the mean of the seven anemometer readings and the wind velocity v_o , determined optically, is shown over a 24-h period in Fig. 6. A 10-min running average has been applied to both curves. The correlation coefficient between v_o and v_a was better than 0.96 for the 24-h period. In Fig. 7 we show a scatter plot of 10-min averaged values of v_o vs v_a for the 24-h period. A least-squares straight-line fit to these data gives a slope of 0.94, indicating that the theoretical relationship between slope and wind velocity is valid. Most of the scatter in Fig. 7 arises from failure of the seven anemometers to measure the true mean wind, even with 10-min smoothing of the data. We know this because a scatter plot of the average of anemometer readings in even and odd position locations contains nearly the same scatter as Fig. 7.

Equation (6) indicates that the optical method measures the wind as weighted by the strength, C_n^2 , of refractive-index turbulence along the path. Random variations of C_n^2 will distort the measured average wind only if they are correlated with the variations in wind speed. A reasonable supposition, certainly not contradicted by the excellent sensor performance shown in Fig. 6, is that turbulence is strongest at locations of maximum wind shear, not at locations of maximum wind speed. If so, the turbulence tends to be uncorrelated with the wind, and the average obtained by the optical sensor is unbiased. Systematic variations of turbulence along the path can be expected in certain cases. For slant paths the resulting bias in the average wind can be reduced by proper choice of the weighting functions shown in Fig. 3. Hilltop-to-hilltop paths have a systematic increase in turbulence near the ends, but this conveniently tends to be counteracted by the insensitivity of the weighting function to winds at ends of the path.

The same system used in the 1-km path tests has now been operating continuously for 5 months on a 15-km north-south path over Boulder, Colorado. A sample record of wind velocity on this path for 12 h is shown in Fig. 8. During part of this period, *Chinook* winds were producing peak gusts as high as 90 mph at Boulder.

Conclusions

We have demonstrated that an optical sensor of average transverse wind, using the natural turbulence of the atmosphere, is an accurate, practical, and potentially useful device. It measures a true average of the wind across the path, being unaffected by non-uniformity of the wind and only slightly affected by nonuniformity of the strength of turbulence along the path.

We plan to explore the possibility of using passive reflectors to permit folding the path. The resulting flexibility of the system would permit measurements to nearly inaccessible locations or would allow a laser beam to surround an area, thus permitting measurement of atmospheric convergence. The possibilities of intentionally varying the weighting function, through the use of different apertures and spacings, so as to deduce the profile of wind over the path warrant exploration.

References

1. S. N. Mitra, *Proc. IEE*, **96-III**, 441 (1949).
2. B. H. Briggs and M. Spencer, *Rept. Progr. Phys.* **17**, 245 (1954).
3. M. H. Cohen, E. J. Gundermann, H. E. Hardebeck, and L. E. Sharp, *Astrophys. J.* **147**, 449 (1967).
4. A. Peskoff, *Proc. IEEE* **59**, 324 (1971).
5. R. W. Lee and J. C. Harp, *Proc. IEEE* **57**, 375 (1969).
6. L. Shen, *IEEE Trans. Ant. Prop.* **AP-18**, 493 (1970).
7. S. F. Clifford, *J. Opt. Soc. Am.* **61**, 1285 (1971).
8. V. I. Tatarski, *Wave Propagation in a Turbulent Medium* (McGraw-Hill, New York, 1961).
9. M. G. Morgan and K. L. Bowles, *Science* **161**, 1139 (1968).
10. Shen follows the same procedure to invert Eq. (5). He shows that a complete numerical inversion can yield only the mean wind and, perhaps, the gradient. We, on the other hand, make direct use of the proportionality between correlation slope and mean wind.
11. G. R. Ochs, *ESSA Tech. Rept. ERL63-WPL2* (U. S. Government Printing Office, Washington, D. C., 1968).
12. G. R. Ochs (to be published, *Rev. Sci. Instrum.*).

Raman Spectroscopy with a Tunable Dye Laser and a Narrow-Band Filter

G. T. McNice

Wave Propagation Laboratory, Environmental Research
Laboratories, NOAA, Boulder, Colorado 80302.

Received 13 December 1971.

Sponsored by Darrell E. Burch, Philco-Ford.

Raman spectra of gases are generally obtained by propagating a fixed-wavelength laser beam through a gas and selecting the Raman component of the scattered light by means of a tunable double monochromator. The double (or even triple) monochromator is desirable for rejection of the strong on-frequency Mie and Rayleigh components. In principle, a similar spectrum can be obtained by tuning the laser rather than the monochromator, thus shifting the Raman wavelength across the fixed passband of the monochromator. The two methods are entirely equivalent if the variation of the Raman cross section over the monochromator passband is ignored.

The advantage of a tunable-laser system lies in its simplicity. With a fixed monochromator, it is not necessary to provide precision tracking of two or three gratings or correct for chromatic aberration in dispersive optical elements. In principle, all that is required is a filter. A stack of absorption filters can provide the required rejection of on-frequency scattering but not a sufficiently narrow passband. Interference filters can have acceptable bandwidths (<1 nm) but reduce the on-frequency scattering by only about 10^4 , which is marginal at best. Since they reflect light that is not transmitted, stacking n interference filters perpendicular to the optical path increases the rejection to only $n \times 10^4$, not 10^{4n} , due to multiple reflections between filters, while tipping them to reduce the reflections degrades transmission and bandwidth. Nevertheless, the simplicity of the tunable-

laser system using a filter was felt to be attractive enough to warrant a preliminary experiment, and the system shown in Fig. 1 was assembled.

The tunable laser was a flashlamp pumped dye laser with the following characteristics:

active medium: calcein blue in water,
 output energy: 5×10^{-4} J/pulse,
 pulse rate: 6 sec⁻¹,
 wavelength: 438–468 nm,
 line width: 0.2 nm,
 pulse width: 0.5 μ sec.

The filter was a stack of four narrow-band interference filters mounted on an EMI 9558 photomultiplier. The filter passbands were centered at 488 nm, three of them being 1 nm wide and the fourth being 3 nm wide. These particular filters were chosen simply because they were available in the laboratory. The optical characteristics of the filter stack were:

peak transmission: 5%,
 half-width: 0.7 nm,
 Transmission at 453.6 nm: less than 10^{-6} .

The filter transmission characteristics were found to be very sensitive to angle of incidence so tipping the filters was not attempted.

The sample compartment consisted of a black cardboard box mounted inside the laser resonator with holes punched for the laser beam and the Raman output. The sample gas was flowed through continuously to displace any air. The box also contained a cylindrical lens to collimate the Raman scattering from the laser beam. The output of the photomultiplier was sampled at the peak of the laser pulse, integrated, and recorded. The

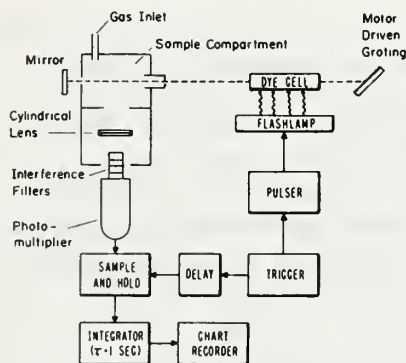


Fig. 1. Schematic diagram of the tunable-laser Raman spectrograph.

Table I. Laser Wavelengths Required to Generate Raman Scattering at 488 nm

| Gas | Transition (cm ⁻¹) | Laser wavelength (nm) |
|----------------|--------------------------------|-----------------------|
| Oxygen | 1555 | 453.6 |
| Carbon dioxide | 1409 | 456.6 |
| | 1388 | 457.0 |
| | 1286 | 459.2 |
| | 1265 | 459.6 |

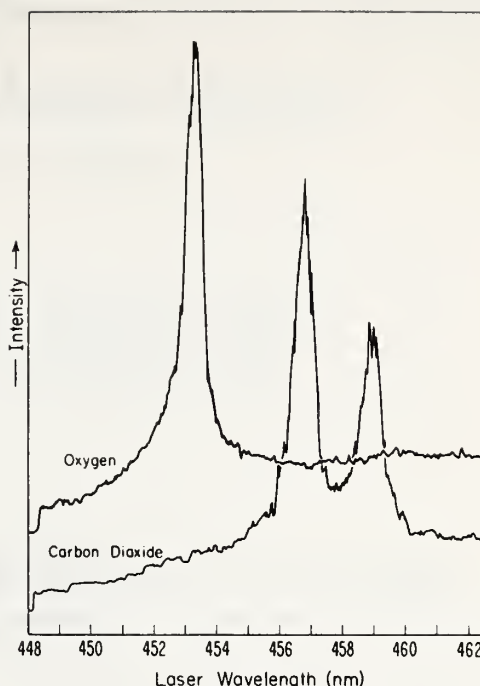


Fig. 2. Representative Raman spectra recorded with the tunable-laser Raman spectrograph.

laser wavelength was calibrated against a mercury spectrum on a Bausch & Lomb 1.5-m grating spectrograph.

Oxygen and carbon dioxide were chosen to test the system, their choice being dictated by their immediate availability as well as their nontoxic and nonodorous nature (the latter being important considerations due to the open structure of the sample compartment). The laser wavelengths required to generate Raman scattering from these gases at 488 nm are shown in Table I.

The sample chamber was first flooded with oxygen and the top spectrum of Fig. 2 obtained. The sample chamber was then flooded with carbon dioxide and the same wavelength region scanned generating the bottom spectrum of Fig. 2. The success of the technique is apparent.

The resolution of the spectra of Fig. 2 is limited primarily by the spectral width of the filter stack (0.7 nm) and to a lesser extent by the laser line width (0.2 nm). System sensitivity was limited by scattered flashlamp light in the passband of the filter and 50% amplitude variations in the laser output. Considerable improvement in both resolution and sensitivity is readily available by placing a Fabry-Perot interferometer in front of the filter stack and using an intracavity etalon in the dye laser. These changes can be expected to produce an instrumental resolution on the order of 0.01 nm along with a significant improvement in sensitivity through reduction of flashlamp feedthrough. Further improvements in sensitivity are available through stabilization of the laser and ratio recording to reduce the effects of the remaining laser fluctuations.

It should be emphasized that this was a very quick and simple experiment requiring neither critical alignment nor special techniques. With care and engineering, this technique should provide a useful and relatively inexpensive tool for the Raman spectroscopist.

TEMPERATURE AND C_n^2 PROFILES MEASURED OVER LAND AND OCEAN TO 3 KM
ABOVE THE SURFACE

G. R. Ochs and R. S. Lawrence

We present a series of profiles of atmospheric temperature and optical refractive-index structure measured to 3 km above the surface. Measurements were made with probes mounted on a moving carriage on ERL's 150-m tower near Haswell, Colorado, and from aircraft-mounted probes flown over eastern Colorado and over the Pacific Ocean southwest of San Diego, California. A brief review of accepted models and theories of height dependence of C_n^2 is included for comparison with the experimental data.

Reprinted from NOAA Technical Memorandum ERL WPL-9, July 1973.

THE NOAA OPTICAL SYSTEM FOR MEASURING AVERAGE WIND

G. R. Ochs and G. F. Miller

The NOAA optical system for measuring average wind is described. Circuit diagrams and adjustment instructions for the instrument are included.

1. INTRODUCTION

The instrument, consisting of the optical receiver and wind computer shown in figure 1, is designed to measure the spatially averaged transverse component of the wind, averaged over an optical path to a laser transmitter. This is accomplished by analysis of the motion of various spatial wavelengths in the scintillating light pattern received from a helium-neon laser. The principle is discussed in detail by Lawrence et al. (1972). The instrument is a somewhat modified version from the one they described, since we correlate the difference of intensity fluctuations between two pairs of photodiode receivers, rather than correlate log-intensity fluctuations in two receivers. This modification has important advantages over the previous technique in that fluctuations in the light source have little effect upon the operation, and less error occurs when optical scintillation approaches the saturated condition. The use of intensity fluctuations results in a variation in the wind calibration with C_N , but this effect is almost entirely eliminated if the sensors are separated 0.3 of a Fresnel zone for the path length used. This separation also gives the most nearly uniform path averaging of the wind and is set up automatically when the path length adjustment is made at the receivers.

A FEASIBILITY STUDY OF AN OPTICAL CROSSWIND MONITOR

G. R. Ochs, S. F. Clifford, and Ting-i Wang*

This report summarizes progress to date on our feasibility study of a laser-beam crosswind-measuring system. In the first section, we consider the laser system concept and discuss its limitations, namely the uncontrollable variability of the path-weighting function and its tendency to peak at less than 10 percent of the path from the transmitter in high refractive turbulence. In the second section, we consider an alternative approach called the "passive" system that uses the naturally occurring, ambient illumination of the target to extract wind information. This technique has the advantage that, unlike the laser system, at least from the point of view of the first-order theory, the path-weighting functions are independent of the level of refractive turbulence and exhibit a reasonable degree of variability with changes in detector spacing. Also included in appendix A are some recent results on the saturation problem. It is quite likely that the effects of saturation will have some influence on both the laser and passive techniques. The size of these effects on the wind-weighting function has yet to be evaluated.

1. INTRODUCTION

During the period from November 1, 1972, to September 30, 1973, we conducted a theoretical and experimental study of the feasibility of a laser-beam crosswind monitor. The system as initially posed consisted of a laser transmitter and a collocated set of receiving optics. The principle of operation of this single-ended system was that a receiver telescope would observe a laser-illuminated target; from an analysis of the atmospherically induced fluctuations in the pattern of illumination (scintillation pattern), information about the crosswind along the path could be derived. The first part of this report is a detailed analysis of the system and a conclusion as to its feasibility. In the second part, we consider an alternative approach and its relative merits.

*Ting-i Wang is with the Cooperative Institute for Research in the Environmental Sciences, an institute sponsored jointly by the University of Colorado and the National Oceanic and Atmospheric Administration.

OPTICAL MEASUREMENT OF CAPILLARY WAVE STRUCTURE

Ronald L. Schwiesow

Remote (optical) sensors may be applied to the measurement of capillary wave structure on an ocean surface. This report analyzes four instrumental systems and associated parameters required to measure the time-dependent relative height of a 1 mm diameter section of surface with a 1 mm height resolution and a frequency response of 100 Hz. Determination of the most promising technique depends on the outcome of some critical experiments, although the CO₂ laser velocity integration system and a mode-locked Nd:YAG laser phase comparison system appear most promising.

Raman Scattering from Pollutant Gases and Air-Water Interfaces

RONALD L. SCHWIESOW*

Environmental Research Laboratories, National Oceanic and Atmospheric Administration, Boulder, Colo.

Remote sensing of environmental constituents by Raman lidar is an attractive method for monitoring molecular environmental pollutants. We report techniques for and results of laboratory measurements of Raman scattering cross sections and depolarization ratios of atmospheric gases, as a function of incident photon energy. The cross section of H_2O (relative to N_2 as a reference) changes by a factor of 2 as the incident photon energy is changed by 5%. Results for SO_2 , NO , and other gases are less dramatic. We also discuss preliminary spectral features of scattering from polluted air-water interfaces.

I. Applications of Spectral Back-Scatter

RAMAN lidar involves the spectral and temporal resolution of the optical back-scatter of a monochromatic pulsed laser source. The intensity-vs-photon-energy characteristics of the scattered spectrum for a given laser photon energy (or frequency) identify the scatterer, and the time delay determines range to the scatterer. In principle, such an atmospheric or air-to-water interface scattering technique is a powerful remote sensor for environmental pollutants.

Our laboratory is involved in studies of the Raman scattering characteristics of gases, aerosols, and air-to-liquid interfaces. The purpose of this paper is to identify some illustrative applications of generalized Raman scatter to pollutant systems, and then to discuss in this applications context some preliminary results of our laboratory measurements. The paper is designed to serve

as a review of applications and theory and as a preview of scattering results.

Enthusiasm for the ability of Raman lidar to both identify and locate a particular polluting constituent must be tempered by the fact that gaseous Raman scattering is very weak compared to Mie or Rayleigh scattering. Scattering cross section and depolarization ratio are the two quantitative parameters which describe the magnitude of the molecular Raman scattering interaction. These parameters will be described in more detail later. Together with the incident laser frequency and the characteristic frequency shift of the particular molecular transition, the cross section and depolarization ratio completely describe the scattering interaction. These four characteristic scattering values, over a range of the incident laser photon frequency as an independent variable, must be known for molecules of interest in order to make realistic system feasibility studies, to calibrate field sensor equipment, and to select laser frequencies for maximum back-scatter intensity. These molecular measurements are discussed here. Similar laboratory studies of gaseous scattering from different molecules from those discussed in this paper have recently been reported by Widhopf and Lederman.¹

Although many investigators have proposed Raman lidar measurements of atmospheric pollutants, Kobayasi and Inaba²

Presented as Paper 71-1086 at the Joint Conference on Sensing of Environmental Pollutants, Palo Alto, Calif., November 8-10, 1971; submitted October 28, 1971; revision received July 31, 1972. Research supported in part by NASA, MSC and EPA, APCO.

Index categories: Atmospheric, Space, and Oceanographic Sciences; Lasers.

* Physicist.

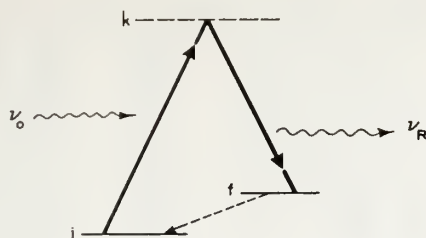


Fig. 1 Representative energy level diagram for discussing the Raman effect.

are among the few to report positive results. Optimization and interpretation of such results require quantitative molecular studies.

We suggest that Raman lidar may also be a useful tool for water pollution studies. Pollution analysis by bulk Raman scattering from samples in small cells has been suggested and demonstrated to a limited extent.³ This paper reports preliminary spectra of Raman scattering from air-to-water interfaces. This method of characterizing water-borne pollutants is excellently suited to remote sensing of large areas from an air-borne platform. Lidar has considerably more flexibility than other methods, such as solar uv absorption, because the active, controlled source allows rapid scanning, ratio detection, and selection of monochromatic pump frequency. One can visualize a remote sensing method utilizing a lateral scan from an aircraft coupled with translation along the aircraft track.

Remote analysis of pollutant systems by Raman back-scatter is currently signal-to-noise limited by technological problems (laser power and optical filter bandwidth) and by lack of understanding of the details of molecular scattering. Advantages of the remote methods over point sampling, including speed, economy and large area coverage, dictate that research on these questions continue.

II. The Raman Effect

At least three types of spectrally-dependent processes are useful for remote constituent sensing. They are resonance radiation, fluorescence, and Raman scattering. At atmospheric pressures only Raman scattering has been observed for molecules, so we will emphasize the Raman effect in the following discussion. Qualitative aspects of the scattering are also useful for understanding resonance radiation and fluorescence effects.

The energy level diagram useful for reviewing the Raman effect is shown in Fig. 1. For molecular pollutants, vibration-rotation levels are applicable, although the theory⁴ applies to pure rotation and electronic energy levels, as well as more complex energy states in solids and liquids. For Raman scattering the level k is a virtual (or unreal) state of the molecule. Level k is introduced as a conceptual aid in visualizing the interaction in terms of energy conservation. The scattering involves the interaction of a molecule and two photons simultaneously, and

$$\sigma(\nu) \propto (\nu_0 + \nu_{if})^4 P_{if}^2$$

$$P_{if} = \frac{1}{h} \sum_k \frac{\langle \psi_i | \vec{r} | \psi_k \rangle \langle \psi_k | \vec{r} | \psi_f \rangle}{\nu_{ki} - \nu_0 + i\delta_k} + \frac{\langle \psi_f | \vec{r} | \psi_k \rangle \langle \psi_k | \vec{r} | \psi_i \rangle}{\nu_{kf} + \nu_0 + i\delta_k}$$

Fig. 2 Quantum mechanical expression for the differential Raman scattering cross section of a gaseous molecule.

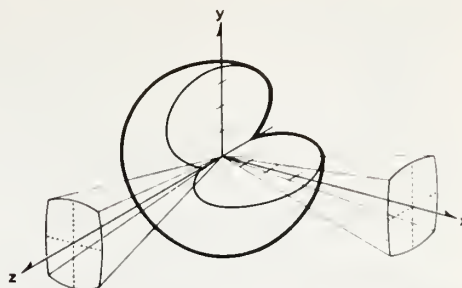


Fig. 3 Representative three-dimensional Raman scattering diagram for scattering intensity as a function of angle. Laser radiation is directed along the y axis polarized in the z direction. Instrumental collection solid angles are indicated for viewing scattering in the x and z directions.

is referred to as a single two-photon interaction. In this context, simultaneously means a time less than 10^{-16} sec. Energy is conserved in the over-all process, but is not conserved in the individual photon destruction and creation subprocesses, where all real states of the molecule are involved. Since the two-photon scattering occurs so rapidly, it is not affected by molecular collisions which typically involve mean time between collisions of the order of 10^{-8} sec.

If state $i \equiv$ state f but k still represents a virtual state, the energy level diagram applies to Rayleigh scattering. This type of scattering is also a two-photon interaction with the molecule, but there is no measurable difference in the incident and scattered photon energies. When k is a real state of the molecule, then the energy level diagram applies to fluorescence if state $i \neq$ state f , and to resonance reradiation if state $i \equiv$ state f . Fluorescence and resonance reradiation involve two separate interactions of the molecule with a single photon at a time. This is referred to as a sequence of two single-photon interactions. The time lapse between stages of the process varies widely but is typically 10^{-6} sec. Energy is conserved in each step of the process. The time lapse between the two single-photon interactions with the molecule allows molecular collisions to nonradiatively de-excite the molecule, quenching the fluorescence or reradiation.

The expression⁵ governing Raman scattering intensity is shown in Fig. 2. The incident photon frequency is ν_0 , and the double subscript frequency $\nu_{if} = \nu_i - \nu_f$ denotes a frequency difference which is proportional to an energy level difference in the molecule. The matrix elements are summed over all real states k of the molecule. The resonance damping factor δ_k may be different for each real state, and is related to the uncertainty or width of the energy level. The equation shows scattering cross-section variation with incident (pump) frequency ν_0 . Since the wave functions ψ are not known for molecules of interest, the expression is not useful for calculation of cross sections directly; laboratory measurements are required. The expression demonstrates the " ν^4 law" characteristic of Raman and Rayleigh scattering alike. This means the scattering cross section is relatively much larger for higher energy incident photons. The resonance denominators are demonstrated and quantified in the next section. Resonance Raman scattering is predicted when the incident frequency is nearly the same as the difference between a real intermediate state and either the initial or final states.⁴ The magnitude of the cross-section change caused by the resonance denominator is the order of 10^6 for some organic liquids.⁵

III. Gaseous Cross Section Studies

Method

In order to measure molecular scattering characteristics, we conduct carefully controlled laboratory experiments. The equip-

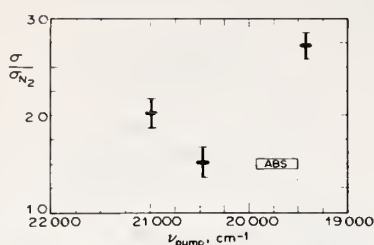


Fig. 4 Relative Raman scattering cross section for water vapor under atmospheric conditions and various laser pump photon energies. A region of weak water vapor absorption is indicated schematically as ABS (the ordinate of the region has no significance) for comparison with Fig. 2.

ment includes a CW argon-ion laser, double monochromator to discriminate against instrumentally scattered on-frequency light and a linear photon-counting detection scheme. All data are taken and processed using digital techniques.

The three-dimensional molecular scattering pattern of a fluid is indicated in Fig. 3, relating intensity and angle. The minimum and maximum radial dimensions of the toroid characterize the scattering and give the cross section and depolarization ratio for the scattering process at some particular pump frequency and molecular frequency shift. The scattering cross section is the magnitude of the maximum radial dimension of the toroid, while the depolarization ratio is the ratio of minimum to maximum dimensions. This depolarization ratio is the same as that obtained by measuring the ratio of y to z polarized scattering for light propagating in the x direction. Because the scattered photons are collected over a large solid angle, the minimum and maximum intensities of Fig. 3 are not available directly, but are obtained from geometrical corrections. Similar corrections are required for the polarization sensitivity of the monochromator.

Pollutant gases are measured in a cell buffered with nitrogen to 760-torr total pressure. The nitrogen reproduces atmospheric pressure-quenching effects and serves as an internal intensity reference. Reported cross sections are given relative to the integrated scattering of the single, isolated Q branch of nitrogen at a shift ν_{if} of 2331 cm^{-1} from the exciting light. In the region of incident photon energy $10,000\text{--}40,000 \text{ cm}^{-1}$, nitrogen has no known absorptions and is presumed to exhibit only the $(\nu_o + \nu_{if})^2$ frequency dependence.

Four argon laser lines have sufficient power to yield significant scattered intensity for useful measurements on gases.

Results

The results reported must be applied with care since further measurements may refine these values. General characteristics of the variation in cross section with pump frequency are believed correct and useful.

Figure 4 graphically illustrates the variation in the Raman scattering cross section of water vapor with incident photon energy. The very weak visible absorption indicated schematically is probably the reason for the weak cross-section resonance. Studies with a tunable dye laser closer to the absorption region are in process, and should help us understand the intensity equation.

The table of scattering cross sections (Table 1) summarizes results to date on pollutant molecules. The values are consistent with other measurements⁶⁻⁸ which were not polarization-analyzed. Larger cross sections are required to extend the range or pollutant concentration limits of present systems.² Resonance studies hold promise of selecting optimum laser frequencies for this extension. Depolarization measurements are an important part of understanding the resonance denominators.⁴

An excitingly large cross section for mixed hydrocarbon vapors

Table 1 Measured relative Raman cross sections ($\sigma_{N_2} = 1$)

| Gas | Laser wave number, cm^{-1} | Relative cross section | Depolarization |
|----------------------|-------------------------------------|------------------------|----------------|
| SO_2 | 20 981 (476.5nm) | 5.2 | 0.04 |
| | 20 487 (488.0nm) | 5.5 | 0.05 |
| | 20 135 (496.5nm) | 5.5 | 0.04 |
| | 19 430 (514.5nm) | 5.6 | 0.05 |
| NO | 20 981 | 0.45 | 0.11 |
| | 20 487 | 0.45 | 0.10 |
| | 20 135 | 0.43 | 0.11 |
| | 19 430 | 0.49 | 0.08 |
| H_2O | 20 981 | 2.5 | |
| | 20 487 | 1.9 | |
| | 19 430 | 3.3 | |

is indicated in Fig. 5. This data has not yet been analyzed for cross section, but on the basis of relative integrated spectral areas and sample partial pressures, it appears that the average hydrocarbon cross section is approximately 115 times that of nitrogen. The spectrum is the result of the C—H stretch in the molecules, where the energy shift for each bond depends on the host molecule and bond location. This molecular combination results in a broad spectrum compared to the nitrogen spectrum. Further analysis of this pollutant system is important for remote sensing purposes.

IV. Air-Liquid Interface Studies

Raman scattering in liquids is comparatively more intense than scattering in gases. An air-liquid interface scatters with a spectrum very similar to that of the bulk liquid. Based on results discussed in this section, Raman (or fluorescent) scattering is a useful analytical tool in water pollution studies.

The apparatus for laboratory studies is basically the same as that described for gaseous measurements. Samples are contained in quartz tubes for 90° bulk scattering, or the air-water interface is illuminated and examined at near-normal incidence. The latter sampling method more realistically models the situation involved in remote sensing. A deep cell is used for interface measurements so that the transmitted beam is removed from the scattering region.

Remote measurements of water temperature are possible using the Raman effect. Such remote temperature measurements are valuable for a study of thermal water pollution using the sensing techniques outlined in Sec. I. Scattering is independent of the surface emissivity and intervening atmospheric temperature.

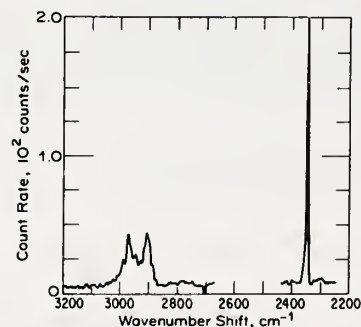


Fig. 5 Raman scattering spectrum of mixed hydrocarbons in gasoline vapor. Nitrogen reference is at a shift of 2331 cm^{-1} with the hydrocarbon spectrum in the region of $2850\text{--}3050 \text{ cm}^{-1}$ shift. Data not corrected for instrumental response.

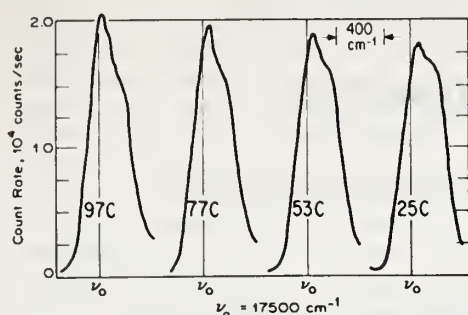


Fig. 6 Raman scattering spectrum of synthetic sea water at four different temperatures. Laser pump at 20487 cm^{-1} . ν_0 indicates photon frequency fiducial point for comparison of spectra.

These latter two parameters affect infrared radiometer measurements of water temperature. Raman spectra of the principal liquid water peak in a synthetic ocean water sample as a function of temperature are shown in Fig. 6. These results are similar to measurements in pure water made by Walrafen.⁹ A significant observation is that the presence of ionic solutes in the water does not change the temperature dependence of the spectrum. By measuring the ratio of scattered intensity at the two peaks (or at one shoulder and the isosbestic point near 3460 cm^{-1} shift), one has a self-calibrating determination of water temperature. This can be measured at the same time that other pollutant aspects are measured by scattering, as discussed below. These spectra were taken in bulk samples (volume scattering), as were Walrafen's, but one expects identical results from interface scattering.

To detect trace constituents by Raman scattering, one must suppress the liquid water spectrum. In very recent data, taken digitally, we have subtracted point-by-point the pure water spectrum from the polluted water spectrum. Such difference spectra have been run on samples of water from the Miami, Florida and Washington, D. C. areas. These samples were provided by the National Ocean Survey. The analysis has progressed only far enough to say that there are significant differences in the samples in broadband features and in a few sharp spectral features. For example, a spectral peak is associated with ocean

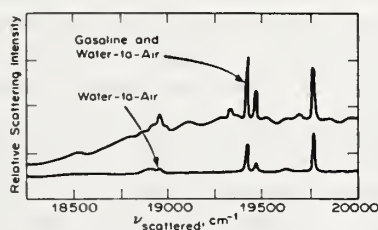


Fig. 7 Raman spectrum of an air to gasoline on water interface. Laser pump at 20487 cm^{-1} . Air-to-pure-water interface scattering shown for comparison.

samples but not with upper-river or NaCl solution samples. More research is required on controlled samples, but the potential for remote sensing of actual water pollution is demonstrated.

Interface scattering from air to pure water and from air to gasoline on water interfaces is sketched in Fig. 7. Details of the spectrum are not yet analyzed. An obvious conclusion is that there is a significant difference in the spectra. The broadband increase and some of the enhanced spectral peaks in the gasoline-on-water spectrum are most likely instrumental scattering and grating ghost effects associated with the increased on-frequency particulate scattering of the polluted interface. Other spectral features of the upper spectrum are due to the presence of the gasoline film on the water.

V. Conclusions

Raman lidar is a potentially useful tool for remote sensing of atmospheric and water-borne pollution distributions at least in near-source concentrations.

Our laboratory studies of pollutant systems have provided quantitative cross sections for some gaseous pollutants, and have demonstrated that significant changes in cross section occur with small changes in pump frequency. Proper selection of laser pump is important to optimize Raman lidar systems.

Studies of chemically and thermally polluted air-water interfaces have demonstrated the feasibility of mapping water-pollutant distributions by Raman lidar. Detailed analysis of the spectra is yet required to evaluate the practicality of the schemes.

References

- Widhopf, G. F. and Lederman, S., "Specie Concentration Measurements Utilizing Raman Scattering of a Laser Beam," *AIAA Journal*, Vol. 9, No. 2, Feb. 1971, pp. 309-316.
- Kobayasi, T. and Inaba, H., "Spectroscopic Detection of SO_2 and CO_2 Molecules in Polluted Atmosphere by Laser-Raman Radar Technique," *Applied Physics Letters*, Vol. 17, No. 4, Aug. 1970, pp. 139-141; "Laser-Raman Radar for Air Pollution Probe," *Proceedings of the IEEE*, Vol. 58, No. 10, Oct. 1970, pp. 1568-1571.
- Bradley, E. B. and Frenzel, C. A., "On the Exploitation of Laser Raman Spectroscopy for Detection and Identification of Molecular Water Pollutants," *Water Research*, Vol. 4, No. 1, Jan. 1970, pp. 125-128.
- Placzek, G., "Rayleigh-Streuung und Raman-Effekt," *Handbuch der Radiologie*, Vol. 6, edited by E. Marx, Akademische Verlagsgesellschaft, Leipzig, Germany, 1934, pp. 209-374; UCRL Translation No. 526 (L) by A. Werbin.
- Behringer, J., "Observed Resonance Raman Spectra," *Raman Spectroscopy*, edited by H. A. Szymanski, Plenum Press, New York, 1967, pp. 168-223.
- Leonard, D. A., "Measurement of NO and SO_2 Raman-Scattering Cross Sections," *Journal of Applied Physics*, Vol. 41, No. 10, Sept. 1970, pp. 4238-4239.
- Fouche, D. G. and Chang, R. K., "Relative Raman Cross Section for N_2 , O_2 , CO , CO_2 , SO_2 , and H_2S ," *Applied Physics Letters*, Vol. 18, No. 12, June 1971, pp. 579-580; "Relative Raman Cross Section for O_3 , CH_4 , C_3H_8 , NO , N_2O , and H_2 ," *Applied Physics Letters*, Vol. 20, No. 7, April 1972, pp. 256-257.
- Penney, C. M., Goldman, L. M., and Lapp, M., "Raman Scattering Cross Sections," *Nature Physical Science*, Vol. 235, No. 58, Feb. 1972, pp. 256-257.
- Walrafen, G. E., "Raman Spectral Studies of the Effects of Temperature on Water Structure," *The Journal of Chemical Physics*, Vol. 47, No. 1, July 1967, pp. 114-126.

Atmospheric Water Vapor Measurement by Raman Lidar

R. G. STRAUCH, V. E. DERR, and R. E. CUPP

*Wave Propagation Laboratory, ERL, National Oceanic and Atmospheric Administration,
Department of Commerce, Boulder, Colorado*

Measurements of atmospheric water vapor using the Raman backscatter from a pulsed laser were directly compared with measurements from meteorological instruments located on a tower. The experimental conditions and precautions required in making these observations in the atmosphere are discussed. The results indicate that water vapor profile measurement to a range of approximately 4 km is feasible with the lidar used in this experiment.

Key Words: Atmospheric water vapor, Lidar, Raman lidar, Raman backscatter, Remote sensing.

Introduction

The development of remote sensing methods for the study of man's geophysical environment offers a wealth of new data and new insights (Derr and Little, 1970). Remote sensing allows the measurement of atmospheric parameters over large volumes, in essentially real time, revealing structure and dynamics in ways not possible with *in-situ* measurements (Bean, 1971). However, because remote sensing methods often probe where no independent measurements are possible, the interpretation of the data and the limitations of that interpretation must be clearly established in order to prevent erroneous conclusions.

Although the theoretical feasibility of using laser radar to measure molecular density has been established (Derr and Little, 1970), the realization of the method, in the field, is not trivial because of the problems created by a very small signal-to-noise ratio, the spectral impurity of laser sources having usefully high power, the fluorescence in elements of the receiving system created by the on-frequency return from the atmosphere, the fluorescence of atmospheric constituents and the interference of natural and man-made radiation.¹ The magnitude of the uncertainty introduced is such that, without great care, the signal observed in a simple lidar system with a filter at the H₂O Raman wavelength will probably not be due to the water vapor Raman backscatter. Even after achieving an observation of atmospheric humid-

ity by these methods, it is necessary to make a systematic evaluation of the limitations in order to evaluate the practicality of such systems in atmospheric observation. It is the purpose of this paper to determine to what extent the feasibility of the method has been proven, to advise the directions in which improvement can be achieved, and to present the calculations from which the ultimate limitations can be determined.

Field measurement of water vapor profiles have been performed by Melfi (1969) and Cooney (1969). Each compared the normalized water vapor profile, as determined by the Raman lidar, with the profile determined by radiosondes and in addition (Cooney, 1969), with sondes borne by helicopters. The general agreement was excellent, but their experiments suffer from lack of immediacy; the water vapor profiles determined by the lidar and by the other methods were too far separated in space and time to consider the experiments conclusive, although the statistical confidence level was high. The relatively poor accuracy of radiosonde humidity measurements prevents precise comparisons, and of greater importance, the variability of the atmosphere is so large that homogeneity and stationarity can not be assumed for the distances and time periods involved. Radiosondes measure only instantaneous values at the time and place of their ascent. It is known now that even the clear atmosphere is so variable that extrapolation of such measurements in time and space cannot be assumed valid (Bean, 1971).

A convincing demonstration of the method, shown in this paper, can be obtained by examining

¹ The 3654 Å radiation from mercury street and road lights falls very near the N₂ Raman wavelength (3658 Å) under irradiation from a 3371 Å laser.

the lidar return from an atmospheric scattering volume very near a standard humidity meter. The close contiguity in space and time will allow both devices to register changes in atmospheric water vapor whenever such changes are sufficiently large to be observed within the signal-to-noise ratio limitation. After calibration, the absolute atmospheric water vapor content can be determined if mechanical, optical, and electronic stability are maintained. In addition, this work demonstrates the feasibility of measuring the fluctuations, and hence the structure functions, of atmospheric water vapor by the use of a laser producing 100 pulses per second.

Raman Spectra

The Raman spectrum of a molecule consists of scattered radiation at a different frequency from the irradiating frequency. The frequency difference between the incident radiation and the scattered radiation is a fixed, unique characteristic of the molecule and can be used to identify the molecule. By using a pulsed laser and a time-gated receiver, the density of an atmospheric constituent can be determined as a function of position.

The integrated intensity of Raman scattering is dependent on the frequency of the irradiation and on resonance denominators as shown by Behringer (Szymanski, 1967)

$$I = \frac{2^7 \pi^5}{3^2 c^4} I_0 (\nu_0 - |\nu_{mn}|)^4 \sum_{\rho\sigma} |\alpha_{\rho\sigma, mn}|^2,$$

where α is the $\rho\sigma$ ($= x, y, z$) component of the scattering dyadic

$$\alpha_{mn} = \frac{1}{h} \sum_r \left(\frac{\mu_{rn} \mu_{mr}}{\nu_{mn} - \nu_0 + i\delta_r} + \frac{\mu_{mr} \mu_{rn}}{\nu_{rn} + \nu_0 + i\delta_r} \right).$$

The intensity of the incident radiation (plane polarized) of frequency ν_0 is I_0 , ν_{mn} is a vibronic transition frequency, μ_{rn} is the transition moment of the dipole moment operator, δ_r is the damping constant of state r , c is the velocity of light, and h is Planck's constant. When the resonance denominators of α_{mn} are not small, the intensity varies approximately as the fourth power of the output frequency. Significant improvement can be made in signal power if suitable high frequency tunable lasers can be developed and irradiating frequencies chosen which will make the resonance denominators small. Initial studies on water

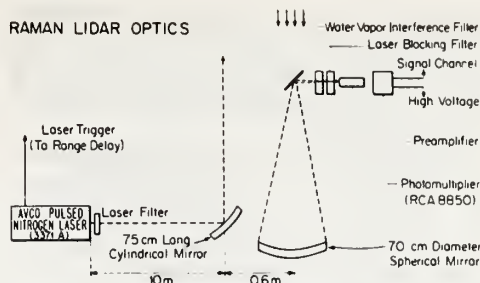
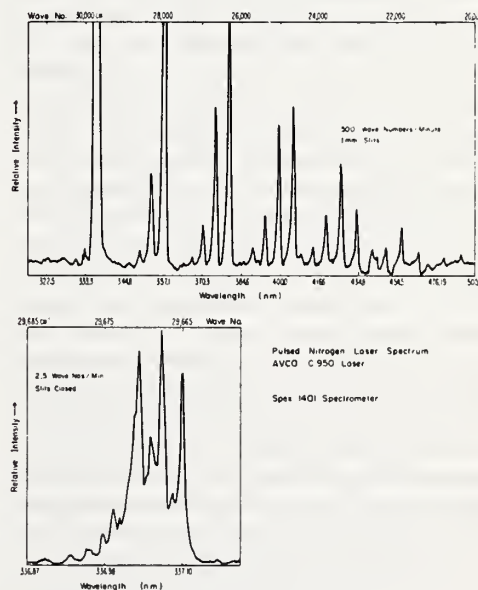


FIG. 1. Raman lidar system.

vapor have indicated an improvement in scattering cross section by resonance effects (Derr and Little, 1970).

Experimental Apparatus and Procedure

Measurements of atmospheric water vapor were made with two independent instruments, a microwave refractometer, and the Raman lidar. The refractometer was located at the 30.5-m level of a meteorological tower and the laser beam passed approximately one meter from the microwave cavity. The backscattered laser signal was observed from a region approximately 20 cm in



diameter and 5 m in length centered at the height of the microwave cavity. The length of the backscattering region was determined by the geometry of the crossing of the transmitter and receiver beams.

The transmitter consisted of an Avco-Everett model C950 pulsed nitrogen laser, an interference filter centered at the transmitter wavelength (337.1 nm) and a 75-cm aperture cylindrical focusing mirror located approximately 10 m from the transmitter. The lidar arrangement is shown in Fig. 1. The peak power output of the laser is 100 kW with a 10-ns pulse width and a repetition rate of 100 pulses per second. The power and repetition rate provide signal returns that allow electronic processing of analog signal levels rather than oscilloscope photography and photon counting. The laser has provided excellent field reliability. It has two disadvantages for atmospheric Raman scattering measurements; the beam divergence is large (specified at 2×27 -milliradian half angle), and the output spectrum contains fluorescent lines that can interfere with Raman measurements. The 27-milliradian beam divergence is partially corrected by the cylindrical mirror shown in Fig. 1, so that the resulting beam pattern can be collimated with approximately 2×5 mr half angle, or as in this experiment, focused at the 30.5 m level of the meteorological tower to a spot about 20×10 cm. (This arrangement has disadvantages for profile experiments because coaxial receiver-transmitter optics are not practical. Coaxial optics allow transmitted and received beams to overlap even at short ranges.) The output spectrum of the laser is shown in Fig. 2. The desired output occurs from a group of lines separated by about 0.1 nm centered near 337.1 nm as shown in the lower trace. The upper trace shows the principal undesired outputs. A photographic plate, not shown, taken on a Bausch and Lomb 2-m dual grating spectrograph shows these spectra are the heads of emission bands. The strongest of these bands occurs at 357.7 nm. A backscattered signal trace using a Jarrel-Ash Model 28-410 spectrometer showed that this strongest emission gave an on-frequency backscattered signal from aerosols approximately equal to the Raman backscatter from atmospheric oxygen when no laser filter was used. The undesired emissions are weak in the wavelength region of the Raman water return (384.4 nm), and are adequately suppressed by the

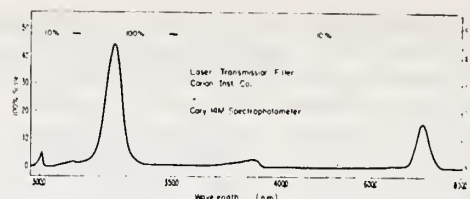


FIG. 3. Spectral response of laser transmission filter.

interference filter whose response is shown in Fig. 3. The transmittance of this filter is 43% at the laser output, with less than 0.1% transmittance in the region of the strongest undesired emission. A spectrograph of the backscattered signal shows only nitrogen, oxygen, and water vapor Raman spectra in addition to the strong on-frequency scattering when the laser transmission filter is used.

The receiver arrangement is also shown in Fig. 1. A 70-cm-diameter spherical mirror was used in an f/3 Newtonian telescope. The received signal passed through an interference filter centered at the water vapor Raman wavelength followed by a laser blocking filter. The blocking filter is a 1-cm path length water solution (0.2 gms/liter) of 2,7 dimethyl-3,6 diazacyclohepta-1,6 diene perchlorate (Leonard, private communication) with CuSO_4 (100 gms/liter) in a quartz vial. The interference filter was placed in front of the laser blocking filter because it exhibits less fluorescence from the strong on-frequency return. The liquid blocking filter characteristics are shown in Fig. 4. The CuSO_4 provides the visible cutoff in the red where both the laser transmission filter and the water vapor interference filter leak and where the photomultiplier

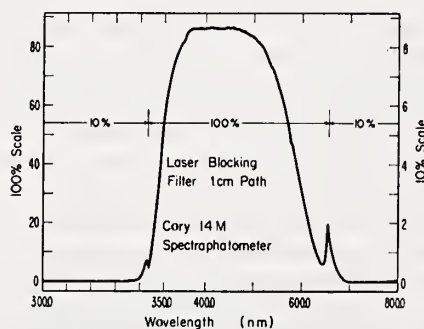


FIG. 4. Spectral response of laser blocking filter.

response is still significant. The dye solution provides nearly total attenuation at the laser output frequency. Transmission at 337.1 nm through this filter is less than a factor of 10^{-6} . The strong on-frequency returns are reduced by a factor less than 10^{-9} , and the on-frequency backscatter from the principal undesired laser emissions are reduced by a factor less than 10^{-5} by the combination of the laser interference filter and the two receiver filters. Thus, except for the desired Raman signals, the filter combination provides blocking over the entire range of the RCA 8850 photomultiplier response. The filter combination does not provide adequate filtering for backscattered nitrogen and oxygen Raman signals. The interference filter transmittance shown in Fig. 5 has a leakage of about 0.15% for

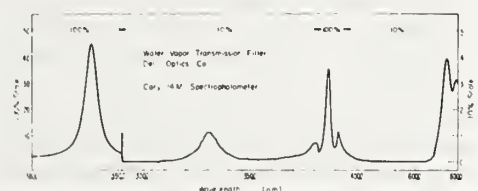
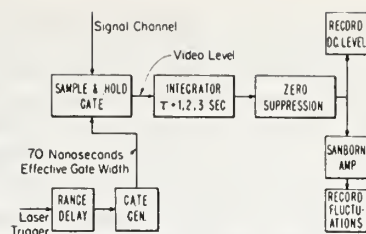


FIG. 5. Spectral response of water vapor transmission filter.

nitrogen Raman (365.8 nm) and about 0.05% for oxygen Raman (355.6 nm) as compared with a peak transmittance of 43%. (The average transmittance at 384.4 nm is less than 43% because the center frequency of the filter is not exactly 384.4 nm and because of the angular transmittance characteristics. The transmittance at 365.8 and 355.6 nm is not sensitive to angle variations for the $f/3$ optics. The average transmittance of the filter combination at the water vapor Raman frequency is estimated at 25%.) Since the N_2/H_2O pressure ratio for these experiments is about 150, some N_2 Raman signal leakage is anticipated. (See discussion.) Subsequent to performing these experiments, a suitable filter was found for passing the H_2O Raman and rejecting N_2 and O_2 Raman signals. It consists of a 1-cm path of a solution of Alpha-NPO (0.2 gm/liter of methyl alcohol).

The lidar electronic data processing system is shown in Fig. 6. The video level from the photomultiplier preamplifier is sampled after each pulse and a voltage proportional to the peak signal level



RAMAN LIDAR ELECTRONIC DATA PROCESSING

FIG. 6. Raman lidar electronic data processing system.

during the sampling period is held until the next pulse. The step-like signal level is smoothed with a 3-second time constant and recorded on one channel of a Sanborn strip chart recorder. This type of processing is useful for signals consisting of 1 or more photons received per pulse as in this experiment. A low-frequency counter on the sampled video level can be used to count photons if the signal level is less than 1 photon per pulse.

The meteorological measurements of water vapor were made using a Colorado Research Corp., Model 504900 microwave refractometer, a thermistor mounted approximately 5 cm from the microwave cavity, a Wallace and Tiernan Model FA 181 pressure gauge located at ground level, and a psychrometer located at the 30.5-m. tower level. Thermistor temperature and refractive index were continuously recorded with a 3-second time constant on other channels of the strip chart.

The experiments were conducted in November 1970 at Gunbarrel Hill, about 10 miles east of Boulder, Colorado. The water vapor content averaged 4 mb² (total pressure was approximately 830 mb). The temperature range for these experiments was 0–15°C. Dry bulb and wet bulb temperature were measured about every 30 minutes. The pressure was read at ground level and a 30.5-m altitude correction was made. Pressure was read about every 30 minutes or whenever a measurable (0.1 mb) pressure change occurred. Thermistor temperature and microwave refractive index were continuously recorded with calibration checks about every 30 minutes. The experiments were performed at night, and the background and dark current were low enough to make the Poisson noise of the signal the dominant

² 1 millibar = 10^3 dyne cm^{-2} .

lidar system noise. The signal level was continuously recorded with frequent zero level checks made by blocking the transmitter beam. The background noise level, with the laser beam blocked, was negligible shortly after sundown. The receiver and transmitter were aligned optically and electronically (range calibration) using a fluorescent target. The laser beam passed the 30.5-m level approximately one meter from the microwave cavity. An attempt to duplicate alignment, laser power settings and electronic gain from night to night was only partially successful, because of lack of electronic and mechanical stability. Experiments were conducted during nights when relatively large fluctuations of refractive index and Raman signals indicated that volumes of air with varying water vapor content were passing the laser beam.

Experimental Results

The experimental results were analyzed to allow them to be presented as a graph of Raman signal level versus water content. The meteorological equipment recorded temperature (T) in degrees Kelvin, microwave refractive index³ (N), and atmospheric pressure (P) in millibars. The partial pressure of water vapor (E) in millibars can be computed by (Bean and Dutton, 1966) Eq. (1),

$$E = \frac{NT^2 - 77.6PT}{3.75 \times 10^5 - 5.6T} \quad (1)$$

The absolute water content must be determined by using the partial pressure of water vapor, the total atmospheric pressure, the temperature, and the gas law. In the experiments reported the absolute water content is approximately proportional to the partial pressure, since the temperature and pressure variations average less than 2°.

In applying this equation, it is necessary to know the accuracy of the P , T , and N measurement in order to know the accuracy of E . Temperature accuracy is $\pm 0.2^\circ\text{K}$; the uncertainty is due mainly to strip chart reading and drift. The thermistor calibration was checked with dry bulb temperature readings and the dry bulb thermometer was checked with an ice bath. The

³ The refractive index n is often measured in "N units" where $N = (n - 1) \times 10^6$.

pressure was read on the ground and compensation was made for the 30.5-m elevation of the cavity. The Wallace and Tiernan pressure gauge was calibrated with a precision mercury barometer, and thus pressure measurements were accurate to ± 0.2 mb. The microwave refractometer was calibrated by using a psychrometer and pressure gauge to calculate N by Eq. (1). The N values recorded by microwave refractometer and those calculated using psychrometer and pressure measurements differed by 4 ± 2 N units. The uncertainty arises not from the refractometer but from variations in wet bulb-dry bulb readings. Several psychrometers were used and all exhibited variations in temperature readings. Different psychrometers did not give agreement in calculating N to better than ± 2 N units. The large wet bulb depression could account for some of the variations. Using these uncertainties, the uncertainty in E for the average conditions for this experiment can be found from Eq. (1) as 0.42 mb. This uncertainty can be regarded as the uncertainty in the zero of the scale for E . The relative uncertainty of E values during an experiment is less than 0.42 mb since the changes in E do not rely on the psychrometer data. The relative uncertainties are $\pm 0.2^\circ\text{K}$, ± 0.2 mb, and ± 0.2 N units giving a relative uncertainty in E of 0.04 mb. The uncertainty in relative N values is due primarily to strip chart reading and drift. The accuracy of the measurement of water vapor fluctuations is more significant than the absolute accuracy in this experiment.

The signal-to-noise ratio of the Raman lidar output is determined by the signal statistics. The number of Raman water vapor signal photons received at the photomultiplier output per transmitted pulse is given by (neglecting attenuation)

$$N_R = \frac{N_T \eta_T \sigma_{H_2O} \rho_{H_2O} L A_R \eta_R \eta_q}{r^2},$$

where

N_T = number of photons transmitted per laser pulse (1.7×10^{15}),

η_T = transmitter efficiency (filter and collimating mirror) ($\approx 36\%$),

σ_{H_2O} = cross section of water vapor at 3371 nm ($\approx 1.86 \times 10^{-33}$ m²/steradian) (Derr and Little, 1970),

ρ_{H_2O} = density of water molecules (1.06×10^{23} m⁻³ for $E = 4$ mb),

L = path length of interaction (5 m),
 A_R = receiver aperture (0.36 m²),
 η_R = receiver efficiency ($\approx 20\%$),
 η_d = detector quantum efficiency ($\approx 25\%$),
 and
 r = range (30.4 m).

The approximate signal photon count per transmitted pulse using the estimates in parentheses is 14. The expected signal-to-noise ratio for a 3-second integration time and a pulse repetition rate of 100 per second is 65. The actual signal-to-noise ratio observed for a typical experiment was approximately 30 for the total return signal.⁴

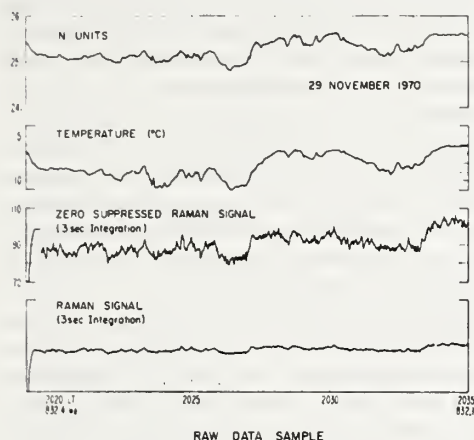


FIG. 7. Raman lidar data sample.

As exemplified in Fig. 7, the changes in water vapor were usually neither large nor frequent in the dry Colorado climate. In order not to bias the choice of data points they were chosen every 400 seconds and also chosen more frequently when large fluctuations of water content occurred. By the latter choice, large changes were always included, regardless of where the data spaced by 400 seconds fell, and the spaced data included trends in the data so that possible instability of optical and electronic equipment would be detected by a failure of correlation between the refractometer and the lidar measurements. Specifically, "large" fluctuations were defined as

⁴ The uncertainty in the value of the scattering cross section can account for the difference in the measured and calculated signal-to-noise ratio.

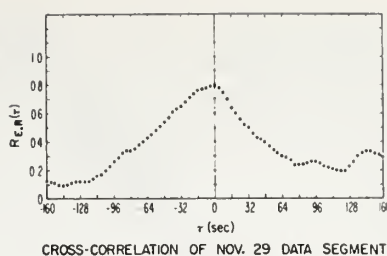


FIG. 8. Cross correlation of water vapor raman backscatter intensity with the water vapor as measured by a microwave refractometer.

changes exceeding 10% of full scale. The number of points chosen by each criterion were approximately equal. After selecting the data points, E was computed and the relative Raman signal level (R) was read. The data points were plotted and a least squares fitting of the data to the equation $R = SE + B$ was made, where S is the slope and B is the Raman signal intercept at $E=0$. The section of record shown in Fig. 7 was analyzed by reading data points every 4 seconds (237 points) and performing a cross correlation of the E and R time records. This correlation is shown in Fig. 8. The peak correlation is 0.8 and falls to 0.4 at about a 1-minute delay. The decay time is indicative of the scale size of the atmospheric fluctuations and of the wind speed. Figure 9 shows the data from one night, and the mean and rms deviation of the experimental R values from the calculated straight line are listed. The positive intercept indicates

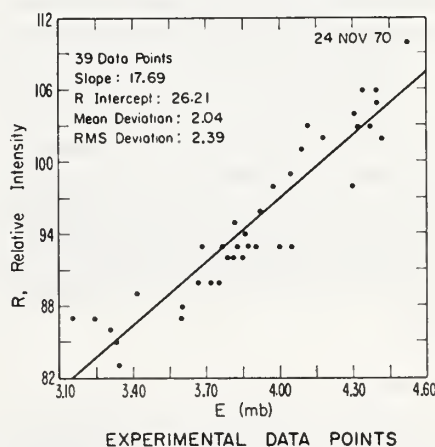


FIG. 9. Relative raman backscatter intensity versus measured water vapor content.

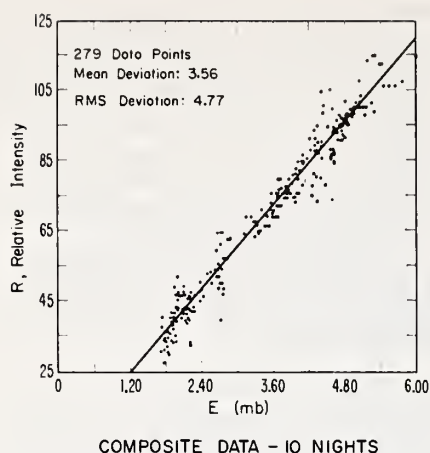


FIG. 10. Composite data: relative raman backscatter intensity *versus* measured water vapor content.

that the backscattered signal does not consist only of H_2O Raman. Most of the extraneous signal is from N_2 Raman scattering, but a portion of it could be from fluorescence. Variations in laser power, gain settings, mirror reflectivity, alignment, etc. on different nights were accounted for by normalizing the data to a fixed slope (20) for the straight line fit. The normalized intercept varied for different nights. The N_2 Raman signal would contribute an approximately constant normalized intercept. The variations of the intercept arise from two factors: (1) during any single night, the variation of H_2O was limited to approximately 1 mb so the accuracy of the intercept determined from a single experiment is low and (2) variations in fluorescence will cause a varying extraneous signal. Fluorescent signals can be caused by pollutant molecules, aerosols, or from a very small backscattered signal from structural supports near the microwave cavity. The data from each night were normalized to make the equation of the fitted straight line have a slope of 20, and zero intercept. Composite data from 10 different nights are shown in Fig. 10. Experiments in which the total range of water vapor variations was less than 0.5 mb were not included.

Discussion

In examining the data it is important to remember that the Raman lidar is observing backscatter from a column of atmosphere

approximately 20 cm in diameter and 5 m in length whereas the refractometer measurement of water vapor is from an X-band microwave cavity and point measurement of temperature. Perfect correlation is not expected because the instruments are observing changing conditions in the atmosphere and the lidar is observing a column of air while the refractometer measurements, by comparison, are nearly point measurements. The average total time represented by the data points for a single experiment is approximately 2 hours. A better correlation would be expected if only data points representing changes of water vapor with scales much larger than the lidar observation volume were plotted. Changes of this type do not occur sufficiently often to perform the experiment in this manner. The expected correlation between measurements taken with a volume sensor and those taken with a point sensor will depend on the dimensions of the volume observed by the volume sensor, the inner and outer scales of turbulence and the wind velocity. It should also be noted that these experiments were conducted in relatively dry air ($E = 1.7\text{--}6$ mb) which reduces the S/N ratio and accentuates any signal variations not arising from water vapor.

The average value of the signals that are not backscattered from H_2O can be attributed to N_2 Raman backscatter. As discussed earlier, the most likely cause of extraneous signal in this experiment is due to Raman nitrogen backscatter leaking through the receiver interference filter. The average N_2 pressure is approximately 644 mb and the $\text{N}_2/\text{H}_2\text{O}$ transmittance ratio is approximately 165. S is the Raman signal level per mb of H_2O and if the N_2 and H_2O cross sections are equal at 337.1 nm, an intercept of $644/165$ would be anticipated. The average intercept from the computed straight line fits is $1.26 S$. These experiments lead to the conclusion that the $\text{H}_2\text{O}/\text{N}_2$ cross section at 337.1 nm is approximately 3. This ratio was estimated by Cooney (1969) as 5 using a doubled ruby laser transmitter.

The effect of leakage of the Raman scattering of N_2 through the H_2O interference filter can be eliminated by simple filtering. However the fluorescence of aerosols or pollutant molecules at or near the Raman wavelength is more serious since it can not be easily separated from the desired Raman signal. Fluorescent backscatter from molecules or aerosols exactly at the Raman wavelength would be indistinguishable from the

desired Raman signal and contribute an uncertainty to the measurements. Fluorescence at the Raman wavelength was not found in this experiment (conducted in a rural environment) but may be a problem in urban areas. The Raman line width is much narrower than presently available filter bandwidths so that improved filters will assist in removing extraneous signals from all causes. Compensation for broadband interference can be made by monitoring the backscatter in a wavelength region slightly removed from the Raman wavelength.

Although in the present experiment only a single atmospheric region was probed, this equipment can be expanded to perform average $\text{H}_2\text{O}/\text{N}_2$ profile measurements by the addition of sequentially delayed sampling gates. Transmitter-receiver alignment, beam overlap, aerosol attenuation and $1/r^2$ attenuation could be programmed into the gates to give a straight line profile for N_2 Raman return. The H_2O profile would then be observed directly by substituting the appropriate interference filter. Using the measured values obtained in this experiment for signal returns, 50-meter range resolution, a 5-minute observation time, a constant $\text{H}_2\text{O}/\text{N}_2$ mixing ratio, 50% relative humidity and 20°C , the maximum altitude for observation of the $\text{H}_2\text{O}/\text{N}_2$ ratio with a S/N ratio of 10 (at night) would be 4.25 km. Improved filters and a more powerful transmitter with better collimation are obvious ways to extend the range capability. Daylight operation of Raman lidars probing the atmosphere to useful ranges will be possible with laser transmitters operating at wavelengths where ozone attenuation essentially eliminates solar background noise (less than 2900 nm). Such operation would be confined to the lower atmosphere where the ambient ozone absorption would not substantially interfere with the laser propagation.

This experiment demonstrates the need for highly critical feasibility evaluations of remote sensing methods to determine their potentialities and limitations. After initial design and construction of the instrumentation, only poor

correlation could be obtained between the Raman lidar signal and the microwave refractometer measurement of H_2O . Investigation showed that the cause of the poor correlation was the strong fluctuating signals caused by the fluorescence of the interference filter under irradiation by on-frequency returns from aerosols. Background fluorescence from the dust on the mirror and from the black paint of the telescope were also troublesome. Difficulties such as these can be observed and corrected best by a direct comparison of remote sensing techniques with instruments whose validity has been previously established. These problems were corrected to produce the excellent agreement shown in Fig. 10 by utilizing the optical arrangement shown in Fig. 1.

An effective tool for the measurement of humidity as a function of position, over large volumes, in almost real time, has been proven feasible. The present apparatus is now being developed for profile measurements.

The authors are grateful to the National Weather Service (then Weather Bureau) for some financial support early in the project and to Donald Leonard, AVCO-Everett, for data, discussion and encouragement, and to J. Cooney and H. Melfi for informative discussions.

References

- B. R. Bean, in the Proceedings of NATO Advanced Study Institute "Statistical Methods and Instrumentation in Geophysics" Skeikampen, Norway, 1971, Teknologisk Forlag A/S, Oslo, Norway (to be published).
- B. R. Bean and E. J. Dutton, *Radio Meteorology*, NBS Monograph 92 (1966).
- J. A. Cooney, *J. Appl. Meteorol.* **9**, 182 (1969).
- V. E. Derr and C. G. Little, *Appl. Opt.* **9** 1976 (1970).
- D. Leonard, AVCO Corp., Everett, Mass. (private communication).
- S. H. Melfi, J. D. Lawrence, Jr., and M. P. McCormick, *Appl. Phys. Lett.* **15**, 295 (1969).
- H. A. Szymanski (Ed.), *Raman Spectroscopy*, Plenum Press, New York (1967).

Application of Backus-Gilbert Inversion Technique to Determination of Aerosol Size Distributions from Optical Scattering Measurements

E. R. Westwater and A. Cohen

The inversion technique of Backus and Gilbert is applied to the determination of size distributions of spherical particles from optical scattering measurements. The spatial resolution inherent in a set of multiwavelength measurements is studied as a function of number of measurements, measurement noise level, and radius. The inversion technique is then applied to computer simulated intensity data to recover size distributions. These examples indicate that the distribution can be recovered at selected points without using a priori assumptions about the shape of the distribution.

1. Introduction

Light scattering (and extinction) measurements in the atmosphere polluted with particulate matter (aerosols) depend on the physical properties of the specific aerosol. Such measurements can thus provide an indirect way of inferring these properties. In general, the properties can be divided into two categories:

(1) Properties that appear as parameters in the exact theoretical scattering functions: sizes of spherical aerosols, (low) number densities, relative indices of refraction, etc.;

(2) Properties that involve an approximation in the theoretical scattering functions: nonspherical shapes, orientations in respect to the scattering plane, high number densities (= multiple scattering), etc.

The theory for any inversion method is based upon the assumption that the scattering functions are known for each particle size and for each wavelength, scattering angle (ϕ), and polarization. As a consequence, most of the theoretical work dealing with the inversion problem introduces the following approximations:

(1) The particles are either spherical or can be considered as being spherical with respect to their scattering properties. A limited number of experiments have indicated this assumption is valid for unpolarized light over a restricted range of scattering angles.^{1,2}

(2) The scattering from most aerosols is mainly (>90%) single scattering (excluding water and ice clouds).

Although these two approximations reduce the number of the aerosol parameters considerably, the scattering intensity I is still a function of several possible variables, e.g., size distribution, refractive index, etc.

One of the first widely used approaches of relating scattering information to aerosol properties was to calculate I values for a number of atmospheric aerosol models³⁻⁵ and compare the results with the scattering measurements.⁶ This method is limited in its applicability whenever the real atmosphere is of concern, and other inversion methods were developed.⁷⁻¹⁰ Most of such new inversion methods involve the following assumptions:

(1) The index of refraction is known and unique. This assumption suggests that all particles may differ from one to another only in respect to their radii.

(2) A best fit to one of the suggested possible size distribution functions should be the target of the inversion procedure, or in some cases⁹ a close resemblance to an initial guess of the particle size spectrum.

The technique used in this paper does not require a trial distribution or an initial guess to achieve results. Instead, it determines quantitatively both the resolution obtainable at an arbitrary point from a given set of measurements and the accuracy achievable from the measurements as a function of noise level. Below we summarize the main features of the Backus-Gilbert¹¹ inversion procedure and, after a discussion of the relevant weighting functions for scattering, apply the technique to the particle size distribution inversion problem.

The authors are with the National Oceanic and Atmospheric Administration, Environmental Research Laboratories, Boulder, Colorado.

Received 26 December 1972.

II. Summary of the Backus-Gilbert Inversion Technique

Linear inverse problems frequently reduce to inferring properties of $f(r)$ from the integral equation

$$g_i = \int_a^b K_i(r) f(r) dr, \quad i = 1, 2, \dots, n, \quad (1)$$

where g_i is the result of the i th of n physical measurements, and $K_i(r)$ is the known weighting function at radius r . In general, g_i is measured with an error ϵ_i . We assume the errors are distributed with mean zero and a known covariance matrix S_i given by

$$S_i = E\{\epsilon\epsilon^T\}, \quad (2)$$

where E is the expected value operator over the joint probability density of errors $\epsilon = [\epsilon_1, \epsilon_2, \dots, \epsilon_n]^T$. The superscript T represents matrix transposition.

Below, we summarize basic equations and ideas developed by Backus and Gilbert¹¹ in solving Eq. (1) that are later applied to remote sensing of size distributions.

Weighted linear averages of a function $f(r)$ over a region (a, b) are formed by

$$\langle f, A \rangle = \int_a^b A(r) f(r) dr, \quad (3)$$

where the unimodular averaging kernel $A(r)$ satisfies

$$\int_a^b A(r) dr = 1. \quad (4)$$

The Backus-Gilbert technique constructs averaging kernels with properties suitable for an inversion algorithm. The averaging kernels can be formed as a linear combination of the weighting functions $K_i(r)$ as

$$A(r) = \sum_{i=1}^n a_i K_i(r). \quad (5)$$

The average given by Eq. (3) can be considered as representative of the local value of f at r_0 if A is large around this point and small elsewhere, i.e., if $A(r) \sim \delta(r - r_0)$, where $\delta(r)$ is the Dirac delta function. We can thus choose $a_i = a_i(r_0)$ to best approximate the delta function (in the mean square sense)

$$\begin{aligned} g(\mathbf{a}) &= \int_a^b [A(r) - \delta(r - r_0)]^2 dr \\ &= \min \end{aligned} \quad (6)$$

and determine the local average of f

$$\begin{aligned} \langle f(r) \rangle_{r_0} &= \int_a^b A(r_0, r) f(r) dr \\ &= \sum_{i=1}^n a_i(r_0) g_i. \end{aligned} \quad (7)$$

A somewhat more useful quantity to minimize is the spread $s(r_0)$,

$$s(r_0) = 12 \int_a^b (r - r_0)^2 A^2(r) dr, \quad (8)$$

$$= \mathbf{a}^T S \mathbf{a}, \quad (9)$$

where matrix elements of S are given by

$$S_{ij} = 12 \int_a^b (r - r_0)^2 K_i(r) K_j(r) dr, \quad (10)$$

and

$$\mathbf{a} = [a_1, a_2, \dots, a_n]^T. \quad (11)$$

The spread is normalized such that a rectangular averaging kernel centered at r_0 with width = l and height = l^{-1} has $s(r_0) = l$. Minimizing either Eq. (6) or Eq. (8) yields values of \mathbf{a} that can be used in the inversion algorithm Eq. (7). In addition, the spread $s(r_0)$ can be used to express the amount of resolution inherent in the set of weighting functions K_i .

In addition to resolution, it is necessary to consider the effect of errors in g_i on the error in $\langle f(r) \rangle_{r_0}$. The variance of

$$\langle f(r) \rangle_{r_0}, \quad V[\langle f(r) \rangle_{r_0}] \text{ is given by } V[\langle f(r) \rangle_{r_0}] = \mathbf{a}^T S \mathbf{a}. \quad (12)$$

As is shown in Backus-Gilbert, improvement in accuracy (reduction in variance) is achieved only by degrading the resolution (increasing the spread), and for any physical problem some compromise between these quantities must be made. This compromise can be specified by choosing a point on a trade-off curve between error variance and resolution. If we parametrize this curve by θ , where $0 \leq \theta \leq \pi/2$, the Backus-Gilbert inversion equations are

$$\mathbf{a}(\theta) = [\mathbf{u}^T W(\theta)^{-1} \mathbf{u}]^{-1} W(\theta)^{-1} \mathbf{u}, \quad (13)$$

where

$$(\mathbf{u})_i = \int_a^b K_i(r) dr, \quad (14)$$

and

$$W(\theta) = S \cos \theta + w S_i \sin \theta, \quad (15)$$

and w is an arbitrary numerical constant.

Note that $\theta = 0$ yields the minimum spread (maximum variance) solution, while $\theta = \pi/2$ yields the opposite extreme of minimum variance (maximum spread). Also, the minimum variance solution is independent of r_0 . A convenient choice of w is such that S and $w S_i$ will be of comparable numerical size. In a practical problem, an entire trade-off curve should be drawn from which an appropriate choice of θ is selected.

In addition to immediate application to inversion of data, the Backus-Gilbert technique can be applied to a variety of considerations relevant to experimental design. Among these are: (1) what is the effect of measurement error on resolution? (2) what is the effect on the resolution when the number of measurements is increased?

In the following sections, we apply the Backus-Gilbert formalism to these questions that arise in remote inference of size distributions.

III. Optical Weighting Functions

We shall now examine briefly the behavior of the kernel of the integral equation (1), namely, the Mie scattering intensities (MSI) as a function of the parameters radius r , wavelength λ , scattering angle ϕ , refractive index m , and polarization P . The main characteristics of the dependence on the size-parameter $\alpha = 2\pi r/\lambda$ are the nonmonotonic fluctuations of the scattering intensity as a function of the aerosol size; for example, three periodicities can be found^{12, 13}: $\sim 0.8 \cdot \alpha$, $\sim 2(m-1) \cdot \alpha$, and $0.277 \cdot \alpha$. When calculating the intensity, for an α , the number of maxima (or minima) is dependent on the sampling interval $\Delta\alpha$ used in the computation. For example, when $\Delta\alpha = 0.1$ the MSI curve for $m = 1.33$, $\phi = 90^\circ$, and $30.0 \leq \alpha \leq 60.0$ contains 89 pairs of extremum α values vs 131 pairs, when $\Delta\alpha = 0.01$. These results illustrate that caution should be exercised when choosing an appropriate sampling interval. This choice should depend on the wavelength or angular resolution of the measuring system, as well as on some physical assumptions on the distribution of the particles sizes. For example, to determine particle radii to 1%, say $r = 1.0 \pm 0.005 \mu\text{m}$, the use of a common dye laser near $\lambda = 0.6 \mu\text{m}$ and $\Delta\lambda \leq 0.1 \text{ nm}$ for the scattering measurement will make the use of $\Delta\alpha$ steps smaller than 0.1 unnecessary (in this example, $10.42 \leq \alpha \leq 10.52$). This is based on the assumption that the MSI curves calculated for well defined α values in steps of $\Delta\alpha = 0.1$ represent to a

good approximation the MSI curves of the scattering values averaged over a range of $\Delta\alpha = 0.1$.

An experimental measurement of the MSI's as a function of wavelength performed by one of us¹⁴ provides additional evidence to the validity of the above assumption, as well as a verification for the applicability of the Mie scattering theory to real spheres. Another result of this laboratory experiment is the sensitivity of the MSI to small variations of the refractive index. It is shown by comparing the experimental Mie curve for a wavelength range of 30 nm ($441 \text{ nm} \leq \lambda \leq 471 \text{ nm}$) and monosized scattering particles of $r = 2.956 \mu\text{m}$ (in one of the experiments), to the MSI computed curve, a shift in the positions of the maxima and minima is obtained (with respect to α values) when an average refractive index is assumed for the whole wavelength range. In Fig. 1 an example of this effect can be seen by comparing the MSI curve obtained for $r = 4.5 \mu\text{m}$ and $m = 1.33$ in the visible range with the one calculated for $m = f(\lambda)$. For specific α values the ratio of the two MSI values $\{I(m = 1.33)/I[m = f(\lambda)]\}$ can reach a value of 100 or more, but since the method of inversion yields the number density of particles for a range of r , the effect of small variations of the refractive index is reduced, but not negligible. Thus, in calculating the MSI's for different wavelengths the refractive index dispersion effect should be taken into account.

The MSI's show also nonmonotonic fluctuations as a function of the scattering angle ϕ with an increasing number of fluctuations for a range of ϕ as α increases. The main characteristics of the dependence on the scattering angle is the much stronger forward scattering efficiency as compared with other scatter-

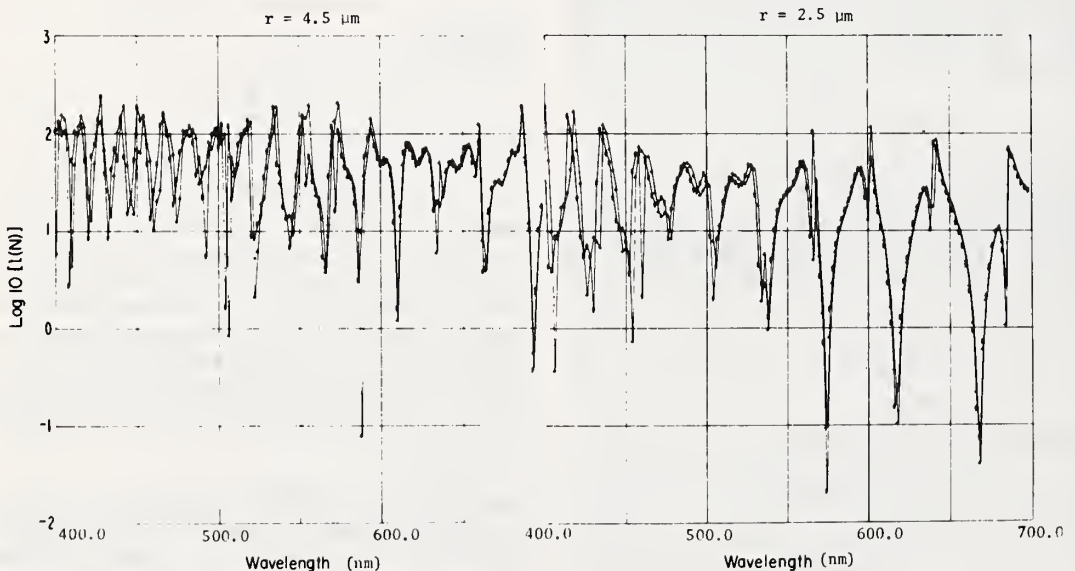


Fig. 1. MSI curves at radii of $4.5 \mu\text{m}$ and $2.5 \mu\text{m}$ for $m = 1.33$ and $m = f(\lambda)$. $i(n)$ is the scattering intensity of the component normal to the scattering plane, for a scattering angle of 90° . $+$ — $m = 1.33$; $-$ — $m = f(\lambda)$.

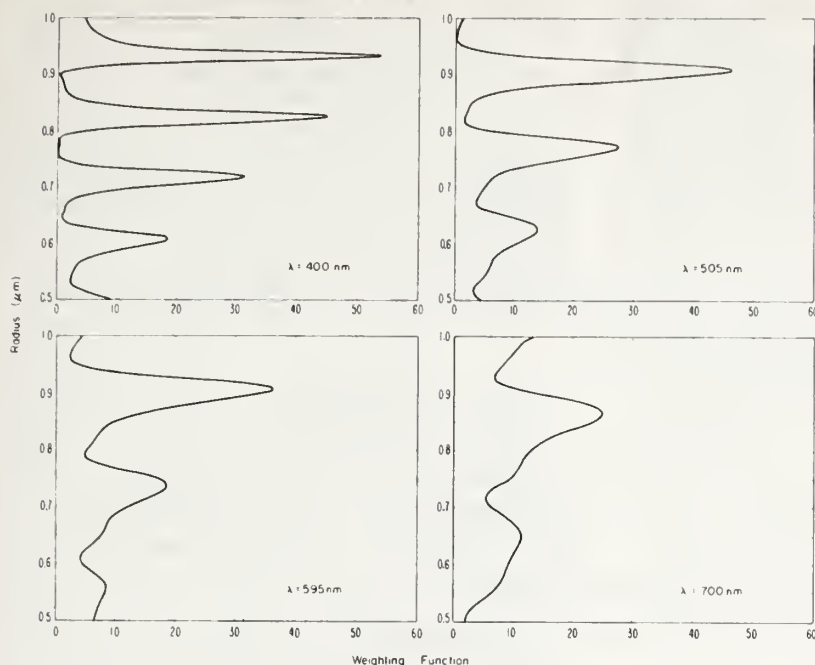


Fig. 2. Weighting functions for multispectral 90° scattering in relative units.

ing angles. The minimal scattering efficiency is obtained near $\phi \sim 90^\circ$. Since the variations of intensity with scattering angle also contain information on the size distribution⁸ it is important to note that the method of inversion described here can be applied to scattering measurements with an arbitrary combination of scattering angle and wavelength. Since the MSI's can also be separated into the four Stokes parameters, additional information can be achieved by polarization measurements, for which weighting functions can be calculated.

Note that extinction measurements can also be inverted using the Backus-Gilbert method, but since extinction processes involve scattering in all angles (and absorption) the resulting extinction curves as a function of α show less fluctuations (relative amplitude and frequency) than the corresponding scattering curve. This suggests that the extinction measurements in different wavelengths are less independent than those obtained by scattering measurements.

In the following sections we study inversion of multiwavelength scattering measurements to determine size distributions. This example supplements an experiment being done by one of us (AC) and provides a new application of the Backus-Gilbert technique.

IV. Averaging Kernel Calculations

In addition to the assumptions mentioned above, the feasibility of remote sensing of size distributions depends on the spatial resolution inherent in the

measurements and of the effect of experimental errors on this resolution. Numerical examples are given below to illustrate the applicability of the Backus-Gilbert technique to studies of these questions.

A basic set of twenty-one weighting functions representing 90° scattering was chosen over the wavelength interval 400–700 nm in steps of 15 nm, and the size range 0.5–1.0 μm . The refractive index was $m = f(\lambda)$ (~ 1.33) as discussed in Sec. III. Typical examples of the weighting functions are shown in Fig. 2. The MSI of all functions was expressed in the same relative units. This was achieved by multiplying all intensity values (calculated as a function of the size parameter α) by the corresponding λ^2 . The other constants determining the absolute scattering irradiances are common to all wavelengths. For a given size range, decreasing the wavelength increases the fluctuations in the weighting functions; conversely, increasing the size range increases the number of maxima and minima for all wavelengths. As discussed in Sec. II, the Backus-Gilbert inversion method constructs an approximation to a delta function at r_0 from a linear combination of weighting functions. This construction will be successful only if enough independent measurements are available to allow cancellation except at radii near r_0 . Intuitively, this number will be somewhat higher than the number of oscillations that the weighting functions exhibit over the size range of particles. To illustrate the Backus-Gilbert technique, we restricted the size distribution to $0.5 \mu\text{m} \leq r \leq 1.0 \mu\text{m}$. For a larger interval, both a larger

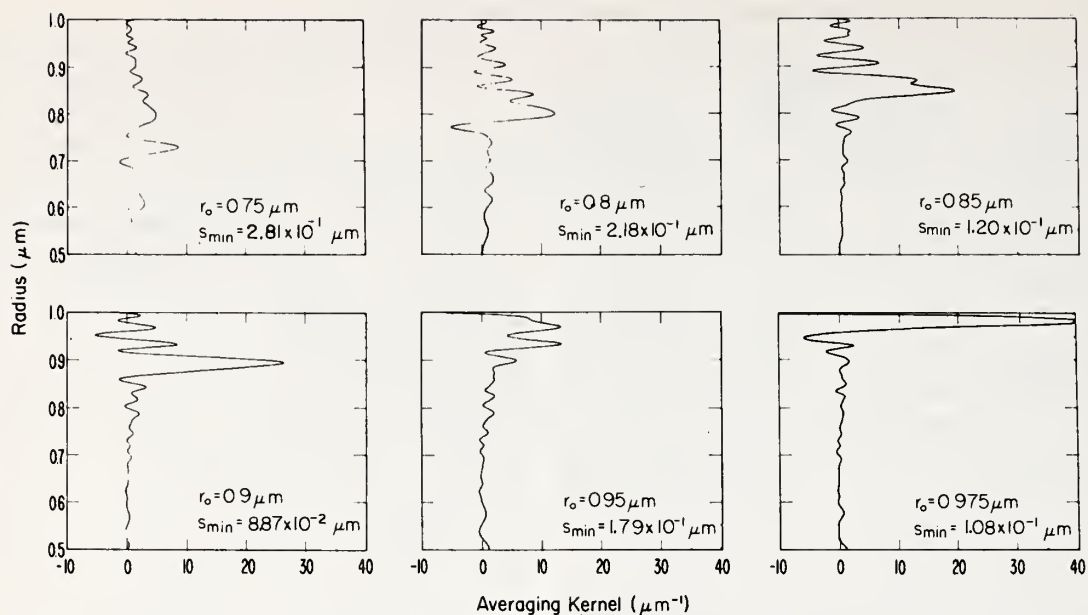


Fig. 3. Averaging kernels constructed from twenty-one multispectral weighting functions. The wavelength interval was 400-700 nm.

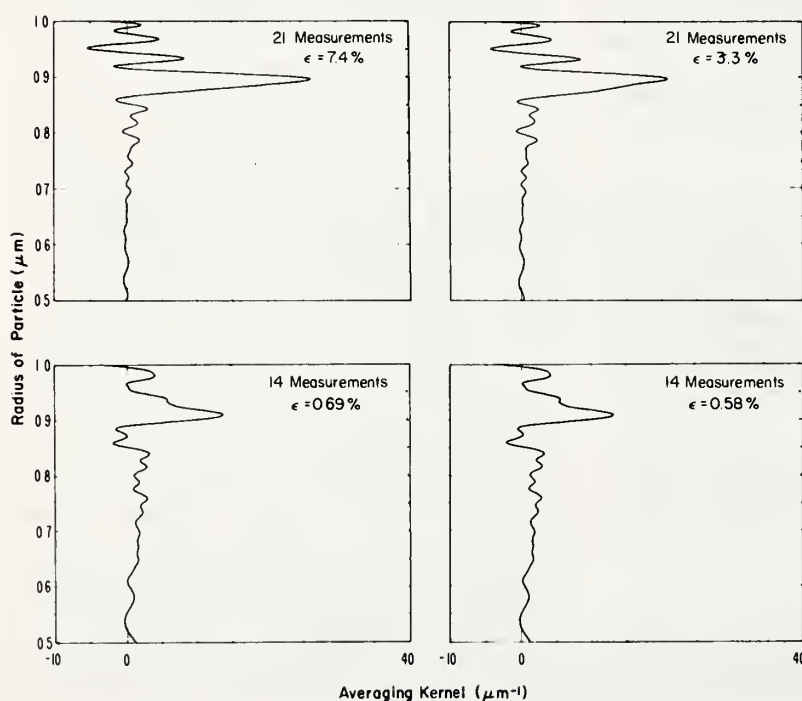


Fig. 4. Averaging kernels at $r_0 = 0.9 \mu\text{m}$ constructed from fourteen and twenty-one multispectral weighting functions. The wavelength intervals were 400-595 nm and 400-700 nm. The two curves on the right have greater than minimum spread.

number of measurements and a larger wavelength interval are necessary to construct adequate averaging kernels.

Averaging kernels were constructed from the set of twenty-one weighting functions using Eq. (5). The coefficients $a_i = a_i(r_0)$ were determined by minimizing the spread $s(r_0)$ given by Eq. (8). Each of the elements of the spread tensor S_{ij} was calculated by integration with Simpson's rule using 751 points. The results are shown for a variety of radii r_0 in Fig. 3. As would be expected from the increasing contribution to the weighting functions at larger radii, the averaging kernels generally show better resolution at larger r_0 . Table I shows minimum spreads for several choices of radii r_0 .

In general, because of the oscillatory nature of the weighting functions, the spread $s(r_0)$ may be a fairly sensitive function of r_0 . An example of this sensitivity is shown by the averaging kernels at $0.95 \mu\text{m}$ and $0.975 \mu\text{m}$. The function at $0.95 \mu\text{m}$ is a rather poor averaging kernel, while the one at $0.975 \mu\text{m}$ has a much smaller spread. Thus, in inferring a smooth distribution from a set of point inversions, it might be possible to infer the entire curve from a few well-chosen points. Attempts to construct delta functions at $r_0 = 0.90 \mu\text{m}$ were also made with seven, fourteen, and twenty-one weighting functions. Averaging kernels constructed from seven weighting functions bore little resemblance to the desired function. With fourteen wavelengths, the approximation was better with $s_{\text{min}} = 3.6 \times 10^{-1} \mu\text{m}$ (72% of the interval). The addition of seven more weighting functions resulted in $s_{\text{min}} = 8.9 \times 10^{-1} \mu\text{m}$ (18% of the interval). The results obtained with any subset of the twenty-one measurements will depend on the particular elements of the subset as well as the total number of elements. Here we chose the first seven, the first fourteen, etc., without making any attempt to determine an optimum subset. The degradation of resolution by experimental error was also simulated for these measurements. A covariance matrix of the form $S_i = \sigma_i^2 I$ was assumed (I is the identity matrix). The choice of σ_i^2 corresponded to errors in the integral of the product of assumed size distributions (see Sec. V) with the weighting functions of roughly 1%. Figure 4 shows averaging kernels at $r_0 = 0.9 \mu\text{m}$ for fourteen and twenty-one measurements. The two curves on the left correspond to minimum spread and maximum error in $\langle f(r) \rangle_{r_0}$. The two curves on the right correspond to another point on the trade-off curve in which resolution is degraded to achieve better accuracy. Typical trade-off curves at $r_0 = 0.9 \mu\text{m}$ are shown in Fig. 5 for fourteen and twenty-one measurements. Each of the curves corresponds to an error covariance matrix of the form $S_i = \sigma_i^2 I$. Several features of these curves should be noted: the minimum spread s_{min} is, of course, independent of measurement error. However, the error associated with s_{min} is directly proportional to σ_i (if $S_i = \sigma_i^2 I$). Although, the minimum spread is four times smaller in the twenty-one

measurement case, the associated error is roughly 10 times larger.

As suggested by Backus and Gilbert,¹¹ it is usually desirable to work away from the extremes of the trade-off curves, so that large sacrifices in error or spread are avoided. This is particularly true when narrow resolution is obtainable, as in the twenty-one measurement case. The units on these curves need discussion. The relative error in inferring the size distribution function [i.e., relative error = $(\mathbf{a}^T S_i \mathbf{a})^{1/2} / \langle f(r) \rangle_{r_0}$] depends somewhat on the distribution itself. For the size distributions I, II, and III discussed in the next section, the units on the curves are such that multiplying the abscissas' value by 7.8, 11.9, and 8.5 gives the percentage error in the size distribution function at $r_0 = 0.9 \mu\text{m}$ for distributions I, II, and III. Thus, with 1% measurement error, about 10% error in the distribution function is obtained with $s \approx 9.6 \times 10^{-2} \mu\text{m}$ resolution. In addition, the difference between $\langle f(r) \rangle_{r_0}$ and $f(r_0)$ also depends on the distribution because of the side lobes of $A(r_0, r)$.

The achievable spread, for a given set of measurements, is quite sensitive to the assumed upper range of particle radius. Figure 6 shows averaging kernels at $r_0 = 0.75 \mu\text{m}$ constructed over the 0.5 – $1.0 \mu\text{m}$

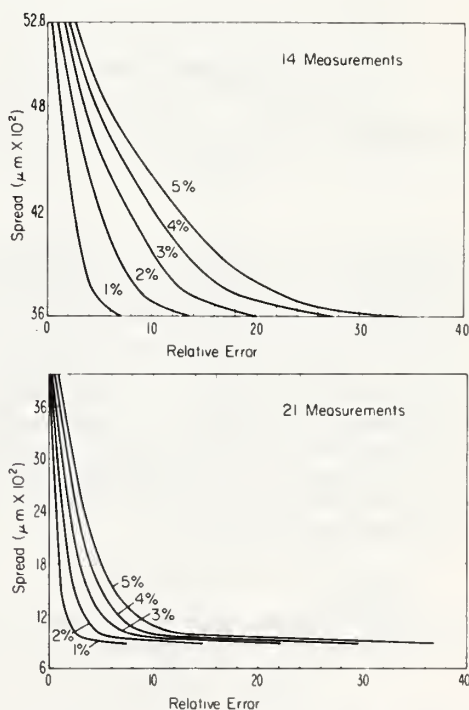


Fig. 5. Error-spread trade-off curves for fourteen and twenty-one measurements. The units are such that multiplying the abscissas' value by 7.8, 11.9, and 8.5 gives the percentage error in inferring the size distribution at $r_0 = 0.9 \mu\text{m}$ for distributions I, II, and III of Sec. IV. The curves are labeled with the assumed measurement errors.

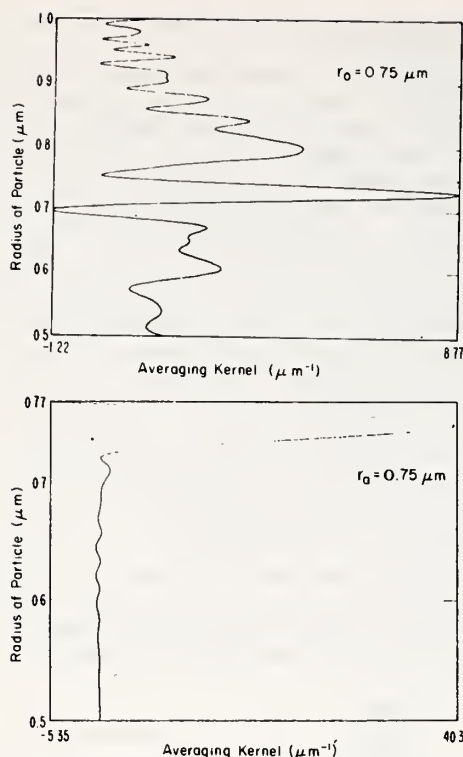


Fig. 6. Averaging kernels at $r_0 = 0.75 \mu\text{m}$ constructed from twenty-one weighting functions over the range $0.5\text{--}1.0 \mu\text{m}$ and $0.5\text{--}0.77 \mu\text{m}$.

interval and the $0.5\text{--}0.77\text{-}\mu\text{m}$ interval. The sharpness obtained in the smaller range is striking and occurs because of the elimination of the relatively higher amplitude oscillations above $0.77 \mu\text{m}$. Note the change in abscissa values which now range from minimum to maximum value of averaging kernel.

The number of particles in a given interval can also be directly inferred using a slight extension of the Backus-Gilbert technique. Suppose that instead of a delta function, we approximate some other unimodal function, say $F(r)$, as a linear combination of weighting functions $K_i(r)$:

$$\hat{F}(r) = \sum_{i=1}^n K_i(r) a_i$$

If we choose a mean square error as our norm, we choose coefficients a_i which minimize

$$\int_a^b [\hat{F}(r) - F(r)]^2 dr$$

subject to the constraint

$$\int_a^b \hat{F}(r) dr = 1.$$

An example of this type of approximation is shown in Fig. 7 in which a rectangular function of total

width $0.1 \mu\text{m}$ centered at $0.75 \mu\text{m}$ is approximated by a linear combination of twenty-one measurements. An obvious extension of this technique allows a direct inference of the total number of particles over all sizes.

IV. Inversion of Simulated Data

Three distributions were chosen to check the results of Sec. III using simulated measurements. The

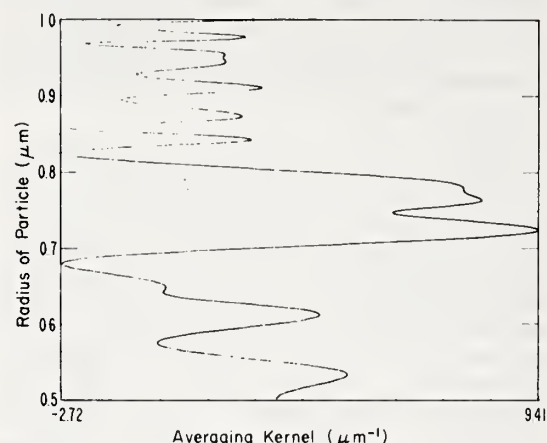


Fig. 7. Approximation of rectangular function at $0.75 \mu\text{m}$ with total width $= 0.1 \mu\text{m}$ by a linear combination of twenty-one weighting functions.

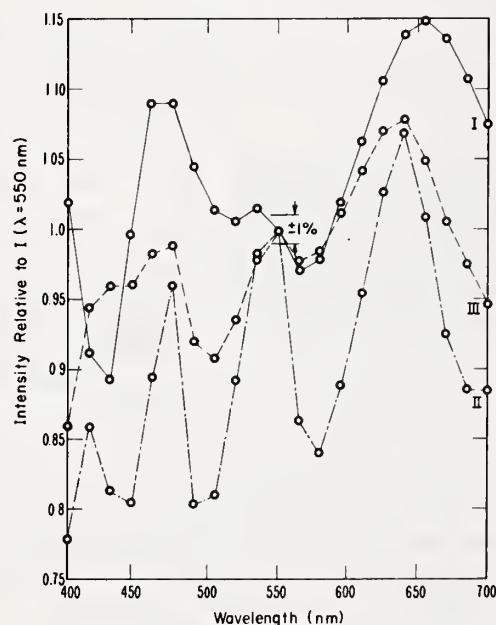


Fig. 8. Scattering intensities relative to $I (\lambda = 550 \text{ nm})$ for distributions I, II, and III. The lines drawn between points are not meant to suggest values for intermediate points.

first distribution (distribution I) represents a haze or a fog having a sharp distribution function similar to that reported by Mason.¹⁵ The second distribution (distribution II) assumes a constant number of particles for the entire range. As will be seen the accuracy achieved for the inversion of such a distribution is very high. Distribution II is therefore a measure (or rather a check) for the theoretical results calculated for various accuracies assumed in the measurements. The third distribution (distribution III) follows a power law in accordance with the well known Junge distribution and thus permits high contribution to the scattering by smaller particles. The exponent chosen in this example is -4 .

In calculating the expected scattering value for distributions I-III and the twenty-one wavelengths, the total number of particles was kept constant in the three distributions. This normalization was used to facilitate comparison of the three sets of inversion results. The intensities calculated for the distributions are shown in Fig. 8. The calculated points are connected by straight lines to differentiate between the distributions and are not meant to suggest values for intermediate points. Error bars corresponding to $\pm 1\%$ measurement error are drawn in the center of the figure. A rough measure of the SNR of the observations is the ratio of total range of intensity variation to the error. For these examples, the ratio is about 18 to 1 (in terms of standard deviations).

In inverting for the size distribution at the six radii shown in Fig. 3, the minimum spread coefficients were used with errorless intensity data while a central point on the trade-off curve appropriate to 1% error was used with data contaminated with 1% Gaussian error. The results are shown in Fig. 9. A check on the inferred results was obtained by numerically integrating the averaging kernels with the three distributions and comparing the answers directly with the inverted data. Note the inferred values of $\langle f(r) \rangle_{r_0}$ for distributions I and III are consistently higher than the true value of f . This occurs because the side lobes are positive, on the average, in regions where there are a large number of particles. The exact opposite would occur if there were a large

number of particles where the side lobes are negative. The spread (and resemblance to a delta function) of averaging kernels for radii less than $0.70 \mu\text{m}$ rapidly deteriorated, and estimates of sizes at these points were determined to be erroneous (see Table I). A useful feature of averaging kernel and spread calculations is the ability to discard *a priori* points whose spread is too large, while retaining points at which accurate results are achievable.

V. Conclusion

In this paper we have applied the inversion technique of Backus-Gilbert to the recovery of spherical size distributions from multiwavelength scattering measurements. The technique is applicable to inferring size distributions from any combination of independent wavelength, scattering angle, or polarization data. The principal advantages of the techniques are:

Table I. Minimum Spread as a Function of Radius for Twenty-one Measurements

| $r_0(\mu\text{m})$ | $s(\mu\text{m}) \times 10^2$ | Percent of total size range |
|--------------------|------------------------------|-----------------------------|
| 0.975 | 10.8 | 21.6 |
| 0.95 | 17.9 | 36.0 |
| 0.90 | 8.9 | 19.2 |
| 0.85 | 12.0 | 48.0 |
| 0.80 | 21.8 | 43.2 |
| 0.75 | 28.2 | 56.4 |
| 0.70 | 27.8 | 55.2 |
| 0.65 | 37.7 | 75.6 |
| 0.60 | 61.2 | 122.4 |
| 0.55 | 105.8 | 211.2 |
| 0.525 | 134.8 | 270.0 |

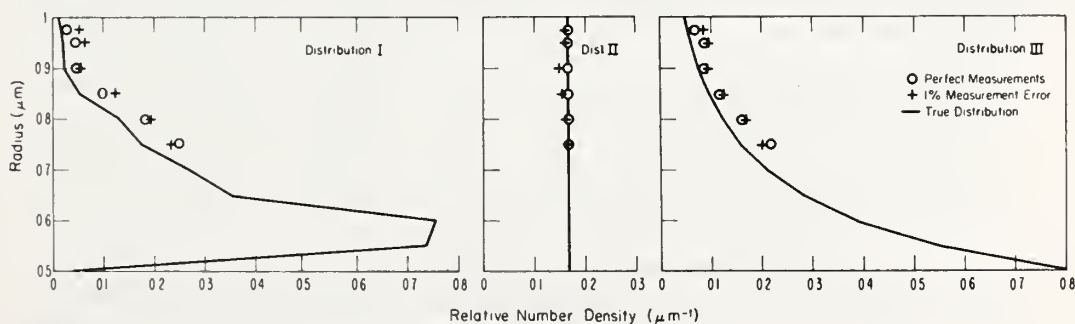


Fig. 9. Inferred size distribution function at six radii from twenty-one multispectral simulated measurements.

(1) For a given set of measurements, definite statements can be made about the achievable resolution and accuracy at any radius. The compromise between resolution and accuracy can be controlled by choosing a point on the trade-off curve.

(2) No *a priori* knowledge about the size distribution is required. However, for the type of weighting functions we encountered the achievable spatial resolution is sensitive to the total radius range of the distributions.

(3) If one is inverting for a smooth distribution, only a few accurate points are needed to infer an entire profile. The Backus-Gilbert technique allows optimum point selection.

(4) By studying the characteristics of averaging kernels at various radii, qualitative statements can be made about distinguishability of different size distributions prior to measurement of scattering intensities.

(5) The technique offers a criterion for optimum measurement ordinates, i.e., the set of measurements that gives the minimum spread for a given accuracy. Different kinds of measurement techniques can be compared by a quality criterion that does not depend on the distribution.

To illustrate the technique, we considered the problem of recovering the size distribution whose range was 0.5–1.0 μm from multispectral measurements of 90° scattering from spherical particles of known refractive index. Twenty-one equally spaced measurements from 400 μm to 700 μm were adequate to obtain spatial resolutions of less than 55% of the total range for radii greater than 0.7 μm . The accuracies in estimating averages appropriate to these resolutions were shown to be about 10% with 1% measurement accuracy. For radii below 0.7 μm the achievable spreads deteriorated rapidly. The effect of measurement number and measurement accuracy on the resolution was also studied.

Future work will include the analysis and comparison of variable scattering angle vs multispectral techniques. To provide a useful operational tool, the allowable range of sizes must be increased greatly over this study. However, the use of a tuneable dye laser at a variety of scattering angles would lead to a large volume of data from which high resolution averaging kernels could be constructed. Another

optimization study of interest is the best placement of measurement ordinates, given that the range and number of measurements are fixed.

Since this method does not depend on *a priori* assumptions about the distribution function, it could also be used to construct an initial estimate required in other inversion techniques.^{8,9} In particular, when any *a priori* assumption is questionable, this technique is appropriate. We plan to compare iterative inversions having initial estimates determined by the Backus-Gilbert method with other methods in cases when an *a priori* guess is, and is not, justified.

The authors acknowledge the helpful criticisms of the manuscript by Leonard Johnson, CIRES, University of Colorado, and Gerald Grams, National Center for Atmospheric Research.

A. Cohen is on leave from the Hebrew University of Jerusalem, Department of Atmospheric Sciences.

References

1. A. C. Holland and G. Gagné, *Appl. Opt.* **9**, 1113 (1970).
2. R. Eiden, *Appl. Opt.* **5**, 569 (1966).
3. D. Deirmendjian, *Appl. Opt.* **3**, 187 (1964).
4. E. de Bary, B. Braun, and K. Bullrich, *Tables Related to Light Scattering in a Turbid Atmosphere*, Special Rept. 33, AFCRL-G5-710, Cambridge, Mass. (1965).
5. M. P. McCormick, J. D. Lawrence, Jr., and F. R. Crowfield, *Appl. Opt.* **7**, 2424 (1968).
6. E. W. Barrett and O. Ben-Dav, *J. Appl. Meteor.* **6**, 505 (1967).
7. J. V. Dave, *Appl. Opt.* **8**, 1161 (1969).
8. J. V. Dave, *Appl. Opt.* **10**, 2035 (1971).
9. B. M. Herman, S. R. Brawning, and J. A. Reagan, *J. Atmos. Sci.* **28**, 763 (1971).
10. H. Grassl, *Appl. Opt.* **10**, 2534 (1971).
11. G. Backus and F. Gilbert, *Philos. Trans. Roy. Soc. London* **266**, 123 (1970).
12. H. C. van de Hulst, *Light Scattering by Small Particles* (Wiley, New York, 1957).
13. T. S. Fahlen and H. C. Bryant, *J. Opt. Soc. Am.* **58**, 304 (1968).
14. A. Cohen, V. E. Derr, G. T. McNice, and R. E. Cupp, *The Measurement of Mie Scattering Intensities from Monodispersed Spherical Particles as a Function of Wavelength*, to be published in *Appl. Opt.* (1973).
15. B. J. Mason, *The Physics of Clouds* (Clarendon Press, Oxford, 1971).

Reprinted with permission from *Boundary Layer Meteorology*
Vol. 4, 449-474, June 1973

PLANETARY BOUNDARY-LAYER TURBULENCE STUDIES FROM ACOUSTIC ECHO SOUNDER AND IN-SITU MEASUREMENTS

B. R. BEAN and A. S. FRISCH

*U.S. Dept. of Commerce, National Oceanic and Atmospheric Administration,
Environmental Research Laboratories, Boulder, Colo., U.S.A.*

and

L. G. McALLISTER and J. R. POLLARD

*Australian Defence Scientific Service, Dept. of Supply,
Weapons Research Establishment, Adelaide, South Australia*

(Received 15 August, 1972)

Abstract. Clear-air plume and wave-like structures are revealed in the atmospheric boundary layer by combined acoustic remote sensing and meteorological tower measurements. The magnitude of turbulent production and dissipation plus properties of velocity and temperature spectra determined from the tower measurements are well correlated with phenomena indicated by the acoustic sounder. Interpretation of either set of records is greatly enhanced by the other. For example, the onset of a sudden burst of turbulent production from the tower measurements may correspond to plume passage or breaking of stable waves recorded by the acoustic echo sounder.

1. Introduction

During the last meeting of the IUCRM (Stockholm, 1969), questions were raised about energy exchange between waves and turbulence, the general partition of energy under various meteorological conditions, and the cause of the intermittent nature of many time series of atmospheric variables. This paper presents some of the results of an experiment specifically designed to answer some aspects of these questions. The basic configuration was to measure the atmosphere's turbulent characteristics with sensitive *in-situ* sensors located on a tower while an acoustic sounder continually monitored atmospheric structure over the height of the tower. This, then, allowed us to determine the relative contributions of the various terms in the energy equations under many different conditions, such as thermal plumes, stable layers, breaking waves, mixing under nocturnal inversions, etc. The experiment was conducted at Haswell, Colorado, during the fall of 1969. A major goal of the experiment was to use tower data to explain quantitatively the phenomenon indicated by the sound scattered in the atmosphere by turbulent fluctuations of temperature and wind.

A discussion of acoustic echo sounding is given by Little (1969). He gives the scattered power, per unit volume, per unit incident flux, per unit solid angle at an angle θ from the initial direction of propagation as

$$\sigma(\theta) = 0.03 k^{1/3} \cos^2 \theta \left\{ \frac{C_v^2}{C^2} \cos^2 \frac{\theta}{2} + \frac{C_T^2}{T^2} \right\} \sin \frac{\theta^{-11/3}}{2},$$

where C_v and C_T are obtained from the velocity and temperature structure functions, and k is the wave number of the acoustic wave.

The sounder used for this experiment used a direct backscatter mode, which is then independent of C_v , along with another receiver which was sensitive to both C_T and C_v . C_T is sensitive to the rate of production of turbulent temperature fluctuations, $\overline{w'\theta'} (\partial\bar{\theta}/\partial z)$ (Wyngaard *et al.*, 1971) and slightly sensitive to ε , the rate of turbulent dissipation of kinetic energy. θ is the potential temperature, w the wind in the vertical direction, z . The prime indicates departure from the mean quantity denoted by an overbar. Thus, $\overline{w'\theta'}$ is the covariance of θ and w .

The first step in this analysis was to examine the acoustic echo patterns, compute the available turbulent quantities, and compare these with what is generally known about the turbulent boundary layer. In so doing it was immediately apparent that the acoustic echo sounder aids in studies of intermittency, i.e., that small percentage of the time series of wind and temperature, etc., that contains a significant percentage of the total variance. Further, it appears that acoustic echo-sounder pattern classification allows the qualitative determination of the turbulent characteristics of the atmosphere thus providing more physical insight into the nature of the quantitative *in-situ* tower measurements.

We present the results of an analysis of five time periods selected to show the wide variability in the meteorological conditions measured from the tower and by the acoustic echo sounder.

Case I (Emmanuel *et al.*, 1972) is a stable wave where very little turbulence is present. Case II may be described as a 'herringbone' type structure of sharply defined, almost vertical acoustic returns described by Emmanuel *et al.* (1972) as an unstable wave. Case III, a rising temperature inversion, follows the transition from stable conditions just after sunrise to the beginning of convective conditions. Case IV shows thermal plumes just after the inversion has been destroyed by convection. Case V is a complex wave structure that appears to be composed of several types of waves.

2. Method of Analysis

The turbulent energy was determined from the tower data and related to the various patterns observed by the acoustic echo sounder.

It is impossible to evaluate all of the terms in the turbulent energy equation from a single tower. However, in the surface layer, with averages of about an hour, horizontal gradients become small, the mean flow can be represented as two-dimensional, the average vertical velocity and pressure terms are approximately zero, and the system is approximately stationary (Lumley and Panofsky, 1964). For these conditions, the turbulent energy equation may be written as

$$\frac{\partial \bar{e}}{\partial t} = -\overline{u'w'} \frac{\partial \bar{u}}{\partial z} + \frac{g}{T} \overline{w'\theta'} - \frac{\partial \overline{w'e}}{\partial z} - \varepsilon = 0, \quad (1)$$

| | | | | |
|------|---|----|-----|----|
| Term | I | II | III | IV |
|------|---|----|-----|----|

where u is the component of the wind in the x direction (taken as the direction of the mean wind), and w is the vertical or z component of velocity. u' , w' and θ' are defined as

$$\begin{aligned} u' &= u - \bar{u} \\ w' &= w - \bar{w} \\ \theta' &= \theta - \bar{\theta}, \end{aligned}$$

where

$$\bar{u} = \frac{1}{\tau} \int_0^{\tau} u dt$$

and τ is some predetermined averaging time.

In addition,

$$e \equiv \frac{1}{2} (u'^2 + v'^2 + w'^2),$$

and where θ is the potential temperature and T is the local temperature.

Term I is called the mechanical production term; it is usually positive (including sign) indicating energy is transferred from the mean flow into turbulent energy. Term II is the buoyancy production term; it is positive during convective conditions and indicates a source of turbulent energy in this case. It is usually negative indicating the temperature stratification normally suppresses turbulence. Term III is a measure of the vertical divergence of the vertical turbulent energy flux, i.e., the redistribution of energy with height. Term IV gives the turbulent energy dissipation or the rate at which energy is lost through viscosity. This term is always positive.

Since the production of the mechanical energy depends upon $\overline{u'w'}$ and the shear of the mean flow, it is informative to see how $\overline{u'w'}$ is generated and to examine the size of the various terms. Making similar assumptions as before, we write the differential equation for $\overline{u'w'}$ as

$$\frac{\partial}{\partial t} \overline{u'w'} = -\overline{w'^2} \frac{\partial \bar{U}}{\partial z} + \frac{g}{T} \overline{u'\theta'} - \frac{\partial}{\partial z} \overline{u'w'^2} \dots \quad (2)$$

The first term in the right-hand side is the production of Reynolds stress through shear in the mean flow and variance in the vertical velocity. The second term is that due to turbulent horizontal transport of temperature fluctuations (or horizontal turbulent heat flux) and the third term redistributes $\overline{u'w'}$ with height. Similarly, the buoyancy production may be written as

$$\frac{\partial}{\partial t} \overline{w'\theta'} = -\overline{w'^2} \frac{\partial \bar{\theta}}{\partial z} + \frac{g}{T} \overline{\theta'^2} - \frac{\partial}{\partial z} \overline{w'^2 \theta'} \dots, \quad (3)$$

where the first term on the right-hand side represents the production of vertical temperature flux through the mean temperature gradient, the second, the variance

of the temperature fluctuations, and the third term, the redistribution of $\overline{w'\theta'}$ with height. A detailed discussion of these equations is given by Stewart (1959).

Estimates of $\overline{u'w'}$, $g/T \overline{w'\theta'}$, $\overline{w'e}$, ε , etc., were made by measuring u , w and θ at a point, detrending the appropriate fluctuating quantities, and averaging for a pre-determined time. The fourth term, ε , is estimated by using the horizontal wind structure function $D_u(r)$ where r is the spatial separation of the two measurements of u . This should have the form in the inertial subrange of

$$D_u(r) = Ae^{2/3} r^{2/3}$$

Record and Cramer (1966) have extensively studied this relationship. They find $A=2.0$ to be the best value for their studies. A correction for the response of the anemometer was used and is given by (after Volkovitchaya and Ivanov, 1970)

$$\varepsilon \simeq \frac{0.37}{\bar{U}} \left(\frac{D_u}{\tau_2^{3/2} - \tau_1^{3/2}} \right)^{3/2},$$

where τ_2 is the time lag corresponding to r , \bar{U} the mean wind speed, and τ_1 the time constant of the anemometer. The value for τ_1 is about 1 s for a wind speed of 1 m s^{-1} .

The mechanical production in Equation (1) was determined by averaging $\overline{u'w'}$ across the two levels of measurement and multiplying by $\Delta \bar{U}/\Delta Z$, where $\Delta \bar{U}$ was the difference in the average wind speed between the two levels, and ΔZ was the spacing between these levels. There was no stress measurement below 39 m, and the value at 39 m was used for the $z=0$ level. This undoubtedly underestimates the mechanical production term, in this region, since $\overline{u'w'}$ during stable conditions decreases with height in this range. The fluctuations in the horizontal wind speed, u'_s , were used for computational efficiency rather than the vector fluctuation along the mean flow. That this is a reasonable approximation, may be seen by the following. Let $u'_s = u' \cos \phi'$ where ϕ' is the fluctuation in azimuth between the average wind direction and the instantaneous wind direction. Then,

$$\overline{u'_s w'} = \overline{u' \cos \phi' (w')} = \overline{u' w' (1 - \phi'^2/2 + \dots)} \simeq \overline{u' w'} - \overline{u' w' \phi'^2}/2$$

yields an error of less than 5% when ϕ varies as much as 20° . Indeed the variance in the azimuth is quite small over two minutes for most of our data.

Another and sometimes a larger source of error is the assumption that the mean wind does not change direction with height. The mechanical term should actually be computed by resolving the horizontal velocity components along two orthogonal horizontal axes. By using the wind speed, the resultant error can amount to as much as 40% underestimation of the mechanical production. However, this error is small relative to that of the measurement of the wind gradient, which is discussed in each particular case.

Power spectra were determined for u , w , and t after linear trends were removed from the data. The spectra were smoothed by dividing each decade into ten equal logarithmic intervals and averaging all points within each interval.

3. Measurements and Data Reduction

The site and measurements have been described by Emmanuel *et al.* (1972). In summary, the measurements were made near Haswell on the plains in the south-eastern part of Colorado. The site elevation is 1307 m, and is sparsely covered with 15-cm high clumps of buffalo grass for a minimum of 3 km in any direction from the tower. The meteorological characteristics are those of the high plains, strong solar heating during the day and radiative cooling at night. Velocity and temperature measurements were made at 39, 93, and 149 m from a 152-m tower. The acoustic sounder was 250 m northwest of the tower. It operated at a frequency of 950 Hz, 20 ms-pulse duration every 2 s, and an acoustic power output of 8 W.

The acoustic-sounder data were recorded on a facsimile to give a height vs. time record of the backscattered intensity (McAllister *et al.*, 1969). The measurements taken on the tower were recorded by FM tape recorders, digitized at 5 samples s^{-1} .

4. Results

The results of estimates of means and the terms in Equations (1), (2), and (3), for the five time periods used a two-minute averaging time. Spectra for the various time intervals were estimated from measurements at 93 m on the tower. The two-minute averages were somewhat arbitrary. In treating the last case, for example, it appeared desirable to resolve selected portions of the pattern shown by the acoustic echo. The two-minute averaging time was determined as the longest sample length that could be used without masking the detailed structure. The value of 10 min for the spectral estimates was used in order to obtain reliable estimates of the spectral peaks which could occur with frequencies below one or two minutes. Care was taken to try to make these estimates during the time the acoustic echo sounder showed the least change in the patterns for the interval. In one case, the 'stable wave' spectral estimates were made for an hour, since this feature appeared to exist during most of the one-hour interval, and had much lower frequencies appearing in the echo return than the other cases. The following quantities were determined:

$$A_z, \bar{U}, \bar{T}, \overline{u'w'}, \frac{\partial \bar{U}}{\partial z}, \frac{g}{T} \overline{w'\theta'}, \frac{\partial}{\partial z} \overline{w'e}, \varepsilon, \\ \overline{w'^2} \frac{\partial \bar{U}}{\partial z}, \frac{g}{T} \overline{u'\theta'}, \frac{\partial}{\partial z} \overline{u'w'^2}, \overline{w'^2} \frac{\partial \bar{\theta}}{\partial z}, \frac{g}{T} \overline{\theta'^2}, \text{ and } \frac{\partial}{\partial z} \overline{w'^2 \theta'},$$

where A_z is the azimuth in degrees from the north, \bar{U} is the average wind speed, \bar{T} is the average temperature. These are plotted in detail as a function of time for the last case; the other cases, however, are described with representative values for pertinent events on the sounder record. All times are local standard time.

CASE 1. 'STABLE WAVE' (OCTOBER 8, 1969) 0100 TO 0200

During this interval, the observed acoustic echo-sounder pattern from the direct

backscatter measurements shows a sinusoidal wave structure (Figure 1) described as a 'stable wave' by Emmanuel *et al.* (1972). The stable wave will not grow with time and will gradually disappear because of frictional forces within the wave. Measurements are not available at 39 m (from 01 00 to 01 30) because of instrumental problems.

The wind speed measurements indicate that the wind has minimum values at times corresponding to the peak heights of the wave shown by the acoustic sounder (01 09, 01 18, and 01 29 h and the 93-m level). The temperature shows very little change during this interval.

HASWELL, COLORADO

OCTOBER 8, 1969

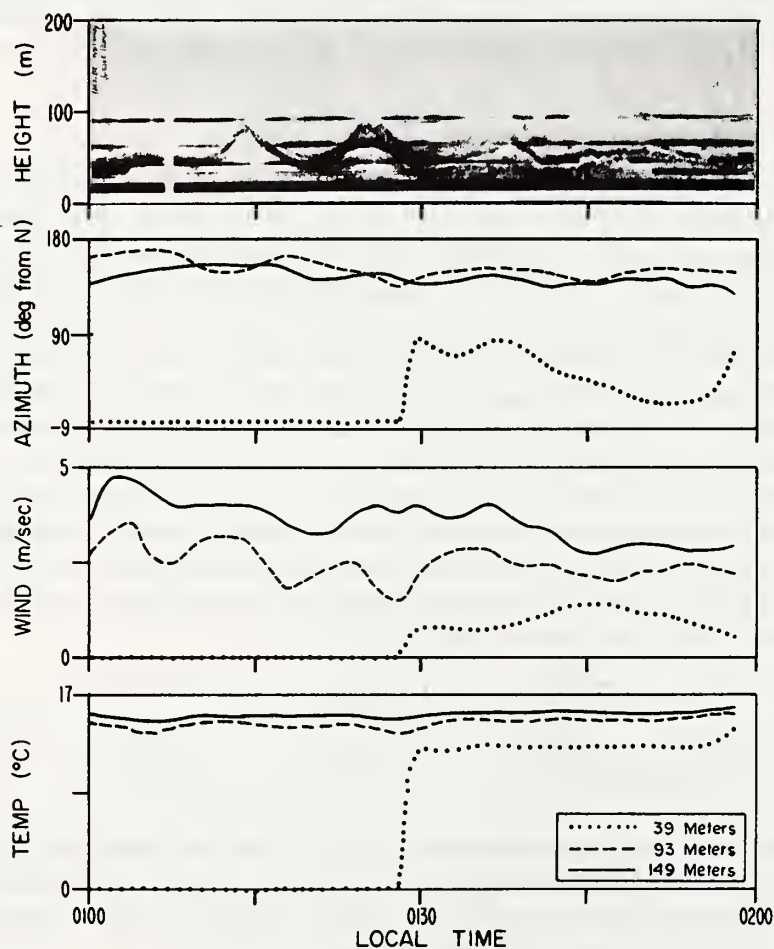


Fig. 1. Stable wave. - Top: Acoustic echo return vs. height and time. Average values determined from measurements at the three fixed levels on the Haswell tower for: Second from top: Azimuth. Third from top: Wind speed. Bottom: Temperature. Note that the measurements at the 39-m level are not available for the first 28 min.

The estimated terms in the energy budget are shown in Figure 2 for 0103. All terms are essentially zero, although at later time periods ϵ increases to about $10 \text{ cm}^2 \text{ s}^{-3}$, while the mechanical term never gets larger than 2 or 3. Emmanuel *et al.* (1972) show the profile of wind and temperature measured from an instrumented carriage which ascended during this time interval. The maximum wind shear occurred at the same level as the acoustic echo-sounder return and has a value of about 0.4 s^{-1} , compared to the 0.05 s^{-1} measured across the two fixed levels.

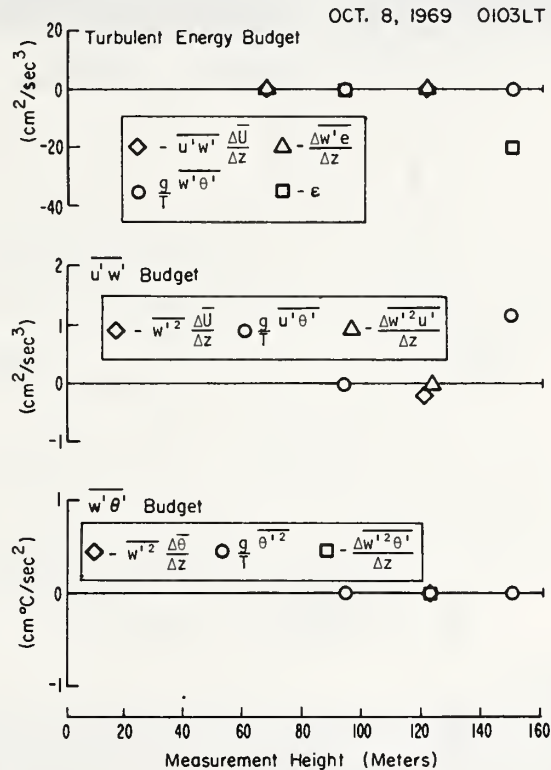


Fig. 2. Stable wave: Turbulent energy budget. – Evaluated terms using a detrended two-minute average for: *Top*: Turbulent energy equation. *Middle*: Reynolds stress equation. *Bottom*: Buoyancy production equation. – Everything is essentially zero for this case and the particular time averages used.

The production of the Reynolds stress and the vertical temperature flux is shown in Figure 2 for 0103. Figure 3 shows the u , w , and θ spectra for the 93-m level computed for a one-hour sample from 0100 to 0200. There is a rapid decrease in the energy in all three variables. These spectra all go to zero near $2 \times 10^{-2} \text{ Hz}$. The sounder return indicates the long wave-like structure occurs about every 8 min or 480 s. This has a frequency of $2.1 \times 10^{-3} \text{ Hz}$. The temperature spectrum displays a maximum at this frequency although the u and w do not. The horizontal component of wind at these frequencies is an order of magnitude greater than the vertical velocity component.

CASE II. 'HERRINGBONE WAVE STRUCTURE' (OCTOBER 9, 1969) 0540 TO 0620

This structure, shown in Figure 4, appears as a herringbone-type structure. The azimuth shows a large change in wind direction with height. This variation persists throughout the interval, except at 0603 to 0605 and at 0619. These time periods occur just before those periods for which the acoustic echo-sounder data show almost no return. Figure 4 also shows wind speed minima coincident with the maximum heights observed by the sounder. These periods of wind minima also show large variation in wind shear. The first minimum at 0553 has relatively strong shear, while

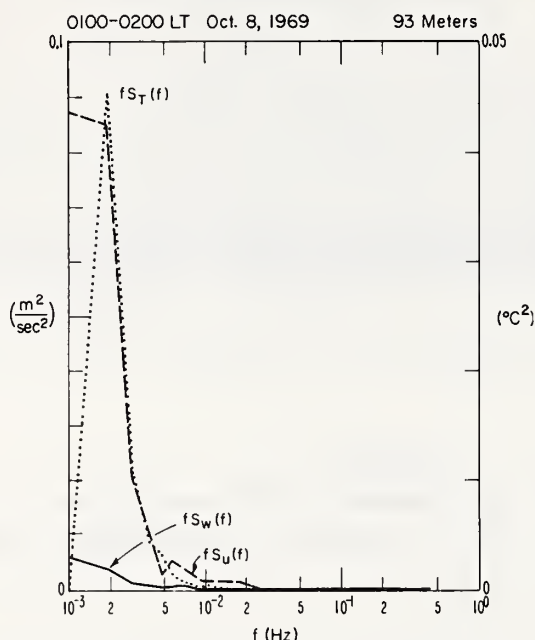


Fig. 3. Stable wave. — Estimates of frequency times the power spectra vs. $\log f$ (Hz) for u (horizontal wind speed), w (vertical velocity), and T (temperature). The horizontal amplitude is more than an order of magnitude larger than the vertical component over most of the frequency range, indicating that even though there is appreciable shear, the production of the Reynolds stress would be small through the $\overline{w'^2}(\partial \bar{U}/\partial z)$ term; hence very little turbulence will be generated through the shear production term. This also means that the motion of this wave is in the horizontal plane.

the one at 0611 has very small wind shear corresponding to sounder returns at all heights for the former, but not for the latter. Figure 4 shows only about a 3°C temperature difference with height, with the maximum difference between the 93 and 149 m levels.

Figure 5 shows the energy budget terms at 0559. The lowest level shows a change in sign for $-\overline{u'w'}$ ($\partial \bar{U}/\partial z$), which may be interpreted such that the energy is being taken from the herringbone structure and put into the mean motion. This conjecture is given additional support by the increase in wind speed at higher elevations accom-

HASWELL, COLORADO

OCTOBER 9, 1969

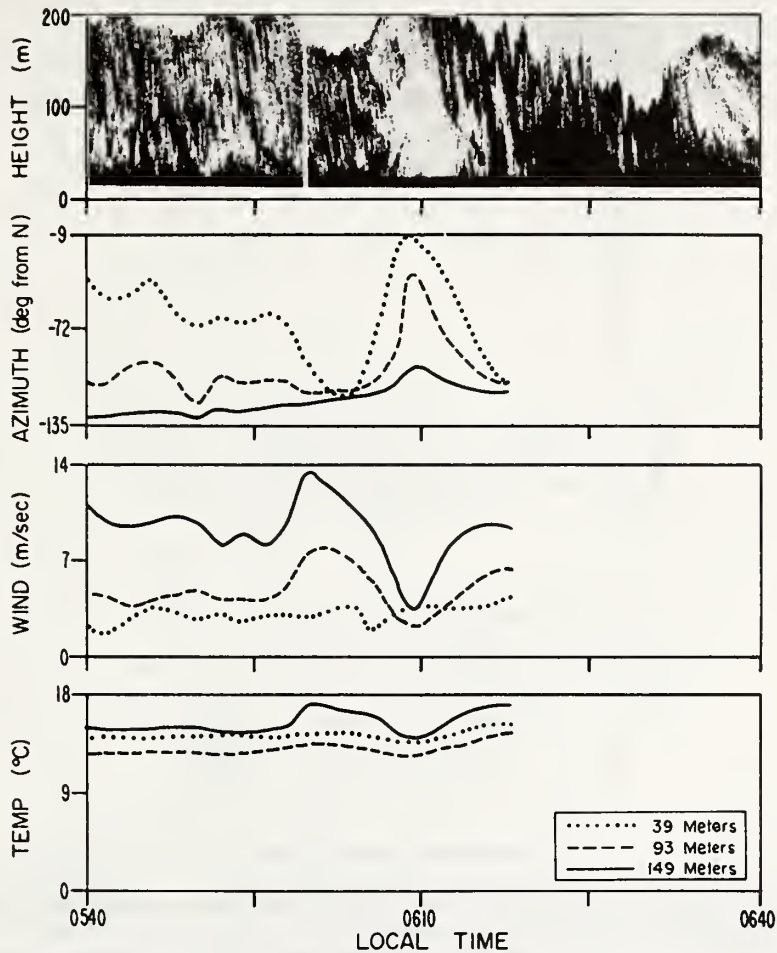


Fig. 4. 'Herringbone' wave structure. - *Top*: Acoustic echo return as a function of height and time. Average values determined from measurements at the three fixed levels on the Haswell tower for: *Second from top*: Azimuth. *Third from top*: Wind speed. *Bottom*: Temperature. - Note the very small wind shear at 0611, corresponding to the region of no acoustic echo return.

panied by an increase in turbulent dissipation many times greater than that observed in Case I.

These Reynolds stress terms are also shown in Figure 5. The relative values of $-\overline{w'^2} (\partial \bar{U} / \partial z)$ are about three orders of magnitude larger for this case than for the stable wave case. The buoyancy and vertical gradient terms are negligible.

The power spectrum of u (Figure 6) shows that higher frequencies are contributing to the turbulent energy compared to the stable case. In this case almost all of the

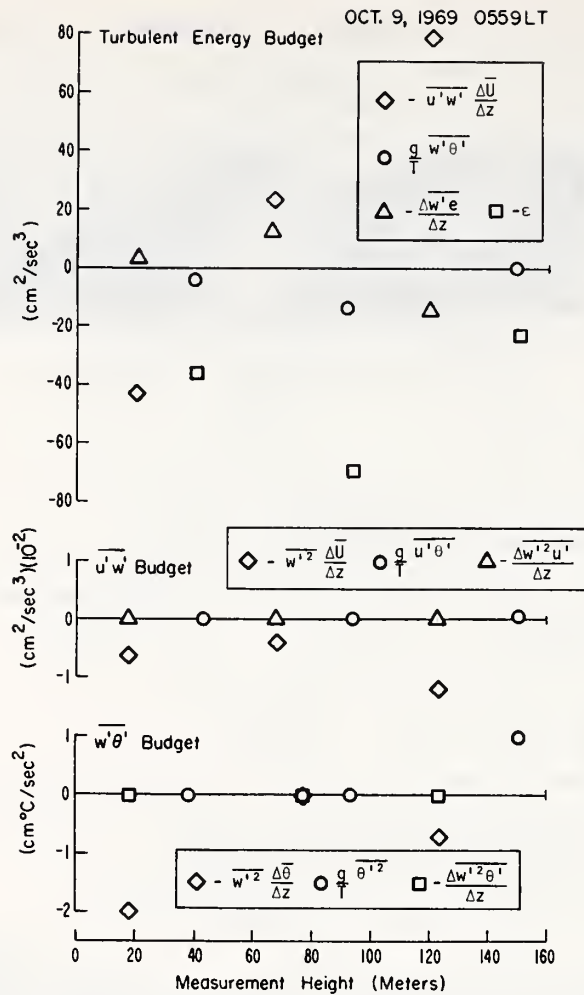


Fig. 5. 'Herringbone' wave structure. – Evaluated terms using a detrended two-minute average for: *Top*: Turbulent energy equation. *Middle*: Reynolds stress equation. *Bottom*: Buoyancy production equation. – Note the large increase in the relative magnitude of almost all the terms compared to the stable wave case.

energy was produced at frequencies higher than 5×10^{-3} Hz while in the first case the energy was concentrated below 5×10^{-3} Hz.

CASE III. RISING INVERSION TO CONVECTION (SEPTEMBER 23, 1969) 0750 TO 0900

The acoustic echo-sounder return (Figure 7) shows most of the return originates from below 94 m until about 0831. Figure 7 also shows that during this time there is almost no change in the wind direction with height, except for a time at the 39-m level. The wind at 39 m is practically zero until 0821. However, at 93 m the wind speed is about 3 m s^{-1} , and 4.4 m s^{-1} at 149 m, increasing toward the end of the time period. The

temperature (Figure 7) increases at 39 m for a few minutes then decreases at 0821, starts increasing from that time, and at 0825 the air at 39 m becomes statically unstable when compared to the 93-m level.

Figure 8 shows terms in the energy budget as the inversion rises. Initially, the inversion is very shallow and the rates of turbulent energy production are small at all heights. As the inversion rises, the buoyancy production below the inversion increases and becomes largest at 0855 when the inversion is just below the 149-m level.

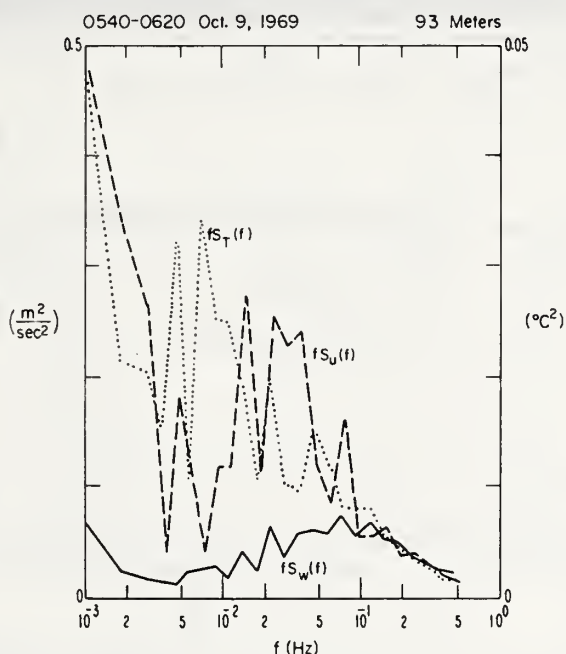


Fig. 6. 'Herringbone' wave structure. — Estimates of $fS(f)$ vs. $\log f$ for u (horizontal wind speed), w (vertical wind speed), and T (temperature). The power spectra for this case show: (1) increased power at higher frequencies compared to the stable wave case; (2) the amplitude of $S_w(f)$ relative to $S_u(f)$ has increased an order of magnitude at the higher frequencies. This means that the shear production of Reynolds stress will be larger, and consequently the shear production term in the turbulent energy equation should also increase.

The Reynolds stress budget and buoyancy budget for the same time periods are shown in Figures 9 and 10. They show that the magnitudes of these terms are largest below the inversion level.

The estimates of power spectra at 93 m for u , w , and T were made for two periods during this case (Figures 11 and 12). The first, 0800 to 0815, was made while the inversion, as seen by the acoustic sounder, was below 93 m. The second, 0840 to 0900, was made after the inversion was higher than 93 m.

The first set of spectra shows the u spectrum (Figure 11) peak at 3×10^{-2} Hz, with a maximum amplitude of $1(\text{m}^2 \text{ s}^2)/\text{Hz}$, and the w spectrum with no well defined peak.

HASWELL, COLORADO

SEPTEMBER 23, 1969

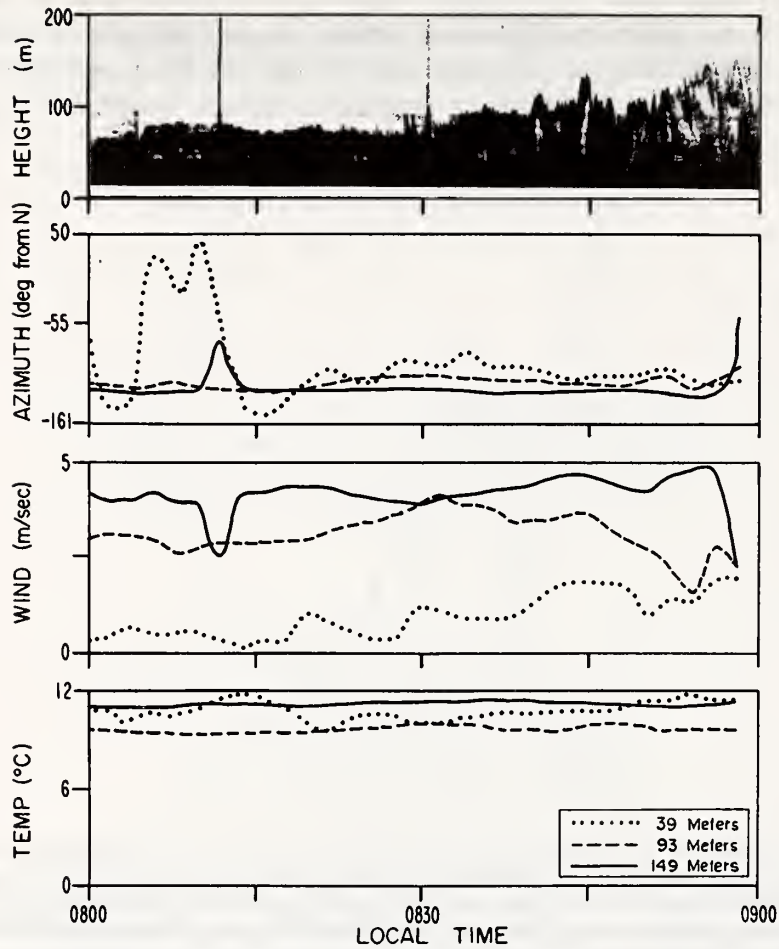


Fig. 7. Rising inversion to convection. — *Top*: Acoustic echo return as a function of height and time. Average values determined from measurements at the three fixed levels on the Haswell tower for: *Second from top*: Azimuth. *Third from top*: Wind speed. *Bottom*: Temperature.

The temperature spectrum has a similar shape to that of u (with a peak amplitude of $0.1^{\circ}\text{C}^2 \text{ Hz}^{-1}$). In contrast, after the inversion rises above 93 m, the u spectrum (Figure 12) shows a peak at $2 \times 10^{-2} \text{ Hz}$, and an amplitude of $4 (\text{m}^2 \text{ s}^{-2}) \text{ Hz}^{-1}$, almost four times larger. The w spectrum does not have a sharp peak but the amplitude has increased by another order of magnitude. The peak of the temperature spectrum has shifted to $5 \times 10^{-2} \text{ Hz}$ and the amplitude has increased to $0.4^{\circ}\text{C}^2 \text{ Hz}^{-1}$, a factor of four over the previous peak. These data, especially the w spectra, indicate that the

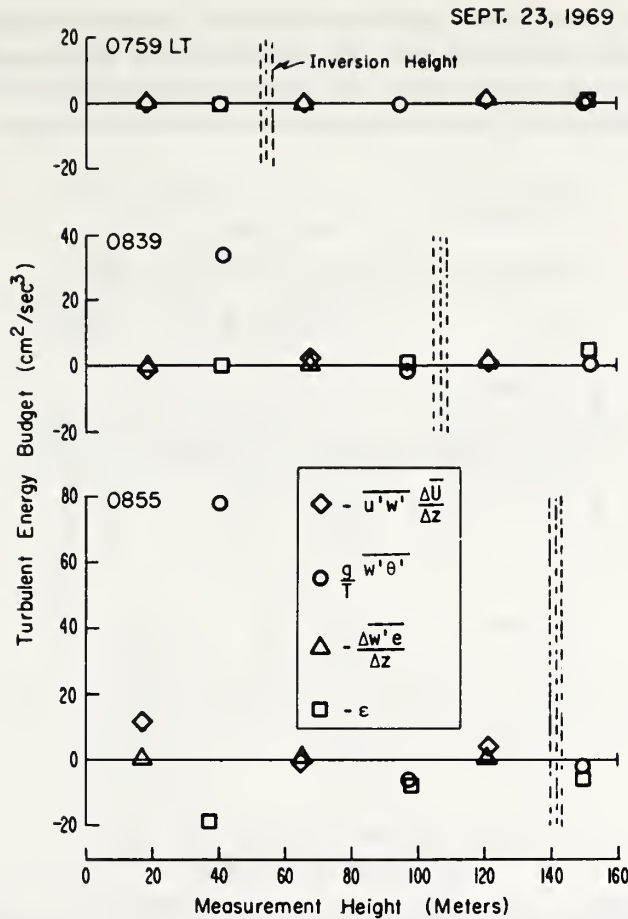


Fig. 8. Rising inversion to convection. – Three time periods showing two-minute average estimates of some of the terms in the turbulent energy equation. The height of the inversion, indicated by the acoustic echo sounder, is shown by the dashed line. The magnitudes of the terms increase below the inversion as the inversion lifts, but not above the inversion.

acoustic echo delineates between the 'mixing' region of the surface layer and the region above it where very little exchange of variables takes place.

CASE IV. CONVECTIVE CASE (SEPTEMBER 23, 1969) 0900 TO 1000

Plume-like structures are observed by the echo sounder (Figure 13) after the convective breakup of the inversion of the previous case. Initially, the azimuth shows very little variation with height until 0935 when the wind at 149 m drops below 1 m s^{-1} . The air is statically unstable from the ground to 93 m and is stable from 93 to 140 m. The convection above this height should stop and, indeed, the echo returns indicate that most of the echo return is below this level.

Figure 14 shows the energy terms, the Reynolds stress and buoyancy terms for

0915. In general, all the terms decrease with height. The spectral estimates of u , w , and T from 0900 to 1000 at 93 m are shown in Figure 15. The u spectrum displays energy over practically the entire frequency range analyzed, and the T and w spectrum has increased nearly two orders of magnitude over the previous case.

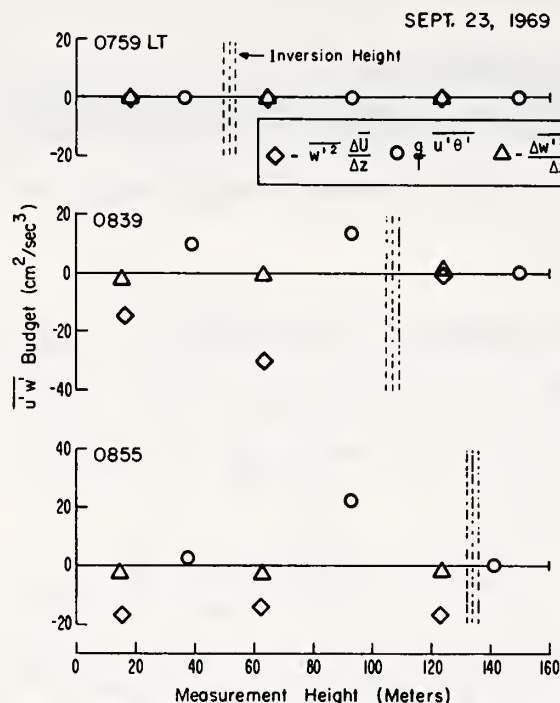


Fig. 9. Rising inversion to convection. — Three time periods showing the two-minute average estimates of some of the terms in the Reynolds stress equation. The height of the inversion, indicated by the acoustic echo sounder, is shown by the dashed line. As in Figure 8, the relative magnitudes of these terms are important below the inversion but not above it. This indicates that the echo return can delineate regions of Reynolds stress production for this type of phenomenon.

CASE V. COMPLEX WAVES (OCTOBER 9, 1969) 0800 TO 0900

The echo-sounder return for this case (Figure 16) indicates rather complex structures that we shall analyze in more detail than the earlier cases. Initially, a thick diffuse layer is indicated between 50 and 125 m. The top of this layer rises to 200 m and develops a wave-like structure. A series of undulating layers appear by 0822 with small scale instabilities superposed upon the main waves of 120 m (Emmanuel *et al.*, 1972). Plots of azimuth, average wind speed and temperature shown in Figure 16 follow the contours of the acoustic recording.

The acoustic record is discussed in three sections. Part A which shows a diffuse layer occurring from 0800 to 0810; Part B, a region of no echo from 50 to 100 m occurring from 0812 to 0822; and Part C where undulating layers are observed (0825–0835).

The echo returns are shown at the top of Figure 17 while the terms in the kinetic energy budget are shown below. Part A shows, with the exception of dissipation, that the various terms are relatively small (less than $15 \text{ cm}^2 \text{ s}^{-3}$). A sharply defined wave structure is observed between 100 and 200 m at 0806. Simultaneously, this region

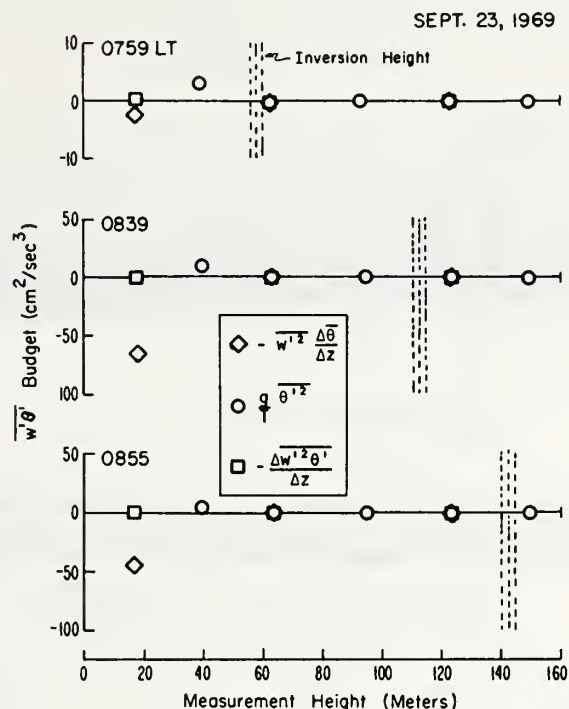


Fig. 10. Rising inversion to convection. — Three times showing the two-minute average estimates of some of the terms in the buoyancy equation. The height of the inversion, indicated by the acoustic echo sounder, is shown by the dashed line. The main difference in this equation is the term $\overline{w'^2}(\partial\bar{\theta}/\partial z)$ using temperature measurements at the surface and at the 39-m level.

shows a marked increase in the mechanical production, a slight increase in dissipation and a large negative buoyancy term.

Figure 18 shows some of the terms in the Reynolds stress equation. Part A shows a slight increase in $\overline{w'^2}(\partial\bar{U}/\partial z)$ at 0806, and a dramatic increase in $(g/T)\overline{u'\theta'}$ at the 149-m level. This increase corresponds to the time that the diffuse structure appears to change to the undulating type structure at heights of 150 m and above. The divergence term of the transport of the Reynolds stress is small during interval A. The buoyancy equation (Figure 19) is dominated by the mean vertical temperature gradient near the surface, as seen in the plot of the $-\overline{w'^2}(\partial\bar{\theta}/\partial z)$ term.

During interval B, (Figure 17), the echo return shows a layer above 125 m, and a low-level layer below 80 m. The mechanical production between 93 and 149 m has decreased, and is very small between the other levels. The buoyancy production term

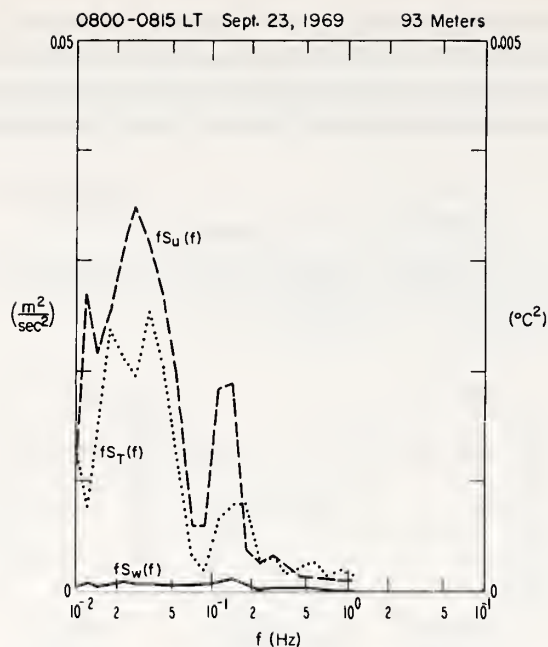


Fig. 11. Rising inversion to convection. — Above the Inversion. Estimates of $fS(f)$ vs. $\log f$ for u (horizontal wind speed), w (vertical wind speed), and T (temperature). The relative magnitude of $S_w(f)$ is between one to two orders of magnitude smaller than $S_u(f)$ over the whole frequency range.

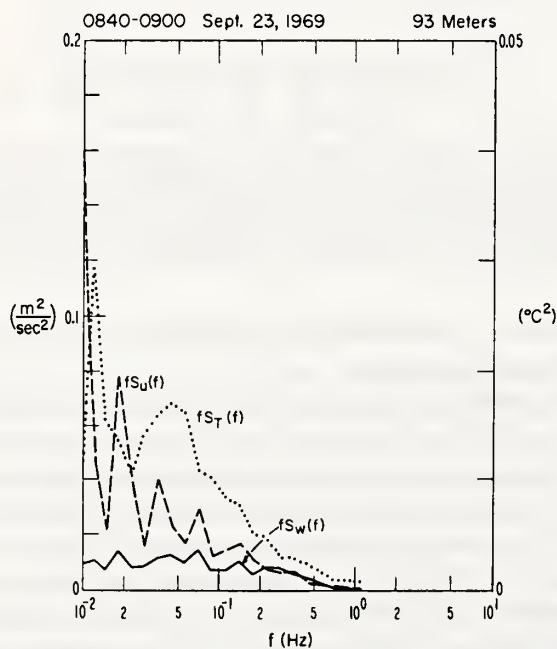


Fig. 12. Rising inversion to convection. — Below the Inversion. Estimates of $fS(f)$ vs. $\log f$ for u (horizontal wind speed), w (vertical wind speed), and T (temperature). The relative magnitude of $S_w(f)$ has increased dramatically relative to $S_u(f)$.

HASWELL, COLORADO

SEPTEMBER 23, 1969

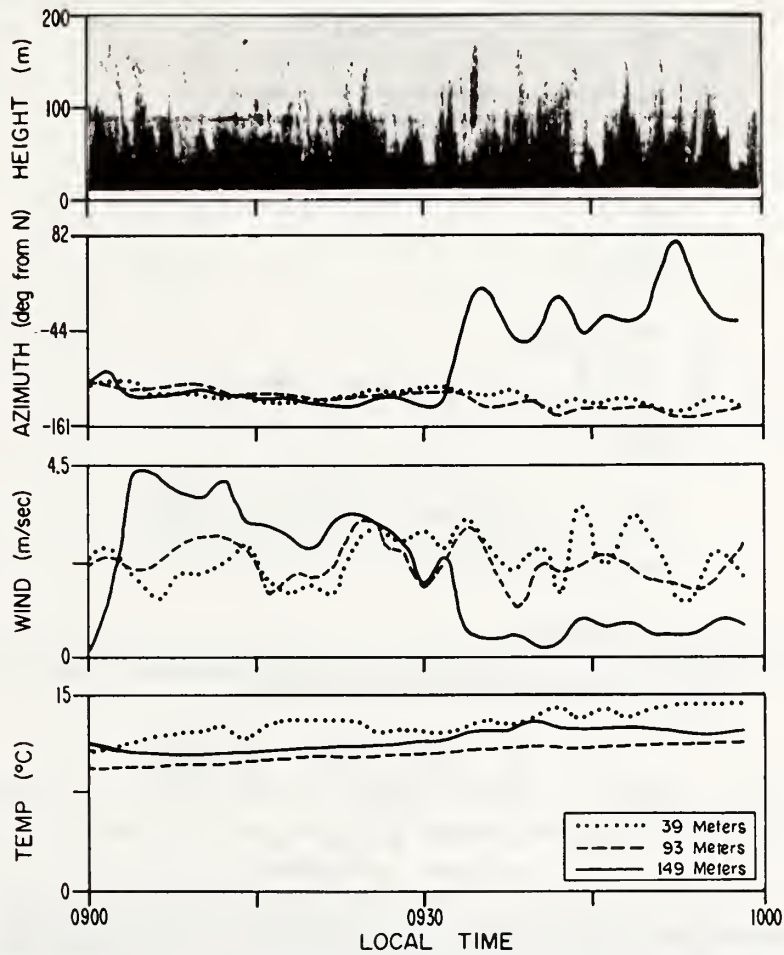


Fig. 13. Convective case. - *Top*: Acoustic echo return as a function of height and time. Average values determined from measurements at the three fixed levels on the Haswell tower for: *Second from top*: Azimuth. *Third from top*: Wind speed. *Bottom*: Temperature.

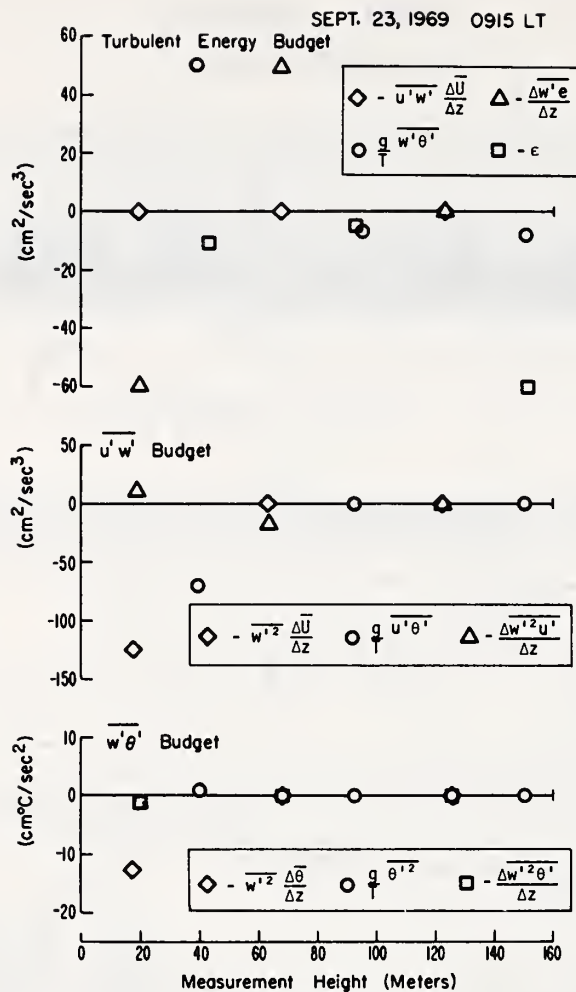


Fig. 14. Convective case. – Evaluated terms using a detrended two-minute average for: *Top*: Turbulent energy equation. *Middle*: Reynolds stress equation. *Bottom*: Buoyancy production equation. – These terms show little change over the last part of the rising inversion.

is also smaller at 149 m, although it increases rapidly toward the end of this interval, corresponding to the appearance of an 'undulating' surface crossing this level. Since this surface has the small-scale instabilities described by Emmanuel *et al.* (1972), then one would expect relatively large vertical motions which would tend to produce the buoyancy term through Equation (3). Similarly, the divergence and dissipation terms are small in the turbulent energy production equation for interval B.

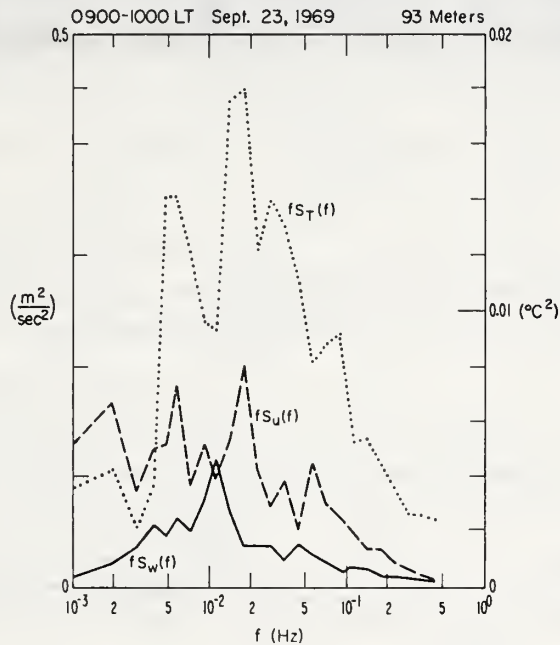


Fig. 15. Convective case. – Estimates of $fS(f)$ vs. $\log f$ for u (horizontal wind speed), w (vertical wind speed), and T (temperature). These spectra show much more power in all three variables than any of the other cases at this height.

The production of Reynolds stress terms shown in Figure 18 are small for this interval (B) with the exception of $g/T \overline{u'\theta'}$, which shows a similar behaviour as the $(g/T) \overline{w'\theta'}$ term, with an opposite sign.

During period C (0825 to 0835), the undulating surface extends from about 20 to 150 m. The terms in the energy equation (Figure 17), all show increases in magnitude, correlated to the occurrence of these undulating surfaces at the particular heights of measurement. The same result holds for the Reynolds stress equation and to a lesser extent in the buoyancy equation (Figures 18 and 19, respectively).

The terms involving the mean gradients may be underestimated. Emmanuel *et al.* (1972) show the measurements from a carriage traverse on the tower. If one uses the wind shear for estimates from the fixed levels on the tower, it appears that terms involving the shear could be underestimated by as much as a factor of 2 or 3. This

HASWELL, COLORADO

OCTOBER 9, 1969

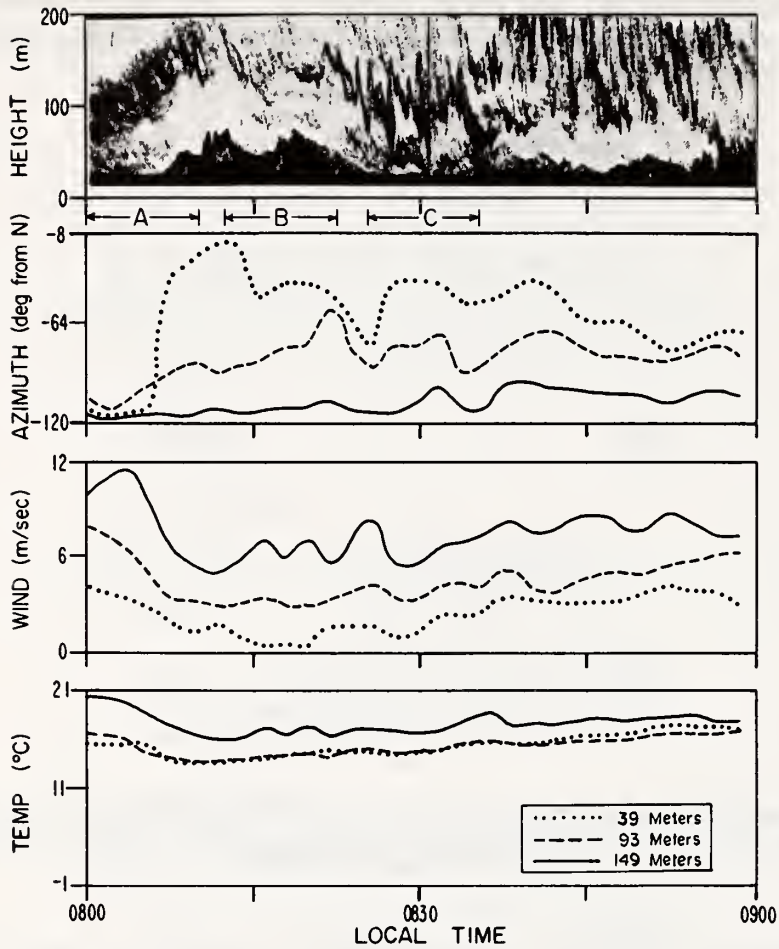


Fig. 16. Complex waves. – *Top*: Acoustic echo return as a function of height and time. – *Note*: the period denoted by A contains a diffuse layer, period B has a region of no echo return below a region where a few wave-like returns appear, and period C, contains what Emmanuel *et al.* (1972), describe as undulating surfaces with small-scale instabilities superimposed on them. Average values determined from measurements at the three fixed levels on the Haswell tower for: *Second from top*: Azimuth. *Third from top*: Wind speed. *Bottom*: Temperature.

HASWELL, COLORADO
OCTOBER 9, 1969

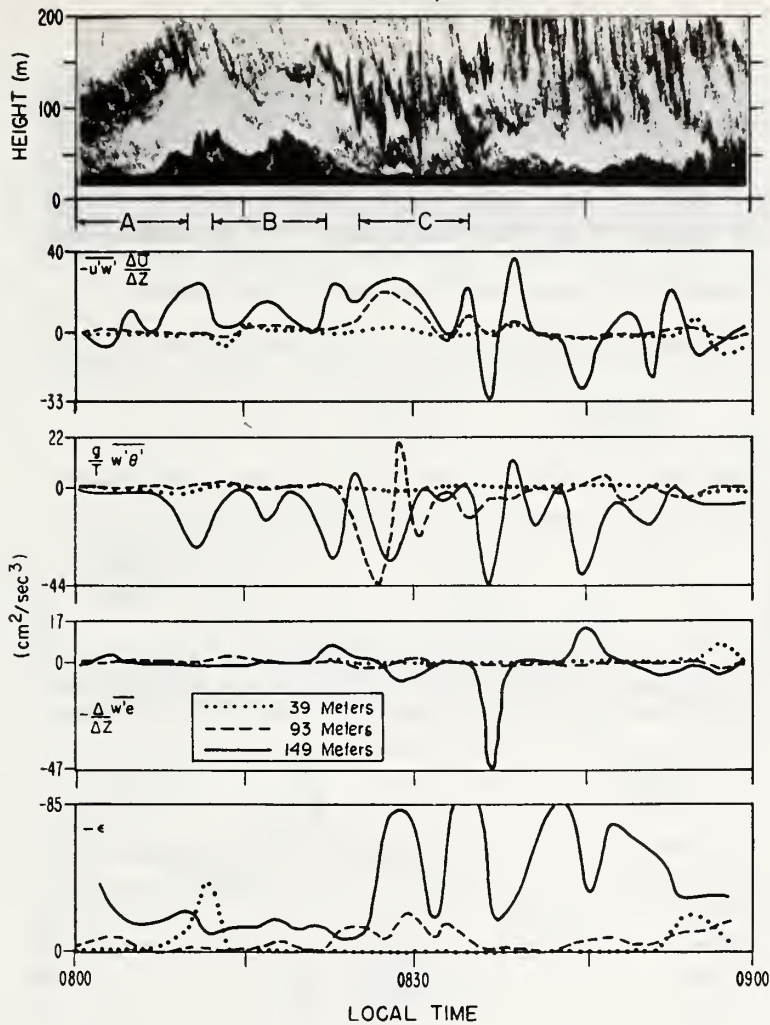


Fig. 17. Complex waves: Turbulent energy equation. - *Top*: Acoustic echo return as a function of height and time. *Second from Top*: Mechanical production. The upper height used to calculate the wind speed difference is indicated by the dotted, dashed or full line. Note the increase in this term corresponding to the occurrence of the small-scale instabilities. *Third from Top*: Buoyancy energy production term. As before, there is an increase in the buoyancy production term corresponding to the occurrence of the unstable waves. If one replaces g/T with qc_p , this represents the vertical heat flux, which indicates that almost all the downward heat transport for this condition was by the unstable waves. *Fourth from Top*: Vertical divergence of the vertical flux of turbulent kinetic energy. The upper height used to calculate the gradient estimates is indicated by the dotted, dashed or full line. This term is relatively small compared to the other terms. *Bottom*: Turbulent dissipation. The dissipation increases at times corresponding to: (1) the diffuse structure appearing in period A; (2) the unstable wave condition in period C.

HASWELL, COLORADO

OCTOBER 9, 1969

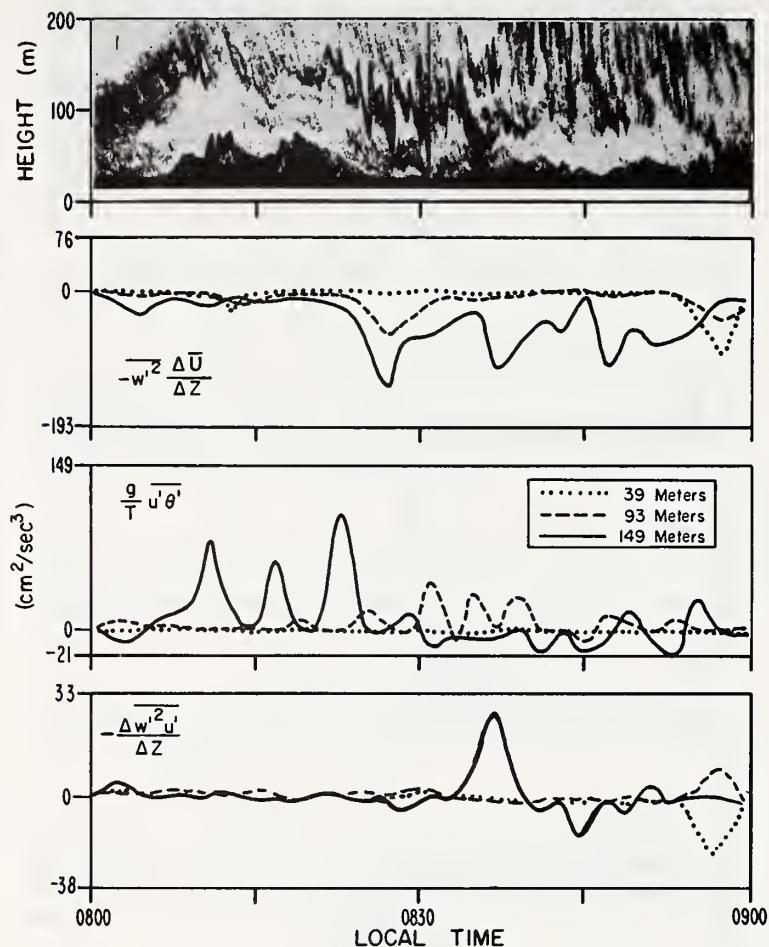


Fig. 18. Complex waves: Reynolds stress equation. - *Top*: Acoustic echo return as a function of height and time. *Second from Top*: Production of the Reynolds stress through vertical shear. The upper height used to calculate the mean wind speed difference is indicated by the dotted, dashed or full line. The very large increase in magnitude of this term coincides with the portion of the acoustic echo showing the unstable wave structure at time interval C and later. *Third from Top*: Buoyancy term due to the horizontal flux of temperature. The largest values occur at 150 m at A and B corresponding to the apparent unstable waves occurring around the 150 m level. During period C, the largest three values are greater at 93 m and are coincidental with the three times the unstable waves appear at that level. *Bottom*: Vertical divergence of the vertical turbulent flux of Reynolds stress. The upper height used to calculate the gradient estimates is indicated by the dotted, dashed or full line. The largest value occurs during C, when the unstable wave appears across the 93-m level, but not the 150-m level.

HASWELL, COLORADO

OCTOBER 9, 1969

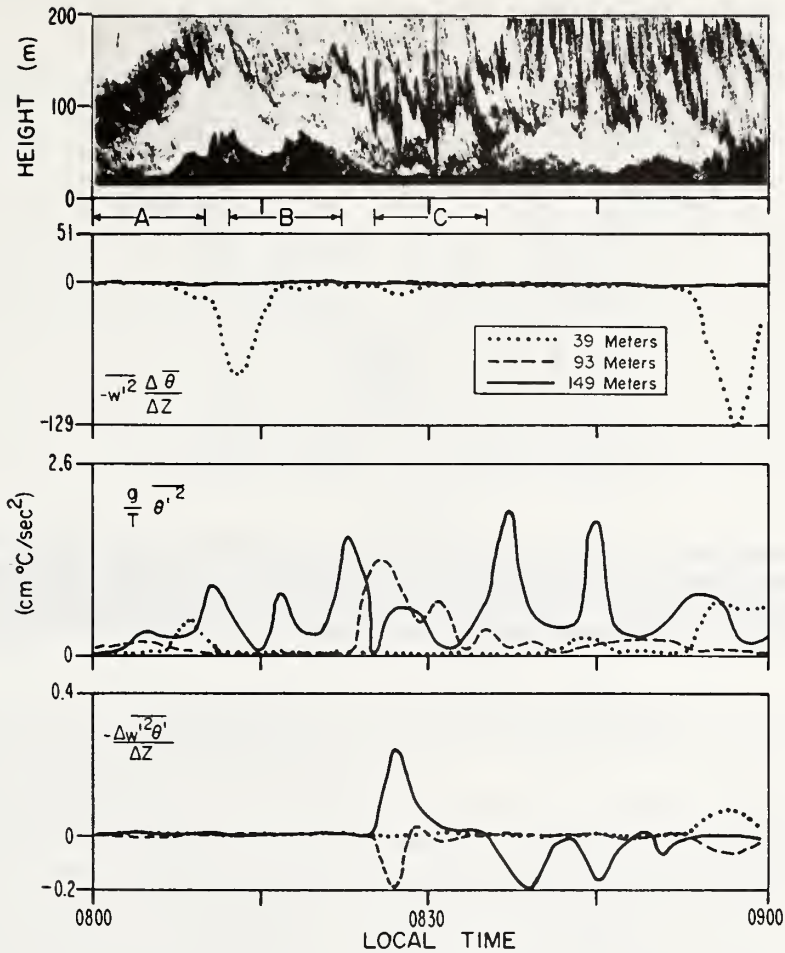


Fig. 19. Complex waves: buoyancy production equation. - *Top*: Acoustic echo return as a function of height and time. *Second from Top*: Production of buoyancy due to the mean vertical temperature gradient. The upper height used to calculate the average potential temperature gradient estimates is indicated by the dotted, dashed or full line. This is dominated by the surface layer production. *Third from Top*: Production due to temperature fluctuations. Note that the increase coincides reasonably well with the times that the structure appears at the measurement height. *Bottom*: Vertical divergence of the vertical flux of the temperature flux. The upper height used to calculate the gradient estimates is indicated by the dotted, dashed or full line.

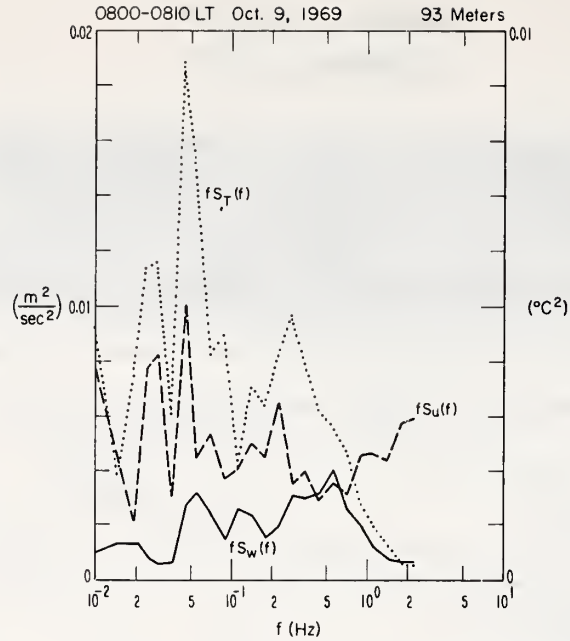


Fig. 20. Complex waves. — Estimates of $fS(f)$ vs. $\log f$ for u (horizontal wind speed), w (vertical wind speed), and T (temperature) during period A. Note the relatively low amplitudes of all variables. This corresponds to the region of the diffuse structure. However, there is a secondary peak in temperature at about 0.4 Hz, which does not occur for period B, where no echo return is observed (Figure 21).

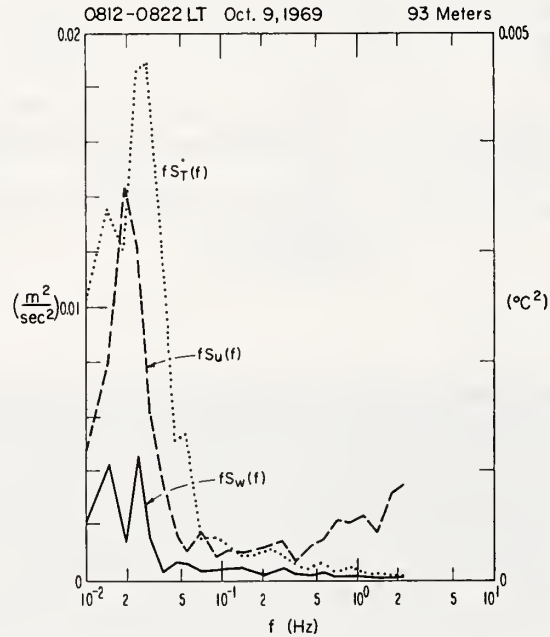


Fig. 21. Complex waves. — Estimates of $fS(f)$ vs. $\log f$ for u (horizontal wind speed), w (vertical wind speed), and T (temperature). This is for period B at 93 m, corresponding to the region below the diffuse echo return. Note the small spectral amplitudes, and the absence of the secondary peak in temperature at 0.4 Hz, compared to period A (Figure 20).

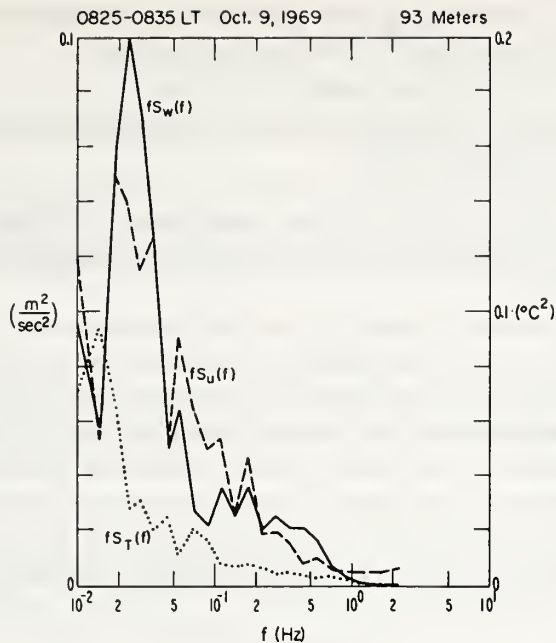


Fig. 22. Complex waves. — Estimates of $fS(f)$ vs. $\log f$ for u (horizontal wind speed), w (vertical wind speed), and T (temperature). This is for period C at 93 m, corresponding to the time when the unstable waves crossed this level. Note the very large increase in the amplitudes of u and especially w at all frequencies. This amplitude of w increases by a factor of 15 to 30 at 2×10^{-2} Hz compared to periods A and B.

would increase the mechanical energy production term by the same amount as well as the shear production of the Reynolds stress.

Spectra are estimated for u , w , and T for the periods A, B, and C at the 93-m level. Figure 20 shows spectra for period A; Figure 21 for period B; and Figure 22 for period C. The main difference between the spectrum estimated for A and that for B, appears to be a secondary peak in the spectrum of temperature for period A, occurring at about 0.3 Hz. The difference in the acoustic-sounder record between A and B is the very diffuse layer covering the 93-m level during A, and no return at this level during B. The spectra from the 93-m level during C, when the undulating layer appears at this height, shows a marked change from the spectra during A and B. The peaks of u and w occur around 3×10^{-2} Hz and have peak amplitudes of 20 and 30 ($\text{m}^2 \text{s}^{-2}$) Hz^{-1} respectively, compared to about 0.3 and 0.1 ($\text{m}^2 \text{s}^{-2}$) Hz^{-1} for the previous periods at the same frequency. Similarly, the amplitude of the temperature spectrum is much higher at 3×10^{-2} Hz, than during either period A or B.

5. Conclusions

From this study, we can see that acoustic echo sounding can help to identify atmospheric phenomena and aid in the following:

- (1) Determination of averaging times for estimates of turbulent quantities, for a given phenomenon, particularly in the stable boundary layer.
- (2) The study of the mixed layer below an inversion.
- (3) Aid in the interpretation of spectral estimates by knowing when the phenomenon starts and stops at a particular level.

In addition, the effects of wave phenomena on the turbulent quantities in the stable boundary layer have been seen. The stable wave motion is horizontal; it generates almost no turbulence, and is relatively unimportant in the transfer of heat and momentum in the vertical.

In contrast, the unstable or breaking wave has a strong vertical component, and as a result, this type of wave is important in the transport of heat in the vertical and horizontal, and momentum in the vertical. The downward and horizontal heat fluxes are orders of magnitude greater in the unstable wave than the stable wave. In addition, because of the increase in the Reynolds stress production through the shear, the mechanical production of turbulence is much greater than for the stable wave. Finally, the unstable wave can be one of the mechanisms for the intermittent generation of high frequency fluctuations in the stably stratified atmosphere.

References

- Emmanuel, C. B., Bean, B. R., McAllister, L. G., and Pollard, J. R.: 1972, 'Observations of Helmholtz Waves in the Lower Atmosphere with an Acoustic Sounder', *J. Atmospheric Sci.* **29**, 886-892.
- Little, C. G.: 1969, 'Acoustic Methods for the Remote Probing of the Lower Atmosphere', spec. issue on *Remote Environ. Sensing*, *Proc. IEEE* **7**, 571-578.
- Lumley, J. L. and Panofsky, H. A.: 1964, *The Structure of Atmospheric Turbulence*, Interscience Publications.
- McAllister, L. G., Pollard, J. R., Mahoney, A. R., and Shaw, P. J. R.: 1969, 'Acoustic Sounding - A New Approach to the Study of Atmospheric Structure', spec. issue on *Remote Environ. Sensing*, *Proc. IEEE* **7**, 579.
- Record, F. A. and Cramer, H. E.: 1966, 'Turbulent Energy Dissipation Rates and Exchange Processes Above a Non-Homogeneous Surface', *Quart. J. Roy. Meteorol. Soc.* **92**, 519-532.
- Stewart, R. W.: 1959, 'The Problem of Diffusion in a Stratified Fluid', *Adv. Geophys.* **1955**, **6**, *Int. Symp. on Atmos. Diffusion and Air Pollut.*
- Volkovitchaya, Z. I. and Ivanov, V. N.: 1970, 'Turbulent Energy Dissipation in the Atmospheric Boundary Layer', *Izv., Atmospheric Ocean Phys.* **6**, 435-444.
- Wyngaard, J. C., Izumi, Y., and Collins, S. A.: 1971, 'Behavior of the Refractive-Index-Structure Parameter Near the Ground', *J. Opt. Soc. Amer.* **61**, 1646.

Reprinted with permission from Remote Sensing of Environment
Vol. 2, 223-234, 1973.

The Comparison of Sensitivities of Atmospheric Echo-Sounders

RUSSELL B. CHADWICK

*Wave Propagation Laboratory, National Oceanic and Atmospheric Administration, U.S. Department of Commerce, Boulder, Colorado **

and

C. GORDON LITTLE

Wave Propagation Laboratory, National Oceanic and Atmospheric Administration, U.S. Department of Commerce, Boulder, Colorado

When comparing the sensitivities of atmospheric sounders, the entire system must be considered rather than just the physical phenomenon causing the scattered signal. A method is presented for the systematic comparison of the sensitivities of atmospheric sounders. The method is illustrated by three examples: the first involves the comparison of two microwave radars, the second the comparison of a microwave radar with an acoustic echo sounder, and the third the comparison of two continuous wave radars.

1. Introduction

The purpose of this paper is to present a systematic method for the comparison of relative sensitivities of different types of atmospheric echo sounders. The technique is illustrated by three examples: the first compares the sensitivities of two electromagnetic sounders, the second compares an acoustical and electromagnetic sounder, and the third compares two continuous wave sounders. The comparison can be made without detailed knowledge of how the sounders are implemented.

The comparison philosophy used here is that the systems should be operating under identical conditions and that these conditions should be as close to the normal operating conditions as possible. Thus, the systems are assumed to view the same atmospheric target, with identical range resolution, for the same length of time. The length of time the target is viewed could be different if the systems had scanning capability, but in the present analysis the viewing times are assumed equal.

In radar measurements, the controlling factor is the ratio of the peak output signal power to the average output signal power to the average output noise power. This is known as the output signal-to-noise ratio (SNR), and determines the probability of detecting the re-

turn signal. For a given target, the output SNR determines the sensitivity of that particular sounder; the ratio of output SNR for two systems, viewing the same target, is a direct comparison of their sensitivities.

In most systems the interfering signal is Gaussian additive noise and is assumed to have constant spectral density across the passband of the receiver, i.e., the noise is white Gaussian additive noise. It is well known that, for this type of noise, the optimum receiver (i.e., the receiver that maximizes the output SNR) is a matched filter, and the maximum output SNR is the ratio of the signal energy of the (two-sided) spectral density of the noise. Thus, to determine the SNR, it is sufficient to assume that the system has been realized in an optimum manner and then make adjustments in this SNR for known departures from the optimum receiver.

In Sec. 2, the output SNR of the receiver is related to the target by using the radar equation and the matched filter concept. The comparison equation is derived by forming a ratio of output SNR's. In Sec. 3, we compare the Wallops Island radar with the Institute for Telecommunication Sciences FM-CW radar, while in Sec. 4, the FM-CW radar is compared to the Wave Propagation Laboratory acoustic sound-

© American Elsevier Publishing Company, Inc., 1973

* Formerly with Institute for Telecommunication Sciences, Office of Telecommunications, U.S. Department of Commerce, Boulder, Colorado.

der. In Sec. 5, a pseudo-noise channel sounder, used in a backscatter configuration is compared to the FM-CW sounder.

2. Output Signal-to-Noise Ratio

A general model for the receiver structure of atmospheric echo sounders is given in Fig. 1. The received signal is $s(t)$ and the noise is $n(t)$. In almost all cases of interest, the noise (which is often due to thermal effects in the first active stage of the receiver) can be assumed to be a white, Gaussian random process. In acoustic sounding, the noise is due to random acoustical noise received by the antenna (Little, 1969). This case still fits the model in Fig. 1 since the acoustic noise is (relatively) wideband Gaussian noise and can be assumed to have a constant spectral density over the passband of the receiver.

The integrator components in Fig. 1 have many different names. Coherent integration is usually performed in the $i - f$ stage and hence is sometimes called $i - f$ or bandpass integration. Since it is before the detector, it is also sometimes called predetection integration. Incoherent integration is sometimes called video integration, lowpass integration, or postdetection integration. As a general rule, coherent integration is the more effective type of integration, but incoherent integration is easier to implement.

The coherent integrator which maximizes the output SNR is a matched filter (e.g., Cooper and McGillem, 1971). The SNR out of the matched filter is simply the ratio of signal energy to noise spectral density and is independent of signal shape. This SNR is further increased by the incoherent integrator, and this increase depends on the type of target and on the signal-to-noise ratio. DiFranco and Rubin (1968) give information about the SNR gain due to incoherent integration for different types of fluctuating targets. For rough estimates of radar performance, the gain due to incoherent integration can be taken as the square root of

the number of samples incoherently integrated when this number is small. As this number becomes large, a better approximation can be obtained from the graph on p. 405 of DiFranco and Rubin (1968). To develop an equation useful for comparison purposes, the square root of the number of samples will be used, but when the number of samples is larger, one should refer to DiFranco and Rubin (1968).

Thus, the SNR out of the incoherent integrator of Fig. 1 is

$$\text{SNR} = M^{1/2} \frac{\int_0^T s^2(t) dt}{N_0}, \quad (1)$$

where M is the number of samples incoherently integrated, N_0 is the (two-sided) noise spectral density, and T is the coherent integration time. For most sounders, T is approximately the reciprocal of the receiver bandwidth.

The signal-to-noise ratio of Eq. (1) can be rewritten in terms of received power as in Eq. (2):

$$\text{SNR} = \frac{M^{1/2} T P_r}{N_0}, \quad (2)$$

where P_r is the received power averaged over T (this is commonly referred to as peak power in pulse systems). The radar equation can be used to relate P_r to the radar target. The assumptions used are that the antenna has effective area A with an idealized circular beam and that the resolution cell is filled. If P is the transmitted peak power, η is the radar cross-section per unit volume, Δ is the range resolution cell, and R is the range to the target.

$$P_r = \frac{PA\eta\Delta}{4\pi R^2}. \quad (3)$$

This yields for the output signal-to-noise ratio

$$\text{SNR} = \frac{M^{1/2} T P A \eta \Delta}{4\pi R^2 N_0}. \quad (4)$$

Equation (4) assumes that the coherent integrator is a matched filter and that the signal propagates without loss. In practical applications this may not be the case; hence, the signal-to-noise ratio will be degraded and these degradations must be taken into account. Therefore, two additional terms must enter into Eq. (4), a loss term and a departure from



FIG. 1. Receiver structure.

matched filter term. Let L denote attenuation in the two-way path and f denote fraction of matched filter performance. Both terms are between zero and unity. Thus Eq. (4) becomes

$$\text{SNR} = \left(\frac{M^2 T P A \eta \Delta}{4\pi R^2 N_0} \right) (L f). \quad (5)$$

The sensitivity of sounder No. 1 compared to sounder No. 2 is readily found by forming a ratio of output signal-to-noise ratios. A meaningful comparison of the signal-to-noise ratios

$$C_{12} = \frac{\text{SNR}_1}{\text{SNR}_2}, \quad (6)$$

requires that the sounders view the same target with the same range resolution. In this case,

$$C_{12} = \left(\frac{M_1}{M_2} \right)^2 \frac{T_1 P_1 A_1 \eta_1}{T_2 P_2 A_2 \eta_2} \left(\frac{N_1}{N_2} \right)^{-1} \frac{L_1 f_1}{L_2 f_2}, \quad (7)$$

where the parameters of sounder No. 1 have been indexed by 1 and those of sounder No. 2 by 2.

It is convenient to express C_{12} logarithmically. When this is done, the comparison of sensitivity becomes

$$\begin{aligned} (C_{12})_{\text{dB}} = & \frac{1}{2} \left(\frac{M_1}{M_2} \right)_{\text{dB}} + \left(\frac{T_1}{T_2} \right)_{\text{dB}} \\ & + \left(\frac{P_1}{P_2} \right)_{\text{dB}} + \left(\frac{A_1}{A_2} \right)_{\text{dB}} \\ & + \left(\frac{\eta_1}{\eta_2} \right)_{\text{dB}} - \left(\frac{N_1}{N_2} \right)_{\text{dB}} \\ & + \left(\frac{L_1}{L_2} \right)_{\text{dB}} + \left(\frac{f_1}{f_2} \right)_{\text{dB}}, \end{aligned} \quad (8)$$

where the $()_{\text{dB}}$ denotes 10 log of the term inside the parentheses.

Equation (8) was derived for the monostatic case of collocated receiver and transmitter. If, in a bistatic situation, the two transmitting and two receiving beamwidths are equal and a common geometry is assumed, the trigonometric factors common to the numerator and denominator of Eq. (6) will cancel. Thus, Eq. (8) will remain valid for the bistatic situation provided that any required change in the radar cross section term is taken into account. The

examples presented here are in each case for the monostatic situation.

In comparing acoustic and electromagnetic probing systems, account must be taken of the differences in the scattering efficiencies of the atmosphere for the two types of waves. As has been stressed by Little (1969), acoustic waves are scattered much more strongly than radio waves, the scattering cross sections often being many orders of magnitude larger in the acoustic case than in the microwave case. We turn first to a comparison of the acoustic and microwave scattering cross sections of gaseous fluctuations in atmospheric refractive index, and then to the scatter of microwaves and acoustic waves by hydrometeors.

2.1 Scatter of Acoustic Waves and Radio Waves by a Nonhomogeneous Gaseous Atmosphere

Atmospheric turbulence, whether produced dynamically by the flow of air over a rough surface or convectively by solar heating of the ground, results in localized fluctuations in atmospheric parameters such as temperature, humidity, and velocity. These localized variations in atmospheric conditions correspond to fluctuations in local refractive index for electromagnetic and acoustic waves. The resultant three-dimensional field of refractive index is most conveniently expressed in terms of the three-dimensional spectrum of acoustic or microwave refractivity, i.e. the intensity (power) of the refractive index fluctuations as a function of spatial wavelength and direction.

A radar wave traversing such an irregular medium is weakly scattered by the fluctuations in refractive index. As shown by Booker and Gordon (1950), the radar waves are sensitive only to that Fourier component of the refractivity spectrum which meets the Bragg condition for scatter from periodic structures. The corresponding acoustic and microwave scattering cross sections will be given by

$$\begin{aligned} \sigma_a(\theta) &= 2\pi k^4 \cos^2 \theta \Phi_a[2k \sin(\theta/2)], \\ \sigma_r(\theta) &= 2\pi k^4 \sin^2 \chi \Phi_r[2k \sin(\theta/2)], \end{aligned} \quad (9)$$

where $4\pi\sigma_a(\theta)$ and $4\pi\sigma_r(\theta)$ are the scattering cross sections for acoustic and radio waves, as a function of scatter angle θ . The terms $\Phi_a[2k \sin(\theta/2)]$ and $\Phi_r[2k \sin(\theta/2)]$ are the

spectral intensities of the acoustic and radio refractive index fluctuations at the spatial number $2k \sin(\theta/2)$, this being the spatial wave number at which a bistatic radar, of wave number $k = 2\pi/\lambda$, is sensitive when operating at a scatter angle θ . The $\cos^2\theta$ and $\sin^2\chi$ terms in the two equations result from the differing polarizations of the two kinds of waves. The longitudinally polarized acoustic wave produces no scatter at a scatter angle of 90° ; the transversely polarized electromagnetic wave produces no scatter if the polarization angle χ (the angle between the scattered wave direction and the electric field vector in the incident wave) is zero. The symbols σ_a and σ_r denote the fraction of the incident power scattered, per unit volume, per unit solid angle, in a direction θ relative to the incident direction and, in the electromagnetic case, at a polarization angle χ .

At the acoustic and microwave wavelengths normally used in atmospheric studies, the turbulence is usually thought to be in the Kolmogorov inertial subrange and, therefore, locally homogeneous and isotropic. Under such circumstances, it is convenient to describe the refractivity fluctuations in terms of the structure constant of the refractivity C_n , defined by

$$D_n(r) = \overline{[n(x) - n(x+r)]^2}_{av} = C_n^2 r^{2/3}, \quad (10)$$

where $D_n(r)$ is the structure function of the refractivity and describes the way in which the mean square difference in refractivity between two test points, x and $x+r$, varies as a function of their spacing, r . The indicated average is over the possible realizations of refractive index. Thus, for a Kolmogorov spectrum of turbulence, C_n is the rms difference in refractive index at two points unit distance apart.

For radiowaves, the refractivity, N , of air is given by

$$N = (77.6/T)[P + 4810e/T], \quad (11)$$

where $N = (n-1) \cdot 10^6$, n = refractive index, T = absolute temperature in Kelvins, and e and P are, respectively, the partial pressure of water vapor and the total pressure of the air in mbars. Thus we see that, at microwave frequencies, the refractive index fluctuations are primarily due to local fluctuations in temperature

and/or water vapor. It is therefore convenient to look at these fluctuations separately in terms of the structure constants for temperature C_T and for humidity C_e , defined by

$$\begin{aligned} D_T(r) &= \overline{[T(x) - T(x+r)]^2}_{av} \\ &= C_T^2 r^{2/3}, \\ D_e(r) &= \overline{[e(x) - e(x+r)]^2}_{av} \\ &= C_e^2 r^{2/3}. \end{aligned} \quad (12)$$

For typical surface air conditions ($T = 288^\circ$, $P = 1013 \text{ mbar}$, $e = 10 \text{ mbar}$.)

$$\begin{aligned} C_{n,r} &= 1.26 \times 10^{-6} \text{ if} \\ C_T &= 1 \text{ kelvin meter}^{-1/3}, \end{aligned} \quad (13)$$

and

$$\begin{aligned} C_{n,r} &= 4.50 \times 10^{-6} \text{ if} \\ C_e &= 1 \text{ mbar meter}^{-1/3}. \end{aligned} \quad (14)$$

(The C_n values will vary slightly from these values as the mean atmospheric temperature or pressure is changed.)

For acoustic waves, because of the much stronger dependence of the phase velocity of sound on atmospheric temperature and humidity, we have

$$\begin{aligned} C_{n,a} &= 1720 \times 10^{-6} \text{ if} \\ C_T &= 1 \text{ kelvin meter}^{-1/3}, \\ C_{n,a} &= 138 \times 10^{-6} \text{ if} \\ C_e &= 1 \text{ mbar meter}^{-1/3}. \end{aligned} \quad (15)$$

In addition, the acoustic refractive index (unlike the electromagnetic refractive index) is affected by the wind velocity or, more specifically, by the component of the wind velocity along the acoustic ray path. Hence, in the presence of turbulence, the acoustic refractive index of the medium will be nonuniform (even if no temperature or humidity fluctuations exist); moreover, the acoustic refractive index field is a function of direction from which the medium is viewed.

Defining

$$C_v^2 = \overline{\left[\frac{u(x) - u(x+r)}{r^{1/3}} \right]^2}, \quad (16)$$

where u is the velocity of the component of the wind in the $+x$ direction at a position x , r is measured along the x axis, and the bar denotes the time-averaged value, then

$$\begin{aligned} C_{n,u} &= 4000 \times 10^{-6} \cos^2(\theta/2) \text{ for} \\ C_t &= 1 \text{ msec}^{-1} \text{ m}^{-1/3} \end{aligned} \quad (17)$$

The corresponding formulae for the scattering cross sections in the inertial subrange of a Kolomogorov spectrum of velocity, temperature, and humidity fluctuations are

$$\begin{aligned} \sigma_u(\theta) &= 0.016 k^{1/3} \cos^2 \theta [\sin(\theta/2)]^{-11/3} C_{n,u}^2, \\ \sigma_r(\theta) &= 0.016 k^{1/3} \sin^2 \theta [\sin(\theta/2)]^{-11/3} C_{n,r}^2, \end{aligned} \quad (18)$$

where

$$\begin{aligned} C_{n,u}^2 &= \left[1.85 \frac{C_t^2}{C^2} \cos^2(\theta/2) + \frac{C_t^2}{4T^2} \right. \\ &\quad \left. + \frac{0.02 C_e^2}{p^2} \right] \end{aligned} \quad (19)$$

and

$$C_{n,r}^2 = [1.59 C_t^2 + 20.1 C_e^2] \times 10^{-12}. \quad (20)$$

In these expressions, it has been assumed that, on the spatial scale $[2k \sin(\theta/2)]^{-1}$, the velocity, humidity, and temperature fields are uncorrelated and that the total scattered power is therefore the sum of the power scattered from the separate refractive index fluctuation fields.

The scattering cross sections for acoustic waves and for microwaves are proportional to $(C_{n,u})^2$ and $(C_{n,r})^2$, respectively. Hence, for temperature fluctuations alone, assuming that the two radars operate on the same wavelength,

$$\begin{aligned} (\eta_u, \eta_r)_T &= \left(\frac{10^{12}}{1.59 \times 4T^2} \right) \sim 2 \times 10^6 \\ &= 63 \text{ dB}. \end{aligned} \quad (21)$$

Similarly, for humidity fluctuations alone,

$$\begin{aligned} (\eta_u, \eta_r)_e &= \left(\frac{2 \times 10^{10}}{20.1 \times p^2} \right) \sim 1 \times 10^3 \\ &= 30 \text{ dB}. \end{aligned} \quad (22)$$

For a Kolomogorov spectrum of turbulence, the scattering cross sections are proportional to $\lambda^{1/3}$. If the wavelength of sounder No. 1 is λ_1 and of sounder No. 2 is λ_2 , the scattering cross section will require an additional term

$$\left[\left(\frac{\lambda_2}{\lambda_1} \right)^{1/3} \right]_{\text{dB}}$$

or 1 dB per two-fold difference in wavelength.

2.2 Scatter of Acoustic and Radio Waves by Hydrometeors

The above discussion dealt with the scattering cross section of gaseous atmosphere resulting from random, small-scale fluctuations in refractive index produced by localized fluctuations in temperature, humidity, or velocity. We turn now to the case of the per-unit-volume reflectivity of the atmosphere due to hydrometeors (i.e., when the rain, snow, hail, cloud, or fog particles are present).

The radar reflectivity of hydrometeors for microwaves and for acoustic waves have been compared by Little (1972). For the normal case, in which the operating wavelength is large compared with the hydrometeor diameter, the (backscatter) radar reflectivities per unit volume are given by

$$\begin{aligned} \eta_r &= \frac{\pi^5}{\lambda^4} \frac{1}{V} \sum_v D^6 K^2, \\ \eta_a &= \frac{25\pi^5}{36\lambda^4} \frac{1}{V} \sum_v D^6, \end{aligned} \quad (23)$$

where $\sum_v D^6$ represents the sum over the range cell of the diameter of each drop raised to the sixth power and $K^2 = (m^2 - 1)/(m^2 + 2)^2$, where m is the complex refractive index of the hydrometeor to microwaves, i.e., $m = n_1 - in_2$. In each case, we see the Rayleigh λ^{-4} dependence typical of scatter of energy by particles small compared with the wavelength; in both cases the echo power is proportional to $\sum_v D^6$.

The acoustic radar cross section of small water spheres is essentially independent of whether the water is solid or liquid. For microwaves, K^2 is of the order 0.9 for liquid water and 0.2 for ice. Substituting these values, we find that the ratio of radar reflectivity of hydrometeors for acoustic waves and microwaves of the same wavelength is

$$(\eta_a - \eta_r)_{\text{water}} = 0.77 \simeq -1 \text{ dB.} \quad (24)$$

and

$$(\eta_a - \eta_r)_{\text{ice}} = 3.5 \simeq +5 \text{ dB.} \quad (25)$$

If the radars differ in wavelength, then an additional correction term

$$\left[\left(\frac{\lambda_2}{\lambda_1} \right)^4 \right]_{\text{dB}}$$

is required, where λ_1 is the wavelength of the sounder No. 1 and λ_2 the wavelength of sounder No. 2. In this case, a two-fold difference in wavelength will result in an additional ± 12 dB correction to the relative scattering cross section.

In order to make a comparison of the relative sensitivity of two different sounders, it is necessary to determine the numerical values of each of the eight terms in Eq. (8). This is done in the next section in a comparison of the relative sensitivity of two electromagnetic sounders. In Sec. 4 an electromagnetic sounder and an acoustic sounder are compared; in Sec. 5, two continuous-wave microwave sounders are compared.

3. Comparison of Two Electromagnetic Sounders

In this section the sensitivity of the S-band radar at the Radar Atmospheric Research Facility on Wallops Island (WI) is to be compared to the sensitivity of the Institute for Telecommunication Sciences (ITS) FM-CW radar which the first-named author has worked with extensively. The parameters for the two systems are given in Tables 1 and 2.

The terms of Eq. (8) can now be found. The two sounders will be compared over a time of 100 msec, since this is the basic period of the

TABLE 1

Parameters for Wallops Island S-Band Pulse Radar
(Cox, 1969)

| | |
|-----------------------|---------------------|
| Frequency | 2.7 - 2.9 GHz |
| Peak power | 3 MW |
| Pulse width | 0.1 - 1.3 μ sec |
| Pulse repetition rate | 320 pps |
| Noise figure | 4 dB |
| Antenna diameter | 60 ft |

TABLE 2

Parameters for ITS FM-CW Radar

| | |
|-----------------------------|----------------------|
| Frequency range (max) | 2.9 - 3.1 GHz |
| Power (avg. or peak) | 200 W |
| Sweep duration | 50 msec |
| Effective noise temperature | 1000°K |
| Antenna diameter | 10 ft |
| Sweep repetition frequency | 10 sec ⁻¹ |

FM-CW radar. In 0.1 sec the WI radar incoherently integrates 32 pulses, while the FM-CW radar integrates 1 sweep. Since the comparison is the WI radar with respect to the FM-CW radar, the incoherent integration term is

$$\frac{1}{2} \left(\frac{M_1}{M_2} \right)_{\text{dB}} = \frac{1}{2} \left(\frac{32}{1} \right)_{\text{dB}} = +7 \text{ dB.} \quad (26)$$

where the subscripts 1 and 2 denote the WI radar and the FM-CW radar, respectively.

The coherent integration term can be found by assuming that the pulse length of the WI radar is 1 μ sec or the range cell is 150 m. From Table 2, the coherent integration time for the FM-CW radar is 50 msec since the range resolution is changed by changing the frequency range rather than signal length. Therefore

$$\left(\frac{T_1}{T_2} \right)_{\text{dB}} = \left(\frac{10^{-6}}{0.05} \right)_{\text{dB}} = -47 \text{ dB.} \quad (27)$$

The power term can be found directly from Tables 1 and 2.

$$\left(\frac{P_1}{P_2} \right)_{\text{dB}} = \left(\frac{3 \times 10^6}{200} \right)_{\text{dB}} = +42 \text{ dB.} \quad (28)$$

The antenna term can also be found from Tables 1 and 2, with the assumption that the antenna efficiencies are equal. Thus, the antenna term is given by a ratio of the physical areas of the antennas. Since the FM-CW radar uses both a transmitting and a receiving antenna, it is possible for the efficiency to be small if the overlap between the patterns is small. Here, we assume that the antennas have been well adjusted for the range of interest and hence, any loss due to non-overlapping patterns is negligible.

$$\left(\frac{A_1}{A_2} \right)_{\text{dB}} = \left[\left(\frac{60}{10} \right)^2 \right]_{\text{dB}} = +16 \text{ dB.} \quad (29)$$

The radar cross-section term is zero decibels

since the radar cross sections per unit volume for the two sounders are identical.

$$\left(\frac{\eta_1}{\eta_2}\right)_{\text{dB}} = (1)_{\text{dB}} = 0 \text{ dB.} \quad (30)$$

The receiver noise term can be found by converting the noise figure for the W1 radar to effective noise temperature, since the noise temperature of the FM-CW radar is given. Using the standard relation between noise figure, N_f , (in numbers) and noise temperature, T_k ,

$$T_k = (N_f - 1)290^\circ = 440^\circ \text{ K} \quad (31)$$

Then since the noise spectral densities are directly related to noise temperature,

$$-\left(\frac{N_1}{N_2}\right)_{\text{dB}} = -\left(\frac{440}{1000}\right)_{\text{dB}} = +3 \text{ dB.} \quad (32)$$

Since both sounders are electromagnetic, the loss terms will be small and equal. Therefore the loss term is

$$\left(\frac{L_1}{L_2}\right)_{\text{dB}} = \left(\frac{1}{1}\right)_{\text{dB}} = 0 \text{ dB.} \quad (33)$$

It is realistic to assume that the receiver for the W1 pulse radar approaches a matched filter and, thus, f_1 is unity. Since the output of the coherent integrator for the FM-CW radar is bandpass rather than lowpass, f_2 is 0.5.

$$\left(\frac{f_1}{f_2}\right)_{\text{dB}} = \left(\frac{1.0}{0.5}\right)_{\text{dB}} = +3 \text{ dB.} \quad (34)$$

Adding these terms gives +24 dB, or the W1 radar is 24 dB more sensitive than the FM-CW radar when the range resolution is 150 m. If the range resolution requirement is 15 m, the coherent integration time of the W1 radar is reduced by a factor of ten while all other parameters remain the same. The comparison then shows that the W1 radar is 14 dB more sensitive than the FM-CW radar. The comparison is summarized in Table 3.

Two things should be kept in mind when considering Table 3. First, returns from the range at which the W1 radar normally operates are so small that large range cells are required to provide the spatial integration required to detect these small signals. Thus, the comparison at 15 m resolution may not be realistic.

TABLE 3
Sensitivity of Wallops Island Radar
with Respect to the FM-CW Radar

| Range Resolution | C_{12} |
|------------------|----------|
| 150 m | + 24 dB |
| 15 m | + 14 dB |

Second, the FM-CW radars described in Bean et al. (1971) and Richter (1969) have minimum detectable signals which range 8 - 20 dB above that predicted by theory. In the absence of information on the exact causes of this loss in sensitivity, it is not possible to predict a number to use in the comparison equation. For this reason and since different equipment realizations may result in a smaller (or larger) value for this degradation, this loss has not been considered in this comparison or the comparison to follow.

In the next section, a more difficult comparison is undertaken, namely, the comparison of an acoustic system and an electromagnetic system.

4. Comparison of Acoustic and Electromagnetic Atmospheric Sounders

Here the sensitivity of the Wave Propagation Laboratories' (WPL) acoustic sounder is compared with the FM-CW radar. The parameters for the pulsed-type acoustic sounder are given in Table 4. These values for pulse width and pulse repetition frequency result in a maximum range of 170 m and a range resolution cell of 1.7 m for short range work, or a maximum range of 1.7 km at a range resolution of 17 m for longer range work.

The sensitivity of the FM-CW radar with respect to that of the acoustic sounder operating in the short range mode will first be calculated, using the acoustic repetition period of 1 sec as the measuring period. During this time the FM-CW radar incoherently integrates 10 samples while the acoustic sounder receives 1 pulse. The incoherent integration term therefore is

$$\frac{1}{2} \left(\frac{M_1}{M_2}\right)_{\text{dB}} = \frac{1}{2} \left(\frac{10}{1}\right)_{\text{dB}} = +5 \text{ dB.} \quad (35)$$

The coherent integration time of the FM-CW radar is, as before, 50 msec. The coherent

TABLE 4
Acoustic Sounder Parameters (Freeman Hall, private communication)

| | Short Range Mode | Long Range Mode |
|----------------------------|---------------------|-----------------------|
| Peak Power | 10 W | 30 W |
| Pulse Width | 10 msec | 100 msec |
| Pulse Repetition Frequency | 1 sec ⁻¹ | 0.1 sec ⁻¹ |
| Carrier Frequency | 4 kHz | 2 kHz |
| Antenna Diameter | 1.22 m | 1.22 m |
| Efficiency Factor | 0.1 | 0.1 |
| Receiver Bandwidth | 100 Hz | 30 Hz |
| System Noise (above kTB) | 10 dB | 10 dB |

integration time of the acoustic sounder is the reciprocal of the receiver bandwidth, or 10 msec. The coherent integration term is

$$\left(\frac{T_1}{T_2}\right)_{\text{dB}} = \left(\frac{0.05}{0.01}\right)_{\text{dB}} = +7 \text{ dB.} \quad (36)$$

The transmitted power term is found by referring to the sounder specifications for transmitted power. This term is

$$\left(\frac{P_1}{P_2}\right)_{\text{dB}} = \left(\frac{200}{10}\right)_{\text{dB}} = +13 \text{ dB.} \quad (37)$$

The antenna term can be found as easily. The geometrical collecting areas are in the ratio $(D_1/D_2)^2$; in addition, the acoustic transducer has an efficiency of only 0.1 compared with the unity efficiency of the microwave transducer. The term for the effective collecting areas is therefore

$$\left(\frac{A_1}{A_2}\right)_{\text{dB}} = \left(\frac{D_1}{D_2}\right)^2 + 10 = +18 \text{ dB.} \quad (38)$$

The radar cross section term is dependent upon the nature of the source of the refractive index fluctuations. For a Kolmogorov spectrum of temperature fluctuations, as indicated above,

$$\left(\frac{\eta_1}{\eta_2}\right)_{\text{dB}} = -63 \text{ dB.} \quad (39)$$

The noise level of the acoustic sounder is 10 dB and thus the effective noise temperature is approximately 3000°K. The FM-CW sounder has an effective noise temperature of approximately 1000°K. The noise level term therefore is

$$-\left(\frac{N_1}{N_2}\right)_{\text{dB}} = +5 \text{ dB.} \quad (40)$$

The loss term is dependent upon atmospheric conditions because of the strong variation of acoustic absorption with humidity. For the frequencies and ranges postulated, a figure of 10 dB is appropriate for the acoustic sounder; the absorption for the microwave radar is negligible. Hence,

$$\left(\frac{L_1}{L_2}\right)_{\text{dB}} = \left(\frac{1}{0.1}\right)_{\text{dB}} = +10 \text{ dB.} \quad (41)$$

The departure from matched filter performance can be estimated in exactly the same manner as in Sec. 3. In fact, the same numbers can be used:

$$\left(\frac{f_1}{f_2}\right)_{\text{dB}} = \left(\frac{0.5}{1.0}\right)_{\text{dB}} = -3 \text{ dB.} \quad (42)$$

When these terms are added, the result is -8 dB, or the sensitivity of the FM-CW sounder to temperature fluctuations is 8 dB below that of the acoustic sounder for the short-range mode of operation. Considering now humidity fluctuations instead of temperature fluctuations, the cross-section term becomes

$$\left(\frac{\eta_1}{\eta_2}\right)_{\text{dB}} = -30 \text{ dB.} \quad (43)$$

(instead of -63 dB); for humidity fluctuations, the FM-CW sounder is therefore 25 dB more sensitive than the acoustic echo sounder.

For the 1.7 km range, 17 meter range resolution, long-range mode of operation, the relative sensitivities may be shown to be

$$\text{for temperature echoes } \left(\frac{\text{SNR}_1}{\text{SNR}_2}\right)$$

$$= -13 \text{ dB.}$$

$$\text{for humidity fluctuations } \left(\frac{\text{SNR}_1}{\text{SNR}_2}\right)$$

$$= +20 \text{ dB.}$$

Considering now the case of hydrometeors, the relative sensitivity of the FM-CW and acoustic echo sounder (with the latter operating in the short-range mode) can be shown to be as summarized in Table 5.

TABLE 5

Analysis of Relative Sensitivity of FM-CW and Acoustic Sounders When Viewing Hydrometeors

| | |
|---------------------------------------|---------|
| Incoherent integration term | + 5 dB |
| Coherent integration term | + 7 dB |
| Transmitted power term | + 13 dB |
| Antenna term | + 18 dB |
| Radar cross section term (snow) | - 8 dB |
| Radar cross section term (rain) | - 2 dB |
| Noise level term | + 5 dB |
| Loss term (snow) | + 20 dB |
| Loss term (rain) | + 10 dB |
| Matched filter term | - 3 dB |
| Resultant relative sensitivity (snow) | + 57 dB |
| Resultant relative sensitivity (rain) | + 53 dB |

In deriving the values given in Table 5, the first four terms are as for atmospheric echoes. The relative scattering cross-sections are as indicated in Sec. 2 and include allowance for the difference in wavelength. The noise levels are assumed unchanged by the presence of precipitation; any increase of ambient acoustic noise level during precipitation would produce a corresponding degradation of the relative performance of the acoustic echo sounder. The loss term is assumed unchanged during rain, but is assumed increased by 10 dB during snow to allow for the known increase of attenuation associated with the lower absolute humidity at the lower temperatures.

We see that the present FM-CW sounder is some 53 dB to 57 dB more sensitive to hydrometeors than the present acoustic echo sounder, depending upon whether the hydrometeors are solid or liquid.

However, in considering this comparison, one should keep in mind that the FM-CW radar may have a sensitivity significantly less than that of the matched filter. (See the paragraph preceding Table 3.)

5. Comparison of Two Continuous-Wave Sounders

In this section we compare the FM-CW sounder with a pseudonoise continuous-wave (PN-CW) sounder, when both are viewing the clear atmosphere. The specific PN-CW sounder used for this comparison is the Institute for Telecommunication Sciences wideband tropospheric channel sounder operated in a monostat-

ic mode. Since the PN-CW sounder has a 100% duty cycle, separate transmitting and receiving antennas must be used and here the antennas are assumed identical to those used for the FM-CW sounder.

The PN-CW sounder transmits a signal with the phase coded according to a pseudo-noise sequence which is sometimes called a pseudo-random sequence or a shift register sequence. Here we will consider binary sequences and thus the phase of the carrier is either 0° or 180° depending on the current value of the sequence. Binary pseudonoise sequences are easily generated by an n stage shift register with appropriate feedback, and if the sequence is a maximal length sequence, it will have $2^n - 1$ binary symbols or bits before it repeats. Since the number of stages in the shift register can be fairly large (a common value of n is 10 for some communication applications), the sequences can be extremely long and hence the coherent integration time for the PN-CW sounder can be large.

Since we desire to compare the two sounders having equal range resolution, it is necessary to specify the bit length from the equation for range resolution Δ ,

$$\Delta = \frac{C\tau}{2} = \frac{C}{2B}, \quad (44)$$

where τ is the bit time length and B is the transmitted signal bandwidth. We will assume an electromagnetic signal, but this would also apply for acoustic signals. Assuming a Δ of 15 m, τ must be 100 nsec and B must be 10 MHz. The coherent integration time is

$$T = \tau(2^n - 1), \quad (45)$$

and a shift register of 9 stages will yield a coherent integration time of approximately 50 μ sec. The coherent integrator, in this case, is not a matched filter, but rather a correlator with a delayed version of the pseudonoise sequence as a reference signal. The processing here is also done simultaneously in the quadrature channel so that there are actually two correlators, which are realized by inexpensive components.

Several coded CW sounders have been described in the literature (Barrow et al., 1969; Reid, 1969). All CW sounders have the prob-

lem of signal leakage from the transmitter antenna to the receiver. The easiest way to solve this problem is to operate in the bistatic mode as described by Barrow et al. (1969). In the FM-CW radar the leakage signal is displaced in frequency from the return signal and can be filtered out, but this is not the case with the PN-CW sounder. Another way of solving the problem is to achieve as much isolation as possible and then coherently cancel as much of the leakage as possible. It is possible to achieve transmitter to receiver isolation of up to 160 dB using separate antennas in conjunction with a cancellation method (Nathanson, 1969). However, if the processor is linear, as is the case here, the correlator will significantly reduce the direct leakage signal. For the sounder described here, the direct leakage signal power at the output is reduced by 54 dB with respect to an equal power signal to which the correlator is matched. In addition, the output due to the leakage signal is a constant and simply biases the output slightly. Thus, the only requirement on the leakage signal is the same as for the FM-CW sounder, i.e., the leakage signal must not saturate the $r-f$ amplifier. This requirement is easy to achieve with shielded antennas.

Pertinent information on the ITS PN-CW sounder is given in Table 6. The first author has worked with this sounder. Since it is assumed that the PN-CW sounder and FM-CW sounder use identical antennas, the antenna parameters do not enter into the comparison. Also, since the two sounders have nearly identical receiver noise temperatures, the receiver noise does not enter into the comparison. Since both sounders are electromagnetic, the comparison equation reduces to

$$(C_{12})_{dB} = \frac{1}{2} \left(\frac{M_1}{M_2} \right)_{dB} + \left(\frac{T_1}{T_2} \right)_{dB} + \left(\frac{P_1}{P_2} \right)_{dB} + \left(\frac{f_1}{f_2} \right)_{dB} + \frac{1}{3} \left(\frac{\lambda_2}{\lambda_1} \right)_{dB}, \quad (46)$$

where the FM-CW sounder is indexed by 1 and the PN-CW sounder by 2.

The coherent integration time for the FM-CW sounder is the sweep duration, 50 msec, while the coherent integration time of the PN-CW sounder is the length of the pseudonoise

TABLE 6
PN-CW Parameters

| | |
|----------------------------|----------------|
| Transmitted power | 1 kW |
| Receiver noise temperature | 1000°K |
| Range resolution | 15 m |
| Code length (511 bits) | 51.1 μ sec |
| Center frequency | 2.17 GHz |

code, which is approximately 50 μ sec. Hence, the coherent integration term is

$$\left(\frac{T_1}{T_2} \right)_{dB} = \left(\frac{50 \times 10^{-3}}{50 \times 10^{-6}} \right)_{dB} = +30 \text{ dB}. \quad (47)$$

The comparison is made over 0.1 sec which is the basic time interval of the FM-CW sounder, so during this time, the FM-CW sounder incoherently integrates one sweep output. During the same time interval, the PN-CW sounder incoherently integrates 2000 outputs, i.e., in a 0.1 sec interval there are 2000, 50 μ sec subintervals. Hence, the incoherent integration term is

$$\frac{1}{2} \left(\frac{M_1}{M_2} \right)_{dB} = \frac{1}{2} \left(\frac{1}{2000} \right)_{dB} = -16 \text{ dB}. \quad (48)$$

The power term is found in a straightforward manner.

$$\left(\frac{P_1}{P_2} \right)_{dB} = \left(\frac{200}{1000} \right)_{dB} = -7 \text{ dB}. \quad (49)$$

The departure from matched filter term can be found by recalling that an ideal FM-CW sounder is 3dB below the matched filter and observing that Nathanson (1969) stated that practical PN sounders have sensitivities approximately 2 dB below the matched filter. The departure from matched filter term is given by

$$\left(\frac{f_1}{f_2} \right)_{dB} = -1 \text{ dB}. \quad (50)$$

The last term in the comparison arises because the radar cross sections for the two sounders are slightly different due to the difference in wavelength. This term is

$$\frac{1}{3} \left(\frac{\lambda_2}{\lambda_1} \right)_{dB} = \frac{1}{3} \left(\frac{0.138}{0.1} \right)_{dB} = +0.4 \text{ dB}, \quad (51)$$

and is small as one would expect.

When these four terms are added, we obtain +5 dB or the FM-CW sounder is 5 dB more sensitive than the PN-CW sounder. There are two things which will tend to decrease this 5 dB figure and tend to make the PN-CW sounder more sensitive than the FM-CW sounder. First, practical realizations of the FM-CW sounder appear to have a sensitivity significantly worse (8 – 20 dB) than the idealized FM-CW sounder. This is perhaps due to the fact that the modulating waveform is analog and can never be realized exactly. On the other hand, the PN-CW sounder has a digital modulation and the exact digital signal is easily generated. Practical realizations of PN sounders are only slightly less sensitive (2 dB) than the ideal sounder. The second effect which will tend to further reduce the relative sensitivity is that the one-half in the incoherent integration term in the comparison equation is a rule-of-thumb is overly pessimistic toward incoherent integration when the target is fluctuating (Di-Franco and Rubin 1968, p. 405).

A final item that should be noted in this comparison is that the PN-CW sounder can be modified to extract Doppler spectra from any given range. The first range ambiguity is approximately 7.5 km and at this range the first velocity ambiguity is approximately 2 km per sec or far in excess of that of any atmospheric target.

6. Summary

This paper presents a method of comparing atmospheric sounder sensitivities. The comparison is made by forming the ratio of output signal-to-noise ratios when the sounders are viewing the same atmospheric target for the same length of time. The advantage of the method is that the comparison is made systematically, and that the effects of changes in any parameter are readily identified. The comparison equation considers eight different factors: incoherent integration, coherent integration, transmitted power, effective aperture, radar cross section, receiver noise, propagation loss, and departure from the matched filter.

Three examples were presented. First, the Wallop Island ultrasensitive radar was compared to the FM-CW radar. At 150 m range resolution the WI radar was 24 dB above the

FM-CW radar, and at 15 m range resolution the difference was 14 dB.

The second comparison was between the FM-CW radar and the acoustic sounder. For 170 m range and 1.7 m range resolution, the WPL acoustic sounder is some 8 dB more sensitive than the ITS FM-CW sounder when looking at temperature irregularities, but some 25 dB less sensitive when looking at humidity fluctuations. At 1.7 km range and 17 m range resolution, temperature eddies would have 13 dB greater SNR on the acoustic sounder; humidity eddies would show 20 dB less SNR on the acoustic sounder, relative to the FM-CW sounder. The acoustic sounder is much less sensitive than the FM-CW sounder to hydrometeors. Using the acoustic sounder in the 170 m range, 1.7 m range resolution mode, the SNR ratio relative to the FM-CW radar is –53 dB for rain and –57 dB for snow.

The FM-CW sounder was then compared to a PN-CW sounder when both are used in a monostatic mode for clear air targets. The idealized FM-CW sounder is 5 dB more sensitive than a PN-CW sounder, but this advantage may be significantly reduced when a practical FM-CW sounder is considered.

Nomenclature

| | |
|------------------|-----------------------------------------------------------------|
| $s(t)$ | received signal |
| $n(t)$ | noise |
| M_1 | number of samples incoherently integrated for the first sounder |
| T_1 | coherent integration time for first sounder |
| P_1 | transmitted power for first sounder |
| A_1 | effective aperture area for first sounder |
| η_1 | radar cross section per unit volume for first sounder |
| N_1 | noise spectral density for first sounder |
| L_1 | loss term for first sounder |
| f_1 | departure from matched filter term for first sounder |
| SNR ₁ | output signal-to-noise ratio for sounder No. 1 |
| C_{12} | sensitivity of sounder No. 1 with respect to sounder No. 2 |
| N_0 | spectral density of white noise |
| Δ | range resolution cell |
| R | range to target |
| τ | element length of PN code |
| B | bandwidth |

Reprinted with permission from *Boundary Layer Meteorology*
Vol. 2, 371-380, March 1972.

ATMOSPHERIC WAVES OBSERVED IN
THE PLANETARY BOUNDARY LAYER USING AN ACOUSTIC
SOUNDER AND A MICROBAROGRAPH ARRAY

W. H. HOOKE, J. M. YOUNG, and D. W. BERAN

*Wave Propagation Laboratory,
Environmental Research Laboratories,
National Oceanic and Atmospheric Administration,
Boulder, Colo. 80302, U.S.A.*

(Received 1 September, 1971)

Abstract. Acoustic sounder and microbarograph records of atmospheric waves propagating in the planetary boundary layer over Table Mountain, Colorado, are presented and compared. The two observing techniques are complementary in that the array provides wave amplitude, horizontal phase speed, direction, and wavelength, while the sounder provides a detailed picture of temporal changes in the structure of the lowermost kilometer or so of the Earth's atmosphere.

This paper describes preliminary comparisons of observations of atmospheric waves in the planetary boundary layer made using an acoustic sounder (McAllister, 1968; McAllister *et al.*, 1969; Little, 1969; Beran, 1970; Beran *et al.*, 1971) and a microbarograph array (Cook, 1962, 1969; Cook and Young, 1962).

The sounder emits acoustic pulses and utilizes the echo returns from small-scale atmospheric temperature fluctuations to provide a detailed picture of temporal changes in boundary-layer structure over the site, while the microbarograph array provides continuous records of the time rate of change of the atmospheric pressure as passively measured at ground level at several separate locations, in this case separated from each other by a kilometer or so. The fluctuations in the individual pressure traces provide wave period (in the frame of reference of an observer fixed with respect to the ground) as well as wave amplitude; phase shifts between the pressure patterns at the different elements of the array provide horizontal wave phase speed, direction of travel, and horizontal wavelength. The acoustic sounder record also provides wave period as well as an indirect measure of wave amplitude; in addition it may provide some estimate of vertical phase velocity and wavelength. (The last two estimates are usually quite crude, however, as for example when the vertical wavelength is large compared to the boundary-layer thickness.) In addition, the sounder presents a vivid picture of boundary-layer dynamics that can, under suitable circumstances, provide insight into the mechanisms responsible for the wave generation and subsequent wave behavior.

The observing instruments were located on Table Mountain, a very flat mesa located approximately 10 km north of Boulder, Colorado. The microphones were situated atop the mesa itself, while the sounder was in a ravine at the mesa's northeast edge. The experimental configuration is shown in Figure 1. The points marked M1, M2, M3, M4 denote the positions of the microbarographs, while the point marked A denotes the position of the acoustic sounder.



Fig. 1. Location of the observing instruments on Table Mountain. The circles marked M1, M2, M3, and M4 indicate the positions of the microbarographs, and the circle marked A represents the position of the acoustic sounder. The entire system is located just east of the foothills of the Rocky Mountains.

This system has gathered many hours of data in the first half of 1971, but here we shall be concerned only with the night of March 2–3. Figure 2 shows the acoustic sounder record and the four pressure traces for the 0000 to 0400 LT period on the morning of March 3. The vertical axis of the acoustic sounder record is the height, 850 m full scale (with roughly the lowest 50 m blanked to avoid ground clutter), and the horizontal axis is the time; dark areas in the figure represent time-height intervals of strong echo returns. As displayed above the sounder record, the four pressure traces have been time-shifted relative to one another so as to provide maximum cross-correlation between 0100 and 0200 LT; as displayed below it, they have been time-shifted to provide maximum cross-correlation between 0300 and 0330 LT. In both cases, the correlation among the four pressure traces, while obvious, is by no means perfect; the lack of complete correspondence may result either from the dispersive

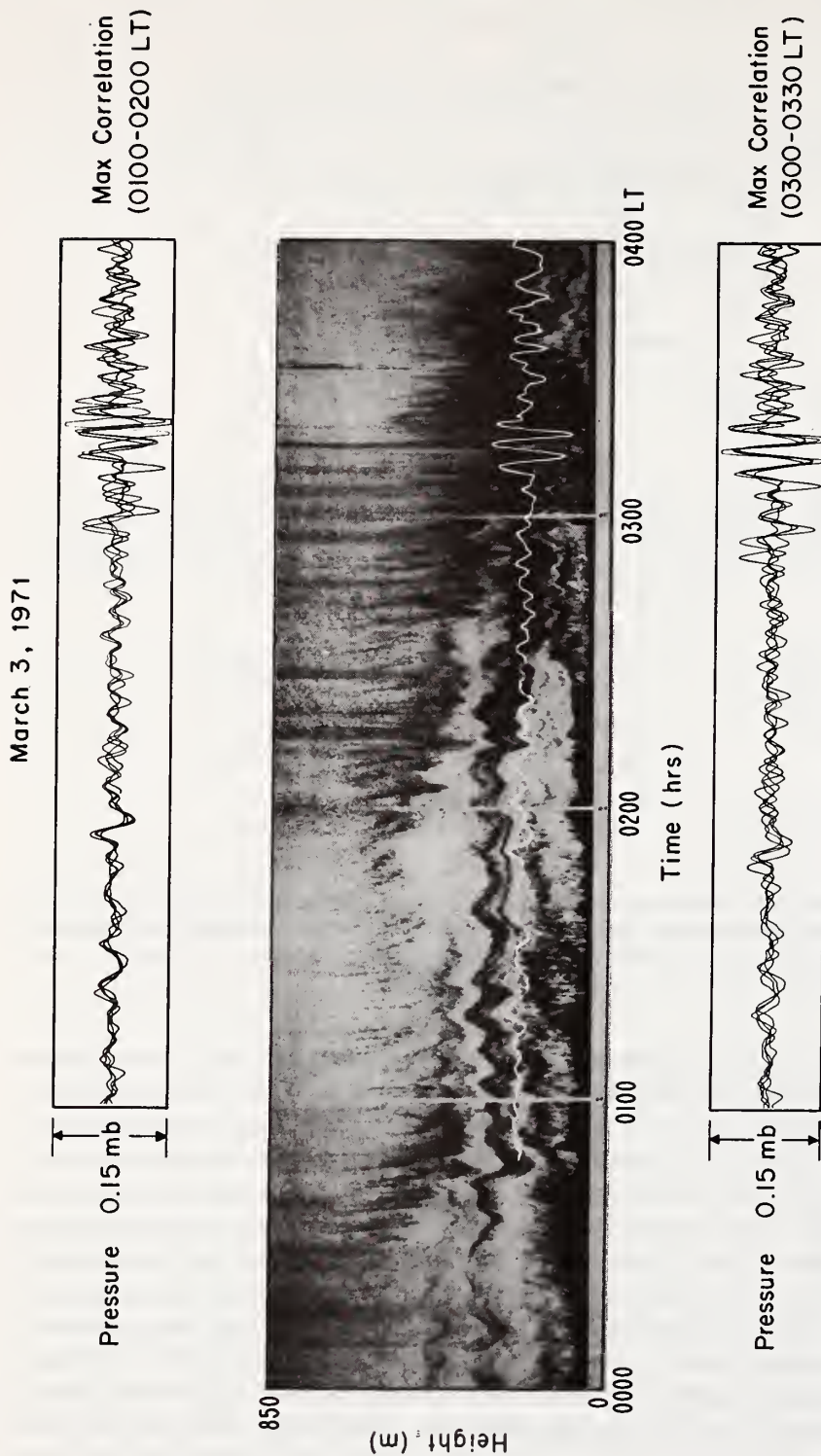


Fig. 2. Microbarograph and acoustic sounder records for the early morning of March 3, 1971. The dark portions of the acoustic sounder record represent height-time intervals of strong echo returns. As displayed above the sounder record, the microbarograph pressure traces have been time shifted relative to one another so as to provide maximum cross-correlation in the 0100-0200 LT time interval. As displayed below it, they have been shifted to provide maximum cross-correlation for the event occurring at about 0315 LT. (In both cases, time shifts are of the order of 2 minutes.) During the 0200-0300 LT and 0330-0400 LT intervals, no single wave component dominates. The white line superimposed on the sounder record is the pressure trace of the M3 microbarograph. Time scales are the same for all records. (Strictly speaking, the microbarographs directly measure dp/dt , not the pressure p ; the pressure scale shown assumes a wave of 7-min period.)

character of the waves or from their interaction with and distortion by the medium as they propagate. The pressure traces for the 0000 to 0100 LT interval are not shown because the pressure fluctuations and the correlation between them during this period were quite weak.

In order to show more clearly the degree of correlation between the pressure fluctuations and variations in the heights of strata of strong echo returns, the pressure trace recorded by the northernmost microphone (M3 in Figure 1; the unit closest to the sounder) has been overlaid on the sounder record as a white line. As among the four pressure traces themselves, there is good, but not perfect, correspondence between features of the sounder record and this pressure trace, and as before, the lack of perfect correlation results in part from the large distance between the sounder and the microphone. In part, however, the discrepancies here arise from a fall off in the response of the microbarograph system at very low frequencies (curve N3 of Figure 2, Chrzanowski *et al.*, 1961). This fall off appears to account both for the deterioration in the correspondence between the two records in the 0100–0200 LT interval, when the dominant fluctuations are of 9-min period, and for the failure of the microphones to detect any pressure changes associated with fluctuations in boundary-layer thickness over periods of several hours.

It might be noted that the good correlation between the pressure changes and fluctuations in the height of the strata of strong echo returns is itself of some interest, since such a good correspondence between the two types of records is not a foregone conclusion. This is because for waves of such long periods, the pressure fluctuations primarily reflect changes in the weight of the total air column above the sensor; waves having vertical wavelengths small compared to a scale height and elevated disturbances of very small vertical extent produce minimal pressure fluctuations at the ground. In several such cases examined, there is indeed a notable lack of correspondence between the sounder records and the pressure traces.

Several features of the records in Figure 2 are of interest:

(a) *The weakness of the returns in the early part of the record.* When used in the monostatic, or backscatter mode, as here, the acoustic sounder receives echoes from atmospheric temperature fluctuations only. When the temperature lapse rate of the atmosphere is nearly adiabatic, these fluctuations are quite weak. Thus, the weak strength of the echoes in the early part of the record may result in part because the nighttime inversion has not yet become well established.

(b) *The presence of a number of strata in the echo returns.* It follows from what was said immediately above that these strata are regions of enhanced turbulent temperature fluctuations, produced either by local increases in the dynamic instability or by local lapse rate conditions favoring increased temperature fluctuations for a given turbulence intensity. Early results from comparison of acoustic sounder records with *in situ* meteorological measurements on an instrumented tower suggest that both effects are typically at work, with those of the temperature lapse rate perhaps predominating (C. B. Emmanuel, private communication). In any event, the sounder record strikingly reveals the lack of homogeneity and stationarity in the atmospheric boundary layer.

(c) *The wavelike undulations of the strata.* The atmospheric wave motions revealed by these undulations are quite obviously a major dynamical feature of the stable atmospheric boundary layer. They pervade the entire record, and appear to have a broad range of temporal and (presumably) spatial scales. The undulations of longest period are not in fact revealed very well in Figure 2; they appear as oscillations of the entire boundary layer of several-hours period, and cause the boundary layer to have a maximum apparent thickness of roughly 500–600 m at about 0130–0200 LT, and a minimum thickness of perhaps less than 100 m at about 0315 LT. The longer-period undulant structure is better seen in Figure 3, which shows the acoustic sounder record for the entire night. It is worth noting that fluctuations of such long period are a common feature of the nighttime acoustic sounder records. As mentioned above, the microbarograph array as presently engineered does not detect fluctuations of such long period, and the sounder information alone does not permit us to say whether these are propagating waves, generated elsewhere, or some type of standing oscillation produced by local orographic features. It is tempting, for example, to relate such motions to the upper-level mesoscale structure observed by Mantis (1963), Kao and Woods (1964), Pinus *et al.* (1967), and others, and to the mesoscale pressure fluctuations studied by Herron and Tolstoy (1969) and attributed to tropospheric wind structure. In the future, the microbarograph system will be modified to permit study of these long-period fluctuations.

The sounder record also reveals other oscillations of considerable interest, in particular the oscillation of roughly 9-min period prevailing between 0100 and 0200 LT, and the strongly nonlinear oscillation of roughly 4.5-min period occurring between 0300 and 0330 LT. (During the 0200–0300 LT intervals, no single wave component dominates.) The wave parameters for these two events as determined from the time shifts of the pressure traces in Figure 2 are given in Table I. Table I also gives wave phase velocities and directions of travel as computed from the amplitude of the pressure fluctuations and anemometer data taken near the sounder, using the ‘impedance’ relation (Gossard and Munk, 1954)

$$V_{ph} = p' / (\rho_0 u'), \quad (1)$$

TABLE I
Wave Parameters for the Two Events of March 3, 1971

| Wave Parameters | 0100–0200 LT | 0300–0330 LT |
|-------------------------------------------------------|------------------------|-------------------------|
| Period | 525 s | 265 s |
| Horizontal phase speed | 13 m s ⁻¹ | 6.5 m s ⁻¹ |
| Horizontal wavelength | 6.8 km | 1.7 km |
| Direction of arrival | 270° | 295° |
| Pressure amplitude | 0.044 mb | 0.132 mb |
| Wind velocity amplitude | 0.25 m s ⁻¹ | 2 m s ⁻¹ |
| Phase speed (estimated from ‘impedance’ relation) | 13.5 m s ⁻¹ | 5.1 m s ⁻¹ |
| Direction of arrival (estimated from anemometer data) | 284° | 259° |
| Mean surface wind speed | 1 m s ⁻¹ | < 0.2 m s ⁻¹ |
| Mean surface wind direction | 220° | 240° |

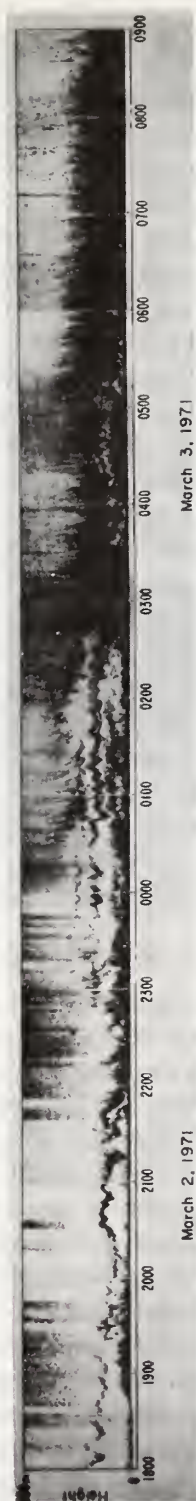


Fig. 3. The acoustic sounder record for the entire night of March 2-3, 1971, showing the long-period fluctuations (\sim several hours) in boundary-layer thickness.

where V_{ph} is the horizontal wave velocity, p' and u' are the amplitudes of the wave-associated pressure and horizontal wind perturbations, respectively, and ρ_0 is the background atmospheric density. The direction of wave propagation is the direction of the wave-associated wind perturbation at the time of maximum pressure. The good agreement between the two methods may be to some extent fortuitous in view of the light and variable winds prevailing at the time.

The 0100–0200 LT event had a 9-min period and a 13 m s^{-1} horizontal phase velocity, giving an estimate for its horizontal wavelength of 6.8 km. It is perhaps worth noting that if we use this figure to convert the time sequence of Figures 2 and 3 into a spatial picture, we find that the 0100–0200 LT interval corresponds to a spatial interval of the order of 50 km, implying a roughly fifty-fold increase in the width of this portion of the record to give a true spatial representation of the wave.

The 0300–0330 LT event had a 4.5 min period and a 6.5 m s^{-1} horizontal phase velocity, giving a horizontal wavelength of only 1.7 km. This event, shown in detail in Figure 4, is striking because of its large amplitude and cusped shape, features which are qualitatively similar to the shapes of the internal waves observed by Gossard *et al.* (1970) using an FM-CW radar (Richter, 1969) and discussed by Gossard and Richter (1970). The acoustic sounder records we have examined suggest that such events occur relatively frequently. There is also some indication that they may occur preferentially at those times when the apparent thickness of the boundary layer, as indicated by the height of the highest echo return, appears to be least, i.e., they may occur only at certain phases of the longer-period oscillations prevailing in the boundary layer. We hope to investigate these features of the records more systematically in the future, but we merely note here that such behavior appears consistent with the qualitative description given by Phillips (1966), Hodges (1967), Orlanski and Bryan (1969), Gossard *et al.* (1971), and others, of the physics underlying the intermittent behavior of oceanic and atmospheric turbulence.

In a particular application of such concepts, G. Chimonas (private communication) has recently pointed out that in cases where the ambient Richardson number is close to, but just above $1/4$, as often occurs in the stable atmospheric boundary layer (Webb, 1970; Oke, 1970; Businger *et al.*, 1971), if internal gravity waves propagating in the boundary layer can stimulate the onset of turbulence in those regions of the wave profile where the wave has lowered the Richardson number below $1/4$, this will result in a complicated energy and momentum exchange between the mean flow, the wave, and the turbulence, leading to instability and explosive growth of wave and turbulence amplitudes. In the present application of Chimonas' general result, it might seem appropriate to identify the wave of several-hour period as a trigger for the turbulence. The 0300–0330 LT interval might then represent a region where the wave-associated changes in boundary-layer wind and temperature structure are such that the Richardson number has been driven below $1/4$. The cusped wave would then be presumed to be the most unstable wave mode in this region and would represent a first step in the onset of turbulence.

Alternatively, with the apparent reduction in boundary-layer thickness occurring at this time, it is tempting to suppose that the small-scale waves ducted in the boundary-

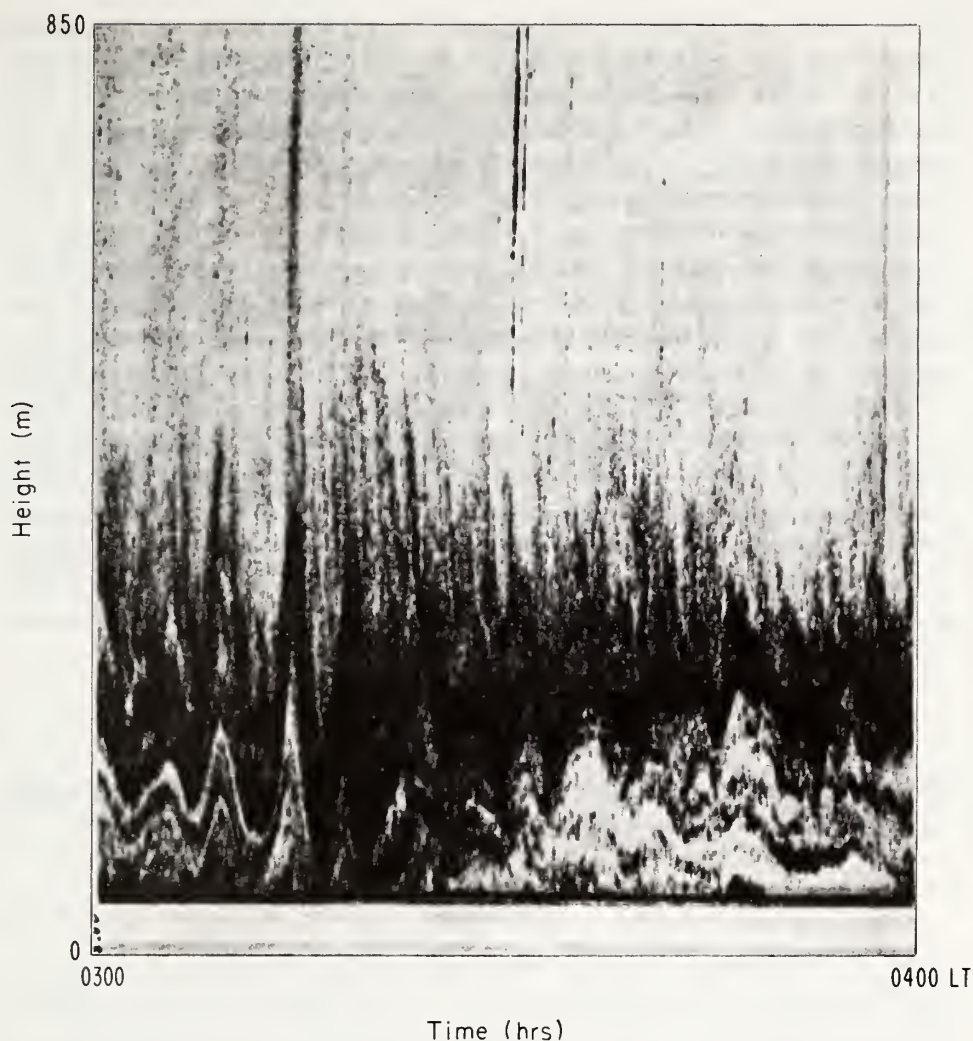


Fig. 4. A detail of the acoustic sounder record for the 0300–0400 LT March 3, 1971, period, showing the large-amplitude cusped waves of 4.5-min period similar in shape to the waves studied by Gossard and Richter (1970); these authors have interpreted the wave shape as resulting from propagation on a fluid interface just above a rigid lower boundary.

layer inversion might be increasing in amplitude as the duct thickness decreases, just as ocean waves steepen on a sloping beach; apart from some reflection, the total wave energy would remain constant, but would be confined to a smaller area, resulting in an increase in wave energy flux and amplitude.

Interpretation of observations such as these must remain essentially speculative, however, until we can supplement these data with concurrent meteorological information, in particular, background wind and temperature profiles, thus providing a more complete picture of boundary-layer structure and specifying whether individual

strata of strong echo returns are strata of low Richardson number or steep lapse rate or both. With such information, and with the use of Doppler acoustic sounding (Beran *et al.*, 1971), it should then be possible to relate the height fluctuations of these strata to the wave amplitude, to determine the directions and magnitudes of the associated wave energies and momentum fluxes, and determine the energy exchanges between the wave, the turbulence, and the background flow.

The original manuscript ended here, but we have appended a brief comment in response to a question asked by a referee, who has inquired about the 'grass' which appeared to be present atop the boundary layer throughout the acoustic-sounder record, but which became particularly prominent at about 0240 LT. This feature of the records is actually fairly common (see, for example, some of the records in the paper by McAllister *et al.* (1969)) and has not escaped our attention; we did not comment on it originally simply because of a lack of detailed information. We do know, however, from results of other experiments, not yet reported, that this structure appears to represent wavefronts of quite small-scale waves (vertical wavelengths ~ 100 m, horizontal wavelengths ~ 500 m, so that the fronts are in fact nearly horizontal, despite their appearance on the compressed horizontal scale of these records). Their exact role in boundary-layer dynamics is not yet understood.

Acknowledgements

Gary E. Greene, John W. Wescott, and Ben C. Willmarth aided in various aspects of the data acquisition and analysis.

References

- Beran, D. W.: 1970, 'Turbulence Detection', Ph. D. Thesis, University of Melbourne.
- Beran, D. W., Little, C. G., and Willmarth, B. C.: 1971, 'Acoustic Doppler Measurements of Vertical Velocities in the Atmosphere', *Nature* **230**, 160–162.
- Businger, J. A., Wyngaard, J. C., Izumi, Y., and Bradley, E. F.: 1971, 'Flux-Profile Measurements on the Atmospheric Surface Layer', *J. Atmospheric Sci.* **28**, 181–189.
- Chrzanowski, P., Greene, G., Lemmons, K. T., and Young, J. M.: 1961, 'Traveling Pressure Waves Associated with Geomagnetic Activity', *J. Geophys. Res.* **66**, 3727–3733.
- Cook, R. K.: 1962, 'Strange Sounds in the Atmosphere, Part I', *Sound* **1**, 12–16.
- Cook, R. K.: 1969, *Atmospheric Sound Propagation*, Final Rept. Panel on Remote Atmospheric Probing, of the Committee on Atmospheric Sciences NAS-NRC, 633–669.
- Cook, R. K. and Young, J. M.: 1962, 'Strange Sounds in the Atmosphere, Part II', *Sound* **1**, 25–33.
- Gossard, E. E. and Munk, W. H.: 1954, 'On Gravity Waves in the Atmosphere', *J. Meteorol.* **11**, 259–269.
- Gossard, E. E., Richter, J. H., and Atlas, D.: 1970, 'Internal Waves in the Atmosphere from High-Resolution Radar Measurements', *J. Geophys. Res.* **75**, 3523–3536.
- Gossard, E. E. and Richter, J. H.: 1970, 'The Shape of Internal Waves of Finite Amplitude from High-Resolution Radar Sounding of the Lower Atmosphere', *J. Atmospheric Sci.* **27**, 971–973.
- Gossard, E. E., Jensen, D. R., and Richter, J. H.: 1971, 'An Analytical Study of Tropospheric Structure as Seen by High-Resolution Radar', *J. Atmospheric Sci.* **28**, 794–807.
- Herron, T. J. and Tolstoy, I.: 1969, 'Tracking Jet Stream Winds from Ground Level Pressure Signals', *J. Atmospheric Sci.* **26**, 266–269.

- Hodges, R. R., Jr.: 1967, 'Generation of Turbulence in the Upper Atmosphere by Internal Gravity Waves', *J. Geophys. Res.* **72**, 3455–3458.
- Kao, S. K. and Woods, H. D.: 1964, 'Energy Spectra of Mesoscale Turbulence along and across the Jet Stream', *J. Atmospheric Sci.* **21**, 513–519.
- Little, C. G.: 1969, 'Acoustic Methods for the Remote Probing of the Lower Atmosphere', *Proc. IEEE* **57**, 571–578.
- Mantis, H. T.: 1963, 'The Structure of the Winds of the Upper Troposphere at Mesoscale', *J. Atmospheric Sci.* **20**, 94–106.
- McAllister, L. G.: 1968, 'Acoustic Sounding of the Lower Troposphere', *J. Atmospheric Terrest. Phys.* **30**, 1439–1440.
- McAllister, L. G., Pollard, J. R., Mahoney, A. R., and Shaw, P. J. R.: 1969, 'Acoustic Sounding – A New Approach to the Study of Atmospheric Structure', *Proc. IEEE* **57**, 579–587.
- Oke, T. R.: 1970, 'Turbulent Transport Near the Ground in Stable Conditions', *J. Applied Meteorol.* **9**, 778–786.
- Orlanski, I. and Bryan, K.: 1969, 'Formation of the Thermocline Step Structure by Large Amplitude Internal Gravity Waves', *J. Geophys. Res.* **74**, 6975–6983.
- Phillips, O. N.: 1966, *The Dynamics of the Upper Ocean*, Cambridge University Press, 261 pp.
- Pinus, N. S., Reiter, E. R., Shur, G. N., and Vinnichenko, N. K.: 1967, 'Power Spectra of Turbulence in the Free Atmosphere', *Tellus* **19**, 206–213.
- Richter, J. H.: 1969, 'High Resolution Tropospheric Radar Sounding', *Radio Sci.* **4**, 1261–1268.
- Webb, E. K.: 1970, 'Profile Relationships: The Log-Linear Range, and Extension to Strong Stability', *Quart. J. Roy. Meteorol. Soc.* **96**, 67–90.

Remote Sensing of the Atmosphere

*C. Gordon Little,
NOAA Wave Propagation
Laboratory*

The attainable quality and scope of an atmospheric forecasting service is determined by the observational data set on which it is based—and especially by the density in time and space of the relevant observations. During the past several years it has become increasingly apparent that the steadily growing need for short-term, local weather forecasts cannot be met by a mere expansion of our present radiosonde networks. A major breakthrough in atmospheric measurement capability is required. Ideally, one would like to use ground-based instrumentation capable of remotely measuring the relevant atmospheric parameters in the three-dimensional space around the instrument, out to a range of many kilometers.

Conceptually, such a measurement capability would have many advantages. First, the measurements would be taken remotely and would not require that in situ sensors be carried to the atmospheric region to be measured. Second, unlike the zero-dimensional measurements provided by stationary in situ sensors, or the basically one-dimensional data supplied by aircraft or radiosonde instrumentation, remote sensing instruments often have the ability to scan the surrounding atmosphere in two or three

dimensions. Third, remote sensing instrumentation often provides much better resolution in time and space than that available from in situ instrumentation, implying a much more complete data set. Fourth, while standard radiosondes are limited to measurements of temperature, humidity, and wind, remote sensing instrumentation is capable (at least conceptually) of measuring more sophisticated parameters, such as spectrum of turbulence, or momentum flux. Fifth, the measurement system does not modify the parameter being measured, a matter of serious concern in some in situ systems, such as those aboard aircraft. Sixth, the remotely sensed measurements involve some integration along a line, or over an area, or throughout a volume. As such, they are likely to be more representative of the medium than measurements from a single point sensor, which may be

adversely affected by local or transient perturbations. Seventh, unlike radio-sonde and aircraft systems, remote sensing instrumentation is usually automatic and can provide data 24 hr per day with greatly reduced or even no manpower.

This paper summarizes the present status of attempts to create atmospheric remote sensing systems possessing many of the advantages listed above.

Methods of Remote Sensing

Remote sensing relies on the quantitative observation and interpretation of the interaction of some form of wave acoustic or electromagnetic—with the atmosphere. In reviewing the status of ground-based remote sensing, it is helpful to recognize that the different types of waves interact differently with the atmosphere, and therefore have different measurement capabilities. Considering the gaseous components of the atmosphere, we find that acoustic

waves interact very much more strongly with the atmosphere than do electromagnetic waves; hence acoustic systems may be readily used, for example, to monitor the internal structure of the atmospheric boundary layer. On the other hand, because of this strong interaction, acoustic observations are likely to be limited to ranges of only a few kilometers.

Electromagnetic waves interact very weakly with the gaseous atmosphere in the optical and radio parts of the spectrum, and remote sensing of the clear air by electromagnetic waves is therefore relatively difficult. Nevertheless, our highly developed radar technology does permit clear air echoes to be obtained, at least for research purposes. Similarly, with the advent of lasers it is being recognized that certain spectroscopic interactions (resonant interactions which occur at certain frequencies or bands of frequency) can be used, especially at the higher frequencies. New remote sensing methods based on

Raman scatter or on spectroscopic absorption techniques are now being developed. In the long run, and especially as laser technology develops further, we may expect that optical interrogation of the clear atmosphere will increase greatly.

Turning now to hydrometeors and aerosols, we find that much of the difference between acoustic and electromagnetic waves disappears. In both cases, the interaction is weak if the wavelength is large compared with the diameter of the scattering particles, but increases rapidly as the wavelength becomes comparable to that diameter. Thus, unlike the much shorter optical waves, microwave radar waves readily penetrate clouds; they are, however, readily scattered by raindrops. Similarly, radar waves are essentially unaffected by aerosols; these tiny particles can, however, be readily detected by optical waves. By appropriate selection of the electromagnetic frequency it is therefore possible to interrogate both

Table 1
STATUS OF WIND MEASUREMENTS

| | DOPPLER | | | SCINTILLATION | | | ECHO CORRELATION | | |
|-----------------------------------------|------------|-----------|----------|---------------|-----------|---------|------------------|-----------|---------|
| | Microwave* | Acoustic† | Infrared | Microwave‡ | Acoustic‡ | Optical | Microwave* | Acoustic† | Optical |
| Mean Values | | | | | | | | | |
| Transverse | | | | X | X | X | | X | X |
| Longitudinal | X | | F | | | | | | |
| Vertical Profiles | | | | | | | | | |
| Horizontal Wind | X | X | F | | | F | | X | X |
| Vertical Motion | X | X | F | | | | | | |
| Turbulence | X | X | F | | | | | | |
| Structure Constant (energy dissipation) | | X | | | | | | | |
| Flux | | | | | | | | | |
| Momentum | X | | F | | | | | | |
| Energy | X | | F | | | | | | |
| 2-D Coverage | X | F | F | | | | | | |
| 3-D Coverage | X | | F | | | | | | |
| Spectra of Turbulence | X | | F | | | | | | |
| Convergence/Divergence | X | | F | | | X | | | |
| Verticity | X | X | F | | X | | | | |

*Requires precipitation or chaff †Not in rain or hail ‡Not in precipitation or cloud X Already demonstrated F Expected in next 3-5 years

the clear atmosphere and hydrometeors, with some prospect that the intermediate (infrared) frequencies will be useful for both purposes.

Observations Required

In order to provide measurements of the atmosphere adequate for modern, short-range local forecasting, six atmospheric parameters must be measured: these are wind, temperature, humidity, precipitation, cloud particles, and aerosols. Ideally, three-dimensional distribution of these parameters is desired. In this connection, remote sensing offers a potentially broad range of different types of measurements of a single parameter, as compared with the zero-dimensional point measurement of a stationary, in situ, instrument. These measurements range from simple line integrals and averages to vertical profiles and measurements of flux and spectra. The range of measurements is particularly wide in the case of a vector field, such as the wind.

Status of Remote Sensing

The status of ground-based remote sensing of wind is summarized in Table 1. Here, three different approaches to remote velocity measurement are considered:

- *The doppler method.* The frequency shift of the signal scattered from a moving target is used to derive the radial component of velocity of the scatterer.

- *The scintillation method.* The transverse drift of the forward-scattered signal pattern is used to derive information on the mean velocity of the air across the beam.

- *The echo-correlation techniques.* The back-scattered field is sampled to derive information on the profile of velocity transverse to the beam.

For each of these methods, it is appropriate to consider microwave, acoustic, and optical versions of the technique. Table 1 is given, therefore, in the form of a matrix of measurement method (technique) against type of velocity measurement (e.g., line average,

Table 2
STATUS OF TEMPERATURE MEASUREMENTS

| | TIME OF FLIGHT | | 5-mm O ₂ Emission | Radio-Acoustic | Raman Lidar | Acoustic Sounding |
|------------------------------------------------------------------------|----------------|----------|------------------------------|----------------|-------------|-------------------|
| | Optical | Acoustic | | | | |
| Mean Value | X | X | | | | |
| Vertical Profiles Temperature Structure Constant Flux of Heat | | | X | X | F F | X |
| 2-D Coverage | | | X | | | |
| 3-D Coverage | | | | | | |

vertical profile, etc.). An X shows that the method has already been demonstrated experimentally; anticipated progress in the near future is indicated by the letter F where it seems likely that research leading to such measurements will be conducted within the next few years. The corresponding information for remote sensing of temperature, humidity, precipitation, cloud particles, and aerosols is given in Tables 2 through 6.

Wind

Of all the meteorological parameters considered, this is the one most readily measured by ground-based remote sensing techniques. As shown in Table 1, a wide range of acoustic, microwave, and

optical techniques has been identified, and many have been tested experimentally. The prospects of optical doppler (actually infrared doppler, using a 10.6- μ m CO₂ laser) are believed to be particularly important, because of its unique ability to operate under a relatively wide range of meteorological conditions. Other advantages include smaller size and better angular resolution than microwave radars, without the severe range limitations and degradation of daytime performance experienced by visible-wavelength optical doppler systems.

Temperature

Time-of-flight measurements of optical or acoustic waves have been used to

Table 3
STATUS OF HUMIDITY MEASUREMENTS

| | Passive Microwave | Differential Absorption | FM/CW Radar | Raman Lidar |
|-------------------------------------------------------------|-------------------|-------------------------|-------------|-------------|
| Line Integral | X | | | |
| Mean Value | | F | | |
| Vertical Profiles Humidity Structure Constant Flux | | F | F | X F |
| 2-D Coverage | | | | |
| 3-D Coverage | | | | |

| Table 4 STATUS OF PRECIPITATION MEASUREMENTS | | |
|-------------------------------------------------|-------------------|-----------------|
| | Passive Microwave | Microwave Radar |
| Line Integral | X | |
| Vertical Profile | | X |
| Vertical Flux | | X |
| 2-D Coverage | | X |
| 3-D Coverage | | X |

| Table 5 STATUS OF CLOUD MEASUREMENTS | | | | |
|-----------------------------------------|-------------------|-----------------|-----------------------|----------------|
| | Passive Microwave | Microwave Radar | CO ₂ Radar | Optical Liders |
| Line Integral | X | | | |
| Mean Value | | | | |
| Vertical Profile | | X | F | |
| 2-D Coverage | | X | F | |
| 3-D Coverage | | X | | |
| Ice/Water Identification | F | | | F |
| Drop Size Distribution | | | | F |

| Table 6 STATUS OF AEROSOL MEASUREMENTS | | | |
|-------------------------------------------|-------------------|---------------|----------------------|
| | Solar Attenuation | Optical Lidar | Multiparameter Lidar |
| Line Integral | X | | |
| Vertical Profile | | X | F |
| Vertical Flux | | | |
| 2-D Coverage | | X | |
| 3-D Coverage | | F | |
| Particle Size Distribution | | | F |

measure average temperature along the propagation path, and microwave radiometry in the 5 - mm O₂ absorption band has been used to measure temperature distribution in one or two dimensions. Temperature profiles have also been derived using a hybrid radio-acoustic system in which radio waves track the velocity of a sonic pulse. Temperature profiles of the mesosphere have already been derived from measurements of the decay of the Rayleigh scattered signal with height; it is anticipated that the much weaker Raman signal from atmospheric nitrogen will be used to measure temperature profiles in the atmospheric boundary layer within the next few years. However, the ability to sense the three-dimensional temperature field remotely seems to be many years away.

Humidity

Passive microwave radiometry at about 20 GHz has been used to measure integrated water vapor content under clear sky conditions. Differential absorption of two optical signals shows promise of permitting measurement of the mean value of humidity on a two-ended path; profiles of humidity should be measurable using two-wavelength optical lidar systems. Vertical profiles of humidity have been measured by Raman lidar techniques, although considerable integration is required, especially under daylight conditions. For this reason, the ability to sense the three-dimensional humidity field remotely also seems to be many years away.

Precipitation

The remote measurement of precipitation by microwave radar is a well-advanced field, and as indicated in Table 4, modern research weather radar systems have the ability to describe the three-dimensional distribution of the precipitation. In addition, passive microwave radiometry at frequencies on the order of 5 - 10 GHz have been used to measure the integrated liquid water content of the atmosphere.

Cloud Measurements

The height of the cloud base has long been measured remotely by optical systems using triangulation techniques. Microwave radars having very short wavelength (e.g., $\lambda = 8$ mm) are capable of giving three-dimensional information on cloud particle distribution; optical and/or infrared lidar systems are likely, in the reasonably near future, to be evaluated for ice/water identification and drop size distribution measurements.

Aerosols

Optical lidar systems have already been used to obtain one- and two-dimensional measurements of aerosol content. There is also a prospect that multiparameter systems (e.g., multiple wavelength, polarization, or scatter angle) could be used to derive coarse information on the particle size distribution.

Pattern Recognition

Up to this point, we have been concerned with the status of various remote sensing techniques for making quantitative measurements. It is important to recognize that much of the value of these techniques lies not in the ability to reproduce the kinds of quantitative data the meteorologist is accustomed to, but in the ability to provide in real time totally new types of data and data presentations. These data can often take the form of "maps" or two-dimensional displays of the intensity of some parameter. Examples of such maps are the PPI plots of radar echo intensity, or the height-vs-time facsimile recordings from monostatic acoustic echo sounders. Figure 1 is such an echo-sounding record, taken around sunrise under clear sky conditions. The herringbone echoes reaching approximately 170 m at the beginning of the record are from the ground-based radiation inversion produced by nocturnal cooling of the ground. At approximately 0830, or 2.5 hr after sunrise, thermal plumes begin to appear at the bottom of the

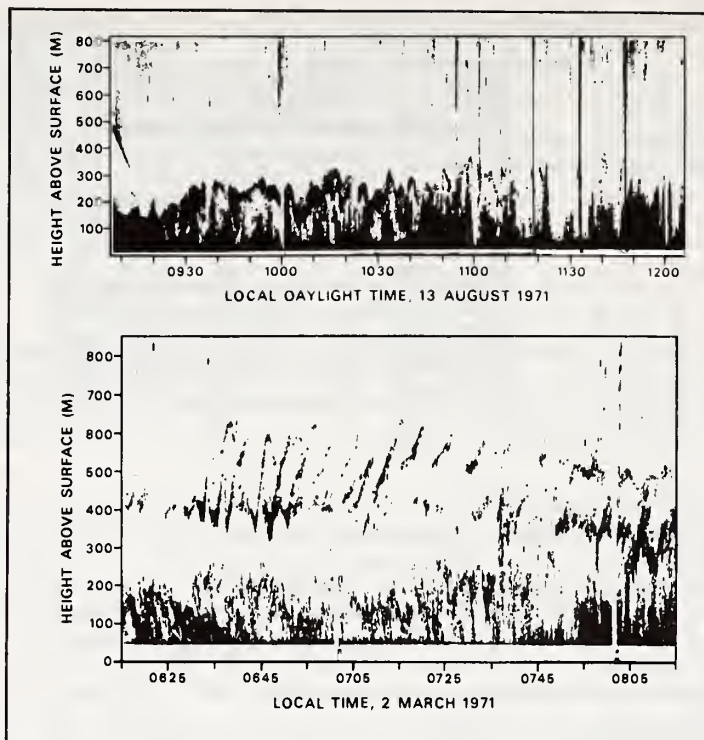


Fig. 1 (top) Acoustic echo sounding record showing dissipation of nocturnal ground-based radiation inversion by thermal plumes. Fig. 2 (bottom) Second record shows braided pattern characteristic of breaking waves occurring above a ground-based radiation inversion. (Photos courtesy Freeman F. Hall Jr., NOAA)

record, increasing in height with time and eroding the inversion until the latter has completely disappeared by noon. Another example, taken under stable nocturnal conditions is shown in Fig. 2. The lowest strip of echoes, reaching to about 200 m, is once again due to a ground-based radiation inversion, with thermal plumes beginning to appear at about 0745 local time. The braided echoes occurring in the height range of about 400 to 600 m are characteristic of breaking Kelvin-Helmholtz waves; similar records have been obtained from the clear atmosphere by pulsed high-power microwave radar, and also by FM-CW radar.

Pattern recognition (as opposed to full quantitative analysis) will initially play a major role in the use of two-dimensional displays such as those in Figs. 1 and 2. Man has long been accustomed to using his eyes as a superb

passive optical remote-sensing system; it is important to recognize that in this case the information is processed by pattern recognition, not by quantitative physical measurements. (The large grey structure over there is a thunderstorm. That transient line of enhanced brightness was a flash of lightning. In that direction it is raining already and over there the sky is clearing.)

Under clear sky conditions, the human eye and the weather radar receive no information (other than the fact that there is no pattern) but already new remote sensing techniques permit the internal structure of the boundary layer to be monitored continuously under clear sky and precipitation conditions. In recent years, we have learned how to use many different tracers for radar-like measurements and displays. Specifically, small-scale (about $\lambda/2$) fluctuations in temperature and velocity

can be used to acoustically monitor the internal structure and processes of the atmosphere; similarly, small-scale humidity fluctuations can be used as tracers of boundary layer structure by FM-CW radar techniques. At optical wavelengths, aerosol particles are readily detected by lidar techniques and may therefore be used to monitor the boundary layer. The resultant echo patterns are already being recognized in terms of thermal plumes, inversions, internal gravity waves, and breaking waves. As the local weather forecaster gains skill in recognizing patterns in mesoscale and microscale maps of parameters such as velocity, temperature, and humidity (and their small-scale structure parameters, C_v^2 , C_T^2 , and C_e^2), he should greatly enhance his ability to identify the existence, location, and intensity of significant meteorological phenomena or processes, and hence to observe and predict their development. Note that these maps do not need to have high absolute accuracy; the many orders of magnitude variability of parameters such as C_T^2 , C_v^2 , C_e^2 , and radar and lidar reflectivities means that

relative accuracies of 3 dB and absolute accuracies of 10 dB may be acceptable for pattern recognition purposes. The wide range of two- or three-dimensional maps potentially available to the meteorologist of the future will provide him with totally new abilities in his continuing watch for changing atmospheric conditions, and hence will radically affect both the nature and scope of future mesoscale research and services. We may also expect that the growing ability to use computers for pattern recognition will eventually result in the automatic processing and interpretation of many of the patterns revealed by the remote sensing systems of the future.

For Further Reading

- Derr, V. E. (Ed.), 1972: *Remote Sensing of the Troposphere*, Government Printing Office, Washington, D.C.
- Little, C. G., 1972: Status of remote sensing of the troposphere. *Bull. Amer. Meteor. Soc.* 53 (10), 936-949. ●



C. Gordon Little is currently serving as Director of the NOAA Wave Propagation Laboratory. He received the Honors Physics degree from the University of Manchester, England, in 1948, and was awarded a Ph.D. in radio astronomy by the same institution in 1952. Prior to joining the Department of Commerce in Boulder in 1958, he served as Deputy Director of the Geophysical Institute at the University of Alaska, conducting research on the auroral ionosphere. He is a Fellow of the Institute of Electrical and Electronic Engineers, the Royal Astronomical Society (London), and the American Association for the Advancement of Science.

status of remote sensing of the troposphere

C. Gordon Little

Wave Propagation Laboratory

National Oceanic and Atmospheric Administration

Boulder, Colo. 80502

Abstract

This paper attempts to summarize the status of remote sensing of the troposphere. It opens with a statement of the need for remote sensing and identifies the potential advantages inherent to such techniques. The main material is in the form of a series of tables which identify the stage of development of each method (acoustic, radio, or optical) for the measurement of the different meteorological parameters relevant to the troposphere. The tables are used to differentiate between those capabilities which as yet are limited to the boundary layer, and those applicable to the full height range of the troposphere; and also between those techniques which are limited to clear air as opposed to those which can operate in the presence of cloud particles and/or precipitation. Examples of the current capabilities of various active and passive acoustic, optical, and radio remote sensing systems are presented in the form of figures, primarily from the work of the Wave Propagation Laboratory.

1. The role of remote sensing in the troposphere

As the size and complexity of our society increases, the number and complexity of its interactions with our atmospheric environment grows. As a result, the economic costs to commerce, transport, communications, and agriculture of natural disasters such as blizzards, ice storms, hurricanes, tornadoes, floods, droughts, etc., increase year by year. This growing sensitivity to weather conditions has, of course, led to a greatly expanded need for atmospheric information and forecasts of many different types, for many different purposes.

The attainable quality and scope of an environmental information or forecasting service is determined by the nature of the observational data set on which it is based—and especially by the density in time and space of the relevant observations. Thus, the present meteorological observing system of ground-released radiosondes and satellite measurements is well matched to synoptic-scale weather patterns, i.e., to space scales of the order 1000 km and time scales (at one location) of the order one or two days. But recent analyses of national needs for improved weather services show that these needs lie primarily in the area of short-term local weather fore-

casts, e.g., forecasts for a local area 1 to 100 km in size, for time periods ranging from 0 to 6 hours. These improved short-term local weather forecasts inevitably will require a much denser array of meteorological data than is currently available from the present observational networks. The required increase in space-time density of relevant observations is huge—at least four orders of magnitude relative to the twice-per-day, 500-km horizontal spacing of the upper air radiosonde observing system. Cost estimates indicate that it is totally impracticable to achieve this desired increase in density of observations by mere expansion of the existing radiosonde network. Satellite remote sensing of meteorological conditions is, of course, already playing a very important role; however, because of the great need for improved resolution in height, time, and space, especially in the boundary layer of the atmosphere and under conditions of cloud or precipitation, satellites can only provide a very incomplete answer. Obviously, some new breakthrough in weather observing is required. The proponents of ground-based remote sensing claim that these techniques offer such a breakthrough; moreover, they claim that their use will radically change the nature and scope of the atmospheric research and services of the future.

The potential advantages of remote sensing are major, and may be listed as follows:

- a) The observations are taken remotely, i.e., without requiring that *in situ* instrumentation be carried to the region of atmosphere to be measured.
- b) Ideally, remote sensing permits the measurement of the relevant parameters of the atmosphere in 1, 2, or 3 spatial dimensions, all as a function of time.
- c) Excellent resolution and continuity of data in time and/or space are usually obtainable.
- d) An increasingly broad range of parameters of the atmosphere may be sensed. While a standard radiosonde is limited to measurements of temperature, humidity, and wind, parameters such as spectrum of turbulence or momentum flux can be measured remotely, e.g., by Doppler radars.
- e) The measurement system does not modify the parameter being measured. In some *in situ* measurement

systems this can be of serious concern, as in the case of aircraft or meteorological tower observations.

f) The remote sensing measurements typically provide a line, area, or volume integration. This helps to ensure that the observations are more representative of the medium than those from a single point sensor, which may be adversely affected by local or transient perturbations.

g) Remote sensing instrumentation is usually automatic and often can provide fully processed data 24 hr per day with a minimum of manpower.

It should be noted that the above are potential advantages, which, though generally applicable to the field of remote sensing, in most cases have yet to be fully realized.

2. Categorization of the status of remote sensing

In attempting to describe the status of remote sensing of the troposphere, it is necessary to describe the progress in terms of several different aspects or interfaces of remote sensing. First, the range of parameters to be measured is large. Thus, a reasonably full knowledge of the condition of the atmosphere around the observing site requires information on the 3-dimensional distribution of seven parameters, all as a function of time. These parameters are: wind; temperature; humidity; cloud particles; precipitation; aerosols; and gaseous pollutants.

For each of these parameters, different types of measurements may be required ranging from the relatively simple average value of the parameter along some line to the full 4-dimensional distribution of the parameter in time and space. These different types of measurements form a hierarchy of increasing information content (and usually of difficulty in acquisition) as follows:

Line integral—the integrated value of the parameter along a line through the whole atmosphere

Line average—the average value of the parameter along some line of known length

Line profile—the distribution of the parameter along some line of known length

2-dimensional coverage—the distribution of the parameter over a plane

3-dimensional coverage—the distribution of the parameter in space around the instrument

Structure constant—a measure of the intensity of small-scale fluctuations of the parameter in space and time

3-dimensional spectrum—the 3-dimensional power spatial spectrum of variability of the parameter in space—i.e., how strong are the variations of the parameter as a function of the spatial size of the irregularity

Flux—the rate at which mass, momentum, or heat is being transported (usually in the vertical direction).

Remote sensing is based on measurements of the interaction of waves with the medium under study. In

remote sensing of atmospheric conditions, it has been found important to make use of the unique advantages peculiar to acoustic, radio, and optical waves, and to recognize that passive remote sensing systems (using waves of natural origin) as well as active systems (using man-made waves) each have their own particular advantages.

At this point, we illustrate some of the present capabilities of remote sensing, using different remote sensing techniques (acoustic, radio, and optical) to illustrate the full range of the eight different types of measurement (from line integral to vertical flux) of various meteorological parameters. Implicit in these illustrations are many of the advantages cited earlier. For reasons of convenience, most of the examples are from the work of colleagues in the Wave Propagation Laboratory; it should, of course, be recognized that similar and in some cases more striking examples are available from the work of other groups within the U.S.A. or elsewhere.

Fig. 1 plots contours of the line integral of liquid water of a thunderstorm, as obtained by Decker and Dutton (1970) using a 10-GHz microwave radiometer in a steerable 60-ft diameter parabolic antenna. The development of the storm in a period of one hour is shown in the series of four contour plots, taken approximately 15 min apart. Note the changing azimuth of the storm with time, and its separation into two cells after originating as a single cell.

In Fig. 2, the measurement of the average value of a meteorological parameter (in this case, the transverse component of wind velocity across a laser beam) is illustrated. These data are taken from a paper by Lawrence *et al.* (1972), which describes the use of measurements of the motion of the scintillation pattern to derive the mean transverse component of the wind. The upper curve shows the average value of transverse wind across the 1-km laser path as derived optically, the lower curve as derived from seven anemometers spaced evenly along the path. In both cases, the data have been smoothed with a ten-minute running average. The agreement between the two data sets is obviously extremely good; investigation indicates that much of the residual discrepancy is due to the failure of the seven anemometers to measure the true mean wind, even after smoothing for 10 min.

The measurement of the line profile of a meteorological parameter is illustrated by Fig. 3, taken from a paper by Snider (1972). In this study, multifrequency, passive radiometric data were obtained in the 5–6 mm O_2 absorption band, using four different frequencies and observations at several antenna elevation angles. The inferred temperature profile is compared with that obtained by a radiosonde released locally. Note the excellent general agreement between the two sets of data, though (as is typical of this kind of radiometric measure-

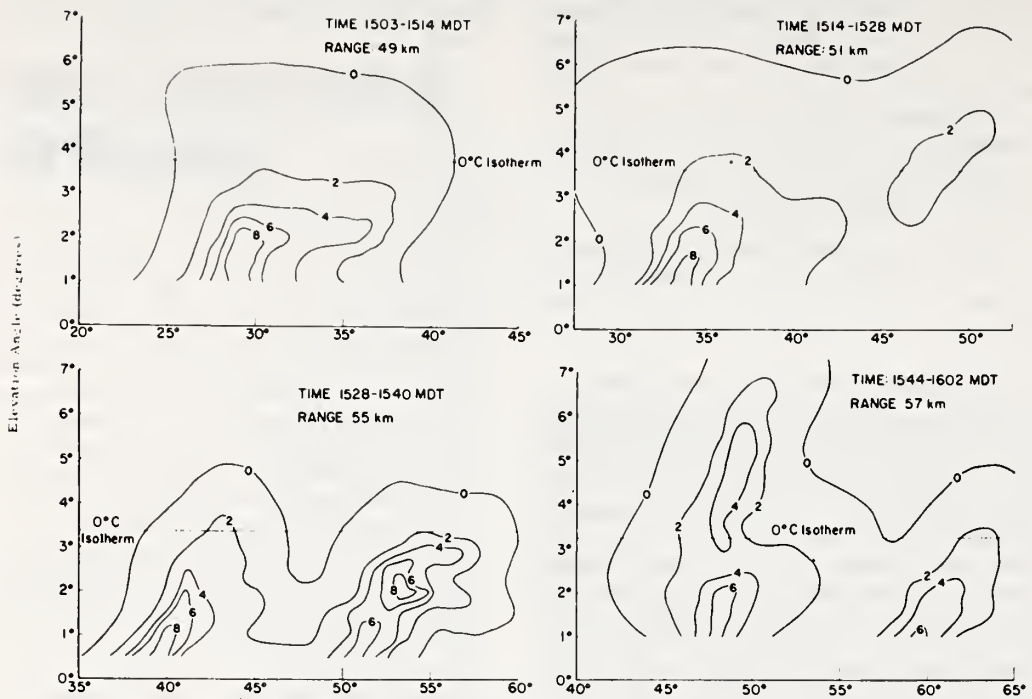


FIG. 1. Contours of liquid water content (kg m^{-2} column) for an 18 July 1967 thunderstorm near Boulder, Colo., obtained using a 10.7 GHz radiometer. Note the changes in azimuth as a function of time; also the breaking of the storm into two cells. (From Decker and Dutton, 1970.) Abscissas show azimuth in degrees from true north.

ment) the sharp ground-based radiation inversion is somewhat smoothed in the radio measurements.

A two-dimensional scan of aerosol content is given in Fig. 4, taken from work of Johnson and Utne of Stanford Research Institute. In this case, an optical radar system was scanned in elevation at fixed azimuth to produce this range-height plot of the intensity of the optical signal backscattered from the aerosol. Note how clearly the 1.5-km depth of the mixing layer is defined; also the smoke plume seen at a range of about 3 km.

Three-dimensional coverage is illustrated in Figs. 5, 6, and 7, taken from recent unpublished work by Strauch and his colleagues of the Wave Propagation Laboratory. These two-dimensional plots show the velocity field of snow particles, obtained using two spaced Doppler radars (Lhermitte, 1969). Fig. 5 shows the velocity in a plane including both radars and inclined at an elevation of 4° . This velocity field shows relatively little structure; however, on subtracting from each point value the *average* velocity of the particles in the plane, a strong eddy pattern immediately becomes apparent (Fig. 6). Approximately 0.5 min later, the two radars scanned a different

plane, the corresponding eddy flow being as shown in Fig. 7. In this way, a large 3-dimensional region of a storm can be scanned by two Doppler radars to give the 3-dimensional velocity field down to resolutions comparable to the pulse volume.

In Fig. 8, the ability of radar systems to measure profiles of the structure constant of refractive index is illustrated. These data were obtained using a monostatic acoustic echo sounder directed overhead. In this case the echoes are due to $\lambda/2$ sized temperature eddies, and the echo power can therefore be immediately expressed in terms of the structure constant for temperature, C_T . Two main regions of strong C_T are shown, separated by a region of much lower C_T values; this pattern results from thermal plumes separated by regions of relatively homogeneous, descending air between the plumes (Hall, 1972).

Measurements of the spectrum of turbulence are shown in Fig. 9, due to Lhermitte (1968). These data were taken during a snowstorm in Oklahoma, using a single Doppler radar scanning at low elevation angles in the upwind and downwind directions. Lhermitte also

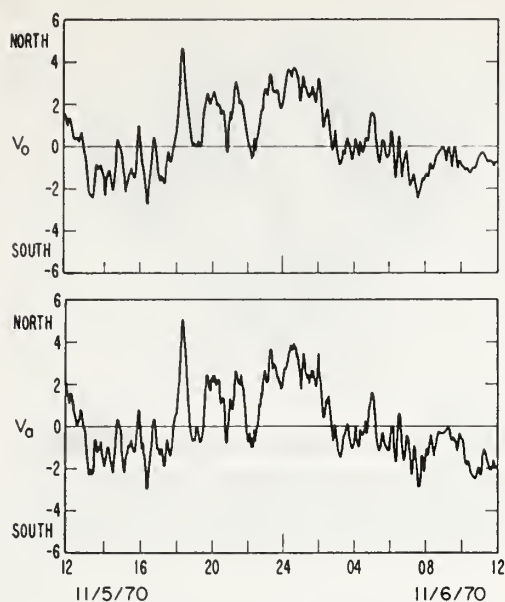


FIG. 2. Comparison of optical measurements of the mean transverse component of wind, in meters per second, across a 1-km laser beam path (upper curve) with the average transverse velocity registered by seven propeller-type anemometers spaced evenly along the path. (From Lawrence *et al.*, 1972.)

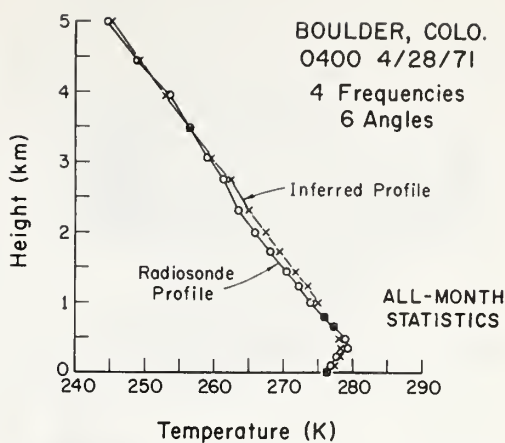


FIG. 3. Comparison of temperature profiles obtained remotely by multi-frequency, multi-elevation angle radiometric observations in the 5-6 mm wavelength oxygen absorption band, with those obtained by a standard radiosonde. (From Snider, 1972.)

showed that the difference between the spectra measured in the upwind and downwind directions are due to the correlation between the horizontal and the vertical velocity fluctuations, and are therefore a direct measure of the momentum flux.

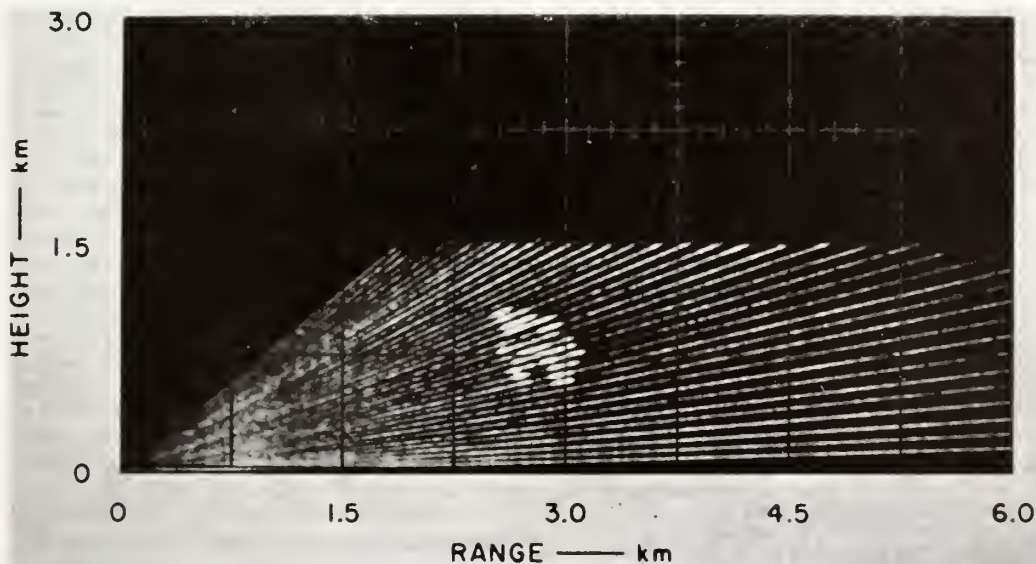


FIG. 4. Lidar observations of atmospheric structure in relatively clear air. Vertical cross section through smoke plume from 245-m stack at Homer City Power Plant, Pa., 3 May 1970, 1842 EDT. The section was made 1 km downwind of the stack at which distance the smoke was virtually invisible to the eye. Turbid boundary layer extended to a height of 1.5 km. (Courtesy Dr. R. T. H. Collis.)

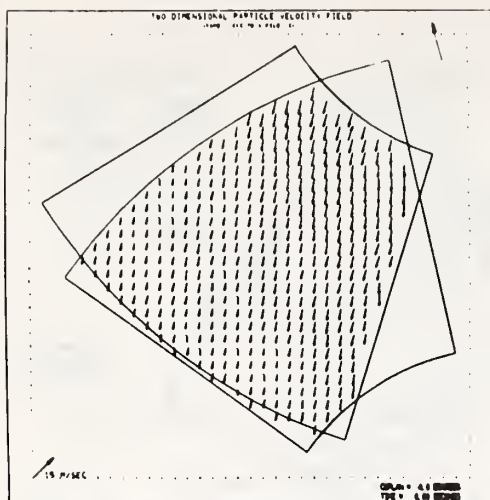


FIG. 5. Two-dimensional map of velocity of snowflakes, measured by a two-station microwave Doppler system. The plane in which the vectors lie is inclined at 4° elevation, and includes the two radars (located at the intersection of the converging radii). The length of the arrow at the bottom left of the diagram corresponds to 15 m sec⁻¹. (Miller, 1972.)

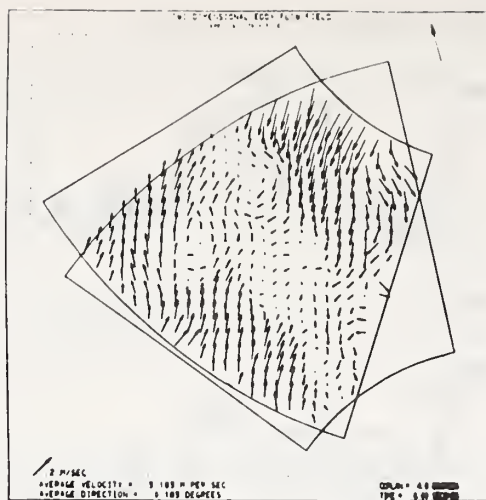


FIG. 6. Two-dimensional map of the eddy flow field in the same plane as Fig. 5, obtained by subtracting the mean value of the velocity of the particles in the plane from each vector of Fig. 5. (Miller, 1972.) The length of the arrow at the bottom left of the diagram corresponds to 2 m sec⁻¹.

In general, the development of a remote sensing concept can be seen to follow a logical sequence. In the first step (Step A), the concept is identified, and preliminary first-order estimates made of its feasibility. In Step B, the potential capabilities and limitations of the concept are analyzed theoretically in considerable detail. If the concept still appears attractive, the development of a research equipment for the experimental evaluation of these capabilities and limitations takes place in Step C. Assuming that this quantitative experimental evaluation of the concept is successful, the next stage (Step D) is to replace the research model with a developmental model which is thought of as a prototype of an operational unit that will be capable of being used routinely in the field by research workers or technicians other than the original research group. If the concept continues to show promise, Step E involves working with industry to obtain commercially built prototype units for field evaluation. Once this stage has been successfully completed, the final stage (Step F) requires that fully evaluated commercial units be routinely available for procurement.

The status of the remote sensing of the troposphere is now discussed in terms of these stages, A–F, of development of acoustic, radio, and optical remote sensing techniques for the different types of measurement of the seven meteorological parameters listed above.

3. Acoustic remote sensing of the troposphere

Table 1 summarizes the status of acoustic remote sensing

of the boundary layer under clear air conditions, using letters to denote the sequence of stages described in the previous section. The footnotes below Table 1 and succeeding tables refer to the superscript numbers in the table, and indicate the nature of the equipment responsible for each specific measurement category. Where possible, a recent reference is given to the work on which the entry was based.

The status of acoustic echo sounding of the boundary layer under cloud or fog conditions is summarized in Table 2. Present experience with the operation of acoustic echo sounders under conditions of cloud, fog, rain or snow is very limited. Analysis by Little (1972a) indicates that hydrometeor echoes should be readily obtainable (at least in the lowest few hundred meters), provided frequencies of the order several thousand Hz are used. The use of these high frequencies (required to obtain adequate scattering cross section from the hydrometeors) increases the absorption of acoustic energy by the atmosphere, and acoustic studies of the precipitation or cloud particles themselves will be limited to the lower boundary layer. Because of the λ^4 dependence of the hydrometeor scattering cross section upon wavelength, the effects of the hydrometeor echoes can be greatly reduced by using low acoustic frequencies. It is therefore possible to probe the atmosphere, under clear sky or cloudy conditions, provided that sufficiently long wavelengths (e.g., $\lambda \gtrsim 30$ cm) are used.

The status of acoustic echo sounding of the boundary layer under precipitation conditions is indicated in

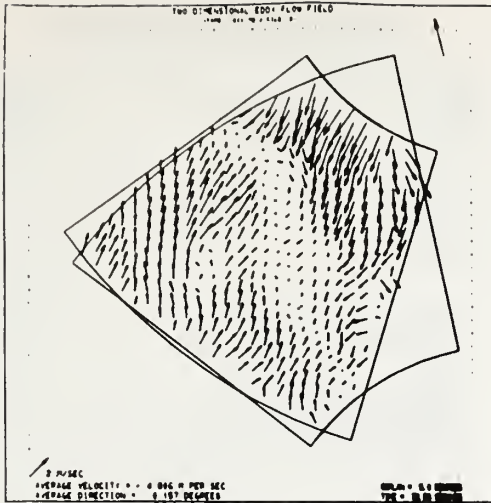


FIG. 7. Two-dimensional map of the eddy flow field in a plane at an elevation angle of 5° , taken 32 sec after the data in Figs. 5 and 6. (Miller, 1972.) The length of the arrow at the bottom left of the diagram corresponds to 2 m sec^{-1} .

Table 3. Precipitation in the form of rain or hail would increase the noise level at the receiving antenna and might preclude successful operation; presumably drizzle and snow would not have such effects, though the presence of these particles might enhance the absorption. The theoretical work of Cole and Dobbins (1970, 1971) indicates that this absorption will not be significant if the cloud and precipitation are in the form of liquid drops, but it is possible that the enhanced surface areas of snowflakes and ice crystals might result in enhanced absorption. To summarize, present information suggests that cloud, fog and drizzle conditions should have little effect upon acoustic echo sounders operating at frequencies below about 1 kHz, though snow conditions might enhance the acoustic absorption and rain or hail could seriously enhance the ambient noise level at the receiving antenna. Parentheses are therefore used in Table 3 to denote that acoustic echo-sounding systems will experience serious degradation or failure during rain or hail conditions.

Although acoustic echoes have on occasion been observed at heights up to several kilometers, quantitative measurements have not yet been made above the boundary layer. However, prospects for acoustic echo-sounding of the clear or cloudy troposphere are good; for a discussion of these prospects, the reader is referred to Little (1972b).

4. Radio remote sensing of the troposphere

In general, radiowaves interact more weakly with the clear atmosphere than optical waves or acoustic waves. Nevertheless, both passive and active radio systems have

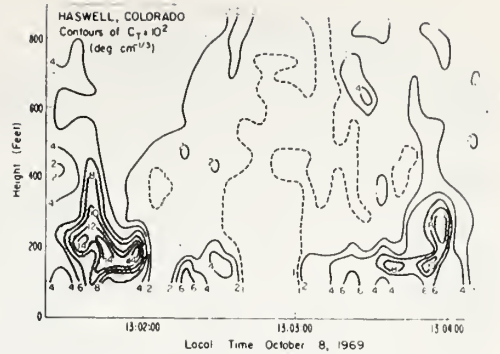


FIG. 8. Height-time contours of temperature structure constant, C_T , measured using a monostatic acoustic echo sounder during convective conditions. The shaded regions are regions of enhanced C_T due to thermal plumes. (Hall, 1972.)

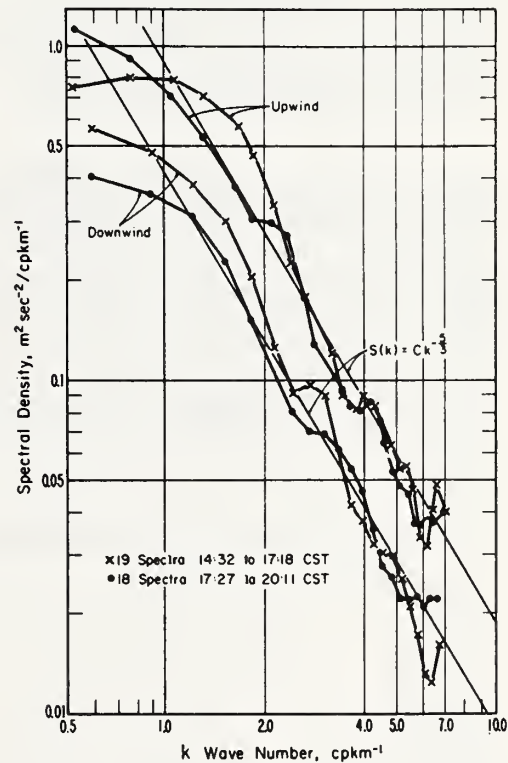


FIG. 9. Spectra of turbulence observed in the upwind and downwind directions during a snow storm, using a single microwave Doppler radar system. The difference in the spectral intensity in the upwind and downwind directions is due to the covariance of the vertical and horizontal fluctuations in velocity, and is therefore a direct measure of the momentum flux. (Hermitte, 1969.)

TABLE 1. Status of acoustic remote sensing of the boundary layer under clear air conditions.

| Type of measurement \ Parameter | Wind | | Temperature | Humidity | Aerosol | Gaseous pollutants |
|---------------------------------|----------------|----------------|-----------------|----------------|---------|--------------------|
| | Transverse | Longitudinal | | | | |
| Line average | C ¹ | C ² | C ³ | | | |
| Line profile | C ² | C ² | A ³ | A ⁴ | | |
| 2-D coverage | | A ¹ | | | | |
| 3-D coverage | | | | | | |
| Structure constant | | A ⁵ | C ¹⁰ | | | |
| 3-D spectrum | | A ⁶ | | | | |
| Flux | | A ⁷ | A ¹¹ | | | |

¹ Spaced line-of-sight, cross-correlation techniques (Mandies, 1971).

² Sonic anemometer (Little, 1969).

³ Doppler echo sounding (Beran and Clifford, 1972).

⁴ Steerable or multibeam Doppler echo sounding (Hall, private communication).

⁵ Bistatic echo sounding (Little, 1969).

⁶ Doppler echo sounding (Little, 1969).

⁷ Doppler echo sounding (Little, 1972b).

⁸ Sonic anemometer/thermometer (Little, 1969).

⁹ Multi-frequency monostatic echo sounding (Gething and Jensen, 1971).

¹⁰ Monostatic echo sounding (Little, 1969).

¹¹ From C_T measurements (Wyngaard *et al.*, 1971).

been used. The passive systems rely on the absorption (and therefore emission) of radio waves by water vapor at about 1.35 cm wavelength, and by oxygen at 5-6 mm wavelength. Such systems are capable of measuring integrated water vapor and profiles of temperature, respectively. The active systems include line-of-sight and forward scatter systems, as well as radar systems. The back-scattering radar cross section due to clear air is usually very low, and high sensitivity radars (either high power pulsed systems, or FM-CW systems) are required. Even these systems do not give continuous echoes from all volumes, but detect only the regions of most intense

TABLE 2. States of acoustic remote sensing of the boundary layer under cloudy conditions.

| Type of measurement \ Parameter | Wind | | Temperature | Humidity | Cloud | Aerosol | Gaseous pollutants |
|---------------------------------|----------------|----------------|----------------|----------|----------------|---------|--------------------|
| | Transverse | Longitudinal | | | | | |
| Line average | C ¹ | C ² | | | | | |
| Line profile | C ² | C ² | | | B ³ | | |
| 2-D coverage | | A ¹ | | | | | |
| 3-D coverage | | | | | | | |
| Structure constant | | A ⁵ | C ⁸ | | | | |
| 3-D spectrum | | A ⁶ | | | | | |
| Flux | | A ⁷ | A ⁹ | | | | |

¹ Spaced line-of-sight, cross-correlation techniques (Mandies, 1971).

² Sonic anemometer (Little, 1969).

³ Doppler echo sounding (Beran and Clifford, 1972).

⁴ Steerable or multibeam Doppler echo sounding (Hall, private communication).

⁵ Bistatic echo sounding (Little, 1969).

⁶ Doppler echo sounding (Little, 1969).

⁷ Doppler echo sounding (Little, 1972b).

⁸ Monostatic acoustic echo-sounding (Little, 1969).

⁹ From C_T measurements (Wyngaard *et al.*, 1971).

¹⁰ High frequency acoustic echo sounding to a few hundred meters range (Little, 1972b).

fluctuations in radio-frequency refractivity. Alternatively, artificial targets (chaff) may be introduced into the atmosphere; more rarely, the density of small insects may be sufficiently high that their echoes can be used as tracers of the air motion.

Tables 4 and 5 give the status of radio remote sensing of the clear atmosphere in the boundary layer and troposphere, respectively, and indicate in parentheses those radio remote sensing capabilities which are dependent upon the presence of chaff. Also included in Table 4 is a hybrid acoustic-radiowave technique, variously designated EMAC (electromagnetic-acoustic) or RASS (radio-acoustic sensing system), which may be used to derive temperature and/or wind profiles. In these studies, a powerful acoustic pulse is tracked by a radar system, which obtains echoes because of the spatial modulation of radio frequency refractive index created by the pressure oscillations of the acoustic wave. As implied in Tables 4 and 5, radio waves are essentially unaffected by

TABLE 3. Status of acoustic remote sensing of the boundary layer under precipitation conditions.

| Type of measurement \ Parameter | Wind | | Temperature | Humidity | Precipitation | Aerosol | Gaseous pollutants |
|---------------------------------|-------------------|-------------------|-------------|----------|-------------------|---------|--------------------|
| | Transverse | Longitudinal | | | | | |
| Line average | | | | | | | |
| Line profile | (A ¹) | (A ¹) | | | (B ³) | | |
| 2-D coverage | | (A ¹) | | | (A ³) | | |
| 3-D coverage | | | | | | | |
| Structure constant | | (A ²) | | | | | |
| 3-D spectrum | | (A ¹) | | | | | |
| Flux | | (A ¹) | | | | | |

¹ Doppler acoustic echo sounding (Beran and Clifford, 1972).

² Bistatic echo sounding (Little, 1969).

³ High frequency echo sounding to a few hundred meters range (Little, 1972a).

Note: The parentheses are used to denote that system performance will be degraded by enhanced ambient noise level if the precipitation is in the form of rain or hail.

TABLE 4. Status of radio remote sensing of the boundary layer under clear air conditions.

| Parameter Type of measurement | Wind | | Temperature | Humidity | Aerosol | Gaseous pollutants |
|----------------------------------|---------------------------------------------------------------------------------------|-------------------------------|-------------|----------------|---------|--------------------|
| | Transverse | Longitudinal | | | | |
| Line average Line profile | C ¹ (C ²) A ³ , (C ³) A ³ | E ¹ C ³ | | C ⁶ | | |
| 2-D coverage | (C ²) | | | | | |
| 3-D coverage | (B ²) | | | | | |
| Structure constant | (A ²) | | | C ⁷ | | |
| 3-D spectrum | (A ²) | | | | | |
| Flux | (A ²) | | | | | |

¹ Spaced line-of-sight cross-correlation techniques (Lee and Waterman, 1968).

² Multi-station Doppler radar, using chaff (Lhermitte, 1969).

³ Single station Doppler radar, using chaff (Lhermitte, 1969).

⁴ Passive multi-frequency and/or multi-angle scan of O₂ absorption at ~5 mm (Snider, 1972; Hosler and Lemmons, 1972).

⁵ Hybrid acoustic-radio (RASS) echo sounding (Marshall *et al.*, 1972).

⁶ Line-of-sight time-of-flight measurements of integrated refractivity (Bean *et al.*, 1969).

⁷ From FM-CW radar echo power, assuming refractivity fluctuations are primarily caused by water vapor (Bean, 1971).

Note: The parentheses are used to denote that chaff will be required for these measurements in clear air.

aerosol and gaseous pollutants at the densities normally found in the atmosphere.

The abrupt change in radio frequency refractive index represented by a hydrometeor is enormously larger than the refractivity fluctuations present in clear air, and hence appreciable radio power is scattered, especially for wavelengths comparable in size with the drop. (At much longer wavelengths, the scattering is weak and can

TABLE 5. Status of radio remote sensing of the troposphere under clear air conditions.

| Parameter Type of measurement | Wind | | Temperature | Humidity | Aerosol | Gaseous pollutants |
|-----------------------------------------------|-------------------|-------------------|----------------|----------------|---------|--------------------|
| | Transverse | Longitudinal | | | | |
| Line integral Line average Line profile | C ¹ | (A ²) | E ¹ | C ² | | |
| 2-D coverage | (A ²) | | | | | |
| 3-D coverage | (A ²) | | | | | |
| Structure constant | (A ²) | | | C ⁶ | | |
| 3-D spectrum | (A ²) | | | | | |
| Flux | (A ²) | | | | | |

¹ Forward scatter Doppler measurements with RAKE system (Birkemeier *et al.*, 1969).

² Single station Doppler radar, using chaff (Lhermitte, 1969).

³ Multi-station Doppler radar, using chaff (Lhermitte, 1969).

⁴ Passive O₂ radiometer measurements (to ~5 km height only) (Snider, 1972; Hosler and Lemmons, 1972).

⁵ Passive 20 GHz radiometer measurements (Guiraud *et al.*, 1972).

⁶ FM-CW radar (Richter, 1969).

Note: The parentheses are used to denote that chaff will be required for these measurements in clear air.

be ignored. Using this fact, it is possible to probe the clear atmosphere above the clouds by using long enough wavelengths.) For many years, microwave radar echoes from precipitation have been used to monitor the location and intensity of precipitation. In the past decade, major efforts have been made to use Doppler techniques to determine the velocities of the precipitation, and hence of the horizontal velocity field of the air. The

TABLE 6. Status of radio remote sensing of the boundary layer and troposphere under conditions of precipitation or cloud.

| Parameter Type of measurement | Wind | | Temperature | Humidity | Precipitation | Aerosol | Gaseous pollutants |
|-----------------------------------------------|------------|----------------------------------|-------------|----------|----------------------------------------------------|---------|--------------------|
| | Transverse | Longitudinal | | | | | |
| Line integral Line average Line profile | | C ¹ C ¹ | | | C ⁴ C ⁵ C ⁵ | | |
| 2-D coverage | | C ² | | | C ⁶ | | |
| 3-D coverage | | B ³ | | | C ⁶ | | |
| Structure constant | | | | | | | |
| 3-D spectrum | | C ¹ | | | C ⁶ | | |
| Flux | | C ¹ | | | C ⁷ | | |

¹ Single station Doppler radar (Lhermitte, 1969).

² Scanning single Doppler radar in a plane will give 2-D plot of *radial* velocity. Two-dimensional coverage of the *vector* wind requires two Doppler radars, preferably operating in the coplane mode (Lhermitte, 1969).

³ Three (or more) Doppler radar system (Lhermitte, 1969).

⁴ From echo power on calibrated radar, or passive microwave radiometry at 5-10 GHz (Atlas, 1964; Decker and Dutton, 1970).

⁵ Calibrated radar (Atlas, 1964).

⁶ Scanning calibrated radar (Atlas, 1964).

⁷ From Z-R relationships (Atlas, 1964).

status of this work is shown in Table 6, which covers both boundary layer and troposphere studies of radio remote sensing under conditions of precipitation or clouds. Implicit in the absence of the parentheses in Table 6 is the assumption that the radars used have wavelengths and sensitivities such that echoes are obtained from cloud particles, or alternatively, that chaff is released to increase the reflectivity of the medium. This table also covers the use of passive microwave radiometric techniques to derive integrated liquid water content along the beam, using the 5–10 GHz radio waves emitted by the water drops.

5. Optical remote sensing of the troposphere

The interaction of optical waves with the constituents of the atmosphere is extraordinarily rich and varied, and we may therefore expect that in the long run optical techniques will eventually become dominant in remote sensing of the clear atmosphere. While passive optical remote sensing systems will undoubtedly be used, the principal progress is likely to come with the development of the field of "lidar spectroscopy." This field combines the remote sensing advantages of radar with the chemical specificity of spectroscopy, and the coherent properties of lasers, to permit (in concept at least) the remote interrogation of very small volumes of the atmosphere for specific constituents. The potential advantages of lidar spectroscopy, relative to radio or acoustic techniques, may be listed as: excellent angular resolution; excellent range resolution; excellent Doppler resolution; excellent chemical specificity; very fast information rate; and broad range of parameters conceptually available. This latter point is well illustrated in Table 7, which indicates the status of optical remote sensing of the (clear) boundary layer. A very full range of remote sensing measurements is *conceptually* practicable though as of this time relatively few optical measurement techniques have been tested experimentally. Currently, the problem is primarily technological. Ideally, one would like to be able to transmit short (e.g., 10 nanosecond) pulses, at very high power (e.g., 10^{10} photons/pulse), at high pulse repetition rates (e.g., 10^4 pulses per second) from highly directive telescopes (beam divergence $\leq 10^{-4}$ radian) using tunable laser systems capable of operating in the UV, optical, and near infrared. While these parameters can be met or exceeded separately, they cannot yet be attained simultaneously in the same system. Nevertheless, laser technology continues to make rapid progress. It should also be emphasized that much of the detailed spectroscopic information needed for remote sensing purposes is not available, and will have to be obtained if the field is to advance efficiently.

The possibility of optical Doppler studies of motions in the clear boundary layer is obviously important, and is at the heart of many of the velocity or flux measuring concepts listed in Table 7. At the moment, the likelihood of optical Doppler measurements of clear air at distances of several kilometers seems remote, and hence

Table 8, which gives the status of optical remote sensing in the troposphere, is much less complete than for the corresponding boundary layer table Table 7.

Under conditions of cloud and fog, optical wavelengths are scattered very strongly, and penetration depths may be limited to a few tens of meters. It therefore seems very unlikely that optical waves will be of much use in meteorological remote sensing of the interior of clouds. Cloud height, however, can be readily determined, and it is possible that differences in the depolarization characteristics of liquid particles and ice crystals might permit the remote identification of the nature of the cloud particles. It is also possible that multiwavelength lidar probing of clouds from the outside could give some information on the size distribution of the particles in the outer tens of meters. Radiometric measurements could also be used to give their temperature.

Under conditions of precipitation, the optical scattering cross section per unit volume of the boundary layer

TABLE 7. Status of optical remote sensing of the boundary layer under clear air conditions.

| Parameter Type of measurement | Wind | | Temperature | Humidity | Aerosol | Gaseous pollutants |
|----------------------------------|----------------|----------------|----------------|-----------------|-----------------|--------------------|
| | Transverse | Longitudinal | | | | |
| Line average | C ¹ | A ³ | C ⁵ | C ⁸ | C ¹¹ | A ¹³ |
| Line profile | B ² | B ² | C ⁶ | C ⁹ | C ¹¹ | A ¹⁴ |
| 2-D coverage | A ⁴ | | A ⁶ | A ⁹ | C ¹¹ | A ¹¹ |
| 3-D coverage | A ⁴ | | A ⁶ | A ⁹ | A ¹¹ | A ¹¹ |
| Structure constant | A ⁴ | | | | | |
| 3-D spectrum | A ⁴ | | A ⁶ | A ⁹ | A ¹¹ | A ¹⁴ |
| Flux | A ⁴ | | A ⁷ | A ¹⁰ | A ¹² | A ¹⁵ |

¹ Laser beam scintillation transverse wind system (Lawrence *et al.*, 1972).

² Spaced lidar beams, cell correlation method (Derr and Little, 1970).

³ Laser beam scintillation, longitudinal wind component system (Lawrence, private communication).

⁴ Optical Doppler (Owens, 1969; Lawrence *et al.*, 1972).

⁵ Line-of-sight, time-of-flight measurements of integrated refractivity (Lawrence, 1969).

⁶ Lidar, using nitrogen Raman density measurement; or Stokes anti-Stokes ratio (Strauch *et al.*, 1971; Salzman *et al.*, 1971).

⁷ Eddy correlation method, using optical Doppler and N₂ Raman.

⁸ Relative absorption of HCN laser lines (Derr, private communication).

⁹ Lidar, using H₂O Raman, or differential absorption in vicinity of water vapor line (Strauch *et al.*, 1972; Schotland, 1969).

¹⁰ Eddy correlation method, using optical Doppler and H₂O Raman.

¹¹ On frequency lidar (Collis, 1970).

¹² Eddy correlation method, using optical Doppler and aerosol scatter.

¹³ Infrared absorption (Hanst, 1970).

¹⁴ Raman, resonance Raman of fluorescent spectroscopy (Derr and Little, 1970).

¹⁵ Eddy correlation method, using optical Doppler and spectroscopic lidar.

TABLE 8. Status of optical remote sensing of the troposphere under clear air conditions.

| Type of measurement \ Parameter | Wind | | Temperature | Humidity | Aerosol | Gaseous pollutants |
|---------------------------------|----------------|----------------|----------------|----------------|----------------|--------------------|
| | Transverse | Longitudinal | | | | |
| Line integral | A ¹ | | C ³ | C ⁴ | C ⁵ | |
| Line average | A ² | A ² | C ³ | C ⁴ | C ⁶ | |
| Line profile | | | | | | |
| 2-D coverage | | | A ³ | A ⁴ | C ⁶ | |
| 3-D coverage | | | | | A ⁶ | |
| Structure constant | | | | | | |
| Flux | | | | | | |

¹ Laser beam scintillations, using geostationary satellite-borne sensor.

² Spaced cell correlation method, using aerosol scatter (Derr and Little, 1970).

³ Lidar, using nitrogen Raman density measurements (Strauch *et al.*, 1971) or Stokes/anti-Stokes ratio (Salzman *et al.*, 1971).

⁴ Lidar, using H₂O Raman density measurement (Strauch *et al.*, 1972).

⁵ Solar extinction measurements (Fegley *et al.*, 1972).

⁶ On-frequency lidar (Collis, 1970).

is much smaller than for clouds, and lidar systems may be able to probe vertically to the base of the clouds. Table 9 summarizes the prospects for optical remote sensing of the boundary layer under precipitation conditions. Here it is assumed that spectroscopic and Doppler techniques would permit separate measurements of the precipitating particles and the gases of the atmosphere.

6. Estimates of accuracy of remote sensing measurements

The specification of accuracy of a remote sensing system involves very many qualifications (e.g., at what range; with what integration time; under what meteorological

conditions; with what background noise level; etc., etc.). A further problem is that the accuracy of remote sensing instrumentation is often not well known, primarily because of the difficulty of obtaining data from an appropriate network of accurate, *in situ* sensors. Also, there is the question of what do we mean by accuracy? For example, absolute accuracy, or relative accuracy, or precision? Despite these difficulties, Tables 10-13 have been prepared in order to give the reader some feeling for the accuracy believed available from the respective remote sensing systems when operating under designed operating conditions. It must be emphasized that the very limited entries in these tables are at best order of magnitude estimates. It is believed that the experimental accuracies actually attained with present systems typically are within a factor of three of these numbers, and that the relative accuracies of adjacent measurements made by the same system would be perhaps 3 to 10 times better. In most cases, the theoretical limits to the accuracy of the measurement system are much smaller than those presently attained, and we may expect significant improvement in measurement accuracy with time.

For more detailed information on the performance of remote sensing systems, the reader is referred to Derr (1972).

7. Pattern recognition in remote sensing

Up to this point, this paper has been concerned with the status of various remote sensing techniques to make *quantitative* measurements, of various levels of information content and sophistication, of meteorologically significant parameters. It is important to recognize that much of the value of remote sensing techniques lies not in the ability to reproduce the kinds of quantitative data the meteorologist is accustomed to, but in the ability to provide in real time totally new types of data and data presentations. These data can often take the form of "maps" or 2-dimensional displays of the intensity of some parameter. Examples of such maps are the PPI plots of radar echo intensity, or the height vs time

TABLE 9. Prospects for optical remote sensing of the boundary layer under precipitation conditions.

| Type of measurement \ Parameter | Wind | | Temperature | Humidity | Precipitation | Aerosol | Gaseous pollutants |
|---------------------------------|----------------|----------------|----------------|----------------|---------------|---------|--------------------|
| | Transverse | Longitudinal | | | | | |
| Line average | | | A ² | | | | |
| Line profile | A ¹ | A ¹ | A ² | A ⁴ | | | |
| 2-D coverage | | A ² | A ² | A ⁴ | | | |
| 3-D coverage | | A ² | A ² | A ⁴ | | | |
| Structure constant | | A ² | | | | | |
| 3-D spectrum | | A ² | A ² | A ⁴ | | | |
| Flux | | A ² | | | | | |

¹ Spaced lidar beam, cell correlation method (Derr and Little, 1970).

² Optical Doppler (Owens, 1969; Lawrence *et al.*, 1972).

³ Lidar, using nitrogen Raman density measurement; or Stokes/anti-Stokes ratio (Strauch *et al.*, 1971; Salzman *et al.*, 1971).

⁴ Lidar, using H₂O Raman, or differential absorption in vicinity of water vapor line (Strauch *et al.*, 1972; Schotland, 1969).

TABLE 10. Estimates of accuracy of wind velocity measurements.

| Type of measurement | Technique | Estimated accuracy | | |
|---------------------------------------|------------------------------|------------------------------------|------------------------------------|-----------------------------------|
| | | Acoustic | Radio | Optical |
| Line average of transverse velocity | Line-of-sight scintillations | $\pm 10\% \pm 0.5 \text{ ms}^{-1}$ | $\pm 10\% \pm 0.5 \text{ ms}^{-1}$ | $\pm 5\% \pm 0.3 \text{ ms}^{-1}$ |
| Line average of longitudinal velocity | Sonic Anemometer | $\pm 5\% \pm 0.3 \text{ ms}^{-1}$ | | |
| Line profile of transverse velocity | Multistation Doppler | $\pm 10\% \pm 0.5 \text{ ms}^{-1}$ | $\pm 5\% \pm 0.3 \text{ ms}^{-1}$ | |
| Line profile of longitudinal velocity | Single station Doppler | $\pm 5\% \pm 0.3 \text{ ms}^{-1}$ | $\pm 5\% \pm 0.2 \text{ ms}^{-1}$ | |
| 2-D coverage of vector wind | Multistation Doppler | | $\pm 5\% \pm 0.3 \text{ ms}^{-1}$ | |

Note: Remote measurements of the spectrum of turbulence and of the momentum flux are currently available only by microwave Doppler radar. The accuracies of these spectra and flux measurements will be determined by the accuracies (estimated above) of the original Doppler measurements from which they are calculated.

facsimile recordings from monostatic acoustic echo sounders. Fig. 10 is such an echo-sounding record, taken around sunrise under clear sky conditions. The "herring-bone" echoes reaching up to approximately 170 m at the beginning of the record are from the ground-based radiation inversion produced by nocturnal cooling of the ground. At approximately 0830, 2-1/2 hr after sunrise, thermal plumes began to appear at the bottom of the record, increasing in height with time and eroding the inversion until the latter had completely disappeared by noon. Another example, taken under stable, nocturnal conditions is shown in Fig. 11. The lowest strip of echoes, reaching up to about 200 m, is once again due to a ground-based radiation inversion, with thermal plumes beginning to appear at about 0745 local time. The "braided" echoes occurring in the height range ~400 to 600 m are characteristic of breaking Kelvin-Helmholtz waves; similar records have been obtained from the clear atmosphere by high power microwave radars, and also by the FM-CW radar.

Pattern recognition (as opposed to full quantitative analysis) will initially play a major role in the use of 2-dimensional displays such as Figs. 10 and 11. Man has long been accustomed to using his eyes as a superb passive optical remote sensing system; it is important to recognize that the information is processed by pattern recognition and *not* by quantitative physical measurements. (The large grey structure over there is a thunderstorm. That transient line of enhanced brightness was a flash of lightning. In that direction it is raining already. Over there the sky is still clear, etc., etc.)

It is only in the last 25 years that local weather forecasters have been able to supplement the local weather information available from the human eye with an additional remote sensing capability—namely, weather radar. Again, pattern recognition (in this case while looking at "maps" of echo strength) is important to the interpretation of the data.

Under clear sky conditions, the human eye and the weather radar receive no information (other than the fact that there is no pattern) but already new remote sensing techniques permit the internal structure of the boundary layer to be monitored continuously under

TABLE 11. Estimates of the accuracy of temperature measurements.

| Type of measurement | Technique | Estimated accuracy | | |
|---------------------|----------------------------------------|-----------------------|-----------------------|-------------------------|
| | | Acoustic | Radio | Optical |
| Line integral | Time-of-flight | $\pm 1^\circ\text{K}$ | | $\pm 0.2^\circ\text{K}$ |
| Line profile | Multifrequency O_2 radiometer | $\pm 2^\circ\text{K}$ | | |
| | N_2 Raman lidar | | | $\pm 1^\circ\text{K}$ |
| | Hybrid radio-acoustic | | $\pm 1^\circ\text{K}$ | |
| Structure constant | Monostatic acoustic sounder | $\pm 50'$ | | |

TABLE 12. Estimates of accuracy of water vapor content.

| Type of measurement | Technique | Estimated accuracy | | |
|---------------------|----------------------------|--------------------|------------------------------------|----------------------|
| | | Acoustic | Radio | Optical |
| Line integral | Microwave radiometry | | $\pm 10\% \pm 1 \text{ gram/cm}^2$ | |
| Line average | Time-of-flight HCN laser | | $\pm 10\%$ | |
| Line profile | H_2O Raman | | | $\pm 0.1 \text{ mb}$ |
| Structure constant | FM-CW radar | | Factor of 2 | $\pm 0.1 \text{ mb}$ |

TABLE 13. Estimates of accuracy of aerosol reflectivity.

| Type of measurement | Technique | Estimated accuracy | | |
|---------------------|----------------|--------------------|-------|-----------------|
| | | Acoustic | Radio | Optical |
| Line profile | Lidar | | | Factor of 2^* |
| 2-D coverage | Scanning lidar | | | Factor of 2^* |

* Relative accuracy of adjacent measurements with the same system should be within $\pm 10\%$.

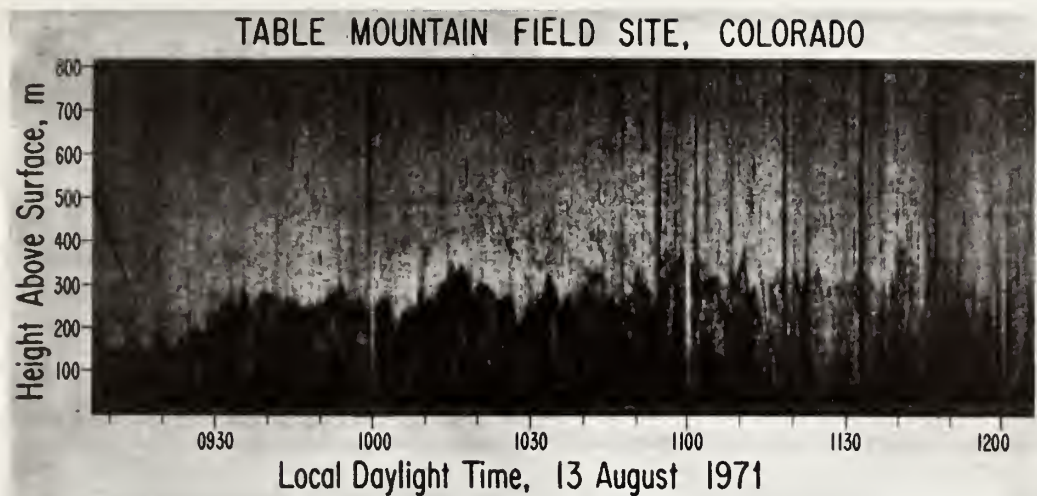


FIG. 10. Acoustic echo sounding record showing dissipation by thermal plumes of nocturnal ground-based radiation inversion. (Courtesy Dr. Freeman F. Hall)

clear sky conditions. In recent years, we have learned how to use many different tracers, additional to hydrometeors, for radar-like measurements and displays. Spe-

cifically, small scale (of order $\lambda/2$) fluctuations in temperature and velocity can be used acoustically to monitor the internal structure and processes of the atmosphere;

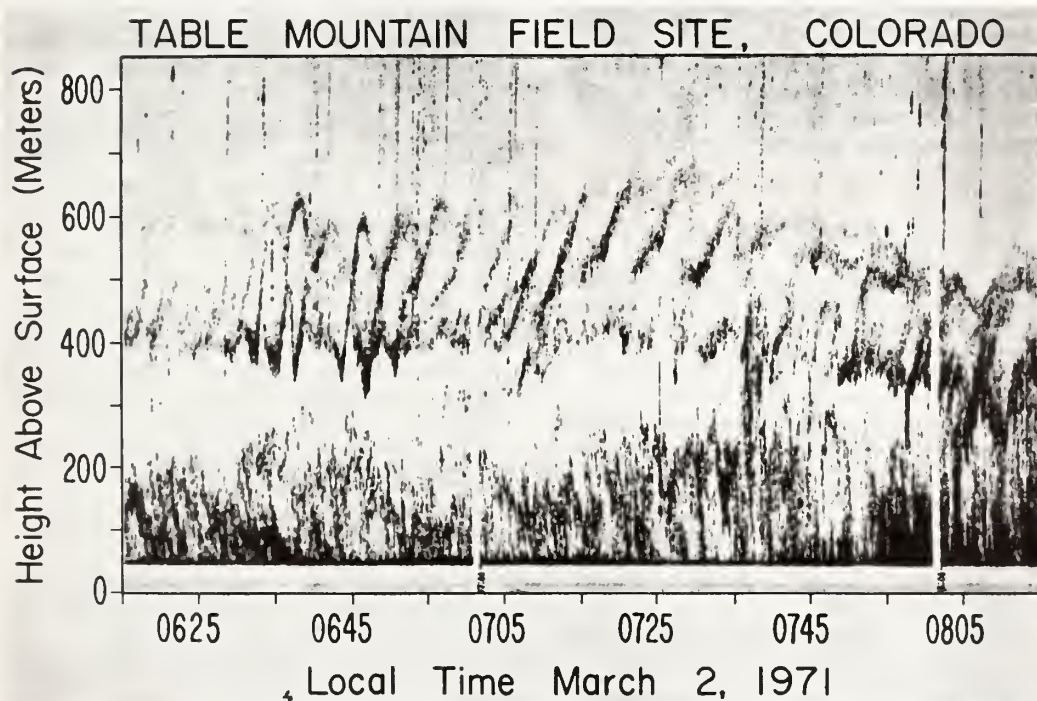


FIG. 11. Acoustic echo sounding record showing "braided" pattern characteristic of breaking waves occurring above a ground-based radiation inversion. (Courtesy Dr. Freeman F. Hall)

similarly, the small scale humidity fluctuations can be used as tracers of boundary layer structure by FMCW radar techniques. At optical wavelengths, aerosol particles are readily detected by lidar techniques and may therefore be used to monitor the boundary layer. The resultant echo patterns are already being recognized in terms of thermal plumes, inversions, internal gravity waves, breaking waves, etc. As the local weather forecaster gains skill in recognizing patterns in mesoscale and microscale maps of parameters such as velocity, temperature and humidity (and their small-scale structure parameters, C_x^2 , C_r^2 , and C_z^2), so he should greatly enhance his ability to identify the existence and location of meteorological phenomena or processes (e.g., thermal plumes, radar hook echoes, and temperature inversions) and hence to observe and predict their development. Note that these maps do not have to have high absolute accuracy; the many orders of magnitude variability of parameters such as C_x^2 , C_r^2 , C_z^2 , and radar and lidar reflectivities mean that relative accuracies of 3 db and absolute accuracies of 10 db may be acceptable for pattern recognition purposes. The wide range of 2-dimensional or 3-dimensional maps potentially available to the meteorologist of the future will provide him with totally new abilities to watch for changing atmospheric conditions, and hence will radically affect both the nature and scope of future mesoscale research and services. We may also expect that the growing ability to use computers for pattern recognition purposes will eventually result in the automatic processing and interpretation of many of the patterns revealed by the remote sensing systems of the future.

Acknowledgments. I am grateful to my colleagues in the Wave Propagation Laboratory for many helpful discussions on remote sensing, and to the authors and the cited journals for permission to reproduce Figs. 1-11.

References

- Atlas, D., 1964: Advances in radar meteorology. *Advan. in Geophys.*, **10**, 317-478.
- Beau, B. R., 1971: Comparison of remote and *in situ* measurements of meteorological parameters and processes. *Proc. of NATO Adv. Study Inst.*
- , R. E. McGavin, C. B. Emmanuel, and R. W. Krinks, 1969: Radiophysical studies of evaporation at Lake Hefner, 1966 and 1967. ESSA Tech. Rept. ERL 115-WPL7.
- Beran, D. W., and S. F. Clifford, 1972: Acoustic Doppler measurements of the total wind vector. *Proc., Sec. Symp. on Meteorological Observations and Instruments, Amer. Meteor. Soc.*
- Birkemier, W. P., P. F. Duvoisin, A. B. Fontaine, and D. W. Thomson, 1969: Indirect atmospheric measurements utilizing RAKE tropospheric scatter techniques—Part II, Radiometric interpretation of RAKE channel-sounding observations. *Proc. IEEE*, **57**, 552-559.
- Cole, J. E., and R. A. Dobbins, 1970: Propagation of sound through atmospheric fog. *J. Atmos. Sci.*, **27**, 426-434.
- , and R. A. Dobbins, 1971: Measurements of the attenuation of sound by a warm air fog. *J. Atmos. Sci.*, **28**, 202-209.
- Collis, R. T. II., 1970: Lidar. *Appl. Opt.*, **9**, 1782.
- Decker, M. T., and E. J. Dutton, 1970: Radiometric observations of liquid water in thunderstorm cells. *J. Atmos. Sci.*, **27**, 785-790.
- Derr, V. E., 1972: *Remote Sensing of the Troposphere*. Gov't. Printing Office.
- , and C. G. Little, 1970: A comparison of remote sensing of the clear atmosphere by optical, radio and acoustic radar techniques. *Appl. Opt.*, **9**, 1976-1992.
- Fegley, R. W., I. H. Billford, Jr., and D. A. Gillette, 1972: A comparison of measured atmospheric solar extinction with that predicted from direct aerosol data (to be published).
- Gething, J. T., and D. Janssen, 1971: Measurements of temperature and humidity by acoustic echo sounding. *Nature*, **231**, 198-200.
- Gnirand, F. O., M. T. Decker, and F. R. Westwater, 1972: Experimental investigation of the convection of electrical range by passive microwave radiometry. NOAA Tech. Rept. ERL 221-WPL19.
- Hall, F. F., 1972: Temperature and wind structure studies by acoustic echo sounding. Chapter 18, *Remote Sensing of the Troposphere*, V. E. Derr (Ed.) Gov't Printing Office.
- Hanst, P. L., 1970: Infrared spectroscopy and infrared lasers in air pollution research and monitoring. *Appl. Spectrosc.*, **24**, 161.
- Hosler, C. R., and T. J. Lemmons, 1972: Radiometric measurements of temperature profiles in the planetary boundary layer. *J. Appl. Meteor.*, **11**, 311-318.
- Lawrence, R. S., 1969: Remote atmospheric probing by ground-to-ground line-of-sight optical methods. Report of Remote Atmospheric Probing Panel, Committee on Atmospheric Sciences, Nat'l Acad. of Sci.-Nat'l. Research Council, **2**, 91-110.
- , G. R. Ochs, and S. F. Clifford, 1972: The use of scintillations to measure average wind across a light beam. *Appl. Opt.*, **11**, 239-243.
- Lawrence, T. R., D. J. Wilson, C. E. Craven, I. P. Jones, R. M. Huffaker, and J. A. L. Thomson, 1972: A laser velocimeter for remote wind sensing. *Rev. Sci. Instr.*, **43**, 512-518.
- Lee, R. W., and A. T. Waterman, Jr., 1968: Space correlations of 35 GHz transmissions over a 28-km path. *Radio Sci.*, **3**, (New Series), 135-139.
- Lhermitte, R. M., 1968: Turbulent air motion as observed by Doppler radar. 13th Radar Meteorology Conf., McGill Univ., Montreal, Canada.
- , 1969: Atmospheric probing by Doppler radar. Rept. of Remote Atmos. Probing Panel, Committee on Atmos. Sci., Nat'l Acad. of Sci.-Nat'l. Res. Council, **2**, 253-285.
- Little, C. G., 1969: Acoustic methods for the remote sensing of the lower atmosphere. *Proc. IEEE*, **57**, 571-578.
- , 1972a: On the detectability of fog, cloud, rain and snow by acoustic echo-sounding methods. *J. Atmos. Sci.*, **29**, 748-755.
- , 1972b: Prospects for acoustic echo sounding. Chapter 19, *Remote Sensing of the Troposphere*, V. E. Derr (Ed.) Gov't Printing Office.
- Mandics, P. A., 1971: Line-of-sight acoustic probing of atmospheric turbulence. Tech. Rept. 4502-1, Stanford Elect. Labs., Stanford University.
- Marshall, J. M., A. M. Peterson, and A. A. Barnes, Jr., 1972: Combined radar-acoustic sounding system. *Appl. Opt.*, **11**, 108-112.

- Miller, L. Jay, 1972: Dual-Doppler radar observations of circulation in snow conditions. *Proc. 15th Radar Meteor. Conf., Amer. Meteor. Soc.*
- Owens, J. C., 1969: Optical Doppler measurement of micro-scale wind velocity. *Proc. IEEE*, **57**, 530-536.
- Richter, J. H., 1969: High resolution tropospheric radar sounding. *Radio Sci.*, **4**, 1261-1268.
- Salzman, J. A., W. J. Masica, and T. A. Coney, 1971: Determination of gas temperatures from laser-Raman scattering. NASA TN D-6336.
- Schotland, R. M., 1969: Some aspects of remote atmospheric sensing by laser radar. Rept. of Remote Atmos. Probing Panel, Committee on Atmos. Sci., Nat'l Acad. of Sci. Nat'l Res. Council, **2**, 179-200.
- Snider, J. B., 1972: Ground-based sensing of temperature profiles from angular and multi-spectral emission measurements. *J. Appl. Meteor.*, **11**, 958-967.
- Strandh, R. G., V. E. Deni, and R. E. Cupp, 1971: Atmospheric temperature measurement using Raman lidar. *Appl. Opt.*, **10**, 2665-2669.
- , V. E. Deni, and R. E. Cupp, 1972: Atmospheric water vapor measurement using Raman lidar. *Remote Sensing of Environment* (in press).
- Wyngaard, J. E., V. Izumi, and S. A. Collins, Jr., 1971: Behavior of the refractive-index-structure parameter near the ground. *J. Opt. Soc. Amer.*, **61**, 1646-1650.

Reprinted with permission from *Boundary Layer Meteorology*
Vol. 4, 47-89, April 1973

RADAR AND SODAR* PROBING OF WAVES AND TURBULENCE IN STATICALLY STABLE CLEAR-AIR LAYERS

HANS OTTERSTEN

Research Institute of National Defence, Stockholm, Sweden

KENNETH R. HARDY

Air Force Cambridge Research Laboratories, Bedford, Mass., U.S.A.

and

C. GORDON LITTLE

Environmental Research Laboratories, NOAA, Boulder, Colo., U.S.A.

(Received 8 August, 1972)

Abstract. This paper reviews the remote sensing of waves and turbulence in statically stable atmospheric layers, utilizing sodar and microwave radar echoes from the small-scale inhomogeneities in gaseous refractive index caused by localized fluctuations in temperature, humidity, and velocity. Scattering theory and sounding methodology are reviewed briefly, and the relative performance of typical radar and sodar systems compared.

The main section of the paper takes the form of a summary and discussion of experimental progress since 1969, showing how the echo patterns obtained may be applied to the interpretation of multiple layering, gravity waves, internal fronts and the details of dynamic instability and the genesis of turbulence in stably stratified shear layers. In addition, methods for the measurement of the intensity of the small-scale ($\sim \lambda/2$) variability of wind, temperature and water vapor from the observed radar or sodar echo intensities, and the use of Doppler techniques for the measurement of mean velocity and turbulence are discussed.

1. Introduction

In statically stable air, overturning and turbulence are generated by kinetic energy extracted from the mean flow. The mixing distorts and breaks up the mean gradients of potential temperature and specific humidity, resulting in small-scale temperature and water vapor contrasts. The refractive-index variability resulting from fluctuations in temperature, water vapor, and wind causes scattering of microwaves and acoustic waves (Batchelor, 1955; Megaw, 1957; Wheelon, 1959; Tatarski, 1961; Kallistratova, 1961; Monin, 1961), which provides a means for remote sensing of the structure within the clear atmosphere. The backscattering is of particular interest because radar and sodar sounding in monostatic configuration can produce informative, directly interpretable images of atmospheric cross-sections. Regions of turbulent activity and enhanced refractive-index variability can be identified with good spatial resolution.

Microwave scattering depends primarily on fluctuations in temperature and water vapor. Normally, contrasts in water vapor determine the scattering, but in the higher and drier parts of the atmosphere temperature variations may dominate. Both temperature and wind variability affect acoustic-wave scattering, while the influence of contrasts

* SODAR from SOUNd Detection And Ranging in analogy to RADIo Detection And Ranging.

in water vapor usually may be neglected. For the special case of acoustic-wave backscattering, only temperature fluctuations contribute.

No degree of turbulence is detectable by radar or by monostatic sodar unless air layers are present with gradients in potential refractive index (i.e., contrasts in potential temperature and specific humidity). In statically stable air, the vertical gradient of potential temperature guarantees the generation of temperature irregularities in the presence of turbulence, and some scattering will result. Moreover, shears in the mean flow build up in association with layers of enhanced static stability, and increased temperature variability will be a consequence of dynamic instability and turbulence in shear layers. Water-vapor gradients also tend to be accentuated in statically stable shear layers and further enhance refractive-index variability in overturning air. This is of particular importance for microwave scattering in the lower, humid atmosphere. As a consequence, stably stratified shear layers will be marked by small-scale refractive-index irregularities which scatter interrogating waves and serve as tracers which outline larger-scale configurations. It becomes possible to obtain radar and sodar images of clear-air structure which reveal phenomena associated with quasi-horizontal stratification. Multiple layering, gravity waves and internal fronts, details of dynamic instability and the genesis of turbulence have all been studied with radar and sodar techniques. Through direct analysis of echo patterns, information on levels, configurations, and scales of various atmospheric structures may be obtained. This information is particularly valuable when combined with conventional meteorological profiles and microbarograph data.

Sodar and radar backscattering also provides quantitative information on the intensity of fluctuations in refractive index within a very narrow range of eddy sizes, centered at one-half the interrogating wavelength. Combining bistatic and monostatic sodar sounding with radar probing, it should be possible to determine separately the variability of wind, temperature, and water vapor at the smallest scales. With the assumption of a Kolmogorov spectrum, average values are obtained for the rate of dissipation of kinetic energy, and for the rate of reduction of inhomogeneity in temperature and water vapor fields. Implicit in this information is also some knowledge of the mean vertical gradients of horizontal velocity, potential temperature, and specific humidity, because the small-scale structure results from a transfer of kinetic energy and inhomogeneity from the mean fields. Finally, Doppler frequencies in backscattered signals reflect the distribution of radial velocities in the sampled volume and may be analyzed for information on the motion field. Although the technique has been used with success for several years in weather radar studies of storm systems, Doppler radar measurements of clear-air motion have only recently been obtained and much work remains in their interpretation and application to atmospheric dynamics. Doppler sodar measurements, on the other hand, have quickly become a useful technique for studies of motion in the lower clear atmosphere. Both vertical motions and the mean horizontal wind field have been measured using monostatic and bistatic sodar, separately or in combination.

Radar and sodar sounding of the clear atmosphere has experienced an intensifying

interest in various parts of the world during the last 5 to 10 years (Atlas, 1964; Atlas and Hardy, 1966; Yaglom and Tatarski, 1967; Lane, 1967; Hardy and Katz, 1969; Ottersten, 1969a; Hardy, 1972; Proc. Radar Meteor. Conf., 1966, 1968, 1970; McAllister, 1968; McAllister *et al.*, 1969; Little, 1969, 1972; Hall, 1972). The interaction between atmospheric structure and interrogating waves has received a satisfactory description (Tatarski, 1961; Monin, 1961; Smith and Rogers, 1963; Ottersten, 1964, 1969a, b, c, 1972; Little, 1969). Imaging techniques have been developed to display the distribution of the intensive refractive-index variability associated either with convection due to hydrostatic instability, or with hydrodynamic instability and turbulence in layers of enhanced static stability. The methods provide unique information on clear-air structure, of value primarily in basic meteorological research. New results have been obtained on thermal convection (Konrad, 1970; Beran *et al.*, 1971a), land- and sea-breezes (Meyer, 1971), atmospheric waves and internal fronts (Gossard *et al.*, 1970, 1971; Gossard and Richter, 1970, 1972; Hooke *et al.*, 1972; Boucher, 1970; Katz, 1972; Reed and Hardy, 1972; Starr and Browning, 1972), dynamic instability and the genesis of turbulence (Atlas *et al.*, 1970; Browning and Watkins, 1970; Browning *et al.*, 1970; Ottersten, 1970a; Browning, 1971; Hardy *et al.*, 1973). Operational applications of this type of radar and sodar sounding in meteorological observation techniques have not yet been realized, but efforts toward this goal are in progress (Derr and Little, 1970; Little *et al.*, 1970; Beran, 1971; Beran and Willmarth, 1971; Beran *et al.*, 1971c; Gething and Jenssen, 1971; Simmons *et al.*, 1971; Harrold and Browning, 1971).

The scope of this paper is restricted to remote sensing of waves and turbulence in statically stable atmospheric layers, utilizing sodar and microwave radar for observation of scattered returns from variability in gaseous refractive index. We will focus on backscattering in essentially monostatic systems but bistatic sodar will also receive some consideration. Sounding methodology and scattering theory will be reviewed briefly to allow an extensive exposure of experimental progress since 1969 by exemplifying and summarizing recent experimental results. The deliberate trend toward joint exploration with indirect systems in combination with *in-situ* sensors is satisfying. Such investigations have established that radar and sodar sounding provides essential meteorological information which together with the acquisition of intermittent wind and temperature profiles by conventional meteorological sensors allow an improved delineation of tropospheric structure and a better visualization of irregularities in the motion field.

2. Methodology

2.1. GENERAL

Radar and sodar methods are attractive for atmospheric remote sensing because they permit interrogation of the surrounding medium with good spatial and temporal resolution. The spatial resolution is achieved through the combination of directive antennas and echo-delay ranging, which together define the minimum resolution cell of the system. With fixed antennas, the medium is probed in only one dimension, but with steerable antennas, two-dimensional and three-dimensional scans of the surround-

ing atmosphere can be achieved, with a time resolution determined by the dwell-time required to provide adequate integration of the echo from each resolution cell.

Backscattering from the clear atmosphere is sensitive only to refractive-index fluctuations of size one-half the interrogating wavelength. Below about 1 cm in scale, the intensity of refractive-index fluctuations decreases rapidly with size, causing the backscattered intensity to decrease rapidly for wavelengths shorter than a few centimeters. Therefore, a wavelength no shorter than 5–10 cm should be selected for monostatic sounding of clear-air structure. On the other hand, a reasonably short wavelength is favorable for good angular resolution. Microwaves have therefore been found particularly suitable for clear-air radar sounding with an optimum wavelength of around 10 cm, although wavelengths of up to about 6 m have been used (Woodman and Guillen, 1972). Similar wavelengths, which correspond to audible frequencies, should be used for acoustic echo sounding. In this case, however, there are additional restrictions because of the excessive environmental audio noise at low acoustic frequencies and the rapidly increasing atmospheric attenuation at high frequencies. This limits the useful frequency interval for atmospheric sodar probing to about 200–5000 Hz, corresponding to wavelengths in air of about 170 to 7 cm. The short wavelengths give very limited range, typically only 100–200 m, because of high attenuation.

Radar research on clear-air structure with the objective of furthering our understanding of statically stable shear flows is currently proceeding along two different lines. High powered pulse radars with large, steerable antennas are being used to sense and resolve turbulent structures in clear air up to high altitudes (<35 km) and out to long ranges (~100 km), and can provide spatial and temporal coverage of atmospheric structures for determination of their three-dimensional configuration and evolution with time. Ultra-high resolution radars with fixed, vertically-pointing antennas are being used successfully in the lower, clear atmosphere (<2 km) to outline fine-scale structure of the air mass drifting through the radar beam, displaying detailed features of atmospheric stratification, gravity waves and dynamic instability in a time-height plane. Both of these approaches have combined radar observation with simultaneous *in-situ* sounding in efforts to relate parameters obtainable from radar visualization of the flow to measurements of mean profiles and fluctuating quantities.

Table I lists approximate values for important parameters of five high-powered pulse radars with steerable antennas which have been devoted to studies of the clear atmosphere. The three sensitive radars at Wallops Islands, Virginia, were the first to be used intensively for investigations of clear air (Hardy *et al.*, 1966; Katz, 1966). Note that the 10.7-cm wavelength radar, which is a pulse Doppler radar, is almost 100 times more sensitive than the WSR-57, a 10.4-cm radar used for detection of precipitation and included in the table only for comparison. In 1968, Crane (1970) investigated clear-air turbulence (CAT) with the Westford 23.2-cm radar, the most sensitive radar in Table I. Ground clutter is severe for this radar, however, and atmospheric measurements within a 50-km range are difficult to obtain. The 10.7-cm

TABLE I

Characteristics of five high-powered pulse radars with steerable antennas which have been used for studies of clear atmosphere. For comparison, the characteristics of the WSR-57 radar, used by the U.S. National Weather Service for precipitation detection, are included. The minimum detectable reflectivity is the value of the minimum detectable radar cross-section per unit volume obtained when averaging over the resolution cell. Note that the value for the Westford radar has been evaluated at a range of 100 km.

| | | Wallops Island, Virginia | | | Defford, England | Westford, Mass. | (WSR-57) |
|----------------------------------------------|--------------|--------------------------|---------------------|---------------------|---------------------|---------------------|---------------------|
| Wavelength | (cm) | 3.2 | 10.7 | 71.5 | 10.7 | 23.2 | 10.4 |
| Antenna diameter | (m) | 10.4 | 18.4 | 18.4 | 25 | 25.6 | 3.6 |
| Beamwidth | (deg) | 0.2 | 0.5 | 2.9 | 0.33 | 0.6 | 2.0 |
| Pulse length | (μ s) | 2 | 1.3 | 1 | 1.25 | 10 | 4 |
| Peak power | (MW) | 0.9 | 3.0 | 6.0 | 1 | 4 | 0.4 |
| Minimum detectable reflectivity ^a | (m^{-1}) | 6×10^{-15} | 4×10^{-16} | 5×10^{-17} | 10^{-15} | 6×10^{-17} | 3×10^{-14} |
| At a range of | (km) | 10 | 10 | 10 | 10 | 100 | 10 |

^a For thin layers, only partially filling the radar resolution cell, higher average reflectivities are required before detection is possible. For the Westford radar in particular, the resolution cell will never be completely filled and detectable layers will always have average reflectivities exceeding $6 \times 10^{-17} m^{-1}$. For layer thickness of about 100 m, average reflectivities of about $10^{-15} m^{-1}$ are required, before detection is possible with the Westford radar at a range of 100 km.

radar located in Defford, England (Browning and Watkins, 1970; Watkins, 1971; Browning, 1972) is a pulse Doppler radar with clutter suppression and has more recently been brought into operation for meteorological studies of the clear atmosphere. It has produced excellent data on horizontal stratification and dynamic instability and some unique results on lee waves in clear air.

The ultra-high resolution radar developed by Richter (1969) is a vertically-pointing FM-CW (Frequency-Modulated Continuous Wave) radar which has high sensitivity and a range resolution of about 1 m and which is essentially free of ground clutter. This radar has been used for the visualization of a wide variety of atmospheric structures in the marine layer of San Diego which were never before resolved in such detail (Richter and Gossard, 1970). The same type of radar, with essentially the same parameters but in a mobile version, has been used by Bean *et al.* (1971a, b) adjacent to a 150 m high, micrometeorological tower at Haswell in the high plains of eastern Colorado. Both of these radars are restricted to vertical sounding and provide time-height displays of atmospheric structures propagating or being advected in the planetary boundary layer. In this issue, however, Richter *et al.* describe a second generation FM-CW radar sounder which is fully mobile and which incorporates scanning capability. This radar has revealed for the first time true spatial pictures of complex clear-air structures with a range resolution of 1 m.

Chadwick and Little (1972) have compared the respective sensitivities of the Wallops Island 10.7-cm pulse radar and the 10-cm FM-CW radar, using the parameters in Table II for evaluation of radar performance. They conclude that the pulse radar will

TABLE II

Parameters used in a comparison of the sensitivities of the Wallops Island 10.7-cm pulse radar, the ultra-high resolution 10-cm FM-CW radar developed by Richter (1969), and the Wave Propagation Laboratory sodar (Wescott *et al.*, 1970). (From Chadwick and Little, 1972)

| | | |
|------------------------------------|------------------|-----------------|
| Wallops Island 10.7-cm pulse radar | | |
| Frequency | 2.7–2.9 GHz | |
| Peak power | 3 MW | |
| Pulse width | 0.1–1.3 μ s | |
| Pulse repetition frequency | 320 Hz | |
| Noise figure | 4 dB | |
| Antenna diameter | 18 m | |
| 10-cm FM-CW radar | | |
| Frequency range (max) | 2.9–3.1 GHz | |
| Power (average or peak) | 200 W | |
| Sweep duration | 50 ms | |
| Effective noise temperature | 1000 K | |
| Antenna diameter | 3 m | |
| Sweep repetition frequency | 10 Hz | |
| WPL Mark I Sodar | Short range mode | Long range mode |
| Peak power | 10 W | 30 W |
| Pulse width | 10 ms | 100 ms |
| Pulse repetition frequency | 1 Hz | 0.1 Hz |
| Carrier frequency | 4 kHz | 2 kHz |
| Antenna diameter | 1.22 m | 1.22 m |
| Efficiency factor | 0.1 | 0.1 |
| Receiver bandwidth | 100 Hz | 30 Hz |
| System noise (above kTB) | 10 dB | 10 dB |

be about 24 dB more sensitive than the FM-CW radar over a common range resolution cell of 170 m, although the difference will be only about 14 dB if a range resolution of 17 m is used. (It is assumed that the pulse repetition rate is kept constant, which means that the average power of the pulse radar is reduced by a factor of 10, thereby accounting for the decrease in relative sensitivity.)

At short ranges, however, the sensitivity of the pulse radar is greatly reduced because of ground clutter. These problems are much less severe on the FM-CW radars, which attain unique sensitivities because of their ability to operate at full sensitivity at relatively close ranges. As a result, very high space resolution can be obtained, and FM-CW radars are able to observe and resolve small-scale features in the reflectivity structure in unparalleled detail.

Vertically-pointing pulse radars have also been used for clear-air studies (Lane, 1969; Ottersten, 1970b; Scoggins, 1970; LaGrone and Deam, 1971) but with their coarse range resolution they cannot compete with FM-CW radars in the observation of details of internal gravity waves and shear instability. They can be simple and reasonably inexpensive devices, however, for continuous monitoring of inversion levels and zones of enhanced turbulence in the lower clear atmosphere.

Chadwick and Little (1972) also made a comparison of the sensitivities of an

FM-CW radar and a sodar, using the parameters in Table II. Operating at the 170-m range in the 4-kHz, 1.7-m resolution mode, they show that the sodar would be 8 dB *more* sensitive than the FM-CW radar for pure temperature fluctuations, and about 25 dB *less* sensitive for pure humidity fluctuations. For a 1.7-km range and 17-m resolution, the FM-CW sounder would be 2 dB less sensitive than the sodar for temperature fluctuations and 31 dB more sensitive for humidity fluctuations. In Table III, we summarize the relative sensitivities of the three systems in terms of

TABLE III
Minimum detectable reflectivities and C_n^2 values for the systems described in Table II.

| System | Range | | | | | |
|------------------------|-----------------------|--------------------------|-----------------------|--------------------------|-----------------------|--------------------------|
| | 0.1 km | | 1.0 km | | 10 km | |
| | $\eta(\text{m}^{-1})$ | $C_n^2(\text{m}^{-2/3})$ | $\eta(\text{m}^{-1})$ | $C_n^2(\text{m}^{-2/3})$ | $\eta(\text{m}^{-1})$ | $C_n^2(\text{m}^{-2/3})$ |
| High power pulse radar | — | — | — | — | 1×10^{-17} | 1.2×10^{-17} |
| FM-CW radar | 2×10^{-17} | 2.5×10^{-17} | 2×10^{-16} | 2.5×10^{-16} | 2×10^{-15} | 2.5×10^{-15} |
| WPL Mark I sodar | 6×10^{-12} | 7×10^{-12} | 2×10^{-11} | 3×10^{-11} | — | — |

their minimum detectable reflectivities at ranges of 0.1, 1.0 and 10 km. The corresponding minimum detectable C_n^2 values have been computed using Equation (13); Table IV may be used to convert these C_n^2 values to corresponding values of C_T^2 , C_e^2 or C_v^2 . Note that, because of ground clutter problems, no figures are given at the two lower ranges for the high-power pulse radar, and that, because of absorption, the sodar does not operate at the longest range. The range resolutions are assumed to be equal for each system, and respectively 1.7 m at a 0.1-km range, 17 m at a 1.0-km range and 170 m at a 10-km range. In each case, a 1-s integration period is assumed. It is also assumed that the pulse volume is completely filled with a homogeneous isotropic field of refractive-index irregularities; if the volume is incompletely filled, then the minimum detectable values of η and C_n^2 will, of course, be larger. The calculations of sodar sensitivity have assumed that the total round-trip absorption in each case is 10 dB, though this value could vary by at least a factor of two in each direction, depending upon meteorological conditions.

It should be noted that the above calculations assume ideal performance of the radars, and include the effect of incoherent integration of the pulse within the 1-s integration period. In general, the sensitivity figures given in Table I (which were taken from the cited references), correspond more closely to the minimum detectable reflectivities to be expected from a single pulse.

The numbers given in the above comparisons will change quickly in favor of FM-

CW radars and sodars, since improvements in performance are anticipated. One characteristic of sodar is also its high degree of flexibility, and several of the parameters listed in Table II may be varied for the one and same sodar to vary the wavelength and the amount of integration, and to extend the range. A variety of sodar designs have also been tested (Mahoney, 1969; McAllister and Pollard, 1969; Beran, 1970; Beran *et al.*, 1970, 1971b; Hall *et al.*, 1971; Parry and Sanders, 1972), many of them with better sensitivity than the sodar in Table II. Various types of acoustic antennas have been tried, including concrete parabolas, parabolic horn antennas, and acoustic arrays, employing various types of shielding to improve acoustic noise rejection and clutter suppression. With anechoic absorbers surrounding the antenna, typical minimum ranges of 30 m can be achieved and the sounder can be operated in noisy urban environments, as indicated in the feasibility study by Simmons *et al.*, (1971) which deals extensively with sodar system analysis and sounder design. The feasibility of sodar for atmospheric probing, including aspects of atmospheric attenuation of sound waves, is also discussed by Little (1969) and Hall (1972), and prospects for acoustic echo sounding are given by Little (1972) who concludes that very large improvements in sodar system performance are conceivable.

Bistatic configurations of acoustic echo sounding may be superior in applications where continuous monitoring of atmospheric returns is desirable, since forward scatter signals are typically much stronger than echoes received in the monostatic mode. The turbulent fluctuations in wind contribute substantially to the forward scatter of acoustic waves which opens the possibility of monitoring turbulence intensity with bistatic sodar, as indicated in Section 3. Wind variability and temperature fluctuations may be separated by combined monostatic and bistatic sodar measurement. For Doppler techniques, the stronger and more continuous signals of forward scatter are advantageous, and bistatic sodar has been employed successfully for Doppler measurement of wind, as discussed in Section 2.2. For the measurement of horizontal wind, it is desirable that the axis of Doppler resolution be well inclined to the vertical. This is difficult to accomplish in a bistatic configuration, however, and therefore monostatic Doppler sodar is also attracting considerable attention. If bistatic sodar is employed, it is important to avoid scattering angles close to 90° , since no power is scattered in directions orthogonal to the direction of incidence of the acoustic wave.

2.2. DOPPLER TECHNIQUES

Various methods for wind measurement with sodar have been suggested (Derr and Little, 1970), including angle-of-arrival determination of acoustic beam bending by wind gradients, and time-lagged cross-correlation analysis of spaced sounding measurements. Here we only consider the wind-induced Doppler frequency shifts contained in signals received both in monostatic and bistatic scatter systems. Since Doppler shifts provide velocity information specific to the associated echo region, Doppler techniques for wind velocity measurements appear superior for detailed analysis of structural features of waves and turbulence. Doppler radar for atmospheric

probing has long been an established technique (Lhermitte, 1968), but only recently have Doppler radar measurements provided useful information on clear-air motion (Browning *et al.*, this issue, p. 91). Doppler sodar measurement has quickly become a useful method for studies of motions in the planetary boundary layer (Beran *et al.*, 1971a; Beran and Willmarth, 1971; Beran and Clifford, 1972). Mahoney *et al.* (this issue, p. 155) have obtained some unique sodar wind measurements using both angle of arrival and Doppler techniques, and Beran *et al.* (this issue, p. 133) have determined the vector wind profile by Doppler sodar probing.

In a scatter geometry with wave vectors \mathbf{k}_0 and \mathbf{k}_s for the incident and scattered waves, respectively, we receive a Doppler shifted signal f_s differing from the impinging frequency f_0 by an amount $\Delta f = f_s - f_0$ proportional to the velocity \mathbf{V} of the motion of the scattering medium. The Doppler shift is given by

$$\Delta f = (2\pi)^{-1} (\mathbf{k}_s - \mathbf{k}_0) \cdot \mathbf{V} \quad (1)$$

and we note that from the Doppler shift can be determined the wind component along $\text{dir}(\mathbf{k}_s - \mathbf{k}_0)$, which is the bisector of the angle formed by the incident beam and the beam scattered toward the receiver. Neglecting the difference in wavelength λ between the incident and scattered waves, we have

$$\Delta f \approx 2\lambda^{-1} \sin(\theta/2) V \cos \beta, \quad (2)$$

where β is the angle between the wind vector \mathbf{V} and $\text{dir}(\mathbf{k}_s - \mathbf{k}_0)$. We have $k_s \approx k_0 = 2\pi\lambda^{-1}$, and the scattering angle θ is the angle between \mathbf{k}_s and \mathbf{k}_0 .

We note that in a bistatic configuration with \mathbf{k}_0 vertical and \mathbf{k}_s well inclined to the vertical, a component of the horizontal wind contributes to the Doppler shift. With \mathbf{k}_0 and \mathbf{k}_s at the same inclination to the vertical and still in the same vertical plane, only vertical motions can be measured, however. Swinging both beams out of the vertical plane, again a horizontal wind component starts to contribute, in addition to the Doppler shift from vertical motion.

Ordinarily we use the wave vectors at the transmitter and receiver, respectively, for \mathbf{k}_0 and \mathbf{k}_s in Equation (1), which means that we neglect the effects of refraction, or beam bending, due to a varying mean value of the atmospheric refractive index. For electromagnetic waves, this is an excellent approximation at short ranges, which is equally applicable at long ranges provided that we avoid the lowest elevation angles for which refraction may be substantial. For acoustic waves, however, refraction is potentially serious already at short ranges and, in order to avoid misinterpretation, an analysis of the influence of beam bending is proper for every experimental configuration in atmospheric sodar probing. Beran and Clifford (1972) have considered the three basic effects of refraction on Doppler sodar wind determination, namely the relocation of the scattering volume, the shift in the axis of resolution of the Doppler wind component, and the change in magnitude of the measured wind. For a bistatic configuration with one beam vertical and one beam at 45° elevation, they conclude that within ranges of about 300 m, the wind speeds derived by the use of Equation (2) without accounting for refraction, in most circumstances will be in error by no more

than 5%. Similar conclusions were reached by Georges and Clifford (1972) for Doppler sodar sounding to heights of about 1 km.

For pure backscattering, Equation (2) reduces to

$$\Delta f \approx 2\lambda^{-1}V \cos \beta, \quad (3)$$

where β now is the angle between the wind vector V and the radial direction of the beam. Thus, monostatic Doppler radar and Doppler sodar can only measure the radial component of the wind. Vertically-pointing systems can only provide vertical motions, but by tilting of the beam, a horizontal component of the wind will also be sensed in the Doppler frequency shift. Further, by slewing the beam in azimuth at a fixed elevation angle, velocity-azimuth-display (VAD) technique, various horizontal wind components will be sensed and, under certain assumptions, the horizontal vector wind and the vertical motions may be determined separately (Little *et al.*, 1970). Until now, VAD technique has been applied successfully only to Doppler radar measurement when snow, rain and occasionally insects provide ample scatterers in the entire region surrounding the radar.

With a distribution of velocities within the scattering volume, a spectrum of Doppler frequencies occurs in the scattered return, rather than a single component as indicated by Equation (2). (The additional spread of the spectrum due to the slight variation of $\text{dir}(\mathbf{k}_s - \mathbf{k}_0)$ within the scattering volume is usually small and may be neglected for narrow beams.) Each Doppler frequency in the Doppler spectrum corresponds to a particular magnitude according to Equation (2) of the wind component along $\text{dir}(\mathbf{k}_s - \mathbf{k}_0)$, and the spectral densities in the Doppler spectrum reflect the distribution of velocity values present in this component within the scattering volume, although this distribution will be weighted by the antenna diagrams and by the reflectivity distribution when converted into a Doppler spectral density. Thus, in the monostatic mode, the Doppler spectrum represents the distribution of radial velocities within the resolution cell, and to every radial velocity $V \cos \beta$ corresponds a Doppler frequency according to Equation (3).

From the mean frequency of the Doppler spectrum, the mean motion of the scattering medium along $\text{dir}(\mathbf{k}_s - \mathbf{k}_0)$ may be obtained, and the spread of the spectrum reflects the spread of velocities within the scattering volume due to the combined effects of wind shear and turbulence within the resolution cell. As yet, the variance of the Doppler sodar spectrum has not been analyzed in terms of atmospheric motions, but, since the resolution cell can be quite small in sodar probing, the evaluation of the mean Doppler velocity and its variation in space and time still provides a wealth of detail about the atmospheric motion field (Beran *et al.*, 1971a; McAllister, 1971). In Doppler radar analysis of atmospheric motions, both the mean and variance have proved to be useful quantities, and in this issue Browning *et al.*, p. 91, demonstrate how Doppler radar spectra obtained from clear-air returns at various altitudes may be used to evaluate the main component of the mean wind, the vertical shear of the same component, and from the variance of the Doppler spectrum, an estimate of the turbulence intensity.

From nearly simultaneous determinations of Doppler shifts in three different directions but from almost the same scattering volumes, the mean value of the total wind vector may be synthesized. If vertical motions can be neglected or accounted for, determinations in two directions suffice. Such methods have been implemented for Doppler radar studies of storm systems, but the cost for two or three high-powered Doppler radars for clear-air studies almost seems prohibitive. Also, with the total absence of echo in large regions and with comparatively limited range elsewhere, extensive Doppler radar mapping of the total wind field in the clear atmosphere does not appear feasible. Doppler sodar measurement of the total wind vector in the planetary boundary layer has already been implemented (Beran and Clifford, 1972), however, and in this issue Beran *et al.*, p. 133, present results from an early test of a technique for determining the vector wind profile. One method relies on three separate monostatic sodar systems. In another concept, two orthogonal components of the horizontal wind are evaluated from the Doppler shifts observed on two orthogonal, bistatic sodar links, using separate receiver beams tilted to intersect a common vertically-pointing transmitter beam. The influence of vertical motion on these Doppler shifts may be accounted for, if also the Doppler shift in the backscattered signal is measured in a third receiver, sharing the transmitter antenna to determine vertical motions separately.

3. Scattering Theory

3.1. REFRACTIVE INDEX

The radio refractive index of air n in terms of absolute temperature T , total pressure p mb, and partial pressure of water vapor e mb is expressed in N -units:

$$N = (n - 1) 10^6 = 77.6T^{-1} [p + 4810eT^{-1}]. \quad (4)$$

An acoustic refractive index may be defined in a similar way starting from the phase velocity of sound waves given by

$$C = 20.05T^{1/2} [1 + 0.14ep^{-1}] + V \cos \phi. \quad (5)$$

Note that the wind component $V \cos \phi$ normal to the wave fronts is of importance, ϕ being the angle between wave and wind vectors.* We obtain the real part of an acoustic refractive index n_a as $C_0 C^{-1}$, where $C_0 = 20.05T_0^{1/2}$ is a reference phase velocity at a reference temperature T_0 in dry, stagnant air. In N_a -units we have

$$N_a = (n_a - 1) 10^6 \approx 10^6 \left\{ \frac{T_0 - T}{2T_0} - 0.14 \frac{e}{p} - \frac{V \cos \phi}{C_0} \right\}. \quad (6)$$

This expression is useful with good accuracy for $|C - C_0| \ll C_0$. For instance, with

* Since the atmosphere is the transmitting medium for sound waves, also the wind component parallel to the wave fronts is influential by introducing translatory motion of wave packets but without affecting phase velocity. Gradients of this component cause no refraction but only slide the wave fronts relative to each other, leaving their orientation unaffected.

$T_0 = 288$ K we have $C_0 \approx 340$ m s⁻¹, and it follows from Equation (6) with $p = 1000$ mb that fluctuations of 1°C in temperature, 1 mb of water vapor pressure, or 1 m s⁻¹ in wind speed, correspond to N_a -unit changes in acoustic refractive index of about 1700, 140 and 0–3000, respectively. Note that the refractive-index change due to wind depends on the direction of acoustic wave propagation relative to the wind direction. The corresponding N -unit changes for microwaves, about 1, 4, and 0, respectively, can be obtained from Equation (4). For sound waves we note that wind and temperature fluctuations dominate, humidity contrasts usually being unimportant. For microwaves, wind effects are negligible and the influence of humidity usually exceeds that of temperature. The imaginary part of refractive index, describing absorption of waves propagating through the atmosphere, is also typically much larger for acoustic waves than for microwaves. Little (1969) notes that the 3-cm wavelength radio wave is attenuated 0.01 dB km⁻¹ in the lower, clear atmosphere, while the 3-cm acoustic wave will experience an attenuation of order 100 dB km⁻¹. Attenuation increases rapidly with decreasing wavelength, both for microwaves and acoustic waves.

3.2. SCATTERING CROSS-SECTION

Irregular small-scale fluctuations in refractive index produce scattering of electromagnetic and acoustic waves propagating through the turbulent clear atmosphere. The scattering cross-section σ per unit volume per unit solid angle is a measure of the fraction of the incident power scattered in a given direction. General expressions obtained by Tatarski (1961) and Monin (1961) for electromagnetic and acoustic waves, respectively, are:

$$\begin{aligned}\sigma_{em} &= 2\pi k^4 \sin^2 \chi \phi_n(\mathbf{K}), \\ \sigma_a &= 2\pi k^4 \cos^2 \theta \phi_{na}(\mathbf{K}), \\ \mathbf{K} &= \mathbf{k}_s - \mathbf{k}_0; \quad K = 2k \sin(\theta/2).\end{aligned}\tag{7}$$

The polarization angle χ , the angle between the scattered wave direction and the electric field vector of the incident wave, enters the expression for the transversely polarized electromagnetic waves. For the longitudinally polarized acoustic waves, $\cos^2 \theta$ reflects the dependence on the scattering angle θ , the angle between the wave vectors \mathbf{k}_0 and \mathbf{k}_s for the incident and scattered waves, respectively. We have $k_s = k_0 = k = 2\pi\lambda^{-1}$.

The scattering angle θ together with the wavelength λ of the incident wave also determines the Fourier component \mathbf{K} in the three-dimensional spatial power-spectral densities ϕ_n and ϕ_{na} of refractive-index fluctuations that is sensed in a given scattering geometry. Scattering in an inhomogeneous medium is of a resonant nature in the sense that for scattering in the direction \mathbf{k}_s , only the variability in the direction $\text{dir}(\mathbf{k}_s - \mathbf{k}_0)$ and of scale size $2\pi K^{-1} = 0.5\lambda \sin^{-1}(\theta/2)$ contributes substantially to the scattered power. Clearly, for pure backscattering ($\theta = 180^\circ$), only the variability of scale size 0.5λ and variability along the radial vector determine the return. Also, by

varying λ and/or the scattering geometry, the spatial power spectrum of the refractive-index variability as a function of \mathbf{K} may be explored (Gjessing, 1969).

For acoustic waves, the power spectrum ϕ_{na} of refractive-index variability at any given wave number \mathbf{K} displays a dependence on scattering angle because the influence of wind variability on the refractive-index field depends on the scattering geometry. To illustrate this, we separate the spatial power-spectral densities of wind and temperature fluctuations, $E(\mathbf{K})$ and $\phi_T(\mathbf{K})$, respectively, neglecting humidity variations and assuming that the wind and temperature fluctuations are uncorrelated (for limitations of this expression, see Little, 1969).

$$\phi_{na}(\mathbf{K}) = C^{-2} E(\mathbf{K}) \cos^2(\theta/2) + (2T)^{-2} \phi_T(\mathbf{K}). \quad (8)$$

The mean values of sound velocity and temperature in the scattering volume are used for C and T .

It follows from Equation (7) that there will be no scatter of electromagnetic waves for a polarization angle of 0° , and that for acoustic waves, no scatter will occur in directions orthogonal to the direction of incidence. From Equation (8) we note that the scattered acoustic power is the sum of the powers scattered from the variability in velocity and temperature, the influence of velocity fluctuations being weighted by the factor $\cos^2(\theta/2)$; as a result, the backscattered acoustic power is entirely due to the temperature field.

For a Kolmogorov spectrum of turbulence (Tatarski, 1961), we may substitute

$$\begin{aligned} E(\mathbf{K}) &\equiv 0.061 C_V^2 K^{-11/3} \\ \phi_n(\mathbf{K}) &\equiv 0.033 C_n^2 K^{-11/3} \\ \phi_T(\mathbf{K}) &\equiv 0.033 C_T^2 K^{-11/3} \end{aligned} \quad (9)$$

and, assuming that $2k \sin(\theta/2)$ falls within the inertial subrange, we obtain

$$\begin{aligned} \sigma_{em} &= 0.016 k^{1/3} \sin^2 \chi C_n^2 \sin^{-11/3}(\theta/2) \\ \sigma_a &= 0.016 k^{1/3} \cos^2 \theta [1.84 C^{-2} C_V^2 \cos^2(\theta/2) + (2T)^{-2} C_T^2] \sin^{-11/3}(\theta/2). \end{aligned} \quad (10)$$

These expressions are valid only when the 'effective wave number' $2k \sin(\theta/2)$ of our interrogating scatter geometry lies within the inertial subrange of locally homogeneous and isotropic fields of radio refractive index, wind, and temperature fluctuations. We note that the scattered power varies weakly with wavelength and that most of the scatter is in the forward hemisphere, $\sigma \sim \lambda^{-1/3} \sin^{-11/3}(\theta/2)$.

The structure constants C_V^2 , C_T^2 , and C_n^2 may serve as measures of the variability within the inertial subrange of velocity, temperature, and radio refractive index, respectively. In analogy with the electromagnetic case, we may define a structure constant for acoustic refractive index C_{na}^2 equal to the expression within brackets in Equation (10). It is important to note, however, that C_{na}^2 applies to scattering only, depends on the scattering angle θ , and differs from the structure constant of acoustic refractive index which may be defined for the description of amplitude and

phase fluctuations in a propagating sound wave and which is given as $(C^{-2}C_v^2 + (2T)^{-2}C_T^2)$ by Tatarski (1961).

The influence of turbulent fluctuations of temperature, humidity, and wind on the refractive-index variability of acoustic waves and microwaves is illustrated in Table IV. The quoted values are typical in regions of enhanced variability in the lower

TABLE IV

The influence of fluctuations in temperature, C_T^2 , humidity, C_e^2 , and wind, C_v^2 , on the refractive-index variability of acoustic waves, C_{na}^2 , and microwaves, C_n^2 , at 1000 mb and 288 K. The structure constant C_x^2 for variability in a parameter x is defined from the structure function $D_x(r) = C_x^2 r^{2/3}$. The influence of temperature and humidity variability on the microwave refractive-index fluctuations has been separated according to $C_n^2 = (77.6 \times 10^{-6} p T^{-2})^2 (1 + 9620 e p^{-1} T^{-1})^2 C_T^2 + (0.373 T^{-2})^2 C_e^2$, neglecting the effects of pressure fluctuations and assuming that temperature and humidity fluctuations are uncorrelated within the inertial subrange.

| | $C_{na}^2 \times 10^6 \text{m}^{-2/3}$ | $C_n^2 \times 10^{12} \text{m}^{-2/3}$ |
|-------------------------------------------------|----------------------------------------|----------------------------------------|
| $C_T^2 = 1 (\text{°C})^2 \text{m}^{-2/3}$ | 3 | 1 |
| $C_e^2 = 1 (\text{mb})^2 \text{m}^{-2/3}$ | 0.02 | 20 |
| $C_v^2 = 1 (\text{m s}^{-1})^2 \text{m}^{-2/3}$ | 0-16 | 0 |

troposphere. The refractive-index variability, and consequently the scattering, are typically 5 to 6 orders of magnitude stronger for acoustic waves than for microwaves. For microwave scattering, the contribution of humidity fluctuations may exceed the influence of temperature variability by more than an order of magnitude, while for acoustic waves, the humidity variations ordinarily can be neglected with an error of less than 1% in scattered power. Moreover, the influence of wind variability on sound scattering depends on the scattering angle, with no contribution for pure backscattering. Thus, wind variability and temperature variations may be obtained separately by combining monostatic and bistatic sodar, and the joint use of monostatic radar and sodar allows separate determination of fluctuations in humidity and temperature.

3.3. BACKSCATTERING

Since the monostatic radar and sodar configurations are of particular interest, we also give explicitly the corresponding scattering cross-sections in the case of pure backscattering, the general form in Equation (11), and the special case of a Kolmogorov spectrum of turbulence in Equation (12).

$$\begin{aligned}\sigma_{\text{em}} &= 2\pi k^4 \phi_n(2\mathbf{k}_s) \\ \sigma_a &= 2\pi k^4 (2T)^{-2} \phi_T(2\mathbf{k}_s).\end{aligned}\quad (11)$$

We are sampling the power spectral density of radio refractive index and temperature, respectively, along the radial vector at a scale size of 0.5λ .

$$\begin{aligned}\sigma_{\text{em}} &= 0.016 k^{1/3} C_n^2 \\ \sigma_a &= 0.016 k^{1/3} (2T)^{-2} C_T^2.\end{aligned}\quad (12)$$

We may introduce reflectivity $\eta = 4\pi\sigma$, the backscattering cross-section per unit volume, and together with $k = 2\pi\lambda^{-1}$ reduce Equation (12) to the familiar forms

$$\begin{aligned}\eta_{em} &= 0.38 C_n^2 \lambda^{-1/3} \\ \eta_a &= 0.38 (2T)^{-2} C_T^2 \lambda^{-1/3}.\end{aligned}\quad (13)$$

We note that the combined monostatic radar and sodar experiment allows determination of C_n^2 and C_T^2 , from which C_e^2 may be evaluated (Table IV).

For the particular case of dry air, we have

$$C_n^2 = [77.6 \times 10^{-6} p T^{-2}]^2 C_T^2 \quad (14)$$

and we may at a given wavelength directly evaluate the ratio of sodar to radar reflectivity for backscattering from temperature fluctuations.

$$\eta_a \eta_{em}^{-1} \sim 40 \times 10^6 T^2 p^{-2}. \quad (15)$$

At the surface, about 1000 mb at 288 K, we obtain $\eta_a \eta_{em}^{-1} \sim 3 \times 10^6$, while ratios of about 50×10^6 would be obtained at tropopause levels with 200 mb and 220 K. Although these values imply an effectiveness of backscattering more than one million times better for sodar than for radar, a proper comparison of sounder performance must take into account the total system performance by evaluation of propagation loss and system parameters such as transmitted power, effective aperture, receiver noise, and spatial and temporal integration (Chadwick and Little, 1972).

In the planetary boundary layer, the influence of temperature variability on C_n^2 is often negligible compared with the effect of humidity fluctuations, and we have

$$C_n^2 \approx (0.373 T^{-2})^2 C_e^2. \quad (16)$$

In such situations, a useful estimate of the ratio of sodar to radar reflectivity at a given wavelength may be obtained from

$$\eta_a \eta_{em}^{-1} \sim 1.8 T^2 C_T^2 C_e^{-2}. \quad (17)$$

4. Experimental Results

Atlas (1964) has reviewed some of the early studies of radar echoes from stratified layers. These layers usually correspond in height to regions having sharp vertical gradients in refractive index. Additional evidence for the existence of clear-air radar layers associated with large variations of refractive index has been given by Saxton *et al.* (1964), Hardy *et al.* (1966), and Kropfli *et al.* (1968). Multiple stratifications have been reported recently by Ottersten (1969a), Katz (1969), Crane (1970), Kropfli (1971) and Starr and Browning (1972). The scattering layers may be quite shallow, perhaps only a few meters thick as reported by Gossard *et al.* (1970), or they may be of the order of 1 km in depth. Ottersten (1970a) describes the clear-air scattering layers as occurring within stable regions in particular zones of enhanced static stability where vertical shear of the horizontal wind is accentuated. As the shears are

strengthened by larger-scale processes, small-scale overturning and turbulence may break out within the thin zones or layers. The layers are outlined by sensitive radars due to backscattering from the associated perturbations in temperature and water vapor. If the turbulence within thin layers is not able to erode the accentuating shear forces fast enough, breakdowns at progressively larger scales take place. This overturning is outlined by the previously turbulent thin lamina, although the new instability of larger scale may intensify the refractive-index variability and the radar returns. Deformation of the wind field by dynamical processes such as internal fronts, gravity waves, and mountain waves may lead to rapid local accentuation of the vertical wind shear; on occasion the final breakdown may take place over large vertical depths with escalation of the turbulence to scales and intensities of concern for aviation. Whether the breakdown occurs within thin lamina or over large vertical depths, the instability generally takes the form of regularly spaced two-dimensional rolls of lateral extension. The configuration exhibits the same structural characteristics as billow clouds. Thus, the overturning very much resembles the dynamic instability of the Kelvin-Helmholtz (K-H) type which occurs within a hydrostatically stable flow with both an inflection point in the velocity profile and a sufficiently strong vertical shear. Because of its periodic appearance, the instability is often referred to as 'unstable K-H waves' although the configuration does not propagate in the flow; instead, initial wavelike disturbances arise within the flow and roll up while the entire vortex sheet moves with the velocity of the mean flow.

With the vertically-pointing ultrahigh-resolution FM-CW radar (Richter, 1969), Richter and Gossard (1970) have been able to study the breakdown mechanism in detail and to reveal the influence of some of the processes responsible for the deformation of the mean fields leading to dynamic instability and small-scale breakdown in the flow. In a series of important papers (Gossard and Richter, 1970, 1972; Gossard *et al.*, 1970, 1971) and in this issue, Gossard *et al.* have interpreted the FM-CW radar observations, in terms of the influence of trapped and untrapped internal gravity waves on statically stable shear flows in the lower clear atmosphere. They have analyzed the distribution of Richardson number, Ri , in trapped and untrapped gravity waves and concluded that *untrapped internal gravity waves* whose propagation vector is directed nearly vertically within very stable height regions may reduce Ri below the critical value in thin lamina and cause dynamic instability. The resulting overturning takes an organized form resembling *K-H instability within thin lamina* no more than a few meters deep, and the associated small-scale deformations of the refractive-index field scatter electromagnetic (and acoustic) waves and outline the thin lamina on the time-height display of the FM-CW radar. *Trapped gravity wave systems* propagating in the stable boundary layer cause undulations on the thin lamina which may be monitored by the FM-CW radar for analysis with concurrent microbarograph data. Moreover, *a higher generation of dynamic instability, also resembling trains of K-H instability structures*, is often seen to perturb the thin, previously already unstable lamina. These larger-scale vortices are seen on the FM-CW radar by virtue of the backscattering from previously existing small-scale de-

formations in the refractive-index field within the thin turbulent lamina, but it also appears that the refractive-index variability and the radar return are enhanced when the stream surfaces are deformed by the larger-scale instability.

Figure 1, from Richter and Gossard (1970), contains features in the echo patterns

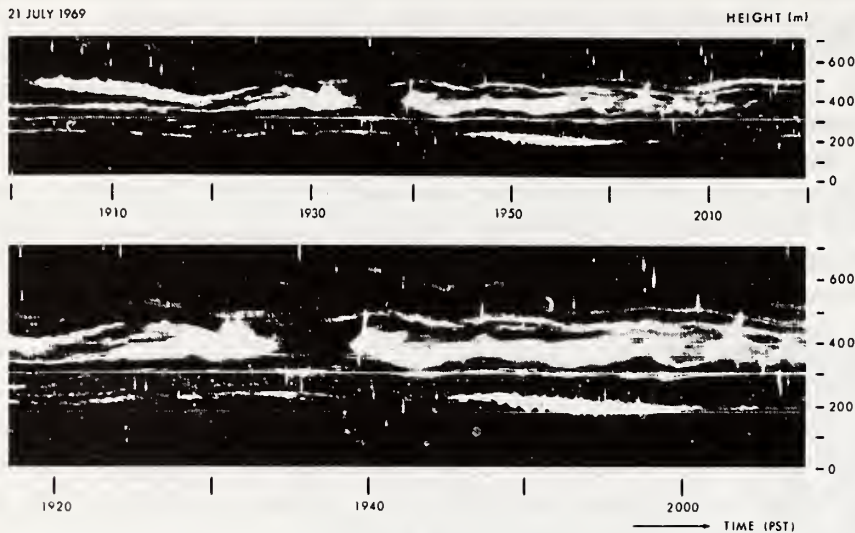


Fig. 1. Intensity-modulated display of time-height record obtained with a vertically-pointing FM-CW radar, with the record enlarged in the lower diagram. Notable features in the echo patterns indicate three types of structures in the clear atmosphere: thin, multiple layers, some of regular vertical spacing, are dynamically unstable lamina which contain small-scale overturning and which probably are created by untrapped internal gravity waves with nearly vertical propagation vectors in very stable height regions; slow, sinusoidal undulations on the layers are trapped gravity wave systems of higher frequencies, ordinarily representing the fundamental mode of gravity waves propagating in the stable boundary layer; small-scale vortex features, some of cusped appearance, resemble trains of K-H instability structures which occur as a result of dynamic instability in statically stable shear flows. Detailed analysis has revealed that the overturning within thin lamina also resembles K-H instability, probably a result of reduction in the Richardson number due to superposition of wave-induced shear from the untrapped wave on the background shear. (From Richter and Gossard, 1970.) (All figures reproduced with permission of the authors.)

which give evidence of three of these four types of processes in the clear atmosphere. Thin, multiple layers, some of regular vertical spacing, are dynamically unstable lamina which are created by *untrapped internal gravity waves* with nearly horizontal equiphase surfaces in very stable zones. Detailed analysis has revealed that the overturning within thin lamina resembles K-H instability (not resolved in Figure 1), probably a result of reduction in Ri due to superposition of wave-induced shear from the untrapped wave on the background shear. Slow, sinusoidal undulations on the layers are *trapped internal waves* of higher frequencies, ordinarily representing the fundamental mode of gravity waves propagating in the stable boundary layer. Vortex features which resemble trains of K-H instability structures perturb some of the layers, which presumably contain K-H instability on a smaller scale not resolved

in Figure 1. We infer that these visible vortices evidence a *higher generation of K-H instability* which develops as a result of consecutive shear instability at successively larger scales (Ottersten, 1970a).

Many of the structures observed by the FM-CW radar have not yet obtained satisfactory explanations, but it appears that the processes which have been identified and much of the analysis they have received are also relevant to statically stable shear layers observed by high-powered pulse radars in clear air at higher altitudes and longer ranges. Internal fronts and gravity waves in the free atmosphere, and mountain waves and lee waves in particular, deform the mean fields of static stability and wind, resulting in local reduction of Ri below critical values in statically stable shear zones. The scale of overturning will often be too small to be resolved at long ranges and the echoes will appear as almost featureless, stratified layers. Moreover, at high altitudes these layers will not be detectable unless large-scale overturning develops and intensifies temperature variability and radar reflectivity. We have no reason to assume, then, that the first vortex features that the radar is able to detect and resolve are also evidence for the first unstable scale. On the contrary, we may suspect that once the radar reveals overturning over scales of a hundred meters or more, we are witnessing the last event in a sequence of consecutive shear instability, starting possibly at meter scales and escalating in several steps to successively larger scales. Each event may well be a case of K-H instability, the later events representing recurrences of K-H instability over larger spatial and longer temporal scales. Thin layers of small-scale overturning are of little concern for aviation and give weak radar echoes, unless they coincide with sharp vertical gradients in water vapor contents. Large-scale overturning over deeper layers gives stronger radar echoes and these huge vortices with the associated trail of lesser whirls represent a hazard for many aircraft.

4.1. KELVIN-HELMHOLTZ INSTABILITY

Hicks and Angell (1968) were the first to analyze the structure observed by high-power radars in dynamically unstable shear flows in a clear atmosphere. This was rapidly followed by other studies (Hicks, 1969; Boucher, 1970; Ottersten, 1970a; Browning and Watkins, 1970; Atlas *et al.*, 1970; Gossard *et al.*, 1970).

Figure 2, from Browning and Watkins (1970), illustrates the stages in the development of 'K-H billows', a wave-like pattern which often leads to cloud formation at the crests (Ludlam, 1967; Scorer, 1969a). The stage with the closed rotor corresponds to overturning of the layer into a structure which is often observed with radar. In fact, radar structures which are observed throughout the history of billow development are indicated by the darker line. The light line represents the stream surface in the portion of the structure which breaks; usually this detail can only be resolved with ultrahigh resolution radar (see Figure 7). Note that in the overturned or 'braided' stage, the radar outlines mainly the boundaries of the rotor circulation. This is so because the overturning will accentuate the gradients at the boundaries where the air parcels have their maximum displacement, while weaker contrasts inside the rotor are destroyed by turbulence. In the final stage, the echoes are in the form of 'stretched

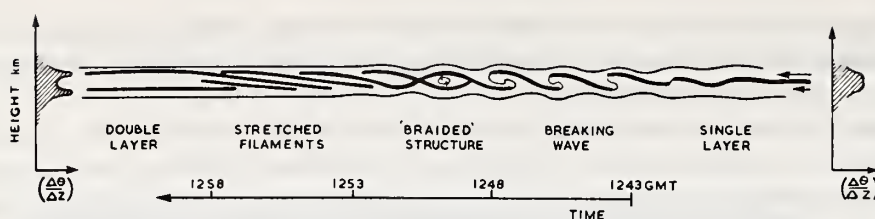


Fig. 2. Schematic representation of the life cycle of an individual K-H billow based on high-power radar observations. Time progresses from right to left. Thick lines correspond to the detectable clear-air radar echo, which started as a single layer at 1243 and finished as a double layer at 1258 GMT. Schematic vertical profiles of potential temperature gradient ($\Delta\theta/\Delta z$) are indicated before and after the occurrence of K-H instability. (From Browning and Watkins, 1970.)

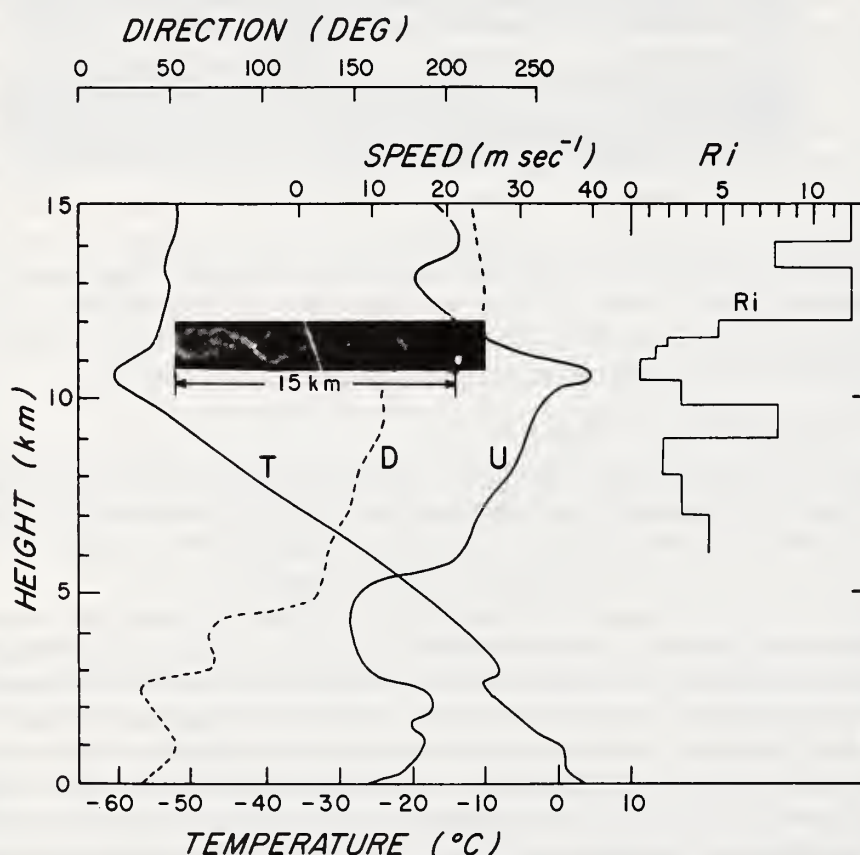


Fig. 3. Meteorological situation associated with 'braided' clear-air radar echoes obtained at Wallops Island, 1968 February 7, shown in the insert. The curve marked *T* is the temperature profile; *U*, the wind speed profile; *D*, the wind direction; and *Ri*, the Richardson number profile. Note that the clear air billows occur in a region of pronounced static stability and strong shear, with a low value of *Ri*.

filaments' and a layer forms both at the bottom and top boundaries of the original overturned layer. Modification of the profile of potential temperature gradient, $d\theta/dz$, by the overturning and turbulence is shown by the sketches to the right and left of the billow development. An initial single layer of large $d\theta/dz$ is modified to form two regions of large $d\theta/dz$ at the upper and lower boundaries of the overturned layer.

An outstanding example of clear-air billows observed by high-power radar and the associated meteorological sounding are shown in Figure 3. The pattern appeared near a height of 11 km above an extensive region of cloud and precipitation. It is seen that the structure occurs within a region of strong stability and marked wind shear. The gradient Richardson number Ri , which is the ratio of the negative buoyancy force to the inertial forces, is plotted to the right of Figure 3. It has its lowest value within the zone of the radar echoes. This feature is consistent with the requirements for the development of K-H instability. Other striking examples of clear-air billows observed by high-power radar are shown by Boucher (1970) and Browning (1971).

Browning (1971) obtained radiosonde measurements within one hour of the occurrence of large amplitude billows as observed with the 10.7-cm radar in Defford, England. He restricted his study to billows of large amplitude because these were easy to resolve with high-power radar and because only in these cases was it possible to obtain profiles of stability and shear with the necessary resolution for a meaningful

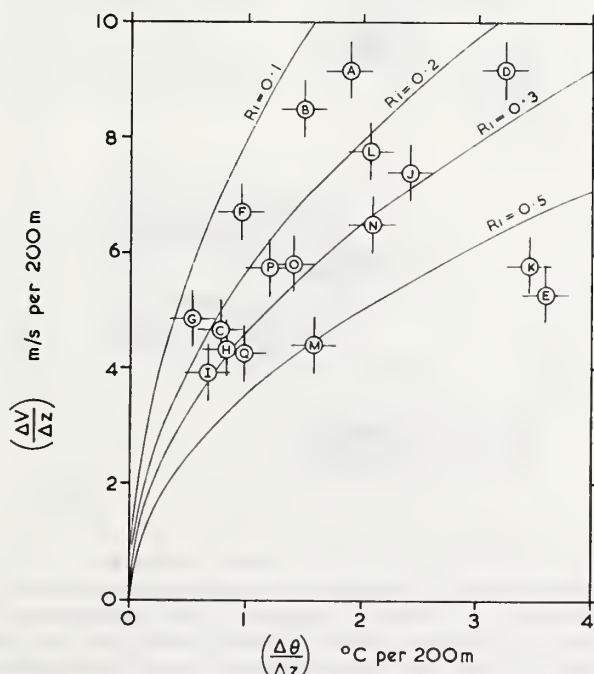


Fig. 4. The maximum value of the wind shear, $\Delta V/\Delta Z$, over layers 200 m deep within the height interval occupied by K-H billows, plotted against the corresponding value of the vertical gradient of potential temperature, $\Delta\theta/\Delta Z$, for 17 cases. Solid lines are isopleths of Ri over the corresponding layers. (From Browning, 1971.)

comparison with the radar data. Most of the billows had a crest-to-trough amplitude between 300 and 400 m and occurred at heights between 5.6 and 10.7 km. On the basis of linear theory, Ri should be less than or equal to 0.25 before K-H instability can be initiated (Miles and Howard, 1964). In the 17 cases investigated, Browning (1971) found that the minimum value of Ri when evaluated over layers 200 m deep was usually in the range 0.15–0.3. The results for the 17 cases are shown in Figure 4. Considering the difficulty of investigating this phenomenon, the agreement between experimental and theoretical results is remarkable.

Browning *et al.* (1970) describe some radar observations of clear-air billows at the tropopause in association with lee-wave development east of the South Wales mountains. Simultaneous measurements were obtained with a fully instrumented aircraft

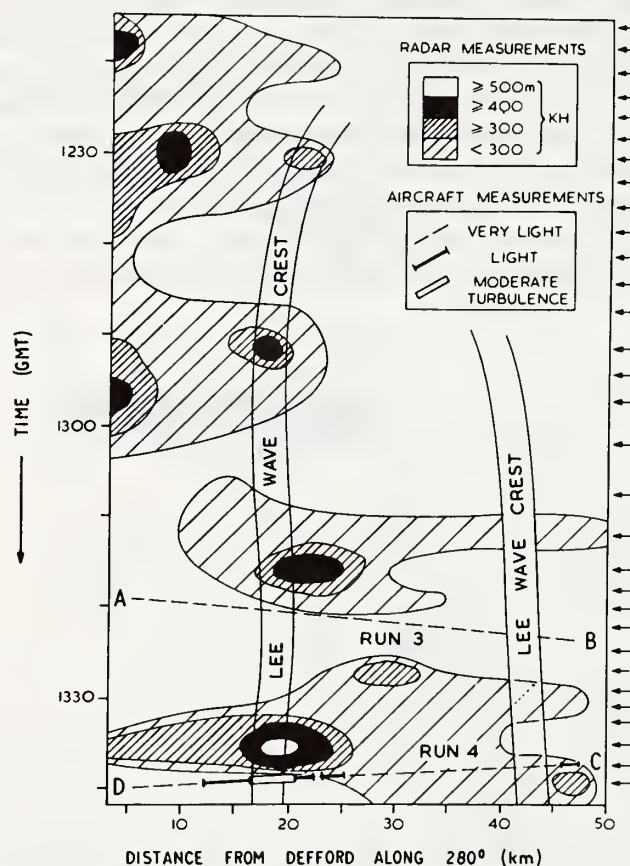


Fig. 5. Locations of detectable 10.7-cm wavelength radar echoes associated with K-H billows at the tropopause on 1970 February 3, near Defford, England with the radar pointing towards 280°. The crest-to-trough amplitude of the billows is indicated by shading (see key in figure). Also shown are the positions of crests in the lee wave pattern as observed by radar. Arrows on the right side of the diagram denote times of individual RHI scans. Aircraft turbulence reports along the path AB and CD are plotted according to the code indicated in the key. Time and space registration between the radar and aircraft data is thought to have been closer than 1 min and 3 km, respectively. (From Browning *et al.*, 1970.)

in a specific patch of K-H billows where the aircraft experienced moderate CAT. The aircraft and radar observations on that occasion are shown in the distance-time diagram in Figure 5 where distance is the range upwind from the radar. The shaded areas in this figure represent patches of billows detected by the radar at heights from 10.5 to 11 km. The two lines AB and CD represent two aircraft flight paths made at a height of 10.9 km. Although the aircraft appears to have missed the billows of largest amplitude, the maximum rms vertical acceleration of 0.65 g (corresponding to moderate, almost severe turbulence) occurred close to the patch of 500-m amplitude billows observed by radar. It is also noted that there is a tendency for the maximum billow amplitude to occur in the vicinity of the most pronounced lee-wave crest.

Mather and Hardy (1970) also have presented instrumented aircraft measurements in the vicinity of clear-air radar structures resembling K-H billows. Their preliminary analysis seemed to preclude an explanation in terms of K-H instability, but after a more detailed investigation, Hardy *et al.* (1973) conclude that all the information on this case leads to a picture of two-dimensional K-H billows. Figure 6 shows the aircraft data observed at the same time that the radar was detecting the wave-like struc-

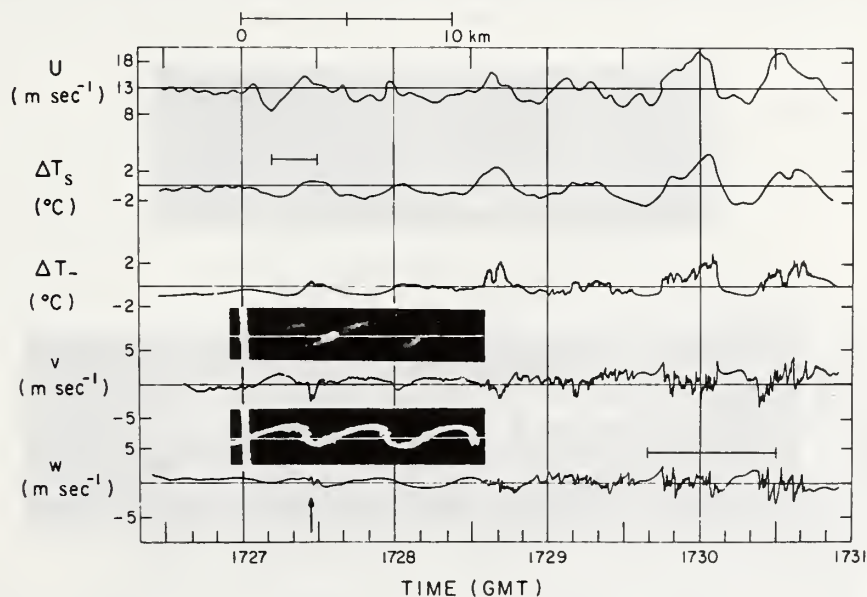


Fig. 6. Data obtained by a T-33 aircraft on 1970 February 19 at a height of 2600 m near Wallops Island, Virginia, along an azimuth of 073°. Time histories show longitudinal wind speed U , differential static temperature ΔT_s , differential total temperature ΔT_T , and lateral component v and vertical component w of turbulence measured in a layer giving clear-air radar echoes. The upper inset is a photograph of the 10.7-cm wavelength RHI scope and the lower inset is a retouched photo of the same data. The RHI photo was taken about 1727:15 GMT along an azimuth parallel to the aircraft track but the two sets of data were displaced by about 5 km. The radar pattern was enlarged to match the equivalent range sampled by the aircraft and the pattern was shifted slightly in the figure in order that the wave structure and aircraft data would be mutually consistent. The white horizontal line is the altitude of the flight path with respect to the waves. Note that the turbulence is associated mainly with the troughs of the waves. (From Hardy *et al.*, 1973.)

ture. A portion of the radar-observed 'wave' which occurred in the vicinity of the aircraft is shown as an inset in the figure. The line on the inset represents the flight path through the structure. The increasing turbulence along the path may occur because the aircraft was flying a little higher and in the more central portions of the structure as time increased.

The top trace in Figure 6 is the component of the wind parallel to the aircraft track (073°), averaged over 2.5 s. The second trace is the differential static temperature averaged in the same way. Trace 3 (ΔT_T) is the differential total temperature measured by a fast-response temperature probe with a frequency response flat to 10 Hz. It is shown here to illustrate the sharpness of the density gradient across the interface between the smooth and turbulent flows. The bottom two traces are the lateral (v) and vertical (w) components of turbulence measured in the layer. Since the displacement of the air is approximately an adiabatic process, temperatures will be lower than the mean when the aircraft is sampling air brought up from below and vice versa for air brought down. Consequently, the stream surface will be exactly out of phase with the temperature structure. Similarly, the U-component of wind is also out of phase with the stream surface, since the wind increased with height throughout the layer.

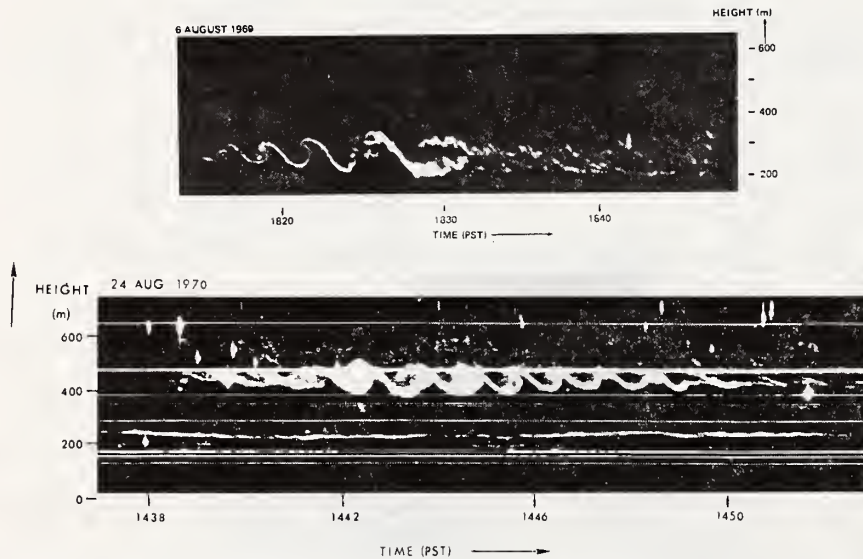


Fig. 7. Two trains of clear-air billows observed drifting through the beam of a vertically-pointing FM-CW radar. Presumably, evolution is negligible while one billow is advected over the radar, and the temporal picture of one individual billow very nearly gives its spatial structure. Both vortex sheets are probably manifestations of K-H shear instability. The top sequence seems to illustrate all phases of growth, breaking, mixing across the interface, and eventual stretching by shear. Note details in the third billow such as thin line in stream surface prior to breaking, and wrinkled upslope possibly evidencing secondary instabilities. Examination of fine structure in the thin layer at 200 m in the bottom sequence has revealed organized overturning, resembling K-H instability, also within this layer, at meter scales. We infer that the billow train above, at 400 m, is a higher generation of K-H instability, perturbing a thin, already unstable layer containing K-H instability at meter scales.

(From Gossard *et al.*, 1971.)

Figure 6 can be thought of as a slice through the layer at an instant in time, since the aircraft speed is large compared to the motion of the structure. Six cycles of the periodic structure have been measured. As the amplitude of the 'wave' grows, bursts of turbulence are observed in the troughs (1727:27 and 1728:40) until, at 1729:45, a 20-s outbreak of moderate turbulence is experienced in the large amplitude trough. As seen from the sharp changes in ΔT_T in the last two cycles, the turbulent mixing process appears to be intensifying the density gradient across the bottom interface between the smooth and turbulent layers. This could also enhance the radar echo from the structure.

The FM-CW radar often resolves clear-air billows in the planetary boundary layer in remarkable detail. In Figure 7, from Gossard *et al.* (1971), two samples of billow trains are shown drifting through the vertically-pointing radar beam. Gossard *et al.* (1970) present evidence that one individual billow moves past the radar with the mean wind at its altitude, ordinarily in such a short time that the temporal picture from the radar display very nearly gives the spatial structure of an individual billow. The top sequence in Figure 7 seems to illustrate, in successive billows, all phases of growth, breaking, mixing across the interface, and eventual stretching by shear. Note details in the third billow such as the thin line in the stream surface prior to breaking, and the

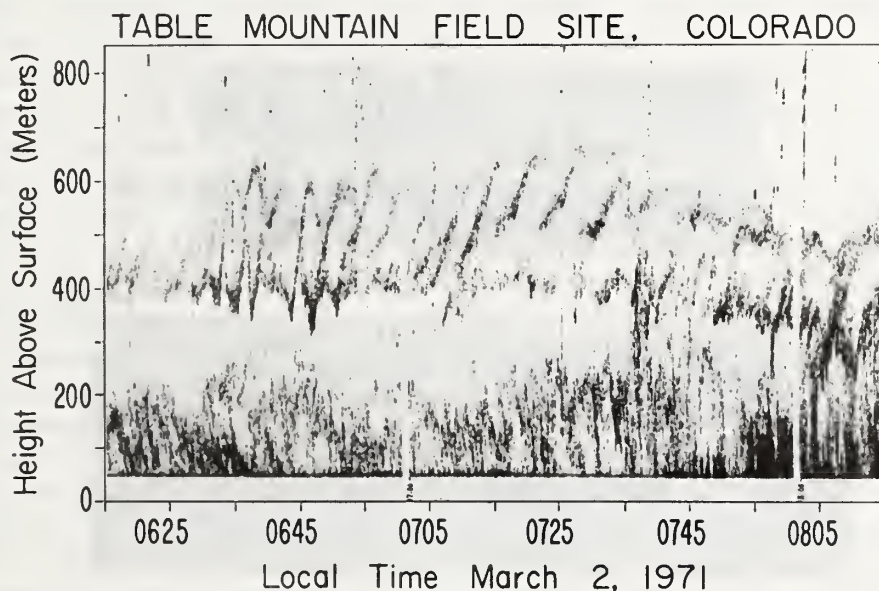


Fig. 8. This time-height record, evidencing dynamic instability in the statically stable boundary layer, was obtained with a vertically-pointing monostatic sodar, receiving backscatter from temperature irregularities. Evidently, the structures at 400 to 600 m resemble the clear-air billows in Figure 7, when the differences in time scale and, probably, advecting wind are considered. We infer that also this structure is a manifestation of K-H shear instability in clear air, although the sodar displays the temperature variability while the radar returns in Figure 7 originate from centimeter-scale water vapor fluctuations. Note enhanced returns in upslopes and weakly reflecting, diffuse breaking portions. (From Hall, 1971.)

wrinkled upslope which may be evidence of secondary instabilities (Scorer, 1969b; Ottersten, 1970a) and a probable reason for the enhancement of radar echo from the upslope. When the sub-structure of thin layers, such as the lower layer at 200 m in the bottom sequence of Figure 7, is examined in detail, it is revealed that these thin layers also contain organized structures resembling K-H billows at meter scales (Gossard *et al.*, 1971). From this we infer that the billow train at 400 m in the lower sequence of Figure 7 is a higher generation of K-H instability, perturbing a thin, already unstable layer containing K-H instability at meter scales.

Kelvin-Helmholtz instability structures are also often observed by vertically-pointing sodars probing statically stable shear flows in the planetary boundary layer (Mahoney, 1969; McAllister *et al.*, 1969; Emmanuel *et al.*, 1972). One example is shown in Figure 8, which is a time-height record obtained with a vertically-pointing monostatic sodar receiving backscatter from temperature irregularities (Hall, 1971). Considering the differences in time scale and advecting wind, the structures at 400 to 600 m in Figure 8 resemble the clear-air billows in Figure 7, and we infer that both types of structures are manifestations of K-H shear instability, although the sodar displays the temperature variability while the radar returns in Figure 7 originate from small-scale water vapor fluctuations. The enhanced returns in upslopes and the weakly reflecting, diffuse breaking portions on the sodar record in Figure 8 are also con-

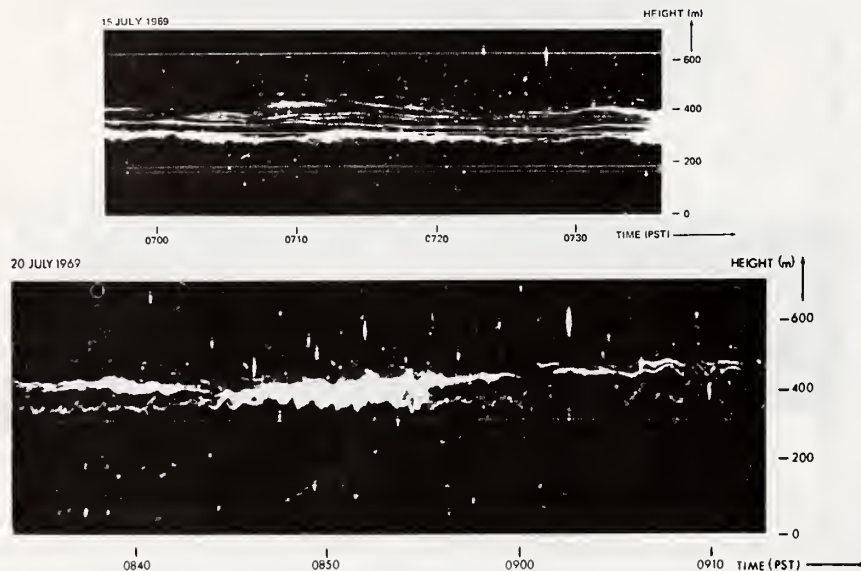


Fig. 9. FM-CW radar records of multiple layers in clear air. Thin lamina periodically spaced in the vertical (top) are layers of reduced Ri propagating with the nearly horizontal equi-phase surfaces of untrapped gravity waves. Dynamic instability occurs in these lamina since, in the presence of background shear, the untrapped wave can reduce Ri below the critical level in the vicinity of crests or troughs, depending on direction of background shear. Lower frame shows two intersecting layers which resemble upward and downward propagating waves. Enhanced instability and turbulence are indicated at their intersection. (From Gossard *et al.*, 1971.)

sistent with features of K-H billows observed by radar. Enhanced variability of both water vapor and temperature would result if secondary instabilities develop in the upslopes and deform and wrinkle an interface with gradients in both temperature and water vapor.

4.2. INTERNAL GRAVITY WAVES

As illustrated in the top frame of Figure 9, many of the FM-CW radar records show multiple layers more or less regularly spaced in the vertical so that it is natural to consider the possibility that untrapped gravity waves with nearly vertical propagation vectors produce the multiple layering. In an extension of an earlier analysis (Gossard *et al.*, 1971) Gossard *et al.* demonstrate in this issue, p. 113, that for an untrapped gravity wave propagating into a region of enhanced static stability (or a zone of different wind speed), the wave vector tilts toward the vertical and the vertical wavelength decreases so that the ratio of amplitude to wavelength increases. This reduces the Richardson number at some phase of the wave and, in the presence of background shear, critical values are reached in the vicinity of crests or troughs, depending on the direction of background shear. It is, therefore, concluded that dynamic instability in untrapped wave systems imbedded in a medium of strong static stability and some shear would generate a structure of regularly spaced, horizontally stratified, multiple layers, similar to the thin multiple layers seen by FM-CW radar within temperature inversions and exemplified in the top frame of Figure 9.

Untrapped waves may propagate upwards or downwards through the stable zones and on occasion, waves from above and below will meet and possibly interact in these zones. The lower frame in Figure 9, which is no isolated occurrence, shows a case of two intersecting layers which resemble upward and downward propagating waves. Enhanced instability and turbulence are indicated at their intersection.

The multiple lamina, which have been attributed to low-frequency, untrapped gravity waves, more often than not display sinusoidal undulations propagating horizontally. Gossard *et al.* (1970) have investigated these trapped higher frequency waves with concurrent wind and microbarograph data and conclude that they represent the fundamental mode of oscillation for a stable planetary boundary layer. These waves have periods in the order of 10 min, wavelengths of a few kilometers, and amplitudes of about 100 m. Their phase velocities, of order 10 m s^{-1} , always differ from the wind speed and are generally much larger, so that the wind plays a minor role, except that it causes some Doppler shift in the observed frequency. Gossard *et al.* (1970) speculate that waves with velocities comparable with the airstream velocity component in the direction of propagation are destroyed by shear instability. Periods greater than about 10 min will be most commonly observed since they ordinarily escape destruction, having higher phase velocities than the range of trapped waves with higher frequencies.

Nonlinear effects become important in trapped waves at a fluid interface when the wave amplitude cannot be considered small compared to the depth of the lower fluid, as may be the case in the atmosphere with a strong temperature inversion near the ground. Figure 10, from Gossard and Richter (1970), shows such a case with the

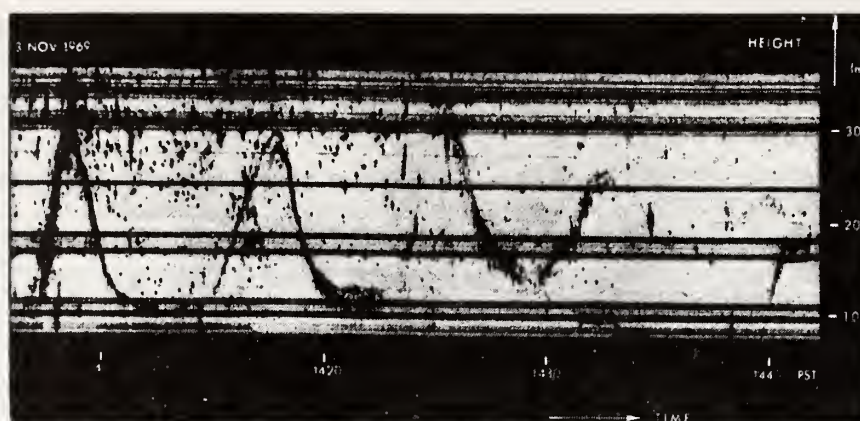


Fig. 10. FM-CW radar record of finite-amplitude internal gravity wave with crests sharper than troughs, indicating importance of nonlinear effects. This shape of internal waves at a fluid interface develops when the wave amplitude cannot be considered small compared to the depth of the lower fluid, as may be the case in the atmosphere with a strong temperature inversion near the ground. The characteristics of this wave have been adequately described in the Stokes form of third-order nonlinear theory applied to a two-layer model. (From Gossard and Richter, 1970.)

FM-CW radar record displaying a trapped gravity wave of finite amplitude with the crests sharpened and the troughs flattened due to nonlinear effects because of the proximity of the stable interface to the ground. The characteristics of this type of wave have been adequately described by the Stokes form of third-order nonlinear theory applied to a two-layer model (Gossard and Richter, 1970).

The wavetrain in Figure 10 also illustrates that the local Ri structure within trapped waves is not the dominant factor for the control of dynamic instability and enhancement of refractive-index variability and radar reflectivity. The fairly uniform radar return from all phases of the wave in Figure 10 and the general absence of crest and trough enhancement in other large-amplitude waves imply that the theoretically inferred, self-induced reduction in Ri at crests and troughs in trapped wave systems (Gossard *et al.*, 1971) is at most a secondary factor in producing the radar patterns of trapped gravity waves. It appears probable that the trapped waves generally are seen by the radar only because of the presence of the thin, dynamically unstable lamina of enhanced radar reflectivity which have been attributed to low frequency, untrapped gravity waves. In this issue, p. 113, however, Gossard *et al.* show some examples of large-scale waves with evidence of instability or breaking which may represent the effect of self-induced reduction in Ri within trapped waves.

Evidence of atmospheric gravity waves propagating in the planetary boundary layer is also common in sodar records. Hooke *et al.* (1972) note that these undulations are a major dynamical feature of the stable atmospheric boundary layer, which at nighttime may contain waves of a broad range of temporal and presumably spatial scales, from periods of a few minutes to oscillations of the entire boundary layer of several-hours period. The record in Figure 11, from Hall (1971), was obtained by a

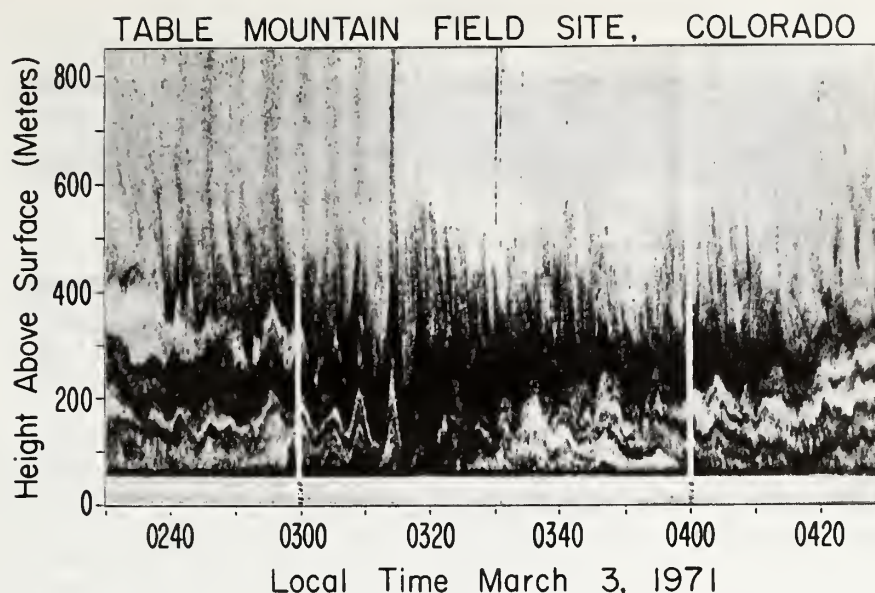


Fig. 11. Monostatic sodar record of large-amplitude atmospheric gravity waves propagating in the planetary boundary layer. Possibly, the strong wind shear caused dynamic instability at the top of the nocturnal radiation inversion, resulting in oscillations in the stable, cold air trapped below. Nonlinear effects, discussed in Figure 10, are apparent in some waves. For a detailed analysis of this record, see Hooke *et al.* (1972). (From Hall, 1971.)

monostatic sodar observing such gravity wave structures in the nocturnal inversion. Hall notes that the strong wind shear at the top of the inversion may have induced dynamic instability in the inversion layer, resulting in oscillations in the stable cold air below. Hooke *et al.* (1972) have studied the event in Figure 11 in detail together with concurrent data from a microbarograph array and have deduced the wave parameters for some of the oscillations. The large-amplitude oscillations between 0300 and 0330 local time display the same shape as the radar-observed waves in Figure 10, and it appears probable that nonlinear effects due to the proximity of the ground are in play. Fine examples of this type of nonlinear wave have also been observed by McAllister *et al.* (1969) in the nocturnal radiation inversion using a monostatic sodar. These waves are often seen as undulations in multiple lamina and we note that the radar return ordinarily is uniform from all phases of the wave, while enhancement at crests and troughs would be expected if dynamic instability due to self-induced reduction in Ri in the trapped wave were responsible for the generation of the back-scattering fine-scale temperature variability. The question arises whether the multiple lamina of enhanced temperature variability often observed in sodar records also are manifestations of untrapped gravity waves generating dynamic instability in nearly horizontal equiphase surfaces, as suggested by Gossard *et al.* (1971) to explain multiple lamina observed by FM-CW radar.

The FM-CW radar record in Figure 12, from Bean *et al.* (1971b), also displays non-

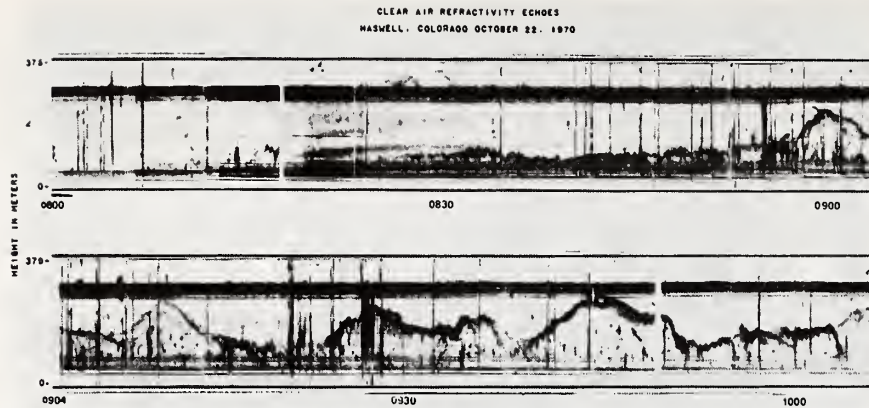


Fig. 12. FM-CW radar record displaying nonlinear third-order Stokes waves (0810) followed by returns from the radiation inversion, lifting during the morning hours. In addition to possible shear instability, the small-scale features in the inversion surface are the result of convective activity modulating and lifting the inversion during the growth of the well-mixed layer below. Note also large-amplitude heaving of the entire inversion surface in several instances. (From Bean *et al.*, 1971b).

linear third-order Stokes waves, which are followed by returns from the radiation inversion, lifting during the morning hours. This record was obtained with a mobile FM-CW radar in an experiment at Haswell in the high plains of eastern Colorado, where an instrumented 150-m tower provided the opportunity to verify with excellent temporal and spatial correspondence that the radar returns outlined the rising temperature inversion during the convective expansion of the well-mixed layer below. Particularly interesting in Figure 12 are several instances of large-amplitude heaving of the entire inversion surface. These events appear as singular disturbances propagating in the boundary layer and have little resemblance to trains of trapped gravity waves.

The association between lee waves and clear-air billows observed with the high powered 10.7-cm Defford radar was noted by Browning *et al.* (1970). In situations of strong lee-wave activity, clear-air layers are relatively abundant, although many layers appear almost featureless. Presumably, the coarse radar resolution fails to resolve small-scale billow trains in such layers. Radar detects the lee waves by observing the distortion of clear-air layers by lee-wave flow, offering a direct and elegant method of observing three-dimensional lee-wave patterns. Starr and Browning (1972) have exploited this for some unique lee-wave studies. The Defford radar is situated 60 km east of the lee slope of the South Wales mountains, a suitable location for observation of organized lee waves. An example of these waves is shown in Figure 13. The RHI photograph was taken while the radar scanned toward 270° , the upwind direction. Echoes below 4.5 km were mainly from clear air, those above 6 km were from cirrus; echoes in between had contributions from both sources. On this occasion, two families of lee waves existed. One family, with a wavelength of 8–10 km, had a maximum crest-to-trough amplitude of only about 200 m at a height of 4 km; this is

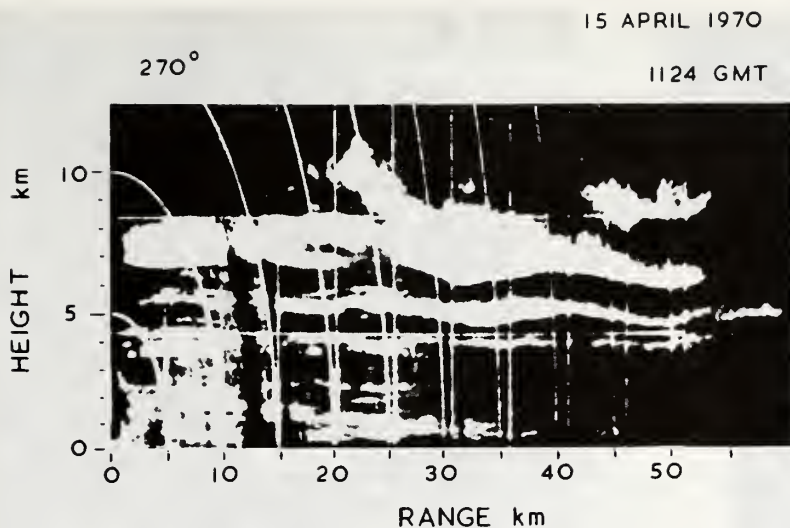


Fig. 13. Photograph of RHI along azimuth 270° deg (upwind direction) at 1124 GMT on 1970 April 15 taken with the 10.7-cm radar at Defford, England. Note the waves of rather large amplitude between 5- and 7-km height. Echoes above 6 km are from cirrus particles; those below 4.5 km are from the clear air. (From Starr and Browning, 1972.)

difficult to see in Figure 13. The other family of lee waves, with a wavelength of 19 km, attained a maximum amplitude of as much as 700 m at a height of 6–7 km. Both the short and long waves maintained fixed positions with respect to the ground in the lee of the Welsh mountains.

Reed and Hardy (1972) describe some long waves which, in contrast to the stationary lee waves observed by Starr and Browning (1972), were embedded within the mean flow. A portion of one of the waves is shown in Figure 14. It has a wavelength of about 30 km and a crest-to-trough amplitude of 1.8 km; other RHI photographs showed more than one full wavelength of the long wave. Large secondary billows (Scorer, 1969b) formed in the upslope of the long wave as shown in Figure 14. These billows developed where the wind (increasing with altitude) and the tilting by the wave together accentuated the vertical wind shear and induced dynamic instability. The billows have a wavelength of about 1.6 km and a crest-to-trough amplitude of about 200 m. Moderate to severe turbulence was encountered by a NASA T-33 aircraft as it probed the clear-air wave patterns observed by the radar.

With regard to the aircraft turbulence encountered within regions of clear-air radar echoes, various investigations have been conducted (Hicks *et al.*, 1967; Glover *et al.*, 1968, 1969; Hardy *et al.*, 1969; Crane, 1970; Browning *et al.*, 1970; Boucher and Glover, 1971). Glover and Duquette (1970) found that all altitude intervals corresponding to clear-air radar layers between 0.5 and 15 km, when probed with fighter jet aircraft, were turbulent. Only about 12% of the light or greater turbulence above 6 km was not detected by the radar.

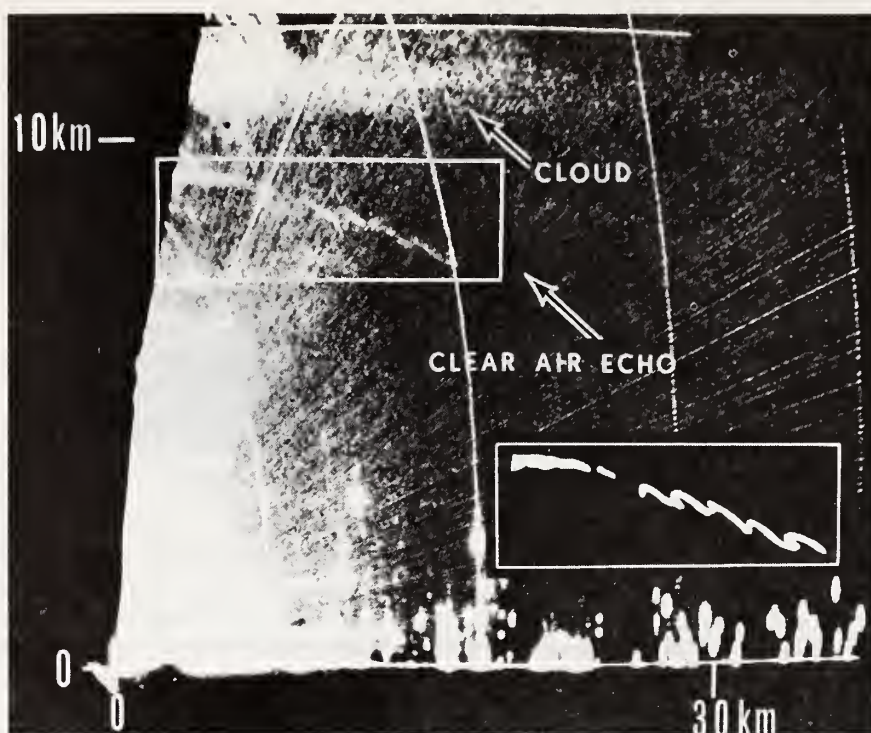


Fig. 14. Photograph of RHI at radar wavelength of 10.7 cm, 03 32 GMT, 1969 March 18, azimuth 270° , Wallops Island, Virginia. The wind and shear are directed toward the left in this photo. Note the portion of the long arch and the superposition of the billow structure. The vertical scale is expanded by a factor of about three and this accounts for the seemingly large slope of the long wave. The inset is a tracing from the original record. (From Reed and Hardy, 1972.)

4.3. WIND AND TEMPERATURE STRUCTURE IN THE OSCILLATING BOUNDARY LAYER

Characteristic for the development of radar and sodar probing and its successful application to atmospheric research have been concerted experimental investigations with remote probes and *in-situ* sensors for comparison and verification, and for acquisition of complementary data for delineation of the detailed structure of waves and turbulence in statically stable clear-air layers. In this issue Browning *et al.*, p. 91, and Readings *et al.*, p. 275, demonstrate how tethered balloons and high powered pulse Doppler radar may be employed for joint investigations of the turbulent mechanisms in temperature inversions in the planetary boundary layer. An arsenal of tools has been used for support of fixed beam, high resolution probing by radar and sodar, including free balloons (Richter and Gossard, 1970), tethered balloons (Beran and Clifford, 1972) instrumented towers (Bean, 1971, 1972; Emmanuel *et al.*, 1972) and aircraft (Metcalf and Atlas, this issue, p. 7). In addition, records of wave perturbations in surface wind and microbarograph pressure (Gossard *et al.*, 1970), or data from microbarograph arrays (Hooke *et al.*, 1972), have been employed for evaluation

of wave amplitude and the horizontal phase speed and direction of internal gravity waves observed in the lower stable regions by FM-CW radar and sodar.

The micrometeorological tower at Haswell, Colorado, has been used by Bean (1971), Emmanuel *et al.* (1972), and Emmanuel (next issue), for comparison of sodar or FM-CW-radar records with the detailed structure of wind and temperature as obtained at fixed tower levels and by an instrumented carriage which travels the height of the 150 m-tower. At the start of the monostatic sodar record in Figure 15, from Bean (1971), the 16°C isotherm parallels the top of the strong returns from the noc-

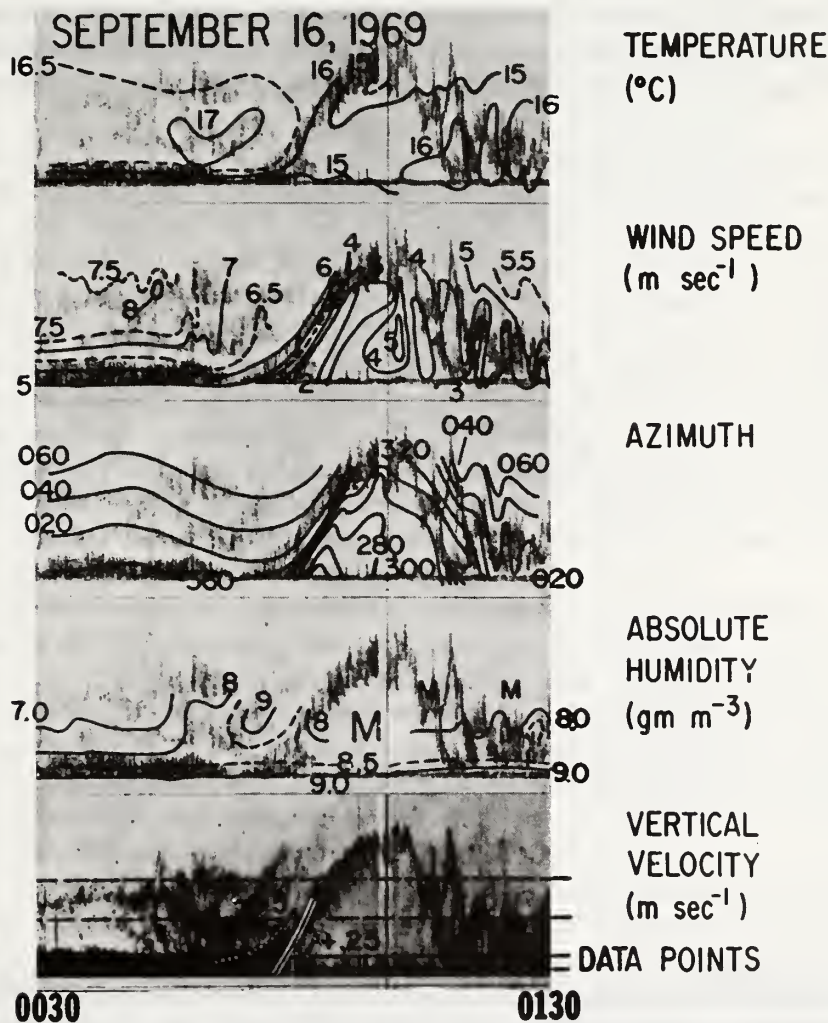


Fig. 15. Comparison of monostatic sodar returns to meteorological fields determined at an adjacent, 150 m high, instrumented tower during an event of large-amplitude heaving of the nocturnal radiation inversion. The 150-m level is the top level marked in the lower frame of the 1-h record. Note how the 16°C isotherm follows the inversion surface as the wind slows down and nearly isothermal air slides in from the side during the heaving. (From Bean, 1971.)

turnal surface inversion. During an event of large-amplitude heaving, the diagram illustrates how the entire surface inversion rises above the tower level with the 16°C isotherm following, and a nearly isothermal, and echo-free, region developing below. Simultaneously, the wind slows down and the dramatic change in wind direction reveals that the lifting of the surface inversion is connected with an event of cold air sliding in from the side.

In Figure 16, from Bean *et al.* (1971b), FM-CW radar returns from a temperature inversion are compared with the profiles of temperature and horizontal wind speed (top) and with the profiles of refractive index and refractive-index variability (bottom), determined in the six minutes required for the carriage to travel through the interesting zone. The top diagram shows a very strong temperature inversion coinciding with the strongest radar return, and a small temperature kink below corresponds to a

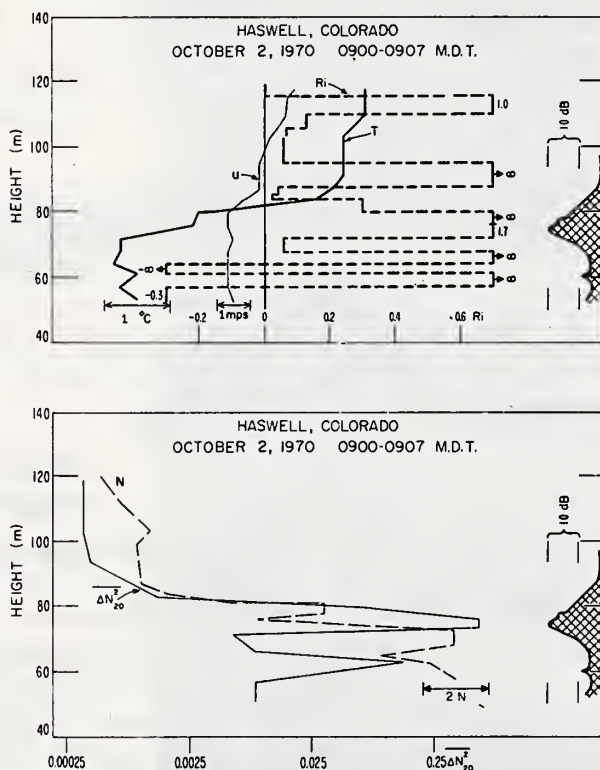


Fig. 16. Comparison of FM-CW radar returns from a temperature inversion with the profiles of temperature and horizontal wind speed (top) and with the profiles of refractive index in N -units and refractive-index variability (bottom). Meteorological profiles were obtained by an instrumented carriage travelling the height of a 150-m tower adjacent to the radar. Two microwave refractometer cavities separated by 20 cm in the vertical were used to determine $\overline{\Delta N^2_{20}}$, the refractive-index variability over 20-cm scales. Site elevation is 1300 m and this dry morning temperature variability dominates the refractive-index fluctuations and the radar return, while the contrary ordinarily is true. Note double peak in radar return and detailed correspondence in profiles. (From Bean *et al.*, 1971b.)

secondary echo maximum. Some wind shear is evident at the strong inversion but the Ri-profile appears erratic. A microwave refractometer with two cavities was used to obtain the profiles in the lower diagram and, for the primary radar return in particular, the correspondence with the strong decrease in mean refractive index and with the maximum in refractive-index variability is evident. The data in Figure 16 were obtained during a dry morning and, since the site elevation is 1300 m, the temperature variability dominates the refractive-index fluctuations and the radar returns for this particular case, while ordinarily the contributions from water vapor variability will be most important in the boundary layer. Moreover, Bean *et al.* (1971b) have compared the radar reflectivities measured by the FM-CW radar and evaluated by the refractive-index variability, assuming an inertial subrange for small-scale fluctuations. The data were obtained in a thin inversion layer and the two reflectivities showed excellent agreement over a range from 10^{-15} to 10^{-13} m^{-1} .

Richter and Gossard (1970) have presented a large amount of simultaneous FM-CW radar and radiosonde soundings which also demonstrate excellent agreement between echo layers and refractive-index gradients, generally caused by sharp decreases in water vapor contents. Evidence of enhanced static stability and some wind shear is also generally present. Moreover, support for the hypothesis that untrapped gravity waves are responsible for the generation of multiple lamina has been obtained from analysis of oscillations observed in the wind profiles (Gossard *et al.*, 1970). In this issue, Browning *et al.*, p. 91., and Readings *et al.*, p. 275, use Doppler radar data and fine-scale measurements of wind, temperature, and refractive-index to demonstrate that convective circulations in the boundary layer perturb the shallow inversion above, thereby producing local enhancement of wind shear at the crests of hummocks where evidence of small-scale K-H billows is obtained and absence of an inertial subrange is indicated.

Doppler sodar data have also proved to be useful for delineation of flow configurations in the stable boundary layer, as demonstrated by Mahoney *et al.* p. 155, and Beran *et al.* p. 133, in this issue. One example, from Beran *et al.* (1971a), is shown in Figure 17 which displays the Doppler-derived vertical velocity field in an oscillating nocturnal inversion. The data were obtained by a vertically-pointing monostatic sodar. An interpretation in terms of a breaking wave is indicated in the derived streamline pattern at the bottom of Figure 17. Possibly, the structure is the result of the development of one single K-H vortex roll.

Beran and Clifford (1972) have established that measurement of the horizontal wind with Doppler sodar techniques is perfectly feasible. In an earlier experiment, Beran and Willmarth (1971) had demonstrated that a component of the horizontal wind could be measured with Doppler sodar both in monostatic and bistatic configurations. The winds in Figure 18, from Beran *et al.* (this issue, p. 133), were obtained using three separate monostatic Doppler sodars which allowed the total wind vector to be determined. Figure 18 shows a time section of isotachs for the total horizontal wind, superimposed on the sodar facsimile record obtained during an oscillating nocturnal inversion.

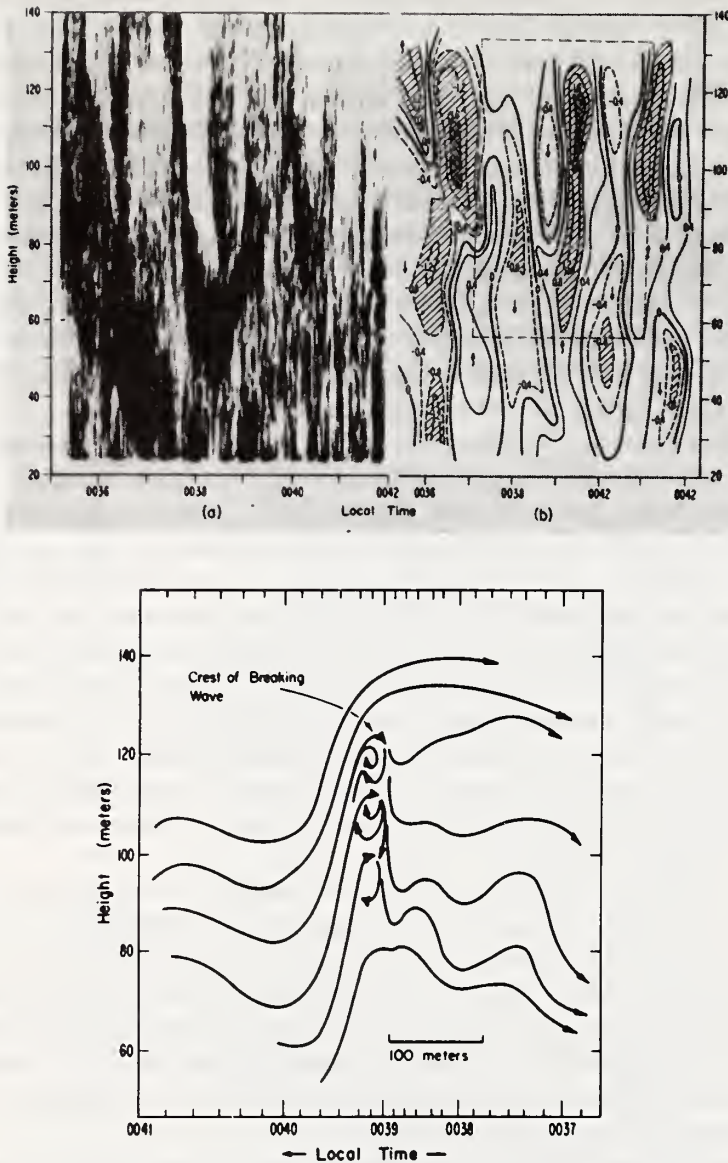


Fig. 17. Monostatic sodar echoes and Doppler-derived vertical velocity field (top) under a nocturnal inversion exhibiting oscillations and local overturning. Contour interval is 0.4 m s^{-1} ; velocities $< 0.8 \text{ m s}^{-1}$, single hatching; $< 1.6 \text{ m s}^{-1}$, double hatching; upward vertical velocities, solid lines; downward vertical velocities, dashed lines. Derived streamline pattern for area boxed to the right is shown at the bottom. (From Beran *et al.*, 1971.)

TABLE MOUNTAIN COLORADO

19 August 1971

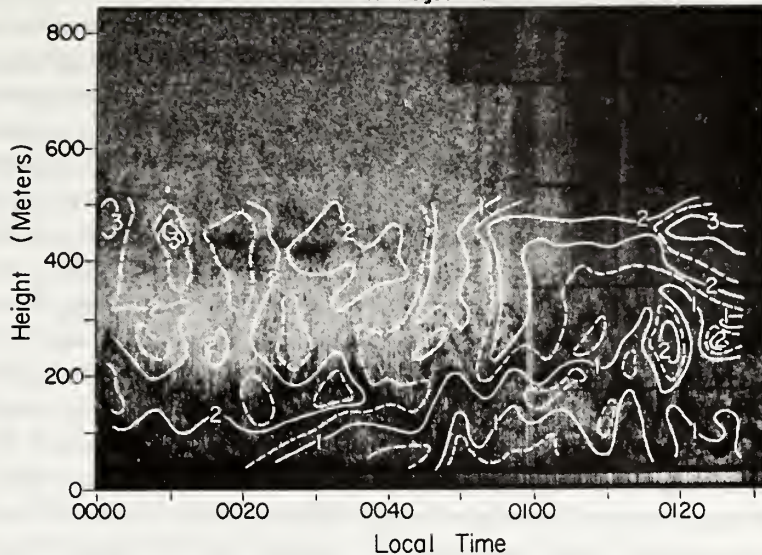


Fig. 18. Time section of isotachs for total horizontal wind (ms^{-1}) superimposed on monostatic sodar echoes from an oscillating inversion. Winds were derived solely from Doppler sodar measurements using three separate monostatic systems. From the respective Doppler frequency shifts at a given level, radial velocities in three different directions were obtained, from which the total wind vector may be synthesized. All altitudes were monitored simultaneously in a fixed beam configuration. With a common volume only at one altitude, radial wind components were obtained from horizontally separated volumes and time averaging over one minute was used to reduce the effects of horizontal inhomogeneity. (From Beran *et al.*, this issue, p. 133)

5. Conclusions

In the statically stable atmosphere, overturning and turbulence result when the destabilizing force of vertical vector wind shear overcomes the balancing influence of static stability. Static stability is mainly determined by the vertical gradient of potential temperature which tends to suppress vertical motions for potential temperatures increasing with height. Pronounced vertical wind shears develop across quasi-horizontal strata of enhanced static stability which are present in stably stratified air from the planetary boundary layer throughout the troposphere and in the stratosphere. Temperature inversions when probed in detail often reveal a substructure of thin stratified lamina, characterized by enhanced static stability and some vertical shear. At the tropopause, because temperature inversions are often particularly deep, vertically extensive zones of pronounced shears develop. The water vapor distribution is also affected by the structuring of the clear atmosphere by wind and temperature fields. Differences in water vapor between adjacent air masses concentrate across inversion zones and may exhibit drastic contrasts in the lower atmosphere, e.g., as in the marine layer.

Local dynamics of the stable strata are controlled by larger-scale irregularities in the motion field. Accentuation of vertical wind shear and reduction in Richardson number to sub-critical values result when the mean fields of wind and temperature in statically stable shear zones are deformed in gravity waves and internal fronts (Dutton, 1971; Dutton and Panofsky, 1970). Evidence has been presented that untrapped gravity waves in the lower atmosphere may restructure shear and stability in stable zones to the point where dynamic instability occurs (Gossard *et al.*, 1971). Untrapped waves with nearly vertical propagation vectors in very stable zones may be the very generating mechanism for multiple layering within stable strata. Multiple layers of regular vertical spacing have been observed in the marine layer with ultrahigh resolution radar, presumably because dynamic instability is induced by the untrapped wave train in several thin lamina which are detected by radar due to wrinkling and breakup of interfaces with sharp gradients in water vapor and temperature. Trapped internal gravity waves which propagate in the stable boundary layer are seen as undulations on the thin lamina, but self-induced reduction in Ri at crests and troughs in trapped wave systems is generally not the cause of dynamic instability and enhanced radar reflectivity in thin lamina. The trapped waves are seen by radar because of the presence of the thin, unstable lamina, attributed to low-frequency untrapped waves. In this issue, however, Gossard *et al.*, p. 113, present some evidence also of dynamic instability due to self-induced reduction in Ri in trapped waves.

It has been revealed that when the surplus shear (supplied by a wave for example) upsets the balance in a shear layer, the instability generally takes the form of regularly spaced two-dimensional rolls of lateral extension. The configuration exhibits the same structural characteristics as billow clouds. Thus, the overturning very much resembles the dynamic instability of the K-H type which occurs within a hydrostatically stable flow with both an inflection point in the velocity profile and a sufficiently strong vertical shear.

Much evidence has been gathered which indicates that these clear-air billows are indeed manifestations of K-H instability. Moreover, their common occurrence in shear layers of widely different vertical extension seems to imply that K-H instability is the dominant mechanism responsible for the destruction of the shears which are concentrated across strongly stable zones by external processes. Similarly, this instability of the flow and the resulting intermittent generation of more random turbulence on a range of smaller scales lead to vertical transfer of other properties, heat, humidity, etc., because the mixing strives to eliminate vertical gradients. As a result, gradients across the stable layer prior to the event disappear in the mixing zone and are accentuated at upper and lower boundaries.

Also, the vertical wind shear will be consumed and the turbulence will decay when this energy source is drained. Simultaneously, we must recognize the importance of the external condition which originally supplied the surplus shear and triggered the instability. We may expect that in highly dynamical situations, the accentuation of shear is sufficiently violent, not only to maintain the shear against erosion by turbulence, but actually to supply momentum at a rate which exceeds the distributing capability of the

original K-H instability and its trail of lesser vortices. Indications from radar observations are that in such situations the turbulence escalates, not by expanding the original instability, but rather through initiation of a new instability in the flow, also in the form of laterally extended rolls resembling K-H instability, but now of larger size in order that momentum distribution at the faster rate can be accomplished. Sequential radar studies of shear zones in a clear atmosphere (Ottersten, 1970a) have revealed that turbulence evolves by consecutive instability at successively larger scales, and ultrahigh resolution radar data (Gossard *et al.*, 1971) support this conclusion. After initial shear-instability at small scales, the flow breaks down into larger vortices with subsequent escalation of the turbulence scale.

Consecutive shear-instability at successively larger scales implies a close spatial and temporal connection between large-scale overturning and the generation of cm-scale refractive-index variability responsible for radar and sodar echoes. The initial K-H instability over thin layers, sometimes no deeper than a few meters, together with associated smaller vortices of more random orientation will cause wrinkling of the stable stratum with deformation and break-up of gradients. As a result, a fine-scale refractive-index structure with variability in various directions will be superimposed on the vertical gradient of the strongly anisotropic mean field. This fine structure will scatter microwaves and acoustic waves in all directions. Since monostatic radar and sodar returns evidence no marked aspect-sensitivity, it appears that the backscattering dominates over the partial reflection from the mean gradient. (We may expect, however, that with increasing interrogating wavelength, or with decreasing scatter angle for bistatic probing, partial reflections from vertical gradients in the stratified mean field become more substantial.) If the turbulence escalates due to rapid shear accentuation, the fine-scale refractive-index structure from the initial breakdown will outline the flow configuration when higher generations of roll-instabilities develop. As a result, the larger vortices are revealed on radar and sodar images and it appears that the refractive-index variability is enhanced along the rotor boundaries. Presumably, the deeper overturning accentuates the gradients because of deformation and vertical displacement of stream surfaces. Also, there is some evidence that smaller, secondary instabilities develop locally along the upslopes of vortex rolls and enhance small-scale contrasts by wrinkling of the interface with sharp gradients in water vapor and/or temperature.

In the statically stable planetary boundary layer, high-resolution remote probes have cast some light on the detailed breakdown mechanisms of dynamic instability as well as on the external processes which are responsible for the deformation of the wind and temperature fields, resulting in reduction of the Richardson number to sub-critical values. Some of the observations in the boundary layer have not yet received satisfactory explanations, but it appears that the phenomena which have been identified and much of the analysis which they have received also are relevant to the processes in play in baroclinic zones in the free atmosphere, in internal fronts and in mountain waves and lee waves. High-powered pulse radars with large, steerable antennas have provided some unique information on waves and turbulence in stratified shear layers

in the free atmosphere. For continued exploration of these phenomena and for further clarification of the interaction between internal waves, the atmospheric background fields of wind and temperature, and dynamic instability and turbulence, ultrahigh-resolution remote probes with long-range capability would be of particular value. The FM-CW radar can be developed into such an instrument (Richter *et al.*, this issue, p. 179), which will be of outstanding value once it can be tied to a steerable antenna of good angular resolution. With further development of sodar techniques, acoustic echo sounding of higher altitudes may also prove feasible. Concerted experimental investigations with remote probes and *in-situ* sensors are necessary for further advances in the exploration of waves and turbulence in statically stable clear-air layers.

Acknowledgements

The authors are grateful for the careful and helpful review of the manuscript by Dr Keith A. Browning. We gratefully acknowledge permission from the respective authors and cited journals to reproduce Figures 1–18.

References

- Atlas, D.: 1964, 'Advances in Radar Meteorology', *Adv. Geophys.* **10**, 317–478.
- Atlas, D. and Hardy, K. R.: 1966, 'Radar Analysis of the Clear Atmosphere: Angels', *Proc. XV Gen. Assembly of URSI*, Munich, Germany, pp. 401–469.
- Atlas, D., Metcalf, J. I., Richter, J. H., and Gossard, E. E.: 1970, 'The Birth of "CAT" and Micro-scale Turbulence', *J. Atmospheric Sci.* **27**, 903–913.
- Batchelor, G. K.: 1955, 'The Scattering of Radio Waves in the Atmosphere by Turbulent Fluctuations in Refractive Index', Research Report EE 262, School of Elect. Eng., Cornell University, Ithaca, N.Y.
- Bean, B. R.: 1971, 'Comparisons of Remote and In-Situ Measurements of Meteorological Parameters and Processes', in A. G. Kjelaas (ed.) *Stat. Meth. and Instr. in Geophysics*, Teknologisk Forlag, Oslo, pp. 181–196.
- Bean, B. R.: 1972, 'Application of FM-CW Radar and Acoustic Echo-Sounder Techniques to Boundary Layer and CAT Studies', *Course in Remote Sensing of the Troposphere*, University of Colorado, Ch. 20, 28 pp.
- Bean, B. R., Dougherty, H. T., and McGavin, R. E.: 1971a, 'Remote Probes for the Study of Atmospheric Sources of Fading on Optical and Microwave Line-of-Sight Paths', *Proc. 1971 Int. Symp. Ant. and Prop.*, Japan, pp. 237–238.
- Bean, B. R., McGavin, R. E., Chadwick, R. B., and Warner, B. D.: 1971b, 'Preliminary Results of Utilizing the High Resolution FM Radar as a Boundary-Layer Probe', *Boundary-Layer Meteorol.* **1**, 466–473.
- Beran, D. W.: 1970, *Proj. EAR (Environ. Acoustic Res.)* **1**, University of Melbourne, Meteorol. Dept. Pub. No. 15.
- Beran, D. W.: 1971, 'Acoustics: A New Approach for Monitoring the Environment Near Airports', *AIAA J. Aircraft* **8**, 934–936.
- Beran, D. W. and Clifford, S. F.: 1972, 'Acoustic Doppler Measurements of the Total Wind Vector', in *Proc. 2nd Symp. Meteorol. Observ. and Instr.*, Amer. Meteorol. Soc., Boston, Mass. pp. 100–109.
- Beran, D. W. and Willmarth, B. C.: 1971, 'Doppler Winds from a Bistatic Acoustic Sounder', in *Proc. 7th Int. Symp. Remote Sensing of Environment*, University of Michigan, pp. 1699–1714.
- Beran, D. W., Reynolds, R. M., and Gething, J. T.: 1970, *Proj. EAR (Environ. Acoustic Res.)* **5–7**, University of Melbourne, Meteorol. Dept. Pub. No. 17.
- Beran, D. W., Little, C. G., and Willmarth, B. C.: 1971a, 'Acoustic Doppler Measurements of Vertical Velocities in the Atmosphere', *Nature* **230**, 160–162.

- Beran, D. W., McAllister, L. G., and Mahoney, A. R.: 1971b, 'Extension of Acoustic Sounding Experiments to the Upper Atmosphere', WRE Tech. Note A208 (AP), Dept. of Supply, Weapons Res. Est., Salisbury, South Australia.
- Beran, D. W., Hall, F. F., Wescott, J. W., and Neff, W. D.: 1971c, 'Application of an Acoustic Echo Sounder to Air Pollution Monitoring', *Air Pollution Turb. and Diffus. Symp.*, Dec. 7-10, New Mexico State University, Las Cruces, New Mexico.
- Boucher, R. J.: 1970, 'CAT at a Subsidence Inversion: A Case Study', *J. Appl. Meteorol.* **9**, 534-537.
- Boucher, R. J. and Glover, K. M.: 1971, 'Radar, Aircraft, and Meteorological Observations of Shear Induced Clear Air Turbulence', in *Proc. Int. Conf. Atmos. Turb.*, London, England, B9, 10 pp.
- Browning, K. A.: 1971, 'Structure of the Atmosphere in the Vicinity of Large-Amplitude Kelvin-Helmholtz Billows', *Quart. J. Roy. Meteorol. Soc.* **97**, 283-299.
- Browning, K. A.: 1972, 'Atmospheric Research Using the Defford Radar Facility', *Weather* **27**, 2-13.
- Browning, K. A. and Watkins, C. D.: 1970, 'Observations of Clear Air Turbulence by High Power Radar', *Nature* **227**, 260-263.
- Browning, K. A., Watkins, C. D., Starr, J. R., and McPherson, A.: 1970, 'Simultaneous Measurements of Clear Air Turbulence at the Tropopause by High-Power Radar and Instrumented Aircraft', *Nature* **228**, 1065-1067.
- Chadwick, R. B. and Little, C. G.: 1972, 'The Comparison of Sensitivities of Atmospheric Echo Sounders' (in publication).
- Crane, R. K.: 1970, 'Measurement of Clear Air Turbulence in the Lower Stratosphere Using the Millstone Hill L-Band Radar', Preprints 14th Radar Meteorol. Conf. Amer. Meteorol. Soc., Boston, Mass., pp. 101-106.
- Derr, V. E. and Little, C. G.: 1970, 'A Comparison of Remote Sensing of the Clear Atmosphere by Optical, Radio, and Acoustic Radar Techniques', *Appl. Opt.* **9**, 1976-1992.
- Dutton, J. A.: 1971, 'Clear-Air Turbulence, Aviation, and Atmospheric Science', *Rev. Geophys. Space Phys.* **9**, 613-657.
- Dutton, J. A. and Panofsky, H. A.: 1970, 'Clear Air Turbulence: a Mystery May be Unfolding', *Science* **167**, 937-944.
- Emmanuel, C. B., Bean, B. R., McAllister, L. G., and Pollard, J. R.: 1972, 'Observations of Helmholtz Waves in the Lower Atmosphere with an Acoustic Sounder', *J. Atmospheric Sci.* **29**, 886-892.
- Georges, T. M. and Clifford, S. F.: 1972, 'Acoustic Sounding in a Refractive Medium', submitted to *J. Acoust. Soc. Amer.*
- Gething, J. T. and Jenssen, D.: 1971, 'Measurements of Temperature and Humidity by Acoustic Echo Sounding', *Nature* **231**, 198-200.
- Gjessing, D. T.: 1969, 'Atmospheric Structure Deduced from Forward-Scatter Wave Propagation Experiments', *Radio Sci.* **4**, 1195-1210.
- Glover, K. M. and Duquette, E. F.: 1970, 'A Study of Clear Air Turbulence Using Sensitive Radars', Preprints 14th Radar Meteorol. Conf., Amer. Meteorol. Soc., Boston, Mass., pp. 89-94.
- Glover, K. M., Boucher, R. J., Ottersten, H., and Hardy, K. R.: 1968, 'Radar, Aircraft, and Meteorological Investigation of Clear Air Turbulence', in *Proc. 13th Radar Meteorol. Conf.*, Amer. Meteorol. Soc., Boston, Mass., pp. 242-247.
- Glover, K. M., Boucher, R. J., Ottersten, H., and Hardy, K. R.: 1969, 'Simultaneous Radar, Aircraft, and Meteorological Investigations of Clear Air Turbulence', *J. Appl. Meteorol.* **8**, 634-640.
- Gossard, E. E. and Richter, J. H.: 1970, 'The Shape of Internal Waves of Finite Amplitude from High-Resolution Radar Sounding of the Lower Atmosphere', *J. Atmospheric Sci.* **27**, 971-973.
- Gossard, E. E. and Richter, J. H.: 1972, 'FM-CW Radar Studies of Production of Turbulent Instability within Thermally Stable Layers by Internal Waves', in *Effects of Atmos. Gravity Waves on Electromag. Wave Prop.*, AGARD Conf. Proc. **115**, Wiesbaden, Germany, Ref. No. 20, 14 pp.
- Gossard, E. E., Richter, J. H., and Atlas, D.: 1970, 'Internal Waves in the Atmosphere from High-Resolution Radar Measurements', *J. Geophys. Res.* **75**, 3523-3536.
- Gossard, E. E., Jensen, D. R., and Richter, J. H.: 1971, 'An Analytical Study of Tropospheric Structure as Seen by High-Resolution Radar', *J. Atmospheric Sci.* **28**, 794-807.
- Hall, F. F.: 1971, 'Acoustic Remote Sensing of Temperature and Velocity Structure in the Atmosphere', in A. G. Kjelaas (ed.), *Stat. Meth. and Instru. in Geophys.* Teknologisk Forlag, Oslo, pp. 167-180.
- Hall, F. F.: 1972, 'Temperature and Wind Structure Studies by Acoustic Echo-Sounding', in *Course in Remote Sensing of the Troposphere*, University of Colorado, Ch. 18, 26 pp.

- Hall, F. F., Wescott, J. W., and Simmons, W. R.: 1971, 'Acoustic Echo Sounding of Atmospheric Thermal and Wind Structure', in *Proc. 7th Int. Symp. Remote Sensing of Environ.*, University of Michigan, pp. 1715-1732.
- Hardy, K. R.: 1972, 'Studies of the Clear Atmosphere Using High Power Radar', *Course in Remote Sensing of the Troposphere*, University of Colorado, Ch. 14, 34 pp.
- Hardy, K. R. and Katz, I.: 1969, 'Probing the Clear Atmosphere with High Power, High-Resolution Radar', *Proc. IEEE* **57**, 468-480.
- Hardy, K. R., Atlas, D., and Glover, K. M.: 1966, 'Multiwavelength Backscatter from the Clear Atmosphere', *J. Geophys. Res.* **71**, 1537-1552.
- Hardy, K. R., Glover, K. M., and Ottersten, H.: 1969, 'Radar Investigations of Atmospheric Structure and CAT in the 3 to 20-km Region', in Y.-H. Pao and A. Goldburg (eds.), *Clear Air Turbulence and Its Detection*, Plenum Press, New York, pp. 402-416.
- Hardy, K. R., Reed, R. J., and Mather, G. K.: 1973, 'Radar, Instrumented Aircraft, and Meteorological Measurements of Developing Kelvin-Helmholtz Billows', submitted to *Quart. J. Roy. Meteorol. Soc.*
- Harrold, T. W. and Browning, K. A.: 1971, 'Identification of Preferred Areas of Shower Development by Means of High Power Radar', *Quart. J. Roy. Meteorol. Soc.* **97**, 330-339.
- Hicks, J. J.: 1969, 'Radar Observations of a Gravitational Wave in Clear Air Near the Tropopause Associated with CAT', *J. Appl. Meteorol.* **8**, 627-633.
- Hicks, J. J. and Angell, J. K.: 1968, 'Radar Observations of Breaking Gravitational Waves in the Visually Clear Atmosphere', *J. Appl. Meteorol.* **7**, 114-121.
- Hicks, J. J., Katz, I., Landry, C. R., and Hardy, K. R.: 1967, 'Clear Air Turbulence: Simultaneous Observations by Radar and Aircraft', *Science* **157**, 808-809.
- Hooke, W. H., Young, J. M., and Beran, D. W.: 1972, 'Atmospheric Waves Observed in the Planetary Boundary Layer Using an Acoustic Sounder and a Microbarograph Array', *Boundary-Layer Meteorol.* **2**, 371-380.
- Kallistratova, M. A.: 1961, 'Experimental Investigation of Sound Wave Scattering in the Atmosphere', *Trudy Inst. Fiz. Atmos. Turbulentnost* **4**, 203-256.
- Katz, I.: 1966, 'Probing the Clear Atmosphere with Radar', APL Tech. Digest, Applied Physics Laboratory, Johns Hopkins University, Sept-Oct., 2-8.
- Katz, I.: 1969, 'Probing the Optically Clear Atmosphere with Radar', in Y.-H. Pao and A. Goldburg (eds.), *Clear Air Turbulence and Its Detection*, Plenum Press, New York, pp. 417-424.
- Katz, I.: 1972, 'The Detection and Study of Gravity Waves with Microwave Radar', in *Effects of Atmos. Gravity Waves on Electromag. Wave Prop.*, AGARD Conf. Proc. **115**, Wiesbaden, Germany, Ref. No. 21, 9 pp.
- Konrad, T. G.: 1970, 'The Dynamics of the Convective Process in Clear Air as Seen by Radar', *J. Atmospheric Sci.* **27**, 1138-1147.
- Kropfli, R. A.: 1971, 'Simultaneous Radar and Instrumented Aircraft Observations in a Clear Air Turbulent Layer', *J. Appl. Meteorol.* **10**, 796-802.
- Kropfli, R. A., Katz, I., Konrad, T. G., and Dobson, E. B.: 1968, 'Simultaneous Radar Reflectivity Measurements and Refractive-Index Spectra in the Clear Atmosphere', *Radio Sci.* **3**, 991-994.
- LaGrone, A. H. and Deam, A. P.: 1971, 'Study of the Relationship Between Radar Returns from Clear Air and the Mechanical Energy Regime in the Atmosphere', in *Proc. 1971 Int. Symp. Antennas and Prop.*, Japan, pp. 235-236.
- Lane, J. A.: 1967, *Structure of the Lower Atmosphere and Electromagnetic Wave Prop.*, NATO Advanced Study Institute, directed by J. A. Lane, 2-15 Sept. 1967, Aberystwyth, Wales.
- Lane, J. A.: 1969, 'Radar Echoes from Clear Air in Relation to Refractive-Index Variations in the Troposphere', *Proc. IEE* **116**, 1656-1660.
- Lhermitte, R. M.: 1968, 'Atmospheric Probing by Doppler Radar', in *Proc. NAS-CAS Panel on Remote Atmos. Probing*, Chicago, Illinois, pp. 253-285.
- Little, C. G.: 1969, 'Acoustic Methods for the Remote Probing of the Lower Atmosphere', *Proc. IEEE* **57**, 571-578.
- Little, C. G.: 1972, 'Prospects for Acoustic Echo-Sounding', *Course in Remote Sensing of the Troposphere*, University of Colorado, Ch. 19, 10 pp.
- Little, C. G., Derr, V. E., Kleen, R. H., Lawrence, R. S., Lhermitte, R. M., Owens, J. C., and Thayer, G. D.: 1970, 'Remote Sensing of Wind Profiles in the Boundary Layer', ESSA Tech. Rept. ERL 168-WPL 12, Boulder, Colorado 123 pp.

- Ludlam, F. H.: 1967, 'Characteristics of Billow Clouds and Their Relation to Clear Air Turbulence,' *Quart. J. Roy. Meteorol. Soc.* **93**, 419-435.
- Mahoney, A. R.: 1969, 'A Review of Acoustic Sounding Experiments', WRE Tech. Note CPD (T) 180, July.
- Mather, G. K. and Hardy, K. R.: 1970, 'Instrumented Aircraft Measurements in the Vicinity of Clear Air Radar Structures', Preprints 14th Radar Meteorol. Conf., Amer. Meteorol. Soc., Boston, Mass., pp. 49-52.
- McAllister, L. G.: 1968, 'Acoustic Sounding of the Lower Troposphere', *J. Atmospheric Terrest. Phys.* **30**, 1439-1440.
- McAllister, L. G.: 1971, 'Wind Velocity Measurements in the Lower Atmosphere Using Acoustic Sounding Techniques', WRE Tech. Note - A 204 (AP), Dept. of Supply, Weapons Res. Est., Salisbury, South Australia, 10 pp.
- McAllister, L. G. and Pollard, J. R.: 1969, 'Acoustic Sounding of the Lower Atmosphere' in *Proc. 6th Int. Symp. Remote Sensing of Environ.*, University of Michigan, pp. 436-450.
- McAllister, L. G., Pollard, J. R., Mahoney, A. R., and Shaw, P. J.: 1969, 'Acoustic Sounding - A New Approach to the Study of Atmospheric Structure', *Proc. IEEE* **57**, 579-587.
- Megaw, E. C. S.: 1957, 'Fundamental Radio Scatter Propagation Theory', *Proc. IEE*, London, **104C**, 441.
- Meyer, J. H.: 1971, 'Radar Observations of Land Breeze Fronts', *J. Appl. Meteorol.* **10**, 1224-1232.
- Miles, J. W. and Howard, L. N.: 1964, 'Note on a Heterogeneous Shear Flow', *J. Fluid Mech.* **20**, 331-336.
- Monin, A. S.: 1961, 'Characteristics of the Scattering of Sound in a Turbulent Atmosphere', *Akust. Zh.* **7**, 457-461, (*Soviet Phys. - Acoustics* **7**, (1962), 370-373).
- Ottersten, H.: 1964, 'A Theoretical Treatment of Microwave Backscattering from Tropospheric Turbulence', Swedish Res. Inst. Nat. Def. Rept. A 623, Stockholm, 16 pp.
- Ottersten, H.: 1969a, 'Atmospheric Structure and Radar Backscattering in Clear Air', *Radio Sci.* **4**, 1179-1193.
- Ottersten, H.: 1969b, 'Radar Backscattering from the Turbulent Clear Atmosphere', *Radio Sci.* **4**, 1251-1255.
- Ottersten, H.: 1969c, 'Mean Vertical Gradient of Potential Refractive Index in Turbulent Mixing and Radar Detection of CAT', *Radio Sci.* **4**, 1247-1249.
- Ottersten, H.: 1970a, 'Radar Observations of the Turbulent Structure in Shear Zones in the Clear Atmosphere', Preprints 14th Radar Meteorol. Conf., Amer. Meteorol. Soc., Boston, Mass., pp. 111-116.
- Ottersten, H.: 1970b, 'Radar Angels and Their Relationship to Meteorological Factors', *Swedish Res. Inst. Nat. Def., FOA Repts.* **4**, No. 2, Stockholm, 33 pp.
- Ottersten, H.: 1972, 'Radar Monitoring of Turbulence at the Tropopause Level', NOAA Tech. Rept. ERL-WPL, Boulder, Colorado, 69 pp.
- Parry, H. D. and Sanders, M. J.: 1972, 'The Design and Operation of an Acoustic Radar', *IEEE Trans. GE* **10**, 58-64.
- Preprints 14th Conf. Radar Meteorol.: 1970, Amer. Meteorol. Soc., Boston, Mass., 465 pp.
- Proc. 12th Conf. Radar Meteorol.: 1966, Amer. Meteorol. Soc., Boston, Mass., 510 pp.
- Proc. 13th Conf. Radar Meteorol.: 1968, Amer. Meteorol. Soc., Boston, Mass., 565 pp.
- Reed, R. J. and Hardy, K. R.: 1972, 'A Case Study of Persistent, Intense Clear Air Turbulence in an Upper Level Frontal Zone', *J. Appl. Meteorol.* **11**, 541-549.
- Richter, J. H.: 1969, 'High-Resolution Tropospheric Radar Sounding', *Radio Sci.* **4**, 1261-1268.
- Richter, J. H. and Gossard, E. E.: 1970, 'Lower Tropospheric Structure as Seen by a High-Resolution Radar', Naval Elect. Lab. Center, Rept. TR 1718, San Diego, 66 pp.
- Saxton, J. A., Lane, J. A., Meadows, R. W., and Mathews, P. A.: 1964, 'Layer Structure of the Troposphere - Simultaneous Radar and Microwave Refractometer Investigations', *Proc. IEE* **3**, 275-283.
- Scoggins, J. R.: 1970, 'Relationship Between Meteorological Parameters, CAT, and Variations in the Index of Refraction Measured by Airplane and Radar', *Antennas and Prop. Div.*, Rept. P-45, University of Texas, 51 pp.
- Scorer, R. S.: 1969a, 'Mechanisms of Clear Air Turbulence', in Y.-H. Pao and A. Goldburg (eds.), *Clear Air Turbulence and Its Detection*, Plenum Press, New York, pp. 34-50.
- Scorer, R. S.: 1969b, 'Billow Mechanics', *Radio Sci.* **4**, 1299-1307.

- Simmons, W. R., Wescott, J. W., and Hall, F. F.: 1971, 'Acoustic Echo Sounding as Related to Air Pollution in Urban Environments', NOAA Tech. Rept. ERL 216-WPL 17, Boulder, Colorado, 77 pp.
- Smith, P. L. and Rogers, R. R.: 1963, 'On the Possibility of Radar Detection of Clear-Air Turbulence', in *Proc. 10th Weather Radar Conf.*, Amer. Meteorol. Soc., Boston, Mass., pp. 316-322.
- Starr, J. R. and Browning, K. A.: 1972, 'Observations of Lee Waves by High-Power Radar', *Quart. J. Roy. Meteorol. Soc.* 98, 73-85.
- Tatarski, V. I.: 1961, *Wave Propagation in a Turbulent Medium*, McGraw-Hill Book Co., Inc., New York, N.Y., 285 pp.
- Watkins, C. D.: 1971, 'High-Power Radar for Meteorological Studies in Clear Air', *Proc. IEE* 118, 519-528.
- Wescott, J. W., Simmons, W. R., and Little, C. G.: 1970, 'Acoustic Echo-Sounding Measurements of Temperature and Wind Fluctuations', ESSA Tech. Memo. ERLTM-WPL 5, Boulder, Colorado, 24 pp.
- Wheelon, A. D.: 1959, 'Radio-Wave Scattering by Tropospheric Irregularities', *J. Res. NBS* 63, D205.
- Woodman, R. F. and Guillen, A.: 1972, 'Observations of the Mesosphere and Stratosphere with the Jicamarca Radar' (in process).
- Yaglom, A. M. and Tatarski, V. I. (eds.): 1967, *Atmospheric Turbulence and Radio Wave Propagation*, *Proc. Int. Colloq., Moscow, June, 15-22, 1965*, Nauka, Moscow, 376 pp.

FM/CW RADAR STUDIES OF PRODUCTION OF TURBULENT INSTABILITY
WITHIN THERMALLY STABLE LAYERS BY INTERNAL WAVES

Earl E. Gossard
 Wave Propagation Laboratory
 NOAA Environmental Research Laboratories
 Boulder, Colorado, U.S.A. 80302

J. H. Richter
 Naval Electronics Laboratory Center
 San Diego, California, U.S.A. 92152

ABSTRACT

A recent development in radar sounding has made the detailed structure of the troposphere visible to a degree previously not approachable. The radar sounder is an FM/CW system designed and built by Dr. J. H. RICHTER (1969).

The most outstanding features evident in the records are internal gravity waves, features resembling Kelvin/Helmholtz instability structures, multiple layering often displaying lamina only a few meters thick, and convection cells within the marine layer (GOSSARD, RICHTER and ATLAS, 1970; GOSSARD, JENSEN and RICHTER, 1971).

Considerable doubt has existed as to just what the radar is "seeing." It is evident from the records that the returns come from regions of large refractive index gradient, but whether the return is backscatter from a thin region of intense, small scale turbulence (either "fossil" or mechanical) or whether it may include coherent partial reflection from gradient layers of refractive index remains a question.

This paper shows a variety of atmospheric structural patterns and compares them with several hypothetical models of internal wave structures to obtain more insight into the atmospheric processes at work. Special attention is given to the distribution of Richardson's Number in trapped and untrapped gravity waves. It is concluded that the multiple layers result from untrapped internal gravity waves, whose propagation vector is directed nearly vertically within very stable height regions. The layers are concluded to be caused by Kelvin/Helmholtz instability resulting from reduction in Richardson's Number due to growth of the amplitude-to-wavelength ratio as the waves propagate into thermally stable height regions of the atmosphere.

1. INTRODUCTION

Radar pictures of the structure of the clear atmosphere reveal many patterns suggestive of some kind of dynamic instability. They provide fundamental new information about the manner in which turbulence in the atmosphere is created and the role played by thermal stratification in fluid dynamics.

Correct interpretation of the radar patterns in terms of atmospheric motion and structure is necessary in order to make radar sounding an effective tool in weather forecasting. The proper interpretation of many patterns seen, and even the precise mechanism for reflection (or scattering) of the radar waves, remains in doubt. It is the purpose of this paper to extend an earlier analysis (GOSSARD, JENSEN and RICHTER, 1971) (hereafter referred to as GJR), to include effects of finite amplitude and compressibility in the medium. In the earlier analysis GJR proposed that the mechanism for generating and maintaining thin regions of intense, small scale turbulence within thermally stable layers was the propagating upwards or downwards of untrapped gravity waves. They analyzed the distribution of Richardson's Number through internal waves in terms of wave structures seen by a special high resolution radar sounder (RICHTER, 1969).

Only the case of infinitesimally small amplitude perturbations was considered by GJR in the analysis. Furthermore, it was pointed out that the perturbation wave equations are linear in the variables $\rho(z)^{1/2}\eta$, $\rho(z)^{1/2}(u, v, w)$ and $\rho(z)^{-1/2}p$ but they ignored the dependence of density, ρ , on height, z , when computing the distribution of Richardson's Number within the wave. In their notation u, v, w are the x, y, z components of perturbed velocity, η is amplitude of parcel displacement and p is pressure perturbation. As they stated, the neglect of the height dependence of $\rho(z)$ is permissible when the inverse scale height, $\chi = -\rho^{-1}d\rho/dz = g/c^2$, is negligible compared with the inverse vertical scale, or skin depth, of the wave system. In other words, their analysis was applicable to the usual wave systems seen by the radar which are confined to relatively thin height ranges in the troposphere in the neighborhood of temperature inversions.

It is the purpose of the present paper to extend the earlier analysis to the case of finite amplitude and to examine (1) the shape of the isotherms (and refractive index isopleths); (2) examine the

effect of neglecting the height dependence of $\rho(z)$ when taking the height derivatives required in the calculation of wave Richardson's Number.

Specifically, the shape of the isotherms corresponding to Frame III of Figure 3 in the GJR paper is computed in order to consider the question of whether the radar is "seeing" isopleths of perturbed refractive index within a height gradient or some passive trace constituent carried with the displaced parcel (e.g., fossil turbulence). Furthermore, the Richardson's Number within the stable layer is recalculated for a hypothetical case in which the atmospheric scale height is not large compared with the vertical scale of the wave system.

2. FINITE AMPLITUDE WAVES

One classical approach to finite amplitude theory is the method of successive approximations in which a nonlinear wave equation is made linear by substitution of a lower order solution in the nonlinear terms and solved. Equations corresponding to successively higher order solutions result. The sum of the solutions describes finite amplitude effects as long as $k\eta$ is small, where k is horizontal component of wave number and η is parcel displacement. The lowest order of differential equation is linear with the usual small amplitude solution. This solution is introduced into the nonlinear, next higher order equation, etc. The method is well described and illustrated by THORPE (1968, page 579). For an incompressible fluid, the method is fairly convenient. The most practical form of the wave equation is the vorticity equation in the stream function χ and density, ρ . The form of finite amplitude solution which results from this approach will be derived here assuming an incompressible fluid and a first order wave perturbation of the form $\chi_1 = A_{\chi_1} \cos(kx + nz - \sigma t)$, $\rho_1 = \rho_0 \cos(kx + nz - \sigma t)$ for unbounded waves. The velocity perturbations, $u, w = \partial\chi/\partial x, -\partial\chi/\partial z$. The solution desired is for the displacement, δ , of the surfaces of equal density in a stably stratified fluid. For infinitesimally small amplitude, the solutions for both χ and η are sinusoidal in both x and z .

The vorticity equation is (see, for example, THORPE, 1968):

$$\frac{\partial}{\partial t} \nabla^2 \chi + u \frac{\partial}{\partial x} \nabla^2 \chi + w \frac{\partial}{\partial z} \nabla^2 \chi = \frac{g}{\rho_0(z)} \frac{\partial \rho}{\partial x} \quad (1)$$

and the equation of continuity for an incompressible fluid is:

$$\frac{d\rho}{dt} = \frac{\partial \rho}{\partial t} + u \frac{\partial \rho}{\partial x} + w \frac{\partial \rho}{\partial z} = 0 \quad (2)$$

Taking $\chi = \alpha \chi_1 + \alpha^2 \chi_2 + \alpha^3 \chi_3 \dots$

and $\rho = \rho_0 + \alpha \rho_1 + \alpha^2 \rho_2 + \alpha^3 \rho_3 \dots$

where the power of α is the indicator of order of perturbation, the successively higher order solutions for χ and ρ are:

$$\chi_1 = A_{\chi_1} \cos(kx + nz - \sigma t)$$

$$\chi_2 = A_{\chi_1} \cos 2(kx + nz - \sigma t)$$

$$\chi_3 = A_{\chi_3} \cos(kx + nz - \sigma t) + B_{\chi_3} \cos 3(kx + nz - \sigma t)$$

$$\rho_1 = A_{\rho_1} \frac{k}{\sigma} \frac{d\rho_0}{dz} \cos(kx + nz - \sigma t)$$

$$\rho_2 = \frac{1}{4} A_{\rho_1}^2 \left(\frac{k}{\sigma}\right)^2 \frac{d^2 \rho_0}{dz^2} \cos 2(kx + nz - \sigma t)$$

$$- A_{\rho_2} \frac{d\rho_0}{dz} \left(\frac{k}{\sigma}\right) \cos 2(kx + nz + \text{const})$$

so

$$\chi = \chi_1 + \chi_2 + \chi_3 \dots \quad (3)$$

where

$$A_{x2} = \frac{1}{4} A_{x1}^2 \frac{\frac{d^2 \rho_0}{dz^2} \left(\frac{k}{\sigma} \right)}{4\sigma^2 \left(\frac{1}{k^2} + 1 \right) - N^2}$$

$$A_{x3} = \frac{1}{8} A_{x1}^3 \frac{\frac{d^3 \rho_0}{dz^3} - \frac{\frac{d^4 \rho_0}{dz^4}}{4 \left(\frac{\sigma}{R} \right)^2 (n^2 + k^2) - N^2}}{\sigma^2 (n^2 + k^2) - k^2 N^2}$$

$$B_{x3} = \frac{1}{8} A_{x1}^3 \frac{\frac{d^3 \rho_0}{dz^3} - \frac{\frac{d^4 \rho_0}{dz^4}}{4 \left(\frac{\sigma}{k} \right)^2 (n^2 + k^2) - N^2}}{9\sigma^3 (n^2 + k^2) - k^2 N^2}$$

It is evident that all the higher order perturbation terms in χ are multiplied by higher order derivatives of the unperturbed density profile. Therefore, if $\rho_0(z)$ is linear with height, or perhaps exponential with a large scale depth, χ (and therefore the velocity field) is little affected by nonlinearity in the equations of motion.

Our main concern lies with the displacement of the density surfaces, because the same reasoning applies to the displacement of potential temperature and of refractive index surfaces. Expanding the density in a Taylor's series the displacement, δ , of a surface of constant density is determined by

$$\rho(z_0 + \delta) = \text{const} = \rho_0(z_0) + \delta \frac{\partial \rho}{\partial z} + \frac{1}{2} \delta^2 \frac{\partial^2 \rho}{\partial z^2} \dots \quad (4)$$

where

$$\rho(z_0) = \rho_0(z_0) + \alpha \rho_1(z_0) + \alpha^2 \rho_2(z_0) + \alpha^3 \rho_3(z_0) \dots$$

$$\delta = \alpha \delta_1 + \alpha^2 \delta_2 + \alpha^3 \delta_3 \dots$$

Since the first term in the expansion of $\rho(z_0)$ cancels $\rho_0 z_0$:

$$\begin{aligned} & \alpha \rho_1 + \alpha^2 \rho_2 + \alpha^3 \rho_3 \dots \\ &= -(\alpha \delta_1 + \alpha^2 \delta_2 + \alpha^3 \delta_3 \dots) \frac{\delta(\rho_0 + \alpha \rho_1 + \alpha^2 \rho_2 + \alpha^3 \rho_3 \dots)}{\partial z} \dots \end{aligned}$$

so

$$\begin{aligned} \delta_1 &= \delta_0 \cos(kx + nz - \sigma t) \\ \delta_2 &= \delta_0^2 n \cos(kx + nz - \sigma t) \sin(kx + nz - \sigma t) \\ \delta_3 &= \delta_0^3 n^2 [\cos(kx + nz - \sigma t) - \frac{3}{2} \cos 3(kx + nz - \sigma t)] \end{aligned} \quad (5)$$

and

$$\begin{aligned} \frac{\delta}{\delta_0} &= \frac{\delta_1 + \delta_2 + \delta_3}{\delta_0} = \left(1 - \frac{1}{8} (n \delta_0)^2 \right) \cos(kx + nz - \sigma t) \\ &\quad - \frac{1}{2} n \delta_0 \sin 2(kx + nz - \sigma t) - \frac{3}{8} (n \delta_0)^3 \cos 3(kx + nz - \sigma t) \dots \end{aligned}$$

plus terms which are products of $d^2\rho_0/dz^2$ or higher order. If $\rho_0(z)$ is exponential, note that $dk\rho_0/dz^k = (N^2/g)^k$

where

$$n = k \sqrt{\left(\frac{N}{g}\right)^2 - 1} \quad \text{and} \quad \frac{N^2}{g} = -\frac{1}{\rho_0} \frac{d\rho_0}{dz}$$

for an incompressible fluid (see ECKART, 1960). The above approach to the problem of nonlinear effects is laborious and the physics is obscured by the mechanical complexity, so we consider an equivalent but conceptually different approach.

Suppose we consider only equations (4) and (2). Equation (2) yields the perturbation equation of continuity as:

$$\frac{\partial \rho}{\partial t} = -w \frac{d\rho_0}{dz}$$

where ρ and w are the perturbed values of density and vertical velocity and $\rho_0(z)$ is the unperturbed density distribution. Noting that $w = d\eta/dt$, where η is the parcel displacement, and integrating, we have

$$\rho - \rho_0 = -\eta \frac{d\rho_0}{dz}$$

so that

$$\frac{d\rho}{dz} = \frac{d\rho_0}{dz} - \frac{\partial \eta}{\partial z} \frac{d\rho_0}{dz} = \frac{d\rho_0}{dz} \left(1 - \frac{\partial \eta}{\partial z}\right) \quad (6)$$

and

$$\frac{d^2\rho}{dz^2} = \frac{d\rho_0}{dz} \left(\frac{\partial^2 \eta}{\partial z^2}\right) \quad (7)$$

if $d^2\rho_0/dz^2$ is negligible. Also the fluctuations in density at z_0 for small wave perturbations are described by

$$\rho(z_0) - \rho_0(z_0) = \eta \frac{d\rho_0}{dz} = \frac{d\rho_0}{dz} \eta_0 \cos(kx + nz - \sigma t)$$

so that (4) gives

$$\eta_0 \cos(kx + nz - \sigma t) = -\delta \left(1 - \frac{\partial \eta}{\partial z}\right) + \frac{\delta^2}{2} \left(\frac{\partial^2 \eta}{\partial z^2}\right) + \dots \quad (8)$$

Dividing by $1/2(\partial^2 \eta / \partial z^2)$ gives an expression quadratic to this order; i.e.,

$$\delta^2 - \delta \left(\frac{1 - \frac{\partial \eta}{\partial z}}{\frac{\partial^2 \eta}{\partial z^2}}\right) - \frac{2\eta}{\frac{\partial^2 \eta}{\partial z^2}} \dots = 0 \quad (9)$$

Expanding, using successive approximations, and assuming $\eta = \eta_0 \cos(kx + nz - \sigma t)$, we find

$$\begin{aligned} \frac{\delta}{\eta_0} &= \left(1 - \frac{1}{8} n^2 \eta_0^2\right) \cos(kx + nz - \sigma t) - \frac{1}{2} n \eta_0 \sin 2(kx + nz - \sigma t) \\ &\quad - \frac{3}{8} (n \eta_0)^2 \cos 3(kx + nz - \sigma t) \dots \end{aligned} \quad (10)$$

This is the same as equation (5) to 3rd order, where terms in $d^2\rho_0/dz$ have again been ignored, if it is recognized that the 1st order isotherm displacement, δ_1 , is the same as particle displacement, η .

Two important conclusions can apparently be stated:

A. To this order, the shape of the isopycnals in an incompressible fluid are not apparently affected by nonlinearity in the equations of motion, but only by nonlinearity resulting from higher order terms in the Taylor expansion. Thus, other nonlinear effects will be quite negligible compared with the

effect on shape. The reason nonlinearity in the equations of motion is not very important can be seen when written in the form of the vorticity equation (1). The important nonlinearity is in the inertial terms, the second and third terms from the left. However, they cancel since

$$u \frac{\partial}{\partial x} (\nabla^2 \chi) + w \frac{\partial}{\partial z} (\nabla^2 \chi) = \frac{\partial \chi}{\partial z} \frac{\partial}{\partial x} (\nabla^2 \chi) - \frac{\partial \chi}{\partial x} \frac{\partial}{\partial z} (\nabla^2 \chi) = 0$$

Thus, the stream function $\chi = \chi_1 + \chi_2 + \chi_3 \dots = \chi_1$ to third order, and departures from this form depend on second and higher derivatives of $\rho_0(z)$ of z , i.e., velocity perturbations remain essentially sinusoidal.

B. If (A) is true for an incompressible fluid, it implies that the linear form of the solution for the compressible case (for which no comparable vorticity equation can be written) can be used in the Taylor expansion to achieve a valid description of the potential temperature isotherms in a compressible fluid.

The linear form of solution for displacement in a compressible fluid is

$$\eta \rho_0(z)^{1/2} = \eta_1 \rho_0(z_0)^{1/2} \cos(kx + nz - \sigma t) \quad (11)$$

for atmospheric layers in which the coefficients of the differential equations are constant; i.e., $(g/\theta)(d\theta/dz) = N^2 = \text{constant}$, $c = \text{constant}$ and $(2\rho_0)^{-1} d\rho_0/dz + g/c^2 = \Gamma = \text{constant}$. The density and displacement amplitudes are ρ_0 , η_0 , respectively, at a reference level. θ is potential temperature.

Rewriting (4) for isotherm displacement

$$\theta_0(z_0) = \theta(z_0) + \delta \frac{\partial \theta}{\partial z} + \frac{1}{2} \delta^2 \frac{\partial^2 \theta}{\partial z^2} \dots$$

where to 1st order

$$\theta_0(z_0) - \theta(z_0) = \eta \frac{d\theta_0}{dz}$$

and

$$\frac{\partial \theta}{\partial z} = \frac{d\theta_0}{dz} \left(1 - \frac{\partial \eta}{\partial z} \right), \quad \frac{\partial^2 \theta}{\partial z^2} = - \frac{d\theta_0}{dz} \frac{\partial^2 \eta}{\partial z^2} \quad (12)$$

Thus, for the compressible fluid case, an equation identical to (9) results, but $\eta(z)$ and its derivatives now include an additional dependence on z through $\rho_0(z)^{-1/2}$ according to (11).

The isotherm (or isopycnal) displacements for the two cases of incompressible and compressible fluids are shown by the black curves in Figures 1 and 2, respectively. The difference in shape is indistinguishable to the scale shown. The model for the figures is a three-layer model in which the upper and lower fluids have small stability and extend to infinity. The value for N is constant and the same in the upper and lower layers and greater in the middle layer. This model was discussed in detail by GOSSARD, JENSEN and RICHTER (1971) and these figures correspond to their frame III, figure 3. The eigen equation for this model, plotted in Figure 3, is:

$$\tan n \Delta h = \frac{2n\gamma}{n^2 - \gamma^2} \quad (13)$$

where

$$n = k \sqrt{\left(\frac{N_2}{\sigma} \right)^2 - 1} \quad \gamma_{1,3} = k \sqrt{1 - \left(\frac{N_{1,3}}{\sigma} \right)^2}$$

Note that $n_k = i\gamma_k$ in a layer, k , in which the waves are evanescent.

The important points to note are: A) the wave troughs are sharpened and crests flattened above the center of the stable layer. B) the wave crests are sharpened and the troughs flattened below the center of the stable layer. C) at the center, both crest and trough are flattened.

For purposes of illustration, an amplitude-to-vertical wavelength ratio corresponding to $n\eta_0 = 0.75$ has been assumed in the figures. This value was chosen as not being so large as to make the approximate methods used in calculating wave shape completely invalid, while being sufficiently large that the changes in shape are visibly obvious.

In addition to the three layer model, the case of untrapped waves was computed and is shown in Figure 4. In contrast with the trapped waves in the model above, the introduction of finite amplitude now leads to an asymmetry in the wave shape that is reminiscent of some of the waves seen by the radar as shown in Figure 5. However, untrapped waves should exhibit a phase shift with height and such a phase shift is seldom seen by the radar. Therefore, the resemblance in shape of the waves in Figure 4 to the asymmetric, breaking waves seen by the radar should not be interpreted as necessarily providing the correct physical explanation of the waves.

The second mode waves for the three layer model were also computed and the isotherm displacements are shown by the thin wavy lines in Figure 6. The displacement curves display a pattern reminiscent of the figure eight or "cat's eye" patterns so often seen by the radar as shown in Figure 7. Once again, this is probably fortuitous since the patterns seen by the radar usually are associated with a breaking sequence and do not seem to be typically a steady state phenomenon.

3. RICHARDSON'S NUMBER

In addition to isotherm shape, the Richardson's Number must be considered a very important parameter in the interpretation of the radar records. The gradient Richardson's Number is defined as

$$R_i = \frac{\frac{g}{\theta} \frac{\partial \theta}{\partial z}}{\left(\frac{\partial u}{\partial z} \right)^2} = \frac{N^2}{\left(\frac{\partial u}{\partial z} \right)^2} \quad (14)$$

and is generally considered to be an important criterion for the onset of wave instability (breaking) or turbulence. Work by TAYLOR (1931), MILES (1961), MILES and HOWARD (1964), and CHIMONAS (1970) indicate that reduction of the Richardson's Number to less than 0.25 is a necessary condition for the development of wave instability.

GJR proposed that the propagation of untrapped gravity waves into a height region of large thermal stability can reduce R_i sufficiently to cause the onset of dynamic instability at the crests or troughs of the waves, if some shear already exists in the propagation medium. It is, therefore, argued that many of the thin, multiple layers commonly seen by the radar can be explained in terms of untrapped gravity waves propagating into a height region of great thermal stability as shown schematically in Figure 8. As the stability increases, the wave vector tilts toward the vertical so that equiphase surfaces are nearly horizontal. If the vertical energy flux is constant with height, the ratio of amplitude to vertical wavelength, n/ρ_0 , will increase, reducing the (numerator of) Richardson's Number to a level of dynamic instability at some phase of the wave. A record which may be an example of this phenomenon is shown as Figure 9.

From (12), it follows that the numerator of (14) can be written in terms of the wave induced displacement η , as

$$\frac{g}{\theta} \frac{\partial \theta}{\partial z} = \frac{g}{\theta} \frac{d\theta}{dz} \left(1 - \frac{\partial \eta}{\partial z} \right) \quad (15)$$

In order to derive the relation between u and displacement, η , needed in the denominator we require the two-dimensional equation of continuity for a compressible fluid:

$$\frac{\partial u}{\partial x} + \frac{\partial w}{\partial z} = -\frac{1}{\rho_0} \left(\frac{D\rho}{Dt} + w \frac{\partial \rho_0}{\partial z} \right) \quad (16)$$

and the 1st Law of Thermodynamics:

$$\frac{D\rho}{Dt} + w \frac{\partial \rho_0}{\partial z} = \frac{1}{c^2} \left(\frac{Dp}{Dt} + w \frac{\partial p}{\partial z} \right) \quad (17)$$

where D/Dt is the operator $\partial/\partial t + v \partial/\partial x$; p , ρ , w , u are the perturbed pressure, density, vertical velocity and horizontal velocity, and ρ_0 , p , c are the unperturbed density, pressure and sound velocity. V is the unperturbed horizontal wind speed.

Eliminating ρ and using the hydrostatic relation $\partial p/\partial z = -\rho_0 g$, (15) becomes

$$\frac{\partial u}{\partial x} + \frac{\partial w}{\partial z} - \frac{g}{c^2} w = -\frac{1}{\rho_0 c^2} \frac{Dp}{Dt} \quad (18)$$

where p is related to u by the 1st equation of motion, i.e.,

$$\frac{Du}{Dt} = -\frac{1}{\rho_0} \frac{\partial p}{\partial x} \quad (19)$$

so

$$\frac{D^2 u}{Dt^2} = -\frac{1}{\rho_0} \frac{D}{Dt} \left(\frac{\partial p}{\partial x} \right) \quad (20)$$

Taking the partial of (18) with respect to x we get

$$\left(\frac{\partial^2}{\partial x^2} - \frac{1}{c^2} \frac{D^2}{Dt^2} \right) u = - \left(\frac{\partial}{\partial z} - \frac{g}{c^2} \right) \frac{\partial w}{\partial x}$$

For solutions of the form $F(z)\exp[i(kx - \sigma t)]$

$$(\sigma^2 - k^2 c^2)u = -ikc^2 \left(\frac{\partial}{\partial z} - \frac{g}{c^2} \right) w$$

so

$$u = \frac{i}{k \left(1 - \frac{C^2}{c^2} \right)} \left(\frac{\partial}{\partial z} - \frac{g}{c^2} \right) w \quad (21)$$

where $C = \sigma/k$. If we define $(u, w)\rho^{1/2} = U, W$, then

$$\frac{\partial W}{\partial z} = \rho_0^{-1/2} \left(\frac{\partial W}{\partial z} - \frac{1}{2\rho_0} \frac{\partial \rho_0}{\partial z} W \right)$$

If we return to (18) we get on substitution

$$U = \frac{i}{k \left(1 - \frac{C^2}{c^2} \right)} \left(\frac{\partial}{\partial z} - \Gamma \right) W$$

Equations (20) and (21) are equations used by GOSSARD, RICHTER, ATLAS (1970), and GJR. They do not include shear within the medium. Noting that $w = D\eta/Dt$ and assuming $C^2 \ll c^2$

$$\frac{\partial u}{\partial z} = \frac{\sigma}{k} \left(\frac{\partial}{\partial z} - \frac{g}{c^2} \right) \frac{\partial \eta}{\partial z} \quad (23)$$

So that

$$R_1 = \frac{N_0^2}{C^2} \frac{1 - \frac{\partial \eta}{\partial z}}{\left[\left(\frac{\partial}{\partial z} - \frac{g}{c^2} \right) \frac{\partial \eta}{\partial z} \right]^2} \quad (24)$$

For untrapped waves, a solution of the form $\eta = \eta_0 \cos(kx + nz - \sigma t)$ may be assumed. For the three-layer model discussed above.

$$\begin{aligned} \eta_1 &= \eta_0 \cos \left(n \frac{\Delta h}{2} \right) \exp \{ \gamma_1 (x + \Delta h/2) \} \\ \eta_2 &= \eta_0 \cos nz \\ \eta_3 &= \eta_0 \cos \left(n \frac{\Delta h}{2} \right) \exp \{ -\gamma_3 (z - \Delta h/2) \} \end{aligned} \quad (25)$$

where the subscripts 1, 2, 3 apply to the lower, middle and upper layers respectively, and where the origin is chosen at the middle layer. The Richardson's Numbers in Figures 1 and 2 were calculated using equations (24) and (25) assuming $[N_{1,3}/\gamma_{1,3} C]^2 = 0.25$, $n\eta_0 = 0.75$. For Figure 1 it was assumed that $g/c^2 \ll \partial/\partial z$ and the effect of the height dependence in $\rho_0(z)^{-1/2}$ on η and its derivatives was ignored (incompressibility assumption). Figure 4 shows the corresponding patterns of R_1 in untrapped waves, where R_1 is represented by sloping straight lines; and Figure 6 shows patterns of R_1 in 2nd mode trapped waves where R_1 is shown by heavy lines.

If g/c^2 is negligible the numerator and denominator of (24) go to zero together as $n\eta_0 \rightarrow 1.0$ at a limiting $R_1 = 0.5$. Further increase in $n\eta_0$ leads to negative R_1 which implies that the wave can produce super-adiabatic gradients. This is important because it means that the wave cannot reduce R_1 to the level of dynamic instability, i.e., $R_1 = 0.25$, but may, instead, produce convective instability. For the case of untrapped waves, this might argue that layers of convective instability and superadiabatic temperature gradients as proposed by ORLANSKI and BRYAN (1969) might be observed instead of dynamically unstable lamina resulting from reduced R_1 . However, our balloon soundings have failed to detect

superadiabatic temperature gradients within temperature inversion layers [RICHTER and GOSSARD, 1970], and GJR pointed out that the substructure revealed by the radar within the lamina resembles the Kelvin/Helmholtz instabilities seen at larger scales and commonly attributed to dynamic instability. When any background shear in the medium is included, it is found that the limiting $R_i = 0.5$ no longer applies and R_i decreases smoothly to $R_i = 0.25$ as $n\eta_0$ increases. We therefore propose that dynamic instability in untrapped wave systems, imbedded in a medium with some shear, is responsible for the creation of the thin layers of turbulent instability seen by the radar within temperature inversions.

4. REFERENCES

- CHIMONAS, G., 1970, "The Extension of the Miles-Howard Theorem to Compressible Fluids," J. Fluid Mech. 43, 833-836.
- ECKART, C., 1960, "Hydrodynamics of Oceans and Atmospheres," Pergamon Press, New York, p. 107.
- GOSSARD, E.E., D. R. JENSEN, and J.H. RICHTER, 1971, "An Analytical Study of Tropospheric Structure as Seen by High-Resolution Radar," J. Atmospheric Sci. 28, No. 5, 794-807.
- GOSSARD, E.E., J.H. RICHTER, and D. ATLAS, 1970, "Internal Waves in the Atmosphere from High Resolution Radar Measurements," J. Geophys. Res. 75, 903-913.
- MILES, J.W., 1961, "On the Stability of Heterogeneous Shear Flows," J. Fluid Mech. 10, 496-508.
- MILES, J.W., and L.N. HOWARD, 1964, "Note on Heterogeneous Shear Flow," J. Fluid Mech., 20, 331-336.
- ORLANSKI, I., and K. BRYAN, 1969, "Formation of the Thermocline Step Structure by Large Amplitude Internal Gravity Waves," J. Geophys. Res., 74, 6975-6983.
- RICHTER, J.H., and E.E. GOSSARD, 1970, "Lower Tropospheric Structure as Seen by a High-Resolution Radar," Naval Electronics Lab. Center Technical Report 1718, p. 26.
- RICHTER, J.H., 1969, "High Resolution Tropospheric Radar Sounding," Radio Science 4, 1261-1268.
- THORPE, S.A., 1968, "On the Shape of Progressive Internal Waves," Proc. Royal Soc. London, 263, 563-614.
- TAYLOR, G.I., 1931, "Effect of Variation in Density on the Stability of Superposed Streams of Fluid," Proc. Roy. Soc. A, 132, 499-523.

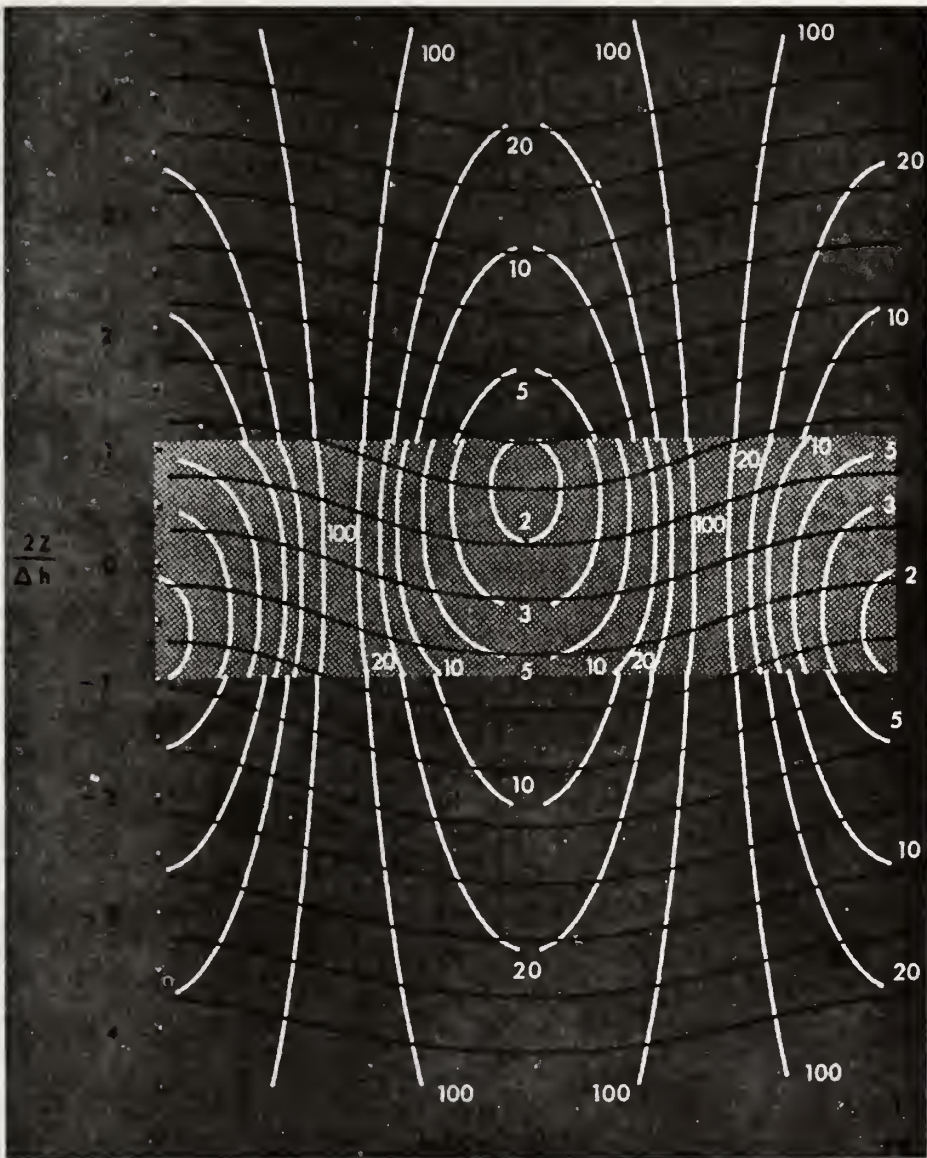


Fig.1 Plot of R_i (white curves) and wave shape (black curves) through a three-layer model wave system. Waves evanescent above and below a stable layer in which ratio of amplitude to vertical wavelength is $0.75/2\pi$ (i.e., $n\eta_0 = 0.75$). It is assumed that $N_2/N_{1,3} = 5.5$, $n^2h/2 = 0.375$ and $N_{1,3} k/\omega n = 0.5$ (see text). Terms in g/c assumed negligible compared with n (i.e., incompressibility condition in which plane wave solution assumed for η). No shear.

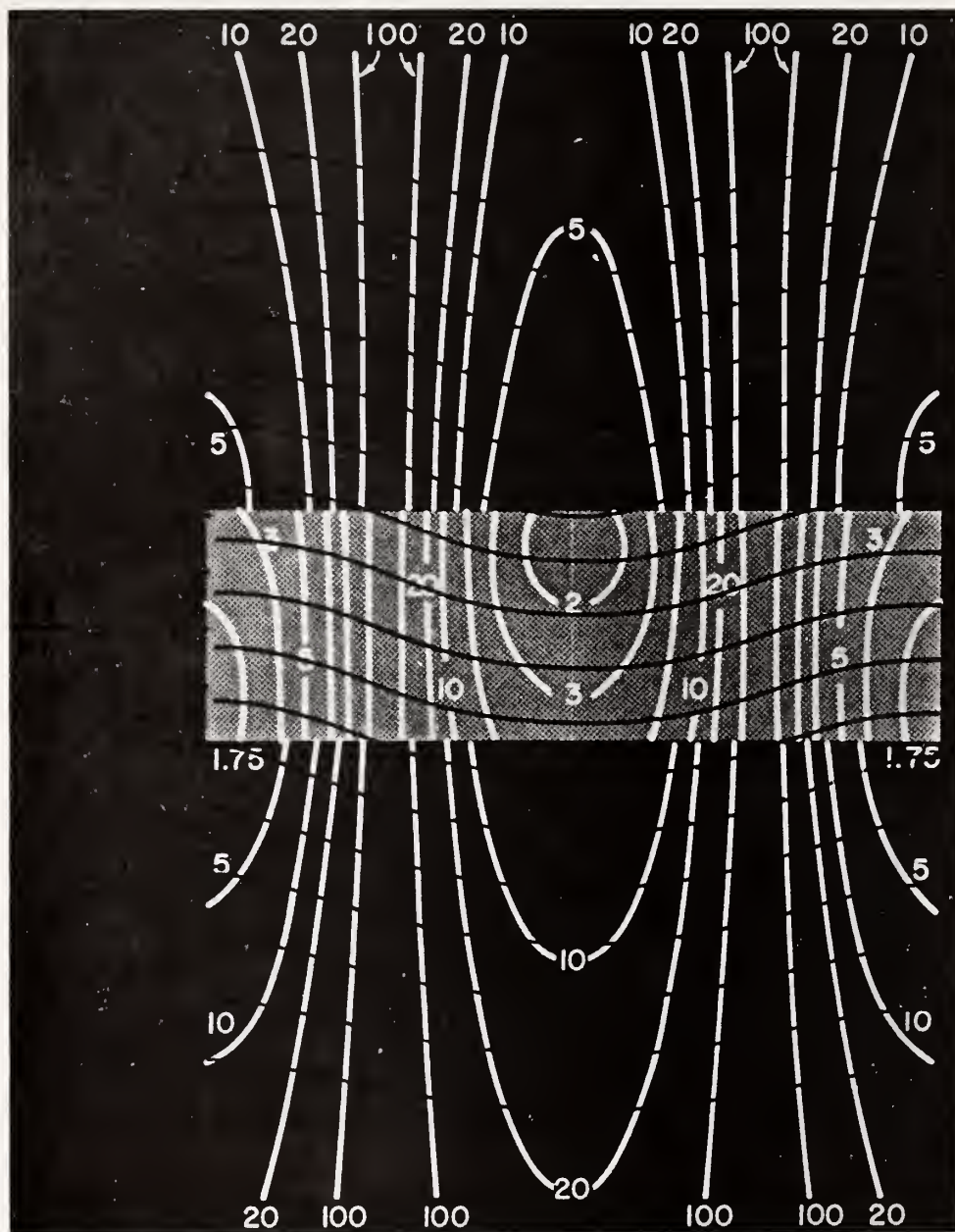


Fig.2 Conditions same as those of Figure 1 except plane wave solution assumed for $\eta\rho_0(z)^{1/2}$ where $\rho_0^{-1}d\rho_0/dz \approx -g/c^2$ and it is assumed that $g/c^2/2n = 0.1$. Note that this inclusion of compressibility makes virtually no difference in wave shape and little difference in R_1 even for the extreme condition assumed.

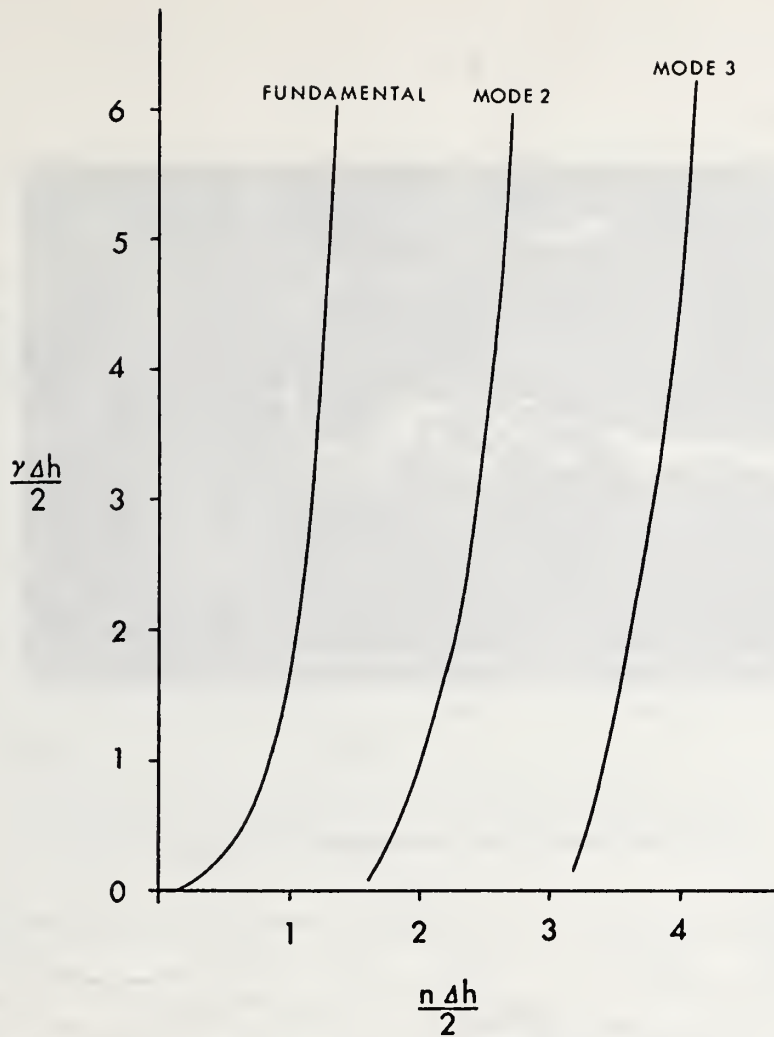


Fig.3 Plot model relation, equation (13).

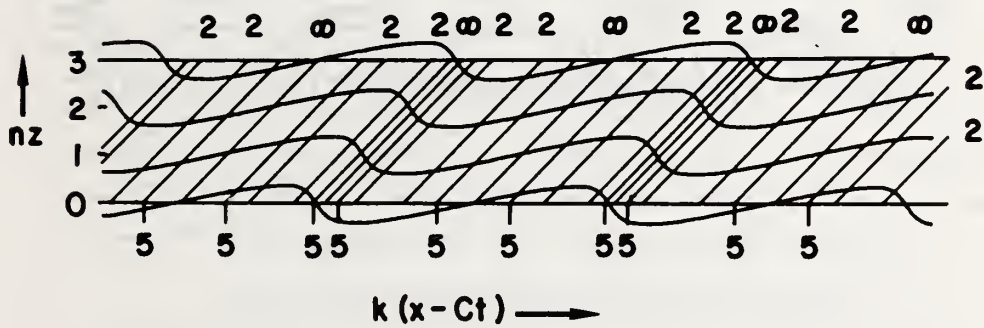


Fig.4 Wave shape and R_i for untrapped wave model assuming same conditions as in Figure 2.

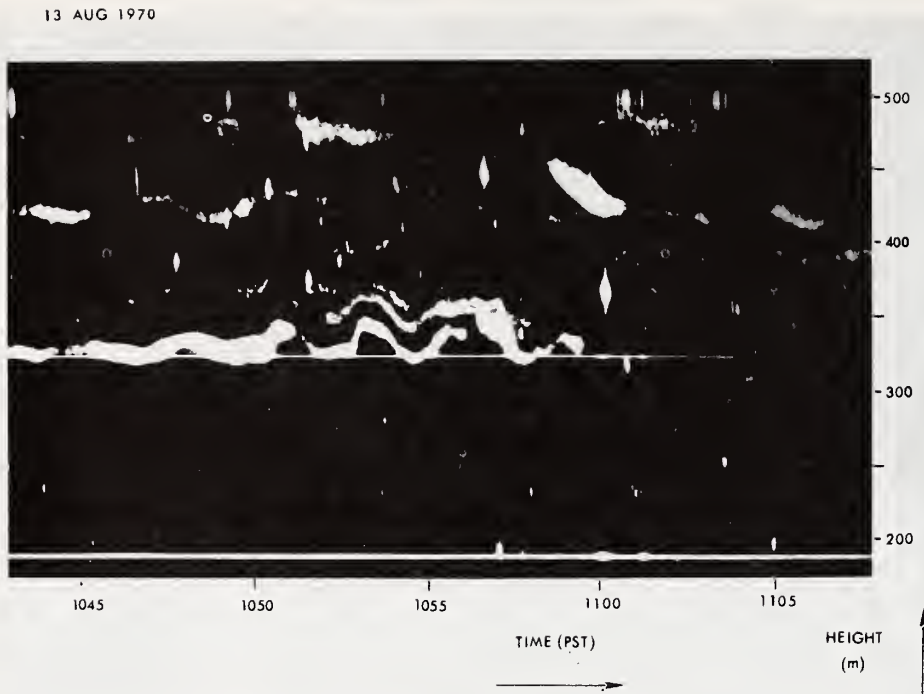


Fig.5 Example of record showing similar wave shape to that of Figure 4.

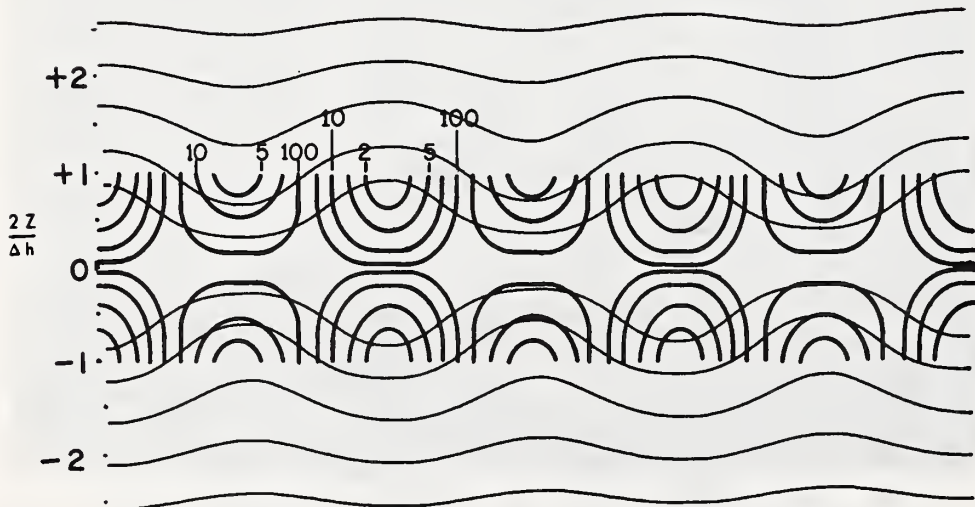


Fig.6 Wave shape and R_l for 2nd mode assuming same model as Figure 2.

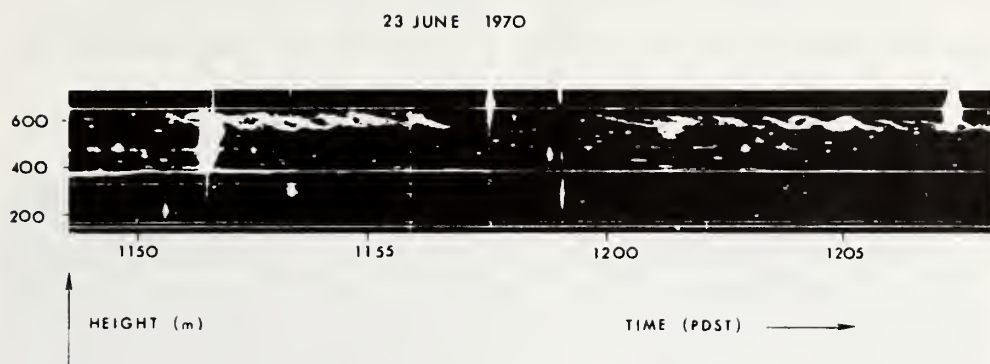


Fig.7 Example of record showing "cat's eye" pattern similar to wave shape of Figure 6.

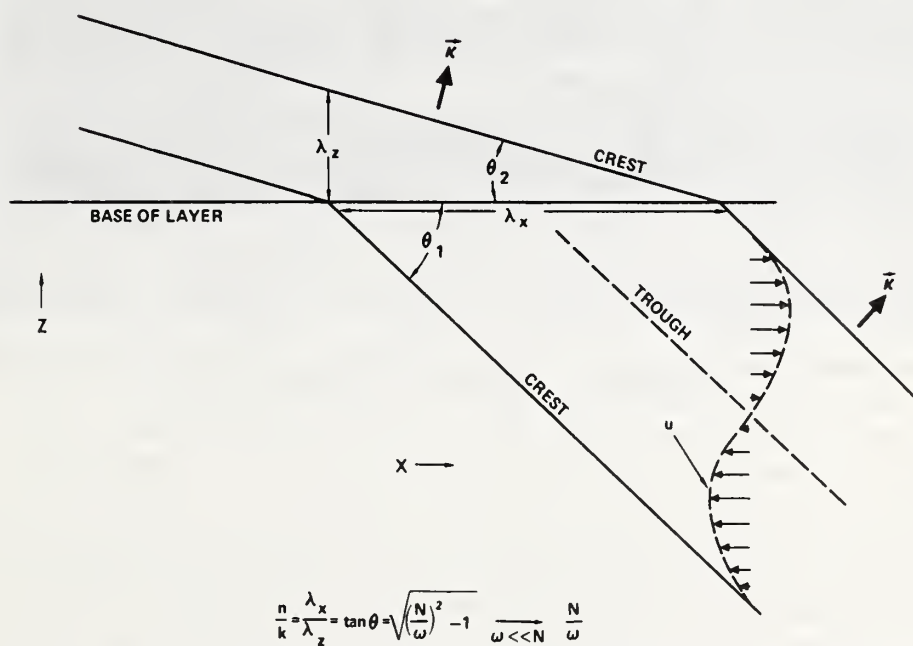


Fig.8 Schematic illustration of reduction in λ_z due to untrapped wave propagating into stable region of atmosphere.

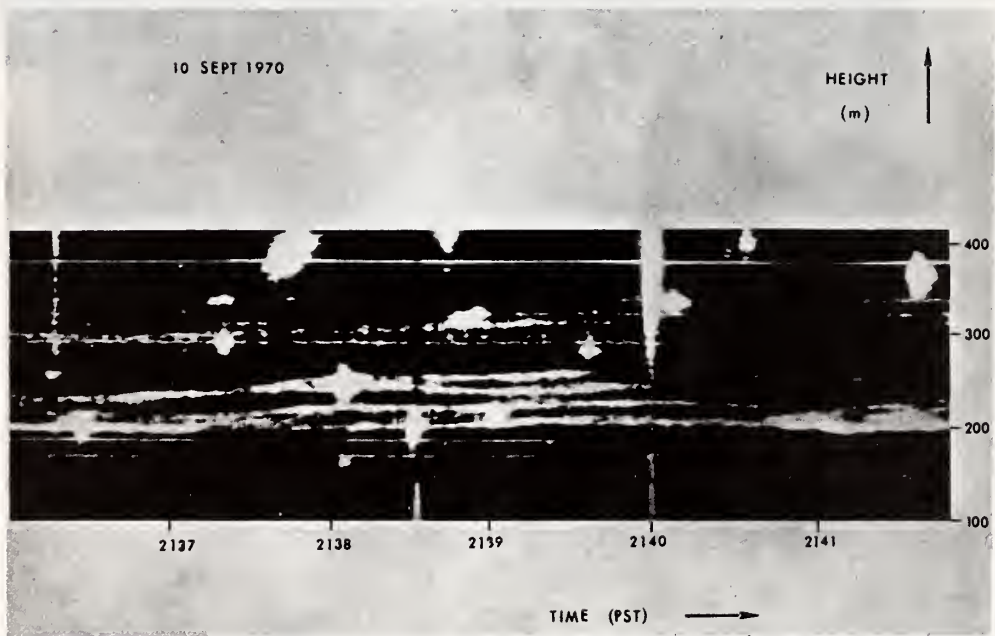


Fig.9 Example of record showing wavelike structures which illustrate regions of reduced R_1 propagating in the vertical (as well as horizontal) direction with untrapped gravity waves.

Reprinted with permission from D. Reidel Publishing Company
Boundary Layer Meteorology Vol. 4, 113-131, 1973

EFFECT OF WIND SHEAR ON ATMOSPHERIC WAVE INSTABILITIES REVEALED BY FM/CW RADAR OBSERVATIONS

E. E. GOSSARD, J. H. RICHTER,* and D. R. JENSEN*

*Wave Propagation Laboratory, NOAA Environmental Research Laboratories,
Boulder, Colo. 80302, U.S.A.*

(Received 8 August, 1972)

Abstract. An FM/CW radar sounding system designed and built by one of us (Richter, 1969) reveals atmospheric wave structure in unparalleled detail.

The most outstanding features evident in the record are; internal gravity waves; features resembling Kelvin/Helmholtz instability structures; and multiple layering, often with lamina only a few meters thick.

This paper shows a variety of atmospheric structural patterns and compares them with several hypothetical models of internal waves to obtain more insight into the atmospheric processes at work. Special attention is given to the distribution of the Richardson number in trapped and untrapped gravity waves. It is proposed that the multiple layers result from untrapped internal gravity waves whose propagation vector is directed nearly vertically within very stable height regions. It is argued that the layers are caused by dynamic instability resulting from reduction in the Richardson number due to wave induced shear and to some background wind shear when the amplitude-to-wavelength ratio grows during propagation into thermally stable height regions of the atmosphere.

1. Introduction

Radar pictures of the structure of the clear atmosphere reveal many patterns suggestive of wavelike motions and of various kinds of dynamic instability. They provide fundamental new information about the manner in which turbulence in the atmosphere is created and the role played by thermal stratification in fluid dynamics.

The most common perturbations of the echo layers are features with the appearance of simple plane waves. They are the phenomenon causing the perturbations in surface pressure and surface wind studied over the last twenty years or more by many observers (e.g., Stilke, this issue, Gossard and Munk, 1954). Their main characteristics are describable by linear theory. Some of these characteristics include their dispersion (Gossard and Richter, 1970), and their amplitude variation with height and atmospheric stability (Gossard *et al.*, 1970). Their propagation velocity is generally very different from the local wind speed and they often propagate against the wind, probably because their coherence would otherwise be destroyed by some kind of dynamic instability associated with a critical region.

Other kinds of structures commonly seen in the radar records resemble billows, braids and cat's eyes. There is mounting evidence (e.g., Emmanuel, next issue; Hooke *et al.*, next issue; Gossard *et al.*, 1970) that these features travel essentially with the mean wind at their height of occurrence and represent some kind of dynamic insta-

* Propagation Technology Division, Naval Electronics Laboratory Center, San Diego, Calif. 92152, U.S.A.

bility in the presence of vertical wind shear. They are probably not adequately described by linear theory.

In this paper we will deal mainly with the first category of wave phenomenon, but we suggest that under some conditions, these waves can become dynamically unstable and the manifestation of this instability may have the appearance of the second category above. We further suggest that there is no particular reason why natural sources should only generate gravity waves in the frequency range where they are trapped (i.e., energy propagating only horizontally, and waves evanescent in layers above and below the layer on which they propagate). If their frequency is below the Väisälä-Brunt frequency, they will have a component of propagation in the vertical as well as the horizontal direction. We believe such vertically propagating waves commonly exist in the troposphere and will be found to be an important mechanism for the vertical redistribution of energy and momentum. Through their interaction with the mean flow, they may under some circumstances influence the circulation patterns of the lower atmosphere. We believe that these waves may be responsible for the generation of the more-or-less periodically-spaced (in height) layers commonly seen on the radar. This paper will extend an earlier study by Gossard *et al.* (1971), hereafter referred to as GJR, in which they proposed that such vertically propagating waves, propagating into height regions of stable temperature stratification, would be shortened sufficiently to become dynamically unstable at their 'crests' and/or 'troughs', thus producing layers of small-scale turbulence seen by the radar. In this paper, we will extend the earlier analysis to include the effects of weak non-linearity on the waves, and we will take into account the effects of a *weak* background shear in the wind field in a more rigorous way. Using the method of successive approximations, we find that the primary effect of the non-linearity is to change the wave shape (e.g., the isotherm shape) and that the wind field is not affected to first order since its non-linearity depends on the curvature of the density (or potential temperature) profile which in our model is small. Thus the Richardson number deviates little from that of linear theory even for fairly extreme non-linear changes in shape.

2. The Richardson Number

The gradient Richardson number Ri must be considered a potentially important parameter in the interpretation of the radar records. For flow in the x direction, Ri is defined as

$$Ri = \frac{g}{\theta} \frac{\partial \theta}{\partial z} \frac{1}{\left(\frac{\partial u}{\partial z}\right)^2} = \frac{N^2}{\left(\frac{\partial u}{\partial z}\right)^2} \quad (1)$$

and is generally considered to be an important criterion for the onset of wave instability (breaking) or turbulence. Work by Taylor (1931), Miles (1961), Miles and

Howard (1964), and Chimonas (1970) indicates that reduction of Ri to less than 0.25 is a necessary condition for the development of wave instability.

GJR proposed that the propagation of untrapped gravity waves into a height region of large thermal stability can reduce Ri sufficiently to cause the onset of dynamic instability at the crests or troughs of the waves, if some shear already exists in the propagation medium. In that paper, the wave-induced shear in a quiescent medium was simply added to the mean shear to examine the effect of shear on Ri . In the present paper, this assumption is examined and the problem of 'background shear' is treated with more rigor. It will be found that the results are only slightly modified, and the conclusion that a small background shear, in addition to the wave-induced shear, can reduce Ri to a point of dynamic instability, remains valid. It will therefore be argued that many of the thin, multiple layers commonly seen by the radar can be explained in terms of untrapped gravity waves propagating into a height region of great thermal stability as shown schematically in Figure 1. As the stability increases, the wave vector tilts toward the vertical so that equiphase surfaces are nearly hori-

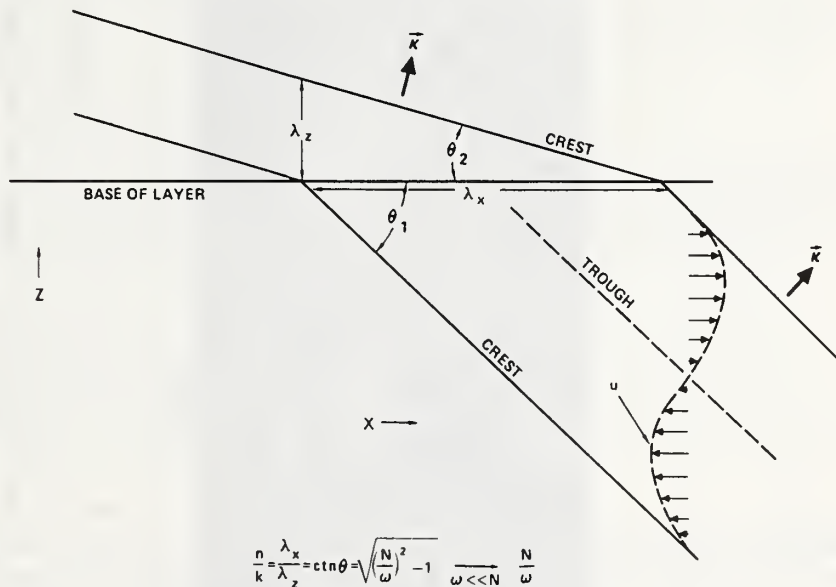


Fig. 1. Schematic illustration of reduction in λ_z due to untrapped wave propagating into a stable region of the atmosphere.

zontal. If the vertical energy flux is constant with height, the ratio η_0/λ_z of amplitude to vertical wavelength will increase, reducing (the numerator of) Ri to a condition of dynamic instability at some phase of the wave. A record which may be an example of nearly horizontal phase surfaces in a wavetrain propagating upwards is shown in Figure 2. Exactly the same schematic picture applies to the effect on waves propagating into a layer of different wind speed; near a critical level, the rays of energy

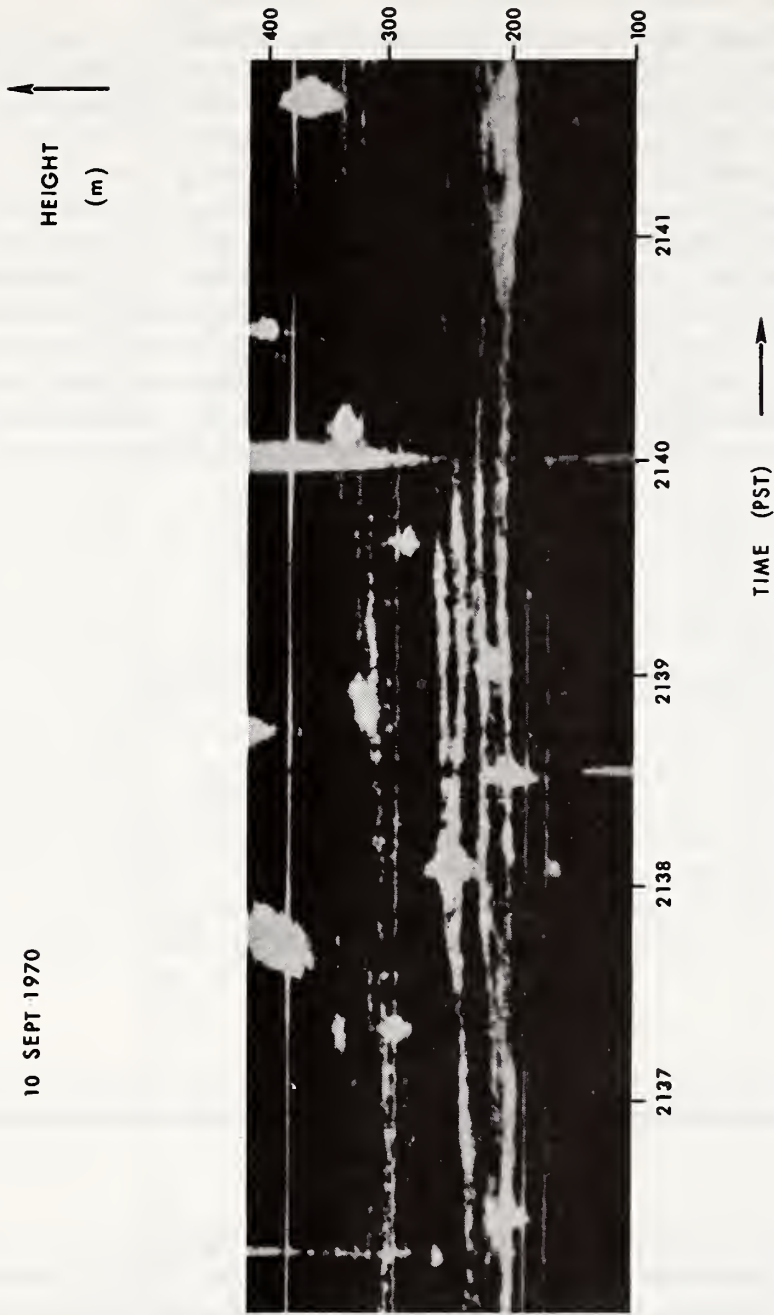


Fig. 2. Example of record showing wavelike structures which may illustrate regions of reduced Ri propagating in the vertical (as well as horizontal) direction with untrapped gravity waves.

tend to become horizontal and, again, the propagation vector tilts toward the vertical; the vertical wavelength decreases and equiphase surfaces become nearly horizontal. Near the critical level, the problem becomes mathematically difficult and the simple expressions from linear theory shown in Figure 1 no longer apply. A treatment of propagation near the critical level using ray tracing has been given by Georges (1972).

It will also be argued that the same mechanism, operating to reduce Ri in trapped wave systems, can explain some of the characteristic wave shapes commonly seen by the radar. For example, the ejection of 'puffs' from sharp wave crests might be expected when the shear is positive while ejection from sharp wave troughs would be expected if the shear is negative.

If the unperturbed potential temperature, θ_0 , varies linearly with height, the potential temperature distribution that results from the wave perturbation, η , is related to θ_0 and η as

$$\frac{\partial \theta}{\partial z} = \frac{d\theta_0}{dz} \left(1 - \frac{\partial \eta}{\partial z} \right). \quad (2)$$

It follows that the numerator of (1) can be written in terms of the wave-induced displacement η , as

$$\frac{g}{\theta} \frac{\partial \theta}{\partial z} = \frac{g}{\theta} \frac{d\theta_0}{dz} \left(1 - \frac{\partial \eta}{\partial z} \right). \quad (3)$$

In order to derive the relation between u and displacement needed in the denominator, we require the two-dimensional equation of continuity for a compressible fluid which is

$$\frac{\partial u}{\partial x} + \frac{\partial w}{\partial z} = - \frac{1}{\rho_0} \left(\frac{D\rho}{Dt} + w \frac{\partial \rho_0}{\partial z} \right) \quad (4)$$

and the First Law of Thermodynamics:

$$\frac{D\rho}{Dt} + w \frac{\partial \rho_0}{\partial z} = \frac{1}{c^2} \left(\frac{Dp}{Dt} + w \frac{\partial p}{\partial z} \right), \quad (5)$$

where D/Dt is the operator $\partial/\partial t + V\partial/\partial x$, p , ρ , w , u are the perturbed pressure, density, vertical velocity, and horizontal velocity, respectively, and ρ_0 , P , c , and V are the unperturbed density, pressure, sound velocity, and wind speed, respectively.

Eliminating ρ and using the hydrostatic relation $\partial P/\partial z = -\rho_0 g$, Equation (4) becomes

$$\frac{\partial u}{\partial x} + \frac{\partial w}{\partial z} - \frac{g}{c^2} w = - \frac{1}{\rho_0 c^2} \frac{Dp}{Dt}. \quad (6)$$

The pressure p is related to u by the first equation of motion, i.e.,

$$\frac{Du}{Dt} = - \frac{1}{\rho_0} \frac{\partial p}{\partial x}, \quad (7)$$

so

$$\frac{D^2 u}{Dt^2} = -\frac{1}{\rho_0} \frac{D}{Dt} \left(\frac{\partial p}{\partial x} \right).$$

Taking the partial of (6) with respect to x , we get

$$\left(\frac{\partial^2}{\partial x^2} - \frac{1}{c^2} \frac{D^2}{Dt^2} \right) u = - \left(\frac{\partial}{\partial z} - \frac{g}{c^2} \right) \frac{\partial w}{\partial x}. \quad (8)$$

For solutions of the form $F(z) \exp[i(kx - \sigma t)]$, we get

$$(\sigma^2 - k^2 c^2) u = -ikc^2 \left(\frac{\partial}{\partial z} - \frac{g}{c^2} \right) w,$$

so

$$u = \frac{i}{k \left(1 - \frac{C^2}{c^2} \right)} \left(\frac{\partial}{\partial z} - \frac{g}{c^2} \right) w, \quad (9)$$

where $C = \sigma/k$. If we define $(u, w) \rho^{1/2} = U, W$, then

$$\frac{\partial w}{\partial z} = \rho_0^{-1/2} \left(\frac{\partial W}{\partial z} - \frac{1}{2\rho_0} \frac{\partial \rho_0}{\partial z} W \right).$$

If we return to (9), we get on substitution

$$U = \frac{i}{k \left(1 - \frac{C^2}{c^2} \right)} \left(\frac{\partial}{\partial z} - \Gamma \right) W, \quad (10)$$

where $\Gamma = \frac{1}{2} \rho_0^{-1/2} \partial \rho_0 / \partial z + g/c^2$.

Equations (9) and (10) are equations used by Gossard *et al.* (1970), and GJR. They do not include shear within the medium. Noting that $w = D\eta/Dt$ and assuming $C^2 \gg c^2$

$$\frac{\partial u}{\partial z} = \frac{\sigma}{k} \left(\frac{\partial}{\partial z} - \frac{g}{c^2} \right) \frac{\partial \eta}{\partial z}, \quad (11)$$

so that

$$Ri = \frac{N_0^2}{C^2} \frac{1 - \frac{\partial \eta}{\partial z}}{\left[\left(\frac{\partial}{\partial z} - \frac{g}{c^2} \right) \frac{\partial \eta}{\partial z} \right]^2}. \quad (12)$$

Ri , from this equation, is plotted as the white curves in Figure 3 for a three-layer model.

For the three-layer model of Figure 3, the upper and lower fluids have relatively small stability and extend to infinity. The thickness of the stable layer is Δh . N is

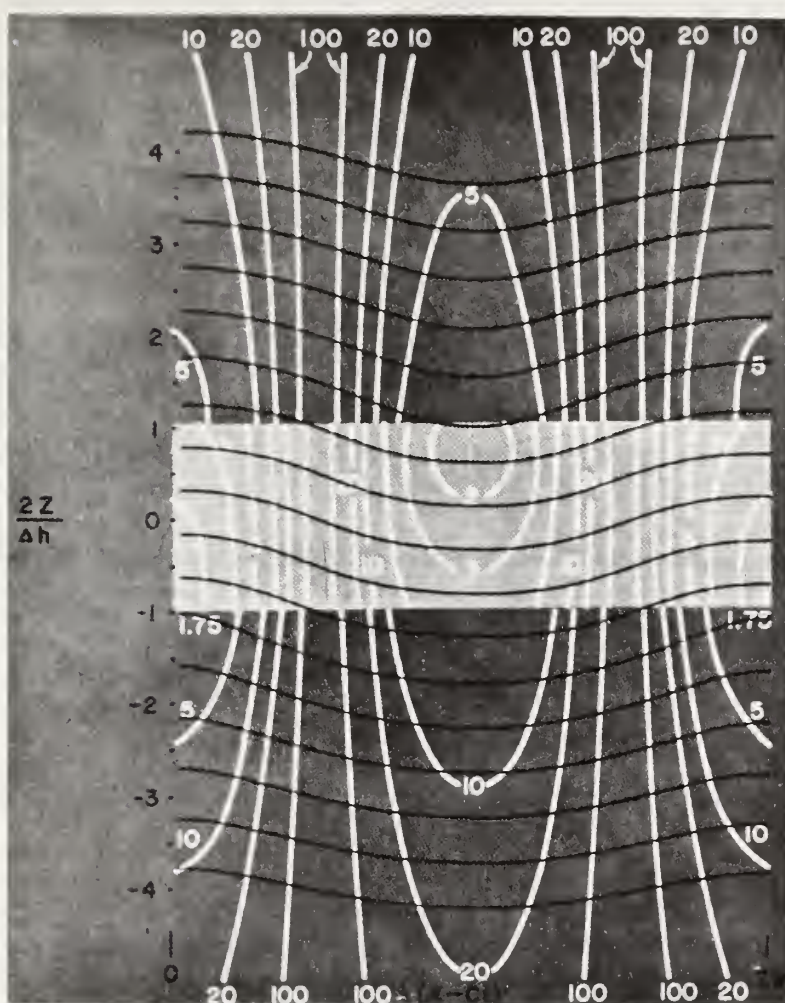


Fig. 3. Plot of Ri (white curves) and wave shape (black curves) through a three-layer model wave system. Waves evanescent above and below a stable layer in which ratio of amplitude to vertical wavelength is $0.75/2\pi$ (i.e., $n\eta_0 = 0.75$). It is assumed that $N_2/N_{1,3} = 5.5$, $n\Delta h/2 = 0.375$ and $N_{1,3}k/\omega n = 0.5$. The slight asymmetry of Ri at crest vs. trough is caused by the fact that $\eta_0 \propto (\varrho(z)/\bar{\varrho})^{-1/2}$, thus influencing derivatives of η with z .

constant in each layer and is the same in the upper and lower layers. The eigenvalue equation is

$$\tan n\Delta h = \frac{2n\gamma}{n^2 - \gamma^2}, \quad (13)$$

where

$$n_2 = k \sqrt{\left(\frac{N_2}{\sigma}\right)^2 - 1}, \quad \gamma_{1,3} = k \sqrt{1 - \left(\frac{N_{1,3}}{\sigma}\right)^2}. \quad (14)$$

Note that $n_\kappa = i\gamma_\kappa$ in a layer, κ , in which the waves are evanescent. Equation (13) is plotted in Figure 4.

The first-order particle displacements in the three layers of this model are

$$\begin{aligned}\eta_1 &= \eta_0 \cos\left(n \frac{\Delta h}{2}\right) \exp[\gamma_1(z + \Delta h/2)] \\ \eta_2 &= \eta_0 \cos nz \\ \eta_3 &= \eta_0 \cos\left(n \frac{\Delta h}{2}\right) \exp[-\gamma_3(z - \Delta h/2)]\end{aligned}\tag{15}$$

where a factor of $\cos(kx - \sigma t)$ is understood. The corresponding isotherm displacements, δ , are of the form

$$\frac{\delta_\kappa}{\delta_0} = a_\kappa + b_\kappa \cos(kx - \sigma t) + c_\kappa \cos 2(kx - \sigma t) + d_\kappa \cos 3(kx - \sigma t) \dots,\tag{16}$$

where $\delta_0 = \eta_0$ is the amplitude of the first-order isotherm displacement at a reference

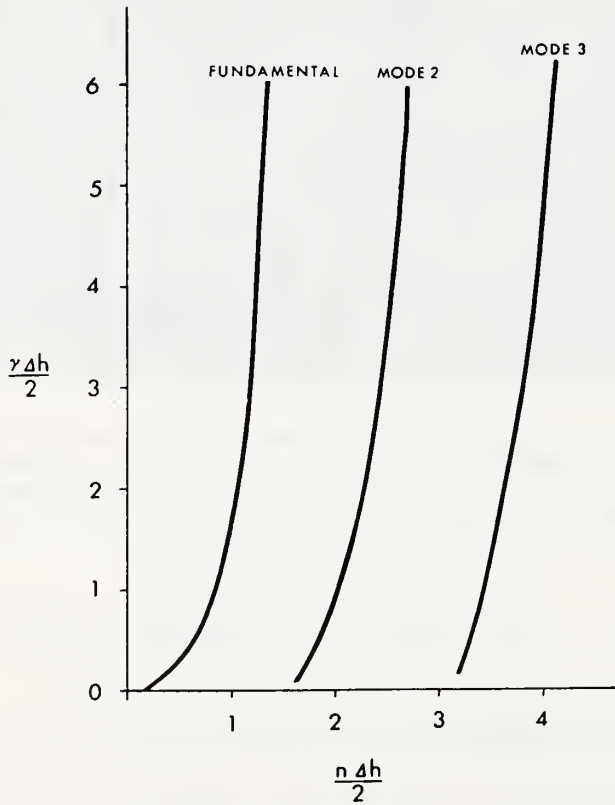


Fig. 4. Plot of modal relation, Equation (13).

height within the layer. The coefficients are evaluated for finite amplitude by the method of successive approximations. The procedure is straightforward but laborious and is described elsewhere (Gossard and Richter, 1972). The general method is thoroughly reviewed by Thorpe (1968, p. 584). The isotherm displacements are indicated by the dark curves of Figure 3 and show the well known sharpening of crests below the stable region and sharpening of the troughs above. The wave-induced pattern of Ri calculated from Equation (12) is shown by the white curves. The pattern for the second mode is shown in Figure 5, and is of interest because of its similarity in ap-

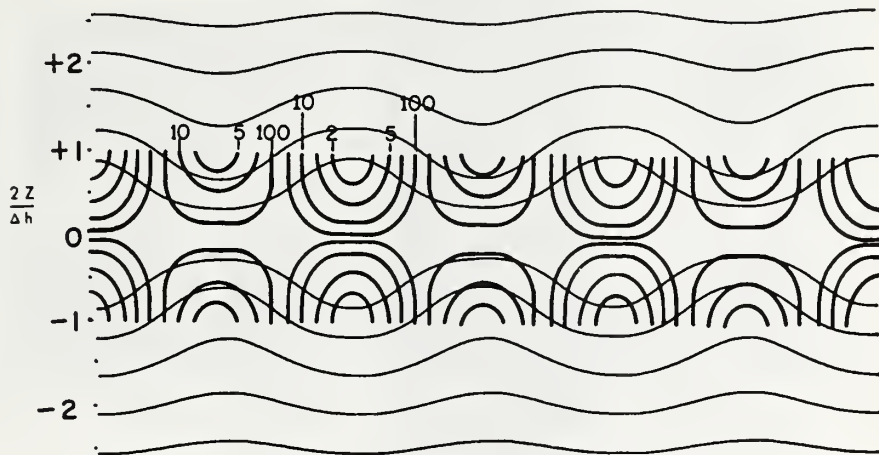


Fig. 5. Wave shape (light curves) and Ri (heavy curves) for 2nd mode, assuming same model as Figure 3.

pearance to the 'cat's-eye' pattern (see Figure 6) so often seen in the records. This similarity is probably accidental, since the 'cat's eye' often seems to appear as a stage in a developing sequence of dynamic instability as shown in Figure 7. For untrapped waves, we assume a first-order displacement of the form $\eta = \eta_0 \cos(kx + nz - \sigma t)$ and the isotherm displacement is then given by

$$\frac{\delta}{\delta_0} = b \cos(kx + nz - \sigma t) + c \sin 2(kx + nz - \sigma t) + d \cos 3(kx + nz - \sigma t) \dots \quad (17)$$

The constant term is absent and the isotherm displacement is no longer symmetrical about crest and trough as shown in Figure 8. The dark sloping lines are isopleths of Ri . The crucial wave parameter is $n\eta_0$ which is the ratio of wave amplitude to vertical wavelength multiplied by 2π . For layers in which the waves are evanescent, the corresponding ratio is amplitude to skin depth of the layer. A value of $n\eta_0 = 0.75$ was chosen for the figures. This value was chosen as a compromise between values so large that convergence of Equations (16) and (17) to third order would be quite un-

23 JUNE 1970

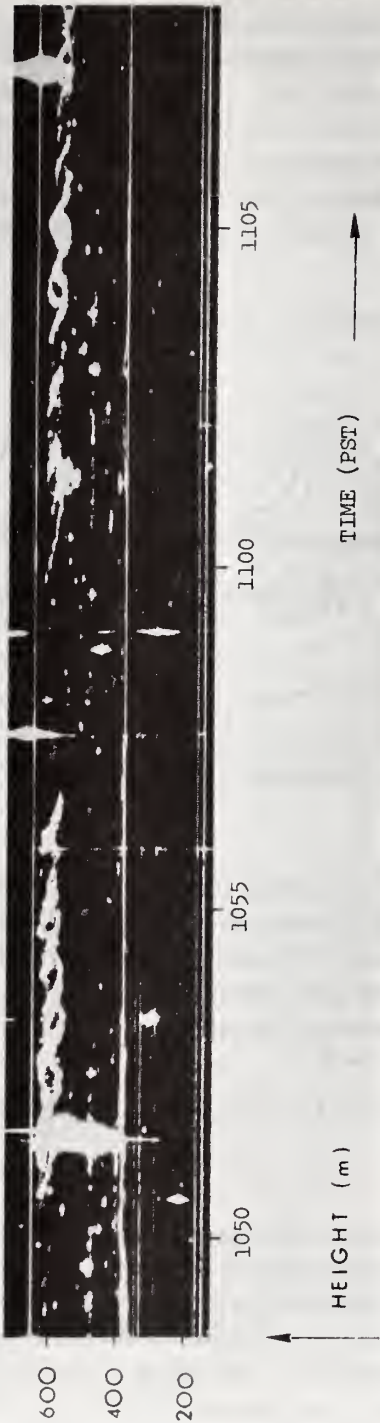


Fig. 6. Example of record showing 'cat's-eye' pattern similar to wave shape of Figure 5.

28 SEPT 1971

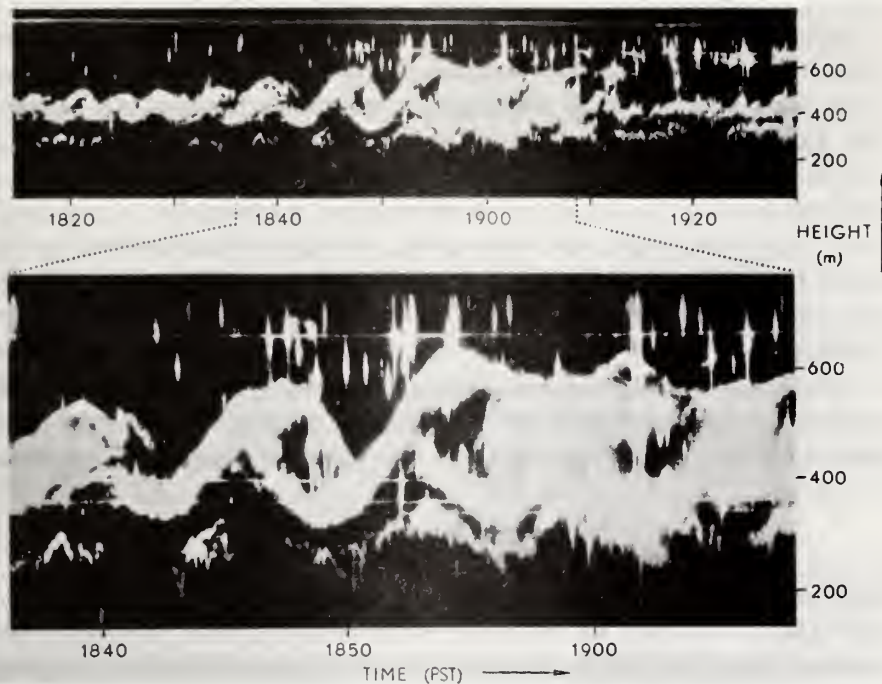


Fig. 7. A breaking wave sequence that probably pictures the morphology of the formation of 'cat's-eye' patterns and 'braided' structures.

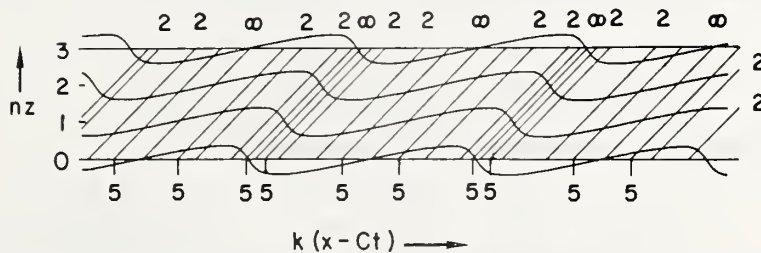


Fig. 8. Wave shape and Ri for untrapped wave model assuming same conditions as in Figure 3.

satisfactory and values so small that patterns in wave shape and Ri would not be clear. The effect of non-linearity on the velocity field turns out to be small, appearing only in higher-order terms depending on curvature of the density (or potential temperature) profile.

If g/c^2 is negligible, the numerator and denominator of Equation (12) go to zero together as $n\eta_0 \rightarrow 1.0$ at a limiting $Ri = 0.5$. Further increase in $n\eta_0$ leads to negative Ri which implies that the wave can produce superadiabatic gradients. This is important because it means that the wave cannot, without shear in the background

flow, reduce Ri to the level of dynamic instability, i.e., $Ri=0.25$, but may, instead, produce convective instability. Although Equation (12) is rigorously applicable only to infinitesimal amplitude disturbances, this might argue that layers of convective instability and superadiabatic temperature gradients might be observed instead of dynamically unstable lamina resulting from reduced Ri . However, our balloon soundings have failed to detect superadiabatic temperature gradients within temperature inversion layers (Richter and Gossard, 1970) even though the rate of ascent and the time constants of the sensor should permit good representation of any layers more than 10 m thick. Even more importantly, the substructure revealed by the radar within the lamina resembles the Kelvin/Helmholtz instabilities seen at larger scales and commonly attributed to dynamic instability. When any ambient shear in the medium is included, it will be found that the limiting $Ri=0.5$ no longer applies and Ri decreases smoothly to $Ri=0.25$ as $n\eta_0$ increases. We therefore propose dynamic instability in untrapped wave systems imbedded in a medium with some shear, to be responsible for the creation of the thin layers seen by the radar within temperature inversions.

3. Effect of Wind Shear on Ri

In this section, the effect of vertical shear in the medium on the wave-induced pattern of Ri is examined. The effect of shear on wave shape is ignored. This places restrictions on the model which will be discussed later, but the model is clearly not applicable near the critical level.

Consider the total wind, U_T , to consist of a background component $U(z)$ in the x direction and a wave-induced component, u . Returning to Equation (6) and defining as before $D/Dt = ik(U - \sigma/k)$, we find

$$u = \frac{i}{k} \frac{\partial w}{\partial z} + \frac{1}{\varrho_0 c^2} \left[\frac{\sigma}{k} - U(z) \right] p - \frac{i}{k} \frac{g}{c^2} w. \quad (18)$$

Using the first equation of motion, as before, we find

$$p = \varrho_0 \left(\frac{\sigma}{k} - U(z) \right) u + \frac{i}{k} \frac{\partial U(z)}{\partial z} \varrho_0 w. \quad (19)$$

Eliminating p from (18)

$$u = \frac{i}{k} \frac{\left(\frac{\partial}{\partial z} - \frac{g}{c^2} \right) + \frac{1}{c^2} \left(\frac{\sigma}{k} - U(z) \right) \frac{\partial U(z)}{\partial z}}{1 - \frac{1}{c^2} \left(\frac{\sigma}{k} - U(z) \right)^2} w. \quad (20)$$

To relate u to η , note that

$$w = \frac{D\eta}{Dt} = ik \left(U(z) - \frac{\sigma}{k} \right) \eta$$

and

$$\frac{\partial w}{\partial z} = ik \left\{ \left[U(z) - \frac{\sigma}{k} \right] \frac{\partial \eta}{\partial z} + \frac{\partial U(z)}{\partial z} \eta \right\}.$$

Finally

$$u = - \frac{1}{1 - \frac{1}{c^2} \left[\frac{\sigma}{k} - U(z) \right]^2} \left\{ \left[U(z) - \frac{\sigma}{k} \right] \left(\frac{\partial}{\partial z} - \frac{g}{c^2} \right) \eta + \eta \frac{\partial U(z)}{\partial z} \right. \\ \left. \times \left[1 - \frac{\left(\frac{\sigma}{k} - U(z) \right)^2}{c^2} \right] \right\}. \quad (21)$$

For the slow class of waves $(\sigma/k - U(z))^2 \ll c^2$, and the total wind

$$U_T \cong U(z) + \left[\frac{\sigma}{k} - U(z) \right] \left(\frac{\partial}{\partial z} - \frac{g}{c^2} \right) \eta - \eta \frac{\partial U(z)}{\partial z} \quad (22)$$

Then

$$\left(\frac{\partial U_T}{\partial z} \right)^2 = \left\{ \frac{\partial U(z)}{\partial z} \left(1 - 2 \frac{\partial \eta}{\partial z} + \frac{g}{c^2} \eta \right) + \left[\frac{\sigma}{k} - U(z) \right] \frac{\partial^2 \eta}{\partial z^2} - \frac{\partial^2 U(z)}{\partial z^2} \eta \right\}^2.$$

Assuming no curvature in the profile of $U(z)$ and letting $\omega/k = (\sigma/k - U)$, where ω is the wave frequency noted by an observer drifting with the wind, and assuming $g/c^2 \ll \partial/\partial z$ as in GJR (1971), we have

$$Ri = R_L \frac{1 - \frac{\partial \eta}{\partial z}}{\left[1 - 2 \frac{\partial \eta}{\partial z} + \frac{\frac{\omega}{k}}{\frac{dU}{dz}} \frac{\partial^2 \eta}{\partial z^2} \right]^2}, \quad (23)$$

where $R_L = N_0^2 / (dU/dz)^2$.

By contrast, the corresponding GJR (1971) expression was

$$Ri = R_L \frac{1 - \frac{\partial \eta}{\partial z}}{\left[1 + \frac{\frac{\omega}{k}}{\frac{dU}{dz}} \frac{\partial^2 \eta}{\partial z^2} \right]^2} = R_L \frac{\left(1 - \frac{\partial \eta}{\partial z} \right)}{\left\{ 1 - n\eta \left[\frac{N_0^2}{\left(\frac{dU}{dz} \right)^2} - \frac{\omega^2}{\left(\frac{dU}{dz} \right)^2} \right]^{1/2} \right\}^2} \quad (24)$$

which assumed the background shear and wave-induced shears were, in effect, independent. The difference in the two expressions turns out to be minor and a plot of

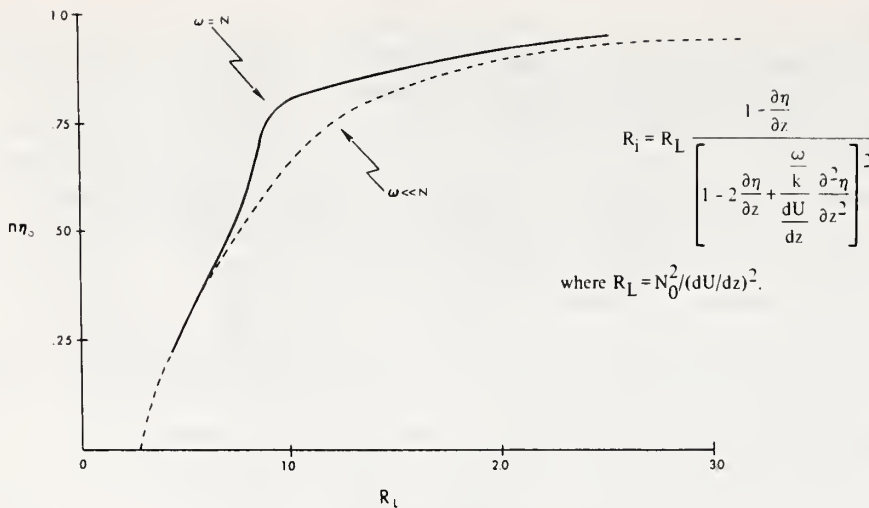


Fig. 9. Effect of shear on minimum Ri . Plot of $n\eta_0$ vs. Ri of unperturbed layer for condition that minimum $Ri=0.25$. See Equation (23).

R_L vs. $n\eta_0$ is shown in Figure 9 for the condition that $Ri=0.25$. In the figure, it has been assumed that solutions of the form $\eta=\eta_0 \cos(kx+nz-\sigma t)$ apply. The form of the wave equation (with shear) shows that this solution is applicable away from the critical level for layers in which $N/(U-\sigma/k)=\text{const.}$, or for layers in which the wind shear is small (then small R_L implies small thermal stability). Nearer the critical level, the appropriate solution has a height dependence given by Bessel functions of order $(\frac{1}{4}-R_L)^{1/2}$ (see Taylor, 1931).

Aside from the mathematical and physical complexity associated with the critical level, it may be concluded that the influence of background shear is mainly to enhance the reduction of Ri at some phase of the wave, and permit the onset of dynamic instability which may, in the case of untrapped waves propagating into a stable layer, produce lamina of intense, small-scale, turbulence-like structures. Although the above theoretical development is based on small-amplitude theory, while the actual calculations of Ri are based on a ratio of vertical wavelength to amplitude equal to about 8.4 (i.e., $n\eta_0=0.75$), we believe the calculated patterns to be essentially correct.

The distribution of Ri within the stable layer corresponding to Figures 3 and 8 is shown in Figures 10 and 11 with positive wind shear included such that $R_L=2.0$. Figure 11 illustrates the proposed mechanism of formation of nearly horizontal layers of reduced Ri created by untrapped waves. If $n\eta_0$ had been assumed to be 0.9 instead of 0.75, Ri would have been reduced to 0.25 at the crest or trough, depending on whether dU/dz was positive or negative.

The radar records have so far failed to reveal any important intensification of the echo near the crest or trough of trapped gravity waves. This lack of correlation of intensity with phase of the sinusoidal fluctuations in layer height is illustrated in

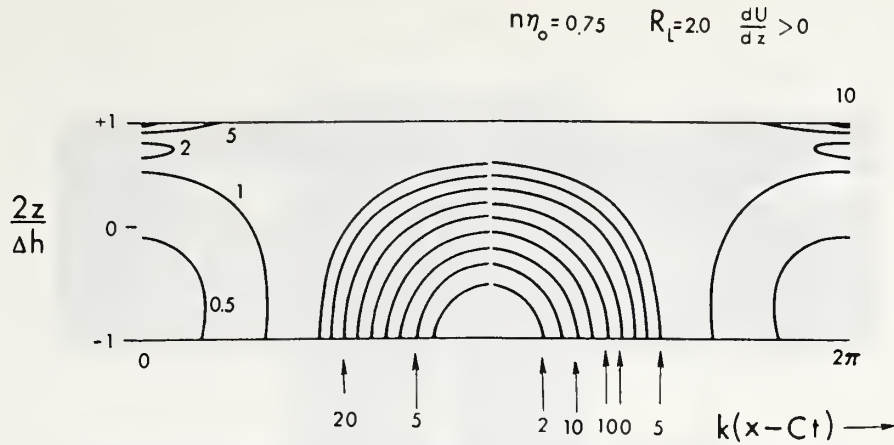


Fig. 10. Ri trapped waves. Same conditions as Figure 3 but assuming positive wind shear with $R_L = 2.0$. (Middle layer only).

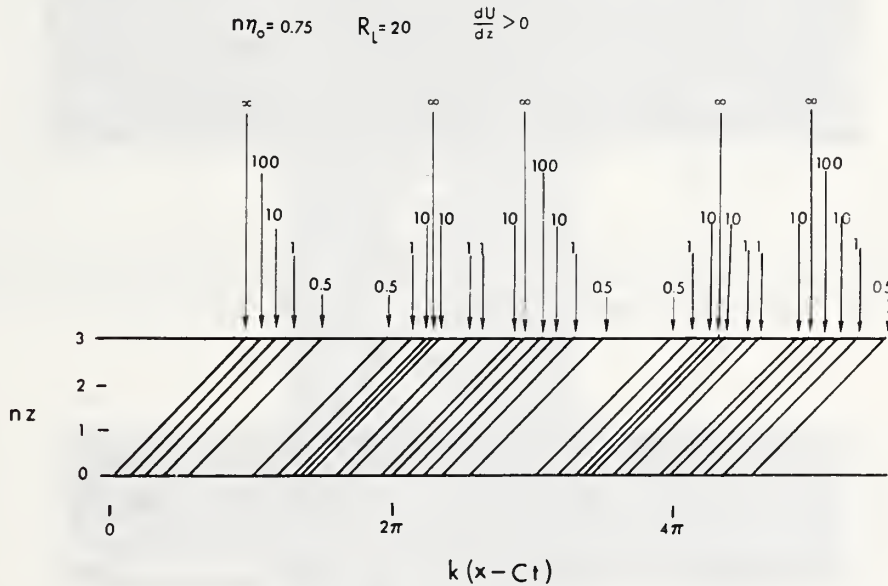


Fig. 11. Ri , untrapped waves. Same conditions as Figure 7 but assuming positive wind shear with $R_L = 2.0$.

Figure 12. The top frame of the figure shows the familiar thin lamina commonly revealed by the radar which are here attributed to low-frequency, untrapped gravity waves. These layers are perturbed in a more-or-less sinusoidal way by trapped, higher frequency gravity waves. In the lower frame, the same record is shown at reduced film exposure in order to reveal the braided fine structure of which the echo layers are composed. If the braiding were caused by instability resulting from self-induced

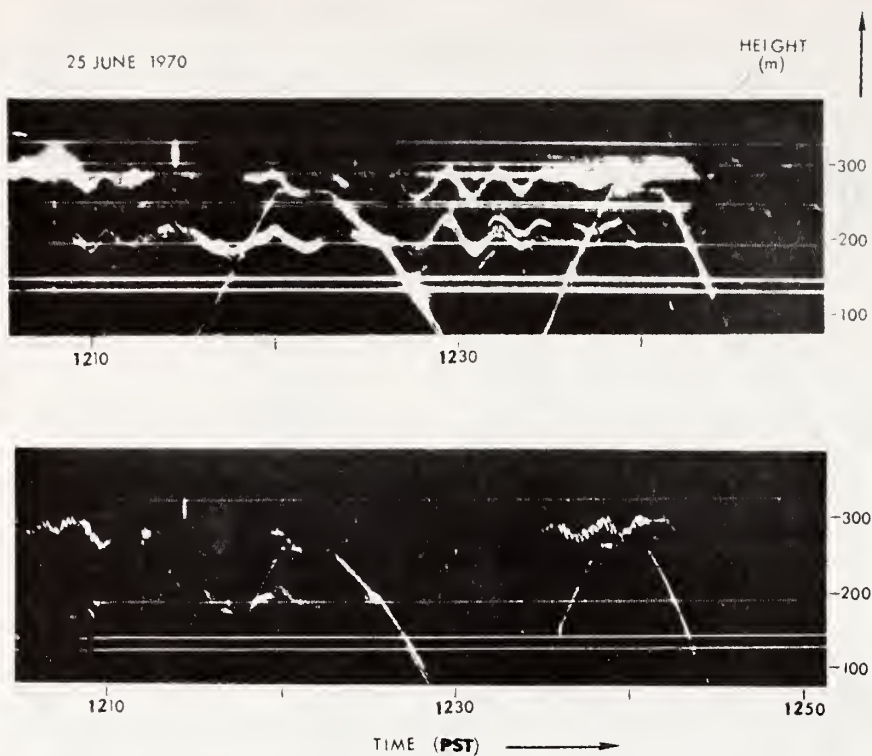


Fig. 12. Top frame shows gravity waves in which radar return is apparently not phase-related. Bottom frame shows same record with reduced film exposure and reveals Kelvin-Helmholtz sub-structure which apparently accounts for the radar return. Sloping straight lines are captive balloon echoes.

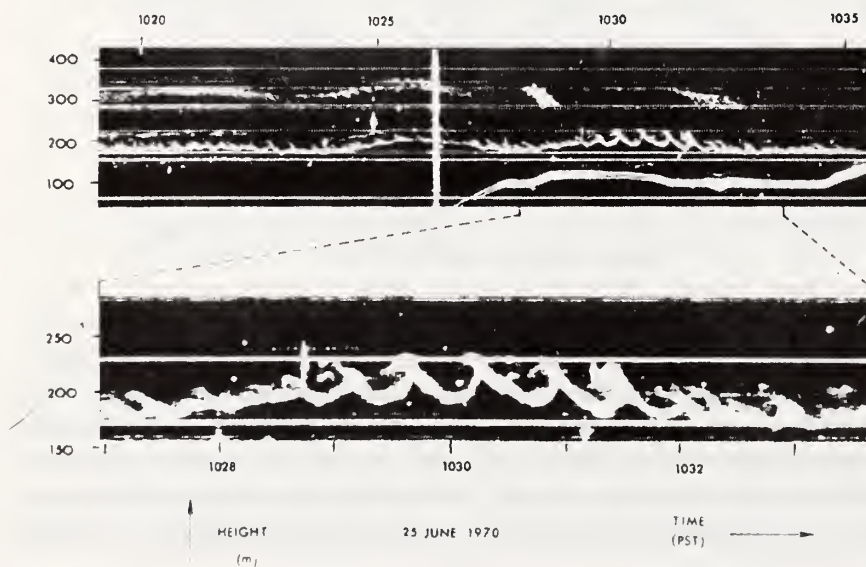


Fig. 13. Record that may illustrate the condition of Figure 10 for positive wind shear. Double trace at lower right is captive balloon echo.

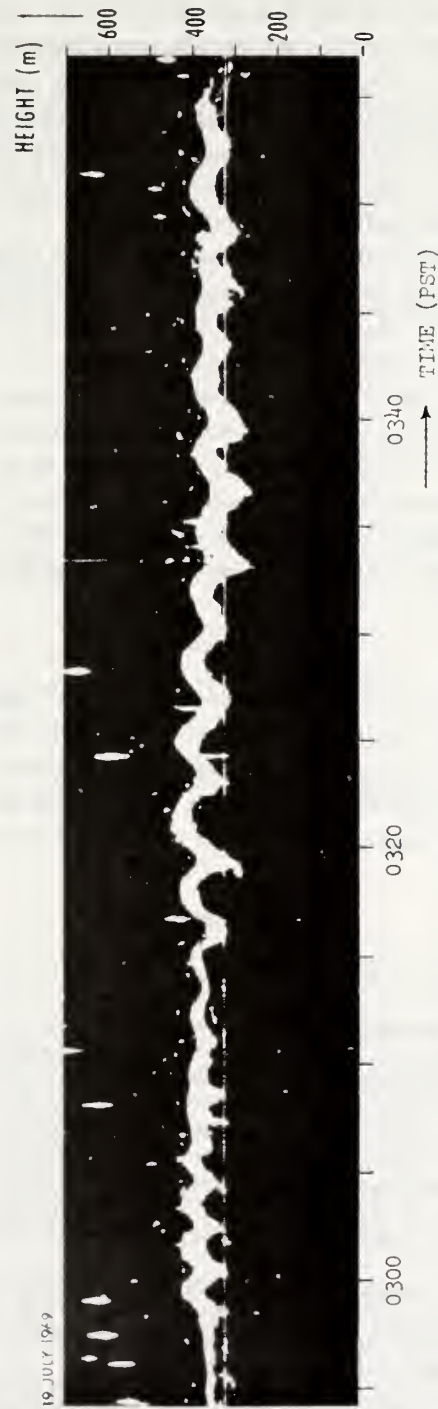


Fig. 14. Record that may illustrate the condition of Figure 10 for negative wind shear.

reduction of Ri in the trapped waves, it would be expected that these features would appear at the crests or at the troughs depending on the sign of the vertical wind shear. Although the radar records may show some slight enhancement of echo intensity at the crests, it is evident that the braiding occurs over the whole wave, regardless of phase. We therefore interpret this phenomenon to be produced by the untrapped wave effect which we suggested above to be a possible mechanism for the formation of the (turbulent?) lamina producing radar return. The horizontally propagating waves merely cause sinusoidal perturbations of these layers.

On the other hand, many large-scale, horizontally propagating waves show a 'breaking', which gives them an appearance similar to that of the fine-scale structures of Figure 12. Examples are shown in Figures 13 and 14. These figures often display ejection of plumes, or breaking at sharp crests or at troughs, respectively. Although the process is too complicated for easy interpretation, it seems likely that it is this characteristic which represents the effect of self-induced reduction in Ri within trapped waves. If this is the case, the pattern breaking upward may be an indication of positive wind shear and that breaking downward may indicate negative shear. This hypothesis can, and should, be verified experimentally. In practice, wind soundings are rarely obtained during an appropriate event because of their transient nature.

4. Conclusions

Wind shear evidently plays an important role in the kind of atmospheric wave motion revealed by high resolution radar. Self-induced reduction in Ri by the waves together with shear in the medium can account for most of the observed patterns. The lamina revealed by the radar are tentatively attributed to untrapped gravity waves propagating into statically stable height regions in the presence of vertical shear in the mean flow.

References

- Chimonas, G.: 1970, 'The Extension of the Miles-Howard Theorem to Compressible Fluids', *J. Fluid Mech.* **43**, 833–836.
- Emmanuel, C. B.: 1973, 'Richardson Number Profiles Through Shear Instability Wave Regions Observed in the Lower Planetary Boundary Layer', *Boundary-Layer Meteorol.*, in press.
- Georges, T. M.: 1972, Proc. of EPP-AGARD Specialists Meeting on 'Effects of Atmospheric Gravity Waves on Electromagnetic Wave Propagation', Wiesbaden, Germany, April 17–21, 1972.
- Gossard, E. E. and Munk, W.: 1954, 'On Gravity Waves in the Atmosphere', *J. Meteorol.* **11**, 259–269.
- Gossard, E. E. and Richter, J. H.: 1970, 'The Shape of Internal Waves of Finite Amplitude from High-Resolution Radar Sounding of the Lower Atmosphere', *J. Atmospheric Sci.* **27**, 971–973.
- Gossard, E. E. and Richter, J. H.: 1972, Proc. of EPP-AGARD Specialists Meeting on 'Effects of Atmospheric Gravity Waves on Electromagnetic Wave Propagation', Wiesbaden, Germany, April 17–21, 1972.
- Gossard, E. E., Jensen, D. R., and Richter, J. H.: 1971, 'An Analytical Study of Tropospheric Structure as Seen by High-Resolution Radar', *J. Atmospheric Sci.* **28**, 794–807.
- Gossard, E. E., Richter, J. H., and Atlas, D.: 1970, 'Internal Waves in the Atmosphere from High-Resolution Radar Measurements', *J. Geophys. Res.* **75**, 903–913.
- Hooke, W. H., Hall, F. F., Jr., and Gossard, E. E.: 1973, 'Observed Generation of an Atmospheric Gravity Wave by Shear Instability in the Mean Flow of the Planetary Boundary Layer', *Boundary-Layer Meteorol.*, in press.

- Miles, J. W.: 1961, 'On the Stability of Heterogeneous Shear Flows', *J. Fluid Mech.* **10**, 496-508.
- Miles, J. W. and Howard, L. N.: 1964, 'Note on Heterogeneous Shear Flow', *J. Fluid Mech.* **20**, 331-336.
- Orlanski, I. and Bryan, K.: 1969, 'Formation of the Thermocline Step Structure by Large Amplitude Internal Gravity Waves', *J. Geophys. Res.* **74**, 6975-6983.
- Richter, J. H.: 1969, 'High Resolution Tropospheric Radar Sounding', *Radio Sci.* **4**, 1261-1268.
- Richter, J. H. and Gossard, E. E.: 1970, 'Lower Tropospheric Structure as Seen by a High-Resolution Radar', Naval Electronics Lab. Center Technical Report 1718, p. 26.
- Stilke, G.: 1973, 'Occurrence and Features of the Ducted Modes of Internal Gravity Waves Over Western Europe and Their Influence on Microwave Propagation', *Boundary Layer-Meteorol.*, this issue, p. 493.
- Taylor, G. I.: 1931, 'Effect of Variation in Density on the Stability of Superposed Streams of Fluid', *Proc. Roy. Soc. A* **132**, 499-523.
- Thorpe, S. A.: 1968, 'On the Shape of Progressive Internal Waves', *Proc. Roy. Soc. London* **263**, 563-614.

OBSERVED GENERATION OF AN ATMOSPHERIC GRAVITY WAVE BY SHEAR INSTABILITY IN THE MEAN FLOW OF THE PLANETARY BOUNDARY LAYER

W. H. HOOKE, F. F. HALL, Jr., and E. E. GOSSARD

*Wave Propagation Laboratory, Environmental Research Laboratories, National Oceanic and
Atmospheric Administration, Boulder, Colo. 80302, U.S.A.*

(Received 8 August, 1972)

Abstract. Observations of a single boundary-layer event – the generation of an atmospheric gravity wave by an unstable shear flow at Haswell, Colorado on November 12, 1971 – are briefly described and discussed. The observations were made using: (a) an acoustic echo sounder, (b) anemometers mounted at two fixed levels on a 150-m tower, (c) an anemometer and a thermometer mounted on a movable carriage on the tower, and (d) a microbarograph array, including one microbarograph mounted atop the tower. The wave phase velocity ($\approx 3.5\text{--}4.0\text{ m s}^{-1}$) was found to equal the wind velocity in the middle of the shear flow, as assumed by other authors. The wave-associated vertical fluxes of momentum and energy measured just above the wave critical layer were estimated to be $\approx -5\text{ dyn cm}^{-2}$ and $\approx 800\text{ erg cm}^{-2}\text{ s}^{-1}$, respectively. These are large values. The annual average vertical flux of momentum at temperate and high latitudes is $\approx 0.25\text{ dyn cm}^{-2}$, while the average kinetic energy dissipation rate in a unit column of atmosphere is $\approx 5 \times 10^3\text{ erg cm}^{-2}\text{ s}^{-1}$. If the region of wave generation was itself propagating horizontally, its propagation velocity was large compared with the horizontal phase speed of the small-scale waves generated. Wave generation appeared to occur over an area large compared with the size of the microbarograph array (i.e., $\gg 2\text{ km}$).

1. Introduction

Recently, Emmanuel and co-workers (Emmanuel, 1973; Emmanuel *et al.*, 1972) have reported observations of gravity-wave generation by shear instability in the boundary-layer flow at Haswell, Colorado, during October of 1969. They used an acoustic echo-sounder and a 150-m tower instrumented with bivane anemometers and temperature sensors mounted at several fixed levels and on a movable carriage. By assuming that the wave phase velocity was equal to the wind velocity in the middle of the shear layer, they found that the observed horizontal wavelengths were in agreement with those predicted theoretically by Drazin (1958) and a number of later workers.

In the present note we describe the observation of a similar event at Haswell in the fall of 1971. As before, the event was observed using an acoustic echo-sounder and an instrumented tower. This time, however, we supplemented the anemometers and thermometers with a microbarograph atop the tower and a ground-based microbarograph array. We were thus able to measure directly the wave phase velocity and the wave-associated vertical fluxes of energy and horizontal momentum at the top of the tower, just above the height of wave generation. In the next section, we describe the observations of the boundary-layer wind and temperature profiles and the wave-associated pressure and wind fluctuations. We use these data to show that the boundary layer was dynamically unstable at the height of the observed wave generation,

to determine the wave parameters, and to estimate the wave-associated vertical fluxes of energy and horizontal momentum. In the third section we present the data from the ground-based microbarograph array.

2. Acoustic Echo-Sounder and Tower Observations

The experimental configuration is shown schematically in Figure 1. The acoustic echo-sounder, a second-generation version of the one used in the 1969 experiments, was located at the point marked A. Sensors on the movable carriage provided the

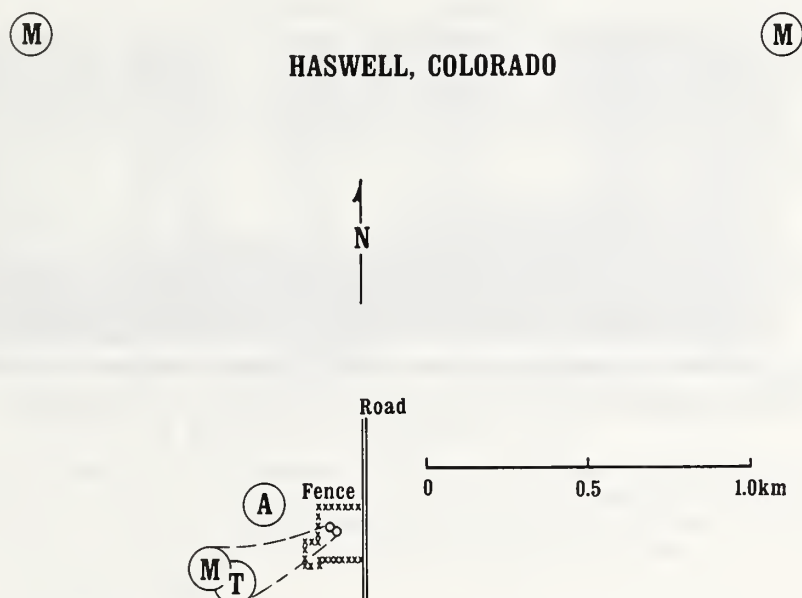


Fig. 1. The experimental configuration of the 1971 Haswell experiment. The acoustic echo-sounder was located at the point marked A. The instrumented tower was located at the point marked T. Microbarographs were located at the three points marked M, as well as at the top of the tower.

wind and temperature profiles used to determine the Richardson number of the flow; only the 150- and 2-m levels of the tower (marked T) were instrumented. There were no instruments at intermediate fixed levels, as had been the case at Haswell in 1969 (the 1971 experiment was in support of electromagnetic wave-propagation tests, with the boundary-layer studies given a lower priority); this proved to be unfortunate for reasons discussed later. Three microbarographs were located at the positions marked M; a fourth was installed atop the tower.

The acoustic echo-sounder was operated in a monostatic, or backscatter, mode with the antenna beam directed vertically. The sounder data were stored on facsimile records and on magnetic tape, so that the Doppler shift in the echo returns resulting from wave-associated vertical winds above the sounder could be measured in the

manner described by Beran *et al.* (1971); however, the Doppler data have not yet been analyzed. The microbarograph, anemometer, and thermometer data were also recorded on magnetic tape, as well as on paper strip charts.

The event to be described here occurred during the evening of November 12, 1971. The acoustic echo-sounder facsimile record for this interval is shown in Figure 2. Wave generation occurs between 1710 and 1730LT as evidenced on the facsimile record by the braided (or breaking wave, or cat's-eye) structure characteristic of this type of event (McAllister *et al.*, 1969; Gossard *et al.*, 1970; Emmanuel *et al.*, 1972); the wave period is ≈ 100 s. The raw microbarograph and anemometer records from

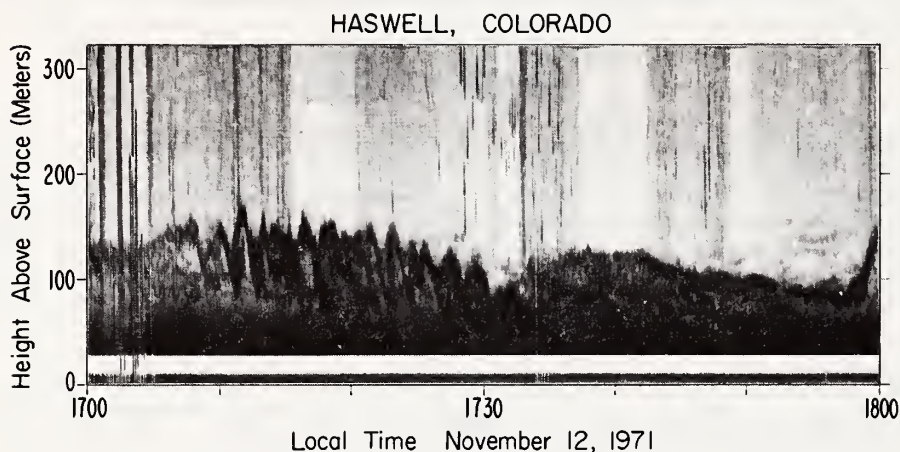


Fig. 2. The acoustic echo-sounder facsimile record for 1700-1800 LT, Nov. 12, 1971. Dark areas of the plot represent height-time intervals of strong echo returns. The event of interest is the breaking-wave structure evident between 1710 and 1730 LT at heights between 80 and 150 m. The wave period deduced from this record and the tower data was ≈ 100 s.

atop the tower ($z=150$ m) are shown in Figure 3a; the 100-s period wave-associated wind and pressure fluctuations are several times greater than the fluctuations in wind and pressure occurring before and after the event. Also shown in Figure 3a is the elevation angle of the surface wind, as recorded by an anemometer mounted at the 2-m level of the tower; it is included to show that the turbulence intensity in the surface boundary layer is considerably enhanced during the period of gravity-wave generation.

The movable carriage on the tower yielded two wind and temperature profiles during this event, shown in Figures 4 and 5. (Noise from the hoist motor shows as an increase in facsimile darkness in Figure 2.) Each carriage traverse of the tower requires roughly ten minutes, compared to the wave period of 100 s; thus the profiles may hardly be considered instantaneous, and most of the detailed height structure they reveal is in fact temporal variation. Nevertheless, the carriage data do suggest that the boundary-layer flow between the surface and the top of the tower divides rather naturally into three regions: a shear zone between 0 and 44 m, which might

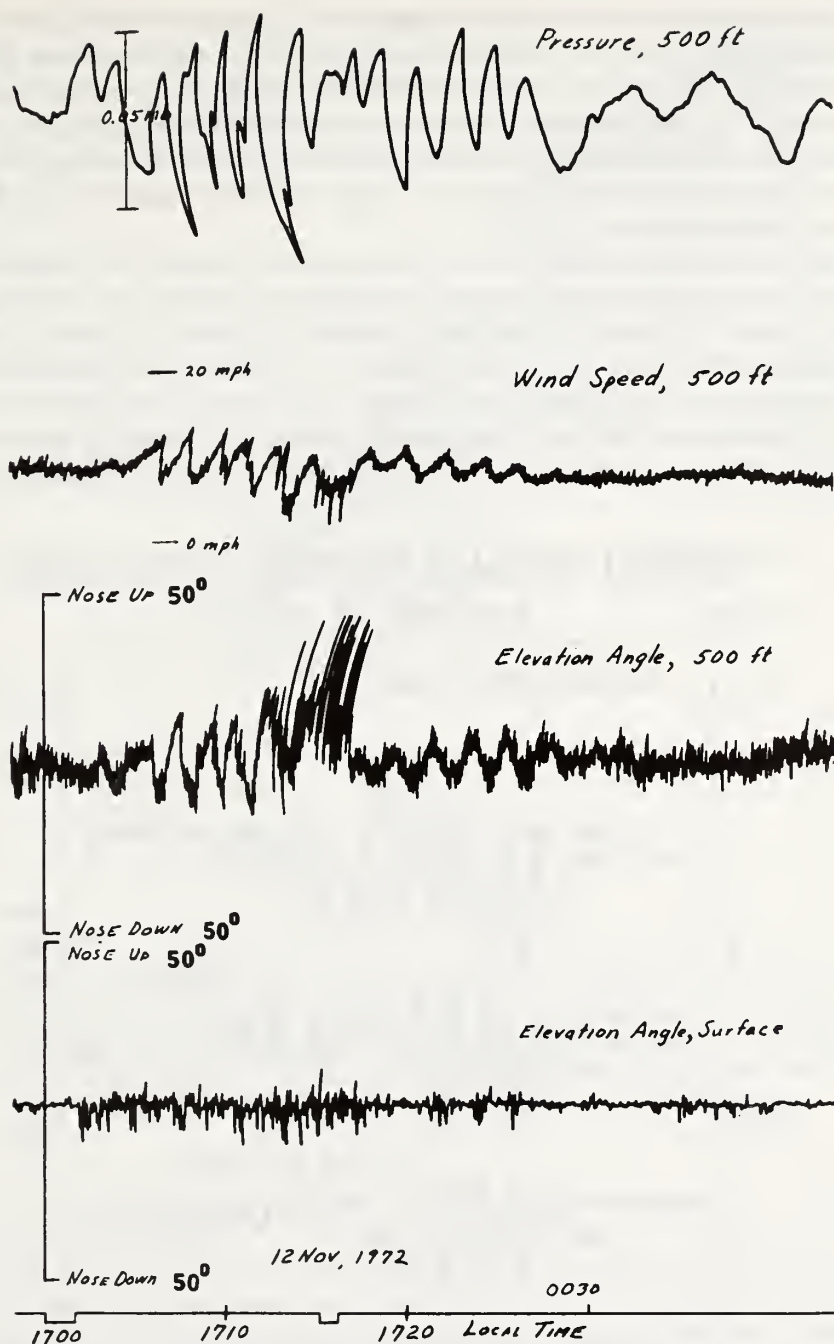


Fig. 3a. Raw microbarograph and anemometer records from the top of the 150-m tower, showing the large-amplitude perturbations in pressure and horizontal and vertical velocities accompanying the wave-generation event observed by the acoustic echo-sounder. The elevation angle of the surface wind recorded at a height of 2 m is also shown, to indicate that the wave generation was accompanied by an increase in the turbulence intensity of the surface boundary layer.

perhaps be identified as the surface boundary layer, a region of roughly constant wind speed between 44 and 100 m, and a second shear zone between 100 and 150 m. By averaging the two carriage traverses, we obtained the mean Richardson number Ri for each of the three boundary-layer regions; these are indicated in Figure 5. The very small values of Ri in the two shear zones suggest that the flow in the upper region was very probably dynamically unstable and that the surface boundary-layer flow was at least intermittently so.

The wave-associated fluctuations in wind speed and direction, as measured at the fixed level atop the tower, can be used to determine the direction of wave propagation (e.g., Gossard and Munk, 1954) and the results are shown in Figure 6. The wave propagation direction is found to be perhaps $5\text{--}15^\circ$ different from the wind direction in the shear zone. At present, we are unable to say whether this difference between the two directions is significant, since there is a great deal of variability in the apparent direction of wave propagation, and since the tower produces perturbations in the

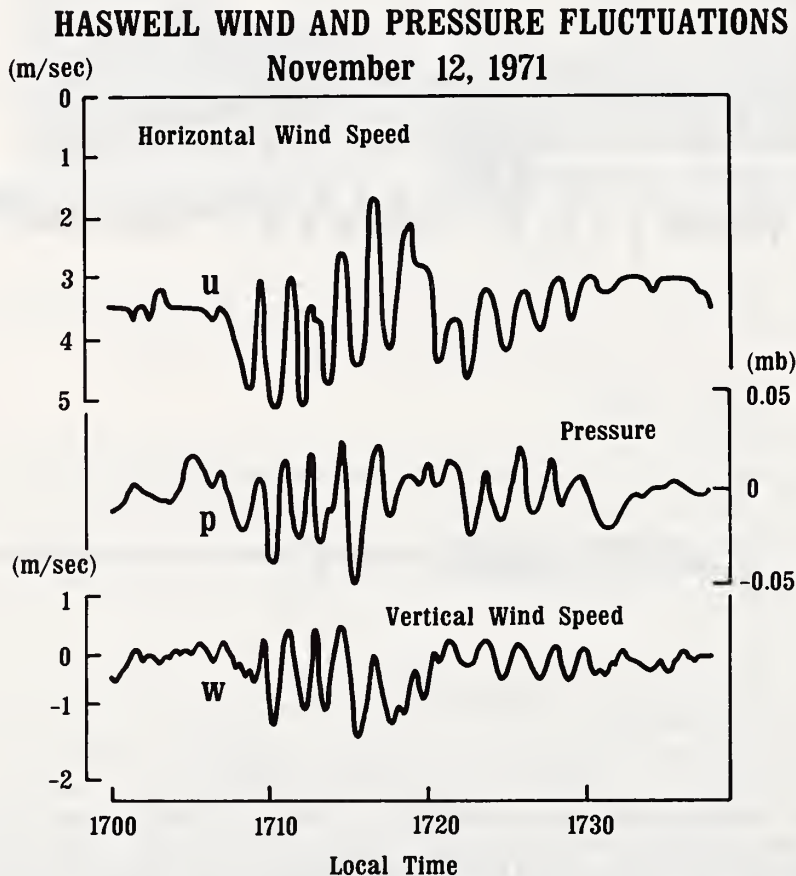


Fig. 3b. Microbarograph and anemometer records replotted on a rectilinear scale, to make it easier to discern the phase relations between the pressure and the wind fluctuations.

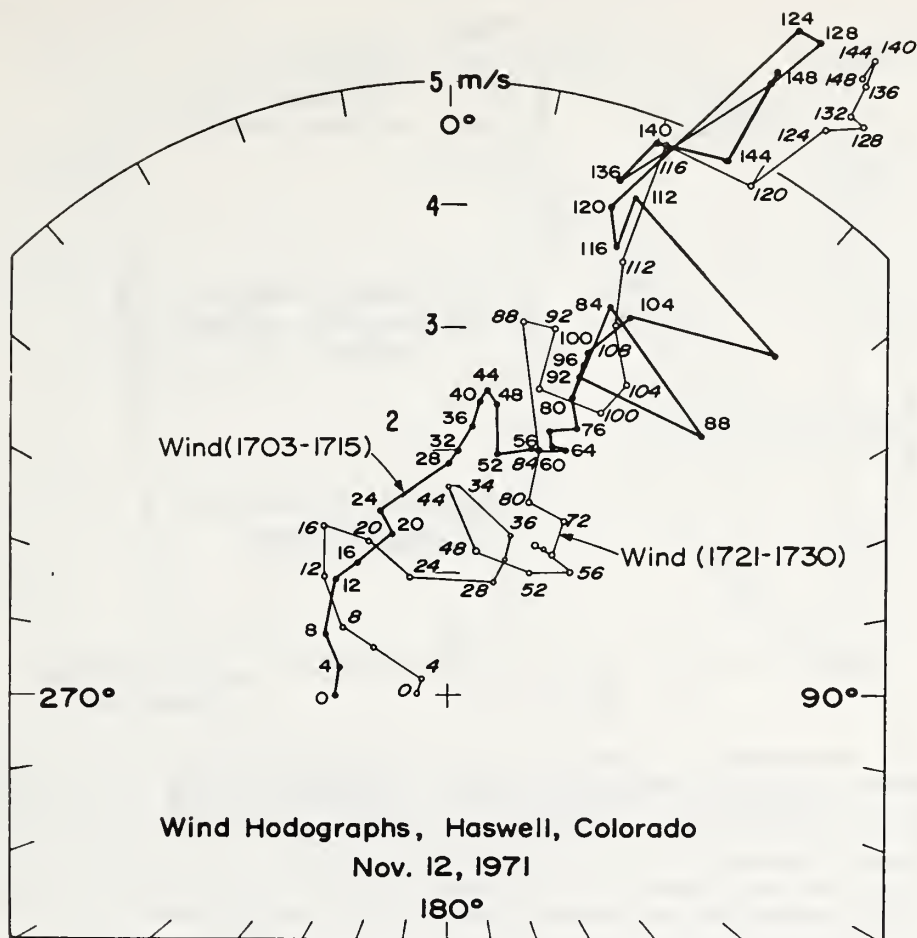


Fig. 4. Hodographs of the Haswell boundary-layer winds between the surface and 148 m during the wave-generation event, as obtained by a movable carriage mounted on the tower. The darker curve was taken from the carriage run up the tower between 1703 and 1715 LT; the lighter curve was taken from the carriage run down between 1721 and 1730 LT. The numbers beside the curves indicate the height; the points indicate the tip of the wind vector with its tail at the origin, in other words, the magnitude of the wind speed and the direction *toward which it blows* (the opposite to the meteorological convention).

airflow in its vicinity that may introduce spurious directional changes in the airflow with changes in wind speed.

Using the data described in the previous paragraphs and shown in the figures, we can obtain the wave phase velocity and the wave-associated vertical fluxes of energy and momentum at a height of 150 m. The horizontal wave phase speed can be determined from the so-called 'wave impedance relation' (Gossard and Munk, 1954), which gives

$$V_p = \frac{\Delta p}{\rho_0 \Delta u}. \quad (1)$$

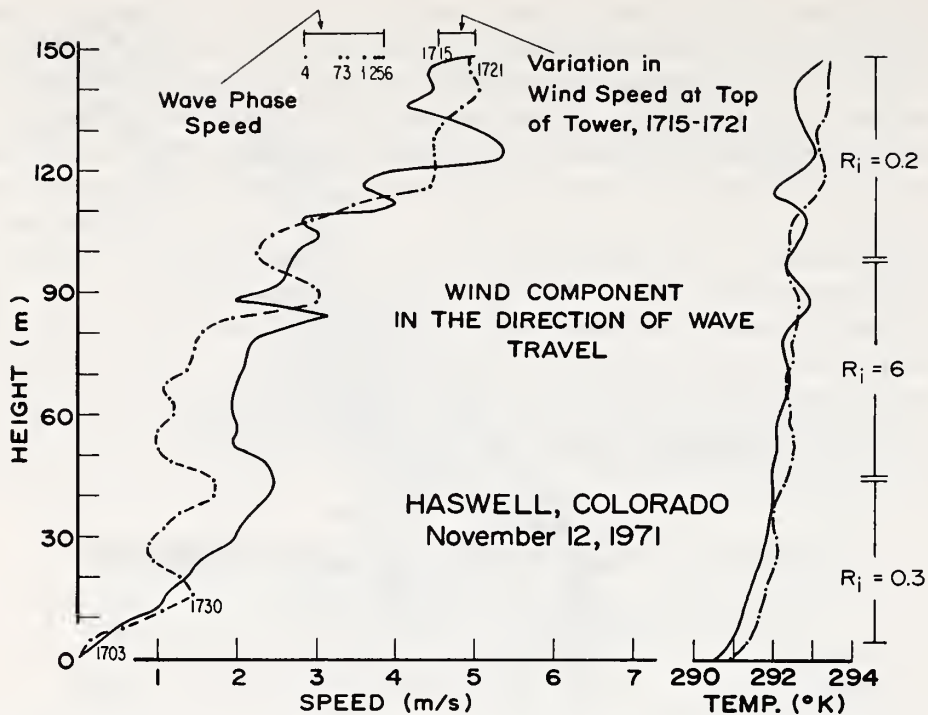


Fig. 5. Height profiles of temperature and the wind component in the direction of wave travel, as obtained by a movable carriage mounted on the tower. The solid curves pertain to the carriage run up the tower between 1703 and 1715 LT; the broken curves pertain to the carriage run down between 1721 and 1730 LT (The direction of wave propagation was taken from the analysis of Figure 6.) Also indicated are the range of the wind speed variation between 1715 and 1721 LT at the top of the tower, the wave phase speed as deduced for the wave cycles indicated, and the Richardson numbers Ri for the three boundary-layer zones discussed in the text. These values are averages for the two runs.

Here Δp and Δu are the wave-associated pressure and horizontal velocity perturbations, respectively, and ρ_0 is the background atmospheric density. It is important to note that V_p is *not* the horizontal wave phase speed measured relative to a frame of reference fixed with respect to the ground; rather it is the phase speed measured in a reference frame moving with the mean wind-speed component in the direction of wave propagation at the observation height. We can see immediately from the pressure and wind velocity traces of Figure 3b that the pressure and wind velocity fluctuations are in antiphase, so that relative to the ground, the wave phase speed is smaller than the wind speed at the height of observation. In the present case, the V_p values (estimated by reading crest-to-trough fluctuations in pressure and horizontal wind speed for successive wave cycles) lie between -0.8 and -1.9 m s^{-1} . As indicated in Figure 5, which shows height profiles of the wind component parallel to the direction of wave propagation, this implies a wave phase velocity *relative to an observer fixed at the ground* of 2.9 – 3.8 m s^{-1} (roughly 3.5 m s^{-1} on the average). Figure 5 also shows that the wave phase speed is very nearly equal to the mean wind speed in the upper

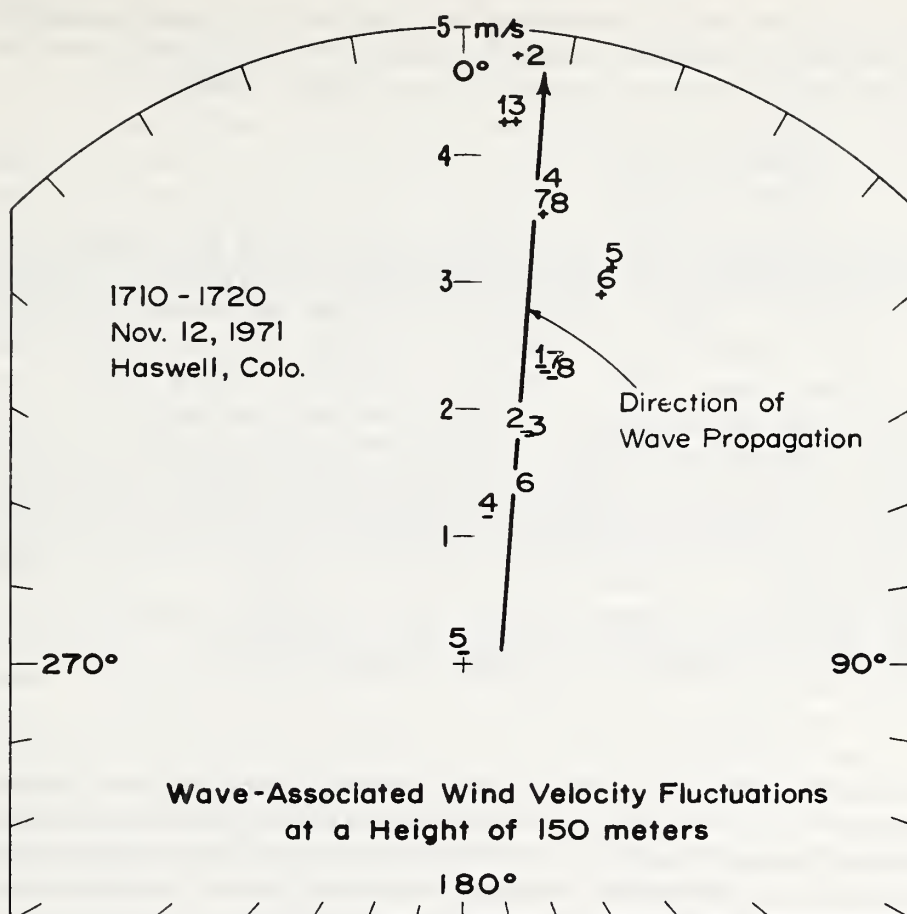


Fig. 6. Determination of the azimuthal direction of wave propagation from an examination of the fluctuation of the horizontal velocity vector of the wind at the top of the tower. The (+) signs indicate the position of the tip of the velocity vector at the wind maxima; the (-) signs indicate the position of the tip of the velocity vector at the wind minima. The numerals indicate the number of the wave cycle, and correspond to the numbers shown in Figure 5.

shear zone, i.e., the wave has a critical level ($V_p=0$) between 110 and 120 m. This agrees very closely with the center height of the braided structure on the acoustic echo-sounder facsimile record. Using the measured wave phase speed and period, we deduce a horizontal wavelength $\lambda \approx 350$ m for the wave; this wavelength falls just outside the neutral curve derived from Drazin's (1958) analysis and shown in Figure 4 of Emmanuel (1973). Considering the uncertainties in our estimate of the shear zone thickness, the governing Richardson number, and the other problem parameters as well as Drazin's assumption of a hyperbolic-tangent wind profile, we regard this agreement as satisfactory.

As a check on the consistency of the data, and the degree of confidence we should have in them, we have compared the observed ratio of the amplitudes of the hori-

zontal and vertical velocity perturbations with those predicted from the ratio of the wave frequency Ω measured in a frame of reference moving with mean wind at the observing height and the local value of the Brunt-Väisälä frequency N :

$$\left(\frac{N^2}{\Omega^2} - 1\right)^{1/2} = \frac{\Delta u}{\Delta w}. \quad (4)$$

The average value of the ratio $\Delta u/\Delta w$ is ≈ 1.2 , while the value of N estimated from Figure 5 is $\approx 2.7 \times 10^{-2} \text{ s}^{-1}$; when substituted into Equation (4), these values yield $\Omega \approx -1.7 \times 10^{-2} \text{ s}^{-1}$ (where the minus sign arises from the retrogression of wave phase relative to the wind at this height). On the other hand, $\Omega = 2\pi V_p/\lambda$; using $V_p \approx -1.4 \text{ m s}^{-1}$ and $\lambda \approx 350 \text{ m}$ yields $\Omega \approx -2.5 \times 10^{-2} \text{ s}^{-1}$. These values do not agree. However, the latter estimate of Ω is quite sensitive to the values of V_p and λ ; the extreme values measured were $V_p \approx -0.8 \text{ m s}^{-1}$ and $\lambda \approx 380 \text{ m}$, and these values yield $\Omega \approx -1.3 \times 10^{-2} \text{ s}^{-1}$. Considering the uncertainties inherent in the estimates of N and V_p , the observations appear to be consistent with a value for the wave phase speed relative to the ground of between 3.5 and 4.0 m s^{-1} and a horizontal wavelength of 350 to 400 m .

The wave-associated vertical flux of horizontal momentum may be expressed in terms of the horizontal and vertical velocity fluctuations as

$$P = \rho_0 \langle \Delta u \Delta w \rangle, \quad (2)$$

where the brackets indicate a time average. Again using the data of Figure 3, we find $P \approx -5 \text{ dyn cm}^{-2}$ at the top of the tower, where the minus sign indicates either a downward flux of positive momentum (directed parallel to the mean wind in the upper shear zone) or an upward flux of negative momentum. (The flux P was estimated by computing $\Delta u \Delta w$ products for twelve wave cycles.) Since the wave source is below this level, and since the wave phase progression is retrogressive relative to the mean wind at the top of the tower, it would seem most appropriate to interpret this as an upward flux of negative momentum.

The magnitude of P is quite large. To put it into perspective, recall that the annual average value of this quantity at temperate and high latitudes is $\approx 0.25 \text{ dyn cm}^{-2}$ (e.g., Palmén and Newton, 1969). Thus, to the extent that wave generation by shear instability is a relatively frequent event over regions of wide geographical extent, such events may account for a significant fraction of the total. The effect of the observed momentum flux should be to increase the momentum content of the boundary-layer below by an amount $\sim 5 \times 10^3 \text{ g cm}^{-1} \text{ s}^{-1}$ in a 10-min interval. The carriage data indicate, however, no significant change in the momentum content of the shear zone in which the wave was generated, and a *decrease* in the momentum content of the flow between roughly 50 and 100 m amounting to $\sim 2 \times 10^3 \text{ g cm}^{-1} \text{ s}^{-1}$ (as estimated from Figure 5).

The wave-associated vertical flux of energy E is usually defined in terms of the pressure fluctuations Δp and the vertical velocity fluctuations Δw by the expression

(e.g., Eckart, 1960)

$$E = \langle \Delta p \Delta w \rangle. \quad (3)$$

Using the data of Figure 3, we find $E \approx 800 \text{ erg cm}^{-2} \text{ s}^{-1}$ at the top of the tower, which is just above the wave critical layer. The fact that $E > 0$ implies that the wave source indeed lies below the height of measurement. (Apparently, then, the physics of this event is rather different from the August 6, 1969 event observed by Gossard *et al.* (1970) and discussed by Hines (1970).) Recently, Hines and Reddy (1970) have argued that in the presence of a mean flow, Equation (3) must be modified, E now being given by

$$E = \langle \Delta p \Delta w \rangle + \rho_0 U_0 \langle \Delta u \Delta w \rangle, \quad (4)$$

where U_0 is the background wind at the height of observation (although whether the source is above or below the observation height is still to be determined by the sign of $\langle \Delta p \Delta w \rangle$). The additional term reflects the coupling between the wave perturbation and the mean flow. Its value quite obviously depends upon the choice of reference frame in which it is measured, as does the kinetic energy of the background flow itself. For example, as measured in a reference frame moving with the wave, $\rho_0 U_0 \langle \Delta u \Delta w \rangle \approx -500 \text{ erg cm}^{-2} \text{ s}^{-1}$; as measured in a reference frame fixed with respect to the ground, $\rho_0 U_0 \langle \Delta u \Delta w \rangle \approx -2500 \text{ erg cm}^{-2} \text{ s}^{-1}$. Thus, in the ground-fixed reference frame, $E = -1700 \text{ erg cm}^{-2} \text{ s}^{-1}$. This, too, is a large value. It can be compared with the rate of kinetic energy dissipation per unit column of the atmosphere; Brunt (1939), for example, estimated this to be $\approx 5000 \text{ erg cm}^{-2} \text{ s}^{-1}$. It implies that in ten minutes or so, the kinetic energy content of the mean boundary-layer flow below the 150-m level should increase by about 10^6 erg cm^{-2} . In fact, examining Figures 4 and 5, we find a decrease, $\sim 2 \times 10^5 \text{ erg cm}^{-2}$.

The apparent discrepancies between the observed changes in the boundary-layer momentum and energy and those predicted from the wave-associated momentum and energy fluxes at 150 m are not as serious as they might at first seem. In the first place, the turbulent momentum and energy fluxes in the surface boundary layer were undoubtedly enhanced during the wave generation, as indicated in Figure 3a; if these were larger in magnitude than the 150-m fluxes, the results could be readily explained. In the second place, the wave-associated fluxes should affect the boundary-layer flow downstream from the observing site, rather than at the site itself. Finally, the estimates ignore mesoscale, reversible changes in the wind-shear profile that might be associated with gravity-wave motions of longer period and wavelength (see the discussion of Section 3).

It would therefore have been useful to have measured the turbulent fluxes of momentum and energy in the surface boundary layer. It would have been useful to have analyzed changes in the mean boundary-layer flow downstream from the site of wave generation. It would also have been of interest to have measured the wave-associated vertical fluxes of momentum and energy just beneath the wave critical level, since with this information we could have analyzed the energy and momentum budgets

of the upper shear zone and the zone with zero shear separately. We hope to improve our observations in at least some of these respects in further experiments currently contemplated, so as to elucidate better the role played by atmospheric gravity waves in the momentum and energy transports in the atmospheric circulation.

3. Observations from the Ground-Based Microbarograph Array

The pressure fluctuations associated with the waves generated by the shear flow instability are much stronger at the 150-m level than they are at the ground. Nevertheless, the event was detected at the surface, as shown in Figure 7, which reproduces the pressure traces from the three ground-based microbarographs (whose positions are indicated in Figure 1). In Figure 7a, the three pressure traces are shown individually. Each reveals large-amplitude fluctuations of rather long period (~ 10 min) associated with a wave motion of mesoscale (phase velocity $\approx 18 \text{ m s}^{-1}$; wavelength ≈ 22 km); in addition, each shows, for a 15- to 30-min interval, weak fluctuations of roughly 100-s period. The pressure fluctuations are largest in amplitude near the base of the tower; an overlay of the pressure traces from the base and the top of the tower shows the pressure fluctuations to be very nearly in phase, as shown in Figure 7b. However, there are uncertainties in the phase determination amounting to perhaps as much as $\pm 20^\circ$, and there is a phase shift $\approx 15^\circ$ introduced by the 20-m spacing between the surface microbarograph and the base of the tower.

Figure 7c shows the three surface microbarograph records overlaid and time-shifted by an amount corresponding to the 3.5 m s^{-1} phase speed of the smaller-scale waves; it is impossible to see any evidence of a peak-to-peak correlation, suggesting that the array spacing was an order of magnitude too large to measure the micro-scale wave phase speed directly. What is interesting about Figure 7c is that it indicates little if any overlap of even the disturbed intervals on the three records. To improve the overlap of the disturbed intervals, it is necessary to use much smaller time shifts. For example, the time shifts required to maximize the cross-correlation of the pressure fluctuations of roughly a 10-min period also provide good overlap of the disturbed intervals, as shown in Figure 7d; these yield a propagation velocity of $\approx 18 \text{ m s}^{-1}$ from 210° . One possibility, then, is that the microscale waves generated by the shear instability were highly dispersive, with a group velocity much higher than the wave phase speeds; this is quite unlikely. Another possibility is that the wave generation resulted from the passage, at relatively high speeds, of mesoscale waves, which perturbed the stability of the very nearly unstable boundary-layer shear flow in the course of their propagation. This interpretation would be in conformance with theoretical notions concerning the origins of the so-called 'intermittency' of atmospheric turbulence put forth by Phillips (1966), Gossard *et al.* (1971), Chimonas (1972), and others, and it is not inconsistent with the reappearance of wave generation events of the type described here at half-hour intervals or so for several hours. Unfortunately the response of the microbarographs we used falls off very rapidly at low frequencies, making it impossible to detect wave motions of such long periods. We hope to con-

MICROBAROGRAPH RECORDS Haswell Colo. Nov. 12, 1971

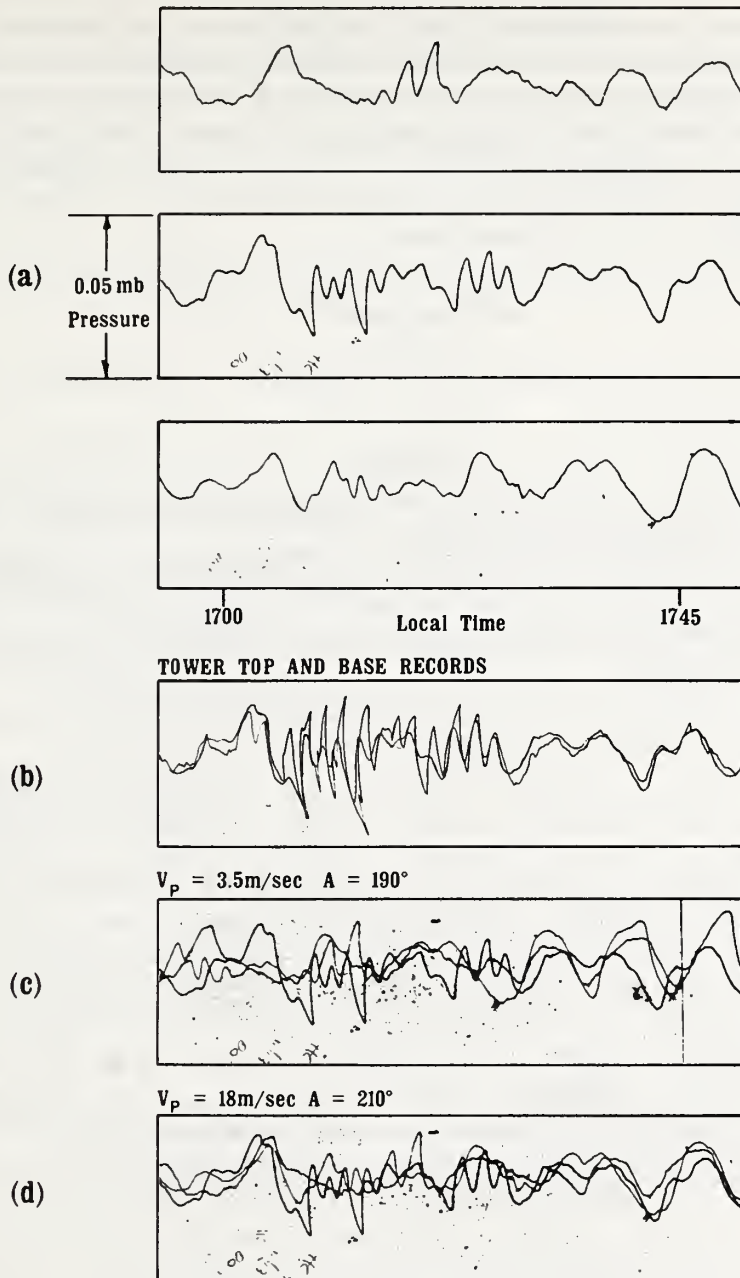


Fig. 7. Surface microbarograph records. (a) The three records displayed individually, each revealing oscillations of roughly 10-min period throughout the observing interval, and oscillations of roughly 100-s period for a 15- to 30-min interval. (b) The records from the top and the base of the tower superimposed. (c) The three surface records superimposed and time-shifted to correspond to a 3.5 m s^{-1} propagation velocity. (d) The three surface records superimposed and time-shifted to maximize the cross-correlation of the 10-min period oscillations; the phase velocity thus determined is $\approx 18 \text{ m s}^{-1}$ from 210° .

firm or reject such an interpretation by using pressure sensors with improved low-frequency response in future work. In addition, we intend to decrease the array spacing in order to determine more accurately the propagation velocity of the region of generation. The present data do appear good enough to suggest that the region of wave generation is propagating with a velocity $> 10 \text{ m s}^{-1}$, however. Together with the fact that the generation persists for 10 min or more, this implies a region of dynamical instability $> 6 \text{ km}$ in horizontal extent.

Acknowledgement

G. E. Greene, R. W. Krinks, and B. C. Willmarth aided in various aspects of the data acquisition and analysis.

References

- Beran, D. W., Little, C. G., and Willmarth, B. C.: 1971, 'Acoustic Doppler Measurements of Vertical Velocities in the Atmosphere', *Nature* **230**, 160–162.
- Brunt, D.: 1939, *Physical and Dynamical Meteorology*, Cambridge University Press, Cambridge.
- Chimonas, G.: 1972, 'The Stability of a Coupled Wave-Turbulence System in a Parallel Shear Flow', *Boundary-Layer Meteorol.* **2**, 444–452.
- Drazin, P. G.: 1958, 'The Stability of a Shear Layer in an Unbounded Heterogeneous Inviscid Fluid', *J. Fluid Mech.* **4**, 214–224.
- Eckart, C.: 1960, *Hydrodynamics of Oceans and Atmospheres*, Pergamon Press, London.
- Emmanuel, C. B.: 1973, 'Richardson Number Profiles Through Shear Instability Wave Regions Observed in the Lower Planetary Boundary Layer', *Boundary-Layer Meteorol.* **5**, 19–27.
- Emmanuel, C. B., Bean, B. R., McAllister, L. G., and Pollard, J. R.: 1972, 'Observations of Helmholtz Waves in the Lower Atmosphere with an Acoustic Sounder', *J. Atmospheric Sci.* **29**, 886–892.
- Gossard, E. E. and Munk, W. H.: 1954, 'On Gravity Waves in the Atmosphere', *J. Meteorol.* **11**, 259–269.
- Gossard, E. E., Richter, J. H., and Atlas, D.: 1970, 'Internal Waves in the Atmosphere from High-Resolution Radar Measurements', *J. Geophys. Res.* **75**, 3523–3536.
- Gossard, E. E., Jensen, D. R., and Richter, J. H.: 1971, 'An Analytical Study of Tropospheric Structure as Seen by High-Resolution Radar', *J. Atmospheric Sci.* **28**, 794–807.
- Hines, C. O.: 1970, 'Comments on Paper by E. E. Gossard and J. H. Richter, and D. Atlas, 'Internal Waves in the Atmosphere from High Resolution Radar Measurements'', *J. Geophys. Res.* **75**, 5956–5959.
- Hines, C. O. and Reddy, C. A.: 1970, 'On the Propagation of Atmospheric Gravity Waves through Regions of Wind Shear', *J. Geophys. Res.* **72**, 1015–1034.
- McAllister, L. G., Pollard, J. R., Mahoney, A. R., and Shaw, P. J. R.: 1969, 'Acoustic Sounding – A New Approach to the Study of Atmospheric Structure', *Proc. IEEE* **57**, 579–587.
- Palmén, E. and Newton, C. W.: 1969, *Atmospheric Circulation Systems*, Academic Press, New York.
- Phillips, O. M.: 1966, *The Dynamics of the Upper Ocean*, Cambridge University Press.

Reprinted with permission from Boundary Layer Meteorology
Vol. 4, 311-322, 1973.

GENERATION AND DISSIPATION OF MICROWAVE REFRACTIVE-INDEX FLUCTUATIONS IN THE BOUNDARY LAYER

P. A. MANDICS

*Wave Propagation Laboratory, Environmental Research Laboratories, National Oceanic and
Atmospheric Administration, Boulder, Colo. 80302, U.S.A.*

(Received 5 September, 1972)

Abstract. The index of refraction and its short-term variations have been measured on a 152-m meteorological tower at three fixed levels and on a moveable platform. Analysis of the data reveals that the time rates of production and dissipation of refractivity fluctuations are approximately in balance under a variety of meteorological conditions, and that changes in the rate of dissipation usually coincide with comparable changes in the rate of production. Under reasonably stationary conditions, terms corresponding to the rate of change and vertical diffusion of refractivity variance are found to be negligible. Power spectral densities of the variations increase when the rate of generation (and dissipation) increase, and conversely. Comparison of the results with simultaneous acoustic sounder returns provides a valuable insight into the mechanisms responsible for changes in the rates of production and dissipation.

1. Introduction

Temporal and spatial variations of the index of refraction at radio wavelengths are of interest to specialists working in a wide variety of fields. For example, random fluctuations of refractive index cause errors in radar tracking of space vehicles (Barton and Ward, 1969) and degrade the performance of millimeter-wave communications links (Roche *et al.*, 1970). In a markedly different application, Shen (1970) uses refractive-index perturbations of the same kind to infer, by remote measurements, wind velocity and its variations along a line-of-sight propagation path.

Although the radio refractive index depends on pressure, temperature, and humidity in the lower atmosphere, its fluctuations are due mainly to changes in humidity and temperature; the effects of pressure variations are negligible. By assuming that the time rates of production and destruction of refractive-index inhomogeneities are equal and that the turbulent flow is stationary, Tatarski (1961) obtained an expression for the refractive-index structure parameter C_n (a quantity essentially indicating the strength of refractive-index variations) in terms of measurable mean field quantities such as the gradient of the wind velocity and potential refractivity.

This paper examines in more detail the various terms appearing in the budget of refractivity variance. In addition to evaluating the time rates of production and dissipation of refractivity fluctuations from experimental data, we also estimate the rate of change and vertical diffusion of the variance of refractivity. The data are analyzed along with simultaneous acoustic echo-sounder returns obtained nearby. Even though the acoustic sounder (in the present configuration) responds only to

temperature fluctuations, its description of the atmospheric turbulence structure proves to be a valuable guide in interpreting the data.

2. Theoretical Background

Recognizing the fact that the generation of refractive-index inhomogeneities depends to a large extent on the gradient of the so-called potential refractive index, we first derive an expression for this gradient in terms of measured quantities. An equation for the budget of refractive-index variance is developed next.

Bean and Dutton (1968) showed that at radio frequencies:

$$N = (n - 1) 10^6 = \frac{77.6}{T} \left(P + \frac{4810e}{T} \right), \quad (1)$$

where n is the refractive index, N is the refractivity in N units (ppm in n), T is the absolute temperature in K , P is the total pressure in millibars (mb), and e is the partial pressure of water vapor in millibars. By introducing the potential temperature

$$\Theta \approx T + \gamma_a z \quad (2)$$

(here γ_a is the adiabatic lapse rate, $\gamma_a = 0.0098 \text{ K m}^{-1}$ and z is the height above the surface in meters) and the specific humidity

$$q \approx 0.622 e/P, \quad (3)$$

we can recast Equation (1) as

$$\begin{aligned} N &= \frac{77.6 P}{\Theta - \gamma_a z} \left(1 + \frac{7733 q}{\Theta - \gamma_a z} \right) \\ &= N[z, P(z), \Theta(z), q(z)]. \end{aligned} \quad (4)$$

Note that both Θ and q are conservative (that is, they remain constant when subjected to adiabatic temperature changes). Horizontal homogeneity is assumed here; the various quantities in Equation (4) depend only on the vertical space coordinate z .

The gradient of refractivity thus reduces to

$$\frac{dN}{dz} = \frac{\partial N}{\partial z} + \frac{\partial N}{\partial P} \frac{dP}{dz} + \frac{\partial N}{\partial \Theta} \frac{d\Theta}{dz} + \frac{\partial N}{\partial q} \frac{dq}{dz}. \quad (5)$$

Tatarski (1961, p. 57) points out that when a parcel of air is displaced adiabatically in the vertical direction by turbulent mixing, changes in N occur only due to the last two terms in Equation (5). It is, therefore, convenient to express the mean vertical gradient of (generalized) potential refractivity (Ottersten, 1969) as

$$\frac{d\phi}{dz} \approx \frac{\partial N}{\partial \Theta} \frac{d\Theta}{dz} + \frac{\partial N}{\partial q} \frac{dq}{dz}. \quad (6)$$

Note that ϕ is defined in such a manner that it does not vary with height in an adia-

batic atmosphere (see Bean and Dutton, 1968). Because dN/dz is measured, we may write for $d\phi/dz$

$$\begin{aligned}\frac{d\phi}{dz} &\approx \frac{dN}{dz} - \left(\frac{\partial N}{\partial z} + \frac{\partial N}{\partial P} \frac{dP}{dz} \right) \\ &\approx \frac{dN}{dz} - \frac{77.6 P}{T^2} \left\{ \gamma_a - \frac{g}{R} + 7733 \left(2\gamma_a - \frac{g}{R} \right) \frac{q}{T} \right\},\end{aligned}\quad (7)$$

where Equation (4), the barometric equation $dP/dz = -g\rho$, and the equation of state $P = R\rho T$, have been used (here g is the acceleration due to gravity, $g = 9.81 \text{ m s}^{-2}$, ρ is the air density, and R is the gas constant, $R = 287 \text{ J (kg)}^{-1} \text{ K}^{-1}$, for dry air). Using measured values of dN/dz , P , T , and q , we may evaluate $d\phi/dz$ from Equation (7).

Up to this point the time dependence of ϕ has not been considered. Time-dependent variations of ϕ may be studied by introducing the diffusion equation (Landau and Lifshitz, 1959),

$$\frac{\partial \phi}{\partial t} + \frac{\partial}{\partial x_i} \left(\phi v_i - D \frac{\partial \phi}{\partial x_i} \right) = 0, \quad (8)$$

where $v_i = (v_1, v_2, \text{ and } v_3)$ represent the three orthogonal components of the wind velocity (here v_1, v_2 , and v_3 are the longitudinal, lateral, and vertical components of the wind, respectively), and D is the molecular diffusion coefficient of ϕ . Let

$$\phi = \bar{\phi} + \phi'$$

and

$$v_i = \bar{v}_i + v'_i,$$

where the overbar indicates an average and the primed quantities denote fluctuations about this average ($\overline{\phi'} = \overline{v'_i} = 0$ by definition). Substituting the above quantities into Equation (8) and averaging yields

$$\frac{\partial \bar{\phi}}{\partial t} + \frac{\partial}{\partial x_i} \left(\bar{\phi} \bar{v}_i + \overline{\phi' v'_i} - D \frac{\partial \bar{\phi}}{\partial x_i} \right) = 0. \quad (9)$$

Next, subtract Equation (9) from Equation (8)

$$\frac{\partial \phi'}{\partial t} + \frac{\partial}{\partial x_i} \left(\phi' \bar{v}_i + \bar{\phi} v'_i + \phi' v'_i - \overline{\phi' v'_i} - D \frac{\partial \phi'}{\partial x_i} \right) = 0. \quad (10)$$

Multiplying by ϕ' and averaging results in

$$\frac{1}{2} \frac{\partial}{\partial t} \overline{\phi'^2} + \frac{1}{2} \frac{\partial}{\partial x_i} (\overline{\phi'^2 \bar{v}_i} + \overline{\phi'^2 v'_i}) + \overline{\phi' v'_i} \frac{\partial \bar{\phi}}{\partial x_i} - \overline{\phi' \frac{\partial}{\partial x_i} \left(D \frac{\partial \phi'}{\partial x_i} \right)} = 0, \quad (11)$$

where it was assumed that the fluid is incompressible, i.e., $\partial v_i / \partial x_i = 0$. Several additional assumptions are needed to simplify further the above equation: (1) the motion is

horizontally homogeneous; (2) the mean flow is horizontal and depends only on the height above the ground; and (3) transport by molecular action can be neglected, i.e.

$$\frac{\partial}{\partial x_i} \left(\phi' D \frac{\partial \phi'}{\partial x_i} \right) = 0.$$

Equation (11) thus becomes

$$\frac{1}{2} \frac{\partial}{\partial t} \overline{\phi'^2} + \frac{1}{2} \frac{\partial}{\partial x_3} \overline{\phi'^2 v'_3} + \overline{\phi' v'_3} \frac{\partial \bar{\phi}}{\partial x_3} + D \left(\frac{\partial \phi'}{\partial x_i} \right)^2 = 0. \quad (12)$$

Because the fluctuations in ϕ and N are identical, it is permissible to replace ϕ' by N' . Also let $x_3 = z$, $v'_3 = w'$, and $D(\partial \phi' / \partial x_i)^2 = G_N$. Equation (12) finally takes the form

$$\frac{1}{2} \frac{\partial}{\partial t} \overline{N'^2} + \frac{1}{2} \frac{\partial}{\partial z} \overline{w' N'^2} + \overline{w' N'} \frac{\partial \bar{\phi}}{\partial z} + G_N = 0. \quad (13)$$

The first term above corresponds to the time rate of change of the variance of the refractivity fluctuations. The rate of vertical diffusion of the fluctuations is represented by the second term. The third term, consisting of the product of the refractivity flux $\overline{w' N'}$ and the gradient of potential refractivity, is related to the rate of production of N variations. The last term gives the time rate of dissipation of the refractivity inhomogeneities.

While it is possible to calculate (or at least estimate) the magnitude of the first three terms in Equation (13), G_N cannot be evaluated directly from the experimental data. Recalling the relation for the structure function of a conservative passive additive (Tatarski, 1961),

$$D(r) = a \varepsilon^{-1/3} G r^{2/3}, \quad (14)$$

we may write for the rate of dissipation

$$G_N = D_N(r) a^{-1} \varepsilon^{1/3} r^{-2/3}, \quad (15)$$

where $D_N(r) = \overline{[N(\mathbf{r}_1) - N(\mathbf{r}_2)]^2}$ is the structure function of the refractivity, $r = |\mathbf{r}_1 - \mathbf{r}_2|$ is the separation between the two observation points, ε is the rate of dissipation of turbulent energy, and a is a constant, $a \approx 3.2$ (Wyngaard and Coté, 1971). We assume that the turbulent flow is both homogeneous and isotropic. The structure function of the horizontal wind

$$D_u(r) = b \varepsilon^{2/3} r^{2/3} \quad (16)$$

may be used to determine ε . Here b is a constant, $b \approx 2.0$ (Panofsky, 1969).

3. Experimental Results

The data are obtained from a 152-m meteorological tower situated in the middle of a 20-km bowl-like depression in south-eastern Colorado, near Haswell. Three fixed

levels (at 39, 95, and 151 m) and a moveable platform (the 'carriage'), capable of travelling from the bottom of the tower to the top in about 11 min, are instrumented to measure refractivity, temperature, wind velocity, relative humidity, and pressure.

Simultaneous acoustic soundings are made 240 m away from the tower to obtain information about the structure of the lower few hundred meters of the atmosphere. The sounder (McAllister *et al.*, 1969) operates in the backscatter mode at 950 Hz and emits 20 ms pulses (8 W of radiated acoustic power) at 2-s intervals. The returns are recorded by a facsimile recorder as intensity modulation of the paper.

Refractivity variations are detected by measuring changes in the resonant frequency (nominally $f \approx 10$ GHz) of a microwave sampling cavity exposed to the free atmosphere. The overall accuracy of the instrument is 0.1 N unit and it is capable of fully resolving refractivity variations separated by 0.75 m (Gilmer *et al.*, 1965). Thermocouples consisting of welded, 2-mil copper-constantan junctions measure the air temperature. Their accuracy is 0.1 °C, and they have a uniform response from dc to 10 Hz. The wind velocity is measured with propeller-driven anemometers attached to bidirectional vanes; the distance constant of the propellers is 0.75 m, and for wind speeds over 2.7 m s⁻¹ all wind direction fluctuations up to 0.5 Hz are recorded accurately. Variable resistance barium fluoride elements deposited on glass strips are used to measure relative humidity to better than a 2% accuracy. Atmospheric pressure and its slower variations are recorded by microbarographs on paper chart.

After preprocessing by appropriate signal conditioning equipment, the data are recorded on analog magnetic tape. Subsequently, the recorded information is prepared for computer analysis by digitizing at the rate of 5 samples per second and re-recording on IBM-compatible digital tape.

Figure 1 illustrates two 50-min data samples taken from the morning of 1969 September 20. Although several different averaging times have been tried, 2-min detrended (mean and linear trend are removed) data averages are plotted here mainly because they give reasonably reliable statistical estimates and still allow us to resolve some of the finer atmospheric structures encountered. Solid lines are the rate of destruction of refractivity fluctuations, evaluated with the help of Equations (15) and (16). Because the sensors provide only a point measurement of the desired meteorological quantities, it is necessary to invoke Taylor's hypothesis and replace space lags with time lags to evaluate the structure function of refractivity and horizontal wind. This means that $r = \bar{u}\tau$ is substituted into Equations (15) and (16), where \bar{u} is the mean horizontal wind flow and τ is the time lag ($\tau = 1$ s, usually).

The rate of generation of refractivity variations $\overline{w'N'}(\partial\bar{\phi}/\partial z)$ is indicated by dashed lines in Figure 1. Although $\overline{w'N'}$ can be evaluated in a straightforward manner from the data, the same is not true for $\partial\bar{\phi}/\partial z$. Normally the gradient of refractivity dN/dz is determined from N profiles, which are obtained from carriage traverses made about twice (sometimes three times) every hour; the gradient $\partial\bar{\phi}(z, t)/\partial z \equiv d\phi(z)/dz$ is then evaluated from Equation (7). Here it is assumed that no significant changes occur in the refractivity profile during the 11-min carriage traverse. Although intervening values of $\partial\bar{\phi}/\partial z$ are determined by linear interpolation, this procedure is considered to

HASWELL, COLORADO
20 September 1969

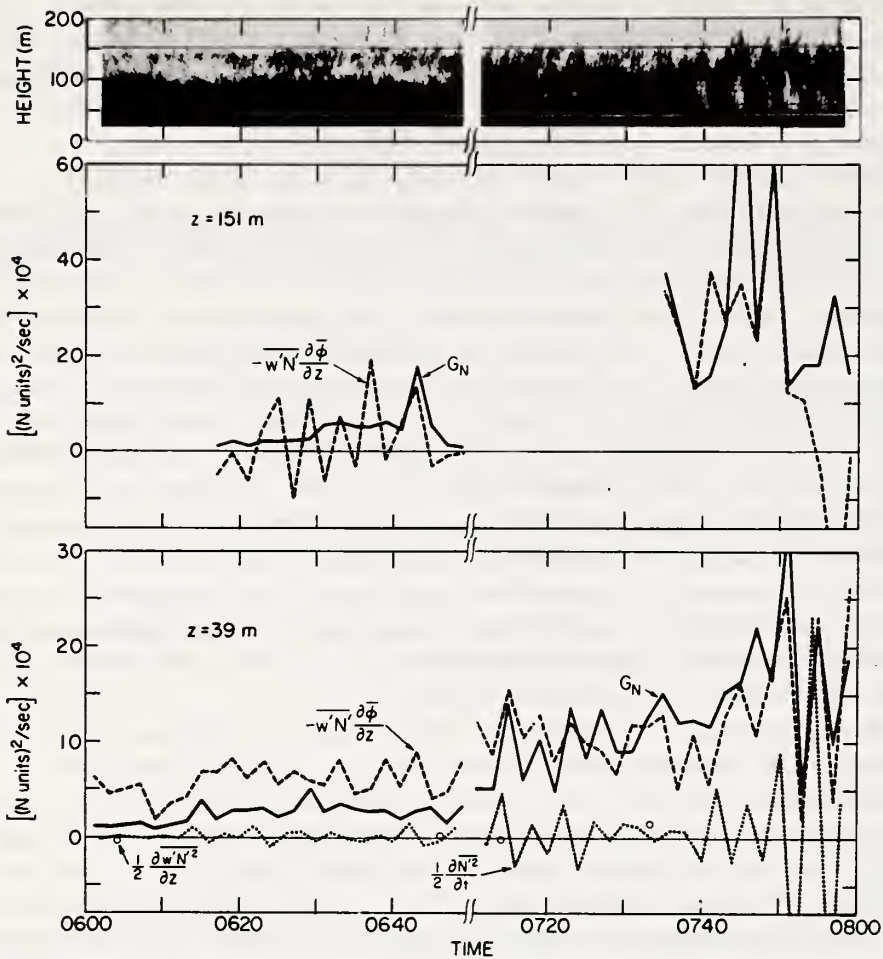


Fig. 1. Time rates of production and dissipation of refractivity fluctuations at two fixed tower levels. The time rate of change and vertical diffusion of refractivity variance are also shown for the 39-m level.

be rather inaccurate whenever more rapid (of the order of 10 min) changes occur. When no carriage profiles are available, a crude estimate of dN/dz is obtained by taking the difference between refractivity readings at two fixed levels and dividing by the separation. It is concluded, therefore, that because of the various uncertainties encountered in evaluating the gradient of refractivity, rather substantial errors may contaminate the resultant $\partial \bar{\phi}/\partial z$ estimate.

For the 39-m level, the time rate of change of variance $(1/2) \partial (\overline{N'^2})/\partial t$ (dotted lines) and vertical diffusion $(1/2) \partial (\overline{w'N'^2})/\partial z$ (open circles) terms are also shown.

Because the diffusion term must be evaluated from carriage measurements, estimates for this term are available only when the carriage crosses the 39-m level. This occurs at 0604, 0646, 0714, and at 0734.

At the top of Figure 1 is a photograph of the acoustic sounder echo returns. Horizontal lines at 39 and 151 m indicate the locations of the two fixed levels for which data are available.

An examination of the 39-m level plots reveals that the production and dissipation terms are approximately in balance; by comparison, the diffusion and change in variance terms are negligibly small during most of the period. As the Sun's heating becomes more appreciable, the intensity of the turbulent fluctuations increases, and this is reflected by corresponding increases in both $\overline{w'N'\partial\phi/\partial z}$ and G_N . Superimposed on this gradually increasing trend are numerous short-term (2- to 6-min) fluctuations. Significantly, many of these more rapid variations in production and dissipation are well correlated; this is especially true for the 0710 to 0800 period. The acoustic sounder returns show essentially uniform intensity of scattering for $z=39$ m from 0600 to 0800; no significant structure is readily discernible at this level.

Unfortunately, no refractivity data are available at the 95-m level, and only two shorter segments could be analyzed for the 151-m level. Although at $z=151$ m the generation and dissipation terms are usually within an order of magnitude of each other, a fairly substantial discrepancy develops after 0752. Also, while $\overline{w'N'\partial\phi/\partial z}$ exhibits some marked fluctuations between 0618 and 0650, most of these are not observed in G_N . Part of the disagreement may be caused by errors in the dN/dz estimates which were mentioned earlier. In addition, the carriage cannot ascend above $z=151$ m, which makes it even more difficult to obtain reliable estimates of the refractivity gradient for this level.

From 0618 until 0650, the intensity of refractivity fluctuations (as judged from the variance N'^2) is approximately twice as large at the 151-m level as at the 39-m level; this is to be contrasted with the acoustic echo sounder data, indicating consistently stronger returns from the lower elevation. The intensity of the fluctuations is more nearly equal at the two levels between 0734 and 0800. Two pronounced peaks in G_N correspond to regions of enhanced acoustic scattering crossing the 151-m tower level at 0744 and 0748. No other obvious correlation between the refractivity variations and acoustic returns is evident, however.

A considerably more complex situation is illustrated in Figure 2. Because Bean *et al.* (1973) examine the turbulent energy budget and Emmanuel (1972) investigates the hydrodynamic stability of the wave structure for this same time period, the reader's attention is directed to these two papers for additional details that are not discussed here.

Figure 2 shows that the generation and dissipation terms are in good agreement at both the 39-m and the 95-m levels. Pronounced increases are observed in G_N and $\overline{w'N'\partial\phi/\partial z}$ whenever the convective layer crosses the 39-m level (indicated by intense, almost uniform acoustic scattering near the ground); this occurs at 0808 and again at 0854. Similarly, G_N and $\overline{w'N'\partial\phi/\partial z}$ show marked increases when the undulating wave

HASWELL, COLORADO
9 October 1969

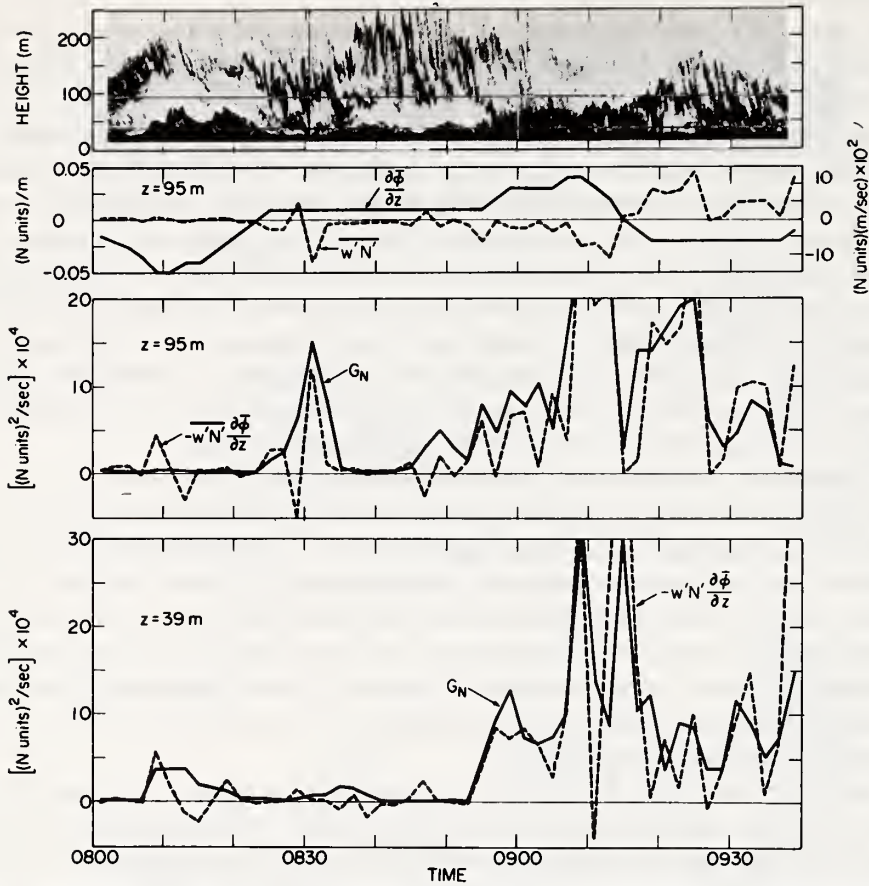


Fig. 2. Time rates of production and dissipation of refractivity fluctuations at two fixed tower levels. The refractivity flux and potential refractivity gradient are also shown for the 95-m level.

structure crosses the 95-m level between 0826 and 0834. An interesting aspect of the 95-m plots is that as the gradient of potential refractivity changes its sign (at 0823 and 0915), a corresponding, but opposite sign change takes place in the refractivity flux term; the result is that $-\overline{w'N'\partial\phi/\partial z}$ remains positive and continues to be in balance with G_N . Figure 3 illustrates two smoothed refractivity profiles, one before and one after the 0915 sign change.

A notable feature of the results is that plots of G_N at the 39- and 95-m levels show very little correlation, and the same is true for $\overline{w'N'\partial\phi/\partial z}$. This is not surprising when we note that the acoustic sounder-returns indicate rather different atmospheric structures at the two levels. Similar comments apply for the results shown in Figure 1.

Additional insight into the problem can be gained by examining plots of power

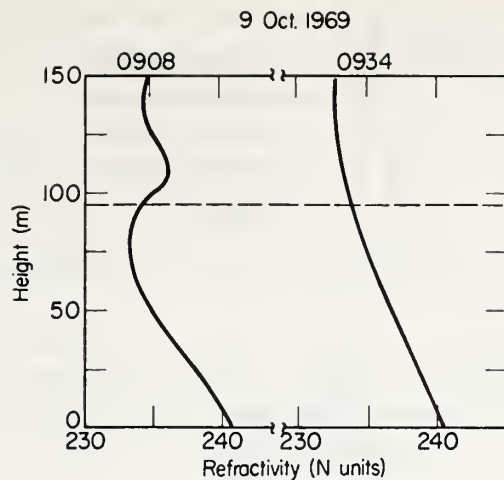


Fig. 3. Refractivity profiles obtained from carriage traverses.

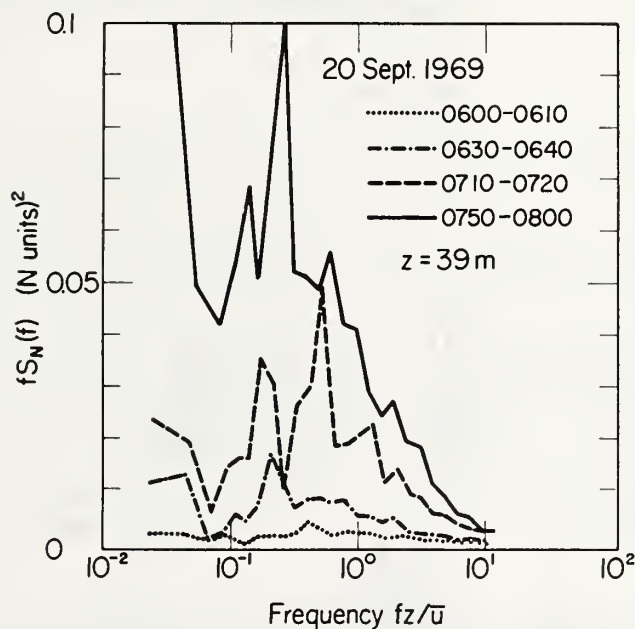


Fig. 4a. Power spectral densities of refractivity fluctuations.

spectral densities of refractivity variations. Figures 4a, b, and c show some typical examples. Ten-min data samples are analyzed on the computer by using a Fast Fourier Transform routine. The spectral outputs $S_N(f)$ are averaged so that approximately 10 equally spaced (on a logarithmic scale) outputs are plotted per decade along the frequency axis. The spectra are multiplied by the fluctuation frequency f (Hz);

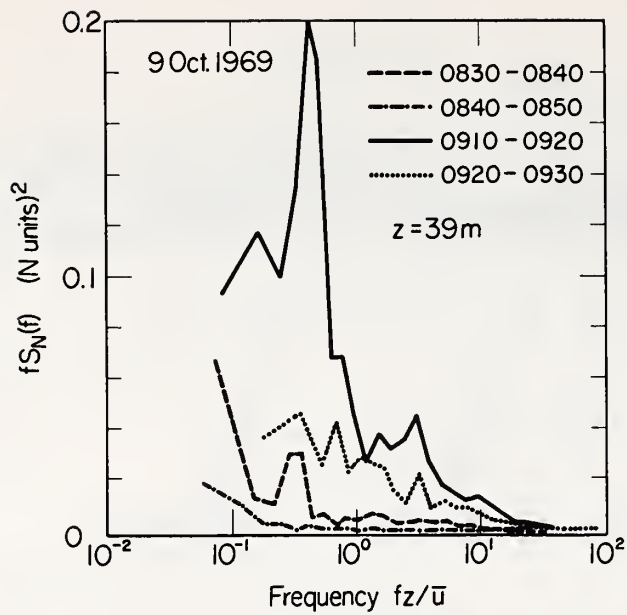


Fig. 4b.

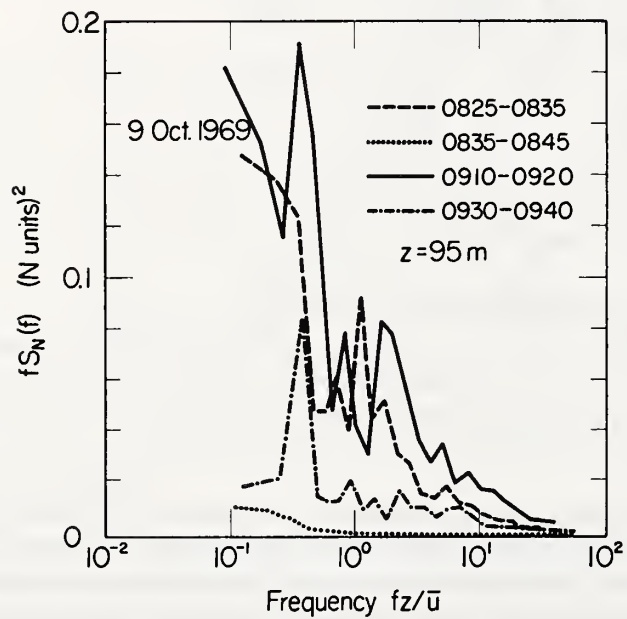


Fig. 4c.

consequently, equal areas under the curves correspond to equal contributions to the total variance $\overline{N'^2}$. The frequency scale is normalized by multiplying f with z and dividing by \overline{u} ; as a result, $fz/\overline{u} = z/l$ becomes dimensionless (here l is the spatial wavelength in meters).

Figures 1 and 4a convincingly demonstrate that as the rates of production and dissipation increase at $z = 39$ m, so do the corresponding spectral estimates. For example, for 0600–0610, $G_N \approx 1.2 \times 10^{-4} (N \text{ unit})^2 \text{ s}^{-1}$, and $fS_N(f)$ peaks at $4 \times 10^{-3} (N \text{ unit})^2$; for 0750–0800, the corresponding numbers are $1.6 \times 10^{-3} (N \text{ unit})^2 \text{ s}^{-1}$ and $1 \times 10^{-1} (N \text{ unit})^2$.

Another interesting feature of Figure 4a is the marked dip that occurs at $z/l \approx 0.07$ ($l = 560$ m). We may speculate that this 'spectral gap' is caused by the separation of mesoscale and microscale phenomena; however, because of the considerable statistical uncertainty in the low-frequency spectral estimates, it is not possible to draw a definite conclusion.

An examination of Figures 4b and c with Figure 2 reveals that increases and decreases in the rates of production and dissipation are again well correlated with corresponding changes in the power spectra.

4. Conclusions

In spite of the difficulties encountered in estimating the gradient of potential refractivity, the production and dissipation rates of refractivity fluctuations agree well in most cases. More important than the actual numerical agreement between these two terms is the fact that changes in the production and dissipation terms are usually well correlated at any given tower level. Under stationary conditions, the time rate of change and vertical diffusion of refractivity variance are about an order of magnitude smaller than the rates of production or dissipation. Larger contributions due to the time rate of change of variance term are observed during the more active time periods.

Because the acoustic sounder is sensitive only to temperature variations, quantitative comparison of acoustic echo returns with refractivity fluctuation data is not possible. Nevertheless, by delineating regions of turbulent activity, the acoustic returns help to explain the observed increases and decreases in the rate of production and dissipation.

Power spectral densities of refractivity variations exhibit changes that are closely related to corresponding changes occurring in the rate of production and dissipation.

Acknowledgments

The author would like to thank Dr B. R. Bean and Dr A. S. Frisch for many valuable discussions. He is indebted to Mr R. E. McGavin, Mr R. W. Krinks, and Mr C. E. Case for taking the meteorological data, and to Mr L. G. McAllister and Mr J. R. Pollard for making the acoustic echo-sounder records available.

References

- Barton, D. K. and Ward, H. R.: 1969, *Handbook of Radar Measurement*, Prentice-Hall, Inc., Englewood Cliffs, N. J., 426 pp.
- Bean, B. R. and Dutton, E. J.: 1968, *Radio Meteorology*, Dover Publications, Inc., New York, 435 pp.
- Bean, B. R., Frisch, A. S., McAllister, L. G., and Pollard, J. R.: 1973, 'Planetary Boundary-Layer Turbulence Studies from Acoustic Echo Sounder and *in-situ* Measurements', *Boundary-Layer Meteorol.*, this issue, p. 449-474.
- Emmanuel, C. B.: 1972, *Observations of Helmholtz Waves in the Lower Atmosphere with an Acoustic Sounder*, Ph.D. Dissertation, Colorado State University, Fort Collins, Colorado, 94 pp.
- Gilmer, R. O., McGavin, R. E., and Bean, B. R.: 1965, 'Response of NBS Microwave Refractometer Cavities to Atmospheric Variations', *Radio Sci.* **69D**, 1213-1217.
- Landau, L. D. and Lifshitz, E. M.: 1959, *Fluid Mechanics*, Addison-Wesley Publishing Company, Inc., Reading, Mass., 536 pp.
- McAllister, L. G., Pollard, J. R., Mahoney, A. R., and Shaw, P. J. R.: 1969, 'Acoustic Sounding - A New Approach to the Study of Atmospheric Structure', *Proc. IEEE* **57**, 579-587.
- Ottersten, H.: 1969, 'Mean Vertical Gradient of Potential Refractive Index in Turbulent Mixing and Radar Detection of CAT', *Radio Sci.* **4**, 1247-1249.
- Panofsky, H. A.: 1969, 'Spectra of Atmospheric Variables in the Boundary Layer', *Radio Sci.* **4**, 1101-1109.
- Roche, J. F., Lake, H., Worthington, D. T., Tsao, C. K. H., and DeBettencourt, J. T.: 1970, 'Radio Propagation at 27-40 GHz', *IEEE Trans. Antennas Propagat.* **AP-18**, 452-462.
- Shen, L. C.: 1970, 'Remote Probing of Atmosphere and Wind Velocity by Millimeter Waves', *IEEE Trans. Antennas Propagat.* **AP-18**, 493-497.
- Tatarski, V. I.: 1961, *Wave Propagation in a Turbulent Medium*, McGraw-Hill Book Company, Inc., New York, 285 pp.
- Wyngaard, J. C. and Coté, O. R.: 1971, 'The Budgets of Turbulent Kinetic Energy and Temperature Variance in the Atmospheric Surface Layer', *J. Atmospheric Sci.* **28**, 190-201.

Demonstration of Distortion in Envelope Detection of SSB Signals

DONALD E. BARRICK

Abstract—Examples are presented illustrating graphically the envelope distortion inherent to SSB signals and the dependence of this distortion upon the amount of carrier present with the sideband.

INTRODUCTION

One of the more difficult topics to present satisfactorily to an electrical engineering undergraduate for the first time (i.e., in his second or third year) is that of single sideband (SSB) signals and their detection. The instructor can easily sketch the appearance of an arbitrary signal, $f(t)$, in the time domain after (i) modulation and (ii) envelope detection for either normal AM modulation or suppressed-carrier double sideband (DSB) modulation. The simple extension of these chalk-eraser techniques to SSB signals in the time domain is not possible, however; one usually draws an arbitrary signal Fourier transform, symmetrical about the carrier, and erases the upper or lower half to illustrate the meaning of SSB signals in the frequency domain. Invariably a student asks the question: what does the signal or its envelope look like in the time domain? It is here that the lack of a quick physical picture leaves an aura of mystery about the subject.

One can of course spend two or three periods introducing Hilbert transform concepts in order to cover SSB signals, and some recent treatments of this subject [e.g., Schwartz*] provide a maximum of insight with a minimum of mathematics. This author has found, however, that the sophistication required to master Hilbert techniques obscures the simple but important physical concepts of SSB for the average student on his first exposure to modulation.

Yet an important practical example of envelope detection of SSB (or more precisely, vestigial sideband) signals occurs with the video portion of the normal TV signal. It is desirable to illustrate the effect of the carrier amplitude on the amount of distortion. This is difficult to calculate with Hilbert transforms, and one can use phasor diagrams [Deutsch*] to show how a large carrier minimizes distortion. Again, however, the unavailability of a ready pictorial representation of a detected signal makes quantitative comparisons difficult. This is especially true for realistic modulating signals, $f(t)$, which have finite bandwidth, in contrast to $f(t) = \sin \omega_m t$, a signal with infinitesimal bandwidth.

Hence, this author has found it useful to cover this subject in one of two ways: (1) Simply present the charts below showing examples of the SSB envelopes for three periodic modulating signals, $f(t)$, (square wave, triangular wave, sine wave) with various amounts of carrier present, or (2) Have the student as a special project plot the envelope shape for an

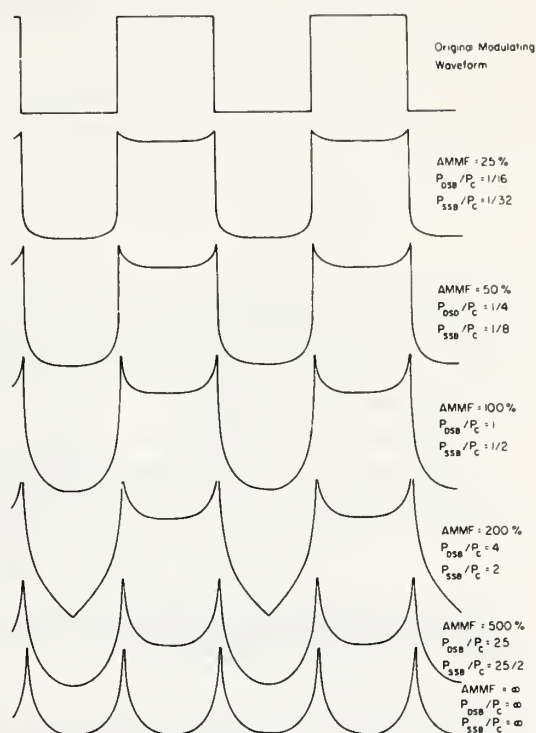


Fig. 1. Envelope of SSB signal for square-wave modulation with various amounts of carrier strength. AMMF is the normal AM modulation factor; P_{DSB}/P_C and P_{SSB}/P_C are the ratios of power in both or one sideband to the power in the carrier.

assigned carrier level and periodic modulating signal, $f(t)$; this can readily be accomplished with the equations below and a time-share computer terminal.

MATHEMATICAL DEFINITIONS

Consider an arbitrary, even, periodic modulating function $f(t)$, normalized such that $f_{MAX}, f_{MIN} = +1, -1$ and $f_{AVE} = 0$, with Fourier series

$$f(t) = 2 \sum_{n=1}^{\infty} d_n \cos n\omega_m t = \sum_{n=-\infty}^{\infty} d_{|n|} e^{jn\omega_m t}.$$

Manuscript received April 15, 1971; revised April 4, 1972.

The author was with the Department of Electrical Engineering, Ohio State University, Columbus, Ohio 43210. He is now with the Wave Propagation Laboratory, National Oceanic and Atmospheric Administration, Boulder, Colo. 80302.

*Schwartz, M., *Information Transmission, Modulation and Noise*, 2nd Ed., pp. 218-228, McGraw-Hill, New York, 1970.

*Deutsch, S., *Theory and Design of Television Receivers*, pp. 17-23, McGraw-Hill, New York, 1951.

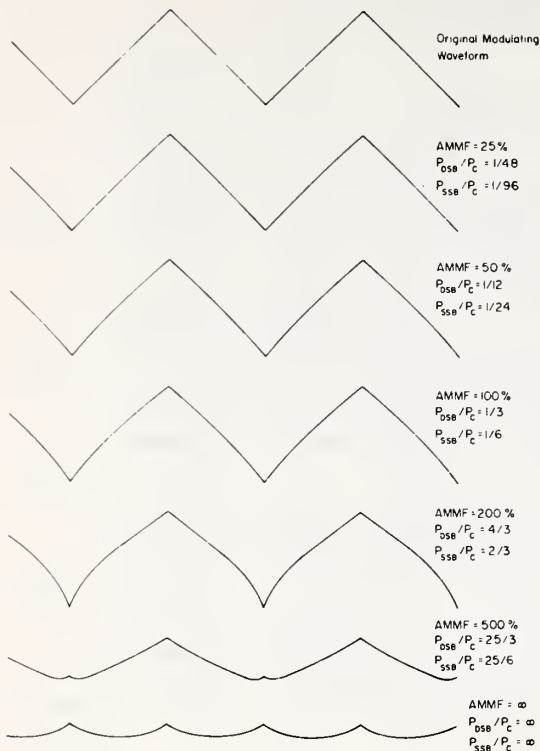


Fig. 2. Envelope of SSB signal for triangular-wave modulation with various amounts of carrier strength. AMMF is the normal AM modulation factor; P_{DSB}/P_C and P_{SSB}/P_C are the ratios of power in both or one sideband to the power in the carrier.

When $f(t)$ is multiplied by $\cos \omega_c t$ and an arbitrary amount of carrier signal, $c_0 \cos \omega_c t$, is added to the result, it is straightforward to show that the envelope of the SSB signal is[†]

$$f_{ENV}(t) = \left[\left(c_0 + \sum_{n=1}^{\infty} d_n \cos n\omega_m t \right)^2 + \left(\sum_{n=1}^{\infty} d_n \sin n\omega_m t \right)^2 \right]^{1/2}$$

(The DSB envelope is the same, but with lower summation limits $-\infty$.)

When $c_0 = 1$, 100% modulation is obtained for the normal AM signal; $c_0 > 1$ represents less than 100% modulation while $c_0 < 1$ produces overmodulation or envelope distortion. The normal AM modulation factor can be defined as $AMMF \equiv (1/c_0) \times 100\%$.

Another quantity useful in measuring communication efficiency is the ratio of average power in the information-carrying sidebands to the average power in the carrier, i.e., P_{DSB}/P_C and P_{SSB}/P_C , for DSB and SSB signals. These ratios can be computed for simple periodic modulation functions without the use of the Fourier series; note that $P_{DSB} = 2P_{SSB} = (1/2T) \int_{-T/2}^{T/2} f^2(t) dt$.

Using the above equations, we compute the SSB envelopes for the square wave, triangular wave, and sine wave with various amounts of carrier present. These are shown in Figures 1-3. The vertical scales are the same for each waveform, but any DC levels contained in the envelopes are not shown since they carry no information. The SSB envelope for the simple sine wave for $f(t)$ can of course be written in closed form, in contrast with the other two.

[†]This can be left as an exercise for the student.

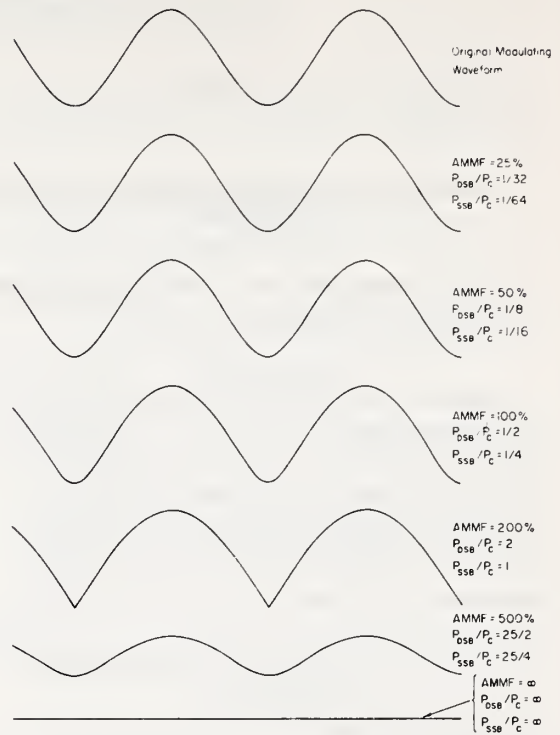


Fig. 3. Envelope of SSB signal for sine-wave modulation with various amounts of carrier strength. AMMF is the normal AM modulation factor; P_{DSB}/P_C and P_{SSB}/P_C are the ratios of power in both or one sideband to the power in the carrier.

DISCUSSION

While the three waveforms considered here are far from all-inclusive, there are several characteristics common to all three that should allow some qualitative inductive observations.

(1) Whereas envelope detection of DSB signals can reproduce perfectly the modulating signal so long as the AMMF is less than 100%, some envelope distortion always occurs with SSB signals.

(2) SSB envelope distortion is generally not too serious until the AMMF approaches 100%; it becomes more serious near 200%, but may still be acceptable for some applications because the envelope depth (between -1 and $+1$) and basic period ($T_m = 2\pi/\omega_m$) are still clearly unchanged.

(3) For an AMMF greater than 200%, the depth of the envelope swing decreases and serious envelope distortion results. In the limit of zero carrier, the basic period of $f(t)$ is no longer even T_m , a clearly intolerable situation.

(4) The nature of the distortion is such that the peaks are broadened and valleys narrowed.

(5) Discontinuities in $f(t)$ (such as the sides of the square wave) produce logarithmic envelope singularities; a fact which may be checked using Hilbert transforms. The effect of a finite post-detector filter bandwidth will in practice suppress these "ears" to a considerable extent.

(6) Suitable SSB transmission of PCM signals could take place at an AMMF of 200% with proper selection of the shape of $f(t)$ to represent a binary digit. Thus a maximum voltage swing at the detector output would be realized with a minimum signal bandwidth and minimum of power transmitted in the carrier.

FM/CW RADAR SIGNALS AND DIGITAL PROCESSING

Donald E. Barrick

ABSTRACT

The use and processing of the FM/CW signal for radar and acoustic sounder systems are examined in this note. This signal--along with real-time digital processing via minicomputers--is currently being used by several groups for HF over-the-horizon radars. A comparative analysis of the different processing techniques for general radar applications has yet to be undertaken. This note therefore attempts to promulgate details of these techniques so that they may find use in other systems. An example involving an HF backscatter radar is used to permit the reader to see how the techniques are applied to an actual problem.

A linearly swept-frequency signal format is used in a 100% duty-factor mode. In the receiver, a replica of the linear FM signal is mixed with the received waveform at an offset such that the desired range window is observed with the lowest possible IF frequency variation. This pulse train is then analog-to-digital (A/D) converted and ready for computer processing. Two techniques are described and analyzed for digitally processing the signal via the Fast-Fourier-Transform (FFT) algorithm. The first is a double-FFT process; the first FFT set is done within a pulse-repetition-interval (PRI) to give range information. The next FFT set is done over N PRIs to give Doppler information. In the second technique, a single long FFT is used over N PRIs, giving simultaneously both range and Doppler information. It is shown that both techniques are identical, in that they produce the same information and require the same number of computer steps in executing the required FFTs. Both techniques yield *unambiguous* range and Doppler, for both discrete and distributed targets; the note shows how and where this information is contained in the processor output. The note also describes how two weighting functions are normally applied to the pulse train time samples to reduce objectionable range and Doppler sidelobes. Finally, simple "cookbook" rules are given for obtaining the signal and processing parameters based on the radar and target range/velocity specifications.

THE DESIGN OF A TEMPERATURE-INDEPENDENT DC FLOW RESISTOR

A.J. Bedard, Jr., National Oceanic and Atmospheric Administration, U.S. Department of Commerce

A flow resistance in conjunction with a volume and pressure transducer has been used as a high-pass filter in a National Oceanic and Atmospheric Administration microbarograph system. Any change in the value of the resistance with temperature results in changes in system response characteristics. Therefore, a flow resistor that does not show changes in resistance with temperature was desired.

Considerations in the design of flow resistors and the details of a resistor showing a value of resistance almost independent of temperature are discussed in the section that follows. The experimental techniques used in determining the flow resistance are presented. The type of flow of interest in this work is laminar, steady-state flow. Air was used in all tests, but the basic principle is applicable to both other gases and liquids. The means for adjustment of the resistance are also described.

Design Considerations

The Capillary

A common form of flow resistor is the capillary tube of circular cross section. The resistance of such a tube can be calculated from the Hagen-Poiseuille law

$$R = 8\mu l / \pi a^4 \quad (1)$$

where R is the value of flow resistance, μ is the viscosity of air, l is the length of the tube, and a is the tube radius. It is assumed in the following that the tube is long enough that end corrections can be neglected. Also, flow velocities are assumed low enough that kinetic energy corrections are not

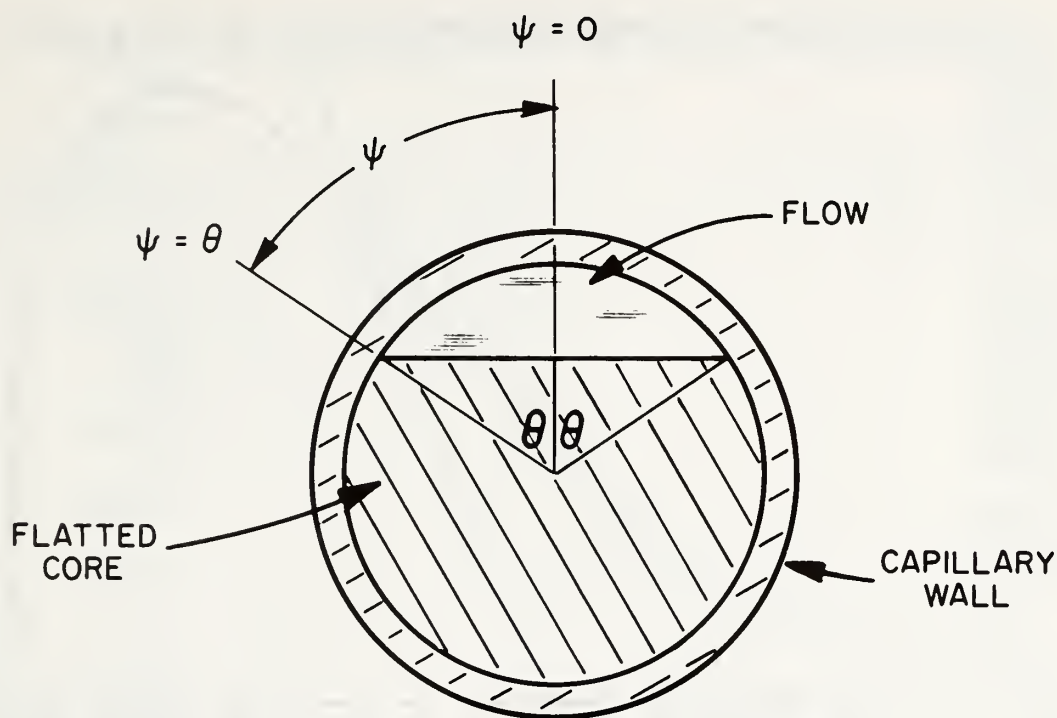


Figure 1a. Sectionary, Cross-Sectional View

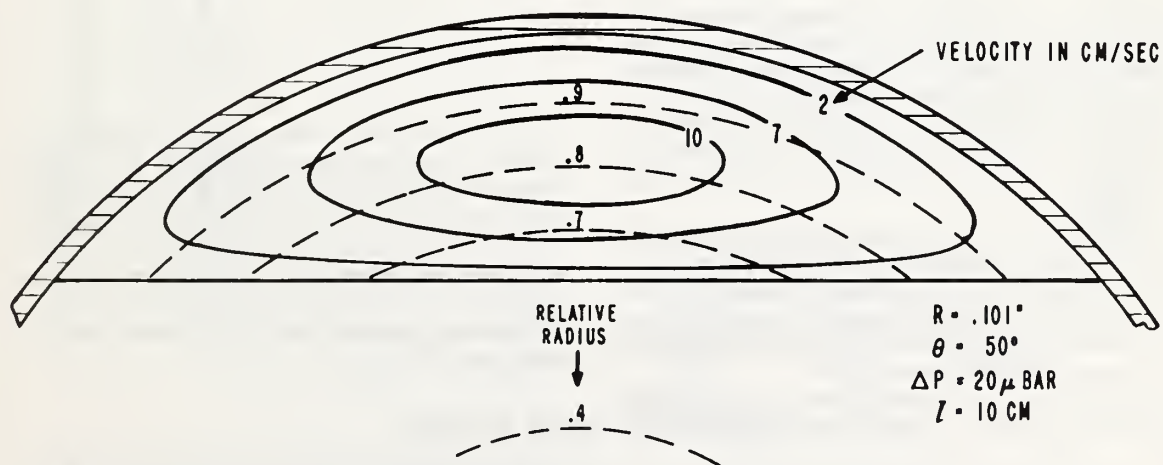


Figure 1b. Constant Velocity Profile through Sectionary

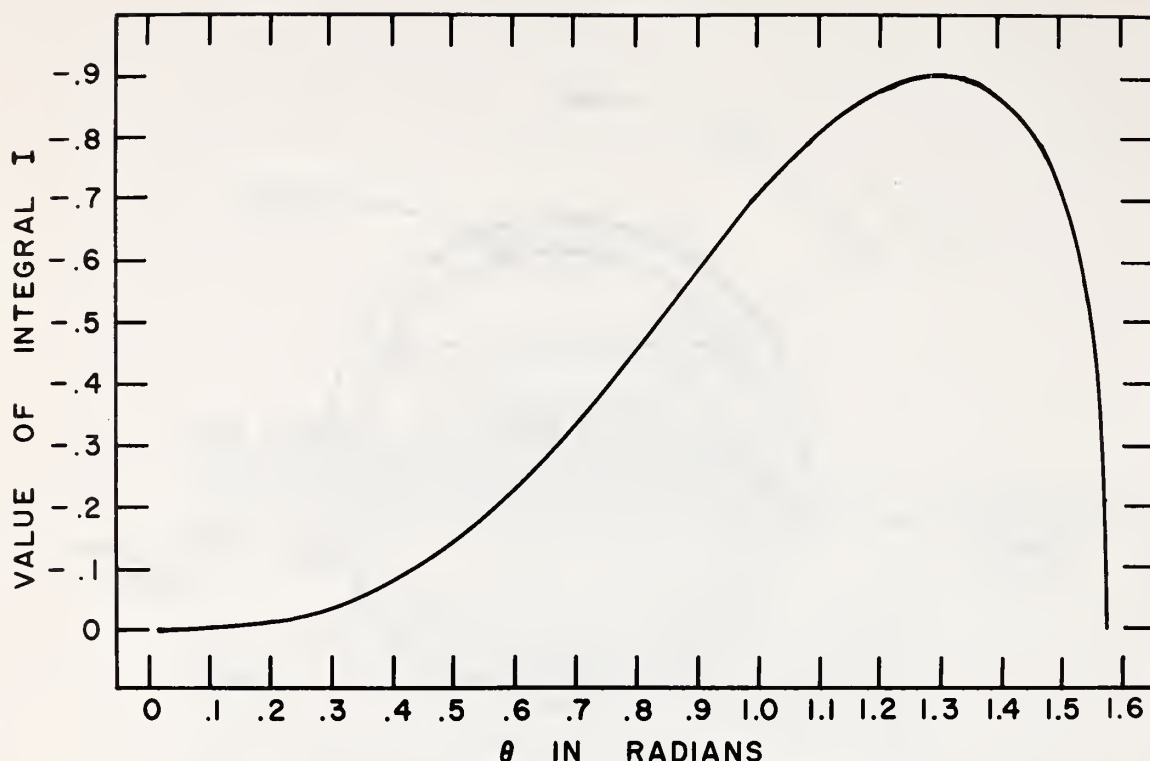


Figure 2. Evaluation of Integral I as a Function of θ . Used in Evaluation of Equation 6

significant. As temperature changes, the physical dimensions of the capillary leak change. Changes in air viscosity will also occur with temperature at 0.536 micropoise per degree Centigrade at 20 degrees Centigrade.¹ A typical value of air viscosity is 190 micropoises. Note that for gases the viscosity increases with temperature, for liquids the viscosity decreases with increasing temperature.

The linear coefficient of expansion per degree Centigrade of capillary tubing materials is in the proper direction to compensate for the air viscosity change. However, it can be shown that the magnitude is too small for practical materials. It is assumed that the longitudinal and transverse coefficients are equal.

For air with $\mu = 190$ micropoises, $d\mu/dT = 0.536$ micropoise per degree Centigrade and setting $dR/dT = 0$

$$(1/a)(da/dT) =$$

$$(1/3) \{ (1/\mu)(d\mu/dT) \}$$

or

$$(1/a)(da/dT) = 95 \times 10^{-5} / ^\circ\text{C} \quad (2)$$

This is the value of the linear coefficient of expansion required to provide compensation for air viscosity changes. No material with a linear coefficient of expansion in this range that could be made into a capillary could be found. The coefficient of stainless steel is too low by a factor of about 100. Elastomers are a factor of about 3 too low. There seems to be no method of obtaining temperature compensation for the configuration of a simple capillary.

The Annulary

The next possibility considered was that of utilizing two materials of greatly differing linear coefficients of expansion in the hope that large differential changes in dimension with temperature would provide compensation. The

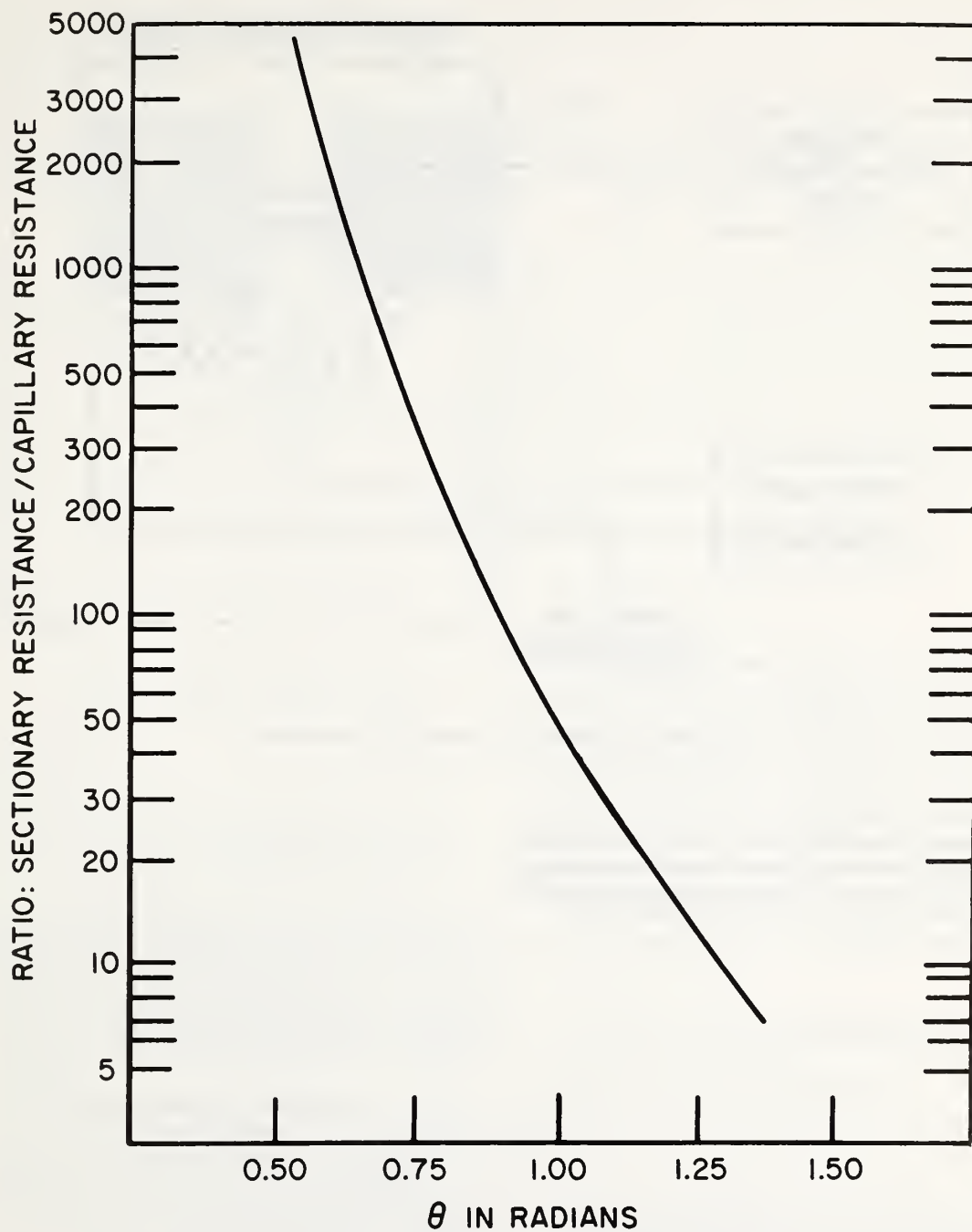


Figure 3. Resistance of Sectionary as a Function of θ expressed in Terms of Its Ratio to that of a Capillary of Circular Cross Section with the Same Bore and Length. Curve was computed from Equation 5

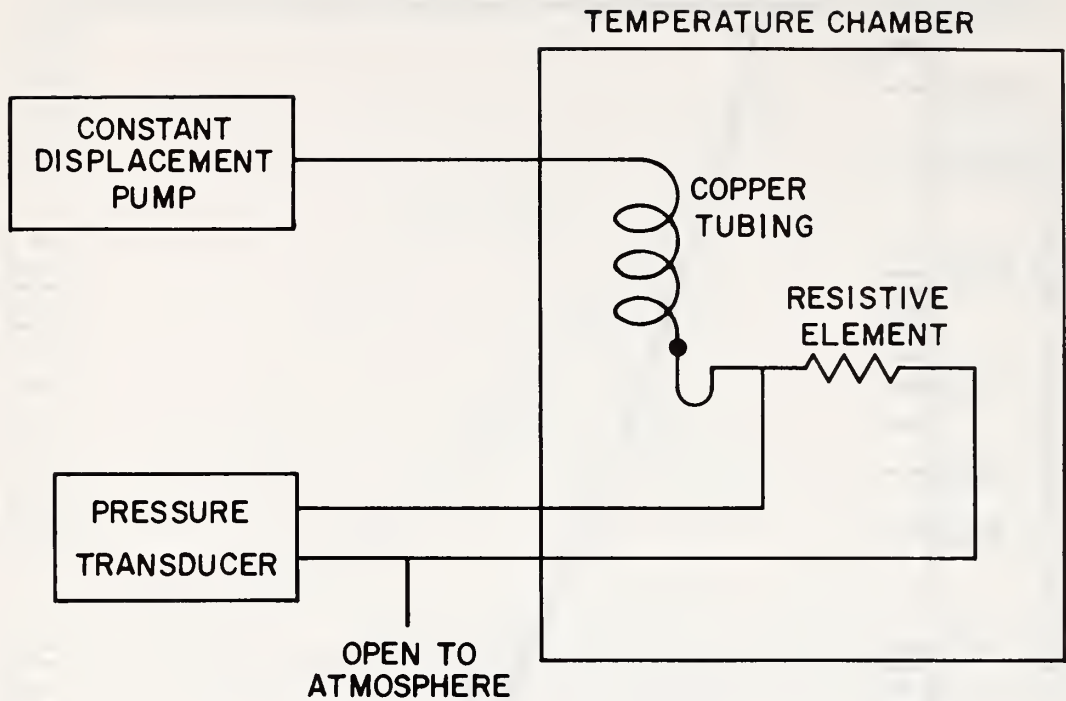


Figure 4. Experimental Setup for the Measurement of Flow Resistance

first configuration investigated was the case for flow through an annulus, a device we will refer to as an annularity. Annular flow resistance has been shown to be²

$$R = (8\mu l / \pi) [(a_1^4 - a_2^4) + (a_1^2 - a_2^2)^2 / \ln(a_2/a_1)]^{-1} \quad (3)$$

where a_1 is the inner radius of the capillary, a_2 is the radius of the core and \ln is the natural log.

It may be shown (Appendix I) that to obtain temperature compensation for the annularity

$$\begin{aligned} (1/a_1)(da_1/dT) = & \left\{ (1/\mu)(d\mu/dT)[(a_1^4 - a_2^4) + (a_1^2 - a_2^2)^2 / \ln(a_2/a_1)] \right. \\ & + (1/a_2)(da_2/dT)[2a_2^2 + (a_1^2 - a_2^2) / \ln(a_2/a_1)]^2 \left. \right\} / \\ & \left\{ [2a_1^2 + (a_1^2 - a_2^2) / \ln(a_2/a_1)]^2 - [(a_1^4 - a_2^4) + (a_1^2 - a_2^2)^2 / \ln(a_2/a_1)] \right\} \end{aligned} \quad (4)$$

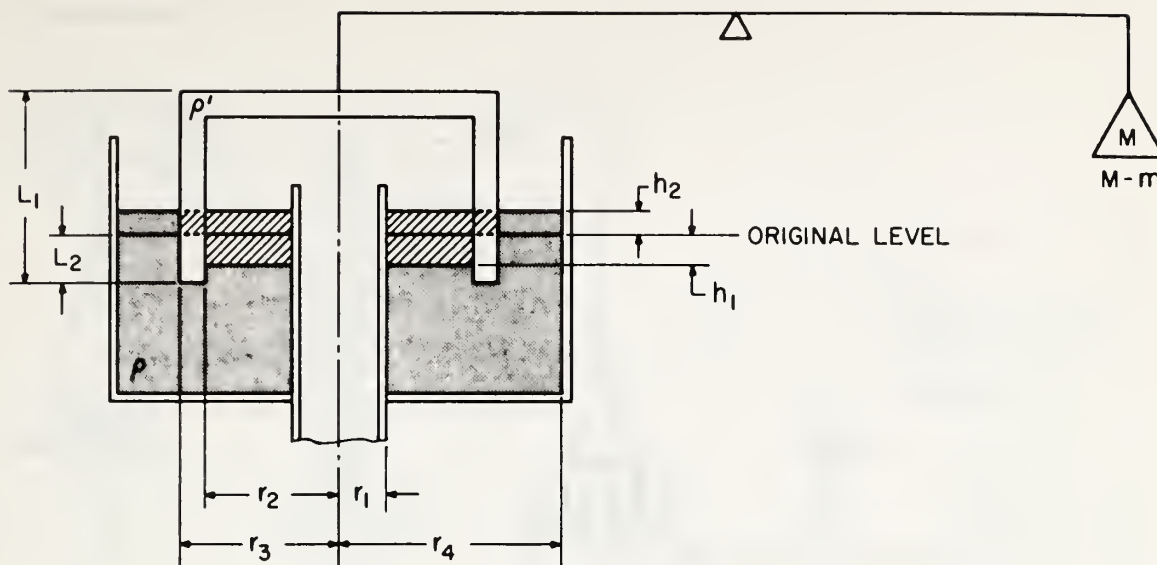


Figure 5. Static Calibrator

Assuming

$$(1/\mu)(d\mu/dT) = 284 \times 10^{-5}/^{\circ}\text{C}$$

(for air) and

$$(1/a_2)(da_2/dT) = 1 \times 10^{-5}/^{\circ}\text{C}$$

(for stainless steel) it is found that it is possible to attain temperature compensation with available materials. Such an annulary was designed and built, and is described in a following section. However, although temperature compensation was attained, one feature of the annulary rendered this approach to the problem impractical.

The annulary resistance is also a function of the position of the core in the capillary tube. The variation of annulary resistance as a function of core position was determined experimentally for a particular unit, as described later, and was found to be quite large. Because of the difficulty of maintaining the core in a centered configuration the annulary was not considered practical.

The Sectionary

It was thought that flow through a section of the tube might provide the necessary temperature compensation while not showing the dimensional instability of the annulary. Flattening a core section with an outer radius equal to the inner radius of the capillary was thought to be a convenient method of insuring that there would be no motion of the core. The core and the capillary would be made from materials with differing linear coefficients of expansion. A flow resistor of this type, Figure 1a, will be referred to as a "sectionary."

For flow through a section of the tube the resistance can be found from the expression (Appendix 2)

$$R = (8\mu l/a^4) \left\{ 1/\left[\theta + \sin\theta \cos\theta + \left[(2/3)\sin^2\theta - 1\right] + 1\right] \right\} \quad (5)$$

where θ is shown in Figure 1a. It is half the angle subtended by the flattened portion of the core. The "a" is the radius of the tube.

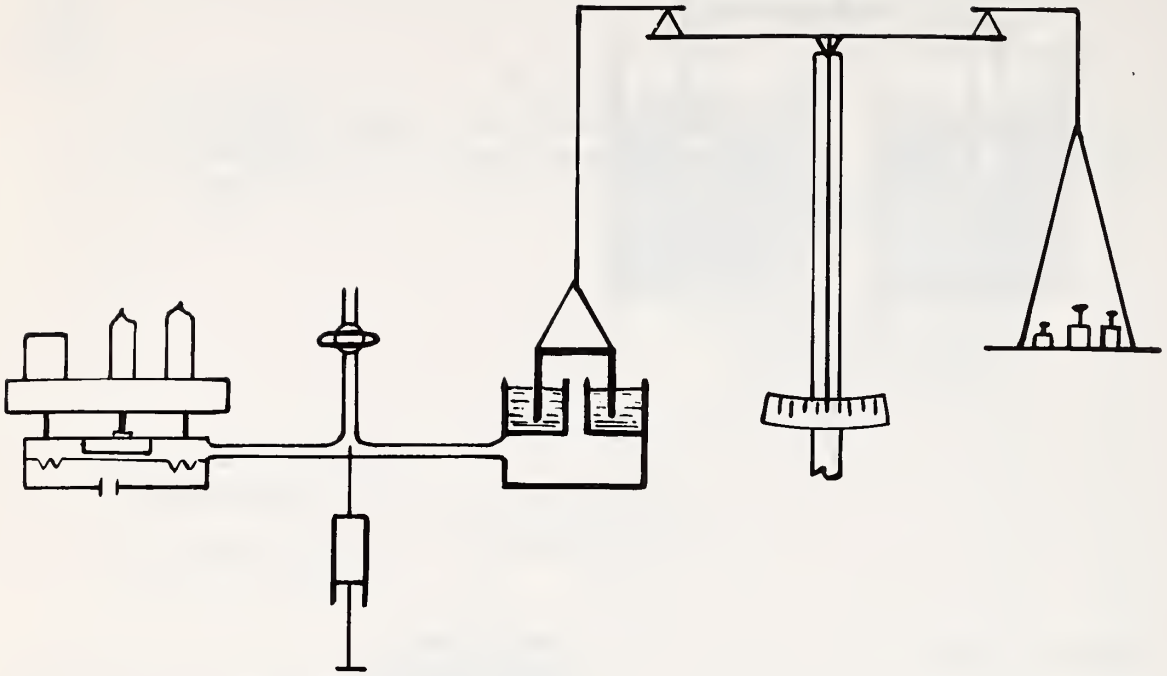


Figure 6. Static Calibrator Test Setup

The term I is

$$I = \int_{\Phi=0}^{\Phi=\theta} \left\{ \left[\left(\frac{\cos^2 \theta}{\cos^2 \Phi} \right) - 1 \right]^2 / \right. \\ \left. \ln(\cos \theta / \cos \Phi) \right\} d\Phi \quad (6)$$

The values of this integral between $\theta=0$ and $\theta=\pi/2$ are plotted in Figure 2. The value of Φ ranges from zero at the center of the flattened portion to θ at the ends.

It is reasonable to assume that the velocity changes very little as a function of Φ for constant r except in the corners of the sectionary. A basic assumption in the development (see Appendix 2) of Equation 5 has been that the second derivative of the velocity with respect to Φ is negligible in the Navier-Stokes equation. Because of the assumption this equation would be expected to yield reasonable predictions only over a limited range of

geometries. Figure 1b shows a typical cross section view of a velocity profile calculated from Equation 21 in Appendix 2 for a typical geometry used. The tube radius used was 0.101 inch, the length 10 cm, and $\theta=50$ degrees with a ΔP of $20\mu\text{bar}$. An exact solution for this geometry could be obtained with the bounding techniques described by Kearsley.³ For the range of flow velocities used here Equation 5 has been found to be sufficient for design purposes and good quantitative predictions have been made. Deviations from the assumed geometry caused by curing of the silicone rubber used for the capillary seem to be the chief source of differences between computed and observed resistances.

Figure 3 presents a plot of resistance as a function of the angle θ in radians computed from Equation 5. It is based on the assumption that the value of resistance determined using a simple Hagen-Poiseuille law calculation for the bore diameter of interest is unity. Thus, to use this curve determined the bore of interest and calculated the resistance from the Hagen-Poiseuille law. Multiplying this value by the relative resistance found in Figure 3 for the θ used will predict the flow resistance of the sectionary. In practice, corrections will have to be

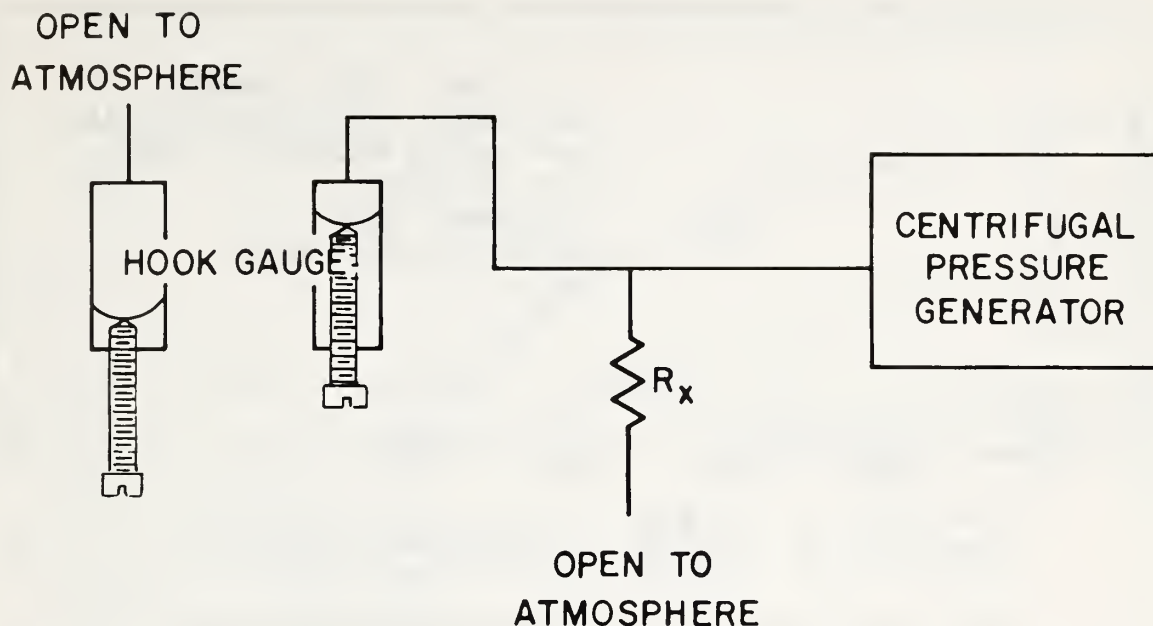


Figure 7. Experimental Setup using Centrifugal Calibrator. R_x is the Unknown Flow Resistor

made if the core piece does not run the entire length of the capillary.

The combination giving temperature independence was found by empirically testing sectionaries consisting of capillaries made from material having a high coefficient of expansion and stainless steel cores having various values of θ . The results, presented in a following section, show that temperature compensation was attained. Tests with capillary sections made from both glass and a silicone potting compound showed that for glass capillaries the theoretical values of resistance determined from Equation 5 agree well with the observed values. The observed values of resistance obtained using silicone potting compound for the capillary material were consistently higher, probably because of dimensional changes during the process of forming the capillaries from the silicone rubber.

The sectionary form of flow resistor can be easily and reproducibly changed by adjusting the length of the core within the capillary section. This longitudinal motion of the core within the capillary routes a portion of the flow through a capillary of circular cross section and the remaining flow through the flattened section. The relative

length of these segments changes as the core is moved within the capillary. If the resistance of the segment of circular cross section is significant compared with the sectionary flow, corrections should be made. In practice, the resistance due to capillary flow of circular cross section will usually be insignificant.

Experimental Method

Various methods of measuring flow resistance have been devised.^{4,5,6} Figure 4 shows a diagram of the experimental setup used in the measurements described here. Since

$$R = \Delta P / Q$$

where R is the flow resistance in acoustic ohms, ΔP is the pressure difference across the resistive element in μ bars, and Q is the flow rate in cubic centimeters per second, the technique for measuring flow resistance reduces to the generation of a known flow through the

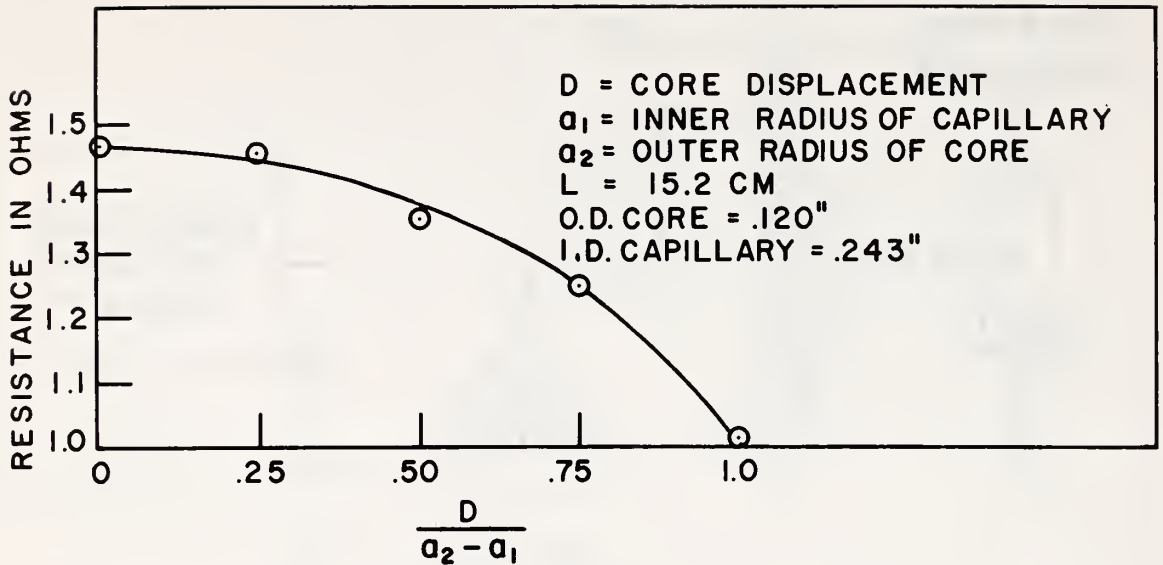


Figure 8. Resistance as a Function of Annular Core Position. Data taken using Centrifugal Calibrator Test Setup

resistive element and measuring the resulting differential pressure across the resistive element. A constant displacement pump provided the known flow rate in these tests. A capacitive pressure transducer⁷ was used to measure ΔP . The pressure transducer was calibrated at low differential pressures with a device devised in the past by the Infrasonics Group at the National Bureau of Standards. The basic principle is a variation of a device used in measuring flow resistance.⁶ The late Peter Chrzanowski of the National Bureau of Standards was chiefly responsible for the adaptation of this device to the generation of small, known, pressure differentials (Appendix 3).

The static calibrator for low differential pressure absolute calibration (Figures 5 and 6) consists of a chemical balance and a cup inverted in a liquid holding container with a centrally located tube sampling the pressure under the inverted cup. It can be shown that a relation exists between the radii of the container, cup and central tube; the mass on the balance pan; and the resulting pressure beneath the cup. The resulting pressure change does not depend upon the density of the liquid used. Dow Corning fluid 200, 1 centipoise, has been used in this system. This liquid has a low viscosity and excellent wetting properties which minimize draining and surface tension effects. The pressure relation is (Appendix 3)

$$\Delta P = \frac{m g (r_4^2 - r_3^2 + r_2^2 - r_1^2)}{[\pi r_3^2 (r_2^2 - r_1^2) + \pi r_2^2 (r_4^2 - r_3^2)]} \quad (8)$$

The radii are defined in Figure 5. The transducer used in these flow resistance measurements was calibrated by this method.

The pump and the pressure transducer were located outside the temperature chamber. The temperature chamber was a Delta Design Inc., Model 1060W. Because the precision pump was operated outside the temperature chamber, it was necessary to apply corrections for the differences in air density between the chamber and the pump. The coiled copper tubing was used to insure that the air attained the temperature of the chamber before passing through the flow resistive element.

The volume flow inside the chamber is

$$(dV_c / dt) = (T_c / T_p) (dV_p / dt) \quad (9)$$

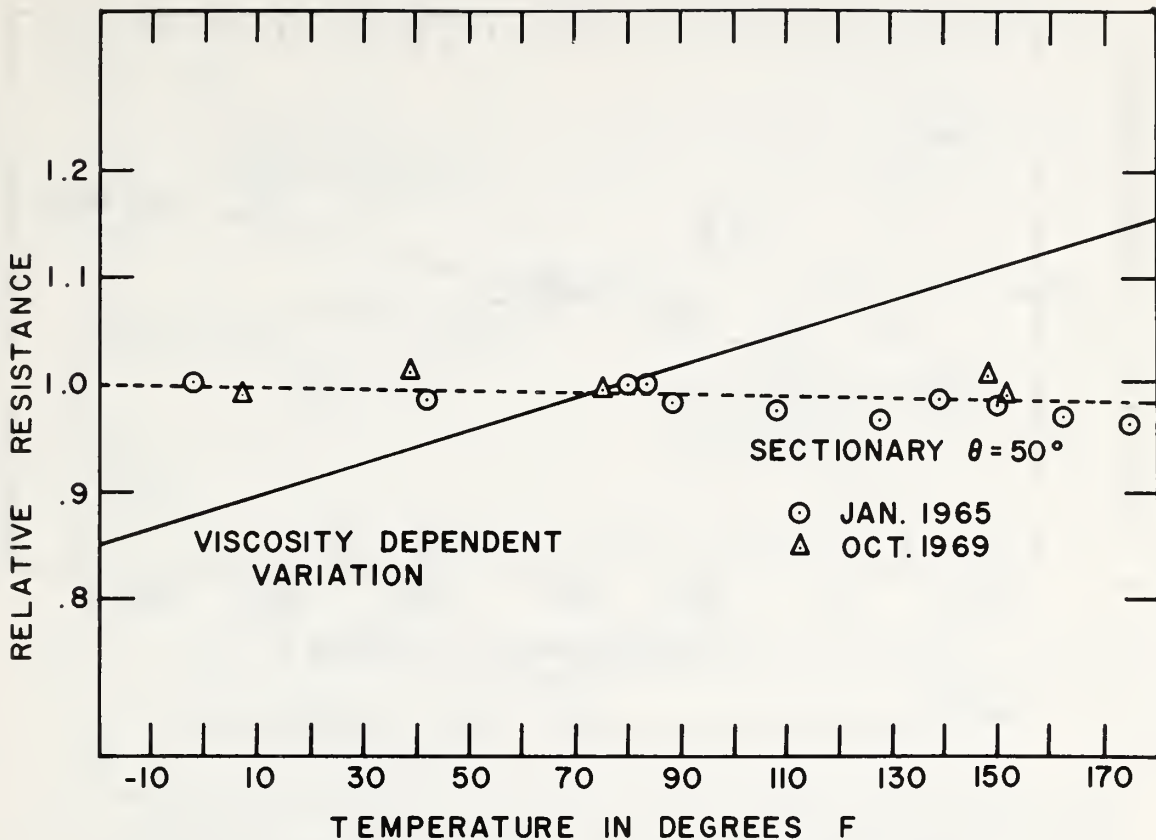


Figure 9. Resistance as a Function of Temperature for Sectionary, illustrating Compensation. The Element had the Following Dimensions: $\theta = 50$ degrees, Core Diameter = 0.119 inches, Length = 4.3 cm., and Outside Diameter of Capillary = 0.43 inches

where T_c is the chamber air temperature and T_p is the pump air temperature in degrees Kelvin, dV_c/dt is the volume velocity in the temperature chamber, and dV_p/dt is the volume velocity at the pump. One end of the resistive element and one end of the pressure transducer were left open to the atmosphere.

A different technique was necessary to determine the change in flow resistance of an annular with eccentricity of the core. To specify accurately the core position, the annular dimensions were made large, resulting in a low value of flow resistance. The method chosen to estimate the change in resistance as a function of core position was to measure the change in loading on a form of centrifugal pressure generator (see Figure 7 and Reference 8).

The centrifugal pressure generator used was a device possessing a low output impedance. If the resistive element is approximately equal in impedance to the output impedance of the centrifugal calibrator, a pressure sensor can be used to detect resistance changes. The centrifugal calibrator will be discussed in more detail in a later paper.

Experimental Results

This section contains the results of some of the experiments performed on flow resistors. Figure 8 shows the dimensions of the annular, tested at various core positions, and the data obtained. The centrifugal calibra-

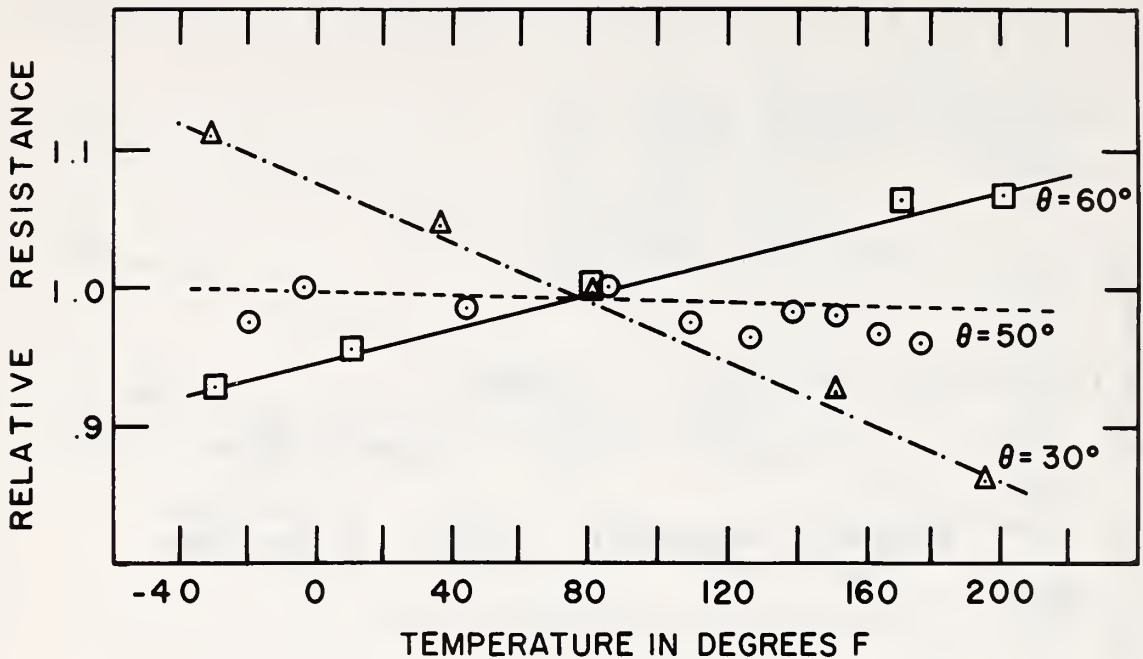


Figure 10. Sectionary Resistance as a Function of Temperature for Several Values of θ .

tor was used to perform this experiment. These results show that a large change in flow resistance occurs with a shift in core position. The measured change was not as great as would be expected from the results obtained by Johnson and Sparrow.⁹

Performing tests as shown in Figure 4, resistance data were obtained for various flow resistors as a function of temperature. The type of resistive element is described for each of the cases presented. The ratio of the resistance at room temperature to the resistance at chamber temperature has been plotted as a function of chamber temperature for various resistive elements. These results appear in Figures 9, 10 and 11.

The particular elements presented are as follows: The solid line curve in Figure 9 shows the expected change in resistance due to the air viscosity change with temperature for uncompensated capillary flow. The dashed line shows the measured resistance as a function of temperature for a sectionary with the following characteristics: $\theta = 50$ degrees; core material=stainless steel, 0.119 inch diameter; and length of section=4.3 centimeters. The capillary material was RTV-615 manufactured by the General Electric Company. This material was cast on a

rod 0.119 inches in diameter and cured for one hour at 100 degrees Centigrade. The outside diameter was 0.43 inches. The total resistance for this unit at 80 degrees Fahrenheit was 1200 ohms. The linear coefficient of expansion for the RTV-615 material was 34×10^{-5} per degree Centigrade. The measured resistances at various temperatures have been normalized with respect to the value at room temperature. For use with a microphone the resistance was adjusted to 840 ohms.

This sectionary was placed in the field (6/28/68), operated in an infrasonic microphone for over one year, and then retested (10/14/69). The characteristics of the device were found to have remained stable. The data taken after the field test are also plotted in Figure 9.

The absolute resistance value of this particular resistor is about a factor of 2 higher than predicted by theory. Better agreement was obtained for other sectionaries made from silicone rubber. A set of sectionaries made from glass capillaries on the other hand had agreed well at room temperature with the value predicted by theory (see Figures 12 and 13). This discrepancy probably results from shrinkage of the silicone rubber capillary during the curing process.

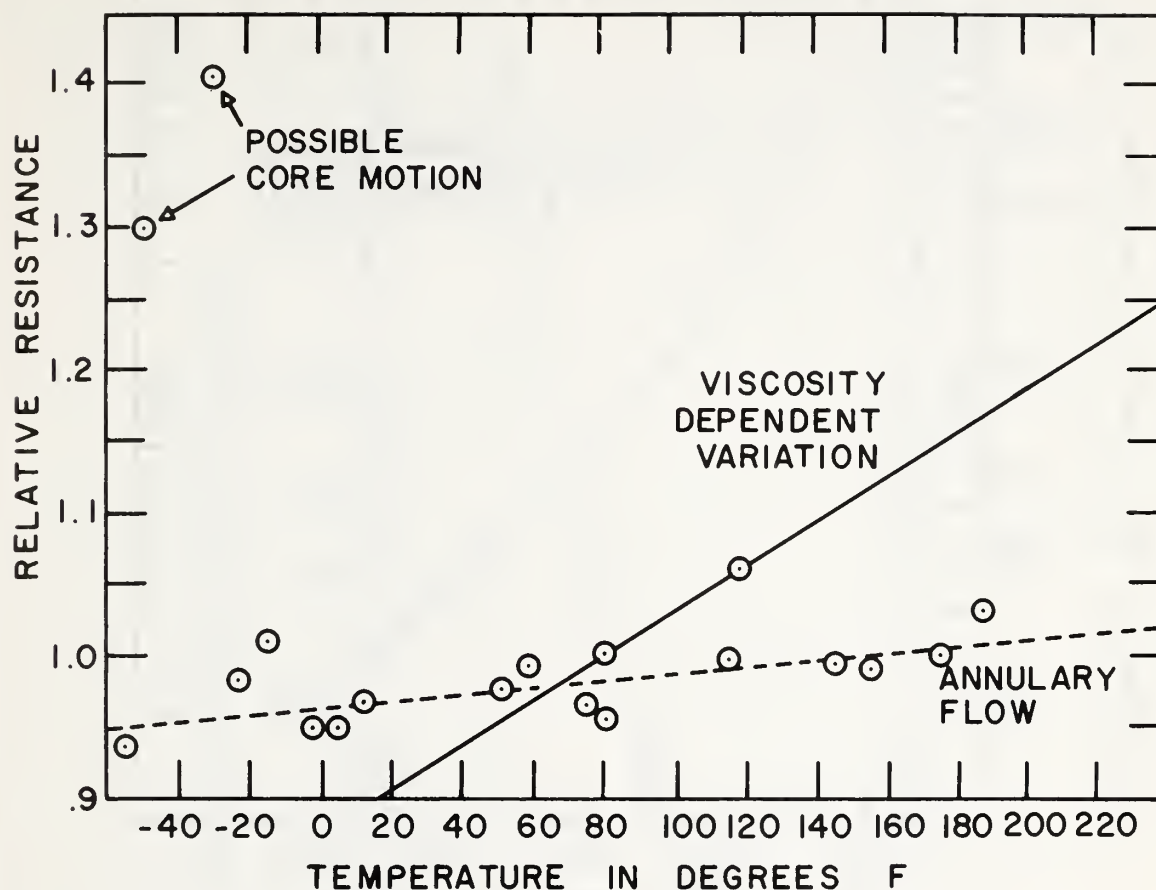


Figure 11. Resistance of a Function of Temperature for an Annular.
Core piece = 0.085 inch Diameter, Silicone Rubber Inside
Diameter = 0.120 inches and Length = 8 cm

This slight shrinkage will cause the silicone rubber tubing to deviate from a circular cross section with the rod inserted. This slight reduction of the passage area will cause the flow resistance to increase relative to the geometry assumed.

Figure 9 shows that the temperature dependence of this sectionary was greatly reduced because the differential coefficients of expansion caused dimensional changes in the air passage that compensate to a large degree for the change in air viscosity with temperature. The angle θ necessary to accomplish this was determined empirically for the materials and dimensions used.

Figure 10 illustrates the effect of the angle θ on the variation of sectionary resistance with temperature using

a silicone rubber tube. At $\theta=60$ degrees partial temperature compensation is obtained with respect to standard capillary flow. The data on resistance variation at $\theta=50$ degrees are the same data as those plotted in Figure 9. At $\theta=30$ degrees over-compensation is attained. Thus it would seem that by the proper choice of the angle θ and the materials used compensation should be attainable for a variety of gases. Making the core the larger coefficient of expansion piece would be the proper approach when working with liquids.

Figure 11 shows the experimental data on the resistance of an annular as a function of temperature. The viscosity-caused variation is also presented for reference. Two anomalous points in this data below -20 degrees

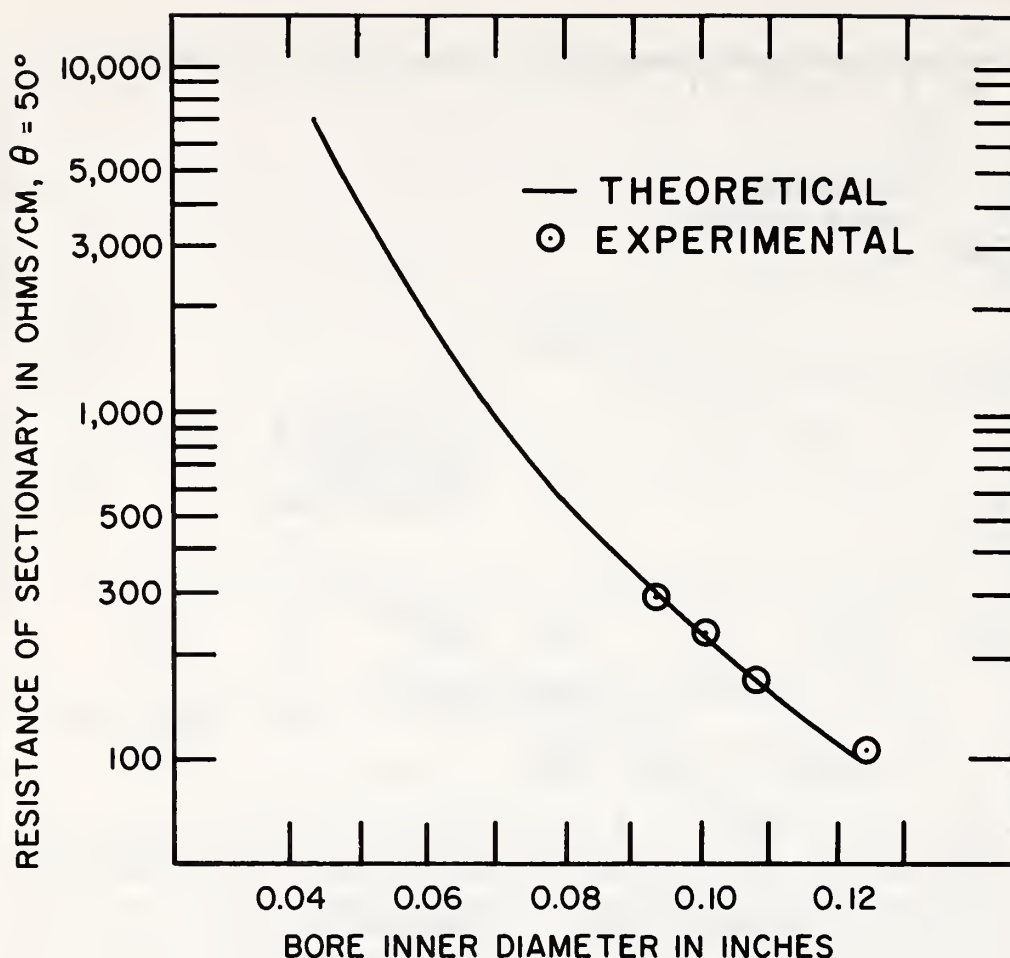


Figure 12. Sectionary Resistance as a Function of Bore Radius, Theoretical and Experimental using Glass Tubes for $\theta = 50$ degrees at Room Temperature

Fahrenheit are attributed to a movement of the core piece. The temperature chamber was moved before and after these readings. Much of the scatter in the plot is probably due to slight motions of the core caused by vibration of the temperature chamber. The annular was made from a 0.085 inch O.D. stainless steel core piece and a 0.120 inch capillary section made from a G.E. silicone rubber compound RTV-602. These data and the data presented in Figure 8 indicate the problem posed in maintaining the core centered in this configuration.

Figures 12 and 13 present theoretical and

experimental data for the sectionary. In Figure 12, the sectionary resistance is plotted as a function of core radius, with θ constant at 50 degrees. Glass capillaries were used. The resistance in ohms per centimeter length at room temperature has been plotted as a function of θ in Figure 13. A glass capillary was used (inside diameter - 0.101 inches) with various cores in obtaining these experimental points. Agreement with the values calculated from Equation 5, the solid line, is good. The data presented in Figures 12 and 13 were obtained at room temperature.

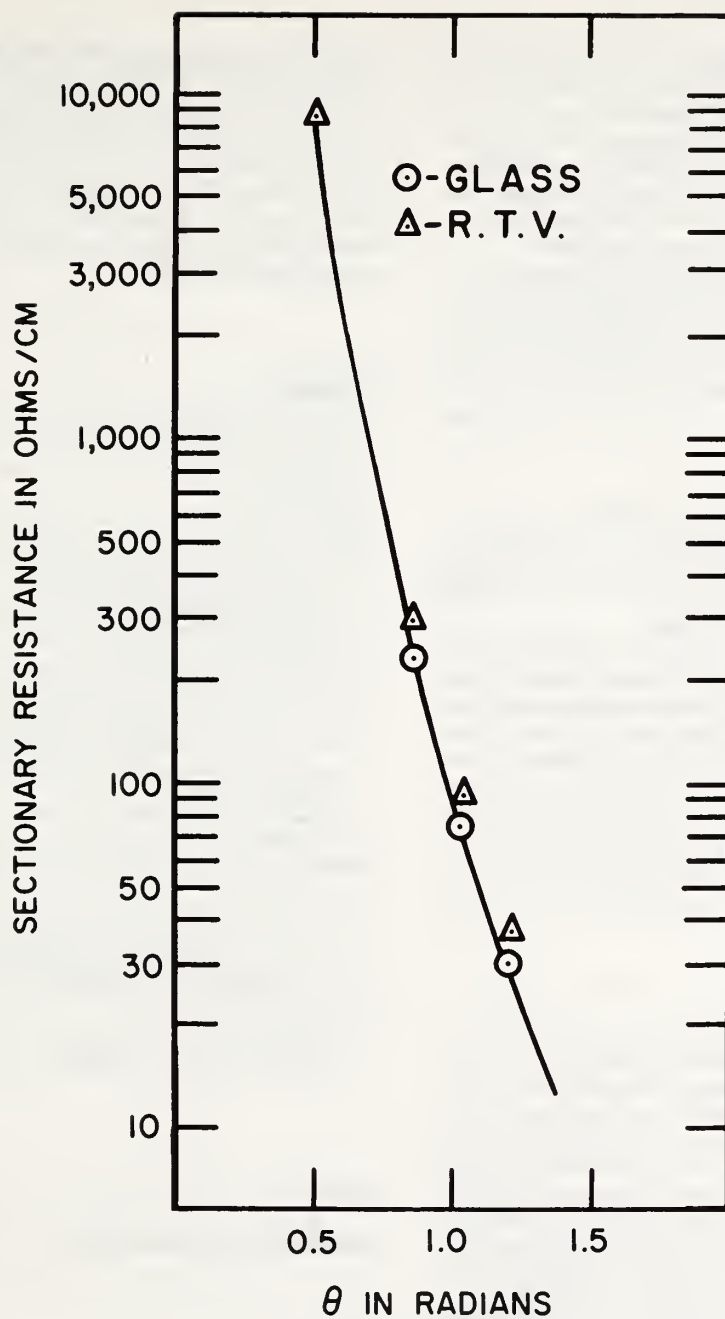


Figure 13. Sectionary Resistance as a Function of θ . Theoretical and Experimental for both Glass and Silicone Rubber Tubes Inside Diameter = 0.101 inches at Room Temperature

Using tubes of silicone rubber RTV-615 (G.E.) in place of the glass capillaries yields values of resistance about 20-30 per cent higher than the theoretical as shown by the triangles on Figure 13. A 25 per cent factor would seem to be a good value to use in design work with these materials. This factor is probably dependent upon the curing process. However, no work has been done to investigate the effect of the curing temperature.

The sectionary will not compensate for variations in air viscosity caused by variations in humidity. Viscosity changes due to humidity changes are small however, in comparison with viscosity changes due to temperature,¹⁰ and are typically less than 3 per cent at the temperatures of interest.

Conclusions

The attainment of temperature independence using a form of annularity is accompanied by the basic difficulty of keeping the core centered. Misalignments and shifts in core position can cause changes of resistance larger than those due to temperature changes.

It is possible to attain temperature independence by using a sectionary. Good stability has been observed both for short-term measurements of various sectionaries and for long-term tests of a sectionary under field conditions.

The theoretical relation developed in Equation 5 can be used to design sectionaries. Although theory and practice agree quite well, more work should be done to investigate the effect of variations in the curing process.

The resistance of the sectionary form of flow resistor can be adjusted by varying the length of the core within the capillary.

Acknowledgments

I am most grateful to Mr. Harry Matheson of the Geoacoustics Group of the National Oceanic and Atmospheric Administration for suggestions, and the presentation of the problem. Dr. Daniel P. Johnson of the National Bureau of Standards was also a source of excellent advice. The late Mr. Peter Chrzanowski of the National Bureau of Standards was chiefly responsible for the development of the differential pressure calibrator (Figure 6) used in these measurements. The equation for this form of the device was originally developed by Dr. Guy Cook of the National Bureau of Standards.

I have learned recently through a private communication from George E. Lindemann, formerly of Republic Flow Meters Co., that a similar pressure calibrator was built by his group in 1931. Unfortunately their device was not formally documented.

Mr. Walter Gilbert formerly of the National Bureau of Standards, provided considerable assistance with

computer programming and with the evaluation of the integral, Equation 6. Mr. Henry Schmidt and Mr. E.M. King of the Geoacoustics Group arranged for the fabrication of many of the flow resistors tested.

[This paper was first presented at the 93rd Winter Annual Meeting of the ASME held 26-30 November 1972 in New York City. Please refer to Volume 5, Issue Number 1 (January 1973) for details about other fluidics papers presented—Editor.]

References

1. *American Institute of Physics Handbook*, 2nd edition, New York: McGraw-Hill, 1963, Table 2u-5, p. 2-227.
2. H. Lamb. *Hydrodynamics*, New York: Dover Publications, 1945, pp. 585-587.
3. E. A. Kearsley. "Bounds on the Dissipation of Energy in Steady Flow of a Viscous Incompressible Fluid Around a Body Rotating Within a Finite Region," *Archive for Rational Mechanical Analysis*, Vol. 5, No. 4 (1960), pp. 347-354.
4. J. E. Anderson. "Acoustical-Impedance Characteristics of Sintered Stainless Steel," *Journal of the Acoustical Society of America*, Vol. 36, No. 5 (May 1964), pp. 811-815.
5. R. Brown and R. Bolt. "The Measurement of Flow Resistance of Porous Acoustic Materials," *Journal of the Acoustical Society of America*, Vol. 13, No. 4 (April 1942), pp. 337-344.
6. R. W. Leonard. "Simplified Flow Resistance Measurements," *Journal of the Acoustical Society of America*, Vol. 17, No. 3 (January 1946), pp. 240-241.
7. F. Cordero, H. Matheson and D. P. Johnson. "A Nonlinear Instrument Diaphragm," *Journal of Research - National Bureau of Standards*, Vol. 58, No. 6 (June 1957), pp. 333-337.
8. J. F. Kemp. "Centrifugal Manometer," *Transactions of the ASME, Journal of Basic Engineering*, September 1959, pp. 341-348.
9. V. K. Johnson and E. M. Sparrow. "Results of Laminar Flow Analysis and Turbulent Flow Experiments for Eccentric Annular Ducts," *American Institute of Chemical Engineering*, Vol. 2, No. 6 (November 1965), pp. 1143-1145.
10. J. Kestin and J. H. Whitelaw. *Measurements of the Viscosity of Dry and Humid Air, Humidity and Moisture*, New York: Reinhold Publishing Corp. Vol. 3, pp. 301-314.

Appendix 1

Temperature Compensation of an Annularity

For

$$R = (8\mu l / \pi) [(a_1^4 - a_2^4) + (a_1^2 - a_2^2)^2 / \ln(a_2/a_1)]^{-1} \quad (10)$$

consider the case for $dR/dT = 0$ and set $l = Na_1$. Then

$$\begin{aligned} (dR/dT) &= (8\mu N/\pi) \left(\frac{d}{dT} \right) \left\{ a_1 / [(a_1^4 - a_2^4) \right. \\ &\quad \left. + (a_1^2 - a_2^2)^2 / \text{Ln}(a_2/a_1)] \right\} \\ &+ (8N/\pi) \left\{ a_1 / [(a_1^4 - a_2^4) \right. \\ &\quad \left. + (a_1^2 - a_2^2)^2 / \text{Ln}(a_2/a_1)] \right\} \\ &\quad (d\mu/dT) = 0 \end{aligned} \quad (11)$$

$$\begin{aligned} (1/\mu) (d\mu/dT) &= \left\{ -1 / \left[a_1 / [(a_1^4 - a_2^4) \right. \right. \\ &\quad \left. \left. + (a_1^2 - a_2^2)^2 / \text{Ln}(a_2/a_1)] \right] \right\} \\ (d/dT) &\left\{ a_1 / [(a_1^4 - a_2^4) \right. \\ &\quad \left. + (a_1^2 - a_2^2)^2 / \text{Ln}(a_2/a_1)] \right\} \end{aligned} \quad (12)$$

Note that a_1 and a_2 are functions of T .

Performing the differentiation and expansion gives

$$\begin{aligned} (1/\mu) (d\mu/dT) &= -(1/a_1) (da_1/dT) \\ &+ \left\{ (da_1/dT) / [(a_1^4 - a_2^4) \right. \\ &\quad \left. + (a_1^2 - a_2^2)^2 / \text{Ln}(a_2/a_1)] \right\} \\ &\quad \left\{ 4a_1^3 + [4a_1^3 / \text{Ln}(a_2/a_1)] \right. \\ &\quad \left. - [4a_1 a_2^2 / \text{Ln}(a_2/a_1)] \right. \\ &\quad \left. + [(a_1^2 + a_2^2)^2 / a_1 \text{Ln}(a_2/a_1)] \right\} \\ &\dots + \left\{ (da_2/dT) / [(a_1^4 - a_2^4) \right. \end{aligned}$$

$$\begin{aligned} &\quad \left. + (a_1^2 - a_2^2)^2 / \text{Ln}(a_2/a_1)] \right\} \\ &\quad \left\{ -4a_2^3 - [4a_2 a_1^2 / \text{Ln}(a_2/a_1)] \right. \\ &\quad \left. - [4a_1 a_2^2 / \text{Ln}(a_2/a_1)] \right. \\ &\quad \left. + [(a_1^2 - a_2^2)^2 / a_2 \{ \text{Ln}(a_2/a_1) \}^2] \right\} \end{aligned} \quad (13)$$

Combining and solving for

$$(1/a_1) (da_1/dT)$$

yields

$$\begin{aligned} (1/a_1) (da_1/dT) &= \\ &\quad \left\{ (1/\mu) (d\mu/dT) [(a_1^4 - a_2^4) \right. \\ &\quad \left. + (a_1^2 - a_2^2)^2 / \text{Ln}(a_2/a_1)] \right. \\ &\quad \left. + (1/a_2) (da_2/dT) [2a_2^2 \right. \\ &\quad \left. + (a_1^2 - a_2^2) / \text{Ln}(a_2/a_1)]^2 \right\} / \\ &\quad \left\{ [2a_1^2 + (a_1^2 - a_2^2) / \text{Ln}(a_2/a_1)]^2 \right. \\ &\quad \left. - [(a_1^4 - a_2^4) \right. \\ &\quad \left. + (a_1^2 - a_2^2)^2 / \text{Ln}(a_2/a_1)] \right\} \end{aligned} \quad (14)$$

Appendix 2

Sectionary Flow

The angles θ and Φ are defined in Figure 1, V is the fluid velocity along the length of the section, and a is the radius of the capillary tube. From the Navier-Stokes equation in polar coordinates

$$(1/r)(d/dr)[r(dV/dr)] = -\Delta P/\mu l \quad (15)$$

$$V = -(\Delta P/4\mu l)r^2 + b \ln r + c \quad (16)$$

where b and c are constants. The boundary conditions to be used are the following:

1. $V = 0$ for $r = a$, and
2. $V = 0$ for

$$r = a(\cos \theta / \cos \Phi)$$

From condition 1:

$$(\Delta P a^2 / 4\mu l) = b \ln a + c \quad (17)$$

From condition 2:

$$\begin{aligned} (\Delta P a^2 \cos^2 \theta / 4\mu l \cos^2 \Phi) = \\ b \ln [a(\cos \theta / \cos \Phi)] + c \end{aligned} \quad (18)$$

$$\begin{aligned} c = (a^2 \Delta P / 4\mu l) \left\{ 1 - (\ln a) \right. \\ \left. [(\cos^2 \theta / \cos^2 \Phi) - 1] \right\} / \\ \ln(\cos \theta / \cos \Phi) \end{aligned} \quad (19)$$

$$\begin{aligned} b = (a^2 \Delta P / 4\mu l) \\ \left\{ [(\cos^2 \theta / \cos^2 \Phi) - 1] / \right. \\ \left. \ln(\cos \theta / \cos \Phi) \right\} \end{aligned} \quad (20)$$

After substituting in Equation 16 for b and c , we have

$$\begin{aligned} V = (\Delta P / 4\mu l) [a^2 - r^2] + (a^2 \Delta P / 4\mu l) \\ \left\{ [(\cos^2 \theta / \cos^2 \Phi) - 1] / \right. \\ \left. \ln(\cos \theta / \cos \Phi) \right\} \ln(r/a) \end{aligned} \quad (21)$$

$$\begin{aligned} Q = \frac{\text{volume flow}}{\text{unit time}} \\ = 2 \int_a^a (\cos \theta / \cos \Phi) \int_{\Phi=0}^{\Phi=\theta} r V d\Phi dr \end{aligned} \quad (22)$$

Substituting for V gives

$$\begin{aligned} Q = (\Delta P / 2\mu l) \int_a^a (\cos \theta / \cos \Phi) \\ \int_{\Phi=0}^{\Phi=\theta} \left\{ (a^2 - r^2) r d\Phi dr \right. \\ \left. + a^2 [(\cos^2 \theta / \cos^2 \Phi) - 1] / \right. \\ \left. \ln(\cos \theta / \cos \Phi) \dots \right. \\ \left. \dots (r \ln r - r \ln a) d\Phi dr \right\} \end{aligned} \quad (23)$$

Performing this integration yields for the first term

$$\begin{aligned} (\Delta P / 8\mu l) a^4 \left\{ \theta - \sin \theta \cos \theta \right. \\ \left. [(2/3) \sin^2 \theta + 1] \right\} \end{aligned} \quad (24)$$

Now, performing integration on the second term of Equation 23 gives

$$\begin{aligned}
 & (\Delta P a^4 / 8 \mu l) \int_{\Phi=0}^{\Phi=\theta} \\
 & \left\{ \left[\left(\cos^2 \theta / \cos^2 \Phi \right) - 1 \right]^2 / \right. \\
 & \quad \left. \ln(\cos \theta / \cos \Phi) \right] \\
 & - 2(\cos^4 \theta / \cos^4 \Phi) + (\cos^2 \theta / \cos^2 \Phi) \Big\} \\
 & \quad d\Phi \\
 & \quad (25)
 \end{aligned}$$

The first term of Equation 25 has been evaluated over the interval $\Phi = 0$ to $\Phi = \pi/2$ (See Figure 2). Integrating and combining the remaining two terms inside the brackets yields

$$(4/3) \cos \theta \sin^3 \theta \quad (26)$$

Combining Equations 24 and 26 and the term

$$\begin{aligned}
 I = \int_{\Phi=0}^{\Phi=\theta} & \left\{ \left[\left(\cos^2 \theta / \cos^2 \Phi \right) - 1 \right]^2 / \right. \\
 & \left. \ln(\cos \theta / \cos \Phi) \right\} d\Phi
 \end{aligned}$$

This yields for Q

$$\begin{aligned}
 Q = (\Delta P / 8 \mu l) a^4 & \left\{ \theta - \sin \theta \cos \theta \right. \\
 & \left[(2/3) \sin^2 \theta + 1 \right] + I \\
 & \left. + (4/3) \cos \theta \sin^3 \theta \right\} \\
 & (27)
 \end{aligned}$$

But since

$$\begin{aligned}
 R &= \Delta P / Q \\
 R &= (8 \mu l / a^4) \left\{ 1 / \left[\theta + \sin \theta \cos \theta \right. \right. \\
 & \quad \left. \left. \left[(2/3) \sin^2 \theta - 1 \right] + I \right] \right\} \\
 & (28)
 \end{aligned}$$

Appendix 3

The Static Calibrator (Figures 5 and 6)

When $P_{in} = P_{out}$, and the system is in equilibrium

$$\begin{aligned}
 M &= \pi(r_3^2 - r_2^2) L_1 \rho' \\
 & - \pi(r_3^2 - r_2^2) L_2 \rho + \pi r_2^2 L \rho' \\
 & (29)
 \end{aligned}$$

When P_{in} is greater than P_{out} , and the system is brought back to equilibrium by subtracting a weight m from the balance pan

$$\begin{aligned}
 M - m &= \pi(r_3^2 - r_2^2) L_1 \rho' \\
 & - \pi(r_3^2 - r_2^2) (L_2 + h_2) \rho \\
 & - \pi r_2^2 (h_1 + h_2) \rho + \dots \\
 & \dots \pi r_2^2 L \rho' \\
 & (30)
 \end{aligned}$$

Subtract Equation 29 from Equation 30 to obtain

$$m = \pi r_3^2 h_2 \rho + \pi r_2^2 h_1 \rho \quad (31)$$

Note

$$\pi r_3^2 h_2 + \pi r_2^2 h_1$$

is the volume represented by the shaded area in the diagram.

Now, the volume of liquid depressed inside the can equals the volume elevated outside the can

$$h_1 (\pi r_2^2 - \pi r_1^2) = h_2 (\pi r_4^2 - \pi r_3^2) \quad (32)$$

Define

$$A = h_2 / h_1$$

$$= (\pi r_2^2 - \pi r_1^2) / (\pi r_4^2 - \pi r_3^2) \quad (33)$$

$$h_2 = h_1 A \quad (34)$$

Substitute Equation 34 into Equation 31 to obtain

$$m / \pi \rho = r_3^2 h_1 A + r_2^2 h_1 \quad (35)$$

from which we get

$$h_1 = m / \pi \rho (r_3^2 A + r_2^2) \quad (36)$$

due to m . The Δp , the change of pressure inside the can, is

$$\Delta p = (h_1 + h_2) \rho g$$

$$\Delta p = h_1 (1 + A) \rho g \quad (37)$$

Substitute in Equation 37 for h_1 from Equation 36

$$\Delta p = [m g (1 + A)] / [\pi (r_3^2 A + r_2^2)] \quad (38)$$

Using Equation 33 to eliminate A gives

$$\Delta p = [m g (r_4^2 - r_3^2 + r_2^2 - r_1^2)] /$$

$$[\pi r_3^2 (r_2^2 - r_1^2)$$

$$+ \pi r_2^2 (r_4^2 - r_3^2)] \quad (39)$$

Thus, the pressure inside the can depends only on the relative dimensions and mg . If the can had a zero wall thickness, then the differential pressure would be the excess mass times the acceleration of gravity divided by the section area of the can. For a can with finite wall thickness all four radii are involved in the equation. The density of the liquid is not involved.

The static calibrator is based on modifying a chemical balance. The balance constant, $\Delta p/m$, has been determined by careful measurements of the involved radii. This constant is usually designated in terms of $\Delta p/m$, $\mu\text{bar per gram}$.

Nomenclature

| | |
|-------|-------------------------------------------------------------------|
| A | Ratio of liquid height displacements, h_1/h_2 |
| a | Inner radius of capillary |
| a_1 | Inner radius of capillary portion of annularity |
| a_2 | Radius of core |
| b | Constant appearing in Equation 16 |
| c | Constant appearing in Equation 16 |
| D | Core displacement distance |
| g | Acceleration due to gravity |
| h_1 | Height of liquid displaced outside cup above equilibrium position |
| h_2 | Height of liquid displaced inside cup below equilibrium position |
| I | The integral defined by Equation 6 |
| L_1 | Length from top of static calibrator cup to base |
| L_2 | Length of static calibrator cup submerged in liquid initially |
| l | Length of capillary tube |
| m | Weight subtracted from pan of static calibrator |
| N | Number of radii equal to length of tube $= l/A$ |

| | |
|------------|---------------------------------------------------------------------------------------------------------------------------|
| Q | Volume velocity |
| R | Flow resistance |
| r | Distance from center of capillary |
| r_1 | Outer radius of central tube of static calibrator |
| r_2 | Inner radius of cup of static calibrator |
| r_3 | Outer radius of cup of static calibrator |
| r_4 | Inner radius of container of static calibrator |
| T | Temperature of medium |
| T_c | Chamber air temperature |
| T_p | Pump air temperature |
| V | Fluid velocity along length of section |
| dV_c/dt | Volume velocity in temperature chamber |
| dV_p/dt | Volume velocity at the pump |
| ΔP | Pressure difference |
| θ | Half the angle subtended by the flatted portion of the core |
| μ | Viscosity of medium |
| ρ | Density of static calibrator liquid |
| ρ' | Density of cup material |
| Φ | The angle from a line bisecting the center of the flatted portion of the core piece to a radii. May not exceed θ . |

Analysis of Four Optical Distance Measuring Instrument Configurations Using Electrooptical Polarization Modulators

E. Norman Hernandez

Four configurations for optical distance measuring instruments using electrooptical polarization modulators are analyzed. Criteria are developed to compare the systems. A summary of the systems is presented, and their advantages and disadvantages are discussed.

Introduction

Recent progress in lasers and high-frequency modulation techniques has spurred the development of optical geodetic distance-measuring instruments.¹ As the final accuracy of the distance measurement depends upon the modulation frequency of the optical beams, it is desirable to have devices that allow modulation at microwave frequencies.

Electrooptic phase modulators are capable of polarization modulation of optical beams at microwave frequencies. Recently, several distance-measuring instruments have been constructed using this type of modulator.²⁻⁵ It is necessary to optimize such optical configurations since the typical value of Γ_0 , the peak phase retardation of the modulator, is usually small.

This paper analyzes four instrument configurations and compares their expected performances. The optimal configuration depends on various parameters including bandwidth of the receiving-intensity detector, whether the system is one way or two way, and the maximum frequency of modulation necessary.

Most electrooptic modulators in the microwave band have small Γ_0 . In this case of small Γ_0 , two important criteria are discussed: *amplitude for small Γ_0 and dc residue*. The first is the amplitude of the applied signal, used as a measure of the strength of the signal containing the phase information. The second is the value of the dc optical term, which, as in the case of a photomultiplier (PM) tube, can saturate the intensity receiver.

The author was with the National Oceanic and Atmospheric Administration, Environmental Research Laboratories, when this work was done; he now has a joint appointment with the Applied Physics Laboratory, University of Washington, Seattle, Washington 98105.

Received 5 August 1971.

Theory of Electrooptic Modulator

Consider the electrooptic crystal depicted in Fig. 1. The following equations are computed from Jones's matrices shown in the figure. The fast axis, y , and slow axis, x , of the crystal are oriented at 45° to the cleavage (x, y). A vertically polarized optical plane wave is incident on the crystal face. The electric field of the optical plane wave is represented by

$$\mathbf{E}_{in} = A \cos(\omega_c t) \mathbf{a}_y, \quad (1)$$

where A is the amplitude, ω_c is the optical frequency in radians, and \mathbf{a}_y is the y direction unit vector. The electric field is retarded by the crystal, resulting in

$$\mathbf{E}_{out} = \left[\frac{A}{2} \cos(\omega_c t + \Phi_1) + \frac{A}{2} \cos(\omega_c t + \Phi_2) \right] \mathbf{a}_y + \left[\frac{A}{2} \cos(\omega_c t + \Phi_1) - \frac{A}{2} \cos(\omega_c t + \Phi_2) \right] \mathbf{a}_x, \quad (2)$$

where Φ_1, Φ_2 are the phase retardations along the y^1 and x^1 axes, respectively. For simplicity, we assume that a net phase retardation occurs only on the y^1 axis, so

$$\mathbf{E}_{out} = \left[\frac{A}{2} \cos(\omega_c t + \Gamma) + \frac{A}{2} \cos(\omega_c t) \right] \mathbf{a}_y + \left[\frac{A}{2} \cos(\omega_c t + \Gamma) - \frac{A}{2} \cos(\omega_c t) \right] \mathbf{a}_x. \quad (3)$$

Defining V and H by

$$\mathbf{E}_{out} = V \mathbf{a}_y + H \mathbf{a}_x, \quad (4)$$

we can write the intensity for the vertical, V , and horizontal, H , components as

$$V^2 = A^2 \left[\cos^2\left(\frac{\Gamma}{2}\right) \cos^2\left(\omega_c t + \frac{\Gamma}{2}\right) \right], \quad (5)$$

$$H^2 = A^2 \left[\sin^2\left(\frac{\Gamma}{2}\right) \sin^2\left(\omega_c t + \frac{\Gamma}{2}\right) \right] \quad (6)$$

A device, such as a PM tube, is used to detect the horizontal or vertical components. Such devices are sensitive only to the intensity and will not respond to oscil-

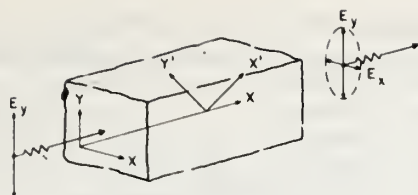


Fig. 1. Electrooptic crystal.

lation at optical frequencies. This reduces Eqs. (5) and (6) to

$$V^2 = \frac{A^2}{4} (1 + \cos \Gamma), \quad (7)$$

$$H^2 = \frac{A^2}{4} (1 - \cos \Gamma). \quad (8)$$

In a distance measuring instrument, Γ contains information concerning the path phase delay, that is, Γ is a function of Φ , where Φ is the phase delay introduced by the propagation path's transit time. Suppose that the modulator is being modulated at ω_m rad/sec. Then Γ has the form,

$$\Gamma = \Gamma_0 \cos(\omega_m t), \quad (9)$$

where Γ_0 is the peak phase retardation of the crystal modulator. Substituting Eq. (9) into either Eq. (7) or (8) yields the phase modulated form,

$$\cos(\Gamma_0 \cos \omega_m t). \quad (10)$$

Expanding this function in a Fourier series gives (for the horizontal term)

$$H^2 = 1 - J_0(\Gamma_0) + 2J_2(\Gamma_0) \cos(2\omega_m t) + \dots + \theta(2n\omega_m t), \quad (11)$$

where $\theta(2n\omega_m t)$ is taken to mean frequency components of order $2n\omega_m t$ and higher. If we used a quarter-wave plate, Eq. (9) would become

$$\Gamma = \Gamma_0 \cos(\omega_m t) + (\pi/2). \quad (12)$$

Expanding as in Eq. (11) we obtain

$$H^2 = 1 + 2J_1(\Gamma_0) \sin(\omega_m t) + \dots + \theta[(2n+1)\omega_m t]. \quad (13)$$

Comparing Eqs. (11) and (13) we see that a quarter-wave plate shifts the energy into the odd harmonics. In the case of small Γ_0 , Eq. (11) becomes

$$H^2 \approx 1 + J_0(\Gamma_0) - 2J_2(\Gamma_0) \cos(2\omega_m t), \quad (14)$$

and Eq. (13) becomes

$$H^2 \approx 1 + 2J_1(\Gamma_0) \sin(\omega_m t). \quad (15)$$

Three Configurations

Systems II, IIIb, IVa, and IVb (see Table I) have been built and are in various stages of testing. For convenience, we reserve final comparison until after we have analyzed each system separately.

Systems I and II: Amplitude Modulation (AM System)

This system (I) is constructed, as shown in Fig. 2, with a $\lambda/4$ retardation plate on the transmitting side and a polarizer and PM tube on the receiver side. Computing Jones's matrices we obtain at the output of the polarizer for the horizontal intensity

$$H^2 \approx 1 - \sin[\Gamma_0 \cos(\omega_\mu t + \Phi)], \quad (16)$$

where the terms are previously defined. Reducing this equation for small Γ_0 yields

$$H^2 \approx 1 - 2J_1(\Gamma_0) \cos(\omega_\mu t + \Phi) + \theta(3\omega_\mu t), \quad (17)$$

where $\theta(n\omega_\mu t)$ is previously defined. Detection of the amplitude of the cosine term requires either a demodulating PM tube or a PM tube that can respond to the ω_μ frequency. In any event the important parameter is $2J_1(\Gamma_0)$ and the dc residue is 1. System II in Fig. 2 does not have the $\lambda/4$ plate, yielding for the horizontal intensity

$$H^2 \approx 1 - \cos[\Gamma_0 \cos(\omega_\mu t + \Phi)]. \quad (18)$$

Expanding this equation gives

$$H^2 \approx 1 - J_0(\Gamma_0) + 2J_2(\Gamma_0) \cos(2\omega_\mu t + 2\Phi), \quad (19)$$

and for small Γ_0 ,

$$H^2 \approx \frac{\Gamma_0^2}{4} + \frac{\Gamma_0^2}{4} \cos(2\omega_\mu t + 2\Phi). \quad (20)$$

Here the intensity receiver must respond to $2\omega_\mu$ but the dc residue is of the order of the received amplitude.

System III: Two-Modulator Intermediate Frequency (IF) System

This system uses two modulators and is a one-way system; that is, the transmitter is on one end of the propagation path, and the receiver is on the other end. Jones's matrices yield

$$H^2 \approx 1 - \sin \left[2\Gamma_0 \cos \left(\frac{\omega_1 - \omega_2}{2} t + \frac{\Phi}{2} \right) \cos \left(\frac{\omega_1 + \omega_2}{2} t + \frac{\Phi}{2} \right) \right]. \quad (21)$$

Table I. System Comparisons

| System | Frequency | Amplitude | Amplitude. small Γ_0 | dc Residue |
|--------|-----------------------------------------|-----------------------------------|--------------------------------|------------------------------------------------|
| I | $\omega t + \Phi$ | $2J_1(\Gamma_0)$ | Γ_0 | 1 |
| II | $2\omega t + 2\Phi$ | $2J_2(\Gamma_0)$ | $\Gamma_0^2/4$ | $1 - J_0(\Gamma_0) \approx \{(\Gamma_0^2/4)\}$ |
| IIIa | $\omega t + \Phi$ | $2J_1[2\Gamma_0 \cos(\Phi/2)]$ | $2\Gamma_0 \cos(\Phi/2)$ | 1 |
| IIIb | $[(\omega_1 - \omega_2)/2]t + (\Phi/2)$ | $2\Gamma_0$ | $2\Gamma_0$ | 1 |
| IVa | dc | $1 - J_0[2\Gamma_0 \cos(\Phi/2)]$ | $(\Gamma_0^2/4)(1 + \cos\Phi)$ | — |
| IVb | $(\omega_1 - \omega_2)t + \Phi$ | $\Gamma_0^2/2$ | $\Gamma_0^2/2$ | $\Gamma_0^2/2$ |

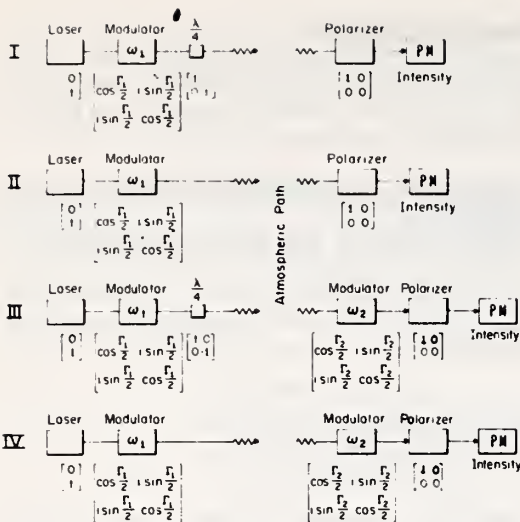


Fig. 2. Various optical distance measuring instrument configurations.

This reduces, in the case of small Γ_0 , to

$$H^2 \approx 1 - 2J_1 \left[2\Gamma_0 \cos\left(\frac{\omega_1 - \omega_2}{2}t + \frac{\Phi}{2}\right) \right] \cos\left(\frac{\omega_1 + \omega_2}{2}t + \frac{\Phi}{2}\right) \quad (22)$$

If the PM tube can follow frequencies of the order of ω where $\omega_1 = \omega_2 = \omega$, the amplitude term is given by $2J_1(2\Gamma_0 \cos\Phi/2)$ and the dc residue is 1. Detection of this signal requires a PM tube with a frequency response of ω .

If $\omega_1 \neq \omega_2$ and Γ_0 is small, Eq. (21) becomes

$$H^2 \approx 1 - 2\Gamma_0 \cos\left(\frac{\omega_1 - \omega_2}{2}t + \frac{\Phi}{2}\right). \quad (23)$$

The PM tube needs only a response of $(\omega_1 - \omega_2)/2$, has an output with amplitude $2\Gamma_0$, and a dc residue of 1.

Systems IV: One- or Two-Modulator, dc, or DF System

This system can use two modulators for a one-way propagation path, or, with a folded propagation path, it can use a single modulator.⁶ Computing H^2 we obtain

$$H^2 \approx 1 - \cos \left[2\Gamma_0 \cos\left(\frac{\omega_1 - \omega_2}{2}t + \frac{\Phi}{2}\right) \cos\left(\frac{\omega_1 + \omega_2}{2}t + \frac{\Phi}{2}\right) \right]. \quad (24)$$

With $\omega_1 = \omega_2 = \omega$, Eq. (21) becomes

$$H^2 \approx 1 - J_0(2\Gamma_0 \cos\Phi/2) + \theta(\omega t). \quad (25)$$

The output dc term is $1 - J_0(2\Gamma_0 \cos\Phi/2)$.

If $\omega_1 \neq \omega_2$ and Γ_0 is small,

$$H^2 \approx \Gamma_0^2 \{ 1 + \cos[(\omega_1 - \omega_2)t + \Phi] \}. \quad (26)$$

The amplitude is $\Gamma_0^2/2$, and the dc residue $\Gamma_0^2/2$.

Comparison

Table I summarizes the pertinent quantities used in comparing the different systems. The various systems are labeled I through IV. For each system the frequency and phase of the used output are given under the column, FREQUENCY. The amplitude of this signal and the value of the amplitude in the case of small Γ_0 are given under columns AMPLITUDE and AMPLITUDE SMALL Γ_0 . The final column labeled, DC RESIDUE, refers to the cases where the amplitude of the ac signal is accompanied by a dc term. In some systems this dc term can saturate the receiver. For example, system IIb has an amplitude of $2\Gamma_0$ compared with $\Gamma_0^2/2$ for system IVb. If Γ_0 is less than four (which is true for ω_1, ω_2 in the microwave range for most modulators), it appears that system IIb is better than system IVb. The basic systems differ only by a $\lambda/4$ plate. If, however, a standard PM tube is used and if $\Gamma_0 \ll \frac{1}{2}$, the ac signal in system IIb will be dominated by the dc term, rendering the system useless. Under this condition, system IVb is preferable. This demonstrates that the dc residue term is as important as the amplitude term. Systems I and II require light detectors with either a frequency response of ω (or 2ω) or an internal heterodyning system. Clearly, at microwave frequencies, this is a disadvantage. System I suffers from a large dc residue compared to the amplitude of received signal whereas system II does not. Wood and Thompson² of the Institute for Telecommunication Sciences (ITS) have built a version of system II with an effective modulation frequency of 120 MHz.

System IIIa has the disadvantages of system I and requires two modulators.

System IVa is a dc system and requires different techniques to obtain the phase information Φ . In the other systems, the ac signal has a phase $(\Phi + \Phi/2)$ equal to the propagation path phase. System IVa has the advantage of needing only a single modulator (by folding the beam via a retroreflector). The disadvantage is that the phase information is contained in a term whose amplitude is $\Gamma_0^2/4$, the smallest of any of the systems. This system has been built by Hernandez and Earnshaw of the Environmental Research Laboratories.^{3,4} Systems IIb and IVb have been built by R. Gilmer, also of the Environmental Research Laboratories (private communication, paper to be published).

Conclusion

This paper has discussed four possible optical configurations for optical distance-measuring instruments. For very high frequencies (S band and higher), it appears that only systems IIb, IVa, and IVb are practical (Table I). Of these four systems, IIb has the worst dc residual-to-modulation amplitude ratio, for easily attainable Γ_0 [typically for KH_2PO_4 (KDP) modulators $\Gamma_0 < 0.1\pi$]. The two remaining systems have been built, tested, and checked with the theoretical results. System II has been built and tested but for lower modulation frequencies ($\omega = 120$ MHz).

This work was partially supported by AFCRL under

project order Y69-829 and by NASA under project order W12,929.

References

1. L. E. Wood, Trans. AGU **52**, 17 (1971).
2. L. E. Wood and M. C. Thompson, Jr., "Differential Phase Techniques for Measuring Atmospheric Refractivity," Proc. of Electro-Optic Systems Design Conference (September 1970), pp. 921-926.
3. K. B. Earnshaw and E. Norman Hernandez, Appl. Opt. **11**, in press (1972).
4. K. B. Earnshaw and J. C. Owens, IEEE J. Quantum Electron. **QE-3**, 11 (1967).
5. K. D. Froome and L. Essen, *Velocity of Light and Radio Waves* (Academic, New York, 1969).
6. L. E. Wood and M. C. Thompson, Nature **211**, 173 (1966).

Reprinted with permission from the Proceedings IEE Conference
RADAR, Present and Future, London, October 23-25, 74-80, 1973,
Publication 105

NON-REDUNDANT PHASED-ARRAY RADAR

W. K. Klemperer

I. Introduction

The considerable advantages of electronically steerable, phased-array radars over the more traditional mechanically steered systems are widely appreciated. However, it has become painfully clear that phased-array radars are outrageously expensive, unusually heavy if fully implemented, and generally unreliable. If one examines the system requirements of most phased-array radars, one finds that these requirements can well be met by certain skeletal arrays of far fewer elements. Of course, then the array gain is reduced and the sidelobe level is increased over what it would have been for a completely filled aperture. For many applications, the advantages outweigh the disadvantages. The per-element transmitted power can be increased and, in particular, with fewer elements one can afford better low-loss components and low-noise receivers. Sidelobe levels can be reduced by the enlightened application of proper weighting functions. By far the most important consideration is that with fewer elements one can significantly reduce the vast amount of redundant information which the usual array processor is forced to deal with. The following section briefly outlines the general approach and historical development of non-redundant antennas. Section III introduces some new two-dimensional array configurations of 15, 18, 27 and 30 elements. In the concluding section, some further remarks are addressed specifically to the application of element non-redundancy to the design of modern phased-array radar.

II. Non-Redundant Phased Arrays

It is by now generally appreciated that certain unfilled, incomplete or "skeletal" arrays can provide angular resolution comparable to that afforded by filled arrays of similar overall dimensions. All that is required of the incomplete array is that the various spatial Fourier components of the radiowave field be determined from a set of interferometer combinations, taking elements of the incomplete array two at a time. The resolution (but not the gain) of a filled aperture can then be obtained by synthesis. The sensitivity of an antenna to these spatial Fourier components is given by its spectral sensitivity function (s.s.f.) which is the complex autocorrelation function of the aperture distribution. The power radiation pattern of the array is the Fourier transform of its s.s.f. In the optics literature, antenna power radiation patterns are known as "spread functions" and the s.s.f.'s are called "transfer functions."

An appreciation of the discrete-interval (sampling) theorem is also helpful for the design of unfilled arrays. A filled array has a great many redundant spacings. On the other hand, a good skeletal array determines

W. K. Klemperer is with the National Oceanic and Atmospheric Administration, Environmental Research Laboratories, Boulder, Colorado, U.S.A.

the required Fourier components only once. Its s.s.f. or transfer function is characteristically flat. It can be shown that a non-redundant array yields the highest possible resolution* for a given aperture size [1].

One-dimensional arrays of minimum redundancy have received a good deal of attention, and a few representative arrays have been built [2],[3]. Figure 1 shows a plot of the number of elements vs. the number of spacings obtainable. Linear arrays of zero redundancy fall on the boundary between the shaded and the unshaded region (the curve $y = x(x - 1)/2$). Various minimum redundancy linear arrays of up to ten elements are marked by triangles. Ordinary, completely-filled linear arrays fall on the dashed line between the unshaded and the cross-hatched region of the figure. With minimum redundancy schemes, the number of spacings obtainable rises very steeply with the number of elements employed.

Suitable configurations for two-dimensional, non-redundant arrays have only recently been proposed [4]-[6]. Two-dimensional arrays of zero redundancy always sample $m(m-1)/2$ unique points of the u,v plane, where m is the number of aeriels. A special sub-class of all arrays of zero redundancy has the property of uniformly and completely sampling the central portion of the u,v plane out to some maximum radius. Following Golay [5] one can calculate a figure of merit for such arrays as the ratio of the minimum possible moment to the given moment of all the points of the transfer function in the $u-v$ plane. Another useful parameter is the core number, defined as the total number of points in the central portion of the $u-v$ plane within a limiting circle just passing through the unoccupied points closest to the center, to which is added one-half of the number of points falling on the circumference of that circle. In practice, a small proportion (5-10%) of holes in the transfer function can be tolerated. Accordingly, the core number parameter is a very conservative estimate of equivalent filled-array antenna performance.

III. Two-Dimensional, Non-Redundant Arrays

A number of new non-redundant array configurations for up to 30 elements are shown in the remaining figures, along with their transfer functions. Figures-of-merit and core numbers are given in the following table. These arrays are all based on a triangular or interlaced grid. Such an arrangement requires 13.4% fewer elements than an equivalent array arranged on a rectangular grid pattern.

Finding good, non-redundant array configurations is not a trivial problem (which is perhaps one reason why few previous examples have been published). The brute force approach is quite impractical: note that the number of possible arrangements of 36 antennas on a grid of 64×64 points exceeds 10^{130} . The problem may be defined as one of choosing, from a large number of non-redundant arrays, those which best satisfy criteria of compactness (figure-of-merit) and large core number. The patterns shown were all generated from known six-point patterns of zero redundancy, adding three new points at a time and using a computer to sort the resulting patterns by core number and compactness. Even better patterns may yet be found.

* Highly impractical "supergain" arrays (those with very large evanescent fields) are excluded.

It is interesting to speculate whether really superb array configurations of low redundancy exist; only zero redundancy cases have been examined so far. A small amount of redundancy is useful: identical spatial Fourier components acquired from widely separated portions of a low-redundancy array can then be compared and thus provide a good check on the performance of correlators and other equipment.

IV. Applications to Phased-Array Radar

As mentioned in the introduction, the problems with present-day phased-array radars are numerous; and at least some of these could be solved by using non-redundant arrays. A great deal of effort has gone into the design of array elements to minimize mutual coupling problems (which are the cause of array blindness in certain directions). Generally, these solutions limit the system bandwidth. With thinned arrays, mutual coupling is much reduced and it should be possible to design airborne multi-frequency radars capable of doing a number of tasks, a list which could include terrain avoidance, IFF, mapping, navigation, and even weather radar--all with the same array. Although the non-redundant array has much less gain than its completely-filled counterpart, there are many radar tasks other than long-range search for which high resolution and agility are far more important. With fewer elements to program and collect information from, the time and computational effort required for beam formation and beam-steering can be reduced by a large factor. Some earlier work in phased-array radar adopted the strategy of arranging elements in random two-dimensional patterns, achieving some of the advantages of the thinned and space-tapered arrays familiar in one-dimensional theory. Placing elements in a random arrangement avoids the periodicities inherent in non-random arrangements (which are the cause of unwanted grating responses). However, very large numbers of elements ($\sim 10^4$) are required in order to achieve uniformity and freedom from statistical clumping. The non-redundant array, which requires the least number of elements to obtain a given angular resolution, should find considerable application in modern radar.

Acknowledgment

The author wishes to thank John L. Melanson for implementing the rather intricate computer program used to find the new non-redundant, two-dimensional arrays shown in figures 2 and 3.

TABLE 1.
NUMBER OF SPACINGS, FIGURES OF MERIT,
AND CORE NUMBERS FOR THE ARRAYS

| No. of Elements | No. of Spacings | Figure of Merit | Core Number |
|-----------------|-----------------|-----------------|-------------|
| 15 | 210 | 0.79 | 141 |
| 18 | 306 | 0.62 | 174 |
| 27 | 702 | 0.57 | 120 |
| 27 | 702 | 0.42 | 255 |
| 30 | 870 | 0.42 | 294 |

References

- [1] Moffet, A. T., "Minimum-redundancy linear arrays," IEEE Trans. Antennas Propagat., vol. AP-16, pp. 172-175, Mar. 1968.
- [2] Arsac, J., "Etude Théorique des réseaux d'antennes en radioastronomie et réalisation expérimentale de l'un d'eux" ("Theoretical study of the spacings of radioastronomical antennas and experimental realization of one of them"), Ph.D. dissertation, University of Paris, Paris, France, 1956.
- [3] Colvin, R. S., and L. R. D'Addario, "The Stanford five-element array: An instrument for real time fan beam synthesis and fast rotation synthesis," presented at the Symposium on the Collection and Analyses of Astrophysical Data, Charlottesville, Va., November 13-15, 1972.
- [4] Goodman, J. W., "Imaging with low-redundancy arrays," in Applications of Holography, Edited by E. S. Barrekette and others, Plenum Press, New York, p. 54, 1971.
- [5] Golay, M. J. E., "Point arrays having compact, nonredundant autocorrelations," J. Optical Soc. America Ltrs., vol. 61, pg. 272, 1971.
- [6] Klemperer, W. K., "Very large array configurations for the observation of rapidly varying sources," Astronomy and Astrophysics Supplemental Series, in press, 1973.

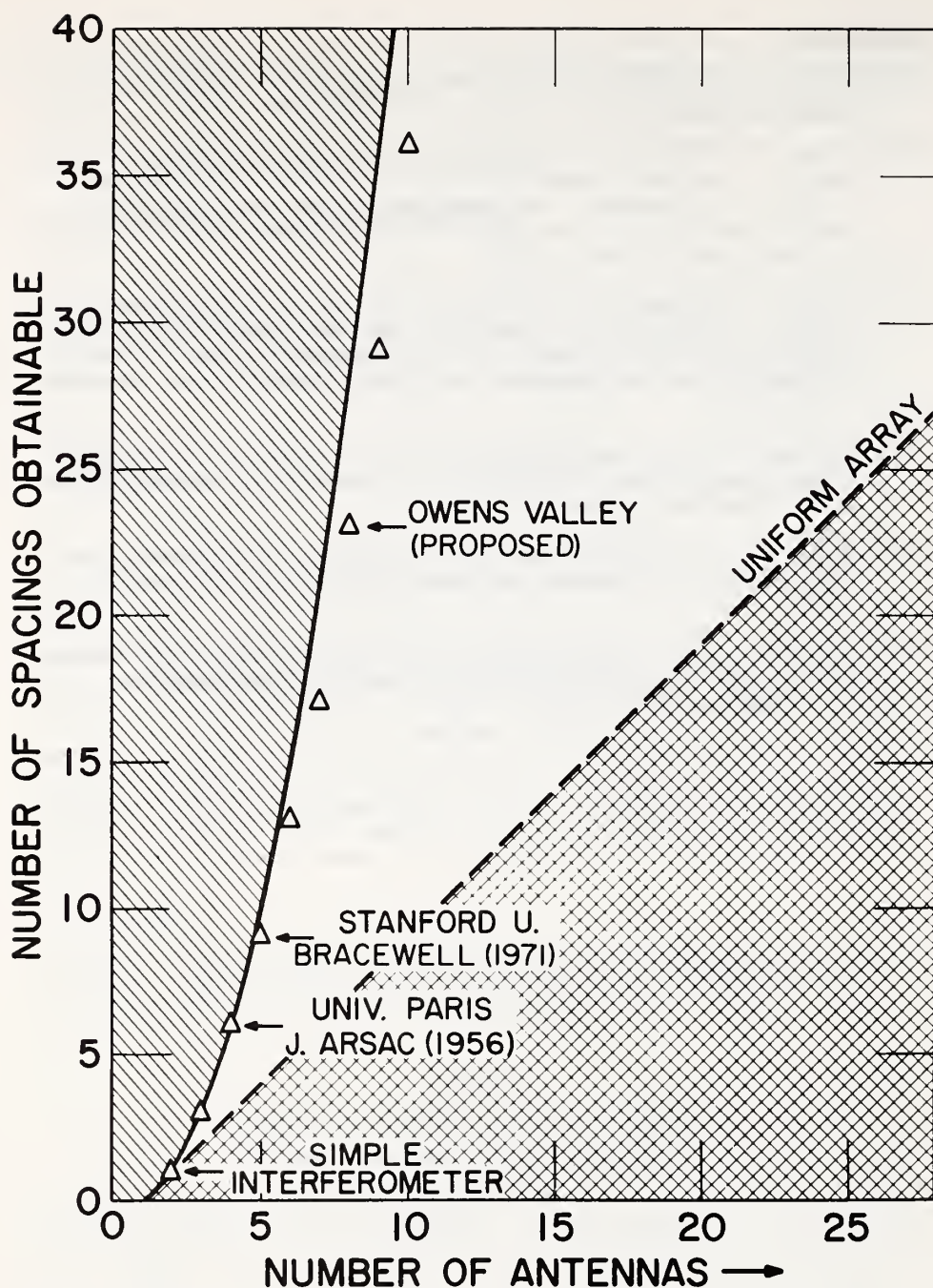


Figure 1. The number of spacings obtainable with various linear, one-dimensional array configurations. Those for minimum-redundancy arrays of up to ten elements are marked with triangles.

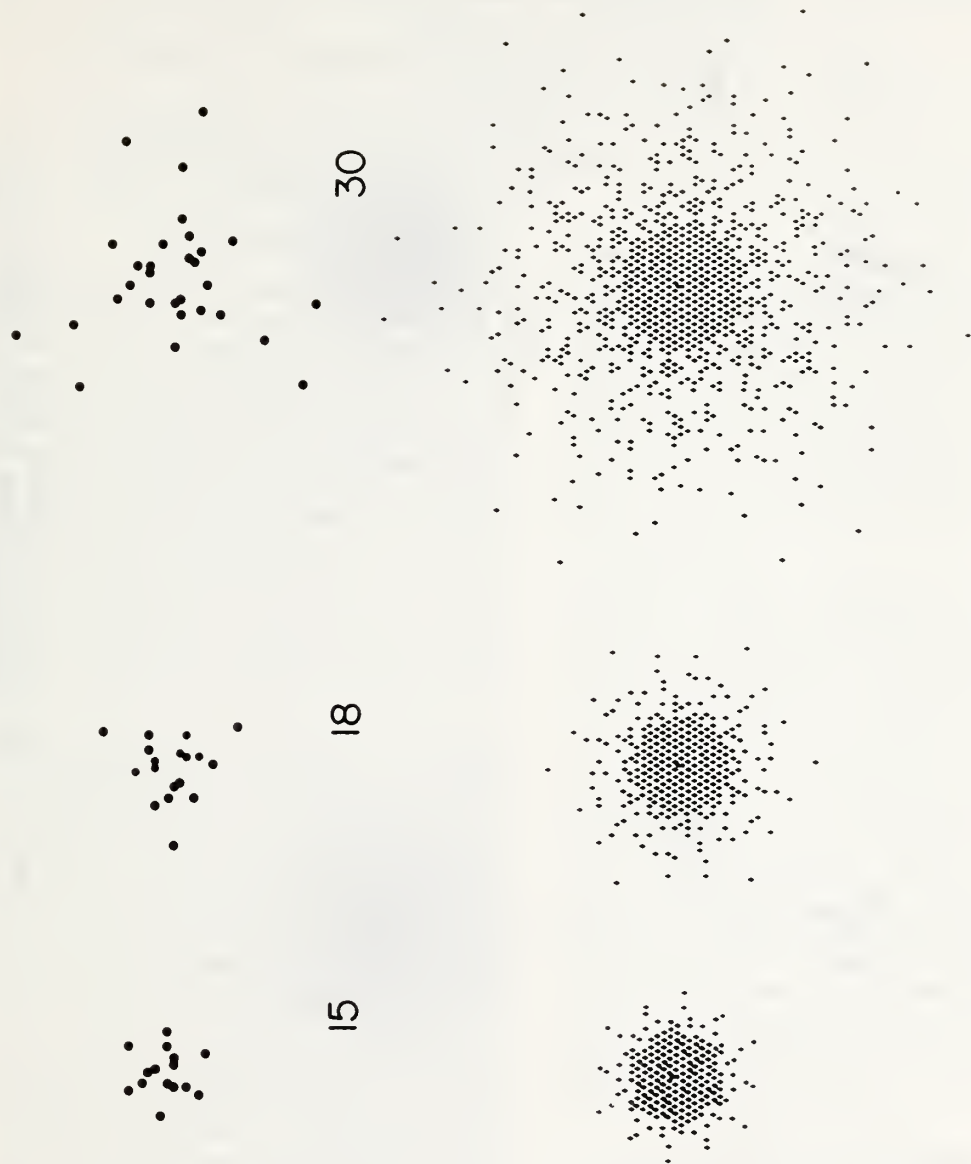


Figure 2. Two-dimensional non-redundant array configurations for 15, 18, and 30 elements with their respective transfer functions.

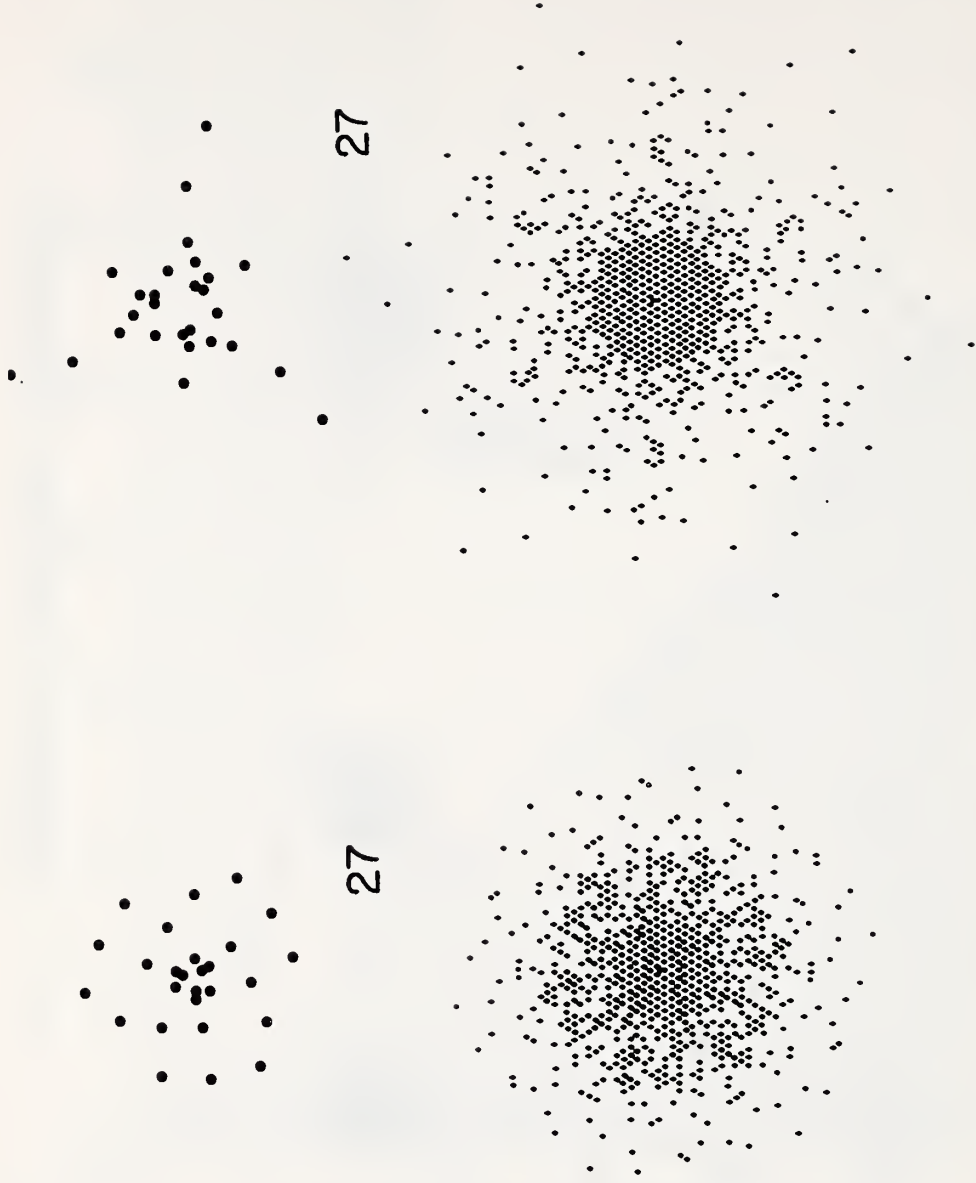


Figure 3. Two non-redundant arrays of 27 elements:
a) relatively compact transfer function (left),
b) transfer function with a large core (right).

Reprinted with permission from the Review of Scientific Instruments
Vol. 43, No. 6, 879-882, June 1972.

Pattern Velocity Computers: Two Types Developed for Wind Velocity Measurement by Optical Means

GERARD R. OCHS AND GLEN F. MILLER

National Oceanic and Atmospheric Administration, Environmental Research Laboratories, Boulder, Colorado 80302

(Received 30 July 1971)

We describe two types of pattern velocity computers that have been developed specifically to measure average wind across an optical beam by observing the light scintillation in two spaced receivers. The technique is applicable to a wide variety of problems of this nature.

INTRODUCTION

In many situations, it is desirable to obtain the mean velocity of moving irregular patterns of various types. In some cases, such as a moving map, the pattern is not changing with time; whereas in others—turbulent atmospheric flow for example—the moving pattern evolves with time. While, in principle, it is possible to obtain the mean flow velocity by calculation from various measurements, it is not always convenient to do so. The two types of analog pattern velocity computers that we have designed compute the velocity in real time and may be convenient to apply to a variety of problems of this nature. To illustrate the principle, we will describe the computer design considerations related specifically to the problem of wind measurement by optical means. A discussion of the theory of optical detection of wind velocity may be found in Lawrence *et al.*¹

If two sensors are used to detect pattern irregularities, and they are spaced in the direction of a moving pattern, the mean pattern velocity may be determined in some sense if both the spatial statistics of the pattern and the time-lagged covariance function of the fluctuations seen by the two sensors are known. For some applications, it is possible to determine the pattern velocity (or a related quantity such as mean wind from optical pattern motion) from something less than the complete function. The two computers to be described make use of this principle.

In Fig. 1, a plan view is shown of the system used to measure wind velocity normal to an optical path. A laser light source is diverged slightly and directed toward two photomultiplier receivers. Refractive index inhomogeneities carried across the light beam by the wind result in a moving light pattern of irregular intensity at the detectors. The pattern velocity computer measures the mean pattern velocity by comparing the intensity fluctuations seen by the detectors and provides an output suitable for a chart recorder or digitizer.

In one technique (which we shall call the time delay method), the delay of one signal is continuously adjusted relative to the other by the amount necessary to maximize the normalized covariance of the two signals. If the pattern does not change during its passage across the sensors, the pattern velocity is equal to the sensor separation divided by the appropriate delay (see Fig. 2). If the pattern is

changing with time, the pattern velocity derived by this method will be too high.² However in many cases, enough is known about the resulting covariance function so that pattern velocities may be obtained even though the pattern is changing with time. In the case of a uniform wind normal to a divergent optical beam, geometrical amplification along the path produces a scintillation pattern at the receivers that changes with time. The uniform wind velocity responsible for the moving pattern can be shown to be one-half the pattern velocity found by the time delay method.¹

The second technique (which we shall call the slope method) relies upon a measurement of the slope of the normalized covariance at zero delay, the slope indicated in Fig. 2. This method largely avoids the problems of pattern decay since the measurement involves comparing features at nearly the same instant. This second technique is much more suitable for the measurement of average winds by optical means since the slope remains proportional to the component of wind velocity along the separation of the sensors and at right angles to the optical path, even though the winds along the path are varying in velocity and direction. Computation of wind velocity under these conditions by the time delay method will not give the correct answer. An extreme example may be cited where the wind is blowing across one-half the optical path in one direction and with equal velocity in the other direction across the other half of the path. In this case, the covariance function will peak at zero delay. The slope technique gives the right answer, zero mean velocity, while the time delay technique would indicate infinite velocity.

TIME DELAY COMPUTER

Basically this circuit servocontrols the delay of one of the sensor signals in order to maximize the correlation be-

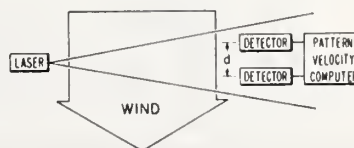


FIG. 1. A plan view of the system used to measure wind velocity normal to an optical path.

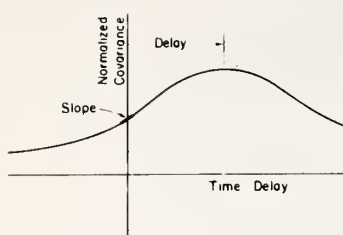


FIG. 2. The time lagged covariance of two sensors observing a moving irregular pattern. One computer measures the reciprocal of the time delay to the peak of the function; the other measures its slope at zero time delay.

tween the two fluctuating sensor signals. This delay is, of course, the time to the peak of the covariance function. A block diagram of the circuit is shown in Fig. 3. The combination of two clippers and any of the "exclusive or" circuits forms a 1 bit correlator, which computes the normalized correlation of waveforms having a Gaussian amplitude distribution.³

The variable delay shift register provides three delayed outputs, in the ratio 2:5:8. The normalized covariance of signal 1 and signal 2 delayed by 2 bits and also of signal 1 and signal 2 delayed by 8 bits are formed. The difference of these two is integrated and used to control a voltage controlled generator. The output of the VCG controls the delay line, completing a servoloop arranged to provide that delay required to maintain a normalized covariance difference of zero. If the covariance function is symmetric around its peak, then the peak delay lies halfway between the 2 and 8 bit delays, as shown in the plot to the right of zero delay in Fig. 4. Thus the delay at which the peak occurs is continuously tracked. Since the shift register delay is inversely proportional to the clocking frequency, this frequency is proportional to the pattern velocity. If the VCG is linear, then its output is also proportional to pattern velocity.

The system may be conveniently calibrated by measuring the clocking frequency f . Since $5/f$ is the time delay to the peak of the covariance function, the pattern velocity is

$$v = fd/5,$$

where the sensors are separated a distance d in the direction

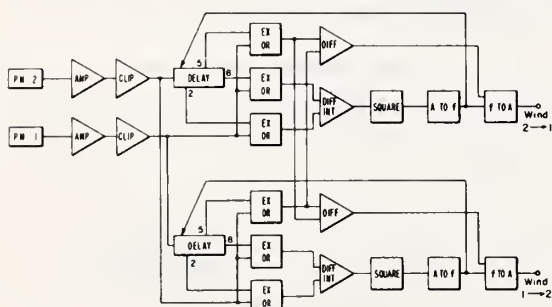


FIG. 3. A block diagram of the time delay computer.

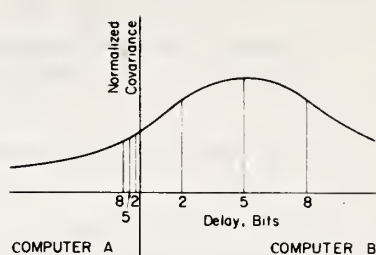


FIG. 4. The time lagged covariance of two sensors observing a moving irregular pattern. The time delay computer locates the peak by adjusting the time delay of one of the signals until the covariance at 2 and 8 bits of delay is equal.

of pattern motion, and the pattern is not changing with time.

The above outlines the principle of operation. The instrument must necessarily be more complex to assure satisfactory operation with actual signals. The following discussion concerns some of the design considerations and additional circuitry required for practical operation.

The high frequency cutoff of a shift register is approximately one-half the clocking frequency. This cutoff is inversely proportional to delay and hence proportional to wind velocity, a desirable feature, as the signal bandwidth increases with wind velocity. By selection of the proper number of bits (a total of eight in our case), the signal-to-noise ratio (S/N) can be held approximately constant over a wide wind velocity range. Signal conditioning also requires a low frequency cutoff. Ideally, this should be automatically varied also. In our system, however, it is not varied. In a general sense, the bandwidth requirements are dictated by the spatial frequencies in the moving pattern and the separation of the sensors.

It requires more time to make an estimate of normalized covariance at low wind velocity than at high velocities. Hence, a linear voltage controlled generator is unsatisfactory, and one with a characteristic $f = kv^2$, which increases error loop gain with frequency, is used. This function also improves the lock-on capability of the system. The VCG must not be allowed to go to zero frequency since the shift register would not transmit a signal, and the servo system could not lock on. A minimum frequency, corresponding to a minimum readable velocity (and minimum HF cutoff) must be set for the system. This setting corresponds to a wind velocity of approximately 0.44 m/sec. Since the fluctuating servo system voltage cannot go below that minimum, the mean wind reading may be slightly high near the minimum. The VCG square law conversion tends to minimize this error.

The wind may blow across the path from either direction, so that it is necessary to delay signal 1 relative to 2 as well as 2 relative to 1. Essentially duplicate computers have been constructed to take care of the two cases. In addition,

a normalized covariance measurement is made at 5 bits of delay in both computers to indicate which computer is giving a valid reading. In Fig. 4, a typical covariance function is shown with computer B locked on the signal. Computer A is attempting to lock onto the signal by trying to equalize the covariances at the 2 and 8 bit delay points. As a result the servo system goes to minimum delay (maximum velocity reading), which is not a valid reading. The fact that the 5 bit reading of computer B is above that of the 5 bit reading of computer A indicates that computer B has the correct reading. In this situation, an inhibit circuit turns off the output of computer 2 but passes the reading of computer 1.

As mentioned earlier, the covariance function will peak up near zero time delay when the mean drift is small, if winds having random directional components are large by comparison. This situation is especially likely when the mean wind direction is close to the optical path direction. To prevent a false reading in this situation, a rudimentary check is made of the shape of the covariance function. This is accomplished by requiring the difference in the normalized covariance at plus and minus 5 bits of delay to be greater than a preset value (approximately 0.05 of full scale). If this is not satisfied both outputs will be inhibited.

SLOPE COMPUTER

The circuit employed to measure the derivative of the normalized covariance at zero delay is somewhat simpler since it does not require servo systems, and a single circuit measures winds in either direction across an optical path. A block diagram is shown in Fig. 5. Again, the 1 bit correlator principle is used. The normalized covariance is measured at a small time delay on either side of zero. The magnitude of the difference is then a measure of the slope at zero delay. A third covariance measurement is made at zero delay and this value is used in the calibration procedure to be described later.

In a 1 bit correlator, the output voltage of the correlator is a nonlinear function of the normalized covariance C , i.e.,

$$C = \sin[(\pi/2)R], \quad (1)$$

where R is the ratio of output voltage to one-half the output voltage difference between a covariance of +1 and

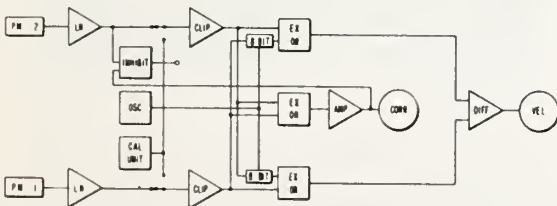
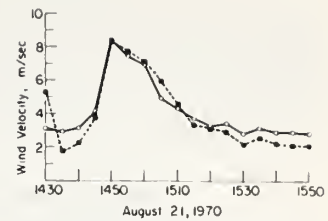


FIG. 5. A block diagram of the slope computer.

FIG. 6. Comparison of anemometer and optical wind measurement using the time delay computer. ○—Optical; ■—weighted average 7 anemometers.



—1. The waveforms to be correlated are assumed to have a Gaussian amplitude distribution. Since the optical signal intensity fluctuations are log normally distributed, this condition is satisfied by taking the logarithms of the signals.

For optical measurement of wind, the slope of the covariance function at zero delay dC/dt is proportional to wind velocity, and the proportionality constant may be calculated in most circumstances.¹ Assuming this proportionality constant is known, we can relate it to the output dR/dt of the computer as follows. Differentiating (1) and substituting, we obtain

$$\frac{dC}{dt} = \frac{\pi}{2} (1-C^2)^{1/2} \frac{dR}{dt}. \quad (2)$$

Thus we can obtain dC/dt from known values of C and dR/dt .

A convenient means of relating dR/dt to the output voltage of the computer is included in the system. It consists of a generator of variable frequency having two square wave outputs differing in phase by 90° . The expected normalized covariance of these two signals is a triangular waveform, with zero covariance at zero delay. It so happens that the output voltage of the 1 bit correlator is linear with covariance for the particular amplitude distribution of the square wave, so that the resulting triangular waveform is not distorted. For a square wave of frequency f , the slope at zero delay is $4f$, the sign being determined by which signal is leading. Thus a calibrating signal of known slope is available, through the relation

$$dR/dt = 4f. \quad (3)$$

Combining (3) with (2), we have the convenient relationship

$$f = \frac{dC/dt}{2\pi(1-C^2)^{1/2}}, \quad (4)$$

where f is the calibrating frequency necessary to simulate a slope dC/dt for a normalized covariance C .

An inhibit circuit is included in the system so that either an excessively low signal or low normalized zero delay covariance will be detected. If the laser signal is lost in the daytime, the covariance will go to zero even though ambient background light may be intense enough to pre-

vent low signal turnoff, since the noise in the detectors under these conditions is uncorrelated. If the laser signal is lost at night, the low signal turnoff is effective. The covariance may not be excessively low, however, due to correlated stray pickup in the absence of other signals.

MEASUREMENTS

Some examples of average wind velocity measurements calculated by each computer from optical pattern velocity observations are shown in Figs. 6 and 7. The tests were made over a 1 km path instrumented with seven propeller anemometers fixed in position to read the wind component normal to the path. A comparison of the time delay optical measurement with that of the anemometer average is shown in Fig. 6. Five-minute averages are plotted.

In Fig. 7 a plot of wind velocity V_0 derived from the slope method is shown with the seven anemometer average, V_a . A 5 min running average has been applied to these curves. The slope method is preferable to the time delay technique for optical wind measurement, as it can measure more accurately a small mean wind flow in the presence of large velocity components of random direction. On the other hand, the slope technique will be adversely affected by the addition of uncorrelated noise to the sensor inputs (which will reduce the slope), but the time delay method

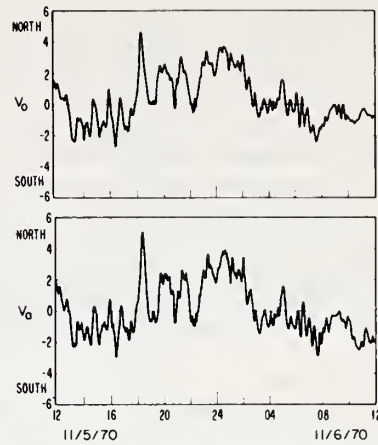


FIG. 7. Comparison of anemometer and optical wind measurement using the slope computer.

will not be affected seriously as long as the S/N ratio is sufficient to measure time delay to the peak of the covariance function.

¹ R. S. Lawrence, G. R. Ochs, and S. F. Clifford, *Appl. Opt.* **11**, 239 (1972).

² M. G. Morgan and K. L. Bowles, *Science* **161**, 1139 (1968).

³ G. R. Ochs, ESSA Tech. Rep. ERL 63-WPL 2, 1968.

Analytical Representation for Standards of Spectral Irradiance over the 300–1200 nm Range

R. L. Schwiesow

Wave Propagation Laboratory, Environmental Research Laboratories, National Oceanic & Atmospheric Administration, Boulder, Colorado 80302.
 Received 15 February 1972.

Tungsten-halogen incandescent lamps are widely used as standards of spectral irradiance in many types of spectroradiometric calibration. The purpose of this communication is to present results related to an analytic expression for spectral irradiance as a function of wavelength.

With the increasing application of automatic data processing in spectroscopic experiments, it becomes necessary to present standard lamp calibration data in a computer-compatible format. An analytic expression, compared to a table look-up and interpolation technique, increases accuracy by data smoothing and reduces storage requirements for the reference data at the cost of a possible slight increase in computation time. Such an analytic expression has been extremely useful in the computer assisted determination of over-all quantum efficiency for input optics, spectrometer, photomultiplier, and photon counting electronics in the automated processing of light scattering data, for example.

Stair *et al.* have reported the basic calibration work¹ on a quartz-iodine standard of spectral irradiance. Their data are presented in tabular form with spectral irradiance (in μW per cm^2 per nm bandwidth at a distance of 43 cm) given at spectral intervals between 10 nm and 100 nm, depending on how rapidly the data are changing in each region. Calibration data from commercially available standard lamps are given in similar form or in a graphical presentation.

We have fitted the calibration data for the lamps of Stair *et al.* and for a commercial lamp to a function given by Planck's Law² with a linearly and a quadratically varying tungsten emissivity³ over the spectral range of interest. The fit utilized an iterative least squares method⁴ to linearize the error derivatives, coupled with a matrix algebra solution of the resulting simultaneous equations. The adjustable parameters were chosen to minimize the weighted root mean squared fractional error, rather than the more common root mean squared error, because the spectral irradiance varies over two orders of magnitude in the spectral region considered. The general form for the spectral irradiance is

$$P(\lambda) = [A_1 + A_2(\lambda - 300) + A_3(\lambda - 300)^2] \lambda^5 \times [\exp(A_4/\lambda) - 1]^{-1}, \quad (1)$$

where P is the spectral irradiance in watts per unit area per unit spectral bandwidth, λ is the wavelength in nanometers in the range 300–1200 nm, A_1 includes emissivity and $8\pi hc$, A_2 , and A_3 relate to the falloff of emissivity, and A_4 includes a factor of hc/k and the reciprocal of the effective color temperature of the source. The experimental data points were weighted for fitting purposes by the reciprocal of the estimated uncertainty ratio given by Stair *et al.*¹ We assigned a weight of $\frac{3}{8}$ at 250 nm varying linearly to a weight of 1 at 400 nm and constant for all longer wavelengths, based on estimated uncertainties of 8% at 250 nm and 3% at 400 nm. While the weighting procedure increases the fractional root mean squared error slightly, it results in a more faithful representation of the irradiance standard.

Parameter values for the best fit analytic functions for two different sets of lamp data are shown in Table I. The maximum fractional error refers to the largest error in the visible region. Comparison of the fitting error with the estimated uncertainty in the data reveals that a three or four parameter fitting function provides a satisfactory representation of the spectral irradiance data. Actual measured and calculated values for the data of Stair *et al.*¹ are shown in Table II for a four parameter fit.

It is apparent that the additional parameter in the quadratic emissivity fit serves primarily to reduce the larger fitting errors, without significantly lowering the fractional root mean squared error. Because of the reduction in maximum error, the four parameter analytic expression is to be preferred for most work. The error distribution shown in Table II is not random. Allowing a higher order polynomial approximation to the emissivity would improve the fit, but the analytic complication is not justified for typical applications.

The fit to the graphical data for a commercial standard of spectral irradiance⁵ is closer than the fit to the data of Stair *et al.*¹ This is probably because the graphical data are already somewhat smoothed. Note that similar lamps require significantly different parameters for a best fit in the least squares sense.

This study has shown the utility of an analytic representation for the output of standards of spectral irradiance. The reported parameters are directly useful for standards that are sufficiently characterized by the data of Stair *et al.*¹ and are indicative of approximate parameter values for tungsten-halogen lamps in general. Maximum errors of fitting are consistent with uncertainties in the experimental data. The analytic representation is

Table I. Fitting Parameters for Standard Lamps

| | Stair <i>et al.</i> | Commercial |
|--------------------------|--------------------------|--------------------------|
| Linear emissivity | | |
| A_1 | 0.7624×10^{18} | 0.8721×10^{18} |
| A_2 | -0.7188×10^{14} | -0.9514×10^{14} |
| A_4 | 4665 | 4659 |
| fractional rms error | 2.3% | 1.7% |
| maximum fractional error | 4.1% | 2.7% |
| Quadratic emissivity | | |
| A_1 | 0.4183×10^{18} | 0.6483×10^{18} |
| A_2 | 0.5379×10^{15} | 0.3203×10^{15} |
| A_3 | -0.4184×10^{12} | -0.2770×10^{12} |
| A_4 | 4478 | 4567 |
| fractional rms error | 2.1% | 1.7% |
| maximum fractional error | 3.0% | 2.3% |

Table II. Comparison of Experimental and Calculated Irradiance^a

| Wavelength (nm) | Measured | Calculated | Error (%) |
|-----------------|----------|------------|-----------|
| 300 | 0.0548 | 0.0567 | -3.4 |
| 320 | 0.105 | 0.107 | -1.9 |
| 350 | 0.242 | 0.235 | 3.0 |
| 370 | 0.374 | 0.363 | 3.0 |
| 400 | 0.647 | 0.628 | 2.9 |
| 450 | 1.26 | 1.265 | -0.4 |
| 500 | 2.04 | 2.10 | -3.0 |
| 550 | 2.96 | 3.04 | -2.9 |
| 600 | 3.94 | 4.00 | -1.6 |
| 650 | 4.91 | 4.88 | 0.6 |
| 700 | 5.72 | 5.63 | 1.6 |
| 750 | 6.32 | 6.21 | 1.8 |
| 800 | 6.69 | 6.62 | 1.1 |
| 900 | 6.94 | 6.95 | -0.2 |
| 1000 | 6.73 | 6.76 | -0.6 |
| 1100 | 6.25 | 6.26 | -0.2 |

^a In $\mu\text{W per cm}^2 \text{ per nm}$ at a distance of 43 cm. See Stair *et al.*¹

particularly useful for reference calibration data in automatic data processing of spectroradiometric experimental results.

References

1. R. Stair, W. E. Schneider, and J. K. Jackson, *Appl. Opt.* 2, 1151 (1963).
2. See, for example, R. W. Ditchburn, *Light* (Wiley-Interscience, New York, 1963), p. 679.
3. M. Pivovonsky and M. R. Nagel, *Tables of Blackbody Radiation Functions* (Macmillan, New York, 1961).
4. H. Margenau and G. M. Murphy, *The Mathematics of Physics and Chemistry* (Van Nostrand, Princeton, 1956), p. 517.
5. Nominally 3050 K, 200 W quartz-iodine lamp at 40-cm distance.

Reprinted with permission from the Journal of the
Optical Society of America Vol. 62, No. 5, May 1972

Departures from the Electrostatic Crystal-Field Model for Gd^{3+} in Six Hexagonal Crystals*

R. L. SCHWIESOW†

Wave Propagation Laboratory, Environmental Research Laboratories,
National Oceanic and Atmospheric Administration, Boulder, Colorado 80302

(Received 11 November 1971)

Using the experimental energy levels of Gd^{3+} in six hexagonal crystals as a basis, we discuss modifications to the electrostatic-approximation crystal-field model caused by nonlinear shielding, nephelauxetic, and covalency-induced molecular orbital effects. The crystal-field fit improves when levels belonging to different irreducible representations (crystal quantum numbers) are fitted separately and when levels of different spectroscopic terms are fitted separately. Nephelauxetic and covalency effects are related for the same crystal structure and are strongly structure dependent. Nonlinear shielding and/or term-dependent configuration-interaction effects are shown to be important but not simply related to the host structure.

INDEX HEADINGS: Spectra; Crystals; Gadolinium.

The Gd^{3+} ion is a particularly useful rare earth for a crystal-field probe. For the $4f^7$ electronic configuration in the limit of Russell-Saunders (*LS*) coupling, diagonal matrix elements of crystal-field operators are zero.^{1,2} All crystal-field splitting is then due to higher-order effects, which are relatively more obvious in Gd^{3+} than in ions that exhibit strong first-order crystal-field splitting.

The major contribution to the splitting of Gd^{3+} free-ion energy levels in a crystal host is the electrostatic crystal-field interaction with the intermediate-coupling electronic wave functions. We discuss here significant evidence for additional contributions to the crystal-field energy-level splitting from nonlinear shielding, nephelauxetic and covalency-induced molecular-orbital effects. In particular, the Gd^{3+} ion is studied in six different hosts, each with an identical $\bar{6}$ (C_{3h}) site symmetry at the ion. This variation in host configuration, but with a consistent, high site symmetry, provides a unique way of demonstrating the effects of higher-order crystal-field interaction.

I. EXPERIMENTAL DATA

The measured energy levels for Gd^{3+} in $LaBr_3$, $LaCl_3$, $GdCl_3$, $Y(OH)_3$, $Gd(OH)_3$, and LaF_3 have been reported previously^{3,4} and will not be repeated here. Experimental technique and data-reduction procedures are similarly described. Typical uncertainties of energy levels range from 0.03 cm^{-1} in $LaBr_3$ to 0.5 cm^{-1} in the concentrated salts.

Point symmetry at the site of the rare-earth ion is established as $\bar{6}$ (C_{3h}) in $LaBr_3$,⁵ $LaCl_3$,⁵ $GdCl_3$,⁶ $Y(OH)_3$,⁷ and $Gd(OH)_3$.⁸ In LaF_3 the site symmetry is dominantly $\bar{6}$,⁹ although a distortion of the order of 1% of a_0 , which will be ignored here, has been reported.¹⁰ This distortion does have a strong effect on some selection rules, however. The LaF_3 structure differs in type from the five $LaBr_3$ -type hosts, having an additional triangle of ligands in a plane normal to the optic axis and through the ion site. The five $LaBr_3$ -type hosts differ in ligand type and lattice dimension only. The different crystal hosts exhibit different near-

ligand configurations, which give rise to systematic differences between observed and calculated crystal-field splittings.

II. FORMALISM

A. Free-ion Eigenfunctions

We assume that the crystal field is a small perturbation on the free-ion hamiltonian. Free-ion eigenfunctions are used as basis states for constructing a matrix representation of the crystal-field contribution to the total hamiltonian. The intermediate-coupling free-ion calculation used for this analysis is performed in the usual way, parametrized by the radial integrals P^k ($k=0, 1, 2, 3$) of Racah¹¹ and by $\alpha L(L+1)$, which parametrizes one of the effective operators for configuration interaction.¹² Details of the particular free-ion diagonalization used are discussed elsewhere.³ Subsequent free-ion studies using additional parameters for spin-other-orbit and spin-spin interactions¹³ have been fit to extended Gd^{3+} data.¹⁴ Crosswhite has also suggested additional empirical tensor operators to refine the eigenfunction basis for the crystal-field hamiltonian and improve the fit to the $^6I_{7/2}$ group.

These subtle free-ion refinements may improve the mean error of fitting calculated to experimental energy levels, but are not expected to modify the observations on improvement of the fitting by considering non-electrostatic crystal-field effects.

B. Crystal-Field Parameters

In the electrostatic approximation, the crystal-field hamiltonian summed over all $4f$ electrons is written as

$$H_{cf} = \sum_i eV(r_i, \theta_i, \phi_i).$$

This crystal potential is expanded in terms of r^k and the unit irreducible tensor operator $U_q^{(k)}$ of Racah.¹⁵ Coefficients of this expansion, including the $\langle r^k \rangle$, which is constant for all spectroscopic terms in a given configuration, are the crystal-field parameters B_k^q . Only

B_2^0 , B_4^0 , B_6^0 , and B_6^6 are nonzero and observable in this symmetry.

Matrix elements of the $U_q^{(k)}$ are evaluated using the vector-recoupling formalism of Judd,¹⁶ published tables of reduced matrix elements,¹⁷ and $u-j$ symbols.¹⁸ The four crystal-field parameters and fourteen free-ion level parameters are allowed to vary to make a best fit, in the least-squares sense, of calculated to experimental energy levels. The assignment of S , L , and J quantum numbers to the experimental energy levels has been described.³

C. Nonelectrostatic Effects

In addition to the electrostatic-model effects discussed above, the crystal field acting on closed $5s5p$ electronic shells in the Gd^{3+} ion may also result in a shielding effect, which has been postulated in an attempt to explain the discrepancy between *a priori* electrostatic-model calculations¹⁹ and empirical crystal-field parameters. The shielding recognizes that the f^n wave functions contain contributions from states of higher configurations. Linear (isotropic) shielding affects all crystal levels equally as a scale factor on crystal-field strength and cannot be detected by any observations made in this study. Nonlinear (angularly dependent) shielding results from a distortion of the closed shells by the crystal field and depends on the S and L quantum numbers in the $4f$ shell, and empirically means that different B_k^q are associated with crystal levels arising from different spectroscopic terms.²⁰ Possible effects of nonlinear shielding on the results of this study are evaluated by examining improvements of crystal-field fits when each spectroscopic term is considered separately. Resulting fitting improvement does not prove the existence of significant nonlinear shielding effects, because configuration interaction and other wave-function distortions are also in part compensated for by the separate-term fits.

The electrostatic approximation considers the free ion to be acted on only by an electrostatic field with a point symmetry at the ion site identical to the site symmetry of the crystal. In fact, lattice and ion dimensions suggest that the rare-earth-ion and the surrounding-ligand wave functions overlap.²¹ This overlap gives rise to a nephelauxetic effect, which is an expansion of the ion wave function as a result of overlap with those of surrounding ligands.²² This is most clearly observed as a shift of Stark-multiplet mean energy (which we take as the free-ion energy) for the Gd^{3+} ion in different hosts. Ideally, a separate free-ion calculation should therefore be done for each crystal host. However, because nephelauxetic shifts are of the same order or smaller than the fitting errors of the free-ion calculation in the present analysis, no significant improvement would result from separate diagonalizations.

Note that by fitting the free-ion calculated energies to the empirical crystal Stark-multiplet centers, the

nephelauxetic effect on energy, but not the more complicated effect on wave functions, is automatically included in the free-ion calculation. Similarly, a correct choice of free-ion parameters can include the effects of linear and nonlinear shielding on ion energy levels. It must be emphasized that a set of free-ion parameters chosen on the basis of best energy fit does not necessarily result in the most realistic set of wave functions when effective, rather than actual, operators are involved.

No modification of the free-ion parameters can account for a mixture of ligand wave functions into the central-ion wave functions. The existence of this covalency is shown in the present study by the wave-function overlap required to explain the observed nephelauxetic effect. Increased wave-function overlap between the central ion and ligands results in greater radial-wave-function expansion, which depresses the Stark-multiplet centers relative to the 4S ground state. Lower multiplet centers are identified with increased covalency in Sec. II D. So-called molecular orbitals are suitable combinations of central-ion and ligand wave functions. Formal molecular-orbital calculations²³ show that the crystal-field-splitting parameters can have different values for each group of states belonging to a different irreducible representation. In the case of $4f^7$, this means empirically that if covalent-bonding effects are important to the crystal-field calculation, an improvement of fit between experimental and calculated Stark levels will result from fitting crystal levels separately for each value of crystal quantum number μ , because μ is the same for all states belonging to a given irreducible representation of the group corresponding to the point symmetry of the crystal at the ion site.

A recent review²⁴ discusses rare-earth crystal-field theory in additional detail.

D. Results

Table I shows the free-ion-level energies that give the best fit to experimental data for each crystal. These values are at most 4 cm^{-1} different from the Stark-multiplet means, and in typical cases are less than 0.5 cm^{-1} from the means. The free-ion levels were calculated using parameters $E_{av}=878.9$, $E^1=5754.7$, $E^2=28.083$, $E^3=576.69$, $\zeta=1477.7$, $\alpha=19.96$, $\beta=-525.6$, $\gamma=1425$, and $M^0=M^2=M^4=1.5$. All these parameter values are in units of cm^{-1} . The latter seven values parametrize such free-ion refinements as configuration interaction and spin-other-orbit and spin-spin interactions, and are discussed more fully elsewhere.¹⁴

The shift of free-ion energy levels evident in Table I is a clear example of the nephelauxetic effect. Crystals of approximately the same structure in which the Gd^{3+} levels are lower show stronger interaction with the host by a larger crystal-field splitting. The effect is strongly structure dependent, however. $Gd:LaF_3$, which differs in structure (but very little if at all in site symmetry) from the five $LaBr_3$ -type crystals, shows the

TABLE I. Effective free-ion levels of Gd³⁺ in various crystalline hosts. All energy levels in cm⁻¹.

| Level | Calc free ion | 1% Gd:LaBr ₃ | 5% Gd:LaCl ₃ | GdCl ₃ | 2% Gd:Y(OH) ₃ | Gd(OH) ₃ | 0.2% Gd:LaF ₃ |
|--------------------------------|---------------|-------------------------|-------------------------|-------------------|--------------------------|---------------------|--------------------------|
| ⁸ S _{7/2} | -32 | 0.0 | 0.0 | 0.0 | 0.0 | 0.0 | 0.0 |
| ⁶ P _{3/2} | 32 224 | 32 097.0 | 32 121.5 | 32 084.1 | 32 036.8 | 32 054.9 | 32 197.8 |
| ⁶ P _{5/2} | 32 816 | 32 692.3 | 32 717.7 | 32 679.5 | 32 627.8 | 32 647.1 | 32 791.1 |
| ⁶ P _{7/2} | 33 341 | 33 263.1 | 33 288.3 | 33 251.7 | | 33 221.1 | |
| ⁶ I _{7/2} | 35 933 | 35 825.0 | 35 849.4 | 35 807.9 | 35 767.0 | 35 783.5 | 35 959.4 |
| ⁶ I _{9/2} | 36 247 | 36 166.3 | 36 194.3 | 36 151.0 | 36 111.9 | 36 127.1 | 36 304.2 |
| ⁶ I _{11/2} | 36 309 | 36 199.9 | 36 245.0 | 36 206.0 | 36 174.7 | 36 190.8 | 36 360.8 |
| ⁶ I _{13/2} | 36 514 | 36 439.3 | 36 471.3 | 36 429.7 | 36 389.2 | 36 403.9 | 36 582.2 |
| ⁶ I _{15/2} | 36 627 | 36 546.8 | 36 589.0 | 36 546.6 | 36 513.1 | 36 525.7 | 36 702.1 |
| ⁶ I _{17/2} | 36 660 | 36 586.3 | 36 622.5 | 36 581.0 | 36 548.2 | 36 563.0 | 36 727.8 |
| ⁶ D _{3/2} | 39 675 | 39 507.0 | 39 555.5 | 39 508.1 | | 39 502.3 | |
| ⁶ D _{5/2} | 40 615 | 40 428.2 | 40 492.4 | 40 444.5 | | 40 424.9 | |
| ⁶ D _{7/2} | 40 674 | 40 516.4 | 40 586.7 | 40 538.7 | | 40 531.3 | |
| ⁶ D _{9/2} | 40 847 | 40 679.2 | 40 745.4 | 40 694.1 | | 40 680.7 | |
| ⁶ D _{5/2} | 40 967 | 40 786.2 | 40 900.0 | 40 856.6 | | 40 806.0 | |

smallest nephelauxetic shift and the largest crystal-field splitting of all. Note that, in general, the relative order of nephelauxetic depression for the various crystals changes between ⁶I and ⁶D terms, indicating a possible variation of ligand-induced configuration interaction. The desirability of a separate free-ion diagonalization for each host is apparent.

The question of a separate free-ion diagonalization for each host has been studied for Pr³⁺ and reported in detail.²⁵ In the case of Gd³⁺, such improvement would not be so marked as in Pr³⁺, in which first-order crystal-field effects are important.

Table II lists the B_k^q in the Racah expansion of the crystal field and the mean error of fitting for each crystal host. The mean error of fitting, σ , is given by

$$\sigma = \left(\sum_{\text{levels}} \text{squared residual} / D \right)^{1/2},$$

where the squared residual is $(E_{\text{expt}} - E_{\text{calc}})^2$ and D is the number of experimental levels fitted minus the number of free parameters. These values are the reference electrostatic-fit parameters that we attempt to improve by considering other crystal-field interaction mechanisms.

Mixing of the ligand wave functions with the wave function of the central ion results in a different set of crystal-field parameters being associated with levels having different crystal quantum numbers, as previously discussed. To check this so-called covalency or molecular-orbital effect, separate crystal-field fits were

performed for experimental levels associated with each value of μ . The B_k^q were allowed to vary, but the free-ion-level parameters were fixed at values determined in the all-value fits and shown in Table I. Three crystals showing good resolution in ⁶I and representative of three degrees of nephelauxetic depression and two types of structure were fitted. Table III records the results of the fitting. Mean error σ is that associated with the crystal-field parameters in Table II; improved mean error σ' is the best-fit value associated with the parameters in Table III.

In order to evaluate the degree of improvement attributable to the separate fitting procedure, the σ' 's for each crystal were averaged, weighing σ' for each μ by the number of levels in each subgroup. These weighted averages are entered in Table IV. For comparison, the mean error of the all-level fit is also shown.

TABLE III. Reduction in mean error by separate fits to levels having the same crystal quantum number—(covalency). All values in cm⁻¹.

| | | 1% Gd:LaBr ₃ | 2% Gd:Y(OH) ₃ | 0.2% Gd:LaF ₃ |
|---------------------|------------|-------------------------|--------------------------|--------------------------|
| $\mu = \frac{1}{2}$ | σ | 3.59 | 3.49 | 5.71 |
| | σ' | 3.43 | 3.21 | 5.16 |
| | $B_2^0(U)$ | -358 | -500 | -327 |
| | $B_4^0(U)$ | -351 | -570 | 2270 |
| | $B_6^0(U)$ | 980 | 810 | -2400 |
| | $B_8^0(U)$ | -1050 | -1950 | 200 |
| $\mu = \frac{3}{2}$ | σ | 3.40 | 3.83 | 6.11 |
| | σ' | 3.19 | 3.13 | 5.83 |
| | $B_2^0(U)$ | -367 | -577 | -257 |
| | $B_4^0(U)$ | -187 | -695 | 1980 |
| | $B_6^0(U)$ | 60 | -300 | -2700 |
| | $B_8^0(U)$ | -1560 | -1930 | 2760 |
| $\mu = \frac{5}{2}$ | σ | 4.16 | 3.65 | 5.56 |
| | σ' | 3.46 | 2.82 | 5.37 |
| | $B_2^0(U)$ | -306 | -438 | -253 |
| | $B_4^0(U)$ | -330 | -724 | 2070 |
| | $B_6^0(U)$ | -160 | 1690 | -2050 |
| | $B_8^0(U)$ | -2150 | -1160 | 2340 |

TABLE II. Least-squares-fit crystal-field parameters for Gd³⁺ in various hosts. All parameters and errors in cm⁻¹.

| Crystal | $B_2^0(U)$ | $B_4^0(U)$ | $B_6^0(U)$ | $B_8^0(U)$ | Mean error | Levels fit |
|--------------------------|------------|------------|------------|------------|------------|------------|
| 1% Gd:LaBr ₃ | -349 | -323 | 870 | -1530 | 3.60 | 58 |
| 5% Gd:LaCl ₃ | -294 | -311 | 1150 | -1220 | 2.58 | 56 |
| GdCl ₃ | -363 | -369 | 1250 | -1650 | 3.51 | 43 |
| 2% Gd:Y(OH) ₃ | -478 | -700 | 730 | -1740 | 3.43 | 41 |
| Gd(OH) ₃ | -500 | -517 | 1730 | -2260 | 3.76 | 36 |
| 0.2% Gd:LaF ₃ | -290 | 2110 | -2530 | 2290 | 5.42 | 37 |

TABLE IV. Dependence of mean error σ on fitting method. σ in cm^{-1} .

| Crystal | All levels | By μ | By term |
|--------------------------|------------|----------|---------|
| 1% Gd:LaBr ₃ | 3.50 | 3.35 | 3.03 |
| c_c improvement | | 4.3% | 13.4% |
| 5% Gd:LaCl ₃ | 2.48 | | 2.28 |
| c_c improvement | | | 8.1% |
| GdCl ₃ | 3.24 | | 2.69 |
| c_c improvement | | | 17% |
| 2% Gd:Y(OH) ₃ | 3.27 | 3.05 | 2.65 |
| c_c improvement | | 6.7% | 19% |
| Gd(OH) ₃ | 3.53 | | 3.26 |
| c_c improvement | | | 7.7% |
| 0.2% Gd:LaF ₃ | 5.08 | 5.45 | 4.47 |
| c_c improvement | | (-7.2%) | 12% |

This all-level σ is slightly smaller than the value in Table II because it was computed allowing only the B_k^q to vary with all free-ion-level parameters fixed. This means that all mean errors entered in Table IV are calculated by the same method and are directly comparable.

Gd:LaF₃ shows no improvement attributable to the molecular-orbital fit. The mean error actually increases because the number of levels entering into each fit (and hence the number of degrees of freedom) is reduced in the μ -fit case, whereas the actual calculated errors remain the same or decrease only slightly. This result is not at all surprising. From the relatively small nephelauxetic depression, we predict slight or negligible overlap of central-ion and ligand wave functions. Hence ligand wave functions will have little or no effect on the crystal energy levels. Free-ion-level depressions lead us to expect that molecular-orbital effects will be more important in Gd:LaBr₃ and still more important in Gd:Y(OH)₃. The results of crystal-quantum-number fits in Table IV bear out these predictions.

This result is also consistent with qualitative notions of ligand size or spatial extent of ligand wave function. We would expect the ligands to increase in size as F⁻, Br⁻, and (OH)⁻. The relative increase of fitting improvement as wave-function overlap increases is evidence of a significant molecular-orbital effect in Gd:LaBr₃-type crystals and is a qualitative validation of the formal molecular-orbital formulation²³ as applied to rare-earth salts.

Separate crystal-field fits were also performed for Stark levels arising from different spectroscopic terms in each crystal. Fitting procedure, fixed and variable parameters, and weighted averaging methods were identical to those discussed for the molecular-orbital fits. Improvement of the term fit over the all-level fit is evidence for nonlinear shielding and/or configuration-interaction wave-function distortion in an unknown ratio. Results of the term-fitting procedure are shown in Table V, where σ and σ' refer to mean errors with all-level and term-only crystal-field parameters, respectively. This improvement is consistent with related earlier results.²⁶

Comparative fitting improvement is evident in Table IV. Shielding and configuration-interaction effects together are clearly more important than molecular-orbital effects. There is no obvious relation between term-fitting improvement and crystal structure, wave-function overlap, free-ion-level depression, or any other distinctive crystal characteristic. It is therefore possible to associate an average fitting improvement of about 13% with recognition that nonlinear shielding and/or term-dependent configuration-interaction effects affect and modify the free-ion wave function in a crystalline environment. A somewhat lesser improvement is associated with a consideration of molecular-orbital effects involving the host lattice.

TABLE V. Reduction in mean error by separate fits to spectroscopic terms. All values in cm^{-1} .

| | 1% Gd:LaBr ₃ | 5% Gd:LaCl ₃ | GdCl ₃ |
|-----------|--------------------------|-------------------------|--------------------------|
| σ | 3.69 | 2.77 | 3.48 |
| σ' | 3.00 | 2.31 | 2.43 |
| 6P | $B_2^0(U)$ | -302 | -312 |
| | $B_2^2(U)$ | -310 | -566 |
| | $B_4^0(U)$ | 873 | 1250 |
| | $B_4^2(U)$ | -1530 | -1650 |
| 6I | σ | 3.42 | 2.91 |
| | σ' | 3.24 | 2.60 |
| | $B_2^0(U)$ | -268 | -292 |
| | $B_2^2(U)$ | -369 | -509 |
| 6D | $B_4^0(U)$ | 1100 | 1110 |
| | $B_4^2(U)$ | -1220 | -1300 |
| | σ | 4.83 | 3.73 |
| | σ' | 2.37 | 2.91 |
| 6D | $B_2^0(U)$ | -448 | -438 |
| | $B_2^2(U)$ | -345 | -341 |
| | $B_4^0(U)$ | -141 | 1730 |
| | $B_4^2(U)$ | -2120 | -2470 |
| | 2% Gd:Y(OH) ₃ | Gd(OH) ₃ | 0.2% Gd:LaF ₃ |
| σ | 3.72 | 3.80 | 5.87 |
| σ' | 0.49 | 2.71 | 3.11 |
| 6P | $B_2^0(U)$ | -447 | -257 |
| | $B_2^2(U)$ | -186 | 3280 |
| | $B_4^0(U)^a$ | 727 | -2530 |
| | $B_4^2(U)^a$ | -1740 | 2290 |
| 6I | σ | 3.35 | 5.06 |
| | σ' | 2.93 | 4.79 |
| | $B_2^0(U)$ | -699 | -452 |
| | $B_2^2(U)$ | -639 | 2000 |
| 6D | $B_4^0(U)$ | 1030 | -2850 |
| | $B_4^2(U)$ | -1550 | 2410 |
| | σ | 4.55 | |
| | σ' | 4.33 | |
| | $B_2^0(U)$ | -544 | |
| | $B_2^2(U)$ | -511 | |
| | $B_4^0(U)$ | 982 | |
| | $B_4^2(U)$ | -1930 | |

^a Not allowed to vary.

E. Conclusions

For Gd^{3+} , nonelectrostatic crystal-field effects make significant contributions to the ion energy levels in crystal hosts.

Empirical corrections that are expressed as separate sets of crystal-field parameters for energy levels belonging to a given irreducible representation (crystal quantum number) account for the covalency-induced molecular-orbital effect. For a given crystal structure, the molecular-orbital interaction correlates in direct proportion with nephelauxetic energy-level depression and with crystal-field splitting. This is reasonable because both effects result from overlap between ion and ligand wave functions. The molecular-orbital effect does not correlate with crystal-field splitting for different host structures.

Empirical corrections expressed by separate fits to each spectroscopic term are indications of nonlinear shielding and/or configuration interaction. No correlation between energy-level fit and crystal-host characteristics is evident from a study of Table III. Analyses with an improved semiempirical hamiltonian^{13,14,24} to reduce configuration interaction effects in the wave functions used to evaluate the $L'^{(4)}$ matrix elements may help isolate configuration-interaction effects from residual nonlinear shielding.

REFERENCES

- * Work supported in part by the U. S. Atomic Energy Commission.
 † Work done while the author was with Department of Physics, The John Hopkins University, Baltimore, Md. 21218.
¹ G. Racah, *Phys. Rev.* **63**, 367 (1943).
² W. A. Runciman, *J. Chem. Phys.* **36**, 1481 (1962).
³ R. L. Schwiesow and H. M. Crosswhite, *J. Opt. Soc. Am.* **59**, 592 (1969).

- ⁴ R. L. Schwiesow and H. M. Crosswhite, *J. Opt. Soc. Am.* **59**, 602 (1969).
⁵ W. H. Zachariasen, *Acta Cryst.* **1**, 265 (1948).
⁶ D. H. Templeton and C. H. Dauben, *J. Am. Chem. Soc.* **76**, 5237 (1954).
⁷ K. Schubert and A. Seitz, *Z. Anorg. Allgem. Chem.* **254**, 116 (1947); R. Fricke and W. Dürbacher, *Z. Anorg. Allgem. Chem.* **259**, 305 (1949).
⁸ R. Fricke and A. Seitz, *Z. Anorg. Allgem. Chem.* **254**, 107 (1947).
⁹ R. W. G. Wyckoff, *Crystal Structures*, Vol. 2, 2nd ed. (Wiley-Interscience, New York, 1964), pp. 60ff and 77ff; J. D. H. Donnay and G. Donnay, *Crystal Data*, 2nd ed. (American Crystallographic Association, New York, 1963); I. Oftedal, *Z. Physik. Chem.* **5B**, 272 (1929); K. Schlyter, *Arkiv Kemi* **5**, 73 (1952).
¹⁰ R. P. Bauman and S. P. S. Porto, *Phys. Rev.* **101**, 842 (1967); G. E. Stedman and D. J. Newman, *J. Phys. Chem. Solids* **32**, 109 (1971).
¹¹ G. Racah, *Phys. Rev.* **76**, 1352 (1949).
¹² K. Rajnak and B. G. Wybourne, *Phys. Rev.* **132**, 280 (1963).
¹³ B. R. Judd, H. M. Crosswhite, and H. Crosswhite, *Phys. Rev.* **169**, 130 (1968); H. Crosswhite, H. M. Crosswhite, and B. R. Judd, *Phys. Rev.* **174**, 89 (1968).
¹⁴ H. M. Crosswhite, R. L. Schwiesow, and W. T. Carnall, *J. Chem. Phys.* **50**, 5032 (1969).
¹⁵ G. Racah, *Phys. Rev.* **62**, 438 (1942).
¹⁶ B. R. Judd, *Operator Techniques in Atomic Spectroscopy* (McGraw-Hill, New York, 1963), pp. 42 and 72.
¹⁷ C. W. Nielson and G. F. Koster, *Spectroscopic Coefficients for the p^n , d^n and f^n Configurations* (MIT Press, Cambridge, Mass., 1963).
¹⁸ M. Rotenberg, R. Bivins, N. Metropolis, and J. K. Wooten, Jr., *The 3-j and 6-j Symbols* (MIT Press, Cambridge, Mass., 1959).
¹⁹ A. J. Freeman and R. E. Watson, *Phys. Rev.* **133**, A1571 (1964); **139**, A1606 (1965).
²⁰ B. G. Wybourne, *Spectroscopic Properties of Rare Earths* (Wiley-Interscience, New York, 1965), p. 215.
²¹ M. T. Hutchings and D. E. Ray, *Proc. Phys. Soc. (London)* **81**, 663 (1963).
²² C. K. Jorgensen, *Orbitals in Atoms and Molecules* (Academic, New York, 1962).
²³ H. S. Jarrett, *J. Chem. Phys.* **31**, 1579 (1959).
²⁴ D. J. Newman, *Advan. Phys.* **20**, 197 (1971).
²⁵ D. A. Wensky and W. G. Moulton, *J. Chem. Phys.* **53**, 3957 (1970).
²⁶ J. C. Eisenstein, *J. Chem. Phys.* **39**, 2128 (1963).

AUTHOR INDEX

- Abshire, N. L. (with Schwiesow), *Relative raman cross section of O_3 for four Ar^+ laser frequencies*, 42-44.
- Atlas, D. (with Gossard and Richter), *Reply*, 110-112.
- Barrick, D. E., *Demonstration of distortion in envelope detection of SSB Signals*, 467-469.
- Barrick, D. E., *First-order theory and analysis of MF/HF/VHF scatter from the sea*, 120-129.
- Barrick, D. E., *FM/CW radar signals and digital processing*, 469.
- Barrick, D. E., *The use of skywave radar for remote sensing of sea states*, 129-134.
- Barrick, D. E. (with Westwater), *Interpretation and application of second-order HF sea-echo doppler spectrum*, 134-141.
- Barrick, D. E. (with Headrick and Snider), *Some features of sea echo at HF (U)*, 154-167.
- Bean, B. R. (with Frisch, McAllister, and Pollard), *Planetary boundary-layer turbulence studies from acoustic echo sounder and in-situ measurements*, 299-325.
- Bedard, A. J., Jr., *The design of a temperature-independent DC flow resistor*, 470-490.
- Beran, D. W. (with Clifford), *Acoustic doppler measurements of the total wind vector*, 44-54.
- Beran, D. W. (with Hooke and Clifford), *Acoustic echo-sounding techniques and their application to gravity-wave, turbulence, and stability studies*, 54-75.
- Beran, D. W. (with Hooke and Young), *Atmospheric waves observed in the planetary boundary layer using an acoustic sounder and a microbarograph array*, 336-346.
- Beran, D. W. (with Hall, Wescott, and Neff), *Application of an acoustic sounder to air pollution monitoring*, 75-82.
- Brown, E. H. (with Clifford), *Amplitude spectra of acoustic pulses in the ocean*, 1-5.

- Brown, E. H. (with Clifford), *Spectral broadening of an acoustic pulse propagating through turbulence*, 5-9.
- Calfee, R. F. (with Schwiesow), *Nu-averaged infrared absorption coefficients of water vapor*, 41.
- Chadwick, R. B. (with Cooper), *Measurement of distributed targets with the random signal radar*, 141-149.
- Chadwick, R. B. (with Little), *The comparison of sensitivities of atmospheric echo-sounders*, 325-336.
- Clifford, S. F. (with Beran), *Acoustic doppler measurements of the total wind vector*, 44-54.
- Clifford, S. F. (with Brown), *Amplitude spectra of acoustic pulses in the ocean*, 1-5.
- Clifford, S. F. (with Brown), *Spectral broadening of an acoustic pulse propagating through turbulence*, 5-9.
- Clifford, S. F. (with Georges), *Acoustic sounding in a refracting atmosphere*, 32-41.
- Clifford, S. F. (with Beran and Hooke), *Acoustic echo-sounding techniques and their application to gravity-wave, turbulence, and stability studies*, 54-75.
- Clifford, S. F. (with Lawrence and Ochs), *Use of scintillations to measure average wind across a light beam*, 267-272.
- Clifford, S. F. (with Ochs and Wang), *A feasibility study of an optical crosswind monitor*, 276.
- Cohen, A., *The size spectrum determination of spherical aerosols by light scattering. Part 1: Method*, 231-238.
- Cohen, A. (with Westwater), *Application of Backus-Gilbert inversion technique to determination of aerosol size distributions from optical scattering measurements*, 290-299.
- Cohen, A. (with Derr, McNice, and Cupp), *Measurement of mie scattering intensities from monodispersed spherical particles as a function of wavelength*, 238-242.
- Cook, J. C. (with Goforth and Cook), *Seismic and underwater responses to sonic boom*, 9-20.

- Cooper, G.R. (with Chadwick), *Measurement of distributed targets with the random signal radar*, 141-149.
- Cupp, R.E. (with Strauch and Derr), *Atmospheric water vapor measurement by raman lidar*, 282-290.
- Cupp, R.E. (with Cohen, Derr, and McNice), *Measurement of mie scattering intensities from monodispersed spherical particles as a function of wavelength*, 238-242.
- Decker, M.T. (with Guiraud and Westwater), *Correction of electrical path length by passive microwave radiometry*, 149-154.
- Derr, V.E., *Research problems in the use of lidar in anti-pollution studies*, 242-254.
- Derr, V.E. (with Strauch and Cupp), *Atmospheric water vapor measurement by raman lidar*, 282-290.
- Derr, V.E. (with Cohen, McNice, and Cupp), *Measurement of mie scattering intensities from monodispersed spherical particles as a function of wavelengths*, 238-242.
- Earnshaw, K.B. (with Hernandez), *Two-laser optical distance-measuring instrument that corrects for the atmospheric index of refraction*, 254-260.
- Earnshaw, K.B. (with Hernandez), *Field tests of a two-laser (4416A and 6328A) optical distance-measuring instrument correcting for the atmospheric index of refraction*, 262-267.
- Emmanuel, C.B. (with Mandics), *A feasibility study for the remote measurement of underwater currents using acoustic Doppler techniques*, 82.
- Frisch, A.S. (with Bean, McAllister, and Pollard), *Planetary boundary-layer turbulence studies from acoustic echo sounder and in-situ measurements*, 299-325.
- Georges, T.M., *Acoustic ray paths through a model vortex with a viscous core*, 20-24.
- Georges, T.M. *3D ray tracing for acoustic-gravity waves*, 24-32.
- Georges, T.M., *Infrasound from convective storms: examining the evidence*, 83-107.
- Georges, T.M., *Infrasound from severe storms*, 107-110.
- Georges, T.M. (with Clifford), *Acoustic sounding in a refracting atmosphere*, 32-41.

- Goforth, T. (with Cook and Cook), *Seismic and underwater responses to sonic boom*, 9-20.
- Gossard, E.E. (with Richter), *FM/CW radar studies of production of turbulent instability within thermally stable layers by internal waves*, 409-423.
- Gossard, E.E. (with Hooke and Hall), *Observed generation of an atmospheric gravity wave by shear instability in the mean flow of the planetary boundary layer*, 442-455.
- Gossard, E.E. (with Richter and Atlas), *Reply*, 110-112.
- Gossard, E.E. (with Richter and Jensen), *Effect of wind shear on atmospheric wave instabilities revealed by FM/CW radar observations*, 423-442.
- Guiraud, F.O. (with Decker and Westwater), *Correction of electrical path length by passive microwave radiometry*, 149-154.
- Hall, F.F., Jr., *New Heights for atmospheric optics*, 260-262.
- Hall, F.F., Jr. (with Hooke and Gossard), *Observed generation of an atmospheric gravity wave by shear instability in the mean flow of the planetary boundary layer*, 442-455.
- Hall, F.F., Jr. (with Beran, Wescott, and Neff), *Application of an acoustic sounder to air pollution monitoring*, 75-82.
- Hardy, K.R. (with Ottersten and Little), *Radar and sodar probing of waves and turbulence in statically stable clear-air layers*, 366-409.
- Headrick, J.M. (with Barrick and Snider), *Some features of sea echo at HF(U)*, 154-167.
- Hernandez, E.N., *Analysis of four optical distance measuring instrument configurations using electrooptical polarization modulators*, 490-494.
- Hernandez, E.N. (with Earnshaw), *Field tests of a two-laser (4416A and 6328A) optical distance-measuring instrument correcting for the atmospheric index of refraction*, 262-267.
- Hernandez, E.N. (with Earnshaw), *Two-laser optical distance-measuring instrument that corrects for the atmospheric index of refraction*, 254-260.
- Hooke, W.H. (with Beran and Clifford), *Acoustic echo-sounding techniques and their application to gravity-wave, turbulence, and stability studies*, 54-75.

- Hooke, W.H. (with Hall and Gossard), *Observed generation of an atmospheric gravity wave by shear instability in the mean flow of the planetary boundary layer*, 442-455.
- Hooke, W.H. (with Young and Beran), *Atmospheric waves observed in the planetary boundary using an acoustic sounder and a microbarograph array*, 336-346.
- Jensen, D.R. (with Gossard and Richter), *Effect of wind shear on atmospheric wave instabilities revealed by FM/CW radar observations*, 423-442.
- Klemperer, W.K., *Non-redundant phased-array radar*, 494-501.
- Lawrence, R.S. (with Ochs), *Temperature and C_n^2 profiles measured over land and ocean to 3 km above the surface*, 274.
- Lawrence, R.S. (with Ochs and Clifford), *Use of scintillations to measure average wind across a light beam*, 267-272.
- Little, C.G., *On the detectability of fog, cloud, rain and snow by acoustic echo-sounding methods*, 112-120.
- Little, C.G., *Remote sensing of the atmosphere*, 346-352.
- Little C.G., *Status of remote sensing of the troposphere*, 352-366.
- Little C.G. (with Chadwick), *The comparison of sensitivities of atmospheric echo-sounders*, 325-336.
- Little, C.G. (with Ottersten and Hardy), *Radar and sodar probing of waves and turbulence in statically stable clear-air layers*, 366-409.
- Mandics, P.A., *Generation and dissipation of microwave refractive-index fluctuations in the boundary layer*, 455-467.
- Mandics, P.A. (with Emmanuel), *A feasibility study for the remote measurement of underwater currents using acoustic Doppler techniques*, 82.
- McAllister, L.G. (with Bean, Frisch, and Pollard), *Planetary boundary-layer turbulence studies from acoustic echo sounder and in-situ measurements*, 299-325.
- McNice, G.T., *Raman spectroscopy with a tunable dye laser and a narrow-band filter*, 272-274.
- McNice, G.T. (with Cohen, Derr, and Cupp), *Measurement of mie scattering intensities from monodispersed spherical particles as a function of wavelength*, 238-242.

- Miller, L.J., *Dual-Doppler radar observations of circulation in snow conditions*, 167-173.
- Miller, S.F. (with Ochs), *Pattern velocity computers: Two types developed for wind velocity measurement by optical means*, 501-505.
- Miller, S.F. (with Ochs), *The NOAA optical system for measuring average wind*, 275.
- Neff, W.D. (with Beran, Hall, and Wescott), *Application of an acoustic sounder to air pollution monitoring*, 75-82.
- Ochs, G.R. (with Lawrence), *Temperature and C_n^2 profiles measured over land and ocean to 3 km above the surface*, 274.
- Ochs, G.R. (with Miller), *Pattern velocity computers: Two types developed for wind velocity measurement by optical means*, 501-505.
- Ochs, G.R. (with Miller), *The NOAA optical system for measuring average wind*, 275.
- Ochs, G.R. (with Clifford and Wang), *A feasibility study of an optical crosswind and monitor*, 276.
- Ochs, G.R. (with Lawrence and Clifford), *Use of scintillations to measure average wind across a light beam*, 267-272.
- Ottersten, H.K. (with Hardy and Little), *Radar and sodar probing of waves and turbulence in statically stable clear-air layers*, 366-409.
- Pollard, J.R. (with Bean, Frisch, and McAllister), *Planetary boundary-layer turbulence studies from acoustic echo sounder and in-situ measurements*, 299-325.
- Richter, J.H. (with Gossard), *FM/CW radar studies of production of turbulent instability within thermally stable layers by internal waves*, 409-423.
- Richter, J.H. (with Gossard and Atlas), *Reply*, 110-112.
- Richter, J.H. (with Gossard and Jensen), *Effect of wind shear on atmospheric wave instabilities revealed by FM/CW radar observations*, 423-442.
- Schwiesow, R.L., *An analytical representation for standards of spectral irradiance over the 300-1200 nm range*, 505-507.

- Schwiesow, R.L., *Departures from the electrostatic crystal-field model for Gd 3^+ in six hexagonal crystals*, 507-513.
- Schwiesow, R.L., *Optical measurement of capillary wave structure*, 277.
- Schwiesow, R.L., *Raman scattering from pollutant gases and air-water interfaces*, 278-282.
- Schwiesow, R.L. (with Abshire), *Relative raman cross section of O_3 for four Ar⁺ laser frequencies*, 42-44.
- Schwiesow, R.L. (with Calfee), *Nu-averaged infrared absorption coefficients of water vapor*, 41.
- Snider, J.B., *Ground-based sensing of temperature profiles from angular and multi-spectral microwave emission measurements*, 173-183.
- Snider, J.B., *Recent results in ground-based sensing of atmospheric temperature profiles*, 183-193.
- Snider, J.B. (with Headrick and Barrick), *Some features of sea echo at HF (U)*, 154-167.
- Strauch, R.G. (with Derr and Cupp), *Atmospheric water vapor measurement by raman lidar*, 282-290.
- Taylor, W.L., *An electromagnetic technique for tornado detection*, 193-195.
- Taylor, W.L., *Electromagnetic radiation from severe storms in Oklahoma during April 29-30, 1970*, 195-212.
- Taylor, W.L., *Evaluation of an electromagnetic tornado-detection technique*, 212-216.
- Wang, T. (with Clifford and Ochs), *A feasibility study of an optical crosswind monitor*, 276.
- Wescott, J.W. (with Beran, Hall, and Neff), *Application of an acoustic sounder to air pollution monitoring*, 75-82.
- Westwater, E.R., *Ground-based determination of low altitude temperature profiles by microwaves*, 216-230.
- Westwater, E.R., *Microwave emission from clouds*, 230.
- Westwater, E.R. (with Barrick), *Interpretation and application of second-order HF sea-echo doppler spectrum*, 134-141.

- Westwater , E.R. (with Cohen), *Application of Backus-Gilbert inversion technique to determination of aerosol size distributions from optical scattering measurements*, 290-299.
- Westwater, E.R. (with Decker and Guiraud), *Correction of electrical path length by passive microwave radiometry*, 149-154.
- Young, D.W. (with Hooke and Beran), *Atmospheric waves observed in the planetary boundary layer using an acoustic sounder and a microbarograph array*, 336-346.

References for Further Reading

Book: Derr, V. E., Editor, Remote Sensing of the Troposphere, Government Printing Office, Catalogue No. C55.602:T75, Stock No. 0323-0011. (\$9.00)

Guiraud, F. O., M. T. Decker, and E. R. Westwater, Experimental Investigation of the Correction of Electrical Range Errors by Passive Microwave Radiometry, *NOAA Technical Report ERL 221-WPL 19*, 90 pages, December 1971.

Hall, F. F., and C. M. Giorgi, Methodology Study Infrared-Optical Propagation Investigation, Final Report, *U.S. Army EPG-FR-735*, March 1972.

Lawrence, R. S., Irradiance Fluctuations in Optical Transmission through the Atmosphere, *Journal of the Optical Society of America* 62, p. 701, 1972.

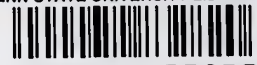
Lawrence, R. S., The Effects of the Clear, Turbulent Atmosphere on Laser Beams, *Sixth Instrumentation Symposium of the Albuquerque Section of the Instrument Society of America*, 23 pp, April 1972.

R. L. Schwiesow, and N. L. Abshire, Raman Spectroscopy in the Atmosphere and Oceans, *RAMAN Newsletter* 43, p. 12, July 1972.

Emmanuel, C. B., and P. A. Mandics, Feasibility of Remote Underwater Current Measurement Using Acoustic Doppler Technique, *Proceedings of Ocean '73*, IEEE International Conference on Engineering in the Oceanic Environment, published by the Institute of Electrical and Electronic Engineers, Inc., New York, pp. 59-63 (IEE Pub. No. 73 CHO 774-00CC), 1973.



PENN STATE UNIVERSITY LIBRARIES



A000072832820